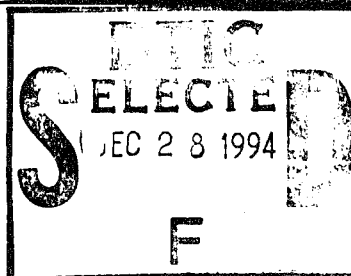


# Electronic Properties of Two-Dimensional Systems



Proceedings of the  
10th International Conference on  
Electronic Properties of Two-Dimensional Systems

Newport, RI, USA, 31 May – 4 June 1993

Edited by  
B. McCombe  
A. Nurmikko

This document has been approved  
for public release and sale; its  
distribution is unlimited.

19941223 131

North-Holland

## Electronic Properties of Two-Dimensional Systems



# EP2DS-10

# Proceedings of the 10th International Conference on Electronic Properties of Two-Dimensional Systems

Newport, RI, USA  
31 May – 4 June 1993

*Guest Editors:*

B. McCombe  
*University at Buffalo, NY, USA*

A. Nurmikko  
*Brown University, Providence, RI, USA*

1	OF 481	<input checked="" type="checkbox"/>
2	1113	<input type="checkbox"/>
3	1113	<input type="checkbox"/>
4	1113	<input type="checkbox"/>
5	1113	<input type="checkbox"/>
6	1113	<input type="checkbox"/>
7	1113	<input type="checkbox"/>
8	1113	<input type="checkbox"/>
9	1113	<input type="checkbox"/>
10	1113	<input type="checkbox"/>
11	1113	<input type="checkbox"/>
12	1113	<input type="checkbox"/>
13	1113	<input type="checkbox"/>
14	1113	<input type="checkbox"/>
15	1113	<input type="checkbox"/>
16	1113	<input type="checkbox"/>
17	1113	<input type="checkbox"/>
18	1113	<input type="checkbox"/>
19	1113	<input type="checkbox"/>
20	1113	<input type="checkbox"/>
21	1113	<input type="checkbox"/>
22	1113	<input type="checkbox"/>
23	1113	<input type="checkbox"/>
24	1113	<input type="checkbox"/>
25	1113	<input type="checkbox"/>
26	1113	<input type="checkbox"/>
27	1113	<input type="checkbox"/>
28	1113	<input type="checkbox"/>
29	1113	<input type="checkbox"/>
30	1113	<input type="checkbox"/>
31	1113	<input type="checkbox"/>
32	1113	<input type="checkbox"/>
33	1113	<input type="checkbox"/>
34	1113	<input type="checkbox"/>
35	1113	<input type="checkbox"/>
36	1113	<input type="checkbox"/>
37	1113	<input type="checkbox"/>
38	1113	<input type="checkbox"/>
39	1113	<input type="checkbox"/>
40	1113	<input type="checkbox"/>
41	1113	<input type="checkbox"/>
42	1113	<input type="checkbox"/>
43	1113	<input type="checkbox"/>
44	1113	<input type="checkbox"/>
45	1113	<input type="checkbox"/>
46	1113	<input type="checkbox"/>
47	1113	<input type="checkbox"/>
48	1113	<input type="checkbox"/>
49	1113	<input type="checkbox"/>
50	1113	<input type="checkbox"/>
51	1113	<input type="checkbox"/>
52	1113	<input type="checkbox"/>
53	1113	<input type="checkbox"/>
54	1113	<input type="checkbox"/>
55	1113	<input type="checkbox"/>
56	1113	<input type="checkbox"/>
57	1113	<input type="checkbox"/>
58	1113	<input type="checkbox"/>
59	1113	<input type="checkbox"/>
60	1113	<input type="checkbox"/>
61	1113	<input type="checkbox"/>
62	1113	<input type="checkbox"/>
63	1113	<input type="checkbox"/>
64	1113	<input type="checkbox"/>
65	1113	<input type="checkbox"/>
66	1113	<input type="checkbox"/>
67	1113	<input type="checkbox"/>
68	1113	<input type="checkbox"/>
69	1113	<input type="checkbox"/>
70	1113	<input type="checkbox"/>
71	1113	<input type="checkbox"/>
72	1113	<input type="checkbox"/>
73	1113	<input type="checkbox"/>
74	1113	<input type="checkbox"/>
75	1113	<input type="checkbox"/>
76	1113	<input type="checkbox"/>
77	1113	<input type="checkbox"/>
78	1113	<input type="checkbox"/>
79	1113	<input type="checkbox"/>
80	1113	<input type="checkbox"/>
81	1113	<input type="checkbox"/>
82	1113	<input type="checkbox"/>
83	1113	<input type="checkbox"/>
84	1113	<input type="checkbox"/>
85	1113	<input type="checkbox"/>
86	1113	<input type="checkbox"/>
87	1113	<input type="checkbox"/>
88	1113	<input type="checkbox"/>
89	1113	<input type="checkbox"/>
90	1113	<input type="checkbox"/>
91	1113	<input type="checkbox"/>
92	1113	<input type="checkbox"/>
93	1113	<input type="checkbox"/>
94	1113	<input type="checkbox"/>
95	1113	<input type="checkbox"/>
96	1113	<input type="checkbox"/>
97	1113	<input type="checkbox"/>
98	1113	<input type="checkbox"/>
99	1113	<input type="checkbox"/>
100	1113	<input type="checkbox"/>



1994

ELSEVIER

AMSTERDAM-LONDON-NEW YORK-TOKYO

OTIC QUALITY INSPECTED

© 1994 Elsevier Science B.V. All rights reserved

*No part of this publication may be reproduced, stored in a retrieval system, or transmitted in any form or by any means, electronic, mechanical, photocopying, recording or otherwise, without the written permission of the Publisher, Elsevier Science B.V., Copyright & Permissions Department, P.O. Box 521, 1000 AM Amsterdam, The Netherlands.*

*Special regulations for readers in the USA: This publication has been registered with the Copyright Clearance Center Inc. (CCC), Salem, Massachusetts. Information can be obtained from the CCC about conditions under which photocopies of parts of this publication may be made in the USA.*

*All other copyright questions, including photocopying outside of the USA, should be referred to the Publisher.*

*No responsibility is assumed by the Publisher for any injury and / or damage to persons or property as a matter of products liability, negligence or otherwise, or from any use or operation of any methods, products, instructions or ideas contained in the material herein. Although all advertising material is expected to conform to ethical standards, inclusion in this publication does not constitute a guarantee or endorsement of the quality or value of such product or of the claims made of it by its manufacturer.*

*This volume is printed on acid-free paper.*

Reprinted from:  
SURFACE SCIENCE 305 (1994)

The Manuscripts for the Proceedings were  
received by the Publisher: 5 October 1993

PRINTED IN THE NETHERLANDS

their many contributions to the local arrangements and the smooth operation of the registration desk, and the staff at SUNY at Buffalo, Anna Isom and Cindy Nydahl, who handled abstracts, manuscripts and various mailings with efficiency. Numerous students and postdocs also provided valuable assistance at different stages of the process: at SUNY at Buffalo – J.L. Wang, L.P. Fu, S.R. Ryu, J. Kono, W.J. Li and his wife Spring, Z.X. Jiang and Y.J. Wang; at Brown University – M. Fritze, A. Krapivka, D. Some and W. Walecki. Finally, I thank my wife, Renée Bush, for her tolerance and understanding during the long hours and many mood swings accompanying my efforts as chairman of the organizing committee during the past year.

Bruce D. McCombe  
September 1993

## Preface

This volume contains 114 contributed and 13 invited manuscripts of papers presented at the Tenth International Conference on Electronic Properties of Two-Dimensional Systems (EP2DS-10), which was held in Newport, Rhode Island, 31 May–4 June, 1993. Over 250 scientists attended the conference, making it the largest in the series to date. 142 papers were presented at the conference, either orally or as posters. In order to maintain the small size and lively, informal atmosphere that has been traditional in this series, only about 40% of the submitted abstracts were accepted by the Program Committee as contributed papers. The selection process is difficult and fraught with potential for error, but I believe that the papers contained in these proceedings constitute a representative cross section of the recent work in this field, and contain among them some of the best recent work.

As has been the case in previous conferences the focus of EP2DS-10 was the fundamental physics and phenomena related to electronic excitations in systems exhibiting dimensionality less than three. In spite of the specificity and limited dimensionality of the conference title, a large fraction of the papers presented was concerned with dimensionality *less* than two, consistent with the trends of the past few conferences. Approximately 30% of the papers presented were concerned with electronic phenomena associated with one and zero dimensions, reflecting the general directions of this field. A large number of papers again were concerned with the quantum Hall effect, the fractional quantum Hall effect and the regime of electron densities, temperatures and magnetic fields associated with the Wigner crystal. A large fraction of the meeting was also devoted to quantum wires and dots and to mesoscopic phenomena, including chaotic motion of carriers in laterally patterned nanostructures. There was a special invited symposium featuring studies of few-electron transport in lateral nanostructures, and a focused session on low-dimensional organic crystals, a new topic for this series.

The conference would not have been possible without substantial sponsorship from government agencies. I am grateful to those agencies listed on the following page for their support, and particularly to Larry Cooper, Clive Perry and Michael Strosio. Additional support was provided by the Department of Physics at SUNY at Buffalo and the Center for Advanced Materials Research at Brown University.

No conference can take place without many hours of hard work by many people. I enjoyed working with the members of the organizing committee, and I thank them for their many contributions over the past (almost) two years in planning, organizing and executing this conference. The Program Committee, under the guidance of Emilio Mendez, had a particularly trying task in selecting a relatively small fraction of the more than 300 excellent abstracts received. I am grateful to the members of this committee for their long hours and conscientious efforts during this process. The International Advisory Committee made numerous suggestions for invited speakers and topics; many of these suggestions are reflected in the program. Local arrangements were handled expertly by Sue Masoian and her staff under the watchful eye of Arto Nurmikko. I am particularly grateful to Sue for the splendid arrangements for registration, housing, meals, reception and conference dinner at Salve Regina University and the conference excursion, as well as for her diplomatic dealings with a large number of scientists with their myriad of requests for both standard and special treatment. Thanks are also due to the staff at Brown University, Susan Whitney and Toni Barbosa, for

## Committees

### Organizing Committee

S. Das Sarma, Financial Aid  
B.D. McCombe, Chairman  
E. Mendez, Program  
A. Nurmikko, Finance and Local Arrangements  
A. Pinczuk  
M. Reed

### Program Committee

S.J. Allen, Jr.  
J. Eisenstein  
A. MacDonald  
E. Mendez, Chairman  
M. Reed  
L.J. Sham

### International Advisory Committee

G. Abstreiter (Garching)	T. Ando (Tokyo)
E. Andrei (New Brunswick)	G. Bauer (Linz)
A. Chaplik (Novosibirsk)	R. Clark (Kensington)
A. Dahm (Cleveland)	M. D'Iorio (Ottawa)
L. Eaves (Nottingham)	L. Esaki (Tsukuba)
E. Gornik (Garching)	P. Hawrylak (Ottawa)
O. Hipolito (Sao Carlos)	M. Kastner (Cambridge)
S. Kawaji (Tokyo)	F. Koch (Garching)
J.P. Kotthaus (München)	G. Landwehr (Würzburg)
J.C. Maan (Nijmegen)	R. Nicholas (Oxford)
M. Pepper (Cambridge)	J.J. Quinn (Knoxville)
M. Saitoh (Osaka)	B. Shanabrook (Washington)
F. Stern (Yorktown Heights)	P.J. Stiles (Providence)
H. Störmer (Murray Hill)	C. Tejedor (Madrid)
V.B. Timofeev (Chernogolovka)	D.C. Tsui (Princeton)
H. van Houten (Eindhoven)	K. von Klitzing (Stuttgart)
M. Voos (Paris)	F.I.B. Williams (Gif-sur-Yvette)
J.M. Worlock (Salt Lake City)	H.Z. Zheng (Beijing)

## Sponsors

### Federal

Army Research Office  
National Science Foundation  
Office of Naval Research

### Other

Department of Physics and Astronomy, SUNY at Buffalo  
Center for Advanced Materials Research, Brown University

Ultrasonic approach to the integer and fractional quantum Hall effect A. Esslinger, R.W. Winkler, C. Rocke, A. Wixforth, J.P. Kotthaus, H. Nickel, W. Schlapp and R. Lösch	83
Phonon measurements of the energy gap in the fractional quantum Hall state R.H. Eyles, C.J. Mellor, A.J. Kent, K.A. Benedict, L.J. Challis, S. Kravchenko, N.N. Zinov'ev and M. Henini	87
Thermoelectric properties of GaAs/Ga <sub>1-x</sub> Al <sub>x</sub> As heterojunctions in the fractional quantum Hall regime U. Zeitler, R. Fletcher, J.C. Maan, C.T. Foxon, J.J. Harris and P. Wyder	91
Wigner solid in two-dimensional electron system in silicon in the extreme quantum limit? V.T. Dolgoplov, G.V. Kravchenko, S.V. Kravchenko and A.A. Shashkin	96
High temperature perturbation study of two-dimensional interacting electrons in a partly-filled Landau level L. Zheng and A.H. MacDonald	101
<b>Quantum Hall effect – phase diagram</b>	
Termination of the quantized Hall effect by the electron solid V.M. Pudalov, M. D'Iorio and J.W. Campbell	107
Collective insulating state at zero magnetic field in a dilute 2D electron system M. D'Iorio, V.M. Pudalov, S.V. Kravchenko and J.W. Campbell	115
Magnetic-field-induced transition from an Anderson insulator to a quantum Hall conductor H.W. Jiang, I. Glozman, C.E. Johnson and S.T. Hannahs	120
Observation of finite-frequency scaling in the integer quantum Hall effect L.W. Engel, D. Shahar, Ç. Kurdak and D.C. Tsui	124
Quantum Hall liquid–Wigner solid phase boundary R. Price, P.M. Platzman, S. He and X. Zhu	126
<b>Integer quantum Hall effect and edge channels</b>	
Transport properties between quantum Hall plateaus D.B. Chklovskii and P.A. Lee	133
Direct determination of the density of states in two-dimensional systems by magnetocapacitances of biased double barrier structures A. Song, H. Zheng, F. Yang and Y. Li	139
Transitions between edge and bulk channels in the quantum Hall regime C.A. Richter, R.G. Wheeler and R.N. Sacks	145
Conductivity peaks in the quantum Hall regime: broadening with temperature, current, and frequency D.G. Polyakov and B.I. Shklovskii	151
“Intrinsic” quantum Hall effect in InAs/Ga <sub>1-x</sub> In <sub>x</sub> Sb crossed gap heterostructures in high magnetic fields K.S.H. Dalton, M. van der Burgt, M. Lakrimi, R.J. Warburton, M.S. Daly, W. Lubczyński, R.W. Martin, D.M. Symons, D.J. Barnes, N. Miura, R.J. Nicholas, N.J. Mason and P.J. Walker	156
Magnetic field dependence of the device-width-dependent breakdown current in the quantum Hall effect S. Kawaji, K. Hirakawa, M. Nagata, T. Okamoto, T. Fukase and T. Goto	161
Effects of electron–electron interactions on the ground state of quantum Hall edge states B.Y. Gelfand, J. Dempsey and B.I. Halperin	166
Total suppression of the inter-edge-channel scattering in a GaAs/AlGaAs heterostructure R.J.F. van Haren, F.A.P. Blom, W. de Lange and J.H. Wolter	172
Junctions between coplanar 2D gases: a probe of boundary effects in the quantized Hall regime B.E. Kane, L.N. Pfeiffer and K.W. West	176

# Contents

Preface	vii
Committees and sponsors	ix
 <b>Quantum Hall effect – even fractions</b>	
Theories for $\nu = 1/2$ in single- and double-layer systems B.I. Halperin	1
New collective quantum Hall states in double quantum wells G.S. Boebinger, S.Q. Murphy, J.P. Eisenstein, L.N. Pfeiffer, K.W. West and S. He	8
One-component to two-component transitions of fractional quantum Hall states in a wide quantum well Y.W. Suen, H.C. Manoharan, X. Ying, M.B. Santos and M. Shayegan	13
Experimental evidence for composite particles in the fractional quantum Hall effect R.R. Du, D.C. Tsui, H.L. Stormer, L.N. Pfeiffer and K.W. West	18
 <b>Fractional quantum Hall effect and Wigner lattice – optical studies</b>	
Occurrence of a bulk-like electron phase in the cyclotron resonance of GaAs inversion channels in the extreme quantum limit C.M. Engelhardt, E. Gornik, M. Besson, G. Böhm and G. Weimann	23
Cyclotron resonance to 100 mK of a GaAs heterojunction in the ultra-quantum limit J.G. Michels, S. Hill, R.J. Warburton, G.M. Summers, P. Gee, J. Singleton, R.J. Nicholas, C.T. Foxon and J.J. Harris	33
Time-resolved magneto-photoluminescence measurements of the integer QHE, fractional QHE and extreme quantum limit S.A. Brown, A.G. Davies, A.C. Lindsay, R.B. Dunford, R.G. Clark, P.E. Simmonds, H.H. Voss, J.J. Harris and C.T. Foxon	42
Time-resolved photoluminescence in the fractional quantum Hall regime D. Heiman, A. Pinczuk, M. Dahl, B.S. Dennis, L.N. Pfeiffer and K.W. West	50
Time-resolved magnetoluminescence and Raman scattering measured in the regime of the fractional quantum Hall effect and of the Wigner solid I.V. Kukushkin, R.J. Haug, K. von Klitzing, K. Eberl and K. Ploog	55
Quasi-particle recombination and spatial ordering of 2D electrons in the extreme quantum limit I.N. Harris, H.D.M. Davies, R.A. Ford, J.F. Ryan, A.J. Turberfield, C.T. Foxon and J.J. Harris	61
Photoluminescence and the Wigner crystal: can you see it? H.A. Fertig, D.Z. Liu and S. Das Sarma	67
Numerical studies of the photoluminescence spectrum of quantum Hall systems X.M. Chen and J.J. Quinn	71
 <b>Fractional quantum Hall effect and Wigner lattice – DC and dynamical conductivity studies</b>	
Surface acoustic wave studies of electron correlations in the 2DES R.L. Willett	76

**Organic conductors**

- Magnetic ordering and Fermi surface effects in the low-dimensional organic conductor  $\alpha$ -(BEDT-TTF)<sub>2</sub>RbHg(SCN)<sub>4</sub>  
S.J. Klepper, J.S. Brooks, G.J. Athas, X. Chen, M. Tokumoto, N. Kinoshita and Y. Tanaka 181
- The influence of magnetic order in quasi-2D organic conductors  
M. Doporto, J. Caulfield, S. Hill, J. Singleton, F.L. Pratt, M. Kurmoo, P.J.T. Hendriks, J.A.A.J. Perenboom, W. Hayes and P. Day 187

**Heterostructures, quantum wells and superlattices – energy states and optical properties**

- Electronic excitations in parabolically confined electron systems  
A. Wixforth 194
- Transition from 2D to 3D collective response: surface sensitivity  
E.L. Yuh and E.G. Gwinn 202
- Resonant inelastic light scattering in remotely doped wide parabolic GaAs/Al<sub>x</sub>Ga<sub>1-x</sub>As quantum wells in a magnetic field  
J.H. Burnett, H.M. Cheong, R.M. Westervelt, W. Paul, P.F. Hopkins, M. Sundaram and A.C. Gossard 208
- Spectroscopy of quasi-2D D<sup>-</sup> ions in the presence of excess electrons  
W.J. Li, J.L. Wang, B.D. McCombe, J.-P. Cheng and W. Schaff 215
- Transition energies of D<sup>-</sup> centers in a superlattice  
J.M. Shi, F.M. Peeters and J.T. Devreese 220
- Negatively charged excitons X<sup>-</sup> in the electron gas in CdTe/Cd<sub>1-x</sub>Zn<sub>x</sub>Te quantum wells  
K. Kheng, R.T. Cox, Y. Merle d'Aubigné, M. Mamor, N. Magnea, H. Mariette, K. Saminadayar and S. Tatarenko 225
- Exciton-capture mechanism at impurities in GaAs/Al<sub>x</sub>Ga<sub>(1-x)</sub>As quantum wells  
C.I. Harris, B. Monemar, P.O. Holtz, H. Kalt, M. Sundaram, J.L. Merz and A.C. Gossard 230
- Time-resolved four wave mixing studies of a two-dimensional electron gas in a magnetic field  
S. Bar-Ad, I. Bar-Joseph, Y. Levinson and H. Shtrikman 234
- Femtosecond studies of excitonic optical non-linearities in GaAs/Al<sub>x</sub>Ga<sub>1-x</sub>As multiple quantum wells under in-plane uniaxial strain  
M. Wraback, H. Shen, J. Pamulapati, M. Dutta, P.G. Newman, M. Taysing-Lara and Y. Lu 238
- Terahertz electromagnetic transients as probes of a two-dimensional electron gas  
W.J. Walecki, D. Some, V.G. Kozlov and A.V. Nurmikko 243
- Raman scattering on modulation-doped quantum wells: intrinsic spin splitting of the GaAs conduction band  
B. Jusserand, D. Richards, H. Peric and B. Etienne 247
- Optical measurements of warped valence bands in quantum wells  
J.A. Kash, M. Zachau, M.A. Tischler and U. Ekenberg 251
- Exciton spin dynamics and polarized luminescence in quantum wells  
M.Z. Maialle and L.J. Sham 256
- Hole spin relaxation in a n-doped quantum well structure  
Ph. Roussignol, R. Ferreira, C. Delalande, G. Bastard, A. Vinattieri, J. Martinez-Pastor, L. Carraresi, M. Colocci, J.F. Palmier and B. Etienne 263
- Plasmons localized at point charges in semiconductor quantum wells  
S. Rudin and T.L. Reinecke 267
- Spin-resolved cyclotron resonance in a 2D electron gas  
M.J. Yang, R.J. Wagner, P.J. Lin-Chung, B.V. Shanabrook, J.R. Waterman, W.J. Moore and J.L. Davis 271
- Cyclotron effective mass of holes in strained Si<sub>1-x</sub>Ge<sub>x</sub>/Si quantum well structures  
J.-P. Cheng, V.P. Kesan, D.A. Grützmacher and T.O. Sedgwick 275



Far infrared emission from magnetically quantised 2DEGs in GaAs/(AlGa)As heretojunctions N.N. Zinov'ev, R. Fletcher, L.J. Challis, B. Sujak-Cyrul, A.V. Akimov and A.F. Jezierski	280
Reflectivity, transport and magneto-optical studies of holes in the p-type HgZnTe/CdTe superlattice J.B. Choi, J.R. Meyer, C.A. Hoffman, G. Karczewski, J.K. Furdyna, K.H. Yoo and J.P. Faurie	285
Crossing of cyclotron and spin resonances in a 2D electron gas V.I. Fal'ko	290
Multicomponent envelope function problems: the ultimate concept R. Winkler and U. Rössler	295
<b>Heterostructures, quantum wells and superlattices – transport</b>	
2DEG in strained Si/SiGe heterostructures F.F. Fang	301
Valence band Landau level mixing and anisotropy in $\text{Si}_{1-x}\text{Ge}_x$ investigated by resonant magnetotunneling A. Zaslavsky, D.A. Grützmacher, S.Y. Lin, T.P. Smith III and T.O. Sedgwick	307
Effect of electronic-state modulation on mobility in quantum wells T. Tsuchiya and T. Ando	312
Wave function modification via controlled potential perturbation K. Ensslin, H. Baum, P.F. Hopkins and A.C. Gossard	317
Non-uniform resonant coupling effect on 2D electron transport in $\delta$ -doped double quantum well structures Y. Ohno, M. Tsuchiya, T. Matsusue, T. Noda and H. Sakaki	322
Disappearance of magnetophonon resonance at high magnetic fields in GaAs/GaAlAs heterojunctions D.R. Leadley, R.J. Nicholas, J. Singleton, W. Xu, F.M. Peeters, J.T. Devreese, L. van Bockstal, F. Herlach, J.A.A.J. Perenboom, J.J. Harris and C.T. Foxon	327
Current induced “spin” separation in p-doped asymmetric double quantum wells G. Goldoni and A. Fasolino	333
Quantum transport in $\text{InAs}_{1-x}\text{Sb}_x/\text{InSb}$ strained layer superlattices T. Le, A.G. Norman, W.T. Yuen, L. Hart, I.T. Ferguson, J.J. Harris, C.C. Phillips and R.A. Stradling	337
Crossover from a two- to three-dimensional electronic structure in Si spike doped GaAs superlattices A.B. Henriques and L.C.D. Gonçalves	343
Transverse magnetic focusing and the dispersion of GaAs 2D holes at (311)A heterojunctions J.J. Heremans, M.B. Santos and M. Shayegan	348
<b>Resonant tunneling in quasi-2D systems</b>	
Intrinsic bistability in the electroluminescence spectrum and current–voltage characteristics of triple-barrier p–i–n resonant tunneling devices P.A. Harrison, L. Eaves, P.M. Martin, M. Henini, P.D. Buckle, M.S. Skolnick, D.M. Whittaker and G. Hill	353
Excitonic correction to resonant tunneling G.E.W. Bauer	358
Electron confinement in variable-area resonant tunnelling diodes using in-plane implanted gates C.J. Goodings, H. Mizuta, J.R.A. Cleaver and H. Ahmed	363
Electron transport via resonantly coupled energy levels in triple barrier structure investigated by magnetotunneling spectroscopy H. Kurata and H. Sakaki	369
Optical spectroscopy of inverted electron populations in double-barrier resonant-tunnelling structures J.W. Cockburn, R.J. Teissier, M.S. Skolnick, P.D. Buckle, D.M. Whittaker, A.R.K. Willcox, G.W. Smith, G. Hill and M.A. Pate	375

Resonant inter-Landau-level tunneling of electrons and holes in superlattices W. Müller, H.T. Grahn, K. von Klitzing and K. Ploog	380
Superlattice transport in intense terahertz electric fields B.J. Keay, P.S.S. Guimaraes, J.P. Kaminski, S.J. Allen, Jr., P.F. Hopkins, A.C. Gossard, L.T. Florez and J.P. Harbison	385
Terahertz response of resonant tunneling diodes J.S. Scott, J.P. Kaminski, S.J. Allen, D.H. Chow, M. Lui and T.Y. Liu	389
<b>Electron interactions in coupled quasi-2D layers</b>	
Tunneling between highly correlated 2D electron systems J.P. Eisenstein, L.N. Pfeiffer and K.W. West	393
One-electron Green's function and electron tunneling in a two-dimensional electron system in a strong magnetic field S. He, P.M. Platzman and B.I. Halperin	398
Coupled electron-hole transport: generalized random-phase approximation and density functional theory H.C. Tso, P. Vasilopoulos and F.M. Peeters	400
Observation of an abrupt double-to-single-layer transition in a double-quantum-well structure Y. Katayama, D.C. Tsui, H.C. Manoharan and M. Shayegan	405
<b>Effects of lateral potentials on quasi-2D electrons</b>	
Magnetotransport in antidot arrays D. Weiss, K. Richter, E. Vasiliadou and G. Lütjering	408
Scattering of ballistic electrons by magnetic flux tubes A.K. Geim, S.J. Bending and I.V. Grigorieva	419
Resistivity and Hall resistance of a two-dimensional electron gas in the presence of magnetic flux tubes L. Brey and H.A. Fertig	424
Electronic states and collective excitations of a two-dimensional electron gas in spatially modulated magnetic fields X. Wu and S.E. Ulloa	428
Two-dimensional tunneling through magnetic barriers A. Matulis, F.M. Peeters and P. Vasilopoulos	434
Influence of a periodic potential on the integer quantum Hall effect B. Huckestein and R.N. Bhatt	438
Negative magnetoresistance and anomalous diffusion of two-dimensional electrons in a disordered array of antidots G.M. Gusev, P. Basmaji, Z.D. Kvon, L.V. Litvin, Yu.V. Nastaushev and A.I. Toropov	443
<b>Contacts and ballistic transport</b>	
Anti-collimation of ballistic electrons by a potential barrier P.T. Coleridge, R.P. Taylor, A.S. Sachrajda and J.A. Adams	448
Charge oscillations in edge states and double-frequency Aharonov-Bohm effects around a tunable obstacle P.J. Simpson, C.J.B. Ford, D.R. Mace, I. Zailer, M. Yosefin, M. Pepper, J.T. Nicholls, D.A. Ritchie, J.E.F. Frost, M.P. Grimshaw and G.A.C. Jones	453
Control of ballistic electrons in (AlGa)As/GaAs heterostructures by means of superconducting niobium gate structures T. Schäpers, F. Müller, A. Förster, B. Lengeler and H. Lüth	460

Metal/2DEG contact – a microscopic model Y.B. Levinson	465
Superconductors coupled with a two-dimensional electron gas in GaAs/AlGaAs and InAs/AlGaSb heterostructures J.R. Gao, J.P. Heida, B.J. van Wees, T.M. Klapwijk, G. Borghs and C.T. Foxon	470
Influence of gate voltage on the transport properties of superconductor/2DEG systems K.-M.H. Lenssen, L.A. Westerling, C.J.P.M. Harmans, J.E. Mooij, M.R. Leys, W. van der Vleuten and J.H. Wolter	476
<b>Fluctuations and chaos in low-dimensional systems</b>	
Conductance fluctuations in a quantum dot in the tunneling regime: crossover from aperiodic to regular behavior C.M. Marcus, R.M. Westervelt, P.F. Hopkins and A.C. Gossard	480
Universal fluctuation effects in chaotic quantum dots A.D. Stone and H. Bruus	490
Weak localization and conductance fluctuations in a chaotic quantum dot M.J. Berry, J.A. Katine, C.M. Marcus, R.M. Westervelt and A.C. Gossard	495
Magnetotransport in a chaotic scattering cavity with tunable electron density M.W. Keller, O. Millo, A. Mittal, D.E. Prober and R.N. Sacks	501
Conductance fluctuations of 2D electrons in a strong magnetic field D.E. Khmelnitskii and M. Yosefin	507
Tunneling into classically chaotic orbits in quantum wells T.M. Fromhold, M.L. Leadbeater, L. Eaves, T.J. Foster, P.C. Main and F.W. Sheard	511
Low-temperature equilibrium vertical transport through a two-dimensional electron gas P.C. van Son, F.P. Milliken, E.E. Mendez and W.I. Wang	516
<b>Few electron effects and charging in quantum dots</b>	
Coulomb blockade in the presence of adiabatically transmitted edge channels B.W. Alphenaar, A.A.M. Staring, H. van Houten and C.T. Foxon	520
Electron–electron interactions and the magnetoconductance of submicron quantum dots A. Sachrajda, R.P. Taylor, C. Dharma-wardana, J.A. Adams, P. Zawadzki and P.T. Coleridge	527
Coulomb blockade of Andreev reflection in the NSN single-electron transistor T.M. Eiles, M.H. Devoret and J.M. Martinis	536
Correlation effects on transport through few-electrons systems J.J. Palacios, L. Martin-Moreno and C. Tejedor	541
Charging effects in small-area modulation-doped double-barrier heterostructures S. Tarucha, T. Honda, T. Saku and Y. Tokura	547
A non-evasive voltage probe to measure Coulomb charging C.G. Smith, M. Field, M. Pepper, D.A. Ritchie, J.E.F. Frost, G.A.C. Jones and D.G. Hasko	553
Energy levels of an artificial atom probed with single-electron capacitance spectroscopy R.C. Ashoori, H.L. Stormer, J.S. Weiner, L.N. Pfeiffer, K.W. Baldwin and K.W. West	558
Evidence for spin singlet–triplet transitions of two electrons in a quantum dot observed via single-electron tunneling B. Su, V.J. Goldman and J.E. Cunningham	566
Coulomb oscillation amplitude enhancement and envelope modulation in a magnetic field and activated tunneling M. Stopa, Y. Aoyagi and T. Sugano	571

**Optical studies of quantum wires and dots**

Magneto-optics of quantum wires grown on V-grooved substrates A.S. Plaut, K. Kash, E. Kapon, D.M. Hwang and E. Colas	576
Fermi-edge singularities in InGaAs and GaAs quantum wires M. Fritze, A.V. Nurmikko and P. Hawrylak	580
Photoluminescence intensity and multiple phonon Raman scattering in quantum dots: evidence of the bottleneck effect P.D. Wang, C.M. Sotomayor Torres, H. McLelland, S. Thoms, M. Holland and C.R. Stanley	585
Information on the confinement potential in GaAs/AlGaAs wires from magnetoluminescence experiments F. Hirler, R. Strenz, R. K��chler, G. Abstreiter, G. B��hm and G. Weimann	591
Magneto-optics of interacting electrons in quantum dots P. Hawrylak	597
Magnetoplasmons and FIR response of an antidot array G.Y. Wu and Y. Zhao	601
FIR spectroscopy of the intra-Landau level excitations of strongly correlated quantum dots X.C. Xie, S. Das Sarma and S. He	606
Quantum dots in tilted magnetic fields B. Meurer, D. Heitmann and K. Ploog	610

**Transport studies of quantum wires and dots**

The influence of reduced dimensionality on the spin-splitting in GaAlAs/GaAs quantum wires J. Wr��bel, F. Kuchar, K. Ismail, K.Y. Lee, H. Nickel, W. Schlapp, G. Grabecki and T. Dietl	615
Determination of the quantum wire potential and hot electron spectroscopy using point contacts G. Fasol, Y. Nagamune, J. Motohisa and H. Sakaki	620
Resonant tunnelling between edge states in mesoscopic wires A.K. Geim, P.C. Main, C.V. Brown, R. Taboryski, H. Carmona, T.J. Foster, P.E. Lindelof and L. Eaves	624
Gate tuned transition to the insulating phase of one-dimensional electrons in high magnetic fields S.W. Hwang, D.C. Tsui and M. Shayegan	629
Observation of 1D electron states at the boundary between an MOS and a Schottky contact on Si(100) by electron tunneling U. Kunze, T. Drebingen, B. Klehn and J. Lindolf	633
Magnetophonon resonances in quantum wires G. Berthold, J. Smoliner, E. Gornik, G. B��hm, G. Weimann, T. Suski, P. Wisniewski, C. Hamaguchi, N. Mori and H. Momose	637
Anharmonic periodic modulation in lateral surface superlattices R. Cusc��, M.C. Holland, J.H. Davies, I.A. Larkin, E. Skuras, A.R. Long and S.P. Beaumont	643
Fabrication and characterisation of multi-level lateral nano-devices R.P. Taylor, Y. Feng, A.S. Sachrajda, J.A. Adams, M. Davies, P.T. Coleridge and P. Zawadzki	648
Magnetotransport study of GaAs/AlGaAs quantum wires R.G. Mani, K. von Klitzing, E. Vasiliadou, P. Grambow and K. Ploog	654
Transport properties of dual quantum dots K. Ogawa, R.J. Blaikie, J.D. White, J. Allam and H. Ahmed	659
Lateral transport through a single quantum dot with a magnetic field parallel to the current J. Weis, R.J. Haug, K. von Klitzing and K. Ploog	664
Aharonov-Bohm conductance oscillation of an antidot Y. Takagaki and D.K. Ferry	669

**Electrons on liquid helium**

The AC Hall effect for electrons on liquid helium in ultra-high magnetic fields

P.J.M. Peters, P. Scheuzger, M.J. Lea, W.P.N.M. Jacobs and R.W. van der Heijden 674

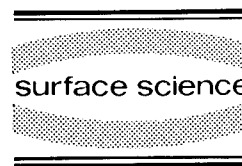
Author index 678

Subject index 694



ELSEVIER

Surface Science 305 (1994) 1–7



# Theories for $\nu = 1/2$ in single- and double-layer systems

Bertrand I. Halperin

*Physics Department, Harvard University, Cambridge, MA 02174, USA*

(Received 30 April 1993)

## Abstract

Recent experiments have shown that a quantized Hall plateau can occur in double-layer systems at total filling factor  $\nu = 1/2$ , though there is no plateau at  $\nu = 1/2$  in a normal single-layer system. For the single-layer system, considerable insight has been provided by a theory based on the fermion Chern–Simons picture, where the electrons are transformed into fermions that carry two flux quanta of a Chern–Simons gauge field. A similar picture can be used to characterize ground states which have been proposed for the two-layer system.

## 1. Introduction

During the course of the past few years, as experiments have continued to reveal the structure of electronic states in a partially filled Landau level, a variety of theoretical approaches have been developed to understand these systems. One of the most useful of these approaches employs a singular gauge transformation to convert the electrons to a system of particles interacting with a Chern–Simons gauge field [1–11]. In this description, a flux tube containing an integer number  $\tilde{\phi}$  of quanta of the Chern–Simons magnetic field is attached to each particle. If  $\tilde{\phi}$  is an even integer [5–11], then the transformed particles obey Fermi statistics. The motivation for employing this singular gauge transformation is that for various rational values of the Landau-level filling factor  $\nu$ , with an appropriate choice of  $\tilde{\phi}$ , if one treats the transformed system in a simple Hartree approximation, the resulting ground state is nondegenerate, and therefore has

a reasonable chance of being a good first approximation to the true ground state of the system. Moreover, one may hope to calculate corrections to the ground state and study the dynamic response of the system by using standard techniques of diagrammatic perturbation theory, beginning with the Hartree ground state [9,10,12].

As an important example, if  $\nu = p/(2p + 1)$ , where  $p$  is a positive or negative integer, and if we choose  $\tilde{\phi} = 2$ , then the mean-field ground state of the transformed system is a collection of fermions in an *effective* magnetic field whose strength is such that exactly  $|p|$  Landau levels are filled by fermions. The ground state is, therefore, stabilized by an energy gap separating it from the excited states. This provides a natural explanation for the most prominent fractional quantized Hall states, which are observed at these filling fractions. At the mean-field level, the fermion Chern–Simons description is essentially equivalent to Jain's composite fermion description of these quantized Hall states [8].

In a recent paper (HLR), P.A. Lee, N. Read, and the present author employed the fermion Chern–Simons method to analyze the properties of a single layer system, at  $\nu = 1/2$  and at various other even fractions, where the quantized Hall effect has not been observed [10]. At  $\nu = 1/2$ , if one chooses  $\tilde{\phi} = 2$ , the average Chern–Simons field just cancels the external magnetic field, so that the Hartree ground state is just a filled Fermi sea of particles, in zero magnetic field, with Fermi wavevector  $k_F = (4\pi n_e)^{1/2}$ . (Here  $n_e$  is the areal density of the electrons. We assume that the electron spins are fully aligned by the Zeeman field.) Although there is no energy gap in this case, the density of states for low energy particle–hole excitations is small, so that there is reason to hope that the mean-field ground state may be stable with respect to the particle–particle interactions, similar to the case of an ordinary Fermi liquid. The detailed analysis of HLR gives rise to predictions for various properties of the  $\nu = 1/2$  system, which seem to be in excellent qualitative agreement with experiments and with exact calculations of finite system. The most striking of these predictions is an explanation for the surface acoustic wave anomalies observed by Willett and coworkers [13,14]. A summary of the most important results of the fermion Chern–Simons theory in the single layer system will be given in Section 2 below.

As is now well known, a quantized Hall plateau at total filling  $\nu = 1/2$  has recently been observed in certain double-layer systems by groups at Princeton and Bell Laboratories [15,16]. A plateau at filling fraction  $\nu = 5/2$  was observed earlier in single-layer systems by Willett et al. [17]. Although various explanations for these states have been advanced, there remains a considerable amount of debate about the precise form of the ground state in various cases. I am not able to settle these questions, but I will try to outline in Section 3 below how the various postulated quantized Hall states may be at least formulated in terms of the fermion Chern–Simons picture as states with various forms of BCS pairing among the particles near the Fermi surface. This suggests a simple phase diagram for how the various states may be connected.

## 2. The single-layer system

We summarize here some of the key results of the analysis of HLR [10] for a fully polarized single-layer system at  $\nu = 1/2$ .

The density and current response functions have been obtained using the random phase approximation (RPA) or time-dependent Hartree approximation. Here the transformed fermions are treated as free particles which respond to the self-consistent Chern–Simons electric and magnetic field  $\langle e(\mathbf{r}, t) \rangle$  and  $\langle b(\mathbf{r}, t) \rangle$ , as well as to the external electromagnetic field and the self-consistent Coulomb potential of the particles [9,10,12]. The equations for  $\langle b \rangle$  and  $\langle e \rangle$  are

$$\langle b \rangle = 2\pi\tilde{\phi}\langle \rho \rangle, \quad (2.1)$$

$$\langle e \rangle = -2\pi\tilde{\phi}\hat{z} \times \langle \mathbf{j} \rangle, \quad (2.2)$$

where  $\langle \rho \rangle$  and  $\langle \mathbf{j} \rangle$  are the particle density and current, respectively, and  $\tilde{\phi} = 2$ . The system is found to be “compressible” at long wavelengths, which means more precisely that the static density response function  $\chi_{\rho\rho}(q)$  is determined by the diverging Coulomb interaction for  $q \rightarrow 0$ :

$$\chi_{\rho\rho}(q)^{-1} \approx v(q) = \frac{2\pi e^2}{\epsilon q}. \quad (2.3)$$

The frequency-dependent density response function  $\chi_{\rho\rho}(q, \omega)$  has, in addition to the pole at the cyclotron frequency that exhausts the  $f$ -sum rule for  $q \rightarrow 0$ , a diffusive pole at a low frequency  $\omega = -i\gamma_q$  which we write in the form

$$\gamma_q = q^2 v(q) \sigma_{xx}(q), \quad (2.4)$$

where  $\sigma_{xx}(q)$  is the wavevector-dependent longitudinal conductivity (we assume  $\mathbf{q} \parallel \hat{x}$ ). According to the RPA, for a system without impurities,  $\sigma_{xx}(q)$  is given by [10]

$$\sigma_{xx}(q) = \frac{e^2}{8\pi\hbar} \frac{q}{k_F}. \quad (2.5)$$

More generally, if impurity scattering is taken into account, we expect that (2.5) applies for  $q \gg l^{-1}$ , where  $l$  is the transport mean free path at  $\nu = 1/2$ . For  $q \rightarrow 0$ , the conductivity goes to a finite value which may be obtained by replacing  $q$

on the right-hand side of (2.5) by  $(2l^{-1})$ . The value of  $l$  is expected to be much smaller than the transport mean free path in zero magnetic field. This is because the dominant mechanism for scattering of carriers at  $\nu = 1/2$  comes from static fluctuations of the Chern-Simons magnetic field due to inhomogeneities in the electron density induced by random variations in the density of charged impurities in the doping layer, a mechanism which does not occur for electrons in zero magnetic field [18]. A crude estimate of  $l$ , at  $\nu = 1/2$ , was obtained by assuming that the charged impurities are uncorrelated within the doping layer, and are equal in number to the electrons in the conducting layer. If scattering is treated in the Born approximation, one finds a value of  $l$  which is just equal to the setback distance  $d_s$  of the doping layer in this model [10]. Experiments suggest that our crude estimate for  $l$  is about a factor of three smaller than the actual values in the highest mobility samples [14,19].

An important effect arising from dynamic fluctuations of the Chern-Simons vector potential is a large renormalization of the effective mass of the transformed fermions. If the bare mass is small, so that the cyclotron energy is large compared to the scale of the electron-electron interactions, then the effective mass becomes independent of the bare mass, and is determined by the electron-electron interaction. Using a self-consistent analysis based on the leading diagrams in perturbation theory, HLR propose that there is a logarithmic divergence of the effective mass at the Fermi energy for Coulomb interactions, and a stronger power-law divergence for short range interactions, but that the most essential features of Fermi liquid theory are preserved in either case. Note that expressions (2.3)–(2.5) for the density response function and the conductivity are independent of the electron mass, and we believe that they are not affected by the divergent mass renormalization. (The results for the mean free path in the presence of impurities are also independent of the electron mass.)

One place where the effective mass enters directly is in the expression of HLR for the energy gaps  $E_g^{(\nu)}$  for the principal quantized Hall states at  $\nu = p/(2p + 1)$ . For an interaction that

behaves like  $e^2/\epsilon r$  at large distances, HLR predict the following asymptotic form for the energy gap at large  $p$ :

$$E_g^{(\nu)} \approx \frac{4}{\pi} \frac{e^2}{\epsilon l_0} \frac{1}{D(\ln D + C)}, \quad (2.6)$$

where  $D = |2p + 1|$  is the denominator of the fraction and  $C$  is a constant which depends on the short distance behaviour of the potential. (This formula is based on a self-consistent analysis of the leading correction to the quasiparticle self-energy arising from interactions with fluctuations in the transverse gauge field; it is possible that it may be modified by other singular contributions.) A good fit to numerical estimates [20] of the energy gaps at  $\nu = 1/3$ ,  $2/5$ , and  $3/7$ , for a pure Coulomb interaction, may be obtained by choosing  $C \approx 2.5$  in that case. The effects of finite layer thickness and inter-Landau-level mixing, which occur in any real sample, would tend to increase the value of  $C$  still further. An energy gap of the form (2.6), with a relatively large value of  $C$ , also gives a good fit to the data of Du et al. [21], provided that one accepts the proposal of those authors that the effects of impurity scattering may be taken into account by subtracting a constant  $\Gamma$ , independent of  $\nu$ , from the theoretical energy gap.

The linear wavevector dependence of  $\sigma_{xx}(q)$ , predicted by (2.5) for  $\nu = 1/2$ , is just what is needed to explain the anomalous surface acoustic wave propagation, seen at short wavelengths by Willett et al. [14]. The absolute values of  $\sigma_{xx}(q)$  extracted by Willett et al. from their data are larger than the theoretical values obtained from (2.5), however, by a factor of  $\sim 2$ . The theory of HLR also predicts that the width of the anomaly should depend linearly on  $q$  as the magnetic field is varied away from the field corresponding to  $\nu = 1/2$ . This is in good agreement with the experimental observations.

Quasiparticle states for the transformed fermions which lie close to the Fermi energy should not have a significant overlap with the wavefunction of a single electron added to the ground state of a  $\nu = 1/2$  system. A recent analysis by He, Platzman and Halperin [22], building



on the results of HLR, suggests that the spectral density  $A(\omega)$  for the electron Green's function vanishes as  $e^{-\omega_0/|\omega|}$ , for  $|\omega| \rightarrow 0$ , where  $\omega_0$  is a constant. Following this analysis, they predict a pseudogap in  $A(\omega)$ , which is in reasonable agreement with recent tunneling experiments [23].

The general methods of HLR can be applied to various other even-denominator fractions, including  $\nu = 1/4, 3/4, 3/2, 3/8$ , etc. Chklovskii and Lee have shown, however, that a more sophisticated analysis is necessary to understand the value of the electrical conductivity  $\sigma_{xx}$  at the higher order even fractions, because the Born approximation for scattering becomes quite poor in this situation [24].

### 3. Double-layer systems

As a model to describe a double-layer system, we shall introduce an “isospin” index  $\tau = \pm 1$ , which distinguishes between the two layers, in addition to the position  $\mathbf{r}$  in the  $x$ - $y$  plane. The Coulomb interaction between two electrons then has different forms  $V_{++}(\mathbf{r} - \mathbf{r}')$  and  $V_{+-}(\mathbf{r} - \mathbf{r}')$ , depending on whether the two electrons are in the same or in different layers [25]. In the simplest case where each separate layer is considered to be of zero thickness, we may write

$$V_{++}(r) = e^2/\epsilon r, \quad (3.1)$$

$$V_{+-}(r) = e^2/\epsilon(r^2 + d^2)^{1/2}, \quad (3.2)$$

where  $d$  is the separation between the layers. In addition, we introduce a term to represent tunneling between the layers, which we write as

$$H_t = -tI_x, \quad (3.3)$$

where  $t$  is the tunneling matrix element, and  $I_x$  is the  $x$  component of the total isospin operator  $\mathbf{I}$ . We assume that the actual spins of the electrons are completely polarized in the direction of the magnetic field, and we consider only the case where there is a mirror symmetry between the two layers. In our discussions we consider that the system employed in Ref. [15], consisting of a single wide quantum well in which the self-consistent Coulomb potential creates a barrier in the

middle of the well, with maxima in the electron density at the two edges, is equivalent to a double-layer system with a relatively large value of the tunneling matrix element  $t$ .

We shall limit our discussions here to the case where the *total* filling factor  $\nu$  is equal to  $1/2$ ; i.e. there is a total of one electron per flux quantum in the two layers combined. Then, if the system is confined to the lowest Landau level, there are essentially two dimensionless parameters in our model  $\tilde{d} \equiv d/l_0$ , and  $\tilde{t} \equiv t/(e^2/\epsilon l_0)$ .

Let us first consider the case where  $\tilde{d} = 0$ , so that  $V_{++} = V_{+-}$ . If  $\tilde{t}$  is also equal to zero, then the Hamiltonian  $H_0$  possesses full SU(2) symmetry in the isospin  $\mathbf{I}$ . In fact,  $H_0$  is equivalent to the Hamiltonian for a single-layer system with two spin states and no Zeeman term to split the degeneracy. The simplest assumption (though not universally believed [26]) is that the ground state of the single layer system would be completely polarized at  $\nu = 1/2$ , even in the absence of Zeeman interactions. If this is the case, then for the two-layer system with  $\tilde{d} = 0$ , the effect of  $H_t$ , for any positive value of  $\tilde{t}$ , is simply to align the isospin polarization in the  $x$ -direction. Specifically, this means that every electron is restricted to the isospin state  $I_x = 1/2$ , i.e., the lowest subband, which is the even combination of states in the two layers. Since the Hamiltonian is equivalent to that of a fully polarized single-layer system, we expect, as discussed in Section 2 above, that the ground state can be described by gauge transformed fermions with a single Fermi surface, having  $k_F = (4\pi n_e)^{1/2} = l_0^{-1}$ , and no quantized Hall effect.

Let us now consider the case where  $\tilde{d}$  is nonzero and  $\tilde{t}$  is infinite. Every electron must have  $I_x = 1/2$ , and hence all electrons have the same interaction,  $\bar{V}(r) = \frac{1}{2}[V_{++}(r) + V_{+-}(r)]$ . If  $\tilde{d}$  is very large, then  $V_{+-} \approx 0$ , and  $\bar{V}(r) \approx \frac{1}{2}V_{++}(r)$ . Therefore, for large  $\tilde{d}$ , the ground state is the same as for  $\tilde{d} = 0$ , and we expect to find a Fermi surface with no quantized Hall effect. (The only change from  $\tilde{d} = 0$  is that the energy scale is reduced by a factor of 2.)

According to the numerical calculations of Greiter, Wen and Wilczek [27] for a two-layer system with  $\tilde{t} = \infty$ , there should exist an interme-

diate range  $\tilde{d}'_{\min} < \tilde{d} < \tilde{d}'_{\max}$ , where a quantized Hall effect does occur at  $\nu = 1/2$ . Their calculations suggest that the quantized Hall state has a very high overlap with the so-called Pfaffian state, originally described by Moore and Read [5], and further analyzed by Greiter et al. [7]. From the point of view of the ground state symmetry, this state can also be understood in terms of the fermion Chern–Simons picture as a state where the fermions near to the Fermi surface are paired in a BCS-like state, with orbital angular momentum  $l_z = -1$ , and isospin  $I_x = 1$ . (In terms of untransformed electrons, the state may be crudely described as made up of pairs with angular momentum  $l_z = 1$ , which are then “condensed” into a Laughlin state of degree  $m = 8$ .) Moore and Read have suggested that the charged excitations of the Pfaffian state have a different kind of statistics from what might be expected in a simple pairing state, and perhaps there are other subtle differences as well. We shall not distinguish here, however, between the Pfaffian state and the Chern–Simons BCS state with pairing  $l_z = -1$  and  $I_x = 1$ .

Let us next consider the case  $\tilde{t} = 0$ ,  $\tilde{d} \neq 0$ . Now,  $I_z$  is a good quantum number of the system, and if there is equal population of the two layers, the ground state must have  $I_z = 0$ . (For  $\tilde{d} \neq 0$ , the Hamiltonian does not commute with  $I_x$ . The ground state has  $\langle I_x \rangle = 0$ , for  $t = 0$ , but is not generally an eigenstate of  $I_x$ .) In the limit  $\tilde{d} \rightarrow \infty$ , for  $\tilde{t} = 0$ , the system becomes two uncoupled layers, with  $\nu = 1/4$  in each layer. Experiments on single-layer systems show that there should be no quantized Hall effect in this case [14]. According to the theory of HLR, there should be a separate Fermi surface of transformed fermions in each layer (seeing separate Chern–Simons field, with  $\tilde{\phi} = 4$ , in each layer), and a Fermi wavevector  $k_F = (2\pi n_e)^{1/2} = (2I_0^2)^{-1/2}$ .

Numerical calculations for systems with  $\tilde{t} = 0$  again indicate that for an intermediate range  $\tilde{d}'_{\min} < \tilde{d} < \tilde{d}'_{\max}$ , there should exist a quantized Hall plateau at  $\nu = 1/2$  [28–30]. The ground state in this case has been found to have a high degree of overlap with the so-called 331 state, first proposed in 1983 as a possible generalization of Laughlin’s wavefunctions to an even denominator

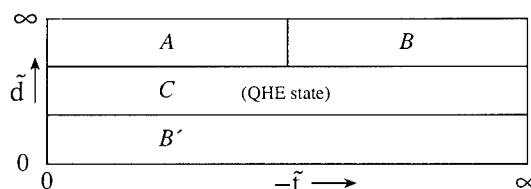


Fig. 1. Possible schematic phase diagram for the ground state of a two-layer system at total filling  $\nu = 1/2$ . Variables  $\tilde{d}$  and  $\tilde{t}$  are respectively the separation between layers, in units of the magnetic length  $l_0$ , and the tunneling strength between layers, in units of  $e^2/\epsilon l_0$ . Phase *A* has two essentially independent layers of filling factor  $\nu = 1/4$ , with a separate Fermi surface in each layer, and no quantized Hall effect. Phases *B* and *B'* behave like a single layer at  $\nu = 1/2$ , with electrons in the subband which is an even combination of states in the two layers. These phases have a single Fermi surface for the gauge transformed fermions, and no quantized Hall effect. Phase *C* is a quantized Hall state which evolves continuously as a function of  $\tilde{t}$  from a state with the symmetry of the “331 state” at  $\tilde{t} = 0$ , to a state with the symmetry of the “Pfaffian” state at  $\tilde{t} = \infty$ .

fraction [31]. The 331 state has been characterized by various authors as a system of two types of fermions (or bosons) with a  $2 \times 2$  matrix of Chern–Simons interactions [32]. However, the state may also be characterized in the spirit of Greiter et al. [7] as a system of fermions coupled to a single Chern–Simons field (with coupling strength  $\tilde{\phi} = 2$ ), whose ground state has BCS pairing with  $l_z = -1$  and  $I_z = 0$ .

What happens for intermediate values of  $\tilde{t}$ , when  $\tilde{d} \neq 0$ ? A simple schematic phase diagram, compatible with our previous discussion, is presented in Fig. 1.

The phase labeled *A* consists of two essentially independent layers with  $\nu = 1/4$  and a separate Fermi surface for transformed fermions in each layer. Phases *B* and *B'* have a large value of  $\langle I_x \rangle$ , and contain a single Fermi surface for transformed fermions with isospin  $I_x = 1/2$ , the even combination of states in the two layers.

The phase labeled *C*, which occurs for intermediate values of the parameter  $\tilde{d}$ , is a quantized Hall state. Within the fermion Chern–Simons picture, we characterize the entire phase as a state with a BCS gap at the Fermi surface due to

pairing in a state of isospin 1 and  $I_z = -1$ . Specifically, we expect pairing of the form

$$c_{k\tau} c_{k'\tau'} \approx Q(\mathbf{r})(k_x - ik_y) f_{\tau\tau'} e^{i(\mathbf{k}+\mathbf{k}')\cdot\mathbf{r}}, \quad (3.4)$$

where  $c_{k\tau}$  is the annihilation operator for a transformed fermion with wavevector  $\mathbf{k}$  and isospin  $\tau$ , the wavevectors  $\mathbf{k}$  and  $\mathbf{k}'$  are close to the Fermi surface at diametrically opposite points, and  $Q(\mathbf{r})$  is an order parameter whose pair correlation function  $\langle Q^+(\mathbf{r})Q(\mathbf{r}') \rangle$  falls off at large separations as a power of  $|\mathbf{r} - \mathbf{r}'|$  (i.e., the system has “quasi-long-range order” in the ground state). The matrix  $f_{\tau\tau'}$  is symmetric in the isospin indices, and we hypothesize that it varies continuously as a function of the tunneling strength  $\tilde{t}$  between the two limits:

$$f_{\tau\tau'} \rightarrow \delta_{\tau, -\tau'}, \quad \text{for } \tilde{t} \rightarrow 0, \quad (3.5)$$

$$f_{\tau\tau'} \rightarrow 1, \quad \text{for } \tilde{t} \rightarrow \infty, \quad (3.6)$$

corresponding to pairs with  $I_z = 0$  and  $I_x = 1$ , respectively. We also expect that the expectation value  $\langle I_x \rangle$  for the total isospin of the electron system should increase continuously from  $\langle I_x \rangle = 0$  at  $\tilde{t} = 0$  to  $\langle I_x \rangle = N/2$  (full polarization) at  $\tilde{t} = \infty$ .

Numerical calculations by He et al. [29,30] suggest that for the values of  $\tilde{t}$  and  $\tilde{d}$ , which correspond to the Princeton and Bell Laboratories experiments, there is a high degree of overlap between the ground state at  $\nu = 1/2$  and the 331 state, which has  $I_z = 0$ . Thus, it appears that there is only a small amount of  $\langle I_x \rangle$  polarization, even for the Princeton experiment where  $\tilde{t}$  is relatively large.

The calculations of He et al. [30] support the conjecture that a quantized Hall state should exist for an intermediate range of separations  $\tilde{d}$ , for any value of the parameter  $\tilde{t}$ . The conjecture that the 331 state can be continuously connected with the quantized Hall state at  $\tilde{t} = \infty$  is also compatible with the observation by Greiter et al. [7] that the Pfaffian state is realized by taking the fully antisymmetric part of the spatial portion of the 331 wavefunction.

We do not address here the nature of the phase transitions between the various regions of Fig. 1. Of course, we cannot exclude at this stage

the possibility that the actual phase diagram is more complicated, with various other intermediate phases occurring. Moreover, if our starting assumption, that the ground state for  $\tilde{t} = \tilde{d} = 0$  has complete spontaneous alignment of the isospin vector  $\mathbf{I}$ , is *not* correct, then there must be a more complicated phase structure than we have indicated near the lower left corner of Fig. 1. Among the theoretical possibilities for the ground state at  $\tilde{t} = \tilde{d} = 0$  are the following: (1) there might be an isospin singlet ground state with some type of energy gap, which would thus exhibit a quantized Hall effect; (2) there might be an isospin singlet ground state with no energy gap, described within the fermion Chern–Simons picture as having a single Chern–Simons field, with  $\tilde{\phi} = 2$ , and a Fermi surface, with  $k_F = (2\pi n_e)^{1/2}$ , for each isospin state; or (3) the 331 state might exist as a stable ground state all the way down to the point  $\tilde{t} = \tilde{d} = 0$ . Since the 331 state is not an eigenstate of  $I^2$ , it cannot be the true ground state for a finite system at  $\tilde{t} = \tilde{d} = 0$ ; however, it could be the ground state of an infinite system if there is a spontaneously broken isospin symmetry.

We note that BCS pairing, in the fermion Chern–Simons picture with  $\tilde{\phi} = 2$ , has also been used to discuss the spin-singlet “hollow-core” ground state of Haldane and Rezayi [33], originally proposed as an explanation for the quantized Hall state of a single layer at  $\nu = 5/2$ . (This is a state where the lowest Landau level is completely full and there is a one-half electron per flux quantum in the second Landau level.) In this case the BCS pairing has  $I_z = -2$  for the transformed fermions, corresponding to pairs with  $I_z = 0$  for the original electrons [5,7].

*Note Added at Conference.* Numerical calculations by R. Morf, reported at this conference, suggest that the correct ground state for  $\tilde{t} = \tilde{d} = 0$  is an isospin singlet ground state with no energy gap, as in possibility (2) mentioned above. If this is correct, then the lower left corner of Fig. 1 should contain a new phase  $D$ , having a single Chern–Simons field with  $\tilde{\phi} = 2$ , and two Fermi surfaces, with radii  $k_{F+}$  and  $k_{F-}$ , corresponding to fermions with  $I_x = 1/2$  and  $I_x = -1/2$ , respectively. As  $\tilde{t}$  is increased, the ratio  $k_{F-}/k_{F+}$

should decrease continuously in phase *D* from the value unity, at  $\tilde{t} = 0$ , until the boundary with phase *B* is encountered, where  $k_{F-} = 0$ . The sum  $k_{F-}^2 + k_{F+}^2$  must be a constant,  $4\pi n_e$ .

Experimental results reported by Y.W. Suen at this conference suggest that in actual double-layer systems, contrary to the model calculations of Ref. [27], the quantized Hall state may be absent regardless of the value of  $\tilde{d}$ , when  $\tilde{t}$  is sufficiently large. If this is correct, then the QHE state *C* should not extend all the way to the right-hand boundary of Fig. 1. Phases *B* and *B'* may then be united into a single phase, connected in the right-hand portion of the figure.

#### 4. Conclusion

Although many details remain to be understood, it seems clear that the transformation to fermions with a Chern-Simons field is a powerful tool for understanding the behavior of electrons at  $\nu = 1/2$ , in both single- and double-layer systems.

#### 5. Acknowledgments

This review has benefited greatly from discussions with P.A. Lee, N. Read, S. He, R.H. Morf, F. Wilczek, P.M. Platzman, J.P. Eisenstein, and R.L. Willett. The work has been supported in part by NSF grant DMR-91-15491.

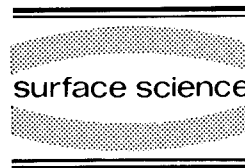
#### 6. References

- [1] S.M. Girvin and A.H. MacDonald, Phys. Rev. Lett. 58 (1987) 1252.
- [2] S.-C. Zhang, H. Hanson and S. Kivelson, Phys. Rev. Lett. 62 (1989) 82; Phys. Rev. Lett. 62 (1989) 980(E); S.-C. Zhang, Int. J. Mod. Phys. B 6 (1992) 25; D.-H. Lee and M.P.A. Fisher, Phys. Rev. Lett. 63 (1989) 903.
- [3] D.-H. Lee, S. Kivelson and S.-C. Zhang, Phys. Rev. Lett. 68 (1992) 2386; S. Kivelson, D.-H. Lee and S.-C. Zhang, Phys. Rev. B 46 (1992) 2223.
- [4] D. Schmeltzer, Phys. Rev. B 46 (1992) 1591.
- [5] G. Moore and N. Read, Nucl. Phys. B 360 (1991) 362.
- [6] M. Greiter and F. Wilczek, Mod. Phys. Lett. B 4 (1990) 1063.
- [7] M. Greiter, X.-G. Wen and F. Wilczek, Phys. Rev. Lett. 66 (1991) 3205; Nucl. Phys. B 374 (1992) 567; M. Greiter and F. Wilczek, Nucl. Phys. B 370 (1992) 577.
- [8] J.K. Jain, Phys. Rev. Lett. 63 (1989) 199; Phys. Rev. B 40 (1989) 8079; Phys. Rev. B 41 (1990) 7653; J.K. Jain, S.A. Kivelson and N. Trivedi, Phys. Rev. Lett. 64 (1990) 1297.
- [9] A. Lopez and E. Fradkin, Phys. Rev. B 44 (1991) 5246.
- [10] B.I. Halperin, P.A. Lee and N. Read, Phys. Rev. B 47 (1993) 7312.
- [11] V. Kalmeyer and S.-C. Zhang, Phys. Rev. B 46 (1992) 9889.
- [12] R.B. Laughlin, Phys. Rev. Lett. 60 (1988) 2677; A.L. Fetter, C.B. Hanna and R.B. Laughlin, Phys. Rev. B 39 (1989) 9679; Q. Dai, J.L. Levy, A.L. Fetter, C.B. Hanna and R.B. Laughlin, Phys. Rev. B 46 (1992) 5642.
- [13] R.L. Willett, M.A. Paalanen, R.R. Ruel, K.W. West, L.N. Pfeiffer and D.J. Bishop, Phys. Rev. Lett. 54 (1990) 112.
- [14] R.L. Willett, R.R. Ruel, M.A. Paalanen, K.W. West and L.N. Pfeiffer, Phys. Rev. B 47 (1993) 7344.
- [15] Y.W. Suen, L.W. Engel, M.B. Santos, M. Shayegan and D.C. Tsui, Phys. Rev. Lett. 68 (1992) 1379.
- [16] J.P. Eisenstein, G.S. Boebinger, L.N. Pfeiffer, K.W. West and S. He, Phys. Rev. Lett. 68 (1992) 1383.
- [17] R.L. Willett, J.P. Eisenstein, H.L. Stormer, D.C. Tsui, A.C. Gossard and J.H. English, Phys. Rev. Lett. 59 (1987) 1776.
- [18] This scattering mechanism was also discussed by V. Kalmeyer and S.-C. Zhang in Ref. [11].
- [19] H.L. Stormer, K.W. Baldwin, L.N. Pfeiffer and K.W. West, Solid State Commun. 84 (1992) 95.
- [20] N. d'Ambrumenil and R.H. Morf, Phys. Rev. B 40 (1989) 6108.
- [21] R.R. Du, H.L. Stormer, D.C. Tsui, L.N. Pfeiffer and K.W. West, Phys. Rev. Lett. 70 (1993) 2944.
- [22] S. He, P.M. Platzman and B.I. Halperin, Phys. Rev. Lett. 71 (1993) 777.
- [23] J.P. Eisenstein, L.N. Pfeiffer and K.W. West, Phys. Rev. Lett. 69 (1992) 3804.
- [24] D.B. Chklovskii and P.A. Lee, Phys. Rev. B, in press.
- [25] T. Chakraborty and P. Pietiläinen, Phys. Rev. Lett. 59 (1987) 2784.
- [26] L. Belkhir and J.K. Jain, Phys. Rev. Lett. 70 (1993) 643.
- [27] M. Greiter, X.-G. Wen and F. Wilczek, Phys. Rev. B 46 (1992) 9586.
- [28] D. Yoshioka, A.H. MacDonald and S.M. Girvin, Phys. Rev. B 39 (1989) 1932.
- [29] S. He, X.C. Xie, S. Das Sarma and F.C. Zhang, Phys. Rev. B 43 (1991) 9339.
- [30] S. He, S. Das Sarma and X.C. Xie, Phys. Rev. B 47 (1993) 4394.
- [31] B.I. Halperin, Helv. Phys. Acta 56 (1983) 75.
- [32] See, for example, D. Schmeltzer and J.L. Birman, Phys. Rev. B 47 (1993) 10939.
- [33] F.D.M. Haldane and E. Rezayi, Phys. Rev. Lett. 60 (1988) 956; Phys. Rev. Lett. 60 (1988) 1886(E).



ELSEVIER

Surface Science 305 (1994) 8–12



# New collective quantum Hall states in double quantum wells

G.S. Boebinger<sup>\*</sup>, S.Q. Murphy, J.P. Eisenstein, L.N. Pfeiffer, K.W. West, Song He

*AT & T Bell Laboratories, Murray Hill, NJ 07974, USA*

(Received 21 April 1993; accepted for publication 30 August 1993)

## Abstract

Transport studies on double-layer two-dimensional electron systems in GaAs double quantum wells have revealed quantum Hall states at total filling fraction  $\nu = 1/2$  and  $\nu = 1$ . We conclude that these states arise from interlayer Coulomb correlations, based on studies of samples with different densities and layer separations and experiments utilizing tilted magnetic fields.

## 1. Introduction

The standard model of the fractional quantum Hall effect (FQHE) describes a myriad of observed odd-denominator FQHE states in terms of a fully spin-polarized two-dimensional electron system (2DES) [1]. Recent work has revealed novel unpolarized spin configurations for the FQHE states at various Landau-level filling fractions [2,3]. If the spin-flip energy is not too large, the 2DES can exploit the spin degree of freedom and form FQHE states not contained within the standard model. In particular, the only known even-denominator FQHE in a conventional single-layer 2DES (at Landau-level filling fraction  $\nu = 5/2$ ), is thought to be an example of such an unpolarized state [4]. By analogy, a *double-layer* 2DES possesses an extra degree of freedom, the layer index, that is expected to give rise to new FQHE states not present in single-layer systems [5–7].

Yoshioka et al. [7] systematically outlined the possibilities for new FQHE states in double-layer systems using the two-component Jastrow wavefunction proposed by Halperin [8]:

$$\Psi_{m,m',n} = \prod (z_i - z_{i'})^m (w_j - w_{j'})^{m'} (z_k - w_{k'})^n.$$

In this wavefunction, the positions of electrons in one well are given by  $z_i$ , positions in the other well by  $w_j$ . The exponents  $m$  and  $m'$  govern the intra-layer correlations, while the cross-term exponent,  $n$ , governs the inter-layer correlations. Note that only  $m$  and  $m'$  are constrained to be odd by the requirement for an odd-parity wavefunction. In the regime where inter-layer Coulomb interactions are comparable to the ordinary intra-layer interactions, the  $\Psi_{3,3,1}$  and  $\Psi_{1,1,1}$  states have been proposed as candidate ground states for a double-layer FQHE at  $\nu = 1/2$  and  $\nu = 1$ , respectively. Since the magnetic length  $l_B = (\hbar/eB)^{1/2}$  sets the length scale for intra-layer Coulomb interactions, these new FQHE states are most stable in double-layer 2DES with  $d/l_E \approx 1$ , where  $d$  is the inter-layer spacing.

<sup>\*</sup> Corresponding author.

Insofar as intra-layer correlations are concerned, the  $\Psi_{3,3,1}$  wavefunction is quite similar to the original Laughlin  $1/3$ -state and the  $\Psi_{1,1,1}$  wavefunction is quite similar to the integral QHE state at  $\nu = 1$ . However, each state contains additional *inter-layer* correlations which, in effect, keep electrons in adjacent layers from occupying the same position in the 2D plane. Since inter-layer tunneling will suppress this anticorrelation, these new FQHE states weaken in a double-layer 2DES if the symmetric–antisymmetric tunneling gap,  $\Delta_{\text{SAS}}$ , is not substantially smaller than characteristic Coulomb energies,  $e^2/\epsilon l_B$  [9].

In this paper we review the discovery of a new FQHE state at total filling factor  $\nu = 1/2$  in a double-layer 2DES [10]. We present evidence that both this and the quantized state at  $\nu = 1$  arise from an interplay of intra- and inter-layer Coulomb interactions.

## 2. Experimental results

For these experiments a series of modulation-doped GaAs/AlGaAs double quantum well (DQW) structures were grown by molecular beam epitaxy. These samples were designed to have minimal tunneling and yet still to be coupled via Coulomb interactions. The details of the sample growth are given in Ref. [10]. The electron density was balanced between the two wells and standard low-frequency magnetotransport techniques were employed. We define the Landau-level filling fraction as  $\nu = hN_{\text{tot}}/eB$ , with  $N_{\text{tot}}$  the total carrier density in the structure and  $B$  the magnetic field. (Thus, a widely-spaced double-layer system will exhibit only even-integer QHE states and fractional QHE states with even numerators.) Unless otherwise noted, all data presented in this paper come from a sample with two 180 Å wide GaAs quantum wells separated by a 31 Å wide undoped pure AlAs barrier layer (giving  $d = 211$  Å and  $\Delta_{\text{SAS}} \approx 0.9$  K).

Fig. 1 shows the diagonal resistivity  $\rho_{xx}$  and Hall resistivity  $\rho_{xy}$  at  $T = 150$  and 430 mK, respectively. Four quantum Hall states, both integral and fractional, are noted by their total filling fraction  $\nu$  as defined above. As the figure shows,

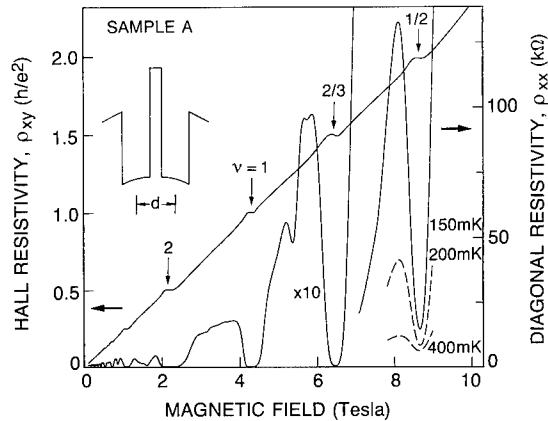


Fig. 1. Diagonal resistivity at  $T = 150$  mK and Hall resistivity at  $T = 430$  mK. Note the  $\nu = 1/2$  fractional quantum Hall state. Temperature dependence of  $\rho_{xx}$  near  $\nu = 1/2$  is also shown. The  $\rho_{xx}$  trace for  $B < 7$  T has been amplified ten-fold. Inset: Schematic conduction-band diagram of the double quantum well.

a new FQHE state, with the requisite deep minimum in  $\rho_{xx}$  and flat Hall plateau, is observed at filling fraction  $\nu = 1/2$ . This state has also been observed in single quantum wells which are sufficiently wide that the electrons concentrate near the two interfaces [11].

Three additional samples, listed in Ref. [10] were studied in order to clarify the role of inter-layer correlations in the observed  $\nu = 1/2$  FQHE. The  $\nu = 1/2$  state was found to monotonically weaken as the density increases. This is an unusual observation since the single-layer FQHE generally becomes stronger at higher magnetic fields owing to the increasing Coulomb energy ( $e^2/\epsilon l_B \propto B^{1/2}$ ). For a double-layer system, however, the relative magnitude of intra- and inter-layer Coulomb energies,  $d/l_B$ , plays a critical role. The data span the range of  $d/l_B$  increasing from 2.4 to 2.9 as the  $\nu = 1/2$  state weakens. Further increasing  $d/l_B$  to 3.6 (by increasing the barrier thickness to 99 Å) obliterates all evidence of a FQHE at  $\nu = 1/2$ . This provides compelling evidence that the  $\nu = 1/2$  FQHE derives from inter-layer electron–electron interactions.

Fig. 1 contains several QHE features in addition to the new state at  $\nu = 1/2$ . The states observed at  $\nu = 2$  and  $2/3$  both have well-known

counterparts in single-layer systems. For  $\nu = 2$ , this is the ordinary integral QHE obtained when the Fermi level lies in the spin gap of the lowest Landau level. Similarly, the FQHE seen at  $\nu = 2/3$  corresponds to the canonical Laughlin  $1/3$ -state in each single layer. Finally, the data in Fig. 1 also reveal a strong QHE at  $\nu = 1$ , for which there is no similar single-layer analog. As previously discussed, this  $\nu = 1$  state could arise from the inter-layer correlations built into the  $\Psi_{1,1,1}$  state [5–7]. A  $\nu = 1$  state could also arise, however, if the two layers are close enough to be coupled by substantial tunneling. If the tunneling gap between the lowest-lying symmetric and anti-symmetric states is experimentally resolved, then odd-integer QHE states result when the Fermi energy lies in this single-electron energy gap [12].

Thus, the observed QHE state at  $\nu = 1$  could have two possible origins: single-particle tunneling or inter-layer many-body effects. The low-temperature resistivity data shown in Fig. 2 supports the many-body alternative. Consider the lower trace taken with the magnetic field perpendicular to the 2DES ( $\theta \equiv 0^\circ$ ). Strong QHE minima are observed at  $\nu = 9, 7, 5$ , and 1. (We will discuss the absence of the  $\nu = 3$  QHE later.) Application of an in-plane magnetic field,  $B_{\parallel}$ , has

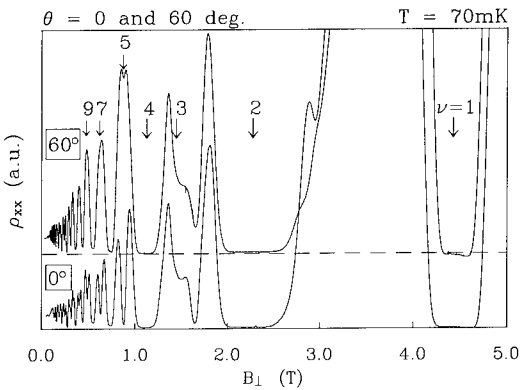


Fig. 2. Low-field  $\rho_{xx}$  at  $T = 70$  mK versus the perpendicular component of the magnetic field for magnetic field tilted  $0^\circ$  and  $60^\circ$  from normal to the 2DES. Note the  $\nu = 9, 7$ , and 5 states are destroyed by an in-plane magnetic field, while the  $\nu = 1$  is not. This is evidence that the  $\nu = 1$  state arises from inter-layer Coulomb interactions. The missing  $\nu = 3$  state is discussed in the text.

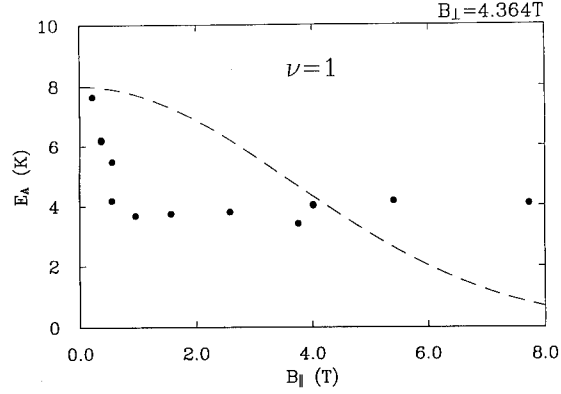


Fig. 3. Activation energy of the quantized state at  $\nu = 1$  versus in-plane magnetic field,  $B_{\parallel}$ . The dashed line (normalized to the data at  $B_{\parallel} = 0$ ) is the calculated dependence of a single-particle tunneling gap at  $\nu = 1$ . The relative independence of the activation energy over the range  $1 < B_{\parallel} < 8$  T is strong evidence that the  $\nu = 1$  state of Fig. 2 does not arise from single-particle tunneling.

been shown to destroy  $\nu = \text{odd}$  QHE states which arise from tunneling [12]. This effect is due to a reduction of the tunneling matrix element stemming from the requirement of conserved canonical momentum. It assists us in discriminating between the single-particle and collective variants of the  $\nu = 1$  QHE. The upper trace in Fig. 2 shows the destruction of the QHE states at  $\nu = 9, 7$ , and 5 upon tilting the magnetic field by  $60^\circ$ . We therefore attribute these states to the finite tunneling gap in this sample. The  $\nu = 1$ , by contrast, remains strong, even in the presence of a 7.6 T in-plane magnetic field. Activation energies measured at  $\nu = 1$  as a function of  $B_{\parallel}$  are shown in Fig. 3. The dashed line (normalized to the data at  $B_{\parallel} = 0$ ) is the calculated  $B_{\parallel}$ -dependence of a tunneling gap at  $\nu = 1$  [13]. Although the sharp enhancement of the activation energy very near  $B_{\parallel} = 0$  is not understood, the relative independence of the activation energy over the range  $1 < B_{\parallel} < 8$  T is strong evidence that the  $\nu = 1$  state of Figs. 1 and 2 does not arise from single-particle tunneling.

We now re-examine the lower trace of Fig. 2. The absence of the  $\nu = 3$  QHE state is reminiscent of previous studies of the destruction of low-order integral QHE states in double-layer

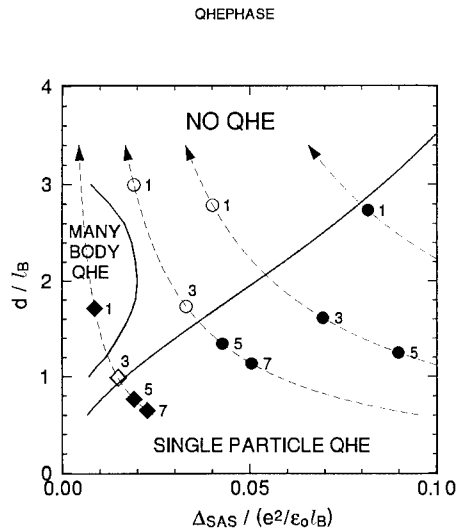


Fig. 4. Schematic phase diagram of the quantized states at  $\nu = \text{odd}$  in a double quantum well, adapted from Refs. [9,15], including data from Ref. [12] (circles) and new data from Fig. 2 (diamonds). Since the axes are each scaled by the magnetic length,  $l_B$ , the dashed arrows represent increasing magnetic field for a given sample (fixed  $d$ ,  $\Delta_{\text{SAS}}$ , and  $N_{\text{tot}}$ ). Filled/open symbols denote observed/missing quantum Hall states labelled by filling factor  $\nu$ . The solid lines are schematic phase boundaries representing the Coulomb-driven destruction of the single-particle tunneling QHE and the re-emergence of a many-body QHE in the regime of  $d/l_B \approx 1$  and  $\Delta_{\text{SAS}} \rightarrow 0$ .

systems [12,14]. These studies find a phase transition in which inter-layer Coulomb interactions destroy the single-particle tunneling gap. A well-defined boundary [15,16] exists between the larger odd-integral filling factors for which the single-particle tunneling gap, and, hence, the QHE, survives, and the smaller odd integers for which it is collapsed and the QHE is quenched. Within this picture then, inter-layer interactions have destroyed the tunneling gap in our sample for all  $\nu \leq 3$ . Thus, the *reappearance* of a QHE at  $\nu = 1$  suggests these same inter-layer interactions are now strong enough to create a new, many-body gap to replace the tunneling gap. We therefore propose in Fig. 4 a refinement [9] of a previously proposed phase diagram for the QHE at  $\nu = \text{odd}$  [15]. The two axes (interwell distance,  $d$ , and single-particle tunneling gap,  $\Delta_{\text{SAS}}$ ) are each scaled by the magnetic length,  $l_B$ . The dashed arrows represent increasing magnetic field for a

given sample (fixed  $d$ ,  $\Delta_{\text{SAS}}$ , and  $N_{\text{tot}}$ ). Filled/open circles denote observed/missing quantum Hall states from Ref. [12], labelled by filling factor  $\nu$ . Filled/open diamonds denote observed/missing quantum Hall states from the  $\theta = 0^\circ$  data of Fig. 2. The solid lines are schematic phase boundaries representing the Coulomb-driven destruction of the single-particle tunneling QHE and re-emergence of a many-body QHE in the regime of  $d/l_B \approx 1$  and  $\Delta_{\text{SAS}} \rightarrow 0$ . In the regime of large  $\Delta_{\text{SAS}}$ , the observed  $\nu = \text{odd}$  QHE arises from the single-particle tunneling gap. The new phase in Fig. 4, labelled "MANY BODY QHE", includes the  $\nu = 1$  state observed in Figs. 1 and 2.

### 3. Conclusions

Two new quantized states have been observed in a double-layer 2D electron system at filling fractions  $\nu = 1/2$  and  $\nu = 1$ . Studies of samples with different densities and layer separations and experiments with in-plane magnetic fields establish a strong argument that these two states arise from an interplay between intra- and inter-layer Coulomb interactions.

### 4. References

- [1] For reviews, see: R.E. Prange and S.M. Girvin, Eds., *The Quantum Hall Effect* (Springer, New York, 1987); T. Chakraborty and P. Pietilainen, *The Fractional Quantum Hall Effect*, Vol. 85 of Springer Series in Solid State Physics (Springer, Berlin, 1988).
- [2] J.P. Eisenstein, H.L. Stormer, L.N. Pfeiffer and K.W. West, *Phys. Rev. Lett.* 62 (1989) 1540.
- [3] R.G. Clark, S.R. Haynes, A.M. Suckling, J.R. Mallett, P.A. Wright, J.J. Harris and C.T. Foxon, *Phys. Rev. Lett.* 62 (1989) 1536.
- [4] R.L. Willett, J.P. Eisenstein, H.L. Stormer and D.C. Tsui, *Phys. Rev. Lett.* 59 (1987) 1776.
- [5] E.H. Rezayi and F.D.M. Haldane, *Bull. Am. Phys. Soc.* 32 (1987) 892.
- [6] T. Chakraborty and P. Pietilainen, *Phys. Rev. Lett.* 59 (1987) 2784.
- [7] D. Yoshioka, A.H. MacDonald and S.M. Girvin, *Phys. Rev. B* 39 (1989) 1932.
- [8] B.I. Halperin, *Helv. Phys. Acta* 56 (1983) 75.
- [9] Song He, S. Das Sarma and X.C. Xie, *Phys. Rev. B* 47 (1993) 4394.

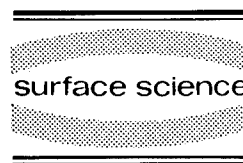


- [10] J.P. Eisenstein, G.S. Boebinger, L.N. Pfeiffer, K.W. West and Song He, *Phys. Rev. Lett.* 68 (1992) 1383.
- [11] Y.W. Suen, L.W. Engel, M.B. Santos, M. Shayegan and D.C. Tsui, *Phys. Rev. Lett.* 68 (1992) 1379.
- [12] G.S. Boebinger, H.W. Jiang, L.N. Pfeiffer and K.W. West, *Phys. Rev. Lett.* 64 (1990) 1793; G.S. Boebinger, in: *High Magnetic Fields in Semiconductor Physics III*, Ed. G. Landwehr, Vol. 101 of Springer Series in Solid State Physics (Springer, Berlin, 1992) p. 155.
- [13] J. Hu and A.H. MacDonald, *Phys. Rev. B* 46 (1992) 12554.
- [14] G.S. Boebinger, L.N. Pfeiffer and K.W. West, *Phys. Rev. B* 45 (1992) 11391.
- [15] A.H. MacDonald, P.M. Platzman and G.S. Boebinger, *Phys. Rev. Lett.* 65 (1990) 775.
- [16] L. Brey, *Phys. Rev. Lett.* 65 (1990) 903.



ELSEVIER

Surface Science 305 (1994) 13–17



## One-component to two-component transitions of fractional quantum Hall states in a wide quantum well

Y.W. Suen <sup>\*</sup>, H.C. Manoharan, X. Ying, M.B. Santos, M. Shayegan

*Department of Electrical Engineering, Princeton University, Princeton, NJ 08544, USA*

(Received 20 April 1993; accepted for publication 22 June 1993)

### Abstract

We report measurements of the quasi-particle excitation gaps for different fractional quantum Hall (FQH) states of a low-disorder, symmetric electron system in a 770 Å wide GaAs quantum well as a function of density,  $N_s$ . At filling factor  $\nu = 1/2$ , the electron system undergoes phase transitions from a compressible (metallic) state to an incompressible (FQH) state and then to an insulating phase as  $N_s$  is increased. The  $\nu = 1/2$  FQH state, observed in the range  $1.0 \times 10^{11} \leq N_s \leq 1.4 \times 10^{11} \text{ cm}^{-2}$ , is remarkably strong and its excitation gap reaches  $\approx 0.9 \text{ K}$  at  $N_s = 1.16 \times 10^{11} \text{ cm}^{-2}$ . Our data suggest that this  $1/2$  FQH state has a two-component origin. We also observe a dramatic transition from a one-component to a two-component FQH state at  $\nu = 2/3$  as  $N_s$  is increased.

Recently, observations of new FQH states at the *even-denominator* Landau level filling factor  $\nu = 1/2$  have been reported for quasi-two-dimensional electron systems (2DESs) in either a wide single quantum well (WSQW) [1,2] or a double quantum well (DQW) [3]. Theoretically, in two-component systems, such as a spin-unpolarized 2DES or a double-layer electron system, the extra (spin or layer-index) degree of freedom can lead to even-denominator FQH states [4–8]. The  $1/2$  FQH state for DQWs in experiments of Eisenstein et al. is clearly a two-component state and fits the theoretical predictions very well. The origin of the  $1/2$  FQH state in a WSQW is more subtle, however, since such a system possesses the duality of a double-layer and a *thick*, single-layer

system. In fact, both one-component [9] and two-component [10] theoretical models have been recently proposed to explain the  $1/2$  FQH state observed in WSQWs. Our previous studies [1,2] show that a 2DES in a symmetric WSQW does undergo a transition from a one-layer to a two-layer system as the density ( $N_s$ ) increases, and that the  $1/2$  state is observed in a range of intermediate  $N_s$ . However, because of the relative weakness of the observed  $1/2$  state, we could not reveal its origin unambiguously.

In this paper, we present data for a new, very high-quality, 770 Å wide, GaAs WSQW sample which shows remarkably strong FQH states at  $\nu = 1/2$  as well as other fractional  $\nu$ . In particular, we report the quasi-particle excitation gaps of different FQH states for varying  $N_s$ , ranging from  $\sim 4 \times 10^{10}$  to  $\sim 2 \times 10^{11} \text{ cm}^{-2}$ . Our detailed study of these states reveals their origin. In the discussion, we will focus on: (i) the origin of the

<sup>\*</sup> Corresponding author.

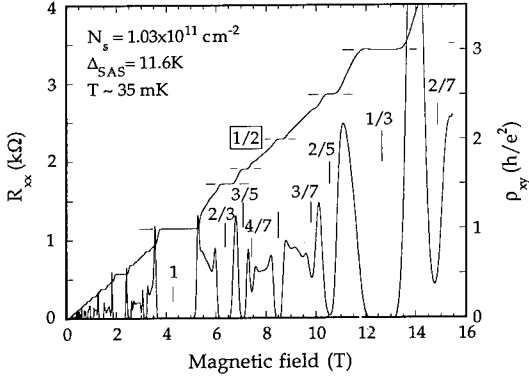


Fig. 1. Magnetotransport data for a 770 Å wide GaAs well with  $N_s = 1.03 \times 10^{11} \text{ cm}^{-2}$ .

1/2 FQH state and phase transitions at  $\nu = 1/2$ ; and (ii) the transition from a one-component to a two-component state for different FQH states as  $N_s$  increases. (The reason we use “one-/two-component state” instead of “one-/two-layer state” will become clear later.)

The sample was grown by molecular beam epitaxy and consists of a wide GaAs well bounded on each side by an undoped  $\text{Al}_{0.35}\text{Ga}_{0.65}\text{As}$  spacer layer and Si  $\delta$ -doped layers. The density in the well is adjusted by front-side and back-side gates and the well is kept symmetric (balanced) for all  $N_s$ . Details of our sample preparation and experimental set-up can be found in our previous work [1,2,11]. The energy difference between the symmetric and antisymmetric subbands ( $\Delta_{\text{SAS}}$ ) is obtained from analysis of the low-field Shubnikov-de Haas data and agrees very well with the  $\Delta_{\text{SAS}}$  determined from self-consistent Hartree-Fock calculations using the local-density-functional approximation for the exchange term [1,2,11].

In Fig. 1 we show the diagonal resistance ( $R_{xx}$ ) and Hall resistivity ( $\rho_{xy}$ ) as a function of magnetic field ( $B$ ), applied perpendicular to the sample plane, for a well-balanced system with  $N_s = 1.03 \times 10^{11} \text{ cm}^{-2}$  (measured  $\Delta_{\text{SAS}} = 11.6 \text{ K}$ ). Excluding the 1/2 FQH state, the structure of all

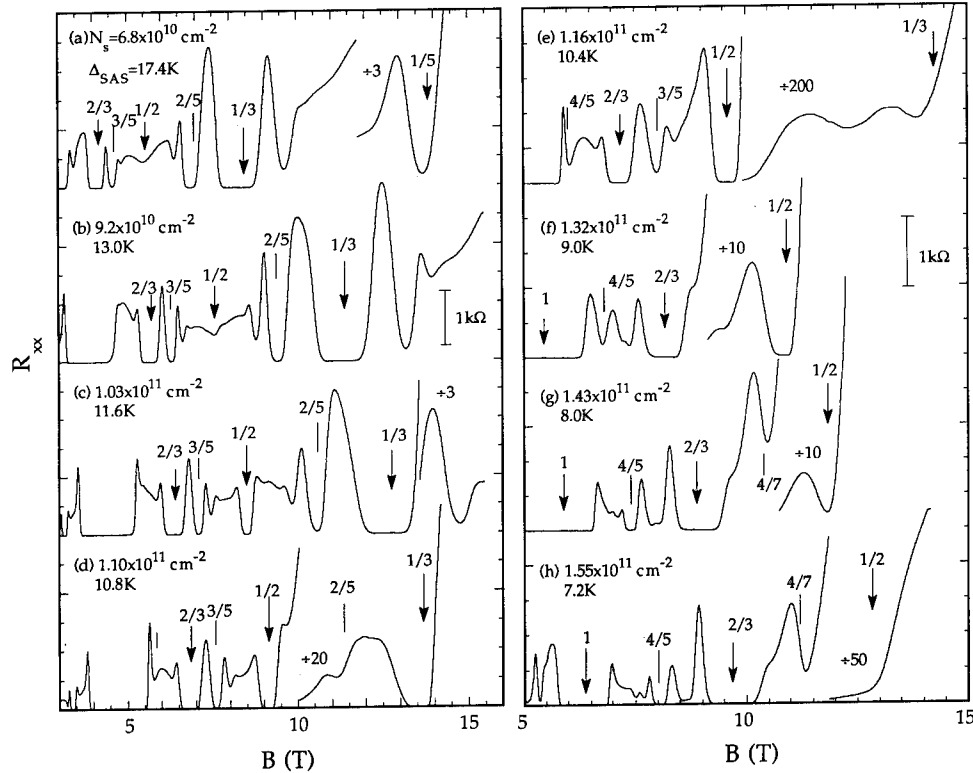


Fig. 2. The evolution of the FQH states in a symmetric 770 Å wide well as  $N_s$  is varied. All the data were taken at  $T \approx 35 \text{ mK}$ .

other IQH and FQH states is strikingly similar to that of a high-quality, standard 2DES in a single heterostructure.

We present the  $R_{xx}$  data at  $\sim 35$  mK for  $\nu \leq 1$  for different  $N_s$  along with the measured  $\Delta_{SAS}$  in Fig. 2. Compared to our previous data [2], the much higher quality of the present sample is evidenced by the presence of stronger and also new (higher order) FQH states even though the electron mobility ( $\mu$ ) is similar ( $\mu \approx 1 \times 10^6$  cm<sup>2</sup>/V·s for  $N_s \approx 1 \times 10^{11}$  cm<sup>-2</sup>). In particular, the 1/2 state develops remarkably stronger than any previously reported data [1–3], allowing us to measure its quasi-particle excitation gap ( $\Delta_{1/2}$ ) in a very large range of  $N_s$ . The 1/2 FQH state is strongest at  $N_s = 1.16 \times 10^{11}$  cm<sup>-2</sup> and has a gap of  $\sim 0.9$  K. Also noteworthy in the data of Fig. 2 is the appearance of an insulating phase (IP), manifested by a diverging  $R_{xx}$  as  $T \rightarrow 0$ , at high  $B$ . (We also observed a similar IP in Ref. [2].) The origin of this IP is not clear, but we believe it is not a result of single-particle localization since it moves to higher  $\nu$  as  $N_s$  (and  $\mu$ ) increase, and also it is reentrant around well-developed FQH states (e.g., around the 1/3 FQH state at  $N_s = 1.1 \times 10^{11}$  cm<sup>-2</sup> and around the 1/2 state at  $N_s = 1.3 \times 10^{11}$  cm<sup>-2</sup>). In this paper we will not discuss this IP further, except to note that the weakening of the 1/2 FQH state at high  $N_s$  is partially caused by this IP.

To begin the discussion, we introduce several important parameters. The relevant length scales are the well width ( $w$ ) and the magnetic length  $l_B = (\hbar/eB)^{1/2}$ . The relevant energies at  $T = 0$  are: (1)  $\Delta_{SAS}$ ; (2)  $Ce^2/\epsilon l_B$ , the in-plane Coulomb correlation energy, where  $C$  is a constant  $\sim 0.1$ ; and (3)  $e^2/\epsilon d$ , the Coulomb energy along the normal of the 2DES plane, where  $d \approx w$  is a measure of the effective interlayer separation. For a 2DES in a WSQW, the transitions between one- and two-component states are determined by the competition between these three energies [12]. Here, we neglect the spin degree of freedom, assuming that it is frozen out at large  $B$  where the correlated states are observed.

When  $Ce^2/\epsilon l_B \lesssim \Delta_{SAS}$ , i.e. when the subband separation is large compared to the in-plane (intra-layer) correlation energy, the upper (antisym-

metric) state is unlikely to mix into the many-body ground state. For  $\nu < 1$ , the 2DES occupies the lowest Landau level of the symmetric subband and exhibits one-component FQH states, such as 1/3, 2/3, 3/5, etc., similar to a normal 2DES in a single heterojunction but with reduced strength due to the thickness of the electron layer [13]. On the other hand, if the in-plane correlation energy is sufficiently strong ( $Ce^2/\epsilon l_B \gtrsim \Delta_{SAS}$ ), the anti-symmetric state can mix into the correlated ground state to lower its energy. This mixing can result in a reduction and eventual collapse of  $\Delta_{SAS}$  [14]. Such a system then behaves as a two-component system, the “components” being the (degenerate) symmetric and antisymmetric states [15]. Now in a WSQW, as in a double-layer electron system in a DQW, two types of two-component FQH states may be possible, depending on the strength of the “interlayer” Coulomb interaction ( $\sim e^2/\epsilon d$ , but note that  $d$  is hard to define for a WSQW in a  $B$  field). When  $e^2/\epsilon d$  is sufficiently small, the system behaves as two independent layers in parallel, each with a density equal to  $N_s/2$ . An example of a two-component FQH state in such a system is the  $\Psi^{330}$  state which has  $\nu = 2/3$  (1/3 filling for each layer) [7,8]. Note that such FQH states always have a  $\nu$  with even numerator and, since each layer is a single-component 2DES, odd denominator. On the other hand, if  $e^2/\epsilon d$  is large enough, a second type of FQH state, one with strong interlayer correlation, is possible. Such a FQH state is unique to two-component systems and can be at even-denominator  $\nu$ ; an example is the  $\Psi^{331}$  FQH state with  $\nu = 1/2$ .

In Fig. 3, we plot the measured quasi-particle excitation gaps ( $\Delta_\nu$ ) for FQH states of different  $\nu$  versus the relevant energy ratio  $\alpha \equiv \Delta_{SAS}/(e^2/\epsilon l_B)$ . Based on the arguments of the preceding paragraphs we expect that, for a given  $\nu$ , the one- or two-component FQH states become stronger at larger or smaller  $\alpha$ , respectively. (Note also that for fixed  $\nu$ ,  $\alpha$  increases with decreasing  $N_s$  as both  $\Delta_{SAS}$  and  $l_B$  are larger for smaller  $N_s$ .) This is clearly evidenced in Fig. 3: the one-component states such as 1/3 and 3/5 get weaker at lower  $\alpha$  and eventually collapse at sufficiently small  $\alpha$ . The 4/5 state, on the other hand, shows

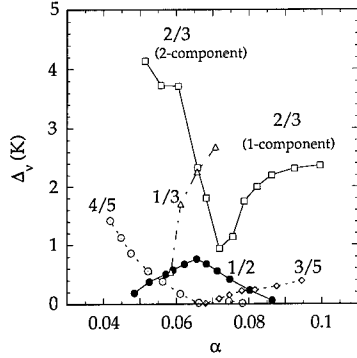


Fig. 3. The quasi-particle excitation gaps ( $\Delta_\nu$ ) vs. the ratio of the symmetric to antisymmetric energy gap to the in-plane correlation energy,  $\alpha \equiv \Delta_{\text{SAS}}/(e^2/\epsilon l_B)$ , for different filling factors ( $\nu$ ). Toward larger  $\alpha$ , one-component states are more stable; toward smaller  $\alpha$ , two-component states are more stable and one-component states collapse.

the opposite behavior; this state can be associated with a two-component state ( $2/5$  filling for each layer). The  $\nu = 2/3$  state exhibits a pronounced minimum in  $\Delta_{2/3}$  as a function of  $\alpha$ . We attribute this behavior to a phase transition from a one-component FQH state at large  $\alpha$  to a two-component ( $\Psi^{330}$ ) state at low  $\alpha$  [16]. We can identify the one- and two-component states by examining the transport behavior while unbalancing the well with  $N_s$  fixed. The details of this experiment will be reported elsewhere.

The dependence of  $\Delta_{1/2}$  on  $\alpha$  is more subtle. As  $\alpha$  decreases below about  $\sim 0.09$ ,  $\Delta_{1/2}$  increases suggesting that the  $1/2$  FQH state in this system has a two-component origin.  $\Delta_{1/2}$  then decreases for  $\alpha < 0.065$  and vanishes when  $\alpha < 0.045$ . We believe that this weakening of the  $1/2$  FQH state at low  $\alpha$  is a result of the dramatic rise in  $R_{xx}$  and the insulating phase that sets in at low  $\nu$  and large  $N_s$  in WSQWs (see Fig. 2 and also data of Ref. [2]). We emphasize, however, that even in the absence of the insulating phase, a two-component  $1/2$  FQH state is likely to be stable only in a finite range of  $\alpha$  [10]. We conclude, therefore, that both the behavior of  $\Delta_{1/2}$  with  $\alpha$  and also the value of  $\alpha$  ( $\sim 0.09$ ) below which the  $1/2$  FQH state starts to emerge are

suggestive that this state has a two-component origin.

We thank D.C. Tsui and S. He for informative discussions, and L.W. Engel for technical assistance. H.C. Manoharan acknowledges fellowship support from the Fannie and John Hertz Foundation. This work was supported by the National Science Foundation.

## 1. References

- [1] Y.W. Suen, L.W. Engel, M.B. Santos, M. Shayegan and D.C. Tsui, Phys. Rev. Lett. 68 (1992) 1379.
- [2] Y.W. Suen, M.B. Santos and M. Shayegan, Phys. Rev. Lett. 69 (1992) 3551.
- [3] J.P. Eisenstein, G.S. Boebinger, L.N. Pfeiffer and S. He, Phys. Rev. Lett. 68 (1992) 1383.
- [4] B.I. Halperin, Helv. Phys. Acta 56 (1983) 75.
- [5] E.H. Rezayi and F.D.M. Haldane, Bull. Am. Phys. Soc. 32 (1987) 892.
- [6] T. Chakraborty and P. Pietilainen, Phys. Rev. Lett. 59 (1987) 2784.
- [7] D. Yoshioka, A.H. MacDonald and S.M. Girvin, Phys. Rev. B 39 (1989) 1932.
- [8] S. He, X.C. Xie, S. Das Sarma and F.C. Zhang, Phys. Rev. B 43 (1991) 9339.
- [9] M. Greiter, X.G. Wen and F. Wilczek, Phys. Rev. B 46 (1992) 9586.
- [10] S. He, S. Das Sarma and X.C. Xie, Phys. Rev. B 47 (1993) 4394.
- [11] Y.W. Suen, J. Jo, M.B. Santos, L.W. Engel, S.W. Hwang and M. Shayegan, Phys. Rev. B 44 (1991) 5947; Surf. Sci. 263 (1992) 152.
- [12] The Coulomb correlation is also sensitive to the shape of the electron wavefunctions and the charge distribution. However, it is hard to parametrize them, specially in the presence of magnetic field.
- [13] M. Shayegan, J. Jo, Y.W. Suen, M. Santos and V.J. Goldman, Phys. Rev. Lett. 65 (1990) 2916.
- [14] Similar arguments have been used to explain the magnetic-field-induced collapse of integer quantum Hall states in DQWs. See, e.g., G.S. Boebinger, L.N. Pfeiffer and K.W. West, Phys. Rev. B 45 (1992) 11391; and A.H. MacDonald, P.M. Platzman and G.S. Boebinger, Phys. Rev. Lett. 65 (1990) 775.
- [15] The two components may also be thought of as “layers”, the basis states labeled by layer index simply being linear combinations of symmetric and antisymmetric wavefunctions.
- [16] We note the  $2/3$  transition we observe occurs at  $B \approx 7.5$  T. This is much larger than  $B \approx 3.3$  T, where a  $2/3$

transition has been reported for single-layer 2DES in a standard GaAs/AlGaAs heterojunction and has been attributed to the spin polarization of the electron system. R.G. Clark, S.R. Haynes, J.V. Branch, A.M. Suckling, P.A. Wright, P.M. Oswald, J.J. Harris and C.T. Foxon, *Surf. Sci.* 229 (1990) 25;

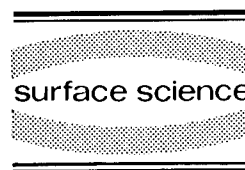
J.P. Eisenstein, H.L. Stormer, L.N. Pfeiffer and K.W. West, *Phys. Rev. B* 41 (1990) 7910;

L.W. Engel, S.W. Hwang, T. Sajoto, D.C. Tsui and M. Shayegan, *Phys. Rev. B* 45 (1992) 3418.



ELSEVIER

Surface Science 305 (1994) 18–22



## Experimental evidence for composite particles in the fractional quantum Hall effect

R.R. Du <sup>\*,a</sup>, D.C. Tsui <sup>a</sup>, H.L. Stormer <sup>b</sup>, L.N. Pfeiffer <sup>b</sup>, K.W. West <sup>b</sup>

<sup>a</sup> Princeton University, Princeton, NJ 08544, USA

<sup>b</sup> AT&T Bell Laboratories, Murray Hill, NJ 07974, USA

(Received 31 May 1993; accepted for publication 15 July 1993)

### Abstract

We have measured the temperature dependence of the transport coefficient  $\rho_{xx}$  at the lowest Landau level fractional quantum Hall effect filling factors  $\nu = p/(2p \pm 1)$ , up to  $p = 5$ , in a high-quality two-dimensional electron system. Our data establish that the gap energies separating the excitations from their quantum liquid ground states are linear with  $\Delta B$ , the magnetic field deviation from exact half-filling. We interpret this linearity as evidence for Landau level quantization of composite particles and deduce the effective mass and the scattering times of the particles.

### 1. Introduction

While the origin of the fractional quantum Hall effect (FQHE) [1] at primary filling factor  $\nu = 1/m$  ( $m$  odd) is well understood in terms of Laughlin's wavefunction and its fractionally charged quasiparticle excitations [2,3], theoretical models for the higher-order FQHE state at  $\nu = p/q$  remain controversial. The nature of the higher-order states gains additional interest since it affects also our general view of the FQHE.

The quasi-particle condensation hierarchy constructed by Haldane [4], Halperin [5], and Laughlin [3] invokes formations of Laughlin states of fractionally charged quasiparticles from lower-order quantum liquids. This process can be con-

tinued *ad infinitum* and covers all odd-denominator rational filling factors. Wavefunctions of such states are expressed in terms of quasiparticle coordinates and so far could not be formulated in terms of electron coordinates. Translating energy calculations for Laughlin's wavefunction to the pseudo-wavefunctions of quasiparticles, Halperin derived approximate gap energies which scale as  $|1/q|^{5/2}$ , where  $q$  is the denominator of the rational filling factor [5]. A conceptual difficulty in the hierarchical scheme was stressed later by Jain [6]. It questions the validity of the quasiparticle picture when the density of the quasiparticles required by condensation becomes exceedingly large.

Despite their importance, the gap energies of the FQHE states at  $\nu = p/(2p \pm 1)$  have not been widely pursued, both in theory and in experiment. Few-electron numerical calculations of gap energy at  $\nu = 1/3$  have converged to  $0.10 e^2/\epsilon l_0$  for

\* Corresponding author.

the ideal case, where  $l_0 = (\hbar/eB)^{1/2}$  is the magnetic length, and  $\epsilon$  is the dielectric constant. Numerical results for other filling fractions have so far been limited to  $2/5$ ,  $3/7$  and  $2/7$  [7]. Much uncertainty remains for the states  $\nu = p/(2p \pm 1)$  as  $p$  become large. The experimental gap energy at  $\nu = 1/3$ , as determined in very high mobility GaAs/AlGaAs heterostructure, has only recently approached the theoretical value, after proper corrections for their non-ideality had been made [8]. Preliminary experimental results [9] indicated that gap energies of higher-order states in fact deviated considerably from the scaling of  $|1/q|^{5/2}$ .

Currently promoted theories provide a new perspective on our general view of the FQHE. Jain has constructed a trial wavefunction for the spin-polarized states, in which the FQHE is the integer quantum Hall effect of composite fermions. A composite fermion is an electron bound to an even number of flux quanta [6]. By introducing a Chern–Simons gauge field interacting with electrons, Halperin, Lee and Read (HLR) have developed a Fermi liquid theory for the half-filled Landau level [10]. Kalmeyer and Zhang similarly propose that the  $\nu = 1/2$  is a metallic phase [11].

It is most remarkable that even in the presence of potential fluctuations, a well-defined Fermi surface of wave vector  $k_F = 1/l_0$  exists at  $\nu = 1/2$ , where the effective magnetic field  $\Delta B$  seen by the fermions is zero. The external magnetic field  $B$  corresponding to  $\nu = p/(2p \pm 1)$  satisfies

$$\Delta B = (B - B_{1/2}) = \pm [h/e]n/p,$$

where  $B_{1/2} = 2nh/e$  is the magnetic field corresponding to  $\nu = 1/2$  at electron density  $n$ . HLR predict that apart from a logarithmic correction, the gap energies are proportional to  $1/p$  in the limit of large  $p$ , in contrast with  $|1/q|^{5/2} = |1/(2p \pm 1)|^{5/2}$ . There remains some uncertainty, however, for the case where  $p$  is small, i.e., the filling factor deviates considerably from half.

In this paper we report on a careful experimental determination of the higher-order FQHE gaps at fraction  $\nu = p/(2p \pm 1)$ , up to  $p = 5$ , in a high-quality two-dimensional electron system

(2DES). Our data establish that the gap energies are *linear* with  $\Delta B$ , the magnetic field deviation from  $\nu = 1/2$ .

## 2. Experimental

We have measured temperature ( $T$ ) dependence of the transport coefficient  $\rho_{xx}$  on a series of modulation doped GaAs/AlGaAs heterostructure samples. Our data focused on two samples each having density  $n = 1.12 \times 10^{11} \text{ cm}^{-2}$ , low  $T$  mobility  $\mu = 6.8 \times 10^6 \text{ cm}^2/\text{V} \cdot \text{s}$  (sample A) and  $n = 2.30 \times 10^{11} \text{ cm}^{-2}$ ,  $\mu = 12 \times 10^6 \text{ cm}^2/\text{V} \cdot \text{s}$  (sample B). In both samples the distance between the electron layer and the Si doping layer is  $d_s = 800 \text{ \AA}$ . Both samples are  $5 \text{ mm} \times 5 \text{ mm}$  square with eight In contacts. The low  $T$  data were taken in a modified Oxford  $^3\text{He}/^4\text{He}$  dilution refrigerator, capable of achieving  $\sim 25 \text{ mK}$  base temperature in a 30 T field of a hybrid magnet. For  $T$  ranging from 0.5–4.2 K we used a  $^3\text{He}$  and a  $^4\text{He}$  cryostat.

An overview of the FQHE (sample B) around  $\nu = 1/2$  is displayed in Fig. 1, where  $\nu = 1/3$  is at  $B = 28.5 \text{ T}$ . For both samples, we observed  $\rho_{xx}$  minima up to fractions  $9/19$  and  $9/17$ . The lower density sample (sample A, Fig. 2) also shows FQHE states descending from  $\nu = 1/4$ , in a se-

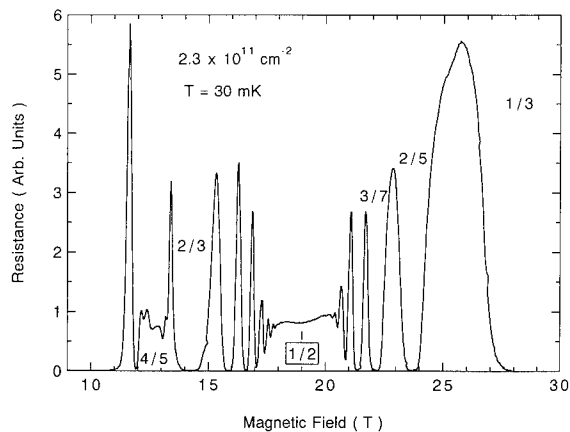


Fig. 1. Fractional quantum Hall effect states around  $\nu = 1/2$  in sample B.



ries of  $p/(4p-1)$ . We omit here the activation energy results for  $\nu < 1/4$  since the proximity of the insulating phase [12] leads to an increase resistivity at low  $T$ .

We derive the gap energy,  $\Delta$ , from the temperature dependence of  $\rho_{xx} \propto \exp(-\Delta/2kT)$  via an Arrhenius plot. The diagonal resistivity is proportional to the conductivity since  $\sigma_{xx} = \rho_{xx}/(\rho_{xx}^2 + \rho_{xy}^2)$  and  $\rho_{xx} \ll \rho_{xy}$ , throughout our experiments.

A recent study of the FQHE activation energies in high mobility samples proposes that a prefactor  $1/T$  should be invoked when  $kT$  exceeds the half-width  $\gamma$  of the extended states [13]. In our case  $kT \approx \gamma$  and both fitting formulas result in values which agree with one another within 15%. We deduce  $\Delta$  from fittings which neglect the prefactor.

Temperature dependences of the resistance minima at filling fractions  $1/3$ ,  $2/5$ ,  $3/7$ ,  $4/9$  and  $5/11$  for sample A are plotted in Fig. 3. Except for the last fraction, regions of activated resistivity extend over more than one decade in  $\rho_{xx}$ . We also include data for the fraction  $\nu = 5/11$  (and  $6/11$ ) to exemplify the limits of this procedure. The observation of well-defined plateaus in  $\rho_{xy}$ , while missing for yet higher-denominator fractions, increases our confidence in assigning a gap energy to these fractions.

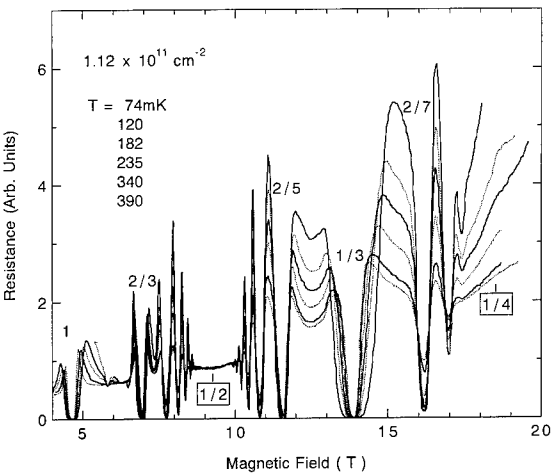


Fig. 2. Resistivity  $\rho_{xx}$  of sample A at various temperatures.

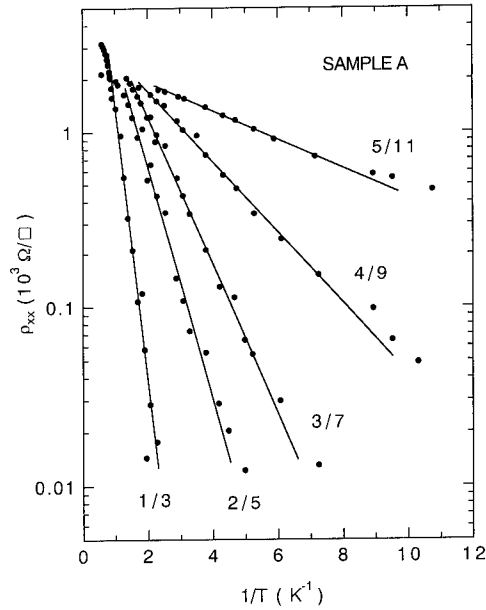


Fig. 3. Temperature dependence of resistivity  $\rho_{xx}$  for various fractions in sample A.

### 3. Results and discussion

We observe a striking linearity between experimental gap energies and the magnetic field for the sequence of higher-order states around filling factor  $\nu = 1/2$ .

Fig. 4 shows data for sample A (closed circles) as well as sample B (open circles) in a single graph. The magnetic axes have been scaled, so that equivalent filling factors coincide. The linearity is emphasized by four straight line sections emanating from  $\nu = 1/2$ . All lines intercept  $\nu = 1/2$  at negative energies. These offsets are nearly identical for the upper and the lower sequence of fractions in each sample. We make the following observations.

(a) We can characterize our findings phenomenologically in very simple terms once we establish  $B_{1/2}$  at  $\nu = 1/2$  as a new origin for  $B$  and adopt its deviation from this value,  $\Delta B$ , as the *effective magnetic field*. Since the gap energies are linear in  $\Delta B$  they can be characterized by an effective mass  $m^*$  via  $\hbar\omega_c = \hbar e(\Delta B)/m^*$  in analogy to the Landau level spectrum and the field dependent occupation of electrons in the

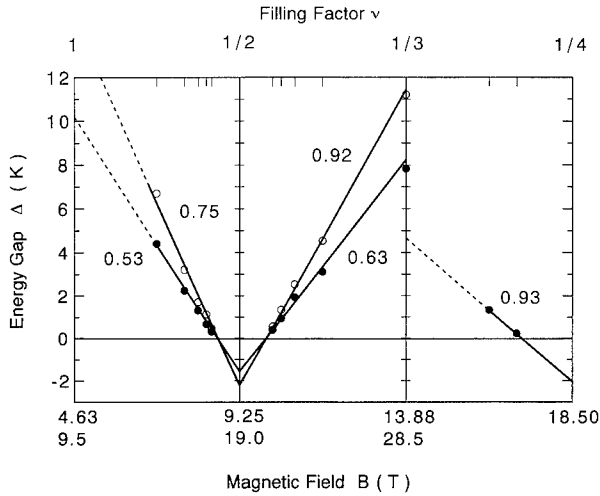


Fig. 4. Gap energies for FQHE states in the vicinity of  $\nu = 1/2$  and  $\nu = 1/4$  in sample A (closed circles) and B (open circles) plotted vs. magnetic field. Straight lines are a guide to the eye. The number associated with each line represents the effective mass in units of  $m_e$ .

presence of a magnetic field. The value of  $\hbar\omega_c$  is reduced by a broadening factor  $\Gamma$  of the levels, assumed to be field independent.

(b) The effective masses are about one order of magnitude bigger than the band electron mass  $m_b \approx 0.07 m_e$  of GaAs. The values for  $m^*$  (in units of free electron mass  $m_e$ ) are indicated in Fig. 4. The mass deviates from the band mass of the electron since it is purely a measure for the strength of the many-particle interaction. In an ideal 2DES, we expect them to scale as  $l_0^{-1}$  and hence as  $B^{1/2}$ . This scaling is closely observed in our samples where density and hence magnetic

field scales differ by a factor of 2 and mass ratios are very close to  $\sqrt{2}$ .

(c) The scattering behavior of the composite particles is strongly modified from regular electrons around zero field. We list in Table 1 three relevant scattering times. The transport scattering time  $\tau^t = m^*/ne^2\rho$  is derived from the resistivity  $\rho$  and the mass  $m^*$  of the carrier. The relaxation time  $\tau^r = \hbar/\Gamma$  is derived from the level broadening  $\Gamma$ . We also define a cyclotron scattering time  $\tau^c = 1/\omega_c$  from the onset of oscillations in  $\rho_{xx}$ .

It is interesting to contrast the scattering behavior of the composite particles with electrons. The ratio  $\tau_e^t/\tau_e^c \approx 30$  and 100 for sample A and B, respectively, exemplifies the well documented [14] weak scattering behavior of electrons in modulation-doped GaAs. The equivalent ratio  $\tau_f^t/\tau_f^c = 2$  and 2.8 for the carriers in the same samples clearly classifies the scattering in these particles as very strong. At the same time  $\tau^c$  varies by less than a factor of 1.5 between electrons and the composite particles for each sample. The data indicate that the rate at which carriers are being scattered is nearly identical but the scattering strength differs widely between electrons and the composite particles.

In conclusion, we have established that the gap energies of the FQHE at  $\nu = p/(2p \pm 1)$  are linear with  $\Delta B$ , the magnetic field deviated from half-filling. We regard this linearity as evidence for Landau level quantization of the composite particles. We have also been able to deduce two important parameters of the particle. The effective masses of the new particles are found to be almost one order of magnitude bigger than the band electron mass and their scattering behavior is strongly modified.

The experiments were performed at FBNML in Cambridge, MA, USA. R.R.D. and D.C.T. are supported in part by the AFOSR (AFOSR-910353) and a grant from the NEC corporation.

#### 4. References

- [1] D.C. Tsui, H.L. Stormer and A.C. Gossard, Phys. Rev. Lett. 48 (1982) 1559.

Table 1  
Scattering times  $\tau$  (in  $10^{-12}$  s) for sample A and B

	Sample A	Sample B
$\tau_e^t$	270	480
$\tau_e^c$	9	4.5
$\tau_f^t$	12	14
$\tau_f^c$	6	5
$\tau_f^r$	5.1	3.3
$\tau_f^t$ (1/4)	2.3	—
$\tau_f^c$ (1/4)	6	—
$\tau_f^r$ (1/4)	3.8	—

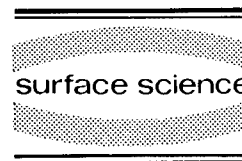
Except where indicated by (1/4) the subscript f refers to  $\nu = 1/2$ .

- [2] R.B. Laughlin, *Phys. Rev. Lett.* 50 (1983) 1395.
- [3] R.E. Prange and S.M. Girvin, Eds., *The Quantum Hall Effect* (Springer, New York, 1990).
- [4] F.D. Haldane, *Phys. Rev. Lett.* 51 (1983) 605.
- [5] B.I. Halperin, *Phys. Rev. Lett.* 52 (1984) 1583; *Phys. Rev. Lett.* 52 (1984) 2390(E).
- [6] J.K. Jain, *Phys. Rev. Lett.* 63 (1989) 199; *Phys. Rev. B* 40 (1989) 8079; *Phys. Rev. B* 41 (1990) 7653.
- [7] N. d'Ambrumenil and R.H. Morf, *Phys. Rev. B* 40 (1989) 6108.
- [8] R.L. Willett, H.L. Stormer, D.C. Tsui, A.C. Gossard and J.H. English, *Phys. Rev. B* 37 (1988) 8476.
- [9] H.W. Jiang, H.L. Stormer, D.C. Tsui, L.N. Pfeiffer and K.W. West, unpublished.
- [10] B.I. Halperin, P.A. Lee and N. Read, *Phys. Rev. B* 47 (1993) 7312.
- [11] V. Kalmeyer and S.C. Zhang, *Phys. Rev. B* 46 (1992) 9889.
- [12] H.W. Jiang, R.L. Willett, H.L. Stormer, D.C. Tsui, L.N. Pfeiffer and K.W. West, *Phys. Rev. Lett.* 65 (1990) 633.
- [13] K. Katayama, D.C. Tsui and M. Shayegan, *Phys. Rev. B*, to be published.
- [14] S. Das Sarma and F. Stern, *Phys. Rev. B* 32 (1985) 8442.



ELSEVIER

Surface Science 305 (1994) 23–32



# Occurrence of a bulk-like electron phase in the cyclotron resonance of GaAs inversion channels in the extreme quantum limit

C.M. Engelhardt <sup>\*,a</sup>, E. Gornik <sup>b</sup>, M. Besson <sup>a</sup>, G. Böhm <sup>a</sup>, G. Weimann <sup>a</sup>

<sup>a</sup> Walter Schottky Institut, TU München, Am Coulombwall, D-85748 Garching, Germany

<sup>b</sup> Institut für Festkörperelektronik, TU Wien, A-1040 Wien, Austria

(Received 30 April 1993; accepted for publication 12 July 1993)

## Abstract

Cyclotron resonance (CR) of 2D electron gases in GaAs has been systematically studied in the extreme quantum limit. Below a critical filling factor of about  $1/9$  a splitting is observed in the resonance line. For very low filling factors ( $\sim 1/20$ ) the splitting becomes nearly identical to the bulk GaAs CR spin-splitting. At intermediate filling factors the behaviour of the splitting strongly differs from the expected single particle spin-splitting. Above the critical filling factor a single hybridized resonance is observed. The characteristics of the transition regime are investigated by a careful analysis of CR masses, carrier densities and scattering rates. Electron–electron interaction as well as localization effects are discussed in the interpretation of the observations.

## 1. Introduction

Cyclotron resonance (CR) has been successfully applied to the investigation of nonparabolicity [1], screening effects [2], scattering mechanisms [3] and resonant subband Landau level coupling [4] in recent years. An unanswered question is the different signature of the Zeeman splitting in the CR of bulk and 2D electron systems. The energy dependence of the  $g$ -factor induced by nonparabolicity causes a splitting of the CR. For the three-dimensional systems this spin-splitting is observed [5,6] in accordance with

theory [7,8]. It is expected as well for the 2D case, but has not been found so far [9,10]. This hybridization of the CR transitions from different spin levels, as observed in most investigations, could not be explained consistently until present. Theoretical approaches to the hybridization involve strong electron–electron interactions. Only recently, the first observations of nonparabolicity-split CR transitions originating from different Landau and spin levels have been reported for strongly nonparabolic InAs/AlSb quantum wells [11,12] in a restricted mobility regime.

A sudden appearance of a splitting in the CR of GaAs 2DEGs in the extreme quantum limit has been reported independently by two groups [13,14]. These works discuss the possible link of the observed phase transition to the formation of

\* Corresponding author.

a short range ordered electron solid. In addition, the similarity of the splitting to the bulk GaAs spin-splitting has been mentioned [14].

In this work we have investigated the possible parameters leading to the suppression of the splitting at higher filling factors. On the basis of most recent data and careful analysis of CR masses, carrier densities and scattering rates a detailed description of the properties of the transition from the presumably spin-split CR to the hybridized CR is given. Possible mechanisms involved in the interpretation of the splitting are discussed.

## 2. Experimental technique

The cyclotron resonance measurements are performed in a standard arrangement of a commercial rapid scan Fourier transform spectrometer connected via a lightpipe to a  $^4\text{He}$  cryostat.

Temperatures down to 0.4 K were accessible by the use of a  $^3\text{He}$  insert. The maximum investigated temperatures were 70 K. A superconducting magnet provided magnetic fields up to 17 T. The transmitted far infrared radiation is detected with a silicon bolometer. The resolution of the spectrometer has been set to  $0.05\text{ cm}^{-1}$ . The carrier densities in the 2DEGs could be increased typically by a factor of 1.5 after illumination of the sample with a red LED by the persistent photo-effect. The spectra are divided by a spectrum taken at  $B = 0\text{ T}$ , yielding the normalized transmission  $T(B)/T(0)$ .

The investigated samples consist of a one-side modulation doped 60–80 Å wide GaAs/AlGaAs single quantum well (SQW) which is separated by a 1400 Å wide  $\text{Al}_{0.41}\text{Ga}_{0.59}\text{As}/\text{GaAs}$  superlattice (sample 1 and 3), or a 500 Å  $\text{Al}_{0.37}\text{Ga}_{0.63}\text{As}$  barrier (sample 2), from a 2  $\mu\text{m}$  thick buffer layer on top of the semi-insulating GaAs substrate. At the interface of the superlattice or the barrier with the buffer a second 2DEG forms (Fig. 1a). In this paper we will be concerned with this inversion channel. It exhibits low carrier densities of  $(0.9\text{--}6.0) \times 10^{10}\text{ cm}^{-2}$  which enables the observation of very low filling factors  $\nu$  ( $\nu = n_s h/eB$ ) down to 1/30. In the SQW carrier densities of

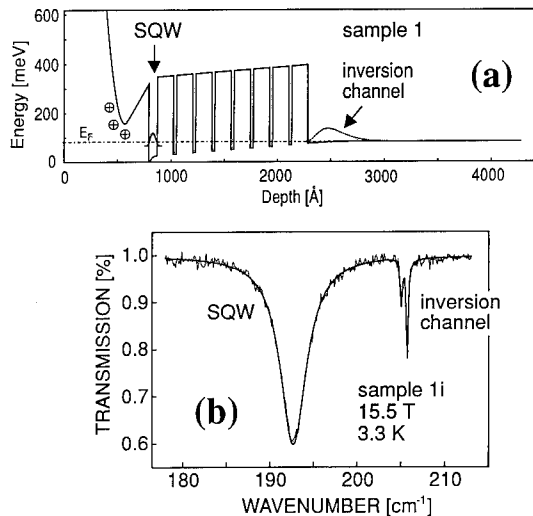


Fig. 1. (a) Conduction band of sample 1 (schematically). The samples incorporate two 2DEGs: A one-side-modulation-doped single-quantum well and an inversion channel at the interface between superlattice and buffer. (b) Typical spectrum for the illuminated sample 1i. The smooth curve represents the fit with a Drude model as described below. The broad resonance corresponds to the quantum well; the sharp and split resonance is that of the inversion channel. In the following, only the latter resonance is discussed.

$(3.0\text{--}7.1) \times 10^{11}\text{ cm}^{-2}$  and mobilities of 50 000 to 265 000  $\text{cm}^2/\text{V}\cdot\text{s}$  are found in transport measurements. The inversion channel could not always be contacted. The carrier densities from magnetotransport were found to match the results of the Drude evaluation of the spectra (see below). The parallel conduction in the SQW however prohibited the determination of the inversion channels mobility by magnetotransport.

The cyclotron resonance lines of the two channels are clearly separated, as shown in Fig. 1b. The broad resonance of the SQW is shifted to lower energy due to the nonparabolicity according to its higher subband energy as compared to the inversion channel. The resonance of the inversion channel is found to be remarkably narrow, FWHMs down to  $0.15\text{ cm}^{-1}$  are observed. The small linewidths are mainly attributed to the free carrier redistribution taking place at filling factors below 1 under the influence of repulsive scatterers of the p-type background doping [3,15]. The SQW is found to stabilize the carrier density

in the inversion channel for weeks. As  $\nu = 2$  is passed in the SQW a change in the intensity of the inversion channels CR of up to 30% is measured. This has been previously attributed to a reduced oscillator strength of the novel electron phase [13]. However, according to the most recent data this has to be interpreted as a reduction in carrier density. Due to the oscillating chemical potential in the SQW, steps in the carrier density evaluated for the inversion channel are found if an even filling factor is passed in the SQW. No influence of the SQWs filling-factor-dependent screening on the scattering rate of the inversion channel is found.

We have used a Drude model to fit the CR lines. The normalized transmission of a system with different types of carriers is calculated from

$$\frac{T(B, \omega = \omega_c)}{T(0, \omega = \omega_c)} = 0.5 + 0.5 \frac{(1 + n_{\text{GaAs}})^2}{|1 + n_{\text{GaAs}} + (1/\epsilon_0 c) \sum \sigma_j|^2},$$

with the index of refraction  $n_{\text{GaAs}}$  and the dynamical conductivities of the different carrier systems

$$\sigma_j = \frac{e^2 n_{sj}}{m_{cj}} \frac{i}{[\omega - \omega_{cj} + (i/\tau_j)]}.$$

The fitting parameters are the CR frequencies  $\omega_{cj}$  (related to the CR mass  $m_{cj}$  by  $\omega_{cj} = eB/m_{cj}$ ), the scattering rates  $1/\tau_j$  and the carrier densities  $n_{sj}$  corresponding to the integrated intensities of the different resonances.

Table 1 gives the typical values of the carrier densities in the presented inversion channels. As

already mentioned, variations with magnetic field occur due to the changing chemical potential in the SQW. Also listed are the lowest intersubband spacings as determined by resonant subband Landau level coupling (RSLC) at full field, which for the low densities investigated here are expected to give the plain intersubband energies [16]. The RSLCs are observed due to the small residual tilt of the samples with respect to the magnetic field direction. They result in an increased CR scattering rate when the CR energy  $\hbar\omega_c$  equals the energy difference  $E_{0-s}$  between 0th and  $s$ th subband. These energies have to be kept in mind in the discussion of higher temperature data, where thermal population of higher 2D subbands occurs ( $2.5 \text{ meV} \approx k_B \times 30 \text{ K}$ ).

### 3. Experimental results

The main feature of the observations is the appearance of an additional resonance above a critical magnetic field. In Fig. 2 the abrupt change in the CR with magnetic field is illustrated for the illuminated sample 1i at 1.2 and 3.0 K. The high energy resonance (in the following labelled (+)) increases in intensity with increasing magnetic field and decreasing temperature at the cost of the low energy resonance (–). At lowest temperatures all oscillator strength is transferred to the (+) resonance. The most drastic change is observed at about 13 T. The evaluation of the spectra shows that this is mostly due to the change in linewidth. The energy separation between the two lines increases with temperature and saturates for temperatures above  $\sim 6 \text{ K}$ . The extrapolated vanishing point of the (+) intensity is for all temperatures 11 T. This onset of the splitting is shifted to lower magnetic field for the unilluminated sample 1 which has less carrier density. Viewed over the scale of filling factor the appearance of the splitting looks much the same in both cases.

To characterize the observed transition, a critical filling factor  $\nu_c$  indicating the onset of the splitting is introduced. In the following  $\nu_c$  will be calculated from the extrapolated magnetic field  $B_c$  at which the (+) resonance vanishes and from

Table 1  
Carrier density and lowest intersubband spacing for the presented inversion channels

Sample No.	$n_s$ ( $10^{10} \text{ cm}^{-2}$ )	$E_{0-1}$ (meV)
1	2.0	6.2
1i	3.5	2.1
2i	2.0	11.2
3	5.5	2.7

Index i: after illumination with a red LED.

the carrier density which is found from the integrated intensity of the resonance at this field. For sample 1 ( $n_s = 2.0 \times 10^{10} \text{ cm}^{-2}$  at  $B_c = 6.5 \text{ T}$ ) and sample 1i ( $n_s = 3.5 \times 10^{10} \text{ cm}^{-2}$  at  $B_c = 11.0 \text{ T}$ ) before and after illumination a critical filling factor of  $\nu_c = 0.13 \approx 1/8$  is found.  $\nu_c$  appears to be sample dependent. Thus for sample 2i a critical filling factor  $\nu_c = 0.11 \approx 1/9$  is evaluated and sample 3 gives  $\nu_c = 0.17 \approx 1/6$ .

At higher temperatures the increasing size of the energy splitting approaches the value found

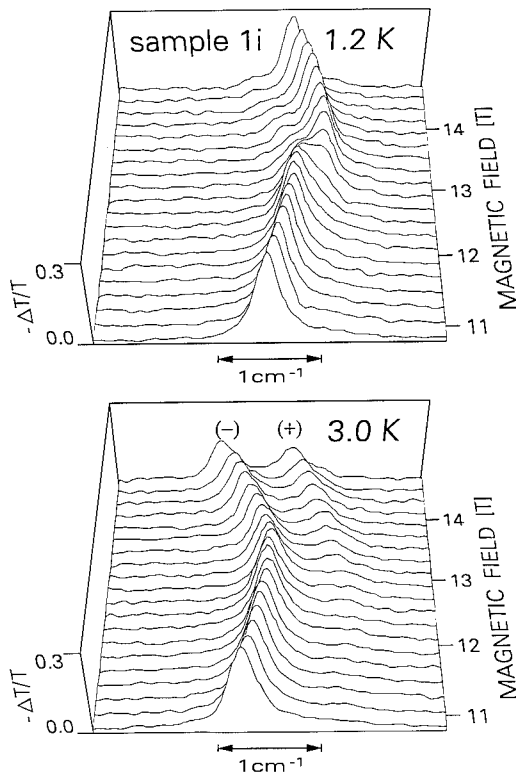


Fig. 2. Two series of CR spectra taken at magnetic fields from 10.8 to 14.6 T at temperatures of 1.2 and 3.0 K illustrating the sudden onset of the splitting. The CR absorption  $-\Delta T/T = 1 - T(B)/T(0)$  is plotted above a relative energy scale. For convenience the spectra have been shifted linearly with magnetic field in energy to come to lie behind each other. For 1.2 K, near 13 T an abrupt exchange of oscillator strength from the low energy (-) to the high energy (+) resonance can be observed. At 3.0 K the change over is not total; most intensity remains in the low energy resonance and the energy separation of the two lines has increased. At high temperatures the size of the splitting approaches the value of the spin-splitting in bulk GaAs (see Fig. 3).

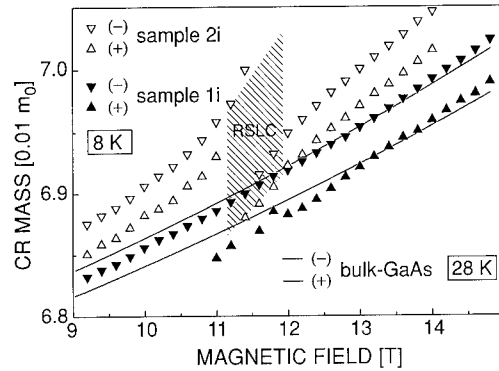


Fig. 3. Comparison of CR masses of sample 1i (filled triangles) and 2i (open triangles) measured at 8 K with the CR masses from the measurement of the spin-split CR of the bulk GaAs at 28 K. The CR positions of the 2DEG are found to be very similar to the bulk spin-splitting positions plus a mass shift due to the 2D subband nonparabolicity. At 11.4 T a resonant subband Landau level coupling is observed for sample 2i, shown by the hatched region.

for the spin-splitting of the CR of free electrons in bulk GaAs. In a nonparabolic dispersion the Zeeman splitting of the Landau levels  $\Delta E = g^* \mu_B B$  is energy dependent. This may be described by an effective  $g$ -factor [17,18]

$$g^* = g_0 + g_1(n + 1/2)B,$$

with the Landau level index  $n$ . This dependency has been confirmed by electron spin resonance investigations of GaAs heterostructures [18]. The accepted value for the conduction band edge  $g$ -factor of GaAs is  $g_0 = -0.44$  [19]. The resulting energy difference in the CR transitions is then  $\Delta \hbar \omega_c = g_1 \mu_B B^2$ . This splitting is observed in bulk GaAs [5,6] and other bulk semiconductors in CR measurements. It is expected as well for 2D electron systems but has not been observed so far [9], even when the CR linewidth has been reduced much below the expected splitting [10].

For a better comparison the CR of a bulk 5  $\mu\text{m}$  thick MBE-grown Si-doped GaAs layer has been measured. In Fig. 3 the CR masses for sample 1i (filled symbols) and sample 2i (open symbols) are plotted along with the CR mass for the spin-splitting in bulk GaAs (lines). The CR of the free electrons in the bulk sample could only be observed for temperatures above 20 K because

of magnetic freeze out. From the slope of the energy splitting plotted over the squared magnetic field a value of  $g_1 = 0.0097 \text{ T}^{-1}$  is found for the bulk CR in good agreement with the findings of Refs. [5,6]. The energy splitting for the 2D samples at temperatures above 6 K has the same value, thus also obeying the  $B^2$  law. The absolute CR masses are shifted to higher values due to the subband nonparabolicity, as shown in Fig. 3. This shift is most pronounced for sample 2i with the highest intersubband spacing (see Table 1). For this sample a coupling of the CR to the  $E_{0-2}$  intersubband energy is observed at 11.4 T. An anticrossing behaviour is resolved, indicated by the hatched area in Fig. 3.

In the following we present data from the transition range between the non-split CR at high filling factors and the spin-splitting-like CR in the extreme quantum limit. Two series of temperature dependent spectra are displayed in Fig. 4a (sample 3, 17 T,  $\nu \approx 1/7$ ) and Fig. 4b (sample 1, 16.7 T,  $\nu \approx 1/20$ ) illustrating the different behaviour of the splitting close to the critical filling factor as opposed to that at very low occupation. Two pronounced features are distinguishable from the spectra. First, in the extreme quantum limit no temperature dependence of the CR positions can be seen (Fig. 4b); however, in the transition regime near  $\nu_c$  (Fig. 4a) the two lines approach each other with decreasing temperature. Second, in Fig. 4a at quite low temperature (about 3 K) the intensities of the two lines invert, while in the extreme quantum limit almost equal occupation is approached at higher temperatures. The corresponding CR masses  $m_c$ , carrier densities  $n_s$  and scattering rates  $1/\tau$ , evaluated according to the above described Drude model are shown in Fig. 5 for the temperature series of Fig. 4b and in Fig. 6 for the series of Fig. 4a.

Fig. 5a displays the CR masses of the (–) and (+) resonances for sample 1 at  $B = 16.7 \text{ T}$ , corresponding to  $\nu \approx 1/20$ . The masses show no significant dependence on temperature; the energy splitting matches the size of the bulk spin-splitting (see above). At low temperatures the intensities of the lines (Fig. 5b) show an activation behaviour corresponding to an effective  $g^*$ -factor of  $g^* = -0.35$ . A model is used where the sys-

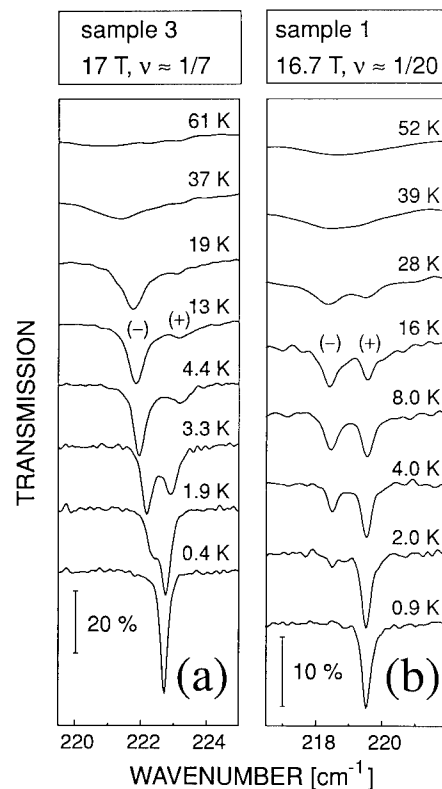


Fig. 4. Temperature dependent measurements for (a): sample 3 at 17 T corresponding to  $\nu \approx 1/7$  and (b): sample 1 at 16.7 T,  $\nu \approx 1/20$ , illustrating the different behaviour of the splitting close to the critical filling factor with respect to the case of very low occupation. In this graph CR transmission  $T(B)/T(0)$  is plotted. The evaluation of the temperature series of (b) is displayed in Fig. 5, the series of (a) is evaluated in Fig. 6.

tem is represented by two  $\delta$ -like densities of states separated by  $g^* \mu_B B$  and populated according to a Fermi distribution. This  $g^*$  is close to the spin-splitting value of  $-0.36$ , calculated from  $g_0$  and  $g_1$  for 16.7 T.

At higher temperatures an inversion of the intensities is found, this effect is much more pronounced at higher filling factors and is in contrast to the expected spin-splitting. In the limit of infinite temperatures the thermal population of two levels with equal density of states should result in equal occupation. This point will



be discussed in detail below. For all samples a slight increase in total carrier density  $n_{s(-)} + n_{s(+)}$  is observed at higher temperatures. This is attributed to thermal ionization of shallow impurities in the vicinity of the channel.

Both scattering rates (Fig. 5c) of the two lines show the same increase with temperature which is similar for all samples at higher temperatures and is attributed to increasing impurity scattering according to the model of free carrier redistribution [15] and phonon scattering.

Figs. 6a–6c show the evaluation of the spectra of sample 3 at 17 T corresponding to a filling factor of about 1/7 (Fig. 4a). All three quantities show a behaviour quite different from spin-splitting. The following characteristics are found for the transition region between the non-split resonance and the spin-splitting behaviour in the extreme quantum limit: First, the two transitions

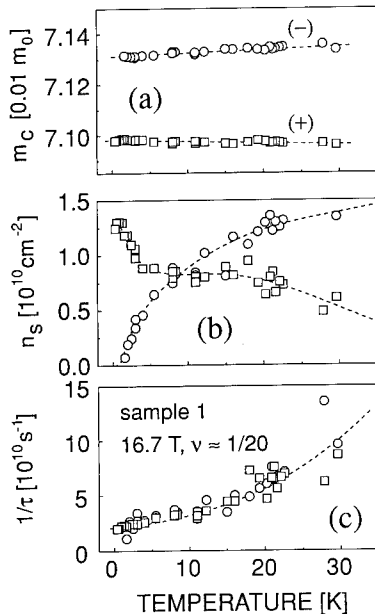


Fig. 5. Evaluation of the temperature series of sample 1 at 16.7 T (corresponding to the spectra of Fig. 4b). (a) CR mass  $m_c$ , (b) carrier density  $n_s$ , corresponding to the integrated intensity of the lines, and (c) scattering rate  $1/\tau$ . The observed size of the splitting and the activation of the intensities are close to the expectations for bulk spin-splitting. The circles correspond to the low energy (-) and the squares to the high energy (+) resonance, the dashed lines are guides to the eye. This convention is also used in the following graphs.

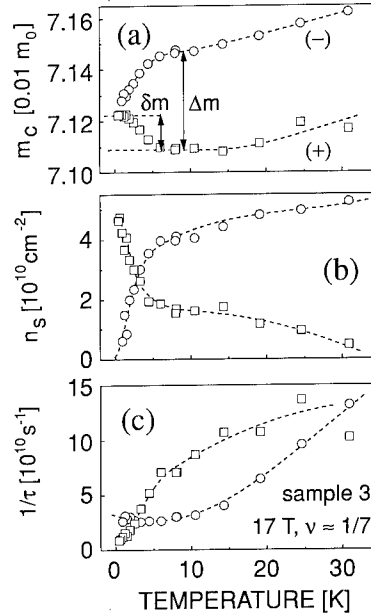


Fig. 6. Evaluation of the temperature series (Fig. 4a) of sample 3 at 17 T. Characteristics of the CR at transition filling factors are (a) the merging of the two transitions at low temperatures as seen in the CR masses  $m_c$ , (b) an inversion of the intensities at medium temperatures displayed by the evaluated carrier densities  $n_s$  and (c) a different behaviour of the scattering rates  $1/\tau$  for the two transitions showing increased scattering for the minority occupation. In (a) the quantities  $\delta m$  and  $\Delta m$ , describing the merging of the transitions at low temperatures, are labelled. These values are used for the evaluation in Fig. 9.

merge for low temperatures and the CR mass slightly increases at higher temperatures (Fig. 6a). Second, the intensities of the two resonances invert at medium temperatures (Fig. 6b), and third, the scattering rates of the two states exhibit a different behaviour (Fig. 6c). All three characteristics become more pronounced as  $\nu_c$  is approached.

In Fig. 6a the quantities  $\delta m$  and  $\Delta m$  describing the mass shift at low temperatures are depicted. They are used for the evaluation shown in Fig. 9. The mass shift  $\delta m$  appears to be related to the change in occupation as seen in the evaluated carrier densities, suggesting a decreasing CR mass for decreasing occupation.

From the activation behaviour of the evaluated carrier densities in Fig. 6b for lowest tempera-

tures a  $g^* = -0.2$  is calculated, which differs from the value of  $-0.36$  expected for spin-splitting. At increasing temperatures,  $g^*$  has to reach even higher values growing well above  $+1$  to account for the inversion of the intensities. This two level model assuming identical densities of states for both states, therefore, implies a crossing of the levels with temperature. If, on the other hand, the energy gap between the two levels is kept constant, a pronounced difference in the density of states for the two levels has to be assumed (see Ref. [13]).

In the transition region the scattering rates of the  $(-)$  and  $(+)$  states strongly differ from each other. Increased scattering is found for the lesser occupied state. Close to the critical filling factor the following relation is found:  $n_{s(-)} \times 1/\tau_{(-)} \approx n_{s(+)} \times 1/\tau_{(+)}$ . For all measurements equal scattering rates are found at the point of equal occupation.

Fig. 7 illustrates the characteristics of the transition regime close to the critical filling factor for sample 1i. The CR masses of six temperature series at magnetic fields from 9.5 T up to 17 T are shown. At higher magnetic fields the masses are shifted to higher values due to the influence of nonparabolicity from the increasing energy of the Landau levels. The increase of CR mass with temperature is attributed to the influence of free carrier redistribution [15]. At filling factors below  $\nu_c$ , that is for magnetic fields 12.5 to 17.0 T the splitting is observed. The  $(+)$  resonance vanishes (like in Fig. 5b) with increasing magnetic fields at higher temperatures. The total carrier density in the channels increases with temperature as already mentioned. As function of filling factor the splitting again vanishes at  $\nu_c$  due to the increased carrier density.

A systematic behaviour of the merging of both transitions at low temperature can be observed. The splitting extrapolates to a finite value for  $T \rightarrow 0$ . The corresponding mass shift is strongest close to  $\nu_c$ . For purpose of comparison the range from the bulk  $(-)$  to the bulk  $(+)$  transition is indicated by the hatched regions. For 9.5 and 11.0 T no splitting and even no broadening of the CR is observed. The mass shift at low temperatures is half the size of the spin-splitting in bulk,

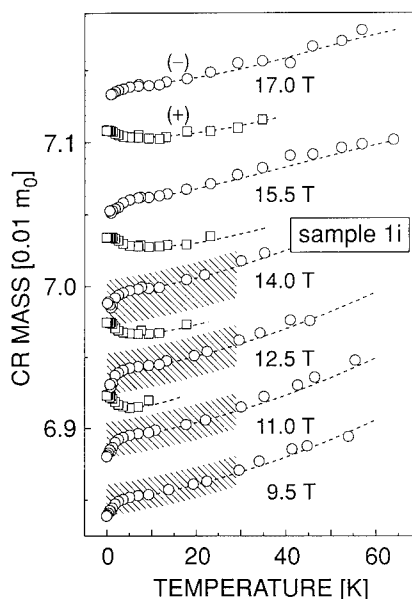


Fig. 7. CR masses for six temperature series of sample 1i at magnetic fields from 9.5 T up to 17 T. For magnetic fields  $\geq 12.5$  T the splitting is observed. The hatched regions provide a comparison to the bulk spin-splitting. In the scale of the mass they extend from the measured  $(-)$  bulk position to the  $(+)$  bulk position, with temperature they follow the overall tendency found in the 2D data.

suggesting that the averaged position of the two hybridized resonances is observed. If the corresponding temperature dependent population of the two states is calculated under this assumption, an activation energy a little below the bulk spin gap is found. In the region of the splitting the  $(-)$  resonance still follows this trend, whereas the  $(+)$  resonance shows a downward shift for increasing temperatures. Therefore, the behaviour of both resonances may be described by an occupation dependent downward shift in CR mass.

Fig. 8 gives an example how the varying intensities of the two lines in the transition regime are expressed by the occupations of the two states. The separate occupations of the two states  $\nu_{(-)}$  and  $\nu_{(+)}$  are calculated with the definition for  $\nu$  (see above) for the corresponding carrier densities  $n_{(-)}$  and  $n_{(+)}$ , so that  $\nu_{(-)} + \nu_{(+)} = \nu$ . Between 11 and 12 T a RSLC disturbs the evaluation of the integrated intensities. It turns out that

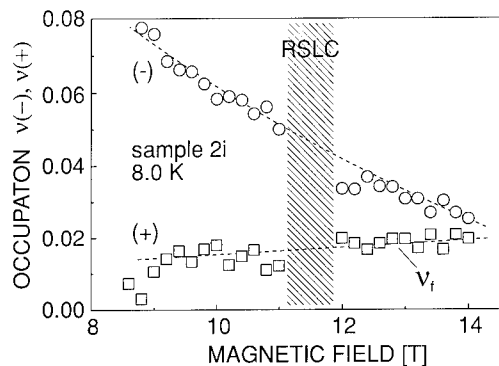


Fig. 8. Separate occupations  $\nu_{(-)}$  and  $\nu_{(+)}$  determined from the intensities of the two transitions for sample 2i at 8 K. Between 11 and 12 T (hatched region) a resonant subband Landau level coupling (RSLC) disturbs the evaluation of the integrated intensities.

the observed inversion of the intensities, which is less pronounced as the filling factor is lowered, is manifested in an almost constant occupation of the (+) state. With increasing magnetic field the reduced filling factor only appears in  $\nu_{(-)}$ . At even lower filling factors  $\nu_{(+)}$  starts to decrease as soon as it is reached by  $\nu_{(-)}$ , which is seen in temperature dependent measurements at lowest filling factors. In the transition region where  $\nu_{(+)}$  keeps almost constant it may be labelled a fixed

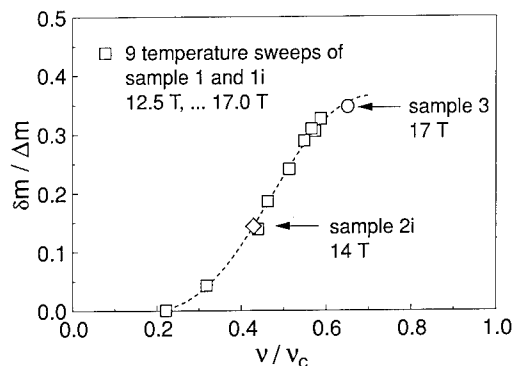


Fig. 9. Low temperature mass shift  $\delta m$  as a fraction of the spin-splitting  $\Delta m$  ( $\delta m$  and  $\Delta m$  as given in Fig. 6a) from the evaluation of eleven temperature sweeps, plotted versus filling factor  $\nu$  as a fraction of the critical filling factor  $\nu_c$ . This graph illustrates the merging of the spin transitions as the critical filling factor is approached.

occupation  $\nu_f$ . For a given temperature  $\nu_f$  is found to depend on sample as  $\nu_c$  does. The constant occupation  $\nu_f$  itself corresponds to a density of states which is proportional to magnetic field.

The mass shift  $\delta m$  as a feature of the transition regime is found to obey a relation independent of the sample, magnetic field and carrier density as shown in Fig. 9. The mass shift  $\delta m$  is normalized by the mass difference  $\Delta m$  corresponding to the size of the spin splitting (both are evaluated as depicted in Fig. 6a). Following the observation that the merging becomes more pronounced as the critical filling factor  $\nu_c$  is approached, the relative filling factor  $\nu/\nu_c$  is calculated. The correlation of  $\delta m/\Delta m$  versus  $\nu/\nu_c$  is surprisingly good.

#### 4. Summary of observations

The 2D character of the investigated inversion channels is reflected by the observed resonant-subband-Landau-level couplings and the subband nonparabolicity appearing in the increased CR mass. The CR in the extreme quantum limit is attributed to a bulk-like phase of 2D electrons in the sense that the observed splitting becomes increasingly similar to the bulk spin-splitting for very low filling factors. In the transition regime a process leading to the hybridization of the spin transitions at higher filling factors is observed.

- The critical filling factor  $\nu_c$ , defined as the onset of the splitting, is sample dependent, indicating an influence of sample quality on the observed effect.  $\nu_c$  does not vary under changed illumination condition, that is for varied carrier densities in the channel.
- At filling factors above  $\nu_c$  no splitting and no broadening of the lines is observed. The mass shift at low temperatures resembles half the spin gap, suggesting that an averaged mass for the transitions from the two thermally populated states is observed. The activation energy deduced under this assumption is found to be little below the spin gap expected for the bulk case.
- The size of the splitting at medium temperatures (around 8 K) obeys the  $B^2$  dependence

according to the same  $g_1$  factor found for bulk. In the extreme quantum limit the activation of the intensities at low temperatures yields values for the spin gap compatible with the  $g_0$  and  $g_1$  factors of the bulk spin-splitting.

A description of the characteristics of the transition regime may provide hints to the understanding of the hybridization of the spin transitions. The main features are:

- The apparent inversion of the intensities can be described by a constant occupation  $\nu_f$ . In the extreme quantum limit almost equal occupations of the  $(-)$  and  $(+)$  states are found. As soon as the  $(+)$  states reaches  $\nu_f$  the surplus intensity is shifted to the  $(-)$  state.  $\nu_f$  shows the same sample dependence as  $\nu_c$ .
- The scattering rates of the  $(-)$  and  $(+)$  transitions strongly differ in this regime. The lesser occupied state exhibits the higher scattering rate. Near  $\nu_c$   $n_{s(-)} \times 1/\tau_{(-)} \approx n_{s(+)} \times 1/\tau_{(+)}$  is obeyed, suggesting a scattering between the two states. At equal occupation the scattering rates are always found to be identical.
- The mass shift at low temperatures as a fraction of the total splitting expressed by  $\delta m/\Delta m$  is found to correlate to  $\nu/\nu_c$ . The merging of the lines is most pronounced at filling factors close to  $\nu_c$ . The extrapolated CR masses (or positions) do not coincide for  $T \rightarrow 0$ . At filling factors below  $1/3 \nu_c$ , the mass shift vanishes. The merging appears not to be an effect of the two spin transitions having equal transition energies, it rather looks like an occupation dependent mass shift for the  $(-)$  and the  $(+)$  transition.

## 5. Discussion of the results

The first observation of a hybridization of CR transitions for different types of electrons has been made by Stallhofer et al. [20] for strained Si(100) where different valleys are occupied. For the explanation of these findings Appel and Overhauser [21] studied the electron–electron interaction in a two component plasma and found hybridization of the CR transitions in the case of strong electron–electron interaction, that is for  $1/\tau_e \gg 1/\tau$  when electron–electron scattering

dominates over electron impurity scattering. Takada and Ando [22] employed the Landau–Fermi liquid theory to show hybridization of CR transition in the case of strong electron–electron interaction.

MacDonald and Kallin [23] used a generalized single mode approximation to calculate the magnetoplasmon dispersion for filling factors  $2 < \nu < 3$ . A magnetoplasmon-like, a spin-wave-like and a non-infrared-active mode is predicted. The magnetoplasmon-like excitation mixes the  $n = 0$  to  $n = 1$  and  $n = 1$  to  $n = 2$  transitions in the limit of strong electron–electron correlation, but spin-splitting should remain observable for vanishing wave vector  $k = 0$ . Translational invariance is necessary to exclude influences of electron–electron interactions on the CR according to Kohn’s theorem [24]. The translational invariance can be broken by nonparabolicity. Therefore electron–electron interactions will couple the transitions until the nonparabolicity exceeds the Coulomb energy.

All these calculations of hybridization of distinct CR transitions involve strong electron–electron interaction. This may suggest for our case an abrupt change in electron–electron interaction at the critical filling factor, which might be introduced by localization of the electrons in the extreme quantum limit, leading to decreased electron–electron scattering. Formation of an electron solid as appears to be observed in magnetotransport, luminescence and microwave experiments (see citations in Refs. [13,14]) might have a similar effect.

The finding of a constant occupation  $\nu_f$  for the  $(+)$  transition at a given temperature suggests a density of states for the associated level which is proportional to magnetic field. The same dependence of  $\nu_f$  and  $\nu_c$  on sample seems to support this interpretation. The downward shift of the  $(+)$  CR masses in Fig. 7 with respect to the extrapolated behaviour of the bulk CR masses would be compatible with stronger binding of the electrons in impurity potentials according to the model for the influence of impurity potentials on the CR energy [25]. The observation of vanishing spin- and Landau-splitting for highest mobilities in the InAs system [12] by Scriba et al. also

indicates the importance of localization for the occurrence of spin-splitting.

We have demonstrated the transition of the 2DEG in the extreme quantum limit from a phase which exhibits bulk-like spin-splitting to a system with hybridized resonances. The hybridization is related to strong electron–electron interaction, which appears to be weakened in the extreme quantum limit under the influence of weak localization induced by magnetic field.

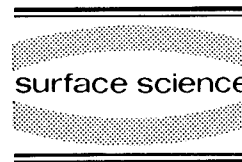
## 6. References

- [1] M.A. Hopkins, R.J. Nicholas, M.A. Brummell, J.J. Harris and C.T. Foxon, *Phys. Rev. B* 36 (1987) 4789.
- [2] M. Besson, E. Gornik, G. Böhm and G. Weimann, *Surf. Sci.* 263 (1992) 650.
- [3] J. Richter, H. Sigg, K. von Klitzing and K. Ploog, *Phys. Rev. B* 39 (1989) 6268.
- [4] Z. Schlesinger, J.C.M. Hwang and S.J. Allen, Jr., *Phys. Rev. Lett.* 50 (1983) 2098.
- [5] H. Sigg, J.A.A.J. Perenboom, P. Pfeffer and W. Zawadzki, *Solid State Commun.* 61 (1987) 685.
- [6] M.A. Hopkins, R.J. Nicholas, P. Pfeffer, W. Zawadzki, D. Gauthier, J.C. Portal and M.A. DiForte-Poisson, *Semicond. Sci. Technol.* 2 (1987) 568.
- [7] M. Braun and U. Rössler, *J. Phys. C* 18 (1985) 3365.
- [8] H. Mayer and U. Rössler, *Phys. Rev. B* 44 (1991) 9048.
- [9] U. Merkt, M. Horst, T. Evelbauer and J.P. Kotthaus, *Phys. Rev. B* 28 (1983) 2271, and references therein.
- [10] M. Watts, R.J. Nicholas, N.J. Pulsford, J.J. Harris and C.T. Foxon, in: *The Physics of Semiconductors*, Eds. E.M. Anastassakis and J.D. Joannopoulos (World Scientific, Singapore, 1990) p. 1465.
- [11] J. Scriba, A. Wixforth, J.P. Kotthaus, C.R. Bolognesi, C. Nguyen, G. Tuttle, J.H. English and H. Kroemer, *Semicond. Sci. Technol.* 8 (1993) 133.
- [12] J. Scriba, A. Wixforth, J.P. Kotthaus, C. Bolognesi, C. Nguyen and H. Kroemer, unpublished, 1992.
- [13] E. Gornik, M. Besson, C.M. Engelhardt and G. Weimann, in: *Low Dimensional Electronic Systems: New Concepts*, Springer Series in Solid-State Sciences, Vol. 111, Eds. G. Bauer, F. Kuchar and H. Heinrich (Springer, Berlin, 1992) p. 226; M. Besson, E. Gornik, C.M. Engelhardt and G. Weimann, *Semicond. Sci. Technol.* 7 (1992) 1274.
- [14] R.J. Nicholas, G.M. Summers, M. Watts, R.J. Warburton, J. Michels, R.A. Lewis, J.J. Harris and C.T. Foxon, in: *Low Dimensional Electronic Systems: New Concepts*, Springer Series in Solid-State Sciences, Vol. 111, Eds. G. Bauer, F. Kuchar and H. Heinrich (Springer, Berlin, 1992) p. 232; G.M. Summers, R.J. Warburton, J.G. Michels, R.J. Nicholas, J.J. Harris and C.T. Foxon, *Phys. Rev. Lett.* 70 (1993) 2150.
- [15] H. Drexler, P. Graf, M. Besson, E. Gornik and G. Weimann, *Phys. Rev. B* 44 (1991) 3105.
- [16] J. Pillath, E. Batke, G. Weimann and W. Schlapp, *Phys. Rev. B* 40 (1989) 5879.
- [17] G. Lommer, F. Malcher and U. Rössler, *Phys. Rev. B* 32 (1985) 6965.
- [18] M. Döbers, F. Malcher, G. Lommer, K. von Klitzing, U. Rössler, K. Ploog and G. Weimann, in: *High Magnetic Fields in Semiconductor Physics II*, Springer Series in Solid-State Sciences, Vol. 87, Ed. G. Landwehr (Springer, Berlin, 1989) p. 386.
- [19] C. Hermann and C. Weisbuch, *Phys. Rev. B* 15 (1977) 823.
- [20] P. Stallhofer, J.P. Kotthaus and F. Koch, *Solid State Commun.* 20 (1976) 519.
- [21] J. Appel and A.W. Overhauser, *Phys. Rev. B* 18 (1978) 758.
- [22] Y. Takada and T. Ando, *J. Phys. Soc. Jpn.* 44 (1978) 905.
- [23] A.H. MacDonald and C. Kallin, *Phys. Rev. B* 40 (1989) 5795.
- [24] W. Kohn, *Phys. Rev.* 123 (1961) 1242.
- [25] R.J. Nicholas, M.A. Hopkins, D.J. Barnes, M.A. Brummell, H. Sigg, D. Heitmann, K. Ensslin, J.J. Harris, C.T. Foxon and G. Weimann, *Phys. Rev. B* 39 (1989) 10955.



ELSEVIER

Surface Science 305 (1994) 33–41



## Cyclotron resonance to 100 mK of a GaAs heterojunction in the ultra-quantum limit

J.G. Michels <sup>\*,a</sup>, S. Hill <sup>a</sup>, R.J. Warburton <sup>a</sup>, G.M. Summers <sup>a</sup>, P. Gee <sup>a</sup>, J. Singleton <sup>a</sup>,  
R.J. Nicholas <sup>a</sup>, C.T. Foxon <sup>b</sup>, J.J. Harris <sup>c</sup>

<sup>a</sup> Clarendon Laboratory, The University of Oxford, Parks Road, Oxford OX1 3PU, UK

<sup>b</sup> Physics Department, Nottingham University, Nottingham, UK

<sup>c</sup> Semiconductor IRC, ICST, Prince Consort Road, London, UK

(Received 27 April 1993; accepted for publication 12 October 1993)

### Abstract

A helium dilution refrigerator has been modified to enable cyclotron resonance measurements to 100 mK on low-density, 2D electron systems in the ultra-quantum limit. Previous cyclotron resonance work to 300 mK indicates the presence of a phase boundary at a filling factor of  $\nu_c \approx \frac{1}{10}$ , separating gas-like behavior at  $\nu < \nu_c$ , and a new mixed-spin liquid at  $\nu \geq \nu_c$ . The present experiment probes the ground state of these phases, as the temperature is lowered to the Wigner solid regime. We find that, even at 100 mK, the system is spin polarized only at low values of  $\nu$ .

### 1. Introduction

The availability of high-quality heterostructures has led to many studies of the two-dimensional electron system (2DES) formed at the interface of two materials, in the presence of a perpendicular magnetic field. Description of such systems is usually in terms of the variables carrier concentration  $n_s$ , temperature  $T$ , and the filling factor  $\nu = n_s h / eB$  used to detail the number of Landau levels fully occupied by the carriers. It is postulated that a reduction in filling factor to a critical value  $\nu = \nu_c$  will lead to crystallization of the dilute electron gas and the formation of a “Wigner solid” (WS) [1].

Up until recently, the experimental tools for probing 2DES have been magnetotransport [2,3] and radio-frequency spectroscopic [4,5] or conductivity [6] techniques. From transport measurements, it is generally accepted that at  $\nu = \frac{1}{3}$  and  $\frac{1}{5}$ , the ground state of the system is an incompressible fractional quantum Hall liquid, which produces plateaus in the Hall resistance and associated minima in the diagonal resistivity. The region around  $\nu = \frac{1}{5}$  has emerged as critical with transport-generated AC “noise” [7], and diagonal resistance versus temperature studies [8] indicating possible Wigner crystal formation just below and reentrant above the  $\nu = \frac{1}{5}$  liquid ground state. These studies are not inconsistent with the best currently available theoretical estimates of  $\nu_c = \frac{1}{6.5}$  [9] and  $\frac{1}{9}$  [10].

A significant breakthrough in 2DES investiga-

\* Corresponding author.

tions was the correlation of photoluminescence intensity with filling factor associated with the fractional and integral quantum Hall effects [11,12]. Optical investigation was now possible with some further studies showing the presence of an additional line in the luminescence spectra below a critical filling factor of  $\nu_c = 0.28$  [13]. This additional line almost disappeared at fractional filling factors  $\nu = \frac{1}{5}$ ,  $\frac{1}{7}$ , and  $\frac{1}{9}$ , where the electrons were thought to condense into the incompressible Laughlin liquid of the fractional quantum Hall effect (FQHE), giving cause to equate the appearance of this new line with the formation of a WS.

An attempt to correlate optical and transport data has been made by Kukushkin and co-workers [14] who monitored luminescence intensity while applying an electric field. Indicated by the appearance of the low-energy photoluminescence peak, the solid is said to exist in regions below  $\nu_c = 0.27$  and, surprisingly, up to temperatures of 1.5 K. Only the low-energy luminescence peak intensity is affected by the electric field, showing an enhancement attributed to depinning of the Wigner crystal. Indication is also given for a two-stage melting process which agrees with earlier experiments on classical systems [15] and theoretical predictions for the existence of an intermediate “hexatic” phase between the liquid and solid phases in a 2DES [16].

An alternative optical technique, cyclotron resonance (CR), constitutes the most recent of the experimental methods tried to date in an attempt to probe the phase diagram of the 2DES. The most important conclusion from these measurements has been to show that, in contrast to all previous assumptions, there is a considerable population of both spin states of the lowest Landau level even in the extreme quantum limit [17,18]. A particular advantage of CR is that in the limit of a perfect system, the absorption intensity is determined by the classical single-particle oscillator strength, and according to Kohn’s theorem, is insensitive to electron–electron interactions [19]. CR, then, should be an indication of the single-particle composition of the interacting 2DES and how this may change around  $\nu_c$  and  $T_c$ .

This paper concerns itself with CR measurements performed on the 2DES present in high-quality GaAs/GaAlAs samples. Our previous work down to temperatures of  $\sim 360$  mK is summarized. Extension of those measurements to much lower temperatures, well below the classical Wigner solid melting temperature,  $T_c$ , around 200–400 mK for the densities employed, enables us to find that a transition also occurs in this regime from a higher-density mixed-spin configuration to a spin-polarized system at very low densities.

## 2. Experimental setup

Two GaAs/GaAlAs heterojunctions grown by MBE at Philips Research Laboratory, Redhill [20], were studied, with spacer layers of 480 and 80 nm resulting in carrier concentrations at the interface of  $3.6$  and  $12 \times 10^{10} \text{ cm}^{-2}$  and 2 K mobilities of  $2.5$  and  $4 \times 10^6 \text{ cm}^2 \text{ V}^{-1} \text{ s}^{-1}$ , respectively. In addition, continuous reduction of the density by up to 70% was achieved in situ by using above barrier illumination from a HeNe laser, as will be described shortly.

We have modified a helium dilution refrigerator in the bore of a 17.5 T magnet to include a light pipe and optical fiber. The highly polished, evacuated brass light pipe carried far-infrared (FIR) radiation from a  $\text{CO}_2$ -pumped laser to the sample. Blackbody radiation presented a problem, requiring filters to be added at room-temperature, 4.2, and 1 K stages of the refrigerator. Suitable filter materials (quartz and black polythene) were selected such that only wavelengths longer than  $\sim 50 \mu\text{m}$  passed through, essentially blocking all but the long-wavelength tail of the room-temperature Planck distribution, and conveniently just letting through the  $57 \mu\text{m}$  laser line needed to match the cyclotron frequency for fields of  $\sim 13$  T. We achieved base sample temperatures between 50 and 100 mK, as measured with  $\text{RuO}_2$  resistors. Cyclotron resonance measurements were made in the range from 50–1000 mK. The intensity of the transmitted FIR radiation was determined by a Si bolometer mounted below the sample and cooled to 2 K by the  $^4\text{He}$

bath. The extreme sensitivity of this bolometer enabled FIR power to be kept to a minimum ( $\sim 0.1 \mu\text{W}$ ) and no heating effects were observed in the refrigerator from the  $57 \mu\text{m}$  laser light.

A 1 mm glass optical fiber was similarly inserted through the refrigerator to provide continuous illumination of the sample with red or green HeNe laser light. With energy greater than the AlGaAs band gap, this light served to further depopulate the 2DES; power density  $\sim 10^{-4} \text{ W/cm}^2$  reduced the lower bound on the carrier concentration to  $1 \times 10^{10} \text{ cm}^{-2}$ . The power density was altered through the use of externally placed neutral density filters. Little difference in resultant carrier concentration was observed between equivalent power densities of the red and green HeNe. The dilution refrigerator was reasonably tolerant of this added source of heat, holding base temperature for all but the largest power densities, with a full HeNe power of 0.5 mW.

Electrical contacts allowed simultaneous transport measurements to be made on the high-density sample, enabling a precise comparison of optical and transport measurements of the carrier density. Conversion of absorption strength to carrier concentration was made using the classical Drude absorption formula as in previous  $^3\text{He}$  cryostat experiments [17,21] using both the  $\text{CO}_2$ -pumped FIR laser and Fourier transform spectrometer. No differences in CR position or intensity were detected between data taken at comparable densities and temperatures, either between measurements with different samples, different illumination conditions, or different refrigeration systems.

### 3. CR measurements of low-density 2D electron systems

The dilution refrigerator measurements, which extend our previous CR experiments, provide evidence for the existence of a mixed-spin state at temperatures below the classical Wigner solid melting temperature  $T_c$ , and show a tendency towards complete spin polarization only at very low densities and temperatures. The data and

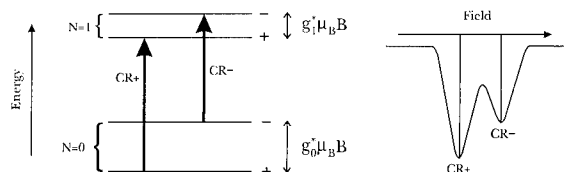


Fig. 1. Possible CR transitions from the  $N=0$  Landau level and the resultant spin splitting.

consequent analysis are best understood within a framework where the range of filling factors is divided into three regions:  $1 < \nu < 2$ ,  $\frac{1}{6} < \nu < 1$ , and  $\nu < \frac{1}{6}$ . While the present study concerns itself with data taken in the ultra-quantum limit ( $\nu \ll 1$ ), it relies to a large extent on previous experimental and theoretical work in each of the listed regimes.

#### 3.1. $1 < \nu < 2$

Generally, spin splitting of the Landau levels is the result of the Zeeman interaction, but only manifests itself in CR measurements because of the energy dependence of the  $g$ -factor, which changes the magnitude of the splitting for successive Landau levels. This is shown schematically in Fig. 1 for bulk GaAs, which has an  $N=0$   $g$ -factor of  $\sim -0.4$ . The two spin-conserving transitions in the CR  $N=0 \rightarrow 1$  absorption are split by 60 mT at 13 T. In GaAs heterostructures, this splitting continues to be determined predominately by the GaAs  $g$ -factor, with the spin(+) state lowest in energy [22]. The predicted field location of the spin(+) and spin(-) transitions is carrier-concentration-dependent due to band non-parabolicity and can be calculated by the formula  $m^*/m = 1 + 2.6\langle T_z \rangle / E_g$ , where  $\langle T_z \rangle$  is the kinetic energy due to the self-consistent quasi-accumulation layer potential, and  $E_g$  the GaAs band gap [23,24].

Initial experiments [25] in very high mobility GaAs/AlGaAs heterojunctions for  $1 < \nu < 2$ , where both spin states are populated, failed to observe a splitting of the CR, despite experimental linewidths that were considerably smaller than the expected splitting. This was attributed to plasma mixing or hybridization of the two spin



transitions [25], resulting in a single coupled resonance at the weighted mean of the two transitions, although no mixing of these transitions is predicted [26] at  $k = 0$ . By contrast, recent work in lower mobility InAs quantum wells, where the  $g$ -factor is much larger ( $\sim 15$ ), does show separately resolved resonances from different spin states of the same Landau level [27]. This splitting disappears, however, for a sample with a higher mobility, leading the authors to conclude that the small number of lattice imperfections in high-mobility samples results in a system with strong translational symmetry and that a hybridization of the two spin-states has occurred due to the removal of scattering centers. This suggestion becomes applicable in discussions concerning the origin of our two observed CR peaks in the ultra-quantum limit.

### 3.2. $\frac{1}{6} < \nu < 1$

Transport data showing several well defined FQHE states in this region led researchers to try and correlate shifts in cyclotron resonance positions or changes in absorption linewidths to filling factors associated with the FQHE [28,29]. These have, on the whole, provided no *conclusive* evidence for the observation of the FQHE by CR, although the majority of experiments have been performed between 0.5 and 2 K, where the FQHE features are not particularly strong. We have extended this work down to 100 mK, and a comparison of our cyclotron masses for a large wavelength range (1223–57  $\mu\text{m}$ ) with simultaneous transport measurements in a sample which shows a strong and clearly resolved series of FQHE features, is shown in Fig. 2. No anomalies in the effective mass are seen at fields corresponding to fractional filling factors, and a single resonance is always seen for  $\nu > \frac{1}{6}$ . Both of these results provide evidence for the insensitivity of the CR to the electron–electron interactions responsible for the FQHE.

While not finding any evidence of FQHE states, recent CR measurements in this regime [17,21] have found a systematic shift in resonance position as the temperature is varied. This temperature dependence appears to have an onset at

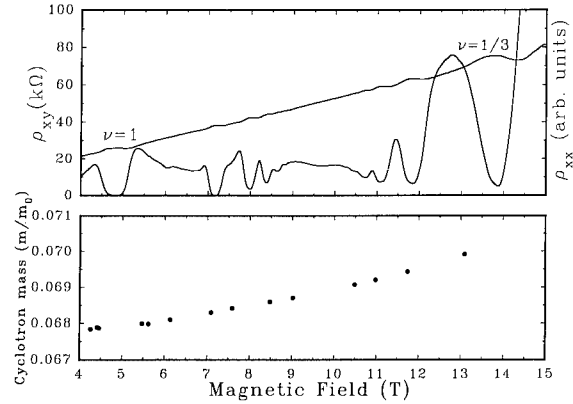


Fig. 2. Data taken at 100 mK, showing a comparison of transport and cyclotron effective mass.

$\nu \approx \frac{1}{3}$  and becomes more pronounced towards smaller filling factors. Changing the temperature from 2 K to 300 mK for  $\nu = \frac{1}{3} - \frac{1}{6}$  resulted in a continuous shift of the resonance position downwards in field. The total shift in position was up to half of the single-particle spin splitting. We will argue later that the temperature dependence of this resonance suggests that it is a coupled resonance similar to that seen for the integral occupancy region  $1 < \nu < 2$ .

### 3.3. $\nu < \frac{1}{6}$

The appearance of a second resonance in CR measurements at filling factors below  $\frac{1}{6}$  was recently reported independently by two groups [18,21]. Existence of a second resonance was striking given the failure to observe splitting at greater occupancies when both spin states are definitely occupied.

Nicholas et al. [21] demonstrated that the magnitude of the observed splitting at very low densities ( $\nu \rightarrow 0$ ) was similar to that in bulk GaAs for  $\Delta g$ -induced spin(+) and spin(−) transitions originating from the lowest Landau level, and postulated that  $\Delta g$  splitting was the origin of the two peaks. This interpretation was largely based on the very good agreement between the high-temperature limit of the observed splitting and the known values for bulk GaAs [23] over a range of magnetic field from 6 to 90 T [21,30]. The possi-

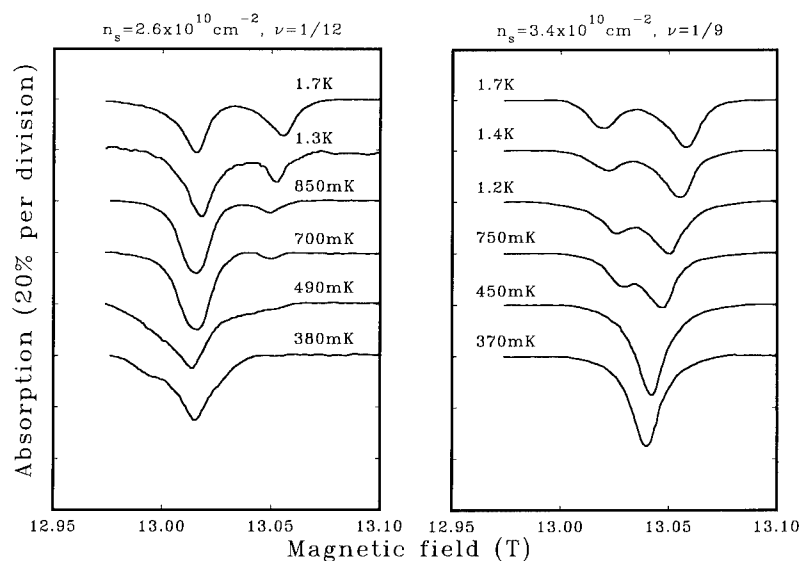


Fig. 3. CR traces are shown as a function of temperature for occupancies  $\frac{1}{2}$  and  $\frac{1}{9}$ , either side of a critical value of  $\sim \frac{1}{10}$ .

bility of impurity-shifted CR was discounted due to the highly systematic dependence of resonance positions and intensities on carrier density which are continuous from one sample to the next, and independent of other factors such as spacer-layer thicknesses, illumination states and cool-down history.

Subsequently, Summers and co-workers [17] plotted the position and intensity of the dual peaks as a function of temperature and filling factor and found a critical occupancy at  $\nu_c = \frac{1}{10}$  which serves to divide regions which differ dramatically in their response to changes in temperature (Fig. 3). Below  $\nu_c$ , the resonance peak positions vary little with decreasing temperature but the *intensity* of the spin(+) transition is increased relative to the spin(−) so that, at low temperatures, most of the carriers are seen to reside in this lower-energy state. In the low-density limit (i.e.,  $\nu \rightarrow 0$ ) the absolute positions of both resonances correspond very accurately ( $\pm 5$  mT) to the field positions in bulk GaAs, measured with the same system. Above  $\nu_c$ , the resonance peak positions merge together with decreasing temperature to join into a single resonance at the mean of the expected spin(+) and spin(−) transitions. The formation of a single resonance at the mid-

point is independent of the relative intensities that existed in either peak prior to cooling.

The existence of a critical occupancy is confirmed by the density-dependent behaviour of the system for a fixed temperature as shown in Fig. 4 at 16 T and 2.2 K, where the occupancy is varied

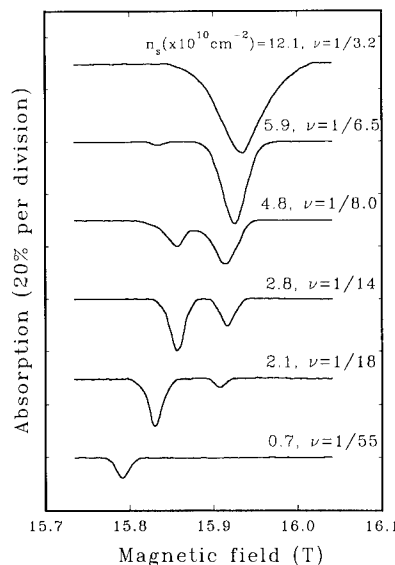


Fig. 4. The density dependence of the CR at 16 T and 2.2 K, covering the occupancy range  $\frac{1}{50}$  to  $\frac{1}{3}$ .

from  $\sim \frac{1}{50}$  to  $\sim \frac{1}{3}$ . At very low densities two resonances are observed with the higher-energy (lower-field) spin(+) resonance as the most intense and the second, weaker resonance at exactly the field expected for the spin(−) transition in bulk GaAs. As the carrier density increases there is a small continuous shift in resonance positions due to the normal effect of band non-parabolicity. At around  $\nu = \frac{1}{10}$  ( $4 \times 10^{10} \text{ cm}^{-2}$ ) there is a rapid change-over in intensity between the two resonances and the resonance positions show an anomalous decrease in splitting, with the minimum corresponding to the point at which both intensities are equal.

Our dilution refrigerator experiments demonstrate the continued existence of this critical filling factor to temperatures below 100 mK. Data was usually taken at a fixed carrier density, controlled by the level of continuous illumination, as a function of increasing temperature. Fig. 5A–5C show transmission spectra obtained for a FIR wavelength of  $57 \mu\text{m}$  at a filling factor which is just above  $\frac{1}{8}$ , just below  $\frac{1}{18}$ , and at the critical occupancy of  $\frac{1}{10}$ . These traces were taken in the dilution refrigerator and are the extension of Fig.

3 to lower temperatures. Analysis of the peak intensities indicates that the total carrier density is constant and independent of temperature and magnetic field.

Very little temperature dependence is seen at  $\frac{1}{18}$  (Fig. 5A), with most of the carriers contained in the low-field (spin(+)) transition. The weak high-field resonance (indicated by an arrow in Fig. 5A) is probably due to a metastable population of the upper spin state, a consequence of the high illumination intensity used to depopulate the heterojunction and the relatively long spin relaxation time. For  $\nu = \frac{1}{8}$  (Fig. 5C), there is little visible shift in resonance position for the single peak as the temperature is lowered. This is due only to our high-temperature limit of  $\sim 600 \text{ mK}$  which fails to show a shift that principally occurs from 500 mK to 2 K.

At the critical occupancy of  $\frac{1}{10}$  (Fig. 5B), a decrease in temperature results in the same merging of the resonances as was seen for a higher range of temperatures, and at  $\sim 540 \text{ mK}$  a single resonance is formed at the mean of the predicted spin(+) and spin(−) transitions. A further reduction in temperature sees a slight shift

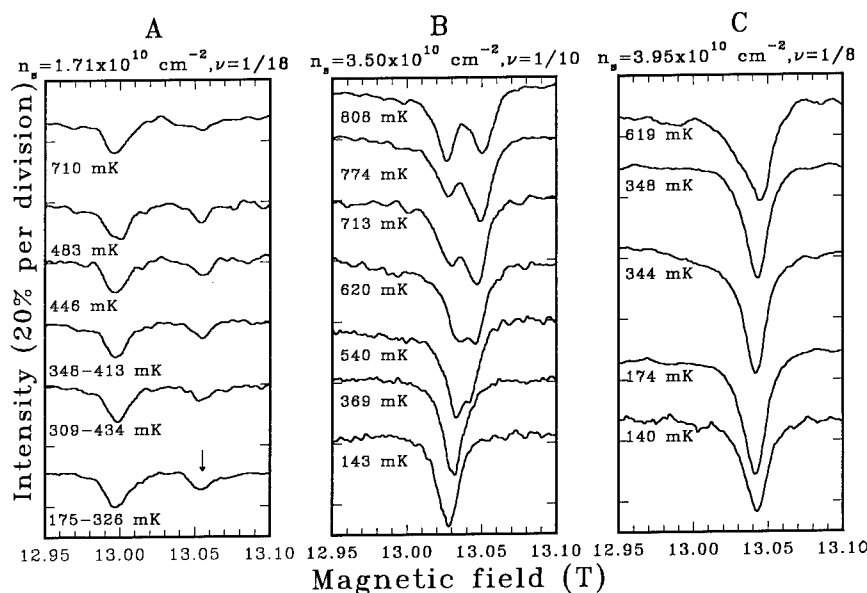


Fig. 5. Experimental traces taken for a FIR wavelength of  $57 \mu\text{m}$  and a filling factor which is (C) just above, (A) below, and (B) at the critical occupancy of  $\frac{1}{10}$ .

of this single resonance towards lower fields but its position of 13.028 T at 143 mK is still much closer to the mean than the predicted spin(+) position of 13.01 T. This is more clearly shown in Fig. 6, a composite picture of the resonance positions as a function of temperature, from 0.1–1.5 K, for a range of carrier concentrations  $\nu = \frac{1}{9} - \frac{1}{11}$  close to the critical occupancy. The range of the plot (60 mT) is equal to the single-particle spin splitting, and demonstrates that the splitting is already well below this value by 1 K, and that the two resonances collapse to a single peak at temperatures below  $\sim 540$  mK. At 540 mK the resonances occur at almost exactly the mean of the two spin(+) and spin(–) transitions and, as previously mentioned, there is a small shift to lower field of the single resonance on cooling to base temperature. The temperature, 540 mK, at which the resonances in Fig. 6 collapse together, corresponds to a temperature of approximately 1.5 times the classical Wigner solid melting temperature for these densities.

The carrier-density dependence of the resonance positions, confirming the existence of a critical occupancy, is shown in Fig. 7, a series

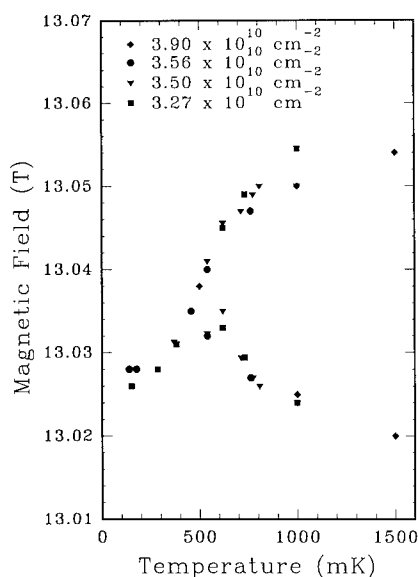


Fig. 6. A composite picture of the resonance positions for a range of carrier concentrations, close to the critical occupancy  $\nu = \frac{1}{10}$ .

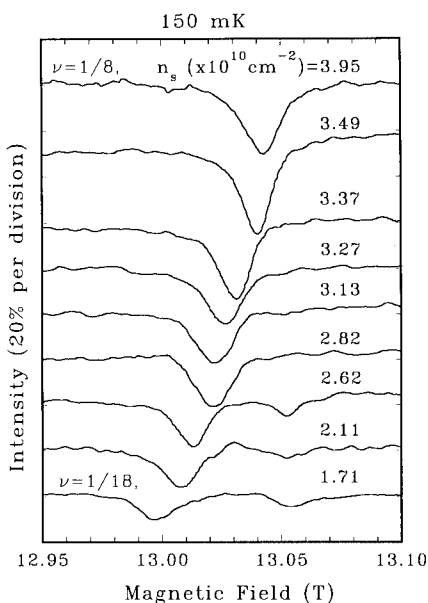


Fig. 7. CR traces taken at 150 mK. The resonance position changes as a function of density showing the progression towards complete spin polarisation at lower carrier densities.

where carrier density is changed at a constant temperature of  $\sim 150$  mK. This figure serves as the low-temperature analog to Fig. 4. Starting at densities near the critical filling factor, the resonance position is shown near the mean of the predicted spin(+) and spin(–) positions. The peak position then shifts systematically downward in field with decreasing carrier density, finally reaching the limit of the predicted spin(+) transition. In Fig. 8, this data is combined with previous  $^3\text{He}$  results at 360 mK to show the systematic trend towards spin polarization at low densities and temperatures. The solid lines show the expected behavior of the spin states due to band non-parabolicity.

#### 4. Discussion and possible phase diagram

Critical in any discussion of these results is the origin of the CR peaks over the range of studied filling factors. The experimental data suggest very strongly that the effects we have observed are related to spin. We therefore interpret CR as a

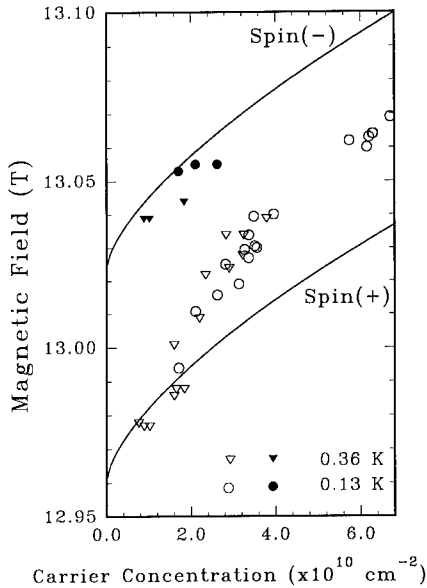


Fig. 8. A composite picture illustrating the shift in resonance position with carrier concentration. The solid lines show the calculated shift due to electron non-parabolicity.

probe of the spin composition of the multi-electron ground state.

The above data lead us to offer a phase diagram shown in Fig. 9. The line defining the region within which the Wigner crystal may exist has been drawn in accordance with previous ex-

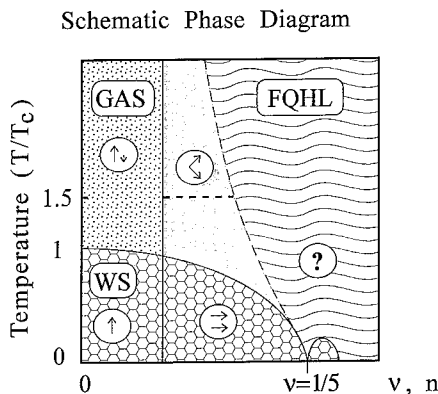


Fig. 9. A schematic phase diagram of the 2DES in the low-occupancy region, showing the expected Wigner solid regime, the FQHE liquid, the regions of single-particle behaviour and the interacting doublet region. The encircled symbols indicate the possible spin configuration of the system in each region.

perimental and theoretical studies. Our cyclotron resonance measurements are not obviously sensitive to this boundary. However, the phase diagram includes two roughly vertical lines at  $\nu \approx \frac{1}{10}$  and  $\frac{1}{6}$ , and a roughly horizontal line at  $T/T_c = 1.5$ , which are delineated by the present experiment.

For filling factors less than  $\frac{1}{10}$ , two CR peaks are seen with a splitting close to that seen in bulk GaAs. The intensity of the carriers in each peak as a function of temperature is satisfactorily explained by single-particle statistics indicating a gas-like state. The low-temperature and low-occupancy region is characterized by almost complete spin polarization with the majority of the carriers in the lower-energy spin(+) state.

We label occupancies greater than  $\nu = \frac{1}{10}$  as a liquid state, characterized by the collapse of the two resonances into a single peak with decreasing temperature. The existence at low temperature of a single peak, lying at the midpoint of the predicted spin(+) and spin(-) transitions, indicates that there is no net spin contribution to the CR. This means that the ground state has  $S = 0$  or  $S_z = 0$ , or even has the spins aligned perpendicular to the field. The horizontal line at  $T/T_c = 1.5$  shows the critical temperature of this liquid phase: for  $T/T_c < 1.5$  the spins behave as if  $S = 0$ , whereas for  $T/T_c > 1.5$  the spins are not exactly coupled, but the interaction continues to influence the CR. A possible suggestion for the origin of the low-temperature state at  $\nu \approx \frac{1}{10}$  has been made very recently by Mouloupoulos and Ashcroft [31]. These authors calculated that, in the absence of Zeeman splitting, the ground state of the three-dimensional Wigner crystal consists of an arrangement of  $S = 0$  spin-paired electrons which then form the electron crystal. A field-induced, non-zero Zeeman energy acts to break the correlation energy that favors spin pairing and, in the limit of a low-density system, results in complete spin polarization.

Our second vertical line at  $\nu \approx \frac{1}{6}$  is drawn to divide the region in which two resonances were observed from higher occupancies where only a single resonance was seen. The  $\nu \approx \frac{1}{6}$  phase boundary is less significant than the one at  $\nu \approx \frac{1}{10}$  due to the continuing temperature dependence of the single resonance up to  $\nu \approx \frac{1}{3}$ . This suggests

# Time-resolved magneto-photoluminescence measurements of the integer QHE, fractional QHE and extreme quantum limit

S.A. Brown <sup>\*,a</sup>, A.G. Davies <sup>a</sup>, A.C. Lindsay <sup>a,b</sup>, R.B. Dunford <sup>a</sup>, R.G. Clark <sup>a</sup>,  
P.E. Simmonds <sup>c</sup>, H.H. Voss <sup>d,1</sup>, J.J. Harris <sup>e</sup>, C.T. Foxon <sup>f</sup>

<sup>a</sup> School of Physics, University of New South Wales, P.O. Box 1, Kensington 2033, Australia

<sup>b</sup> Defence Science and Technology Organisation, Salisbury 5108, Australia

<sup>c</sup> Department of Physics, University of Wollongong, P.O. Box 1144, Wollongong 2500, Australia

<sup>d</sup> Rheinische Friedrich-Wilhelm-Universität, Bonn, Germany

<sup>e</sup> IRC for Semiconductor Materials, University of London, Prince Consort Road, London SW7 2BZ, UK

<sup>f</sup> Department of Physics, University of Nottingham, University Park, Nottingham NG7 2RD, UK

(Received 20 April 1993; accepted for publication 4 June 1993)

## Abstract

Low-temperature, time-resolved magneto-photoluminescence (TRPL) measurements of 2D electron–free-valence-hole recombination have been carried out in the IQHE, FQHE and magnetically induced electron solid regimes of a GaAs/AlGaAs single heterojunction. Clear differences, not present at elevated temperatures, are found in the measured PL decay time ( $\sim 1$  ns) for components of multiple-peak structure observed beyond  $\nu = 1/5$  used previously to construct a phase diagram associated with the Wigner solid. The new TRPL results and earlier PL data, taken together, are consistent with a mechanism in which the spectral feature associated with crystallisation derives from the trapping of excitons within a few Bohr radii ( $z$  separation) of the heterointerface and their subsequent ( $x$ ,  $y$ ) localisation by the presence of a 2D electron system with a degree of spatial order at this interface.

## 1. Introduction

Recent investigations of the two-dimensional electron system (2DES) formed at the interface of a GaAs/AlGaAs single heterojunction (SHJ) have provided strong evidence for the onset of an electron solid phase (magnetically induced Wigner solid (MIWS)) at high magnetic fields (Landau-

level filling factor  $\nu < 1/5$ ) and low temperatures. While the high quality of GaAs heterostructure samples now available is such that the fundamental many-electron interactions are not dominated by disorder, the picture that has emerged from early electrical transport [1], radiofrequency absorption [2] and surface acoustic wave attenuation studies [3] is a MIWS phase broken into domains (length scale  $\sim 1 \mu\text{m}$ ) pinned by host disorder, principally low-level residual impurities (donors, acceptors) that can be situated close to the 2DES [4]. Evidence from these macroscopic probes points to the onset of a

\* Corresponding author.

<sup>1</sup> Exchange student visiting the University of New South Wales.

that some spin interaction is still taking place. With just a single high-temperature CR for  $\nu > \frac{1}{6}$ , it is not possible to be more specific in this filling-factor regime.

In conclusion, we can state that we have clear evidence for the importance of both spin states in determining the collective states of the 2DES at low temperature and high magnetic field.

## 5. References

- [1] E.P. Wigner, Phys. Rev. 46 (1934) 1002; Trans. Faraday Soc. 34 (1938) 678.
- [2] R.L. Willet, H.L. Störmer, D.C. Tsui, L.N. Pfeiffer, K.W. West and K.W. Baldwin, Phys. Rev. B 38 (1988) 7881.
- [3] V.J. Goldman, M. Shayegan and D.C. Tsui, Phys. Rev. Lett. 61 (1988) 881.
- [4] F.I.B. Williams, P.A. Wright, R.G. Clark, E.Y. Andrei, G. Deville, D.C. Glattli, O. Probst, B. Etienne, C. Dorin, C.T. Foxon and J.J. Harris, Phys. Rev. Lett. 66 (1991) 3285.
- [5] E.Y. Andrei, G. Deville, D.C. Glattli and F.I.B. Williams, Phys. Rev. Lett. 60 (1988) 2765.
- [6] M.A. Paalanen, R.L. Willet, P.B. Littlewood, R.R. Ruel, K.W. West, L.N. Pfeiffer and D.J. Bishop, Phys. Rev. B 45 (1992) 11342.
- [7] V.J. Goldman, M. Santos, M. Shayegan and J.E. Cunningham, Phys. Rev. Lett. 65 (1990) 2189.
- [8] H.W. Jiang, R.L. Willet, H.L. Störmer, D.C. Tsui, L.N. Pfeiffer and K.W. West, Phys. Rev. Lett. 65 (1990) 633.
- [9] P.K. Lam and S.M. Girvin, Phys. Rev. B 30 (1984) 473.
- [10] D. Levesque, J.J. Weis and A.H. MacDonald, Phys. Rev. B 30 (1984) 1056.
- [11] A.J. Turberfield, S.R. Haynes, P.A. Wright, R.A. Ford, R.G. Clark and J.F. Ryan, Phys. Rev. Lett. 65 (1990) 637.
- [12] B.B. Goldberg, D. Heimann, A. Pinczuk, L. Pfeiffer and K. West, Phys. Rev. Lett. 65 (1990) 641.
- [13] H. Buhmann, W. Joss, K. von Klitzing, I.V. Kukushkin, A.S. Plaut, G. Martinez, K. Ploog and V.B. Timofeev, Phys. Rev. Lett. 66 (1991) 926.
- [14] I.V. Kukushkin, N.J. Pulsford, K. von Klitzing, K. Ploog, R.J. Haug and S. Koch, Phys. Rev. B 45 (1992) 4532.
- [15] C.A. Murray and D.H. Van Winkle, Phys. Rev. Lett. 58 (1987) 1200.
- [16] B.I. Halperin and D.R. Nelson, Phys. Rev. Lett. 41 (1978) 121.
- [17] G.M. Summers, R.J. Warburton, J.G. Michels, R.J. Nicholas, J.J. Harris and C.T. Foxon, Phys. Rev. Lett. 70 (1993) 2150.
- [18] M. Besson, E. Gornik, C.M. Engelhardt and G. Weimann, Semicond. Sci. Technol. 7 (1992) 1274.
- [19] W. Kohn, Phys. Rev. 123 (1961) 1242.
- [20] C.T. Foxon, J.J. Harris, D. Hilton, J. Hewett and C. Roberts, Semicond. Sci. Technol. 4 (1989) 582.
- [21] R.J. Nicholas, G.M. Summers, M. Watts, R.J. Warburton, J.G. Michels, R.A. Lewis, J.J. Harris and C.T. Foxon, in: Low-Dimensional Electronic Systems, New Concepts, Vol. 111 of Springer Series in Solid-State Sciences (Springer, Berlin, 1992), p. 232.
- [22] U. Rössler, F. Malcher and G. Lommer, in: High Magnetic Fields in Semiconductor Physics II, Vol. 87 of Springer Series in Solid-State Sciences (Springer, Berlin, 1989) p. 376.
- [23] M.A. Hopkins, R.J. Nicholas, P. Pfeffer, W. Zawadzki, D. Gauthiers, J. Portal and M.A. DiForte-Poisson, Semicond. Sci. Technol. 2 (1987) 568.
- [24] H. Sigg et al., Solid State Commun. 48 (1983) 897.
- [25] M. Watts, R.J. Nicholas, N.J. Pulsford, J.J. Harris and C.T. Foxon, in: Proceedings of the Twentieth International Conference on the Physics of Semiconductors, Eds. E.M. Anastassakis and J.D. Joannopoulos (World Scientific, Singapore, 1991) p. 1465.
- [26] A.H. MacDonald and C. Kallin, Phys. Rev. B 40 (1989) 5795.
- [27] J. Scriba, A. Wixforth, J.P. Kotthaus, C. Bolognesi, C. Nguyen and H. Kroemer, Semicond. Sci. Technol. 8 (1993) S133.
- [28] W. Seidenbusch, E. Gornik and G. Weimann, Phys. Rev. B 36 (1987) 9155.
- [29] G.L.J.A. Rikken, H.W. Myron, P. Weyder, G. Weimann, W. Schlapp, R.E. Horstman and J. Wolter, J. Phys. C 18 (1985) L175.
- [30] R.J. Nicholas, D.J. Barnes, N. Miura, J.J. Harris and C.T. Foxon, J. Phys. Soc. Jpn., to be published.
- [31] K. Mouloupoulos and N.W. Ashcroft, Phys. Rev. Lett. 69 (1992) 2555.

MIWS boundary in the  $(\nu, T)$  plane that occurs immediately beyond the fractional QHE (FQHE) ground state at  $\nu = 1/5$ , in agreement with recent calculation [5], with a small MIWS region sandwiched between the  $2/9$  and  $1/5$  FQHE states.

Due to the absence of (ideal) long-range electronic order in real samples, an understanding of the detailed nature of the MIWS phase requires a local experimental probe and there has been intense interest recently in magneto-photoluminescence (PL) experiments [6]. The PL experiments fall into two categories: recombination of 2D electrons with free holes in the GaAs valence band (e–h) in standard SHJ and quantum well (QW) samples [7–10] and, in specialised structures, recombination with localised holes bound to Be acceptor atoms (e– $A^0$ ) [11–13] purposely grown into the GaAs in a  $\delta$ -doped layer ( $n_\delta = 2 \times 10^{10} \text{ cm}^{-2}$ ) 250 Å from the SHJ. A theoretical understanding of the PL data is at an early stage and until recently (see below) has been restricted to the FQHE [14]. For the e– $A^0$  process, two PL lines are observed in the MIWS regime; the lower energy line observed for  $\nu < 0.28$  has been qualitatively attributed to an electron solid phase and the higher energy line present throughout the magnetic field range studied to a coexisting liquid phase, with oscillator strength transferring to the lower line as the temperature is reduced [11]. Recent e– $A^0$  measurements [13c] have shown that the recombination time for the lower line is longer than for the higher energy line. This difference has been exploited to derive a phase diagram for Wigner crystallisation and to additionally distinguish between glass-like and intrinsic solid phases [13c]. However, in a theory subsequently developed for PL in the MIWS phase [15], it is shown that when the deformation of the electron lattice by the potential of the hole is taken into account, structure in the PL spectrum which provides direct confirmation of local crystalline order is lost for the e– $A^0$  process. In contrast, it is concluded that e–h recombination offers the best chance to observe intrinsic, multiple-peak structure imposed by the electron lattice since the free hole has little effect on the crystal structure.

Our previous studies identified a characteristic break-up of the e–h PL spectrum in the MIWS regime [10] that exhibits some similarities to the calculated finite-temperature spectrum [15]. We report low-temperature, time-resolved magneto-photoluminescence (TRPL) measurements of the components that form the multiple peak e–h PL spectrum, which potentially carry quantitative information about the MIWS phase, and compare these to TRPL results in both the FQHE and integer QHE (IQHE) regimes at lower magnetic field. It is significant that all measured recombination times in our TRPL study are *short* ( $\sim 1$  ns) which strongly suggests that the PL results can be understood *entirely* in an excitonic framework. A model of exciton localisation by the onset of an electron lattice, as opposed to a model of coexisting solid and liquid phases, is put forward that provides an overall explanation for the different measured decay times and both the origin and temperature dependence of components of the multiple-peak (e–h) PL spectrum in the MIWS regime.

## 2. Experimental

TRPL measurements of e–h PL were performed on a GaAs/AlGaAs single-heterojunction sample G648 ( $n_s = 3.2 \times 10^{10} \text{ cm}^{-2}$ ,  $\mu = 3 \times 10^6 \text{ cm}^2/\text{V} \cdot \text{s}$ ), using low excitation levels (1–18  $\mu\text{W}$  at the  $2.5 \times 2.5 \text{ mm}^2$  2D layer) from a mode-locked Ti-sapphire laser (200 ps pulses at 180 MHz). PL spectra with pulsed illumination were indistinguishable from those obtained with CW illumination. The sample was mounted in the dilute phase of a dilution refrigerator at field centre of a 15.5 T superconducting magnet. Transport measurements showed sharp QHE structure out to  $\nu = 1/5$  [10]. Optical fibres carried laser light to the sample and PL was collected using a triple spectrometer and a micro-channel plate detector (alternatively, a CCD detector could be selected by means of a rotatable mirror). Single-photon counting techniques were employed with an overall time-resolution of 70 ps. The instrumental response was monitored before and after each TRPL measurement. In the



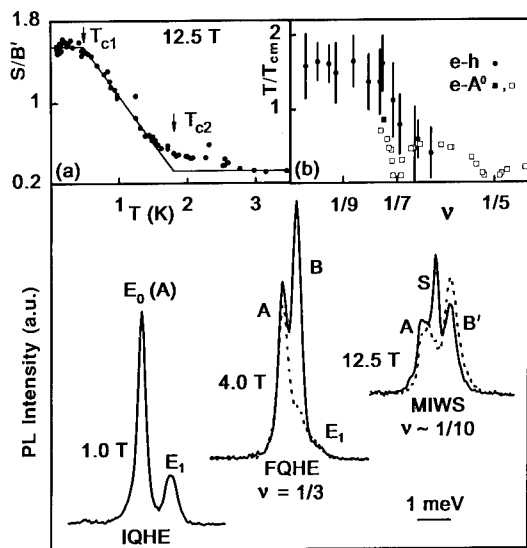


Fig. 1. PL spectra for e-h recombination at 70 mK (full lines) and 2.2 K (dashed lines); energy scale refers to individual spectra. IQHE –  $E_0$ ,  $E_1$  emission; FQHE – doublet A,B structure; MIWS – triplet A,S,B' structure. Insets: (a)  $S/B'$  intensity plot used to determine the electron temperature  $T_e$  under conditions of TRPL measurements [10]. (b) (●) – Optical phase boundary for MIWS from  $S/B'$  intensity ratio analysis [10]; (■, □) –  $e-A^0$  data [13b,c].

extreme quantum limit the PL spectra are comprised of a number of closely spaced components and we have performed TRPL measurements on both the spectrum as a whole and the individual peaks. Measurement of decay times for the latter required an improvement in energy resolution resulting in a significant loss of PL intensity; this necessitated an increase in the excitation intensity to obtain TRPL spectra in reasonable data acquisition times. Well-characterised, low-power ( $0.5 \mu\text{W}$ ) PL spectra [10], taken using the CCD array, were used to monitor the electron temperature  $T_e$  (see below and Fig. 1 inset (a)) at each magnetic field under the conditions of the TRPL measurements.

### 3. Results

An overview of the low-temperature PL spectra for sample G648, detailed elsewhere [10], is shown in Fig. 1. In the IQHE regime, e-h PL

spectra comprise two lines,  $E_0$  (many-body exciton) and  $E_1$  (exciton) [7,10], corresponding to recombination from the densely populated ground and sparsely populated (photoexcited) first-excited state 2D electron subbands, respectively. At  $\nu = 1$ , a sharp  $E_0$  intensity minimum and transfer of intensity into the  $E_1$  line has been explained by a suppression of screening [7–10]. In the FQHE regime, a new line labelled B is resolved intermediate in energy between the  $E_0$  line (re-labelled A) and  $E_1$ , giving rise to a characteristic A,B doublet structure. For the  $\nu = 2/3$  FQHE hierarchy,  $E_0$  (A) intensity minima are observed at  $\nu = 2/3$  and  $3/5$ , whilst the  $E_1$  line, which exhibits weak maxima at these FQHE states, falls to low intensity for  $\nu < 1$  and is barely observable at low temperatures beyond  $\nu \approx 1/2$ . In the  $\nu = 1/3$  FQHE hierarchy, intensity minima are observed in the A line together with maxima in the B line at  $\nu = 1/3$ ,  $2/5$ , and  $3/7$ . The reduced ability of electrons in incompressible FQHE states to screen the potential of photoexcited holes is central to this signature [7,10]. In the MIWS region  $\nu < 1/5$ , the PL structure changes from an A,B doublet to a triplet labelled A,S,B' with evidence of at least one further component (A') within this profile together with an additional weak peak resolved at lowest  $\nu$  split-off to lower energy (arrowed in Fig. 3d below). The A component of the doublet observed in the FQHE regime extends on smoothly in energy from the low-field  $E_0$  line [10]. No discontinuities or splittings in energy are observed in the A (or B) line at QHE states for sample G648, although this is not the case for all samples [7,9]. In the transition to the MIWS region, the A line similarly continues on smoothly in energy, but the B line gives way to the emergent S peak which is shifted to lower energy by  $\sim 0.1$  meV and to the B' peak  $\sim 0.2$  meV higher in energy.

The oscillator strength transfers dramatically from S to B' upon increasing the temperature, and the temperature dependence of the intensity ratio  $S/B'$  identifies two critical temperatures,  $T_{c1}$  and  $T_{c2}$ , shown in Fig. 1, inset (a) for 12.5 T ( $\nu \approx 1/10$ ). The lower-temperature mapping  $T_{c1}(\nu)$  is shown in Fig. 1, inset (b), where the temperature axis is in units of the 2D melting

temperature for the classical electron solid  $T_{\text{cm}} = \Gamma^{-1} e^2 / (4\pi\epsilon_0 k_B a)$  with  $\Gamma = 127$  and  $a = (\pi n_s)^{-1/2}$  ( $T_{\text{cm}} = 320$  mK for sample G648), and correlates with the electron liquid–solid transition established by other techniques [1–3]. This is compared with the MIWS phase boundary established from  $e$ - $A^0$  PL data [13b,c] in Fig. 1, inset (b), showing reasonable agreement, including a step at  $\nu = 1/7$  aligned with re-entrant FQHE behaviour in  $e$ - $A^0$  PL at this filling factor. We make use of the  $S/B'$  ratio plots for each field to determine the electron temperature,  $T_e$ , in the TRPL experiments.

TRPL results for the IQHE regime ( $\nu = 1$  at 1.3 T) are shown in Fig. 2. Selected decay curves for the  $E_0$  line are shown in Fig. 2a, from which measured PL decay times  $\tau_m$  (hole lifetime) are determined. PL spectra at 1.0 and 1.3 T ( $\nu = 1$ ) are shown in Fig. 2b, reflecting the sharp intensity minimum in  $E_0$  and maximum in  $E_1$  that occurs at  $\nu = 1$ . In a common hole model, the  $E_0$  radiative recombination time is given by  $\tau_r = \tau_m / I_{\text{rel}}$ , where  $I_{\text{rel}}$  is the relative intensity of the  $E_0$  emission with respect to the total intensity for all recombination processes;  $I_{\text{rel}} \approx I_0 / I_{\text{tot}}$ , where  $I_0$  is the time-integrated intensity of the  $E_0$  line

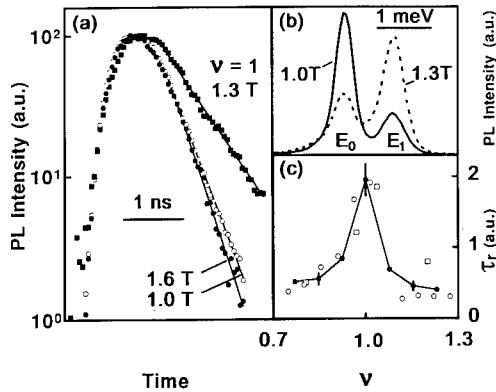


Fig. 2. IQHE,  $\nu = 1$ : (a) normalised TRPL decay curves for  $E_0$  at an electron temperature close to the refrigerator bath temperature  $T_b \approx 100$  mK. Decay curves are aligned on their leading edges for presentation purposes. (b) PL spectra under conditions of TRPL measurements that show  $E_1/E_0$  intensity ratio enhanced at  $\nu = 1$ . (c)  $\tau_r$  – PL radiative time  $\tau_r$  derived from measured decay time and  $E_0, E_1$  intensity data; ( $\square, \circ$ ) – similar data, normalised at  $\nu = 1$ , of Ref. [16], for SHJ and QW samples, respectively.

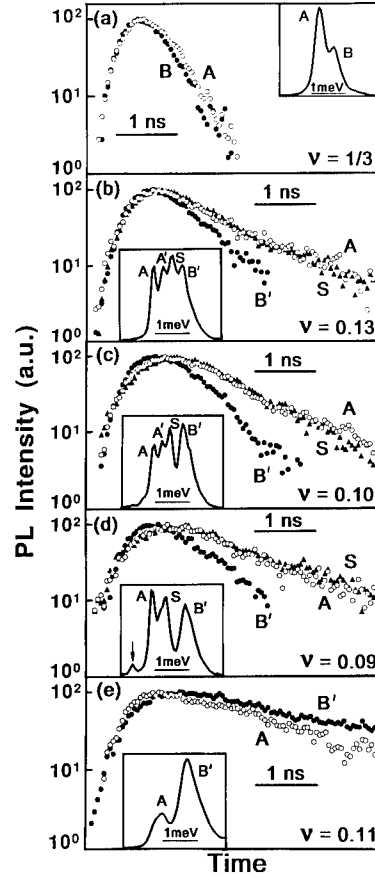


Fig. 3. Normalised and aligned TRPL decay curves for individual components ( $\circ$ ) – A; ( $\bullet$ ) – B', B; ( $\blacktriangle$ ) – S, of PL spectra at  $T_b \approx 100$  mK (a)–(d) and  $T_b = 4.2$  K (e). The insets show the PL spectra under the illumination conditions of the TRPL experiment. No differences are observed in the measured decay times  $\tau_m$  for A and B lines at  $\nu = 1/3$  (a). In the MIWS regime (b–d),  $\tau_m(B')$  is significantly shorter than  $\tau_m(A) = \tau_m(S)$ . At elevated temperature (e),  $\tau_m(B')$  is comparable to  $\tau_m(A)$ .

and  $I_{\text{tot}}$  is the total intensity, estimated by the total radiative intensity which is roughly constant through  $\nu = 1$  [16]. The variation in the low-temperature  $E_0$  radiative time  $\tau_r$  around  $\nu = 1$  is shown in Fig. 2c; the peak in  $\tau_r$  at  $\nu = 1$  is quenched at 4.2 K as expected (not shown). Our low-temperature TRPL measurements over the range  $\nu = 0.7$  to 1.3 are in excellent agreement with the first, comprehensive TRPL study of the  $\nu = 1$  IQHE for both SHJ and QW samples [16]. The five-fold increase in  $\tau_r$  at  $\nu = 1$  corroborates

the view [7–10,16] that the optical (intensity) signature of the IQHE is due to a reduction in screening of photoexcited holes by  $E_0$  electrons.

TRPL decay curves for individual components of PL spectra in the FQHE and MIWS regimes are shown in Fig. 3. These measurements are difficult, requiring both high-resolution and low-excitation power. It has been possible, however, to obtain these results at  $T_e \approx 900$  mK which is above  $T_{c1}(\nu)$  but well below the higher temperature boundary  $T_{c2}(\nu)$  beyond which S structure, the low temperature intensity saturation of which is associated with the solid phase, disappears [10] (Fig. 1, insets (a) and (b)). The Fig. 3 insets show the PL spectra under the illumination conditions of the TRPL measurements – note the appearance of A' structure in Figs. 3b and 3c, and the development of a weak peak at low  $\nu$ , split-off to lower energy, arrowed in Fig. 3d [10]. Low-temperature TRPL measurements of the individual A and B recombination times at  $\nu = 1/3$  are essentially identical ( $\tau_m(A) = \tau_m(B) \approx 0.4$  ns; Fig. 3a). Decay curves for the dominant A,S,B' triplet PL components in the MIWS regime are shown in Figs. 3b–3d for  $\nu = 0.13, 0.10$  and  $0.09$ , respectively. It is found that whereas  $\tau_m(A)$  and  $\tau_m(S)$  are comparable throughout the low- $\nu$  region at low temperature ( $\sim 1.1$  ns at  $\nu \approx 1/10$ ),  $\tau_m(B')$  is shorter than  $\tau_m(S)$  by a factor  $\sim 2$ . The difference is expected to be sustained and possibly increased to lower  $T_e$  (in particular  $T_e < T_{c1}$ ); this follows from the observation that at elevated temperature (4.2 K), where S structure is no longer observed,  $\tau_m(B')$  becomes comparable to  $\tau_m(A)$  (Fig. 3e). The magnitude of the low-temperature measured decay times ( $\tau_m \leq 1$  ns), which are short for this system, is also important (see below). In addition to the clear difference in decay times for emergent S and B' structure observed in the MIWS region, at lowest  $\nu$  (Figs. 3c and 3d) the rise time for S becomes longer than for B' and develops a “flat-top” profile.

Whilst TRPL measurements of individual components of the e–h PL spectra in the MIWS (and FQHE) region inevitably perturb the electron temperature, it is possible to obtain data for the *complete* PL spectrum at electron temperatures below  $T_{c1}$  at low  $\nu$ . Selected TRPL decay

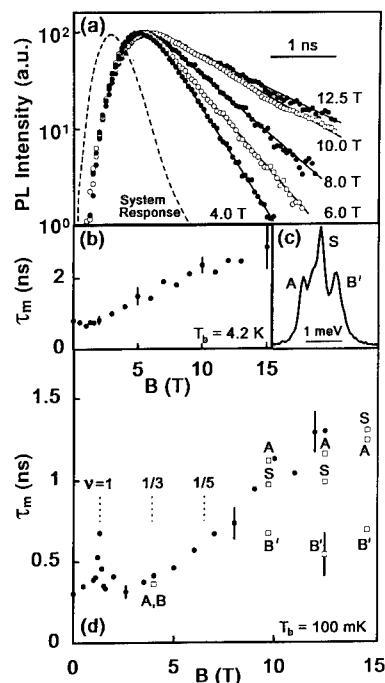


Fig. 4. (a) Normalised and aligned TRPL decay curves beyond 4 T ( $\nu = 1/3$ ) for the complete  $E_0$  PL spectrum, at  $T_e$  close to  $T_b \approx 100$  mK. The system response for the 4 T decay curve is also shown. (b) Plot of  $\tau_m$  for the complete  $E_0$  spectrum against field, at  $T_b = 4.2$  K. (c) PL at 11 T under illumination conditions of low-power TRPL experiment ( $T_e < T_{c1}$  defined in Fig. 1 – see text). (d) Plot of  $\tau_m$  against field, at  $T_b \approx 100$  mK; (●) – complete  $E_0$  spectra, (□) – individual components of the multiple-peak e–h spectra.

curves for the latter are shown in Fig. 4a, at  $T_e < T_{c1}$  (we can only define an upper bound for  $T_e$  since the thermometry provided by plots as in Fig. 1, inset (b) saturates by definition at  $T_{c1}$ ). Also shown in Fig. 4a (dashed line) is the overall measurement system response obtained from reflection of the laser pulse. Measured decay times  $\tau_m$  for the complete spectrum (excluding  $E_1$  emission at low field) are plotted in Fig. 4d (●) together with  $\tau_m$  values for the individual components of the PL spectra from Fig. 3 (□). The former (●) show a steady increase for  $\nu < 1$  with the onset of significant change beyond  $\nu = 1/3$ , from  $\tau_m \approx 0.4$  ns to  $\tau_m \approx 1.3$  ns at  $\nu = 1/10$ . There is no obvious deviation from this overall trend at FQHE states in the  $\nu = 1/3$  hierarchy, although there may be a small increase in  $\tau_m$  at

$\nu = 2/3$ . Setting aside the short B' decay times (see below), we note that the A,S component decay times in the FQHE and MIWS regimes taken under conditions of increased power are similar to the complete spectra data taken with low power. This indicates that the increased electron temperature in the individual-component measurements does not significantly affect  $\tau_m$ . A PL spectrum at 11 T ( $\nu = 0.13$ ) under conditions of the low-power TRPL measurements is shown in Fig. 4c. The entire set of measurements for the complete PL spectrum was repeated at 4.2 K, where decay times are  $\sim 1$  ns longer. The results are plotted in Fig. 4b showing a roughly linear increase in  $\tau_m$  with magnetic field for  $\nu < 1$ . A detailed comparison of Fig. 4b with the low-temperature  $\tau_m$  data in Fig. 4d suggests an increased slope beyond  $\nu \approx 1/5$  that is absent at 4.2 K. This observation is amplified by plots (not shown) of the *relative* increase in  $\tau_m$  (normalised to its zero-field value) with field which identify a two-fold enhancement in the slope of the low-temperature data for  $\nu \leq 1/5$  when compared to the 4.2 K data. This feature, partly masked by the overall field-dependence, is possibly associated with the MIWS phase.

#### 4. Discussion

A general observation from the Fig. 4d plot is that the short, measured decay times ( $\leq 1$  ns) are comparable with those for recombination at low temperature of quasi-2D excitons in QWs, modulation-doped QWs and double heterostructures; see, for example, Ref. [17] (QW situation). Calculations by Balslev [18] for SHJ structures show that photoexcitation at low temperatures is rapidly converted into mobile excitons that diffuse or drift quickly to the high electric field region and form stable states a few exciton Bohr radii from the heterojunction, so-called 2D “interface excitons”; in brief, an exciton created in the bulk will become trapped at the interface. Taken together with the previous model of PL in the IQHE and FQHE regimes, in particular our understanding of the  $E_0$  line as a many-body exciton and the  $E_1$  line as an exciton [7,10] (involving electrons in the

2DES), there is compelling evidence to view the details of the PL [10] summarised in Fig. 1 and the TRPL data assembled in Fig. 4d completely within an excitonic framework.

We put forward the following interpretation: the A ( $E_0$ ) line is a many-body exciton, as before [7,10], corresponding to recombination of photoexcited valence-band holes with 2D electrons in the densely occupied  $E_0$  subband. Its intensity mirrors the correlation of electrons in the vicinity of the hole, principally evidenced by the observation of sharp minima at IQHE, FQHE states; on entering the MIWS region there is no abrupt intensity signature, but rather a general fall-off in PL intensity at low  $\nu$  [7,10]. The absence of PL energy anomalies in sample G648 [10] at QHE states and on transition to the MIWS region could well be explained by the close proximity (in  $z$ ) of electron and hole planes in this structure [14b]; energy anomalies have been observed in other samples [7–9], at  $\nu = 1$  and  $2/3$ . It seems plausible that excitons created in the bulk that have diffused to the interface region could retain the character of a single-electron exciton in their recombination. We attribute the B line to an exciton bound (in  $z$ ) at the interface that does not directly involve electrons in the correlated 2DES. B intensity exhibits maxima at FQHE states as an indirect effect of the reduction of A emission. In this sense it is an analogue of the  $E_1$  exciton [7], with the distinction that  $E_1$  emission observed at low field involves recombination of 2D electrons photoexcited into the  $E_1$  subband. The view of B as a lightly-bound interface exciton of the type described by Balslev [18], and of a different character to A, is reinforced by the temperature dependence over the entire FQHE region [10]; B is significantly weaker than A at 2.2 K, whereas at 70 mK they are comparable (Fig. 1). The slope of the (roughly parallel) A and B energy trajectories (shift rate of transitions) is found to increase with magnetic field [10], an observation also reported for (bulk) magnetoexcitons, which supports our interpretation. The continuous increase in the measured decay time  $\tau_m$  for the complete PL spectrum throughout the high-field region  $\nu < 1/3$  in Fig. 4d indicates that the luminescence retains its essential excitonic

character at high field. A similar increase, observed in  $\delta$ -doped structures [13c], has been attributed to reduced magnetic length but it is not clear that this is valid for e–h PL.

Whilst the A line continues smoothly on entering the MIWS region, the B line is replaced by emergent S and B' structure [10]. There are two possibilities for the effect of the formation of a MIWS phase on B emission – the B exciton becomes localised in some way by the Wigner lattice at, say, an interstitial position or by formation of a Bloch state, resulting in the observed S line to slightly lower energy, or it remains unlocalised but nevertheless influenced by the changed electronic background conditions at low  $\nu$ , resulting in the B' line to higher energy. *Two principal experimental observations are consistent with this model.* Firstly, the transfer of intensity from S to B' on increasing the temperature, at a threshold temperature  $T_{c1}$  which correlates with the liquid–solid transition, [10] (Fig. 1, inset (a)) is then explained by delocalisation of the S exciton, resulting from melting of the electron lattice. Secondly, the measured decay time  $\tau_m$  for the B' line is significantly shorter than for S (Figs. 3b–3d and 4d). From our picture it is clear that at low temperature, in addition to S, B' radiative channels, there should be a non-radiative channel from B' to S corresponding to the likelihood of a delocalised exciton (B'), becoming localised (S) by spatial electronic order. This has the effect that in the radiative emission of A, S, B' in the MIWS region, which would otherwise be expected to be similar (as for A, B at  $\nu = 1/3$  in a common hole model (Figs. 3a and 4d)), the measured decay time of B' will be shorter. We have performed simple model calculations of this scheme which generate decay curves remarkably similar to the Fig. 3 data, even with respect to details such as the longer rise time and flat-topped character of the S curve, which results from the non-radiative channel B' to S.

Finally, we note that the temperature-dependent transfer of intensity between the S and B' lines and the different measured decay times of S and B' have strong similarities to the behaviour of the two PL lines observed in e–A<sup>0</sup> emission in the MIWS phase [11–13]. Whilst it is not obvious

that the localised exciton mechanism put forward above can be carried across to the very different  $\delta$ -doped structures, our model is consistent with the array of e–h PL and TRPL data summarised in Figs. 1 and 4, respectively.

## 5. Acknowledgements

We thank A.H. MacDonald for helpful discussions and S. Das Sarma for a preprint of Ref. [15].

## 6. References

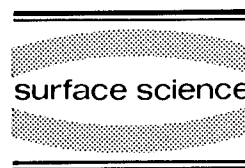
- [1] For a review, see, M. Shayegan, in: *New Concepts for Low Dimensional Electronic Systems*, 7th Int. Winter-school on New Developments in Solid State Physics 1992, Springer Series in Solid State Sciences, to be published.
- [2] F.I.B. Williams, P.A. Wright, R.G. Clark, E.Y. Andrei, G. Deville, D.C. Glatli, O. Probst, B. Etienne, C. Dorin, C.T. Foxon and J.J. Harris, *Phys. Rev. Lett.* 66 (1991) 3285.
- [3] M.A. Paalanen, R.L. Willett, P.B. Littlewood, R.R. Ruel, K.W. West, L.N. Pfeiffer and D.J. Bishop, *Phys. Rev. B* 45 (1992) 11342.
- [4] I.M. Ruzin, S. Marianer and B.I. Shklovskii, *Phys. Rev. B* 46 (1992) 3999.
- [5] A.H. MacDonald, in: *New Concepts for Low Dimensional Electronic Systems*, as for Ref. [1].
- [6] For a review, see, R.G. Clark, in: *New Concepts for Low Dimensional Electronic Systems*, as for Ref. [1].
- [7] A.J. Turberfield, S.R. Haynes, P.A. Wright, R.A. Ford, R.G. Clark, J.F. Ryan, J.J. Harris and C.T. Foxon, (a) *Phys. Rev. Lett.* 65 (1990) 637; (b) *Surf. Sci.* 263 (1992) 1.
- [8] R.G. Clark, R.A. Ford, S.R. Haynes, J.F. Ryan, A.J. Turberfield, P.A. Wright, C.T. Foxon and J.J. Harris, *High Magnetic Fields in Semiconductor Physics III*, Vol. 101 of Springer Series in Solid State Sciences (Springer, Berlin, 1992) p. 231.
- [9] B.B. Goldberg, D. Heiman, A. Pinczuk, L. Pfeiffer and K.W. West, (a) *High Magnetic Fields in Semiconductor Physics III* Vol. 101 of Springer Series in Solid State Sciences (Springer, Berlin, 1992) p. 243; (b) *Phys. Rev. Lett.* 65 (1990) 641; (c) *Surf. Sci.* 263 (1992) 9.
- [10] E.M. Goldys, S.A. Brown, R.B. Dunford, A.G. Davies, R. Newbury, R.G. Clark, P.E. Simmonds, J.J. Harris and C.T. Foxon, *Phys. Rev. B* 46 (1992) 7957; see also *Physica B* 184 (1993) 56.
- [11] H. Buhmann, W. Joss, K. von Klitzing, I.V. Kukushkin, G. Martinez, A.S. Plaut, K. Ploog and V.B. Timofeev, (a) *Phys. Rev. Lett.* 65 (1990) 1056; (b) 66 (1991) 926.

- [12] M.K. Ellis, M. Hayne, A. Usher, A.S. Plaut and K. Ploog, *Phys. Rev. B* 45 (1992) 13765.
- [13] I.V. Kukushkin, N.J. Pulsford, K. von Klitzing, K. Ploog, R.J. Haug, S. Koch and V.B. Timofeev, (a) *Phys. Rev. B* 45 (1992) 30; (b) 4532; (c) *Physica B* 184 (1993) 38.
- [14] (a) V.M. Apal'kov and E.I. Rashba, *Pis'ma Zh. Eksp. Teor. Fiz.* 53 (1991) 420 [*JETP Lett.* 53 (1991) 442]; (b) A.H. MacDonald, E.H. Rezayi and D. Keller, *Phys. Rev. Lett.* 68 (1992) 1939.
- [15] H.A. Fertig, D.Z. Liu and S. Das Sarma, *Phys. Rev. Lett.* 70 (1993) 1545.
- [16] M. Dahl, D. Heiman, A. Pinczuk, B.B. Goldberg, L.N. Pfeiffer and K.W. West, *Phys. Rev. B* 45 (1992) 6957.
- [17] (a) J. Feldmann, G. Peter, E.O. Göbel, P. Dawson, K. Moore, C. Foxon and R.J. Elliott, *Phys. Rev. Lett.* 59 (1987) 2337; (b) H.W. Liu, C. Delalande, G. Bastard, M. Voos, G. Peter, R. Fischer, E.O. Göbel, J.A. Brum, G. Weimann and W. Schlapp, *Phys. Rev. B* 39 (1989) 13537.
- [18] I. Balslev, *Semicond. Sci. Technol.* 2 (1987) 437.



ELSEVIER

Surface Science 305 (1994) 50–54



# Time-resolved photoluminescence in the fractional quantum Hall regime

D. Heiman <sup>\*,a</sup>, A. Pinczuk <sup>b</sup>, M. Dahl <sup>c</sup>, B.S. Dennis <sup>b</sup>, L.N. Pfeiffer <sup>b</sup>, K.W. West <sup>b</sup>

<sup>a</sup> MIT Francis Bitter National Magnet Lab., Cambridge, MA 02139, USA

<sup>b</sup> AT&T Bell Labs., Murray Hill, NJ 07974, USA

<sup>c</sup> Physikalisches Institut der University Wurzburg, Wurzburg, Germany

(Received 22 April 1993; accepted for publication 22 July 1993)

## Abstract

Photoluminescence (PL) spectra from excitons in the 2D electron layer in GaAs shows anomalous behavior that reflects the intrinsic properties of the strongly interacting 2D electron system. In the regime of the fractional quantum Hall effect an additional spectral peak is observed for Landau filling factor  $\nu < 1/2$ . At  $\nu = 1/3$  a dramatic transfer of intensity between the peaks is observed which is coincident with a sharp increase in the PL decay times. This effect is influenced by changes in electron–hole overlap as a result of changes in the polarizability of the Laughlin fluid/electron gas. In the extreme quantum limit  $\nu < 1/4$ , the PL decay time for the higher-energy peak decreases while the lower-energy peak decay time increases.

## 1. Introduction

Recent optical experiments on low-defect 2D electron systems in high magnetic fields have provided information about the intrinsic properties of the complex interaction of electrons in two dimensions [1–6]. Photoluminescence (PL) studies of itinerant electron–hole (exciton) recombination revealed striking spectral signatures corresponding to Shubnikov–de Haas oscillations [1], and the integer and fractional quantum Hall effects (QHE) [2–5]. Interesting phenomena have also been observed in PL from localized carriers [6]. Subsequently there have been a number of

theoretical investigations of optical spectra in the IQHE [7–8] and FQHE [9–12] regimes.

One of the general features of the exciton PL is the emergence of *higher-energy peaks* in the extreme quantum limit  $\nu < 1$ . This was first observed in a 2D system of moderate mobility  $\mu \sim 2 \times 10^5 \text{ cm}^2/\text{V} \cdot \text{s}$ , in which the peaks were split by nearly 1 meV [3]. In previous optical studies, spectral blue shifts and intensity variations were found at both integer and fractional Landau filling factors [3–5]. Now, sample quality has improved considerably ( $\mu > 2 \times 10^6 \text{ cm}^2/\text{V} \cdot \text{s}$ ) and the resulting narrow PL linewidths ( $\sim 0.2 \text{ meV}$ ) permit us to clearly resolve the optical anomalies. In these new materials we have conclusively established that the spectral energy shifts of each component are rather small ( $\leq 0.1 \text{ meV}$ ), but there are large transfers of spectral intensity from

\* Corresponding author.

the lower-energy peak to the upper peak, in correspondence with the QHE.

The first time-resolved PL measurements of the QHE established that the intensity transfer at  $\nu = 1$  resulted from an increase in the radiative lifetime of the ground state [13]. There, we suggested that the electron–hole overlap decreases when the 2D electron sheet becomes insulating at  $\nu = 1$ , which is influenced by the reduced image charge attraction of the hole to the 2D electron sheet. In the present study we examine the time evolution of PL in the regime of the FQHE near  $\nu = 1/3$  and beyond.

## 2. Experiment

Time-resolved PL measurements were made on a 25 nm wide GaAs/(Al,Ga)As single quantum well that was single-side doped with electrons. The electron density  $n = 0.81 \times 10^{11} \text{ cm}^{-2}$  was found to be the same at  $B = 0$ ,  $\nu = 1$  and  $\nu = 1/3$ , as determined from the optically measured Fermi energy and spectral intensity transfers. This is in contrast to most single interfaces and wide ( $\geq 40$  nm) quantum wells which show electron depletion due to optical pumping [14]. A single optical fiber was used to access the  $B = 19$  T magnet and  $^3\text{He}$  cryostat [2]. The spectral resolution was limited to 0.3 meV, although smaller resolutions were able to reveal fine structure in the major spectral peaks, which we ignored here. The PL time response was measured using a pulsed 0.78  $\mu\text{m}$  laser diode, side-on GaAs photomultiplier, and time-correlated single-photon counting technique. For this publication, only the decay time  $\tau_D$  is presented, which was determined from fits to the exponential PL tail at long times, but with the response function subtracted.

## 3. Time-averaged results

Before discussing the time response of the PL we present the time-averaged PL results. Fig. 1 shows selected time-averaged spectra at various magnetic fields  $B$ . Notice the additional peak emerging from the high-energy side of the main

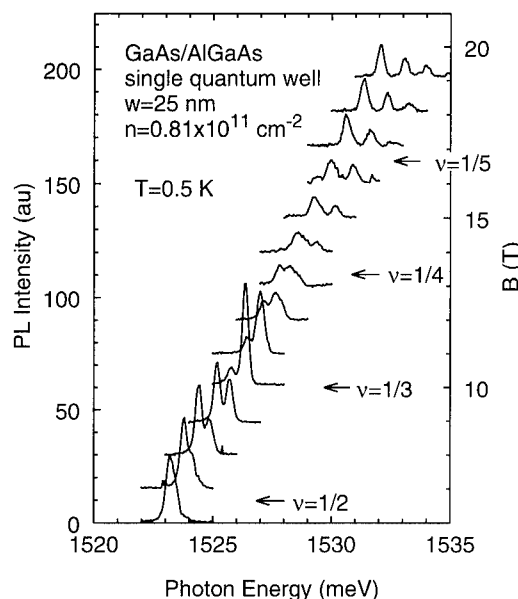


Fig. 1. Time-averaged photoluminescence spectra from excitons in a 2D electron system for various magnetic fields. Spectral resolution = 0.3 meV.

PL peak above  $B = 7$  T ( $\nu < 1/2$ ), and a third higher-energy peak above  $B = 15$  T ( $\nu < 1/5$ ). These three major peaks are labeled A, B and C, for increasing energies, respectively. Closer examination of these peaks revealed fine structure, which is not of interest here.

### 3.1. Energies

Fig. 2 shows the energies  $E_i(B)$  of the PL spectral peaks. First we note that near  $\nu = 1/3$  the peak separation is  $E_B - E_A \approx 0.6$  meV. Although the separation is similar to the FQHE quasiparticle–quasihole gap energy of  $\Delta \approx 1$  meV, it does not scale as the magnetic energy ( $B^{1/2}$ ) and is present over a very wide field range. There are, however, subtle changes in the separation. Above  $B = 9$  T,  $E_A$  is extremely linear with magnetic field, to within  $\pm 0.05$  meV. In  $E_B$  there is a small blue-shift cusp of 0.1 meV at  $\nu = 1/3$ , which is displayed in the inset. This deviation is an order of magnitude smaller than  $\Delta$ . The theory of Ref. [9] predicts magneto-roton satellites separated by approximately  $\Delta$ ; Ref. [11] predicts that for  $\nu > 1/3$  a second peak should appear



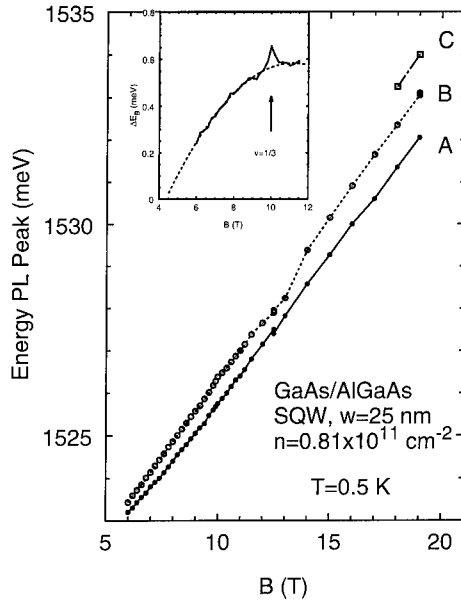


Fig. 2. Energies of spectral peaks in the photoluminescence of a 2D electron system as a function of magnetic field. The inset shows energy difference of A and B peaks.

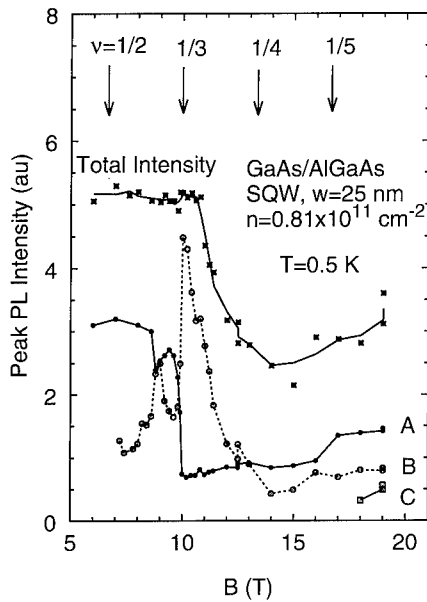


Fig. 3. Time-averaged photoluminescence intensity of A-, B-, and C-peaks versus magnetic field for a 2D electron system. The total intensity data was integrated over the whole spectral peak range.

which is higher in energy by  $\Delta$ ; and Ref. [12] predicts a cusp in the energy at  $\nu = 1/3$ . In the two latter models the magnitude of the effect should go to zero for complete electron–hole  $z$ -overlap. Our sample has a moderate overlap, but we will not quantify it in this paper.

### 3.2. Intensities

Fig. 3 shows the peak intensities  $I_i$ . In the top curve we see that the total integrated PL intensity of all the peaks is constant up to  $B = 11$  T ( $\nu > 0.30$ ); in this region there is a simple transfer of intensity between  $I_A$  and  $I_B$ . Second, we observe a dramatic maximum in  $I_B$  at  $\nu = 1/3$ . The transfer of intensity from the lower- to higher-energy peaks is directly related to the PL time response described below. At higher fields  $B > 11$  T the total intensity decreases.

## 4. Time-resolved results

### 4.1. FQHE regime $1/2 > \nu > 1/4$

The inset of Fig. 4 shows raw data for the PL time response of the A-peak at various magnetic fields, along with the time response of the measuring system. In general, as the magnetic field increases, the PL( $t$ ) data develops a longer tail. The derived PL decay times  $\tau_D(B)$  are displayed in the main part of Fig. 4, where the A-peak data are represented by the solid curve and the B-peak by the dotted curve. There are sharp maxima in  $\tau_D$  at  $\nu = 1/3$  for both peaks. The large  $\tau_D$  maximum in the A-peak coincides with a minimum in intensity. A similar lengthening of decay time at an intensity minimum was also found in measurements at  $\nu = 1$  [13]. If we assume a simple two-level model then the radiative lifetime  $\tau_R \sim \tau_D/I$ , so the rapid drop of intensity enhances the increase in the radiative lifetime. From the data we find that  $\tau_R$  for the A-peak grows by almost  $10\times$  as the  $\nu = 1/3$  FQHE is entered.

### 4.2. Electron solid regime $\nu < 1/4$

For magnetic fields up to  $B = 13$  T, Fig. 4 shows that the decay times for the two PL peaks

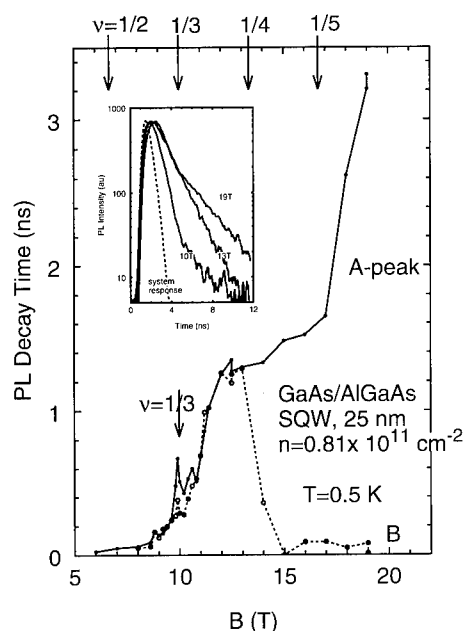


Fig. 4. Photoluminescence decay times of the A-peak (solid curve) and B-peak (dashed curve) for a 2D electron system versus magnetic field. The inset shows the A-peak PL intensity versus time for  $B = 10, 13$ , and  $19$  T; the dashed curve is the system response.

are nearly equal. However, above  $B = 13$  T the decay time for the B-peak  $\tau_D$  goes to nearly zero (resolution limited). This large difference in  $\tau_D$  is accompanied by a relatively large change in the energy separation of the peaks. (Since the character of the B-peak changes considerably at  $B = 13$  T we cannot exclude the possibility that there are actually two different B-peaks above and below  $B = 13$  T.) It is remarkable that although the decay times at  $B = 19$  T are orders of magnitude different their intensities are nearly equal. Finally, at higher temperatures there is a decrease in  $\tau_D$  for the A-peak.

## 5. Discussion

The present photoluminescence study of the FQHE regime reveals a number of results.

(a) Additional spectral peaks emerge at higher energies for  $\nu < 1/2$  (B-peak), and  $\nu < 1/5$  (C-

peak), having a splitting of  $\sim 0.6$  meV at  $\nu \sim 1/3$ , and 1 meV at  $\nu = 1/5$ .

- (b) Near  $\nu = 1/3$  the A-peak energy is smoothly varying with  $\nu$ , but the B-peak energy increases by 0.1 meV precisely at  $\nu = 1/3$ .
- (c) At  $\nu = 1/3$  the PL intensity is dramatically transferred from the A-peak to the B-peak.
- (d) For  $\nu \geq 1/3$  the total PL intensity is independent of  $\nu$ , but decreases significantly for smaller  $\nu$ .
- (e) At  $\nu = 1/3$  both PL peaks show a significant increase in their decay times.
- (f) At  $\nu < 1/3$  the PL decay times continue to increase for increasing field, however, above  $B = 13$  T the decay time for the B-peak is nearly zero; at  $B = 19$  T they differ by several orders of magnitude.

One of the open questions here is what mechanism gives rise to the higher-energy spectral peaks found at small filling factors. The additional spectral peak has been found in almost all PL studies of itinerant electron-hole recombination in high-mobility GaAs structures [2–5]. We find that the energy separation does not scale simply as the magnetic energy  $e^2/\epsilon l_c$ , where  $l_c \sim B^{-1/2}$  is the magnetic length (cyclotron radius). It is likely that these peaks arise from the complex many-body response of the 2D electron system to the valence band hole.

From these time-resolved PL measurements it is clear that at  $\nu = 1/3$  the transfer of spectral intensity between the PL peaks is due to the changing dynamics of the electron-hole system. The radiative lifetime is related to the carrier wavefunctions through the electron-hole overlap. Both the in-plane ( $xy$ ) and perpendicular ( $z$ ) overlap of the wavefunctions may be important [13]. In particular, it may be the difference of the polarizability between the 2D electron gas and the Laughlin fluid that affects the overlap of the electron wavefunction and the hole. One should keep in mind that the itinerant hole resides in a complex self-consistent potential generated by itself and the 2D electron system. The  $z$ -component of the hole wavefunction and its overlap with the electron system is sensitive to this potential. For example, the hole is likely to move away from the electron layer when the polarizability of

the electron system becomes reduced. Likewise, the *xy*-plane electron–hole overlap may change when the electron system is in an insulating state. This could be important in the extreme quantum limit where the electron solid is expected. Experiments are in progress at lower temperatures to explore this regime.

## 6. Acknowledgements

This work was supported by the National Science Foundation through grant DMR-9201614. We also thank H. Okamura for assistance.

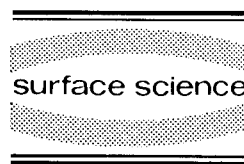
## 7. References

- [1] W. Chen, M. Fritze, A.V. Nurmikko, D. Ackley, C. Colvard and H. Lee, *Phys. Rev. Lett.* 64 (1990) 2434.
- [2] D. Heiman, in: *Semiconductors and Semimetals*, Vol. 36, Eds. R.K. Willardson and A.C. Beer (Academic Press, New York, 1992) p. 1.
- [3] D. Heiman, B.B. Goldberg, A. Pinczuk, C.W. Tu, A.C. Gossard and J.H. English, *Phys. Rev. Lett.* 61 (1988) 605.
- [4] A.J. Turberfield, S.R. Haynes, P.A. Wright, R.A. Ford, R.G. Clark, J.F. Ryan, J.J. Harris and C.T. Foxon, *Phys. Rev. Lett.* 65 (1990) 737.
- [5] B.B. Goldberg, D. Heiman, A. Pinczuk, L.N. Pfeiffer and K.W. West, *Phys. Rev. Lett.* 65 (1990) 641.
- [6] I.V. Kukushkin, N.J. Pulsford, K. von Klitzing, K. Ploog and V.B. Timofeev, *Surf. Sci.* 263, (1992) 30; H. Buhmann, W. Joss, K. von Klitzing, I.V. Kukushkin, G. Martinez, A.S. Plaut, K. Ploog and V.B. Timofeev, *Phys. Rev. Lett.* 65 (1990) 1056.
- [7] P. Hawrylak, N. Pulsford and K. Ploog, *Phys. Rev. B* 46 (1992) 15193.
- [8] T. Uenoyama and L.J. Sham, *Phys. Rev. B* 39 (1989) 11044; S. Katayama and T. Ando, *Solid. State Commun.* 70 (1989) 97.
- [9] S.R. Eric Yang, *Phys. Rev. B* 40 (1989) 1836.
- [10] B.S. Wang, J.L. Birman, Z.B. Su, *Phys. Rev. Lett.* 68 (1992) 1605.
- [11] A.H. MacDonald, E.H. Rezayi and David Keller, *Phys. Rev. Lett.* 68 (1992) 1939.
- [12] V.M. Apalkov and E.I. Rashba, *Phys. Rev. B* 46 (1992) 1628.
- [13] M. Dahl, D. Heiman, A. Pinczuk, B.B. Goldberg, L.N. Pfeiffer and K.W. West, *Phys. Rev. B* 45 (1992) 6957; M. Dahl, D. Heiman, A. Pinczuk, B.B. Goldberg, L.N. Pfeiffer and K.W. West, *Surf. Sci.* 263 (1992) 638.
- [14] D. Heiman, A. Pinczuk, B.S. Dennis, L.N. Pfeiffer and K.W. West, *Phys. Rev. B* 45 (1992) 1492.



ELSEVIER

Surface Science 305 (1994) 55–60



# Time-resolved magnetoluminescence and Raman scattering measured in the regime of the fractional quantum Hall effect and of the Wigner solid

I.V. Kukushkin <sup>\*,1</sup>, R.J. Haug, K. von Klitzing, K. Eberl, K. Ploog

*Max-Planck-Institut für Festkörperforschung, Stuttgart 80, Germany*

(Received 21 April 1993; accepted for publication 2 July 1993)

## Abstract

The kinetics of radiative recombination of 2D-electrons with free holes and with holes bound to acceptors were studied for the first time in the regime of the FQHE and of the Wigner solid. We found that in the extreme quantum limit the recombination rates for both recombination processes became extremely slow due to localization effects.

## 1. Introduction

Magnetoluminescence is known to be a very effective tool to study the properties of 2D-electrons in the regime of the fractional quantum Hall effect (FQHE) and of the Wigner solid [1–6]. There are two different experimental possibilities for investigation of the radiative recombination of 2D-electrons with photoexcited holes. One possibility is the recombination of electrons with holes bound to acceptors [2,7], and another in recombination with free holes [4–6]. It was established both theoretically [8,9] and experimentally [10,11] that in the case of recombination with free holes (located in the same 2D-plane as electrons) there is no contribution from electron–electron interaction to the energy position of luminescence lines (the FQHE appears only in

intensity dependence on filling factor due to screening effects), whereas in the case of holes bound to remote acceptors, the spectral position of the recombination line reflects the dependence of the mean energy of interacting electrons on filling factor. Therefore, the investigation of radiative recombination of 2D-electrons with holes bound to acceptors located far away from the interface is a direct method to study the ground state of the system of interacting 2D-electrons in the extreme quantum limit.

## 2. Experiment

We studied high quality GaAs/AlGaAs single heterojunctions with a 2000 nm GaAs buffer layer in which a monolayer of acceptors (with concentration  $5 \times 10^9 \text{ cm}^{-2}$ ) was created at a distance of  $Z = 30\text{--}50 \text{ nm}$  away from the interface. It was possible to change the concentration of 2D-electrons

\* Corresponding author.

<sup>1</sup> On leave from: Institute of Solid State Physics, RAS, Chernogolovka 142432, Russian Federation.

trons by illumination power in the range of  $(0.3-4) \times 10^{11} \text{ cm}^{-2}$ . The transport mobility of electrons at the lowest concentration was  $2 \times 10^6 \text{ cm}^2/\text{V} \cdot \text{s}$ . For photoexcitation we used pulses of an  $\text{Ar}^+$ -laser with a duration of 20 ns, peak powers of  $10^{-5}-10^{-3} \text{ W/cm}^2$  and frequencies of 1–0.01 mHz [11]. Luminescence was detected by a gated photon counting system. The time resolution of the system was about 30 ns and the spectral resolution was 0.01 meV. We estimated the overheating of 2D-electrons due to illumination from the width of magnetoresistance peaks in the Shubnikov–de Haas oscillations [12] and found that under continuous illumination with the above mentioned power level it does not exceed 20 mK at the bath temperature of 30 mK. Other experimental details can be found in Refs. [10,12].

### 3. Time-resolved magnetoluminescence and the hierarchy of the FQHE states

It follows from theory [8] that the exact correspondence between spectral position of the luminescence line and the mean energy of 2D-electrons does exist for the case when the acceptor is located at an infinite distance from the 2D-channel. However, in real situations we deal with finite distances and therefore it is important that the corrections to this simple expression are small enough. These corrections are defined by the third power of the ratio  $l_h/d$  ( $d$  is the distance to the acceptor, and  $l_h$  is the magnetic length) and therefore, to fulfill the theory requirement for magnetic fields in the range of 5–20 T one has to have  $d$  about 50 nm. However, an increase of the distance between 2D-electrons and the acceptors' monolayer results in an exponential increase of the recombination time [13] and hence in an exponential reduction of the intensity of the corresponding luminescence signal. The consequence of this problem in CW-measurements is an appearance of the bulk signal (donor–acceptor recombination) with an intensity comparable to the 2D-luminescence. The application of the time-resolved technique allowed us to solve this problem and it also results in a much better

resolution of the Landau levels in the luminescence spectra (individual Landau levels became visible starting from  $H = 0.4 \text{ T}$ ). To analyze the dependence of the spectral position of the luminescence line as a function of filling factor, we numerically calculate the normalized first moment –  $M_1$  (center of gravity) of the line [10]. This procedure allows us to observe a very large number of different FQHE states:  $4/5, 5/7, 2/3, 3/5, 4/7, 5/9, 4/9, 3/7, 2/5, 1/3, 2/7, 3/11, 2/9, 1/5, 2/11$ , and to study the hierarchy of the FQHE states in detail [14].

### 4. Kinetics of luminescence in the regime of the Wigner solid

According to our previous observation, in the regime of very small filling factors,  $\nu < 1/4$ , where the Wigner crystal is expected to form the ground state of the electronic system, two phenomena are observed in the luminescence spectra – an appearance of an additional luminescence line accompanied by a strong reduction of the integrated luminescence intensity [3]. Our proposed explanation was based on the localization of both electrons (in the pinned Wigner solid) and holes (on acceptors) in the 2D-plane. In this model the overlap of the wavefunctions of electrons and holes in the 2D-plane decreases with increasing magnetic field and this results in an exponential increase of recombination time, and, hence, in a decrease of the integrated intensity. In this work we performed direct measurements of the kinetics of magnetoluminescence in the regime of Wigner crystallization which confirmed the proposed model. Namely, we found [12,15] that the recombination time for electrons in the pinned Wigner solid is exponentially increasing with magnetic field and became up to several orders of magnitude longer than for electrons in the liquid phase. The difference in recombination times of the 2D-electrons in liquid and solid phases is obvious from the time dependence of the integrated luminescence intensity, presented in Fig. 1 for different magnetic fields. Below  $H < 2 \text{ T}$  (at  $\nu < 1$ ) the decay in intensity is described by a single exponent with  $\tau = 220 \text{ ns}$  ( $Z = 30 \text{ nm}$ ),

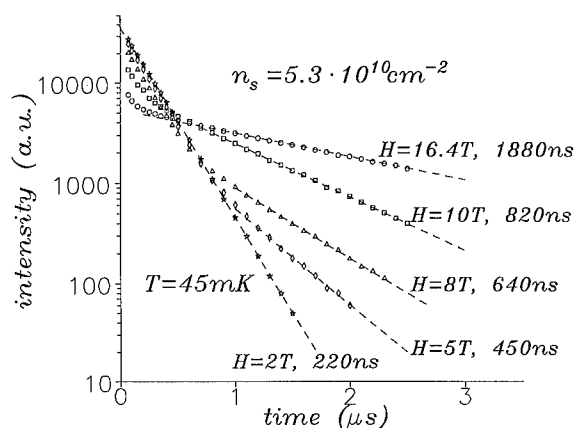


Fig. 1. Kinetics of luminescence measured in different magnetic fields.

corresponding to the recombination of electrons in the liquid phase. As the magnetic field increases, a tail with a slow decay time appears at large delay times due to the recombination of electrons in the solid phase (only the *S*-line remains in the spectra for these delays). We found that the recombination time of 2D-electrons in the solid phase increases exponentially with magnetic field, whereas it remains constant in the liquid phase [12,15]. Different time scales allow us to investigate the properties of liquid and solid phases independently and to derive a phase diagram for the Wigner solid [12,15]. Besides this we were able to distinguish between an extrinsic glass-like phase of localized electrons (due to single-particle localization on disorder sites) and intrinsic solid phase, which we assign to the Wigner solid.

### 5. Recombination of 2D-electrons with free holes

The recombination of 2D-electrons with free holes in a single heterojunction has been intensively studied by different groups [4–6,16]; however, there are many unsolved problems remaining. We observed such recombination only in a few samples (in 3 samples from approximately one hundred studied) and only under the follow-

ing conditions: the GaAs buffer layer is n-type, the concentration of 2D-electrons is less than  $2 \times 10^{11} \text{ cm}^{-2}$  and the temperature is less than a critical temperature  $T_c$  ( $T_c = 4 \text{ K}$  at  $H = 0$ , and it is growing with magnetic field). It is still unclear at what distance from the interface the holes are located and what is their spatial distribution. It follows from the time-resolved measurements that the recombination time of 2D-electrons with free holes is very short (in comparison with recombination with bound holes) – 1 ns [16]. In our samples we found that at zero magnetic field the recombination time of the free holes depends on concentration and that it is in the range of 1–4 ns for concentrations of  $(0.5\text{--}2) \times 10^{11} \text{ cm}^{-2}$  [17]. The luminescence spectra measured for different magnetic fields in one of the samples of this type (sample B) are presented in Fig. 2a. One sees a similarity of these spectra and the spectra measured in Refs. [5,6]: a strong intensity of recombination from the first excited subband at  $\nu > 1$ , splitting of the line into two components A and B at  $\nu < 1$  and an appearance of the *S*-line (sensitive to the temperature) in the regime of Wigner crystallization. We also observed an oscillatory redistribution of the recombination intensities among lines  $E_0$  and  $E_1$  (and among lines A and B) at values of magnetic field and density corresponding to the integer and fractional QHE [5,6]. Another feature visible in Fig. 2a is a reduction of the integral intensity at  $\nu \ll 1$  at low temperatures similar to that observed for the case of recombination with holes bound to acceptors [3]. As we demonstrated for the case of bound holes, this reduction was due to a decrease of the recombination rate in a magnetic field. We investigated also the time evolution of the spectra for 2D-electrons recombining with free holes and found that at low temperatures and high magnetic fields, the kinetics of the recombination became very slow, nonexponential and very sensitive to the temperature (see Fig. 2b). The time evolution of the corresponding luminescence spectra is shown in Fig. 2c. It is obvious from this figure that at long delay times only the *S*-line (and *S*\*-line) remains in the spectrum, whereas the A and B lines disappeared much faster. Such a behaviour is similar to the above mentioned

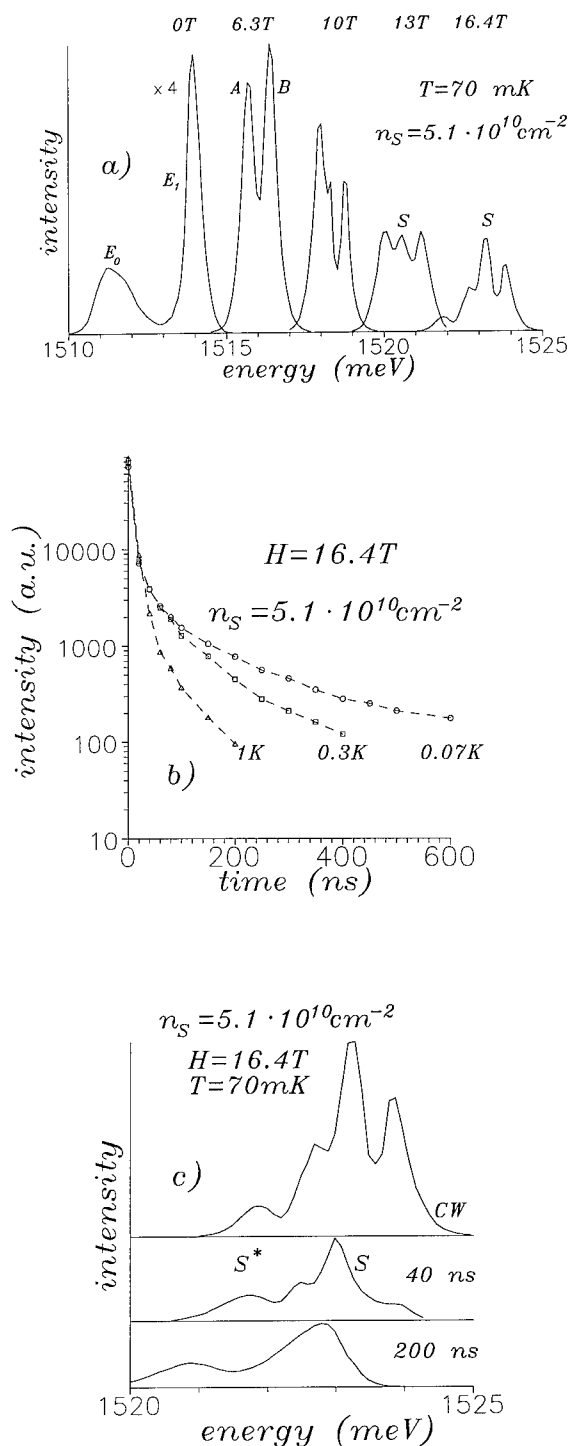


Fig. 2. Spectra of recombination with free holes (a); the kinetics of this recombination (b); and the time evolution of the luminescence signal (c) measured for sample B.

one, found for the recombination with holes bound to acceptors and, therefore, we explained the observed results in terms of recombination of localized 2D-electrons with holes localized on disorder sites (with some distribution in localization energy). The wave functions of both localized electrons and holes are defined by magnetic length and, therefore, their overlap in the 2D plane goes to zero exponentially with increase of magnetic field. An increase in temperature results in delocalization of both electrons and holes, and, consequently, to an increase of recombination rate.

## 6. Reduction of the electron concentration in the extreme quantum limit

A rather old puzzle which attracts interest is the observed reduction of the concentration of 2D-electrons in a strong magnetic field under continuous illumination [5], resulting in the collapse of the intersubband splitting [18]. Up to now, the reason for this reduction is not clear [5,6,18], and the main problem was to explain the fact that the reduction of concentration was observed only at temperatures lower than 2 K. To investigate this phenomenon we studied Raman scattering and time-resolved luminescence and found that the reduction of the electron concentration takes place simultaneously with a reduction of the recombination rate due to the localization of both electrons and holes in the 2D-plane. These two phenomena are observed at  $\nu < 1$  and are similarly sensitive to the magnetic field and to the temperature. In Fig. 3a we show Raman spectra measured at  $H = 0$  for different concentrations of 2D-electrons. In these measurements we used the illumination of an  $\text{Ar}^+$ -laser ( $\lambda = 488 \text{ nm}$ ,  $W = 10^{-6} \times 10^{-4} \text{ W/cm}^2$ ) for variation of the concentration [19], and tunable Ti/sapphire laser ( $\lambda = 740\text{--}750 \text{ nm}$ ,  $W = 10^{-3}\text{--}10^{-1} \text{ W/cm}^2$ ) for Raman measurements. One can see from this figure that the reduction in  $n_s$  results in a reduction of intersubband splitting. In Fig. 3b we show the dependence  $E_{10}(n_s)$  measured for different samples by Raman scattering

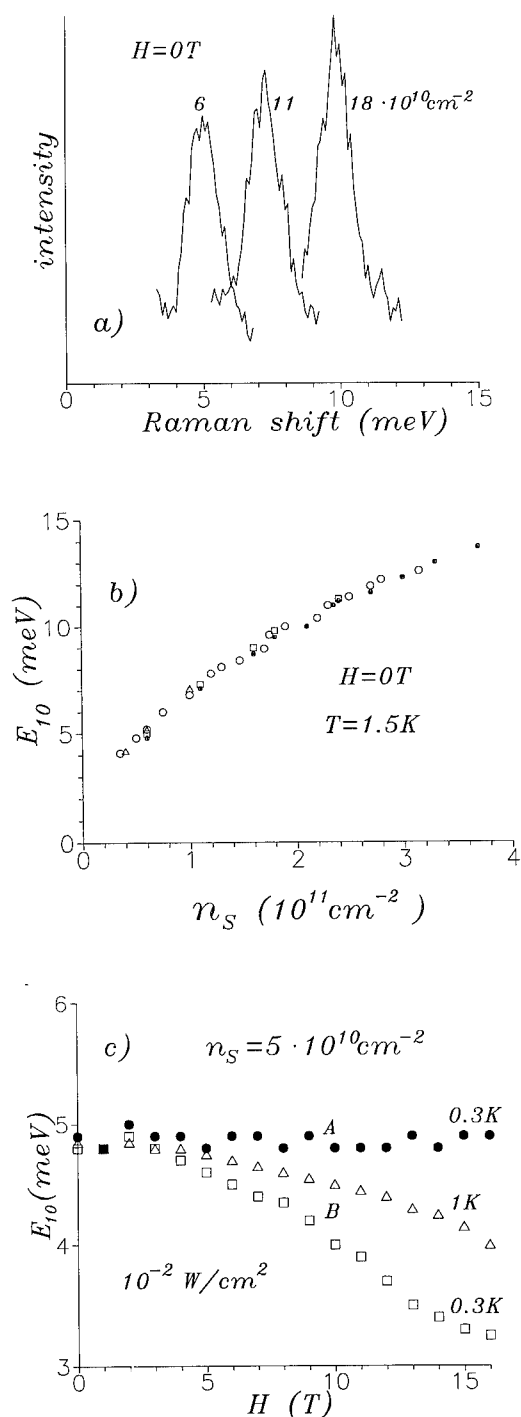


Fig. 3. Raman spectra measured for different concentrations (a); Dependence of intersubband splitting on 2D-electron concentration (b); Dependence of intersubband splitting on magnetic field for different samples (c).

(open symbols) and also by luminescence [20] (closed symbols). A reasonable agreement between the results obtained by these methods is obvious from this figure; therefore, we used Raman scattering as a test of the reduction in the 2D-concentration. In Fig. 3c we present a variation of the intersubband splitting with magnetic field and temperature measured for two different samples (A and B) with similar concentrations of 2D-electrons (at  $H=0$   $n_s = 5 \times 10^{10} \text{ cm}^{-2}$ ). One can see from this figure that the reduction in  $n_s$  happens only for sample B (open symbols), in which the slow recombination with free holes was observed in the same region of magnetic fields and temperatures. We associate the observed reduction in  $n_s$  with a strong increase of the concentration of free holes (comparable with the concentration of 2D-electrons) at low temperatures and high magnetic fields. A simple estimation shows that for an excitation power  $W = 10^{-3} \text{ W/cm}^2$  and recombination time  $\tau = 10^{-6} \text{ s}$  the concentration of the holes  $n_h = W\tau/\hbar\omega = 10^{10} \text{ cm}^{-2}$  ( $\hbar\omega$ , being 1.6 eV, is the energy of photons used for excitation). It is important that there is no upper limit of  $n_h$  in the case of free holes, whereas in the case of holes bound to acceptors the limit is given by the concentration of the acceptors.

## 7. Conclusion

Time-resolved magnetoluminescence and Raman scattering were used to study the properties of 2D-electrons in the regime of FQHE and of the Wigner solid. The hierarchy of the FQHE states is investigated. In the regime of the Wigner solid we found an exponential increase of the recombination time of the electrons in the solid phase, whereas no change in recombination time was observed for the liquid phase. Very similar properties of kinetics of luminescence were obtained for recombination with both free holes and holes bound to acceptors. Raman scattering was used to study the effect of reduction of electron concentration in the extreme quantum limit.



## 8. Acknowledgement

The authors acknowledge support from Volkswagen Foundation Collaborative Program.

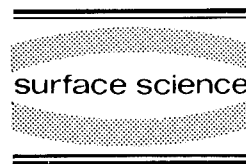
## 9. References

- [1] I.V. Kukushkin and V.B. Timofeev, JETP Lett. 44 (1986) 228.
- [2] H. Buhmann et al., Phys. Rev. Lett. 65 (1990) 1056.
- [3] H. Buhmann et al., Phys. Rev. Lett. 66 (1991) 926.
- [4] D. Heiman et al., Phys. Rev. Lett. 61 (1988) 605; B.B. Goldberg et al., Phys. Rev. Lett. 65 (1990) 641.
- [5] A.J. Turberfield et al., Phys. Rev. Lett. 65 (1990) 637.
- [6] E.M. Goldys et al., Phys. Rev. B 46 (1992) 7957.
- [7] I.V. Kukushkin et al., Phys. Rev. B 40 (1989) 7788.
- [8] V.M. Apal'kov and E.I. Rashba, JETP Lett. 53 (1991) 442; JETP Lett. 54 (1991) 155.
- [9] A.H. MacDonald et al., Phys. Rev. Lett. 68 (1992) 1939.
- [10] I.V. Kukushkin et al., Europhys. Lett. 18 (1992) 63; Surf. Sci. 263 (1992) 30.
- [11] A.J. Turberfield et al., Phys. Rev. B 47 (1993) 4794.
- [12] I.V. Kukushkin et al., Physica B 184 (1993) 38.
- [13] A.F. Dite et al., JETP Lett. 54 (1991) 389.
- [14] I.V. Kukushkin et al., to be published.
- [15] I.V. Kukushkin et al., Europhys. Lett. 23 (1993) 211.
- [16] M. Dahl et al., Surf. Sci. 263 (1992) 638.
- [17] A.F. Dite et al., JETP Lett., to be published.
- [18] D. Heiman et al., Phys. Rev. B 45 (1992) 1492.
- [19] I.V. Kukushkin et al., Phys. Rev. B 40 (1989) 4179.
- [20] I.V. Kukushkin et al., Solid State Commun. 70 (1989) 1015.



ELSEVIER

Surface Science 305 (1994) 61–66



## Quasi-particle recombination and spatial ordering of 2D electrons in the extreme quantum limit

I.N. Harris <sup>a</sup>, H.D.M. Davies <sup>a</sup>, R.A. Ford <sup>a</sup>, J.F. Ryan <sup>a</sup>, A.J. Turberfield <sup>\*,a</sup>,  
C.T. Foxon <sup>b</sup>, J.J. Harris <sup>c</sup>

<sup>a</sup> Physics Department, Clarendon Laboratory, Oxford University, Oxford, UK

<sup>b</sup> Physics Department, The University, Nottingham, UK

<sup>c</sup> Semiconductor Research Centre, Imperial College, London, UK

(Received 26 April 1993; accepted for publication 1 June 1993)

### Abstract

The inter-band photoluminescence spectrum of an incompressible liquid at an ultra-high mobility GaAs heterojunction may show multiple recombination channels in which different integral numbers of fractionally charged excitations participate. The spectrum at  $\nu = 1/2$  is discussed in terms of the proposed composite fermion model of the fractional quantum Hall effect. Changes in the photoluminescence spectrum at higher field lead to the proposal of an experimental test for magnetic-field-induced crystalline order.

### 1. Introduction

Three important and unresolved issues in the physics of electron–electron interactions in degenerate two-dimensional electron systems (2DES) are: the dispersion of neutral excitations of the incompressible liquid states responsible for the fractional quantum Hall effect (FQHE); the nature of the ground state at even filling factors; experimental determination of the ground state at filling factors  $\nu < 1/5$ . We will show here that optical spectroscopy has the potential to address each of these questions. We present measurements of photoluminescence from two ultra-high-mobility GaAs single heterojunctions G641

( $n_s = 10^{11} \text{ cm}^{-2}$ ,  $\mu = 9 \times 10^6 \text{ cm}^2 \text{ V}^{-1} \text{ s}^{-1}$ ) [1] and G648 ( $n_s = 3 \times 10^{10} \text{ cm}^{-2}$ ,  $\mu = 2 \times 10^6 \text{ cm}^2 \text{ V}^{-1} \text{ s}^{-1}$ ) [2]; we explore the physics of the recombination process and demonstrate progress towards the resolution of the three important questions listed above. The experimental technique has been described elsewhere [1–3]. Weak photoexcitation below the band gap of the barrier excites low densities of electrons and holes in continuum states in the GaAs layer; photoexcited holes relax to the valence band edge where they recombine with electrons in the potential well at the interface. Recombination is observed both from electrons in the 2DES in the ground subband and from photoexcited electrons that have scattered into higher subbands. Photoexcited electrons are not in thermal equilibrium with the 2DES, whose temperature is estimated to be approximately 100 mK. Both the energy and inten-

\* Corresponding author.

sity of photoluminescence are sensitive to the effects of correlation in the 2DES; hierarchies of FQHE states are detected [1,2] and the spectrum responds to the onset of a high-field insulating phase at  $\nu \approx 1/5$  [3].

## 2. Quasi-particle recombination and the determination of FQHE energy gaps

The fundamental characteristic property of an incompressible liquid is an excitation energy gap. No measurement of the zero-wavevector gap has yet been possible, although activated transport measurements give an estimate of the energy  $\Delta$  of large-wavevector excitations (quasielectron–quasi-hole pairs). Various anomalies in the energy of photoluminescence at FQH states have been reported which may allow measurement of excitations of the liquid. In the case of acceptor-doped heterojunctions the photoluminescence energy at fractional filling factors  $\nu = p/q$  has been claimed to change discontinuously by  $q\Delta$  [4]; in this model the recombination process either annihilates  $q$  quasi-electrons ( $\nu \geq p/q$ ) or creates  $q$  quasi-holes ( $\nu \leq p/q$ ) each of charge  $\mp 1/q$ . Recent analysis of the data relates  $\Delta$  to discontinuities in the derivative of the luminescence energy with respect to magnetic field [5]. It seems more likely, however, that the strongest recombination channel is always that creating  $q$  quasi-holes within the condensate, even when (for  $\nu \geq p/q$ ) excess quasi-electrons are present, and that weaker satellite lines involving the annihilation of quasi-electrons might appear. MacDonald et al. [6] have recently predicted the appearance of a satellite luminescence peak near  $\nu = 1/3$ : this satellite corresponds to annihilation of one quasi-electron and creation of two quasi-holes in the inter-band recombination process and is higher in energy than the main recombination channel (creation of three quasi-holes) by  $\Delta$ . We present here data near  $\nu = 1/3$  which show structure at higher energies consistent with this interpretation.

Fig. 1a shows the luminescence spectrum of G641 at  $\nu = 1/3$ . We observe a strong  $E_0$  peak, corresponding to recombination from the 2DES in the ground subband, with a wing extending to

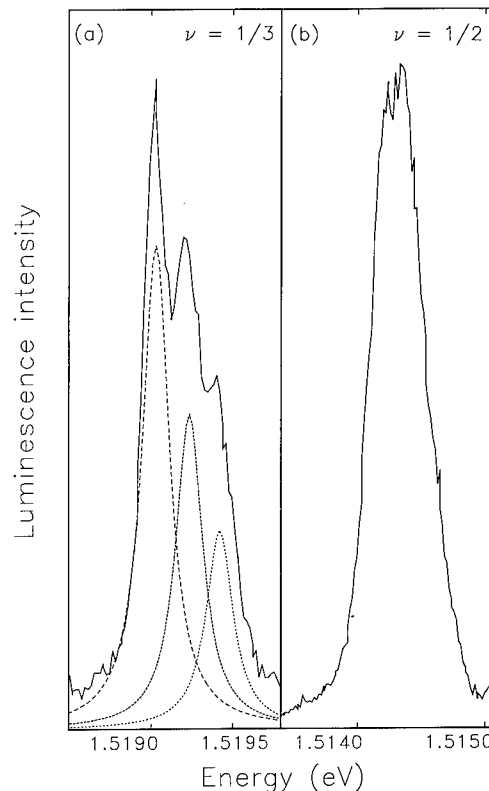


Fig. 1. Luminescence spectra of G641 at 100 mK (a)  $\nu = 1/3$ ; (b)  $\nu = 1/2$ .

high energy. This wing shows structure consistent with the presence of two satellite lines shown by the fitted curves. The strong low-energy component is interpreted as arising from the dominant recombination process involving the generation of 3 quasi-holes. In general, recombination of electrons can proceed by creation of  $n$  quasi-holes and annihilation of  $(q - n)$  quasi-electrons giving rise to  $(q + 1)$  spectral lines separated by  $\Delta$ . The two satellite peaks present in Fig. 1a then correspond to  $n = 2$  and 1 processes. At  $\nu = 1/5$  we observe a high-energy wing but no clearly resolved structure; this may be simply due to the fact that  $\Delta$  is lower than the experimental resolution in this case. The relative efficiencies of these recombination channels are not known, although those involving annihilation of more than one quasi-electron are expected to be weak due to the low probability of quasi-electrons being present

in the same place, i.e. the location of the valence hole; MacDonald et al. [6] find evidence in their finite-size calculations for only the  $n = 3$  and 2 processes at  $\nu = 1/3$ . The line separation observed here is 0.2 meV (2.2 K). This is smaller than the previously published value of  $\sim 5$  K for the  $\nu = 1/3$  gap energy deduced from activated transport measurements at similar fields [7]; it is probable that this measurement of  $\Delta$  is perturbed by interaction between the 2DES and the valence band hole. Apal'kov and Rashba [8] find that at  $\nu = 1/3$  in systems where the electron–electron and electron–valence hole interactions are strongly asymmetric there is an energy minimum in the magnetoexciton dispersion at finite wavevector; recombination from this state requires emission of a magnetoroton to conserve momentum and is therefore lower in energy than recombination from a magnetoexciton at the zone centre by approximately the *magnetoroton* energy rather than the quasi-particle gap.

Halperin et al. [9] have recently extended Jain's composite fermion model of the FQHE [10] to the special cases of even-denominator fractional filling, in particular to  $\nu = 1/2$ . Here the average gauge field cancels the applied magnetic field; the picture that results is that of fermions in zero magnetic field with a well defined Fermi surface. The electron system is gapless at these filling factors. Experimental data for  $\nu = 1/2$  and  $1/4$  are rather limited: the resistivity  $\rho_{xx}$  shows a weak minimum at  $\nu = 1/2$  and is systematically smaller than that at neighbouring even-denominator fractions, as predicted by the model, but the same does not appear to apply at  $\nu = 1/4$  [3,11] (it should be recalled that there is a dramatic increase in  $\rho_{xx}$  for  $\nu \lesssim 1/4$  which may be associated with formation of an electron solid – see below). Our discussion of the use of photoluminescence to detect FQHE gaps suggests the possibility of optical detection of the density of states of this exotic quantum system. Fig. 1b shows the luminescence spectrum of G641 at  $\nu = 1/2$ . The strong  $E_0$  line is remarkably symmetrical in contrast to the complex, asymmetric lineshape observed when the ground state is incompressible as at  $\nu = 1/3$  and  $1/5$ . By analogy with the true zero-field case, the full lumines-

cence linewidth may provide a measure of the Fermi energy; the observed value is  $\sim 0.5$  meV, which corresponds to an effective mass of approximately  $0.35m_e$  (the electron density at  $\nu = 1/2$  with  $B = 11.5$  T is estimated to be  $7 \times 10^{10} \text{ cm}^{-2}$  [3]). This measurement is close to the theoretical estimate of  $0.27m_e$  at  $B = 10$  T [9]. However, this lineshape analysis makes no distinction between the recombination of composite fermions and of ordinary electrons, nor does it take any account of the enhancement of recombination at the Fermi edge observed at zero field.

### 3. "Hot" electron probe of spatial ordering

The high-field ground state of an ideal degenerate two-dimensional electron system is believed to be crystalline. Nonlinear transport [11–13], photoluminescence [3,14] and surface acoustic wave propagation [15] have all provided evidence that a solid phase occurs at filling factor  $\nu \approx 1/5$  for GaAs but the nature and length scale of the order in this phase remains controversial. A clear test for crystalline order is a diffraction measurement, possibly using phonons, but this has not yet been achieved. We describe here a new method which utilises nonequilibrium electrons in higher-energy subbands of the confining potential as a probe of spatial order in the ground subband.

When the two-dimensional electron system in the ground subband is liquid its charge density is spatially uniform; the effective interaction potential experienced by other carriers (electrons in higher subbands and in the continuum, and valence band holes) is therefore also uniform. A magnetic-field-induced electron crystal is easily pinned by fluctuations in the interface potential, however, in which case the charge distribution in the ground subband is not uniform but periodically modulated. A transition from a liquid to a pinned crystal in the ground subband is therefore accompanied by the onset of a periodic perturbation experienced by electrons confined in higher subbands of the potential well. More remote carriers in continuum states, including all valence band states, will be more weakly perturbed. Pho-

toluminescence spectroscopy is sensitive to the densities of states for both electrons and holes and, in the range of filling factors in which crystallisation is expected, luminescence from non-equilibrium electrons in the first excited subband is observed. Spatial order in the ground subband might therefore be detected through its effect on this component of the luminescence spectrum.

In a strong magnetic field the effect of a periodic potential is to broaden the Landau level density of states and split it into bands in a pattern that depends on the symmetry and on the number of flux quanta penetrating a unit cell of the potential [16,17]. (The term Hofstadter band will be used to distinguish these fragments of a Landau level, corresponding to in-plane motion, from the subbands of the potential well confining the electron system.) When the filling factor for a crystalline 2DES in the *ground* subband is a rational fraction  $\nu = p/q$  then  $q/p$  flux quanta penetrate a unit cell and the density of states for electrons in the first excited subband is split into  $q$  bands. Relatively large gaps in the density of states occur at simple filling factors, where there are few bands, and persist over a range of magnetic fields [18]. To confirm the presence of spatial order in the ground subband it is this characteristic pattern of gaps that must be detected.

In the crystalline phase we expect the spectrum of luminescence from photoexcited electrons in the first excited subband to broaden and split into a field-dependent pattern of transitions from Hofstadter bands. It is reasonable to assume that all bands are populated by photoexcitation. The most easily identified feature in this spectrum should be the principal gap which, for  $1/5 < \nu < 1/10$ , is approximately half the total width of the spectrum in magnitude and divides it into a narrow high-energy line and a broader collection of transitions from bands at lower energies. The characteristic energy scale for this structure, the magnitude of the periodic potential, depends on the in-plane charge distribution in the ground subband and on the form of both ground and excited subband wavefunctions normal to the interface; we estimate this to be of order 1 meV. The excitonic character of luminescence from the upper subband [1] will reduce the broadening of

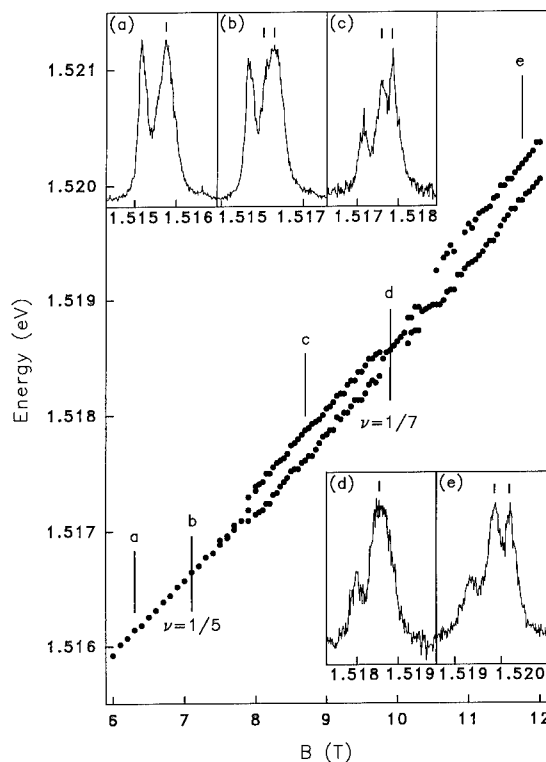


Fig. 2. Upper subband ( $E_1$ ) luminescence peak energies for G648. Representative spectra are inset.

the spectrum as the sign of the perturbation experienced by a valence hole is reversed.

Fig. 2 shows the magnetic-field-dependent energy of  $E_1$  luminescence peaks (corresponding to recombination from states in the lowest Landau level of the first excited subband) for sample G648. Inset spectra show the full luminescence lineshape with  $E_1$  transitions marked; the peak  $\sim 0.5$  meV lower in energy corresponds to  $E_0$  recombination from the degenerate 2DES in the lower subband. At filling factors  $\nu > 1/5$ , where the 2DES is liquid, the  $E_1$  peak is featureless (spectrum a). Between  $\nu = 1/4$  and  $\nu = 1/5$  the  $E_1$  peak broadens from 0.3 meV FWHM to 0.6 meV and at  $\nu = 1/5$ , the suggested threshold for crystallisation, a high-energy shoulder appears (spectrum b); the transition develops into a well-resolved doublet at lower filling factors (spectra c and e). The lower-energy  $E_1$  peak loses intensity as the filling factor is reduced below  $\nu = 1/7$  and at  $\nu = 1/10$  the higher-energy  $E_1$  peak dominates

the spectrum. This characteristic development of the luminescence spectrum correlates with changes in transport properties associated with crystallisation and has been observed previously over a smaller range of filling factors in the higher-density heterojunction G641 [3]. Over a range of filling factors around  $\nu = 1/7$  the  $E_1$  spectrum reverts to the single line (spectrum d) characteristic of higher filling factors  $\nu > 1/5$ .

Changes in the width and structure of the  $E_1$  luminescence transition for  $\nu \leq 1/5$  suggest corresponding changes in the density of states of electrons in the upper subband that are consistent with the effect of crystallisation of the 2DES in the ground subband. The width of the  $E_1$  luminescence transition for  $\nu < 1/5$  is consistent with our estimate of the periodic perturbation due to the electron crystal. The minimum luminescence linewidth measured from this sample is  $\sim 0.3$  meV so we cannot expect to resolve small gaps in the density of states; the shape of the spectrum for  $\nu < 1/5$  is consistent with the calculated density of states if only the principal gap is resolved. The reversion of the spectrum to its low-field form around  $\nu = 1/7$  may indicate a reversion to a liquid ground state of the 2DES: a re-entrant liquid phase at this filling factor has been inferred from measurements of a  $\rho_{xx}$  minimum [13,19]; luminescence spectra of an acceptor-doped system have been interpreted as showing coexisting solid and liquid phases over *all* filling factors  $\nu < 1/5$  [14].

Changes in the luminescence spectrum are not due solely to the orbital wavefunction: the spin states of the  $E_1$  electrons respond differently to spin and spatial ordering of the 2DES. There may be enhancement of the spin splitting in the upper subband due to exchange with the degenerate 2DES in the ground subband; if this were responsible for the structure observed at low filling factors then Fig. 2 shows that there must be a rapid threshold for this interaction at  $\nu \approx 1/5$ . Measurements of the polarisation of the luminescence do not support this interpretation: at  $\nu = 1/5$  both  $E_0$  and  $E_1$  are predominantly left circularly polarised (LCP) with  $I_L/I_R \approx 3$  [2]; the higher-energy  $E_1$  peak that develops for  $\nu < 1/5$  becomes more strongly LCP at lower filling fac-

tors whereas the lower-energy  $E_1$  peak becomes distinctly *unpolarised*. A detailed interpretation of the measurements requires a complete model for electron–valence hole recombination, but the magnitude of the splitting and the polarisation data are not consistent with a simple spin-splitting picture. It would be interesting, however, to investigate whether a transition from spin-polarised liquid to a solid could enhance the magnitude of the exchange interaction with upper subband electrons.

#### 4. Conclusions

Structure in the spectrum of luminescence from an incompressible liquid reveals multiple recombination channels which involve different numbers of quasi-electrons and quasi-holes and allow measurement of the quasi-particle gap  $\Delta$ . The spectral lineshape at  $\nu = 1/2$  is anomalous and may provide information about the compressible ground state at even fractions. Spatial order in the 2DES may be detected by measuring luminescence from photoexcited electrons in a higher subband. Our measurements are consistent with crystallisation at filling factor  $\nu \sim 1/5$  and suggest a reentrant liquid phase around  $\nu = 1/7$ .

#### 5. References

- [1] A.J. Turberfield, S.R. Haynes, P.A. Wright, R.A. Ford, R.G. Clark, J.F. Ryan, J.J. Harris and C.T. Foxon, *Phys. Rev. Lett.* 65 (1990) 637.
- [2] A.J. Turberfield, R.A. Ford, I.N. Harris, J.F. Ryan, C.T. Foxon and J.J. Harris, *Phys. Rev. B* 47 (1993) 4794.
- [3] R.G. Clark, R.A. Ford, S.R. Haynes, J.F. Ryan, A.J. Turberfield, P.A. Wright, C.T. Foxon and J.J. Harris, in: *High Magnetic Fields in Semiconductor Physics III*, Ed. G. Landwehr (Springer, Berlin, 1992) p. 231; A.J. Turberfield, S.R. Haynes, P.A. Wright, R.A. Ford, R.G. Clark, J.F. Ryan, J.J. Harris and C.T. Foxon, *Surf. Sci.* 263 (1992) 1.
- [4] H. Buhmann, W. Joss, K. von Klitzing, I.V. Kukushkin, G. Martinez, A.S. Plaut, K. Ploog and V.B. Timofeev, *Phys. Rev. Lett.* 65 (1990) 1056.
- [5] I.V. Kukushkin, N.J. Pulsford, K. von Klitzing, K. Ploog and V.B. Timofeev, *Surf. Sci.* 263 (1992) 30.
- [6] A.H. MacDonald, E.H. Rezayi and D. Keller, *Phys. Rev. Lett.* 68 (1992) 1939.

- [7] J. Wakabayashi, S. Kawaji, J. Yoshino and H. Sakaki, J. Phys. Soc. Jpn. 55 (1986) 1319.
- [8] V.M. Apal'kov and E.I. Rashba, Pis'ma Zh. Eksp. Teor. Fiz. 55 (1992) 38 [JETP Lett. 55 (1992) 37].
- [9] B.I. Halperin, P.A. Lee and N. Read, Phys. Rev. B 47 (1993) 7312.
- [10] J.K. Jain, Adv. Phys. 41 (1992) 105.
- [11] H.W. Jiang, R.L. Willett, H.L. Stormer, D.C. Tsui, L.N. Pfeiffer and K.W. West, Phys. Rev. Lett. 65 (1990) 633.
- [12] V.J. Goldman, M. Santos, M. Shayegan and J.W. Cunningham, Phys. Rev. Lett. 65 (1990) 2189.
- [13] F.I.B. Williams, P.A. Wright, R.G. Clark, E.Y. Andrei, G. Deville, D.C. Glattli, O. Probst, B. Etienne, C. Dorin, C.T. Foxon and J.J. Harris, Phys. Rev. Lett. 66 (1991) 3285.
- [14] H. Buhmann, W. Joss, K. von Klitzing, I.V. Kukushkin, A.S. Plaut, G. Martinez, K. Ploog and V.B. Timofeev, Phys. Rev. Lett. 66 (1991) 926.
- [15] M.A. Paalanen, R.L. Willett, P.B. Littlewood, K.W. West, L.N. Pfeiffer and D.J. Bishop, Phys. Rev. B 45 (1992) 11342.
- [16] D.R. Hofstadter, Phys. Rev. B 14 (1976) 2239; A.H. MacDonald, Phys. Rev. B 28 (1983) 6713.
- [17] F.H. Claro and G.H. Wannier, Phys. Rev. B 19 (1979) 6068.
- [18] Eq. (5) and Fig. 1 of Ref. [17] give the expected result for a hexagonal potential.
- [19] V.J. Goldman, M. Shayegan and D.C. Tsui, Phys. Rev. Lett. 61 (1988) 881.

## Photoluminescence and the Wigner crystal: can you see it?

H.A. Fertig <sup>\*,a</sup>, D.Z. Liu <sup>b</sup>, S. Das Sarma <sup>b</sup>

<sup>a</sup> *Department of Physics and Astronomy, University of Kentucky, Lexington, KY 40506-0055, USA*

<sup>b</sup> *Center for Superconductivity Research, Department of Physics, University of Maryland, College Park, MD 20742, USA*

(Received 25 January 1993; accepted for publication 11 June 1993)

### Abstract

We develop a theory of photoluminescence from the magnetically induced two-dimensional Wigner crystal. It is found that the photoluminescence spectrum is a weighted measure of the single particle density of states of the electron system, which for an undisturbed electron lattice has the intricate structure of the Hofstadter butterfly. It is shown that the interaction of a localized hole with the electron lattice wipes out this structure, but that an itinerant hole can, in principle, detect it. Experimental implications are discussed.

Recent studies of high mobility heterojunctions in strong magnetic fields have uncovered a number of intriguing properties that in some ways are consistent with the presence of some crystalline order at the lowest available temperatures. Among these, photoluminescence probes have yielded spectra with interesting behavior both as a function of magnetic field and temperature. Photoluminescence experiments on these systems have been performed in two ways. One set of experiments [1] uses a low density of Be dopants that are purposely grown into the sample approximately 250 Å away from the 2DEG. A pulse of light excites a core electron out of a Be<sup>+</sup> acceptor, and the photoluminescence spectrum from recombination of electrons in the 2DEG with the remaining core hole is observed. More recent experiments [2] have also investigated recombina-

tion of electrons with itinerant holes in the host crystal (GaAs) valence band. Both experiments show intriguing and complicated results; among them is the observation of a pair of photoluminescence lines that appear at magnetic fields for which transport anomalies recently associated with the WC are found. At the lowest temperatures, the lower of the two lines has most of the oscillator strength; as the temperature is raised, the oscillator strength transfers to the higher of these lines, until the lower line cannot be distinguished from the background. While it is tempting to associate lower line with a crystal phase, and the upper with a melted phase, the precise interpretation of the data is hampered by a lack of theoretical understanding of what the PL spectrum should look like when the ground state of the 2DEG really is a WC.

To address this question, we have computed the PL spectrum for the Wigner crystal using a time-dependent Hartree–Fock approximation (TDHFA) [3]. A few examples of the PL spec-

\* Corresponding author.



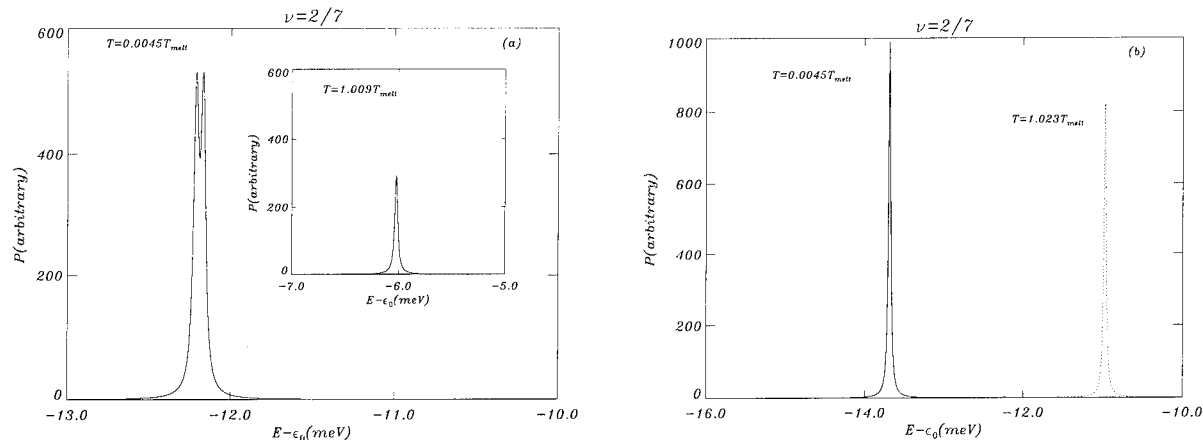


Fig. 1. (a) Photoluminescence for  $\nu = 2/7$ , sheet density  $n = 6 \times 10^{10} \text{ cm}^{-2}$ , with no electron-hole interaction, with  $T$  below the melting temperature  $T_{\text{melt}}$ . Inset: Same, for  $T$  above melting temperature. (b) Photoluminescence for  $\nu = 2/7$ , sheet density  $n = 6 \times 10^{10} \text{ cm}^{-2}$ , with electron-hole interaction, below (solid line) and above (dotted line) melting temperature.

trum obtained in our work are shown in Figs. 1 and 2. Fig. 1a illustrates the PL for a localized hole, where we ignore the interaction of the hole with the lattice, and the filling fraction of electrons is taken to be  $\nu = 2/7$ . The structure of the PL is essentially a double peak, whose origin may be understood as follows. The PL, as will be shown below, is essentially a weighted measure of

the single particle density of states. Within mean field theory (i.e., Hartree-Fock), this is determined by the energy spectrum of a single electron in a magnetic field, moving in the average potential of all the other electrons. Thus, the single particle density of states is that of an electron in a periodic potential. This spectrum has an intricate nature [4]: for rational filling fractions  $\nu = p/q$  there are  $q$  subbands, and in Hartree-Fock,  $p$  of these are filled. We therefore expect that for any filling fraction  $p/q$ , one should expect to see  $p$  lines in the PL for the ideal case of a perfect electron lattice. An observation of this behavior in photoluminescence experiments would yield direct confirmation of the presence of a WC in the system.

Unfortunately, the multiple peak structure is sensitive to perturbations from external potentials. For the case of an unscreened, localized core hole, the primary perturbation is from the electron-hole interaction itself; the PL spectrum when one turns on this interaction is illustrated in Fig. 1b. Here there is a single luminescence peak, which is shifted down in energy from what was seen in Fig. 1a. The structure is best interpreted in terms of the density of states. Direct examination of this reveals a single state that corresponds to an electron bound to the hole. This lowest energy electron state overwhelmingly dominates the PL spectrum, because the overlap of its wave-

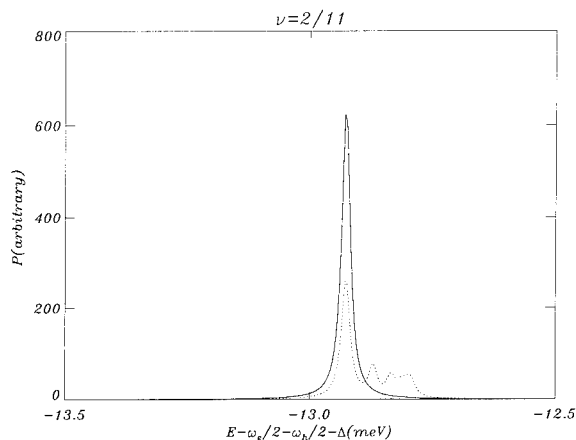


Fig. 2. Photoluminescence for itinerant hole at electron filling  $\nu = 2/11$ , sheet density  $n = 6 \times 10^{10} \text{ cm}^{-2}$ , and hole plane 250 Å away from the electron plane, for  $T \approx 0.005T_{\text{melt}}$  (solid line) and  $T \approx 0.05T_{\text{melt}}$  (dotted line). Electron and hole cyclotron frequencies given here by  $\omega_e$  and  $\omega_h$ , respectively and  $\Delta$  is the conduction band-valence band gap.

function with that of the hole is nearly two orders of magnitude larger than those of the next closest electrons. In essence, the PL spectrum is dominated by a single final state of the ion–electron gas system.

It should be noted that, in most localized hole experiments [1], the dopant atom is a *neutral* acceptor in its initial state. The interaction of the core hole with the electron gas is then quite weak, leading to a negligible deformation of the WC in its initial state. However, the *final* state of the dopant is charged, which introduces a strong perturbation. The net result of this is that the PL spectrum is still dominated by a single final state, one in which a vacancy is bound to the charged ion. The PL spectrum is thus qualitatively the same as described for the case of a strong initial interaction; details will be reported elsewhere [3].

The difficulty of observing local crystalline order directly in PL for the highly localized hole is clearly related to the fact that a single electron dominates the electron–hole recombination. This problem can be alleviated in principle if the hole is not so strongly localized. We thus consider an itinerant hole in the valence band, in a plane 250 Å above the electron plane, a geometry which is only very recently being examined in the WC regime [2]. Typical results for this system are shown in Fig. 2, for filling fraction  $\nu = 2/11$ . For the lowest temperatures, one can only see a single peak in the photoluminescence, essentially because at this filling the splitting between the two filled subbands is too small to resolve numerically [5]. However, an interesting effect occurs when the temperature is raised slightly (although not nearly enough to melt the crystal): one then finds that structure in the PL peak is introduced. This turns out to be due to the density of states for the hole. This also moves in the periodic potential of the electron lattice, and so should be expected to have eleven bands as well. Increasing the temperature moderately allows some non-negligible probability for the hole to occupy the higher bands, each adding a new line to the PL spectrum. Once again, observation of this effect would constitute direct confirmation of crystalline order in the 2DEG. We believe that, with improved sample quality, itinerant hole PL

experiments should offer the best opportunity to observe this type of structure, which is a direct consequence of the presence of a WC.

Our calculated PL spectrum as the temperature is raised so as to melt the WC also has very interesting behavior. In this case, there is an upward shift in the PL peak for the case of a localized hole, as seen in Fig. 1. The increase in energy corresponds directly to the potential energy lost per electron when the carriers are no longer crystallized. What is remarkable about the shift is that it occurs almost precisely at the melting temperature; there is very little motion just above or below the transition. This is in qualitative agreement with experimental observations [2], in which two distinguishable lines are observed, with oscillator strength transferring from the lower to the upper one as the temperature is increased. One could interpret this as finite size domains of the WC with a distribution of melting temperatures, accounting for the continuous transfer of oscillator strength between the two lines. That two such lines are visible in real experiments, rather than a broad continuum PL spectrum, seems consistent with an electrostatic environment for the recombining electrons that is fairly uniform through the sample, indicating that there may be some (substantial) order in the system.

We now outline how we calculate the photoluminescence in the TDHFA. (Details will be given elsewhere [3].) The photoluminescence intensity is given, for a single localized hole state, by

$$P(\omega) = \frac{I_0}{Z} \sum_n \sum_m e^{-E_n/k_B T} |\langle m, 0 | \hat{L} | n, h \rangle|^2 \times \delta(\omega - E_n + E_m), \quad (1)$$

where  $Z = \sum_n e^{-E_n/k_B T}$ ,  $|n, h\rangle$  is a many-body electron state with energy  $E_n$  and  $N$  electrons when there is a core hole present,  $|m, 0\rangle$  is a many-body electron state with  $N-1$  electrons and energy  $E_m$ ,  $\omega$  is the luminescence frequency, and  $\hat{L} = \int d^2x \psi(x) \psi_h(x)$  is the luminescence operator, with  $\psi(x)$  the electron annihilation operator and  $\psi_h(x)$  the hole annihilation operator. As written, the initial state is actually higher in energy than the final state, and we find it conve-

nient to rework the problem in terms of absorption rather than emission. To accomplish this, we add a term  $H' = -E_0 c_0^\dagger c_0$  to the Hamiltonian, where  $c_0^\dagger$  creates a localized hole, and take the limit  $E_0 \rightarrow \infty$ . It is not difficult to show  $P(\omega) = \lim_{E_0 \rightarrow \infty} P'(\omega - E_0)/n_0(E_0)$ , where  $P'$  is the absorption spectrum of the new Hamiltonian, and  $n_0$  is the average occupation of the hole state, which just becomes one in the limit  $E_0 \rightarrow \infty$ . The absorption spectrum is identical to Eq. (1), except one needs to add the energy  $E_0$  to all the quantities  $E_n$  in the expression. After standard manipulations [6], one can show that

$$P'(\omega) = \frac{I_0}{\pi} \frac{1}{1 - e^{\omega/k_B T}} \text{Im } R(\omega + i\delta).$$

The function  $R(\omega + i\delta)$  is a response function, which continued to imaginary frequency has the form

$$R(i\omega) = - \int_0^\beta \langle T_\tau L(\tau) L^\dagger(0) \rangle e^{i\omega\tau} d\tau. \quad (2)$$

To compute this quantity, we consider (for the case of a localized hole state) instead of a single hole, a periodic (hexagonal) lattice of them, with a unit cell that contains as many electrons as can be handled numerically. In addition, since the system is in a strong magnetic field, we project the electron part of the Hamiltonian into the lowest Landau level. Because of the symmetry of the system,  $R(\omega)$  may be written in the form

$$R(\omega) = \frac{n_h \Omega}{2\pi l_0^2} \sum_{\mathbf{G}} R(\mathbf{G}, \omega) e^{-G^2 l_0^2/4}$$

if we approximate the core-hole wavefunctions as delta-functions, where  $n_h$  is the density of holes,  $\Omega$  the volume of the system, and the vectors  $\mathbf{G}$  are the reciprocal lattice vectors of the superlattice. The quantity  $R(\mathbf{G}, \omega)$  may be computed by writing down the equation of motion for  $R(\tau)$  in terms of its commutator with the Hamiltonian, and then applying a Hartree–Fock decomposition to the resulting expression [7,3].

The case of the itinerant hole is treated similarly to the case outlined above, except there is an important simplification: since the hole density is low at all points in space, it is safe to ignore

any deformation of the electron lattice due to the hole. For this situation, we find that Eq. (1) may be written directly in terms of the Green's functions for the electron lattice. Because there are many hole states close in energy on the scale of temperature for the itinerant hole, we also take a thermal average of Eq. (1) over the different hole states that the electrons may decay into. The hole wavefunctions may be generated by numerically computing its Green's function. Details will be given elsewhere [3].

In summary, we have developed a theory of photoluminescence for the WC in a strong magnetic field. We find that one can use PL to unambiguously demonstrate the presence of a WC, by observing a gap structure associated with the unique energy spectrum of an electron in a periodic potential and a magnetic field. We show that electron–hole interactions tend to close these gaps, and argue that the best situation for finding this structure would be in an itinerant hole experiment.

The authors thank the University of Kentucky Center for Computational Sciences for providing computer time. This work is supported by the National Science Foundation through grants No. DMR 92-02255(HAF) and 91-23577(DZL and SDS).

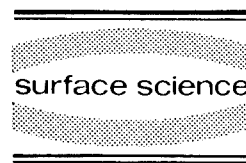
## 1. References

- [1] H. Buhmann et al., Phys. Rev. Lett. 66 (1991) 926; I.V. Kukushkin et al., Phys. Rev. B 45 (1992) 4532.
- [2] E.M. Goldys et al., Phys. Rev. B 46 (1992) 7957; R.G. Clark, Phys. Scri. T 39 (1991) 45, and references therein.
- [3] H.A. Fertig, D.Z. Liu and S. Das Sarma, Phys. Rev. Lett. 70 (1993) 1545; D.Z. Liu, H.A. Fertig and S. Das Sarma, Phys. Rev. B 48 (1993) 11184.
- [4] D. Hofstadter, Phys. Rev. B 14 (1976) 2239.
- [5] D. Yoshioka and P.A. Lee, Phys. Rev. B 27 (1983) 4986, found a similarly small splitting at this filling.
- [6] G. Mahan, Many-Particle Physics (Plenum, New York, 1983).
- [7] R. Côté and A.H. MacDonald, Phys. Rev. Lett. 65 (1990) 2662; Phys. Rev. B 44 (1991) 8759.



ELSEVIER

Surface Science 305 (1994) 71–75



## Numerical studies of the photoluminescence spectrum of quantum Hall systems

X.M. Chen <sup>\*,a</sup>, J.J. Quinn <sup>a,b</sup>

<sup>a</sup> Department of Physics and Astronomy, University of Tennessee, Knoxville, TN 37996, USA

<sup>b</sup> Oak Ridge National Laboratory, Oak Ridge, TN 37831, USA

(Received 19 April 1993; accepted for publication 7 May 1993)

### Abstract

The eigenfunctions and eigenvalues of a system consisting of a finite number of electrons on a two-dimensional plane together with a few holes on a neighboring plane are obtained by numerical diagonalization within the subspace of the lowest Landau level. The energy spectrum and ground state energy per particle are studied as a function of the Landau level degeneracy and the interlayer separation. By evaluating the square of the matrix element of the luminescence operator between the initial state with  $N_e$  electrons and one hole and various final states with  $N_e - 1$  electrons and no hole, and multiplying by a delta function which conserves energy, the luminescence intensity  $I(\omega)$  is obtained.

Recently there has been intense experimental and theoretical interest in the magneto-photoluminescence (PL) of a two-dimensional electron system in the fractional quantum Hall effect (FQHE) regime [1–3]. While experiments have revealed a considerable amount of fine structure in the PL spectrum, the theoretical interpretation of these results is still at the primitive stage. Critical to the understanding of PL spectrum is the role of the photo-excited valence band holes, whether on the same two-dimensional plane as the electrons or separated from the plane by a finite distance, as a perturbation to the electron system in the initial and final state of the recombination process.

In an system which contains both free elec-

trons and valence band holes, strong correlations exist between particles of like charge, as well as between particles of opposite charge. For a system with an equal number of electrons and holes ( $\nu_e = \nu_h$ ) in the same two-dimensional layer, if only the first Landau level is considered, the ground state can be obtained exactly and viewed as a Bose condensed state of noninteracting excitons [4]. As the layer separation is increased, the interlayer correlations become relatively less important, and the system would be expected to undergo a phase transition either to a double FQHE state or to an excitonic charge-density wave state [5]. For a system in which the number of electrons differs from the number of holes ( $\nu_e \neq \nu_h$ ), i.e., for a general electron–hole system, the nature of the ground state is still an unsolved problem. Recently, based on a mapping between the electron–hole system and a two-component

\* Corresponding author.

electron system, the authors of Ref. [6] concluded that in the symmetric case, where electrons and holes are in the same layer, the charged electron–hole fluid should exhibit a FQHE when the filling factor of the excess charge  $\nu_c = \nu_e - \nu_h$  is a fraction with an odd denominator. This prediction follows from the assumption that for a two-component spin-1/2 electron system with a negligible Zeeman splitting, the ground state is always maximally spin polarized. Here we present a numerical study of a finite-size general electron–hole system with an arbitrary layer separation  $d$ . We find that in the symmetric case, neither the chemical potential discontinuity nor the finite energy gap between the ground state and the excited states appears. In the asymmetric case, we find that when the layer separations are of the order of the magnetic length, strong cusps are obtained at  $\nu_c/(1 - \nu_h) = p/q$ , where  $q$  is an odd integer [7].

Let us first consider the symmetric case where electrons and holes are in the same layer. It has been shown that the electron–hole system in this case has a hidden symmetry [6,8,9], which can be easily understood by noticing that the commutator of the Hamiltonian of the system  $\hat{H}$  and the creation operator  $\hat{d}^+(0)$  of a  $k=0$  exciton is proportional to the creation operator itself, that is

$$[\hat{H}, \hat{d}^+(0)] = E_x(0)\hat{d}^+(0). \quad (1)$$

Here  $E_x(0)$  is the binding energy of a single bare exciton. In the Landau gauge the exciton creation operator  $\hat{d}^+(0)$  is given by  $\hat{d}^+(0) = \sum_X a_X^+ b_{-X}^+$ , where  $a_X^+$  (or  $b_X^+$ ) is the creation operator of a free electron (hole) with momentum  $k_y = X/l^2$  in the first Landau level. It follows from Eq. (1) that if  $|N_e, N_h\rangle$  is an eigenstate of a  $N_e$  electron and  $N_h$  hole system with an eigenenergy  $E_0$ ,  $[\hat{d}^+(0)]^n |N_e, N_h\rangle$  will be an eigenstate of a  $N_e + n$  electron and  $N_h + n$  hole system with an eigenenergy  $E_0 + nE_x(0)$ . The introduction of an extra electron–hole pair with a total momentum  $k=0$  changes the energy of the system by  $E_x(0)$ , the single bare exciton energy.

We perform our finite-size calculations in the spherical geometry [10]. Electrons and holes are

put on a sphere of radius  $R^2 = S$  with a magnetic monopole at the center, where  $2S + 1$  is the degeneracy of the first Landau level. The Coulomb interaction between the particles of like charge is taken to be inversely proportional to the chord distance, and the interaction between electrons and holes is modulated by the layer separation  $d$  through the relation  $V_{eh}(|\hat{\Omega}_1 - \hat{\Omega}_2|) = -1/(R^2|\hat{\Omega}_1 - \hat{\Omega}_2|^2 + d^2)^{1/2}$ , where  $\hat{\Omega}$  is a unit vector in radial direction denoting the position of a particle on the sphere. The quantum states of the system are classified by eigenvalues  $L(L+1)$  and  $M$  of the square of the angular momentum operator  $\hat{L}^2$  and its  $z$ -component  $\hat{L}_z$ . The effect of the neutralizing background is included by adding a shift [11] of  $-N_c^2/2R$  to the calculated energy, where  $N_c = N_e - N_h$ . For a seven electrons and one hole system at  $d=0$ , according to the prediction of Ref. [6], one might expect several downward cusps in the plot of ground state energy versus  $S$ . These cusps, however, are not observed in our result. The assumption that the ground state of the spin-1/2 electron system onto which the electron–hole system maps is maximally spin polarized is equivalent, in the electron–hole system, to the assertion that the ground state can be obtained from the ground state of a  $N_c$  electron system by simply adding  $N_h$  excitons of momentum  $k=0$ . Finite size calculations clearly indicate that the ground state for a given  $S$  is not necessarily one of these multiplicative states  $[\hat{d}^+(0)]^{N_h} |N_c\rangle$ , where  $|N_c\rangle$  is a quantum state of a  $N_c$  electron system with the same  $S$ . In Fig. 1, we plotted the energy spectrum for a seven electrons and one hole system at  $S=7$ . The states indicated by diamonds are multiplicative ones, which can be obtained by operating  $\hat{d}^+(0)$  onto the states belonging to a six electron system. Fig. 1 shows that the lowest multiplicative state ( $L=3$ ) is higher than the ground state ( $L=1$ ) by  $0.06e^2/\epsilon l$ , a value which is comparable to the energy gap of  $\nu=1/3$  Laughlin state. This leads us to predict that at  $d=0$  one should not see a peak in the PL spectrum at  $\omega = E_x(0)$  at this filling factor.

For the asymmetric case, in which electrons and holes are on two different layers, the ground state properties, as well as the collective excita-

tions of the system, depend strongly on the inter-layer separation. It is conceivable that in a certain range of the layer separation, each hole may bind only one or two quasielectrons, instead of a whole real electron, because of the weaker interlayer interaction. In Fig. 2a the ground state energy of a system of seven electrons and one hole at  $d = 1.75$  is shown as a function of the Landau level degeneracy  $S$ . A pronounced cusp is revealed at  $S = 8$ . Two other weaker cusps (or kinks) appear at  $S = 6$  and  $5$ . Also plotted in Fig. 2a is the ground state energy of a six electron system. As can be seen, by adding one electron-hole pair to the six electron system the cusps (kinks) corresponding to  $\nu_c = 1/3, 2/5$  and  $2/3$  have all been shifted towards right by  $0.5$  of  $S$  value. We have also calculated the ground state energy for an eight electrons and two holes system at the same layer separation. The result shows that the positions of the cusps (kinks) are all shifted in  $S$  value by one unit towards right relative to those in the six electron system. The systematic shift of the cusps leads us to postulate that the ground state at  $S = 8$  in Fig. 2a consists of a  $\nu = 1/3$  incompressible liquid of seven electrons and a bound state complex of one hole and two Laughlin quasielectrons [12]. In Fig. 2b we show the energy difference  $\Delta E$  between the ground state and the lowest excited state for several  $S$  values. It is found that at the positions where the cusps appear in the ground state en-

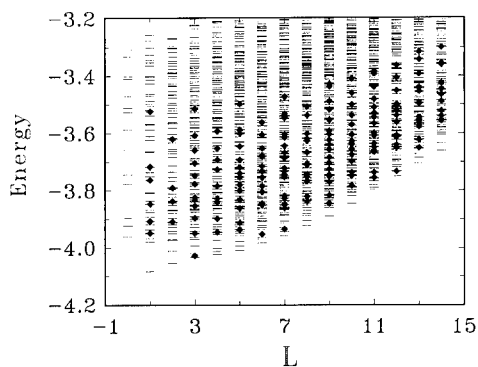


Fig. 1. Energy spectrum of an electron-hole system with  $N_e = 7$ ,  $N_h = 1$ , and  $d = 0$  at  $S = 7$ . The states indicated by diamonds can be obtained by operating  $\hat{d}^+(0)$  onto the states belonging to a six electron system.

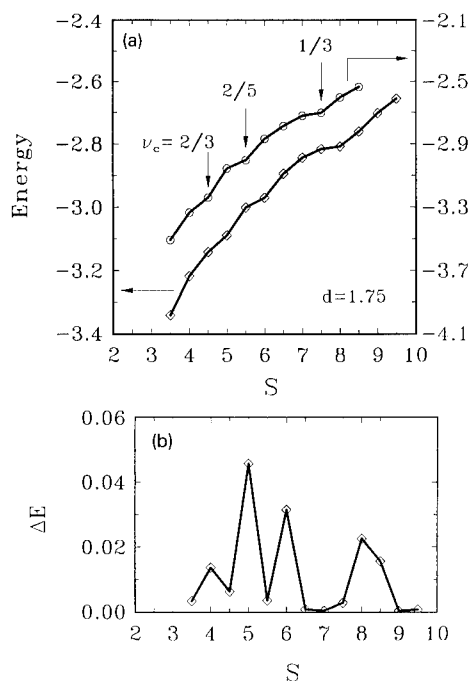


Fig. 2. (a) Ground state energy as a function of  $S$ : Diamonds – electron-hole system with  $N_e = 7$ ,  $N_h = 1$ , and  $d = 1.75$ ; Circles – system with six electrons only. (b) Energy difference between the ground state and the lowest excited state for an electron-hole system with  $N_e = 7$ ,  $N_h = 1$ , and  $d = 1.75$ . Note that the peaks here correspond to the cusps (kinks) in (a).

ergy,  $\Delta E$  displays strong peaks characteristic of a dissipationless system. Calculated results for the electron-hole pair correlation function and the energy spectrum of the system also support the conjecture of the exotic bound state complex [7].

Having investigated the ground state properties of electron-hole systems, we now can proceed to calculate the PL spectrum resulting from recombination of an electron with a valence band hole. The photoluminescence intensity at temperature  $T$ , is given by

$$I(\omega) = \frac{I_0}{Z} \sum_{i,f} e^{-E_i/k_B T} \left| \langle \Phi_f^{(N_e-1,0)} | \hat{d}(0) | \Phi_i^{(N_e,1)} \rangle \right|^2 \times \delta(\omega - E_i + E_f), \quad (2)$$

where  $Z = \sum_i \exp(-E_i/k_B T)$  is the partition function of the initial system.  $\Phi_i^{(N_e,1)}$  and  $\Phi_f^{(N_e-1,0)}$  are the quantum states of initial and final system

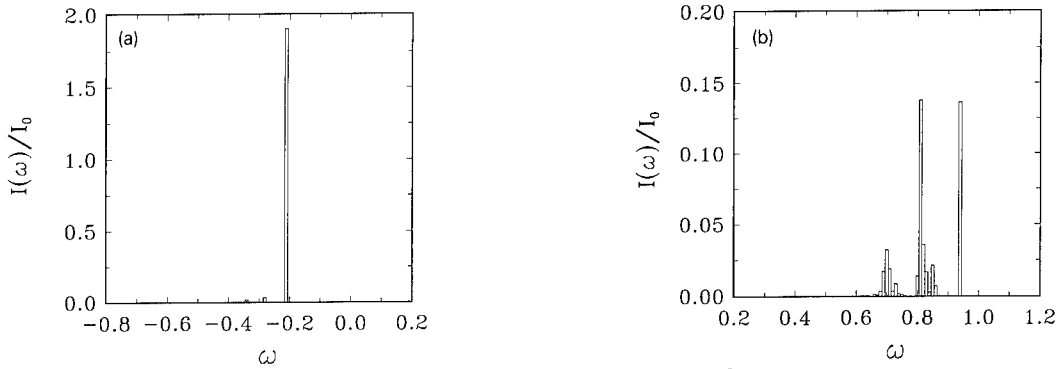


Fig. 3. PL spectrum of a seven electron system at  $S = 8.0$  and  $T = 0.005e^2/\epsilon l$ . (a)  $d = 1.75$ ; (b)  $d = 8.0$ .

with  $N_e$  electrons and one hole, and  $N_e - 1$  electrons and no hole, respectively.

From Eq. (2), the hidden symmetry and what we have discussed in the previous paragraphs, one immediately sees that the low temperature PL intensity at  $d = 0$  will be zero for most of the  $S$  values because the ground state of electron-hole systems is in general not a multiplicative state (Fig. 1). Even at those fillings (for example,  $S = 7.5$  corresponding to  $\nu_e = 1/3$  for a seven electrons and one hole system) where one of multiplicative states does seem to have the lowest energy, the ground state is found to be almost degenerate with several non-multiplicative states, and in the thermodynamical limit the PL intensity from the recombination process simulated by Eq. (2) will be greatly reduced.

For the asymmetric case, where Eq. (1) no longer holds, sharp peaks are obtained in the PL spectrum. In Fig. 3a, we plot the PL intensity at  $d = 1.75$ ,  $S = 8$ . The temperature  $T$  is set to be  $0.005e^2/\epsilon l$  in our calculation. The PL spectrum consists of a strong peak at high energy side and two tiny peaks (which are about 50–100 times smaller and probably too small to be seen) with lower energy. As the layer separation is increased, the two small peaks become stronger and stronger in comparison with the biggest one. For a very large layer separation, the second peak actually becomes the dominant one. Fig. 3b shows the PL spectrum of the system at the same  $S$  and  $T$  values, with  $d = 8$ . The three peaks are almost equally separated by an energy of the order of

the Laughlin gap. If we change the  $S$  value to 8.5, the peak with the highest energy disappears, and only two lower energy peaks remain (at the same energy positions); this is in qualitative agreement with the finding in Ref. [3] for this  $S$  value. A detailed account of our PL results will be given elsewhere.

In summary, our finite-size calculation for electron-hole layers with  $d = 0$  shows no clear signature of an incompressible FQHE state. For most values of the filling factor no PL signal or at best a very weak one should be observed at the exciton binding energy for the coplanar systems (as long as  $\nu_h \ll \nu_e$ ). For the case of  $d \approx 1.5$ , our results reveal that the ground state energy displays a strong cusp (or kink) when plotted as a function of the Landau level degeneracy, and the states responsible for the cusps are interpreted as a mixture of an incompressible liquid of electrons at  $\nu_e = p/q$  and a dilute gas of anyonic ions consisting of a hole bound to Laughlin quasielectrons. The PL spectrum of the system changes dramatically as the layer separation is increased from  $d = 1.5$  to infinite, and as the Landau level degeneracy is varied.

We would like to thank Xiaoguang Xia for helpful discussions. This research was supported in part by the Division of Materials Sciences of the U.S. Department of Energy under Contract No. DE-AC05-84OR21400 with Martin Marietta Energy Systems, Inc., and by US Office of Naval Research under Grant No. N00014-90-J-1915.

## 1. References

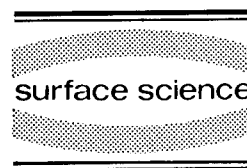
- [1] H. Buhmann et al., *Phys. Rev. Lett.* 65 (1990) 1056;  
A.J. Turberfield et al., *Phys. Rev. Lett.* 65 (1990) 637;  
B.B. Goldberg et al., *Phys. Rev. Lett.* 65 (1990) 641;  
E.M. Goldys et al., *Phys. Rev. B* 46 (1992) 7957.
- [2] Bing-Shen Wang, J. Birman and Zhao-Bin Su, *Phys. Rev. Lett.* 68 (1992) 1605.
- [3] A.H. MacDonald, E.H. Rezayi and D. Keller, *Phys. Rev. Lett.* 68 (1992) 1939.
- [4] I.V. Lerner and Yu.E. Lozovik, *Sov. Phys. JETP* 53 (1981) 763;  
D. Paquet, T.M. Rice and K. Ueda, *Phys. Rev. B* 32 (1985) 5208.
- [5] X.M. Chen and J.J. Quinn, *Phys. Rev. Lett.* 67 (1991) 985.
- [6] A.H. MacDonald and E.H. Rezayi, *Phys. Rev. B* 42 (1990) 3224.
- [7] X.M. Chen and J.J. Quinn, *Phys. Rev. Lett.* 70 (1993) 2130.
- [8] A.B. Dzyubenko and Yu.E. Lozovik, *J. Phys. A* 24 (1991) 415.
- [9] V.M. Apalkov and E.I. Rashba, *Phys. Rev. B* 46 (1992) 1628.
- [10] F.D. Haldane, *Phys. Rev. Lett.* 51 (1983) 605;  
F.D. Haldane and E.H. Rezayi, *Phys. Rev. Lett.* 54 (1985) 237.
- [11] G. Fano, F. Ortolani and E. Colombo, *Phys. Rev. B* 34 (1986) 2670.
- [12] R.B. Laughlin, *Phys. Rev. Lett.* 50 (1983) 13.





ELSEVIER

Surface Science 305 (1994) 76–82



# Surface acoustic wave studies of electron correlations in the 2DES

R.L. Willett

*AT&T Bell Laboratories, Murray Hill, NJ 07974, USA*

(Received 19 April 1993; accepted for publication 17 May 1993)

## Abstract

We have used surface acoustic waves (SAW) to measure the dynamical conductivity  $\sigma_{xx}(\omega, q)$  to high frequency  $\omega$  and wavevector  $q$ . The most important finding is enhanced conductivity at large  $q$  for filling factors  $\nu = 1/n$ , where  $n$  is an even integer. This effect persists to high temperatures, greater than those at which the FQHE is observed, with the enhanced conductivity proportional to  $q$  and the effect width in  $B$  field proportional to  $q$ . These results are consistent with a recent theory describing Fermi surface formation at even denominator  $\nu$ . In addition to these results, at small  $\nu$  near  $1/5$ , we observe a complex  $\sigma_{xx}(\omega, q)$  which we have mapped out as a function of  $\omega$ . This conductivity mode is consistent with a wavevector independent pinning mode in the insulating phase.

The objective of our experiments is to study correlation effects in high quality 2D electron systems using a method that will not adversely perturb the system yet allows measurement of conductivity at small length scales. In addition we want to use a frequency and wavevector adjustable technique to study low energy dispersion. The technique we have employed is propagation of surface acoustic waves (SAW) on GaAs/Al GaAs heterostructures, which allows direct determination of complex  $\sigma_{xx}(\omega, q)$ . In this method [1] we deposit interdigital transducers on both ends of a sample with a 2DES mesa between the transducers (see inset to Fig. 1). Since GaAs is piezoelectric, when the frequency of the voltage applied to the transducer matches the transducer wavelength  $\lambda$  such that  $\lambda\omega = 2\pi v_s$ ,  $v_s$  = sound velocity, a traveling longitudinal wave is pro-

duced. The SAW transverses the 2DES and is detected by the receiving transducer, with the sound wave amplitude and velocity effected by the 2D electron system through a simple relaxation response. This relaxation model gives direct measurement of complex  $\sigma_{xx}(\omega, q)$  from

$$\frac{\Delta v}{v} = \left( \frac{K_{\text{eff}}^2}{2} \right) \frac{1 + \sigma''}{(1 + \sigma'')^2 + (\sigma')^2}, \quad (1)$$

and

$$\Gamma = \left( \frac{K_{\text{eff}}^2}{2} \right) \frac{q\sigma'}{(1 + \sigma'')^2 + (\sigma')^2}, \quad (2)$$

where  $\sigma' = \text{Re } \sigma_{xx}(\omega, q)/\sigma_m$ ,  $\sigma'' = \text{Im } \sigma_{xx}(\omega, q)/\sigma_m$ ,  $\sigma_m = v_s(\epsilon + \epsilon_0)$ , and  $K_{\text{eff}}$  is the piezoelectric coupling constant [2]. The transmitted amplitude is given by  $A = \exp(-\Gamma x)$ , where  $x$  is the sound path length through the 2DES.

Shown in Fig. 1 are  $\sigma_{xx}(\text{DC})$ , which is measured via standard contacts diffused into the periphery of the 2D mesa, and the measured SAW  $\Delta v/v$  and  $A$  [3]. This figure demonstrates the effect of the 2DES on the sound parameters. The DC measurement is used in the above expressions with the results also shown in the figure. Good correspondence between the calculated  $\Delta v/v$ ,  $A$  and the measured  $\Delta v/v$ ,  $A$  means that at this SAW  $\omega$  and  $q$ ,  $\sigma_{xx}(\text{DC}) \approx \sigma_{xx}(\omega, q)$ . In this report we will focus on our findings at  $\nu = 1/2$  and at small filling factors.

### 1. $\nu = 1/2$

Measured SAW parameters for our largest wavevector [4] of  $q \approx 8 \mu\text{m}^{-1}$  are shown in Fig. 2.

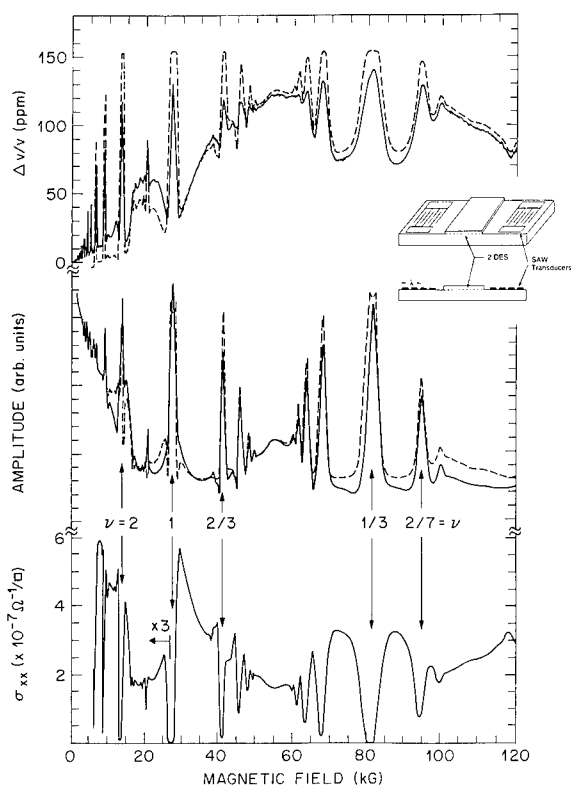


Fig. 1. DC conductivity, SAW amplitude, and SAW velocity shift versus magnetic field at 160 mK and 235 MHz. Solid lines are measured values and dashed lines are results using the measured  $\sigma_{xx}(\text{DC})$  in Eqs. (1) and (2).

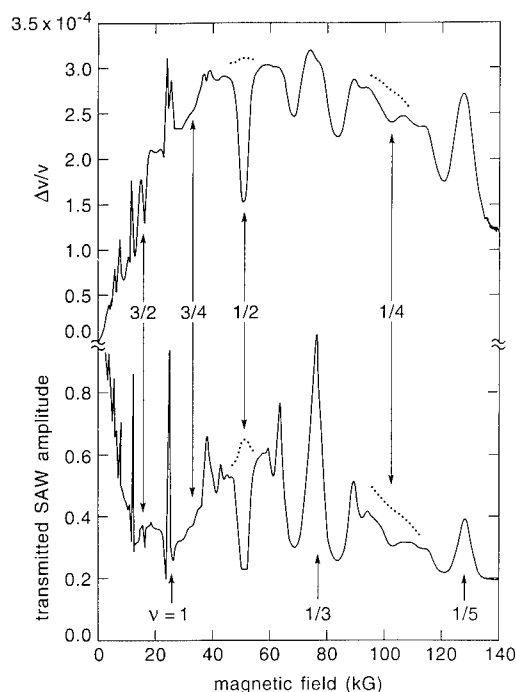


Fig. 2. SAW velocity shift and transmitted amplitude for 3.4 GHz SAW at 120 mK versus magnetic field. The dotted lines represent  $\Delta v/v$  and amplitude calculated from the DC conductivity (offset for clarity).

The DC conductivity taken simultaneously to this is similar to that in Fig. 1, lowest panel. This DC conductivity would give  $\Delta v/v$  and amplitude shown by the dashed lines in the figure near  $1/2$  and  $1/4$ . Rather than maxima, very marked minima in the sound properties are noted at  $\nu = 1/2$ ,  $3/2$  with smaller minima at  $1/4$  and  $3/4$ , representing enhanced  $\sigma_{xx}(\omega, q)$  at large  $q$ . Using the measured amplitude and frequency one can deduce that the enhanced  $\sigma_{xx}(\omega, q)$  at  $\nu = 1/2$  is purely real, not complex.

The temperature evolution of this enhanced conductivity is shown in Fig. 3. Note the remarkable persistence of the enhanced  $\sigma_{xx}(\omega, q)$  (minimum in transmitted amplitude) at  $\nu = 1/2$  to high temperatures. At 3.0 K the effect has survived to a temperature higher than that able to support the FQHE. The minimum in amplitude at  $1/2$  is persistent to  $T > 4$  K, where only the IQHE is visible. The lower panel shows that

the conductivity at  $1/2$  for 3.4 GHz possesses no simple activated temperature behavior. Clearly this effect is robust and pervasive; it occurs at multiple  $\nu$  and is stronger than the FQHE.

The most important findings of our SAW experiments are those for large  $q$  that reveal the specific properties of the enhanced conductivity effect at  $\nu = 1/2$ . Comparison of raw  $\Delta v/v$  data for three SAW frequencies is displayed in Fig. 4, left panel. The effect gets both broader and deeper with increasing frequency. Precisely at  $\nu = 1/2$  measuring  $\Delta v/v$  and  $A$  gives  $\sigma_{xx}(q)$ , and this can be plotted for the full range of  $q$  used on this sample (Fig. 4, right). At small  $q$ ,  $\sigma_{xx}$  is  $q$  independent as seen for the rest of the FQHE  $B$ -field range for all  $q$ . For  $q \geq 2 \mu\text{m}^{-1}$ ,  $\sigma_{xx}(q)$  increases linearly with  $q$ .

The width of the enhanced conductivity clearly increases with increased SAW  $q$ . Fig. 5 shows the full width in  $\Delta B/B$  at half maximum of the effect at  $\nu = 1/2$ , demonstrating a distinct linear dependence in  $q$ .

To summarize the results, enhanced conductivity is observed at multiple even denominator  $\nu$  and is found to be more robust than the FQHE, with  $\sigma_{xx}(q)$  and the width of the effect both increasing linearly in SAW wavevector for large  $q$ .

A recent theory developed by Halperin, Lee and Read [5] may provide a rather complete explanation of the SAW results and in fact may provide a new model for understanding correlations in the 2DES in general. In this theory, a Chern–Simons gauge field is introduced at one-half filling that attaches two flux quanta to each particle. The opposite sense of these flux to the applied field results in a total mean magnetic field of zero:  $B_{\text{TOT}} = B_{\text{CS}} + B_{\text{APP}} = 0$ . An immediate consequence of this construction is that a Fermi surface should form at  $\nu = 1/2$  with  $k_F = (4\pi n_e)^{1/2} = k_F^e \sqrt{2}$ . This Fermi surface will manifest itself near  $1/2$  through the classical cyclotron orbits of the quasiparticles in a  $B$  field  $\Delta B = B_{\text{APP}} - B$  ( $\nu = 1/2$ ). At the smallest values of  $\Delta B$  (near  $1/2$ ) the theory predicts in some detail the SAW results presented above. At  $\nu = 1/2$  these gauge field fermions move in the direction  $q$  of the SAW due to the SAW electric field. If the

SAW  $\lambda > l_0$ , the mean free path of the gauge field fermion, then  $\sigma_{xx}(q)$  is determined only by  $l_0$ . If  $\lambda < l_0$  the quasiparticles will relax along  $q$  without scattering so that  $\sigma_{xx}(q) \propto q$ . This behavior is qualitatively just what is seen in Fig. 4. The inflection in the data at  $q \approx 2 \mu\text{m}^{-1}$  demonstrates a transition from mean free path limited to  $q$  dependent conductivity, and therefore determines the quasiparticle mean free path to be  $\sim 1 \mu\text{m}$ . There is a quantitative discrepancy between the experiment and the theory in the overall conductivity scale of about a factor of two – the etiology of this is not clear.

The width of the effect is also consistent with the picture of Fermi surface formation at  $\nu = 1/2$  and may actually provide a measurement of the gauge field fermion wavevector,  $k_F$ . As shown schematically in Fig. 5, the quasiparticles will

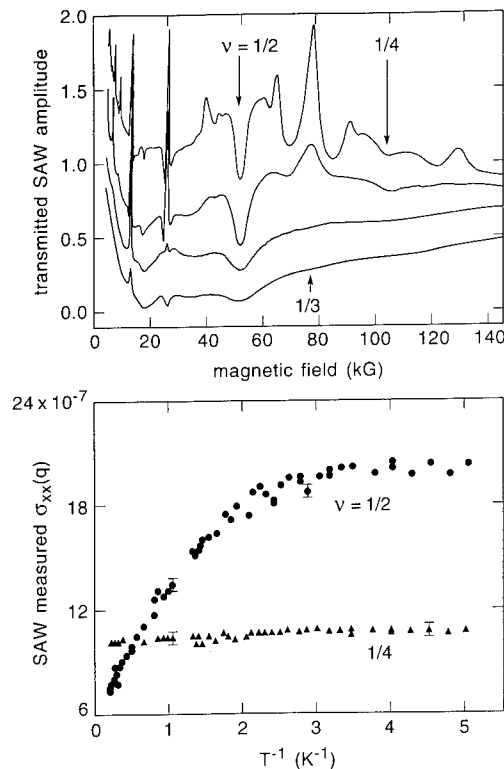


Fig. 3. Temperature dependence of the  $1/2$  and  $1/4$  features. The upper panel shows four transmitted SAW amplitude magnetic field traces at temperatures of 0.45, 1.25, 3.0 and 4.0 K from top to bottom at 3.4 GHz SAW. The lower panel shows SAW derived conductivity at 3.4 GHz.

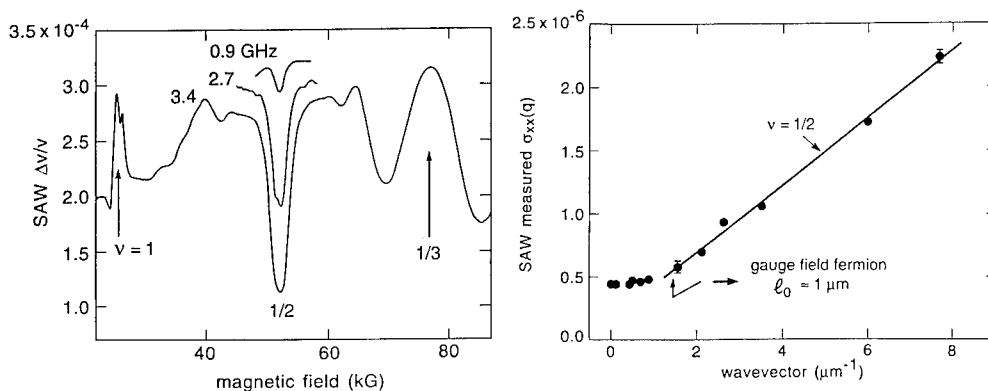


Fig. 4. Left panel: SAW velocity shift for three different frequencies at 50 mK. The traces are offset for clarity. Right panel: wavevector dependent conductivity at  $\nu = 1/2$  as derived from the SAW velocity shift,  $T = 50$  mK.

move in a cyclotron orbit of radius  $R_c = \hbar k_F / e \Delta B$ . We assume here that  $\text{SAW } \lambda < l_0$ . One expects that for small  $\Delta B$  the quasiparticle will move in a sufficiently large orbit  $R_c$  that the particle will still substantially short-out the SAW electric field. However, as  $\Delta B$  increases, the cyclotron radius is reduced to the point that movement of the quasiparticle is essentially transverse to the  $q$  direction of the SAW and as such the quasiparticle motion will not enhance the  $\sigma_{xx}(q)$ . Therefore, the width of the effect at  $1/2$  provides a scale of the quasiparticle Fermi wavevector. If the limit  $R_c \approx \lambda/2$  is selected then  $\Delta B = \hbar k_F q / \pi e$ . This line is shown in Fig. 5. Clearly the SAW electric field shorting will be cut off for a

smaller chosen percentage of  $R_c$ , which will increase the predicted  $\Delta B/B$ . This would bring the theoretical prediction and experimental results into closer agreement than the present discrepancy of  $\sim 20\%$ .

This powerful theory may provide a new perspective on 2D correlations in a  $B$  field. The gauge field fermions we may be observing at  $1/2$  are predicted to occur at other even denominator  $\nu$ , just as we in fact observe experimentally. These particles may well be responsible for the spectrum of FQHE states observed at the principle series  $\nu = p/(2p+1)$ . These directly translate to the IQHE for quasiparticles ( $1/3 \rightarrow \nu' = 1$ ,  $2/5 \rightarrow \nu' = 2$ , etc.). As such, the SAW results may be

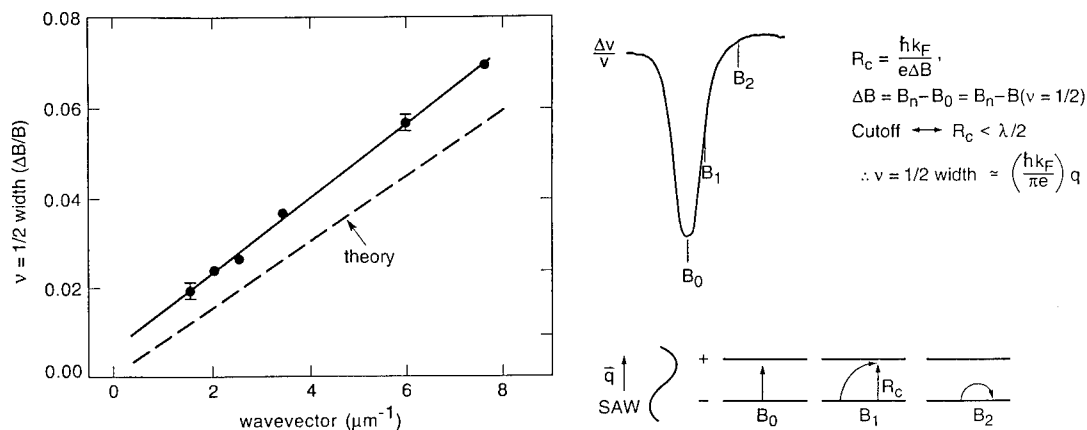


Fig. 5. Left panel:  $\nu = 1/2$  width ( $\Delta B/B$ ) versus SAW wavevector at 50 mK. The width is defined as the full  $B$  field extent at the half maximum. Right panel: map of  $\Delta v/v$  near  $1/2$  and schematic of gauge field Fermion cyclotron radius for  $\Delta B$ .

providing us with a description of the gauge field fermion, which themselves are a manifestation of electron correlation in 2D, and which in fact may be the origin of the fractional quantum Hall effect.

## 2. Small $\nu$

The second focus of our studies has been the small filling factor range near and below  $\nu = 1/5$ , where it is proposed that in this system of quenched kinetic energy the 2DES will condense into an electron solid [6]. A large increase in the DC resistance is expected as solidification occurs, and this effect has been extensively characterized [7]. This property, along with observed  $I$ - $V$  discontinuities [8], are sensitive but not specific symptoms of electron solidification: magnetic localization may likewise present as an insulating state in a similar  $\nu$  range. A specific sign of electron lattice formation is propagation of a shear mode with the magneto-phonon dispersion  $\omega \approx q^{3/2}/B$ . This dispersion will be broadened with the inclusion of disorder and at  $q=0$  a gapped pinning mode will be present [9]. Our surface acoustic wave technique is particularly suited to detect such a mode. In the proposed electron solid  $\nu$  regime, a crossing of the sound dispersion and the magneto-phonon dispersion should appear as an additional real conductivity peak with an imaginary counterpart.

The following data represent our investigations into the electron solid filling factor range and may demonstrate such a mode crossing. Experimentally we measured  $\sigma_{xx}(\omega, q) = \sigma'_{xx}(\omega, q) + i\sigma''_{xx}(\omega, q)$  for a range of  $\omega, q$  using the SAW technique. In these measurements in the vicinity of  $\nu = 1/5$  where the DC measurements show insulating behavior the sound velocity shift and attenuation show that at high frequencies substantial additional conductivity is indeed present. In Fig. 6 one sees that the sound velocity shift ( $\Delta v/v_{\max}$ ) is much lower than expected from the DC measurement (marked THEORY) for  $\nu < 1/5$ . This means additional conductivity at 235 MHz compared to DC [10].

Before proceeding to other  $\omega, q$  we demon-

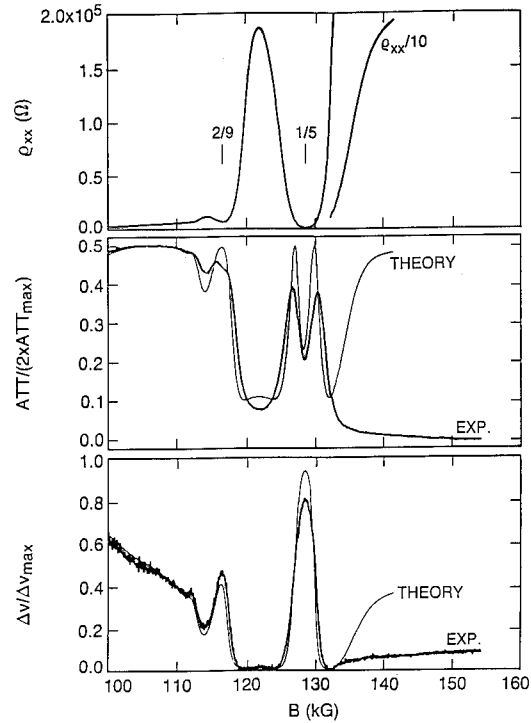


Fig. 6. Magnetic-field dependence of DC resistance  $\rho_{xx}$ , normalized SAW attenuation, and velocity shifts at 80 mK and 235 MHz. The lines marked theory are calculated using  $\rho_{xx}(\text{DC})$  in Eqs. (1) and (2).

strate that one can take advantage of the measurement of both amplitude and velocity to derive both real and imaginary conductivity. If an excitation mode is present in the 2DES and the SAW dispersion crosses the mode, then it is expected that the real part of the conductivity will be peaked at the mode center and the imaginary part of the conductivity will go through zero. The real and imaginary contributions to the conductivity can be seen immediately in a phase plot of the measured SAW attenuation versus velocity. From Eqs. (1) and (2) the phase plot will give a semicircle for only real conductivity and deviations from this semicircle will indicate imaginary conductivity. Fig. 7 shows phase plots for a high  $B$  field point in the insulating range where the temperature is swept from the highest to lowest values. The highest frequency plot shows data lying on the semicircle or real curve over the entire temperature range with only minor deviation at the

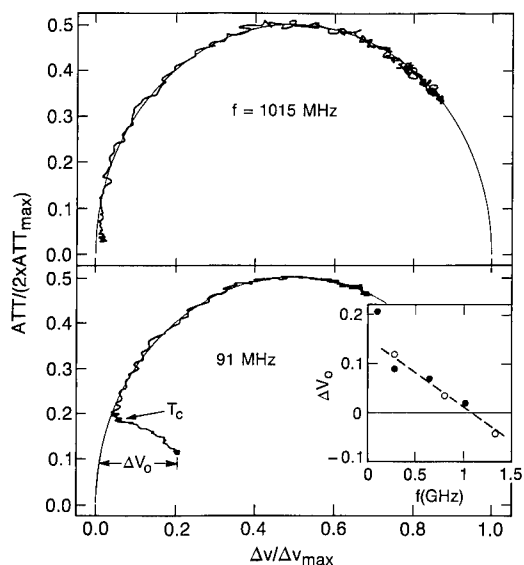


Fig. 7. Phase plots of SAW attenuation vs. velocity shift at two different frequencies at  $\nu = 0.167$ . The theoretical line based on Eqs. (1) and (2) forms a semicircle. In the inset,  $\Delta v_0$  is plotted as a function of frequency for two different samples (( $\circ$ ) and ( $\bullet$ )).

low temperature (velocity) end of the sweep. In the low frequency (91 MHz) plot at the low temperature end a substantial inward deviation occurs, signaling a sizable positive imaginary contribution. This deviation initiates at a distinct temperature  $T_c$ . Intermediate frequencies demonstrate intermediate values of  $\Delta v_0$ , which is defined as the lowest temperature deviation of the SAW velocity from the real conductivity semicircle. These data show that a large imaginary conductivity exists at frequencies near 100 MHz and this conductivity decreases with increasing frequency. These values (and others) of  $\Delta v_0$  are plotted versus frequency in the Fig. 7 inset, and show that  $\Delta v_0$  crosses zero at a frequency of about 1 GHz, indicating a mode crossing.

To examine the real part of the conductivity, one can also perform temperature sweeps at constant magnetic field values in the insulating regime, using Eqs. (1) and (2) to extract  $\sigma'_{xx}(\omega, q)$ . Fig. 8 shows the real conductivity calculated from SAW measurements at four different frequencies and for DC. As the temperature is decreased, different frequency traces have the same conduc-

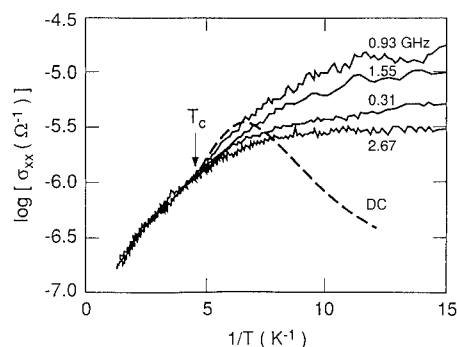


Fig. 8. RF real conductivity versus  $1/T$  for four different frequencies plus DC at filling factor  $\nu = 0.176$ .

tivity down to a well defined temperature  $T_c$ . At  $T < T_c$  the real  $\sigma_{xx}$  behavior is frequency dependent. From these traces one can determine the frequency dependence; Fig. 9 shows the real conductivity versus frequency for four different temperatures but all at the same magnetic field value. It is clear that at sufficiently low temperatures a peak in the real conductivity is crossed as the SAW frequency is increased, with the peak near 1 GHz. Interestingly the mode peak does not change in  $\omega$  appreciably as the temperature is lowered.

Fig. 10 shows the  $\nu$  dependence of this mode. It is important that over the magnetic field range shown here, the mode peak position does not appear to move in frequency. One would expect

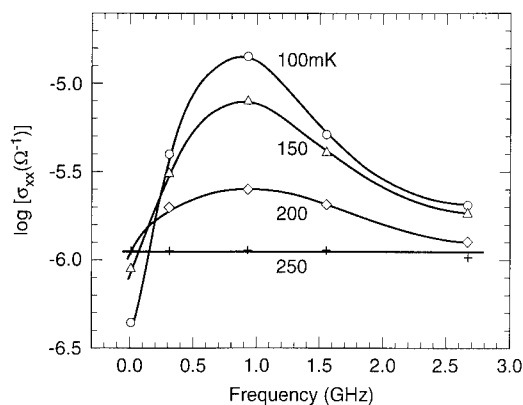


Fig. 9. Finite frequency/wavevector real conductivity mode at filling factor  $\nu = 0.160$  for a set of four different temperatures as measured with SAW.

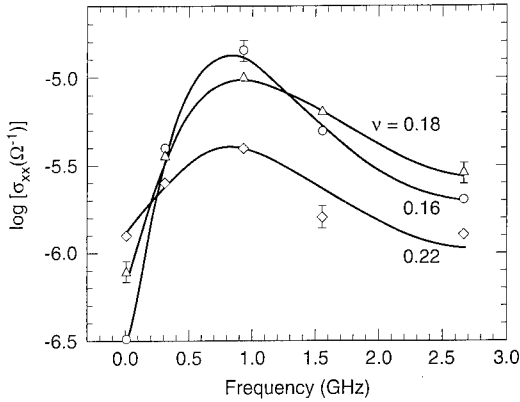


Fig. 10. Finite frequency/wavevector real conductivity mode at  $T = 100$  mK for three different magnetic field values.

that for a pure  $q$  dependent mode the peak position should change with  $B$  field as  $\omega \approx f(q)/B$ . These data therefore suggest a wavevector independent, broad, low energy excitation in the insulating range.

If one is to pursue an electron lattice picture then these results offer at least a determination of an upper bound to the correlation length  $\zeta$ . The peak in the real conductivity in this model represents the peak of a pinning mode. In the long wavelength limit,  $k < 2\pi/\zeta$ , regime, the pinning frequency scales like  $\omega_{\text{pl}}\omega_t/\omega_c$ , where the plasma frequency  $\omega_{\text{pl}}^2 = ne^2k/2\epsilon_p m^*$  and the shear mode frequency  $\omega_t^2 = \eta k^2/nm^*$  are determined at the wavevector  $k = 2\pi/\zeta$  with the cyclotron frequency  $\omega_c = cB/m^*$ . By estimating the shear modulus [11]  $\eta = 4k_B T_c n$  from the transition temperature  $T_c = 200$  mK one obtains  $\zeta = 1 \mu\text{m}$  from our measured pinning frequency at  $\nu = 0.167$ . This value of  $\zeta$  is about 25 lattice spacings but on the order of our minimum wavelength of  $\lambda_{\text{min}} \approx 1.0 \mu\text{m}$ . These findings suggest that the correlation length is no longer than  $1 \mu\text{m}$ , and

that higher frequency SAW may be able to examine the  $q$  dependent range of the solid dispersion.

These results show that a low energy mode is indeed present in the small filling factor range, and if an electron solidification picture is invoked then the mode we have characterized here probably represents a pinning mode of the system. In order to truly demonstrate and study ordering in the system, however, a smaller wavelength probe must be employed.

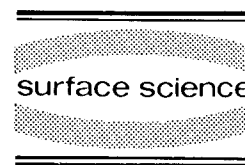
### 3. References

- [1] A. Wixforth, J. Scriba, M. Wassermeier, J.R. Kotthaus, G. Weimann and W. Schlapp, Phys. Rev. B 40 (1989) 7874; Also A. Wixforth, J.P. Kotthaus and G. Weimann, Phys. Rev. Lett. 56 (1986) 2104.
- [2] T.W. Grudkowski and M. Gilden, Appl. Phys. Lett. 38 (1981) 412.
- [3] R.L. Willett, M.A. Paalanen, R.R. Ruel, K.W. West, L.N. Pfeiffer and D.J. Bishop, Phys. Rev. Lett. 65 (1990) 112.
- [4] R.L. Willett, R.R. Ruel, M.A. Paalanen, K.W. West and L.N. Pfeiffer, Phys. Rev. B 47 (1993) 7344.
- [5] B.I. Halperin, P.D. Lee and N. Read, Phys. Rev. B 47 (1993) 7312.
- [6] Y. Lozovik and V. Yudson, Pis'ma Zh. Eksp. Teor. 22 (1975) 26 [JETP Lett. 22 (1975) 11].
- [7] R.L. Willett, H.L. Stormer, D.C. Tsui, L.N. Pfeiffer, K.W. West and K.W. Baldwin, Phys. Rev. B 38 (1988) 7881.
- [8] R.L. Willett, H.L. Stormer, D.C. Tsui, L.N. Pfeiffer, K.W. West, M. Shayegan, M. Santos and T. Sajoto, Phys. Rev. B 40 (1989) 6432; Also Y.P. Li, T. Sajoto, L.W. Engel, D.C. Tsui and M. Shayegan, Phys. Rev. Lett. 67 (1991) 1630.
- [9] H. Fukuyama and P. A. Lee, Phys. Rev. B 18 (1978) 6245.
- [10] M.A. Paalanen, R.L. Willett, P.B. Littlewood, R.R. Ruel, K. W. West, L.N. Pfeiffer and D.J. Bishop, Phys. Rev. B 45 (1992) 11342.
- [11] J.M. Kosterlitz and D.J. Thouless, J. Phys. C 6 (1973) 1181; D.R. Nelson and B.I. Halperin, Phys. Rev. B 19 (1979) 2457.



ELSEVIER

Surface Science 305 (1994) 83–86



## Ultrasonic approach to the integer and fractional quantum Hall effect

A. Esslinger <sup>\*,a</sup>, R.W. Winkler <sup>a</sup>, C. Rocke <sup>a</sup>, A. Wixforth <sup>a</sup>, J.P. Kotthaus <sup>a</sup>,  
H. Nickel <sup>b</sup>, W. Schlapp <sup>b</sup>, R. Lösch <sup>b</sup>

<sup>a</sup> *Sektion Physik, Ludwig-Maximilians-Universität München, Geschwister Scholl Platz 1, D-8000 München 22, Germany*

<sup>b</sup> *Telekom Forschungsinstitut beim FTZ, D-6100 Darmstadt, Germany*

(Received 15 April 1993; accepted for publication 4 June 1993)

### Abstract

The integer and fractional quantum Hall effect is investigated using the acoustoelectric effect in a high mobility two-dimensional electron system. This effect is a result of the interaction of the coherent field of an ultrasonic surface acoustic wave and the completely quantized electron system in strong magnetic fields. The mutual interaction leads to both energy and momentum transfer of the wave to the electrons and is reflected in giant quantum oscillations in the sound-induced currents and voltages in the two-dimensional system. Unlike standard magnetotransport experiments the acoustoelectric effect probes the states of the bulk of the electron system rather than those of the edges and thus is suited to gain insight into the quantum Hall effect from a different point of view.

In piezoelectric semiconductors, the coherent phonon field of a surface acoustic wave (SAW) can couple to mobile carriers via the piezoelectric polarizability of the host material. For the case of a two-dimensional electron system (2DES) like in a GaAs/AlGaAs heterostructure, this interaction is strongest for a small diagonal conductivity  $\sigma_{xx} = \sigma_m \approx 3 \times 10^{-7} \Omega_{sq}^{-1}$  as present under the conditions of the quantum Hall effect or at very low carrier density [1,2] and leads to giant quantum oscillations of, e.g., the attenuation of the SAW. As reported earlier [3] also large SAW-induced acoustoelectric currents and voltages are observed under these conditions. A most remarkable effect in the regime of both the integer and

the fractional quantum Hall effect is the occurrence of a bipolar transverse acoustoelectric field  $E_y$  around integer and fractional Landau level filling factors. Such oscillations are observed in the so-called “open geometry” where no macroscopic currents in the sample are permitted. Here, we concentrate on the quantitative explanation of the observed acoustoelectric voltages. Initial results on the acoustoelectric current as observed in “shorted” configuration are discussed in Refs. [3,4].

The SAW is excited by means of interdigital transducers [1,2] at a center frequency of 144 MHz. Typically, 100  $\mu$ W of RF power is fed into one of the transducers resulting in an acoustic power density of about 1 mW/m. The 2DES is defined into a Hall bar geometry with ohmic contacts serving as voltage probes. Source and

\* Corresponding author.



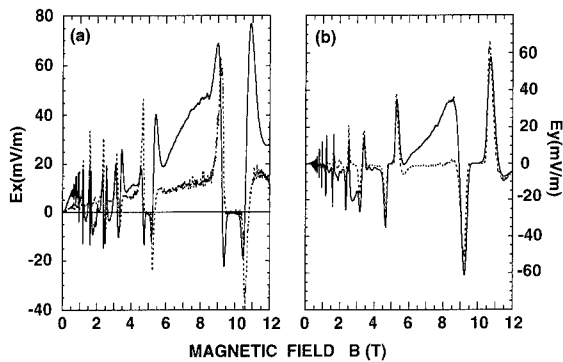


Fig. 1. Experimental results for the acoustoelectric fields  $E_x$  (a) and  $E_y$  (b) in open geometry as a function of the magnetic field  $B$ . The longitudinal field  $E_x$  exhibits a characteristic double-peak structure around integer filling factors, whereas the transverse field  $E_y$  changes sign around those magnetic field values. The dashed lines are the results of a calculation employing the model as described in the text.

drain contacts of  $20\ \mu\text{m}$  width are provided at both ends of the 2DES. The experiments reported here are performed on two different samples: S1 (carrier density  $N_S = 2.4 \times 10^{15}\ \text{m}^{-2}$ ; mobility  $\mu = 150\ \text{T}^{-1}$ ) and S2 ( $N_S = 0.72 \times 10^{15}\ \text{m}^{-2}$ ;  $\mu = 150\ \text{T}^{-1}$ ) in open geometry. Both the sound-induced longitudinal field  $E_x$  and the transverse

field  $E_y$  are monitored at the voltage probes using standard lock-in techniques [3,4].

Typical experimental results for sample S1 are shown in Fig. 1 as solid lines. In Fig. 1a the longitudinal field  $E_x$  and in Fig. 1b the transverse field  $E_y$  are depicted as a function of the magnetic field  $B$ .  $E_x$  exhibits a double peak structure around integer filling factors  $\nu$  similar to those observed in SAW transmission measurements [1,2]. In contrast, the transverse field  $E_y$  displays bipolar double peaks around integer fillings. Similar results are also obtained in the regime of the fractional quantum Hall effect. This is demonstrated for the low density sample S2 at  $T = 0.5\ \text{K}$  and for filling factor  $\nu = 1/3$ , as shown in Fig. 2a.

Existing theories [5] failed to explain some of our observations quantitatively. For example, the non-zero off-diagonal acoustoelectric voltage  $E_y$  in the open geometry is not at all accounted for in Ref. [5]. Also the results as obtained in “shorted geometry” [3,4] are partially in contradiction with this model. More recently, however, a different model of the acoustoelectric interaction has been formulated by Fal’ko and Iordanskii [6] and by Winkler et al. [7]. We here restrict ourselves to a sketch of the basic ideas of this model and refer

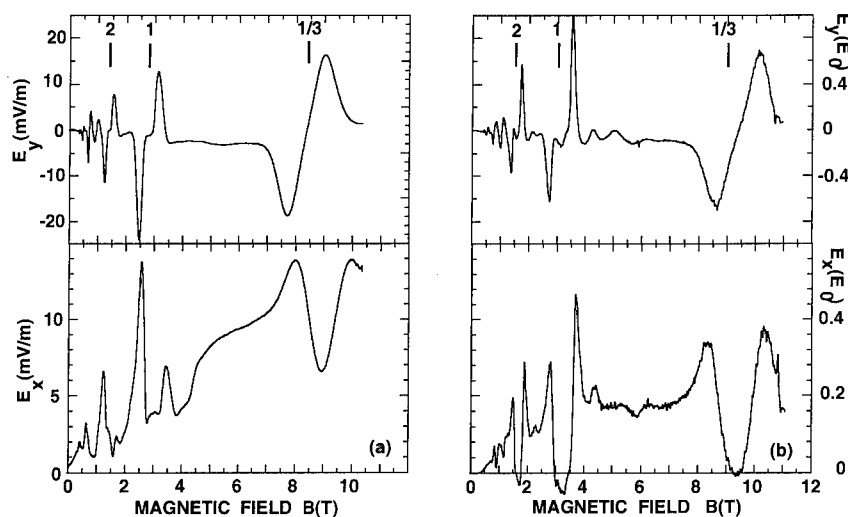


Fig. 2. (a) Experimentally obtained acoustoelectric fields  $E_x$  and  $E_y$  in open geometry for the low-density sample S2. Also for the fractional filling factor  $\nu = 1/3$ , the characteristic signature of the acoustoelectric effect is observed. (b) Calculated acoustoelectric fields using measured magnetotransport tensor components.

the reader to a more detailed description in the original references.

On piezoelectric materials a SAW leads to a piezoelectric field propagating with the speed of sound:

$$E_p(x, t) = -\frac{\partial}{\partial x}\Phi(x, t) = E_m e^{i(kx - \omega t)}. \quad (1)$$

This field is screened by the mobile carriers depending on the local diagonal conductivity  $\sigma_{xx}$  and the effective field is then given by [2]

$$E_{\text{eff}}(x, t) = E_p(x, t) + E_{\text{ind}}(x, t) \\ = \frac{E_p(x, t)}{1 + i(\sigma_{xx}/\sigma_m)}, \quad (2)$$

where  $E_{\text{ind}}$  is phase-shifted with respect to  $E_p$  by  $\Phi = \arctg(\sigma_{xx}/\sigma_m)$ . Thus the generated local acoustoelectric current,

$$j_\alpha(x, t) = \sigma_{\alpha x} E_{\text{eff}}(x, t), \quad \alpha = (x, y) \quad (3)$$

gives rise to a modulated carrier density and thus a modulated local conductivity tensor:

$$N_S(x, t) = N_S^0 + \Delta N_S e^{i(kx - \omega t)}$$

and

$$\sigma(x, t) = \sigma_0 + \frac{\partial \sigma}{\partial N_S} \Delta N_S(x, t) \quad (4)$$

with an amplitude  $\Delta N_S$  much smaller than the equilibrium value  $N_S^0$ . Using the continuity equation, the oscillating part of the charge density can now be related to  $E_{\text{eff}}$ :

$$\Delta N_S(x, t) = -\frac{k\sigma_{xx} E_{\text{eff}}(x, t)}{e\omega} \\ = -\frac{\sigma_{xx} E_{\text{eff}}(x, t)}{ec}. \quad (5)$$

Here,  $c$  denotes the speed of sound, whereas the other symbols have their usual meaning. For  $\Gamma_{xx} = \Gamma_m$  and an amplitude of the SAW  $\mu_z = 0.1 \text{ \AA}$ ,  $\Delta N_S/N_S^0 \approx 1 \times 10^{-3}$ . The time average of the acoustoelectric current has two components.

$$\langle j_\alpha(x) \rangle_t \\ = \left\langle \left( \sigma_{\alpha x}^0 + \frac{\partial \sigma_{\alpha x}}{\partial N_S} \Delta N_S(x, t) \right) E_{\text{eff}}(x, t) \right\rangle_t \\ = -\frac{\partial \sigma_{\alpha x}}{\partial N_S} \frac{1}{ce} \langle (\sigma_{xx}^0 E_{\text{eff}}(x, t)) E_{\text{eff}}(x, t) \rangle_t, \quad (6)$$

because  $\langle \sigma_{\alpha x}^0 E_{\text{eff}}(x, t) \rangle_t = 0$  is zero and there is no phase shift between  $E_{\text{eff}}$  and  $\Delta N_S$ . In other words, the acoustoelectric current is a quadratic function in  $E_{\text{eff}}$  thus representing the local quadratic response of the 2D electron system to the piezoelectric field of the SAW. On the other hand, the attenuation of the wave [1,2] and the relative dissipated power density are given by

$$\langle \Gamma \rangle_t = -\frac{1}{I} \frac{\partial I}{\partial x} = \frac{1}{I} \langle \sigma_{xx} E_{\text{eff}}^2(x, t) \rangle_t, \quad (7)$$

respectively. Here,  $I$  denotes the acoustic intensity of the wave. As  $\Delta N_S \ll N_S^0$ , the expressions (6) and (7) are identical and the acoustoelectric current can be expressed in terms of the attenuation  $\Gamma$ ,

$$\langle j_\alpha(x) \rangle_t = -\frac{\partial \sigma_{\alpha x}}{\partial N_S} \frac{1}{ce} \langle I \cdot \Gamma \rangle_t \hat{e}_x \\ = -\frac{\partial \sigma_{\alpha x}}{\partial N_S} \frac{1}{e} \langle Q \rangle_t \hat{e}_x. \quad (8)$$

Here,  $Q = I \cdot \Gamma / c$  represents a “phonon pressure” proportional to both  $\Gamma$  and  $I$ , and  $\hat{e}_x$  a unit vector in the direction of sound propagation. The acoustoelectric tensor  $\Lambda$  [5] defines the proportionality between the current and the phonon pressure  $\mathbf{Q}$ , namely  $j_i = \Lambda_{il} Q_l$  and is in our model given by

$$\Lambda = -\frac{1}{e} \frac{\partial \sigma}{\partial N_S}. \quad (9)$$

This is the most important result of the above calculation. It is in contrast to Ref. [5] where  $\Lambda$  turns out to be directly proportional to the conductivity tensor  $\sigma$ , whereas in our case it is given by its derivative  $\partial \sigma / \partial N_S$ . Both quantities, however, converge for vanishing magnetic field since here the conductivity is linear in the carrier density. This non-linear relation between the acoustoelectric tensor and the carrier density is essential for the acoustoelectric effect in strong quantizing magnetic fields. Now, the field components  $E_x$  and  $E_y$  can be calculated:

$$E_x = \frac{I \cdot \Gamma}{ceN_S} \left( \nu \rho_{xy} \frac{\partial \sigma_{yx}}{\partial \nu} + \nu \rho_{xx} \frac{\partial \sigma_{xx}}{\partial \nu} \right); \\ E_y = \frac{I \cdot \Gamma}{ceN_S} \left( \nu \rho_{yx} \frac{\partial \sigma_{xx}}{\partial \nu} + \nu \rho_{yy} \frac{\partial \sigma_{yx}}{\partial \nu} \right), \quad (10)$$

where we express the carrier density  $N_S$  in terms of the Landau filling factor  $\nu = N_S h / eB$  using

$$\frac{\partial \sigma}{\partial N_S} = \frac{\partial \sigma}{\partial \nu} \frac{\partial \nu}{\partial N_S} = \frac{\nu}{N_S} \frac{\partial \sigma}{\partial \nu}. \quad (11)$$

Eq. (10) can be regarded as an extension of the famous Weinreich relation [8] both taking into account the tensor nature of the conductivity as well as its nonlinear dependence on the carrier density of a 2DES in strong quantizing magnetic fields.

Experimentally, the resistivity tensor is easily accessible, and hence  $E_x$  and  $E_y$  can be calculated in order to compare the results with the experiments. This is shown in Fig. 1 (dotted lines) and in Fig. 1b only using the SAW intensity  $I$  as fit parameter. Especially for the transverse field  $E_y$  the agreement is very good. The bipolar peaks are well explained by the oscillating derivative  $\partial \sigma_{xx} / \partial \nu$  which changes sign at integer filling factors. It should be noted, however, that standard DC measurements probe the conductivity of edge states rather than SAW experiments where the conductivity of the bulk of the 2DES is important whenever the sample size is larger than the SAW wavelength. This fact might be the origin of the deviations between the experiment and the calculations at present, e.g., in Figs. 1a and 1b around 8 T. The asymmetry of the double peaks of  $E_x$  in Fig. 1a is related to a well-understood asymmetry in the SAW attenuation caused by a sometimes unavoidable small inhomogeneity of the carrier density across the sample [2]. This asymmetry is less pronounced for the sample S2 as presented in Fig. 2.

In summary, we observe giant quantum oscillations in the sound-induced acoustoelectric fields

caused by an interaction between a surface acoustic wave and a high mobility 2DES in a piezoelectric GaAs/AlGaAs heterojunction. The acoustoelectric effect in a 2DES under the conditions of the integer and fractional quantum Hall effect is quantitatively explained using a model that can be regarded as an extension of the Weinreich relation originally formulated for three-dimensional systems in the absence of a magnetic field. The important difference is the non-monotonic dependence of the diagonal component of the magnetoconductivity-tensor on the carrier density (or the Landau-level filling) in strong quantizing magnetic fields.

We gratefully acknowledge stimulating discussions with V.I. Fal'ko and W. Dietsche and appreciate the financial support of the Deutsche Forschungsgemeinschaft.

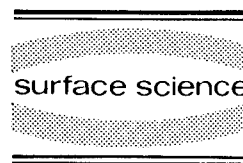
## 1. References

- [1] A. Wixforth, J.P. Kotthaus and G. Weimann, Phys. Rev. Lett. 56 (1986) 2104.
- [2] A. Wixforth, J. Scriba, M. Wassermeier, J.P. Kotthaus, G. Weimann and W. Schlapp, Phys. Rev. B 40 (1989) 7874.
- [3] A. Esslinger, A. Wixforth, R.W. Winkler, J.P. Kotthaus, H. Nickel, W. Schlapp and R. Lösch, Solid State Commun. 84 (1992) 939.
- [4] A. Esslinger, A. Wixforth, R.W. Winkler, S. Manus, J.P. Kotthaus, H. Nickel, W. Schlapp, R. Lösch and G. Weimann, Proceedings of the 21st ICPS in Beijing, People's Republic of China.
- [5] A.L. Efros and Yu.M. Galperin, Phys. Rev. Lett. 64 (1990) 1959.
- [6] V.I. Fal'ko and S.V. Iordanskii, J. Phys.: Condensed Matter 4 (1992) 9201, and preprint.
- [7] R.W. Winkler, A. Esslinger, A. Wixforth and J.P. Kotthaus, to be published.
- [8] G. Weinreich, Phys. Rev. 104 (1956) 321.



ELSEVIER

Surface Science 305 (1994) 87–90



## Phonon measurements of the energy gap in the fractional quantum Hall state

R.H. Eyles, C.J. Mellor <sup>\*</sup>, A.J. Kent, K.A. Benedict, L.J. Challis, S. Kravchenko <sup>1</sup>,  
N.N. Zinov'ev <sup>2</sup>, M. Henini

*Physics Department, Nottingham University, Nottingham NG7 2RD, UK*

(Received 12 April 1993; accepted for publication 14 July 1993)

### Abstract

We have made the first measurements of the energy gap responsible for the fractional quantum Hall effect (FQHE) using ballistic acoustic phonons. This novel technique allows us to measure the FQHE energy gap at the magnetoroton minimum of the excitation spectrum. The gaps measured by this technique are comparable to those deduced for high-quality samples from the temperature dependence of the activated magnetoresistance and by optical luminescence studies. At a filling factor of  $2/3$  at 9 T we find an energy gap of 6.1 K close to the theoretical value.

### 1. Introduction

The accepted explanation of the fractional quantum Hall effect (FQHE) requires the existence of an energy gap for excitations from the two-dimensional quantum liquid ground state. A theory for the collective excitations was proposed by Girvin et al. [1] which draws close analogies with Feynman's theory [2] of the excitations of superfluid helium. Using a single mode approximation (SMA) they find that the dispersion relation for collective excitations  $\Delta(q)$  has a finite gap at  $q = 0$  and a minimum,  $\Delta_{\min}$ , at  $q^* \approx 1.3/l_c$ ,

where  $l_c$  is the cyclotron length;  $\Delta_{\min}$  is approximately  $\Delta(0)/2$ . The excitations near this minimum are known as magnetorotons in analogy with rotons in superfluid helium. The energy of the excitations is lowered for a real two-dimensional system relative to an ideal system due to the finite spread of the wave functions in the vertical direction [1], Landau level mixing [3] and disorder [4].

Experimentally, this energy gap has previously been measured in two ways. Firstly the gap was determined by measuring the temperature dependence of the longitudinal magnetoresistance ( $R_{xx}$ ) at a rational filling factor. This gap, which is due to thermally excited quasiparticles depends strongly on the mobility of the sample [5] and the activation measurements of  $R_{xx}$  are comparable to the theoretical values only in the highest mobility heterojunctions. The second approach has

<sup>\*</sup> Corresponding author.

<sup>1</sup> Permanent address: Institute for High Pressure Studies, Troitsk, Moscow, Russian Federation.

<sup>2</sup> Permanent address: Ioffe Institute, St. Petersburg, Russian Federation.

been to use magneto-optical methods to measure the mean energy of the electrons [6]. These measurements suggest an energy gap comparable to the theoretical values once the overlap of the electronic states with the acceptors is taken into account. In neither case is it clear exactly which gap is being measured. By using ballistic phonons we believe we can probe the dispersion curve close to the magnetoroton minimum.

## 2. Experimental details

The  $3\text{ mm} \times 2\text{ mm}$  Hall bars were fabricated from GaAs/(AlGa)As heterojunctions with a typical carrier density after illumination of  $1.5 \times 10^{11}\text{ cm}^{-2}$  and a mobility of  $1 \times 10^6\text{ cm}^2\text{ V}^{-1}\text{ s}^{-1}$ . The polished back face of the  $0.4\text{ mm}$  thick wafer had two,  $50\ \Omega$  constantan heaters ( $60\ \mu\text{m} \times 600\ \mu\text{m}$ ), evaporated onto it (see Fig. 1). One of the heaters was positioned over the edge of the Hall bar, the other over its centre. The sample was mounted in vacuum on a dilution refrigerator with a base temperature around  $40\text{ mK}$  in magnetic fields  $\leq 17.4\text{ T}$ .

A burst of nonequilibrium ballistic phonons was generated by applying a  $100\text{ ns}$  electrical pulse to one of the heaters. The repetition rate was kept low ( $1\text{ kHz}$ ) to ensure the temperature of the 2DEG remained close to the lattice temperature. The spectral distribution of emitted phonons can be estimated by assuming that it corresponds to the emission from a black body at the tempera-

ture of the heater. This distribution can be derived from the total power dissipated in it using acoustic mismatch theory [7]. These phonons were incident upon the 2DEG through which a constant bias current was flowing. A corresponding increase in the longitudinal voltage was detected. Assuming the voltage pulse to be proportional to the phonon absorption we can measure the absorption as a function of magnetic field and heater temperature. In particular we can measure the dependence of absorption on the heater temperature with the magnetic field fixed so that the system is at a filling factor of  $2/3$ .

## 3. Results

We find no qualitative difference between the heater over the edge of the sample and the one positioned over the bulk of the sample. This may be due to the high current ( $50\text{--}100\text{ nA}$ ) used in these experiments which will result in a significant proportion of the current flowing in the bulk of the sample rather than at the edges. As will be discussed later it may also be the case that phonon focusing is unimportant, allowing both heaters to affect the whole sample. The following results are from experiments in which only the heater over the centre of the sample was used. The results were found to be independent of the measurement current.

When the device was in a FQH state the phonon absorption signal was a minimum. By varying the heater temperature, the transient change in  $R_{xx}$ , which we take to be proportional to the phonon absorption, could be measured. This phonon absorption signal is shown in Fig. 2, for a filling factor of  $2/3$  ( $9\text{ T}$ ) along with a fitted theoretical curve that will be explained in the next section. A simple intuitive theory that gives almost the same result demonstrates the basic physics. If phonons are only absorbed at the density-of-states peak at the magnetoroton minimum then the size of the signal will be proportional to the phonon distribution function at an energy  $\Delta_{\min}$ , i.e. proportional to  $1/[\exp(\Delta_{\min}/k_B T) - 1]$ . This curve fits the data extremely well and gives a value  $\Delta_{\min} = 6.8 \pm 0.5\text{ K}$  compared to

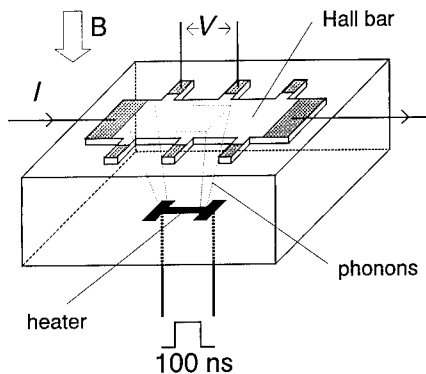


Fig. 1. Schematic diagram of the experiment.

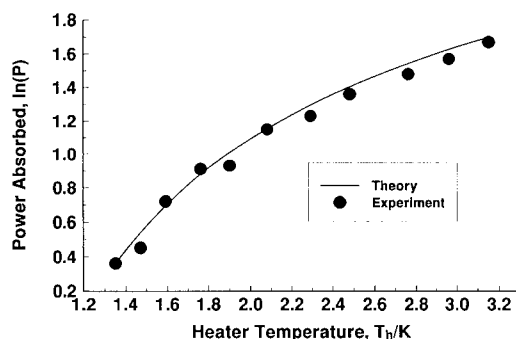


Fig. 2. Experimental absorption data (●) for  $\nu = 2/3$  (9 T), with the fitted theoretical curve (solid line) with  $\Delta_{\min} = 6.1$  K,  $\mu = 5.65m_{\text{eff}}$ .

a value of  $6.1 \pm 0.5$  K obtained from the detailed analysis. At a filling factor of  $1/3$ , measured with a different carrier density so that the minimum of  $R_{xx}$  is at a similar value of magnetic field to the data shown above, we obtain a similar value for the energy gap.

This energy gap measured by phonon absorption is far greater than the activated energy gap of 2.2 K derived from the temperature variation of the minimum of  $R_{xx}$  using  $R_{xx} \propto \exp(-\Delta_{\text{gap}}/2k_B T)$ . However, the phonon absorption energy gap is comparable with values obtained from optical measurements [6] and transport measurements in very high mobility heterojunctions [5]. We therefore ascribe this discrepancy to differences in the way that disorder affects the two types of measurement.

Interpretation of the results at a filling factor of  $3/5$  is less clear. The fitting procedure outlined above does not provide a good fit even at very low energy gaps. We suggest that this may be because the minimum of  $R_{xx}$  is always nonzero in this sample unlike the minima at  $1/3$  and  $2/3$  which are very deep. As a result there are always thermal excitations present which can also absorb the phonons.

#### 4. Analysis and discussion

We can model the system as a 2DEG embedded in an elastic medium. As we are only interested in the interaction with long-wavelength

phonons we can use the isotropic Debye approximation; the consequent neglect of phonon focusing will be justified later. The rate of energy transfer from the phonon pulse to the 2DEG is given by Fermi's golden rule as

$$P(T_h) = \sum_s \int \frac{d^3 Q}{(2\pi)^3} \omega_s(Q) n_s(Q) |M_s(Q)|^2 S(q, \omega), \quad (1)$$

where  $\omega_s(Q)$  is the frequency of phonons of polarization  $s = (\text{LA}, \text{TA}_1, \text{TA}_2)$  and the (3D) wave vector  $Q = (q, q_z)$ ,  $n_s(Q)$  is the number of phonons in the given mode interacting with the 2DEG,  $M_s(Q)$  is the effective coupling between the phonons and the 2DEG (including both deformation and piezoelectric effects) and  $S(q, \omega)$  is the dynamic structure factor of the 2DEG. The number of phonons can be estimated by solving the Boltzmann equation with a source term representing the injection of phonons by the heater. When the 2DEG is at filling factor of the form  $\nu = 1/(2m+1)$  (and  $\nu = 1 - 1/(2m+1)$  by particle-hole symmetry) the single mode approximation gives a particularly simple form for the dynamic structure factor

$$S(q, \omega) = \bar{s}(q) \delta(\omega - \Delta(q)) \quad (2)$$

where  $\bar{s}(q)$  is the projected static structure factor, which can be obtained purely from the form of the ground state wave function. Girvin et al. [1] used the variational wave function of Laughlin [8] to find this and hence the magnetoroton dispersion  $\Delta(q)$ . The fact that  $\bar{s}(q)$  vanishes for small and large  $q$  means that we can use the approximate parabolic form

$$\Delta(q) = \Delta_{\min} + \frac{\hbar^2 (q - q^*)^2}{2\mu}. \quad (3)$$

The numerical value of  $\Delta_{\min}$  and  $\mu$  depend on the finite extent of the 2DEG in the vertical direction and the inevitable disorder in the system. We choose these quantities as fitting parameters to our experimental data.

Fig. 3 shows the integrand  $P_s(q)$ , the rate of absorption for phonons with an in-plane compo-

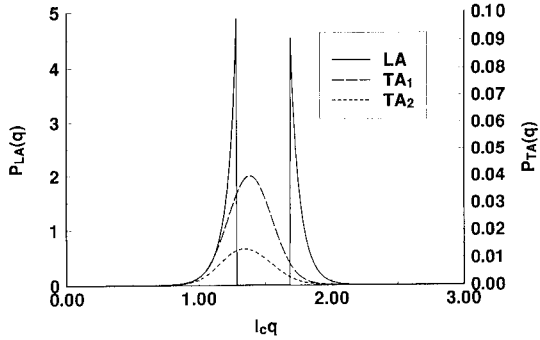


Fig. 3. Relative contributions of the LA and TA modes to  $P_s(q)$  as a function of the in-plane wavevector  $q$  for  $\Delta_{\min} = 6.1$  K,  $\mu = 5.65m_{\text{eff}}$ .

nent of the wavevector in the range  $[q, q + dq]$  for each of the phonon modes at a heater temperature of 3 K using the values of  $\Delta_{\min}$  and  $\mu$  which best fit the experimental data at  $\nu = 2/3$ ,  $B = 9.0$  T. It is clear that the longitudinal (LA) modes make the dominant contribution due to the frequency dependence and isotropy of the deformation potential coupling; the fact that the LA modes are only weakly focused justifies our use of the isotropic Debye approximation and may partially explain why the two heaters give similar results. The origin of the cutoff in the LA part of the integrand can be understood from simple energy conservation considerations. The range of possible energies of a phonon with a given in-plane wavevector,  $q$ , has a lower limit set by the maximum allowed angle of incidence,  $\theta_{\max} \approx 75^\circ$ ; this minimum energy is  $\hbar\omega_{\min}(q) = \hbar c_s q / \sin \theta_{\max}$  where  $c_s$  is the relevant phonon velocity. If, for a given value of  $q$ , this lower limit lies above the magnetoroton curve (as sometimes happens for LA phonons) then a phonon cannot be absorbed at that value of  $q$ . Clearly then, at low heater temperatures, the absorption is going to be dominated by the excitations near the magnetoroton minimum.

In order to fit the data the lowest data point is used to set the absolute scale. The best fit to the data suggests that  $\Delta_{\min} = (0.040 \pm 0.003) \times e^2 / 4\pi\epsilon_0\epsilon_r l_c \approx (6.1 \pm 0.5)$  K. The magnetoroton mass is more difficult to determine but we have assumed, on the basis of the finite thickness correc-

tions that it has a value close to  $6m_{\text{eff}}$  where  $m_{\text{eff}}$  is the effective mass of the conduction electrons in GaAs. The best fit is obtained for  $\mu = (5.65 \pm 0.5)m_{\text{eff}}$ . In our heterojunction the vertical extent of the wavefunction is characterised by a Fang–Howard parameter [9],  $b^{-1}$ , of approximately 4 nm. This leads to a theoretical value of  $\Delta(0) \approx 0.1 \times e^2 / 4\pi\epsilon_0\epsilon_r l_c$  [1] ignoring Landau level mixing. Taking  $\Delta(0)$  to be twice  $\Delta_{\min}$  we obtain experimentally a value of  $0.08 \times e^2 / 4\pi\epsilon_0\epsilon_r l_c$ .

## 5. Conclusions

We have observed absorption of ballistic phonons by a two-dimensional electron system in the fractional quantum Hall state. The energy gap at  $\nu = 2/3$  (9 T) is found to be 6.1 K even though the gap measured by the activated behaviour of  $R_{xx}$  is only 2.2 K. The value of 6.1 K is in broad agreement with values obtained by magneto-optical measurements and transport experiments in high-mobility samples.

## 6. Acknowledgements

We are grateful to the Science and Engineering Research Council, the Royal Society and the European Community for financial support.

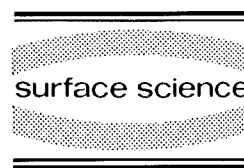
## 7. References

- [1] S.M. Girvin, A.H. MacDonald and P.M. Platzmann, Phys. Rev. B 33 (1986) 2481.
- [2] R.P. Feynman, Phys. Rev. 91 (1953) 1291, 1301; 92 (1954) 262.
- [3] D. Yoshioka, J. Phys. Soc. Jpn. 53 (1984) 3740.
- [4] A.H. MacDonald, K.L. Liu, S.M. Girvin and P.M. Platzmann, Phys. Rev. B 33 (1986) 4014.
- [5] R.L. Willett, H.L. Stormer, D.C. Tsui, A.C. Gossard and J.H. English, Phys. Rev. B 37 (1988) 8476.
- [6] I.V. Kukushkin, N.J. Pulsford, K. von Klitzing, K. Ploog and V.B. Timofeev, Surf. Sci. 263 (1992) 30.
- [7] W. Kappus and O. Weiss, J. Appl. Phys. 44 (1973) 1947.
- [8] R.B. Laughlin, Phys. Rev. Lett. 50 (1983) 1395.
- [9] F.F. Fang and W.E. Howard, Phys. Rev. Lett. 16 (1966) 797.



ELSEVIER

Surface Science 305 (1994) 91–95



## Thermoelectric properties of GaAs/Ga<sub>1-x</sub>Al<sub>x</sub>As heterojunctions in the fractional quantum Hall regime

U. Zeitler <sup>\*,a,1</sup>, R. Fletcher <sup>b</sup>, J.C. Maan <sup>a,c</sup>, C.T. Foxon <sup>d</sup>, J.J. Harris <sup>e</sup>, P. Wyder <sup>a</sup>

<sup>a</sup> High Magnetic Field Laboratory (MPIF-CNRS), B.P. 166, F-38042, Grenoble Cedex 9, France

<sup>b</sup> Physics Department, Queen's University, Kingston, Ontario, Canada K7L 3N6

<sup>c</sup> High Field Magnet Laboratory, University of Nijmegen, 6525 ED Nijmegen, The Netherlands

<sup>d</sup> Department of Physics, University of Nottingham, Nottingham NG7 2RD, UK

<sup>e</sup> Semiconductor Interdisciplinary Research Centre, Imperial College, London SW7 2BZ, UK

(Received 21 April 1993; accepted for publication 11 August 1993)

### Abstract

We present experimental data on the thermoelectric power of a two-dimensional electron gas in the fractional quantum Hall regime. The thermopower is shown to be due to phonon-drag and therefore reflects the coupling of phonons to the electronic quasiparticle states. The general behaviour of the thermoelectric power as a function of applied magnetic field and temperature is compared to recent theoretical predictions of the electron–phonon drag in quantizing magnetic fields.

The thermoelectric power (TEP) of two-dimensional electron gases (2DEG) in GaAs/Ga<sub>1-x</sub>Al<sub>x</sub>As heterojunctions mainly reflects the coupling of the phonons to the electronic states, as opposed to resistivity measurements which are sensitive to the electron-impurity scattering. TEP measurements therefore provide an important complementary tool for a better understanding of the electronic states in a 2DEG. At high magnetic fields, where only the lowest Landau level is occupied, and at low temperature, where the fractional quantum Hall (FQH) states develop, the nature of the phonon coupling to the electronic quasiparticles is an especially interesting

problem. However, only experimental TEP data in the integer quantum Hall regime have been reported previously [1,2].

The aim of our experiments was the investigation of the TEP of a 2DEG in the FQH regime. We will present the overall behaviour of the TEP in this region and will show that its variation as a function of magnetic field and temperature agrees qualitatively with a recent theory of the electron–phonon drag effect in an ideally pure 2DEG [3]. However, an experimentally observed strong decrease of the TEP in very high magnetic fields (filling factors below 1/5) cannot yet be explained.

The thermoelectric power  $S$  of an electron system is due to an applied temperature gradient  $\nabla T$  which leads to a thermal current  $j_{th} = \epsilon \nabla T$  ( $\epsilon$  is the thermoelectric tensor). In the steady state, where no total current is flowing, an oppo-

\* Corresponding author.

<sup>1</sup> Present address: High Field Magnet Laboratory, University of Nijmegen, 6525 ED, The Netherlands.



site current  $j_{\text{el}} = \sigma E$  ( $\sigma$  is the conductivity tensor) has to exist and an electric field is generated  $E = S \nabla T$  to produce this, leading to the relation:  $S = \sigma^{-1} \epsilon$ . For high mobility samples and at high fields, where  $\rho_{xx} \ll \rho_{xy}$ , the two independent components of the TEP in a 2DEG resulting from this equation can be simplified to  $S_{xx} \approx -\epsilon_{yx} \rho_{yx}$  (within 2% for our samples) and  $S_{yx} \approx \epsilon_{xx} \rho_{yx}$  (within 10%).

We have investigated the thermoelectric properties of three different MBE-grown high mobility samples (kindly provided by Philips Research Laboratories, Redhill, UK; labeled G645, G647 and G650 with electron concentrations of 0.86, 0.43, and  $1.0 \times 10^{15} \text{ m}^{-3}$  and mobilities of 230, 270, and  $190 \text{ m}^2/\text{V} \cdot \text{s}$ ). The 2DEG were grown on a semi-insulating GaAs substrate with dimensions of about  $10 \times 3 \times 0.5 \text{ mm}^3$ .

In order to perform TEP measurements, each sample was mounted freestanding inside a vacuum. One end was thermally anchored by soldering it with indium to a copper arm which was in thermal contact with a  $^3\text{He}$  bath, and a strain gauge heater was glued to the other end. By passing a DC current through the heater, a thermal gradient was established in the sample. We measured the temperature  $T$  and the temperature gradient  $\nabla T$  with two calibrated thermometers glued on the rear side of the substrate. Given the known heating power, the thermal conductivity  $\lambda$  of the samples could be calculated. In order to check the thermometry in a magnetic field we have measured  $\lambda$  at various fields; we did not observe any significant change as a function of the field.

The thermal conductivity of sample G647 at zero magnetic field is shown in the insert of Fig. 1. For all three samples the measured heat conductivities behave in a quantitatively similar way and are found to be close to the theoretically expected  $T^3$  dependence in the boundary scattering limit. The slight deviation from  $T^3$  is consistent with earlier published data [1].

The thermopower  $S_{xx}$  and the Nernst–Ettingshausen coefficient  $S_{yx}$  were measured with a phase-sensitive lock-in technique by applying an AC heating at 12 Hz. We verified that the thermal response of the system was fast enough to

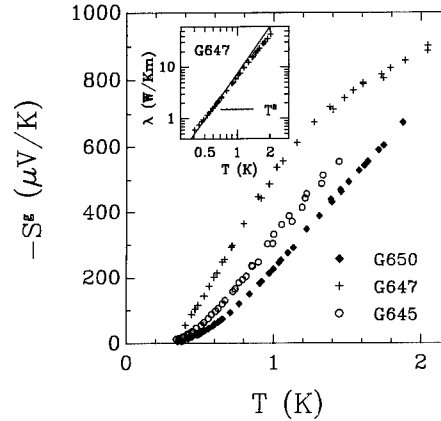


Fig. 1. The phonon-drag thermopower at zero magnetic field for three different samples. The insert shows the measured heat conductivity of the GaAs substrate of G647.

follow this frequency by obtaining the same results for 5–30 Hz, as well as with a DC method.

Generally the TEP is the sum of two contributions: the diffusion of the charge carriers, and the drag of these carriers by phonons. At zero magnetic field the diffusion contribution to the TEP can be written as  $S^d = -(\pi^2 k/3e)(p+1)(T/T_F)$  ( $T_F$  being the Fermi temperature and  $p \approx 1$  expressing the energy dependence of the electron scattering) [4]. For our samples at 1 K we expect  $S^d$  to have a magnitude between 14 and  $30 \mu\text{V/K}$  (taking  $p = 1$ ). The experimental magnitudes are at least an order of magnitude higher and the temperature dependence is much faster than linear, showing that the phonon drag TEP is the dominant contribution in the temperature range explored. We believe that this remains true in a magnetic field (though little is known about the diffusion component in the FQH regime) and so the TEP will continue to reflect the coupling of the phonons to the electronic quasiparticle states.

The zero field phonon drag TEP  $S^g$  (i.e. the experimentally measured TEP after subtracting the above described diffusion contribution using  $p = 1$ ) is plotted in Fig. 1. In the simplest model, the phonon-drag TEP is expected to vary as  $T^3$  [5] (which gives references to more detailed treatments; see also Refs. [6,7]). At higher temperatures the TEP begins to saturate because phonons with  $k_{\parallel} > 2k_F$  can no longer couple to the 2DEG

( $k_{\parallel}$  is the component of the phonon wave vector in the plane of the 2DEG, and  $k_F$  is the Fermi wave vector of the two-dimensional electrons).

In Fig. 2 we show the measured quantities  $S_{xx}$  and  $S_{yx}$  in a magnetic field. At lower fields, i.e. in the integer quantum Hall region, the TEP  $S_{xx}$  as well as the Nernst–Ettingshausen coefficient  $S_{yx}$  show an oscillatory behaviour, the latter resembling the derivative of the former with respect to magnetic field. This behaviour has been reported for many different samples [1,7]. In this region standard theory explains the occurrence as well as the magnitude of the maxima in  $S_{xx}$  [8], whereas  $S_{yx}$  is expected to be zero. A recent theory which relates the thermoelectric tensor to the derivative of the conductivity with respect to filling factor [9] can explain the oscillations of  $S_{yx}$  and its proportionality to the derivative of  $S_{xx}$  with respect to magnetic field.

At higher magnetic fields, when the FQH effect becomes visible, several interesting features appear in the TEP. Some have been reported

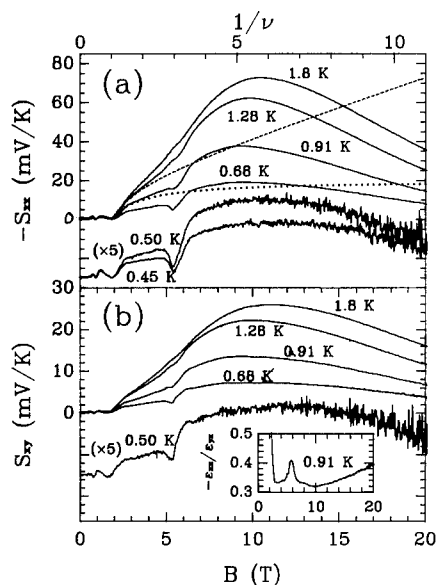


Fig. 2. (a) The TEP  $S_{xx}$  of G647 for different temperatures; the dotted line represents schematically the theoretical variation with only polar interaction; the broken line includes the deformation potential. (b) The Nernst–Ettingshausen coefficient  $S_{yx}$  of G647 for different temperatures with the ratio  $j_x/j_y$  of the thermally induced currents in the insert.

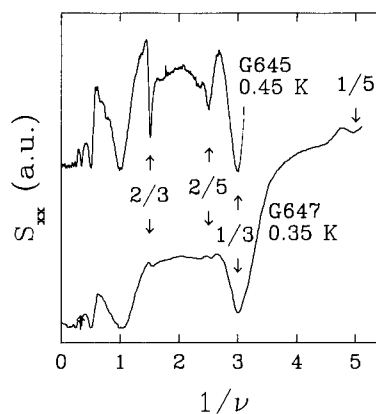


Fig. 3. The low temperature TEP  $S_{xx}$  for two samples showing several well pronounced fractions.

elsewhere [7], and we shall restrict ourselves here to a brief outline. Fractional filling factors (mainly  $1/3$  and  $2/3$ , and below  $0.5$  K also  $1/5$  and  $2/5$ ) are visible in the thermopower  $S_{xx}$  and the Nernst–Ettingshausen coefficient  $S_{yx}$  (Fig. 3), roughly comparable to their visibility in the resistivities  $\rho_{xx}$  and  $\rho_{xy}$  at similar temperatures. This means that the phonons cannot couple to the fractional states, but only to the thermally excited quasiparticles. However, apart from the minima, the TEP in the FQH regime is found to behave differently from the integer regime and also differently as compared to resistivity. For example, in the FQH regime the Nernst–Ettingshausen coefficient  $S_{yx}$  no longer resembles the field derivative of  $S_{xx}$ , as is the case in the integer quantum Hall regime, and in particular does not change sign when  $S_{xx}$  crosses fractional minima.

Moreover  $S_{yx}$  is found to be unexpectedly large, whereas for high mobility samples we expect it to be close to zero, which might be explained as follows. Due to the Lorentz force a phonon flux in the  $x$ -direction induces a thermal electron current turned by the Hall angle, i.e. for  $\rho_{xx} \ll \rho_{xy}$  perpendicular to it. This current must be compensated by a counter current due to an electric field which is again perpendicular to its resulting current. Therefore the electric field points in the direction of the thermal gradient. For a Hall angle  $\Theta$  slightly below  $90^\circ$ , the thermally induced current should be turned by about

$90^\circ$ – $\theta$  with respect to the perpendicular direction to the thermal gradient which corresponds to at most  $2^\circ$  for the present data. This is essentially why  $S_{yx}$  is expected to be zero. In fact, in the FQH regime, except in the narrow field regions where the fractions develop, we observe a constant ratio  $S_{yx}/S_{xx} \approx -\epsilon_{xx}/\epsilon_{yx} \approx 0.35$ , nearly independent of magnetic field and temperature (see insert in Fig. 2c; the slight increase at higher fields is probably due to a decrease of the Hall angle). The effective electric field is thus turned by an angle of about  $20^\circ$  with respect to the temperature gradient. This effect may be due to the phonon anisotropy in the GaAs substrate which has already been observed at zero field [10].

Finally, the TEP is seen to change dramatically when passing through the fractional minimum at  $\nu = 1/3$ , especially at temperatures below 1 K. The TEP increases roughly by a factor of two from above  $\nu = 1/3$  to below  $\nu = 1/3$ . At lower temperatures, and particularly in samples other than presented in Fig. 2, the TEP has actually been shown to be nearly field independent for  $2/3 < \nu < 1/3$ , as well as for  $\nu < 1/3$  [7]. In this previous paper it was concluded that the electronic quasiparticle states are subjected to a different electron–phonon interaction below and above  $1/3$ . This might be due to a change in their cohesive energy [11] leading to a change in the thermodynamic properties of the quasiparticle system [12].

In the following we concentrate on the overall behaviour (i.e. outside the regions where the FQHE minima develop) of the TEP in the quantum limit as a function of field and temperature. Although we present data mainly for the lowest concentration sample G647, we emphasize that all the main features were also observed in the other samples. Indeed from the somewhat limited number of samples that we have examined, we tentatively conclude that the behaviour of  $S_{xx}$  at high fields appears to be universal.

An obvious feature is that  $S_{xx}$  (Fig. 2a) is remarkably high, reaching values of up to 70 mV/K for the presented data of sample G647 at a filling factor of about  $\nu \approx 0.2$ , much higher than expected by conventional theory [13].

Although we cannot yet explain the absolute values of the TEP in the FQH regime, we attempt to describe its general variation using a recent theory which calculates the phonon-drag induced current in an ideal 2DEG [3]. Since for high mobility samples  $\rho_{yx}$  is accurately given by  $\rho_{yx} = B/ne \propto B$  ( $n$  is the electron concentration),  $S_{xx} \approx -\epsilon_{yx}\rho_{yx}$  reflects the properties of the fundamental thermoelectric quantity  $\epsilon_{yx}$ , i.e. of the phonon-drag induced current perpendicular to the thermal gradient, and the theoretically predicted drag current can be directly compared with our experimental TEP data.

The relevant temperature scale for the phonon drag TEP in a magnetic field is defined by the ratio between the thermal energy  $kT$  and the characteristic energy  $\hbar v/l_B$  of the phonons which couple to the 2DEG ( $l_B$  is the magnetic length and  $v$  the phonon velocity), giving a characteristic temperature  $T^* = \hbar v/k l_B$ . At fixed magnetic field and for very low temperatures ( $T \ll T^*$ ), the drag current  $j_{\text{drag}}$  is predicted to be proportional to  $T^5$  [3]. In the intermediate temperature range of  $0.05 < T/T^* < 0.4$ ,  $j_{\text{drag}}$  varies approximately linearly with temperature. Finally, for high temperatures ( $T \geq T^*$ ) it saturates at a value  $j_{\text{max}}$ . This dependence  $f(kT l_B/\hbar v)$  of  $j_{\text{drag}}$  is represented in Fig. 4 for an arbitrarily chosen saturation value  $j_{\text{max}}$ . Comparing the predicted temper-

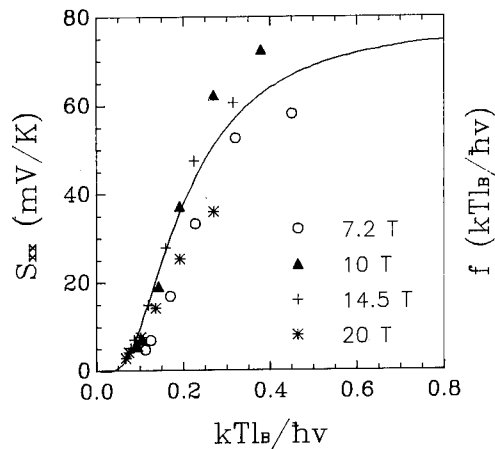


Fig. 4. The temperature dependence of  $S_{xx}$  of G647 at different magnetic fields compared to the theoretically expected phonon-drag current.

ature dependence of  $j_{\text{drag}}$  with the experimentally measured values of  $S_{xx}$  (we do not pretend to explain in detail the field dependence of  $S_{xx} \propto j_{\text{drag}} B$ ), we get good agreement between the experimental and theoretical variations even in the high field range ( $\nu < 0.2$ ,  $B > 10$  T), where the  $B$  dependence of the TEP is not reproduced by the theory (see below).

The magnetic field dependence of the phonon drag current is predicted to be given by [3]:

$$j_{\text{drag}} \propto \nu(1 - \nu) l_B^{-1} f(kT l_B / \hbar v) (1 + \delta)$$

( $\nu \propto 1/B$  is the filling factor,  $\delta$  depends on the ratio between deformation potential and polar interaction). Using  $S_{xx} \propto j_{\text{drag}} B$ , being in a range where  $j_{\text{drag}}$  varies linearly with  $kT l_B / \hbar v$ , and supposing only a polar interaction ( $\delta = 0$ ), the magnetic field dependence of the TEP will then be  $S_{xx} \propto (1 - \nu)$ . We have plotted schematically the corresponding curve in Fig. 2a (dotted line). For higher fields ( $l_B < 100$  Å), the deformation potential interaction becomes dominant, and the theoretical variation including this interaction is also schematically represented by the broken line in Fig. 2a. Up to filling factors of  $\nu \approx 1/4$  the theoretical and experimental variations agree well, i.e., the TEP begins to rise rapidly on entering in the FQH regime and tends to level off at filling factors below  $1/2$ . However, at filling factors lower than  $\nu \approx 0.2$ , the experimental TEP begins to decrease again; there is, to our knowledge, no current theory which can explain this behaviour.

In summary, the low temperature TEP of 2DEG in three different GaAs/Ga<sub>1-x</sub>Al<sub>x</sub>As heterojunctions has been measured in high magnetic fields at temperatures below 1 K. We have shown that the TEP is due to phonon-drag and therefore reflects the nature of the phonon coupling to the electronic states. The general be-

haviour was found to be in good agreement with recent theoretical calculations. However, numerous features are still not fully understood.

Part of this work was supported by NATO and by the National Science and Engineering Research Council of Canada. U.Z. would like to thank V.I. Fal'ko (MPI-FKF, Stuttgart) for stimulating discussions.

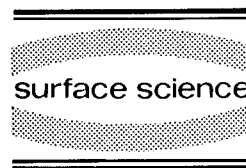
## 1. References

- [1] R. Fletcher, J.C. Maan, and G. Weimann, Phys. Rev. B 32 (1985) 8477;  
R. Fletcher, J.C. Maan, K. Ploog and G. Weimann, Phys. Rev. B 33 (1986) 7122;  
R. Fletcher, M. D'Iorio, W.T. Moore and R. Stoner, J. Phys. C: Solid State Phys. 21 (1988) 2681.
- [2] H. Obloh, K. von Klitzing, K. Ploog and G. Weimann, Surf. Sci. 170 (1986) 292.
- [3] V.I. Fal'ko and S.V. Iordanskii, J. Phys.: Condensed Matter 4 (1992) 9201.
- [4] V.C. Karavolas and P.N. Butcher, J. Phys.: Condensed Matter 3 (1991) 2597.
- [5] M.J. Smith and P.N. Butcher, J. Phys.: Condensed Matter 2 (1990) 2375.
- [6] G.M. Gusev, N.V. Zavaritskii, Z.D. Kvon and A.A. Yurgens, Pis'ma Zh. Eksp. Teor. Fiz. 40 (1984) 275, (JETP Lett. 40 (1984) 1056);  
B.L. Gallagher, J.P. Oxley, T. Galloway, M.J. Smith and P.N. Butcher, J. Phys.: Condensed Matter 2 (1990) 755.
- [7] U. Zeitler, R. Fletcher, J.C. Maan, C.T. Foxon, J.J. Harris and P. Wyder, Phys. Rev. B 47 (1993) 16008.
- [8] S.S. Kubakaddi, P.N. Butcher and B.G. Muliamani, Phys. Rev. B 40 (1989) 1377; S.K. Lyo, Phys. Rev. B 40 (1989) 6458.
- [9] V.I. Fal'ko, S.V. Meshkov and S.V. Iordanskii, Phys. Rev. B 47 (1993) 9911.
- [10] H. Karl, W. Dietsche, A. Fischer and K. Ploog, Phys. Rev. Lett. 61 (1988) 2360.
- [11] B.I. Halperin, Phys. Rev. Lett. 52 (1984) 1583, 2390(E).
- [12] A.H. MacDonald, H.C.A. Oji and K.L. Liu, Phys. Rev. B 34 (1986) 2681.
- [13] N.S. Sankeshwar, S.S. Kubakaddi, B.G. Muliamani and P.N. Butcher, J. Appl. Phys. 68 (1990) 5919.



ELSEVIER

Surface Science 305 (1994) 96–100



## Wigner solid in two-dimensional electron system in silicon in the extreme quantum limit?

V.T. Dolgoplov<sup>a</sup>, G.V. Kravchenko<sup>a</sup>, S.V. Kravchenko<sup>\*,b</sup>, A.A. Shashkin<sup>a</sup>

<sup>a</sup> Institute of Solid State Physics, Chernogolovka, 142432 Moscow District, Russian Federation

<sup>b</sup> Department of Physics and Astronomy, University of Oklahoma, Norman, OK 73019, USA

(Received 12 April 1993; accepted for publication 28 June 1993)

### Abstract

The metal–insulator transition in a 2D electron gas of Si MOSFETs has been investigated. In the extreme quantum limit, the phase boundary in the  $H$ ,  $N_s$  plane has been found to be a straight line with the slope  $\nu_c = 0.53 \pm 0.01$ . Transport properties of the insulating phase have proven to be unexpectedly similar to those of the insulating phase in GaAs/AlGaAs heterostructures where magnetically induced Wigner solid formation has been reported. Strongly nonlinear current–voltage characteristics with linear  $V(I)$  dependence below some threshold voltage,  $V_c$ , and saturation at  $V > V_c$  were observed. The longitudinal resistance corresponding to the linear part of the  $I$ – $V$  characteristics demonstrates an activated temperature dependence. Knowing the values of the threshold voltage and activation energy we obtain a characteristic length that is large compared to the distance between electrons, which excludes a single-electron picture of nonlinearity. The similarity of transport properties strongly suggests the same physical nature of the insulating phases in Si inversion layers and GaAs/AlGaAs heterostructures. However, the value of  $\nu_c$  is somewhat surprising since, in the presence of a long-range potential, the percolation metal–insulator transition is expected at precisely this filling factor. The percolation transition is considered as an alternative explanation of the observed effects.

At sufficiently small Landau-level filling factor,  $\nu$ , the ground state of an ideal 2D electron system is expected to be a Wigner crystal (see, e.g., Refs. [1–3]). Another possible ground state in the extreme quantum limit is the incompressible electron liquid responsible for the fractional quantum Hall effect. Competition between these ground states defines behavior of disorderless 2D electron systems in a high magnetic field. The state of a real 2D electron gas is determined by

the relation between the energy of the electron–electron interaction and the amplitude of the random potential. Anderson localization of electrons is expected in a strong, short-range random potential while the percolation transition can occur in a long-range one. In the latter case, magnetic freeze-out is expected at  $\nu$  close to  $1/2$  [4].

In pioneering work [5,6] it has been experimentally shown that in the extreme quantum limit, a magnetic field does promote an insulating phase in silicon metal–oxide–semiconductor field-effect transistors (MOSFETs). Later, the peak of experimental activity was transferred to

\* Corresponding author.

investigations of magnetic-field-induced metal–insulator transitions in high-mobility GaAs/Al GaAs heterostructures (see, e.g., Refs. [7,8], and references therein). In the majority of cases, the results have been interpreted as evidence for a pinned electron solid although some doubts about this interpretation were expressed in Ref. [7].

In this paper we report magnetotransport data for the insulating phase in high-quality Si MOSFETs in the extreme quantum limit. The results have proved to be unexpectedly similar to those for a 2D electron gas at  $\nu$  around  $1/5$  [7] and a hole gas at  $\nu$  around  $1/3$  [8] in GaAs/AlGaAs heterostructures, as well as for Si MOSFETs in zero and low magnetic field [9,10], which suggests the same physical origin of the insulating states in these systems.

Measurements were made on three Si MOSFETs from different wafers. Peak mobilities were  $\mu_{\text{peak}} \approx 3 \times 10^4 \text{ cm}^2/\text{V} \cdot \text{s}$  at temperature  $T = 1.3 \text{ K}$ . All samples were of the Hall-bar geometry ( $0.25 \times 2.5$  or  $0.8 \times 5 \text{ mm}^2$ ) with distances between the nearest potential probes of 0.625 and 1.25 mm, respectively. The results obtained for different samples were qualitatively similar. Experiments were carried out in a dilution refrigerator TLM-400 with a base temperature of  $\sim 25 \text{ mK}$ . Most of the results were obtained by a four-terminal DC technique using two KEITHLEY 614 DVMs as high-input-resistance preamplifiers.

Typical experimental traces are shown in Fig. 1. At some critical electron density,  $N_c$ , the non-dissipative current through the lowest quantum level disappears and the resistivity  $\rho_{xx}$  grows abruptly. In high magnetic field, the rise of  $\rho_{xy}$  starts at lower density than that of  $\rho_{xx}$  so that the intersection point of these curves is close to  $26 \text{ k}\Omega$ . The growth of resistances indicates a transition into an insulating phase.

The value of resistance corresponding to the metal–insulator transition should be referred to the critical density of electrons,  $N_c$ , at which the temperature dependence of  $\rho_{xx}$  switches between insulator- and metal-like. The critical resistivity,  $\rho_c$ , has proven to be close to  $100 \text{ k}\Omega$ . We used this value to determine the position of metal–insulator transitions in different magnetic fields.

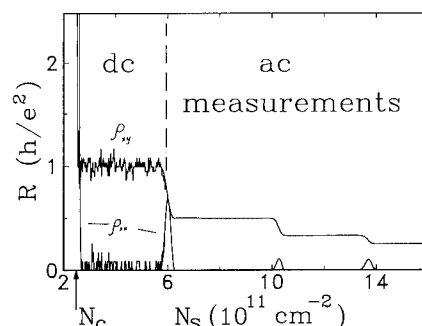


Fig. 1. Experimental dependences of resistivities  $\rho_{xx}$  and  $\rho_{xy}$  on the electron density. The value of  $\rho_{xx}$  is enlarged by a factor of 5. The vertical dashed line separates regions where different experimental techniques were used.  $H = 16 \text{ T}$ ;  $T = 100 \text{ mK}$ .

The complete phase diagram, including low magnetic fields, is shown in Fig. 2. At high magnetic fields the dependences  $N_c(H)$  for all the samples were straight lines with the slope  $\nu_c = (hc/e) \partial N_c / \partial H = 0.53 \pm 0.01$ . One can see that deviation from the linear dependence begins at filling factor  $\nu \gtrsim 1$  (the phase boundary at filling factors  $\nu > 1$  was investigated in detail in Ref. [11]).

Typical  $I$ – $V$  characteristics in the high-field, low- $\nu$  limit are shown in Fig. 3. In the vicinity of

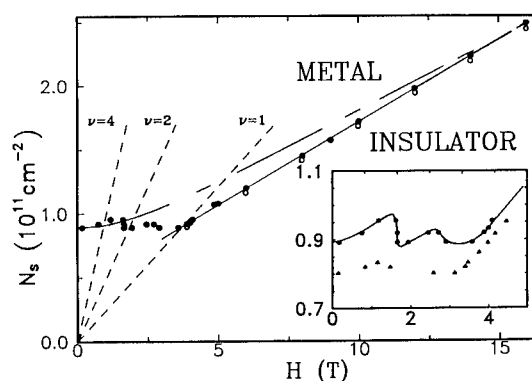


Fig. 2. Phase diagram of the metal–insulator transition. Solid and open circles are the experimental data taken on the samples with  $\mu_{\text{peak}} = 2.9 \times 10^4 \text{ cm}^2/\text{V} \cdot \text{s}$  and  $3.1 \times 10^4 \text{ cm}^2/\text{V} \cdot \text{s}$ , respectively for  $\rho_c = 100 \text{ k}\Omega$ . Dashed lines correspond to filling factors 1, 2, and 4. Dash-dotted line is a fit after Ref. [1]. The inset shows, on an expanded scale, the low-field region of the phase diagram. Triangles represent the data determined at  $\rho_c = 500 \text{ k}\Omega$ .

$I_{sd} = 0$ ,  $V$  is proportional to  $I_{sc}$ , while after exceeding some critical value,  $V_c$ , the differential resistance,  $\partial V / \partial I$ , drops abruptly. Both  $V_c$  and  $\partial V / \partial I$  in the linear part are functions *only* of a point's location in the  $(H, N_s)$  plane and are independent of the path taken to this point. As the temperature increases, the curves become smooth, and at the temperature  $T \geq 300$  mK it is impossible to distinguish a critical voltage at all.

Giant nonlinearity of  $I$ – $V$  characteristics cannot be explained by the heating of the electron system. The minimal power at which we have observed voltage saturation ( $\lesssim 10^{-13}$  W) is too small for this nonlinearity mechanism to take place; in addition, the power dissipated at the threshold voltage changes strongly for different  $H$  or  $N_s$ .

The resistance,  $R$ , corresponding to the linear part of the  $I$ – $V$  characteristics, displays an activated temperature dependence. The activation energy increases when moving from the phase boundary into the insulating phase, i.e., when increasing the distance between the point and phase boundary in the  $(H, N_s)$  plane. An example of this dependence is shown in Fig. 4. The activation energy,  $\epsilon_a$ , is proportional to  $N_c - N_s$  within the experimental accuracy and tends to zero as the point approaches the phase boundary.

Let us now consider the electron solid formation and its depinning in the applied electric field as a possible origin for the observed effects. The equations defining the boundary between the

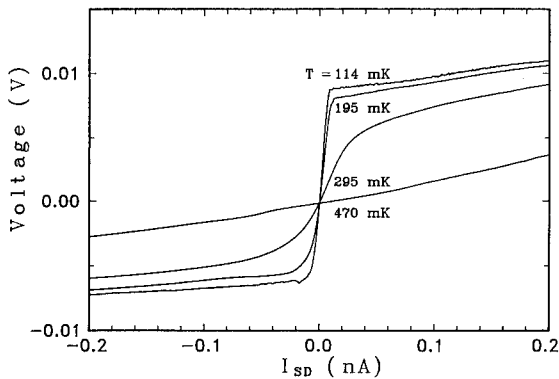


Fig. 3. Typical current–voltage dependencies for different temperatures at  $N_s = 2.1 \times 10^{11} \text{ cm}^{-2}$  and  $H = 14$  T.

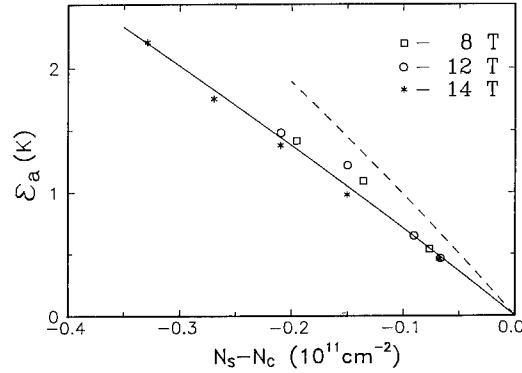


Fig. 4. Activation energy versus electron density for different magnetic fields. Solid and dashed lines are calculated after Ref. [14] for magnetic fields  $H = 14$  T and  $H = 8$  T, respectively.

electron liquid and the Wigner crystal were found by Lozovik and Yudson [1]. It was shown that in high magnetic fields this boundary is a straight line in the  $(H, N_s)$  plane. Since the transport properties of the insulating phase in the extreme quantum limit are similar to those in the absence of a magnetic field [10,12], it seems reasonable to describe the phase boundary by a unified law over the whole range of magnetic fields. Assuming the existence of the electron solid in zero magnetic field, we have for the phase boundary [1]:

$$\frac{eH}{ch} = \frac{1}{2} r_c^{1/2} N_s \left[ 1 - (N_c/N_s)^{1/2} \right]^{1/2}, \quad (1)$$

where  $e$  is the electron charge,  $N_c = 1/\pi(r_c a^*)^{-2}$  is the highest value of  $N_s$  for which an electron solid still exists in zero field,  $a^*$  is the Bohr radius, and  $r_c$  is a dimensionless parameter. The result of calculations of the phase boundary using  $r_c$  as a fitting parameter is shown in Fig. 2 by the dash-dotted line. The best fit is obtained when  $r_c \approx 24$ , which seems to be unrealistically small (expected  $r_c = 37 \pm 5$  for an ideal crystal [13], the low disorder leading to lower  $r_c$ ).

The vanishing activation energy near the phase boundary is an indication of the absence of a first-order transition on the boundary line. Chui and Esfarjani [14] have calculated the current transferred by a bound dislocation pair created at finite temperature. In agreement with Ref. [14],

the activation energy approaches zero as  $\epsilon_a \propto \nu_c - \nu$ . The comparison of experimental results with Ref. [14] is shown in Fig. 4. It should be emphasized that good agreement with experiment can be reached without any fitting parameters.

The existence of a threshold voltage in the electron solid phase has been discussed in previous papers (e.g., Refs. [7,9,10]). The low-electric-field threshold conduction has been considered to be a result of electron solid depinning. As the threshold voltage in our case is of the order of that found in Refs. [9,10], all the arguments used in those papers are equally valid for the present work and exclude a single-particle origin for the threshold conduction.

Despite the astounding similarity of the transport properties of an insulating phase in Si MOSFETs near  $\nu = 1/2$  and those in GaAs/AlGaAs heterostructures around  $\nu = 1/5$  (electron gas) and  $\nu = 1/3$  (hole gas), our results cannot identify the insulating phase to be a magnetically induced Wigner solid. So, it is necessary to discuss another possibility of explaining the experimental observations.

In the case of long-range potential fluctuations, the boundary between metal and insulator states should be straight line with slope  $\partial N_c / \partial H = e/2hc$  [4], just as has been found for all our samples (Fig. 2). The straight line intersects the ordinate axis at the electron density which can be interpreted as the number of electrons strongly coupled by positive ions at the Si–SiO<sub>2</sub> interface. The density of these ions agrees with the results of independent measurements on similar samples [15]. The activation energy in this model is equal to the energy gap between the percolation threshold and the Fermi level of the electrons localized in potential minima. Hence, in accordance with the experiment, the activation energy should vanish on the phase boundary. In an applied electric field, the tilting of the potential relief leads to a shift in the occupied electron states towards the saddle points of the chaotic potential, and at the critical field the area occupied by the electrons is expanded up to saddle points. If we assume the characteristic scale of a cluster to be  $L$  then this critical value of the electric field may be estimated as  $E_c = \epsilon_a / eL$ . The measured  $E_c \approx 10^2$

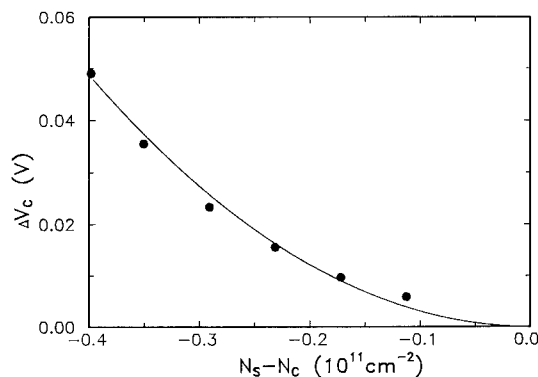


Fig. 5. The dependence of threshold voltage on electron density in magnetic field  $H = 14$  T.

mV/cm and  $\epsilon_a \approx 1$  K correspond to  $L \approx 1 \mu\text{m}$ . Near the phase boundary, the cluster dimension diverges as  $L \propto (\nu_c - \nu)^{-s}$ , where  $s$  is a critical index (for 2D system,  $s = 1.34$  [16]). Taking into account the experimental relation  $\epsilon_a \propto (N_c - N_s)$  (see Fig. 4), one should expect the threshold voltage  $\Delta V_c$  to be proportional to  $(N_c - N_s)^{s+1}$ . As can be seen from Fig. 5, experimental dependences are close to  $\Delta V_c \propto (N_c - N_s)^2$ . The model of a long-range potential satisfactorily explains the experimental results. However, the nature of long-range fluctuations in our samples is unclear.

In summary, we have presented a study of electronic transport in a high-mobility two-dimensional system of Si-MOSFETs in the extreme quantum limit. In a strong magnetic field, the phase boundary in the  $(H, N_s)$  plane has been found to be a straight line with the slope  $\partial N_s / \partial H \approx e/2hc$ , corresponding to  $\nu_c \approx 1/2$  at  $H \rightarrow \infty$ . Two possible mechanisms leading to metal–insulator transition have been discussed: the electron solid formation and the percolation transition in a long-range chaotic potential. Each of them can qualitatively explain part of the experimental results; however, neither one can be unambiguously proved to take place. The similarity of transport properties of Si MOSFETs at  $\nu \leq 1/2$  and GaAs/AlGaAs heterostructures around  $\nu = 1/5$  (electron gas) and  $\nu = 1/3$  (hole gas) strongly suggests the same physical nature of the insulating phases in these systems.



## 1. References

- [1] Y.E. Lozovik and V.I. Yudson, JETP Lett. 22 (1975) 11.
- [2] M. Tsukada, J. Phys. Soc. Jpn. 42 (1977) 391.
- [3] P.K. Lam and S.M. Girvin, Phys. Rev. B 30 (1984) 473.
- [4] A.L. Efros, F.G. Pikus and V.G. Burnett, Solid State Commun. 84 (1992) 91.
- [5] S. Kawaji and J. Wakabayashi, Solid State Commun. 22 (1977) 87.
- [6] M. Pepper, Philos. Mag. 37 (1978) 83.
- [7] H.W. Jiang, H.L. Stormer, D.C. Tsui, L.N. Pfeiffer and K.W. West, Phys. Rev. B 44 (1991) 8107.
- [8] M.B. Santos, Y.W. Suen, M. Shayegan, Y.P. Li, L.W. Engel and D.C. Tsui, Phys. Rev. Lett. 68 (1992) 1188.
- [9] M. D'Iorio, V.M. Pudalov and S.G. Semenchinsky, Surf. Sci. 263 (1992) 49; Phys. Rev. B 46 (1992) 15992.
- [10] V.M. Pudalov, M. D'Iorio, S.V. Kravchenko and J.W. Campbell, Phys. Rev. Lett. 70 (1993) 1866.
- [11] M. D'Iorio, V.M. Pudalov and S.G. Semenchinsky, Phys. Lett. A 150 (1990) 422.
- [12] V.T. Dolgoplov, G.V. Kravchenko, S.V. Kravchenko and A.A. Shashkin, Phys. Rev. B 46 (1992) 13303.
- [13] B. Tanator and D.M. Ceperley, Phys. Rev. B 39 (1989) 5005.
- [14] S.T. Chui and K. Esfarjani, Phys. Rev. Lett. 66 (1991) 652.
- [15] E.A. Vydrov, V.T. Dolgoplov, S.I. Dorozhkin and N.B. Zhitenev, Zh. Exp. Teor. Fiz. 94 (1988) 234 [Sov. Phys. JETP 67 (1988) 998].
- [16] B.I. Shklovskii and A.L. Efros, Electronic Properties of Doped Semiconductors (Springer, New York, 1984).

# High temperature perturbation study of two-dimensional interacting electrons in a partly-filled Landau level

Lian Zheng \*, A.H. MacDonald

*Department of Physics, Indiana University, Bloomington, IN 47405, USA*

(Received 23 April 1993; accepted for publication 19 May 1993)

## Abstract

Using the Matsubara formalism, we have examined the finite-temperature perturbation expansion series for the grand potential of interacting electrons confined to the lowest Landau level of a two-dimensional electron gas. We have evaluated the perturbation expansion exactly up to the third order for the case of the hard-core interaction model. We have also evaluated the infinite-order subseries of the perturbation expansion which gives the leading contribution to the grand potential at small filling factors. In the zero temperature limit this class of diagrams leads to a ground state energy which has a cusp at  $\nu = 1/2$ .

## 1. Introduction

In the strong magnetic field limit all electrons in a two-dimensional electrons gas can be accommodated within a single macroscopically degenerate Landau level and Landau level mixing by interactions is negligible. In this limit the eigenstates of the system are determined completely by electron–electron interactions and descriptions of the electronic properties based on independent electron notions fail qualitatively. The occurrence of the fractional quantum Hall effect [1] (FQHE) in this system is an experimental consequence of cusps in the dependence of the ground state energy on the Landau level filling factor  $\nu$ . ( $\nu \equiv N/N_L$  is the ratio of the number of electrons ( $N$ ) to the number of single-particle states in the

Landau level ( $N_L$ )). From the theory of the FQHE, substantial progress has been made toward understanding the ground states and the lowest lying excited states of this system, especially near the filling factors where the strongest cusps in the ground state energy occur [1]. However, little is known about the higher-lying excited states which control the thermodynamic properties of the systems, except at low temperatures, or indeed about even the ground state at arbitrary filling factors. In this paper, we report preliminary results of an attempt to study the interacting 2D electron gas in the quantum limit at finite temperatures using the Matsubara perturbation theory. Our hope is that this effort will improve our understanding of this system over the full ranges of filling factor and of temperature.

We restrict our attention in this paper to the limit where the electrons are completely spin-polarized. Because of the complete degeneracy of

\* Corresponding author.

the single-particle energy levels, the only energy scales in the problem are the interaction energy scale,  $V$ , and the thermal energy scale  $k_B T$ . There is no small parameter which may be used to estimate interaction corrections to the ground state and the zero-temperature many-body perturbation theory [2] cannot be applied. Interactions can be treated perturbatively only by performing a high-temperature expansion [3] in powers of  $\beta V$ , where  $\beta = 1/k_B T$ . Again, because of the Landau level degeneracy, the terms in the high temperature expansion for this system are generated directly by the Matsubara finite-temperature many-body perturbation theory formalism [2]. The diagrammatic rules for the Matsubara formalism are well established and can readily be adapted to the present problem [4].

As discussed in more detail below, we have evaluated the three leading terms in a Matsubara expansion for the grand potential [5]. These results provide new information about the properties of the strong-magnetic-field two-dimensional electron-gas system at high and moderate temperatures. However, the ultimate aim of our study is to understand the fractional quantum Hall effect from a perturbative point of view. To reach this goal it will be necessary to obtain the ground state energy as a function of  $\nu$ , *i.e.* to obtain results which capture the essential physics of the limit  $\beta \rightarrow \infty$ . We have completed preliminary investigations of two approaches. One approach is to fit the leading terms in the high-temperature series to a Padé approximation and extrapolate the result to low temperatures. In the next section we discuss the evaluation of the three leading terms in the high-temperature expansion and the approximation for the ground state energy of the 2D electrons as a function of  $\nu$  which results from the corresponding Padé approximation. A second method for approximating the  $\beta \rightarrow \infty$  limit is to identify subsets of diagrams which can be summed to infinite order and which capture the essential physics of the system at low temperatures. In Section 3, we discuss the evaluation of the infinite set of particle–particle ladder diagrams. We will argue that this set of diagrams captures some essential features of the fractional quantum Hall effect.

In this paper, we will discuss only the case of the hard-core model electron–electron interaction for which the only non-zero Haldane pseudopotential [6] is the one-for the smallest relative angular momentum channel. This interaction avoids the long wavelength divergence of some terms in the perturbation expansion due to the long range of the Coulomb interaction which plays no essential role in the fractional quantum Hall effect. This model is known to produce cusps in the  $\nu$  dependence of the interaction and hence captures the essence of the FQHE.

## 2. High temperature perturbation expansion

An important aspect of the physics of interacting electrons in a single Landau level is particle–hole symmetry [7]. This symmetry implies that the spectrum of the Hamiltonian is altered only by a constant shift in all eigenenergies when a particle–hole transformation is made changing  $\nu$  to  $1 - \nu$ . The Matsubara perturbation formalism calculates averages in the grand canonical ensemble as a function of the exact chemical potential; the particle number at a given chemical potential is altered by interactions. As a result, the particle–hole symmetry which exists for definite particle numbers is not satisfied order-by-order in perturbation theory. However, we [4] have shown that particle–hole symmetry can be restored order-by-order in the perturbation theory if the expansion is done in terms of the Hartree–Fock propagator (defined below) rather than the free-electron propagator. (The first order (Hartree–Fock) contribution is not particle–hole symmetric and reflects the overall shift in the eigenenergies under particle–hole transformation.) This replacement is particularly straightforward in the present problem, since the Hartree–Fock self-energy is not only independent of frequency but is also independent of the single-particle state index. The replacement of the bare propagator by the Hartree–Fock propagator is thus equivalent to a chemical potential shift. It not only restores order-by-order (in fact diagram-by-diagram) particle–hole symmetry but dramatically reduces the number of diagrams that need to be considered

in any given order without any increase in the complexity of each diagram. This important simplification is the key reason that we are able to carry out the evaluation of the high temperature expansion series to third order.

We use the Matsubara formalism to carry out the high temperature perturbation expansion for the grand potential  $\Omega$ . All the thermodynamic properties are determined once the grand potential is known. We first make some general remarks about the perturbation expansion and then give explicit results up to the third order with the hard core potential  $v(q) = 4\pi l^2 V_1(1 - q^2 l^2)$ .

We start with the coupling constant integration expression for the grand potential [2]

$$\Omega - \Omega_0 = \frac{1}{\beta} \int_0^1 \frac{d\lambda}{\lambda} \sum_{\mathbf{p}, i, p_n} \mathcal{G}_\lambda(\mathbf{p}, i, p_n) \sum_{\lambda} (\mathbf{P}, i, p_n). \quad (1)$$

The diagrams are closed loops formed by connecting a free electron Green's function  $\mathcal{G}_0$  to the two ends of an (in general) improper self-energy. The general form of the diagrams is shown in Fig. 1. The number of diagrams for the grand potential is related to the number of self-energy diagrams in each order and it increases sharply as we go to higher orders. There are two diagrams, direct and exchange, for the first order proper self-energy. There are ten diagrams for the second order self-energy. For the third order, the number of diagrams for the self-energy goes up to seventy-four. Many of these diagrams are eliminated when the expansion is performed in terms of the Hartree–Fock propagator.

We know that Hartree–Fock self-energy is independent of frequency. Due to the complete degeneracy of the single-particle states, it is also independent of the intra-Landau level index. In self-consistent Hartree–Fock approximation, the electron single-particle Green's function is unaffected by the interaction, since the self-energy, being a constant, is canceled by the shift in chemical potential  $\mu$ , i.e.,  $\mathcal{G}_{\text{HF}}(\mu_{\text{HF}}) = \mathcal{G}_0(\mu_0)$ . We can now regard the bare Green's function in the Feynman diagrams as the self-consistent Hartree–Fock Green's function. This identification directly enables us to exclude the diagrams shown

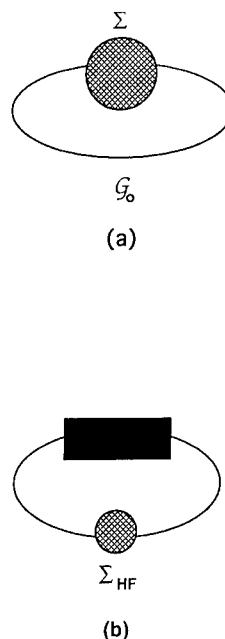


Fig. 1. (a) General structure of Feynman diagrams for grand potential. (b) Diagrams for grand potential which are excluded as a result that Hartree–Fock self-energy is independent of both frequency and single particle eigenstate index.

in Fig. 1, which contain Hartree–Fock self-energy terms dressing Green's function in lower order diagrams, since these diagrams are already included when the bare Green's function is recognized as the self-consistent Hartree–Fock Green's function. The diagrams retained for the grand potential for the second and third order are shown in Fig. 2, where the coefficient associate with each diagram is due to the fact that we use the Feynman rules for Green's function to evaluate the diagrams for grand potential [4,8]. The evaluation of the grand potential up to third order now becomes possible. We can directly verify that the diagrams retained are all particle–hole symmetric. We can also verify that for  $v(\mathbf{r}) = \delta(\mathbf{r})$ , the contributions vanish identically order-by-order as required by the Pauli exclusion principle. We remark that the contribution to the chemical potential of order  $\beta^n$  is a particle–hole symmetric polynomial in  $\nu$  of order  $2n$ .

In the rest of this section, we sketch the evaluation of the grand potential up to third order. We rewrite Eq. (1) as

$$\begin{aligned}\Omega(\mu) &= \Omega_{\text{HF}}(\mu) - \frac{1}{\beta} \\ &\quad \times [\text{Feynman diagrams in Fig. 2}] \\ &= \Omega_{\text{HF}}(\nu_{\text{HF}}(\mu)) + \Omega^{(2)}(\nu_{\text{HF}}(\mu)) \\ &\quad + \Omega^{(3)}(\nu_{\text{HF}}(\mu)),\end{aligned}\quad (2)$$

where the minus sign on the first line is due to the closed fermion loops in the diagrams. Here

$$\nu_{\text{HF}}(\mu) \equiv \frac{1}{\beta} \sum_{i p_n} \mathcal{E}_{\text{HF}}(\mu). \quad (3)$$

At a given value of  $\nu$ , the chemical potential  $\mu$  depends on interactions. If  $\mu = \mu_{\text{HF}} + \Delta\mu$ , then

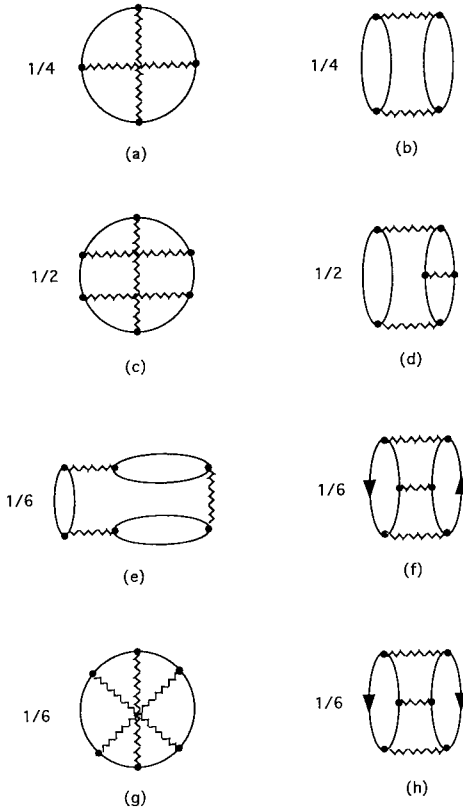


Fig. 2. The second and third order Feynman diagrams for grand potential which are retained. They contain all interaction contributions to grand potential in the second and third orders.

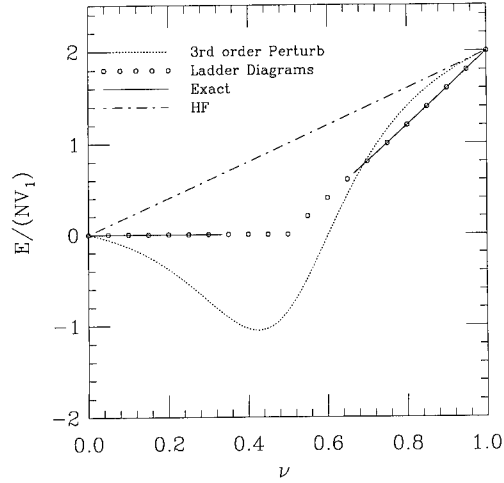


Fig. 3. Ground state energy per electron at zero temperature versus the Landau level filling factor with the hardcore potential  $v(q) = 4\pi l^2 V_1(1 - q^2 l^2)$ . The results shown are: Hartree–Fock approximation (dashed line); Exact result (solid line), it has cusps at  $\nu = 1/3$  and  $\nu = 2/3$  and more complicated hierarchy state structure in between; High temperature perturbation result of Eq. (5) (dotted line); The result from particle–particle ladder diagram summation in Section 3 (marked line).

$\Delta\mu$  is of the second order. Within the third order in Eq. (2), only  $\Omega_{\text{HF}}$  is changed by  $\Delta\mu$ :  $\Omega_{\text{HF}}(\nu_{\text{HF}}(\mu)) = \Omega_{\text{HF}}(\nu) - N\Delta\mu$ . Then with  $F = \Omega + \mu N$ , we obtain

$$\begin{aligned}F(\nu) &= F_{\text{HF}}(\nu) + \Omega^{(2)}(\nu) + \Omega^{(3)}(\nu) \\ &= F_{\text{HF}}(\nu) + \alpha^{(2)}(\nu)\beta + \alpha^{(3)}(\nu)\beta^2,\end{aligned}\quad (4)$$

where  $\alpha^{(2)}$  and  $\alpha^{(3)}$ , independent of temperature, are known by evaluating the diagrams in Fig. 2. The zero-temperature electron energy is obtained from the above equation by a simple Padé approximation:

$$E(T=0) = E_{\text{HF}} - \frac{[\alpha^{(2)}(\nu)]^2}{\alpha^{(3)}(\nu)}. \quad (5)$$

For a hard-core potential  $v(q) = 4\pi l^2 V_1(1 - q^2 l^2)$ , where  $l$  is the magnetic length, the result from Eq. (5) is shown in Fig. 3 (dotted line). The exact result, which has cusps at  $\nu = 1/3$  and  $\nu = 2/3$  and more complicated hierarchy state structures in between, is also shown (solid line) for the range of  $\nu \leq 1/3$  and  $\nu \geq 2/3$  for compar-

ison purpose. Although it is very non-trivial to carry out the evaluation of the grand potential to third order to use the minimum order Padé approximation, the result obtained for the ground state energy is, nevertheless, a very crude approximation. A higher order Padé would require the perturbation expansion to be evaluated out to fifth order which seems to be a prohibitively difficult task. Unless a way is found to simplify the higher order diagrams it will not be possible to reliably extrapolate to low temperatures in this way.

### 3. The particle–particle ladder diagrams

Infinite order subset summation is an alternative method to get a non-trivial zero-temperature result from the high temperature expansion series. In this section, we will discuss the evaluation of the contribution to the grand potential from particle–particle ladder diagrams. It is possible to show [4,10] that at each order in  $\beta$  these diagrams give the contribution to the grand potential which is correctly proportional to  $\nu^2$ . These contributions are the largest for  $\nu \rightarrow 0$  and this subset may be identified as giving the leading order contribution in a small  $\nu$  expansion at all temperatures.

The ladder diagrams for the grand potential are shown in Figs. 4a and 4b. This subset contains all the first and second order diagrams. This subset may be summed by solving the integral equation summarized diagrammatically in Fig. 4c. This integral equation may be solved analytically [9]. The ladder diagrams in Figs. 4c and 4b are related by an integration over the coupling strength:  $\gamma = 1/2 \int_0^1 (d\lambda/\lambda) \Gamma_\lambda$ . From Fig. 4c, it is easy to see that  $\Gamma$  depends only on the relative momentum  $Y$  and  $Y'$  and the total frequency  $i\omega_n$ , so we have

$$\Gamma(Y, Y', i\omega_n) = \langle Y | v | Y' \rangle + \frac{1-2\nu}{i\omega_n - 2\xi} \sum_{Y''} \langle Y | v | Y'' \rangle \Gamma(Y'', Y, i\omega_n), \quad (6)$$

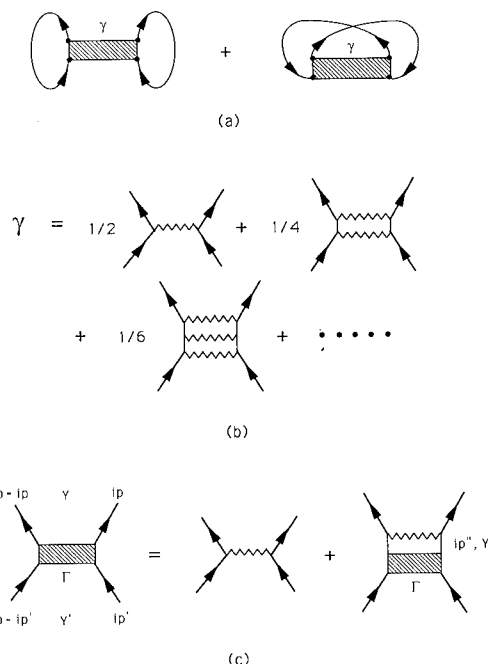


Fig. 4. (a) and (b): Particle-particle ladder diagrams for grand potential. It contains all contribution for the first and second orders and a subset of high order diagrams. (c) A related ladder diagram series  $\Gamma$ , which can be evaluated analytically.

where the factor  $(1-2\nu)/(i\omega_n - 2\xi)$  results from the frequency summation over intermediate states. Using Haldane's pseudopotential parameters  $V_m$ 's, we have  $\langle Y | v | Y' \rangle = \sum_m a_{Ym}^* a_{Y'm} V_m$ , where  $a_{Ym} = \langle \phi_m | \varphi_Y \rangle$  with  $\phi_m$  and  $\varphi_Y$  as single particle eigenstates at symmetric and Landau gauges, respectively. Since  $Y$  and  $Y'$  are separable variables in the matrix elements  $\langle Y | v | Y' \rangle$ , Eq. (6) is an algebraic equation and easily solved. Since  $\sum_Y a_{Ym}^* a_{Yn} = \delta_{mn}$ , the contributions from different  $V_m$ 's are decoupled and additive. With  $\Gamma = \sum_m \Gamma_m$ , Eq. (6) gives

$$\Gamma_m(Y, Y', i\omega) = a_{Ym}^* a_{Y'm} V_m + \frac{a_{Ym}^* a_{Y'm} (1-2\nu) V_m^2}{i\omega - 2\xi - (1-2\nu) V_m}. \quad (7)$$

Evaluating the diagrams in Fig. 4a with the vertex function  $\Gamma_m$  is very straightforward. The total contribution from the two diagrams, labeled

$\mathcal{E}^{(m)}$  below, is related to the grand potential  $\Omega_m$  by an integration over the coupling strengths

$$\mathcal{E}^{(m)} = \frac{[(-1)^m - 1] 2N_L \beta V_m (1 - 2\nu) \nu^2}{(1 - \nu)^2 e^{(1 - 2\nu)\beta V_m} - \nu^2}. \quad (8)$$

For even  $m$ 's,  $\mathcal{E}^{(m)} = 0$  reflecting Fermi statistics. It is easy to verify that  $\mathcal{E}^{(m)} - \mathcal{E}_{\text{HF}}^{(m)}$  is particle-hole symmetric.

The ladder diagram subset gives very interesting results at zero temperature:  $\mathcal{E} \equiv 0$  for  $\nu \leq 1/2$ . All terms in the expansion of the ground state energy in powers of  $\nu$  are zero. This result from the ladder diagram sum is in agreement with the exact result. For the hard-core model, the interaction energy is identically zero for a finite range of filling factors surrounding  $\nu = 0$ . However, the exact ground state energy has a cusp first at  $\nu = 1/3$  rather than at  $\nu = 1/2$ , as shown in Fig. 3. To predict the occurrence of the cusps at the right filling factor values, however, other classes of diagrams will apparently have to be included.

#### 4. Summary

Using the Matsubara perturbation formalism, we have studied the high temperature perturbation expansion series for the grand potential of interacting 2D electrons confined within the lowest Landau level. Making use of the observation that the Hartree-Fock self-energy is independent of both frequency and single-particle eigenstate index, we evaluated the high temperature perturbation series exactly up to the third order, which enables us to extrapolate the ground state energy at zero temperature as a function of the Landau level filling factors. We also evaluated to infinite order the subset of particle-particle ladder diagrams. We identified the subsum as the leading order contribution in the low density expansion for interaction energy and showed that it is iden-

tically zero for small filling factors. We suggested the possibility of using the high temperature perturbation method to study the FQHE, possibly by identifying the subsets of diagrams which develop cusps in the ground state energy as a function of filling factor at zero temperature.

#### 5. Acknowledgment

This work was supported by the National Science Foundation under Grant No. DMR-9113911.

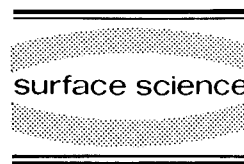
#### 6. References

- [1] For a review of the theoretical work on FQHE, see, A.H. MacDonald, Ed., *Quantum Hall Effect: A Perspective*, (Kluwer, Dordrecht, 1990); R.E. Prange and S.M. Girvin, Eds., *Quantum Hall Effect* (Springer, Berlin, 1987); T. Chakraborty and P. Pietiläinen, *The Fractional Quantum Hall Effect: Properties of an Incompressible Quantum Fluid* (Springer, Berlin, 1988).
- [2] See, for example, G.D. Mahan, *Many-Particle Physics* (Plenum, New York, 1981); A.L. Fetter and J.D. Walecka, *Quantum Theory of Many-Particle Systems* (McGraw-Hill, New York, 1971).
- [3] For an elementary discussion of high-temperature series expansions, see, for example, M. Plischke and B. Bergersen, *Equilibrium Statistical Physics* (Prentice Hall, Englewood Cliffs, NJ, 1989).
- [4] The Feynman rules for the present application will be discussed in detail elsewhere, Lian Zheng and A.H. MacDonald, *Phys. Rev. B*, to be submitted.
- [5] The perturbation expansion for other properties of the system will be discussed elsewhere.
- [6] F.D.M. Haldane, *Phys. Rev. Lett.* 51 (1983) 605.
- [7] See, for example, A.H. MacDonald and E.H. Rezayi, *Phys. Rev. B* 42 (1990) 3224.
- [8] The coefficient associated with each diagram can be determined by systematic ways (A.H. MacDonald, unpublished).
- [9] A.H. MacDonald, H. Akera and M.R. Norman, *Phys. Rev. B* 45 (1992) 10147.
- [10] This statement can be explicitly verified for up to the third order.



ELSEVIER

Surface Science 305 (1994) 107–114



# Termination of the quantized Hall effect by the electron solid

V.M. Pudalov <sup>\*,1,a</sup>, M. D'Iorio <sup>a</sup>, J.W. Campbell <sup>b</sup>

<sup>a</sup> National Research Council Canada, Ottawa, Ontario, Canada K1A 0R6

<sup>b</sup> University of Ottawa, Ottawa, Ontario, Canada K1N 6N5

(Received 18 April 1993; accepted for publication 15 July 1993)

## Abstract

The diagonal and Hall resistance were studied at quantized-Hall-effect-to-insulator transitions in a dilute 2D electron system in Si(100), in the milli-kelvin temperature range. The Hall resistance remains close to its classical value,  $H/nec$ , even when the temperature-activated diagonal resistivity  $\rho_{xx}$  rises to  $4 \times 10^6 \Omega/\square$ . Experimental data show that the insulating state may develop directly from at least 3 metallic states with quantized Hall resistance at filling factors  $\nu = 1, 2$  and 6. Persistence of well resolved Landau levels up to the final insulating stage makes it possible to trace the delocalized states at the QHE to insulator transition. Within experimental uncertainty no evidence for their exit through the Fermi energy has been found. The results are discussed in terms of recent theoretical models for the transition to the insulating state.

## 1. Introduction

The low temperature transition in a two-dimensional electron (2DE) system between the metallic phase in the quantized Hall effect (QHE) regime and the insulating phase (QHE/I transitions) has been the focus of theoretical and experimental interest, since this problem is closely related to the behaviour of the dilute 2D system of interacting electrons in the presence of a quantizing magnetic field and disorder. A decrease in the density  $n_s$  drives the 2DE system towards an ordered lattice due to the increasing electron-electron (e-e) interaction energy compared to

the Fermi energy,  $E_F$ . On the other hand, the decrease in the density is accompanied by an increase in the relative strength of the disorder, which drives the 2DE system towards complete localization. In contrast to the metal-insulator (M/I) transition in 3D systems, the QHE/I transitions provide a unique possibility to trace the delocalized states through the M/I transition. The Hall coefficient is considered to be a sensitive probe to study the mechanism of the transition.

It has been found that for weak disorder, to first order in perturbation theory for a noninteracting 2D Fermi system, localization corrections renormalize the Hall conductivity,  $\sigma_{xy}$ , in such a way, that the Hall resistance,  $R_{xy}$ , remains undisturbed on the metallic side of the transition [1,2]. For interacting electrons in the presence of weak disorder the Hall resistance was predicted [1] to diverge logarithmically at low  $T$ , but at a rate

\* Corresponding author.

<sup>1</sup> On leave from the Institute for High Pressure Physics, Troitsk, Moscow district, 142092, Russian Federation.



twice as fast as that of the diagonal resistivity. Using the scaling theory, Shapiro and Abrahams [3] have found that in the disordered non-interacting 2DE system, both conductivity components vanish at the critical point, while  $\sigma_{xy} \propto (\sigma_{xx})^2$ ; therefore,  $R_{xy}$  retains its classical metallic value at the M/I transition. Considering the disorder-induced insulating transition for non-interacting electrons at the lowest Landau level, Viehweger and Efetov [4] have found that in the low frequency limit,  $\sigma_{xy} \propto (\sigma_{xx})^2 \propto \omega^2$ . The Hall resistance  $R_{xy}$ , therefore, remains finite in the insulating phase when  $\omega \rightarrow 0$  and  $\rho_{xx} \rightarrow \infty$ , in contrast to the band insulator or magnetic freeze-out. It is worthy to note that  $R_{xy}$  in this picture is not related anymore to the number of extended-state bands or to the density of carriers participating in the transport; it has rather a thermodynamic meaning. Halperin [5], Laughlin [6], and Khmel'nitskii [7] predicted that upon increasing disorder, when  $\omega_c \tau \rightarrow 0$ , the energy of delocalized states should rise and therefore they would “float upward like bubbles” and “exit through the Fermi energy”,  $E_F$ . Recently Kivelson et al. [8] suggested a global behaviour for the 2DE system, in particular, at the QHE/I transitions. The existence of the “Hall insulator” has been proven again for non-interacting electrons, and it has been argued that this phase is generic for interacting electrons as well. At  $T=0$  in the Hall insulator phase  $\rho_{xx} \rightarrow \infty$ ,  $\sigma_{xx} \rightarrow 0$ , and  $\sigma_{xy} \rightarrow 0$ , while  $\rho_{xy} = H/(n_s e c)$ .

Summarizing the available predictions for  $\sigma_{xy}$  and  $\rho_{xy}$  behaviour at the metal–insulator transition in 2D (where by definition  $\rho_{xx} \rightarrow \infty$ ), we find a variety of options: (a)  $\sigma_{xy}$  vanishes at the transition  $\propto (n/n_c - 1)^k$  and, depending on the critical exponent  $k$ , the Hall resistance either diverges or remains finite [1–4,9]; (b)  $\sigma_{xy}$  diminishes in a step-like fashion each time an extended state band exits through the Fermi energy, and, eventually,  $\sigma_{xy}$  vanishes  $\propto (\sigma_{xx})^2$  [5–8], providing  $\rho_{xy}$  remains finite; (b) for the Wigner solid with transport due to point defect motion  $\rho_{xy} \rightarrow \infty$  [8], as well as for the magnetic freeze-out; (c) for the Wigner solid and transport via extended defect motion [10]  $\rho_{xy}$  is predicted to maintain its classical value  $H/(n_s e c)$  within  $10^{-8}$ .

Experimentally, since magnetotransport in the insulator phase is nonlinear [11–14],  $R_{xy}$  measurements must be carried out at electric fields below and above its threshold value: this has not been done yet. In Ref. [15] no deviations of  $R_{xy}$  from its classical value have been found in Si MOSFETs at the reentrant QHE/I transitions around  $\nu = 1.5$  and 2.5, despite the growth in  $\rho_{xx}$  up to  $\sim 4h/e^2$ . Anomalies in the Hall voltage in the reentrant insulating phase near fractional filling factors in GaAs/AlGaAs, reported earlier [13,14], were explained later by an admixture of the longitudinal voltage drop due to a misalignment in the Hall voltage probes [16,17]. Finally, the Hall resistance in GaAs/Al(Ga)As was found to remain near its classical value at the fractional QHE to insulator transitions [16,17].

In this paper we report on a detailed study of the Hall and diagonal resistance, through the transitions from three QHE states at filling factors  $\nu = 1, 2$  and 6 to the adjacent insulating phases. We found that  $\rho_{xy}$  does not diverge but remains close to the classical value, when measured below or above the threshold electric field, even when  $\rho_{xx}$  rises to  $5 \times 10^6 \Omega/\square \approx 200 h/e^2$ . Both diagonal and Hall conductivities vanish in the insulating phase, while  $\sigma_{xy} \propto \sigma_{xx}^2$ . We analyze also the topology of the boundary between the QHE states and the insulating state; the experimental data do show that the insulating phase develops directly from each of these QHE states.

## 2. Experimental

We used a high mobility (100) Si-MOSFET sample ( $\mu^{\text{peak}} = 4.3 \times 10^4 \text{ cm}^2/\text{V} \cdot \text{s}$ ) patterned as a Hall bar ( $5 \times 0.8 \text{ mm}^2$ ) with 2 current and 5 potential probes ( $20 \mu\text{m}$  probe width). DC-transport measurements with the highly resistive sample have been done by the 4-terminal technique, using a battery operated differential electrometer ( $10^{14} \Omega$  input resistance). In the Hall voltage measurements, in order to eliminate the admixture of the longitudinal voltage, we subtracted results taken in two opposite magnetic field directions.

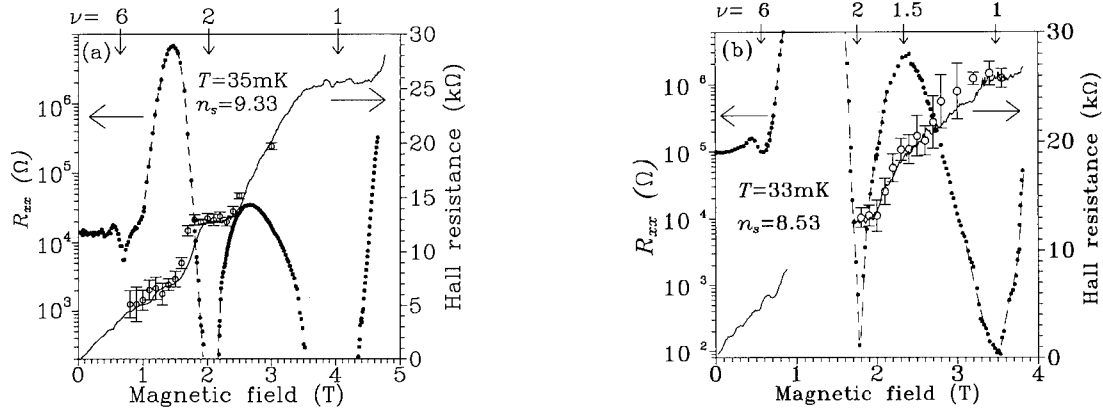


Fig. 1. Diagonal and Hall resistances as a function of the magnetic field in the reentrant insulating regime for electron densities: (a)  $9.326 \times 10^{10}$  and (b)  $8.53 \times 10^{10} \text{ cm}^{-2}$ . Full curves represent  $R_{xy}$  measured at 10 nA, far above the threshold. Open circles with error bars –  $R_{xy}$ , measured at 0.25 nA, half the threshold value. Arrows indicate filling factor positions for the principal extrema in  $R_{xx}$  vs.  $H$ . The dashed line is a guide to the eye.

At low temperature,  $T < 500 \text{ mK}$ , and at low electron density,  $n_s < 9.5 \times 10^{10} \text{ cm}^{-2}$  the sample exhibited a highly resistive phase [11,12] centred at filling factor  $\nu \approx 2.5$ , and at  $n_s < 8.5 \times 10^{10} \text{ cm}^{-2}$  – a similar phase around  $\nu \approx 1.5$ , as shown in Figs. 1a and 1b. Our previous study [11,12,15] showed that the phases, where  $\rho_{xx}$  diverges, represent an electron solid state, but for the purpose of the present study, the most important issue is that these phases are true insulating states: (i)  $\rho_{xx} \gg h/e^2$ , (ii)  $d\rho_{xx}/dT < 0$ , and (iii) the diagonal conduction,  $\sigma_{xx}$ , is characterized by a sharp threshold as a function of applied electric field

[11,12]. The insulating state is interrupted at integer filling factors  $\nu = 1$  and  $2$ . In their vicinity the 2DE system is in the regular 2D metal (or, more precisely, the strongly correlated 2DE gas), in the quantized Hall resistance regime. By this definition we mean that (i) the diagonal resistivity is low,  $\rho_{xx} \ll h/e^2$ , (ii)  $d\rho_{xx}/dT > 0$ , (iii)  $\sigma_{xx}$  does not depend on electric field, and (iv)  $\rho_{xy}$  shows a plateau at a quantized value. Therefore, when we fix electron density and vary magnetic field, as shown in Fig. 1, the observed variations in  $\rho_{xx}$  represent a sequence of reentrant M/I transitions, which are the goal of the present study.

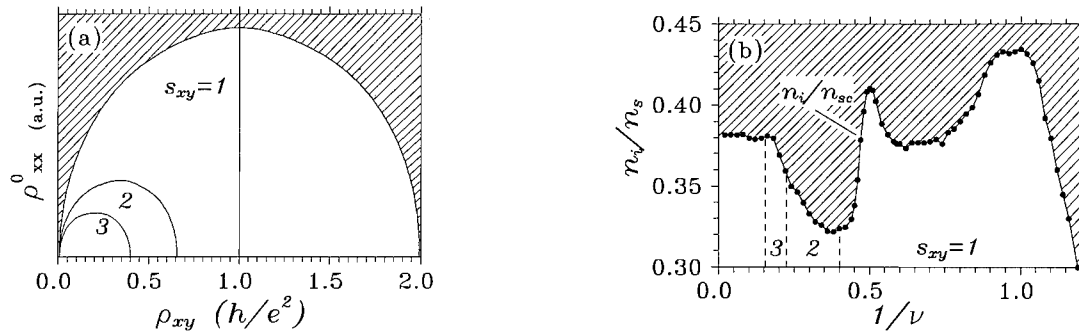


Fig. 2. Phase diagrams for the integer QHE to insulator transition. (a) Theoretical phase diagram [8] at  $T = 0$  as the strength of the disorder vs normalized magnetic field (courtesy of D.-H. Lee); (b) the experimental data taken at  $T = 35 \text{ mK}$ , as the critical density of impurities per electron,  $n_i/n_s$ , vs normalized magnetic field  $(\nu)^{-1} = He/n_s hc$ . Shaded regions designate the insulating phase.

Oscillatory variations of  $\rho_{xx}$  indicate that Landau levels remain resolved at these M/I transitions; it gives us a chance to trace the pathway of the extended states through the transition.

### 3. Hall resistance in the insulating state

Continuous lines in Figs. 1a and 1b show  $R_{xy}$ , measured at source–drain current 10 nA, far above the threshold [11,12], while open circles with error bars –  $R_{xy}$ , measured at 0.25 nA, at half the threshold value. Each of the displayed results was obtained with reversing magnetic field, as mentioned above. It is clearly seen from Fig. 1, that  $R_{xy}$  values are rather close to the classical dependence  $R_{xy} = H/(nec)$  both far above and below the threshold electric field, even when  $\rho_{xx}$  rises to  $\sim 5 \times 10^6 \Omega/\square \approx 200 h/e^2$ . Within the same experimental uncertainty, as shown in Fig. 1, the Hall resistance was found to be independent of temperature as  $T \rightarrow 0$ , while  $\rho_{xx}$  diverges.

### 4. Phase diagram in the plane “disorder-magnetic field”

The theory by Kivelson et al. [8] suggests a global phase diagram to describe the QHE/I transitions in a 2DE system at zero temperature, as shown in Fig. 2a. The y-axis,  $\rho_{xx}^0$ , is a measure of the disorder, while the x-axis,  $\rho_{xy}^0$ , is a measure of the magnetic field. The dashed region represents the insulating phase which spreads towards zero disorder at zero field ( $\rho_{xy}^0 = 0$ ) and at the half-filled lowest Landau level ( $\rho_{xy}^0 = 2h/e^2$ ). The nested curves separate regions which are labelled by the index  $s_{xy}$ , denoting the number of delocalized levels below the Fermi energy. The transition from the initial QHE state with  $s_{xy} = m$  (i.e. from  $m$ th plateau) to the insulator (where  $s_{xy} = 0$ ) would occur in this picture only through a sequence of transitions to lower order QHE states  $s_{xy} = m - 1, m - 2, \dots$ . Any other transitions to and from the insulating phase beyond  $s_{xy} = 1 \leftrightarrow 0$  are forbidden in this approach, as well as in the scaling theory [6,7].

Although the experimental data in Fig. 1 are shown as  $R_{xx}$  versus  $H$ ,  $R_{xx}$  is not an obvious

measure of the disorder, since its magnitude also indicates the onset of the insulating phase. We have chosen the density of impurities at the interface per electron,  $n_i/n_s$ , as a more appropriate measure of the disorder [18]. Experimental points in Fig. 2b [19] are obtained from the critical density  $n_c$ , below which activated transport appears [10], and  $n_i = 3 \times 10^{10} \text{ cm}^{-2}$  calculated from the sample's mobility. The upper shadowed region designates the insulating state, while the regular metallic phase, characterized by the QHE at  $\nu = 1, 2, \dots$  lies below.

To make a proper comparison with theory we have to take into account that in Si(100) there are two electron valleys [20,21], while the theory [8] considered the single-valley and spinless system of electrons. We may choose to neglect e–e interaction and consider the two-valley system as a pair of stacked independent 2DE systems. With this assumption (which is not too realistic), the entire region from  $(\nu)^{-1} = 1/0.5$  to  $1/2.5$  can be attributed to  $s_{xy} = 1$ , the region from  $(\nu)^{-1} = 1/2.5$  to  $1/4.5$  – to  $s_{xy} = 2, \dots$  (see Fig. 2b). The existence of the QHE liquid phase at integer filling factors  $\nu = 1$  and  $2$  surrounded at fixed disorder by insulating phases (or equivalently, the reentrant QHE/I transition around  $\nu = 1$  and  $2$ ) agrees then with Ref. [8]. When  $(\nu)^{-1}$  exceeds  $\sim 1.1$ , the 2DE system is driven to the insulator at weaker disorder, while at  $\nu = 1$  and  $2$  – at stronger disorder, both roughly consistent with Fig. 2a. The absence of QHE/I transitions at  $\nu = 3$  and  $4$  ( $s_{xy} = 2$ ) is also consistent with predictions by Ref. [8], but could originate also from a rapid decrease of the respective energy gap at  $\nu = 3$  as  $H \rightarrow 0$  [21], and from the important role of the polarization [22] in the solid to liquid transition.

There are, however, a couple of caveats: the experimental data [19] show the emergence of a reentrant QHE/I transition around  $\nu = 6$ , and no evidence for the exit of delocalized states through the Fermi energy have been noticed.

### 5. QHE/I transition around $\nu = 6$

The weak feature in the diagonal resistance around  $\nu = 6$  could be seen already in Fig. 1. At

high density,  $n_s > 8.9 \times 10^{10} \text{ cm}^{-2}$ , the 2DE system in the range of  $H = 0.5\text{--}0.9 \text{ T}$  is in the metallic phase with well pronounced quantum Hall effect at  $\nu = 6$ ; it indicates resolved energy levels at  $\nu = 6$  (which is the spin gap [20]). At lower density  $n_s < 8.1 \times 10^{10} \text{ cm}^{-2}$  the insulating state spreads over all range of filling factors  $\nu > 2$ , or, equivalently, magnetic field  $H < 1.5 \text{ T}$ . But in the intermediate range of densities,  $8.6 > n_s > 8.1 \times 10^{10} \text{ cm}^{-2}$ , the exponentially rising magnitude of the Shubnikov-de Haas effect exceeds the maximal value  $h/e^2$  allowed in the gaseous phase [20]; that results in the development of the reentrant metal/insulator transition. This transition appears to be very similar to that discussed above for  $\nu = 1$  and 2.

Detailed experimental study proves that in this range of densities and at magnetic field from 0.45 to 0.5 T, the 2DE system is a true insulator. Fig. 3a shows the diagonal resistivity at fixed electron density  $n_s = 8.34 \times 10^{10} \text{ cm}^{-2}$  at three different temperatures:  $\rho_{xx}^{\text{max}}$  is temperature activated and diverges as  $T \rightarrow 0$ ; in the same range of  $\nu$ , the diagonal conduction is strongly dependent on electric field, exhibiting a sharp threshold, similar to that studied earlier [12] in the insulating phase at  $\nu = 1.5$  and 2.5. At slightly higher magnetic field,  $H = 0.5$  to 0.65 T, at the resistivity minimum  $\nu = 6$  (see Fig. 3a), the 2DE system is in the true metallic phase with  $\rho_{xx}^{\text{min}} < h/e^2$  and

$d\rho_{xx}^{\text{min}}/dT > 0$ . Conduction in this phase does not depend on electric field.

The metallic phase at  $\nu = 6$  is accompanied by the plateau in the Hall resistance, as shown in Fig. 3b, with quantized value  $h/6e^2$  within 5% uncertainty. The Hall resistance through the insulating phase at  $H = 0.45\text{--}0.5 \text{ T}$  follows the classical straight line, similar to that shown in Fig. 1 for  $\nu = 1.5$  and 2.5. Summarizing these observations we have to conclude, that the metal-to-insulator transition around  $\nu = 6$  is one more example of the QHE/I transition, where a variation of the diagonal resistivity through the transition,  $(\rho_{xx}^{\text{max}} - \rho_{xx}^{\text{min}})$ , reaches  $10 \times h/e^2$ . The weak feature in  $\rho_{xx}$  at  $\nu = 10$ , noticeable in Fig. 3, we believe, indicates emergence of one more QHE/I transition, which might be resolved at lower temperature or in a less disordered sample.

## 6. Discussion

The existence of the direct transition from the QHE state at  $\nu = 6$  to the insulator is not consistent with the global phase diagram [8] plotted in Fig. 2a, even when the two-valley system is interpreted as “two folded” 2DE systems. According to the scaling theory [6,7], the energy of delocalized states should rise upon increasing disorder; the delocalized states would then “exit through

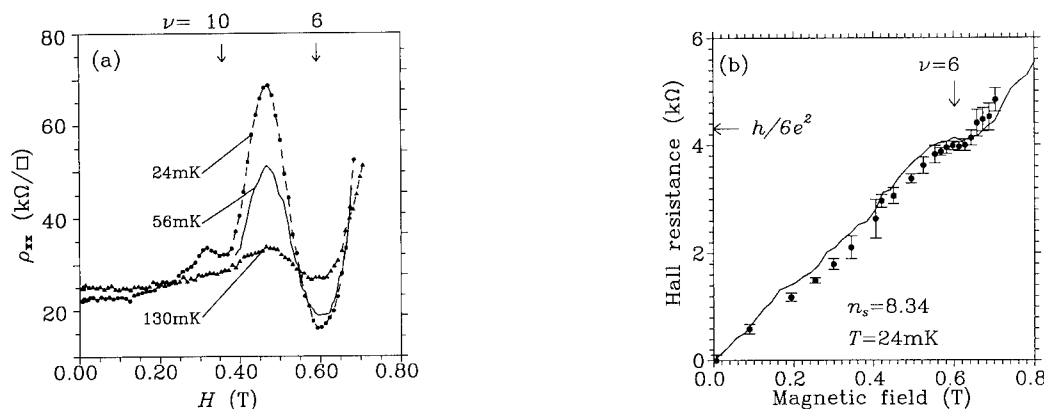


Fig. 3. (a) Magnetic field dependence of the (a) diagonal resistivity at three different temperatures and (b) Hall resistance at the lowest temperature. Arrows indicate filling factor positions for the principal extrema in  $\rho_{xx}$  vs  $H$ . Full curve is  $R_{xy}$  measured at 10 nA, dots with error bars – at 0.25 nA. The electron density is  $8.34 \times 10^{10} \text{ cm}^{-2}$ .

the Fermi energy” [6] during the QHE/I transition. Anomalies in  $\rho_{xx}$  (and possibly in  $\rho_{xy}$ ) would then be observed whenever the boundary between phases with different indices  $s_{xy}$  is crossed (see Fig. 2a). This is not seen experimentally. In particular, the transition from the QHE state at  $\nu = 6$  to the insulator should proceed as a series of transitions from  $s_{xy} = 3 \rightarrow 2 \rightarrow 1 \rightarrow 0$ . This should be seen experimentally as three anomalies in  $\rho_{xx}$  whenever the extended state band exits through the Fermi energy and the  $s_{xy}$  index is changing. The experimental data in Figs. 1 and 3 reveal, however, a smooth exponential rise of the diagonal resistivity and gradual change of the Hall resistance, coinciding with the classical Hall dependence  $H/nec$ , whenever one tunes the transition by varying magnetic field at fixed density, or by varying density at fixed magnetic field.

It appears therefore that the QHE/I transitions develop directly from any liquid phase to the insulator. The same follows from the topology of the boundary in Fig. 2b. A possible reason for this discrepancy could be the non-zero temperature, 30 mK, which may smear the expected features in  $\rho_{xx}$ , since the theoretical predictions [8] have been made for  $T = 0$  and in the limit of low frequencies  $\omega \rightarrow 0$ , while experiments are performed at  $\omega = 0$  and  $T \neq 0$ . It was pointed out [8] that these two limits do not commute.

The direct transitions between the insulator and different QHE phases, and the absence of a signature of the “exit” of delocalized states through the Fermi energy may have an alternative explanation, based upon the collective nature of the reentrant insulating state [12,15,18]. When the 2DE system is pushed towards the insulator by decreasing density rather than by increasing disorder, this is accompanied by an increase in the ratio of the e–e interaction energy to the Fermi energy,  $E_{ee}/E_F \propto n_s^{-1/2}$ , which is  $\sim 12$  at  $n_s = 8 \times 10^{10} \text{ cm}^{-2}$ . It is possible that the delocalized states persisting on the “metallic” side of the transition do not exit, but form an electron lattice which becomes insulating due to pinning by the existing disorder, and provides the insulating transition.

Our preliminary data also indicate that, above the boundary for the QHE/I transition (i.e. at

lower densities) into the electron solid phase [10], plotted in Fig. 3b, there is a crossover from the collective electron state to the single-particle insulator. Its boundary might be consistent with the predictions of Ref. [8].

## 7. Conductivity phase diagram

It is instructive to consider the development of the QHE/I transition when experimental data are plotted as  $\sigma_{xx}$  versus  $\sigma_{xy}$  in Figs. 4a–4c. The phase diagram shown in Fig. 4a for the “metallic” state in the QHE regime is in agreement with the scaling theory [7,23] and consists of a series of arcs, fixed by the QHE states at their endpoints ( $i, 0$ ), where  $i = 1, 2, 3, 4, \dots$  is the number of delocalized states below  $E_F$  in both valleys. During the QHE/I transition, when  $n_s$  at a given magnetic field becomes lower than  $n_c$  (i.e. it crosses the boundary plotted in Fig. 2b), the corresponding point starts deviating from the regular arc. The top points  $t_{i+1/2}$  indicating initial  $\sigma_{xx}$  maxima and located at  $\nu = 3/2$  and  $5/2$  move towards the point of origin (0, 0), as displayed in Fig. 4b. Eventually, all the top points  $t_{i+1/2}$  merge at the origin, approaching it vertically (i.e. with  $\sigma_{xx} \approx \rho_{xx}^{-1} \rightarrow 0$ ,  $\sigma_{xy} \approx \rho_{xy}/\rho_{xx}^2 \rightarrow 0$ ,  $\sigma_{xx}/\sigma_{xy} \rightarrow \infty$ ), while the bottom points stay fixed at their initial positions ( $i, 0$ ).

Figs. 4b and 4c illustrate this behaviour for the energy levels  $i = 1$  and 2; higher levels  $i \geq 3$  become unresolved at low  $n_s$ . When all the top and bottom points are fixed at the origin and at the horizontal axis, the phase diagram displays remarkable universality: both branches starting from the bottom points ( $i, 0$ ) follow the same semicircles of fixed radius  $i/2$ , independent of their Landau level index. It is evident from Figs. 1, 3 and 4, that  $\sigma_{xx}$  drops to zero twice a period for the QHE/I transition on the magnetic field axis: at  $\rho_{xx}$  minima and maxima. It could be interpreted as evidence for the exit of the delocalized states; this interpretation, however, might be applied only in the interval of filling factor  $\nu$  from 1 to 2, and fails for the higher order QHE/I transitions in the intervals  $\nu = 2\text{--}6$  and  $\nu = 6\text{--}10$ . This topological behaviour of the conductivity phase

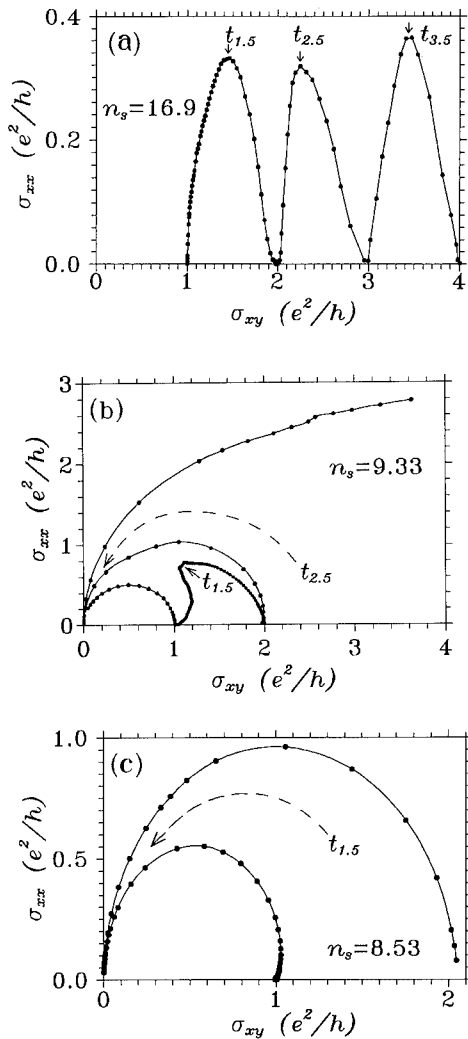


Fig. 4. Experimental phase diagrams as  $\sigma_{xx}$  vs  $\sigma_{xy}$  at three different densities (given in units of  $10^{10} \text{ cm}^{-2}$ ). Dashed arrows in (b) and (c) indicate trajectories for the top points.

diagram first seen in Ref. [15] is again in good agreement with the explanation given above and involving the formation of an electron solid due to the increase in the ratio  $E_{ce}/E_F$ . The e-e interaction has not been considered in Refs. [4–6,20]. Below  $n_s < 6 \times 10^{10} \text{ cm}^{-2}$ , the system is driven towards the Anderson insulator, when all branches of the phase diagram collapse at the origin, approaching it also vertically with  $\sigma_{xx}/\sigma_{xy} \rightarrow \infty$ .

## 8. Summary

Our measurements in the vicinity of the QHE/I transitions have shown that (i) the Hall resistance does not diverge, measured either above or below the threshold electric field, even when  $\rho_{xx}$  rises to  $4 \times 10^6 \Omega/\square$ . While  $\rho_{xx}$  is temperature activated,  $\rho_{xy}$  is not. These results agree with the predictions for both the “Hall insulator” [2,3,7] and the pinned Wigner lattice with transport provided by extended defects [8]. (ii) The disorder-magnetic field diagram for the QHE/I transitions suggests that the insulating state develops directly from the QHE phases at different indices. (iii) The phase diagram  $\sigma_{xx}$ – $\sigma_{xy}$  shows universality different from that of the scaling theory for the QHE in a metallic phase and that of the Hall insulator.

## 9. Acknowledgements

We wish to thank D.-H. Lee for valuable discussions and Donald Brown for his expert technical assistance.

## 10. References

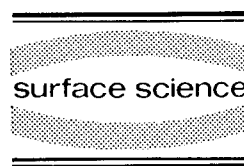
- [1] B.L. Altshuler, D. Khmel'nitskii, A.L. Larkin and P.A. Lee, Phys. Rev. B 22 (1980) 5142.
- [2] H. Fukuyama, J. Phys. Soc. Jpn. 49 (1980) 644.
- [3] B. Shapiro and E. Abrahams, Phys. Rev. B, 24 (1981) 4025.
- [4] O. Viehweger and K.B. Efetov, Phys. Rev. B 44 (1991) 1168.
- [5] B.I. Halperin, Phys. Rev. B 25 (1982) 2185.
- [6] R.B. Laughlin, Phys. Rev. Lett. 52 (1984) 2304.
- [7] D.E. Khmel'nitskii, JETP Lett. 38 (1983) 552.
- [8] S. Kivelson, D.-H. Lee and S.-C. Zhang, Phys. Rev. B 46 (1992) 2223; S.-C. Zhang, S. Kivelson and D.-H. Lee, Phys. Rev. Lett. 69 (1992) 1252.
- [9] X.-F. Wang, Z. Wang, G. Kotliar and C. Castellani, Phys. Rev. Lett. 68 (1992) 2504.
- [10] S.T. Chui, preprint BA 92-53, Bartol Res. Inst. (1992).
- [11] M. D'Iorio, V.M. Pudalov and S.G. Semenchinsky, Phys. Lett. A 150 (1990) 422.
- [12] M. D'Iorio, V.M. Pudalov and S.G. Semenchinsky, Phys. Rev. B 46 (1992) 15992.

- [13] L.W. Engel, T. Sajoto, Y.P. Li, D.C. Tsui and M. Shayegan, *Surf. Sci.* 263 (1992) 44.
- [14] M.B. Santos, Y.W. Suen, M. Shayegan, Y.P. Li, L.W. Engel and D.C. Tsui, *Phys. Rev. Lett.* 68 (1992) 1188.
- [15] S.V. Kravchenko, J.A.A.J. Perenboom and V.M. Pudalov, *Phys. Rev. B* 44 (1991) 13513.
- [16] V.J. Goldman, J.K. Wang, Bo Su and M. Shayegan, *Phys. Rev. Lett.* 70 (1993) 647.
- [17] T. Sajoto, Y.P. Li, L.W. Engel, D.C. Tsui and M. Shayegan, report J27.1, APS March meeting, Seattle, 1993.
- [18] V.M. Pudalov, M. D'Iorio, S.V. Kravchenko and J.W. Campbell, *Phys. Rev. Lett.* 70 (1993) 1866.
- [19] V.M. Pudalov, M. D'Iorio and J.W. Campbell, *JETP Lett.* 57 (1993) 608.
- [20] For the review see: T. Ando, A.B. Fowler and F. Stern, *Rev. Mod. Phys.* 54 (1982) 437.
- [21] V.M. Pudalov, S.O. Semenchinskii and V.S. Edel'man, *JETP* 62 (1985) 1079.
- [22] S.-T. Chui and Tanatar, report J27.10, APS March meeting, Seattle, 1993.
- [23] A.M.M. Pruisken, in: *The Quantum Hall Effect*, 2nd ed., Eds. R.E. Prange and S.M. Girvin (Springer, New York, 1990) p. 117.



ELSEVIER

Surface Science 305 (1994) 115–119



## Collective insulating state at zero magnetic field in a dilute 2D electron system

M. D'Iorio <sup>\*,a</sup>, V.M. Pudalov <sup>1,a</sup>, S.V. Kravchenko <sup>1,b</sup>, J.W. Campbell <sup>c</sup>

<sup>a</sup> National Research Council Canada, IMS, Ottawa, ON, Canada K1A 0R6

<sup>b</sup> University of Oklahoma, Department of Physics and Astronomy, Norman, OK 73019, USA

<sup>c</sup> University of Ottawa, Department of Physics, Ottawa, ON, Canada K1N 6N5

(Received 28 April 1993; accepted for publication 28 June 1993)

### Abstract

We present experimental evidence for the low temperature collective insulator state which sets in upon lowering the electron density at zero magnetic field in high mobility Si-inversion layers. Data on temperature activated and threshold electric field dependent dc conduction are fitted well by a model of transport in a Wigner solid provided by the motion of dislocation pairs. We report weak narrowband noise with a current dependent frequency spectrum on a background of broadband noise.

### 1. Introduction

The observation of a metal–insulator (MI) transition in dilute electron systems around fractional filling factors in GaAs/AlGaAs [1] and integer filling factors in Si-MOSFETs [2] has fueled a debate over the nature of the insulating state at low temperature in the 2D electron system with minimal disorder. There is little doubt that for zero disorder and  $T = 0$ , the 2D electron system will crystallize into a Wigner lattice upon lowering density. It is also known that in the limit of strong disorder, the Anderson single-particle localization (SPL) will set in. Real samples with minimal disorder provide an intermediate regime

where a collective insulating state like the pinned Wigner solid (WS) [3], or the pinned charge density wave (CDW) [4] might exist. In a Si inversion layer, the large effective mass ( $m^* = 0.19m_e$ ) and the low dielectric constant ( $\kappa = 7.7$ ) yield a cold melting density which is at least  $20 \times$  higher than in GaAs [2,5]. This is favourable for the observation of a collective electron solid and raises hope that at low enough disorder, the short range order might be revealed.

We present experimental evidence for the collective character of the low temperature metal–insulator transition at zero field in Si-MOSFETs with weak disorder. As “direct” evidence for the existence of short range order, we report on the observation of narrowband noise whose frequency spectrum reflects the principal lattice spacings. The non-linear dc transport data can be fitted well by a model of generation and motion of extended defects in the pinned electron lattice.

\* Corresponding author.

<sup>1</sup> On leave from the Institute for High Pressure Physics, Troitsk, Moscow District 142092, Russian Federation.



Our data indicate a trend from a collective to a single-particle insulator state with decreasing density or increasing disorder.

## 2. Experimental

The samples for this study were selected to provide a wide range of peak mobilities,  $\mu^{\text{peak}}$ : Si-5 with  $\mu^{\text{peak}} = 4.3 \times 10^4 \text{ cm}^2/\text{V} \cdot \text{s}$ , Si-11 with  $\mu^{\text{peak}} = 3.63 \times 10^4 \text{ cm}^2/\text{V} \cdot \text{s}$ , and Si-2 with  $\mu^{\text{peak}} = 2.42 \times 10^4 \text{ cm}^2/\text{V} \cdot \text{s}$ . The samples were patterned as rectangular Hall bars with a source to drain length  $L = 5 \text{ mm}$ , a width  $w = 0.8 \text{ mm}$ , and an intercontact distance  $l = 1.25 \text{ mm}$ . The carrier density could be varied from  $5 \times 10^{10}$ – $1 \times 10^{12} \text{ cm}^{-2}$  by means of the top gate. The measurements were taken in a temperature range of 25–650 mK. For the dc transport measurements, a four-probe technique was used with a differential electrometer and dc currents as low as 0.1 pA.

The longitudinal resistance  $R_{xx}$  exhibits insulating behavior characterized by an exponential rise and a negative temperature derivative, below a critical carrier density  $n_{sc} \approx 10^{11} \text{ cm}^{-2}$ . The activation energy  $\Delta$  obtained from the temperature dependence  $R_{xx} \propto \exp(\Delta/kT)$  drops linearly to zero at  $n_{sc}$ , as illustrated in Fig. 1a. The value of the critical carrier density is sample dependent, decreasing from  $1 \times 10^{11} \text{ cm}^{-2}$  for Si-2 to

$8 \times 10^{10} \text{ cm}^{-2}$  for Si-5 which has the highest mobility (or the least disorder). The current–voltage characteristics shown in Fig. 2a are also marked by a sharp drop in  $\partial V/\partial I$  above a threshold electric field  $E_t$ . The threshold field goes to zero smoothly at  $n_{sc}$  as shown in Fig. 1a. The data can be fitted well by a power law  $E_t \propto \delta n_s^\gamma$ , where  $\delta n_s = (n_{sc} - n_s)$  and  $\gamma = 1.7$  (see Fig. 1b). The dependencies of  $\Delta$  and  $E_t$  on  $n_s$  are quite similar for all three samples. The sharp rise in conduction is accompanied by a steep increase in the broadband rms-noise voltage  $\langle V_N \rangle$  as a function of current (see Fig. 2b). The broadband rms-noise voltage  $\langle V_N \rangle$  was measured at two nearest potential contacts in a 1–300 kHz frequency band.

To study the frequency spectrum of the generated noise we used an analog technique. Narrow-band amplifiers (1% frequency band) were tuned through the frequency range, point by point and the rms-noise voltage between two closest potential contacts was averaged for a few hours thereby ensuring proper statistics. Below 4 kHz, the diverging  $1/f$  noise signal prevented us from doing measurements at low frequencies, while above 10 kHz the signal was cut-off by the RC time constant of the gated sample. The carrier density was adjusted such that the driving source–drain current near threshold would correspond to a 4–10 kHz frequency range. The narrowband noise shown in Fig. 2c has a reproducible frequency spectrum which shifts to higher frequency as the

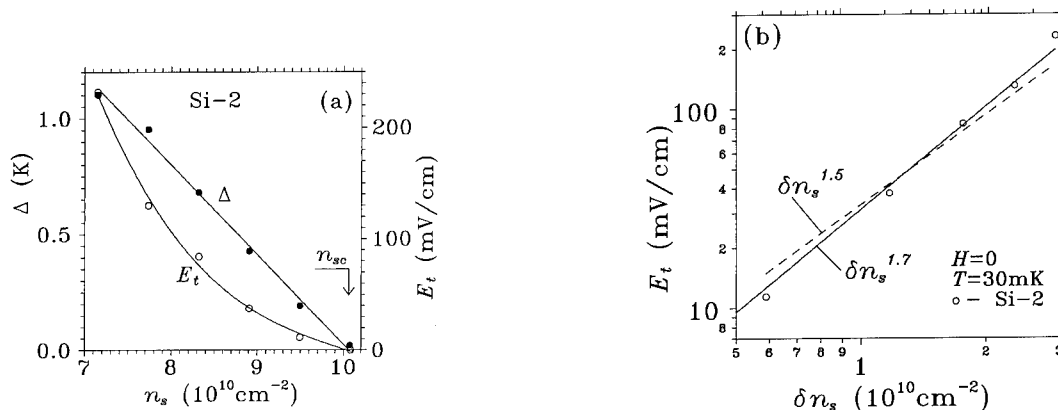


Fig. 1. (a) Activation energy and threshold electric field versus electron density. (b) Threshold electric field versus  $\delta n_s = (n_{sc} - n_s)$ .

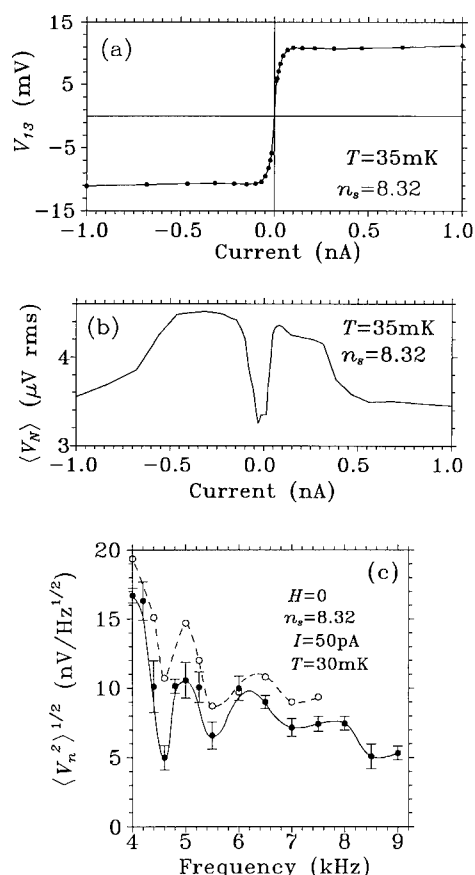


Fig. 2. (a) Typical threshold  $I$ - $V$  characteristic. (b) Broadband noise voltage measured between potential contacts as a function of source-drain current. (c) Two independent spectral measurements of the narrowband noise driven by the dc current. The density is in units of  $10^{10} \text{ cm}^{-2}$ .

driving current is increased. The maxima in the signal amplitude occur at frequencies which can be related to the 2D electron lattice constants.

### 3. Discussion

The depinning mechanism of an electron solid via the creation and separation of dislocation pairs has recently been studied by Chui [6]. In the limit of low impurity density, the depinning field is proportional to the activation energy to the power  $3/2$ . Experimentally the activation energy varies linearly with  $\delta n_s$  (see Fig. 1a) and there-

fore the predicted  $3/2$  power law agrees well with the experimental results where  $E_t \propto \delta n_s^{1.7}$  (see Fig. 1b). The theoretical estimate for the depinning electric field is also of the same order of magnitude as the experimental data.

In the collective insulating state, the transport data cannot be fitted to a SPL model. The threshold field is too low and the localization length is too large and neither hopping nor variable range hopping models can fit the temperature dependence of the conduction [7]. A rough fit to the transport data can be provided by a model for a pinned WS (or pinned CDW) whose transport above threshold is due to the motion of depinned domains [8–10]. The evanescence of the threshold field at  $n_{sc}$  suggests that the transition is not first order or is, at best, a weak first-order transition. It is difficult to account for this transition in the limit of strong pinning [8,9], when both the pinning force and correlation length are given by the impurities. Using the approach of the elastic theory of the CDW [10] in the weak pinning limit, we can estimate the correlation length (domain size)  $L_D$  as  $(K_T a / (2\pi e n_s E_t))^{1/2}$ , where  $K_T$  is the transverse shear modulus,  $a$  is the interelectron spacing and  $E_t$  is the threshold electric field [4,9,10]. Substituting the experimental  $E_t(n_s)$  data in the expression above, we find that  $L_D$  diverges as  $(\delta n_s)^{-0.9}$  [7]. Irrespective of the model used, the correlation length  $L_D$  drops with decreasing density (or increasing  $\delta n_s$ ) thus driving the 2D electron system towards single-particle localization.

The generated broadband noise shown in Fig. 2b is appropriate for depinning of the WS (or for coherent defect motion [6]). If this occurs, one might expect narrowband noise with frequency peaks related to the principal lattice spacings, or, at least, peaks on a broadband background. If we assume that the electron lattice extends across the entire 2D layer of width  $w$  and that the total current  $I$  is only provided by the sliding lattice, then the expected spectral maxima  $f_j$  can be easily related to the principal lattice spacings  $\Lambda_j$  as follows:  $f_j = I / (e n_s w \Lambda_j)$ . For a hexagonal lattice sliding in the random field of point defects, we find  $\Lambda_1 = a$ ,  $\Lambda_2 = \sqrt{3}a$ , and  $\Lambda_3 = 2a$ , where  $a$  is the spacing between nearest neighbour elec-

trons. If, alternatively, the current is provided by extended defects [6] moving through a fixed electron lattice, then an additional distinct spacing is found:  $A_4 = (\sqrt{3}/2)a$ . For  $n_s = 8.32 \times 10^{10} \text{ cm}^{-2}$ ,  $a = 310 \text{ \AA}$  and  $I = 50 \times 10^{-12} \text{ A}$ , we expect frequency peaks at  $f_1 = 15.5 \text{ kHz}$ ,  $f_2 = 9 \text{ kHz}$ ,  $f_3 = 7.75 \text{ kHz}$  and  $f_4 = 18 \text{ kHz}$ . The measured frequency spectrum shown in Fig. 2c exhibits maxima at about 5, 6.2 and possibly 8 kHz. If the weak peak at 8 kHz is ignored, then the two lower peaks can be labeled as  $f_4$  and  $f_1$  scaled down by a factor  $\sim 3$ . The frequency of the spectral maxima increases with current but not in a proportional fashion. It is therefore possible that part of the total current is provided by hopping of carriers beyond the lattice.

We have studied quantitatively the role of disorder in the development of the insulating phase. By using Gold's calculation [11] for the mobility of Si(100) inversion layers, we obtain a satisfactory description of  $\mu^{\text{peak}}$  versus  $n_s$  for our samples. We can use these results to relate  $\mu^{\text{peak}}$  to the density of impurities  $n_i$  which is a more appropriate measure of disorder since impurities are the major source of electron scattering at low  $n_s$  [12]. This is true below  $2 \times 10^{11} \text{ cm}^{-2}$  in our samples. The long dashed line in Fig. 3 illustrates the calculated dependence of  $\mu^{\text{peak}}$  on  $n_i$ . The empty squares depict the experimental data [13] for the Anderson transition. The boundary for SPL, denoted  $n_{\text{SPL}}$ , is estimated from  $n_i$  and shown as a short dashed line. Theoretical calculations of  $n_i$  and  $n_{\text{SPL}}$  [11] have been done specifically to fit the data for low mobility samples assuming particularly large surface roughness parameters. The calculated short-dashed line is taken to be the highest estimate of  $n_{\text{SPL}}$  in our high mobility samples where surface roughness scattering is much lower [14]. The  $n_{\text{sc}}$  values for the three samples, indicated by the full circles are at least  $2 \times$  higher than the  $n_{\text{SPL}}$  values. This agrees with the collective character of the transition at  $n_{\text{sc}}$ .

As direct  $R_{xx}$  measurements down to  $n_s \approx n_{\text{SPL}} \approx 1 \times 10^{10} \text{ cm}^{-2}$  were impossible due to a rapid increase in the probe resistance, we extrapolated the domain length  $L_D$  to lower  $n_s$  in order to examine the validity of our interpretation. The

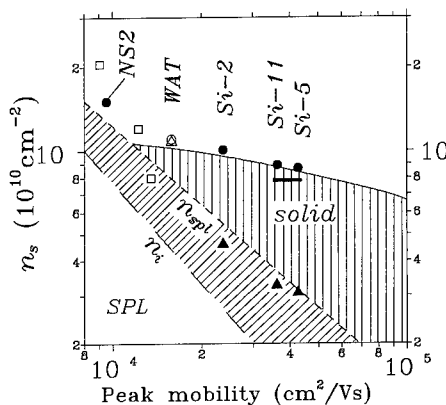


Fig. 3. Critical density versus sample peak mobility. The full circles designate the measured  $n_{\text{sc}}$  values. The full line represents  $n_{\text{cm}}(n_i)$  calculated on the basis of Ref. [3], the dashed lines –  $n_i$  and  $n_{\text{SPL}}$  vs.  $\mu^{\text{peak}}$ . The full triangles indicate the  $n_{\text{SPL}}$  evaluated from our data. The empty circle and triangle are taken from Ref. [15]. The empty boxes denote the onset of activated transport from Ref. [13].

resulting  $n_{\text{SPL}}$  estimates corresponding to the criterion  $L_D = 2a$  are indicated by full triangles in Fig. 3. The WAT empty circle and the triangle designate respectively the onset of the insulating phase and the estimated  $n_{\text{SPL}}$  (using the same criterion), from cyclotron resonance data by Wilson and co-workers [15]. The lower-dashed region is interpreted as a crossover to SPL and there is reasonable agreement with all the data plotted in Fig. 3. The vertically-dashed region designates then a collective insulator phase, confined between the metallic state above the  $n_{\text{cm}}$  boundary and presumably the Anderson insulator below the  $n_{\text{SPL}}$  line.

It is known that weak disorder can stabilize the WS due to the creation of a gap in the phonon spectrum and hence a limited zero point displacement [3]. We calculated the mean square displacement (MSD) of the pinned WS at  $T = 0$  for given  $n_i$  values as the area under the phonon spectral density of the pinned WS for the relative strength of the pinning potential  $\Lambda = 1$  [3]. The full line in Fig. 3 shows the calculated dependence of the cold melting density on  $n_i$  using the MSD as a function of  $n_i$  and a realistic estimate of  $n_{\text{cm}}$  as  $n_i \rightarrow 0$  [7]; the agreement with the data seems quite good. Taking into account numeri-

cally the disorder in our samples, Chui [16] has recently calculated a transition from a polarized WS to a partially polarized liquid at  $r_s \approx 10$  ( $n_s \approx 7.65 \times 10^{10} \text{ cm}^{-2}$ ) in agreement (within 15% accuracy) with the data for Si-5 and Si-11. This is indicated by a bar in Fig. 3. The full line merges with the dashed SPL boundary at  $\mu^{\text{peak}} \approx 10^4 \text{ cm}^2/\text{V} \cdot \text{s}$  which accounts for the lack of collective MI transitions in poorer mobility Si samples.

We conclude that there is mounting experimental evidence for a low temperature transition to a collective insulator at zero magnetic field in high mobility Si-inversion layers. With increasing disorder or decreasing carrier density, the collective insulator state is driven into a single-particle one. The collective insulator state at  $H = 0$  shares many of the features of the pinned Wigner solid. The power law dependence of the threshold electric field on the carrier density agrees well with a model involving the motion of dislocation pairs in an electron lattice. The frequency spectrum of the narrowband noise and its current dependence reflect the presence of at least short-range order. A crossover to an Anderson insulator or SPL regime occurs as disorder is increased.

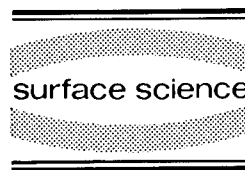
#### 4. References

- [1] E.Y. Andrei, G. Deville, D.C. Glatthi, F.I.B. Williams, E. Paris and B. Etienne, *Phys. Rev. Lett.* 60 (1988) 2765; V.J. Goldman, M. Santos, M. Shayegan and J.E. Cunningham, *Phys. Rev. Lett.* 65 (1990) 2189;
- H.W. Jiang, R.L. Willett, H.L. Stormer, D.C. Tsui, L.N. Pfeiffer and K.W. West, *Phys. Rev. Lett.* 65 (1990) 633.
- [2] M. D'Iorio, V.M. Pudalov and S.G. Semenchinsky, *Phys. Lett. A* 150 (1990) 422; S.V. Kravchenko, J.A.A.J. Perenboom and V.M. Pudalov, *Phys. Rev. B* 44 (1991) 13513; M. D'Iorio, V.M. Pudalov and S.G. Semenchinsky, *Phys. Rev. B* 46 (1992) 15992; S.V. Kravchenko, V.M. Pudalov, J. Campbell and M. D'Iorio, *Pis'ma ZhETF* 54 (1991) 528.
- [3] A.C. Eguiluz, A.A. Maradudin and R.J. Elliott, *Phys. Rev. B* 27 (1983) 4933.
- [4] H. Fukuyama and P.A. Lee, *Phys. Rev. B* 17 (1978) 535.
- [5] B. Tanatar and D.M. Ceperley, *Phys. Rev. B* 39 (1989) 5005.
- [6] S.-T. Chui, *Phys. Lett. A* 180 (1993) 149.
- [7] V.M. Pudalov, M. D'Iorio, S.V. Kravchenko and J.W. Campbell, *Phys. Rev. Lett.* 70 (1993) 1866.
- [8] I.M. Ruzin, S. Marianer and B.I. Shklovskii, *Phys. Rev. B* 46 (1992) 3999.
- [9] P.A. Lee and T.M. Rice, *Phys. Rev. B* 19 (1979) 3970.
- [10] B.G.A. Normand, P.B. Littlewood and A.J. Millis, *Phys. Rev. B* 46 (1992) 3920.
- [11] A. Gold, *Phys. Rev. Lett.* 54 (1985) 1079; A. Gold and W. Gotze, *Phys. Rev. B* 33 (1986) 2495.
- [12] For a review see: T. Ando, A.B. Fowler and F. Stern, *Rev. Mod. Phys.* 54 (1982) 437.
- [13] A. Yagi and M. Nakai, *Surf. Sci.* 98 (1980) 174.
- [14] M.S. Khaikin, A.M. Troyanovskii, V.S. Edelman, V.M. Pudalov and S.G. Semenchinskii, *JETP Lett.* 44 (1986) 245.
- [15] S. Kawaji and J. Wakabayashi, *Solid State Commun.* 22 (1977) 87; B.A. Wilson, S.J. Allen and D.C. Tsui, *Phys. Rev. B* 24 (1981) 5887.
- [16] S.T. Chui and B. Tanatar, APS March meeting, J27 10 (1993).



ELSEVIER

Surface Science 305 (1994) 120–123



# Magnetic-field-induced transition from an Anderson insulator to a quantum Hall conductor

H.W. Jiang <sup>\*,a</sup>, I. Glozman <sup>a</sup>, C.E. Johnson <sup>a</sup>, S.T. Hannahs <sup>b</sup>

<sup>a</sup> Department of Physics, University of California at Los Angeles, Los Angeles, CA 90024, USA

<sup>b</sup> Massachusetts Institute of Technology, Francis Bitter National Magnet Laboratory, Cambridge, MA 02139, USA

(Received 19 April 1993; accepted for publication 15 June 1993)

## Abstract

We report the first experimental observation of a magnetic-field induced transition from an Anderson insulator to a quantum Hall conductor in a two-dimensional electron gas (2DEG) system. With sufficiently strong disorder, the 2DEG is an Anderson insulator with a divergent resistance at  $B = 0$ . The 2DEG is transformed into a quantum Hall conductor when the lowest Landau level is filled. This magnetic-field-induced delocalization is consistent with a recently proposed global phase diagram for the quantum Hall effect.

## 1. Introduction

It is now generally believed that in the absence of a magnetic field all the states of a 2DEG are localized in the presence of any amount of disorder [1]. The effect of an applied magnetic field, however, is still a subject of much debate and has become central to most discussions of localization in quantum Hall systems. The presence of extended states is, of course, implied by the observation of the quantum Hall effect (QHE). However, experimentally, the localization length in a 2DEG is estimated from  $\xi \approx \exp(\pi^2 h / e^2 \rho)$ , here  $\rho$  is the resistivity, to be of the order of a kilometer even in very “dirty” devices. This means that because of its finite size (typically of order 1 mm), a 2DEG system is effectively delocalized at  $B = 0$ .

It has been suggested that even if the system

were completely localized (with no extended states below the Fermi level  $E_F$ ) in zero magnetic field, it might still be possible to observe the QHE since the system may be subject to magnetic-field-induced delocalization. In this regard, a scaling argument has been developed by Khmelnitskii [2] and a gedanken experiment proposed by Laughlin [3]. The idea is that extended states are assumed to be conserved and, as a consequence of changing disorder or magnetic field, may float or sink relative to localized states and possibly past  $E_F$ . A schematic illustration of this possibility is suggested in Fig. 1.

Recently, a novel global phase diagram by Kivelson, Lee and Zhang [4] predicted a series of direct Anderson insulator (a special type called a Hall insulator [5] which has a non-divergent Hall resistance) to quantum Hall conductor transitions as a consequence of delocalization induced by a change in the magnetic field. Motivated by this theoretical phase diagram, we have conducted an

\* Corresponding author.

experiment on a system which can serve as an Anderson insulator defined by having all of its electronic states below  $E_F$  localized due to random potential fluctuations. Experimentally, although the transport properties of the two-dimensional electron gas (2DEG) in the strong localization regime have been explored as early as in the 70's by utilizing silicon inversion layers [6], the delocalization transition has not been observed.

## 2. Results

The samples used in the present work were modulation-doped GaAs/AlGaAs heterostruc-

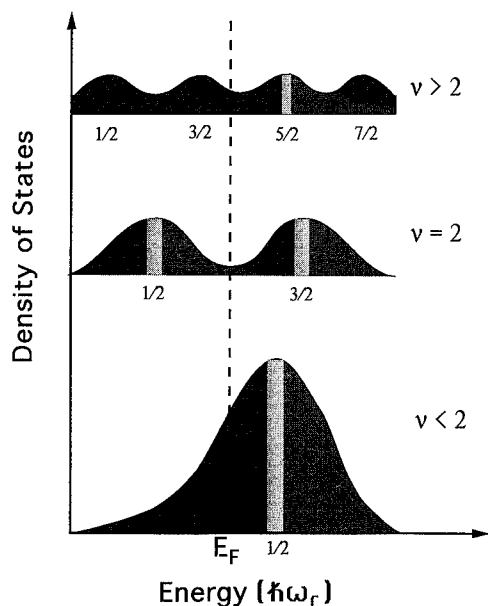


Fig. 1. The density of states versus energy for three different filling factors. For simplicity, spin splitting is assumed to be unresolved. Singular Landau levels are broadened by disorder into bands of extended states (light shading) separated by tails of localized states (dark shading). For  $\nu > 2$  (low magnetic field) and in the presence of sufficient disorder, there are no extended states below the Fermi level; as a result, no QHE is observed and the system is an insulator. The case  $\nu = 2$  corresponds to a quantum Hall conductor; dissipation is precluded by an energy gap between  $E_F$  and the next available extended state into which scattering can take place. For  $\nu < 2$  (high magnetic field), there are once again no extended states below  $E_F$  and the system is a regular insulator.

tures fabricated by molecular beam epitaxy. The active 2D layer was formed on top of a Si-doped AlGaAs layer without the conventional undoped spacer to ensure a large random fluctuation of the impurity potential. A Hall bar pattern was etched out by standard lithographic techniques and an aluminum gate was evaporated onto its surface.

As expected, depletion was achieved by increasing the gate voltage (and thus the disorder) as  $R_{xx}$  rose by several orders of magnitude (see inset of Fig. 4). That is, the localization length decreased dramatically as the screening of the random potential was reduced by depletion. The details of tuning the effective disorder by changing the density is described elsewhere [7]. As shown in the figure, at low  $V_G$  (high density), the 2DEG is nearly metallic, characterized by a temperature independent resistance as  $T \rightarrow 0$ . At high  $V_G$  (low density),  $R_{xx}$  shows an exponential divergence  $R_{xx}$  as  $T \rightarrow 0$  at zero magnetic field and in fact follows the well-known Mott law  $R \approx \exp(T_0/T)^{1/3}$  as expected for an Anderson insulator, as shown in Fig. 2. From this temperature dependence and Mott's law [7], we estimate a localization length of about 1200 Å, corresponding to a strongly localized system.

To determine how magnetic field affects localization, several  $R_{xx}$  versus  $B$  traces were taken in the depleted (strongly localized) regime at

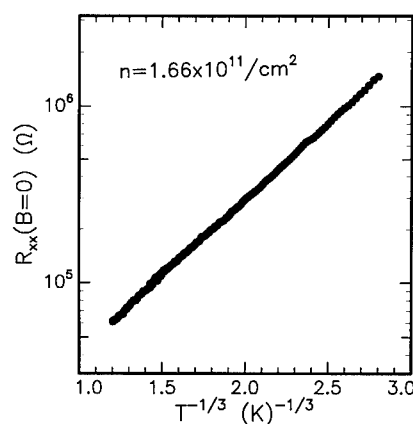


Fig. 2. The logarithmic of the resistance vs.  $T^{-1/3}$  at a density of  $1.66 \times 10^{11}/\text{cm}^2$ . The data show insulator-like behavior for zero magnetic field as  $R$  diverges as  $T \rightarrow 0$ .

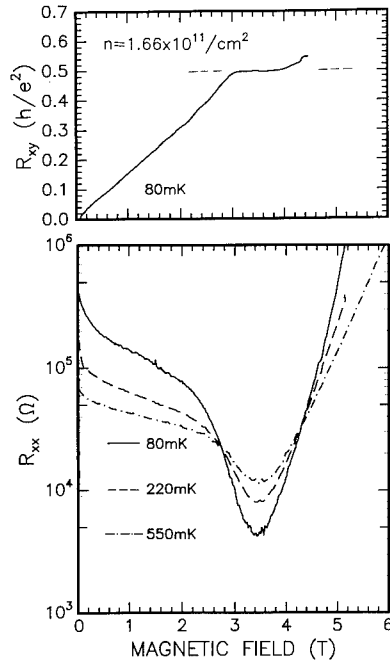


Fig. 3. Top: Hall resistance. For fields away from the Landau level filling factor of  $\nu = 2$ , both above and below,  $R_{xy}$  is nearly classical. A well resolved plateau is developed around  $\nu = 2$  at low-temperature. Bottom: the longitudinal resistance  $R_{xx}$  versus magnetic field at three different temperatures. A minimum is seen at  $\nu = 2$  which deepens as the temperature is lowered.

different temperatures. For fields away from  $\nu = 2$ , both above and below, variable-range hopping behavior was observed similar to the zero-field case and the Hall resistance is approximately classical,  $R_{xy} = B/nec$  (consistent with the behavior of a Hall insulator). On the other hand, at  $\nu = 2$  (defined by a well resolved plateau in  $\rho_{xy}$  with the value of  $(h/e^2)/2$ ) a deep minimum was observed which dropped continuously as the temperature was lowered. This minimum is thus consistent with the onset of a quantum Hall conducting phase. It is also interesting to point out that a well defined “crossing point” of the three curves can be seen around  $B = 2.6$  T. This suggests the possibility of a critical field as shown in Fig. 4 by the horizontal transition and certainly warrants further investigation.

In a further study of the quantum Hall conductor at  $\nu = 2$ , we were able to map out the

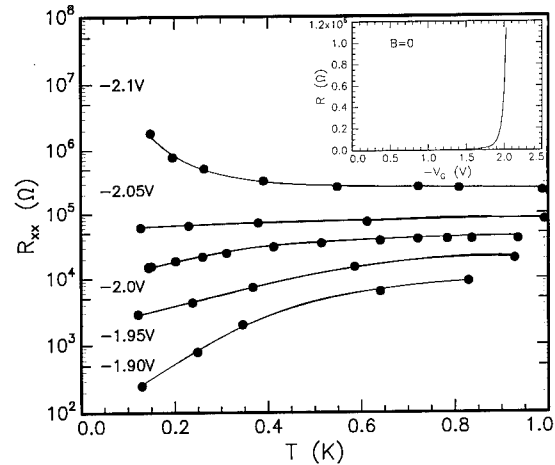


Fig. 4. Semi-logarithmic plot of  $R_{xx}$  versus temperature at different values of the gate voltage  $V_G$  and at  $\nu = 2$ . For higher values of  $|V_G|$ ,  $R_{xx}$  diverges as  $T \rightarrow 0$  as expected for an Anderson insulator. For lower values of  $|V_G|$ ,  $R_{xx}$  approaches zero as  $T \rightarrow 0$  as expected for a quantum Hall conductor. Critical disorder is expected to be at  $V_G \approx -2.05$  V which separates the two regions. The inset shows a divergent  $R_{xx}$  as  $|V_G|$  goes up, implying an increase of disorder as a function of  $V_G$ .

portion of the global phase diagram containing the point of critical disorder on the insulator-quantum Hall conductor phase boundary (Fig. 5).

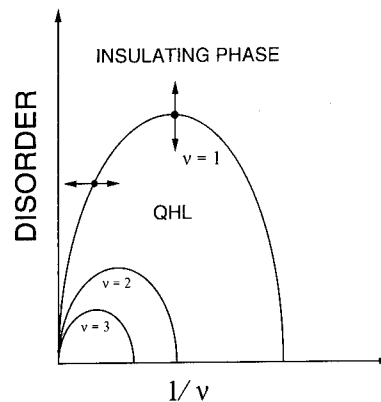
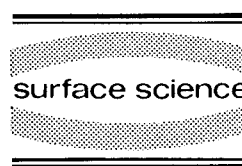


Fig. 5. A simplified global phase diagram for the quantum Hall effect (adapted from Ref. [4] and modified). Of particular relevance are the two types of a transition from an insulating to a quantum Hall conducting phase, one brought on by a change in disorder and the other by a change in magnetic field (or filling factor). Critical disorder is marked by a small circle in the case of the former. Note that spin splitting is not considered.



ELSEVIER

Surface Science 305 (1994) 124–125



## Observation of finite-frequency scaling in the integer quantum Hall effect

L.W. Engel <sup>\*</sup>, D. Shahar, Ç. Kurdak, D.C. Tsui

*Department of Electrical Engineering, Princeton University, Princeton, NJ 08544, USA*

(Received 19 April 1993; accepted for publication 11 May 1993)

### Abstract

We present microwave measurements of the diagonal conductivity  $\sigma_{xx}$ , in the integer quantum Hall regime. Our frequencies  $f$  were between 0.2 and 14 GHz, and the temperature  $T$  was  $\geq 50$  mK. Broadband  $\text{Re}(\sigma_{xx})$ , was measured by a transmission line method. The widths  $\Delta B$  of  $\text{Re}(\sigma_{xx})$  peaks between IQHE minima increase with  $f$  roughly as  $(\Delta B) \propto f^{0.41}$  for  $f \geq 1$  GHz. At lower  $f$  the peak width dependence on  $f$  saturates. We interpret the increase in  $\Delta B$  with  $f$  as due to dynamic scaling. The exponent, together with existing estimates of the localization length exponent  $\nu$ , yields a dynamic exponent  $z \approx 1$ .

In low-mobility 2D samples, transitions between integer quantum Hall effect (IQHE) steps have recently been shown [1] to be characterized by a critical exponent  $\kappa$ , which describes the increasing sharpness of a transition between IQHE plateaus as the temperature  $T$  decreases. The magnetic field width,  $\Delta B$ , of a transition was found to decrease with  $T$  according to  $\Delta B \approx T^\kappa$ , with  $\kappa \approx 0.42$ . Within the context of the scaling theory [2], and assuming that inelastic scattering controls the effective size of the sample, this power law can be related to the divergence of the localization length  $\xi$  as the magnetic field  $B \rightarrow B^*$ , where  $B^*$  is the magnetic field at which the Fermi energy is aligned with a Landau level.

Quite generally for continuous phase transitions, a divergent characteristic length is accom-

panied by a divergent characteristic time. Dynamic scaling [3] describes the time-dependent behavior of the system as determined by this correlation time. Since the transitions between IQHE steps are critical phenomena, as Ref. [1] indicates, with  $\xi$  diverging as  $\xi \approx |B - B^*|^{-\nu}$ , we can expect that there is a concomitantly diverging correlation time  $\tau_c \approx |B - B^*|^{-y} \approx \xi^z$  [4], where  $z = \nu/y$  is the dynamic exponent. Fisher et al. [5] have suggested that  $z = 1$ .

We report on ac measurements of  $\text{Re}(\sigma_{xx})$  in a sample that exhibits the IQHE, for a frequency ( $f$ ) range (0.2–14 GHz) that has not, to our knowledge, been explored previously. Our broadband  $\text{Re}[\sigma_{xx}(f)]$  data are obtained from the measured transmission loss of an Al transmission line that was patterned on the sample surface. The sample was a GaAs/Al<sub>x</sub>Ga<sub>1-x</sub>As heterojunction grown by liquid phase epitaxy, with density  $n \approx 4.2 \times 10^{11} \text{ cm}^{-2}$ , and mobility  $\mu \approx 4 \times 10^4 \text{ cm}^2/\text{V} \cdot \text{s}$ . Its properties were similar to those of other

<sup>\*</sup> Corresponding author.



It turns out that a reasonable parametrization of disorder is achieved by the zero field localization length  $\xi_0$  (estimated from the temperature dependence in the variable-range hopping regime). As we decrease  $\xi_0$  by increasing  $V_G$ , the width in  $B$  of the quantum Hall conductor decreases continuously until finally the QHE disappears altogether at the critical value  $V_G \approx -2.05$  V ( $\xi \approx 800$  Å). For  $|V_G| > 2.05$  V, a pronounced minimum in  $R_{xx}$  survives but diverges as  $T \rightarrow 0$  as shown in Fig. 4. We suggest that this criticality may be described as a percolation threshold. Lakes of mobile 2D electrons (quantum Hall liquids) become intermingled with islands of localized ones. Source–drain conduction becomes likely when the amount of liquid begins to exceed the amount of land as the disorder is reduced. These observed “critical” behaviors are surprisingly similar to the superconductor–insulator transition found in superconducting films [8].

### 3. Conclusion

The ability to tune disorder has of late become a powerful experimental tool in the study of localization phenomena in 2DEG systems. In particular, we have demonstrated a magnetic-field-induced transition from an Anderson insulator (Hall insulator) to a quantum Hall conductor in a disordered 2DEG system. Consistent with

the global phase diagram, two types of transitions were observed, one brought on by a change in the magnetic field and the other by a change in the disorder. Furthermore, above a critical disorder no transition appears to be possible and the insulating phase persists, irrespective of the magnetic field.

### 4. Acknowledgements

We would like to thank S. Kivelson and S. Feng for useful discussions. H.W.J. acknowledges support from the Alfred Sloan Foundation.

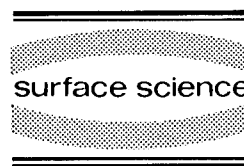
### 5. References

- [1] E. Abrahams, P.W. Anderson, D.C. Licciardello and T.V. Ramakrishnan, *Phys. Rev. Lett.* 42 (1979) 673.
- [2] D.E. Khmel'nitskii, *Phys. Lett.* 106 (1984) 182.
- [3] R.B. Laughlin, *Phys. Rev. Lett.* 52 (1984) 2304.
- [4] S. Kivelson, D.H. Lee and S.C. Zhang, *Phys. Rev. B* 46 (1992) 2223.
- [5] O. Viehweger and K.B. Efetov, *Phys. Rev. B* 44 (1991) 1168.
- [6] For early experimental works see, for example, D.C. Tsui and S.J. Allen, *Phys. Rev. Lett.* 32 (1974) 1200, A.B. Fowler, *Phys. Rev. Lett.* 34 (1975) 15, M. Pepper, *Philos. Mag. B* 37 (1978) 83.
- [7] H.W. Jiang, C.E. Johnson and K.L. Wang, *Phys. Rev. B* 46 (1992) 12830.
- [8] See, for example, M.A. Paalanen, A.F. Hebard and R.R. Ruel, *Phys. Rev. Lett.* 69 (1992) 1604.



ELSEVIER

Surface Science 305 (1994) 126–132



# Quantum Hall liquid–Wigner solid phase boundary

Rodney Price \*, P.M. Platzman, Song He, Xuejun Zhu

*AT&T Bell Laboratories, Murray Hill, NJ 07974, USA*

(Received 7 May 1993; accepted for publication 4 June 1993)

## Abstract

The quantum Hall liquid–Wigner solid phase boundary as a function of filling factor, density (Landau-level mixing) and temperature displays a rich variety of phenomena. More importantly the density and temperature range where these phenomena could take place are in an experimentally accessible regime. This is particularly true because of the availability of hole samples.

We will present results of variational Monte Carlo calculations on the ground-state energy of the liquid and solid. Assuming the transition is first-order, we predict the density-dependent phase boundary at  $T = 0$  for the basic filling factors  $\nu = 1/3, 1/5, 1/7$ , and  $1/9$ . At finite temperatures, treating the excitation spectrum as phonons for the solid and magnetorotons for the liquid, we can calculate the low-temperature properties of the phase boundary. Because the entropy of the solid coming from the low-lying shear modes is large compared to the entropy of the liquid, i.e. there is a gap in the excitation spectrum, we find an interesting regime where the liquid freezes as the temperature is raised. This quantum freezing is analogous to the behavior near the minimum in the melting of the solid helium–superfluid helium boundary.

## 1. Introduction

It is well-known that a two-dimensional system of electrons will form a Wigner solid in two limits: first, as the magnetic field goes to infinity, the size of the cyclotron orbits of the electrons shrinks to the vanishing point, and behaving like classical point charges, they form a Wigner solid; and second, as the density of the system is made very small, the kinetic energy becomes so small with respect to the potential energy of the system

that it is negligible, and again the electrons minimize the potential energy by forming a Wigner solid. In terms of dimensionless parameters  $\nu$  and  $r_s$ , these limits are, respectively,  $\nu \rightarrow 0$  and  $r_s \rightarrow \infty$ .

At the other extreme in density, as  $r_s \rightarrow 0$ , at certain rational filling factors  $\nu = p/q$ , a remarkable quantum liquid, the fractional quantum Hall or Laughlin liquid, forms. Most theoretical work has focused on the Wigner solid–Laughlin liquid phase boundary in the limit of infinite density and magnetic field,  $r_s = 0$ , where no Landau-level mixing occurs [1], which is a good approximation for high-density samples, such as the electron-doped GaAs heterostructures. In these samples,  $r_s$  ranges from 1 to 3 or more, and transport

\* Corresponding author.

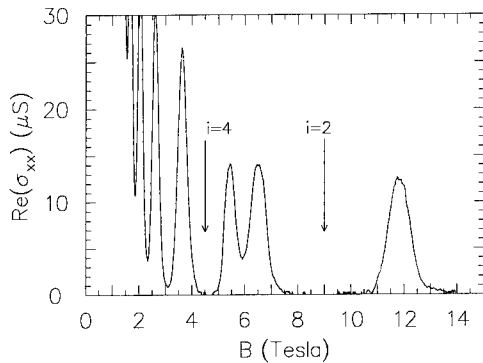


Fig. 1.  $\text{Re}(\sigma_{xx})$  versus  $B$ ;  $f = 6.5$  GHz;  $T \approx 50$  mK.

samples used to study scaling in the IQHE [1,6]. The sample, with a microwave source (implemented with a levelling loop [7]) and a detector, were loaded into the mixing chamber of a top-loading dilution refrigerator. The dc resistances  $R_{xx}$ ,  $R_{xy}$ , and the relative microwave power transmission  $P$  were measured simultaneously.

The transmission line we use is a coplanar waveguide [8] (CPW) meander line. The measured loss in the 2DES occurs mainly under slots in the metallization. The slotwidth  $w \approx 30 \mu\text{m}$ , so the length scale on which the experiment measures  $\sigma_{xx}(f)$  is macroscopic.  $\text{Re}(\sigma_{xx})$  is obtained from the measured  $P$ , by analyzing the CPW arrangement in the quasi-TEM approximation [9].

Fig. 1 shows the  $\text{Re}(\sigma_{xx})$  versus  $B$  at  $f = 6.5$  GHz. The transitions between the 6.5 GHz IQHE minima are wider than the corresponding transitions in dc transport traces. For all our  $f$ ,  $\text{Re}(\sigma_{xx})$  versus  $B$  exhibits broad, flat IQHE minima, with  $\text{Re}(\sigma_{xx}) \rightarrow 0$ , for integer Landau filling factors  $i = 1, 2$  and 4.

For  $f \gtrsim 1$  GHz,  $\sigma_{xx}$  peaks between well-developed IQHE minima widen as  $f$  increases, roughly

as  $(\Delta B) \propto f^\gamma$ , where  $\Delta B$  is the peakwidth, and  $\gamma \approx 0.41$ . The power-law behavior can be interpreted as due to dynamic scaling, where the exponent is related to the  $\tau_c$  exponent as  $\gamma = 1/y$ . The experimentally-determined  $\gamma$  can be combined with existing estimates of  $\nu$  to estimate the dynamic exponent  $z$ . Theoretical [10] and experimental [6] estimates of  $\nu$  are in agreement that  $\nu \approx 7/3$ . This  $\nu$  is close to that obtained from the  $\kappa$  measured in Ref. [1], using  $\nu = p/2\kappa$ , if we assume the effective size of the sample  $L \approx T^{-p/2}$  with  $p = 2$ . Taking  $\nu = 7/3$  together with  $1/y = \gamma \approx 0.41$  gives  $z = \nu/\gamma \approx 1.0$ .

## 1. References

- [1] H.P. Wei, D.C. Tsui, M. Paalonen and A.M.M. Pruisken, Phys. Rev. Lett. 61 (1988) 1294.
- [2] A.M.M. Pruisken, Phys. Rev. Lett. 61 (1988) 1297.
- [3] P.C. Hohenberg and B.I. Halperin, Rev. Mod. Phys. 49 (1977) 435, and references therein.
- [4] S. Kivelson, D.-H. Lee and S.-C. Zhang, Phys. Rev. B 46 (1992) 2223.
- [5] M.P.A. Fisher, G. Grinstein and S.M. Girvin, Phys. Rev. Lett. 64 (1990) 587.
- [6] S. Koch, R.J. Haug, K. von Klitzing and K. Ploog, Phys. Rev. Lett. 67 (1991) 883.
- [7] Hewlett-Packard Application note 183, High Frequency Swept Measurements (1978).
- [8] C.P. Wen, IEEE Trans. Microwave Theory Tech., MTT-17 (1969) 1087.
- [9] T. Itoh, Ed., Planar Transmission Line Structures (IEEE, New York, 1987).
- [10] G.V. Mil'nikov and I.M. Sokolov, JETP Lett. 48 (1988) 536; B. Huckestein and B. Kramer, Phys. Rev. Lett. 64 (1990) 1437; Y. Huo and R.N. Bhatt, Phys. Rev. Lett. 68 (1992) 1375.

experiments [2–4] show strong fractional quantum Hall effects down to the vicinity of  $\nu = 1/5$ . As  $\nu$  approaches  $1/5$ , however, the longitudinal resistivity begins to increase exponentially as the temperature  $T \rightarrow 0$ . At  $1/5$ , the longitudinal resistivity again drops to zero, due to the  $\nu = 1/5$  Laughlin liquid, then below  $1/5$  the steep rise in longitudinal resistivity resumes. This high longitudinal resistivity is widely believed to signal the presence of a pinned Wigner solid.

A recent transport experiment with hole samples [5] has shown a very similar behavior in the vicinity of  $\nu = 1/3$ . The carriers in these samples are heavy holes, and as a consequence of their high effective mass, they can have  $r_s$  from 8 to 15 or more. Landau-level mixing is much more important at high  $r_s$ , as the separation between Landau levels  $\hbar\omega_c \approx 1/\nu r_s^2$ , and the authors cite this increase in Landau-level mixing as the cause of the shift in the phase boundary toward higher  $\nu$ .

Other recent experiments [6,7], done by optical means at somewhat higher temperatures than the transport experiments in electron samples with  $r_s = 1$  to 3, show evidence of fractional quantum Hall states all the way down to  $\nu = 1/9$ . These authors propose a phase diagram in which liquid phases at  $\nu = 1/5$ ,  $1/7$ , and  $1/9$  are surrounded by solid phases, and the solid phase dominates at all  $\nu < 1/9$ .

In this paper we compare the ground-state energies of variational wavefunctions for the liquid and the solid at fixed filling factors  $\nu = 1/3$ ,  $1/5$ ,  $1/7$ , and  $1/9$  as  $r_s$  is allowed to vary. We find a zero-temperature phase transition from liquid to solid at  $r_s^c \approx 22$  for  $\nu = 1/3$ ,  $r_s^c \approx 15$  for  $\nu = 1/5$ , and we find that at zero temperature the solid is always favored over the liquid for  $\nu = 1/7$  and  $1/9$ . Disorder tends to favor the solid phase, lowering  $r_s^c$  somewhat, particularly at  $\nu = 1/5$ . We next calculate free energies for liquid and solid at the same filling fractions by assuming that at low temperatures only the lowest-lying modes are occupied, and we find a curious re-entrant freezing behavior at  $\nu = 1/3$  and  $1/5$  when  $r_s$  is slightly less than the zero-temperature freezing point  $r_s^c$ : as the temperature  $T$  is raised from zero, the liquid freezes into a Wigner solid, then

at still higher temperatures melts again into a Laughlin liquid. At lower filling factors  $\nu = 1/7$  and  $1/9$ , we find melting temperatures consistent with the observation of a Wigner solid in the extremely low-temperature transport experiments, and a Laughlin liquid in the somewhat higher-temperature luminescence experiments.

## 2. Zero temperature

If all the electrons in the system are confined to the lowest Landau level, the ground-state energy  $E_\nu(r_s)$  at a fixed  $\nu$  will go as  $1/r_s$ , since there is no kinetic energy in the system and the potential energy will be on the order of  $e^2/a$ , where  $a = (\pi n)^{-1/2}$ , with  $n$  the particle density. When the magnetic field is finite, however, we can trade off some kinetic energy for an improved potential energy by including basis functions from higher Landau levels in a variational wavefunction. As  $r_s$  increases, the kinetic energy cost of Landau-level mixing drops and the electrons can be localized further, until finally at  $r_s \rightarrow \infty$  the electrons are localized completely and the system forms a Wigner solid with the lowest possible potential energy, the Madelung energy  $E_{cl}(r_s) = -2.212/r_s$ . (Energy is given in units of  $(e^2/\epsilon)/2a_B$ , where  $a_B$  is the Bohr radius.) At  $\nu = 1/3$ , for instance,  $E_{1/3}(r_s) = -2.009/r_s$  for the Laughlin wavefunction, which is entirely in the lowest Landau level. At some intermediate  $r_s$  the total energy must drop more rapidly than  $1/r_s$  to approach the Madelung energy.

A variational wavefunction for the liquid which interpolates in some sense between a wavefunction with the lowest possible kinetic energy, the Laughlin wavefunction, and a wavefunction with the lowest possible potential energy, in which the electrons are completely localized, might be expected to be a good variational choice. To that end, we have chosen a variational wavefunction that consists of the Laughlin wavefunction  $\psi_m$  ( $m = 1/\nu$ ) multiplied by a Jastrow factor  $\prod_{i < j} e^{-\alpha/\sqrt{r_{ij}}}$ , where  $r_{ij}$  is the distance between the  $i$ th and  $j$ th particles and  $\alpha$  is the variational parameter. When  $\alpha = 0$ , we recover the Laughlin

wavefunction, and when  $\alpha \neq 0$ , the wavefunction is no longer analytic and higher Landau levels are mixed in. The Jastrow factor introduces more correlations into the wavefunction, lowering the potential energy, while introducing a kinetic energy cost.

Details of the calculation are given in Ref. [8], so we will only review it briefly here. We used the spherical geometry, in which our wavefunction becomes

$$\psi_m^\alpha = \prod_{i < j} (u_i v_j - u_j v_i)^m \exp\left(\frac{-\alpha}{|u_i v_j - u_j v_i|^{1/2}}\right), \quad (1)$$

where  $u_i \equiv e^{-i\phi_i/2} \cos(\theta_i/2)$ ,  $v_i \equiv e^{i\phi_i/2} \sin(\theta_i/2)$  are convenient spinor coordinates, and the distance between particles  $i$  and  $j$  is taken as the chord distance  $r_{ij} = 2R|u_i v_j - u_j v_i|$ . The Hamiltonian can be written as

$$H = \frac{1}{r_s^2} T + \frac{2}{r_s} V - \frac{2}{r_s} N^{3/2}, \quad (2)$$

where  $T$  is the kinetic energy operator,  $V$  is the potential energy operator and the last term is the contribution from the uniform background charge. Then the energy of the system becomes

$$E_\nu(\alpha, r_s) \equiv \langle \psi_\alpha^\nu | H | \psi_\alpha^\nu \rangle = \frac{1}{r_s^2} T_\nu(\alpha) + \frac{2}{r_s} V_\nu(\alpha) - \frac{2}{r_s} N^{3/2}, \quad (3)$$

where  $T_\nu(\alpha) = \langle \psi_\alpha^\nu | T | \psi_\alpha^\nu \rangle$  and  $V_\nu(\alpha) = \langle \psi_\alpha^\nu | V | \psi_\alpha^\nu \rangle$ . We evaluated the energy of the wavefunction using the Metropolis algorithm, but instead of choosing an  $r_s$  before the Monte Carlo code ran and doing a minimization at that time, we evaluated  $T_\nu(\alpha)$  and  $V_\nu(\alpha)$  for a sufficient number of values of  $\alpha$  to fit a smooth curve to the points, and did the minimization for some particular  $r_s$  after the Monte Carlo code ran. In this way we avoided duplicating calculations for different  $r_s$ , and the curve fitting was used to average out some of the remaining statistical noise in the Monte Carlo estimates of  $T_\nu(\alpha)$  and  $V_\nu(\alpha)$ .

In order to determine the value of  $r_s$  at the liquid–solid phase boundary we need a rather

accurate evaluation of the solid. Lam and Girvin [1] evaluated the energy of a correlated Wigner solid wavefunction

$$\Psi = \exp\left(\frac{1}{4} \sum'_{i,j} \xi_i B_{ij} \xi_j\right) \prod_i \phi_{R_i}(z_i), \quad (4)$$

where  $\xi_i = z_i - R_i$ ,  $B_{ij} \equiv B(R_i - R_j)$ , and

$$\phi_{R_i}(z_i) = \exp\left(-\frac{1}{4} \left[|z_i - R_i|^2 - (z_i^* - z_i R_i^*)\right]\right). \quad (5)$$

Here  $z_i = x_i + iy_i$  is the  $i$ th particle position and  $R_i = X_i + iY_i$  is the  $i$ th lattice site.  $\Psi$  is the harmonic crystal wavefunction restricted to the lowest Landau level, and the variational parameters  $B_{ij}$  are calculated by using the values derived from the harmonic crystal. However, in order to make a reasonable comparison of solid and liquid wavefunctions, we need, as discussed above, a wavefunction which includes Landau-level mixing.

Zhu and Louie [9] have recently completed a study of the ground-state energy of the Wigner crystal including Landau-level mixing. Their calculation is similar to Lam and Girvin's, except that two more variational parameters were added to the wavefunction to put in more correlations at the expense of some Landau-level mixing. They first followed Lam and Girvin's method with the exception that the gaussians in the single-particle wavefunctions (5) were "squeezed" to move the electrons farther away from each other, by making the replacement

$$\exp\left(-\frac{1}{4}|z_i - R_i|^2\right) \rightarrow \exp\left(-\beta|z_i - R_i|^2\right). \quad (6)$$

Varying the parameter  $\beta$  away from  $1/4$  introduces Landau-level mixing into the wavefunction because the single-particle wavefunctions  $\phi_\beta(R_i)$  are no longer eigenstates of the single-particle Hamiltonian. Zhu and Louie then multiply the wavefunction by another Jastrow factor, and the wavefunction, with two variational parameters  $\alpha$  and  $\beta$  is then

$$\Psi = \exp\left(\sum'_{i,j} \left[\frac{1}{4} \xi_i B_{ij} \xi_j - \frac{\alpha}{2} u(|z_i - z_j|)\right]\right) \times \prod_i \phi_\beta(R_i), \quad (7)$$

where

$$u(r) = \frac{1}{\sqrt{r}} (1 - e^{-\sqrt{r/F} - r/2F}), \quad (8)$$

and  $F$  is a constant chosen to optimize the pseudo-potential at small  $r$ . Zhu and Louie varied  $B_{ij}$  as well as  $\beta$ , but found that varying  $B_{ij}$  had very little effect on the energy, as Lam and Girvin had suggested. The quantum Monte Carlo calculations were done with modified periodic boundary conditions [9], which require the addition of an unimportant phase factor to the single-particle wavefunctions (5).

In addition to all uncertainties connected with accuracy in the calculation for the liquid and solid energy in the absence of impurities, we must concern ourselves, at least qualitatively, with the effects of impurities. Even in the best samples we expect the electrons to couple to a rather slowly varying random potential produced by the dopant atoms, typically Si, offset from the interface by hundreds of ångströms. The electrons can in fact lower their energy somewhat by changing their local density to accommodate the local impurity potential. Since the liquid is incompressible at fillings like  $\nu = 1/3$ , to lowest order in the potential fluctuations, it will not be able to do this. The solid on the other hand is compressible. For a weak smoothly varying potential, simple arguments based on an elastic medium description of the WS indicate that the energy gained by the solid is very roughly [10]

$$E_{\text{imp}} \approx \frac{1}{2} m v_t^2 \left( \frac{\alpha}{\xi} \right)^2 = \frac{0.138}{r_s} \left( \frac{\alpha}{\xi} \right)^2, \quad (9)$$

where  $v_t = (0.138 e^2 / m a)^{1/2}$  is the transverse sound velocity in the absence of the magnetic field and  $\xi$  is the correlation length for the distorted WS. Depending on the quality of the sample, we might expect  $5a < \xi < 50a$ . If  $\xi = 50a$ , the effect on the solid energy will be minimal, and the solid energy will be given by the upper solid line in Fig. 1, whereas if  $\xi = 5a$ , the solid energy will be shifted to the value shown by the lower solid line. At  $\nu = 1/3$  the solid energy crosses the liquid energy at a relatively large angle, so if we take  $\xi = 5a$  the transition point may change by  $\Delta r_s \approx 2$  or 3, but at  $\nu = 1/5$ , the

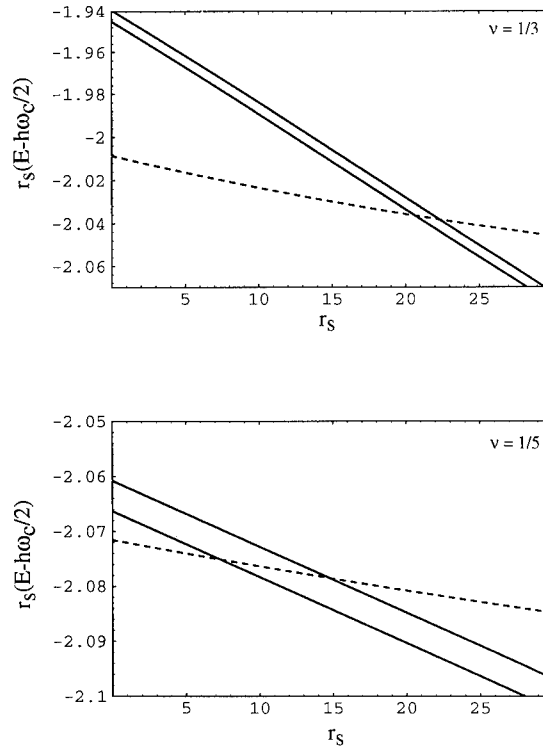


Fig. 1. Liquid and solid energies as a function of  $r_s$  for the  $\nu = 1/3$  and  $\nu = 1/5$  state. The dashed curves are liquid energies, and the solid lines are linear interpolations between the points at  $r_s = 2$  and  $r_s = 20$  of Zhu and Louie, both with and without impurities (assuming  $\xi = 5a$ ).

slope of the two curves is more nearly equal, and the transition point may change by  $\Delta r_s \approx 10$  or more. Of course, we do not know the coherence length, and (9) is only a rough estimate.

### 3. Finite temperature

At finite temperature, we need to know something about the excited states of the system as well as the ground-state energies in order to make comparisons between the liquid and the solid. However, because the temperatures of interest are so low, we need only know the lowest-lying modes  $\omega_k$  of both the solid and the liquid to calculate the free energy. Then the free energy is

$$F = E + T \sum_k \log(1 - e^{-\omega_k/T}), \quad (10)$$

where  $E$  is the ground-state energy and the  $\omega_k$  are the lowest lying excitations of either the liquid or the solid. For the Wigner solid these excitations are the transverse magnetophonons  $\omega_k^{\text{WS}}$ . We evaluated the free energy  $F^{\text{WS}}$  of the solid using the ground-state energy  $E^{\text{WS}}$  from Ref. [9], and the harmonic magnetophonons  $\omega_k^{\text{WS}}$  calculated in the same way as Bonsall and Maradudin [12]. The sum in (10) was evaluated by averaging over the Brillouin zone by the method of Cunningham [13], so the result is exact in the harmonic approximation. It is useful, however, to examine the form of the transverse magnetophonons in the long-wavelength limit

$$\omega_k^{\text{WS}} \approx 0.526 \left( \frac{\nu}{r_s} \frac{e^2/\epsilon}{2a_B} \right) (ka)^{3/2}. \quad (11)$$

Substituting into (10) we find

$$F^{\text{WS}} \approx E^{\text{WS}} - 0.701 \left( \frac{r_s}{\nu} \frac{2a_B}{e^2/\epsilon} \right)^{4/3} T^{7/3}, \quad (12)$$

and the free energy of the solid phase goes as  $T^{7/3}$  at low temperatures.

On the liquid side, since we are interested primarily in the lowest-lying modes of the magnetoroton spectrum, we can approximate the magnetoroton mode by

$$\omega_k^{\text{LL}} = \frac{(k - k_R)^2}{2m_R} + \Delta_R, \quad (13)$$

where  $m_R$  is an effective mass for the magnetorotons near the minimum. Here we have used the magnetoroton spectrum calculated in the lowest Landau level. In Ref. [17] Girvin, MacDonald, and Platzman find that the magnetoroton spectrum becomes flat at large  $k$ , which if continued to  $k \rightarrow \infty$  would cause the free energy to diverge at any  $T > 0$ . Diagonalizations of small systems, however, show that the magnetoroton spectrum always cuts off at some finite  $k$ , followed at higher  $k$  by other states with rapidly rising energy, thus avoiding this divergence. Then only the lowest-lying magnetoroton modes are important, and a parabolic approximation to the spectrum works well.

Rappe, Zhu, and Louie [14] have very recently calculated the magnetoroton spectrum as a func-

tion of  $r_s$  for  $\nu = 1/3$ , and find that at  $r_s = 20$ , the magnetoroton spectrum has fallen only about 10% below the lowest Landau level value. At  $\nu = 1/5$ ,  $1/7$ , and  $1/9$  the amount of Landau-level mixing found in Ref. [8] is much less than that found at  $\nu = 1/3$ , so using the lowest Landau-level spectrum is an excellent approximation. Assuming that only the modes in the vicinity of the minimum contribute, the free energy per particle of the liquid is

$$F^{\text{LL}} = E^{\text{LL}}(r_s) - (2\pi m_R)^{1/2} \frac{k_R l^2}{\nu} T^{3/2} e^{-\Delta_R/T}, \quad (14)$$

which goes exponentially at small  $T \leq \Delta_R$ .

Because the excitations of the liquid display a gap, at very low temperatures  $T \ll \Delta_R$ , even the lowest lying modes at the minimum  $k_R$  remain unoccupied, while the low-lying modes of the solid, which have no gap, begin to fill immediately. The free energy of the solid then falls as a power of  $T$ , while the free energy of the liquid remains constant. In this range of temperature, if we have chosen  $r_s$  such that the liquid ground state is favored only slightly, the growing entropy of the solid can cause the free energy of the solid to drop below that of the liquid, and the system freezes into a Wigner solid as temperature rises. When the temperature begins to approach the roton gap energy, however, the free energy of the liquid begins to fall exponentially as the states become occupied. Because the density of states at the roton gap energy is very large, this exponential rise is very rapid and the liquid free energy quickly falls below that of the solid, and the system melts into a Laughlin liquid once again.

In Fig. 2 we have plotted the phase boundary as a function of  $r_s$  and  $T$  for a hole sample with effective mass  $m^* = 0.3m_e$  at filling factor  $\nu = 1/3$  and  $1/5$ . The phase boundary at  $\nu = 1/3$  behaves as expected: there is a temperature region for  $r_s \leq r_s^c$  where the liquid is stable at  $T = 0$ . The liquid freezes, in this case at a temperature of  $\sim 1$  K, followed by a magnetoroton entropy triggered melting at  $\sim 3$  K. The effects of impurities will shift the boundary to the left by a small amount in  $r_s$ , and may also push the top

of the phase boundary down somewhat. At  $\nu = 1/5$ , impurities play a much larger role, since the energy difference between liquid and solid is much smaller, but we would expect the general features of the phase diagram to remain; that is, below  $r_s^c$ , the system remains a liquid at all temperatures, well above  $r_s^c$  the system is a solid at low temperatures, melting at some point probably lower than shown in Fig. 2, and just above  $r_s^c$  a narrow re-entrant regime exists.

The phase boundaries for  $\nu = 1/7$  and  $1/9$  for an electron sample with  $m^* = 0.068m_e$  are shown in Fig. 3. Here the ground-state energy of the solid is lower than that of the liquid for all  $r_s$ , so there is no re-entrant melting possible. The relationship of the melting temperature, shown as the solid lines, to the size of the magnetoroton gap, shown as the dash-dotted lines, is clearly visible. Melting, as a rule, will occur roughly at some constant fraction of the magnetoroton gap. The melting temperatures we find are roughly comparable to the classical Kosterlitz–Thouless melting temperature, although there is no theoretical reason to expect them to be closely related.

Disorder in the sample will have varying effects on the ground-state and temperature-de-

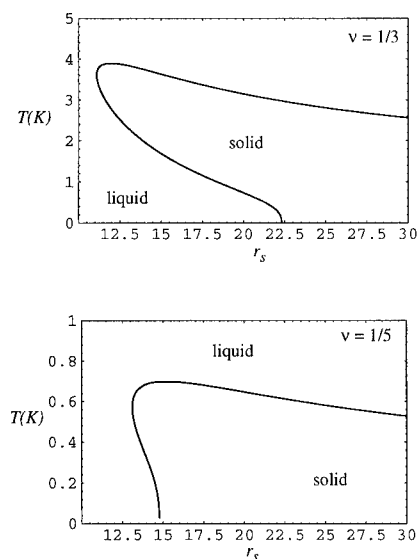


Fig. 2. The finite-temperature liquid–solid phase boundary at  $\nu = 1/3$  and  $1/5$ , where  $m^* = 0.3m_e$ . Impurity effects are not shown in this plot.

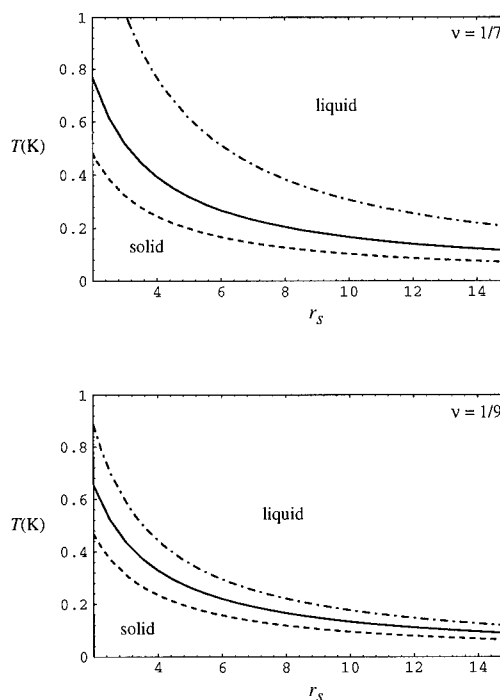


Fig. 3. The phase boundary between Wigner solid and Laughlin liquid at  $\nu = 1/7$  and  $1/9$ . The solid line is the boundary in the absence of disorder, the dashed line is the boundary when an estimate of disorder effects is included, and the dash-dotted line is the theoretical  $\Delta_R$ .

pendent parts of (14) and (12). The ground-state energy of the liquid is to lowest order independent of the disorder in the sample, while as we have seen, the solid ground-state energy falls relative to the liquid by an amount given in (9). The lowest-lying modes of the solid and liquid are affected in different ways as well. The magnetoroton gap of the liquid is significantly reduced by disorder [15,16]. At  $\nu = 1/5$ ,  $\Delta_R$  is measured in transport experiments [3] as 1.1 K, while the single-mode approximation of Ref. [17] which we have used gives  $\Delta_R = 5.6$  K for the sample of Ref. [3]. The luminescence measurements give magnetoroton gaps  $\Delta_R \leq 0.4$  K at  $\nu = 1/7$ , and  $\Delta_R \leq 0.25$  K at  $\nu = 1/9$  for a sample with  $r_s = 2.3$ . These experiments measure the magnetoroton energy at small  $k$ , not at the magnetoroton minimum, so they may be high by a factor of two or more. The presence of disorder will open a small gap in the magnetophonon spectrum, but this gap



will have a negligible effect on the free energy of the solid, since it is centered at the origin of the Brillouin zone, where the density of states is small.

The result of moving the ground-state energy of the solid down by setting the correlation length  $\xi = 5a$  and using the measured values of  $\Delta_R$  from the luminescence experiments are shown in Fig. 3 as the dashed line. In spite of the shift in ground-state energy favoring the solid at low temperatures, the exponential drop in the free energy of the liquid near the magnetoroton gap temperature moves the melting temperature down to about 400 mK for both  $\nu = 1/7$  and  $1/9$ . If the true  $\Delta_R$  is half the measured value, this temperature may be expected to fall very roughly by half as well. Of course, we do not know the precise amount of disorder in the samples, but our calculation shows that the Wigner solid may melt at a temperature equivalent or slightly below those of the luminescence experiments, while remaining a solid at the lower temperatures of the transport experiments.

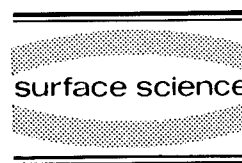
#### 4. References

- [1] P.K. Lam and S.M. Girvin, Phys. Rev. B 30 (1984) 473.
- [2] R.L. Willett et al., Phys. Rev. B 38 (1988) 7881.
- [3] H.W. Jiang et al., Phys. Rev. Lett. 65 (1990) 633.
- [4] V.J. Goldman, M. Santos, M. Shayegan and J.E. Cunningham, Phys. Rev. Lett. 65 (1990) 2189.
- [5] M.B. Santos et al., Phys. Rev. Lett. 68 (1992) 1188.
- [6] H. Buhmann et al., Phys. Rev. Lett. 65 (1990) 633.
- [7] H. Buhmann et al., Phys. Rev. Lett. 66 (1991) 926.
- [8] R. Price, P.M. Platzman and S. He, Phys. Rev. Lett. 70 (1993) 339.
- [9] X. Zhu and S.G. Louie, Phys. Rev. Lett. 70 (1993) 335.
- [10] P. Lee and T.M. Rice, Phys. Rev. B 19 (1975) 3970.
- [11] D. Ceperley, Phys. Rev. B 18 (1978) 3126.
- [12] L. Bonsall and A.A. Maradudin, Phys. Rev. B 15 (1977) 1959.
- [13] S.L. Cunningham, Phys. Rev. B 10 (1974) 4988.
- [14] Rappe, X. Zhu and S.G. Louie, to be published.
- [15] G.S. Boebinger, A.M. Chang, D.C. Tsui and H.L. Stormer, Phys. Rev. Lett. 55 (1985) 1606.
- [16] A.H. MacDonald, K.L. Liu, S.M. Girvin and P.M. Platzman, Phys. Rev. B 33 (1986) 4014.
- [17] S.M. Girvin, A.H. MacDonald and P.M. Platzman, Phys. Rev. B 33 (1986) 2481.



ELSEVIER

Surface Science 305 (1993) 133–138



## Transport properties between quantum Hall plateaus

Dmitri B. Chklovskii \*, Patrick A. Lee

*Department of Physics, Massachusetts Institute of Technology, Cambridge, MA 02139, USA*

(Received 16 April 1993; accepted for publication 13 June 1993)

### Abstract

We propose a unified transport theory for the two-dimensional electron gas (2DEG) in the dissipative quantum Hall regime in the presence of a long-range disorder. We find that the evolution of the longitudinal conductivity peaks as a function of the disorder can be described by a single parameter  $\beta^{-1}$  which is determined by the typical gradient of the electron density fluctuations. In the case of relatively strong disorder we utilize the edge states network model to describe transport in a half-filled Landau level. In the fractional quantum Hall regime we apply the network model to the system of composite fermions finding universal values of the resistivity at even-denominator filling fractions. The breakdown of the network model takes place at weak disorder because the edge channels develop into wide compressible strips and at strong disorder because of the destruction of the incompressible strips, isolating the edge channels. We find the limits of the applicability of the network model in terms of  $\beta$ . In the limit of very weak disorder the system is effectively a Fermi-liquid of composite fermions. We calculate the conductivity in this regime by considering the motion of non-interacting fermions in a spatially varying magnetic field arising from the density fluctuations. The resistivity is found to scale linearly with the magnetic field with the slope given by  $\beta^{-1}$ . Although the presence of the non-local transport makes measurements of the resistivity difficult, we find qualitative and in some cases quantitative agreement with experiment.

Until recently, most studies of the quantum Hall effect focused on the dissipationless regime characterized by a quantized Hall conductance [1]. Much less attention was given to the dissipative regime, which is characterized by an unquantized Hall conductance and a finite longitudinal resistivity. A brief look at experimental data, Fig. 1, reveals an extraordinary diversity of the observed longitudinal resistivity values, which seem to vary from sample to sample. Recently a significant effort was devoted to providing some theoretical basis for the dissipative regime. The sev-

eral approaches to this problem include the network model [2–4], the law of corresponding states [5,6], and the Fermi-liquid description [7,8]. However, it is not clear what the relationship between those theories is and whether they can explain the diversity in experimental data.

The purpose of this paper is to incorporate these approaches into a single picture, in which the relationship between various regimes is determined by a single parameter reflecting the level of disorder, and to find the longitudinal resistivity for different values of the parameter. We are able to do this for the case of high-mobility GaAs heterostructures where disorder is known to be of long-range nature: it comes from a non-uniform

\* Corresponding author.

distribution of donors set back from the 2DEG plane by the spacer thickness  $d_s$ . Due to very good screening by the 2DEG at zero magnetic field the long-range disorder potential is translated into electron density fluctuations. The characteristic length scale of these fluctuations is of the order of  $d_s$ , while the ratio of the average electron density,  $n_e$ , to the typical amplitude of the density fluctuations,  $\delta n_e$ , provides a natural large parameter  $\beta$ , on which our theory is based.

The value of  $\beta$  can be found approximately from the following consideration [9,10]. In an ungated heterostructure the concentration of ionized donors is equal to the electron concentration  $n_e$ . The number of ionized donors in a square with side  $d_s$  is equal to  $n_e d_s^2$ . The typical fluctuation in the number of donors is given by  $(n_e d_s^2)^{1/2}$ . This leads to the value of the relative density fluctuation  $\beta = n_e / \delta n_e \approx \sqrt{n_e} d_s$ . A more rigorous calculation for the case of an uncorrelated donor distribution yields [11]

$$\beta = \sqrt{8\pi n_e} d_s. \quad (1)$$

In typical high-quality heterostructures  $\beta \approx 10$ –40.

Our basic picture is that in a strong magnetic field, at a filling factor between the quantum Hall plateaus, the electron system breaks up into incompressible regions corresponding to the integer or fractional states [9,12], Fig. 2. Those regions are separated by edge channels which form a percolating network. We refer to these channels as the bulk edge channels. Depending on the value of  $\beta$  and the filling factor the bulk edge channels can be either wide or narrow, which turns out to be crucial for transport properties.

Although the longitudinal resistivity is measured at a fixed value of  $\beta$  with magnetic field being varied, it is enlightening to consider the evolution of resistivity between the quantum Hall plateaus with the variation of  $\beta$ , while neglecting the electron spin.

First, let us focus on the resistivity at a half-integer filling factor. In the case of strong disorder (small  $\beta$ ) peaks in longitudinal resistivity between the IQHE plateaus become infinitely sharp at low

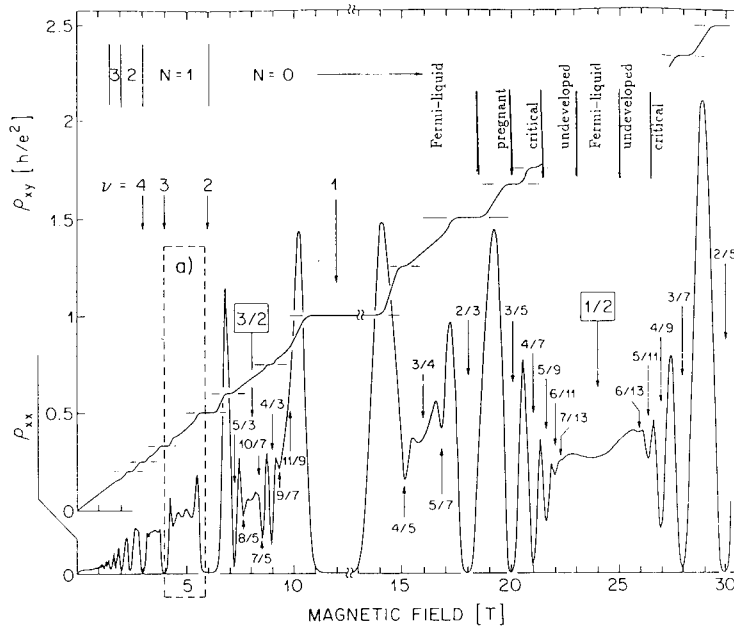


Fig. 1.  $\rho_{xx}$  and  $\rho_{xy}$  as a function of the magnetic field in a very high-mobility heterostructure. (Source: Willett et al. [23].) We have added labels to indicate our diagnosis of the principal sequence peaks. Notice that the scale is reduced by the factor 2.5 for magnetic fields higher than 12 T.

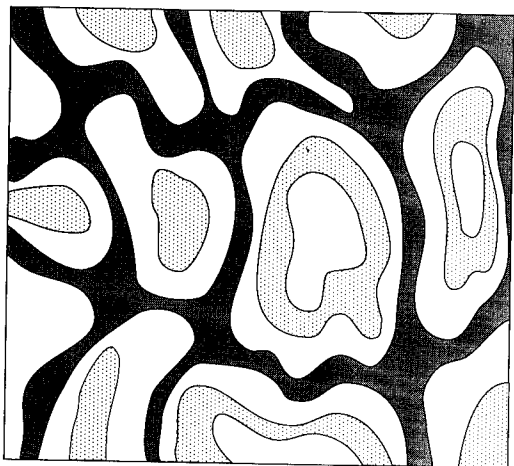


Fig. 2. Break-up of the electron system into the incompressible and compressible liquid regions. White regions represent incompressible liquid, while shaded regions correspond to compressible liquid: localized edge channels are dotted, extended channels are gray.

temperature. The related critical phenomena was studied extensively both theoretically and experimentally [13]. Thus, we call this peak critical. In this case the bulk edge channels are very narrow allowing one to describe them as one-dimensional channels comprised in a network. It was found in Refs. [2,3] by using the Landauer formula that the conductivity tensor of such a network, simplified to a square lattice, Fig. 3, is

$$\begin{aligned}\sigma_{xx}^N &= 1/2(e^2/2\pi\hbar), \\ \sigma_{xy}^N &= 1/2(e^2/2\pi\hbar),\end{aligned}\quad (2)$$

where  $N$  stands for the Landau level number. The same conductivity tensor has been found [14]

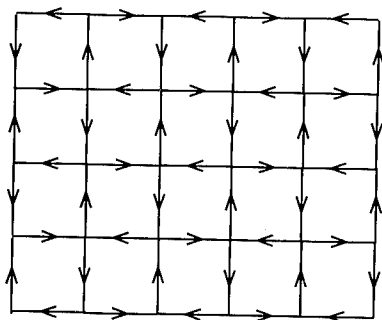


Fig. 3. The simplified network of directed (edge or snake) channels.

in a numerical simulation of a system of non-interacting electrons with short-range disorder, suggesting that this value may be universal. Thus, we find that the contribution of the topmost Landau level is independent of its number. The lower Landau levels contribute only to the Hall conductivity. Therefore, the longitudinal resistivity peaks should scale as magnetic field squared.

As  $\beta$  is increased, the typical gradient of the electron density distribution at zero magnetic field becomes smaller and the bulk edge channels acquire a finite width [10,15–17], developing into strips of compressible liquid. When a bulk edge channel is wide it cannot be described as a one-dimensional channel. The value of the chemical potential may vary across the channel [18,19] making the network model invalid. Consequently, the peak's height is reduced from its critical value and the peak does not look as sharp. We call this peak "pregnant" because it is about (as disorder is reduced) to give birth to the fractional states.

At larger values of  $\beta$  there is a slight depression in the longitudinal resistivity rather than a peak at a half-integer filling factor. The edge channel network disappears because the compressible liquid occupies the whole plane. Such a system is a Fermi-liquid of composite fermions [7,8]. Exactly at a half-integer filling factor the average effective magnetic field acting on fermions is zero. The variation of the filling factor leads to the appearance of the Shubnikov-de Haas oscillations which develop into the quantum Hall effect. Thus, the principal sequence of the FQHE is interpreted in terms of the IQHE for the composite fermions [21]. This leads to a straightforward generalization of the evolution picture to the FQHE regime, in which a quantitative estimate can be carried out.

At sufficiently low disorder (large  $\beta$ ) a peak in the longitudinal resistivity between the FQHE plateaus develops. It becomes critical when the incompressible strips on both sides of the bulk edge channels get wide enough to suppress tunneling across them, which would lead to the admixing of the lower Landau levels to the topmost one. At even larger values of  $\beta$  the fractional peak becomes pregnant because the bulk edge channels acquire a finite width. This shows up in

the reduction of the peak's height. As  $\beta$  is increased further, the peak turns into a Fermi-liquid state and starts giving birth to the daughter states of the next generation of fractions.

To summarize the discussion, the whole lifecycle ( $\beta$  playing the role of time) of a given resistivity peak consists of four periods. The development of the peak is characterized by the growth of the peak's height and the decrease in the resistivity at the adjacent odd denominator fractions. Then the peak becomes critical making it infinitely narrow at zero temperature. In the next stage the peak is pregnant, its height reduced. Then it starts giving birth to the daughter states while staying in the Fermi-liquid regime. At this stage it would be more correct to talk about the even denominator fraction and its vicinity rather than about the peak.

We would like to point out that our picture is for the case of experimentally available temperatures. In the limit of zero temperature the question of localization of the compressible liquid has to be addressed.

Now we can go back to the experimentally relevant situation where the value of  $\beta$  is fixed for a given sample, Fig. 1. We argue [20] that the effective measure of disorder is different from peak to peak or, in other words, the values of  $\beta$  determining transitions between various regimes for a given peak depend on the peak's filling factor. Because of this, in Fig. 1 some peaks are undeveloped, while some are critical and some are pregnant; a few have turned into a Fermi-liquid state.

Let us consider fractions of the principal sequence of the FQHE defined by the filling factor  $\nu = p/(2p+1)$ , where  $p$  is a positive or negative integer [21]. The corresponding resistivity peaks at  $\nu = (2p-1)/(4p)$  fall into one of the following categories as shown in Fig. 1:

$$\begin{aligned} &\text{pregnant peaks,} && \text{if } |p| < p_{c1}, \\ &\text{critical peaks,} && \text{if } p_{c1} < |p| < p_{c2}, \\ &\text{undeveloped peaks,} && \text{if } |p| > p_{c2}. \end{aligned} \quad (3)$$

By developing the approach of Ref. [15], we estimated the widths of compressible and incom-

pressible strips from electrostatic considerations as a function of  $\beta$  and  $p$  [20]. It was found in Refs. [19,20] that a compressible strip width shrinks exponentially fast after becoming of the order of  $p^2 l_H$ , where  $l_H$  is the magnetic length ( $p^2$  appears here because the difference in the filling factors between neighboring principal sequence states is  $\sim 1/p^2$ , while the chemical potential discontinuity is independent of  $p$ ). Based on this result, we find  $p_{c1}$  by setting the compressible strip width equal to  $p_{c1}^2 l_H$ :

$$p_{c1} \approx \sqrt{\beta/2}. \quad (4)$$

Tunneling through an incompressible strip is exponentially suppressed on the scale of the magnetic length in the IQHE regime. We believe that this can be generalized to the FQHE regime by using the effective magnetic length of composite fermions  $l_H^f = l_H \sqrt{2p+1}$ . By setting the typical width of the an incompressible strip equal to  $l_H^f$  we find [20]

$$p_{c2} \approx (\beta/2)^{4/5}. \quad (5)$$

We note that the numerical factors in Eqs. (4,5) should not be taken seriously.

It is possible to calculate the resistivity at even-denominator filling factors in the critical and the Fermi-liquid regime. The values of the resistivity for the critical peaks in the principal sequence can be found by applying Eq. (2) to the fermion system, which is at half integer filling factor. Making transformation to the electron resistivity tensor as outlined in Ref. [7] we find for the principal sequence peaks at filling factor  $(2p-1)/(4p)$ :

$$\begin{aligned} \rho_{xx} &= \frac{2\pi\hbar}{e^2} \frac{1}{2p^2 - 2p + 1}, \\ \rho_{xy} &= -\frac{2\pi\hbar}{e^2} \frac{4p^2 - 2p + 1}{2p^2 - 2p + 1}. \end{aligned} \quad (6)$$

These transport coefficients are identical to those previously obtained in Ref. [6] by mapping the fractional filling factor system onto the dirty boson model and taking the boson conductivity such that it yields the universal value (2) for the IQHE.

Thus, our results are in agreement with the law of corresponding states [5,6]. Eqs. (6) can be straightforwardly generalized to other filling factors [20].

It is difficult to extract the values of resistivity from experimental data because of non-local transport effects [22]. Ignoring this problem we find that the universal resistivity values (6) agree with the relative peak heights observed experimentally [23,24], but only in one case [25] with the absolute values. We believe that the use of the Corbino geometry or non-contact measurements will be helpful to verify our predictions.

The resistivity of the Fermi-liquid states can also be found by considering the composite fermion system. At half-integer filling factors the average effective magnetic field acting on fermions is zero. However, the electron density fluctuations lead to the appearance of the spatially fluctuating magnetic field normal to the electron plane. It was argued in Refs. [7,8] that scattering on these fluctuations gives the main contribution to the resistivity. The problem is effectively reduced to the motion of non-interacting fermions in a spatially fluctuating magnetic field. Although we were able to solve the case of a random magnetic field only approximately, we found an exact solution for the problem in which the effective magnetic field takes only two values. Because the fermion cyclotron radius is smaller than  $d_s$ , the major contribution to conductivity comes from the states that are localized along the lines of zero magnetic field. These are the snake states [26] and they are similar to the edge states in that they can have only one direction of the velocity. The snake states form a network, Fig. 3, similar to the one of Refs. [2–4], for which we find the conductivity tensor by generalizing Eq. (2). Then we make a transformation to the electron resistivity, finding, in agreement with an approximate estimate for the random magnetic field [20] case, that the physical resistivity at half-integer filling factors should scale linearly with the external magnetic field:

$$\rho_{xx} = B/\beta n_e e c. \quad (7)$$

We were able to extend this result to the even-denominator fractions of the principal sequence,

thus explaining the observation made in Refs. [27,28] regarding the linearity of  $\rho_{xx}$ . In fact, the parameter  $\beta$  has been introduced phenomenologically in Ref. [28].

We acknowledge many helpful discussions with B.L. Altshuler, B.I. Halperin, L.S. Levitov, K.A. Matveev, P. McEuen, I.M. Ruzin, B.I. Shklovskii, X.G. Wen. We are grateful to the authors of Refs. [11,19,24,28] for sending us their papers prior to publication. This research was supported by the NSF under grant no. DMR 89-13624.

## 1. References

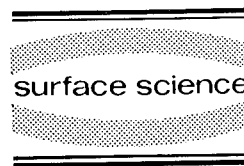
- [1] R.E. Prange and S.M. Girvin, Eds., *The Quantum Hall Effect* (Springer, New York, 1987).
- [2] J. Kucera and P. Streda, *J. Phys. C* 21 (1988) 4357.
- [3] A. Szafer, A.D. Stone, P.L. McEuen and B.W. Alphenaar, *Proceedings NATO ASI on Granular Electronics*, Il Ciocco, 1990.
- [4] J.T. Chalker and P.D. Coddington, *J. Phys. C* 21 (1988) 2665.
- [5] J.K. Jain, S.A. Kivelson and N. Trivedi, *Phys. Rev. Lett.* 64 (1990) 1297, 1993(E).
- [6] S. Kivelson, D.-H. Lee and S.-C. Zhang, *Phys. Rev. B* 46 (1992) 2232; D.-H. Lee, S.A. Kivelson and S.-C. Zhang, *Phys. Rev. Lett.* 68 (1992) 2386.
- [7] B.I. Halperin, P.A. Lee and N. Read, *Phys. Rev. B* 47 (1993) 7312.
- [8] V. Kalmeyer and S.-C. Zhang, *Phys. Rev. B* 46 (1992) 9889.
- [9] S. Luryi, in: *High Magnetic Fields in Semiconductor Physics*, Ed. G. Landwehr (Springer, New York, 1987).
- [10] A.L. Efros, *Solid State Commun.* 65 (1988) 1281.
- [11] F.G. Pikus and A.L. Efros, *Phys. Rev. B* 47 (1993) 16395.
- [12] A.L. Efros, *Solid State Commun.* 67 (1988) 1019.
- [13] See, e.g., H.P. Wei, S.Y. Lin, D.C. Tsui and A.M.M. Pruisken, *Phys. Rev. B* 45 (1992) 3926 and references therein.
- [14] Y. Huo, R.E. Hetzel and R.N. Bhatt, *Phys. Rev. Lett.* 70 (1993) 481.
- [15] D.B. Chklovskii, B.I. Shklovskii and L.I. Glazman, *Phys. Rev. B* 46 (1992) 4026; 46 (1992) 15606(E).
- [16] C.W.J. Beenakker, *Phys. Rev. Lett.* 64 (1990) 216.
- [17] A.M. Chang, *Solid State Commun.* 74 (1990) 871.
- [18] D.B. Chklovskii, K.A. Matveev and B.I. Shklovskii, *Phys. Rev. B* 47 (1993) 12605.
- [19] N.R. Cooper and J.T. Chalker, *Phys. Rev. B* 48 (1993) 4530.
- [20] D.B. Chklovskii and P.A. Lee, *Phys. Rev. B* 48 (1993) 18060.

- [21] J.K. Jain, Phys. Rev. Lett. 63 (1989) 199.
- [22] J.K. Wang and V.J. Goldman, Phys. Rev. Lett. 67 (1991) 749, Phys. Rev. B 45 (1992) 13479.
- [23] R. Willett, J.P. Eisenstein, H.L. Störmer, D.C. Tsui, A.C. Gossard and J.H. English, Phys. Rev. Lett. 59 (1987) 1776.
- [24] R.R. Du, H.L. Störmer, D.C. Tsui, L.N. Pfeiffer and K.W. West, Phys. Rev. Lett. 70 (1993) 2944.
- [25] R.G. Clark, Phys. Scr. T39 (1991) 45.
- [26] J.E. Müller, Phys. Rev. Lett. 68 (1992) 385.
- [27] A.M. Chang and D.C. Tsui, Solid State Commun. 56 (1985) 153.
- [28] H.L. Störmer, K.W. Baldwin, L.N. Pfeiffer and K.W. West, Solid State Commun. 84 (1992) 95.



ELSEVIER

Surface Science 305 (1994) 139–144



## Direct determination of the density of states in two-dimensional systems by magnetocapacitances of biased double barrier structures

Aimin Song, Houzhi Zheng <sup>\*</sup>, Fuhua Yang, Yuexia Li

*National Laboratory for Superlattices and Microstructures, Institute of Semiconductors, Academia Sinica, P.O. Box. 912, Beijing 100083, People's Republic of China*

(Received 12 April 1993; accepted for publication 22 June 1993)

### Abstract

The magnetocapacitive response of a double-barrier structure (DBS), biased beyond resonances, has for the first time been employed as a reliable method to determine the density of states (DOS) of two-dimensional (2D) electrons residing in the accumulation layer on the incident side of the DBS. Model calculations with a Gaussian-like DOS are compared with the experimental  $C$  versus  $B$  curves, measured at different biases and temperatures. The fitting is not only self-consistent but also remarkably good even in well-defined quantum Hall regimes. It is therefore evident that replacing a conventional gated heterostructure by a biased DBS makes it possible that the influence of the magnetoresistance of “lateral” 2D channel may be eliminated completely in the determination of the DOS, while the possible coexistence of three-dimensional (3D) electrons in the accumulation layer can easily be discriminated by experiments.

Knowledge of the density of states (DOS) of a two-dimensional electron gas (2DEG) in magnetic fields is essential for understanding many important behaviors of low-dimensional structures in both weak and strong magnetic fields. Experimental information about the DOS was previously obtained by many groups from measurements of magnetization [1], specific heat [2] and magnetocapacitance [3]. The first two methods had the drawback that the unavoidable inhomogeneities arising from the use of multi-layered samples obscured the determination of the DOS.

Compared with the others, the magnetocapacitance is related to the DOS of Landau levels in a more straightforward way, and could be measured from a small single-layered sample so that the influence of the inhomogeneities might be greatly reduced. However, attempts to study the DOS by measuring the magnetocapacitance of a modulation-doped heterostructure failed in the quantum Hall regimes. The magnetoresistance of the 2DEG mixes increasingly in the measured capacitance and gradually dominates the system response to an AC modulation signal as the magnetic field comes close to the integer fillings of Landau levels. As a result, the charge-sensitive measurement eventually becomes a conductance-

<sup>\*</sup> Corresponding author.



dominant one as pointed out by some previous work [4], and the DOS could no longer be extracted reliably from the magnetocapacitance. There have been several techniques proposed to eliminate such series-resistance effects by means of vertically charging the 2DEG. Smith and Wang [5] measured the DOS for a 2DEG accumulated on the incident side of a single, thick nonconducting AlGaAs barrier, and extended the capacitance measurement into the fractional quantum Hall regime. However, no clear evidence was provided that one can exclude the possible contribution of 3D electrons to the capacitance, which might quite often coexist with the 2DEG in the accumulation layer. Ashoori and Silsbee [6] employed a tunnel barrier to realize vertical charge transfer between an  $n^+$ -GaAs emitter and an undoped GaAs quantum well (where the 2DEG resided), and obtained the Landau DOS up to a magnetic field of 4 tesla. Presumably limited by relatively high tunneling resistance, no information in well-defined quantum Hall regimes was shown.

In the present work we analytically study the magnetocapacitive response of a biased double-barrier structure (DBS), and employ it to determine the Landau DOS of the 2DEG residing in the accumulation layer adjacent to the emitter barrier. It turns out that the main advantage of using a biased DBS lies in two facts. First, the accumulation layer in a DBS is charged or discharged very fast by exchanging electrons “vertically” with the  $n^+$ -GaAs electrode in response to an AC modulation signal and, thus, no “lateral” magnetoresistance of the 2D channel can be involved, as demonstrated in previous work [5]. Second, using peculiar behaviors of resonant magnetotunneling, one may experimentally tell whether only a 2DEG exists in the accumulation layer of a particular DBS, so that the determination of the DOS for the 2DEG will not be obscured by the possible presence of 3D electrons.

To derive the capacitive response, the potential profile of the DBS is schematically depicted in Fig. 1 where the DBS is biased in the voltage range between the first and second resonances. The parameters  $W_e$ ,  $d_e$ ,  $W$ ,  $d_c$ ,  $W_c$  indicated in the figure denote the spacer width on the emitter

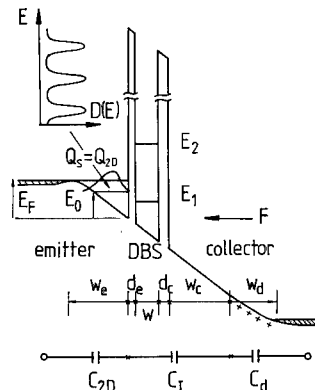


Fig. 1. Conduction-band profile of a positively biased DBS. The inset at the bottom is the lumped circuit of DBS.

side, the thicknesses of the emitter barrier, central well and collector barrier, and the spacer width on the collector side, respectively. Since the DBS is biased beyond the resonance regions, charge build-up in the central well is negligible, and a uniform electric field,  $F$ , will be assumed throughout the regions of  $d_e$ ,  $W$ ,  $d_c$ ,  $W_c$  in the following derivation. The chemical potential difference,  $eV$ , across the DBS may be expressed as

$$eV = E_F + eW_1F + eV_d, \quad (1)$$

where  $W_1 = d_e + W + d_c + W_c$ .  $E_F$  denotes the Fermi level on the emitter side measured from the bottom of the conduction band at the outer interface of the emitter barrier. The last term is the potential energy change over the space charge region near the collector electrode. We label the total space charge on the emitter side by  $Q_s$  ( $Q_s = \epsilon F$ ). To get the capacitive response of the DBS, we differentiate both sides of Eq. (1) with respect to the applied voltage  $V$  and obtain

$$1/C = 1/C_s + 1/C_I + 1/C_d. \quad (2)$$

Here,  $C = dQ_s/dV$  is the total capacitance of the DBS;  $C_s = edQ_s/dE_F$  is defined as the capacitance of the accumulation layer;  $C_d = eN_d\epsilon/Q_s = \epsilon/W_d$  represents the capacitance of the depletion layer  $W_d$ ; and  $C_I = \epsilon/W_1$  is simply the insulator capacitance of the undoped layer  $W_1$ . Eq. (2) demonstrates that the total capacitance of the DBS consists of three capacitors in series, similar

to that of a gated heterostructure. The capacitance term that concerns us mostly is

$$C_S = e \frac{d}{dE_F} \int_{E_0}^{\infty} eD(E, E_0, B) f(E, E_F) dE$$

(for  $T \neq 0$  K and  $B \neq 0$  T). Here, for the moment, we consider only the contribution of the 2D electrons to  $C_S$ . If a variational result for the subband energy  $E_0$  is adopted, the equation can be rewritten as

$$1/C_S = 1/\int_{E_0}^{\infty} e^2 D(E, E_0, B) (-\partial f/\partial E) dE + 11\langle z \rangle/32\epsilon, \quad (3)$$

where  $D(E, E_0, B)$  is the DOS in magnetic fields,  $f(E, E_F)$  is the Fermi distribution function and  $\langle z \rangle$  is the stand-off distance of the 2D electrons in the accumulation layer from the interface.

When three-dimensional electrons on the emitter side also play a role in the capacitive response, then  $Q_S = Q_{3D} + Q_{2D} = \epsilon F$ , and

$$1/C_S = \left\{ \left[ \int_{E_0}^{\infty} e^2 D(E, E_0, B) (-\partial f/\partial E) dE \right]^{-1} + 11\langle z \rangle/32\epsilon \right\} / (1 + \alpha), \quad (4)$$

with  $\alpha = C_{3D}/C_{2D}$ ,  $C_{3D} = e dQ_{3D}/dE_F$  and  $C_{2D} = \int_{E_0}^{\infty} e^2 D(E, E_0, B) (-\partial f/\partial E) dE$ . As verified in our previous work [7,8], it is possible to make all tunneling electrons originate only from 2D electronic states in the accumulation layer by employing wider spacer or thinner emitter barriers. As a result, one is able to avoid the complexity caused by 3D electrons in the determination of the DOS.

The experiments were done in several AlAs/GaAs/AlAs asymmetric DBS samples. An undoped GaAs well of 75 Å was sandwiched between two undoped AlAs barriers of the thicknesses 25 and 15 Å, respectively. Two undoped GaAs spacers of 200 Å were grown immediately outside the DBS. The full composition of the structures and the sample fabrication were described previously [7]. The differential capacitance of the DBS was measured at two different temperatures, 4.2 and 1.5 K, by a HP 4284A LCR

meter with a modulation frequency of 1 MHz and an amplitude of 10 mV as the DBS was biased in the voltage region between the first and second resonance peaks. Special attention was paid to the effect of the modulation frequency on the cusp-like structures of  $C$  versus  $B$  curves. One may note that compared with the frequencies ( $\sim 20$  Hz) used in most previous work [3], a much higher frequency was used in this work. However, even in the vicinity of integer fillings, no falsely deep minima appear in the magnetocapacitance curves, an artifact previously encountered in conventional gated heterostructures due to the extremely high magnetoresistance of the 2D channel and, thus, extremely long  $RC$  time constant. By reducing the modulation frequency from 1 MHz to 10 kHz, we carefully checked that no obvious change in either the shapes or the positions of the cusplike dips was found (although the measured results became increasingly noisy). Another important issue in the experiment was to ensure that all the electrons available for the tunneling were of pure two-dimensional character. This was proved to be true when our DBS was under forward bias, as demonstrated in our early work [7], by checking whether any magneto-oscillatory structure could be revealed in the resonance region. This is also one of the advantages of using the double-barrier structure over a single-barrier structure, where such a discrimination could hardly be made [5].

Accordingly, we only make use of the  $C$  versus  $B$  curves, measured under different forward biases and at two different temperatures (4.2 and 1.5 K), to determine the DOS of the 2DEG. Now, we are in the position to compare the experimental data with the model calculation of the magnetocapacitance, using the derived expressions (2), (3) and a Gaussian-like DOS of the form

$$D_G(E) = \frac{eB}{2h} \sum_n \sqrt{\frac{2}{\pi}} \frac{1}{\Gamma_n} \left[ e^{-(E-E_{n\uparrow})^2/2\Gamma_n^2} + e^{-(E-E_{n\downarrow})^2/2\Gamma_n^2} \right]. \quad (5)$$

Here

$$E_{n\uparrow,\downarrow} = E_0 + (n + 1/2)\hbar\omega_c \mp g^*\mu_B B/2 \quad (6)$$

are the spin-resolved Landau levels. The enhancement of spin splitting due to interaction effects is taken into account in the usual way:

$$g^* = g_0 + (E_{\text{ex}}/\mu_B B)(N_{2D\uparrow} - N_{2D\downarrow}), \quad (7)$$

and

$$N_{2D\uparrow,\downarrow} = \int_{E_0}^{\infty} dE f(E, E_F) \frac{eB}{2h} \times \sum_n \sqrt{\frac{2}{\pi}} \frac{1}{\Gamma_n} e^{-(E-E_{n\uparrow,\downarrow})^2/2\Gamma_n^2}, \quad (8)$$

where  $g_0 = 0.52$  is the Landé factor in the absence of many-body effects,  $E_{\text{ex}}$  is the interaction coefficient and is taken as a fitting parameter,  $N_{2D\uparrow}$  and  $N_{2D\downarrow}$  give the number density of the 2D electrons filled in the spin-up and spin-down states, respectively ( $N_{2D} = N_{2D\uparrow} + N_{2D\downarrow}$ ). The broadening parameter used in Eq. (5),  $\Gamma_n$ , is assumed to have the dependence  $\Gamma = \Gamma_0 B^{1/2}$  on  $B$ . Quite often, due to the inhomogeneities in the structure, one has to introduce a constant background in the model DOS, as given by

$$D_{\text{GB}}(E) = D_G(E)(1-x) + xm^*/\pi\hbar^2. \quad (9)$$

The employed fitting procedure is summarized as follows:

(1) For a particular 2D number density  $N_{2D}$ , self-consistently solve the Schrödinger equation and Poisson equation in the incident region, and obtain the numerical dependence of the subband energy on the 2D number density,  $E_0(N_{2D})$ .

(2) Use the magneto-oscillations observed in the  $C$  versus  $B$  traces to determine  $N_{2D}$  from their reciprocal periods of  $B$  fields,  $\Delta(1/B)$ . We thus obtain the experimental relation  $N_{2D}(V)$  or  $V(N_{2D})$ .

(3) At a given bias  $V$ , self-consistently solve Eqs. (6), (7), (8) and

$$E_F - E_0 = V - E_0(N_{2D}) - eN_{2D}W_1/\epsilon - eN_{2D}^2/2\epsilon N_d$$

(rewritten from Eq. (1)) to get the dependencies on the  $B$  field of  $E_F - E_0$ ,  $g^*$ ,  $E_0$ ,  $N_{2D}$  and  $D(E)$ .

(4) Substitute them into Eqs. (2) and (3) to get  $C$  versus  $B$  curves, and compare them with the measured ones.

(5) Adjust the fitting parameters  $\Gamma_0$ ,  $E_{\text{ex}}$  and  $x$ , and iterate steps (3) and (4) until a satisfactory fitting is finally achieved.

The above fitting procedure has been completed for two different temperatures, 4.2 and 1.5 K, and three different biases, 1.1, 1.2 and 1.3 V. Fig. 2 illustrates the model fitting to the  $C$  versus  $B$  traces measured at the same temperature, 4.2 K, but under two different biases, 1.1 and 1.3 V. In Fig. 3 a similar fitting is performed at two different temperatures, 4.2 and 1.5 K, while the applied bias is fixed at 1.2 V. The inset shows the model DOS obtained from the fitting at  $B = 7$  T and  $T = 1.5$  K. From the figures it is convincing to conclude that the model-fitting completed in the present work is not only self-consistent with a unique set of parameters:  $\Gamma_0 = 0.56$  meV T $^{-1/2}$ ,  $E_{\text{ex}} = 3.143 \times 10^{-11}$  meV cm $^2$  and  $x = 28\%$  used for different biases and temperatures, but also remarkably good over a wide field range up to 7 T, especially in the vicinity of integer fillings,

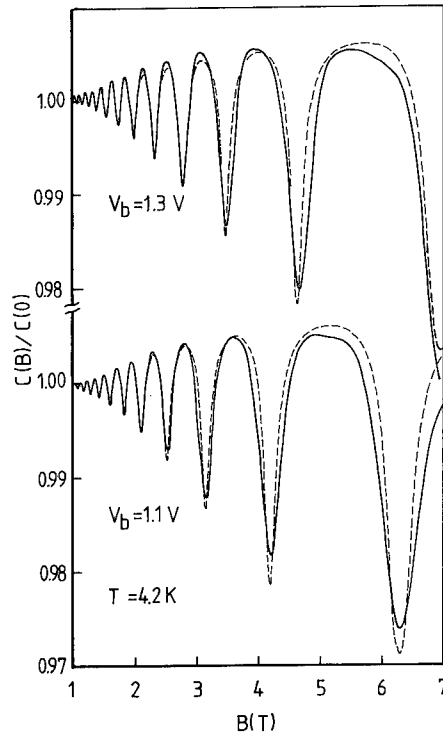


Fig. 2. Normalized  $C$  vs.  $B$  curves plotted at the same temperature 4.2 K but different biases, 1.1 and 1.3 V. The fitting curves are dashed, the solid curves are experimental.

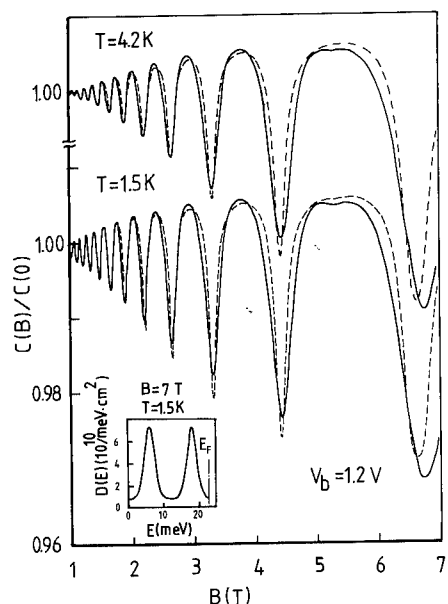


Fig. 3. Normalized  $C$  vs.  $B$  curves plotted at the same bias  $V_b = 1.2$  V but different temperatures, 4.2 K, 1.5 K. The dashed one is the fitting curve. The solid curve is the measured one. The inset shows the model DOS obtained at  $B = 7$  T,  $T = 1.5$  K.

where such a comparison was previously considered as an inappropriate practice using conventional gated heterostructures. The fitting parameters used here are not necessarily the optimized choice.

By using Eq. (4), we have also tried to include the contribution of 3D mobile electrons in the magnetocapacitance to see if it should play some role. For simplicity, we set  $\alpha$  equal to 0.2 and then found substantial decreases in both maxima and minima of the oscillations in the calculated  $C$  versus  $B$  curve. This makes the fitting worse and, thus, further justifies our previous statement that in the accumulation layer only the 2D electrons make a contribution to the structure's capacitance.

Several important conclusions may be drawn from the data. The DOS in strong magnetic fields shows a nonvanishing value (28% of the DOS in zero  $B$  field) between Landau levels. The background DOS may originate from the inhomogeneities in the structure, especially the fluctuation of the 2D number density in the plane. On

the other hand, the effective line width of Landau levels may oscillate as they successively cross  $E_F$  in an increasing magnetic field. A maximum level broadening is expected to occur at the integer fillings. There, small DOS makes the screening to ionized impurities less effective [9]. Our data seem to confirm the  $B^{1/2}$  dependence of the level broadening over a wide  $B$  field range from 1 to 7 T as predicted by the self-consistent Born approximation [10].

In a biased DBS, the chemical potential difference across the structure pins at the value of  $eV$  as given by Eq. (1). This makes the situation different from that in a nongated structure. The model calculation of magnetocapacitance performed in the present work shows that all the physical quantities obtained from the fitting, such as Fermi level ( $E_F - E_0$ ), subband energy  $E_0$ , 2D number density  $N_{2D}$  and effective Landé factor  $g^*$  show oscillatory changes with the magnetic field. However, such oscillatory variations of  $E_0$  and  $N_{2D}$  are very tiny and no larger than  $6 \times 10^{-4}$  and  $1 \times 10^{-3}$ , respectively. In contrast, the effective Landé factor  $g^*$  oscillates drastically and reaches a maximum of about 3.6 at  $B = 5.4$  T

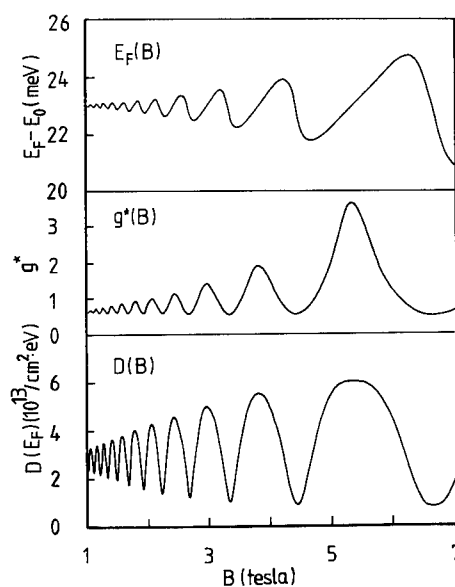


Fig. 4. Dependences on  $B$  fields of  $E_F - E_0$ ,  $g^*$  and  $D(E_F)$  obtained self-consistently from the model fitting at  $T = 1.5$  K and  $V = 1.2$  V.

( $V_b = 1.2$  V,  $T = 1.5$  K). The details for the variations of  $E_F - E_0$ ,  $g^*$  and  $D(E_F)$ , the DOS at the Fermi level with the  $B$  fields, are as shown in Fig. 4.

In summary, we have derived a theoretical expression for the magnetocapacitance of a biased DBS, and fitted it with the experimental  $C$  versus  $B$  curves measured at different temperatures and biases over a wide  $B$ -field range up to 7 T. The fitting is self-consistent and remarkably good, and gives us reliable information about the DOS even in the quantum Hall regimes.

We would like to thank the technical assistance of C.F. Li. The work at the National Laboratory for Superlattices and Microstructures, Institute of Semiconductors, Academia Sinica is supported by the State Council of Science and Technology.

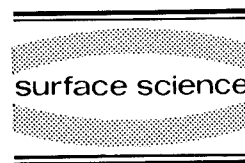
## 1. References

- [1] J.P. Eisenstein, H.L. Stormer, V. Narayanamurti, A.Y. Cho and A.C. Gossard, Phys. Rev. Lett. 55 (1985) 875.
- [2] E. Gornik, R. Lassing, G. Strasser, H.L. Stormer, A.C. Gossard and W. Wiegmann, Phys. Rev. Lett. 54 (1985) 1820.
- [3] T.P. Smith, B.B. Goldberg, P.J. Stiles and M. Heiblum, Phys. Rev. B 32 (1985) 2696.
- [4] R.K. Goudall, R.J. Higgins and P.J. Harrang, Phys. Rev. B 31 (1985) 6597.
- [5] T.P. Smith III and W.I. Wang, Phys. Rev. B 34 (1986) 2995.
- [6] R.C. Ashoori and R.H. Silsbee, Solid State Commun. 81 (1992) 821.
- [7] H.Z. Zheng and F.H. Yang, in: Proc. of Int. Conf. on Semicond. Phys., Eds. E.M. Anastassakis and J.D. Joannopoulos (World Scientific, Singapore, 1990) p. 1317.
- [8] H.Z. Zheng, F.H. Yang and Z.G. Chen, Phys. Rev. B 42 (1990-I) 5270.
- [9] W. Cai and T.S. Ting, Phys. Rev. B 33 (1986) 3967.
- [10] T. Ando and Y. Vemura, J. Phys. Soc. Jpn. 6 (1974) 959.



ELSEVIER

Surface Science 305 (1994) 145–150



## Transitions between edge and bulk channels in the quantum Hall regime

C.A. Richter <sup>a</sup>, R.G. Wheeler <sup>\*,a</sup>, R.N. Sacks <sup>b</sup>

<sup>a</sup> Department of Applied Physics, Yale University, New Haven, CT 06520-2157, USA

<sup>b</sup> United Technologies Research Center, East Hartford, CT 06108, USA

(Received 19 April 1993; accepted for publication 6 July 1993)

### Abstract

An extended network model of the transition regime between two integer quantum Hall plateaus is presented. When it is used to analyze experimental data, two parameters of interest are extracted: the resistivity of the bulk conducting channel due to the energetically topmost Landau level and the scattering length between the bulk channel and the edge channels. The behavior of the equilibration length is studied for transitions between the two spin states of a given Landau level and between Landau levels with different quantum numbers. In some non-ideal devices, the nonlocal aspects of the transition regime cause dramatic and non-intuitive device behavior.

An extended network model (ENM) of the transition regime between two integer quantum Hall (IQH) plateaus has been developed and used to extract parameters of physical interest from experimental data. This theory is an extension of the decoupled network model, first presented by McEuen and co-workers [1,2]. To model transitions, they assumed that the energetically topmost Landau level (LL), which is being backscattered, is completely decoupled from the energetically lower LLs, which are treated as ideal edge states [3]. Recall that in the edge state formalism of the IQH regime, the confining potential causes the discrete LL energies in the bulk of the sample ( $E_j = \hbar\omega_c(j - 1/2)$ , where  $j = 1, 2, 3, \dots$ ) to bend upwards at the sample edges. Where these energy states cross the Fermi level, current carrying edge states arise. When the Fermi energy is pinned between two bulk LLs, the net current flows at the sample edges, and the device is in the IQH regime where  $R_H = (1/N)(h/e^2)$  and  $R_L = 0$ . As the magnetic field is increased so that the bulk of the energetically topmost LL enters the Fermi level, electrons can scatter across the device and are effectively backscattered. This backscattering destroys the quantization and the transition region is entered. As the magnetic field is further increased, the device remains in the transition regime until the topmost LL is completely depopulated, and the next quantized region is entered. The decoupled network model *quantitatively* addressed long standing questions concerning resistances measured in high-mobility devices, and predicted dramatic nonlocal effects that

\* Corresponding author.

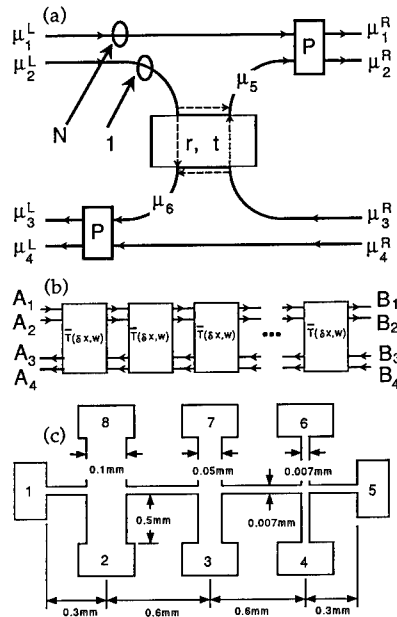


Fig. 1. (a) The extended network model (ENM). The topmost channel is represented by a scattering probability and coupled through the parameter  $P$  to  $N$  ideal edge channels. (b) Schematic of the integration of segments that is necessary to form probes and internal sections. (c) The experimental device geometry. Notice that the total device circumference (excluding the contacts) is  $\sim 10$  mm.

occur during transitions. The agreement of this model with experimental data was remarkable for spin resolved transitions in high-mobility devices. Scattering does occur between the bulk and edge channels, and therefore must be accounted for to explain the resistances measured in most transitions. Much effort has gone into understanding the relationship between inter-channel scattering and measured resistances, and many [4] have presented models to account for this equilibration between LLs.

The ENM presented in this paper treats the topmost LL as being partially coupled to the energetically lower LLs which are treated as rapidly equilibrating ideal edge states. This behavior is in agreement with that observed in studies of inter-edge state scattering in the quantized regions [5]. The attractive features of this model are that it is relatively simple, it can be applied to devices with arbitrary geometries, and the range of equilibration lengths that can be modelled is large. These features make the model readily adaptable so that it can be compared with experimental data for all transitions and in all device geometries. The equilibration length can be extracted from experimental data across the *transition region* as a function of magnetic field.

Fig. 1a shows the model for a device segment (of length  $\delta x$  and width  $w$ ) in the transition region between the  $(N+1)$ th and the  $N$ th plateau. The bulk channel arising from the topmost LL is modelled as a scattering problem, where the electron is transmitted across the device with probability  $t$  and is effectively backscattered, or is forward scattered along the edge of the device (with probability  $r = 1 - t$ ). A resistivity of the  $(N+1)$ th channel alone can be associated with this scattering probability, and in a similar manner as in the decoupled network model  $t = \delta x / \Lambda$ , where  $1/\Lambda = \rho_{xx}^{N+1}(1/w)$ . The coupling between the  $(N+1)$ th, “bulk”, channel and  $N$ , “edge”, channels is represented by the equilibration parameter  $P$ , where  $P$  varies from 0 for no equilibration to 1 for complete equilibration. Associated with this coupling parameter,  $P$ , is an equilibration length along the edge of the sample. For a segment of length  $\delta x$  this equilibration length is defined by  $P = \delta x / L_{eq}$ . A scattering matrix,  $T$ , can be established

[6] for the segment that determines the potentials on the left of the sample given the right-hand side potentials; therefore,  $\mu_{\text{Left}} = T\mu_{\text{Right}}$  where

$$T = \begin{pmatrix} \frac{1}{1-P} \left(1 - \frac{PN}{N+1}\right) & \frac{-P}{(1-P)(N+1)} & 0 & 0 \\ \frac{-PN}{r(1-P)(N+1)} & \frac{1}{r(1-P)} \left(1 - \frac{P}{N+1}\right) & \frac{-t}{r} & 0 \\ \frac{-PNt}{r(1-P)(N+1)} \left(1 - \frac{PN}{N+1}\right) & \frac{t}{r(1-P)} \left(1 - P + \left(\frac{P}{N+1}\right)^2 N\right) & \left(1 - \frac{t}{r}\right) \left(1 - \frac{PN}{N+1}\right) & \frac{PN}{N+1} \\ -\left(\frac{P}{N+1}\right)^2 \frac{tN}{r(1-P)} & \frac{tP}{r(1-P)(N+1)} \left(1 - \frac{P}{N+1}\right) & \left(1 - \frac{t}{r}\right) \left(\frac{P}{N+1}\right) & 1 - \frac{P}{N+1} \end{pmatrix} \quad (1)$$

and the potential vectors are

$$\mu_{\text{Left(Right)}} = \begin{pmatrix} \mu_1^{\text{L(R)}} \\ \mu_2^{\text{L(R)}} \\ \mu_3^{\text{L(R)}} \\ \mu_4^{\text{L(R)}} \end{pmatrix}.$$

There are  $N$  channels at potentials  $\mu_1^{\text{L(R)}}$  and  $\mu_4^{\text{L(R)}}$  while there is only one each at potentials  $\mu_2^{\text{L(R)}}$  and  $\mu_3^{\text{L(R)}}$  (see Fig. 1a). When  $P = 0$ ,  $T$  represents the decoupled network model.

In order to use the ENM with experimental data, a matrix for each probe and internal section of the device must be found. To do this for the  $k$ th element of length  $L_k$  and width  $w_k$ , a sum of the scattering matrices for an infinitesimal segment ( $T(\delta x, w_k)$ ) is performed as schematically shown in Fig. 1b to find ( $T(L_k, w_k)$ ) [6]. The external contacts to the probes are assumed to be ideal. After the scattering matrix for each element is found, they are connected to form a total scattering matrix representing the device. Where the various device elements are connected, current flows only at the edges; scattering diagonally across an intersection is ignored. Once the overall matrix is derived, any possible resistance measurement on a device with that geometry can be simulated.

We have used the single electron picture of edge states to describe the ENM. Recently, a more advanced picture of edge state behavior has been developed [8] where the electrostatic edge potential sensed by electrons is self-consistently calculated. These calculations give rise to strips of compressible and incompressible electron liquids at the sample edges. The formalisms of the ENM are completely compatible with this more complex view of the behavior of electrons at samples edges. The terminology must be adjusted so that scattering occurs between the strips of compressible liquid at the edges and the large compressible liquid in the bulk of the sample. The parameters  $L_{\text{eq}}$  and  $\rho_{xx}^{N+1}$  have the same physical interpretation in both the single electron and self-consistent edge state pictures.

By numerical comparison of the ENM with two experimental magnetoresistance measurements, the bulk resistivity,  $\rho_{xx}^{N+1}$ , and the equilibration length,  $L_{\text{eq}}$ , can be extracted. For example, consider the eight terminal device shown in Fig. 1c which was fabricated from a GaAs/AlGaAs heterostructure having an electron density  $n_s = 3.5 \times 10^{15} \text{ m}^{-2}$  and a mobility of  $\sim 100 \text{ m}^2/\text{V} \cdot \text{s}$ . The device was measured at  $T = 0.5 \text{ K}$  using low frequency lockin techniques at a constant current of 20 nA. The magnetic field direction is such that electron edge states travel clockwise around the sample.

The Hall resistance  $R_{15,37}$  [7] and the longitudinal resistance  $R_{15,34}$  were simultaneously measured, and by comparing these two magnetoresistances with the model for  $N = 2$ ,  $L_{\text{eq}}(B)$  and  $\rho_{xx}^{N+1}(B)$ , are determined for this device. The fits and the extracted parameters are shown in Figs. 2a, 2b, and 2c. The parameters are reasonable:  $\rho_{xx}^{N+1}$  smoothly increases from 0 to  $\infty$  as expected. On the low magnetic field side of the transition, the equilibration length increases exponentially with increasing magnetic field until



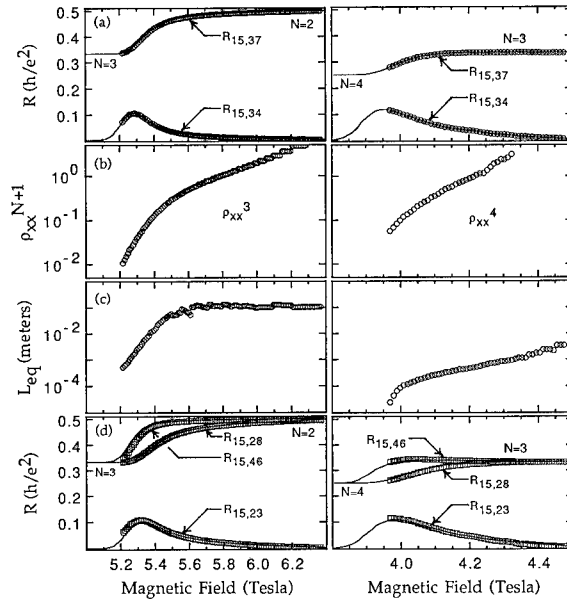


Fig. 2. Comparison of the ENM with experimental data. On the left, the  $N = 3$  to  $N = 2$  transition: a spin resolved transition. (a) (Left) Solid lines are experimental data, open circles are fits using the model. (b) (Left) Resistivity of the energetically lower  $j = 2$ , spin LL extracted using the fits. (c) (Left) The equilibration length between the lower  $j = 2$  spin LL and the  $j = 1$  LL. (d) (Left) Solid lines are experimental data, and open squares are simulations. Figures on the right are for the  $N = 4$  to  $N = 3$  transition: a spin coupled transition. (a) (Right) Solid lines – data; open circles – fits. (b) (Right) Resistivity of the energetically higher  $j = 2$ ; spin LL. (c) (Right)  $L_{eq}$  between the two spin states of the  $j = 2$  LL. (d) (Right) Solid lines – data; open squares – simulations.

saturating at a length that is longer than the device size. The extremely long  $L_{eq}(B)$  justifies the use of the decoupled network model for spin resolved transitions. As a check to the accuracy of the extracted parameters, other pairs of resistance were fit. The extracted  $L_{eq}(B)$  and  $\rho_{xx}^{N+1}(B)$  vary slightly, but all lie within the area bounded by the circles in Fig. 2b and 2c (excluding the region above  $B \approx 5.5$  T, where  $L_{eq}(B)$ , while always long, is variable). Since  $L_{eq}(B)$  and  $\rho_{xx}^{N+1}(B)$  completely characterize the system, other device resistances can be generated using the model and these parameters. Fig. 2d shows three different resistance measurements ( $R_{15,28}$ ,  $R_{15,46}$ , and  $R_{15,23}$ ) and compares them with simulations using the parameters extracted from the fits in Fig. 2a.

At lower magnetic fields where the two spin states are essentially degenerate, the transitions are modelled in a similar manner as the spin resolved case. However, the conductivity of each of the bulk and edge channels must be doubled to account for the two spin states. At higher magnetic fields, to model spin coupled transitions the two spin states of the topmost LL are treated as one bulk state coupled to one edge state: i.e. the topmost LL is modelled in the same manner as a spin resolved transition with  $N = 1$ . Here the energetically lower LLs are modelled as ideal edge states that are completely decoupled from the coupled spin system representing the topmost LL.

As an example of the former, the spin degenerate transition from  $N = 12$  to  $N = 10$  is analyzed in the same manner as the spin resolved case.  $R_{15,37}$  and  $R_{15,34}$  were fit;  $\rho_{xx}^{N=12}$  and the equilibration length  $L_{eq}$  between the  $j = 6$  LL and the other LLs were extracted (Figs. 3a–3c). The extracted parameters were then used to simulate  $R_{15,28}$ ,  $R_{15,46}$ , and  $R_{15,23}$  (see Fig. 3d). Examining  $L_{eq}$ , two features are observed. First, the equilibration length is much shorter than the device size, indicating that unlike in the spin resolved case, a great deal of equilibration is occurring between the bulk and the edge channels.

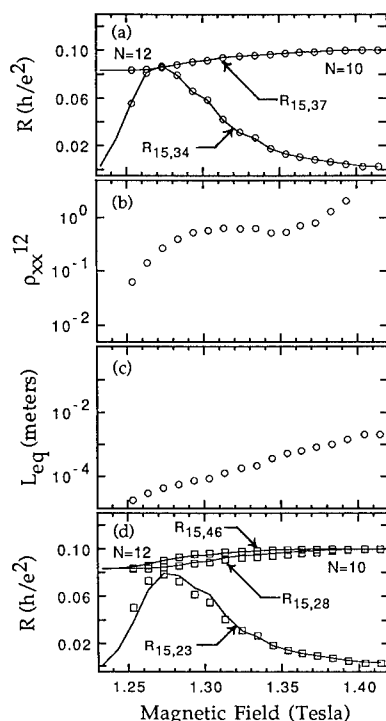


Fig. 3. Comparison of the ENM with experimental data for the  $N = 12$  to  $N = 10$  transition: a spin degenerate transition. (a) Solid lines are experimental data, open circles are numerical fits. (b) Resistivity of the bulk channel (for the  $j = 6$  Landau level). (c) The equilibration length between the bulk channel and the edge states. (d) Solid lines are experimental data, and open squares are simulations.

Secondly, although the equilibration length is short, it is increasing exponentially as  $B$  is increased across the Hall riser.

An example of a spin coupled case, the  $N = 4$  to  $N = 3$  transition is analyzed using the ENM (see Figs. 2a–2d).  $L_{eq}$  is again short indicating that electrons readily scatter between the two spin states. The equilibration length for scattering between two spin states does not simply increase exponentially with increasing  $B$  across a transition, but has a sharp decrease in the equilibration length on the low magnetic field side of the transition as  $B$  is decreased.

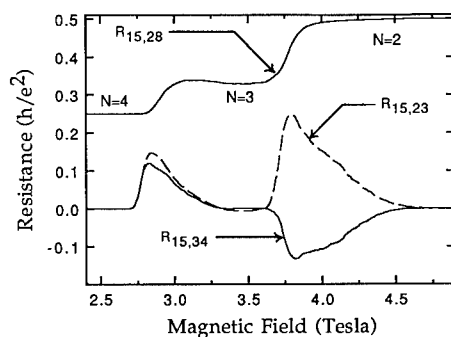


Fig. 4. Experimental data illustrating dramatic nonlocal behavior. Here the edge states flow counterclockwise.

While data from only one of each of the three distinct types of transitions has been shown, an extensive analysis of all transitions in a variety of device geometries and electron gas parameters has been performed. The trends in the behavior of  $L_{\text{eq}}$  versus  $B$  illustrated above hold true in all devices studied. The equilibration length for scattering between different LLs is observed to increase exponentially with increasing magnetic field, while the equilibration length between the two spin states of a given LL is always observed to have sharply increasing  $L_{\text{eq}}$  on the low magnetic field side of a transition followed by a more gentle increase on the higher magnetic side of the transition.

The ENM assumes  $L_{\text{eq}}$  and  $\rho_{xx}^{N+1}$  are uniform throughout the device. This is not always the case. Alphenaar et al. [9] found that the equilibration length is sometimes radically affected by a single impurity. The data in Fig. 4, was taken on a device with the same geometry as the previous device, a slightly lower electron density, and comparable mobility. When  $B$  is such that edge states flow counterclockwise, the resistances  $R_{15,28}$  and  $R_{15,23}$  are superficially “normal”; however, when the resistance  $R_{15,34}$  is measured during the transition from  $N=3$  to  $N=2$ , the potential drop between probes 3 and 4 is reversed from what is expected and appears as a large negative resistance. When the magnetic field is reversed so that the electrons in the edge states flow from probes 4 to 3 to 2, the potential drop between probes 4 and 3 is normal; however, the potential between probes 2 and 3 is now reversed and  $R_{15,23}$  is negative. This surprising result implies that the contact to probe 3 is not ideal [6]. Thus, the resistances measured using probe 3 show dramatic and nonintuitive results and due to the nonlocal nature of the transition regime, *all* the resistances measured on the device are modified.

In conclusion, we have presented an extended network model of transitions in the IQH regime. This model was used to study equilibration lengths between various LLs, and it was found that scattering between the two spin states within a given LL behaves differently than scattering between two different LLs. The nonlocal nature of transitions in high-mobility samples was illustrated by showing dramatic effects due to nonuniformity in a *voltage probe*.

The authors would like to thank Dr. Aaron Szafer for his help which was essential in developing the mathematical model. This work was supported in part by the National Science Foundation under grant No. DMR 9216121.

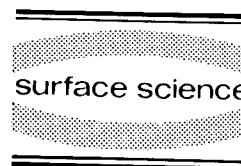
## 1. References

- [1] P.L. McEuen, A. Szafer, C.A. Richter, B.W. Alphenaar, J.K. Jain, A.D. Stone, R.G. Wheeler and R.N. Sacks, Phys. Rev. Lett. 64 (1990) 2062.
- [2] A. Szafer, A. Douglas Stone, P.L. McEuen and B.W. Alphenaar, in: Granular Nanostructures, Eds. David K. Ferry, John R. Barker and Carlo Jacoboni (Plenum, New York, 1992).
- [3] B.I. Halperin, Phys. Rev. B 25 (1982) 2185;  
P. Streda, J. Kucera and A.H. MacDonald, Phys. Rev. Lett. 59 (1987) 1973;  
J.K. Jain and S.A. Kivelson, Phys. Rev. Lett. 60 (1988) 1542;  
M. Buttiker, Phys. Rev. B 38 (1988) 9375.
- [4] J. Faist, Europhys. Lett. 15 (1991) 331;  
V.T. Dolgoplov, G.V. Kravchenko and A.A. Shashkin, Solid State Commun. 78 (1991) 999;  
S. Komiyama, H. Hirai, M. Ohsawa, Y. Matsuda, S. Sasa and T. Fujii, Phys. Rev. B 45 (1992) 1085;  
P. Svoboda, P. Streda, G. Nachtwei, A. Jaeger, M. Cukr and M. Laznicka, Phys. Rev. B 45 (1992) 8763.
- [5] B.W. Alphenaar, P.L. McEuen, R.G. Wheeler and R.N. Sacks, Phys. Rev. Lett. 64 (1990) 667;  
G. Muller, D. Weiss, S. Koch, K. von Klitzing, H. Nickel, W. Schlapp and R. Losch. Phys. Rev. B 42 (1990) 7633.
- [6] C.A. Richter, Transitions in the Quantum Hall Regime, PhD Thesis, Yale University (1993); herein the ENM is discussed in detail.
- [7]  $R_{ij,kl}$  denotes a resistance measured with the current passed between probes  $i$  and  $j$  and the voltage measured between  $k$  and  $l$ .
- [8] C.W.J. Beenakker, Phys. Rev. Lett. 64 (1990) 216;  
A.M. Chang, Solid State Commun. 74 (1990) 871;  
D.B. Chklovskii, B.I. Shklovskii and L.I. Glazman, Phys. Rev. B 46 (1992) 4026.
- [9] B.W. Alphenaar, P.L. McEuen, R.G. Wheeler and R.N. Sacks, Physica B 175 (1991) 235.



ELSEVIER

Surface Science 305 (1994) 151–155



# Conductivity peaks in the quantum Hall regime: broadening with temperature, current, and frequency

D.G. Polyakov <sup>\*,1</sup>, B.I. Shklovskii

*Theoretical Physics Institute, University of Minnesota, Minneapolis, MN 55455, USA*

(Received 16 April 1993; accepted for publication 15 May 1993)

## Abstract

We argue that it is hopping transport that is responsible for broadening of the  $\sigma_{xx}$  peaks in low-mobility samples. Explicit expressions for the width  $\Delta\nu$  of a peak as a function of the temperature  $T$ , current  $J$ , and frequency  $\omega$  are found. It is shown that  $\Delta\nu$  grows with  $T$  as  $(T/T_1)^\kappa$ , where  $\kappa$  is the inverse localization-length exponent. The current  $J$  is shown to act like an effective temperature  $T_{\text{eff}}(J) \propto J^{1/2}$  if  $T_{\text{eff}}(J) \gg T$ . Broadening of the ohmic ac-conductivity peaks with frequency  $\omega$  is found to be determined by the effective temperature  $T_{\text{eff}}(\omega) \approx \hbar\omega/k_B$ .

The integer quantum Hall effect in a disordered two-dimensional electron gas manifests itself more clearly the lower the temperature  $T$ . The steps connecting adjacent plateaus in the dependence of the Hall conductance  $\sigma_{xy}$  on the filling factor  $\nu$  narrow with decreasing  $T$  and so do the peaks in the longitudinal conductance  $\sigma_{xx}$ . In a number of experiments [1–6] a remarkable result has been obtained: the width  $\Delta\nu$  of the peaks shrinks as  $T \rightarrow 0$  according to a power law  $\Delta\nu \propto T^\kappa$ . The exponent  $\kappa \approx 0.4$  was found in Refs. [1,2] to be universal; neither the Landau level index nor the electron mobility are relevant at low temperatures. The measurements have been performed down to temperatures as low as a few tens of millikelvins, thus giving a definite indica-

tion that extended electron states exist at only one energy within the broadened Landau level. Other states should be localized. Although the question as to the nature of the localization still remains unresolved, various computer simulations [7–11] strongly support this concept yielding a power-law divergence of the localization length  $\xi(E) \propto |E|^{-\gamma}$ ,  $\gamma \approx 2.3$ , as the electron energy  $E$  approaches the Landau level center ( $E = 0$ ). Recently, the same value of  $\gamma$  has been directly measured by studying how  $\Delta\nu$  scales with the sample size in the low- $T$  limit [4].

The conventional explanation of the scaling dependence  $\Delta\nu \propto T^\kappa$  is as follows [7,12]. It is assumed that at a finite temperature there exists a phase-coherence length  $L_\phi$  which decreases with increasing  $T$ . One believes that if  $L_\phi \ll \xi(E_F)$ ,  $E_F$  being the Fermi energy, the localization is destroyed, and the electron system exhibits metallic behavior. Similar to the theory of weak localization,  $L_\phi$  is expressed in terms of the dif-

\* Corresponding author.

<sup>1</sup> Permanent address: A.F. Ioffe Physico-Technical Institute, St. Petersburg, 194021, Russian Federation.

fusion coefficient  $\mathcal{D}$  and the phase-breaking time  $\tau_\phi$ :  $L_\phi \approx (\mathcal{D}\tau_\phi)^{1/2}$ . The time  $\tau_\phi$  is proportional to  $T^{-p}$  with the exponent  $p$  depending on the inelastic-scattering mechanism. These arguments lead to the conclusion that the width of the conducting energy band vanishes with decreasing  $T$  as  $T^{p/2\gamma}$ , so that  $\kappa = p/2\gamma$  (to describe the experimental data in this way, one has to admit that  $p \approx 2$ ).

Although such an approach looks very attractive, introducing the phase-breaking time to account for the temperature-induced delocalization at  $\sigma_{xx} \approx e^2/h$  is not obvious. There is no generally accepted theory for  $\tau_\phi$  in the quantum Hall regime. Here we would like to suggest an explanation of the scaling behavior  $\Delta\nu(T)$  in terms of strong localization (approaching a peak from the region where  $\sigma_{xx} \ll e^2/h$ ). We start with the notion that the only possible mechanism of transport in the strongly localized electron system is hopping. It is known that variable-range hopping is predominant in the low-temperature limit. In this regime, due to the existence of the Coulomb gap, the temperature dependence of  $\sigma_{xx}$  should have a form [13,14]

$$\sigma_{xx} = \sigma_0 e^{-(T_0/T)^{1/2}}, \quad (1)$$

where

$$T_0(\nu) = C \frac{1}{k_B} \frac{e^2}{\epsilon \xi(\nu)}, \quad (2)$$

$\xi(\nu)$  is the localization radius of the states on the Fermi level for a given  $\nu$ ,  $\epsilon$  is the dielectric constant,  $k_B$  is the Boltzmann constant, and  $C \approx 6$  in two dimensions [15]. This temperature dependence was observed in the middle of the Hall plateaus [16,17]. Note that Ono [18] also derived Eq. (1) (with a different expression for  $T_0$ ) assuming a finite density of states at the Fermi level and using unperturbed wave functions of isolated impurities  $\psi(\rho) \propto e^{-\rho^2/4\lambda^2}$ , where  $\lambda$  is the magnetic length. It is known [19], however, that tails of wave functions are actually of a simple exponential form  $e^{-\rho/\xi}$  due to multiple scattering of a tunneling electron. Together with the Coulomb gap in the density of states this results in Eqs. (1) and (2). As mentioned above, the length  $\xi(\nu)$

diverges as  $\nu$  approaches a half-integer  $\nu_0$ :

$$\xi(\nu) = \xi_0 |\nu - \nu_0|^{-\gamma}, \quad \gamma \approx 2.3. \quad (3)$$

Correspondingly, the value of  $T_0$  tends to zero as  $\nu \rightarrow \nu_0$ . Hence, at a given temperature, there should exist a characteristic value of  $\nu$  at which the exponential factor in Eq. (1) becomes of the order of unity. It is natural to assume that it is the difference between this value and  $\nu_0$  that determines the half-width of a resistivity  $\rho_{xx}$  peak  $\Delta\nu$ . In this case, solving equation  $T_0(\nu) \approx T$  with the use of the relations (2) and (3) immediately yields a power-law dependence of  $\Delta\nu$  on  $T$ :

$$\Delta\nu = \left( \frac{T}{T_1} \right)^\kappa \quad (4)$$

with  $\kappa = 1/\gamma$ , and

$$T_1 = A \frac{1}{k_B} \frac{e^2}{\epsilon \xi_0}, \quad (5)$$

where  $A$  is the numerical coefficient. For  $\gamma \approx 2.3$  we arrive at the experimental value  $\kappa \approx 0.4$ . As for the characteristic temperature  $T_1$ , to our knowledge, it is the first time an explicit expression for  $T_1$  has been given. Note that  $T_1$  is of the order of  $T_0$  in the middle of an adjacent plateau.

To compare with what is experimentally observed, we should define the elementary length  $\xi_0$  depending on the properties of a random potential. Provided the potential fluctuations are short range, so that their correlation radius is less than or of the order of the magnetic length  $\lambda$ , one may expect that  $\xi_0$  for the lowest Landau levels is  $\sim \lambda$ . One believes that fluctuations of this kind are realized in *InGaAs/InP* heterostructures, the experiment on which Ref. [1] most clearly confirms the universality of the exponent  $\kappa$ . Extracting  $\Delta\nu$  from the data for  $\rho_{xx}$  presented in Ref. [1] we obtain  $T_1 \approx 600$  K for  $\nu = \frac{3}{2}$  (the  $N = 0 \downarrow$  Landau level). Substituting then  $\lambda$  for  $\xi_0$  in Eq. (5) we find  $A \approx 4$ . It should be noted, however, that when the peaks corresponding to the spin-split  $N = 1$  level are treated in the same way,  $T_1 \approx 30$  K is obtained. This temperature is much smaller than what one could expect according to Eq. (5) with  $\xi_0 \approx \lambda$  and  $A \approx 4$ . It is worth comparing  $T_1 \approx 30$  K with the measured

value of  $T_0$  for hopping at  $\nu = 3$  which was found to be 7.8 K for similar samples [17]. This value is of the same order of magnitude as  $T_1$  and also much less than what would be expected from Eq. (2). The fact that both the characteristic temperatures are so small for the spin-split  $N = 1$  level indicates that the length  $\xi_0$  for this level should be much larger than  $\lambda$ . Our approach enables us to relate the anomaly in the values of  $T_0$  and  $T_1$  with another striking phenomenon reported in Ref. [20]: if only one  $\sigma_{xx}$  peak corresponds to the  $N = 1$  level, i.e. its spin splitting is not resolved, the width of the peak follows  $T^{\kappa/2}$  instead of  $T^\kappa$  as for each of the  $\uparrow$  and  $\downarrow$  peaks taken separately. The same phenomenon was observed also for the unsplit  $N = 2$  level [21]. According to direct measurements [21], the localization length exponent in the latter case is much greater than 2.3. Indeed, in our picture, the only thing that may account for the change of the exponent in the dependence  $\Delta\nu(T)$  is a stronger divergence of the localization length as compared with Eq. (3). For example, the value of  $\xi$  for the  $N = 1$  level should behave as

$$\xi(\nu) \approx \xi'_0 |\nu - 3|^{-2\gamma} \quad (6)$$

(if two spin-levels overlap strongly, the values of  $\nu$  corresponding to the extended states are close to an integer in contrast to a half-integer in Eq. (3)). The length  $\xi'_0$  must be proportional to the constant of spin-orbit interaction, so that Eq. (6) may be valid only for  $\xi(\nu) \geq \lambda |\nu - 3|^{-\gamma}$ . By analogy with the derivation of Eqs. (4) and (5), the assumption (6) yields the width of the unsplit level

$$\Delta\nu = (T/T'_1)^{1/2\gamma}, \quad k_B T'_1 \approx e^2 / \epsilon \xi'_0. \quad (7)$$

We think that, even if a  $\sigma_{xx}$  peak is not spin-split, there exist two different energy levels corresponding to delocalized states. The levels are separated by a Zeeman energy  $E_g$ . The reason why two peaks may be not observable is that the hopping conductivity between these two levels is not small. As the Fermi level approaches closely any of the levels,  $\xi(\nu)$  must diverge with the usual exponent  $\gamma$ . Therefore, when  $|\nu - 3|$  becomes  $\sim E_g/\Gamma \ll 1$ , one should expect a

crossover from the dependence (6) to that which is similar to (3) but with much larger “elementary length”  $\sim \xi'_0 (\Gamma/E_g)^\gamma$  resulted from matching in the crossover point. The divergence of  $\xi(\nu)$  should take place at  $\nu = 3 \pm \delta\nu$ , where  $\delta\nu \approx E_g/\Gamma$ . Thus, our conjecture is that the localization length behaves as follows:

$$\xi \approx \xi'_0 \left[ \frac{\Gamma^2}{|E^2 - \frac{1}{4}E_g^2|} \right]^\gamma, \quad E_g \ll \Gamma, \quad (8)$$

where the energy  $E$  is reckoned from the middle of the gap. At  $E = 0$  we get  $\xi \approx \xi'_0 (\Gamma/E_g)^{2\gamma} \gg \lambda$ . Consequently, if the two  $\sigma_{xx}$  peaks are resolved and the hopping conductivity in the middle between them is observed, the value of  $T_0$  should be strongly reduced in comparison with that for large gaps in the density of states:

$$k_B T_0 \approx \frac{e^2}{\epsilon \xi'_0} \left( \frac{E_g}{\Gamma} \right)^{2\gamma}. \quad (9)$$

This equation gives also the characteristic temperature at which the two peaks merge. We would like to draw attention to the extremely strong dependence of  $T_0$  on the ratio  $E_g/\Gamma$ . Indeed, a very high sensitivity of properties of  $\sigma_{xx}$  peaks to the electron mobility [21] as well as to the angle between the normal to the plane in which electrons move and the direction of the magnetic field [22] has been observed for the  $N = 1$  level. To conclude this section, we have to say that we have no clear idea about the mechanism of doubling of the localization-length exponent due to spin-orbit interaction. What we provide is a phenomenological description of the experimental data from the point of view of an approach based on the concept of hopping.

The suggested approach permits us to elucidate yet another interesting phenomenon observed at very low temperatures. It was found in Refs. [23,4] that the width  $\Delta\nu$  of the  $\sigma_{xx}$  peaks grows with increasing current  $J$ , i.e. with the increase of the Hall electric field  $\mathcal{E}_H$ . Let us show that the dependence  $\Delta\nu(\mathcal{E}_H)$  can be understood in terms of the theory of hopping in a strong electric field [24,25]. This theory is based on the fact that there exists a quasi-Fermi level

inclined by the electric field  $\mathcal{E}$ . Zero-temperature hopping with phonon emission becomes then possible and, even though there are no absorption processes, the local Fermi distribution with an effective temperature  $\sim e\mathcal{E}\xi$  is formed [24,25]. On this account, the exponent of the current-voltage characteristics at  $T = 0$  may be obtained from that of the ohmic conductivity by replacing  $T \rightarrow e\mathcal{E}\xi/2$ . In the quantum Hall regime, if the ohmic transport obeys the law (1), the zero-temperature conductivity should behave with increasing electric field as

$$\sigma_{xx} = \sigma_0 e^{-(\mathcal{E}_{H_0}/\mathcal{E}_H)^{1/2}}, \quad \mathcal{E}_{H_0} = \frac{2k_B T_0}{e\xi}. \quad (10)$$

Similar to the case of ohmic conductivity, the width of the  $\sigma_{xx}$  peak is found from the equation  $\mathcal{E}_{H_0}(\xi) \approx \mathcal{E}_H$ . Solving this equation for  $\xi$  we get  $\xi \approx (e/\epsilon\mathcal{E}_H)^{1/2}$ , which yields

$$\Delta\nu = \left( \frac{\mathcal{E}_H}{\mathcal{E}_{H_1}} \right)^\alpha, \quad \mathcal{E}_{H_1} = B \frac{e}{\epsilon\xi_0^2}, \quad (11)$$

where  $\alpha = 1/2\gamma = \kappa/2$  and  $B$  is the numerical coefficient. Comparing Eqs. (11) and (4) and (5) one can notice that the field  $\mathcal{E}_H$  leads to the same broadening of the peak as if there were the temperature

$$T_{\text{eff}} = \frac{1}{k_B} \left( \frac{A^2}{B} \frac{e^3}{\epsilon} \right)^{1/2} \mathcal{E}_H^{1/2}. \quad (12)$$

This relation is remarkably universal: it contains only one parameter of the sample, its dielectric constant  $\epsilon$ . The sensitivity of  $\Delta\nu$  to  $\mathcal{E}_H$  may be viewed as due to heating in the critical region of the metal-insulator transition. In this connection note the unusual square-root dependence of  $T_{\text{eff}}$  on  $\mathcal{E}_H$ . The increase in  $\Delta\nu$  with  $\mathcal{E}_H$  was clearly observed in Refs. [23,4]; however, no treatment in terms of power dependences was presented. Our analysis of the lowest temperature data of both experiments shows that they can indeed be described by introducing  $T_{\text{eff}} \propto \mathcal{E}_H^{1/2}$ .

The third phenomenon we would like to discuss here is broadening of peaks in the ohmic ac-conductivity  $\sigma_{xx}(\omega)$  with frequency  $\omega$  at very low temperatures  $k_B T \ll \hbar\omega$  [26]. In that case

the ac-conduction is related to a resonant absorption of quanta  $\hbar\omega$  by close pairs of localized states. A theory for  $\sigma_{xx}(\omega)$  in three dimensions has been developed in Ref. [27] with the effects of the Coulomb gap taken into account. Straightforward generalization for the two-dimensional case yields the conductivity away from a peak

$$\sigma_{xx}(\omega) = \frac{1}{6}\epsilon\xi\omega, \quad \hbar\omega \gg k_B T. \quad (13)$$

The width of a peak in  $\sigma_{xx}(\omega)$  can be estimated by making use of the condition that the conductivity near the peak is of the order of  $e^2/h$ . This gives

$$\Delta\nu = \left( \frac{T_{\text{eff}}(\omega)}{T_1} \right)^{1/\gamma}, \quad T_{\text{eff}}(\omega) \gg T, \quad (14)$$

where  $k_B T_{\text{eff}} = D\hbar\omega$ ,  $D$  being the numerical coefficient.

Note that measurements of  $\sigma_{xx}$  away from peaks can be very useful. Combining Eqs. (13) and (2) we get a measurable quantity

$$I = k_B T_0 \frac{\sigma_{xx}(\omega)}{\omega} = \frac{C}{6} e^2, \quad (15)$$

which should not depend on  $\nu$ . An experimental observation of this invariance would verify our approach as based on the Coulomb gap theory. At  $\hbar\omega \ll T$ , absorption is related to relaxation losses rather than to resonant transitions. Nevertheless, the expression for  $\sigma_{xx}$  in that case [28],

$$\sigma_{xx} = \frac{1}{12}\epsilon\xi\omega, \quad \hbar\omega \ll k_B T, \quad (16)$$

differs from Eq. (13) only by a factor of 1/2. We would like to stress that, away from peaks, both Eqs. (13) and (16) make it possible to measure directly the value of  $\xi$  as a function of  $\nu$  (see also Ref. [28]). Besides, we think that another way of measuring  $\xi$ , which is based on determination of both temperature and current dependences of  $\sigma_{xx}$  at a given  $\nu$ , may be fruitful. The value of  $\xi(\nu)$  is then obtained as a ratio  $2k_B T_0(\nu)/e\xi_{H_0}(\nu)$ .

Recently, a remarkable observation of the scaling behavior  $\Delta \propto T^\kappa$  in the fractional quantum Hall regime has been reported [29,3]. According to Ref. [29], the exponent  $\kappa \approx 0.4$  is the same as for the integer quantum Hall effect. This gives an indication that our results may be applicable to

the fractional regime, too. If that is the case, the characteristic temperatures  $T_1$  and  $T_0$  contain the fractional charges and so should be much smaller than those for the integer effect. The experimental values of  $T_1$  and  $T_0$  are actually very small [29,30]. Note that one could use the invariant  $I$  to compare effective charges of hopping excitations for different plateaus.

We are grateful to L.W. Engel, S.W. Hwang, C. Kurdak, D. Shahar, D.C. Tsui and H.P. Wei for providing us with the experimental data [22,26]. This work was supported by the National Science Foundation under Grant No. DMR-9020587.

## 1. References

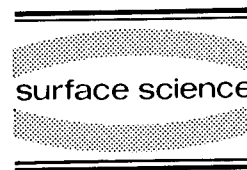
- [1] H.P. Wei, D.C. Paalanen and A.M.M. Pruisken, Phys. Rev. Lett. 61 (1988) 1294.
- [2] H.P. Wei, S.Y. Lin, D.C. Tsui and A.M.M. Pruisken, Phys. Rev. B 45 (1992) 3926.
- [3] S. Koch, R.J. Haug, K. von Klitzing and K. Ploog, Phys. Rev. B 43 (1991) 6828.
- [4] S. Koch, R.J. Haug, K. von Klitzing and K. Ploog, Phys. Rev. B 46 (1992) 1596.
- [5] V.T. Dolgoplov, A.A. Shashkin, B.K. Medvedev and V.G. Mokerov, Zh. Eksp. Teor. Fiz. 99 (1991) 201 [JETP 72 (1991) 113].
- [6] M. D'Iorio, V.M. Pudalov and S.M. Semenchinsky, in: High magnetic fields in Semiconductor Physics, Ed. G. Landwehr (Springer, Berlin, 1992) p. 56.
- [7] H. Aoki and T. Ando, Phys. Rev. Lett. 54 (1985) 831.
- [8] J.T. Chalker and P.D. Coddington, J. Phys. C 21 (1988) 2665.
- [9] B. Huckestein and B. Kramer, Phys. Rev. Lett. 64 (1990) 1437.
- [10] T. Ando, J. Phys. Soc. Jpn. 61 (1992) 415.
- [11] Y. Huo and R.N. Bhatt, Phys. Rev. Lett. 68 (1992) 1375.
- [12] A.M.M. Pruisken, Phys. Rev. Lett. 61 (1988) 1297.
- [13] A.L. Efros and B.I. Shklovskii, J. Phys. C 8 (1975) L49.
- [14] B.I. Shklovskii and A.L. Efros, Electronic Properties of Doped Semiconductors (Springer, Berlin, 1984).
- [15] Nguyen Van Lien, Fiz. Tekh. Poluprovodn. 18 (1984) 335 [Sov. Phys. Semicond. 18 (1984) 207].
- [16] G. Ebert, K. von Klitzing, C. Probst, E. Schubert, K. Ploog and G. Weimann, Solid State Commun. 45 (1983) 625.
- [17] A. Briggs, Y. Guldner, J.P. Vieren, M. Voos, J.P. Hirtz and M. Razeghi, Phys. Rev. B 27 (1983) 6549.
- [18] Y. Ono, J. Phys. Soc. Jpn. 51 (1982) 237.
- [19] B.I. Shklovskii, Pis'ma Zh. Eksp. Teor. Fiz. 36 (1982) 53 [JETP Lett. 36 (1982) 53].
- [20] H.P. Wei, S.W. Hwang, D.C. Tsui and A.M.M. Pruisken, Surf. Sci. 229 (1990) 34.
- [21] S. Koch, R.J. Haug, K. von Klitzing and K. Ploog, Phys. Rev. Lett. 67 (1991) 883.
- [22] S.W. Hwang, H.P. Wei, L.W. Engel, D.C. Tsui and A.M.M. Pruisken, unpublished.
- [23] J.A. Simmons, S.W. Hwang, D.C. Tsui, H.P. Wei, L.W. Engel and M. Shayegan, Phys. Rev. B 44 (1991) 12933.
- [24] B.I. Shklovskii, Fiz. Tekh. Poluprovodn. 6 (1972) 2335 [Sov. Phys. Semicond. 6 (1973) 1964].
- [25] B.I. Shklovskii, E.I. Levin, H. Fritzsche and S.D. Baranovskii, in: Transport, Correlation and Structural Defects, Ed. H. Fritzsche (World Scientific, Singapore, 1990).
- [26] D. Shahar, L.W. Engel and D.C. Tsui, submitted to EP2DS10; L.W. Engel, D. Shahar, D.C. Tsui and C. Kurdak, unpublished.
- [27] B.I. Shklovskii and A.L. Efros, in: Electron–Electron Interactions in Disordered Systems, Eds. A.L. Efros and M. Pollak (North-Holland, Amsterdam, 1985).
- [28] A.L. Efros, Zh. Eksp. Teor. Fiz. 89 (1985) 1834 [JETP 62 (1985) 1057].
- [29] L.W. Engel, H.P. Wei, D.C. Tsui and M. Shayegan, Surf. Sci. 229 (1990) 13.
- [30] G.S. Boebinger, H.L. Stormer, D.C. Tsui, A.M. Chang, J.C.M. Hwang, A.Y. Cho, C.W. Tu and G. Weimann, Phys. Rev. B 36 (1987) 7919.





ELSEVIER

Surface Science 305 (1994) 156–160



## “Intrinsic” quantum Hall effect in InAs/Ga<sub>1-x</sub>In<sub>x</sub>Sb crossed gap heterostructures in high magnetic fields

K.S.H. Dalton <sup>\*,a</sup>, M. van der Burgt <sup>a</sup>, M. Lakrimi <sup>a</sup>, R.J. Warburton <sup>a</sup>, M.S. Daly <sup>a</sup>,  
W. Lubczyński <sup>a,b</sup>, R.W. Martin <sup>a</sup>, D.M. Symons <sup>a</sup>, D.J. Barnes <sup>c</sup>, N. Miura <sup>c</sup>,  
R.J. Nicholas <sup>a</sup>, N.J. Mason <sup>a</sup>, P.J. Walker <sup>a</sup>

<sup>a</sup> Clarendon Laboratory, Physics Department, University of Oxford, Parks Road, Oxford, OX1 3PU, UK

<sup>b</sup> Department of Solid State Physics, Polish Academy of Sciences, 41-800 Zabrze, Kawalca 3, Poland

<sup>c</sup> Institute for Solid State Physics, University of Tokyo, Roppongi, Minato-ku, Tokyo 106, Japan

(Received 30 April 1993; accepted for publication 4 June 1993)

### Abstract

We report a study of the quantum Hall effect and Shubnikov–de Haas oscillations in semimetallic type II heterostructures of the strained layer system InAs/Ga<sub>1-x</sub>In<sub>x</sub>Sb which are almost intrinsic. In high magnetic fields up to 50 T,  $\rho_{xy}$  has large peaks, demonstrating the high degree of charge compensation in the system. Between these peaks, intrinsic quantum Hall minima are observed, where  $\rho_{xy}$  approaches zero.

The quantum Hall effect is well known for single carrier systems such as Si-MOSFET or GaAs/Ga<sub>1-x</sub>Al<sub>x</sub>As structures containing a two-dimensional (2D) electron gas. The longitudinal magnetoresistivity shows Shubnikov–de Haas oscillations which are periodic in inverse magnetic field and, at low temperatures and high magnetic fields, the  $\rho_{xx}$  minima tend to zero. These zeros in  $\rho_{xx}$  occur whenever there is an integer number of filled Landau levels, when the Fermi level,  $E_F$ , lies within localised electron states. At these values of magnetic field, the Hall resistivity,  $\rho_{xy}$ , shows quantised plateaux with  $\rho_{xy} = h/\nu e^2$ , where  $\nu$  is the integer Landau level filling factor [1].

This paper reports a study of the quantum Hall effect in bipolar systems containing a 2D gas of coexisting electrons and holes, using heterostructures formed from the crossed gap system InAs/Ga<sub>1-x</sub>In<sub>x</sub>Sb [2–4]. In these structures, the valence band maximum of GaSb (Ga<sub>1-x</sub>In<sub>x</sub>Sb) lies 150 meV (higher for Ga<sub>1-x</sub>In<sub>x</sub>Sb) above the conduction band minimum of InAs. If the layers of InAs are above a critical thickness ( $\sim 85$  Å for InAs/GaSb), the confined electron levels at zero magnetic field are at lower energy than the hole levels. As a result, there is intrinsic transfer of electrons from the valence band of Ga<sub>1-x</sub>In<sub>x</sub>Sb to the conduction band of InAs and the structure behaves as a semimetal.

In addition to the intrinsic charge, these structures have extrinsic negative charge due to donor interface states [5] and to Fermi level pinning by

\* Corresponding author.

surface states [6]. Previous MBE-grown InAs/GaSb samples had only a small proportion of intrinsic carriers, with electron to hole density ratios  $n_e/n_h$  in the range 4–5 [7]. The important difference in the present study is that the structures have electron to hole density ratios which are much closer to perfect compensation, with typical ratios from 1.5 down to less than 1.1. These samples are semimetallic type II superlattices and double heterojunctions (DHETs) of InAs/GaSb and InAs/Ga<sub>0.9</sub>In<sub>0.1</sub>Sb grown onto a GaSb buffer layer on GaAs substrates by MOVPE [8]. Careful optimisation of the switching sequence of the growth produced structures biased towards an (In–Sb) interface bond [9], which were found to have the highest mobilities. A thick capping layer of GaSb was used in the DHETs to reduce Fermi level pinning at the surface and hence to reduce the extrinsic charge density. The incorporation of In into the GaSb improved the samples in two ways: it increases the band overlap, causing an increase in the intrinsic transfer of charge, and it also biases the system further in favour of (In–Sb) interface formation.

The low field carrier densities and mobilities are found using a classical two-carrier fit [10] to the low field Hall data, which shows that the ratio of electron to hole densities in these samples varies from 1.04 to 1.7, both for single layers of InAs (DHET structures) and for 20 period superlattices. Fourier analyses of the low field resistivity oscillations show that all 20 periods of the superlattices are electrically active, with similar electron densities in each layer. The parameters derived from the low field fitting are shown in Table 1 for the samples studied at high fields. In

general, the structures with Ga<sub>0.9</sub>In<sub>0.1</sub>Sb were closer to the intrinsic limit, due to the additional transfer of charge. These samples also showed higher electron and hole mobilities, which, in the case of the holes, may be due to the considerably larger strain in the system, which leads to a reduction in the hole masses [11]. Further confirmation of the small net charge density in the superlattice structures studied here comes from electron cyclotron resonance measurements in fast pulsed magnetic fields up to 120 T [12]. These magnetic fields are sufficiently large for the zero point energy to cause the lowest Landau levels to uncross, thus inducing a semimetal to semiconductor transition. By 100 T, only the extrinsic carriers remain, and it is found that the carrier density has fallen by factors of 10 to 20. At lower fields, in the range 10–50 T, the intrinsic origin of almost all the carriers and the requirement for a fixed *net* charge lead to large oscillations in the electron and hole densities as the different electron and hole Landau levels cross each other.

Magnetotransport measurements have been carried out on these samples at temperatures down to 1.5 K in slower pulsed magnetic fields up to 50 T [13], and down to 0.33 K in steady fields up to 15 T. We observe two distinct classes of behaviour in the quantum Hall resistance:

(i) For samples with a higher extrinsic contribution to the carrier density, the behaviour of  $\rho_{xx}$  and  $\rho_{xy}$  depends on the extent to which the presence of the hole density compensates for the electron density. Compensated quantum Hall plateaux are observed, as previously studied by Mendez et al. [2]. These plateaux occur when the

Table 1  
Carrier densities and mobilities for the samples in this study

Sample	% In in Ga(In)Sb	InAs thickness (Å)	No. of layers	$n_e$ /layer ( $\times 10^{15} \text{ m}^{-2}$ )	$n_h$ /layer ( $\times 10^{15} \text{ m}^{-2}$ )	$\mu_e$ ( $\text{m}^2/\text{V} \cdot \text{s}$ )	$\mu_h$ ( $\text{m}^2/\text{V} \cdot \text{s}$ )
963/973	0	300	1	7.0	4.1	5.7	0.72
1137	0	280	20	7.2	4.8	4.7	0.11
1249	0	220	20	6.5	6.2	2.5	0.20
1072	10	500	1	6.8	5.3	2.7	0.42
1266	10	500	20	9.2	8.5	10.9	0.80

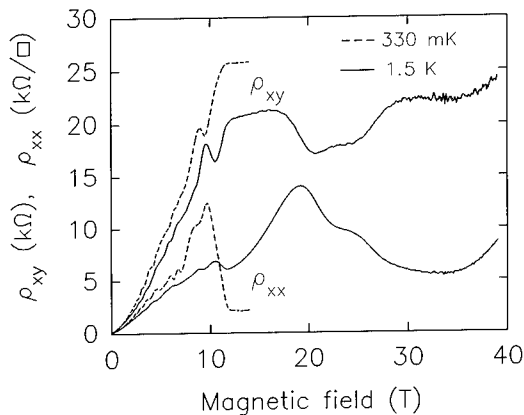


Fig. 1.  $\rho_{xx}$  and  $\rho_{xy}$  for two DHETs with  $n_e/n_h = 1.7$ : sample 963 in pulsed magnetic fields at 1.5 K and sample 973 in steady fields at 0.33 K. Compensated plateaux with  $(\nu_e - \nu_h) = 1$  are seen in  $\rho_{xy}$  around 13 and 30 T, with corresponding minima in  $\rho_{xx}$ . The features are greatly enhanced in the lower temperature data.

Fermi level lies simultaneously in the regions of localised states for both electrons and holes (and hence  $\sigma_{xx} = 0$ ), and the quantised Hall resistance has values corresponding to the net Landau level filling factor. The transverse conductivity is given by the sum of the electron and hole contributions:  $\sigma_{xy} = (\nu_e - \nu_h)e^2/h$ , where  $\nu_e$  and  $\nu_h$  are positive integers. The tensor relationship between the Hall resistivity and the conductivities is  $\rho_{xy} = \sigma_{xy}/(\sigma_{xx}^2 + \sigma_{xy}^2)$ . Since  $\sigma_{xx} = 0$ ,  $\rho_{xy} = 1/\sigma_{xy}$ , and hence the Hall resistivity is  $\rho_{xy} = h/(\nu_e - \nu_h)e^2$  (for  $\nu_e \neq \nu_h$ ).

Fig. 1 shows an example of this behaviour in  $\rho_{xx}$  and  $\rho_{xy}$  of two similar InAs/GaSb DHETs with  $n_e/n_h = 1.7$ . Sample 963 was measured at 1.5 K in fields up to 50 T and sample 973 at 0.33 K and up to 15 T. A compensated quantum Hall plateau is seen around 13 T, with  $(\nu_e - \nu_h) = (2 - 1) = 1$ . (Note that the ratio of effective filling factors is not identical to the carrier density ratio because of the finite densities of localised states.) In the same field range, there is a minimum in  $\rho_{xx}$ . On cooling sample 973 from 4.2 to 0.33 K, the plateau in  $\rho_{xy}$  becomes more accurately quantised and the minimum in  $\rho_{xx}$  is more strongly developed. This is due to the requirement that the Fermi level should lie within the localised states for both carrier types, and thus

the strength of the minimum is determined by the smaller of the two level separations, which is that due to the holes because they have much higher mass than the electrons. The high field  $\rho_{xy}$  shows another plateau around 30 T, this time with  $(\nu_e - \nu_h) = (1 - 0) = 1$ , and a corresponding minimum in  $\rho_{xx}$ .

(ii) For samples which are almost at the intrinsic limit, and at high magnetic fields, a new type of behaviour is seen. The numbers of filled Landau levels for each carrier type are almost equal, and the quantisation condition  $\nu_e = \nu_h$  can be fulfilled. This leads to the special condition for an intrinsic system,  $\sigma_{xy} = 0$ . If  $\sigma_{xy}$  tends to zero faster than  $\sigma_{xx}$ , or if  $\sigma_{xx}$  remains finite for any reason, this will lead to a zero in the Hall resistivity (rather than leading to a plateau as in the extrinsic case). Again, the requirement for observation of quantised behaviour is that the Fermi level should lie within the localised states for both electron and hole Landau levels, but it should be borne in mind that this does not require exact equality of the electron and hole densities, due to the finite width of the localised states. However, if  $\sigma_{xx}$  tends to zero faster than  $\sigma_{xy}$ , there will be a large Hall resistance. Away from the regions where the Fermi level lies within the localised states for both carrier types, there will be imperfect compensation of the Hall conductivity, and a small but finite value of  $\sigma_{xy}$  will result. This too will lead to a large Hall resistance if  $\sigma_{xx}$  is small, and so  $\rho_{xy}$  might be expected to show large oscillations as a function of magnetic field.

Such behaviour is seen in Fig. 2, which shows the longitudinal and Hall resistivities per layer for two 20 period superlattices, samples 1137 and 1249, with electron to hole density ratios 1.5 and 1.04, respectively. The low field Hall resistivities are linear and almost identical because they are dominated by the electrons and  $n_e$  is similar for the two samples. However, at high fields, the more closely compensated sample shows a much larger Hall resistivity due to the smaller net charge density. Large oscillations appear for both samples. An example of the situation where  $\sigma_{xy}$  is small but finite can be seen around 25–30 T for both samples, when  $\rho_{xy}$  becomes very large. Sam-

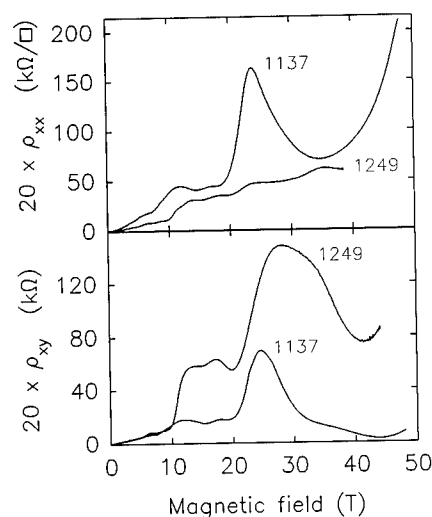


Fig. 2. Longitudinal and Hall resistivity per layer for two 20 period InAs/GaSb superlattices with  $n_e/n_h = 1.5$  (sample 1137) and 1.04 (sample 1249) at 4.2 K. Both samples have field ranges where  $\rho_{xy}$  is large, and sample 1137 shows an intrinsic quantum Hall minimum with  $(\nu_e - \nu_h) = (1 - 1) = 0$ , where  $\rho_{xy}$  approaches zero at 44 T.

ple 1137 also demonstrates the situation where  $\sigma_{xy}$  approaches zero while  $\sigma_{xx}$  remains finite: at 44 T, the quantum Hall resistance is completely compensated, and an intrinsic quantum Hall minimum occurs, with  $\rho_{xy}$  approaching zero at  $\nu_e = \nu_h = 1$  [4].

An even more dramatic example of the intrinsic quantum Hall effect can be seen in Fig. 3, for a 20 period InAs/Ga<sub>0.9</sub>In<sub>0.1</sub>Sb superlattice which has higher electron and hole mobilities and is also very close to the fully compensated (intrinsic) limit, with  $n_e/n_h = 1.08$ . This shows a series of several compensated quantum Hall minima, which alternate with regions where the Hall resistance is high, demonstrating the high degree of charge compensation in the system. In this case, the resistivity,  $\rho_{xx}$ , also shows a series of minima at the same field positions as the minima in  $\rho_{xy}$ ; however, these do not approach zero as strongly as the  $\rho_{xy}$  minima, in contrast with the single carrier case, where only  $\rho_{xx}$  has zeros.

The Hall minima were found to become even more pronounced when hydrostatic pressure was applied to the latter sample in steady magnetic

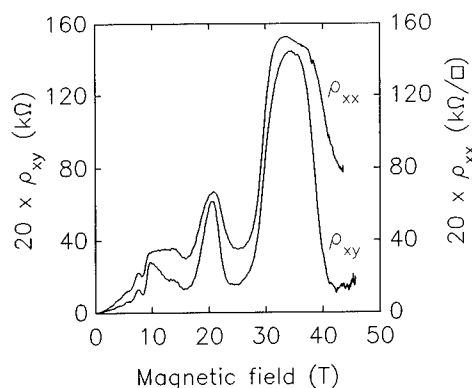


Fig. 3. Longitudinal and Hall resistivity per layer for a 20 period InAs/Ga<sub>0.9</sub>In<sub>0.1</sub>Sb superlattice with  $n_e/n_h = 1.08$  (sample 1266) at 4.2 K.  $\rho_{xy}$  shows large oscillations with a series of intrinsic quantum Hall minima, where  $\rho_{xy}$  approaches zero, while  $\rho_{xx}$  remains finite and larger than  $\rho_{xy}$ .

fields. The pressure causes a reduction in the band overlap of the InAs and Ga<sub>1-x</sub>In<sub>x</sub>Sb, reducing the separation between the electron and hole Landau level fans, and thus reducing the intrinsic electron and hole densities. As a result, specific minima in  $\rho_{xx}$  and  $\rho_{xy}$  are seen to shift linearly with pressure to lower magnetic fields, thus providing further proof of the intrinsic nature of the oscillatory features. This behaviour is shown in Fig. 4, where, with the application of a pressure of 6 kbar, the minima previously seen at higher fields of 25 and 16 T have moved down to

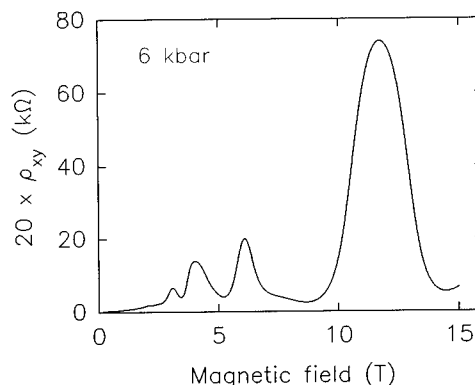


Fig. 4. Hall resistivity per layer for sample 1266 with an applied pressure of 6 kbar at 4.2 K. The minima in  $\rho_{xy}$  have shifted down to lower magnetic fields and have become stronger than in Fig. 3.

14.5 and 9 T, respectively. At the same time, the Hall resistivity minima have become much stronger and are close to zero over a considerable field range.

It is not clear at present why the strongest features are observed in the  $\text{InAs}/\text{Ga}_{1-x}\text{In}_x\text{Sb}$ , rather than the  $\text{InAs}/\text{GaSb}$  structures, and with applied pressure; however, we speculate that the strength of the features is related to the higher mobilities and lower hole masses in the former structures, possibly combined with a particularly favourable alignment of the electron and hole Landau levels achieved by the application of pressure. Detailed 8-band  $\mathbf{k} \cdot \mathbf{p}$  calculations also indicate that the magnitude of the spin-splitting of the hole levels is considerably greater in the  $\text{Ga}_{0.9}\text{In}_{0.1}\text{As}$  structures. Finally, when the pressure is further increased to above 16 kbar, the subband edges of the InAs and the  $\text{Ga}_{0.9}\text{In}_{0.1}\text{Sb}$  become uncrossed and a hydrostatic pressure-induced semimetal to semiconductor transition occurs. Beyond this point, the structure is found to contain a single 2D electron gas, probably at the interface closest to the surface, and conventional extrinsic quantum Hall plateaux for a single carrier system appear.

In conclusion, we have measured the magnetotransport of structures which are very close to the intrinsic limit, and have observed interesting new behaviour in the quantum Hall effect. Large oscillations are seen in  $\rho_{xy}$ : there are high Hall resistances, demonstrating the high degree of charge compensation of the structures, and there are intrinsic quantum Hall minima, where the net Landau level filling factor is zero and  $\rho_{xy}$  approaches zero.

The authors wish to thank the Science and Engineering Research Council (UK) for financial support of this project and the European Commission for two fellowships (for M.v.d.B. and D.J.B.).

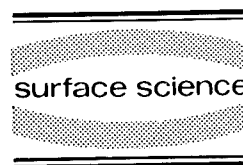
## 1. References

- [1] For a review, see R.E. Prange and S.M. Girvin, Eds., *The Quantum Hall Effect* (Springer, New York, 1987).
- [2] E.E. Mendez, L. Esaki and L.L. Chang, *Phys. Rev. Lett.* 55 (1985) 2216.
- [3] M. Lakrimi, C. López, R.W. Martin, G.M. Summers, G.M. Sundaram, K.S.H. Dalton, R.J. Nicholas, N.J. Mason and P.J. Walker, *Surf. Sci.* 263 (1992) 575.
- [4] K.S.H. Dalton, R. Bogaerts, R.W. Martin, M. Lakrimi, D.M. Symons, R.J. Warburton, R.J. Nicholas, F. Herlach, N.J. Mason and P.J. Walker, *Physica B* 184 (1993) 202.
- [5] J. Luo, H. Munekata, F.F. Fang and P.J. Stiles, *Phys. Rev. B* 38 (1988) 10142.
- [6] M. Altarelli, J.C. Maan, L.L. Chang and L. Esaki, *Phys. Rev. B* 35 (1987) 9867.
- [7] H. Munekata, E.E. Mendez, Y. Iye and L. Esaki, *Surf. Sci.* 174 (1986) 449.
- [8] M. Lakrimi, R.W. Martin, N.J. Mason, R.J. Nicholas and P.J. Walker, *J. Cryst. Growth* 110 (1991) 677.
- [9] C. López, R.J. Springett, R.J. Nicholas, P.J. Walker, N.J. Mason and W. Hayes, *Surf. Sci.* 267 (1992) 176.
- [10] The fit was made using classical magnetotransport expressions, as in: R.A. Smith, *Semiconductors* (Cambridge University Press, Cambridge, 1978) p. 114.
- [11] R.J. Warburton, G.M. Sundaram, R.J. Nicholas, S.K. Haywood, G.J. Rees, N.J. Mason and P.J. Walker, *Surf. Sci.* 228 (1990) 270.
- [12] D.J. Barnes, R.J. Nicholas, N.J. Mason, P.J. Walker, R.J. Warburton and N. Miura, *Physica B* 184 (1993) 168.
- [13] H. Jones, *Proc. 6th Int. Conf. on Megagauss Magnetic Field Generation, Albuquerque, 1992* (Nova Science, New York), in press.



ELSEVIER

Surface Science 305 (1994) 161–165



# Magnetic field dependence of the device-width-dependent breakdown current in the quantum Hall effect

S. Kawaji <sup>\*,a</sup>, K. Hirakawa <sup>a</sup>, M. Nagata <sup>a</sup>, T. Okamoto <sup>a</sup>, T. Fukase <sup>b</sup>, T. Goto <sup>b</sup>

<sup>a</sup> Department of Physics, Gakushuin University, Mejiro, Toshima-ku, Tokyo 171, Japan

<sup>b</sup> Institute for Materials Research, Tohoku University, Sendai 980, Japan

(Received 19 April 1993; accepted for publication 15 June 1993)

## Abstract

Magnetic field dependence of the device-width-dependent breakdown current in the quantum Hall effect is measured in magnetic fields up to 23 T at 0.5 K for GaAs/AlGaAs Hall bars having a total length of 2900  $\mu\text{m}$ , a source- and drain-electrode width of 400  $\mu\text{m}$  and different widths 10, 20 and 35  $\mu\text{m}$  in its central 600  $\mu\text{m}$  long part. Results are explained in terms of localization in Landau levels without edge-state transport.

## 1. Introduction

The quantum Hall effect (QHE), where the Hall conductivity  $\sigma_{xy}$  is quantized as  $\sigma_{xy} = -ie^2/h$  for an integral number  $i$  in two-dimensional (2D) electron systems in strong magnetic fields, was expected from the theoretical study of localization by Ando et al. [1], which showed that the quantization relation  $\sigma_{xy} = -ie^2/h$  holds when the diagonal conductivity  $\sigma_{xx}$  is zero even if the filling factor of Landau levels is not exactly an integral number  $i$ . The QHE was observed in Si-MOSFETs by Kawaji and Wakabayashi [2]. The high precision observation of the quantized Hall resistance by von Klitzing et al. [3] opened a new era in the electrical resistance standard.

Since then, many theoretical studies on the QHE have been done based on the knowledge

that the quantization of the Hall conductance is a bulk property of 2D electron systems in strong magnetic fields [4]. As a supplement to Laughlin's argument [5], the important role of the edge states in the QHE was pointed out by Halperin [6]. Halperin pointed out that the Hall current  $I_H(i)$  is proportional to the chemical potential difference  $\delta\mu = \mu_1 - \mu_2$  between opposite edges of a Hall bar device with a 2D electron system in the QHE condition as  $I_H(i) = (ie/h)\delta\mu$ .

In recent years, understanding of the QHE has been made in terms of the edge-state transport introduced by Büttiker [7]. He restricted the role of the edge states to a function where the Hall current in the QHE is carried by the edge states only. Many experiments have shown phenomena that can be easily explained in terms of the edge-state transport [8]. However, experimental results discussed so far based on edge-state transport are associated with so-called adiabatic transport which appears in nonequilibrium states.

\* Corresponding author.

We reported in a previous paper [9] results of experiments carried out to find evidence of the edge-state transport in the quasi-equilibrium state of the system on which the best present reference standards of electrical resistance in terms of the QHE are based. If the Hall current flows in the edge states only in a simple Hall-bar structure, then the current is confined in two channels along the opposite edges with width of the order of the magnetic length,  $l_B = (\hbar/eB)^{1/2} \approx 100$  Å. The width of the edge channel is supposed to be independent of the total width of the Hall bar  $w$  when the total width is much larger than the edge channel width,  $w \gg l_B$ . Then, the QHE state may break down when the current exceeds a critical value,  $I_{cr}$ . Our experimental results for the Hall plateau with  $i=2$  have shown that the critical current is proportional to the sample width.

In the present paper, results of measurements of the critical current in the Hall plateaus for  $i=1, 2$ , and 4 will be reported.

## 2. Experiments

In the present experiments, we used three samples selected out of five samples in previous experiments [9]. In order to realize a quasi-equilibrium state in the system, as is the case for samples used in the reference standards of electrical resistance, the samples are made from a GaAs/Al<sub>0.3</sub>Ga<sub>0.7</sub>As heterostructure wafer with a relatively low electron mobility of 21 m<sup>2</sup>/V·s. It is known that a nonequilibrium population of electrons occurs at the source- and drain-electrode [10]. In order to keep the same energy dissipation condition at the source- and drain-electrode in different samples, all the samples have the same source- and drain-electrode width of 400 μm. Moreover, in order to equilibrate the electron population in the central part of the sample where the measurement is carried out, all the samples have a large total length of 2900 μm between the source- and drain-electrode. The central part is 600 μm long and has different widths  $w = 10, 20$ , and 35 μm. These numbers of  $w$  are dimensions in the mask used in photolithographic processes. The width in each device is

linearly narrowed down from the source (drain) electrode to the end of the central part. The central part has symmetrically located three pairs of Hall voltage probes separated by 150 μm.

We note here that the structure of the samples in this work is a modification of Hall bars used in the reference standards of electrical resistance and different in nature from the sample with a narrow and short constriction such as used by Bliek et al. [11].

Experiments were carried out at temperatures down to 0.5 K in magnetic fields up to 23 T by using high magnetic fields facilities at the Institute for Materials Research in Tohoku University. The diagonal resistance  $R_{xx}(i)$  for the Hall plateau with the quantum numbers  $i=1, 2$  and 4 was measured by use of a 20 Hz AC constant current whose magnitude ranges from 10 nA to 1 mA as was done in previous experiments. The edge of the Hall plateau was assigned by the magnetic field where  $R_{xx}(i)$  exceeds 0.1 Ω. The critical current  $I_{cr}$  was determined from the current at which the plateau disappeared. Almost all measurements were carried out at 0.5 K. As a typical trace of magnetic field dependence of the diagonal resistance, a result measured in the sample with  $w = 10$  μm at 0.5 K at a current  $I = 10$  μA is shown in Fig. 1.

The critical currents for the breakdown of the QHE measured are shown as a function of  $w$  in Fig. 2. The width  $w$  is the photolithographic mask

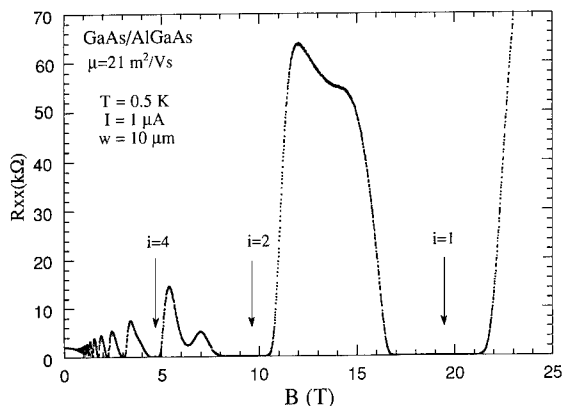


Fig. 1. Typical behaviour of diagonal resistance  $R_{xx}$  vs magnetic field  $B$  in the sample with the width  $w = 10$  μm.

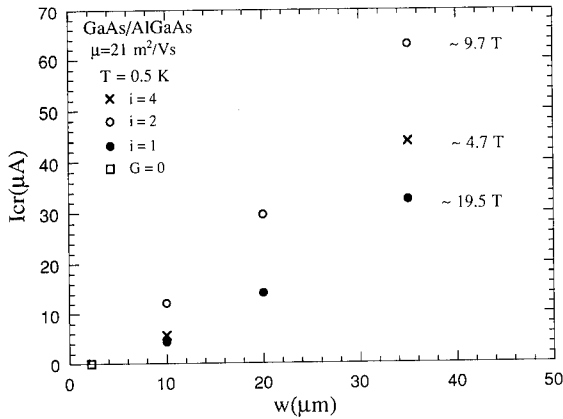


Fig. 2. Sample width dependence of the critical breakdown current of the quantum Hall effect. The open square shows the sample width for zero effective width estimated from conductance vs sample width measurements.

width. The effective width, or the width of the 2D electron sheet, is reduced by chemical etching and formation of the space charge layer at the sample edges. SEM observations of the samples show that the width of each sample is reduced by  $2 \mu\text{m}$  by chemical etching. The effective width estimated from the conductance versus  $w$  plot in the absence of magnetic field is  $w' = w - 2.2 \mu\text{m}$ . The open square in Fig. 2 is the width  $w$  for  $w' = 0$ . In the following discussions, we use the effective width  $w' = w - 2.2 \mu\text{m}$ .

The critical current,  $I_{\text{cr}}$ , the average critical current density,  $J_{\text{cr}}$ , and the average value of the critical field,  $F_{\text{cr}}$ , in the three Hall plateaus measured in the sample with the width  $w = 35 \text{ mm}$  are summarized in Table 1. In Table 1, the drift velocity of electrons,  $v_d$ , determined from the magnetic field  $B$  and the average critical field  $F_{\text{cr}}$  is also calculated for each QHE plateau. In the following section, we discuss possible mechanisms of the breakdown of the QHE.

### 3. Discussions

Some years ago, the breakdown of the QHE in GaAs/AlGaAs heterostructures was experimentally studied. Ebert et al. [12] reported that  $J_{\text{cr}} = 0.5 \text{ A m}^{-1}$  in  $R_{xx}(4)$  at  $T = 1.4 \text{ K}$  and  $B = 4.7 \text{ T}$ . Cage et al. [13] reported that  $J_{\text{cr}} = 0.9 \text{ A m}^{-1}$  in  $R_{xx}(4)$  at  $T = 1.1 \text{ K}$  and  $B = 5.7 \text{ T}$ . Störmer et al. [14] reported that  $J_{\text{cr}} = 1.16 \text{ A m}^{-1}$  in  $R_{xx}(4)$ ,  $R_{xx}(2)$  and  $R_{xx}(1)$  at  $T = 0.5 \text{ K}$  and  $B = 6, 12$  and  $24 \text{ T}$ , respectively. Komiyama et al. [15] reported that  $J_{\text{cr}} = 0.6 \text{ A m}^{-1}$  in  $R_{xx}(4)$  at  $T = 1.9 \text{ K}$  and  $B = 3.8 \text{ T}$ . These critical current densities were obtained in Hall bar devices with somewhat similar dimensions except in the work of Störmer et al. [14] who used a Corbino disk. Störmer et al. [14] obtained the result that the critical current does not depend on the quantum number  $i$  of the Hall plateau which leads to the interesting result that the drift velocity of electrons at the critical current does not depend on the quantum number  $i$ . The constant drift velocity at the breakdown of the QHE appears to favour such a mechanism of the breakdown where the phonon emission like Cerenkov radiation causes the breakdown. However, our result in Fig. 1 and in Table 1 shows that the critical current depends on the quantum number  $i$  and, therefore, the drift velocity of electrons at the breakdown depends on the quantum number  $i$ . Our critical current density for  $i = 4$  is larger than those reported by the authors of Refs. [12–15]. This fact shows that the structure of samples we used is successful in minimizing the effect of the nonequilibrium population of electrons in Landau levels at the breakdown.

The QHE state is characterized by the dissipationless current whose direction is orthogonal to the electric field direction. The breakdown of the QHE means the appearance of energy dissipation

Table 1

Magnetic field  $B$ , critical current  $I_{\text{cr}}$ , average critical current density  $J_{\text{cr}}$ , average critical field  $F_{\text{cr}}$ , average drift velocity  $v_d$ , electric field for inter-Landau-level tunneling  $F_{\text{cr}}(\text{TH})$  and the ratio between  $F_{\text{cr}}$  measured and  $F_{\text{cr}}(\text{TH})$  in the sample with the effective width of  $w' = 32.8 \mu\text{m}$

$i$	$B \text{ (T)}$	$I_{\text{cr}} \text{ (}\mu\text{A)}$	$J_{\text{cr}} \text{ (A/m)}$	$F_{\text{cr}} \text{ (V/m)}$	$v_d \text{ (m/s)}$	$F_{\text{cr}}(\text{TH})$	$F_{\text{cr}}/F_{\text{cr}}(\text{TH})$
1	19.5	32.5	0.99	$2.56 \times 10^4$	$1.3 \times 10^3$	$2.11 \times 10^6$	0.012
2	9.7	62.9	1.92	$2.48 \times 10^4$	$2.6 \times 10^3$	$8.78 \times 10^5$	0.034
4	4.7	43.8	1.34	$8.65 \times 10^3$	$1.84 \times 10^3$	$1.74 \times 10^5$	0.050



due to the current parallel to the electric field. In the structure of the samples in the present experiments, we consider that the breakdown occurs in the central rectangular part with a length of 600  $\mu\text{m}$  and a width  $w'$  in the 2900  $\mu\text{m}$  long samples. Therefore, thermal processes can be eliminated in the transition from the dissipationless state to the dissipative state. A possible process to create mobile electrons and holes along electric field is an inter-Landau-level transition of electrons from the filled Landau level to the empty Landau level.

The eigenfunction of 2D free electrons in a sample with length  $L$  in the  $x$ -direction and width  $w$  in the  $y$ -direction in a perpendicular magnetic field  $B$  in the  $z$ -direction and a parallel electric field in the  $y$ -direction is given by

$$\psi_{n,Y}(x, y) = L^{-1/2} e^{ikx} \phi_n(y - Y), \quad (1)$$

where  $n = 0, 1, 2, \dots$ , is the Landau quantum number, and  $\phi_n(y - Y)$  is the  $n$ th eigenfunction of a harmonic oscillator whose center lies at  $Y$  [16]. A necessary condition for inter-Landau-level transitions is spatial overlap between an eigenfunction  $\phi_n(y - Y)$  of the highest filled Landau level with quantum number  $n$  and an empty state eigenfunction  $\phi_{n+1}(y - Y)$  of the next Landau level, where both states have the same energy at the critical field  $F_{\text{cr}}$  described as  $eF_{\text{cr}}(Y - Y') = \hbar\omega_c$ . If we take the spatial extent of the harmonic oscillator eigenfunction  $\phi_n$  to be given by the classical radius of the Landau orbit  $A_n = (2n + 1)^{1/2} l_B$ , then we have  $Y - Y' = A_n + A_{n+1}$  at the critical breakdown field as described by Eaves and Sheard [17]. Then we can calculate the critical field

$$F_{\text{cr}}(\text{TH}) = \frac{\hbar\omega_c}{el_B[(2n + 1)^{1/2} + (2n + 3)^{1/2}]}, \quad (2)$$

where  $n = 0$  for  $i = 1$  and 2,  $n = 1$  for  $i = 4$ . Here,  $i$  is the quantum number for the Hall plateau as  $R_H = h/ie^2$ . Calculated critical fields for  $i = 1, 2$  and 4 are given in Table 1.

The calculated critical fields  $F_{\text{cr}}(\text{TH})$  are much larger than the corresponding experimental values  $F_{\text{cr}}$ . This fact can be explained in terms of localization. If the range of random potentials is

larger than the radius of a Landau orbit, it is easy to see that the electric field in extended states is enhanced as there are no electric fields in localized regions [16]. In the case of short range random potentials, similar enhancement of the electric field for the extended state electrons is expected because the Hall voltage is fixed against the change in the magnetic field in the QHE. Then it is plausible to consider that the ratio  $F_{\text{cr}}/F_{\text{cr}}(\text{TH})$  is a measure of the ratio (number of extended states)/(total number of states). As shown in Table 1, the ratio  $F_{\text{cr}}/F_{\text{cr}}(\text{TH})$  decreases with increasing magnetic field. This behaviour is reasonable as it is expected that the smaller the radius of the Landau orbit the stronger the localization in Landau levels.

As Fontein et al. [18] observed, enhancement of the Hall field near the edges of a Hall bar sample should take breakdown into consideration. The electric field near the edge  $F_{\text{edge}}(y)$  is calculated at the point  $\xi$  separated from the sample edge for each sample by using Beenakker's formula [19] as

$$F_{\text{edge}}(w'/2 - \xi) = \frac{I_{\text{cr}} R_H(i)}{2\xi[1 + \ln(\omega'/\xi)]}, \quad (3)$$

where  $\xi$  is a characteristic length  $\xi = il_B^2/\pi a^*$ ,  $a^*$  the effective Bohr radius, and  $\xi$  (nm) = 21.0

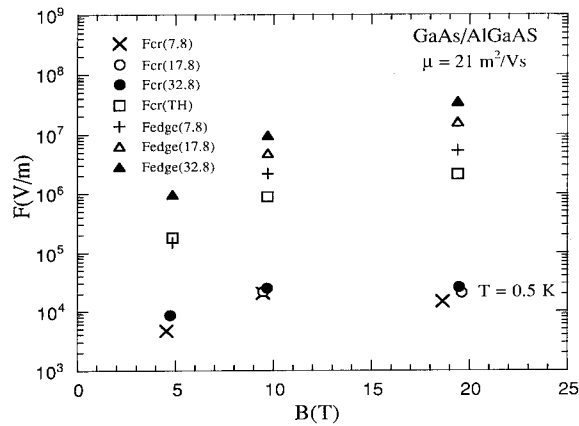


Fig. 3. Sample edge fields  $F_{\text{edge}}(w')$  for each sample at the magnetic fields for  $i = 1, 2$ , and 4 calculated by Eq. (3), critical field for inter-Landau-level transition  $F_{\text{cr}}(\text{TH})$  and experimental critical field  $F_{\text{cr}}(w')$  observed at  $T = 0.5$  K.

$\times (i/B(T))$ . Calculated results are shown in Fig. 3 with experimental results and calculated critical fields  $F_{cr}(TH)$  for the inter-Landau-level transition. The calculated edge fields are larger than  $F_{cr}(TH)$  in each magnetic field and strongly depend on the sample width, whereas the experimental critical fields do not depend on the sample width. Further studies are necessary to treat the field distribution quantitatively.

Recently, Nikopoulos and Trugman [20] studied quantum potential scattering from abrupt scatterers in the quantum Hall regime. They have shown that the inter-Landau-level tunneling is strongly enhanced by spatially extended scatterers. Complex quantum scattering which they studied is another possible mechanism of the breakdown of the QHE.

In conclusion, we have observed the magnetic field dependence of the sample-width-dependent critical breakdown current of the quantum Hall effect, and found that the results can be explained in terms of localization in Landau levels without edge-state transport.

#### 4. Acknowledgements

The authors wish to thank J. Sakai, K. Hirama, K. Aketagawa and Y. Kurata, The 2nd Thin Film Engineering Department, ANELVA Corporation, for providing GaAs/AlGaAs wafers. They thank also Professor H. Nagasawa for his help in SEM observations. This work is supported in part by the Grants-in-Aid for Scientific Research on Priority Area, "Electron Wave Interference Effects in Mesoscopic Structures" from the Ministry of Education, Science and Culture.

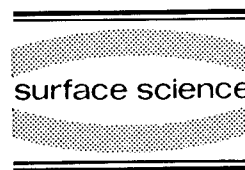
#### 5. References

- [1] T. Ando, Y. Matsumoto and Y. Uemura, J. Phys. Soc. Jpn. 39 (1975) 279.
- [2] S. Kawaji and J. Wakabayashi, Physics in High Magnetic Fields, Eds. S. Chikazumi and N. Miura (Springer, Berlin, 1981) p. 284.
- [3] K. von Klitzing, G. Dorda and M. Pepper, Phys. Rev. Lett. 45 (1980) 449.
- [4] See, for example, The Quantum Hall Effect, Eds. R.E. Prange and S.M. Girvin (Springer, New York, 1987).
- [5] R.B. Laughlin, Phys. Rev. B 23 (1981) 5632.
- [6] B.I. Halperin, Phys. Rev. B 25 (1982) 2185.
- [7] M. Büttiker, Phys. Rev. B 38 (1988) 9375.
- [8] See a review, R.J. Haug, Semicond. Sci. Technol. 8 (1993) 131.
- [9] S. Kawaji, K. Hirakawa and M. Nagata, Physica B 184 (1993) 17.
- [10] P.C. van Son, G.H. Kruithof and T.M. Krapwijk, Phys. Rev. B 42 (1990) 11257.
- [11] L. Bliok, G. Hein, D. Jucknischke, K. Kose, J. Niemeier, G. Weimann and W. Schlapp, Surf. Sci. 196 (1988) 156.
- [12] G. Ebert, K. von Klitzing, K. Ploog and G. Weimann, J. Phys. C 16 (1983) 5441.
- [13] M.E. Cage, R.F. Dziuba, B.F. Field, E.R. Williams, S.M. Girvin, A.C. Gossard, D.C. Tsui and R.J. Wagner, Phys. Rev. Lett. 51 (1983) 1374.
- [14] H.L. Störmer, A.M. Chang, D.C. Tsui and J.C.M. Hwang, Proc. 17th ICPS, 1984, San Francisco, Eds. J.D. Chadi and W.A. Harrison (Springer, Berlin, 1985) p. 267.
- [15] S. Komiyama, T. Takamasu, S. Hiyamizu and S. Sasa, Solid State Commun. 54 (1985) 479.
- [16] S. Kawaji, Proc. Int. Symp. Foundation of Quantum Mechanics, Tokyo, 1983, Eds. S. Kamefuchi et al. (Physical Society of Japan, 1984) p. 327.
- [17] L. Eaves and F.W. Sheard, Semicond. Sci. Technol. 1 (1986) 346.
- [18] P.F. Fontein, P. Hendricks, F.A.P. Blom, J.H. Wolter, L.J. Giling and C.W.J. Beenakker, Surf. Sci. 263 (1992) 91.
- [19] C.W.J. Beenakker and H. van Houten, Solid State Physics, Vol. 44, Eds. H. Ehrenreich and D. Turnbull (Academic Press, New York, 1992) p. 1.
- [20] V. Nikos Nikopoulos and S.A. Trugman, Phys. Rev. Lett. 65 (1990) 779.



ELSEVIER

Surface Science 305 (1994) 166–171



# Effects of electron–electron interactions on the ground state of quantum Hall edge states

B.Y. Gelfand \*, Jed Dempsey, B.I. Halperin

*Lyman Laboratory of Physics, Harvard University, Cambridge, MA 02138, USA*

(Received 27 May 1993; accepted for publication 20 July 1993)

## Abstract

We study the effects of electron–electron interactions on the ground states of integral and fractional quantum Hall edge states. We introduce a realistic model of a mesa-etched sample edge and solve it within an electrostatic approximation. Applying the Hartree–Fock approximation to integral quantum Hall edge states, we show that, in the absence of Zeeman splitting, the outermost edge state undergoes a spontaneous transition between spin-unpolarized and spin-polarized ground states at a confining-potential-dependent critical value of the bulk filling  $\nu_{bulk}^c$ . We apply these general results to our model of mesa-etched sample edges and obtain  $\nu_{bulk}^c$  as a function of model parameters, with  $\nu_{bulk}^c \approx 4$ . The relatively abrupt appearance, in the spin-polarized state, of a sizable (about a magnetic length) separation between edge states of opposite spin should make this transition accessible to a range of magneto-transport experiments. For a 2DEG in the fractional quantum Hall regime we use our electrostatic model to obtain the widths of the fractional quantum Hall strips separating the conducting edge states from each other and from the conducting bulk. This allows us to estimate the quasi-particle scattering rate and the corresponding equilibration length between the edge states and the bulk. We compare these estimates with measurements of non-local resistance.

## 1. Introduction

Edge states in the integral [1–3] and fractional [2–5] quantum Hall regimes have been the subject of intense study in the past few years because of their importance to magnetotransport in a broad range of mesoscopic and macroscopic systems. Attention has increasingly focussed on the effects of electron–electron interactions on edge-state properties [3–6]. To understand the

structure of the ground state we can start with a particular model of the sample edge and solve for the 2DEG density profile using classical electrostatics [3,5]. As long as electron density varies slowly on the scale of magnetic length we can describe edge states as wide compressible regions separated by relatively narrow quantum Hall strips, with the positions and the widths of these strips determined by the electrostatic density profile [3–5]. However, when the electron density varies rapidly on the scale of magnetic length, as may be the case for the outermost edge state, quantum mechanics has to be included more systematically. In particular, for IQHE edge states

\* Corresponding author.

we can use the Hartree–Fock approximation, provided we treat the electron spin properly, i.e. allow each spin state to adjust independently [7,8].

## 2. Electrostatic model

We consider a model of the sample edge appropriate for a mesa-etched sample (Fig. 1, inset). The surface charge  $n_s(z)$  (due perhaps to the occupation of surface states) depletes the 2DEG out to distance  $W_D$  from the mesa wall, which is usually large compared to magnetic length,  $W_D \approx 3000\text{--}5000 \text{ \AA}$  [9]. Within classical electrostatics 2DEG acts like a metal half-plane with movable edge. The corresponding two-dimensional electrostatics problem can be solved by conformal mapping [5]. For any localized  $n_s(z)$  the electron density  $n(x)$  will approach its bulk value as  $n(x)/n_0 \approx 1 - \eta(W_D/x)^{3/2}$  at large distances ( $x \gg W_D$ ). Note that Chklovskii et al. [3] obtain  $1/x$  power-law healing, instead of  $1/x^{3/2}$ . This difference arises from the fact that they use a semi-infinite metal electrode to confine the 2DEG, whereas we use a surface charge confined to a finite region near the edge. If we take  $n_s(z) =$

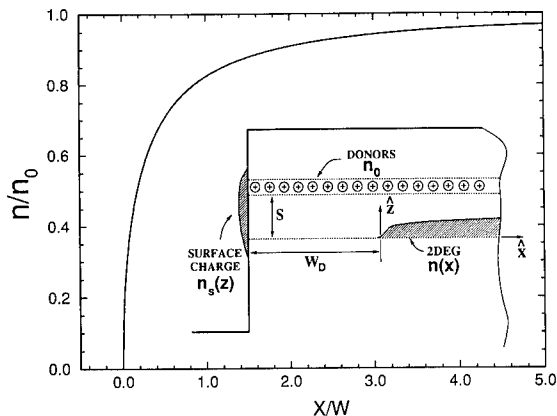


Fig. 1. Electrostatic density profile of the 2DEG for the model shown in the inset. Inset: model of mesa-etched sample edge, with a thin donor layer at distance  $S$  from the 2DEG and the surface charge  $n_s(z)$  on the mesa wall, depleting the 2DEG out to distance  $W_D$  from the wall.

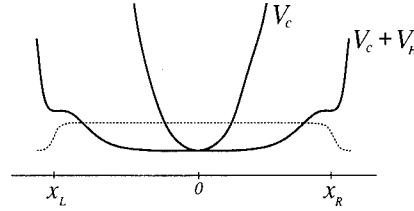


Fig. 2. Potential and density profiles for a wide quantum wire. The bare confining potential  $V_c$  and the total self-consistent potential  $V_c + V_H$  are shown as solid lines, and the electron density as a broken line.

$\lambda \delta(z)$  then the exact solution is easily obtained:  $\lambda = 2n_0(WW_D)^{1/2}$  and

$$n_{es}(x) = \frac{n_0}{\pi} \left[ \frac{2\sqrt{\xi}}{\xi + 1 - \beta^2} + \tan^{-1}(\sqrt{\xi} - \beta) + \tan^{-1}(\sqrt{\xi} + \beta) \right], \quad (1)$$

where  $W = \frac{1}{2}[W_D^2 + (W_D^2 + S^2)^{1/2}]$ ,  $\xi = x/W$ , and  $\beta = S/2W$  (Fig. 1). Note that the electron density changes slowly on the scale of magnetic length everywhere, except near the edge ( $x = 0$ ), where  $n_{es}(x) \sim x^{1/2}$  and the density gradient becomes large.

## 3. Spin-polarizing transition

We now proceed to apply the Hartree–Fock approximation to integral quantum Hall edge states [7]. We consider a wide quantum wire along the  $y$ -axis. In Landau gauge,  $A = Bx\hat{y}$ , the Hartree–Fock single-particle wavefunctions are  $\psi_{nX}^\sigma(x, y) = \exp(-iXy/l^2)\phi_{nX}^\sigma(x)$ , where  $l$  is the magnetic length and  $\phi_{nX}^\sigma(x)$  is an eigenfunction of the Hamiltonian  $H = H_0 + V_c(x) + V_H(x) + H_{ex} + \sigma\epsilon_Z$ , with eigenvalue  $\epsilon_n^\sigma(X)$ . Here  $H_0 = (p_x^2 + \hbar^2 l^{-4}(x - X)^2)/2m$ ,  $V_c(x)$  is the bare confining potential that defines the wire, and  $V_H(x) = -2e^2 \int dx' n(x') \log|x - x'|$  is the Hartree potential (Fig. 2). The 2DEG density is  $n(x) = \sum_{n\sigma X} \nu_n^\sigma(X) |\phi_{nX}^\sigma(x)|^2$ , where  $\nu_n^\sigma(X)$  is the  $X$ -dependent filling factor for each Landau level and spin state. Self-consistency requires that  $\nu_n^\sigma(X) = f(\epsilon_n^\sigma(X))$ , where  $f(\epsilon)$  is the Fermi function. The

spin-dependent terms in the Hamiltonian are the exchange operator  $H_{\text{ex}}^{\sigma}$  and the Zeeman splitting (with  $\epsilon_Z = \frac{1}{2}g\mu_B B$ ), which both conserve  $X$ .

It is convenient to decompose the electron-charge density into a uniform slab of density  $\nu_{\text{bulk}}/2\pi l^2$  and residual distributions of charge concentrated near each edge of the slab:  $n(x) = (\nu_{\text{bulk}}/2\pi l^2)\theta(x - x_L)\theta(x_R - x) + \Delta n^L(x) + \Delta n^R(x)$ , where  $\theta(x)$  is a step function, and  $x_{L,R}$  are chosen so that  $\Delta n^{L,R}$  have each zero net charge. We can not divide  $V_H$  into a term  $V_H^L$  that depends only on  $\Delta n^L$ ,  $x_L$ , and a term  $V_H^R$  that depends only on  $\Delta n^R$ ,  $x_R$ . We lump  $V_H^L$  with  $V_c$  into an effective confining potential  $V_c^{\text{eff}} = V_c + V_H^L$ , which is nearly independent of local rearrangements of charge near  $x_R$ , if the wire is wide. Our approach is to apply Hartree–Fock, treating  $V_c^{\text{eff}}$  as a truly fixed confining potential and  $V_H^R$  as the effective Hartree potential.

In the strong field limit, where we can ignore mixing between Landau levels, we solve the case  $\nu_{\text{bulk}} = 2$  explicitly. We shift the origin to  $x_R$  for notational simplicity and consider a spin-polarized trial state with integral Landau level fillings:  $\nu_0^{\sigma}(X; \Delta X) = \theta(-X - \sigma\Delta X/2)$ . The single-particle energies corresponding to the trial solution depend on spin and on the width parameter  $\Delta X$ :  $\epsilon_0^{\sigma}(X; \Delta X) = \epsilon_c^{\text{eff}}(X) + \epsilon_H(X; \Delta X) + \epsilon_{\text{ex}}^{\sigma}(X; \Delta X) + \sigma\epsilon_Z$  – the sum of contributions from  $V_c^{\text{eff}}$ , Hartree ( $V_H^R$ ), exchange, and Zeeman splitting, respectively. A very hard confining potential will dominate electron–electron interactions and our integer-filling trial state (with  $\Delta X = 0$  for  $\epsilon_Z = 0$ ) will certainly be the Hartree–Fock ground state. We find that, as the confining potential is softened, an integer-filling trial state of the form  $\nu_0^{\sigma}(X; \Delta X)$  still satisfies the Hartree–Fock equations and, in fact, represents a true local minimum in the full space of Hartree–Fock wavefunctions. Eventually, for very soft confining potential, the integer filling state gives way to a solution with fractional filling.

Within the integer-filling regime we can find  $\Delta X^*$  that renders the trial solution self-consistent by minimizing the energy  $E(\Delta X) = \sum_{\sigma X} \nu_0^{\sigma} [\epsilon_0^{\sigma} - \frac{1}{2}(\epsilon_H + \epsilon_{\text{ex}}^{\sigma})]$  numerically for any given  $V_c^{\text{eff}}$ , then checking for self-consistency by calculating  $\epsilon_0^{\sigma}(X; \Delta X)$  explicitly [10]. In addition,

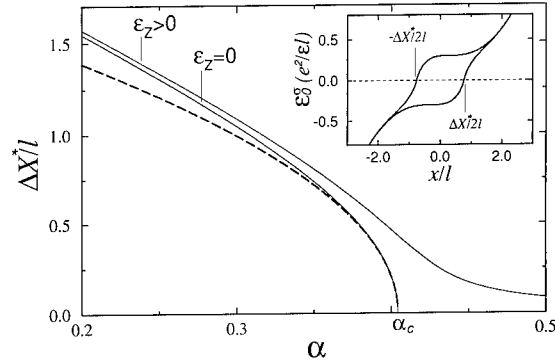


Fig. 3. Equilibrium separation  $\Delta X^*$  of edge states of opposite spin as a function of slope parameter  $\alpha = a_1 l / (e^2 / \epsilon l)$ , with and without the Zeeman energy appropriate for GaAs at  $B = 2$  T (solid lines). Broken line shows the Landau-theory approximation. Inset: self-consistent, single-particle energies  $\epsilon_0^{\sigma}(X; \Delta X^*)$  for  $\alpha = 0.2 < \alpha_c$  (solid lines); Fermi level (dashed line).

we can gain insight by expanding  $\epsilon_c^{\text{eff}}(X) = \sum_m a_m X^m$  and writing

$$E(\Delta X) \approx E(0) + \frac{1}{2\pi l} \left[ -\epsilon_Z \Delta \tilde{X} + \frac{1}{4} \frac{e^2}{\epsilon l} \times (\alpha - \alpha_c) \Delta \tilde{X}^2 + \frac{1}{4!} \frac{e^2}{\epsilon l} \times (\alpha_3 + \beta) \Delta \tilde{X}^4 + \dots \right], \quad (2)$$

an expansion in powers of  $\Delta \tilde{X} \equiv \Delta X/l$ . In this expansion  $\alpha = a_1 l / (e^2 / \epsilon l)$  is the (scaled) slope of  $\epsilon_c^{\text{eff}}$ ,  $\alpha_c = 0.404$ ,  $\beta = 0.318$ , and  $\alpha_3 = \frac{3}{4} l^3 a_3 / (e^2 / \epsilon l)$ . Eq. (2) has the form of Landau free energy for a second-order phase transition, with  $\Delta \tilde{X}$  as the order parameter and  $\epsilon_Z$  as the external field. We see that with  $\epsilon_Z = 0$  there is a spontaneous spin-polarizing transition when  $\alpha$  is reduced below  $\alpha_c$ . The exact numerical solution for  $\Delta X^*$  is shown in Fig. 3 for the case  $\epsilon_c^{\text{eff}} = a_1 X$  and is compared with the approximate result  $\Delta X^*/l = [(3/\beta)|\alpha - \alpha_c|]^{1/2} \theta(\alpha_c - \alpha)$ , found by truncating the series (3) after  $\Delta \tilde{X}^4$ . Note that the Zeeman energy smears out the transition in the region near  $\alpha_c$ .

In Figs. 4a–4d we illustrate the evolution of the edge states as the parameter  $\alpha$  is reduced. For  $\alpha > \alpha_c$  the edge is unpolarized (taking  $\epsilon_Z =$

0), as shown in Fig. 4a. As  $\alpha$  is reduced below  $\alpha_c$ , the electron system undergoes a second-order transition to the spin-polarized state shown in Fig. 4b. As  $\alpha$  is reduced still further the ground state acquires regions with fractional filling, as shown in Fig. 4c. In the limit of very soft potential, the Landau-level filling is fractional and the screening is metallic everywhere except for an incompressible region at  $\nu = 1$  due to the exchange energy gap [3]. When corrections to Hartree–Fock are included, the filling factor  $\nu_0^\sigma(X)$  will no longer be strictly integral even for very hard confining potentials, but a Fermi surface (i.e., a discontinuity in filling) will still exist for each spin state [6], and the limiting cases of an unpolarized ground state for hard-wall confinement and a polarized ground state for soft confinement will still obtain. Hence, the symmetry-breaking transition from a ground state where the Fermi surface positions for the two spin states coincide to one where they are split should persist beyond Hartree–Fock.

To make contact with a realistic system and bring out the physics of the spin-polarizing transition we now apply our results to the outermost edge state, using the mesa-etched sample edge model of Section 2. We fix the electronic charge in the higher Landau levels at its electrostatic density  $n_{es}(x)$  and allow the two spin states in the lowest Landau level to minimize their energy, as discussed above. The appropriate effective con-

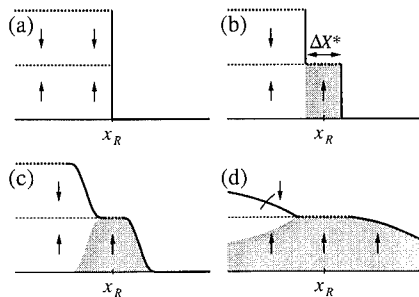


Fig. 4. Evolution of the edge states as the effective confining potential is softened. (a) Unpolarized ground state for steep confining potential ( $\alpha > \alpha_c$ ). (b) Spontaneously polarized integral filling state for  $\alpha < \alpha_c$ . (c) Possible ground state with regions of fractional filling. (d) Ground state with fractional filling in the electrostatic regime. Shading indicates net spin polarization.

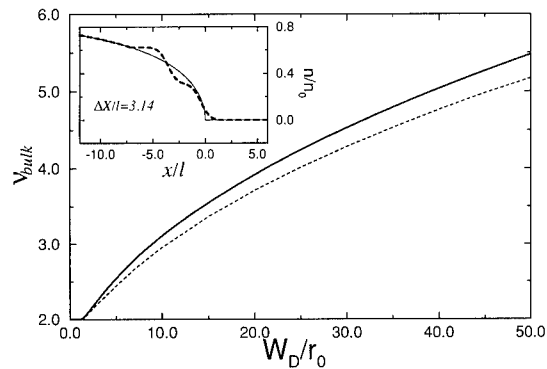


Fig. 5. Solid line shows critical value of bulk filling factor  $\nu_{\text{bulk}}^c$  as a function of  $W_D/r_0$ , where  $W_D$  is the depletion width and  $r_0$  is the interparticle spacing; broken line shows the value of  $\nu_{\text{bulk}}$  where  $\Delta X = l$ . Inset: comparison of classical electrostatic electron density (solid line) to the density given by our approximation (dashed line), with parameters  $\nu_{\text{bulk}} = 3.2$  and  $W_D/r_0 = 25$ .

fining potential  $V_c^{\text{eff}}$  is determined by the depletion width  $W_D$  and bulk filling  $\nu_{\text{bulk}}$ . The Hartree–Fock ground state is then determined by the two-dimensionless parameters  $\nu_{\text{bulk}}$  and  $\tilde{d} \equiv W_D/r_0$ , where  $r_0 = (\pi n_0)^{-1/2}$  is the interelectron spacing. For given  $\tilde{d}$ , there is a critical bulk filling  $\nu_{\text{bulk}}^c(\tilde{d})$  ( $> 2$ ) such that for  $\nu_{\text{bulk}} > \nu_{\text{bulk}}^c$  the lowest Landau level is spin-unpolarized, while for  $\nu_{\text{bulk}} < \nu_{\text{bulk}}^c$  it is spin-polarized, with  $\Delta X^*$  on the order of the magnetic length (Fig. 5).

Within this model the spin-polarizing transition may be understood as follows. If  $\nu_{\text{bulk}}$  is large then the region with  $0 < 2\pi l^2 n_{es}(x) < 2$  is a narrow strip close to the edge, where  $n_{es}(x)$  is steep. The quantum solution can best approximate the electrostatic density by choosing an abrupt drop in filling from 2 to 0, as in Fig. 4a, with no polarization in the outermost edge state. If  $\nu_{\text{bulk}}$  is only slightly greater than 2, however, and if  $W_D \gg l$ , then the region with  $0 < 2\pi l^2 n_{es}(x) < 2$  is wide on the scale of  $l$ , and the quantum solution mimics the more gradual density profile by developing a spin-polarized ground state, as in Figs. 4b–4d. Note that without exchange, which stabilizes the spin-polarized integer-filling state relative to states with fractional filling (because exchange favors completely filled or completely empty spin-split Landau levels), the quantum solution would achieve a gradual den-

sity profile through fractional filling. For  $\nu_{\text{bulk}} \geq 4$ , when the outermost edge state is typically unpolarized, there might nevertheless occur a spontaneous polarization of inner edge states, as these are deeper in the sample, where the density gradient is smaller.

Since a sizable spatial separation between edge states of opposite spin appears rather abruptly when the lowest Landau level becomes spin-polarized, and since  $\nu_{\text{bulk}}$  can be varied by changing  $B$ , the transition should be detectable in several experiments. In measurements of equilibration between opposite spin states in the outermost edge channel [11], for example, the abrupt increase in separation should strongly reduce the scattering rate and increase the equilibration length. In measurements of Aharonov–Bohm (AB) oscillations in conductance, both in quantum dots [12] and in single-point contacts [13], the spatial separation between different spin states will lead to different AB frequencies and to beats in the AB oscillations as a function of magnetic field. In point contacts [2,14], the separation should lead to spin-split conductance steps that depend on the perpendicular and not the in-plane component of  $B$ .

#### 4. Structure of FQHE edge states

The model defined in Section 2 can also be applied to fractional edge states in the slowly varying density regime. In this case conducting channels are separated by a quantum Hall strip when the Landau-level filling  $\nu_{\text{es}}(x) = 2\pi l^2 n_{\text{es}}(x)$  reaches  $\nu_f = p/q$ , i.e. the position  $x_f$  of the strip is given by  $\nu_{\text{es}}(x_f) = \nu_f$ . One approach to obtaining the width  $d_f$  of this strip is to take it to be incompressible, with potential drop across the strip given by  $q\Delta$ , where  $\Delta$  is the FQHE energy gap [3,4]. If we assume the rest of the 2DEG to be perfectly screening, then the problem reduces to one of classical electrostatics. Approximating  $n_{\text{es}}(x)$  by a linear function about  $x_f$ , Chklovskii et al. [3] obtain

$$d_f^2 = \frac{4\gamma q}{\pi^2 l (dn_{\text{es}}/dx)_{x=x_f}}, \quad (3)$$

where  $\gamma = \Delta/(e^2/\epsilon l)$ . However, in the presence of disorder, FQHE liquid will have non-zero compressibility and, at low temperatures, the bulk diagonal conductivity will be extremely small over some range of fillings  $|\nu - \nu_f| < \delta\nu_f$ . Hence, we can obtain an alternative estimate of  $d_f$  by assuming perfect screening for all fillings, i.e. neglecting any deviations from  $n_{\text{es}}(x)$  near  $x_f$  and, by analogy with bulk, assuming that the region given by  $|\nu_{\text{es}}(x) - \nu_f| < \delta\nu_f$  is in the FQHE regime. This approach gives us

$$d_f = |x(\nu_f + \delta\nu_f) - x(\nu_f - \delta\nu_f)|, \quad (4)$$

where  $x(\nu)$  is the inverse of  $\nu_{\text{es}}(x)$  and  $\nu_{\text{bulk}} \geq \nu_f + \delta\nu_f$ .

At low temperatures, equilibration between conducting channels occurs mainly through quasi-particle scattering across the separating FQHE strip. In Born approximation (neglecting multiple scattering), at  $T=0$ , the scattering rate is reduced by a Gaussian factor,  $G(d_f) = \exp(-d_f^2/2l_f^2)$ , where  $l_f = q^{1/2}l$  is the *quasi-particle* magnetic length. In Fig. 6 we plot  $G^{-1}$  (on a logarithmic scale) as a function of bulk filling for  $\nu_f = \frac{1}{3}$  and  $\nu_f = \frac{2}{3}$ , using representative values of the parameters  $\delta\nu_f$  and  $\gamma$ . The value of  $\delta\nu_f$  was estimated from the bulk  $\sigma_{xx}$  plot of Ref. [15] at  $T = 20$  mK. Note that Eq. (4) gives larger  $d_f$  than the incompressible strip approximation (Eq. (3)). In a real system we should be somewhere between the two limits. When  $\nu_{\text{bulk}}$  lies between two successive FQHE plateaus,  $\nu_f < \nu_{\text{bulk}} < \nu'_f$ , the bulk itself forms a (dissipative) conducting channel. As  $\nu_{\text{bulk}}$  approaches  $\nu_f$  from above the  $\nu = \nu_f$ , the FQHE strip becomes wide and, in fact, the equilibration length between the edge states and the bulk ( $L_{\text{eq}}$ ) should become macroscopically large when  $G^{-1} \approx 10^4$ . Non-local resistance measurements by Wang and Goldman [15] show that  $L_{\text{eq}}$  indeed becomes comparable to sample size in the interplateau regions. We believe that there is indication of a transition to macroscopic  $L_{\text{eq}}$  caused by the  $\nu_f = \frac{1}{3}$  strip in the data for one of the edges reported in Ref. [15], and that the same data suggests bounds on a similar transition for  $\nu_f = \frac{2}{3}$  [5]. (These points are shown by the solid square and solid arrow in Fig. 6.) These results are in reasonable agreement

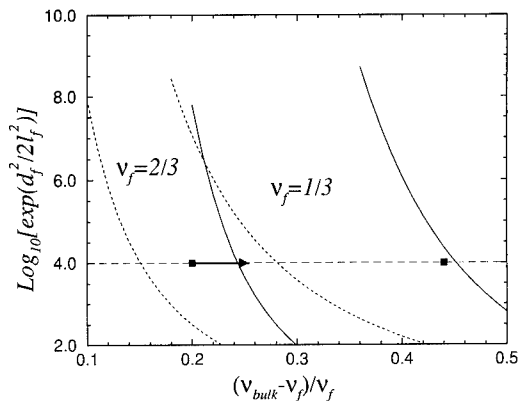


Fig. 6. Gaussian enhancement factor for the edge equilibration length as a function of bulk filling for  $\nu_f = \frac{1}{3}$  and  $\nu_f = \frac{2}{3}$  FQHE strips for parameters  $W_D = 4000 \text{ \AA}$ ,  $n_0 = 8.74 \times 10^{10} \text{ cm}^{-2}$ ,  $\delta\nu_f = 0.017$ , and  $\gamma = 0.03$  (logarithmic scale). Solid lines give the disordered sample estimates (Eq. (4)) and broken lines the incompressible strip estimates (Eq. (3)). Above the long-dashed line the equilibration length  $L_{eq}$  is macroscopically large. Solid square indicates a transition to macroscopic  $L_{eq}$  inferred from the non-local resistance measurements of Ref. [15] ( $\nu_f = \frac{1}{3}$ ), and the arrow indicates the lower bound on a similar transition for  $\nu_f = \frac{2}{3}$ .

with our estimates. The assumption of a Gaussian suppression of the scattering rate will break down at large values of  $d_f$  due to one or another competing process; e.g., multiple (virtual) scattering processes at  $T = 0$  [16], or variable range hopping at  $T \neq 0$ . In either case, the enhancement of the equilibration length will increase more slowly as a function of  $d_f$  than an inverse Gaussian. This would then decrease the steepness of the curves plotted in Fig. 6.

## 5. Acknowledgements

The authors would like to thank J.P. Eisenstein, C.M. Marcus, P.M. Young and Partha Mitra for useful discussions. This work was supported in part by the NSF through the Harvard

Materials Research Laboratory and grant DMR91-15491.

## 6. References

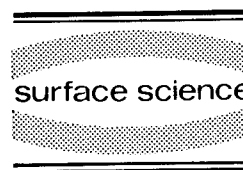
- [1] B.I. Halperin, Phys. Rev. B 25 (1982) 2185; M. Büttiker, Phys. Rev. Lett. 57 (1990) 1761; B.W. Alphenaar, P.L. McEuen, R.G. Wheeler and R.N. Sacks, Phys. Rev. Lett. 64 (1990) 677.
- [2] See, e.g., C.W.J. Beenakker and H. van Houten, in: H. Ehrenreich and D. Turnbull, Eds., Solid State Phys. 44 (1991) 1, and references therein.
- [3] D.B. Chklovskii, B.I. Shklovskii and L.I. Glazman, Phys. Rev. B 46 (1992) 4026.
- [4] C.W.J. Beenakker, Phys. Rev. Lett. 64 (1990) 216; A.H. MacDonald, Phys. Rev. Lett. 64 (1990) 220.
- [5] B.Y. Gelfand and B.I. Halperin, Phys. Rev. B 49 (1994).
- [6] X.G. Wen, Phys. Rev. Lett. 64 (1990) 2206; F.D.M. Haldane, Bull. Am. Phys. Soc. 35 (1990) 254; S.R. Renn, Phys. Rev. Lett. 68 (1992) 658.
- [7] J. Dempsey, B.Y. Gelfand and B.I. Halperin, Phys. Rev. Lett. 70 (1993) 3639.
- [8] P.L. McEuen, E.B. Foxman, J. Kinaret, U. Meirav, M.A. Kastner, N.S. Wingreen and S.J. Wind, Phys. Rev. B 45 (1992) 11419, have included some aspects of spin in quasi-classical self-consistent calculations on quantum dots.
- [9] K.K. Choi, D.C. Tsui and K. Alavi, Appl. Phys. Lett. 50 (1987) 110.
- [10] The trial solution's failure to be self-consistent marks the transition to the fractional-filling regime.
- [11] G. Müller, D. Weiss, A.V. Khaetskii, K. von Klitzing, S. Koch, H. Nickel, W. Schlapp and R. Lösch, Phys. Rev. B 45 (1992) 3932.
- [12] See, e.g., B.J. van Wees, L.P. Kouwenhoven, C.J.P.M. Harmans, J.G. Williamson, C.E.T. Timmering, M.E.I. Broekaart, C.T. Foxon and J.J. Harris, Phys. Rev. Lett. 62 (1989) 2523.
- [13] P.H.M. van Loosdrecht, C.W.J. Beenakker, H. van Houten, J.G. Williamson, B.J. van Wees, J.E. Mooij, C.T. Foxon and J.J. Harris, Phys. Rev. B 38 (1988) 10162.
- [14] See, e.g., B.J. van Wees, L.P. Kouwenhoven, H. van Houten, C.W.J. Beenakker, J.E. Mooij, C.T. Foxon and J.J. Harris, Phys. Rev. B 38 (1988) 3625.
- [15] J.K. Wang and V.J. Goldman, Phys. Rev. Lett. 67 (1991) 749; Phys. Rev. B 45 (1992) 13479.
- [16] T. Martin and S. Feng, Phys. Rev. B 44 (1991) 9084.





ELSEVIER

Surface Science 305 (1994) 172–175



# Total suppression of the inter-edge-channel scattering in a GaAs/AlGaAs heterostructure

R.J.F. van Haren \*, F.A.P. Blom, W. de Lange, J.H. Wolter

*Department of Physics, Eindhoven University of Technology, P.O. Box 513, 5600 MB Eindhoven, Netherlands*

(Received 11 May 1993; accepted for publication 4 June 1993)

## Abstract

We demonstrate that the inter-edge-channel scattering of a two-dimensional electron gas in the quantum Hall regime can be dramatically suppressed when the confining potential at the boundaries of the sample is altered. The confining potential is changed by making use of a half-gated GaAs/AlGaAs heterostructure. This results in a large spatial separation of the respective edge channels. We use an interior contact to detect or feed the separated edge channels. Due to the large spatial separation, it is shown that the equilibration length becomes arbitrarily long, even at a relatively high temperature of 1.2 K.

## 1. Introduction

The Landauer–Büttiker model [1,2] has been very successfully applied to explain many transport properties of a two-dimensional electron gas (2DEG) in the quantum Hall regime. Within this approach the edge channels which are formed at the boundaries of a device play a significant role. These edge channels arise at the periphery of the sample where the Landau levels bend up due to the confining potential and intersect the Fermi level [3]. In equilibrium, each edge channel carries an equal fraction of the current so that the total current is simply determined by the total number of edge channels, i.e. the filling factor. Selective contact can be made to the outermost edge channels, i.e. edge channels lying closest to

the boundary of the sample, by using quantum point contacts [4] or contacts with a cross-gate [5–7]. These, and other experiments reveal many new features, such as the lack of equilibration over macroscopic distances [8].

In this paper we show that the inter-edge-state scattering can be totally suppressed when the edge channels are separated sufficiently far from each other. This separation has been realized by using a half-gated device. An interior contact can be used to directly contact the innermost edge channels. The coupling with the innermost edge channels is controlled by the gate voltage contrary to the interior contacts used in literature [9].

## 2. Sample and setup

The structure presented in this work has been grown by molecular beam epitaxy (MBE) and

\* Corresponding author. Fax: +31 (40) 453587.

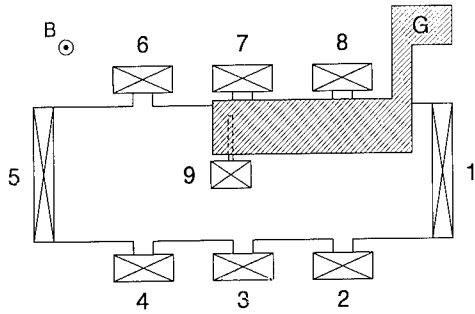


Fig. 1. Top view of the sample used in this work. The gate is indicated by the hatched area. Contact 9 lies on the inner edge that is formed by the groove (dashed line).

contains a two-dimensional electron gas. Starting from the semi-insulating substrate, a 4  $\mu\text{m}$  GaAs layer is grown, followed by a 60 nm undoped  $\text{Al}_{0.33}\text{Ga}_{0.67}\text{As}$  spacer layer, a 38 nm doped (dopant Si:  $1.33 \times 10^{18} \text{ cm}^{-3}$ )  $\text{Al}_{0.33}\text{Ga}_{0.67}\text{As}$  layer, and finally an undoped 17 nm thick GaAs cap layer. By making use of photolithography techniques and subsequently wet-etching, a Hall bar is defined with dimensions  $5.4 \times 2.0 \text{ mm}^2$ . Together with the Hall bar, a groove (860  $\mu\text{m}$  long and 30  $\mu\text{m}$  wide) is etched into the bulk of the sample, as shown in Fig. 1.

Ohmic contacts to the 2DEG are made by lift-off techniques using Ni/AuGe/Ni/Au and annealing at 450°C for 60 s. One of the contacts (number 9) is defined in the middle of the Hall bar, in between contacts 3 and 7, and is connected to the inner edge that is formed by the groove. Finally, the Hall bar is partly covered by a semi-transparent gate (hatched area in Fig. 1) with dimensions  $0.8 \times 2.7 \text{ mm}^2$ . All experiments presented here have been carried out at 1.2 K in magnetic fields up to 7 T. The current  $I_{ij}$  (100 nA) which is applied is sent from contact  $i$  to contact  $j$ . By measuring the voltage  $V_{kl}$  across contact  $k$  and contact  $l$ , we can define a resistance  $R_{ij,kl} \equiv V_{kl}/I_{ij}$ . Prior to the experiments, the sample is illuminated to increase the electron concentration and mobility. Due to the semi-transparent character of the gate, the electron concentration underneath the gate remains somewhat lower than that in the rest of the sample. This difference in electron concentration disappears when a positive gate voltage ( $\sim 100 \text{ mV}$ ) is

applied. From Hall and Shubnikov–de Haas measurements we derive a mobility of  $7.8 \times 10^5 \text{ cm}^2/\text{V} \cdot \text{s}$  and an electron concentration of  $2.3 \times 10^{11} \text{ cm}^{-2}$ .

### 3. Experimental results and interpretation

In Fig. 2 we show the voltage difference  $V_{78}$  (current flows from contact 1 to contact 5) between the probes 7 and 8 as a function of the gate voltage. For bulk filling factors  $b = 2$  and  $b = 4$ ,  $V_{78}$  remains zero, while for  $b = 2\frac{1}{2}$  and  $b = 4\frac{1}{2}$ , a very pronounced structure is visible. For decreasing gate voltage, 2 and 4 minima in the measurements are observed, respectively. These minima correspond to an integer filling factor underneath the gate. Considering the  $b = 2\frac{1}{2}$  case, we see that after the initial vanishing of the Shubnikov–de Haas voltage, the signal comes up again when the gate filling factor (defined as  $g$ ) is not equal to an integer. This means that the extended states underneath the gate couple with the bulk energy states outside the gated region, making backscattering of the electrons possible. At a gate voltage of approximately  $-310 \text{ mV}$ , the electron gas underneath the gate is totally depleted and the voltage probes 7 and 8 are no longer electrically connected with the rest of the sample. If we adjust the magnetic field to an integer bulk filling

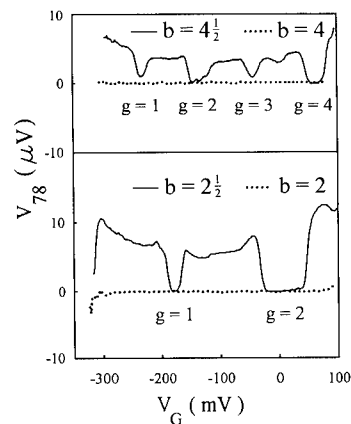


Fig. 2. Measurements of the voltage drop between contacts 7 and 8 as a function of the gate voltage for four bulk filling factors.

factor, the voltages measured between the probes 7 and 8 show no structure at all, i.e. remain zero, when the gate voltage is changed. This means that even in the case where the gate filling factor is not an integer, no resistance is measured. This can be explained by the fact that whole area of the sample outside the gate region has an integer filling factor, thus making backscattering of the electrons impossible. Further, we observe from Fig. 2 that also when the gate filling factor is equal to an integer, the measured voltage  $V_{78}$  remains zero. This can be understood with the help of Fig. 3, where a cross section of the energy states between contacts 7 and 8 is given. In this particular example, we have chosen a bulk filling factor  $b = 2$  and a gate filling factor  $g = 1$ . One edge channel flows along the outer periphery of the sample and is connected to contact 7 and contact 8. The other one follows the edge of the gate and is electrically connected with the interior contact 9. In Fig. 3 it is clearly seen that the edge channels are significantly separated from one another and interaction between the respective edge channels is impossible. From this picture we see that selective contact can be made to the innermost edge channel by means of contact 9, as shown schematically in Fig. 3. In order to test the separation of edge channels experimentally, we can use the interior contact 9 as a

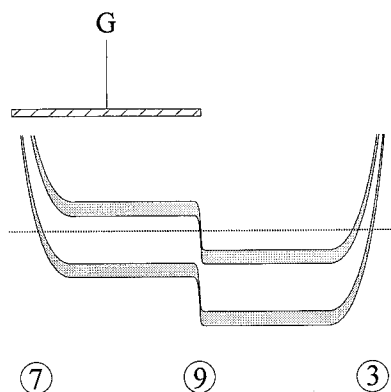


Fig. 3. The effect of the gate (G) on the energy states of the electrons in a magnetic field. In this case, the bulk filling factor  $b = 2$  and the gate filling factor  $g = 1$ . From the picture it is clear that one edge channel is separated by a macroscopic distance. The numbers in the circles indicate the positions of the contacts.

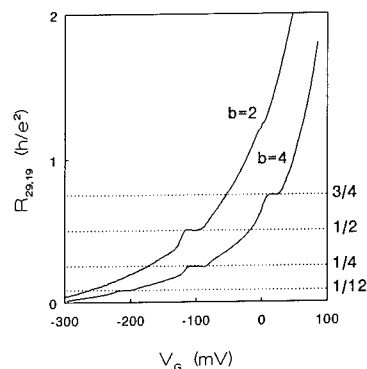


Fig. 4.  $R_{29,19}$  in units of  $h/e^2$  as a function of  $V_G$  at  $b = 2$  and  $b = 4$ . The expected fractions of  $h/e^2$  at which the resistance is quantized are indicated along the right vertical axis.

current injector. Fig. 4 shows the results in case where the current is sent from contact 9 to contact 2 and the voltage is measured between contacts 1 and 9 for two fixed magnetic fields. We observe that the three-terminal resistance goes to infinity when the filling factors of the bulk and the gate are both equal and an integer. All the edge channels flow along the outer boundary of the device and the sample acts like a Corbino disc. When the gate voltage is lowered, we observe plateaus in the resistance according to:

$$R_{29,19} = \frac{h}{e^2} \left( \frac{1}{(b-g)} - \frac{1}{b} \right), \quad (1)$$

when the gate filling factor is equal to an integer.

Measurements of  $R_{29,89}$  reveal that the separated edge channels do not interact with the remaining edge channels underneath the gate. If total equilibration takes place between contact pair 7 and 8, we would expect to measure the quantized resistances given by Eq. (1). Since the measured resistances (see Fig. 5) are equal to:

$$R_{29,89} = \frac{h}{e^2} \left( \frac{1}{(b-g)} \right), \quad (2)$$

we can conclude that the inter-edge-channel scattering between contacts 7 and 8 is totally absent.

In conclusion, we show that in the quantized Hall regime the voltage difference between two contacts on the same side of the sample remains zero when a part of the sample is locally brought

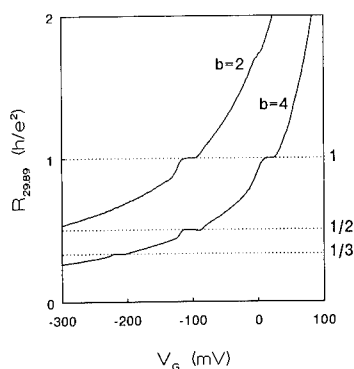


Fig. 5. Measurement of  $R_{29,89}$  versus the gate voltage. From this experiment we can derive that the interaction between the separated and the remaining edge channels is absent.

to another filling factor, provided that the electrons can not backscatter to the opposite side of the sample. The half-gated GaAs/Al<sub>0.33</sub>Ga<sub>0.67</sub>As heterostructure gives us the opportunity to separate the edge channels on the same side of the sample by a macroscopic distance. It is clear that due to the large spatial separation, the inter-

edge-channel scattering is totally suppressed. It is obvious that in this case the meaning of the equilibrium length is no longer well defined.

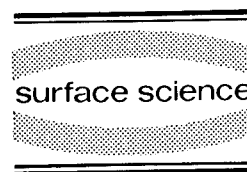
#### 4. References

- [1] R. Landauer, IBM J. Res. Dev. 1 (1957) 223.
- [2] M. Büttiker, Phys. Rev. B 38 (1988) 9375.
- [3] P. Středa, J. Kucera and A.H. MacDonald, Phys. Rev. Lett. 59 (1987) 1973.
- [4] B.J. van Wees, E.M.M. Willems, C.J.P.M. Harmans, C.W.J. Beenakker, H. van Houten, J.G. Williamson, C.T. Foxon and J.J. Harris, Phys. Rev. Lett. 62 (1989) 1181.
- [5] B.W. Alphenaar, P.L. McEuen, R.G. Wheeler and R.N. Sachs, Phys. Rev. Lett. 64 (1990) 677.
- [6] G. Müller, D. Weiss, A.V. Khaetskii, K. von Klitzing, S. Koch, H. Nickel, W. Schlapp and R. Lösch, Phys. Rev. B 45 (1992) 3932.
- [7] S. Komiyama, H. Hirai, M. Ohsawa, Y. Matsuda, S. Sasa and T. Fujii, Phys. Rev. B 45 (1992) 11085.
- [8] R.J. Haug, A.D. Wieck, K. von Klitzing and K. Ploog, Physica B 184 (1993) 192.
- [9] J. Faist, P. Guéret and H.P. Meier, Phys. Rev. B 43 (1991) 9332.



ELSEVIER

Surface Science 305 (1994) 176–180



# Junctions between coplanar 2D gases: a probe of boundary effects in the quantized Hall regime

B.E. Kane \*, L.N. Pfeiffer, K.W. West

*AT&T Bell Laboratories, Murray Hill, NJ 07974, USA*

(Received 19 April 1993; accepted for publication 15 June 1993)

## Abstract

We discuss the behavior of junctions between two coplanar 2D electron gases with different densities in a perpendicular applied magnetic field. The presence of energy gaps in the density of states caused by Landau level quantization and spin splitting leads to behavior in these junctions qualitatively similar to what is observed in a semiconductor p–n junction. We will emphasize aspects of these junctions where the role of electron–electron interactions are important in understanding their properties.

## 1. Introduction

While the physics of uniform density 2D systems has been thoroughly studied, the properties of their boundaries have only recently received attention, most notably in connection with edge states in the quantized Hall regime [1]. Our study of 2D boundaries has focused on junctions between two coplanar 2D gases with different densities in an applied perpendicular magnetic field ( $B$ ). The allowed energies of a 2D system in which disorder and electron–electron (e–e) interactions are neglected are restricted to discrete levels (Fig. 1). If the Fermi energy ( $E_F$ ) lies in different energy levels in two adjoining 2D systems,  $E_F$  must cross between the two levels at their boundary. A semiconductor diode is created

when  $E_F$  crosses between the valence band and the conduction band at the junction. A “Landau level diode” is formed when  $E_F$  crosses between adjacent Landau levels at the junction, while a “spin diode” is created when  $E_F$  crosses between adjacent spin-split levels.

In the usual analysis of a semiconductor diode, the effects of e–e interactions (apart from screening) are entirely ignored since the band gap is much larger than the exciton binding energy (the relevant energy scale for e–e interactions). This simplification is not valid in the study of Landau level diodes and spin diodes implemented in GaAs, since the exciton binding energy is comparable to the Landau level spacing – and greatly exceeds the Zeeman splitting – at typical values of  $B$ ; consequently, phenomena not observable in semiconductor diodes can be expected in these novel junctions. Our observations of spin diodes lead us to propose that a new ground state of the spin polarized 2D electron gas (SP2DEG) can

\* Corresponding author.

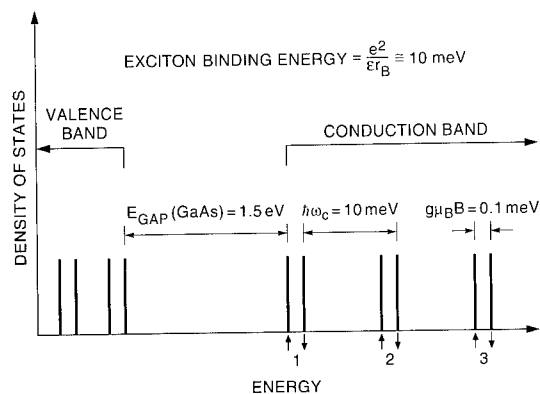


Fig. 1. Density of states as a function of energy for a GaAs quantum well at  $B \cong 5$  T. If  $E_F$  falls between energy levels, the elementary neutral excitations are a bound pair of an electron in the higher level and a vacancy in the lower level. While the binding energy of this exciton is much less than the band gap in GaAs, it is comparable to the cyclotron energy, and greatly exceeds the Zeeman energy.

form in the presence of an electric field  $E$ . Additionally, current–voltage ( $I$ – $V$ ) characteristics of Landau level diodes provide evidence for conduction across these junctions via excitonic states.

## 2. Device fabrication and properties

The devices in our experiments are modulation doped GaAs/ $\text{Al}_x\text{Ga}_{1-x}\text{As}$  heterostructures in which a top gate is used to vary the density in a portion of the structure. Our recent devices have used a self-aligned technique [2] to position the gate immediately adjacent to one of the two ohmic contacts (Fig. 2a). This technique can be extended to make true 2D p–n junctions by using a p-type contact self-aligned to the gate (Fig. 2b). Measurements on Landau level diodes and spin diodes were done on radially symmetric devices: an annular gate lies immediately inside an exterior contact, and surrounds an interior contact. The interior edge of the gate defines the junction. The circumference of the junctions is typically 1 mm.

The width  $W$  of the depletion region (or incompressible region) induced in our structures

can be approximated from the calculations of Chklovskii, Shklovskii, and Glazman [3]:

$$W^2 = \frac{2\epsilon d \Delta E}{\pi^2 e^2 \Delta n},$$

where  $\Delta E$  is the energy gap,  $d$  is the separation between the top gate and the carriers, and  $\Delta n$  is the total change in the 2D carrier density across the junction. Their result is valid in the limit  $W \ll d$ . When  $d = 6000 \text{ \AA}$  and  $\Delta n = 10^{11} \text{ cm}^{-2}$ , we obtain  $W \cong 700 \text{ \AA}$  for a Landau level diode at  $B = 3 \text{ T}$ . Because of the importance of e–e interactions in spin diodes, simply using the Zeeman energy to estimate  $W$  would be inappropriate. We expect that  $W$  for spin diodes is comparable to  $W$  for Landau level diodes.

## 3. Observations

$I$ – $V$  characteristics of the various junctions are plotted in Fig. 3. Positive  $V$  corresponds to forward bias (when the applied  $V$  is reducing the equilibrium  $E$  at the junction). For the 2DEG–2DHG junction (Fig. 3a) the behavior is typical

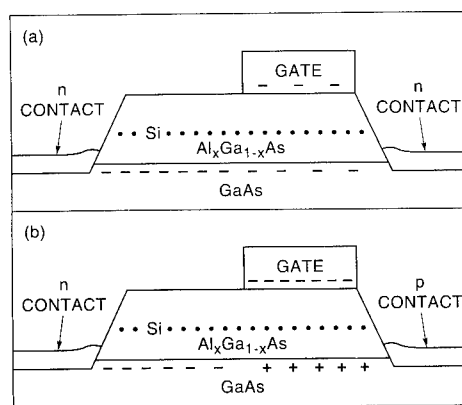


Fig. 2. (a) Side view of a coplanar 2D junction implemented in a modulation doped GaAs/ $\text{Al}_x\text{Ga}_{1-x}\text{As}$  heterostructure. A gate is placed over a portion of the 2DEG, self-aligned to one of the contacts, to regulate the density beneath it. A junction forms at the gate edge when an appropriate bias is applied to the gate. (b) If the self-aligned contact is p-type, it is possible to completely deplete the electrons under the gate and pull holes in from the p contact, forming a coplanar 2DEG–2DHG junction.

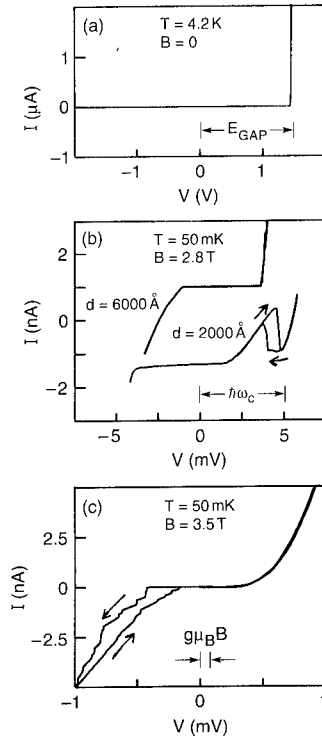


Fig. 3. Experimental  $I$ - $V$  characteristics for various devices. (a) coplanar p-n junction at  $B = 0$ . (b) Landau level diode: a junction between regions of  $\nu = 3/2$  and  $\nu = 5/2$ . The traces for two devices with different gate-2DEG separations are shown and are offset for clarity. (c) Spin diode: a junction between regions of  $\nu = 3/4$  and  $\nu = 5/4$ .  $V$  is slowly swept to obtain this trace.

for a diode: the device abruptly begins to conduct when the forward bias  $V$  exceeds the band gap energy of 1.5 eV. Similar behavior can be seen in the Landau level diode (Fig. 3b): forward bias conduction begins abruptly when  $V$  approaches  $\hbar\omega_c$ ; however, distinct behavior appears in these devices if the gate-2DEG separation is reduced from 6000 to 2000 Å:  $I$  begins to flow when  $V$  is significantly below  $\hbar\omega_c$ . As  $V$  is raised above a point approaching  $\hbar\omega_c$  the device switches to a lower  $I$ . This switching behavior is reminiscent of that observed in double barrier resonant tunneling structures (DBRTS) [4].

Perhaps the most unusual phenomena occurring in coplanar 2D junctions are seen in spin diodes (Fig. 3c). First,  $I$  flowing across a junction

at a given  $V$  is time dependent, often taking several minutes to reach a steady state value. We have established that this behavior is a consequence of dynamic polarization of nuclear spins near the junction when  $I$  is flowing [5,6]. If  $V$  is swept slowly enough so that  $I$  reaches a steady state, the  $I$ - $V$  in reverse bias shows a complex sequence of steps and linear regions. These steps gradually disappear as the temperature is raised [5].

#### 4. Spin diode: evidence for an electric field induced phase transition

While a complete explanation for the structure seen in a spin diode will require an understanding of both nuclear and electronic behavior in these devices, any model must consider the effect of a uniform  $E$  on a SP2DEG, since the depletion region at the junction in the experiments is at  $\nu = 1$ , and since an  $E$  field is present when the diode is in reverse bias. The elementary neutral excitations of a SP2DEG are spin excitons [7], consisting of a bound pair of an electron in the higher spin level and a vacancy or hole in the lower spin level (Fig. 4). This excitation may be pictured classically as an electron-hole pair separated by a constant distance, propagating at a constant velocity in a direction perpendicular to the line connecting them. Quantum mechanically, the excitons are characterized by their wavevector  $k_y$ , and have an electric dipole moment  $\Delta x = k_y l_B^2$ , where  $l_B$  is the magnetic length [7].

The dispersion relation for spin excitons is plotted as the top curve in Fig. 4c. When  $k_y = 0$ , e-e interactions cannot contribute to the energy, and the energy of an exciton is simply the Zeeman energy,  $g\mu_B B$ . Since large  $k_y$  excitons correspond to well separated electron-hole pairs, their energy is the sum of  $g\mu_B B$  and the exciton binding energy, which greatly exceeds  $g\mu_B B$  in GaAs. The ratio  $U(k_y \rightarrow \infty)/U(0) = 20$  that is used to plot Fig. 4c is a value derived from activation energies of a SP2DEG [8], and probably underestimates the true value in GaAs. Notice that all exciton states are bound since a global minimum in  $U(k_y)$  is located at  $k_y = 0$ .

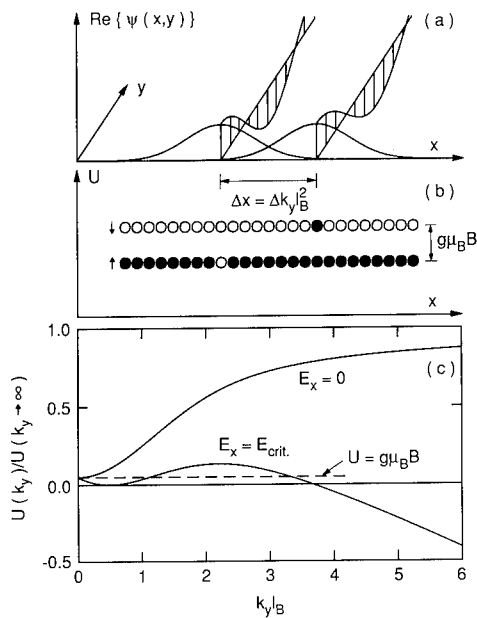


Fig. 4. (a) Lowest Landau level wave functions for electrons confined in the  $x$ - $y$  plane in an applied perpendicular  $B$ . (b) Elementary excitations of a SP2DEG consist of a single electron in a higher spin level and a vacancy in the lower level. (c) Energy of spin excitons as a function of  $k_y$ . When  $E_x \neq 0$ , a new term in the energy appears, proportional to the electric dipole moment of the excitation. When  $E_x = E_{\text{crit}}$ , bound excitons have zero energy and the spin polarized ground state is unstable.

When  $E_x \neq 0$  a new term in the exciton energy appears (bottom trace, Fig. 4c) that is proportional to the exciton electric dipole moment  $\Delta_x$  and to  $k_y$ . For  $E_x$  exceeding some critical field,  $E_{\text{crit}}$ , bound excitonic states will have negative energy with respect to the spin polarized ground state. Electron-hole pairs will then scatter into and accumulate in these states; consequently, the SP2DEG ground state must be unstable when  $E_x > E_{\text{crit}}$ .

The new state of the electrons is presumably a coherent superposition of spin excitons: i.e. a spin density wave with an antiferromagnetic order parameter. The presence of this new order parameter and its interactions with the nuclear spins in the neighborhood of the junction may account for the complex behavior observed in spin diodes in reverse bias. Further investigation is obviously needed.

## 5. Landau level diode: conduction via magnetoexciton states at the junction

We hypothesize that the neutral excitations of a filled Landau level are responsible for the switching behavior seen in the Landau level diode shown in Fig. 3b. In a DBRTS, switching and negative differential resistance are attributable to states between the emitter and collector (between the double barriers) whose occupation can alter the voltage drop within the device [4]. In a Landau level diode, there are states between adjacent Landau levels only in the presence of  $e$ - $e$  interactions. In Fig. 5, the dispersion relation for magnetoexcitons at  $\nu = 2$  is plotted [7]. As is the case for the spin excitons discussed above, these excitations have an electric dipole moment proportional to  $k$ . The energy of the  $k = 0$  exciton is equal to  $\hbar\omega_c$ , as is required by Kohn's theorem; however, the minimum energy excitation occurs at a finite  $k$  and has an electric dipole moment. Using the formulas of Ref. [7], this energy is approximately 1 meV less than  $\hbar\omega_c$  for the conditions relevant to our experiment.

Because of its electric dipole moment, this exciton can further reduce its energy in the pres-

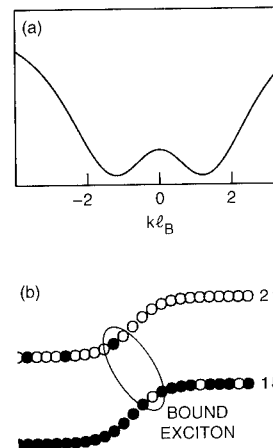


Fig. 5. (a) Magnetoexciton dispersion curve when  $\nu = 2$ . At  $k = 0$  the energy is  $\hbar\omega_c$ . Excitons with minimum energy have an electric dipole moment. (b) Such excitons could be bound by the electric field at the diode junction, providing a pathway for conduction across the junction when the applied bias is less than  $\hbar\omega_c$ .



ence of an electric field; consequently, such an excitation can be bound inside the depletion region of a Landau level diode (Fig. 5b). We hypothesize that these states are responsible for transport across the depletion region when  $eV < \hbar\omega_c$ . As the external bias is increased towards  $\hbar\omega_c$ , the electric field within the depletion region diminishes until excitonic states can no longer be bound there; current across the junction then drops abruptly, as is seen in Fig. 3b. We believe that conduction via excitonic states only occurs in the junction with a small gate–2DEG separation because  $E$  at the junction is larger, reducing the energy of exciton states, and because  $W$  is smaller, allowing efficient scattering between bound excitons and free carriers.

## 6. Conclusions

While it might seem surprising that neutral excitations play an important role in electronic conduction in spin diodes and Landau level diodes, their electric dipole moment can contribute to important effects. Firstly, we believe that a new electronic ground state appears in a

sufficiently strong  $E$  field in a 2DEG at  $\nu = 1$  and manifests itself in spin diodes in reverse bias. Secondly, excitons can be bound by the  $E$  field present in Landau level diodes, introducing a new pathway for conduction across these junctions.

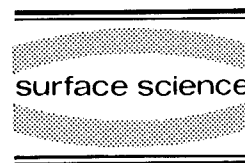
## 7. References

- [1] C.W.J. Beenakker and H. van Houten, in: *Solid State Physics*, Vol. 44, Eds. H. Ehrenreich and D. Turnbull (Academic Press, New York, 1991); M. Buttiker, in: *Semiconductors and Semimetals*, Vol. 35, Ed. M. Reed (Academic Press, New York, 1992).
- [2] B.E. Kane, L.N. Pfeiffer and K.W. West, *Appl. Phys. Lett.*, submitted.
- [3] D.B. Chklovskii, B.I. Shklovskii and L.I. Glazman, *Phys. Rev. B* 46 (1992) 4026.
- [4] V.J. Goldman, D.C. Tsui and J.E. Cunningham, *Phys. Rev. Lett.* 58 (1987) 1256.
- [5] B.E. Kane, L.N. Pfeiffer and K.W. West, *Phys. Rev. B* 46 (1992) 7264.
- [6] The importance of dynamic nuclear polarization in uniform density spin polarized electron systems was previously established. See M. Dobers, K. von Klitzing, J. Schneider, G. Weimann and K. Ploog, *Phys. Rev. Lett.* 61 (1988) 1650.
- [7] C. Kallin and B.I. Halperin, *Phys. Rev. B* 30 (1984) 5655.
- [8] A. Usher, R.J. Nicholas, J.J. Harris and C.T. Foxon, *Phys. Rev. B* 41 (1990) 1129.



ELSEVIER

Surface Science 305 (1994) 181–186



# Magnetic ordering and Fermi surface effects in the low-dimensional organic conductor $\alpha$ -(BEDT-TTF) $_2$ RbHg(SCN) $_4$

S.J. Klepper <sup>\*,a</sup>, J.S. Brooks <sup>b</sup>, G.J. Athas <sup>b</sup>, X. Chen <sup>b</sup>, M. Tokumoto <sup>c</sup>, N. Kinoshita <sup>c</sup>, Y. Tanaka <sup>c</sup>

<sup>a</sup> Francis Bitter National Magnet Laboratory, MIT, Cambridge, MA 02139, USA

<sup>b</sup> Department of Physics, Boston University, Boston, MA 02215, USA

<sup>c</sup> Electrotechnical Laboratory, Tsukuba, Ibaraki 305, Japan

(Received 21 April 1993; accepted for publication 4 June 1993)

## Abstract

Members of the family of low-dimensional organic conductors  $\alpha$ -(BEDT-TTF) $_2$ MHg(SCN) $_4$ , with M = K, Rb, Tl, or NH $_4$ , have a Fermi surface (FS) consisting of both quasi-two-dimensional (Q2D) closed hole orbits and quasi-one-dimensional (Q1D) open orbits. The charge transfer salts with M = K, Rb, and Tl undergo an antiferromagnetic ordering transition at about 10 K, which results in a density wave ground state. We have performed magnetoresistance (MR) measurements on  $\alpha$ -(BEDT-TTF) $_2$ RbHg(SCN) $_4$  in order to understand details of the FS, and the nature of the interaction of the FS with the magnetic ordering in this material.

## 1. Introduction

The group of organic conductors designated by  $\alpha$ -(BEDT-TTF) $_2$ MHg(SCN) $_4$ , where M = Rb [1], K [2], Tl [3], or NH $_4$  [4], is characterized by low-dimensional electron transport. Magnetoresistance (MR) and magnetization are influenced both by the quasi-2D closed hole orbits and the quasi-1D open electron portions of the Fermi surface (FS). Subtle differences in the band structure of these charge-transfer salts, which are isomers of one another, have a dramatic effect on their electronic transport properties. The material with M = NH $_4$  is a low-temperature ( $T_c = 1.0$

K) superconductor; the others have density wave ground states. We have studied transport in the material with M = Rb (“RbHg” for short), at temperatures down to 100 mK and at dc magnetic fields up to 36.5 T. An antiferromagnetic ordering is observed in RbHg below 10.5 K. At temperatures below the ordering temperature, there is a large MR contribution from the open orbits which has a maximum near 17 T. At higher magnetic fields, the MR background drops sharply at a characteristic “kink” field  $H_K$ . Above this field, the antiferromagnetic ordering is destroyed, as are its effects on the FS. Pulsed-field data [5] indicate that  $H_K \approx 32$  T for RbHg at low temperatures. This value for  $H_K$  is confirmed by dc field measurements up to 36.5 T taken in the Hybrid III magnet at the Francis Bitter National Magnet

\* Corresponding author.

Laboratory. We have also studied the MR of RbHg under pressures up to 12 kbar. Pressure suppresses the magnetic ordering, reducing the value of  $H_K$  at fixed temperatures. Angular magnetoresistance oscillations (AMRO), which are seen by rotating the orientation of the conducting planes in RbHg at a fixed field, are radically altered by the magnetic transition. These angular oscillations measure the structure of both the closed-orbit and open-orbit FS.

## 2. Magnetic ordering

Evidence for the magnetic ordering comes from the temperature dependence of the magnetic susceptibility, which shows a strong diamagnetic drop for  $T < 10$  K when field is aligned parallel to the conducting planes, but only a weak paramagnetic rise for field oriented perpendicular to the conducting planes [6]. This behavior is indicative of antiferromagnetic ordering of spins in the conducting plane. Measurements of the temperature dependent resistance show a shoulder in the monotonically decreasing resistance which also occurs at about 10 K [7], and is quite field sensitive below this point. This resistance shoulder signals the existence of a density wave ground state. This ordering can be destroyed through the application of magnetic fields of 32 T. Fig. 1 displays the high-field MR data for a sample at 1.2 K.

Several features are noteworthy. The background magnetoresistance rises to a maximum near 17 T; and drops sharply at the so-called “kink” field,  $H_K = 32$  T. This background is due to the conductance contribution of the open-orbit FS. Superimposed on this MR background is a single frequency series of Shubnikov–de Haas (SdH) oscillations, which arise from the closed-orbit FS. The location of the kink field is hysteretic, being approximately 2 T higher on the upswing than on the downswing. (The apparent slight hysteresis in the phase of the Shubnikov–de Haas oscillations is an artifact, and arises from the long lock-in amplifier time constant (3 s) compared to the rapid sweep of the resistive magnet (20 min to full field), giving a shift of

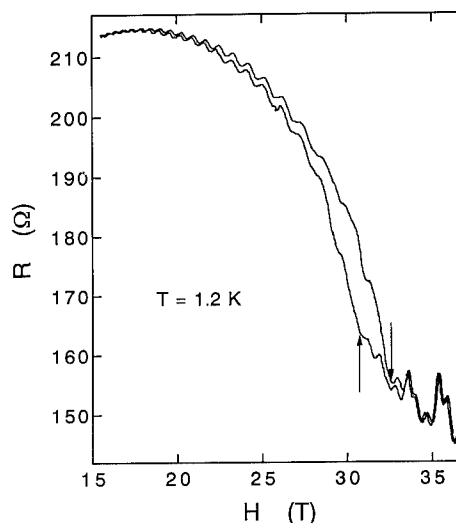


Fig. 1. Magnetoresistance of  $\alpha$ -(BEDT-TTF) $_2$ RbHg(SCN) $_4$  at  $T = 1.2$  K.

$\sim 0.1$  T between up and down sweeps.) The harmonic content of the SdH oscillations is sensitive to the magnetic phase of the material; second and third harmonics can be seen in Fig. 1 above  $H_K$ .

The background MR for RbHg is a hallmark of the density wave ground state. The detailed effect of this ground state on the FS is not yet resolved, but we speculate that the AFM ordering causes nesting of the open orbits. The open-orbit nesting can be lifted with temperature above 10.5 K, with the application of fields above the kink field  $H_K$ , or with pressures of 8 kbar. Sensitive measurements of the SdH oscillations using field modulation techniques show the presence of high frequency components whose corresponding area is similar to that of the first Brillouin zone, which indicates the occurrence of magnetic breakdown above 10 T [8].

We can use the temperature dependence of the kink field to map out a phase diagram for RbHg, as shown in Fig. 2. Above 10.5 K at low fields, the sample is in a normal metallic state. Cooling below this point results in antiferromagnetic ordering and a density wave ground state. Application of high fields at low temperatures breaks the AFM order and returns the sample to

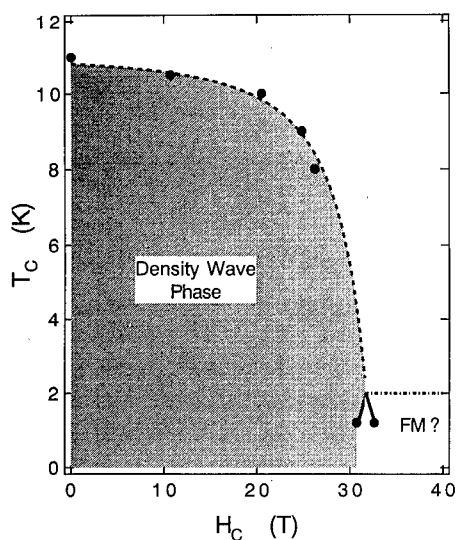


Fig. 2. Magnetic phase diagram of RbHg, showing  $H_K(T)$ .

a normal metallic state. At the lowest temperatures, where the kink field is hysteretic, there may exist a new high field ferromagnetic phase [9]. Magnetization measurements in the KHg sister compound show similar kink field and hysteretic behavior [2].

### 3. Pressure dependence

We have applied hydrostatic pressures up to 12 kbar to members of the  $\alpha$ -(BEDT-TTF)<sub>2</sub>MHg(SCN)<sub>4</sub> family in order to study the effects of altering the Fermi surface. The members of this family of organic conductors have remarkably different properties, due to only small variations in the anion composition. Pressure dependence studies allow the experimenter to alter the Fermi surface of the material under study and to thereby uncover a variety of conducting states in a single sample. These materials are layered, consisting of conducting (BEDT-TTF)<sub>2</sub> donor molecule sheets and anion MHg(SCN)<sub>4</sub> sheets oriented on the triclinic  $a$ - $c$  plane, and alternating along the  $b$  axis. The RbHg material has the largest unit cell in this group. High pressures were achieved hydrostatically by using stan-

dard Be-Cu pressure cell techniques with an inert fluid [10].

Fig. 3 displays magnetoresistance traces of a single RbHg sample at pressures ranging from 0 to 12 kbar; all data are taken at  $T = 120$  mK. The MR maximum moves to lower fields with increasing pressure, which is indicative of suppression of the magnetic phase. By 8 kbar, all evidence for a kink-field behavior in the MR is removed. In Fig. 4 (top), the SdH oscillations at the various pressures are shown. Although the harmonic content of these oscillations is quite sensitive to pressure, there is not a perfect correlation between the destruction of the harmonic content (which occurs by 4 kbar) and the removal of the magnetic ordering (which requires more than 6 kbar). Fig. 4 (bottom) shows the linear variation of SdH frequency with pressure. The removal of harmonic content with pressure, which also returns this material to the normal state, contrasts with the appearance of strong harmonic content in the

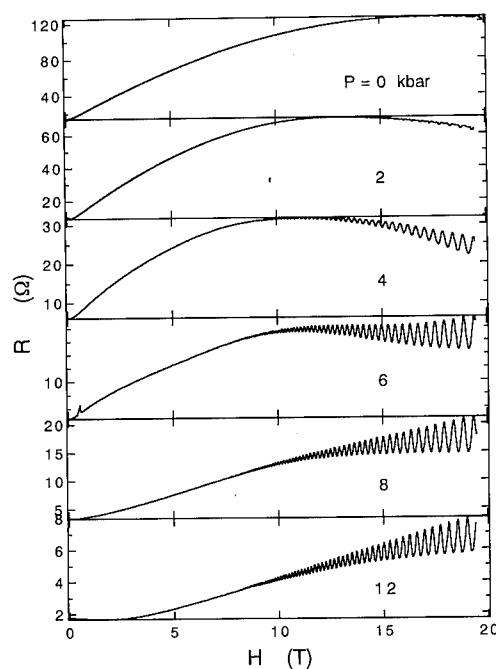


Fig. 3. Pressure dependence of the magnetoresistance for RbHg,  $T = 120$  mK; note the disappearance of the kink field feature and MR maximum by 8 kbar.

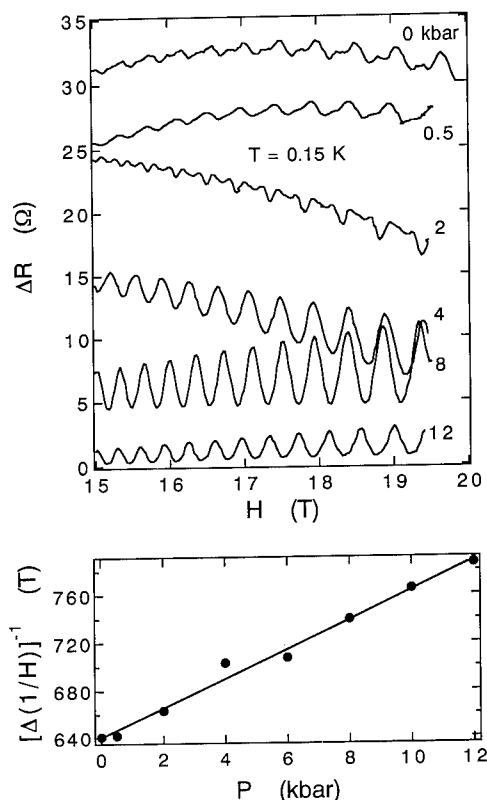


Fig. 4. Pressure dependence of the ShdH oscillations (top) and ShdH frequency (bottom).

SdH oscillations for  $H > H_K$ . This contradictory behavior, and the lack of change in the slope of the ShdH frequency in Fig. 4 (bottom) as the material passes from the density wave to the normal states, indicates that the effect of magnetic ordering on the closed-orbit FS is but incidental. The predominant effect of magnetic ordering is on the open orbits.

The ShdH oscillations result from the closed-orbit FS. The fundamental frequency of 638 T at ambient pressure corresponds to an extremal FS area  $S(P=0)$  of 15.5% of the first Brillouin zone (BZ). This area increases with pressure as  $[dS(P)/dP]/S(0) = 2\%/kbar$ . This pressure dependence is similar to that seen in the KHg and  $NH_4Hg$  compounds. The effective mass for this material is  $m^* = [1.5 \pm 0.2] m_e$ , independent of pressure. The consequences of applying pressure to RbHg as seen by the closed orbits is to expand

the first BZ, and thus the FS topology, changing the band energy by about 5 meV/kbar.

#### 4. Angular magnetoresistance oscillations

Further information about the FS in RbHg has been obtained by studying angular magnetoresistance (AMR) oscillations. Resistance is measured at fixed magnetic field as a function of the angle  $\phi$  measured perpendicular to the conducting  $a$ - $c$  planes. The AMR appears as oscillations with sharp minima below the antiferromagnetic ordering temperature. The period of these oscillations is anisotropic with respect to the plane of rotation cutting through the conducting layers. AMR in the Q2D organic conductors  $(BEDT-TTF)_2X$  ( $X$  is a charge transfer anion) [11] show sharp periodic maxima. The origin of these oscillations was explained by Yamaji as coming from the slight warping of the Q2D FS [12]. At special angles the dispersion along the cylindrical FS axis is removed, and a pure 2D FS arises, resulting in periodic resistance peaks. In contrast, the family of organic conductors  $\alpha$ -(BEDT-TTF) $_2$ MHg(SCN) $_4$  have AMR with minima. Possible explanations for these minima are an anomalous Yamaji effect [13], or an effect arising from the Q1D FS [3].

The FS of  $\alpha$ -(BEDT-TTF) $_2$ RbHg(SCN) $_4$  consists of a weakly warped Q2D cylinder along the  $K_b$  direction, and a pair of weakly warped parallel open-orbit sheets along the  $K_c$  direction that result in Q1D conduction along the  $K_a$  axis [14]. The angle of  $H$  with respect to the  $b^*$  axis ( $\perp$   $a$ - $c$  plane) is  $\phi$ ; the angle of the plane that  $\phi$  cuts through the  $a$ - $c$  plane is  $\theta$ , with  $0^\circ$  being along the  $c$  axis. Fig. 5 shows results for  $\phi$  sweeps taken at various angles  $\theta$  between  $0^\circ$  and  $90^\circ$ . Minima periodic in  $\tan \phi$  are observed superimposed on a  $\cos \phi$  background. This differs from the Yamaji type AMR, where a concave-up background is observed. As pointed out by Kartsovnik [3], the period of the oscillations in  $\phi$  is proportional to  $1/\cos \phi$ . If we use the Yamaji model to explain the oscillations, we get a ratio of  $K_c/K_a > 8$ , disagreeing with the calculated FS. This dependence would, however, be expected for an

open FS oriented perpendicular to the  $a$  axis. AMR oscillations have been observed in Q1D organic conductors [15], occurring at commensurate angles given by:

$$\tan \phi = \cot \alpha + \frac{pK_b}{qK_c \sin \alpha}, \quad (1)$$

where  $\alpha$  is the angle between the  $b$  and  $c$  axis, and  $p$  and  $q$  are integers. Our results compare favorably with this formula for ratios of  $p/q = 0, \pm 2, \pm 4$ , etc. The anisotropy of the  $\tan \phi$  period, commensurate formula fit, and background AMR point towards a Q1D effect.

Fig. 6 shows the temperature dependence for the AMRO at fixed field and  $\theta$  orientation, from 0.5 to 16 K. Below the phase transition, the positions of the minima are field and temperature dependent. Above the transition, the nature of the AMR changes dramatically; the oscillations have vanished and the  $\cos \phi$  background changes to concave-up. This background is similar to that found in Yamaji type materials having only a Q2D FS.

We can now begin to develop a picture of the mechanisms underlying the anomalous AMR in these materials. The conductivity can be separated into open- and closed-orbit contributions,

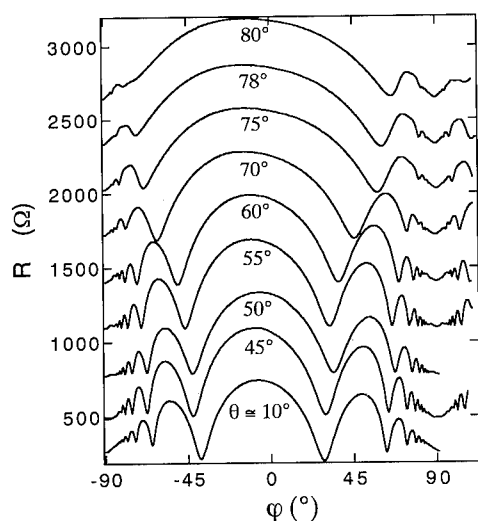


Fig. 5. Angular magnetoresistance oscillations (AMRO) taken at  $T = 0.45$  K for various values of  $\theta$ .

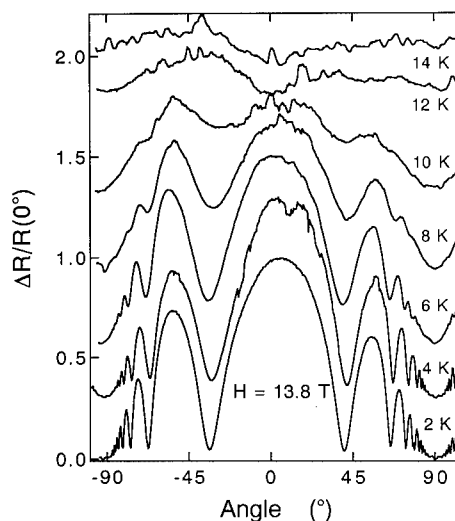


Fig. 6. Temperature dependence of the AMR oscillations for RbHg.

$\sigma = \sigma_0 + \sigma_c$ . Above the phase transition, the open FS conductivity is much higher than the closed FS; hence we see the concave-up dependence in the MR that is seen in the purely Q2D materials. Below the phase transition, the open FS nests, causing an insulating gap. The open FS conductivity drops well below that of the closed FS and the gap increases as temperature is lowered. The open FS magnetoresistance dominates and at some commensurate angles is removed or greatly reduced. Further work in these materials should elucidate the detailed behavior of the open-orbit FS and its interaction with the magnetic phase of the system.

## 5. Acknowledgments

We are indebted to the staff of the Francis Bitter National Magnet Laboratory (supported by NSF); work at Boston University is supported by NSF DMR-92-14889.

## 6. References

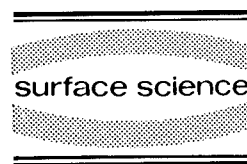
- [1] S.J. Klepper, J.S. Brooks, G.J. Athas, X. Chen, M. Tokumoto, N. Kinoshita and Y. Tanaka, to be published.

- [2] J.S. Brooks, C.C. Agosta, S.J. Klepper, M. Tokumoto, N. Kinoshita, H. Anzai, S. Uji, H. Aoki, A.S. Perel, G.J. Athas and D.A. Howe, *Phys. Rev. Lett.* 69 (1992) 156.
- [3] M.V. Kartsovnik, A.E. Kovalev, V.N. Laukhin and S.I. Pesotskii, *J. Phys. I France* 2 (1992) 223.
- [4] J. Wosnitza, G.W. Crabtree, H.H. Wang, U. Geiser, J.M. Williams and K.D. Carlson, *Phys. Rev. B* 45 (1992) 3018, and references therein.
- [5] C.C. Agosta and G. Boebinger, private communication.
- [6] T. Sasaki, M. Sato and N. Toyota, *Synth. Methods* 44–45 (1991) 2211.
- [7] N. Kinoshita, M. Tokumoto and H. Anzai, *J. Phys. Soc. Jpn.* 60 (1991) 2131.
- [8] S. Uji and H. Aoki, to be published.
- [9] F.L. Pratt, J. Singleton, M. Doport, A.J. Fisher, T.J.B.M. Janssen, J.A.A.J. Perenboom, M. Kurmoo, W. Hayes and P. Day, *Phys. Rev. B* 45 (1992) 13904.
- [10] X. Chen, A.S. Perel, J.S. Brooks, R.P. Guertin and D.G. Hinks, *J. Appl. Phys.* 73 (1993) 1886.
- [11] K. Kajita, Y. Nishio, T. Takahashi, W. Sasaki, R. Kato, H. Kobayashi, A. Kobayashi and Y. Iye, *Solid State Commun.* 70 (1989) 1189; M.V. Kartsovnik, P.A. Kononovich, V.N. Laukhin and I.F. Schegolev, *JETP Lett.* 48 (1988) 541.
- [12] K. Yamaji, *J. Phys. Soc. Jpn.* 58 (1989) 1520.
- [13] T. Osada, R. Yagi, A. Kawasumi, S. Kagoshima, N. Miura, M. Oshima and G. Saito, *Phys. Rev. B* 41 (1990) 5428.
- [14] H. Mori, S. Tanaka, M. Oshima, G. Saito, T. Mori, Y. Maruyama and H. Inokuchi, *Bull. Chem. Soc. Jpn.* 63 (1990) 2183.
- [15] M.J. Naughton, O.H. Chung, M. Chaparala, X. Bu and P. Coppens, *Phys. Rev. Lett.* 67 (1991) 3712, and references therein.



ELSEVIER

Surface Science 305 (1994) 187–193



# The influence of magnetic order in quasi-2D organic conductors

M. Doporto <sup>\*,a</sup>, J. Caulfield <sup>a</sup>, S. Hill <sup>a</sup>, J. Singleton <sup>a</sup>, F.L. Pratt <sup>a</sup>, M. Kurmoo <sup>b</sup>,  
P.J.T. Hendriks <sup>c</sup>, J.A.A.J. Perenboom <sup>c</sup>, W. Hayes <sup>a</sup>, P. Day <sup>b</sup>

<sup>a</sup> Clarendon Laboratory, Parks Road, Oxford OX1 3PU, UK

<sup>b</sup> Royal Institution, 21 Albermarle Street, London W1X 4BS, UK

<sup>c</sup> High Field Magnet Laboratory, 6525 ED Nijmegen, Netherlands

(Received 4 May 1993; accepted for publication 4 June 1993)

## Abstract

We report extensive magnetoresistance (MR) measurements on the charge transfer salts  $\beta''$ -(ET)<sub>2</sub>AuBr<sub>2</sub> and  $\alpha$ -(ET)<sub>2</sub>KHg(SCN)<sub>4</sub>. Our results indicate that spin-density wave (SDW) groundstates in both of these materials modify the Fermi surfaces calculated from room temperature crystal parameters. In the case of  $\beta''$ -(ET)<sub>2</sub>AuBr<sub>2</sub>, the shapes, sizes and orientations of three individual closed two-dimensional (2D) Fermi surface pockets have been deduced at 500 mK. The SDW groundstate in  $\alpha$ -(ET)<sub>2</sub>KHg(SCN)<sub>4</sub> leads to the observation of a resistive “kink” transition at  $\sim 22$  T. MR measurements made as a function of crystal orientation and temperature both above and below this “kink”, allow a qualitative assessment of the change in band structure at the “kink” to be made.

## 1. Introduction

Many ET charge transfer salts have a Fermi surface (FS) consisting of a quasi-two dimensional (Q2D) hole pocket, plus a Q1D electron section. The Q2D holes tend to dominate the low temperature conductivity of the salts, so that phenomena due to the Q1D electrons, such as spin-density wave (SDW) formation (seen in, e.g. TMTSF charge-transfer salts, where the SDW leads to antiferromagnetic behaviour and a band-gap at the FS resulting in a metal–insulator transition), have been ignored by many workers. In this study, we report extensive magnetoresistance (MR) measurements on two metallic ET charge

transfer salts,  $\beta''$ -(ET)<sub>2</sub>AuBr<sub>2</sub> and  $\alpha$ -(ET)<sub>2</sub>KHg(SCN)<sub>4</sub>, both of which exhibit low temperature SDW groundstates; the experiments show that the SDW leads to a modification of the simple Fermi surfaces deduced from band structure calculations.

## 2. Measurements on $\beta''$ -(ET)<sub>2</sub>AuBr<sub>2</sub>

The ET molecules in  $\beta''$ -(ET)<sub>2</sub>AuBr<sub>2</sub> stack along the *a* crystal axis, forming conducting 2D sheets parallel to the *ac* plane, separated in the *b* direction by layers of linear AuBr<sub>2</sub><sup>−</sup> anions (see Ref. [1] and Fig. 3 below for definition of crystal axes). The  $\beta''$  phase results in strong interactions between molecules in different stacks, so that  $\beta''$ -(ET)<sub>2</sub>AuBr<sub>2</sub> is less isotropic than many other

\* Corresponding author.



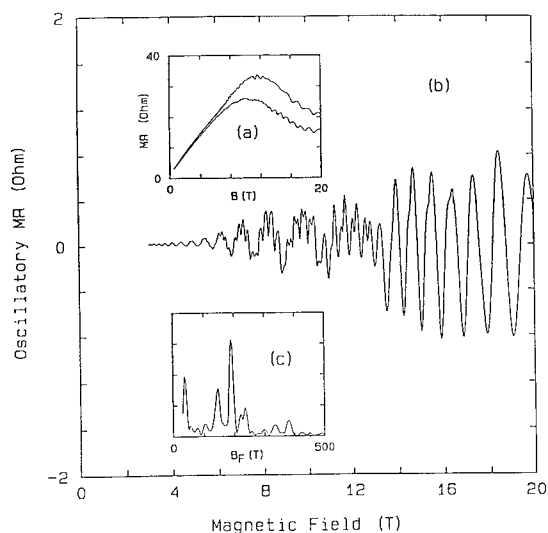


Fig. 1. (a) Magnetoresistance of  $\beta''$ -(ET) $_2$ AuBr $_2$  for  $B||b^*$  (upper trace) and for  $B$  tilted  $30^\circ$  from  $b^*$  about  $a'$  towards  $c$  (lower trace). (b) The oscillatory component of the magnetoresistance for the lower trace in (a). (c) Fourier transform of (b). In all cases  $T = 0.5$  K.

metallic ET salts. Reliable calculations of the transfer integrals and band structure have not yet been established, and those estimated by different groups disagree [2,3]. Evidence for a complex low temperature SDW groundstate is observed in the resistance, which drops sharply at  $\sim 20$  K, and from ESR measurements, which reveal a change in  $g$ -value at  $\sim 6$  K [1].

Fig. 1a shows the MR of  $\beta''$ -(ET) $_2$ AuBr $_2$  for two different angles between the magnetic field and the normal to the 2D conducting planes ( $b^*$ ); the MR is seen to depend strongly on the field direction. Fig. 1b shows the oscillatory component of the MR; Shubnikov-de Haas oscillations (SdHO) of several different frequencies are present. Fourier analysis (Fig. 1c) reveals four strong frequencies (40, 140, 180 and 220 T), together with different harmonic combinations. To progress further, it is necessary to identify which frequencies correspond to actual carrier pockets, and which are merely an artefact of frequency mixing, or a result of crystal twinning. The latter possibility may be ruled out, as the frequencies of all the SdHO are inversely proportional to the cosine of the angle between the magnetic field

and  $b^*$  for all field orientations. The mechanism responsible for frequency mixing is indicated by the strong hysteresis in magnitude and in the phase of the SdHO between up and down sweeps of the magnetic field which is observed below 1 K when the field is parallel to  $b^*$  [4]. This is indicative of strong internal magnetic fields leading to domain formation. In view of this, effects due to the Shoenberg magnetic interaction (MI) [5] between two or more carrier pockets must be considered. These introduce a magnetic feedback term due to the fact that the field experienced by the carriers is  $B = \mu_0(H + M)$ , where  $H$  is the external applied field and  $M$  is the magnetisation containing the oscillatory (de Haas-van Alphen) components. This is thought to be the first observation of such an effect in an organic conductor [6].

The observed SdHO may be partly simulated using two Fermi surface (FS) pockets with areas corresponding to frequencies  $B_{F1} = 40$  T and  $B_{F2} = 180$  T and combinations such as  $B_{F2} \pm B_{F1}$  and  $2 \times B_{F2} \pm B_{F1}$ . Simulations using the MI between the  $B_{F1}$  and  $B_{F2}$  series are successful in accounting for the sidebands at  $180 \pm 40$  T and  $360 \pm 40$  T (Fig. 1c), as well as the disappearance of the 180 T series under certain conditions, but cannot reproduce the dominance of the 40 T and the 220 T frequencies over the 180 T SdHO at higher tilt angles [6]. At large angles, the only surviving second harmonic observed corresponds to the 220 T frequency. Therefore, this frequency ( $B_{F3}$ ) must also correspond to a real carrier pocket and is not merely an artefact of mixing.

Having established that the SdHO frequencies  $B_{F1} = 40$  T,  $B_{F2} = 180$  T and  $B_{F3} = 220$  T correspond to real closed 2D sections of FS, we turn to the angle dependence of the SdHO amplitudes. Fig. 2 shows an example of this for  $B_{F1}$ ,  $B_{F2}$  and  $B_{F3}$  as the sample is rotated about the  $w$  and  $v$  axes; strong oscillations in the amplitude are seen as a function of tilt angle. Rotations about the  $a'$  and  $c$  axes also reveal oscillations in the SdHO amplitudes. These angle-dependent oscillations in SdHO strength are due to a mechanism first proposed by Yamaji [7], who showed that when a magnetic field is applied at certain angles, all the semi-classical  $k$ -space closed orbits around a

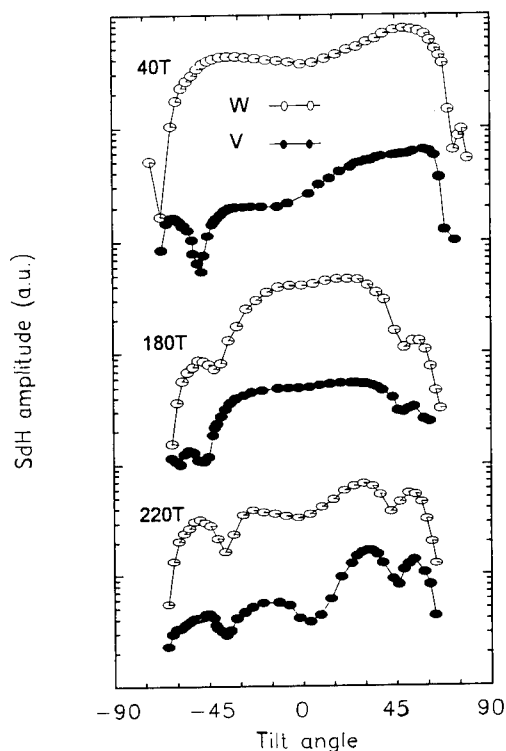


Fig. 2. Fourier amplitudes of the three series of SdHO corresponding to real 2D FS carrier pockets, for tilting about the  $w$  and  $v$  directions ( $T = 0.5$  K).

warped cylindrical FS have approximately the same area. Therefore, at these angles, the density of states at the Fermi energy is enhanced, resulting in a maximum in the background MR, and in the amplitude of the SdHO. The theory was

developed by Kartsovnik et al. [8], who considered materials in which the plane of warping can be inclined with respect to the conducting plane. The tilt angles  $\theta$  at which the maxima occur are given by  $bk_{\parallel}|\tan \theta| = \pi(i - \frac{1}{4}) \pm A(\phi)$ , where  $b$  is the interplane spacing,  $k_{\parallel}$  is the radius of the warped cylindrical Fermi surface at a point where the tangent to the surface is perpendicular to the plane of rotation of the magnetic field,  $i$  is an integer and  $\phi$  is the azimuthal angle describing the plane of rotation of the field. The gradient of a plot of  $|\tan \theta|$  against  $i$  may therefore be used to find one of the dimensions of the FS, and if the process is repeated for several  $\phi$ , the complete FS shape in the conducting plane may be mapped out. ( $A(\phi)$  is determined by the inclination of the plane of warping with respect to the 2D plane, and will not be discussed here.)

Having rotated samples about various axes in the  $ac$  plane ( $a, c, a', c', v$  and  $w$ ), the SdHO amplitudes of each pocket are then plotted against  $\tan \theta$ , where  $\theta$  is the angle between the magnetic field and  $b^*$ . From these data, the shape of the 2D FS pockets can be reconstructed (see Figs. 3c–3e), and, since the areas of the pockets are known from the SdHO frequencies, the unit cell size in the interplane direction can be estimated. In most cases, only a couple of oscillation periods in  $\tan \theta$  are observed, as the resolution of the data does not permit more rapid oscillations to be resolved. It should be noted that the observation of these “Yamaji” oscillations in  $\beta''$ -(ET)<sub>2</sub>AuBr<sub>2</sub> is not necessarily expected since the

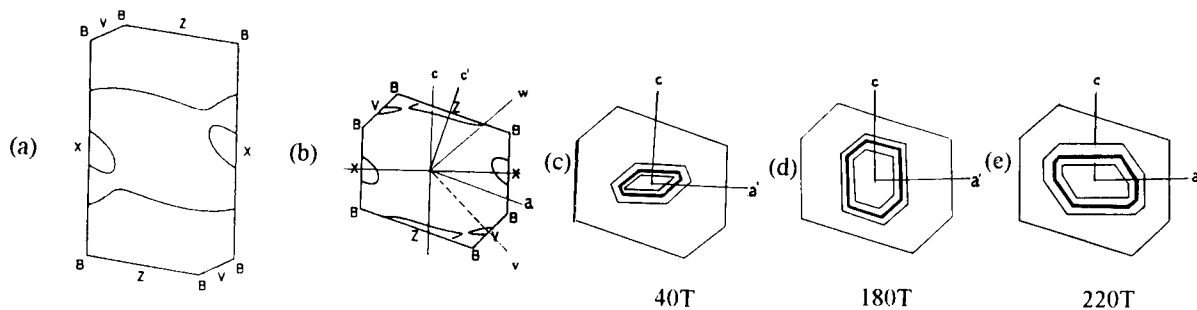


Fig. 3. (a) shows the room temperature Brillouin zone and FS for  $\beta''$ -(ET)<sub>2</sub>AuBr<sub>2</sub> calculated by Mori et al. [2]. (b) Proposed low temperature FS, with two extra closed FS pockets produced by a  $2c$  SDW. (c), (d) and (e) show the shapes (thin lines show worst case) of the different FS pockets, deduced from rotations about 6 crystal axes.

carrier pockets are very small. However, from the data, it is apparent that the Brillouin zone (BZ) boundary in the interplane direction is 2–3 times smaller than the room temperature value (i.e. the unit cell is 2–3 times longer in this direction). In theory, this should not alter the SdHO spectra significantly, as long as the interplane warping remains small. This suggests that there is some interplane component in the SDW ordering.

The shapes of the FS pockets deduced from the angle-dependent oscillations in the SdHO are shown in Figs. 3c–3e. The calculated FS that most resembles the SdHO data on  $\beta''$ -(ET)<sub>2</sub>AuBr<sub>2</sub>, is due to Mori, and has just one closed hole pocket of  $\sim 5\%$  of the room temperature BZ area centred on the X point, together with a pair of open sections [2] (Fig. 3a). Although the closed section is a factor of 2 too large to correspond to the  $B_{F2}$  SdHO series, it should be remembered that this is close to the top of the hole band, so that small adjustments of, e.g., the band overlaps could result in a large reduction in pocket area. However, the FS calculation has no obvious candidate for the  $B_{F1}$  and  $B_{F3}$  series. In view of the magnetic ground state of  $\beta''$ -(ET)<sub>2</sub>AuBr<sub>2</sub>, we propose that the additional SdHO frequencies are the result of closed pockets produced by a SDW modulation with a conduction plane component of  $2c$ , driven by the nesting properties of the Q1D part of the FS. The result of such a modulation would be to fold back sections of the calculated FS leading to a small hole pocket close to  $V$ , together with a larger anisotropic closed section of FS (electron-like) (Fig. 3b). The band filling is such that there should be equal numbers of electrons and holes, so that the total area of the two hole pockets should be the same as the area of the electron pocket. In this way, if we identify the two hole pockets with the SdHO series  $B_{F1}$  and  $B_{F2}$  (Figs. 3c and 3d), the SdHO due to the electron pocket should then occur at the sum of these frequencies, namely  $B_{F3} = 220$  T (Fig. 3e). A comparison of Figs. 3c–3e and Fig. 3b shows that there is reasonable qualitative agreement between the experimental FS shapes and orientations and those of the proposed SDW groundstate.

### 3. Measurements on $\alpha$ -(ET)<sub>2</sub>KHg(SCN)<sub>4</sub>

Charge-transfer salts of the form  $\alpha$ -(ET)<sub>2</sub>MHg(SCN)<sub>4</sub>, where M may be K, Tl, Rb or NH<sub>4</sub>, were first synthesised as possible superconducting modifications of  $\kappa$ -(ET)<sub>2</sub>Cu(SCN)<sub>2</sub> [9]. However, only  $\alpha$ -(ET)<sub>2</sub>NH<sub>4</sub>Hg(SCN)<sub>4</sub> is a superconductor, having a  $T_c \approx 1.1$  K [9]; the others are metals down to  $\sim 100$  mK [10], and in addition exhibit the onset of antiferromagnetic order at  $\sim 8$ – $10$  K, probably due to the onset of a SDW groundstate [11–13]. The materials are isostructural, with identical predicted Fermi surfaces consisting of a rather isotropic Q2D closed hole pocket and a Q1D open electron section (see inset to Fig. 4).

Fig. 4 illustrates the magnetoresistance of  $\alpha$ -(ET)<sub>2</sub>KHg(SCN)<sub>4</sub> for a variety of temperatures; the most noticeable feature is the so-called “kink” transition visible as a dramatic fall in resistance between 22 and 23 T. (Similar “kinks” have now been observed in  $\alpha$ -(ET)<sub>2</sub>TlHg(SCN)<sub>4</sub> at  $\sim 22$  T [14] and in  $\alpha$ -(ET)<sub>2</sub>RbHg(SCN)<sub>4</sub> at  $\sim 35$  T [15], but are absent in the case of  $\alpha$ -(ET)<sub>2</sub>NH<sub>4</sub>Hg(SCN)<sub>4</sub>.) Above the “kink” a single series of SdHO with a frequency of  $670 \pm 15$  T is observed; however, below the “kink”, the MR exhibits hysteresis [11], and the SdHO contain a

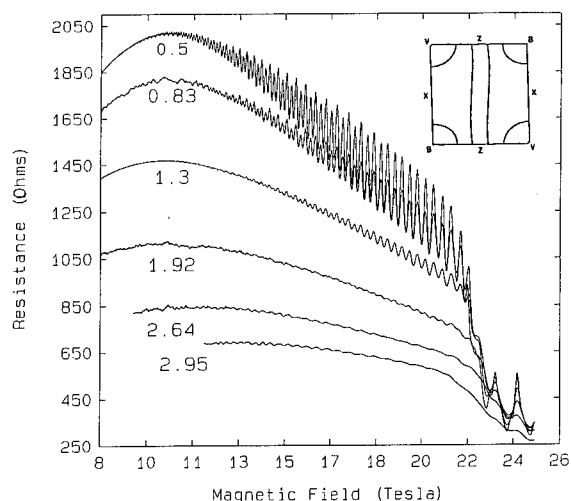


Fig. 4. Magnetoresistance of  $\alpha$ -(ET)<sub>2</sub>KHg(SCN)<sub>4</sub> for several temperatures. SdHO and the field induced resistive “kink” at  $\sim 22$  T can clearly be seen. The inset shows the predicted room temperature Fermi surface.

prominent second harmonic component (see Fig. 4). In addition to the dominant SdHO series with a frequency of  $670 \pm 10$  T, an apparent second series of SdHO, with a sample-dependent frequency between 700 and 870 T has also been observed at low fields [11]. Several workers have linked these phenomena to the presence of the SDW groundstate [11–13]. It is thought that imperfect nesting in the SDW state could lead to the presence of an extra closed 2D carrier pocket in the Fermi surface (c.f.  $\beta''$ -(ET)<sub>2</sub>AuBr<sub>2</sub> described above); the presence of this pocket would lead to the extra SdHO frequency at fields below

the “kink”. The “kink” would signal the destruction of the SDW state by the external field and the depopulation of the pocket would account for the fall in resistance. Others have noted that the complex behavior below the “kink” may be related to possible breakdown orbits between the open and closed sections of FS [15].

Recently, Kartsovnik et al. [14] have proposed a possible SDW groundstate for  $\alpha$ -(ET)<sub>2</sub>MHg(SCN)<sub>4</sub> (M = K, Tl) with a nesting vector which leads to such a small FS pocket and a new 1D FS sheet inclined at  $\sim 26^\circ$  to the 1D sheet shown in Fig. 4. In their scheme the SdHO with a fre-

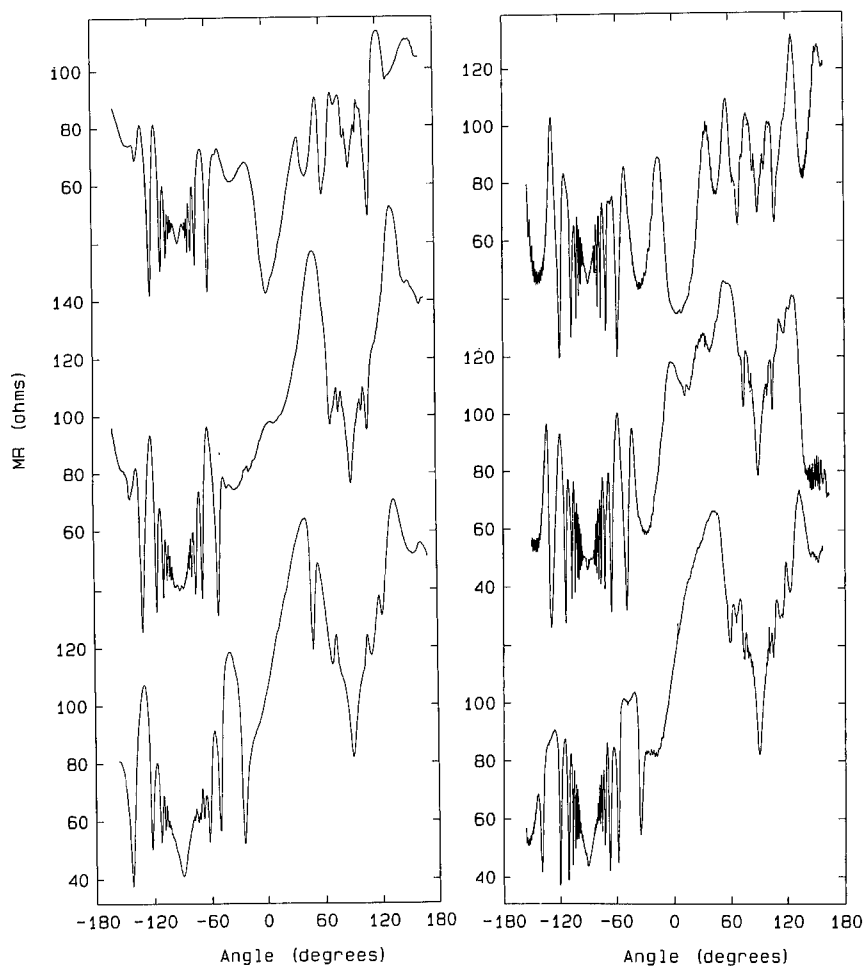


Fig. 5. Magnetoresistance of  $\alpha$ -(ET)<sub>2</sub>KHg(SCN)<sub>4</sub> at  $T = 1.5$  K for fixed fields of 20 T (left-hand side) and 24 T (right-hand side) as a function of rotation angle (see text). The traces correspond to the following angles between the field and the rotation axis: left-hand side top to bottom  $32^\circ$ ,  $42^\circ$  and  $52^\circ$ ; right-hand side top to bottom  $36^\circ$ ,  $46^\circ$  and  $56^\circ$ .

quency of  $\sim 670$  T corresponds to a breakdown orbit between the small 2D FS pocket and the 1D sheet, whilst the 700–870 T series represents mixing between the 670 T frequency and SdHO due to simple orbits around the small pocket. Furthermore, the strong second harmonic observed below the “kink” corresponds to a breakdown orbit of twice the area of that corresponding to the 670 T SdHO frequency, and not to the strong spin splitting proposed by other workers [12,13].

To test these assertions we have fitted data such as those shown in Fig. 4 using the Lifshitz–Kosevich (LK) formula [5] in order to evaluate the carrier effective masses both above and below the “kink” field. Below the “kink” the fitting of the 670 T fundamental frequency is complicated by the presence of the second SdHO frequency  $\sim 700$ –870 T, the amplitude of which has an anomalous temperature dependence. This results in a relatively large uncertainty in the effective mass determined, which lies in the range  $2.0$ – $2.5m_e$ . However, the temperature dependence of the amplitude of the second harmonic at fields below the “kink” is much clearer, and may be fitted using the  $p = 2$  term of the LK formula to reveal an effective mass of  $2.40 \pm 0.05m_e$ . Above the “kink” the temperature dependence of the amplitude of the fundamental 670 T frequency yields a mass of  $2.40 \pm 0.05m_e$ . It therefore appears that the effective mass associated with the FS pocket corresponding to the 670 T frequency is almost unchanged above and below the “kink”. In addition, the very strong second harmonic component seen below the “kink” also exhibits the same effective mass. The latter fact might support the proposal of Kartsovnik et al. [14] that the second harmonic is due to a breakdown orbit of twice the area of the orbit corresponding to the 670 T frequency.

Further information may be obtained by observing the MR as the sample is rotated in magnetic fields above and below the “kink” transition. The experiments were performed in a cryostat which allowed the sample's axis of rotation to be itself tilted in the magnetic field. Typical data are shown in Fig. 5 for fixed fields of 20 T (below “kink”) and 24 T (above “kink”); the traces were obtained by setting the rotation axis (parallel to

the  $c$  axis of the crystal) at a fixed angle with respect to the field and then turning the sample about this axis through  $\sim 300^\circ$  (the rotation angle). In this way, MR data are obtained in all four azimuthal angle quadrants; a disadvantage is that only a restricted range of azimuthal angles are available.

Several notable features are apparent in the data. Firstly, the MR oscillates, and shows minima which are found to be periodic in  $\tan \theta$ , but with a periodicity which is a very strong function of the azimuthal angle defining the plane of tilting of the magnetic field. This is especially notable when one compares data for rotation angles  $0^\circ$  to  $180^\circ$ , corresponding to the azimuthal quadrants  $90^\circ \leq \phi \leq 180^\circ$  and  $270^\circ \leq \phi \leq 360^\circ$  with rotation angles  $0^\circ$  to  $-180^\circ$ , corresponding to quadrants  $0^\circ \leq \phi \leq 90^\circ$  and  $180^\circ \leq \phi \leq 270^\circ$ . The strong azimuthal angle dependence suggests that these oscillations are probably due to the presence of a Q1D section of FS, rather than the 2D FS effect discussed above in the case of  $\beta''$ -(ET) $_2$ AuBr $_2$ . Mechanisms for such oscillations have been proposed by several authors, involving the velocities of electrons in a Q1D band subjected to a magnetic field [16]. If the field is applied in a general direction, the velocity components perpendicular to the 1D direction sweep out all possible values, thus averaging to zero. However, if the field is oriented so that the electron's  $k$ -vector is directed along a reciprocal lattice vector, the transverse velocity takes only a limited set of values determined by the electron's initial position on the FS. Thus its time averaged velocity is non-zero, leading to dips in the MR periodic in  $\tan(\theta)$ . The period of these oscillations is determined by the projection of the plane of rotation of the magnetic field onto the 1D direction, and is proportional to  $1/\cos(\phi - \phi_0)$ ,  $\phi_0$  being the azimuthal angle at which the plane of rotation of the magnetic field is perpendicular to the 1D axis.

The third notable feature of the data in Fig. 5 is that the angle dependence of the MR is very similar, both qualitatively and quantitatively in the oscillation periodicities in  $\tan \theta$ , at 20 and 24 T (i.e. above and below the “kink”). Therefore, although we have as yet insufficient data do

determine the exact orientation of the Q1D sections of the FS, the existing data do appear to indicate that there are no very drastic changes in band structure at the “kink” transition, and that similarly oriented Q1D sections are present at all magnetic fields. This is supported by the similar carrier effective masses observed both above and below the “kink”. Thus, although some of our data give partial support to the band structure for  $\alpha\text{-(ET)}_2\text{KHg(SCN)}_4$  proposed by Kartsovnik et al., much work remains to be done to clarify the mechanism responsible for the “kink” and the low temperature Fermi surface.

#### 4. Note added in proof

Recent measurements of the angle-dependent magnetoresistance in  $\alpha\text{-(ET)}_2\text{KHg(SCN)}_4$  have been carried out using fields up to 30 T. The data show conclusively that the high field “kink” represents a transition from a SDW groundstate, characterised by a quasi-one dimensional Fermi surface sheet tilted by  $\sim 21^\circ$  with respect to the  $b^*c$  plane, to a state with a cylindrical two-dimensional Fermi surface. The two states may be distinguished by the different character of the angle-dependent magnetoresistance oscillations observed above and below the “kink”. See “Magnetoresistance oscillations and field-induced Fermi surface changes in  $\alpha\text{-ET}_2\text{KHg(NCS)}_4$ ”, J. Singleton, J. Caulfield, P.T.J. Hendriks, J.A.A.J. Perenboom, M.V. Kartsovnik, A.E. Kovalev, W.

Hayes, M. Kurmoo and P. Day, *J. Phys.: Condensed Matter*, submitted.

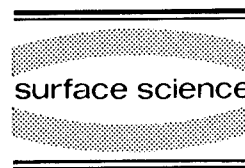
#### 5. References

- [1] M. Kurmoo et al. *Solid State Commun.* 61 (1987) 459.
- [2] T. Mori, F. Sasaki, G. Saitoh and H. Inokuchi, *Chem. Lett.* (1986) 1037.
- [3] K. Kajita et al., *Solid State Commun.* 60 (1986) 811.
- [4] F.L. Pratt et al., *Physica B* 177 (1991) 333.
- [5] D. Shoenberg, *Magnetic Oscillations in Metals* (Cambridge University Press, Cambridge, 1984).
- [6] M. Doporto et al., *Synth. Met.*, 56 (1993) 2572.
- [7] K. Yamaji, *J. Phys. Soc. Jpn.* 58 (1989) 1520.
- [8] M.V. Kartsovnik et al. *J. Phys. I France* 2 (1992) 89.
- [9] T. Ishiguro and K. Yamaji, *Organic Superconductors* (Springer, Berlin, 1990).
- [10] H. Ito et al., *Solid State Commun.* 85 (1993) 1005.
- [11] F.L. Pratt, J. Singleton, M. Doporto, T.J.B.M. Janssen, J.A.A.J. Perenboom, M. Kurmoo, W. Hayes and P. Day, *Phys. Rev. B* 45 (1992) 13904.
- [12] J.S. Brooks et al., *Phys. Rev. Lett.* 69 (1992) 156.
- [13] T. Sasaki and N. Toyota, *Solid State Commun.* 82 (1992) 447.
- [14] M.V. Kartsovnik, A.E. Kovale and N.D. Kushch, *J. Phys. I France*, in press.
- [15] S.J. Klepper, J.S. Brooks, G.J. Athas, X. Chen, M. Tokumoto, N. Kinoshita and Y. Tanaka, *Surf. Sci.* 305 (1994) 181.
- [16] A.G. Lebed and P. Bak, *Phys. Rev. Lett.* 63 (1989) 315; G. Montambaux and P.B. Littlewood, *Phys. Rev. Lett.* 62 (1989) 953; V.M. Yakavenko, *Phys. Rev. Lett.* 68 (1992) 3607; M.J. Naughton, O.H. Chung, M. Chaparaba, X. Bu and P. Coppens, *Phys. Rev. Lett.* 67 (1991) 3712; T. Osada, S. Kagoshima and N. Miura, *Phys. Rev. B* 46 (1992) 1812.



ELSEVIER

Surface Science 305 (1994) 194–201



# Electronic excitations in parabolically confined electron systems

Achim Wixforth

*Sektion Physik, Ludwig-Maximilians-Universität München, Geschwister Scholl Platz 1, D-80539 München, Germany*

(Received 15 April 1993; accepted for publication 4 June 1993)

## Abstract

The dynamic response of electron systems confined in a one-dimensional parabolic potential is investigated experimentally. Such structures are realized in so-called parabolic quantum wells where the parabolic confining potential is achieved by a proper grading of the barriers of a AlGaAs/GaAs quantum well. We present some of our recent studies on both intra- and interband fundamental excitations of such systems like cyclotron resonance, intersubband resonance, plasmon modes and photoluminescence excitations using various experimental techniques and geometries. Detailed studies of the electronic excitations in parabolic wells with intentionally induced deviations from ideal parabolicity allow for a better understanding of the effect of non-parabolic terms in the confining potential also for lateral nanostructures. Due to the simplicity of the confining potentials most of our experimental results can be explained in simple straightforward and transparent ways that also apply to recent investigations of lateral nanostructures and thus may serve for a better understanding also of this rapidly developing field.

## 1. Introduction

The interaction between electron systems in semiconductor quantum well structures and optical fields has been studied intensively during the last two decades [1]. These studies include intersubband absorption, cyclotron resonance in high magnetic fields as well as plasmon emission and absorption. The collective excitation spectrum of an electronic system contains valuable information as it is one of its most fundamental properties. For quasi-two-dimensional electron systems (Q2DES, quantum films) as realized in space charge layers in semiconductors the study of plasmon (intrasubband) excitations as well as intersubband transitions have proven invaluable in the characterization and understanding of these systems [2]. More recently [3], the collective excita-

tions in quasi-one-dimensional (Q1DES, quantum wires) [4,5] and quasi-zero-dimensional electron systems [6] (Q0DES, quantum dots) have also attracted very much attention. This is because in the last few years the realization of lateral nanostructures has become possible, which yielded a rapidly growing field of interest in semiconductor physics. On the other hand, tremendous improvements of semiconductor growth techniques like molecular beam epitaxy (MBE) nowadays offer the possibility to engineer practically every desired kind of bandstructure for semiconductor structures.

A very attractive application of those advanced growth methods are so-called parabolic quantum wells (PQW). Originally invented to represent an attempt towards the theoretical construct of *jellium*, it turned out that there is a striking similar-

ity of many of their properties to the ones of a Q1DES or even a Q0DES. Many experimental results obtained in such nanostructures have in the recent past also been successfully described in a parabolic approximation [3]. For this reason, throughout this report, I shall point out the similarities and the applicability of our experimental and theoretical results to the case of lateral nanostructures and give representative examples.

## 2. Electron systems in parabolic quantum wells

PQWs are grown by computer-controlled molecular beam epitaxy (MBE). The parabolic profiles of both the conduction as well as the valence bands are obtained by properly grading the aluminum content of the ternary  $\text{Al}_x\text{Ga}_{1-x}\text{As}$  alloy. In the range  $0 \leq x \leq 0.3$  its band gap varies nearly linearly with Al mole fraction, such that a controlled variation of  $x$  directly leads to the desired structure. The basic idea of these structures is thus to create a conduction band profile  $E_C(z)$  in the growth direction such that it mimics the parabolic potential of a uniformly distributed slab of positive charge  $n^+$ . Once this structure is remotely doped, the donors release electrons into the well which in turn will screen the man-made parabolic potential and form a wide and nearly homogeneous electron layer. An undoped spacer

between the dopants and the well reduces ionized impurity scattering and thus enhances the electron mobility in the well, as is the case for conventional heterostructures. The fictitious charge  $n^+$  is related to the curvature of the grown PQW by Poisson's equation:

$$n^+ = \frac{\epsilon\epsilon_0}{e^2} \frac{\partial^2 E_C}{\partial z^2} = \frac{8\epsilon\epsilon_0\Delta}{e^2 W^2}. \quad (1)$$

Here,  $\epsilon$  denotes the dielectric constant of  $\text{Al}_x\text{Ga}_{1-x}\text{As}$ ,  $\Delta$  is the energy height of the parabola from its bottom to the edges,  $e$  the electronic charge, and  $W$  the width of the grown PQW. Thus  $n^+$  can be varied over a wide range by proper control of the growth process. Typical curvatures of our samples correspond to  $n^+$  of a few times  $10^{16} \text{ cm}^{-3}$ . Due to the similarity to a real existing positive space charge, this concept has been referred to as “quasi-doping”.

In Fig. 1 we depict the basic results as obtained from a self-consistent calculation of the resulting subband structure and carrier distribution in such a PQW. Since in our experiments we are able to vary the carrier density in the well by application of a gate bias between a semitransparent electrode on top of the sample and the electron system, we plot the above quantities as a function of  $V_g$ . Typical sheet carrier densities in our samples lie in the range of a few times  $10^{11} \text{ cm}^{-2}$ . Usually, up to four subbands are occupied

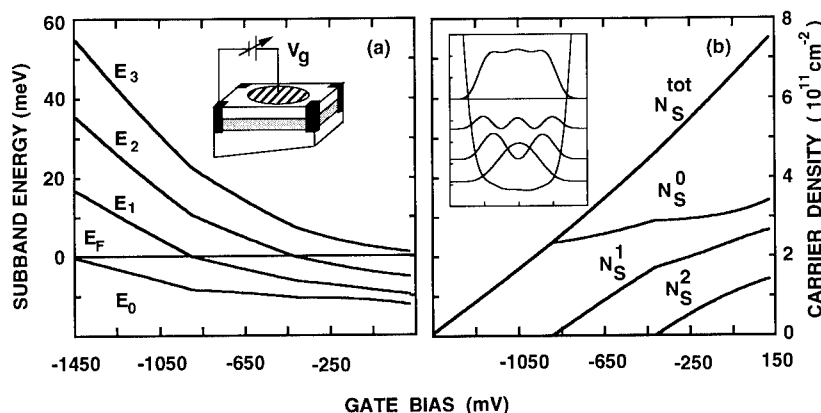


Fig. 1. (a) Self-consistent subband spacing of a wide PQW as a function of the applied gate bias  $V_g$ . The inset depicts a typical sample geometry used in our experiments. (b) Distribution of the carriers in a PQW as a function of gate bias. Decreasing gate voltage tends to deplete the well by depopulating the electrical subbands. The inset depicts the wavefunctions and the total carrier distribution in the well together with the self-consistent Hartree potential at  $V_g = 0 \text{ V}$ .



at  $V_g = 0$  V, and the resulting total carrier distribution is essentially flat over the region of the well. The self-consistent potential in this case also exhibits a flat bottom as expected for a quasi-three-dimensional electron system. Decreasing gate bias depletes the well and simultaneously increases the self-consistent subband spacing as indicated in Fig. 1a. At the same time the electrical subbands become depopulated at specific gate voltages. The slab of mobile carriers narrows thus changing its dimension from quasi 3D towards quasi 2D behavior.

### 3. Far-infrared spectroscopy

Shortly after the first successful realization of remotely doped PQWs, some initial experiments [7,8] stimulated a lot of further experimental as well as theoretical work on this subject. Subsequently, both (magneto-)transport [9,10] as well as FIR investigations [11] uncovered a large amount of new and interesting results which shed some light onto the understanding of many fundamental properties of low-dimensional electron systems.

The most interesting by-product of the initial experimental investigations of the far-infrared (FIR) response of a PQW was the formulation of the generalized Kohn theorem [12]: It states that in a purely parabolically confined electron system long-wavelength radiation only couples to the center of mass (CM) coordinates and its motion. The reason is the decoupling of these modes of the interacting electron gas from its internal modes. Relative coordinates, and thus particularly electron–electron interactions, in such systems do not affect the resonance frequency of the observed transitions. FIR experiments on a PQW thus only allow access to a single well-defined frequency  $\omega_0$  which is related to the CM motion of the whole electron system and is solely determined by the curvature of the external confining potential. For the case of a PQW this resonance frequency can be determined by the growth of the PQW alone, namely

$$\hbar\omega_0 = \left( \hbar^2 \frac{8\Delta}{W^2 m^*} \right)^{1/2}. \quad (2)$$

This mode is of inter-subband type and represents a sloshing of the electron system as a whole in the external parabolic potential. A very power-

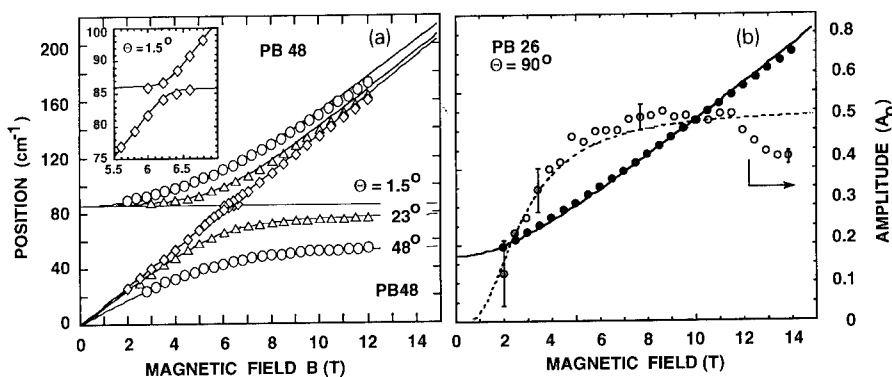


Fig. 2. (a) Experimentally obtained resonance positions for three different tilted field experiments as a function of the total magnetic field strength  $B$ . With increasing tilt angle the mode anticrossing becomes more pronounced. The solid lines are the result of a calculation according to Eq. (3) using no fit parameters for all three measurements. (b) The same experiment with the magnetic field in the plane of the PQW. This leads to a complete hybridization of the CR and the sloshing mode of the PQW. Filled symbols and the solid line represent the extracted and calculated resonance positions, open symbols and the dashed line depict the amplitude of the line as extracted from our experiment together with the theoretical one. The origin of the discrepancies between the oscillator strength as obtained experimentally and theoretically is not known to date.

ful method to investigate this sloshing mode, working well in PQWs, is the use of a tilted magnetic field which couples the in-plane motion of the mobile carriers to the vertical one. This leads to a strong interaction between the cyclotron resonance (CR)  $\omega_c = eB/m^*$  and the sloshing mode represented by  $\omega_0$ , manifested in an anti-crossing around  $\omega_c = \omega_0$ . The result is a splitting of the CR into two lines,  $\omega_+$  and  $\omega_-$ , which are given by the simple analytic expression

$$\omega_{\pm} = \sqrt{\frac{1}{2}(\omega_c^2 + \omega_0^2) \pm \frac{1}{2}\sqrt{\omega_c^4 + \omega_0^4 + 2\omega_0^2(\omega_{c,x}^2 - \omega_{c,z}^2)}}. \quad (3)$$

Here,  $\omega_{c,x} = \omega_c \sin \theta$  and  $\omega_{c,z} = \omega_c \cos \theta$  denote the projections of the CR onto the magnetic field components parallel and perpendicular to the growth direction.  $B$  is tilted by an angle  $\theta$  with respect to the sample surface. For the extreme case of a totally in-plane field, Eq. (3) converts to  $\omega_+^2 = \omega_c^2 + \omega_0^2$  representing the plasma-shifted CR, a hybrid mode between electrical and magnetic confinement. Typical experimental results are given in Fig. 2. Here, we plot the extracted resonance positions of tilted or in-plane field transmission experiments as a function of the total magnetic field. In (a) the results for three different tilt angles are shown. The solid lines represent the calculated positions according to Eq. (3).

In (b) the corresponding results for an in-plane magnetic field and a different sample are shown. Here, we also depict the amplitude of the observed resonance together with the theoretically expected one. As can be seen, the agreement between the simple model of two coupled harmonic oscillators and our experimental results is quite perfect. There is no fit parameter in the calculations, the sloshing mode  $\omega_0$  is simply taken from the growth parameters of our samples. Changing the carrier density does not change the extracted resonance position  $\omega_0$  significantly [13], indicating that Kohn's theorem is valid for our systems. To demonstrate the sensitivity of the above experiments we show in Fig. 3 typical spectra taken at a very small tilt angle and for different magnetic fields between  $B = 2.5$  T and  $B = 4.0$  T. The interaction between the sloshing mode and the CR manifests itself in a sharp dip in the envelope of the spectra in the vicinity of the

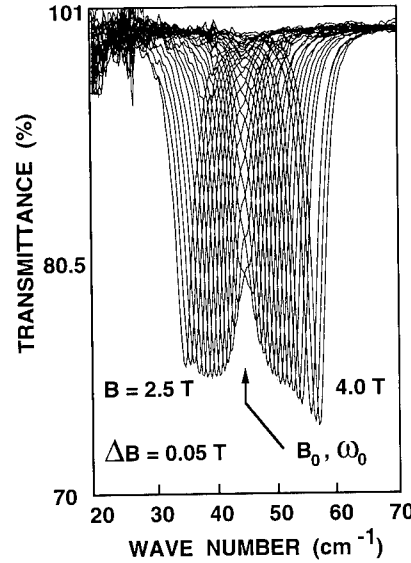


Fig. 3. Experimentally obtained spectra of the cyclotron resonance in a PQW in a tilted magnetic field. The tilt angle in this case is very small ( $\theta = 3^\circ$ ) such that a splitting of both lines according to Eq. (3) is not yet achieved. Nevertheless, a sharp dip in the envelope of the spectrum indicates the region of anticrossing between both lines and allows for an exact determination of the resonance condition.

degeneracy point, although a line splitting at this small angle is not yet resolved.

#### 4. Imperfect parabolic wells

So far, we have demonstrated the FIR response of “ideal” PQWs, where Kohn's theorem is valid. However, it is very interesting to investigate the effect of non-parabolic terms in the confining potential of the FIR spectrum. Here, too, PQWs seem to be a nearly perfect tool. Unlike the case of quantum wires or dots, the external confining potential can be tailored in a very precise and controlled way during the growth. Moreover, optical experiments on imperfect PQWs can yield information not only about the extent to which the confining potential deviates from perfect parabolicity, but also (for small deviations) about the forbidden excitations of an ideal system. Here, we present experimental results obtained in a structure where we intentionally

induced a certain degree of nonparabolicity to study its influence on the FIR spectrum [14]. The sample is a nominally 75 nm wide PQW with  $\Delta = 75$  meV, having vertical sidewalls which are 150 meV high. From the PQW curvature we expect the bare harmonic oscillator frequency to be  $\omega_0 \hat{=} 86 \text{ cm}^{-1}$ . Apart from changing the carrier density in the well by application of a gate bias we can simultaneously change the shape of the confining potential in this special sample. At high well filling the additional vertical sidewalls violate parabolicity, whereas at very low filling the wavefunction is squeezed against the lower vertical sidewall. At intermediate fillings we expect the sample to behave like a “normal” PQW. An experimental spectrum, as obtained using the grating coupler technique [14], is shown in Fig. 4a. Here, we plot the relative change in transmission versus FIR frequency for different carrier densities in the well. As can be seen, the electron

system not only absorbs at the frequency of the bare potential, but side lines appear in the spectrum. Experiments in a tilted magnetic field confirm this observation. Here, we make use of the effect of a certain “contrast enhancement” in such measurements: Although the oscillator strengths of the additional lines may be quite small as compared to the main line, their existence can also lead to a resonant interaction between these modes and the cyclotron resonance. This is demonstrated in Fig. 4b, where we plot the extracted resonance positions from a tilted field experiment for this sample as a function of the magnetic field and for three different gate voltages. Most remarkable is the occurrence of additional lines and the completely changed character of the dispersion as compared to an “ideal” PQW especially for low well fillings.

Recently, Dempsey and Halperin [15] were able to perfectly describe our experimental re-

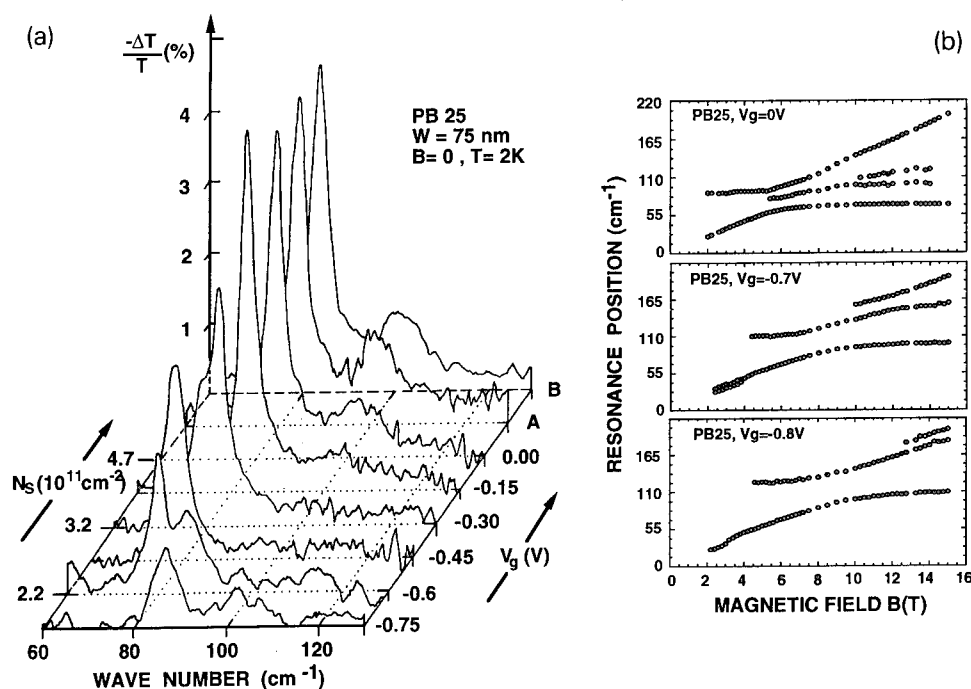


Fig. 4. (a) Grating-coupler-induced spectra for an imperfect PQW. The relative change in transmission is shown for different carrier densities  $N_s$ . In both limits of high and low well filling deviations from the harmonic oscillator picture are observed, manifesting themselves in the occurrence of additional lines [14]. (b) Experimentally obtained resonance positions from a tilted-field experiment on sample PB25 for different well fillings. With decreasing carrier density the spectra deviate more and more from the simple harmonic oscillator picture. Additional lines besides the CM modes appear and the whole spectrum is shifted towards higher energies, indicating a “stiffening” of the confining potential.

sults by using a self-consistent field approach in the local density approximation (LDA-SCF) and, for comparison, also in the random phase approximation (RPA). Since for our samples the shape of the confining potential is extremely well known, it allows for a completely satisfying explanation in terms of theoretical understanding. An important result is the strong mixing of the depolarization-shifted single-particle subband resonances that lead to the complicated spectrum as presented in Fig. 4. Our results together with the theoretical work thus can be regarded as a valuable approach towards the understanding of the FIR spectrum also of quantum wires and dots, where the confining potential is only in first-order parabolic, but not known a priori.

Experiments at finite wave vector are very illustrative in understanding the excitation spectrum of parabolically confined electron systems. Here, we use a grating coupler technique of periodicity  $a$  to couple also to intrasubband plasmon excitations. In a local and strictly two-dimensional treatment, where the wavelength of the

excitation is taken to be much larger than the thickness of the electron system, this dispersion of the intrasubband plasmon reads

$$\omega_p^2 = \frac{e^2 N_s q_x^n}{2\bar{\epsilon} m_p}, \quad \text{with} \quad q_x^n = n \frac{2\pi}{a}. \quad (4)$$

Here,  $N_s$  again denotes the areal carrier density,  $\bar{\epsilon}$  is an effective dielectric function including screening, and  $m_p$  is a plasmon effective mass. It is important that in the near field of the grating,  $z$ -components of the electric field are induced which can be used to excite the intersubband like resonances as discussed in the previous section (cf. Fig. 4a). In the limit of small  $q$  we expect Eq. (4) still to be reasonably valid, even though we are not dealing with a strictly 2D system. For reasonable carrier densities as present in our PQW, and for a wave vector of the order of  $2\pi/1 \mu\text{m}$ , the energies of the intrasubband plasmon  $\omega_p$  are of the same order as  $\omega_0$ . Thus we are able to systematically study the mutual interaction between both modes which is not that easily

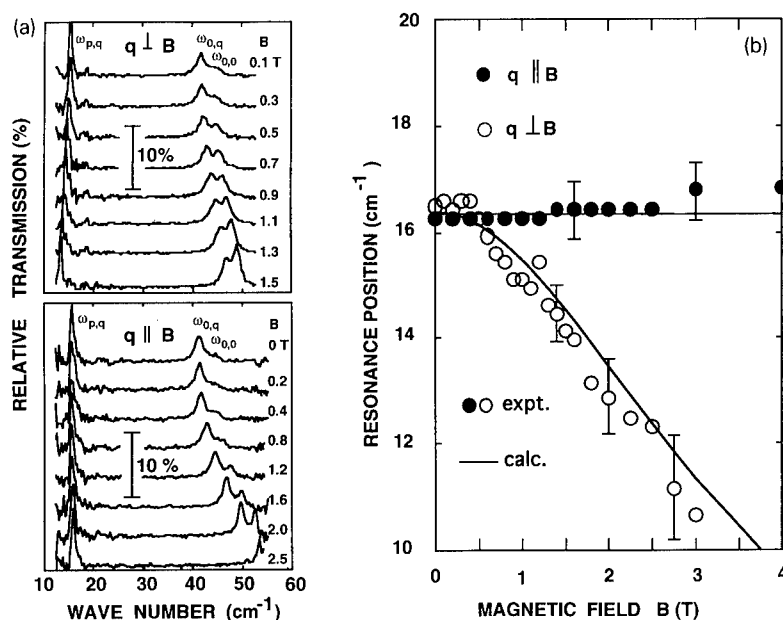


Fig. 5. Plasmon excitations of a PQW subjected to an in-plane magnetic field. The magnetic field induced anisotropy in the subband structure is clearly seen for the intrasubband plasmon resonance at around  $15 \text{ cm}^{-1}$ . For  $q \perp B$  the intra subband plasmon exhibits a negative magnetic field dispersion as it is typical for edge-type plasmons. No such signature is observed for  $q \parallel B$ . The agreement between the simple model as described in the text and the experimental results is quite perfect [17].

achieved on a 2DES. We find that both modes strongly couple if more than one electric subband is occupied, and some asymmetry is induced in the confining potential [16]. Due to the limited space in this report I have to refer the reader to the original paper addressing this mode-coupling phenomenon. There is, however, another very interesting feature about the intrasubband plasmon in a wide PQW: As we have seen before, an in-plane magnetic field hybridizes the cyclotron motion and the sloshing mode of a PQW similar to the magnetic field dispersion of the 1D inter-subband resonance or to the “upper” mode of the characteristic spectrum of a quantum dot. On the other hand, it turns out that the presence of an in-plane magnetic field induces an anisotropy in the subband dispersion. Taking the in-plane magnetic field to be directed along the  $y$ -direction, this dispersion then reads

$$E = \hbar\Omega(n + 1/2) + \frac{\hbar^2 k_x^2}{2m^*} \frac{\omega_{0,q}^2}{\Omega^2} + \frac{\hbar^2 k_y^2}{2m^*}, \quad (5)$$

where  $\Omega^2 = \omega_{0,q}^2 + \omega_{2c}^2$  denotes the effective hybrid mode at finite  $q$ . The free motion in the plane of the electron system is represented by the quasi-momenta  $k_x$  and  $k_y$ . The interesting fact is the occurrence of an anisotropic band structure with respect to the direction of the magnetic field. It is worth mentioning that Eq. (5) has exactly the same form for a Q1DES in the parabolic approximation if one replaces the term containing  $k_y$  by the 2D subband energy of the “starting material” Q2DES. The term containing  $k_x$  is then related to so-called one-dimensional plasmons propagating along the wire [5]. Eq. (5) can also be regarded as to describe a renormalization of the effective mass  $m^*$  with respect of the magnetic field direction. In terms of a collective excitation at finite  $q$ , this leads to a strongly anisotropic magnetic field dispersion, given by

$$\omega_{p,q}^2(q_{\perp}) = \omega_p^2 \left( 1 + \frac{\omega_c^2}{\omega_{0,q}^2} \right)^{-1}; \quad \omega_{p,q}^2(q_{\parallel}) = \omega_p^2. \quad (6)$$

Here, the subscripts of  $q$  have to be taken with respect to the direction of the magnetic field  $B$ . The result of an experiment [17] where we probe this dispersion by a surface plasmon of the type given by Eq. (5) is shown in Fig. 5. In Fig. 5a we depict the experimental spectra for both magnetic field orientations. In all cases we observe three distinct lines with characteristic  $B$ -dispersion. For  $q \perp B$  the low energy line, which we identify with the intrasubband plasmon exhibits a negative dispersion which is characteristic for an edge-type plasmon mode. The lines with positive  $B$ -dispersion are identified as the sloshing mode at  $q = 0$  and at somewhat lower energy the one at finite  $q$  [17]. For  $q \parallel B$ , however, the intrasubband plasmon shows no magnetic field dependence as predicted by Eq. (7). In Fig. 5b we show the extracted resonance position for this plasmon and both magnetic field orientations. Again, there is quite perfect agreement with the calculation according to Eq. (7) as depicted by the solid lines.

As a final example, I would like to present

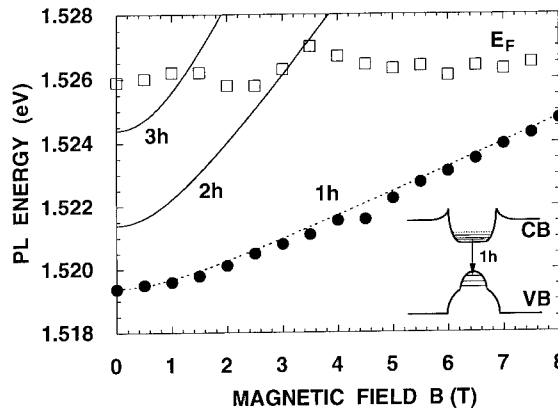


Fig. 6. Magneto-luminescence on a PQW subjected to an in-plane field at an excitation energy of 2.412 eV. In this experiment the single particle subband spectrum is probed by radiative recombination of photoexcited carriers in the quantum well. Strong confinement of the holes also leads to a Fermi edge singularity that allows for a determination of the Fermi level in the system. For symmetry reasons, only the transition 1h is observed. The lines depict the expected dispersion of the magneto-electric hybrid subbands that become depopulated at magnetic fields where the Fermi level exhibits characteristic kinks [courtesy of Ch. Peters, to be published].

some experimental results demonstrating that the single particle spectrum of a PQW is accessible with optical methods. Similar to the work of Plaut et al. [18], we investigated the magneto-photo-luminescence (PL) of our samples in the above 1D geometry, i.e., the magnetic field directed along the plane of the electron system. Then, the magneto-electric hybrid bandstructure is identical to the one observed in quantum wires in a perpendicular magnetic field. Plaut et al. observe a PL signal that is attributed to the radiative recombination of such 1D-confined photoexcited electrons with holes that are provided by a p-type  $\delta$ -layer in close vicinity of the electron system. For a PQW, however, because of the graded alloy, both the conduction as well as the valence band of a PQW are parabolically shaped. This offers the advantage that there is also strong confinement for photoexcited holes, leading to a so-called “Fermi edge singularity” in the PL spectra allowing for a determination of the Fermi energy as a function of the applied magnetic field. In Fig. 6 we depict the result of such an experiment. Clearly the magnetic field dispersion of the lowest hybrid subband as well as the depopulation of the higher subbands is observed, as indicated by the oscillations of the Fermi level as a function of the magnetic field.

## 5. Acknowledgements

I would like to gratefully acknowledge a very fruitful collaboration with many colleagues as cited in the references and thank both the Deutsche Forschungsgemeinschaft and the Volkswagen Stiftung for financial support during the progress of this work.

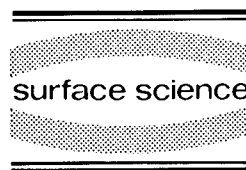
## 6. References

- [1] For an excellent review on the electronic properties of low-dimensional systems, see, e.g., T. Ando, A.B. Fowler and F. Stern, *Rev. Mod. Phys.* 54 (1982) 437.
- [2] See, e.g., D. Heitmann, *Two-Dimensional Systems: Physics and New Devices*, Eds. G. Bauer, F. Kuchar and H. Heinrich (Springer, Berlin, 1986) p. 285.
- [3] For a recent review, see, e.g., W. Hansen, U. Merkt and J.P. Kotthaus, in: *Semiconductors and Semimetals*, Vol. 35, Eds. R.K. Willardson, A.C. Beer and E.R. Weber (Academic Press, San Diego, 1992) p. 279.
- [4] W. Hansen, M. Horst, J.P. Kotthaus, U. Merkt, Ch. Sikorski and K. Ploog, *Phys. Rev. Lett.* 58 (1987) 2586.
- [5] T. Demel, D. Heitmann, P. Grambow and K. Ploog, *Phys. Rev. Lett.* 64 (1990) 788.
- [6] Ch. Sikorski and U. Merkt, *Phys. Rev. Lett.* 62 (1989) 2164.
- [7] K. Karrai, H.D. Drew, H.W. Lee and M. Shayegan, *Phys. Rev. B* 39 (1989) 1426.
- [8] K. Karrai, X. Ying, H.D. Drew and M. Shayegan, *Phys. Rev. B* 40 (1989) 12020.
- [9] E.G. Gwinn, R.M. Westervelt, P.F. Hopkins, A.J. Rimberg, M. Sundaram and A.C. Gossard, *Phys. Rev. B* 39 (1989) 6260.
- [10] K. Ensslin, A. Wixforth, M. Sundaram, P.F. Hopkins, J.H. English and A.C. Gossard, *Phys. Rev. B* 47 (1993) 1366.
- [11] K. Karrai, X. Ying, H.D. Drew, M. Santos, M. Shayegan, S.R.E. Yang and A.H. MacDonald, *Phys. Rev. Lett.* 67 (1991) 3428.
- [12] L. Brey, N.F. Johnson and B.I. Halperin, *Phys. Rev. B* 40 (1989) 647.
- [13] A. Wixforth, M. Sundaram, K. Ensslin, J.H. English and A.C. Gossard, *Surf. Sci.* 267 (1992) 523.
- [14] A. Wixforth, M. Sundaram, K. Ensslin, J.H. English and A.C. Gossard, *Phys. Rev. B* 43 (1991) 10000.
- [15] J. Dempsey and B.I. Halperin, *Phys. Rev. B* 45 (1992) 3902.
- [16] M. Kaloudis, K. Ensslin, A. Wixforth, M. Sundaram, J.H. English and A.C. Gossard, *Phys. Rev. B* 46 (1992) 12469.
- [17] A. Wixforth, M. Kaloudis, M. Sundaram and A.C. Gossard, *Solid State Commun.* 84 (1992) 861.
- [18] A.S. Plaut, H. Lage, P. Grambow, D. Heitmann, K. von Klitzing and K. Ploog, *Phys. Rev. Lett.* 67 (1991) 1642.



ELSEVIER

Surface Science 305 (1994) 202–207



# Transition from 2D to 3D collective response: surface sensitivity

E.L. Yuh \*, E.G. Gwinn

*Department of Physics, University of California at Santa Barbara, Santa Barbara, CA 93106, USA*

(Received 21 April 1993; accepted for publication 7 May 1993)

## Abstract

We present electronic excitation spectra calculated in the random phase approximation (RPA) for bimetallic jellium films with widths ranging from zero to several Fermi wavelengths. We find that for  $q_{\parallel}$  below roughly  $0.1k_F$ , excitation frequencies converge to the surface plasmon frequencies of the Drude model at strikingly different rates as the slab thickens; and that this onset behavior is quite sensitive to the shape of surface potential barriers. At larger wavevectors, the RPA response deviates from local behavior for *all* layer widths.

## 1. Introduction

The collective modes of thin layers of electron gas remain an outstanding problem of current interest [1–3]. To date, the collective behavior of single-density slabs of electron gas (as realized in parabolic AlGaAs heterostructures) has been the subject of several studies [2,3]. However, thin electron gases with *internal* variation in the ground-state electron density,  $n_e$ , have been little explored [4]. Better understanding of such thin gases may allow the design of free electron materials with specific optical and chemical properties that are tailored by choice of the shape of  $n_e$ . In addition, because gases with internal gradients in  $n_e$  support a rich excitation spectrum, studies of such gases provide valuable tests of current theories of the collective behavior of inhomogeneous electron gases, thus far limited primarily to studies of semi-infinite metals [5].

We study the collective mode spectrum of a bimetallic film, for a range of film thicknesses and surface wavevectors,  $q_{\parallel}$ . We choose a bimetallic gas because it has a *single* internal surface between regions of different electron density,  $n_e$ , and is thus the simplest example of an electron layer with strong density gradients in its interior. In AlGaAs heterostructures, widths of electron layers typically do not exceed a Fermi wavelength, so that the electron energy level spectrum is quantized into subbands. We investigate, in the  $q_{\parallel} \ll k_F$  limit, how the excitations of such thin, bimetallic layers evolve toward the surface plasmons (SP) of a fully 3D gas. We show that shapes of the surface potentials that confine the electrons strongly affect the rate at which 3D collective behavior emerges with increasing gas width; and that the emergence of 3D behavior is mode-dependent. Finally, we explore the qualitative difference in response exhibited in two different regimes of  $q_{\parallel}$ : for  $q_{\parallel}$  below roughly  $0.1k_F$ , a local, Drude model describes the response for a sufficiently wide, “3D” layer, while at larger  $q_{\parallel}$ ,

\* Corresponding author.

the local description breaks down regardless of how wide the layer is made.

## 2. Surface potential barriers in “neutral” and “non-neutral” bimetallic jellium

Fig. 1 illustrates ground-state properties of a typical bimetallic film in an AlGaAs heterostructure. A potential well for electrons (Fig. 1a) is formed by the conduction band edge  $E_c(z)$  of  $\text{Al}_{x(z)}\text{Ga}_{1-x(z)}\text{As}$ , in which the Al fraction  $x(z)$  is tailored along the growth direction,  $z$  [6]. By Poisson’s equation for a slab geometry,  $d^2E_c/dz^2 = e^2n_+/ \epsilon_1\epsilon_0$ , the potential shown in Fig. 1a,  $E_c = n_1z^2(e^2/2\epsilon_1\epsilon_0)$  for  $z < 0$  and  $E_c = n_2z^2(e^2/2\epsilon_1\epsilon_0)$  for  $z > 0$ , simulates the presence of adjacent slabs of positive charge with densities  $n_+ = n_1$  for  $z < 0$  and  $n_+ = n_2$  for  $z > 0$ , where  $\epsilon_1 \approx 13$  for GaAs. In the example shown,  $n_1 = 2.7 \times 10^{16} \text{ cm}^{-3}$  and  $n_2 = 1.35 \times 10^{16} \text{ cm}^{-3}$ .

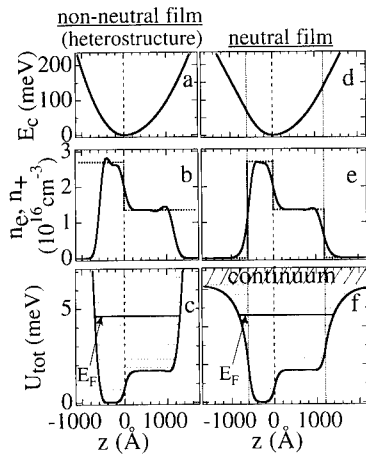


Fig. 1. Ground-state properties of bimetallic slab. In (a)–(f), the dashed, vertical lines at  $z = 0$  separate low- and high-density regions of the positive background density  $n_+$ ; (a)–(c) show a non-neutral film and (d)–(f) its neutral counterpart. (a) Potential  $E_c$  due to  $n_+$ ; (b) electron density  $n_e(z)$  (solid line) and  $n_+$  (dotted line); (c) one-electron potential  $U_{\text{tot}}(z)$ ; dashed horizontal lines show  $\epsilon_n$ ; (b) and (c) are for the well in (a), filled to  $N_e = 3.2 \times 10^{11} \text{ cm}^{-2}$ ; (d)–(f) Neutral bimetallic film with the same  $N_e$ . Dotted vertical lines mark outer surfaces of  $n_+$ .

To screen  $n_+$ , electrons that fill the well form a bimetallic layer (Fig. 1b) with density  $n_e(z) \approx n_1$  for  $z < 0$  and  $n_e \approx n_2$  for  $z > 0$ . In a real structure, Si donors in planes set back from each side of the well provide the electrons, which transfer into the well to reach a constant chemical potential. The small width of the electron gas quantizes the ground-state, single-electron energy spectrum into subbands  $E_n(q_{\parallel}) = \epsilon_n + \hbar^2 q_{\parallel}^2 / 2m^*$ , where  $\epsilon_n$  are eigenvalues of the self-consistent, single-electron potential  $U_{\text{tot}}$ , shown in Fig. 1c. We use the local-density-functional approximation, so  $U_{\text{tot}}$  is the sum of  $E_c$ , the Hartree potential, and an exchange–correlation potential [7].

As shown in Fig. 1b, a *non-neutral* jellium is realized within the well in  $E_c$ :  $n_+$  is wider than the electron gas, and thus produces a steady quadratic rise in  $U_{\text{tot}}$  (Fig. 1c) outside the gas. Fig. 1f shows that conditions at the outer surfaces of a *neutral* jellium are quite different:  $U_{\text{tot}}$  softens and flattens at the outer surfaces, so that the  $\epsilon_n$  above  $E_F$  are closely spaced and form a continuum at high energies. The electronic ground states (i.e.,  $E_F$ , occupied  $\epsilon_n$ ) in both neutral and non-neutral cases are identical, however, as shown. For the neutral film in Figs. 1d–1f, the sheet density of electrons  $N_e = \int n_e(z) dz$  is the same as in Figs. 1a–1c, but  $n_+$  terminates at the dotted vertical lines so that  $N_+ = \int n_+(z) dz = N_e$ .

For much wider bimetallic films and  $q_{\parallel} \rightarrow 0$ , different surface potentials such as in Figs. 1c and 1f do not affect the ordinary SP spectrum: in this limit, ordinary SP frequencies are not sensitive to surface barrier shapes [8]. We show further on that the different surface barriers in Figs. 1c and 1f *do* strongly affect the excitation spectra of the “thin” gases which are the focus of this paper.

## 3. Transition from 2D to 3D collective response: mode specificity and surface sensitivity

In a sufficiently “thin” gas, electrons occupy just a few  $\epsilon_n$ , and two types of collective excitations exist: resonances associated with transitions between subbands (plasma-shifted, intersubband resonances), and a “2D plasmon” intrasubband



mode. As the gas widens, the  $\epsilon_n$  and the excitation spectrum will change rapidly. For a film many Fermi wavelengths wide, however, the  $\epsilon_n$  approach a continuum. If, in addition, the film is wide enough that  $q_{\parallel}w_i \gg 1$  ( $w_i$  is the width of each of the layers of electron density  $n_i$ , that make up the slab), surface excitations on different interfaces of the gas will not be electrostatically coupled to one another. In this limit of a “3D” gas with *decoupled* surfaces, a Drude free electron model gives ordinary SP frequencies exactly [8] in the long wavelength limit  $q_{\parallel} \ll k_F$ . We thus use convergence of the resonance frequencies of the bimetallic gas to those of this model as our criterion for onset of 3D, local dynamic behavior.

The 3D local model uses the Drude dielectric function for the adjacent gases of densities  $n_1$  and  $n_2$ , and finds SP frequencies from the configurations of the oscillating SP charge,  $\delta n$ , that satisfy continuity of  $\phi$  and  $D$  across the three interfaces of the bimetallic gas. Three “ordinary”

SPs exist, with frequencies  $\Omega_{\text{low}}$ ,  $\Omega_{\text{mid}}$  and  $\Omega_{\text{high}}$  that evolve smoothly with slab width, and are related to bulk plasma frequencies  $\omega_1$  and  $\omega_2$  of the high- and low-density gases as shown in Figs. 2a–2c: the left side shows  $\delta n$  and the  $\Omega$ 's for  $q_{\parallel}w_i \ll 1$ ; the right side, for  $q_{\parallel}w_i \gg 1$ . As shown, the  $\Omega$ 's localize at different surfaces for  $q_{\parallel}w_i \gg 1$ . Note that because the model is purely local, it cannot describe any nonlocal effects arising in thin gases due to strong spatial variation in  $n_e$ .

Fig. 2d explores the onset of 3D collective response in the *non-neutral* bimetallic layer (Figs. 1a–1c) by comparing excitation frequencies calculated in the RPA to the 3D, local model, for a wide range of layer thicknesses. Unlike the Drude model, the RPA is microscopic and nonlocal. It has been shown to work well for SPs at surfaces of semi-infinite alkalis at small  $q_{\parallel}$  [5]. The calculation techniques we use are fully described in the literature [9]. We determine the RPA response for an external potential that approximates [10] the effect of the grating couplers often

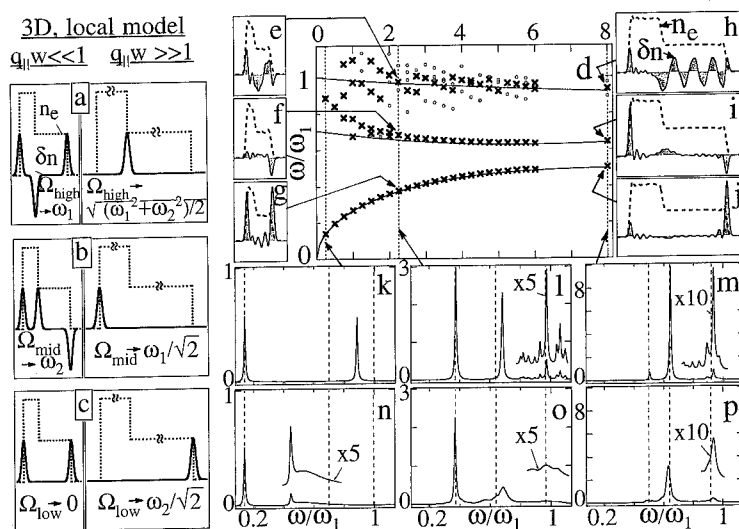


Fig. 2. (a)–(c) SPs of a 3D bimetallic slab, for  $q_{\parallel}w \ll 1$  (left side) and  $q_{\parallel}w \gg 1$  (right side). Dotted line shows  $n_+$  and  $n_e$ ; solid lines sketch oscillating SP charge,  $\delta n$ . (a) Highest mode has frequency  $\Omega_{\text{high}}$ ; (b) middle mode,  $\Omega_{\text{mid}}$ ; (c) lowest mode,  $\Omega_{\text{low}}$ . (d)–(r) Emergence of 3D behavior in a thin electron gas. (d) RPA and 3D resonance frequencies versus gas width  $w_{\text{tot}}$  for  $q_{\parallel} = 3.14 \times 10^4 \text{ cm}^{-1}$ . All frequencies are normalized to  $\omega_1$  (bulk plasma frequency of the denser gas); width is normalized to  $\langle \lambda_F \rangle$ . RPA resonances appear as 0 and x (> 1.8% and > 4.3% of spectral weight, respectively). Solid lines show SP frequencies  $\Omega_{\text{low}}$ ,  $\Omega_{\text{mid}}$  and  $\Omega_{\text{high}}$ . (e)–(j) RPA-calculated  $\delta n$  (snapshots of the oscillating charge of the excitation) and  $n_e$  (dashed line), for resonances indicated by arrows. (k)–(n) RPA absorption (arbitrary units) versus frequency, for  $w_{\text{tot}}$ , marked by vertical dotted lines in (d). Frequency axis is normalized to  $\omega_1$ . (o)–(r) Corresponding RPA spectra for companion *neutral* bimetallic slab.

used experimentally [2,4,11] to couple incident radiation to plasmons with fixed  $q_{\parallel}$ . In Fig. 2d,  $q_{\parallel} = 3.14 \times 10^4 \text{ cm}^{-1} \approx 0.04 \langle k_F \rangle$  (where  $\langle k_F \rangle$  is the mean Fermi wavevector of bulk gases of densities  $n_1$  and  $n_2$ ), placing us in the long wavelength limit in which the 3D, Drude model is accurate for a sufficiently thick gas. Fig. 2d shows dependences of the RPA excitation frequencies, and of the  $\Omega$ 's, on the total width  $w_{\text{tot}}$  of the non-neutral bimetallic gas. In Fig. 2d, frequencies are all normalized to  $\omega_1$ , the bulk plasma frequency of the higher density gas;  $w_{\text{tot}}$  is normalized to the mean Fermi wavelength  $\langle \lambda_F \rangle \approx 765 \text{ \AA}$  of the two gases; and for the largest width shown,  $q_{\parallel} w_{\text{tot}} = 2.1$ . The sheet densities of the adjacent gases are kept equal as the film widens, so that the total sheet density  $N_e$  of the bimetallic film determines the gas width as  $w_{\text{tot}} = 3N_e/4n_2$ , where  $n_2$  is the lower background density. Solid lines are the local SP frequencies  $\Omega_{\text{low}}$ ,  $\Omega_{\text{mid}}$  and  $\Omega_{\text{high}}$ ;  $\times$ 's denote RPA resonances with  $> 3.2\%$  of the integrated spectral weight; and circles, RPA resonances with weight between 0.75 and 3.2%. Figs. 2e–2j show the RPA-calculated  $\delta n$  (shaded) [3], and ground-state density  $n_e$  (dashed lines), for resonances in Fig. 2d marked by arrows. RPA absorption spectra  $A(q_{\parallel}, \omega)$  [10] are shown explicitly in Figs. 2k–2n for selected widths  $w_{\text{tot}}$  marked by vertical dotted lines in Fig. 2d.

Vertical, dashed lines in Figs. 2k–2n locate  $\Omega_{\text{low}}$ ,  $\Omega_{\text{mid}}$  and  $\Omega_{\text{high}}$ .

Fig. 2d shows that the rate at which the RPA resonances approach the  $\Omega$ 's as the gas thickens is strongly mode-dependent. The immediate emergence of the  $\Omega_{\text{low}}$  mode is a general result in the small  $q_{\parallel}$  limit for any electron layer of total width  $w_{\text{tot}}$ , regardless of its  $n_e(z)$ , or whether it is degenerate [3]: for  $q_{\parallel} w_{\text{tot}} \ll 1$ , a “2D” plasmon with frequency proportional to  $(q_{\parallel} N_e)^{1/2}$  always exists. The RPA results in Fig. 2d follow this 2D dispersion for small widths, where the resonance is an intrasubband, “2D” plasmon, and evolve smoothly into the large width limit, in which  $\Omega_{\text{low}} \rightarrow \omega_2/\sqrt{2}$ . In addition to agreement between 3D and RPA frequencies for this plasmon mode, Figs. 2g and 2j show that the RPA-calculated  $\delta n$  resemble their 3D, local model counterparts (Fig. 2c) for all gas widths.

In contrast to the immediate onset of  $\Omega_{\text{low}}$ , Fig. 2d shows that  $\Omega_{\text{mid}}$  emerges gradually from the microscopic response. The RPA intersubband excitations approach  $\Omega_{\text{mid}}$  for  $w_{\text{tot}} \approx 1.5 \langle \lambda_F \rangle$ , and consist of one, or two closely spaced, strong resonances. Figs. 2f and 2i show how the  $\delta n$  of resonances near  $\Omega_{\text{mid}}$  also approach the 3D form (Fig. 2b):  $\delta n$  becomes confined to surface regions and, for  $q_{\parallel} w_{\text{tot}} > 1$ , becomes increasingly localized at the outer surface of the denser gas. Fig. 2i also

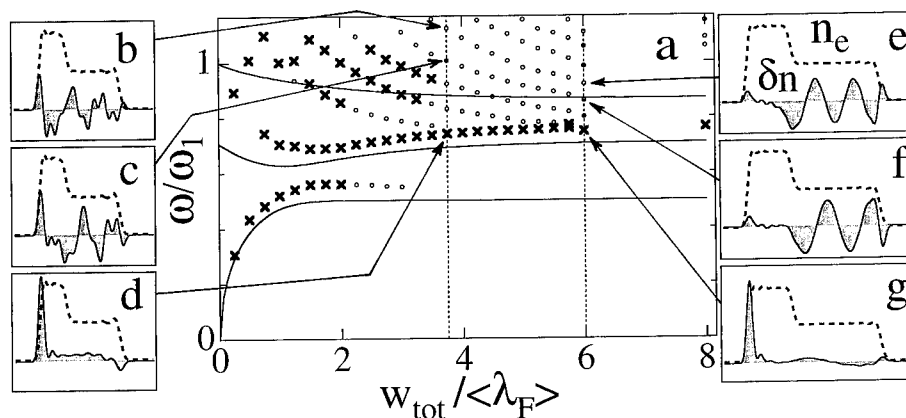


Fig. 3. (a) RPA and Drude resonance frequencies versus  $w_{\text{tot}}$  for  $q_{\parallel} = 1.6 \times 10^5 \text{ cm}^{-1}$ . Frequencies are normalized to  $\omega_1$  and width to  $\langle \lambda_F \rangle$ . RPA resonance frequencies appear as  $\circ$  and  $\times$  ( $> 0.5\%$  and  $> 1.5\%$  of the total integrated spectral weight, respectively); solid lines show Drude SP frequencies  $\Omega_{\text{low}}$ ,  $\Omega_{\text{mid}}$ ,  $\Omega_{\text{high}}$ . (b)–(g) RPA-calculated  $\delta n$  profiles (shaded) and  $n_e$  (dashed line) for resonances indicated by arrows.

shows that  $\delta n$  is most spread out at the internal surface, due to softness of the potential step there.

Unlike  $\Omega_{\text{low}}$  and  $\Omega_{\text{mid}}$ , Fig. 2d shows that the RPA response near  $\Omega_{\text{high}}$  consists of broadly scattered intersubband resonances, even for the largest  $w_{\text{tot}}$  shown. In addition, unlike the  $\delta n$  for RPA resonances near  $\Omega_{\text{low}}$  and  $\Omega_{\text{mid}}$ ,  $\delta n$  profiles (e.g., Fig. 2h) near  $\Omega_{\text{high}}$  have not converged to the 3D form (see Fig. 2a) at large  $w_{\text{tot}}$ : in Fig. 2h,  $\delta n$  does have a large amplitude at the internal surface, but large oscillations also span the low-density gas.

These observations indicate that for typical bimetallic electron-layer widths in AlGaAs ( $N_{\text{e}} \approx 3 \times 10^{11} \text{ cm}^{-2}$ , three occupied subbands, or  $w_{\text{tot}} \approx 1.5\langle\lambda_{\text{F}}\rangle$ ) the absorption will span a narrow frequency range near  $\Omega_{\text{mid}}$ . Near  $\Omega_{\text{high}}$ , however, it will *always* be spread across several plasma-shifted intersubband resonances, spanning a much wider frequency range. These effects have been observed experimentally, as will be described elsewhere [4].

On close inspection of Fig. 2d, the resonances near  $\Omega_{\text{high}}$  are actually seen to be arranged regularly along sweeping lines that intersect  $\Omega_{\text{high}}$ . Each peak is actually a *bulk* plasmon (BP) in the low-density gas, coupled to surface oscillations at the central and vacuum/high-density-gas interfaces. *Within* each line, the number of nodes in  $\delta n$  across the low-density gas is constant; the strongest peaks are those closest to  $\Omega_{\text{high}}$ . Each line differs from the one directly *below* or *above* it by a single node. The modes exist because the dispersion relation for BP's in a 3D, low-density gas,  $\omega_{\text{bulk},2}(q) = [\omega_2^2 + \alpha(q/q_{2\text{F}})^2 + \dots]^{1/2}$ , *always* intersects  $\Omega_{\text{high}}$  for some  $q = q_0$ . Thus, the  $\Omega_{\text{high}}$  SP can never exist alone, but *always* coexists with a BP of wavevector  $q_0$  in the low-density gas [8]. (Here  $q$  and  $q_0$ , to be distinguished from  $q_{\parallel}$ , are wavevectors of a longitudinal, BP oscillation, and point *perpendicular* to the slab) The  $\Omega_{\text{high}}$  SP may actually couple, via electron-hole pairs, to BPs in a *continuous* range of frequencies near  $\Omega_{\text{high}}$ , but since *integral numbers* of half-wavelength oscillations across the low-density gas are preferential, a discrete set of lines about  $\Omega_{\text{high}}$ , rather than a solid band, appears. (*Higher-*

density-gas BPs do not appear prominently in the spectrum, because  $\omega_{\text{bulk},1}(q) = [\omega_1^2 + \alpha(q/q_{1\text{F}})^2 + \dots]^{1/2}$ , intersects none of the three local SPs.)

As we now discuss, our results for the non-neutral bimetallic gas have depended quite critically on the particular shape of the non-neutral barriers. *Neutral* jellium (e.g., Figs. 1d–1f) is the appropriate model for (uncharged) elemental alkalis [5]. Figs. 2o–2r show what happens to the spectra of Figs. 2k–2n when the steep, non-neutral surface barriers are “softened” to those of a neutral bimetallic gas: 3D local dynamic behavior emerges more slowly. Although the integrated absorption is the same in each pair of spectra [9], softer confinement dramatically redistributes the spectral weight: all features above  $\Omega_{\text{low}}$  are broader. In addition, multipole SPs, known to exist at clean elemental metal surfaces [5], reappear in the spectrum, as discussed further elsewhere [3]. They had been suppressed in our non-neutral system, because a steepened electron “selvage” at non-neutral surfaces cannot accommodate within itself the multiple oscillations of  $\delta n$  that characterize multipole SPs [3].

#### 4. Response outside the long-wavelength limit

The discussion up to now has been limited to the long-wavelength limit  $q_{\parallel} \rightarrow 0$ , in which the local, 3D model accurately describes ordinary SPs for a sufficiently wide layer. In this small- $q_{\parallel}$  regime, convergence to the local, 3D model is determined entirely by  $w_{\text{tot}}$ : for all wavevectors  $q_{\parallel}$  below roughly  $0.1\langle k_{\text{F}}\rangle$ , where  $\langle k_{\text{F}}\rangle = 2\pi/\langle\lambda_{\text{F}}\rangle$ , the picture comparing local and RPA excitation frequencies is nearly identical to Fig. 2d. As the  $q_{\parallel}$  of the excitation is increased, however, the local model must become an inadequate description of the response *regardless* of how wide the layer is made. Our calculations show that this change in behavior occurs at rather small  $q_{\parallel}$  just above  $0.1\langle k_{\text{F}}\rangle$ .

As an example of the dynamic response in this “large”  $q_{\parallel}$  regime, Fig. 3a compares the  $\Omega$ 's (solid lines) to RPA excitation frequencies for  $q_{\parallel} = 0.2k_{\text{F}}$ . In Fig. 3a, unlike in Fig. 2d, the RPA frequencies do not converge to any of the Drude

SPs. In particular, RPA frequencies near the “2D” and intermediate-frequency, local response lie above  $\Omega_{\text{low}}$  and  $\Omega_{\text{mid}}$  for all layer widths, while in the small  $q_{\parallel}$  limit explored in Fig. 2d, they converged to  $\Omega_{\text{low}}$  and  $\Omega_{\text{mid}}$ .

The pattern followed by the *highest*-frequency RPA resonances is more easily distinguished in Fig. 3a, than in Fig. 2d. Fig. 3a shows more clearly that the resonance frequencies decrease smoothly with increasing layer width (for  $w_{\text{tot}}$  above  $\sim 2\langle\lambda_F\rangle$ ) along sets of downward-sweeping curves. Figs. 3b, 3c, 3e and 3f illustrate how the mode profile  $\delta n$  is essentially the same at different layer widths along each of these curves, and how at fixed width  $w_{\text{tot}}$ ,  $\delta n$  has an additional half-oscillation in the bulk of the lower-density gas between successive resonances of increasing frequency (compare Fig. 3e to Fig. 3f). The mixed surface/bulk modes appear to merge with the intermediate-frequency SP as the electron layer widens.

## 5. Conclusions

Our results have broad implications for other thin electronic systems. For example, we find that excitations of thin, inhomogeneous gases are quite sensitive to the shape of surface potentials, even in the small  $q_{\parallel}$  limit. We also find that the emergence in thin electron gases of 3D collective behavior is strongly mode dependent. For this reason, we expect that the absorption spectrum for thin gases with strong, internal gradients in  $n_e$  will typically span a wide frequency range (important for potential device applications). Finally, we find that in the bimetallic gas studied here, a local response model begins to break down rather abruptly as  $q_{\parallel}$  increases above  $\sim 0.2\langle k_F\rangle$ , regardless of layer width.

## 6. Acknowledgements

We thank William Schaich, John Dobson and Walter Kohn for numerous helpful discussions. This work was supported in part by NSFDMR-9002491.

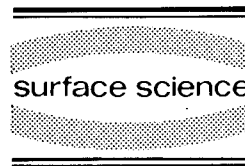
## 7. References

- [1] W.L. Schaich and A.H. MacDonald, Solid State Commun. 83 (1992) 779; W.H. Backes et al., Phys. Rev. B 45 (1992) 8437; O. Heinonen and W. Kohn, to be published.
- [2] P.R. Pinsukanjana et al., Phys. Rev. B 46 (1992) 7284; A. Wixforth et al., Phys. Rev. B 43 (1991) 1991; M. Kaloudis et al., Phys. Rev. B 46 (1992) 12469.
- [3] J.F. Dobson, Phys. Rev. B 46 (1992) 10163; J.F. Dobson, Aust. J. Phys. 46 (1993) 391.
- [4] E.L. Yuh and E.G. Gwinn, to be published.
- [5] K.D. Tsuei, E.W. Plummer and P.J. Feibelman, Phys. Rev. Lett. 63 (1989) 2256; K.D. Tsuei et al., Phys. Rev. Lett. 64 (1990) 44.
- [6] M. Sundaram et al., Superlatt. Microstruct. 4 (1988) 683.
- [7] N.G. Asmar and E.G. Gwinn, Phys. Rev. B 46 (1992) 4752.
- [8] P.J. Feibelman, Prog. Surf. Sci. 12 (1982) 287; Phys. Rev. B 3 (1971) 220, 2974.
- [9] A.G. Eguluz, Phys. Rev. Lett. 51 (1983) 1907; B.N.J. Persson and E. Zaremba, Phys. Rev. B 31 (1985) 1863; A.G. Eguluz and D.A. Campbell, Phys. Rev. B 31 (1985) 7572.
- [10] For an external potential  $\phi_{\text{ext}} \propto \exp[i(q_{\parallel}x - \omega t) - q_{\parallel}z]$ , which approximates the effect of the grating coupler, the absorption spectrum [3,9] is  $A(q_{\parallel}, \omega) = \omega \text{Im}[\int dz e^{-|q_{\parallel}z|} \delta n(z; q_{\parallel}, \omega)]$ . The induced charge  $\delta n(z; q_{\parallel}, \omega)$  is given by  $\int dz' \chi(z, z'; q_{\parallel}, \omega) \phi_{\text{ext}}(z'; q_{\parallel}, \omega)$ . We find  $\chi(z, z'; q_{\parallel}, \omega)$  from the LDA ground state using standard expressions [9]. A realistic calculation of the transmission spectrum that takes into account the parameters of the grating coupler gives results very similar to  $A(q_{\parallel}, \omega)$ : for the 30–70  $\text{cm}^{-1}$  range shown here, there is little change in relative resonance strengths, and a small,  $< 1 \text{ cm}^{-1}$  downward frequency shift (W.L. Schaich, personal communication).
- [11] S.J. Allen, Jr., D.C. Tsui and R.A. Logan, Phys. Rev. Lett. 38 (1977) 980.



ELSEVIER

Surface Science 305 (1994) 208–214



# Resonant inelastic light scattering in remotely doped wide parabolic GaAs/Al<sub>x</sub>Ga<sub>1-x</sub>As quantum wells in a magnetic field

J.H. Burnett \*, H.M. Cheong, R.M. Westervelt, W. Paul

*Department of Physics and Division of Applied Sciences, Harvard University, Cambridge, MA 02138, USA*

P.F. Hopkins, M. Sundaram, A.C. Gossard

*Materials Department and Department of Electrical and Computer Engineering, University of California, Santa Barbara, CA 93106, USA*

(Received 19 April 1993; accepted for publication 16 July 1993)

## Abstract

We have used resonant inelastic light scattering spectroscopy in the  $z(y', x')\bar{z}$  configuration to probe the single-particle excitations of an n-type remotely doped wide parabolic GaAs/Al<sub>x</sub>Ga<sub>1-x</sub>As quantum well, in magnetic fields 0–5 T, oriented perpendicular to the plane of the sample. The well had a design curvature corresponding to an *empty* conduction band harmonic oscillator spacing of 4.4 meV. In zero field the sample revealed two light scattering peaks with energy shifts of 0.85 and 3.0 meV. The peaks were resonant for excitations near the  $E_0 + \Delta_0$  gap of the bulk material at the center of the well, with resonance widths  $< 3$  meV, and the maxima of the resonance curves were separated by an energy given approximately by the scattering peaks separation. This behavior is consistent with a model in which the scattering peaks result from intersubband transitions between square-well-like-spaced subbands of the remotely doped parabolic-well conduction band, which is expected to have a nearly square-well-like effective band-edge potential. For perpendicular magnetic fields, the scattering shifts were independent of field up to 5 T. The resonance energies increased with field approximately linearly by 1 meV for 5 T, an amount less than expected in a simple Landau level model ignoring exciton effects.

## 1. Introduction

Inelastic light scattering has been a useful technique for measuring electronic intersubband spacings in two-dimensional electron-gas (2DEG) systems. Abstreiter and Ploog [1] measured intersubband transitions by carriers in the accumulation layer at a single GaAs/n-Al<sub>x</sub>Ga<sub>1-x</sub>As inter-

face using inelastic light scattering resonant near the  $E_0 + \Delta_0$  gap, and Pinczuk et al. [2] used this technique to measure the intersubband excitations of the multilayer 2DEG in modulation-doped GaAs/Al<sub>x</sub>Ga<sub>1-x</sub>As heterostructure superlattices. In this paper we report resonant inelastic light scattering in n-type remotely doped wide parabolic GaAs/Al<sub>x</sub>Ga<sub>1-x</sub>As quantum wells.

Remotely doped wide parabolic GaAs/Al<sub>x</sub>Ga<sub>1-x</sub>As quantum wells have generated in-

\* Corresponding author.

terest because they have been demonstrated to create relatively thick ( $> 1000$  Å) layers of uniform density, high-mobility electron gas [3–5]. Wide parabolic  $\text{Al}_x\text{Ga}_{1-x}\text{As}$  quantum wells (WPBW) are created in the conduction band (CB), valence band (VB), and spin-orbit split-off band (SOB) by varying the Al concentration in a parabolic profile. The parabolically varying CB edge, by Poisson's equation, mimics a uniform positive charge distribution of 3D density  $n^{3D} = 2\epsilon\Delta E_{CB}/\pi e^2 L_z^2$ , where  $\Delta E_{CB}$  is the difference between the energies at the center of the WPBW and at the edge,  $L_z$  is the width of the well,  $\epsilon$  is the dielectric constant, and  $e$  is the electric charge.

When dopants are introduced outside the parabola, the electrons move to screen this ficti-

tious charge, forming a uniform electron gas of width  $w_e = n_s/n^{3D}$ , where  $n_s$  is the sheet density inside the parabolic well. Self-consistent quantum mechanical calculations verify semiclassical arguments that for filling beyond single subband occupancy, the 3D electron density is nearly uniform, the Fermi level and 3D density are roughly independent of  $n_s$ , and the occupied subband energy levels behave like a square-well spectrum  $E_{n_e} \propto n_e^2/w_{\text{eff}}^2$ , where  $n_e$  is the quantum number and  $w_{\text{eff}}$  is an effective square-well width given by  $w_e$  plus a constant needed to account for the exponential tail of the wavefunction [6]. The VB and SOB edges remain parabolic, but with band-edge curvatures increased by the bare parabolic curvature of the CB. A schematic diagram of the band edges is shown in Fig. 1a, along with a schematic

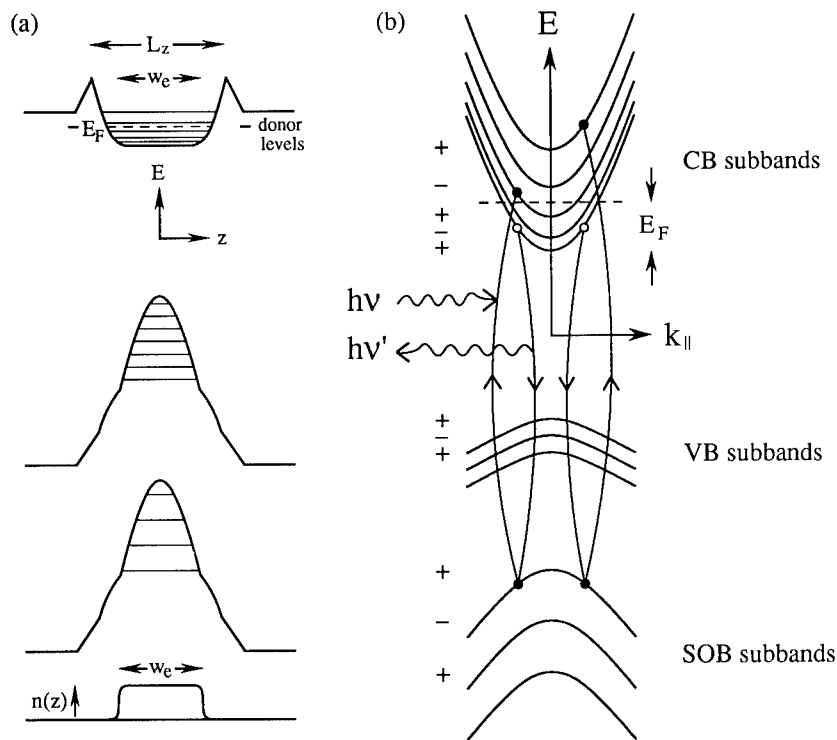


Fig. 1. (a) Schematic diagram of the conduction-band-edge, valence-band-edge and spin-orbit split-off band-edge profiles in an n-type remotely doped  $\text{Al}_x\text{Ga}_{1-x}\text{As}$  parabolic well, with  $k_x = k_y = 0$  energy levels simple-harmonic-like in the VB and SOB, but square-well-like in the CB. (Only the heavy-hole levels in the VB are shown.) The effective width of the square well is given approximately by the width,  $w_e$ , of the electron slab indicated by the charge-density profile shown at the bottom. (b) Schematic diagram of several CB, VB and SOB subbands for the remotely doped parabolic well shown in (a). Two allowed vertical inelastic light scattering transitions, using the lowest SOB subband state as intermediate state, are indicated. The + and - signs on the left of the bands indicate the parity of the states.

of the resulting subbands in Fig. 1b. These predictions of the subband occupancy and spacing, and their dependence on  $n_s$ , have been given support by transport measurements [4,5]. In this work we investigated the predicted square-well-like subband spacing in the CB with inelastic light scattering, using the harmonic-oscillator-like subbands in the SOB as resonance levels.

## 2. Experiment

The WPBW sample was fabricated by molecular beam epitaxy on a (100)GaAs substrate, as described by Sundaram et al. [3]. The parabolic band-edge variations were constructed from a 20 Å period superlattice, each period containing a GaAs and an  $\text{Al}_{0.2}\text{Ga}_{0.8}\text{As}$  layer, with the relative width of the two layers varied using a computer-controlled shutter to produce an average Al concentration with a parabolic profile, with  $x$  near zero at the center. The electrons were introduced into the CB well from Si-doped layers, set back symmetrically from both sides of the well with 300 Å spacer layers. The sample was grown with a nominal WPBW width of  $L_z = 2800$  Å, with  $x = 0.005$  at the center and  $x = 0.2$  at the edge, giving a design density of  $n^{3D} = 1.22 \times 10^{16} \text{ cm}^{-3}$ . The Hall effect sheet density and mobility measured after exposure to light was  $n_s = (1.8 \pm 0.2) \times 10^{11} \text{ cm}^{-2}$  and  $\mu = 0.8 \times 10^5 \text{ cm}^2 \text{ V}^{-1} \text{ s}^{-1}$ , respectively, corresponding to a fractional filling of 0.53 and an effective well width of  $w_{\text{eff}} = \sim 1900$  Å. The Fermi level  $E_F$  determined by  $n^{3D}$  was 2.9 meV.

The sample was cooled to 2 K using a He-vapor-flow optical cryostat, and excited with a dye laser, pumped by an Ar-ion laser. The inelastic light scattering spectra were obtained using a double monochromator, with a cooled GaAs photomultiplier tube, photon-counting electronics, and a computer-controlled data acquisition system. The spectra were obtained in the depolarized backscattering configuration  $z(y', x')\bar{z}$ , with the incident photon energy  $\hbar\omega_i$  (1.89–1.94 eV) near the  $E_0 + \Delta_0$  gap of GaAs. In this configuration the spectra are expected to exhibit electronic single-particle intersubband transitions [7]. We

have neglected corrections for the exchange Coulomb interaction [8], assumed to be small due to the low 3D density of the electron gas. The magnetic-field measurements were made with a superconducting magnet immersed in superfluid He, using the same cryostat.

## 3. Results

Fig. 2a shows a series of inelastic light scattering spectra, taken at 2 K, for excitation energies ranging from 1.927 to 1.936 eV. The focused illumination power density was  $5 \text{ W/cm}^2$  and the instrumental resolution was 0.1 meV. The spectra clearly show two peaks resonant at different excitation energies. Deconvolutions of the double peak structure with Lorentzians show that one peak has an energy shift of  $3.0 \pm 0.3 \text{ meV}$  with a FWHM of  $3.2 \pm 0.4 \text{ meV}$ , which is resonant for excitations near 1.932 eV. The other peak has an energy shift of  $0.85 \pm 0.20 \text{ meV}$  with a FWHM of  $1.0 \pm 0.2 \text{ meV}$ , which is resonant for excitations near 1.930 eV. (The fit with two Lorentzians to one of the curves is shown by triangles in the figure.) The two peaks are spaced apart by an energy of  $2.15 \pm 0.4 \text{ meV}$ . (The upper three curves are seen to be distorted by a broad peak which has an increasing energy shift with increasing excitation energy. In fact, it has a constant peak energy, and is due to the weak luminescence across the  $E_0 + \Delta_0$  gap.) Resonant enhancement curves, showing the excitation energy dependence of the intensities of the two peaks at their maxima, determined from the deconvolution of the double peak structure for the various spectra, are shown in Fig. 2b. These curves show a resonance width (FWHM) for the lower energy shift peak of  $\sim 2.5 \text{ meV}$ , and for the higher energy shift peak of 3.0 meV. The resonant maxima for the two peaks differ by  $2.0 \pm 0.4 \text{ meV}$ , approximately equal to the spacing between the two scattering peaks.

Similar sets of measurements were made on this sample for different angles (from  $0^\circ$  to  $45^\circ$ ) between the incident photon and the normal to the plane of the sample. The peak shifts were independent of this angle, eliminating the possi-

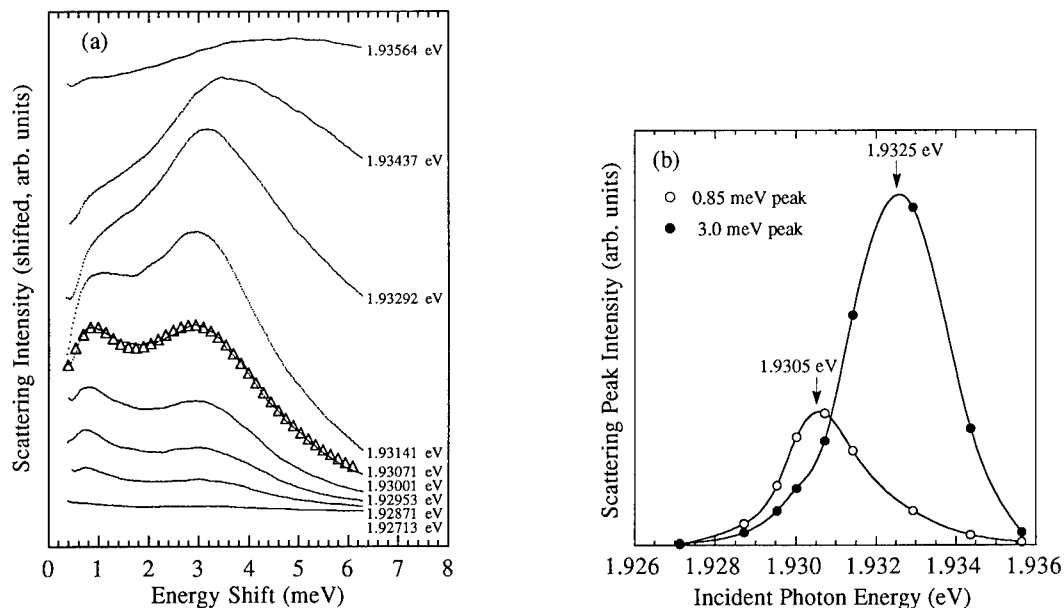


Fig. 2. (a) Light scattering spectra for various excitation energies shown to the right, taken in the  $z(y', x')\bar{z}$  configuration at 2 K. Instrumental resolution is 0.1 meV. All spectra have the same scale factor and the top four are displaced vertically. The figure shows a peak at an energy shift of  $\sim 3.0$  meV, resonant near 1.932 eV and a peak at an energy shift of  $\sim 0.85$  meV, resonant near 1.930 eV. The triangles represent a fit to one of the spectra with two Lorentzians. The broad peak evident in the top two spectra is due to luminescence across the  $E_0 + \Delta_0$  gap. (b) Normalized scattering intensity for the peak maxima of the two light scattering peaks, as a function of incident photon energy. The solid lines are cubic spline fits to the data.

bility of the peaks being associated with plasma oscillations [7]. The peak shifts were also independent of power for power densities ranging from 0.03 to 10 W/cm<sup>2</sup>.

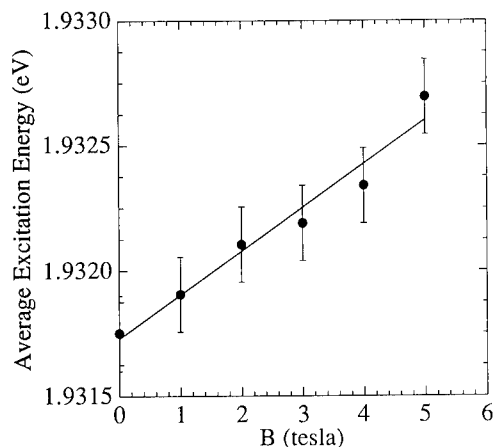


Fig. 3. The average of the resonance maximum excitation energies for the two peaks shown in Fig. 2a, as a function of magnetic field oriented perpendicular to the layers.

The inelastic light scattering peaks were measured as a function of magnetic field  $B_{\perp}$ , oriented perpendicular to the plane of the sample. The peak shifts were independent of  $B_{\perp}$  for fields up to 5 T. The resonance maxima excitation energies, however, increased with field, by the same amount for both peaks. The average of the resonance maximum excitation energies for the two peaks, as a function of  $B_{\perp}$  for 0–5 T, is shown in Fig. 3. The figure shows that the resonance energy increases linearly (within the error bars) with field, by  $\sim 1$  meV for 5 T.

#### 4. Discussion

The  $z(y', x')\bar{z}$  inelastic light scattering spectra shown in Fig. 2a display several noteworthy characteristics: (1) the spectra show peaks with energy shifts near 0.85 and 3.0 meV, which are strongly resonant with excitation energy resonant widths (FWHM) of  $\lesssim 3$  meV; (2) the difference



in energy between the shifts is approximately equal to the energy difference between the peaks of their respective resonance curves; and (3) the widths of the resonance curves are  $\sim E_F \approx 2.9$  meV. These characteristics suggest a model similar to that proposed by Burstein et al. [9] and used by Pinczuk et al. [2] to analyze the inelastic  $z(y', x')\bar{z}$  light scattering spectra of modulation-doped GaAs/Al<sub>x</sub>Ga<sub>1-x</sub>As heterostructure superlattices.

In the scattering mechanism proposed by Burstein et al. [9], for the depolarized backscattering geometry  $z(y', x')\bar{z}$ , the peaks in the inelastic light scattering spectra correspond to single-particle spin-flip transitions from occupied CB subband states below the Fermi level to unoccupied CB subband states above the Fermi level. These transitions can occur if the occupied intermediate states have mixed spins, due, for example, to the spin-orbit interaction, as in the SOB states. For incident and scattered photon wavevectors perpendicular to the heterostructure plane, the transitions must be vertical, i.e. the initial, intermediate, and final states must have the same value for the in-plane wavevector  $k$ . Two such transitions for the remotely doped WPBW structure are illustrated in the  $E$  versus  $k$  diagram in Fig. 1b. Here the initial and final states are in the square-well-level-like subbands of the CB and the intermediate states are in the harmonic-oscillator-level-like subbands of the SOB.

The matrix elements for these spin-flip intersubband transitions for which, as depicted in Fig. 1b, the intermediate state is a SOB subband state, are given by [7,10]

$$M_{if}(k) \propto |\hat{e}_I \times \hat{e}_S| |P_{CB,SOB}|^2 \times \sum_{\nu} \{ \langle \phi_f(z) | e^{ik_I z} | \phi_{\nu}(z) \rangle \times \langle \phi_{\nu}(z) | e^{-ik_S z} | \phi_i(z) \rangle \} \times \{ E(k, \nu) - \hbar\omega_I \}^{-1}. \quad (1)$$

Here  $\hat{e}_I$ ,  $k_I$ , and  $\omega_I$  are the unit polarization vector, wavevector, and frequency of the incident photons;  $\hat{e}_S$  and  $k_S$  are the corresponding quantities for the scattered photons;  $\phi_i(z)$  and  $\phi_f(z)$

are the square-well-like envelope functions of the initial- and final-state CB subbands;  $\phi_{\nu}(z)$  are the harmonic-oscillator-like envelope functions of the intermediate-state SOB subbands;  $k$  is the two-dimensional in-plane wavevector common to all three states;  $P_{CB,SOB}$  is the momentum matrix element between the cell periodic parts of the CB and SOB wavefunctions; and  $E(k, \nu)$  is the resonant energy given by

$$E(k, \nu) = E_G + E_f + E_{\nu} + \hbar^2 k^2 / 2m_e^* + \hbar^2 k^2 / 2m_{so}^*, \quad (2)$$

where  $E_G$  is the  $E_0 + \Delta_0$  gap of bulk Al<sub>x</sub>Ga<sub>1-x</sub>As at the WPBW minimum,  $E_f$  and  $E_{\nu}$  are the  $k = 0$  energies of the final- and intermediate-state subbands measured from the CB and SOB edges of bulk Al<sub>x</sub>Ga<sub>1-x</sub>As at the WPBW minimum, and  $m_e^*$  and  $m_{so}^*$  are the effective masses of the CB and SOB subbands. The sum over  $\nu$  in Eq. (1) is over all intermediate-state subbands. The total scattering intensity resulting from the transitions  $i \rightarrow f$  is proportional to  $|M_{if}(k)|^2$  summed over all  $k$  which correspond to an occupied initial CB subband state and an unoccupied final CB subband state.

In the dipole approximation,  $e^{ik_I z} \approx e^{-ik_S z} \rightarrow 1$ , the selection rules are determined by the product of the envelope-function overlap integrals  $\langle \phi_f(z) | \phi_{\nu}(z) \rangle \langle \phi_{\nu}(z) | \phi_i(z) \rangle$ . Since the remotely doped WPBW structure depicted in Fig. 1a has reflection symmetry about the center of the well, the envelope functions in the matrix element have definite parity, and it is clear that for the matrix element to be non-zero all three states must have the same parity [11]. The envelope functions associated with the lowest subbands of the CB, VB, and SOB all have even parity, and alternate parity for higher subbands as indicated in Fig. 1b. Thus, for example, the lowest-energy-allowed inelastic-scattering intersubband transition is from the first to the third CB subband, CB(1)  $\rightarrow$  CB(3), resonant off the lowest SOB subband, SOB(1), and the next-lowest energy transition from CB(1) is CB(1)  $\rightarrow$  CB(5), as depicted in Fig. 1b. For the assumed square-well-like potentials, the two splittings referred to above have the ratio  $(3^2 - 1^2)/(5^2 - 1^2) = 1/3$ . The transition

energies are independent of  $k$  assuming parabolic subbands and subband-index-independent effective masses, assumptions appropriate for the small  $k$ 's and low-order subbands considered here. Thus, summing over the contributions from all  $k$  obeying the occupancy requirements for the various bands discussed earlier, the two scattering peaks resulting from the two transitions depicted in Fig. 1b should have energy shifts with a ratio 1/3.

We will now use this model to analyze our measurements. We assume an effective well width of  $w_{\text{eff}} \approx 1900 \pm 250$  Å, determined from the measured  $n_s$ , and an average electron effective mass of  $m_e^* = 0.071m_0$ , determined by averaging the Al-concentration-dependent mass over the width of the slab. Then the square-well-like levels are calculated to have splittings of  $E_{\text{CB}(3)} - E_{\text{CB}(1)} = 1.1 \pm 0.2$  meV and  $E_{\text{CB}(5)} - E_{\text{CB}(1)} = 3.4 \pm 0.6$  meV, compared to the measured energy shifts of  $0.85 \pm 0.2$  and  $3.0 \pm 0.3$  meV, respectively. These measured energy shifts for the two peaks have the ratio  $0.85/3.0 \approx 0.28 \pm 0.07$ , consistent within the error bars with the 1/3 ratio expected for square wells. Eqs. (1) and (2) predict that for vertical transitions using the same intermediate state, the peaks of the resonance curves for two different final-state subbands CB(f) and CB(f') should have an energy separation of  $\Delta E \approx (E_{\text{CB}(f')} - E_{\text{CB}(f)})$ . The scattering peaks are separated by  $2.15 \pm 0.4$  meV, which is approximately equal to the separation of the resonance-curve peaks,  $2.0 \pm 0.4$  meV. The resonance-curve widths of 2.5 and 3.0 meV are on the order of the calculated Fermi level  $E_F = 2.9$  meV for this structure, as expected in this model. We have made similar measurements on two other WPBW samples, with sheet densities giving other effective well widths. These samples also show two peaks with peak-shift ratios of  $\sim 1/3$ , and peak-shift magnitudes consistent with effective well widths.

The magnetic field behavior of the spectra can be examined, first ignoring exciton effects, assuming the transitions are between the lowest Landau levels of each of the subbands  $n$ , with field dependence given by  $\frac{1}{2}\hbar\omega_c^n = \frac{1}{2}\hbar(eB_{\perp}/m_n^*c)$ . If the effective mass is the same for each subband,

then the scattering peak shifts should be independent of field, as observed. In this simple model, the resonance energies for the two peaks should increase with field by  $\frac{1}{2}\hbar(eB_{\perp}/\mu c)$ , where  $\mu^{-1} = m_e^{*-1} + m_{\text{so}}^{*-1}$ . For  $m_e^* = 0.067$  and  $m_{\text{so}}^* = 0.154$ , this gives a linear increase of 6 meV for 5 T, a factor of six larger than the measured value of 1 meV (Fig. 3). However, the exciton associated with the SOB to CB intermediate-state transition is expected to have an increasing binding energy with  $B_{\perp}$  [12,13]. Qualitatively, this effect would be expected to counter the increase in resonance energy with  $B_{\perp}$  due to the Landau level effect discussed above, and could account for the smaller increase observed than expected in a simple Landau level model. However, the effects are coupled and a quantitative analysis requires a more sophisticated model.

## 5. Conclusions

Our measurements of the  $z(y', x')\bar{z}$  inelastic light scattering spectra of an n-type remotely doped wide parabolic  $\text{Al}_x\text{Ga}_{1-x}\text{As}$  quantum well have revealed two peaks with energy shifts in the ratio  $\sim 1/3$ , and resonance maxima separated by the energy difference between the peak shifts. Interpreting the peaks in the  $z(y', x')\bar{z}$  spectra as single-particle spin-flip vertical transitions between CB subbands, we have found the observed energy shifts quantitatively consistent with a model for the electron gas in the remotely doped WPBW being distributed as a uniform-density electron slab, with an effective square-well-like potential, giving rise to square-well-like subbands. The  $B_{\perp}$  dependence of the spectra is qualitatively consistent with a simple model for Landau level transitions, but a quantitative accounting for the shift in resonance maximum excitation energies with field requires a more sophisticated model taking into account exciton effects.

## 6. Acknowledgements

The work at Harvard University was supported by the MRL under Contract No. NSF-DMR-89-

20490 and DMR-91-19386. The work at UCSB was supported by the Air Force Office of Scientific Research under Grant No. AFOSR-91-0214.

## 7. References

- [1] G. Abstreiter and K. Ploog, *Phys. Rev. Lett.* 42 (1979) 1308.
- [2] A. Pinczuk, H.L. Störmer, R. Dingle, J.M. Worlock, W. Wiegmann and A.C. Gossard, *Solid State Commun.* 32 (1979) 1001.
- [3] M. Sundaram, A.C. Gossard, J.H. English and R.M. Westervelt, *Superlatt. Microstruct.* 4 (1988) 683.
- [4] T. Sajoto, J. Jo, M. Santos and M. Shayegan, *Appl. Phys. Lett.* 55 (1989) 1430.
- [5] E.G. Gwinn, P.F. Hopkins, A.J. Rimberg, R.M. Westervelt, M. Sundaram and A.C. Gossard, *Phys. Rev. B* 41 (1990) 10700.
- [6] A.J. Rimberg and R.M. Westervelt, *Phys. Rev. B* 40 (1989) 3970.
- [7] See, for example, G. Abstreiter, M. Cardona and A. Pinczuk, in: *Light Scattering in Solids IV*, Eds. M. Cardona and G. Güntherodt (Springer, Berlin, 1984).
- [8] A. Pinczuk, S. Schmitt-Rink, G. Danan, J.P. Valladares, L.N. Pfeiffer and K.W. West, *Phys. Rev. Lett.* 63 (1989) 1633.
- [9] E. Burstein, A. Pinczuk and S. Buchner, in: *Physics of Semiconductors 1978*, Ed. B.L.H. Wilson (The Institute of Physics, London, 1979) p. 1231.
- [10] A. Pinczuk, J.M. Worlock, H.L. Störmer, R. Dingle, W. Wiegmann and A.C. Gossard, *Surf. Sci.* 98 (1980) 126.
- [11] We note that in modulation-doped superlattices Pinczuk et al. (A. Pinczuk, J.M. Worlock, H.L. Störmer, A.C. Gossard and W. Wiegmann, *J. Vac. Sci. Technol.* 19 (1981) 561) observed inelastic light scattering peaks which they ascribe to spin-flip transitions between states of opposite parity, e.g. CB(1)  $\rightarrow$  CB(2). These were not apparent in our spectra and appear to violate the selection rules stated here [7]. However, these selection rules break down if the system does not have perfect reflection symmetry, so it is possible that the apparent “parity violating” transitions in the spectra of Pinczuk et al. are due to unintended asymmetries in the superlattice structure due to the inherent asymmetry of the growth process. The slowly varying average potential of the WPBW may be better able to preserve the reflection symmetry in the presence of symmetry breaking growth processes.
- [12] J.C. Maan, in: *Physics and Applications of Quantum Wells and Superlattices*, Eds. E.E. Mendez and K. von Klitzing (Plenum, New York, 1988).
- [13] A.B. Henriques, E.T.R. Chidley, R.J. Nicholas, P. Dawson, and C.T. Foxon, *Phys. Rev. B* 46 (1992) 4047.

## Spectroscopy of quasi-2D $D^-$ ions in the presence of excess electrons

W.J. Li <sup>\*,a</sup>, J.L. Wang <sup>a</sup>, B.D. McCombe <sup>a</sup>, J.-P. Cheng <sup>b</sup>, W. Schaff <sup>c</sup>

<sup>a</sup> SUNY at Buffalo, Buffalo, NY 14260, USA

<sup>b</sup> Francis Bitter National Magnet Laboratory, MIT, Cambridge, MA 02139, USA

<sup>c</sup> Cornell University, Ithaca, NY 14853, USA

(Received 21 April 1993; accepted for publication 14 June 1993)

### Abstract

Far infrared magneto-spectroscopic studies of quasi-2D  $D^-$  ions have been carried out in several GaAs/ $Al_{0.3}Ga_{0.7}As$  MQW samples with a wide range of controlled doping in the barrier with constant sheet doping in the well. Temperature, carrier density dependence, and polarization studies of a new confinement-related feature on the low frequency side of cyclotron resonance indicate that this feature is likely due to a  $D^-$  triplet transition. The temperature dependence of the relative absorption strength of  $D^-$ ,  $D^0$  and CR were also studied and found to be in qualitative agreement with a calculation that includes the probability of both single and double occupancy (the  $D^-$  states) of a particular donor site in thermal equilibrium in high magnetic field.

A  $D^-$  ion in semiconductors is a negatively-charged ion formed by a shallow impurity donor binding two indistinguishable electrons. The energy spectrum of such a system, the simplest “many-electron system”, provides information about electron–electron correlations in semiconductors.  $D^-$  ions can be created in many-valley bulk semiconductors (Si and Ge) in which one of the valleys is lower in energy due to externally applied stress so that two electrons of a  $D^-$  occupy the same valley [1–5].  $D^-$  ions can also be created metastably in direct gap semiconductors by continuous optical excitation [6]. In recent

years, considerable theoretical and experimental effort has been focused on  $D^-$  ions in quasi-two-dimensional structures [7–14]. Unlike bulk semiconductors, in appropriately doped quantum-well structures such ions can be created and can exist metastably in the absence of optical excitation at low temperatures for very long times, as shown by recent experimental studies [7,8]. Quantum confinement and magnetic field dramatically increase the binding energy of  $D^-$  ions, and in such systems electron–electron correlations can be studied over a range of high magnetic fields that is not achievable in atomic  $H^-$  systems. In addition, due to the lack of continuum states along the confinement/magnetic field axis in quasi-2D structures the optical transitions are much sharper than in 3D.

\* Corresponding author.

In previous far-infrared magneto-optical measurements, the evolution of the electron occupancy process from one-electron ( $D^0$ ) and two-electron ( $D^-$ ) bound impurity states to free-electron Landau states was studied for Si donors confined in GaAs quantum wells [8]. In heavily barrier doped samples ( $N_B > N_w$ , where  $N_B$  and  $N_w$  refer to barrier and well sheet donor densities, respectively) an unexpected increase in the “ $D^-$ ” singlet ( $1S-2P$  ( $M = +1$ )) transition energy with increasing density of excess electrons, and discontinuities in the slope of the magnetic field dependence of this “ $D^-$ ” transition at integer Landau level filling factors, have also been observed [9]. These results have shown the importance of many-electron effects on the  $D^-$  transitions.

A fundamental aspect of  $D^-$  ions confined in QWs at high field is the existence of bound triplet states and associated optical transitions. It is well known from variational calculations [12,15,16] that only one bound state, the singlet state, exists at zero magnetic field. In the presence of a magnetic field, the singlet state becomes deeper and the low-lying triplet states become bound. From the calculation of the infrared absorption spectrum for strictly 2D  $D^-$  centers in the strong magnetic field limit, MacDonald has shown that in addition to the singlet-state transitions, two triplet-state transitions are allowed [13]. In this limit, one of these transitions coincides in energy with the  $\Delta M = +1$  singlet transition, whereas the other lies below the cyclotron resonance (CR) energy.

In this paper, we present detailed studies of a new spectral feature not previously reported. This feature exhibits quasi-2D behavior and appears on the low frequency side of cyclotron resonance with approximately the same magnetic field dependence as CR. We have also extended our earlier studies to include the temperature dependence of the various spectroscopic features ( $D^0$ ,  $D^-$ , and CR) over a wide range of excess electron densities. The observed absorption profiles of  $D^-$ ,  $D^0$ , and CR at several temperatures have been fitted with Lorentzian lineshapes to extract the integrated intensities, which are proportional to the occupancy of the various states. Results

are compared with a calculation that includes the probability of both single and double occupancy of a particular donor site in thermal equilibrium in high magnetic field.

Samples were MBE-grown multiple-quantum-well (MQW) structures (20 periods). The nominal well/barrier width is 200 Å/600 Å. Silicon donors were  $\delta$ -doped at the centers of the wells and the barriers. The doping concentration in the wells,  $2 \times 10^{10} \text{ cm}^{-2}$ , was kept the same for all samples, while the doping concentrations in the barriers are  $2 \times 10^{10}$ ,  $3.5 \times 10^{10}$ ,  $4.0 \times 10^{10}$ , and  $1.5 \times 10^{11} \text{ cm}^{-2}$ , for samples 1 to 4, respectively. Far infrared magneto-transmission experiments were carried out with Fourier transform spectrometers and a 9 T superconducting magnet. The sample temperature varied from 4.2 to 50 K. Samples were tilted away from the field direction in order to separate the quasi-2D  $D^-$  feature from the bulk  $D^0$  ( $1s-2p_+$ ) transition since these two features are only  $2-3 \text{ cm}^{-1}$  apart when the sample is not tilted. The spectra were taken after cross-bandgap illumination from an in-situ light-emitting-diode to remove electrons from the traps in the barriers and to introduce them into the  $D^0$  and  $D^-$  sites in the wells [8].

Temperature dependence of transmission spectra for sample 2 is shown in Fig. 1. Strong absorption lines from CR and  $D^-$  singlet transition are seen at low temperature. At 11 K, a new feature (labeled A) appears at  $94 \text{ cm}^{-1}$ ,  $13 \text{ cm}^{-1}$  below CR. While the  $D^-$  line diminishes rapidly with increasing temperature, feature A grows with temperature up to  $\sim 20 \text{ K}$ . Above 20 K, feature A decreases in strength. This behavior is suggestive of a population process in which electrons are thermally excited to a higher bound state. This bound state is approximately 1.7–2.2 meV (20–25 K) higher than the singlet ground state. The magnetic field dependence of feature A, similar in slope to CR, is indicated in the insert in Fig. 1.

The circular polarization selection rule was studied for transition A at  $118.8 \mu\text{m}$  ( $84 \text{ cm}^{-1}$ ) with a FIR laser and a circular polarizer placed in front of the sample. From measurement of the electron CR transition, it was determined that the laser beam after the polarizer was 90% circu-

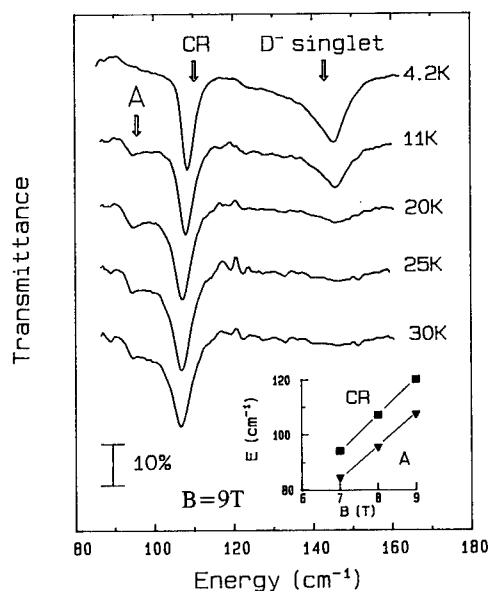


Fig. 1. Transmission spectra of sample 2 ( $N_B = 3.5 \times 10^{10} \text{ cm}^{-2}$ ) at several temperatures. The sample was tilted  $27^\circ$  away from the field direction. Feature A exhibits two-dimensional behavior and is  $13 \text{ cm}^{-1}$  below the peak of CR transition. Field dependence of A and CR are indicated in the insert (this set of data was taken without tilting the sample).

larly polarized. Results show that feature A has the same selection rule as the electron CR-active sense of circular polarization.

When the barrier doping concentration is  $\geq 8 \times 10^{10} \text{ cm}^{-2}$ , feature A is observed even at  $4.2 \text{ K}$  (Fig. 2). The strength of this line decreases rapidly with increasing temperature. This again suggests that feature A is a bound-state transition.

Theoretical calculations [12,13] show that there are four bound states associated with the lowest Landau level (one singlet and three triplet states) for 2D  $D^-$  ions at high magnetic field. The singlet bound state has a total azimuthal angular momentum quantum number  $M=0$ ; the triplet bound states have total azimuthal angular momentum  $M=-1, -2$ , and  $-3$ . We denote the single-particle states by Landau quantum number  $l$  and azimuthal angular momentum  $m$  for electron 1 and 2 as  $(l_1 m_1, l_2 m_2)$ . The total angular momentum is  $M=m_1+m_2$ . The singlet and triplet  $D^-$  states are the symmetric and antisymmetric spatial combinations of the two single-particle states, respectively. The transition selection

rule for radiation with electron CR active sense of polarization is  $\Delta M = +1$ . Thus an electron in the singlet ground state  $M=0$  can make a transition only to the  $M=1$  singlet state. In the single particle notation, the initial state of this transition is  $(00, 00)$  and the final state is  $(00, 11)$ . An electron in the triplet  $M=-1$  ground state can make a transition only to the  $M=0$  excited triplet state. The initial state of this transition is  $(00, 0-1)$ , and there are two possible final states:  $(00, 10)$  and  $(11, 0-1)$ . Since electrons with higher angular momenta are less likely to bind in the Coulomb potential, the  $(11, 0-1)$  state is expected to have higher energy than the  $(00, 10)$  state. Analytical results for the strictly 2D, high field limit [13] show that the singlet transition  $(00, 00) \rightarrow (00, 11)$  occurs at energy  $\hbar\omega_c + \epsilon_0(0)/2$ , where  $\hbar\omega_c$  is the cyclotron resonance energy, and  $\epsilon_0(0)$  is the magnetic field dependent binding energy of a neutral  $D^0$  impurity. The triplet transition  $(00, 0-1) \rightarrow (00, 10)$  occurs at  $\hbar\omega_c - \epsilon_0(0)/4$ , and  $(00, 1-1) \rightarrow (11, 0-1)$  occurs at  $\hbar\omega_c + \epsilon_0(0)/2$ . Note that the singlet transition  $(00, 00) \rightarrow (00, 11)$  and the triplet transition  $(00, 1-1) \rightarrow (11, 0-1)$  have exactly the same energy.

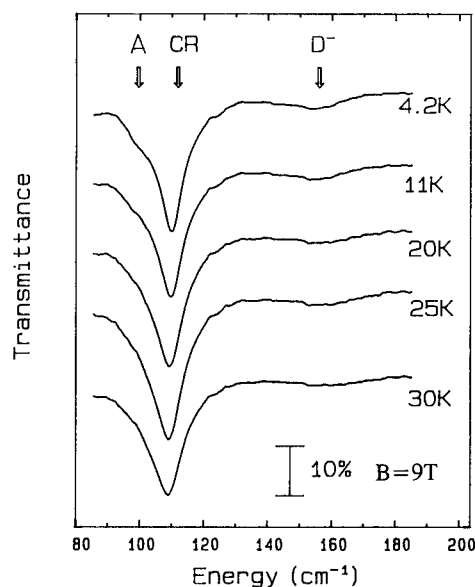


Fig. 2. Temperature dependence of transmission spectra of sample 4 ( $N_B = 1.5 \times 10^{11} \text{ cm}^{-2}$ ). Feature A is only observed at low temperatures.

This energy is also the  $1s-2p^+$  transition energy of a 2D  $D^0$  [17]. Thus in the limit of infinite magnetic field the Coulomb correlations are not optically detectable, as expected from Kohn's theorem [18]. At finite (lower) magnetic field the mixing between different Landau levels by the Coulomb potential reduces the transition energy, thus the  $D^-$  singlet transition takes place with an energy between CR and the  $D^0$  transition, as has been observed in the experiments.

The energy difference between the lowest singlet state  $(00, 00)$  and the lowest triplet state  $(00, 0-1)$  is  $\Delta E = 0.1464\epsilon_0(0)$  [13]. For a 200 Å quantum well at 8 T,  $\epsilon_0(0)$  is approximately 15 meV [19], thus assuming all energies can be scaled by  $\epsilon_0(0)$  as the system deviates from strictly 2D behavior,  $\Delta E \approx 2.2$  meV. This energy is consistent with that estimated from the temperature dependence of the feature A. This result, combined with the quasi-2D nature, the bound state behavior, and the polarization selection rule, are consistent with feature A being the triplet transition  $(00, 0-1) \rightarrow (00, 10)$ . The other triplet transition, as has been shown from the calculation, occurs at an energy close to the singlet transition, and the two features may not be resolvable. For large excess barrier doping densities in which feature A is seen only at low temperature, it is not clear why the  $D^-$  triplet ground state should be favored in a many-electron environment. One possibility is that screening by excess electrons is more effective for the Coulomb repulsion of the triplet electrons (further apart on average than the singlet electrons) than the singlet electrons, leading to a deeper triplet ground state. More detailed theoretical analysis is required to address this point.

Another important aspect of  $D^-$  ions is the statistical population of two electrons in various impurity states in thermal equilibrium. We have studied the evolution of the relative change of absorption strength for  $D^-$ ,  $D^0$ , and CR transition as a function of temperature. Fig. 3 displays the spectra taken from sample 1. Three features of interest are simultaneously observed. Bulk CR ( $125 \text{ cm}^{-1}$ ) and the bulk related donor  $1s-2p^+$  transition ( $159 \text{ cm}^{-1}$ ) from the substrate are also present. To extract information about the num-

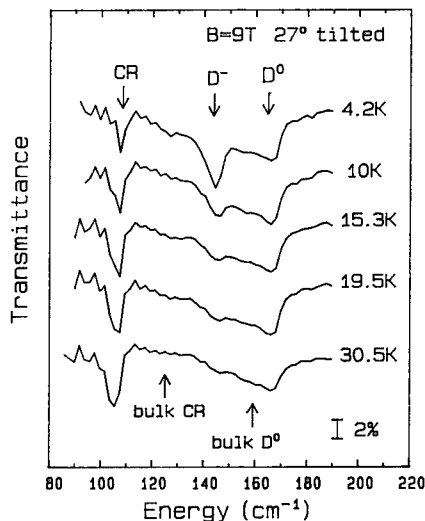


Fig. 3. The evolution of transition intensities of CR,  $D^-$  and  $D^0$  as a function of temperature. Data taken from sample 1 ( $N_B = 2 \times 10^{10} \text{ cm}^{-2}$ ).

ber of carriers, five Lorentzian lines were used to fit the absorption profiles. The area of the individual Lorentzian lineshape is proportional to the carrier density,  $N(T)$ , at temperature  $T$ , and the oscillator strength,  $f$ , of the corresponding transition. Since the oscillator strengths of  $D^-$  and  $D^0$  in a magnetic field are not known, the area of each absorption profile ( $\propto f \cdot N(T)$ ) is ratioed to the corresponding area at 4.2 K ( $\propto f \cdot N(4.2 \text{ K})$ ). Since  $f$  is not a function of temperature, the ratio gives the relative density at  $T$  with respect to the density at 4.2 K.  $N(T)/N(4.2 \text{ K})$  versus temperature is plotted in Fig. 4. It can be seen that the initial increase in temperature depopulates the  $D^-$  state rapidly, and at the same time populates *both* Landau states and  $D^0$  states. This indicates that one of the electrons of a  $D^-$  impurity is thermally promoted to the conduction band, and at the same time a neutral  $D^0$  impurity is created. At higher temperature the electron that is left behind in a  $D^0$  site becomes free. As a result, we see a decrease in  $D^0$  and an increase in CR when the temperature exceeds 15 K.

We have performed a simple statistical calculation in which a donor impurity was modeled as having only three possible states: no occupancy, single occupancy, and double occupancy. Excited

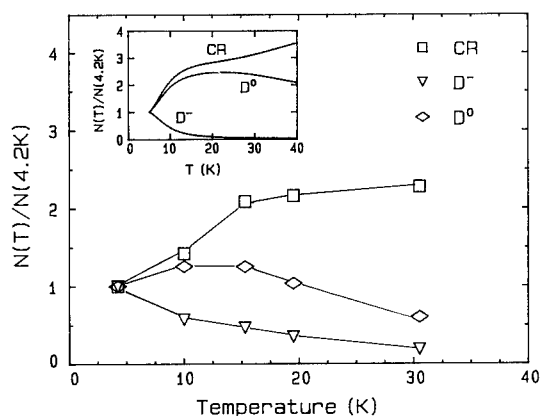


Fig. 4. The relative occupancy of  $D^-$  ions,  $D^0$  neutral donors and free electrons in the Landau levels as a function of temperature. Solid lines are a guide to the eye. Results from a statistical calculation are shown in the insert.

states were not taken into account. The number density of these states was solved numerically from the equation of conservation of total number of electrons, with the measured free electron density  $3 \times 10^9 \text{ cm}^{-2}$ , and neutral donor density  $3.8 \times 10^9 \text{ cm}^{-2}$  at 4.2 K. The total carrier concentration is  $1.5 \times 10^{10} \text{ cm}^{-2}$ . The  $D^0$  binding energy is 15 meV [19] and  $D^-$  binding energy is 4 meV [10] at 8 T. It was assumed that 90% of the electrons were transferred from the barrier into the well. Results (insert of Fig. 4) are in qualitative agreement with the measurements.

In summary, we have carried out detailed magneto-spectroscopic studies of a new feature in well center and barrier center-doped MQWs. The properties of the new feature are consistent with the triplet transition of  $D^-$  centers [13]. The relative occupancy of  $D^-$  and  $D^0$  impurity states, and Landau levels as a function of temperature

has demonstrated the process of creating both free electrons and  $D^0$  impurities from  $D^-$  ions.

This work was supported by the ONR under grant No. N00014-89-J-1673, and ONR/SDIO under the Medical Free Electron Laser programs grant No. N00014-91-J-1939.

## 1. References

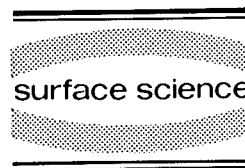
- [1] S. Narita and M. Taniguchi, Phys. Rev. Lett. 36 (1976) 913.
- [2] M. Taniguchi and S. Narita, J. Phys. Soc. Jpn. 43 (1976) 1262.
- [3] D.D. Thornton and A. Hoing, Phys. Rev. Lett. 30 (1973) 909.
- [4] M. Taniguchi, M. Hirano and S. Narita, Phys. Rev. Lett. 35 (1975) 1095.
- [5] P. Norton, J. Appl. Phys. 47 (1976) 308.
- [6] C.J. Armistead, S.P. Najda, R.A. Stradling and J.C. Mann, Solid State Commun. 53 (1985) 1109.
- [7] A. Mandray, S. Huant and B. Etienne, Europhys. Lett. 24 (1992) 181.
- [8] S. Holmes, J.-P. Cheng, B.D. McCombe and W. Schaff, Phys. Rev. Lett. 69 (1992) 2571.
- [9] J.-P. Cheng, Y.J. Wang, B.D. McCombe and W. Schaff, Phys. Rev. Lett. 70 (1993) 489.
- [10] T. Pang and S.G. Louie, Phys. Rev. Lett. 65 (1991) 1635.
- [11] D.E. Phelps and K.K. Bajaj, Phys. Rev. B 26 (1982) 912.
- [12] D.M. Larsen and S.Y. McCann, Phys. Rev. B 45 (1992) 3485.
- [13] A.H. MacDonald, Solid State Commun. 84 (1992) 109.
- [14] E.R. Mueller, D.M. Larsen, J. Waldman and W.D. Goodhue, Phys. Rev. Lett. 68 (1992) 2204.
- [15] A. Natori and H. Kamimura, J. Phys. Soc. Jpn. 44 (1977) 1216.
- [16] D.M. Larsen, Phys. Rev. B 20 (1979) 5217.
- [17] A.H. MacDonald and D.S. Richie, Phys. Rev. B 33 (1986) 8336.
- [18] W. Kohn, Phys. Rev. 123 (1961) 1242.
- [19] R.L. Greene and K.K. Bajaj, Phys. Rev. B 31 (1985) 913.





ELSEVIER

Surface Science 305 (1994) 220–224



## Transition energies of $D^-$ centers in a superlattice

J.M. Shi <sup>\*</sup>, F.M. Peeters, J.T. Devreese <sup>1</sup>

*Departement Natuurkunde, Universiteit Antwerpen (UIA), Universiteitsplein 1, B-2610 Antwerpen, Belgium*

(Received 6 May 1993; accepted for publication 24 June 1993)

### Abstract

We study a negative-donor center ( $D^-$ ) in a GaAs/AlGaAs superlattice in high magnetic fields along the growth axis. The energy levels of the  $D^-$  states are calculated by a variational approach using a trial wave function which (1) includes electron–electron (e–e) correlation for the superlattice case, (2) with, and (3) without e–e correlation for the situation of a quantum well (QW). Polaron effects are included within second-order perturbation theory. A detailed comparison is made of the calculated transition and binding energies with the measured data of Huan et al. [4]. We found that these experimental results should be interpreted as the transition energy between two  $D^-$  states.

### 1. Introduction

Shallow donors ( $D^0$ ) in semiconductors have been the subject of considerable investigation in recent years [1]. In analogy with  $H^-$  ions [2], these donors can bind an extra electron to form negative ions, which are referred to as  $D^-$  centers, and which have been observed in bulk GaAs [3] and in GaAs superlattices [4–7]. These experiments have motivated many theoretical studies [8–13].

Using a Monte Carlo approach, Pang and Louie [8] have studied the ground state of the  $D^-$  center in a QW. In Refs. [9–12] the variational method was applied to calculate the ground state and the lowest excited states. Although there have been a great many theoretical studies of the  $D^-$  center, until now we are unaware of any

calculation of the  $D^-$  states in a *superlattice*. At present all experiments on the  $D^-$  center in a quasi-two-dimensional system are done in multi-quantum wells and superlattices. Polaron effects on the  $D^-$  center in QWs have been discussed in Refs. [11,12]. Here we found that these calculations underestimated these effects systematically.

In this paper, we report on a study of the  $D^-$  center in a GaAs superlattice. The binding and transition energies of the  $D^-$  center are obtained as a function of the magnetic field. To obtain the unperturbed  $D^-$  energies a variational approach is used in Section 2, where we compare the results from three different wave functions. Polaron corrections are calculated within second-order perturbation theory in Section 3 based on an extension of the method given by Platzman [14] for a bound polaron. In Section 4 a detailed comparison of our results is made with the experimental data of Ref. [4]; we found that they should be interpreted as being the transition energy between two  $D^-$  states.

<sup>\*</sup> Corresponding author.

<sup>1</sup> Also at: RUCA and TUE, Eindhoven, The Netherlands.

## 2. Variational calculation

In the effective-mass approximation and in the absence of electron–phonon interaction, a  $D^-$  center at the well center of  $\text{GaAs}/\text{Al}_x\text{Ga}_{1-x}\text{As}$  superlattice in a magnetic field along the growth axis (the  $z$  axis) is described by the Hamiltonian

$$H_{e,e}(\mathbf{r}_1, \mathbf{r}_2) = H_e(\mathbf{r}_1) + H_e(\mathbf{r}_2) + \frac{2}{r_{12}}, \quad (1)$$

where  $H_e(\mathbf{r}_j)$  is the shallow donor Hamiltonian for the  $j$ th electron given by

$$H_e(\mathbf{r}_j) = -\frac{m_w}{m_e^*(z_j)} \left( \nabla_j^2 + i\gamma \frac{\partial}{\partial \phi_j} - \frac{1}{4} \gamma^2 \rho_j^2 \right) - \frac{2}{r_j} + V(z_j), \quad (2)$$

and the superlattice potential is modelled by a square-well potential

$$V(z_j) = \begin{cases} 0, & |z_j| < w/2, \\ V_0, & w/2 < z_j < w/2 + b, \end{cases} \quad (3)$$

which is periodically repeated (i.e.,  $V(z) = V[z + n(w+b)]$ ) with  $w$  the well width,  $b$  the barrier width,  $n$  an integer and  $V_0$  the barrier height given by 60% of the energy-gap difference between the two semiconductors. Here we have used cylindrical coordinates  $(\rho, \phi, z)$  whose origin is at the well center. The effective Bohr radius in GaAs  $a_0^* = \hbar^2 \epsilon_0 / m_w e^2 = 98.7 \text{ \AA}$  is taken as the unit of length, the effective Rydberg  $R^* = e^2 / 2 \epsilon_0 a_0^* = 5.83 \text{ meV}$  as the unit of energy, and  $\gamma = \hbar \omega_c / 2 R^*$  ( $\omega_c$  the electron cyclotron frequency) as the unit of the magnetic field.  $m_e^*(z)$  is the electron effective mass: in the GaAs wells  $m_w/m_e = 0.067$ ; in the  $\text{Al}_x\text{Ga}_{1-x}\text{As}$  barriers  $m_b/m_e = 0.067 + 0.083x$ .  $\epsilon_0 = 12.5$  is the static dielectric constant of GaAs, which is assumed to be the same in both materials. The position of the  $j$ th electron is indicated by  $\mathbf{r}_j = (\rho_j^2 + z_j^2)^{1/2}$ ,  $\rho_j = (x_j^2 + y_j^2)^{1/2}$  being the distance in the  $x$ – $y$  plane, and  $r_{12}$  is the distance between the two electrons.

The Schrödinger equation with the Hamiltonian  $H_{e,e}(\mathbf{r}_1, \mathbf{r}_2)$  cannot be solved exactly; we relied on a variational approach to calculate the

energy levels and wave functions of the  $D^-$  center. The following Chandrasekhar-type variational functions are used for the  $D^-$  states

$$\Psi_{i,j}(\mathbf{r}_1, \mathbf{r}_2) = [\psi_i(\mathbf{r}_1)\psi_j(\mathbf{r}_2) + \psi_j(\mathbf{r}_1)\psi_i(\mathbf{r}_2)] \times [1 + \mu(z_1 - z_2)^2 + \nu(\rho_1 - \rho_2)^2], \quad (4)$$

where in the present work we take the inner orbitals  $\psi_i$  always of a similar form as that of the donor ground state, and the outer orbitals  $\psi_j$  vary depending on the states: for the ground state it is of the same form as  $\psi_i$ , and for the lowest symmetric state it is like that of the donor  $2p^-$  state. We study this excited state which has the same spin configuration as the ground state since the spin configuration cannot be changed in an optical experiment.  $\psi_i$  ( $\psi_j$ ) is taken to be  $\rho^{|m|} f(z) \exp(im\phi - \xi\rho^2 - \eta z^2)$  with  $f(z)$  the wave function of the lowest-energy ( $E_{z,1}$ ) solution of the superlattice. The terms  $(z_1 - z_2)^2$  and  $(\rho_1 - \rho_2)^2$  in Eq. (4) describe e–e correlation in the  $D^-$  center. Thus, there are six variational parameters ( $\xi_i, \eta_i, \xi_j, \eta_j, \mu, \nu$ ) in  $\Psi_{i,j}$  which minimize the energies of the  $D^-$  states

$$E_{i,j}^0 = \frac{\langle \Psi_{i,j}(\mathbf{r}_1, \mathbf{r}_2) | H_{e,e}(\mathbf{r}_1, \mathbf{r}_2) | \Psi_{i,j}(\mathbf{r}_1, \mathbf{r}_2) \rangle}{\langle \Psi_{i,j}(\mathbf{r}_1, \mathbf{r}_2) | \Psi_{i,j}(\mathbf{r}_1, \mathbf{r}_2) \rangle}. \quad (5)$$

In Fig. 1 we present the binding energies of the two  $D^-$  states ( $\Psi_{1s,1s}, \Psi_{1s,2p^-}$ ) as a function of the magnetic field in a superlattice with the following material parameters:  $x = 0.25$ , and  $w = b = 100 \text{ \AA}$  (solid curves). These are compared to the corresponding results in an  $x = 0.25$ ,  $w = 100 \text{ \AA}$  QW for the wave functions with (dashed curves) and without (dotted curves,  $\mu = \nu = 0$ ) e–e correlation terms. Notice that: (1) the binding energies of these two states are defined by

$$E_{i,j}^{\text{binding}} = E_{1s}^0(D^0) + E_{z,1} + \frac{1}{2} \hbar \omega_c - E_{i,j}^0, \quad (6)$$

with  $E_{1s}^0(D^0)$  the energy of the  $D^0$  ground state [15]; (2) the binding energy of  $|1s, 1s\rangle$  is an increasing function of the magnetic field and this state is always bound, while the excited state is not bound and has an opposite  $B$ -dependence, which is consistent with the conclusion of Ref.

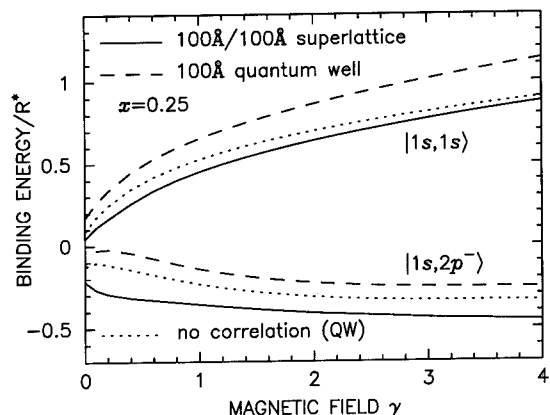


Fig. 1. Binding energies (in units of  $R^*$ ) of the  $|1s, 1s\rangle$  and  $|1s, 2p^-\rangle$  states of the  $D^-$  center at the well center of a GaAs/ $\text{Al}_{0.25}\text{Ga}_{0.75}\text{As}$  superlattice with  $w = b = 100 \text{ \AA}$  (solid curves) versus magnetic field  $\gamma$ . The corresponding results from the wave functions with (dashed curves) and without (dotted curves) e-e correlation terms in the QW are also plotted.

[13] for the 2D case; (3) the binding energy in the superlattice case is appreciably decreased as compared to that of the QW; (4) e-e correlation becomes more important with increasing magnetic field strength. This is a result of the fact that the magnetic field forces the electrons closer to the Si-donor and consequently closer to each other; and (5) a small difference of the binding energies of the  $D^-$  ground state in the QW between the present paper and Ref. [11] for the case of the variational function without e-e correlation is due to the fact that different variational functions were used: a Gaussian function in the present case, and a Gaussian plus exponential one in Ref. [11].

### 3. Polaron correction

For superlattices with not too narrow wells it is a good approximation to include only GaAs bulk-phonon modes in the calculation [15,16]. Therefore, the electron-phonon interaction for a  $D^-$  center in our system can be described by the Fröhlich Hamiltonian

$$H_1(\mathbf{r}_1, \mathbf{r}_2) = \sum_q [V_q b_q (e^{iq \cdot \mathbf{r}_1} + e^{iq \cdot \mathbf{r}_2}) + \text{h.c.}], \quad (7)$$

where  $b_q$ , ( $b_q^\dagger$ ) is the annihilation (creation) operator of a LO phonon with momentum  $\hbar q$  and energy  $\hbar\omega_q$ , and  $|V_q|^2 = 4\pi\alpha(\hbar\omega_{\text{LO}})^{3/2}/q^2\Omega$  with  $\Omega$  the volume. For GaAs we take  $\hbar\omega_q = \hbar\omega_{\text{LO}} = 36.25 \text{ meV}$ , and the electron-phonon coupling constant  $\alpha = 0.068$ .

Because GaAs is a weak polar material, we can use second-order perturbation theory to calculate the polaron correction to the energy of the  $|i, j\rangle$  state of the  $D^-$  center:

$$\Delta E_{i,j} = - \sum_{(i',j')} \sum_q \frac{|\langle i', j'; q | H_1(\mathbf{r}_1, \mathbf{r}_2) | i, j; 0 \rangle|^2}{\hbar\omega_{\text{LO}} + E_{i',j'}^0 - E_{i,j}^0}. \quad (8)$$

In principle we should include all the  $D^-$  ( $|i', j'\rangle$ ) states in Eq. (8) which is a formidable task. Nevertheless, it turns out to be possible to evaluate Eq. (8) approximately in such a way that one needs to know only a few relevant states [14,17].

Using the method of Ref. [14] one can rewrite Eq. (8) into three terms: the first is the leading term ( $-4\alpha\hbar\omega_{\text{LO}}$ ) which is the value of a bipolaron state in the absence of any field, the second becomes zero in the approximation of  $m_w = m_b$ , and the third contains a sum over all the  $D^-$  states. The last term can be approximated by an upper and a lower bound. As a consequence we are able to obtain the minimum and maximum polaron correction to the energy of the ground state and, thus, also the maximum polaron shift to the transition energy between the two  $D^-$  states in the non-resonant region. Notice that in Refs. [11,12] only a finite number of states were included in the sum  $\sum_{(i',j')}$ , which turns out to underestimate the polaron effects considerably.

### 4. Comparison with experiments and conclusions

We now compare our results with the experimental data. In Fig. 2 the solid dots are the measured values which are referred to as being the *binding* energies of the ground state of a  $D^-$  center in an  $x = 0.25$ ,  $w = b = 100 \text{ \AA}$  superlattice

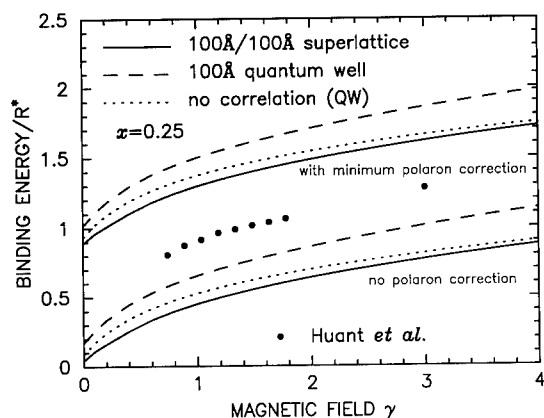


Fig. 2. Binding energy of the  $D^-$  ground state in an  $x = 0.25$ ,  $w = b = 100$  Å superlattice (solid curves) with (in the upper group) and without (in the lower group) polaron correction within the leading term approximation compared to the experimental data (solid dots) in Ref. [4]. The corresponding results from the wave functions with (dashed curves) and without (dotted curves) correlation terms are also depicted for the QW case.

by Huant et al. [4]. The calculated results without polaron effect (the lower group of curves) are much lower than these data, especially for the superlattice case (solid curve). The computer simulations of Ref. [8] for the QW were closer to the experimental results but no polaron effect was included.

In order to correctly describe the polaron correction to the binding energy of the  $D^-$  center one has to study the polaron effects on three different systems: (1) the  $D^-$  center [11,12]; (2) the  $D^0$  donor [15]; and (3) the free electron [18,19]. Within the leading-term approximation we can obtain the minimum polaron shift,  $-2\alpha\hbar\omega_{LO}$ , to the binding energy of the  $D^-$  ground state since it is known that the polaron energy shift to a bipolaron at  $B = 0$  is proportional to  $-4\alpha\hbar\omega_{LO}$ , while to the single donor state and the free electron it is each time proportional to  $-\alpha\hbar\omega_{LO}$ . The theoretical results with this correction are given in Fig. 2 by the upper group of curves. Notice that: (1) the polaron correction increases greatly the binding energy, therefore it is very important to the formation of

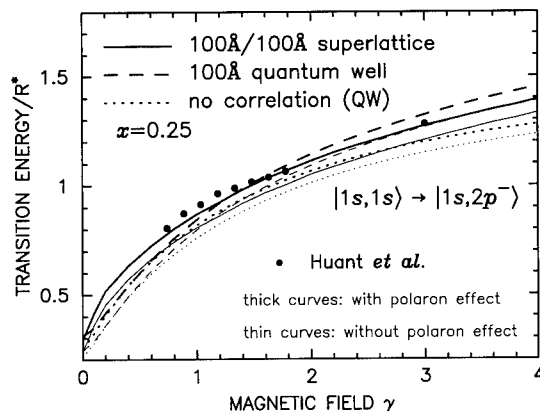


Fig. 3. Transition energy of  $|1s, 1s\rangle \rightarrow |1s, 2p^- \rangle$  as function of magnetic field in an  $x = 0.25$ ,  $w = b = 100$  Å superlattice with (thick) and without (thin solid curve) polaron correction compared to the experimental data (solid dots) in Ref. [4]. The corresponding results from the wave functions with (dashed curves) and without (dotted curves) correlation terms are also plotted for the QW case.

the  $D^-$  center; and (2) the experimental results are not explained as the binding energy of the  $D^-$  center.

In Fig. 3 we plot the transition energy for  $|1s, 1s\rangle \rightarrow |1s, 2p^- \rangle$  with (thick) and without (thin

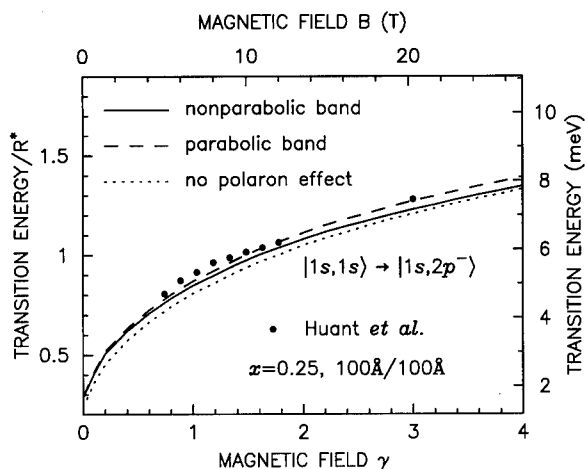


Fig. 4. Transition energy of  $|1s, 1s\rangle \rightarrow |1s, 2p^- \rangle$  as function of magnetic field in an  $x = 0.25$ ,  $w = b = 100$  Å superlattice. The dotted curve is in the absence of any correction, the dashed curve with polaron effect, and the solid curve with the effects of polaron and band non-parabolicity. The solid dots are the experimental results from Ref. [4].

curves) polaron correction and compare them with the previous experimental data. Notice that: (i) a very good agreement is found, especially for the superlattice case; (ii) a small polaron correction is obtained due to the fact that the leading term of the polaron corrections to the energy levels of the  $D^-$  states cancel each other, and (iii) the e–e correlation is particularly important in the high magnetic field region.

Finally we discuss the effect of band non-parabolicity on the transition energy of the  $D^-$  center by using the standard Kane model [17], which is given by  $E_{np} = E_g[-1 + (1 + 2E_p/E_g)^{1/2}]$ , where  $E_{np}$  and  $E_p$  are the  $D^-$  center energies with and without the effect of band non-parabolicity, respectively, and  $E_g = 1520$  meV is the energy gap of GaAs. Here we have taken half of the  $D^-$  energy as the energy of the single electron. The results are plotted in Fig. 4 by the solid curve which shows that this effect on the transition energy is very small which is a consequence of the fact that the energy difference of these two states is small.

## 5. Acknowledgements

One of us (F.M.P.) is supported by the Belgium National Science Foundation. This work is sponsored by Fonds voor Kollektief Fundamenteel Onderzoek, Belgium project No. 2.0093.91, “Diensten voor the Programmatie van het Wetenschapsbeleid”, Belgium, under Contract No. IT/SC/24.

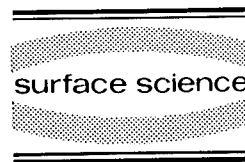
## 6. References

- [1] H. Kamimura and H. Aoki, *The Physics of Interacting Electrons in Disordered Systems* (Clarendon, Oxford, 1989);  
See also, e.g., articles in: *High Magnetic Fields in Semiconductor Physics II*, Ed. G. Landwehr (Springer, Berlin, 1989).
- [2] H.A. Bethe and E.E. Salpeter, *Quantum Mechanics of One- and Two-Electron Atoms* (Springer, Berlin, 1957).
- [3] C.J. Armistead, S.P. Najda, R.A. Strading and J.C. Mann, *Solid State Commun.* 53 (1985) 1109.
- [4] S. Huant, S.P. Najda and B. Etienne, *Phys. Rev. Lett.* 65 (1990) 1468.
- [5] A. Mandray, S. Huant and B. Etienne, *Europhys. Lett.* 20 (1988) 181.
- [6] E. Glaser, B.V. Shanabrook, R.L. Hawkins, W. Beard, J.M. Mercy, B.D. McCombe and D. Musser, *Phys. Rev. B* 36 (1987) 8185.
- [7] S. Holmes, J.P. Cheng, B.D. McCombe and W. Schaff, *Phys. Rev. Lett.* 69 (1992) 2571.
- [8] T. Pang and S.G. Louie, *Phys. Rev. Lett.* 65 (1990) 1635.
- [9] E.R. Mueller, D.M. Larsen, J. Waldman and W.D. Goodhue, *Phys. Rev. Lett.* 68 (1992) 2204.
- [10] X. Xia and J.J. Quinn, *Phys. Rev. B* 46 (1992) 12530.
- [11] J.M. Shi, F.M. Peeters and J.T. Devreese, *Physica B* 184 (1993) 417.
- [12] A.B. Dzyubenko and A.Y. Sivachenko, unpublished.
- [13] D.M. Larsen and S.Y. McCann, *Phys. Rev. B* 45 (1992) 3485.
- [14] P.M. Platzman, *Phys. Rev.* 125 (1962) 1961.
- [15] J.M. Shi, F.M. Peeters, G.Q. Hai and J.T. Devreese, *Phys. Rev. B* 44 (1991) 5692.
- [16] G.Q. Hai, F.M. Peeters and J.T. Devreese, *Phys. Rev. B* 47 (1993) 10358.
- [17] J.P. Cheng, B.D. McCombe, J.M. Shi, F.M. Peeters and J.T. Devreese, *Phys. Rev. B* 48 (1993) 7910.
- [18] F.M. Peeters and J.T. Devreese, *Phys. Rev. B* 31 (1985) 3689.
- [19] X.G. Wu, F.M. Peeters and J.T. Devreese, *Phys. Rev. B* 34 (1986) 8800.



ELSEVIER

Surface Science 305 (1994) 225–229



## Negatively charged excitons $X^-$ in the electron gas in $\text{CdTe}/\text{Cd}_{1-x}\text{Zn}_x\text{Te}$ quantum wells

K. Kheng<sup>a</sup>, R.T. Cox<sup>\*,a</sup>, Y. Merle d'Aubigné<sup>b</sup>, M. Mamor<sup>b</sup>, N. Magnea<sup>a</sup>,  
H. Mariette<sup>b</sup>, K. Saminadayar<sup>a</sup>, S. Tatarenko<sup>b</sup>

<sup>a</sup> CEA / Département de Recherche Fondamentale sur la Matière Condensée, B.P. 85X, 38041, Grenoble Cedex, France

<sup>b</sup> Laboratoire de Spectrométrie Physique, CNRS / Université J. Fourier, B.P. 87, 38402, Saint Martin d'Hères Cedex, France

(Received 16 April 1993; accepted for publication 28 June 1993)

### Abstract

Negatively charged excitons (two electrons bound to one hole),  $X^-$ , are identified for the first time in semiconductor quantum wells. The optical transition corresponding to creation of  $X^-$  is identified  $\sim 3$  meV below the free exciton line X in the magneto-transmission spectra of  $\text{CdTe}/\text{Cd}_{1-x}\text{Zn}_x\text{Te}$  quantum well heterostructures in which a dilute electron gas has been produced either by optical excitation or by modulation doping.

### 1. Introduction

The initial effect of the two-dimensional electron gas (2DEG) on excitons is usually considered to be a reduction of the excitonic binding energy by the screening and phase-space filling effects. This gives the well-known Mahan exciton or Fermi edge singularity enhancement in the optical absorption spectra. However, in a quantum well (QW) system such as  $\text{CdTe}/\text{Cd}_{1-x}\text{Zn}_x\text{Te}$  where the excitonic Rydberg has a rather high value (10.5 meV) one can expect that a first observable effect of the interaction of excitons with a dilute electron gas will be the formation of negatively charged excitons,  $X^-$ . In this paper, we report the identification of the species  $X^-$  in the magneto-transmission spectra of (i) nominally undoped

single QWs under optical excitation and of (ii) modulation-doped multi-QWs.

### 2. Samples and experimental details

The  $\text{CdTe}/\text{Cd}_{1-x}\text{Zn}_x\text{Te}$  strained layer QW samples described in this paper were coherently grown by molecular beam epitaxy directly on (001) orientation  $\text{Cd}_{0.88}\text{Zn}_{0.12}\text{Te}$  substrates (samples 2 and 3) or on a  $2\text{ }\mu\text{m}$  thick (001)  $\text{Cd}_{0.86}\text{Zn}_{0.14}\text{Te}$  buffer layer (sample 1). Sample 1 (Z293) consists of a single  $180\text{ }\text{\AA}$  thick CdTe well layer between the buffer layer and a  $1000\text{ }\text{\AA}$  thick  $\text{Cd}_{0.86}\text{Zn}_{0.14}\text{Te}$  barrier layer. Samples 2 (ZD133) and 3 (ZD130) are  $\text{CdTe}/\text{Cd}_{1-x}\text{Zn}_x\text{Te}$  ( $x \approx 0.16$ ) multi-QWs (10 periods) with identical well widths ( $100\text{ }\text{\AA}$ ) and barrier widths ( $500\text{ }\text{\AA}$ ); the average lattice parameter matches that of the substrate. Sample 2 was planar doped [1] with indium donors at the center

\* Corresponding author.

of the barriers to a nominal sheet concentration of  $4 \times 10^{10} \text{ cm}^{-2}$ . SIMS profiling shows that any broadening of the dopant plane is small at the scale of the SIMS resolution (40 Å). Sample 3 is nominally undoped. Because of the lattice mismatch, the CdTe layers are under strong biaxial compression.

Transmission experiments were performed at 1.7–80 K in the Faraday configuration along the QW growth direction in the magnetic field of a superconducting coil. The samples were illuminated (tungsten source) from the substrate side so that the QWs receive light filtered by the substrate. The transmitted light is detected through a circular polarizer and a monochromator by a GaAs photomultiplier. An additional light source (dye-laser) could be directed onto the front surface of the sample in order to create free carriers.

### 3. Results and discussion

We first present the magneto-transmission results for the undoped single QW (sample 1). The substrate filtering of the incoming light ensures that no (or very little) electron gas is produced during the first measurements. At 2 K and 10 T, the absorption spectra (Fig. 1a) show only the absorption line of the (heavy hole) exciton in the well, labelled X, in both the  $\sigma^+$  and  $\sigma^-$  polarisations. When the sample is additionally optically excited with a defocused laser above or near the barrier bandgap during the transmission measurement, a new absorption feature, labelled Y, appears in the spectrum (Fig. 1b) at 2.8 meV lower in energy than line X. Quite low excitation levels ( $< 1 \text{ mW/cm}^2$ ) are sufficient to saturate the effect.

We propose that the effect of the optical excitation is a transfer of negative charge from ionised acceptor impurities in the barrier to produce a dilute 2DEG in the well and that line Y is related to the presence of this 2DEG. Note that, at low temperature, line Y is much more intense in the  $\sigma^+$  polarisation, which indicates that the initial state of the absorption transition is spin-degenerate (see later). In fact, this line has often been

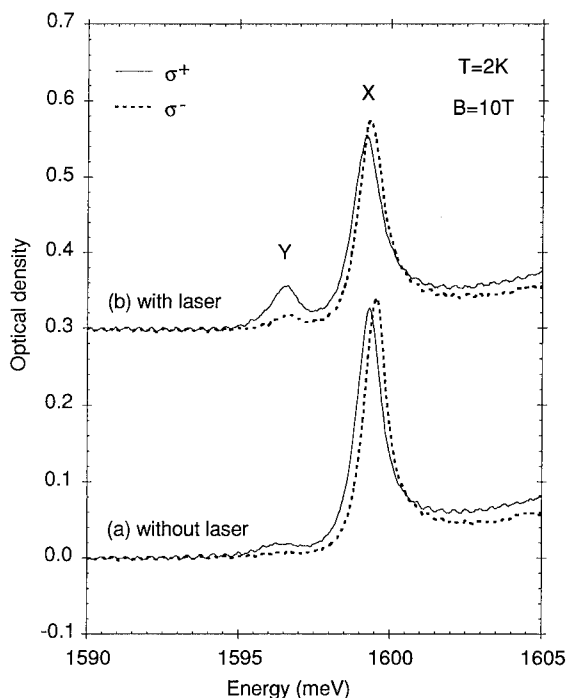


Fig. 1. Absolute optical density spectrum ( $\log_{10}(1/\text{transmission})$ ) of sample 1 (undoped, single 180 Å thick CdTe QW) at 2 K, 10 T. The transmitted light was detected with circular polarizers  $\sigma^+$  (solid lines) and  $\sigma^-$  (dashed lines): (a) Absorption without laser illumination, showing exciton line X; (b) Absorption under additional illumination (defocused laser), showing a new line Y, which is more intense in the  $\sigma^+$  polarisation.

seen in association with line X in the optical spectra, especially the emission spectra, of CdTe/Cd<sub>1-x</sub>Zn<sub>x</sub>Te QW samples [2]. The Y–X separation varies from  $\sim 1 \text{ meV}$  at well-width 700 Å to  $\sim 3 \text{ meV}$  at small well-width, dependent on barrier height. It was initially suggested that line Y could represent the recombination of the species  $D^0X$ : excitons bound to neutral donor impurities present in the CdTe wells. However, the  $D^0X$  line has been definitively identified in spectra of CdTe/Cd<sub>1-x</sub>Zn<sub>x</sub>Te QWs planar doped with indium donors in the well (centre and edge) [3] and is distinctly lower in energy than line Y discussed here (e.g. X– $D^0X$  separation is  $\sim 4 \text{ meV}$  for well-thickness 180 Å). That is, line Y is definitely not associated with donors in the wells, as confirmed by the study of modulation-doped samples which we now describe.

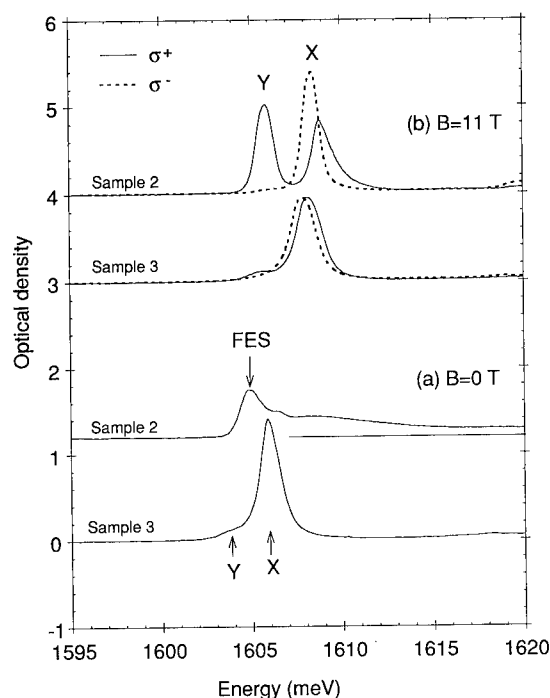


Fig. 2. Absolute optical density spectra of multiple 100 Å well samples (undoped reference sample 3 and modulation-doped sample 2) at 2 K: (a) Zero-field spectra showing line X and a weak Y line for sample 3 and the FES peak for sample 2; (b) 11 T spectra in  $\sigma^+$ ,  $\sigma^-$  polarisations; the FES has transformed into two lines labelled X and Y, with line Y completely polarised  $\sigma^+$ .

Samples 2 and 3 have identical structures except that an indium dopant plane is placed at the centre of the barriers of sample 2. Fig. 2 shows the absorption spectra of both samples at 0 and 11 T. The absorption spectrum of sample 3 (reference sample) shows, at 0 T, the excitonic line with a shoulder on the low energy side corresponding to line Y. At 11 T, line Y is again polarised  $\sigma^+$  and the magnetic splitting of line X is observed. On the other hand, absorption spectra of modulation-doped sample 2 at 0 T show a weaker peak and, because it merges into the interband absorption continuum, we interpret this as a Fermi edge singularity (FES). However at 11 T, the spectrum transforms into 2 narrow lines which we again label Y and X. Line Y is very intense and completely polarised  $\sigma^+$ . The magnetic splitting of line X is observed. Line Y, as

before, is related to the presence of the 2DEG in the QW and is now more intense because the electron density has increased.

In CdTe wells on  $\text{Cd}_{1-x}\text{Zn}_x\text{Te}$  substrates, the lattice mismatch induces a biaxial compression which splits the degeneracy of the valence band maximum (by  $\sim 35$  meV for  $x = 0.12$ ), giving decoupled heavy hole ( $|\pm 3/2\rangle_{\text{HH}}$ ) and light hole ( $|\pm 1/2\rangle_{\text{LH}}$ ) states. Line X is the  $E_1\text{HH}_1$  heavy hole exciton. In the 11 T magnetic field, the heavy hole doublet and the conduction electron doublet ( $|\pm 1/2\rangle_{\text{E}}$ ) are split (Zeeman splitting). Photon absorption creates the exciton states  $|+3/2\rangle_{\text{HH}}|-1/2\rangle_{\text{E}}$  and  $|-3/2\rangle_{\text{HH}}|+1/2\rangle_{\text{E}}$  which are observed in polarisations  $\sigma^+$  and  $\sigma^-$ , respectively. (Note: in CdTe QWs the electron  $g$ -factor is  $-1.6$ ; the heavy hole  $g$ -factor has variable sign and magnitude [4], hence the inversion of the exciton's splitting between 180 and 100 Å thickness in Figs. 1 and 2).

By contrast, an absorption transition involving an electron in the initial state will be seen in one polarisation only, since at low temperature and low filling factor only the lower level  $|+1/2\rangle_{\text{E}}$  of the free electron states is populated. The strong polarisation of line Y at 11 T in Fig. 2 demonstrates that an electron is involved in the initial state of this absorption. This is the feature that leads us to attribute absorption transition Y to the creation of the negatively charged exciton  $X^-$ , that is to the process  $e^- + h\nu \rightarrow X^-$ . The two electrons in the species  $X^-$  have anti-parallel spins so that (see diagram in Fig. 3) the angular momentum of the final state is that of the  $\pm 3/2$  hole.

The identification of  $X^-$  is supported by the temperature dependence of the magneto-absorption spectra, shown in Fig. 3 for sample 2 at 11 T. As expected, the intensity of line Y in polarisation  $\sigma^-$  progressively increases with temperature, as level  $|-1/2\rangle_{\text{E}}$  becomes thermally populated. (Also as expected, this depolarisation effect goes more rapidly with temperature at lower fields, not shown.) Furthermore, one can then see that line Y has similar Zeeman splitting to X, which is required by the model. In Fig. 1b, line Y appears in  $\sigma^-$  polarisation already at 2 K because the potential fluctuations induced by



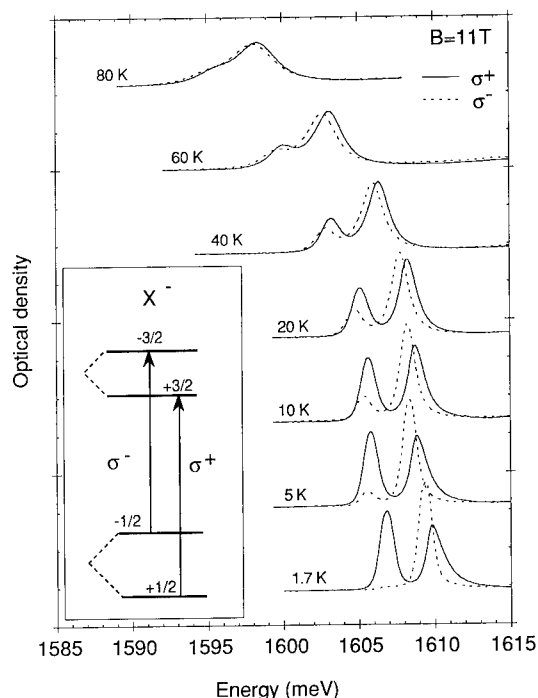


Fig. 3. Temperature dependence of absolute optical density of modulation-doped multi-QW sample 2 at 11 T. The spectra are detected in polarisations  $\sigma^+$  (solid lines) and  $\sigma^-$  (dashed lines): Line Y, totally polarised  $\sigma^+$  at 1.7 K, is seen to appear progressively in  $\sigma^-$  polarisation as the temperature increases. Diagram at left shows transitions creating  $X^-$ , where  $\pm 1/2$  and  $\pm 3/2$  are the angular momenta of the ground and excited states, respectively.

ionised donors randomly distributed in the barriers broaden the electronic density of states. In the doped sample, broadening of the density of states is reduced because, first, the dopant is concentrated in a plane placed at 250 Å from the well and, second, the potential fluctuations are screened by the higher density 2DEG.

The existence of the excitonic negative ion  $X^-$ , analogous to  $H^-$ , was first suggested for bulk semiconductors by Lampert [5]. But in 3D, due to the small binding energy of the second electron ( $\leq 0.055$  Ry, depending on the mass ratio  $m_e/m_h$  [6]), this species has proved very difficult to observe [7]. However, theory predicts that the electron affinity should be greatly increased by quantum confinement, up to 0.47 Ry in the 2D limit [8]. It is this confinement effect, together with the

rather high value of the excitonic Rydberg in CdTe (10.5 meV) that has allowed us to observe the  $X^-$  species. The measured electron affinity ( $X-Y$  separation) at zero magnetic field is 2.3 meV (0.22 excitonic Rydbergs) in the dilute gas of the 180 Å wide QW (but see Ref. [9]).

In sample 2, the carrier density is large enough to screen the Coulomb interaction, reducing drastically the second electron affinity so that line Y can not be distinguished from X at 0 T; indeed the two lines merge into the FES. At 11 T, however, Y and X are well separated. This must be a consequence of magnetic field induced localisation but we have no detailed theory at present.

In conclusion, we propose that (at least for materials systems having high values of the excitonic Rydberg) the first observable consequence of the interaction of excitons with a dilute 2DEG is the formation of the discrete state  $X^-$ , rather than conventional exciton screening. In fact, this interpretation parallels recent thinking about the interaction of the 2DEG with neutral donors  $D^0$  situated in a QW: in that case the electrons first form negatively charged  $D^-$  centres [10] and, subsequently, screened  $D^-$  is observed rather than screened  $D^0$  [11]. Actually, the essential difference between  $X^-$  and  $D^-$  is that now the positive centre (hole) is mobile in the QW layer.

#### 4. References

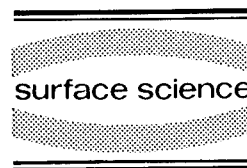
- [1] F. Bassani, S. Tatarenko, K. Saminadayar, N. Magnea, R.T. Cox, A. Tardot and C. Grattapain, *J. Appl. Phys.* 72 (1992) 2927.
- [2] H. Mariette, F. Dal'bo, N. Magnea, G. Lentz and H. Tuffigo, *Phys. Rev. B* 38 (1988) 12443.
- [3] K. Kheng, R.T. Cox, S. Tatarenko, F. Bassani, K. Saminadayar and N. Magnea, in: *Optics of Excitons in Confined Systems*, Eds A. D'Andrea et al. (Institute of Physics, Bristol, 1992) p.333.
- [4] J.J. Davies et al., to be published.
- [5] M.A. Lampert, *Phys. Rev. Lett.* 1 (1958) 450.
- [6] G. Munschy and B. Stébé, *Phys. Status Solidi* 64 (1974) 213.
- [7] T. Kawabata, K. Muro and S. Narita, *Solid State Commun.* 23 (1977) 267; G.A. Thomas and T.M. Rice, *Solid State Commun.* 23 (1977) 359.
- [8] B. Stébé and A. Ainane, *Superlatt. and Microstruct.* 5 (1989) 545.

- [9] Note that the negative charge of  $X^-$  makes it sensitive to the potential fluctuations induced by the distant donor cores  $D^+$  in the barrier; strictly, the electron affinity deduced from the separation of the X and Y lines may be slightly higher than the true, unperturbed value.
- [10] S. Huant, S.P. Najda and B. Etienne, *Phys. Rev. Lett.* 65 (1990) 1486.
- [11] S. Holmes, J.P. Cheng, B.D. McCombe and W. Schaff, *Phys. Rev. Lett.* 69 (1992) 2571.



ELSEVIER

Surface Science 305 (1994) 230–233



## Exciton-capture mechanism at impurities in GaAs/Al<sub>x</sub>Ga<sub>(1-x)</sub>As quantum wells

C.I. Harris <sup>\*,a</sup>, B. Monemar <sup>a</sup>, P.O. Holtz <sup>a</sup>, H. Kalt <sup>b</sup>, M. Sundaram <sup>c</sup>,  
J.L. Merz <sup>c</sup>, A.C. Gossard <sup>c</sup>

<sup>a</sup> Department of Physics and Measurement Technology, Linköping University, Linköping S-581 83, Sweden

<sup>b</sup> Fachbereich Physik, University of Kaiserslautern, Kaiserslautern, Germany

<sup>c</sup> Center for Studies of Quantised Electronic Structures (QUEST), University of California at Santa Barbara, Santa Barbara, CA 93016, USA

(Received 21 April 1993; accepted for publication 4 June 1993)

### Abstract

At low temperatures a neutral impurity is able to capture a free exciton to form a bound exciton state. The capture process is understood in bulk material as a phonon mediated relaxation of the free exciton through successive excited states to the ground state of the bound exciton. The equivalent mechanism in a confined system has not been specifically studied to date. In this paper we present an investigation of the exciton capture process in GaAs/Al<sub>0.3</sub>Ga<sub>0.7</sub>As quantum wells using a picosecond time-resolved photoluminescence technique. We demonstrate that there are significant differences in the capture mechanism for narrow quantum wells in comparison to the bulk. In particular the capture efficiency is shown at first to increase with temperature. This behaviour is understood in terms of the role of localization of the free exciton in the potentials caused by the interface roughness. Higher temperatures destroy this localization process which otherwise limits the total capture rate for the exciton to the impurity. We also conclude that the distinct difference in the near bandgap low temperature excitonic spectra between bulk and confined material at low and moderate doping levels can be understood in terms of the corresponding differences in impurity capture efficiency.

### 1. Introduction

The role of defects and impurities in determining the electrical and optical properties of low dimensional semiconductors remains one of the primary concerns in the technological development of this field. A detailed understanding, in particular of the capture of free carriers and

excitons at defects, is required for a quantitative assessment of the effect of defects/impurities on performance. The optical properties of low dimensional semiconductors are dominated by exciton recombination. It is therefore most relevant in this case to discuss the capture mechanism for free excitons. In this work we make use of resonant excitation of the free exciton at low intensities thereby minimizing the contribution of free electrons and holes to the capture and recombination kinetics. The capture process observed is purely that of the free exciton.

\* Corresponding author.

Despite the importance of impurity capture processes for excitons in bulk material such mechanisms have been discussed only on a limited number of occasions (see for example Refs. [1–3]). A detailed study of exciton capture at neutral shallow impurities in fact exists only for bulk Si [2,3]; in discussing the experimental results we thus make a comparison between bulk and low dimensional behaviour using the data available for Si. The process of capture of a free exciton (FE) by a neutral impurity to form a bound exciton (BE) can be characterized by a capture cross section. In modeling the capture mechanism it is simplest to consider a single-level system, i.e. the particle is either bound or free. The analysis of the predominant capture process is assumed, as a first approximation, to follow the theory of Lax [4], in which he describes a cascade capture mechanism as the particle relaxes through the bound excited states via successive phonon emission. The Lax model is in fact rigidly derived assuming a Coulombic trap for a free carrier; it is therefore not strictly appropriate for the case of exciton capture where the neutral trap provides a limited number of bound excited states. For the purpose of the discussion here it however provides an adequate picture while allowing that the detailed mechanism will be somewhat different. In simple terms the Lax model implies that capture will occur only to those bound states that are deeper than the thermal energy  $k_B T$  from the free particle continuum. Excitons captured to states below this threshold rapidly relax to the ground state via phonon emission, while those in higher lying states are further re-emitted. In calculating the total capture cross section ( $\sigma_t$ ) appropriate to our single level model we must sum over cross sections for each level:

$$\sigma_t = \sum S_j \sigma_j, \quad (1)$$

where  $S_j$  is the so-called sticking probability for the  $j$ th excited level, i.e. the probability that a particle captured in state  $j$  reaches the ground state. From the above model this probability is essentially one for states below  $k_B T$  and zero above. This simplistic model makes no account of the transition rates for the relaxation process;

however, this point is unimportant provided the relaxation is rapid in comparison to the observed decay rates and hence that the bound population predominantly resides in the ground state. The occupancy of excited states is important in determining the thermal emission or release from bound to free states, which in return will represent the temperature dependence of the overall capture mechanism. The work by Hammond and Silver [2] and by Feenstra and McGill [3] for bulk Si has shown that the temperature dependence of the capture cross section can be fitted by a relation of the form  $\sigma \propto 1/T^x$ , where  $x = 0.5$ –4 depending on the impurity measured.

In this work we investigate the dependence of capture rate on temperature in an acceptor doped quantum well. In apparent contradiction to the result obtained in bulk Si, the capture efficiency is found to at first increase with temperature. This result is discussed in terms of the effect of localization in the narrow quantum well system.

## 2. Experimental method

The study described requires well-resolved free and bound exciton peaks to enable a clear analysis of the kinetics even at elevated temperatures. We therefore restrict the discussion in this paper to acceptor doped GaAs/Al<sub>0.3</sub>Ga<sub>0.7</sub>As quantum wells with well width of 100 Å or larger. The samples have been prepared using molecular beam epitaxy (MBE) with non-interrupted growth. The Be dopant was introduced into the central 20 Å of the well only at a concentration of  $1 \times 10^{10} \text{ cm}^{-2}$ . The low temperature photoluminescence experiment was carried out at 2 K, time-resolved measurements were made using a Hamamatsu synchroscan streak camera with a temporal resolution of about 20 ps. Pulsed excitation was provided by a dye laser synchronously pumped using a mode-locked argon laser to give pulse lengths of around 5 ps duration.

## 3. Results and discussion

Fig. 1 illustrates the initial development in the PL signal for the BE emission at four different

temperatures. The rate of onset of the emission corresponds to the rate of capture of resonantly excited free excitons at the neutral Be impurity, given by:

$$dN_{\text{BE}}/dt = C_{\text{FE}} \times (N_{\text{FE}}) \times (A_0 - N_{\text{BE}}), \quad (2)$$

where  $C_{\text{FE}}$  is the capture rate,  $A_0$  the neutral Be acceptor concentration and  $N_{\text{FE}}$ ,  $N_{\text{BE}}$  the concentrations of free and bound excitons, respectively. The capture rate is clearly seen to increase with temperature, the onset time defined by the  $1/e$  value for the rising slope decreases from 55 ps at 2 K to around 46 ps at 20 K. The increasing efficiency with which free excitons are trapped at impurities is also well illustrated in the time integrated luminescence. Fig. 2 shows a series of PL spectra taken at different temperatures, the ratio of BE to FE is found to at first increase with temperature; this trend is however reversed at the highest temperature shown (20 K). Note that there are additional processes resulting from increased temperature which will effect the absolute intensity of the free exciton, these do not affect, however, the maxima in capture efficiency illustrated by Fig. 2.

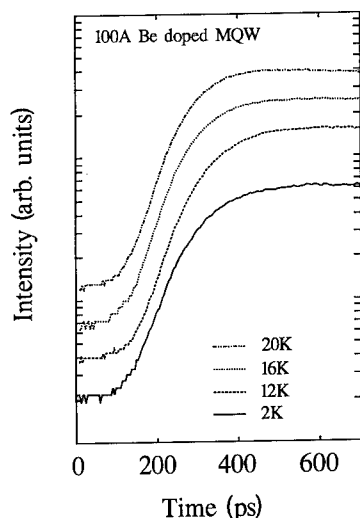


Fig. 1. Temperature dependence of the onset in BE emission for a 100 Å acceptor (Be) doped quantum well, excitation is resonant with the FE. The increasing slope with temperature indicates a faster capture rate of the free exciton at the acceptor.

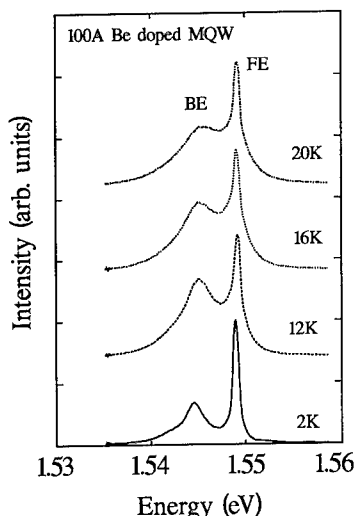


Fig. 2. Time integrated PL signal at different temperatures for the 100 Å acceptor doped quantum well. The increased ratio of BE to FE intensities is indicative of the higher capture efficiency. At the highest temperature (20 K) the trend is reversed illustrating that the decrease in capture cross section is now the dominant contribution to the capture rate.

The capture rate  $C_{\text{FE}}$  is related to the total capture cross section  $\sigma$  by the thermal velocity ( $V_{\text{th}}$ ) such that:

$$C_{\text{FE}} = \sigma_{\text{FE}} V_{\text{th}}. \quad (3)$$

An analysis of the capture process must therefore also take into account the temperature dependence of the thermal velocity [5]:

$$V_{\text{th}} = (8KT/\pi m_{\text{ex}})^{1/2}, \quad (4)$$

where  $V_{\text{th}}$  is the mean thermal velocity of the free exciton and  $m_{\text{ex}}$  is the exciton mass. Given the dependence of capture cross section on temperature suggested by the work on bulk Si this implies an expected negative power law dependence for the capture rate, i.e. the rate should decrease with increasing temperature. The results of Figs. 1 and 2 clearly contradict this model for the QW case since the opposite trend is demonstrated. This apparent anomaly can, we suggest, be understood in terms of the exciton localization in this system. The capture rate is found to be suppressed at low temperatures due to the effect of localization on the free exciton thermal velocity. There are then two competing responses to

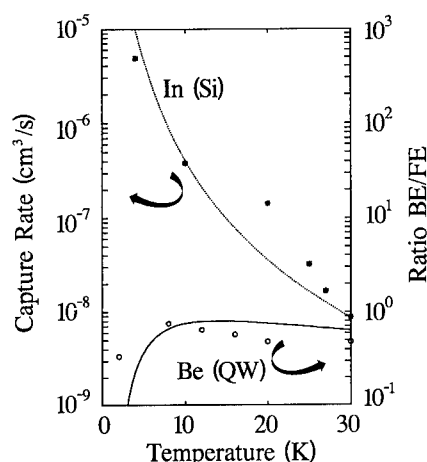


Fig. 3. Comparison of behaviour in bulk material (silicon) with the quantum well measured in this study. The data points (\*) are calculated from the data in Ref. [3] for the capture at the In impurity in Si, the dotted line indicates the  $T^{-4}$  dependence of the capture cross section attributed by the authors. The data (o) are for the quantum well measured in this study and illustrate the ratio of PL intensities for the BE and FE. The solid line is calculated on the basis of an activated thermal velocity for the FE and illustrates the maxima in capture rate at elevated temperatures expected from such a model.

increasing temperature. The capture cross section decreases with increasing temperature as is required by the cascade capture model however, at low temperatures the dominant mechanism is the thermal activation behaviour observed in the thermal velocity of the FE. Fig. 3 compares the trends observed in both the bulk and confined QW systems. For the bulk we use the data for In capture in Si from Ref. [3] to calculate the capture rate. The dotted line indicates the  $T^{-4}$  variation attributed to the capture cross section dependence in that case. In the QW case we have not calculated the absolute capture rates since this requires a detailed analysis of the rate equations which given the small variation implied by the data is not justified within the limits of accuracy of the calculation. A reasonable indication of the behaviour is however obtained directly by taking the ratio of the BE to FE integrated intensities as a function of temperature (this is the same as integrating Eq. (2) assuming a constant

FE population). The data in Fig. 3 have been scaled over the same number of orders of magnitude as the bulk data to indicate the small variation observed over this temperature range. The solid line is the calculated response for the QW capture rate assuming the thermally activated free electron velocity as discussed. The curve illustrates an activation energy equal to the Stokes shift for the exciton emission (1.2 meV) and a capture cross section dependent on  $T^{-1}$ . The calculation suggests a maximum capture rate at approximately 16 K which is consistent with the measured data.

#### 4. Conclusion

The qualitative temperature dependence of the capture rate has been measured for an acceptor doped GaAs/AlGaAs quantum well. The initial increase in capture efficiency with temperature observed is in apparent contradiction to that expected from a cascade capture model and with the behaviour previously reported in bulk material. The mechanism for this increase is believed to be the thermal activation of the localized free exciton such that there is a dramatic increase in the mean thermal velocity of the free exciton. The increase in thermal velocity is the dominant contribution to the capture rate at lower temperatures; at higher temperatures (20 K) the decrease in capture cross section becomes the dominant term and a negative power law dependence can then be observed to dominate.

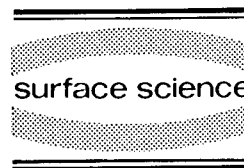
#### 5. References

- [1] D. Bimberg, H. Münzel, A. Steckenborn and J. Christen, Phys. Rev. B 31 (1985) 7788.
- [2] R.B. Hammond and R.N. Silver, Appl. Phys. Lett. 36 (1980) 68.
- [3] R.M. Feenstra and T.C. McGill, Solid State Commun. 36 (1980) 1039.
- [4] M. Lax, Phys. Rev. 119 (1960) 1502.
- [5] K.R. Elliott, D.L. Smith and T.C. McGill, Solid State Commun. 24 (1978) 461.



ELSEVIER

Surface Science 305 (1994) 234–237



## Time-resolved four wave mixing studies of a two-dimensional electron gas in a magnetic field

S. Bar-Ad, I. Bar-Joseph <sup>\*</sup>, Y. Levinson, H. Shtrikman

*Department of Physics, The Weizmann Institute of Science, Rehovot 76100, Israel*

(Received 19 April 1993; accepted for publication 18 July 1993)

### Abstract

We report on experimental investigation of the nonlinear optical response of quantum wells containing a two-dimensional electron gas. As the magnetic field is increased, and the second Landau level is emptied of electrons, we find a *sharp decrease* of the four wave mixing signal at that level.

The optical characterization of the two-dimensional electron gas (2DEG) in semiconductor heterostructures in high magnetic fields has attracted a lot of interest in recent years. Optical measurements of photoluminescence, absorption and inelastic light scattering at very low temperatures have shown that the many body interactions, which give rise to the rich transport phenomena of the integer and fractional quantum Hall effects, influence the optical properties of the system [1–3]. Special attention has been given to the study of the Fermi-edge singularity [4]. This effect, which is seen as a sharp increase of the absorption and photoluminescence intensity at the Fermi energy, is an optical manifestation of the interaction between the optically excited electron–hole pair and the electrons of the 2DEG.

Time-resolved coherent optical spectroscopy has emerged in recent years as an important

experimental tool for solid state research in general and the study of 2DEG in particular [5,6]. A temporal resolution of less than a picosecond, combined with high spectral resolution, allows direct measurements of transient and relaxation phenomena, along with their spectral variation. As a nonlinear optical technique it is sensitive to the diagonal as well as the off-diagonal elements of the density matrix. Thus one can study the temporal evolution of both the population at a given level and the phase coherence between the various states of the system.

In this work we have used time-resolved four wave mixing (FWM) for the study of 2DEG in strong magnetic fields ( $B < 7$  T) at liquid-helium temperature. The FWM technique measures the third order dipole moment, by coherently exciting the sample with two laser pulses at a precisely controlled relative delay, and detecting the signal emitted following the excitation as function of the delay [7]. A schematic FWM setup is shown in the inset of Fig. 1. The two pulses have wave vectors  $k_1$  and  $k_2$  with a small angle between

<sup>\*</sup> Corresponding author.

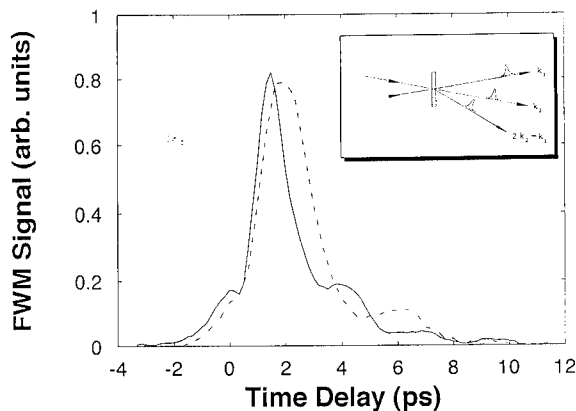


Fig. 1. Quantum beats of the FWM signal at the second LL at 5 and 7 T in the intrinsic sample.

them. The integrated intensity, emitted in the direction  $2\mathbf{k}_2 - \mathbf{k}_1$ , is measured by a slow detector. This integrated intensity decays as function of the delay between the exciting pulses, with a time constant which is proportional to the phase relaxation of the photo-excited carriers in the sample. The temporal resolution of our system is 0.7 ps, fast enough to resolve the relevant temporal processes while maintaining spectral resolution of 1–2 meV.

We have studied a modulation doped (MD) sample, consisting of 30 periods of 100 Å GaAs wells between 500 Å  $\text{Al}_{0.3}\text{Ga}_{0.7}\text{As}$  barriers, the center 100 Å of which were doped with silicon. The electron density was measured to be  $2.4 \times 10^{11} \text{ cm}^{-2}$  in the wells at 4 K. Doped AlGaAs buffer layers were grown on both sides of the heterostructure to suppress bending of the conduction band, while avoiding parallel conduction in the buffer layers. Van der Pauw measurements on the sample gave a mobility of  $5 \times 10^4$  for the 30 in-parallel connected layers (implying a Drude relaxation time of  $\sim 2$  ps). At 4 K and 7 T the Fermi level is in the first Landau level (LL), and the filling factor is 1.4. An intrinsic sample with 30 periods of 120 Å quantum wells (QW) and 120 Å barriers served as a reference. The excitation power densities were chosen to generate a relatively low carrier density, of  $\sim 10^{10} \text{ cm}^{-2}$ , which is only 5% of the electron density in the wells.

The spectrum of the FWM signal at a given

magnetic field in the intrinsic sample consists of well defined peaks, which correspond to the various magneto-exciton transitions of the sample. These peaks get larger with increasing magnetic field strength due to the increased degeneracy and oscillator strength. Fig. 1 shows the temporal evolution of the FWM signal at the second LL in magnetic fields of 5 and 7 T (the two signals are normalized to have the same peak intensity). Decaying oscillations, with a period which is inversely proportional to the magnetic field strength, are clearly seen. A  $\pi$  phase shift is observed between the FWM oscillations obtained with parallel linear polarizations (PP) of the two exciting pulses, and that measured with cross-linear polarizations (CP). These oscillations are quantum beats between Zeeman-split magneto-excitonic states. Their frequency gives directly the Zeeman splitting associated with these transitions and the corresponding Landé  $g$ -factors [8].

The measurements on the MD sample show marked differences with respect to the intrinsic sample. The most pronounced difference is seen when the intensity of the FWM signal is measured at the second LL as a function of the magnetic field. Fig. 2 shows the FWM signals at magnetic fields of 4 and 6.5 T, for which the Fermi level is in the second and first LLs, respectively. We observe a strong *drop* in the signal as the second LL is emptied of electrons – an order of magnitude decrease from 4 to 6.5 T. This

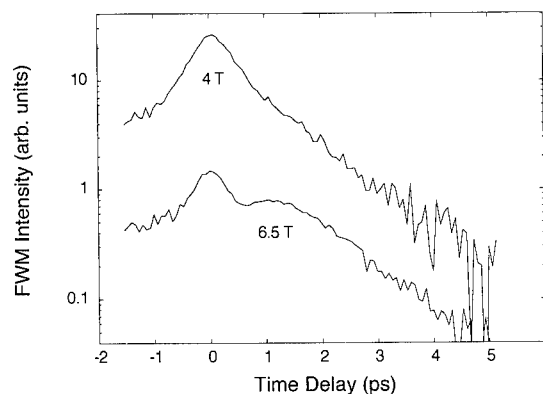


Fig. 2. The temporal evolution of the FWM signal at the second LL at 4 and 6.5 T in the MD sample (on a logarithmic scale). The signal at negative delays is due to scattering.



behavior is opposite to the behavior of the intrinsic sample, where the FWM signal increases with increasing magnetic field. It is evident that the signal at both fields decays with approximately the same time constant of 1.5 ps. The constant relaxation time of 1.5 ps, which is measured throughout this field range, implies that this drop cannot be simply due to different decay rates at the two regimes (a short relaxation time leads to a weak integrated signal).

Examining the temporal evolution of the signal, another important difference between the samples is seen: no quantum beats are observed in the MD sample! Instead, two temporal components, whose relative strength strongly depends on the excitation energy, dominate the signal. The first is an instantaneous component, which rises and falls *within* the pulse autocorrelation time and exists only as long as the two exciting pulses overlap. The second is a slower component, which rises with the pulse autocorrelation time, and decays exponentially with a time constant of 1.5 ps.

Fig. 3 shows the temporal evolution of the signal at 3 different excitation energies in a field of 6.5 T, for which the Fermi level is in the first LL. Panels (a) and (b) show the signal observed when the system is probed at two energies within the second LL transition, while in panel (c) it is probed at the partially filled first LL. The differ-

ences in the relative strength of the two temporal components are evident. It should be noted that the signal at the first LL, just above the Fermi surface, is much more intense than that at the second LL.

The behavior described above is generally true for both the PP and CP cases. An important characteristic of the FWM interaction is the ratio between the signals at the two configurations, PP/CP. We find a clear difference between PP/CP in the first LL, which is approximately unity, and that in the second LL, where the PP signal is much larger than the CP one. At that level PP/CP is  $\sim 10$  at 6.5 T, and  $\sim 5$  at 4 T.

In summarizing our measurements for the MD sample, we observe the following: a strong decrease in the FWM signal at the second LL as it is emptied of electrons; two temporal components, with varying relative intensities, and no Zeeman quantum beats; an energy and magnetic field independent decay constant of 1.5 ps; a marked change in the PP to CP ratio between the first and the second LLs. This rich behavior contains some effects which can be explained within the framework of noninteracting electrons as well as some which cannot.

It is evident that the proximity of the Fermi energy to the second LL critically affects the observed FWM signal from that level. Using a simple two level model, in which we introduce a

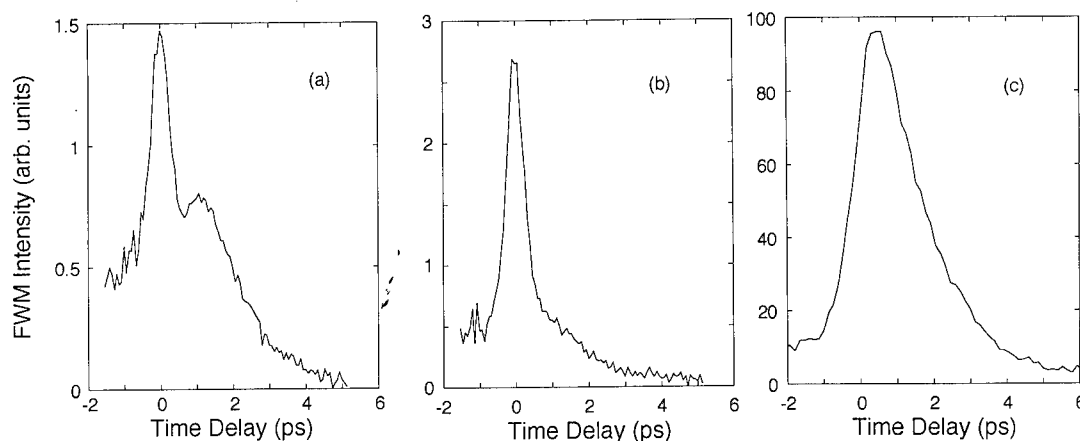


Fig. 3. The FWM signal in the MD sample at 6.5 T in: (a) the second LL – high energy; (b) second LL – low energy; (c) first LL. Note the varying relative strength of the fast and slow components.

sharp cutoff at the Fermi energy in an inhomogeneously broadened LL, we could explain the appearance of the fast and the slow temporal components seen in Fig. 3. Indeed, it can be shown that these two components have different energy dependence at the vicinity of the Fermi energy. However, such a single electron model cannot explain the observed drop of the signal between 4 and 6.5 T. It shows no enhancement of the FWM signal close to the Fermi level, as is the case at 4 T, and no sharp drop as the Fermi level moves away at higher magnetic fields. The fact that this drop of the signal occurs as the Fermi energy moves from the second to the first LL, leads us to conclude that the nonlinear optical response is modified by a many body interaction with the Fermi sea. The nature of this many body interaction, which resembles the Fermi edge singularity, is being studied.

The energy and magnetic field dependence of the ratio between the PP and the CP signals also cannot be explained by simple arguments. This dependence is different from that observed in the intrinsic sample. A model which will attempt to explain these dependencies of the PP to CP ratio,

and the absence of Zeeman quantum beats in the MD sample, should take into account asymmetric filling of the spin split levels, the enhanced spin splitting close to the Fermi level [3] and the mixing between heavy and light hole optical transitions [9].

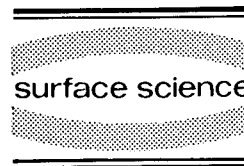
## 1. References

- [1] A.J. Turberfield et al., Phys. Rev. Lett. 65 (1990) 637; B.B. Goldberg et al., Phys. Rev. Lett. 65 (1990) 641; H. Buhmann et al., Phys. Rev. Lett. 65 (1990) 1056.
- [2] D. Heiman, B.B. Goldberg, A. Pinczuk, C.W. Tu, A.C. Gossard and J.H. English, Phys. Rev. Lett. 61 (1988) 605.
- [3] A. Pinczuk et al., Phys. Rev. Lett. 68 (1992) 3623.
- [4] A.J. Turberfield, R.A. Ford, I.N. Harris, J.F. Ryan, C.T. Foxon and J.J. Harris, Phys. Rev. B 47 (1993) 4794.
- [5] W.H. Knox, D.S. Chemla, G. Livescu, J.E. Cunningham and J.E. Henry, Phys. Rev. Lett. 61 (1988) 1290.
- [6] D.S. Kim, J. Shah, J.E. Cunningham, T.C. Damen, S. Scmitt-Rink and W. Schafer, Phys. Rev. Lett. 68 (1992) 2838.
- [7] L. Schultheis, J. Kuhl, A. Honold and C.W. Tu, Phys. Rev. Lett. 57 (1986) 1635, 1797.
- [8] O. Carmel and I. Bar-Joseph, Phys. Rev. B, to be published.
- [9] S.-R. Eric Yang and L.J. Sham, Phys. Rev. Lett. 58 (1987) 2598.



ELSEVIER

Surface Science 305 (1994) 238–242



## Femtosecond studies of excitonic optical non-linearities in $\text{GaAs}/\text{Al}_x\text{Ga}_{1-x}\text{As}$ multiple quantum wells under in-plane uniaxial strain

M. Wraback <sup>\*</sup>, H. Shen <sup>1</sup>, J. Pamulapati, M. Dutta, P.G. Newman, M. Taysing-Lara

*US Army Research Laboratory, Electronics and Power Sources Directorate, AMSRL-EP-EF, Fort Monmouth, NJ 07703-5601, USA*

Y. Lu

*Department of Electrical and Computer Engineering, Rutgers University, Piscataway, NJ 08855-0909, USA*

(Received 22 April 1993; accepted for publication 4 June 1993)

### Abstract

The pump-probe technique was employed in the study of excitonic optical non-linearities at 40 K in a  $\text{GaAs}/\text{Al}_{0.1}\text{Ga}_{0.9}\text{As}$  multiple quantum well under thermally induced in-plane uniaxial strain. We report the first observation of an ultrafast large-angle polarization rotation of the probe light effected by the bleaching of the anisotropic absorption near the heavy hole exciton peak in this material. Dynamic rotations as large as  $42^\circ$  have been measured for a compressive strain of  $\sim 0.2\%$ . In addition, a dependence of the phase space filling produced by resonantly excited excitons on the orientation of the pump polarization vector has been observed which decays with a time constant of 0.5 ps. This decay is attributed to the ionization of excitons into free electron-hole pairs. The subsequent decline of the probe rotation is governed by the removal of these carriers from the wells.

While quantum confinement in the growth ( $z$ ) direction of a multiple quantum well (MQW) breaks the full cubic symmetry of the material, the layered structure still reserves an in-plane four-fold rotation symmetry for growth on (100)-oriented substrates. A necessary consequence of this fact is that the absorption of linearly polarized photons incident normal to the MQW remains independent of the orientation of the electric field vector of the light for transitions near

the  $\Gamma_8-\Gamma_6$  fundamental bandgap. A uniaxial strain created perpendicular to the growth direction reduces the in-plane rotation symmetry of the valence band, producing a mixing of the heavy and light hole wave functions near  $k_{\parallel}=0$  [1] which results in an anisotropy in absorption and concomitant rotation of the light polarization [2,3] most readily observed near the excitonic resonances. In this paper we report the first investigation of excitonic optical non-linearities associated with an ultrafast polarization rotation effected by the bleaching of this anisotropic absorption in a uniaxially strained MQW.

The intrinsic region of the p-i-n structure grown on (100)GaAs used in this study consists of

<sup>\*</sup> Corresponding author.

<sup>1</sup> Also at: Geo Centers, Inc., Lake Hopatcong, NJ 07849, USA.

a 100-period, 150 Å GaAs/50 Å  $\text{Al}_{0.1}\text{Ga}_{0.9}\text{As}$  MQW. The MQW was removed from the GaAs by epitaxial lift-off [4] and bonded at room temperature to a  $\text{LiTaO}_3$  substrate cut such that its thermal expansion coefficient  $\alpha_y$  matches that of the MQW while its orthogonal counterpart  $\alpha_x$  does not. This procedure results in the achievement of a thermally induced compressive in-plane uniaxial strain of  $\sim 0.2\%$  [2] at the measurement temperature of  $\sim 40$  K employed in these experiments. Pulses of 150 fs duration and 83 MHz repetition rate were obtained from a self-mode-locked Ti:sapphire laser [5]. These pulses were split into pump and probe beams, and self-saturation of the probe absorption was avoided through attenuation of the probe beam intensity to one percent of that of the pump. Time-resolved experiments were performed using the conventional pump-probe geometry, with the center frequency of the laser chosen to be in resonance with the lowest excited state of the strain-perturbed system, which we shall label as the first heavy hole exciton. The incident probe polarization was vertical and oriented at  $45^\circ$  with respect to the uniaxial strain ( $x$ ) axis of the sample, while that of the pump pulse was varied using a polarization rotator. A phase compensator and polarizer were used to analyze the transmitted probe light, which was subsequently dispersed by a monochromator placed before the detector.

Fig. 1 shows the spectral dependence of the static probe polarization rotation in the absence of the pump. Measurements of the absorption of light polarized along the  $x$  ( $0^\circ$ ) and  $y$  ( $90^\circ$ ) axes of the sample were performed, with the rotation angle given by [2]

$$\theta = \arctan \left[ \exp \left( \frac{\Delta\alpha d}{2} \right) \right] - 45^\circ, \quad (1)$$

where  $\Delta\alpha = \alpha_x - \alpha_y$ ,  $d$  is the total thickness of quantum wells, and  $\theta$  is positive for angles measured counterclockwise with respect to  $45^\circ$ . Although Eq. (1) does not represent the physical situation exactly because of the presence of a strain-induced birefringence  $\Delta n = n_x - n_y$ , it remains a good approximation near the exciton peaks, where  $\Delta n \approx 0$  [3]. The rotation attained a maximum value of  $\theta = 32^\circ$  and a minimum value

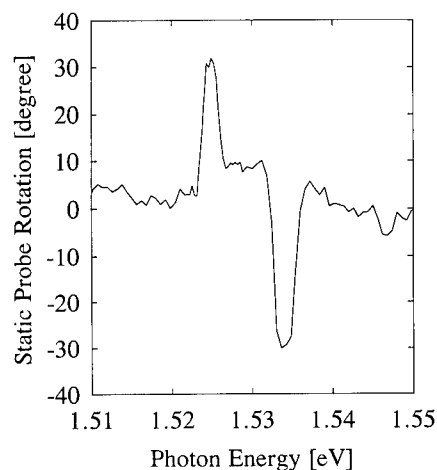


Fig. 1. Polarization rotation of the probe light in the absence of the pump pulse as a function of photon energy.

of  $\theta = -30^\circ$  at the first heavy hole and light hole exciton peaks, respectively, but it was very small elsewhere in the spectrum. These observations indicate that the polarization rotation was primarily due to anisotropic excitonic absorption, with  $\Delta\alpha$  positive (negative) near the heavy (light) hole exciton peak, as predicted by theory [3] for compressive uniaxial strain.

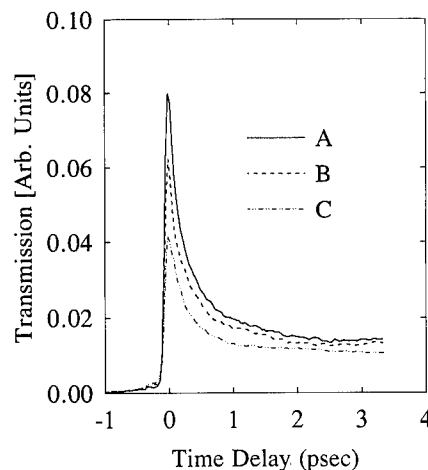


Fig. 2. Photoinduced transmission of the probe as a function of time delay for pump polarization: (A) parallel to the strain axis; (B) parallel to that of probe; (C) perpendicular to the strain axis. The probe polarizer was oriented for minimum transmission at negative time delays.

Shown in Fig. 2 are the results of pump–probe measurements in which the probe polarizer was oriented for minimum transmission at the heavy hole exciton transition energy (1.5239 eV) for the configuration in which the probe pulse precedes the pump. Curves A, B, and C refer to the cases in which the pump polarization was parallel to the strain axis, parallel to that of the probe, and perpendicular to the strain axis, respectively. In all cases the probe transmission exhibited a sharp, pulse-width-limited rise at  $t = 0^+$  which decayed with a sub-picosecond time constant to a plateau within 2 ps. Although the plateau values of all the curves are essentially the same, the maxima for the three pump polarizations are significantly different, with the largest (smallest) peak observed when the pump polarization was parallel (perpendicular) to the strain axis.

The fact that sharp onsets in the data of Fig. 2 occurred at  $t = 0^+$  through a crossed polarizer is clear evidence that the bleaching of the anisotropic excitonic absorption by the pump pulse results in an ultrafast rotation of the probe polarization, which manifests itself in photoinduced transmission when the probe is delayed with respect to the pump. The effect of this rotation on the absorption saturation was separated from that of the bleaching in the absence of the polarizer by performing pump–probe experiments in which the polarizer orientation was perpendicular to that of the previously described measurements. The unpolarized transmission was obtained by adding the curves in Fig. 2 to their counterparts for the perpendicular polarizer orientation, while the dynamic rotation angle was determined from vector addition of the transmitted electric fields for the two polarization orientations, in accordance with Eq. (1).

Figs. 3 and 4 show the unpolarized transmission and dynamic polarization rotation, respectively, of the probe for the three pump polarizations described above. Only one curve is displayed in Fig. 3 because the shape of the unpolarized transmission decays was found to be independent of the orientation of the pump polarization. This curve is characterized by a sharp peak near the zero of time delay followed by a slower decay to a plateau. The peak was most likely due

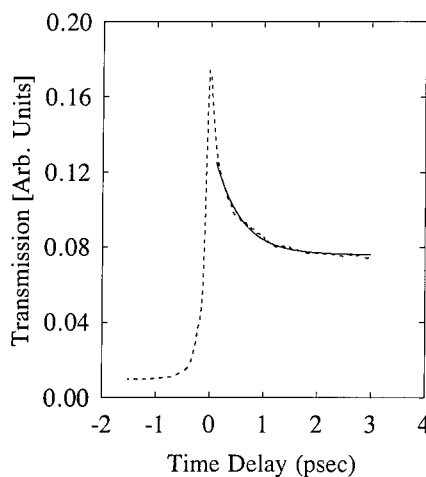


Fig. 3. Unpolarized photoinduced probe transmission as a function of time delay. The shape of the curve is the same for the three pump polarizations discussed in the caption of Fig. 2. The fit is described in the text.

to a coherent non-linear response of the material driven by the temporal coincidence of the pump and probe pulses in the sample. An exponential fit to the subsequent decay yields a time constant of  $0.5 \pm 0.05$  ps. The dynamic probe rotation curves in Fig. 4 are characterized by the same decay constant, but are distinctly different for the

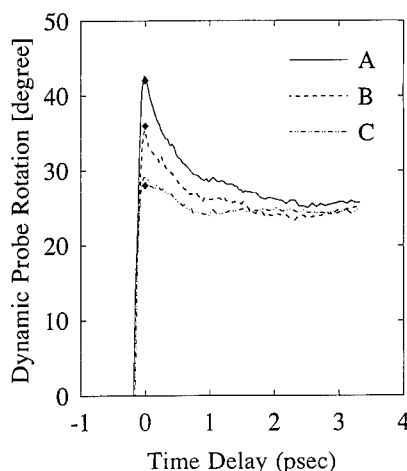


Fig. 4. Dynamic probe rotation as a function of time delay for pump polarization: (A) parallel to the strain axis; (B) parallel to that of the probe; (C) perpendicular to the strain axis. The diamonds correspond to manually measured rotations as described in the text.

three pump polarizations. The rotations exhibited a pulse-width-limited rise to maximum values at  $t = 0^+$  of  $\Delta\theta = 42^\circ$ ,  $35^\circ$ , and  $29^\circ$  for the cases in which the pump polarization was oriented parallel to the strain axis, parallel to that of the probe, and perpendicular to the strain axis, respectively. These numbers were checked by manually orienting the polarizer for minimum transmission at a probe delay of  $t = 0^+$  and measuring its rotation from the angle of minimum transmission at a probe delay such that the probe preceded the pump. The results of these measurements are plotted as points at  $t = 0^+$  in Fig. 4. Excellent agreement with the peak values of the curves was obtained. At longer times a plateau value of  $\Delta\theta \approx 25^\circ$  was observed for all the curves. These data indicate that the differences in the curves of Fig. 2 may be attributed to the temporal evolution of the dynamic probe rotation.

The data shown in Fig. 4 all represent clockwise dynamic rotations with respect to the static rotation of the probe displayed in Fig. 1. This fact indicates that for all the pump polarization orientations the saturation of the absorption in the  $x$  (strain) direction was always stronger than in the  $y$  direction, with the largest (smallest) difference in the photoinduced bleaching between the orthogonal directions obtained when the pump polarization was parallel (perpendicular) to the strain axis. This anisotropy in bleaching is most dramatically displayed in curves 4A and 4B, for which the maximum dynamic rotation exceeds the static rotation, thus illustrating that for these cases  $\alpha_y$  became larger than  $\alpha_x$  at  $t = 0^+$ .

Figs. 3 and 4 also offer insight into the underlying physical processes which determine the shapes of the decay curves. Since the laser was tuned to the first heavy hole exciton transition, the pump pulse resonantly excited cold heavy hole excitons which at  $t = 0^+$  effectively bleached the probe absorption at the heavy hole exciton peak through the exclusion-principle-related mechanisms of excitonic phase space filling and exchange interactions [6,7]. The observation that the magnitude of the maximum dynamic rotation was correlated with the direction of the pump polarization vector indicates that there exists an orientational excitation dependence to the exci-

tonic phase space filling and exchange interactions in a uniaxially strained MQW which persists longer than the temporal overlap of the pump and probe pulses even for the high exciton densities ( $> 10^{11} \text{ cm}^{-2}$ ) generated in our experiments. This orientational behavior may be intuitively understood by noting that the effective shape of the exciton orbit in both real and phase space is no longer circular in our material, with the phase space filling produced by the resultant “ellipsoids” dependent upon the manner in which they were created by the pump. The fact that the disparity in the degree of rotational decay among the curves of Fig. 4 is not reflected in the unpolarized decay of Fig. 3 suggests that the orientational relaxation of the initial absorption saturation is driven by the ionization of excitons into free electron–hole (e–h) pairs rather than the randomization of the excitons. This notion is in concurrence with the experimental behavior that the dynamic rotation angle became independent of pump polarization orientation at longer times, as expected for free e–h pairs. It is interesting to note that in contrast to the very small ( $\sim 1^\circ$ ) polarization rotation associated with the photoinduced anisotropic  $k$ -space filling at  $k \neq 0$  in unstressed GaAs which vanishes on a 100 fs timescale [8,9], the e–h pairs in our material produced a rotation of  $\Delta\theta \approx 25^\circ$  which persisted as long as the carriers remained in the wells.

This interpretation of the data is based upon the assumption that for the two-dimensional case in which the effects of long-range Coulomb screening are negligible [7] cold excitons are more efficient than cool e–h pairs in bleaching the excitonic absorption, a phenomenon which has been both theoretically predicted [10] and experimentally observed [11] in MQWs. While our unpolarized decays bear a distinct resemblance to those observed in Refs. [6] and [11] for resonantly excited heavy hole excitons, it is important to note that their corresponding experiments were performed at room temperature, in contrast to the low-temperature measurements reported here. At 300 K the most significant contribution to exciton ionization comes from the exciton–longitudinal optical (LO) phonon interaction, which results in  $\sim 300$  and  $\sim 100$  fs ionization

times in GaAs/AlGaAs [6] and CdZnTe/ZnTe [11] MQWs, respectively. Identical experiments at 15 K on an unstrained MQW [6] show that the bleaching decay time is  $\sim 10$  ps, which is significantly different from the 0.5 ps value obtained from our measurements. Although the mechanism of this decay in uniaxially strained MQWs is not well understood at the present time, the explanation of this data may be related to the nature of the anisotropic excitonic phase space filling and the possible effects that it may have on both the Coulomb interaction between excitons and the exciton–acoustic phonon interaction.

In conclusion, we report the first observation of an ultrafast large-angle light polarization rotation resulting from optical non-linearities effected by the bleaching of the anisotropic excitonic absorption in a uniaxially strained MQW. Dynamic rotations as large as  $42^\circ$  have been measured for a compressive strain of  $\sim 0.2\%$ . An orientational dependence of the excitonic phase space filling on the direction of the pump polarization was observed which persists longer than the temporal overlap of the pump and probe pulses even for excitation densities exceeding  $10^{11} \text{ cm}^{-2}$  and decays with a time constant of 0.5 ps. The fact that the unpolarized probe transmission curves were independent of the orientation of the pump polarization suggests that this decay occurs by ionization of the excitons into free e–h pairs.

M. Wraback acknowledges the support of an NRC-EPSC research associateship. Y. Lu is supported by NSF-EPSC grant ECS-9216669.

## 1. References

- [1] J. Lee, C. Jagannath, M.O. Vassell and E.S. Koteles, *Phys. Rev. B* 37 (1988) 4164.
- [2] H. Shen, M. Wraback, J. Pamulapati, M. Dutta, P.G. Newman, A. Ballato and Y. Lu, *Appl. Phys. Lett.* 63 (1993) 2908.
- [3] H. Shen, M. Wraback, J. Pamulapati, P.G. Newman, M. Dutta, Y. Lu and H.C. Kuo, *Phys. Rev. B* 47 (1993) 13933.
- [4] E. Yablonovitch, T. Gmitter, T.J. Harbison and R. Bhat, *Appl. Phys. Lett.* 51 (1987) 2222.
- [5] D.E. Spence, P.N. Kean and W. Sibbett, *Opt. Lett.* 16 (1991) 42.
- [6] W.H. Knox, R.L. Fork, M.C. Downer, D.A.B. Miller, D.S. Chemla, C.V. Shank, A.C. Gossard and W. Wiegmann, *Phys. Rev. Lett.* 54 (1985) 1306.
- [7] S. Schmitt-Rink, D.S. Chemla and D.A.B. Miller, *Phys. Rev. B* 32 (1985) 6601.
- [8] M.T. Portella, J.-Y. Bigot, R.W. Schoenlein, J.E. Cunningham and C.V. Shank, *Appl. Phys. Lett.* 60 (1992) 2123.
- [9] J.L. Oudar, A. Migus, D. Hulin, G. Grillon, J. Etchepare and A. Antonetti, *Phys. Rev. Lett.* 53 (1984) 384.
- [10] R. Zimmerman, *Phys. Status Solidi (b)* 146 (1988) 371.
- [11] P.C. Becker, D. Lee, A.M. Johnson, A.G. Prosser, R.D. Feldman, R.F. Austin and R.E. Behringer, *Phys. Rev. Lett.* 68 (1992) 1876.

## Terahertz electromagnetic transients as probes of a two-dimensional electron gas

W.J. Walecki, D. Some, V.G. Kozlov, A.V. Nurmikko \*

*Division of Engineering and Department of Physics, Brown University, Providence, RI 02912, USA*

(Received 30 May 1993; accepted for publication 11 August 1993)

### Abstract

We demonstrate the application of terahertz electromagnetic transients to the study of the dynamical conductivity of a two-dimensional, high mobility electron gas in modulation doped GaAs quantum wells. The transient response of such an electron system on a picosecond time scale occurs in a regime where the implications of electron–electron interaction effects need to be considered.

### 1. Introduction

While the application of dc and low frequency measurements to a high mobility electron gas is routine, there is a notable absence of high speed, real-time techniques and experiments to observe directly dynamical conductivity effects on time scales which are short in terms of scattering from impurities, phonons, defects, etc. Femtosecond laser techniques have been used in the past three years to study the generation of “terahertz electromagnetic transients” off semiconductor surfaces [1,2], thereby producing a new possible source for such transient electron spectroscopy. The THz radiation propagates in the form of a well defined beam in free space so that the conductance of a free electron gas within a semiconductor heterostructure can be measured on a

timescale of  $10^{-12}$  s or less in a contactless way. In a transmission or reflection experiment, a gated ultrafast photoconductive receiver measures the radiation field. In this paper, we demonstrate that it is experimentally practical to employ the real-time THz probes to access an equilibrium electron gas in a semiconductor heterostructure at a low temperature and high magnetic field. We have conducted preliminary studies of the response of a 2D electron gas subject to picosecond transient electric fields in an n-type MQW GaAs/GaAlAs structure.

### 2. Experimental

The experimental arrangement is shown in Fig. 1a, where the THz components are very similar to that of Ref. [2]. The electromagnetic transients are generated by a biased microstrip antenna, gated by 300 fs pulses from a (frequency-doubled)

\* Corresponding author.



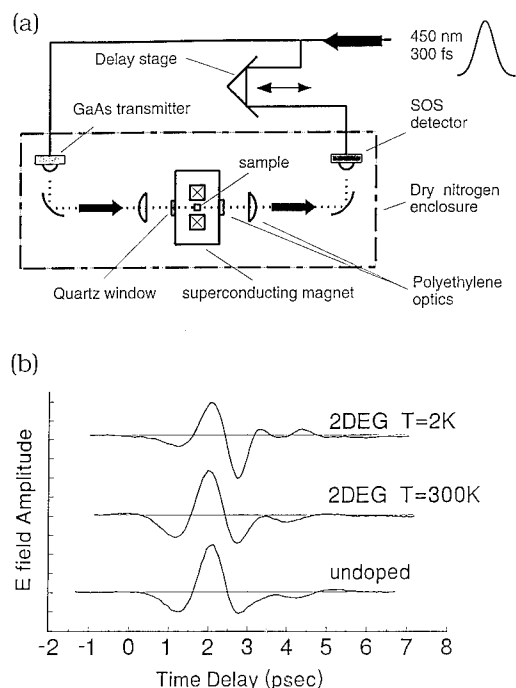


Fig. 1. (a) Experimental arrangement showing the THz transmitter and receiver, with the sample placed in the superconducting magnet cryostat. (b) Transmitted electric field transients through the semi-insulating GaAs control sample at  $T = 2$  K and the doped MQW sample containing the 2D electron gas (2DEG) at  $T = 2$  and 300 K. The curves have been displaced vertically for clarity; the zero amplitude base line is indicated.

sponding to an average flux of  $10^4$ – $10^5$  photons/cm<sup>2</sup> per pulse incident on the samples.

### 3. Results and discussion

The modulation-doped multiple quantum well (MQW) sample consisted of 84 wells of 100 Å individual thickness, with an electron density of  $n_s = 1.5 \times 10^{11}$  cm<sup>-2</sup> and a mobility of  $5 \times 10^5$  cm<sup>2</sup>/V · s, grown on a semi-insulating GaAs substrate and GaAs/AlAs superlattice buffer layer. Fig. 1b shows the comparison of the transmitted THz electric field through the MQW sample at  $T = 2$  and 300 K in comparison with a “control sample” of semi-insulating GaAs at  $T = 2$  K. Apart from a propagation delay, the shape of the THz pulse transmitted through the control sample is identical to that measured through the empty cryostat. Hence the influence of the 2D electron gas is to distort the shape of the transmitted field on the ps timescale in a manner which is directly related to the dynamical conductivity  $\sigma(t)$ . The effect is readily observed in our single beam transmission experiment without modulation techniques.

Fig. 2a shows the transmitted THz electric field as a function of perpendicular magnetic field to  $B_z = 5$  tesla at  $T = 2$  K for parallel incident and transmitted polarizations. Transport measurements verified the presence of strong quantum Hall plateaus in the transverse Hall resistivity  $\sigma_{xy}$  and sharp maxima in the longitudinal resistance  $\sigma_{xx}$ , consistent with results obtained earlier with this material [4]. With increasing magnetic field, the shape of the transmitted pulse reverts back to the form measured with the control sample in the lower portion of Fig. 1. Fig. 2a gives us an indication of the response by the 2D electron gas which is directly connected to the longitudinal “dynamical Hall conductivity”  $\sigma_{xx}(t, B)$ . For example, if one examines the changes in shape of the “trailing” portion of the transmitted pulse (in the time interval of approximately 2–3 ps), we see a clear cross-over behavior at about  $B = 2.4$  T. This coincides with the cyclotron frequency acquiring a value  $\omega_c = 1$  THz, i.e. approximately at the rolloff of our field am-

modelocked Ti:sapphire laser. This radiation is collimated by a high resistivity silicon lens and an off-axis parabolic reflector. The collimated beam passes a free standing wire grid polarizer and is subsequently focused inside a superconducting magnet onto a sample (with a spot size of approximately 6 mm). The transmitted pulse is recollimated, passed through a polarizing analyzer, and focused on a fast, optically gated photoconductive silicon-on-sapphire receiving antenna, similar to that described in Ref. [3]. Nitrogen purging of the experimental enclosure minimized the residual water vapor absorption. The crossed polarizer (power) extinction ratio was about  $4 \times 10^{-4}$ . The average power in the THz beam was measured by a bolometer to be approximately 1 nW, corre-

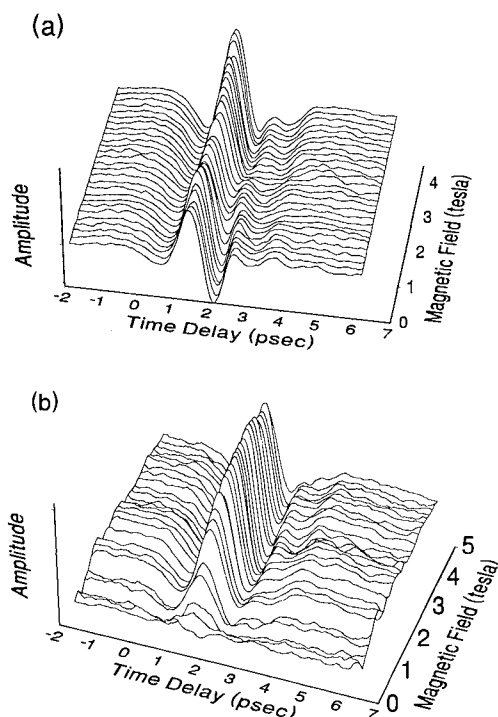


Fig. 2. Transmitted THz transients through the doped MQW sample at  $T = 2$  K as a function of the perpendicular magnetic field, (a) in parallel polarization, and (b) in crossed polarizer configuration.

plitude in frequency domain. The cross-over point is physically related to a transition from inter-Landau level excitations to intra-Landau level excitations.

Fig. 2b displays the contribution by the “transverse dynamical Hall conductivity”,  $\sigma_{xy}(t, B)$  to the transmitted electric field, measured as a function of the magnetic field in the crossed polarizer configuration. The transmitted zero field amplitude is unresolved from the system noise, but becomes readily observable in small fields ( $B < 1$  T) and increases strongly with increasing magnetic field. Overall, the behavior is similar to the classical Hall effect. Notably, the pronounced quantum Hall behavior, clearly identified in the dc transport measurements, is not present in the transient data.

Measurements in the Voigt configuration exhibited no change in the transmitted pulse until

$B = 5$  T, where the cyclotron diameter approaches the quantum well width.

The absence of quantum Hall behavior in the THz measurement is at least partially expected, considering the energetically large excitation regime accessed in our experiment. The electron excess energies  $\Delta E$  are comparable to or larger than the typical activation energies obtained from temperature dependent experiments in the integer QHE regime (1 THz is equivalent to  $T = 48$  K).

We will here only outline some of the arguments about the physical features which are connected with the observations in Figs. 1 and 2. The mean one-electron scattering time (as calculated from the dc mobility) for our sample at  $T = 2$  K is longer than the duration of the electromagnetic probing transients,  $\tau_{sc} \approx 10$  ps  $>$   $\tau_p$ . The transmitted pulses contain a contribution by the incident field itself plus the radiation term by the current induced within the electron gas:  $E_T = E_0 + E_{ind}$ . In linear response theory, the latter is directly related to the conductivity of the electron gas. Analysis of the zero field data in Fig. 1 (by time and frequency domain techniques) then shows a transient response of the electron gas occurring on a timescale of about 1 ps. Scattering involving ionized impurities does not have a frequency dependence which would be enhanced at higher frequencies. Similarly, our calculations about the role of acoustic phonon scattering in the present conditions show that these, too, are ineffective. Hence we are left to consider the role of electron–electron scattering in the data of Figs. 1 and 2.

The electron–electron (e–e) interaction within a 2D electron gas in zero magnetic field has been theoretically formulated by Giuliani and Quinn [5], as well as by Chapik [6]. In such a formulation, the energy dependence of the inelastic scattering rate is calculated for an electron with an excess energy  $\Delta E$  with respect to the Fermi energy (of a cold background gas). In our experiments the “white light” THz source has energy comparable to the Fermi energy of 2DEG ( $\Delta E \approx E_F = 5.2$  meV). The relaxation time of the excited electrons strongly decreases with the increasing energy of excitation. It has been demonstrated

both theoretically [5], and experimentally [7] that the electron–electron relaxation time may be approximated by:

$$\tau_{e-e} = \left\{ \frac{-E_F}{4\pi\hbar} \left( \frac{\Delta E}{E_F} \right)^2 \left[ \ln \left( \frac{\Delta E}{E_F} \right) - \frac{1}{2} \right. \right. \\ \left. \left. - \ln \left( 2 \frac{Q_{TF2}}{p_F} \right) \right] \right\}^{-1},$$

where  $\Delta E$  is the energy of the photon above Fermi sea,  $q_{TF2}$  is Thomas–Fermi screening wave vector in 2D,  $E_F$  is Fermi energy in our gas,  $p_F$  is Fermi wave vector on the surface of the Fermi sea.

Under these transient experimental conditions, dissipation of the excess electronic energy to reservoirs outside the electron system is not measured; thus the phase shift observed in our experiments in zero magnetic field must reflect a dynamical dephasing and phase-space redistribution processes occurring within approximately 1 ps in the 2D electron gas, in reasonable quantitative agreement with predictions in Ref. [8] for an average excess electron energy of 5 meV. At sufficiently high temperatures ( $T$  of 150 K), one returns to the normal dissipation-dominated scattering regime.

In conclusion, we have employed THz transient probes to show the feasibility of detecting

the dynamical response of a 2D electron gas on a timescale which the dc mobility would suggest to be shorter than the elastic scattering time. The intraband excitations are related to transient conductivity, observed under conditions in which effects of electron–electron interactions can be accessed.

This work was supported by National Science Foundation Grants DMR-9112329 and DMR-9121747. We wish to thank X.-C. Zhang and D. Auston for sharing their expertise with the THz techniques, and M. Shayegan and B. Goldberg for providing the samples.

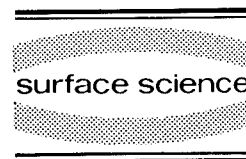
#### 4. References

- [1] Ch. Fattinger and D. Grischkowsky, *Appl. Phys. Lett.* 54 (1988) 490.
- [2] X.-C. Zhang, B.B. Hu, J.T. Darrow and D.H. Auston, *Appl. Phys. Lett.* 56 (1990) 1011.
- [3] M. van Exter, Ch. Fattinger and D. Grischkowsky, *Appl. Phys. Lett.* 55 (1989) 337.
- [4] M. Shayegan, J.K. Wang, M. Santos, T. Sajoto and B.B. Goldberg, *Appl. Phys. Lett.* 54 (1989) 27.
- [5] G.F. Giuliani and J.J. Quinn, *Phys. Rev. B* 26 (1982) 4421.
- [6] A.V. Chaplik, *Sov. Phys. JETP* 33 (1971) 997.
- [7] D.-S. Kim, J. Shah, J.E. Cunningham, T.C. Damen, S. Schmitt-Rink and W. Schafer, *Phys. Rev. Lett.* 68 (1992) 2838.



ELSEVIER

Surface Science 305 (1994) 247–250



## Raman scattering on modulation-doped quantum wells: intrinsic spin splitting of the GaAs conduction band

B. Jusserand <sup>\*,a</sup>, D. Richards <sup>b</sup>, H. Peric <sup>a</sup>, B. Etienne <sup>c</sup>

<sup>a</sup> France Télécom / CNET / Paris-B, Laboratoire de Bagneux, 196 Avenue Henri Ravera, 92220 Bagneux, France

<sup>b</sup> Cavendish Laboratory, Madingley Road, Cambridge CB3 0HE, UK

<sup>c</sup> CNRS, L2M, 196 Avenue Henri Ravera, 92220 Bagneux, France

(Received 22 April 1993; accepted for publication 30 August 1993)

### Abstract

The spin splitting of the conduction band in GaAs is directly observed through the splitting of the intrasubband electronic Raman spectra. Its dependence on the magnitude and orientation of the wavevector is discussed in terms of a simple band structure model.

Due to the lack of inversion symmetry, the lowest conduction band of zincblende compounds is no longer spin degenerate, but a spin-orbit coupling appears, leading to the following additional term in the conduction band energy [1]:

$$E_s = \pm \gamma \left[ k^2 (k_x^2 k_y^2 + k_y^2 k_z^2 + k_z^2 k_x^2) - 9k_x^2 k_y^2 k_z^2 \right]^{1/2}. \quad (1)$$

This term is proportional to  $k^3$  and displays a strong angular anisotropy. The material-dependent coefficient  $\gamma$  has to be determined from experiment or band structure calculations. However, being very small, this splitting has never been observed directly until recently [2]. Extensive indirect evidence has been obtained from depolarization measurements of luminescence [3] or photoemission [4] after optical pumping. This

change in polarization results from the spin precession, induced by the additional  $k^3$  term in the conduction band, the corresponding splitting being neglected with respect to the elastic broadening. These experiments provided consistent determinations of the coefficient  $\gamma$ , ranging between 20 and 25 eV Å<sup>3</sup>, in reasonable agreement with theoretical calculations [5].

Spin precession has also been measured in GaAs based two-dimensional systems either by optical pumping [6] or very recently from anti-weak-localization measurements on modulation-doped heterojunctions [7]. On the other hand, beating of the magnetoresistance due to the slight density difference between the two occupied spin-subbands has never been observed in GaAs, contrary to other systems [8]. The aim of these studies was to investigate the effect of confinement on the spin splitting. This problem was also considered theoretically in Ref. [9], where the intrinsic term due to the confinement was shown to strongly dominate over the Rashba term [10]

\* Corresponding author.

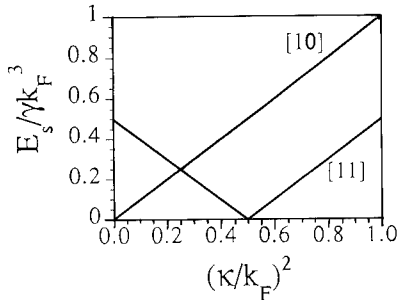


Fig. 1. Dependence on the confinement of the spin splitting along [10] and [11] directions in 2D reciprocal space.

due to the self-consistent electric field. This intrinsic term can be deduced in lowest order in perturbation by replacing in the 3D Hamiltonian  $k_z$  and  $k_z^2$  by the average values 0 and  $\kappa^2$  of the associated operators on the lowest conduction subband wavefunction:

$$E_s = \pm \gamma [\kappa^4 k_{\parallel}^2 - (4\kappa^2 - k_{\parallel}^2) k_x^2 k_y^2]^{1/2}. \quad (2)$$

As in the bulk, the spin splitting displays a large anisotropy, which now depends on the confinement through the parameter  $\kappa$ , as illustrated on Fig. 1. The angular behavior transforms from 3D ( $\kappa = 0$ ) to 2D ( $\kappa \rightarrow \infty$ ) with negligible anisotropy. The corresponding wavevector dependences are cubic and linear, respectively, thus resulting in  $n_s^{3/2}$  and  $n_s^{1/2}$  dependences in modulation-doped heterostructures. In Ref. [7], a 3D behavior, which is very surprising owing to the shape of the confinement potential, was deduced from magneto-transport measurements on samples with different densities.

In this paper we demonstrate that electronic Raman scattering is a particularly powerful technique to study the conduction band spin splitting in GaAs heterostructures. It displays the unique feature, as compared to other methods, that only electron states are probed with magnitude and orientation of the wavevector fixed by the design of the sample and the geometry of the experimental setup, respectively. This allowed us to obtain recently the first spectroscopic evidence of well resolved spin-split conduction bands in GaAs in the absence of any applied magnetic field; we separately observed single-particle Raman scat-

tering by spin-conserving and spin-flipping intra-subband transitions separated by an energy significantly larger than the elastic broadening of the involved states. In this communication, we quantitatively analyze these results and compare them with the predictions of Eq. (2). Furthermore, we show that Raman scattering uniquely provides the angular dependence of the splitting by turning the sample with respect to the scattering plane. The results give new direct insight into the spin-splitting energies in quantum wells.

The structure under investigation is a modulation-doped GaAs quantum well grown by molecular beam epitaxy on a semi-insulating GaAs substrate. Modulation doping of the 180 Å thick well is obtained from Si delta-doping in the top barrier only. Due to the thin spacer layer (100 Å), the electron density reaches  $1.3 \times 10^{12} \text{ cm}^{-2}$  under illumination. The form of the self-consistent electrostatic potential is very similar to that in a heterojunction but the second subband is located above the Fermi energy because of the quantum well confinement. Raman scattering measurements were taken at liquid helium temperature close to the  $E_0$  resonance of the GaAs quantum well, with the polarizations of the incident and scattered light both crossed and parallel, to give depolarized and polarized spectra, respectively. Owing to the symmetry of the GaAs valence band, excitations involving spin-orbit coupling can cause depolarized Raman scattering, while spin-conserving single particle excitations (SPE), allowed in parallel polarization, should be completely screened out due to Coulomb interaction and replaced by the collective plasmon excitations.

We observe both SPE and a plasmon with parallel polarizations, contrary to theoretical expectations. These assignments are supported by Raman measurements at various angles of the sample surface normal with respect to the incident and scattered wavevectors. This allows us to probe excitations in the electron gas with different in-plane wavevectors. As shown in Fig. 2, the observed linear and almost square-root dispersions are in quantitative agreement with the theoretical ones, respectively, for SPE and plasmon excitations of a 2DEG of density  $1.3 \times 10^{12} \text{ cm}^{-2}$ ,

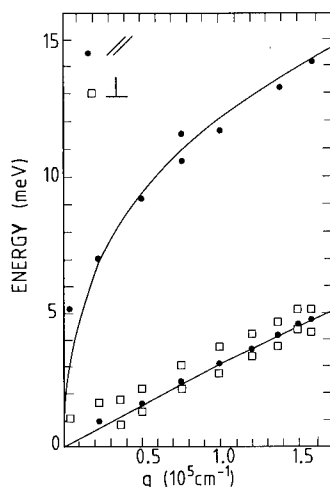


Fig. 2. Dispersion curves of the excitations observed in both polarizations compared with theoretical ones for the plasmon and SPE peaks.

taking into account the dielectric corrections due to the surface. Such an absence of screening has already been observed for inter-subband spectra on the same sample [11] and other quantum wells [12]. It has often been reported on bulk GaAs [13] and its origin is not yet clear. It could be due to an additional Raman process taking place at strong resonance or, in quantum wells, to disorder effects on the intermediate hole states which are confined at the rough interface by the electrostatic potential [11].

Moreover, the low-energy single-particle band splits into two components in the crossed polarization spectra (see Fig. 2 of Ref. [2]). These spectra display linear dispersions parallel to that obtained in parallel polarization. As illustrated schematically in Fig. 3, such observations are well

explained to be a consequence of the conduction band spin splitting. Let us recall that the peak of the intrasubband SPE corresponds to transitions originating from occupied states with a wavevector around  $k_0 = k_F(q/|q|)$ . The associated energy amounts to  $\hbar q v_F$  for spin-conserving and  $\hbar q v_F \pm E_S$  for spin-flip transitions. In these expressions,  $E_S$  is the spin splitting at the well defined wavevector  $k_0$ . We extract a typical value of 0.4 meV for this quantity, while the elastic broadening we deduce from a lineshape analysis amounts to 0.15 meV. We thus get clear evidence in this sample of well resolved spin-split states at low temperature, in contrast to previous reports [3,4,6]. This was possible due to the specific features of our Raman probe and to the modulation doping, which provided a large density with a high mobility.

To compare our experimental results with the predictions of Eq. (2), we need independently determined or fitted values of  $\gamma$  and  $\kappa$ . The latter parameter can be deduced from self-consistent band structure calculations [13] and amounts to  $1.85 \times 10^6 \text{ cm}^{-1}$  in our sample. Using this value, we are able to fit the dispersion curves of Fig. 2 taking  $23.5 \text{ eV \AA}^3$  for  $\gamma$ , in excellent agreement with previous determinations. This clearly demonstrates the validity of our interpretation of this new intra-subband Raman signal in terms of a spin-split conduction band. However, when considering Fig. 1, one realizes that the *anisotropy* of the spin splitting is a very stringent test of the model, as it should strongly vary as a function of the ratio  $\kappa/k_F$ . In our sample, this quantity amounts to around 0.65 and the splitting should significantly decrease when going from the [01] to

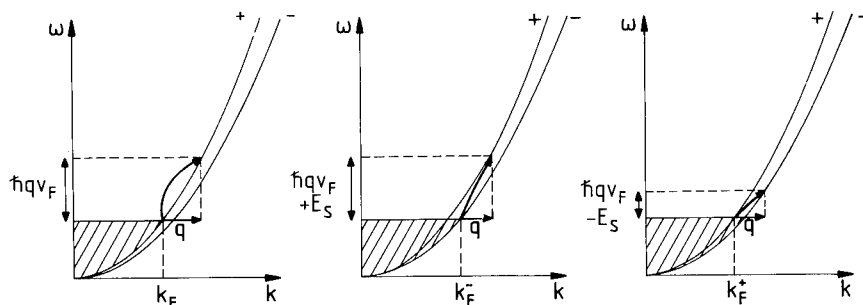


Fig. 3. Schematic representation of the different SPE processes observed by Raman scattering.

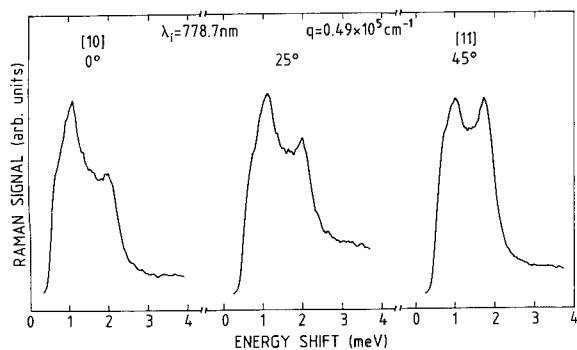


Fig. 4. Depolarized spectra of spin-flip SPE for the same in-plane wavevector along three orientations.

the [11] orientation. This prediction does not agree very well with preliminary experimental results we obtained from different pieces of the same sample fixed side by side at different angles. As shown in Fig. 4, the splitting is only weakly angle-dependent while the overall shape of the SPE spectrum is changing. This result can be reproduced in the framework of our model by fitting simultaneously  $\gamma$  to  $34.5 \text{ eV } \text{\AA}^3$  and  $\kappa$  to  $1.55 \times 10^6 \text{ cm}^{-1}$ . These values are somewhat surprising, however, and lead us to suspect some insufficiencies in the simple model we have presented. Further insight into this problem should be obtained in the near future from additional experiments, including a detailed angular dependence, on samples with different densities.

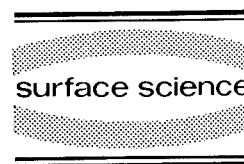
## 1. References

- [1] G.F. Dresselhaus, Phys. Rev. 100 (1955) 580.
- [2] B. Jusserand, D. Richards, H. Peric and B. Etienne, Phys. Rev. Lett. 69 (1992) 848.
- [3] F. Maier and B. Zakharchenya, Eds., Optical Orientation (North-Holland, Amsterdam, 1984).
- [4] H. Riechert, H.J. Drouhin and C. Hermann, Phys. Rev. B 38 (1988) 4136.
- [5] M. Cardona, N.E. Christensen and G. Fasol, Phys. Rev. B 38 (1988) 1806.
- [6] J. Bandet, G. Bacquet, F. Fabre, J. Frandon, R. Planel and G. Le Roux, J. Appl. Phys. 69 (1991) 2532.
- [7] P.D. Dresselhaus, C.M.A. Papavassiliou, R.G. Wheeler and R.N. Sacks, Phys. Rev. Lett. 68 (1992) 106.
- [8] B. Das, D.C. Miller, S. Datta, R. Reifengerger, W.P. Hong, P.K. Bhattacharya, J. Singh and M. Jaffe, Phys. Rev. B 39 (1989) 1411.
- [9] F. Malcher, G. Lommer and U. Rössler, Superlattices Microstruct. 2 (1986) 267.
- [10] Y.A. Bychkov and E.I. Rashba, J. Phys. C 17 (1984) 6039.
- [11] H. Peric, B. Jusserand, D.R. Richards and B. Etienne, Phys. Rev. B, in press.
- [12] A. Pinczuk, S. Schmitt-Rink, G. Danan, J.P. Valladares, L.N. Pfeiffer and K.W. West, Phys. Rev. Lett. 63 (1989) 1633; D. Gammon, B.V. Shanabrook, J.C. Ryan, D.S. Katzer and M.J. Yang, Phys. Rev. Lett. 68 (1992) 1884.
- [13] M.V. Klein, in: Light Scattering in Solids, Ed. M. Cardona (Springer, Heidelberg, 1975) p. 147.
- [14] U. Ekenberg and D.R. Richards, in: Proc. 20th Int. Conf. on the Physics of Semiconductors, Eds. E.M. Anastasakis and J.D. Joannopoulos (World Scientific, Singapore, 1990) p. 1009.



ELSEVIER

Surface Science 305 (1994) 251–255



## Optical measurements of warped valence bands in quantum wells

J.A. Kash <sup>\*,a</sup>, M. Zachau <sup>a</sup>, M.A. Tischler <sup>a</sup>, U. Ekenberg <sup>b</sup>

<sup>a</sup> IBM Research Division, T.J. Watson Research Center, Yorktown Heights, NY 10598, USA

<sup>b</sup> Department of Theoretical Physics, Royal Institute of Technology, S-10044 Stockholm, Sweden

(Received 25 May 1993; accepted for publication 3 June 1993)

### Abstract

The valence subband dispersion of GaAs/AlGaAs quantum wells, including warping, is measured with meV accuracy using the radiative recombination of hot electrons at neutral acceptors. The measurements are shown to be in excellent agreement with  $\mathbf{k} \cdot \mathbf{p}$  calculations. Differences in calculated dispersions from using various sets of Luttinger parameters proposed in the literature are discussed.

The structure of the conduction subbands in quantum wells is relatively simple. For the valence subbands, however, the structure is more complex due to the combined effects of the spin–orbit interaction and the symmetry breaking of the quantum well potential. Experimentally, recent magnetotransport measurements in double barrier tunneling structures [1–3] have demonstrated the ability to qualitatively show the dispersion of subbands in quantum wells. However, these experiments are not sufficiently quantitative to allow direct comparison with  $\mathbf{k} \cdot \mathbf{p}$  calculations. Also, while the anisotropy (warping) of the valence subbands is well established theoretically [4], experimental information [2,3] is scarce and only qualitative.

The recombination of hot electrons at neutral acceptors [5] gives a photoluminescence (PL) spectrum which contains great spectroscopic de-

tail. As indicated schematically in Fig. 1, the energies  $E_e(\mathbf{k})$  and  $E_h(\mathbf{k})$  of the hot electron and hole created by the laser photon can be determined [6,7] from energy conservation as

$$E_e(\mathbf{k}) = \hbar\omega_{\text{PL}} - E_G + E_A \quad (1)$$

and

$$E_h(\mathbf{k}) = \hbar\omega_L - \hbar\omega_{\text{PL}} - E_A. \quad (2)$$

with the terms defined in the caption to Fig. 1. The hot electron and hole have essentially the same wavevector  $\mathbf{k}$ , which can be determined from  $E_e(\mathbf{k})$  using a straightforward calculation [7] of the nearly parabolic and circular  $\Gamma$  valley conduction subband dispersion. In this way, a single point on the valence subband dispersion is determined. By measuring  $\hbar\omega_{\text{PL}}$  as a function of  $\hbar\omega_L$ , the dispersion of the valence subband is mapped out [7].

The polarization dependent matrix elements for the recombination of hot electrons at neutral acceptors [5] can be used to obtain direct information on the valence subband anisotropy [8]. In

\* Corresponding author.



a backscattering geometry, with the laser incident perpendicular to the surface of a  $\langle 001 \rangle$  oriented quantum well, define  $I_{\parallel}$  and  $I_{\perp}$  as the intensity of the hot PL emitted with electric field  $\mathcal{E}_{\text{PL}}$  polarized parallel or perpendicular to the electric field of the laser  $\mathcal{E}_{\text{L}}$ , respectively. Then, one can show [8] that for a pure heavy hole state ( $J = 3/2$ ,  $m_J = \pm 3/2$ ) of in-plane wavevector  $k$

$$I_{\parallel}(k) - I_{\perp}(k) \propto \cos^2(2\phi), \quad (3)$$

where  $\phi$  is the angle between  $\mathcal{E}_{\text{L}}$  and  $k$ . In deriving Eq. (3), we have summed over all equivalent directions  $\pm(\phi + n\pi/2)$ ,  $n = 0, 1, 2, 3$ . A pure light hole state ( $J = 3/2$ ,  $m_J = \pm 1/2$ ) is governed by the same polarization selection rule, except for a change of sign.

Experimentally, the luminescence is measured in two geometries:  $\mathcal{E}_{\text{L}}$  is either along a  $\langle 100 \rangle$  crystal axis (i.e. a  $\langle 10 \rangle$  quantum well axis) or along a  $\langle 110 \rangle$  crystal axis (i.e. a  $\langle 11 \rangle$  quantum well axis). For each geometry we measure the difference spectrum  $I_{\parallel}^{\text{M}} - I_{\perp}^{\text{M}}$ . The measured

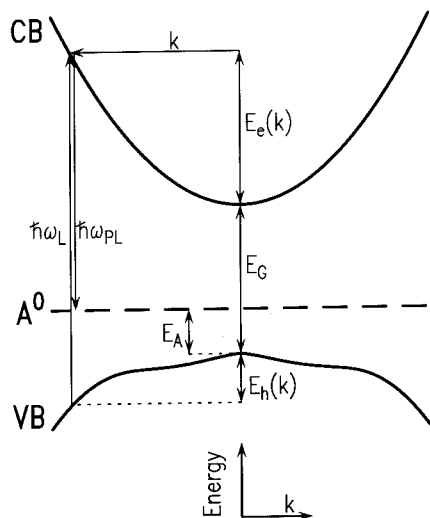


Fig. 1. Schematic of spectroscopy using the recombination of hot electrons at neutral acceptors. CB and VB refer to arbitrary conduction and valence bands, while  $A^0$  is the neutral acceptor level.  $E_e$  and  $E_h$  are the energies of the hot electron and the hot hole of in-plane wavevector  $k$ ,  $E_G$  and  $E_A$  are the band gap and acceptor binding energy,  $\hbar\omega_L$  is the laser energy, and  $\hbar\omega_{\text{PL}}$  is the energy of the hot luminescence peak.

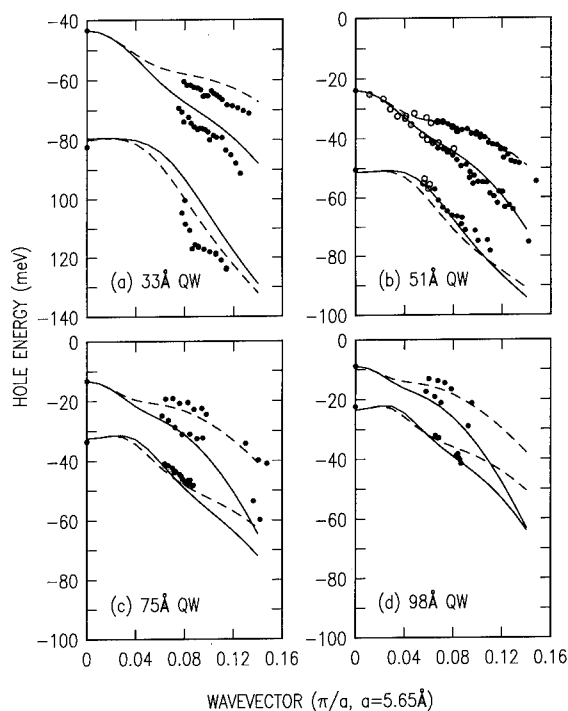


Fig. 2. Measured (points) and calculated (lines) valence band dispersions for the quantum well samples listed in Table 1. Data are derived for the lowest energy heavy and light hole bands, with the calculations for the  $[10]$  direction of in-plane momentum shown as solid lines and the  $[11]$  direction shown as dashed lines. In (b), the solid points are from the conventional quantum well sample, while the open circles are from the coupled well sample. For the calculations, the Luttinger parameters of GaAs are taken from Binggeli and Baldereschi [10].

spectrum contains contributions from hot carriers with all directions of in-plane wavevector, with each direction weighted by Eq. (3). If anisotropy is present in the bands, then different directions of  $k$  will correspond to different values of  $E_e$  and  $E_h$  for a fixed laser energy. From Eq. (3), when  $\mathcal{E}_{\text{L}}$  is parallel to a  $\langle 10 \rangle$  quantum well direction, then  $I_{\parallel}^{\text{M}} - I_{\perp}^{\text{M}}$  has no contribution from carriers in  $\langle 11 \rangle$  directions, and a maximum contribution from carriers in  $[10]$  directions. The reverse is true in the other geometry, where  $\mathcal{E}_{\text{L}} \parallel \langle 11 \rangle$ . A simultaneous lineshape fit [8] of the two difference spectra yields the quantum well dispersion in the  $\langle 10 \rangle$  and  $\langle 11 \rangle$  directions.

Table 1  
GaAs/Al<sub>x</sub>Ga<sub>1-x</sub>As p-doped multiple quantum well samples

Well Width (nm)	Barrier aluminum content $x$	Barrier thickness (nm)	Number of periods	Be-doping (cm <sup>-3</sup> )
9.8	0.38	10.2	100	$3 \times 10^{17}$
7.5	0.32	14.2	30	$2 \times 10^{18}$
5.1	0.315	10.3	100	$10^{18}$
5.1 <sup>a</sup>	0.315	10.3	50	$10^{18}$
3.3	0.325	9.9	100	$10^{18}$

Each well is Be-doped in the central 1.0 nm (3.5 nm for the 9.8 nm wells) at the indicated concentration. In the coupled well sample, the 15.3 nm well is not doped. All samples were grown by molecular beam epitaxy.

<sup>a</sup> Each 5.1 nm well is coupled to a 15.3 nm undoped well by a 2.6 nm Al<sub>0.315</sub>Ga<sub>0.685</sub>As barrier.

The valence band dispersion determined with these experiments is shown in Fig. 2 for quantum wells ranging in width from 3.3 to 9.8 nm, where the well widths and barrier aluminum concentration, listed in Table 1, are determined to an accuracy of 0.1 nm and 1% using X-ray rocking curves and confirmed with electron microprobe measurements and photoluminescence. The splitting between the heavy and light hole bands at  $k = 0$  is determined by conventional photoluminescence excitation measurements. A significant anisotropy is seen for the heavy hole bands. For the light hole bands, no anisotropy was observed, suggesting that the actual anisotropy is less than a few meV.

The band edge luminescence of quantum wells is typically six orders of magnitude stronger than the hot luminescence. This strong band edge emission limits the ability to measure the hot luminescence to those electrons which are well above the conduction band minimum. The lack of data at small wavevectors in Figs. 2a, 2c and 2d is due to this limitation. To obtain the data shown as open circles at small wavevector in Fig. 2b, a coupled quantum well sample was grown as a companion to the conventional 5.1 nm well. In the companion sample, each 5.1 nm Be-doped well is weakly coupled to a 15.3 nm undoped well through a 2.6 nm Al<sub>0.315</sub>Ga<sub>0.685</sub>As barrier. The band edge luminescence from the 5.1 nm well is thereby suppressed about 4 orders of magnitude

by tunneling of the carriers into the wider well. The hot PL is not affected by the tunneling, since it is emitted on a much shorter ( $\sim 100$  fs) timescale. Thus the hot PL can be measured to much lower energies, mapping the dispersion at small  $k$ . As seen in Fig. 2b, measurements were obtained from both samples at  $k = 0$  and in the region  $k \approx 0.07\pi/a$ . These measurements gave essentially the same results, confirming that the weak coupling to the 15.3 nm well does not measurably affect the dispersion of the 5.1 nm well.

Random errors in the dispersion measurements come mainly from the inability to exactly determine the peak energy of the typically 10 meV wide hot luminescence peaks. These random errors are about 1.5 meV. There are three main sources of systematic error. The first is errors in the determinations of  $E_G$  and  $E_A$ , while the second is from the calculated conduction band dispersion. These determinations and calculations are discussed elsewhere [7], and are shown to produce at most a  $\pm 2$  meV error in the hole energy and a  $\pm 5\%$  error in the wavevector. The systematic error may be slightly larger for the narrowest quantum well studied (3.3 nm), where the broad exciton features of the photoluminescence excitation spectrum did not allow an experimental determination of the exciton binding energy. An accurate calculation of the 2s-to-continuum energy of the acceptor [9], which is needed for the determination of  $E_A$ , is also not available for the 3.3 nm well. The third source of systematic error is introduced by the lineshape fitting procedure [8]. Because two spectra are simultaneously fit, the obtained dispersions are insensitive to the details of the fit and an error of only about 0.5 meV is introduced. This is the only significant systematic error in the determination of the anisotropy, as the other errors rigidly shift the  $\langle 11 \rangle$  and  $\langle 10 \rangle$  directions together.

Because of the accuracy of this experimental determination, it is now possible to make a detailed comparison with  $\mathbf{k} \cdot \mathbf{p}$  calculations [4] of the valence band dispersion in GaAs/AlGaAs quantum wells. Such a comparison is shown in Fig. 2. In agreement with theoretical expectations, the measurements show that the heavy hole subband

in the  $\langle 10 \rangle$  directions is more dispersive than in the  $\langle 11 \rangle$  directions. The inability to observe warping of the light hole subbands is also consistent with the calculations. Substantial non-parabolicity is seen in both the data and the calculation. The measurements at small  $k$  demonstrate the inflection of the heavy hole band at  $k \approx 0.04\pi/a$  which results from interaction with the light hole band. It is also evident that the light hole band must have a large and probably negative mass near  $k = 0$ . Overall, the quantitative agreement is quite good. For the 3.3 nm quantum well, the agreement is greatly improved if one assumes a 3 meV larger value for  $E_A$ . As discussed above,  $E_A$  is subject to a larger error for this sample than for the wider wells.

For the calculations shown in Fig. 2, the values for the Luttinger parameters in GaAs are those suggested in the recent analysis of acceptor spectra by Binggeli and Baldereschi [10]. For  $\text{Al}_x\text{Ga}_{1-x}\text{As}$ , Luttinger parameters were derived from a linear interpolation between these values and those for AlAs as suggested by the calculations of E. Hess et al. [11]. The bandgap of  $\text{Al}_x\text{Ga}_{1-x}\text{As}$  is taken as  $1.519 + 1.445x$  eV, with 35% of the bandgap discontinuity occurring in the valence band. Except for the 3.3 nm well, the heavy and light hole confinement energies are much less than the barrier height and very little of the hole wavefunction is present in the barrier. Then, the influence of band gap discontinuity and the Luttinger parameters of  $\text{Al}_x\text{Ga}_{1-x}\text{As}$  on the valence band dispersions is small, and we can compare the effects of various other choices [12–15] for the Luttinger parameters of GaAs. Such a comparison is shown in Fig. 3. Examination of this figure, and analogous figures for the other samples, shows that the calculated differences using the various Luttinger parameters is typically only a few meV. Although these differences are small, some conclusions may still be drawn about the various sets of parameters. Consistently, the parameters of K. Hess et al. [12] and Binggeli and Baldereschi [10] give results for the heavy hole anisotropy which are in agreement with the measurements. Those of Shanabrook et al. [14] and Skolnick et al. [13] consistently underestimate the anisotropy. (The Luttinger parameters proposed

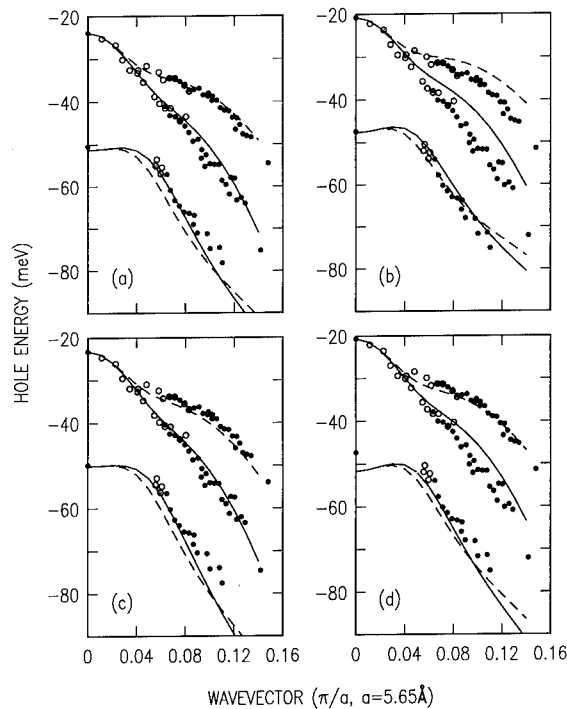


Fig. 3. The effect of varying the Luttinger parameters of GaAs on the calculated dispersion of the 5.1 nm quantum wells. The data in all cases are the same as Fig. 2b, rigidly shifted to match the calculated heavy hole confinement energy at  $k = 0$ . (a) is the same calculation as Fig. 2b. (b) uses the Luttinger parameters of K. Hess et al. [12], (c) uses those of Shanabrook et al. [14], and (d) those of Skolnick et al. [13].

by Molenkamp et al. [15] are essentially the same as those of Shanabrook et al.) The systematic errors in the measurement of the anisotropy are, as discussed above, less than 1 meV. In bulk GaAs, and by extension in  $\text{GaAs}/\text{Al}_x\text{Ga}_{1-x}\text{As}$  quantum wells, the magnitude of the anisotropy is governed by the Luttinger parameters  $\gamma_2$  and  $\gamma_3$  through the value [14] of  $C^2 = 3(\gamma_3^2 - \gamma_2^2)$ . The value of  $C^2$  is significantly larger for K. Hess et al. and Binggeli and Baldereschi than it is for Shanabrook et al. and especially Skolnick et al. Based on the present results, we can say that the larger anisotropy is correct. In addition, the parameters of Skolnick et al. consistently give too large a splitting of heavy and light holes at  $k = 0$ , while the other sets of Luttinger parameters give results within about 2 meV of the measured split-

tings. We have also investigated the effects of changing the valence band offset in the calculations. We find that it has little effect on the calculated dispersions other than to change the splitting of heavy and light holes.

In summary, these optical measurements of valence band dispersions provide meV accuracy and therefore allow detailed comparison with calculated band structure of quantum wells. The main features of the calculations, such as the interaction between heavy and light hole bands and the significant anisotropy of the heavy hole band, are seen in the measurements. Overall, the Luttinger parameters proposed by Binggeli and Baldereschi [10] give the most consistent quantitative agreement with the measurements.

Finally, it is interesting to note that, while none of the hot hole states in the quantum wells examined here are within the valence band of the  $\text{Al}_x\text{Ga}_{1-x}\text{As}$  barriers, the highest energy hot electron states in the quantum wells exceed the conduction band minima of the barriers by more than 70 meV. No unusual broadening or other changes were noted in the luminescence spectra as the conduction band minimum of the barrier was crossed. Thus, these high kinetic energy electron states remain confined to the quantum well even for  $k$ -values large enough that the electron energy is above the  $k = 0$  conduction band energy of the barriers.

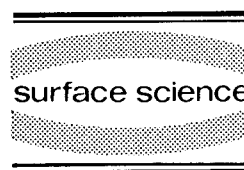
## 1. References

- [1] R.K. Hayden, D.K. Maude, L. Eaves, E.C. Valadares, M. Henini, F.W. Sheard, O.H. Hughes, J.C. Portal and L. Cury, *Phys. Rev. Lett.* 66 (1991) 1749.
- [2] U. Gennser, V.P. Kesan, D.A. Syphers, T.P. Smith III, S.S. Iyer and E.S. Yang, *Phys. Rev. Lett.* 67 (1991) 3828.
- [3] R.K. Hayden, L. Eaves, M. Henini, T. Takamasu, N. Miura and U. Ekenberg, *Appl. Phys. Lett.* 61 (1992) 84.
- [4] U. Ekenberg, W. Batty and E.P. O'Reilly, *J. Phys. (Colloq.)* 48-C5 (1987) 553.
- [5] B.P. Zakharchenya, D.N. Mirlin, V.I. Perel and I.I. Reshina, *Sov. Phys. Usp.* 25 (1982) 143.
- [6] G. Fasol and H.P. Hughes, *Phys. Rev. B* 33 (1986) 2953.
- [7] M. Zachau, J.A. Kash and W.T. Masselink, *Phys. Rev. B* 44 (1991) 4048.
- [8] J.A. Kash, M. Zachau, M.A. Tischler and U. Ekenberg, *Phys. Rev. Lett.* 69 (1992) 2260.
- [9] S. Fraizzoli and A. Pasquarello, *Phys. Rev. B* 42 (1990) 5349.
- [10] N. Binggeli and A. Baldereschi, *Phys. Rev. B* 43 (1991) 14734.
- [11] E. Hess, I. Topol, K.R. Schulze, H. Neumann and K. Unger, *Phys. Status Solidi (B)* 55 (1973) 187.
- [12] K. Hess, D. Bimberg, N.O. Lipari, J.U. Fischbach and M. Altarelli, *Proceedings of the 13th International Conference on the Physics of Semiconductors* (1976) 142.
- [13] M.S. Skolnick, A.K. Jain, R.A. Stradling, J. Leotin, J.C. Ousset and S. Askenazy, *J. Phys. C* 9 (1976) 2809.
- [14] B.V. Shanabrook, O.J. Glembocki, D.A. Broido and W.I. Wang, *Phys. Rev. B* 39 (1989) 3411.
- [15] L.W. Molenkamp, R. Eppenga, G. W. 't Hooft, P. Dawson, C. T. Foxon and K. J. Moore, *Phys. Rev. B* 38 (1988) 4314.



ELSEVIER

Surface Science 305 (1994) 256–262



# Exciton spin dynamics and polarized luminescence in quantum wells

M.Z. Maialle \*, L.J. Sham

*Department of Physics, University of California, San Diego, La Jolla, CA 92093-0350, USA*

(Received 21 April 1993; accepted for publication 22 June 1993)

## Abstract

The time evolution of the polarized luminescence is used to provide a better understanding of the relaxation processes of excitons in quantum wells. We established and solved a coupled set of rate equations for the exciton spin populations in which the spin relaxation mechanisms include the exchange interaction and individual spin-flip of the electrons and holes. A time-dependent energy distribution for the excitons is used to account for the thermalization effect. The dependence of the exchange-driven channel on a longitudinal electric field is shown to be useful in determining its relative importance among various competing spin relaxation channels.

## 1. Introduction

The exciton spin dynamics in quantum wells have been the subject of intense research in recent years, stimulated by advances in ultra-fast laser spectroscopy [1–5]. Since great accuracy in time resolution is obtained, it has been possible now to differentiate between different processes which affect the exciton relaxation before its recombination. For instance, it has been observed [2] that exciton–phonon interaction strongly changes the time dependence of the luminescence intensity giving rise to what is known as the thermalization effects. In part, this process is also responsible for the long lifetimes observed for excitons in confined systems [6], masking the fast

intrinsic recombination processes theoretically predicted [7] from the studies of exciton–photon interaction in these same systems which would occur in the initial stages of the exciton relaxation.

The spin relaxation processes of the excitons are an integral part of the information that needs to be incorporated for a detailed understanding of the exciton dynamics. The use of polarized light in time-resolved experiments makes possible a comprehensive analysis of the exciton dynamics including a proper treatment of the spin variables. Most of the attempts [3,8,9] to understand the spin dynamics of excitons have been based on results obtained from theories that are specifically, and to certain degree successfully, applied to the case where only single-particle spin-flip, either for electrons or holes in doped quantum wells, is considered [10–12]. The excitonic effect has only been qualitatively discussed and its im-

\* Corresponding author.

portance has been clearly evident from experiments in undoped quantum wells [3,8,13].

The purpose of this paper is to present a theoretical study of the time dependence of the polarized luminescence, clarifying some aspects that may be useful in the analysis of future experiments on the exciton spin dynamics. Various relaxation mechanisms are treated using a rate equation approach to determine the time evolution of the exciton spin populations in quantum wells. A brief review of each mechanism is given and emphasis is placed on the spin relaxation channel driven by the exchange interaction, where the use of a longitudinal electric field is also investigated in order to access the relative importance of this interaction in the spin relaxation process. A microscopic theory of the spin relaxation involving exchange was given in Ref. [14] and a preliminary study was initiated there on the competition between exchange and single-particle spin-flip processes. In this paper, the recombination and thermalization processes are treated on an equal footing with the spin relaxation processes, because they also influence the physical picture of the time evolution of the polarized luminescence.

## 2. The relaxation processes

Consider an undoped quantum well being pumped by a pulse of light propagating along its growth direction (call it the  $z$ -direction). Since we are mainly concerned with excitonic effects, we assume a resonant condition in which only the lowest energy heavy-hole exciton states (hhe) are excited. Although this excitation is a special case, it has been the one that most clearly showed [3,8] the importance of relaxation processes which occur more generally and which we wish to investigate in this paper. Here, the spin states in question are those for the hhe, i.e.  $|\pm 2\rangle$  and  $|\pm 1\rangle$ , as shown in Fig. 1. If the initial pump has a positive circular polarization, then angular momentum conservation dictates that a  $|+1\rangle$  spin population is created. The relaxation processes that follow this initial excitation will determine the population of other spin states, as well as the changes in

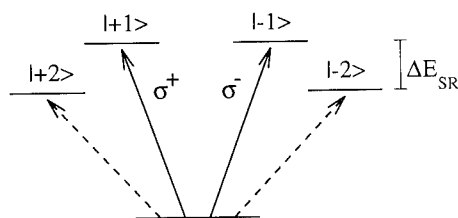


Fig. 1. The energy levels of the ground-state hhe is shown. The energy splitting  $\Delta E_{SR}$  is due to the short-range exchange (see Ref. [14]). The spins are written as  $|\sigma_e + j_h\rangle$ , e.g.  $|+2\rangle = |+\frac{1}{2}, +\frac{3}{2}\rangle$ . Dashed lines indicate forbidden transitions to the dark states.

the distribution of the exciton center-of-mass kinetic energy,  $E$ . Let us define the vector  $N(E) = (N_{+2}, N_{+1}, N_{-1}, N_{-2})$  as the exciton population density at energy  $E$ , whose components specify different spin populations.

The exciton relaxation can be described by a rate equation in the form

$$\frac{dN(E)}{dT} = \int dE' M(E, E') \cdot N(E'), \quad (1)$$

where in the matrix  $M$  are the relaxation processes that affect the exciton dynamics and consequently its luminescence. In the next subsections we examine some of these processes starting with the spin relaxation process driven by the exchange interaction.

### 2.1. The exchange interaction

The exchange interaction is derived [15] from the Coulomb interaction between the electron and hole. It can be seen as the annihilation of the electron-hole pair and its subsequent creation. Since this process is mediated by a Coulomb line it can only be effectively coupled to the optically active spin states  $|\pm 1\rangle$  and, of course, it has to conserve the total angular momentum. Therefore, this interaction by itself cannot flip the exciton spin. An additional mechanism is needed in conjunction with it to create a spin relaxation channel. As an example of how this is accomplished, we consider the contribution given by the long-range part of the exchange interaction, because the short-range part cannot directly flip the hhe

spin and it was shown to be very weak in confined systems (for more details, see Ref. [14]).

The long-range part is just an excitonic dipolar interaction that is responsible for the nonretarded contribution to the polariton effect in bulk [16]. Therefore it depends on the relative direction between the exciton center-of-mass momentum,  $\mathbf{K}$ , and its electric dipole moment. If the momentum state is well defined, so will be the excitonic eigenstates when this interaction is considered, giving rise to the longitudinal–transverse exchange splitting. However, it is well known [17] that the exciton interactions with acoustic phonons, quantum well rough interfaces and impurities are able to quickly scatter the momentum  $\mathbf{K}$ , and in this case the exchange interaction does not yield a spin splitting but rather establishes a spin relaxation channel between the  $|\pm 1\rangle$  spin states. This is similar to other motional narrowing processes [18] in which the spin relaxation time  $\tau_{\text{ex}}$  is given by

$$\frac{1}{\tau_{\text{ex}}(E)} = [\Omega_{\text{ex}}(K)]^2 \tau^*, \quad (2)$$

where  $\Omega_{\text{ex}}(K)$  is the  $K$ -dependent exchange frequency (i.e. the exchange splitting in the quantum well divided by  $\hbar$ ) and  $\tau^*$  is approximately the momentum scattering time [14]. In this equation the  $E$  dependence of  $\tau_{\text{ex}}$  is taken to come only from the momentum dependent term on the right-hand side of (2). This relaxation channel contributes to  $\mathbf{M}$  in the rate equation (1) as (putting  $N$  in a column matrix form)

$$M_{\text{ex}}(E, E') = \delta(E - E') \frac{1}{2\tau_{\text{ex}}(E)} \begin{pmatrix} 0 & 0 & 0 & 0 \\ 0 & -1 & 1 & 0 \\ 0 & 1 & -1 & 0 \\ 0 & 0 & 0 & 0 \end{pmatrix}. \quad (3)$$

The  $\delta$ -function in energies restricts the spin relaxation process to occur within the same energy shell, that is,  $\tau^*$  is determined only by elastic processes. This seems to be a reasonable approximation since the elastic scattering is faster than

the inelastic one [19]. The latter will be included in the thermalization effects below.

## 2.2. Single-particle spin-flip

For free electrons in the conduction band several mechanisms have been identified [20] as being able to relax their spins, all requiring large electronic energies to have sufficient phase space for the scattering process to be effective. Even at these large energies the relaxation of the electron spin is found to be slow, with the shortest relaxation times measured [8] at  $\tau_e \approx 150$  ps in p-doped samples where the electron–hole scattering (BAP mechanism [20]) appeared as the most likely effective process. However, at the present time there is yet no specific theory treating the spin relaxation for individual electrons and holes which are constituent of excitons in quantum wells.

For free holes in the valence band, spin relaxation has been observed [8] to be very fast, relying basically on the strong spin mixing between heavy and light hole states [10,11]. In confined systems this mixing decreases for smaller momenta and we expect a somewhat weaker relaxation for hole in the excitonic state when compared to the processes for free carriers. In the bound state the hole momentum distribution is limited by the exciton binding energy, and that is small enough to slow down the hole spin relaxation.

Even without a detailed knowledge of these processes for excitons in quantum wells, we can phenomenologically incorporate single-particle spin-flip into (1). Here we assume that the spin relaxation times for the electron,  $\tau_e$ , and hole,  $\tau_h$ , are energy independent. The matrix  $M_{\text{sp}}$  for this contribution is the same one given in Eqs. (2.3–2.5) in Ref. [14] and it will not be shown here.

## 2.3. Thermalization effects

At low temperatures it has been observed [2] that the exciton interaction with acoustic phonons is very important in determining the time evolution of the luminescence intensity. The thermalization process should be included in Eq. (1) [21]. This energy relaxation channel can be accounted

for by a term of the form:

$$M_{\text{th}}(E, E') = \left[ \frac{1}{\tau(E, E')} - \delta(E - E') \int \frac{dE''}{\tau(E'', E)} \right] \times \mathbb{I}, \quad (4)$$

where  $\mathbb{I}$  is the  $4 \times 4$  unit matrix and

$$\frac{1}{\tau(E, E')} = \frac{[\tau_{\text{th}} k_B T \ln 2]^{-1}}{1 + e^{(E - E')/k_B T}} \quad (5)$$

is the transition probability of scattering from a state with energy  $E'$  to another with energy  $E$ . The factors in (5) are arranged such that

$$\frac{1}{\tau_{\text{th}}} = \int \frac{dE'}{\tau(E', 0)},$$

a quantity that gives the initial decrease in the luminescence intensity for resonantly excited quantum wells and is estimated from experiments [2,3].

#### 2.4. Recombination

Due to the lack of translational symmetry along the quantum well growth direction the coupling between excitons and photons is substantially modified from the one that takes place in bulk. Now the polariton modes are unstable and a very fast intrinsic recombination process is expected [7,6,22]. These processes must be included in a complete analysis of the time-resolved luminescence data [21]. Only excitons close to the minimum of the kinetic energy,  $K \approx 0$ , are able to couple to radiation, those thermalized to larger- $K$  states cannot recombine until they are scattered back to lower energies inside the light cone. Call this energy limit  $E_1$ . We then approximately describe the recombination rate by

$$M_{\text{R}}(E, E') = -\frac{1}{\tau_{\text{R}}} \delta(E - E') \theta(E_1 - E') \times \begin{pmatrix} 0 & 0 & 0 & 0 \\ 0 & 1 & 0 & 0 \\ 0 & 0 & 1 & 0 \\ 0 & 0 & 0 & 0 \end{pmatrix}, \quad (6)$$

where  $\theta$  is the step function,  $\tau_{\text{R}}$  the recombination time for those excitons with energy smaller than  $E_1$  and we have used the fact that only  $|\pm 1\rangle$  spin states are optically active. We have neglected in Eq. (6) the energy dependence of  $\tau_{\text{R}}$  and also the possible presence of nonradiative processes.

#### 2.5. The generation term

We assume that the incident pulse of light propagating along the  $z$ -direction has a Gaussian shape creating an initial polarized exciton population as a function of time such as [21]

$$M_{\text{G}}(E, E', t) = \delta(E) \delta(E') N_{\text{ex}} \frac{e^{-(t/T)^2}}{\sqrt{\pi} T^2} \times \begin{pmatrix} 0 & 0 & 0 & 0 \\ 0 & \frac{1+P}{2} & 0 & 0 \\ 0 & 0 & \frac{1-P}{2} & 0 \\ 0 & 0 & 0 & 0 \end{pmatrix}, \quad (7)$$

where  $P$  is the initial polarization,  $T = \tau_{\text{p}}/2\sqrt{\ln 2}$  and  $\tau_{\text{p}}$  is the pulse width. In Eq. (7)  $N_{\text{ex}}$  is the exciton density and the resonant condition is used so that only excitons with zero kinetic energy are created.

### 3. Results and discussion

We solved the rate equation (1) numerically. The various parameters that enter the calculation were estimated as follows. To calculate  $\tau_{\text{ex}}(E)$  from Ref. [14] we only need the momentum scattering time which we assumed to be  $\tau^* \approx T_2 \approx 2\hbar/\Gamma_{\text{h}}$ , where  $T_2$  is the exciton dephasing time and  $\Gamma_{\text{h}}$  the homogeneous linewidth. We used  $\tau^* = 6$  ps. For processes involving single-particle spin-flip we used a slow time for the electrons,  $\tau_{\text{e}} = 100$  ps, and a faster one for holes,  $\tau_{\text{h}} = 20$  ps. For the recombination time we used a small value,  $\tau_{\text{R}} = 30$  ps, as theoretically expected [22] and a thermalization time of same order,  $\tau_{\text{th}} = 50$



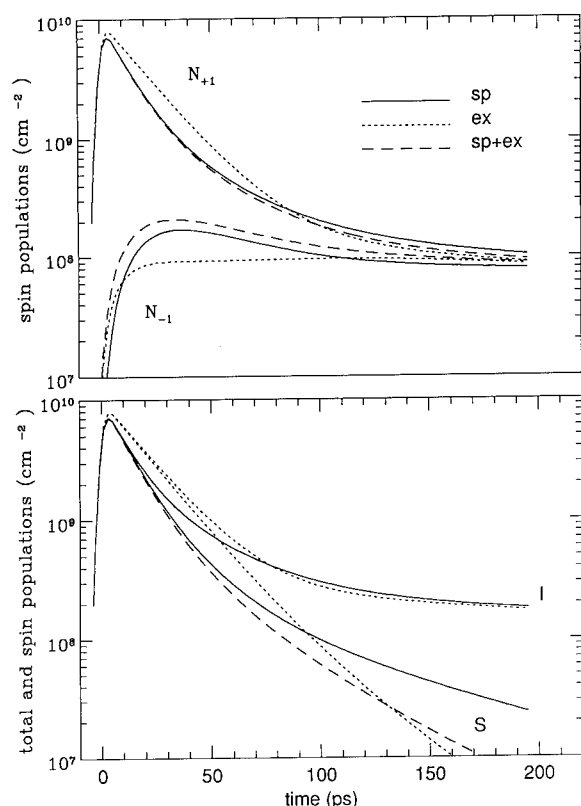


Fig. 2. In the top panel are the spin populations of optically active excitons and in the bottom panel the total and spin intensities as explained in the text.

ps, as experimentally observed [3]. The temperature is kept fixed at 10 K, the pulse width is set to be  $\tau_p = 5$  ps and we consider a 150 Å wide infinity-barrier quantum well. The initial polarization is assumed to be  $P = 1$ ,  $E_1 = 0.2$  meV,  $\Delta E_{SR} = 0.05$  meV and  $N_{ex} = 10^{10}$  cm $^{-2}$ .

In Fig. 2 we show how different spin relaxation processes can affect the polarized luminescence. We studied three distinct cases: (ex) when only the exchange-driven channel is present, (sp) when only single-particle spin relaxation channels are considered, and (sp + ex) when both processes take place simultaneously. In the top panel the spin population of optically active states are shown as a function of time for those excitons which are able to recombine. Therefore this corresponds to the polarized intensities. In the lower panel we plotted the total and spin intensities,

$I = (N_{+1} + N_{-1})$  and  $S = (N_{+1} - N_{-1})$ , respectively.

We first comment on the effects of thermalization. Extremely short intrinsic recombination times for excitons in quantum wells have been predicted in some theoretical studies [7,6,22], although experimental evidence of this fact is not yet fully established. It is believed that the thermalization effects [21,6,22] mask the fast intrinsic recombination because they populate large energy excitonic states that are no longer able to radiate. The net effect expected is then a long decay of the luminescence intensity after thermal equilibrium is partially reached, and that can be interpreted as a long lifetime for exciton in better agreement with the experimental values encountered for the luminescence decay [21]. In Ref. [14] that long lifetime was used to obtain the time dependence of the luminescence. Here, by contrast, full account is taken of the fast recombination and of the thermalization effects. As observed in Fig. 2, the total intensity,  $I$ , does not show a single-exponential decay. The fast initial drop in the intensity is due to the combined effects of thermalization and intrinsic radiative processes and the slow decay follows when the thermal equilibrium phase discussed above sets in. Moreover, if single-particle spin relaxation is present, not only the spin intensity,  $S$ , but also the total intensity,  $I$ , is affected since the excitons are now able to flip their spins to the  $|\pm 2\rangle$  dark states. This can be seen contrasting the cases (ex) and (sp) in the lower panel of Fig. 2. The exchange channel does not contribute to any changes in  $I$  because it only couples the  $|\pm 1\rangle$  states.

From the top panel of this figure we can see that the exchange interaction is very effective in bringing the  $|\pm 1\rangle$  spin populations to equilibrium. This, however, does not happen for the single-particle case where the two populations slowly tend to each other. The reason is that single-particle spin-flip moves  $|\pm 1\rangle$  states to the  $|\pm 2\rangle$  dark states.

When an electric field is applied along the  $z$ -direction it decreases the wave function overlap for the electron-hole pair. Since the exchange interaction depends on the virtual recombination

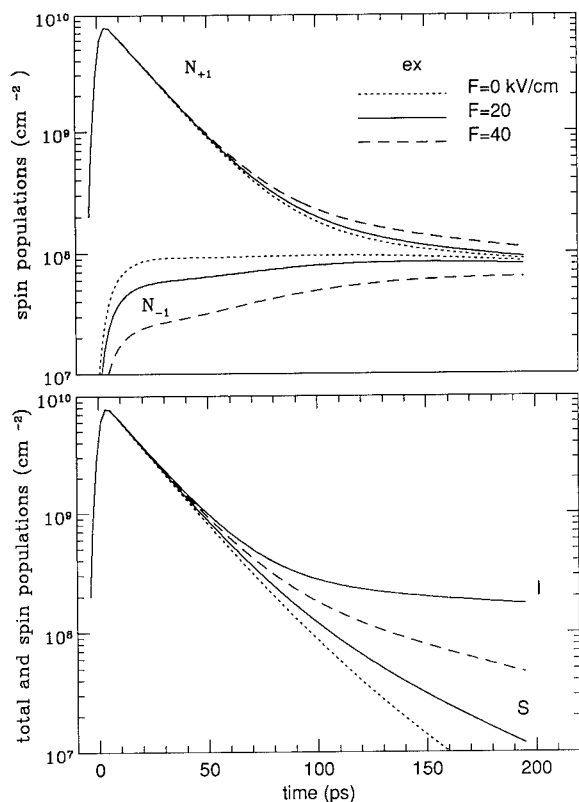


Fig. 3. The time dependence for the spin populations and intensities are shown for spin-flip processes driven only by the exchange interaction (ex) for various strengths of electric field.

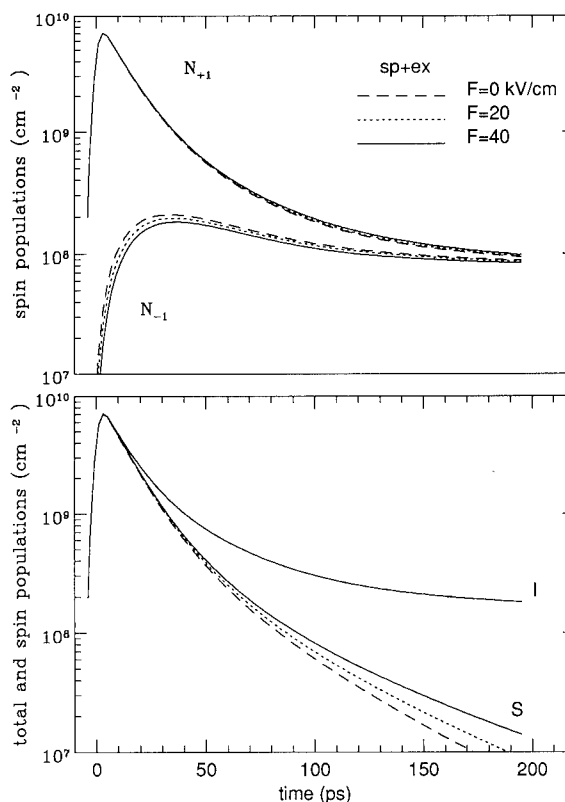


Fig. 4. Time dependence of the spin populations when single-particle and exchange spin-flips are considered (sp + ex).

and creation of the pair, it will be strongly affected [14]. To appreciate better the field effects on the exchange, we keep all the other parameters unchanged with the field and vary only  $\tau_{\text{ex}}$ . In Fig. 3 we show the electric field dependence for the (ex) case, where we clearly see the spin relaxation process being suppressed. However, if there is present any contribution from single-particle spin-flip processes, the field dependence may be much weakened, as shown in Fig. 4 for the (sp + ex) case. Fig. 5 gives an example of how  $\tau_{\text{ex}}$  depends on the exciton kinetic energy,  $E$ , and on the longitudinal electric field,  $F$ , for  $T = 10$  K.

In conclusion, we have presented here a study addressing the time dependence of the polarized luminescence that may be useful in distinguishing contributions from different spin relaxation processes for excitons in quantum wells. A longitudi-

nal electric field is expected to affect strongly the exchange interaction and can be used to detect the importance of processes relying on this inter-

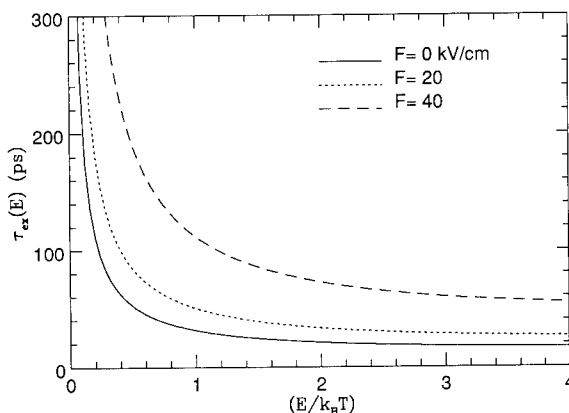


Fig. 5. The energy dependence of the spin relaxation time  $\tau_{\text{ex}}$  obtained from Ref. [14].

action if it plays a prominent role. Thermalization effects are also considered as is the rapid recombinations of confined excitons to describe more realistically the radiative processes in a quantum well.

#### 4. Acknowledgements

We thank J. Shah, A. Vinattieri, and T. Damen for helpful discussions. L.J.S. acknowledges support from NSF DMR-91-17298 and M.Z.M. from CNP<sub>q</sub> (Brazil).

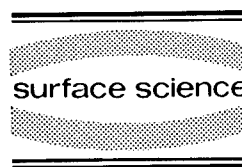
#### 5. References

- [1] W.H. Knox, R.L. Fork, M.C. Downer, D.A.B. Miller, D.S. Chemla, C.V. Shank, A.C. Gossard and W. Wiegmann, *Phys. Rev. Lett.* 54 (1985) 1306.
- [2] T.C. Damen, J. Shah, D.Y. Oberli, D.S. Chemla, J.E. Cunningham and J.M. Kuo, *Phys. Rev. B* 42 (1990) 7434.
- [3] T.C. Damen, K. Leo, J. Shah and J.E. Cunningham, *Appl. Phys. Lett.* 58 (1991) 1902.
- [4] M.R. Freeman, D.D. Awschalom, J.M. Hong and L.L. Chang, *Phys. Rev. Lett.* 64 (1990) 2430; *Proc. 20th Int. Conf. on Physics of Semiconductors*, Eds. E.M. Anastasakis and J.D. Joannopoulos (World Scientific, Singapore, 1990) p. 1129.
- [5] H. Stolz, D. Schwarze, W. von der Osten and G. Weimann, *Superlatt. Microstruct.* 6 (1989) 271.
- [6] L.C. Andreani, F. Tassone and F. Bassani, *Solid State Commun.* 77 (1991) 641.
- [7] E. Hanamura, *Phys. Rev. B* 38 (1988) 1228.
- [8] T.C. Damen, L. Viña, J.E. Cunningham, J. Shah and L.J. Sham, *Phys. Rev. Lett.* 67 (1991) 3432.
- [9] S. Bar-Ad and I. Bar-Joseph, *Phys. Rev. Lett.* 68 (1992) 349.
- [10] T. Uenoyama and L.J. Sham, *Phys. Rev. Lett.* 64 (1990) 3070.
- [11] R. Ferreira and G. Bastard, *Phys. Rev. B* 43 (1991) 9687.
- [12] G. Bastard, *Phys. Rev. B* 46 (1992) 4253.
- [13] Ph. Roussignol, P. Rolland, R. Ferreira, C. Delalande, G. Bastard, A. Vinattieri, L. Carraresi, M. Colocci and B. Etienne, *Surf. Sci.* 267 (1992) 360.
- [14] M.Z. Maialle, E.A. de Andrada e Silva and L.J. Sham, *Phys. Rev. B* 47 (1993) 15776.
- [15] G.E. Pikus and G.L. Bir, *Zh. Eksp. Teor. Fiz.* 60 (1971) 195. [*Sov. Phys.-JETP* 33 (1971) 108].
- [16] L.C. Andreani and F. Bassani, *Phys. Rev. B* 41 (1990) 7536.
- [17] L. Schultheis, J. Kuhl, A. Honold and C.W. Tu, *Phys. Rev. Lett.* 57 (1986) 1797.
- [18] C.P. Slichter, *Principles of Magnetic Resonance* (Harper & Row, New York, 1963) p. 154.
- [19] J. Hegarty and M.D. Sturge, *J. Opt. Soc. Am. B* 2 (1985) 1143.
- [20] F. Meier and B.P. Zachachrenya, Eds., *Optical Orientation* (North-Holland, Amsterdam, 1984).
- [21] Jagdeep Shah, A. Vinattieri and collaborators, private communication.
- [22] D.S. Citrin, *Solid State Commun.* 84 (1992) 281.



ELSEVIER

Surface Science 305 (1994) 263–266



## Hole spin relaxation in a n-doped quantum well structure

Ph. Roussignol <sup>\*,a</sup>, R. Ferreira <sup>a</sup>, C. Delalande <sup>a</sup>, G. Bastard <sup>a</sup>, A. Vinattieri <sup>b</sup>,  
J. Martinez-Pastor <sup>b,d</sup>, L. Carraresi <sup>b</sup>, M. Colocci <sup>b</sup>, J.F. Palmier <sup>c</sup>, B. Etienne <sup>c</sup>

<sup>a</sup> *Laboratoire de Physique de la Matière Condensée de l'Ecole Normale Supérieure, 24 rue Lhomond, 75005 Paris, France*

<sup>b</sup> *Dipartimento di Fisica e LENS, Largo E. Fermi 2, 50125 Firenze, Italy*

<sup>c</sup> *CNET, Centre de Bagneux, 196 avenue Henri Ravera, 92220 Bagneux, France*

<sup>d</sup> *Dept. Fisica Aplicada, Universitat de València, 46100 Burjassot, València, Spain*

(Received 29 April 1993; accepted for publication 4 June 1993)

### Abstract

The dependence of the hole spin relaxation on the electron density is studied in a n-modulation doped 75 Å GaAs/AlGaAs quantum well by means of cw and time-resolved photoluminescence techniques. A slow hole spin relaxation time has been measured ( $\sim 1$  ns) and the polarization has been found to be strongly dependent on the in-plane wavevector of the photocreated holes. Calculations are presented which support the experimental findings.

In bulk semiconductors, due to the fourfold degeneracy of the top of the valence band, holes relax their spin quasi-instantaneously. In quantum-well structures, where this degeneracy is lifted, a substantial change in the hole spin relaxation process is expected [1,2].

In this paper we present an experimental study of cw and time-resolved photoluminescence (PL) on a n-modulation doped 75 Å GaAs/GaAlAs quantum well embedded in a p–i–n diode. The electrons transfer to the well from a Si  $\delta$ -doping plane. AuGeNi–Au contacts are taken both on the p<sup>+</sup> back side and the n<sup>+</sup> cap layer, leaving a 150  $\mu$ m diameter window for optical measurements. The electron density  $N_S$  is estimated from measurement of the Stokes shift between the PL line and the first peak in the PLE spectrum [3]

and varies from  $10^{11}$  to  $10^{12}$  cm<sup>-2</sup>. For this range of electron concentration screening and occupancy effects are sufficient to prevent the existence of excitons [3]. All measurements were done at  $T = 4$  K. CW measurements have been performed by standard dye laser and lock-in techniques. For the time-resolved measurements the optical excitation (5 ps duration and 76 MHz repetition rate) was provided by a pyridine dye laser and the photoluminescence was analysed by a synchroscan streak camera (20 ps effective resolution).

Typically a Stokes shift dependent on the bias voltage is observed between the PL peak and the first peak of the PLE spectrum corresponding to E1\*H1\*, the first band-to-band transition at the Fermi wavevector  $k_F$ . A second peak corresponding to the E1\*L1\* transition and a small structure at higher energy, corresponding to the band-to-band transition E2H1 at  $k_{||} = 0$  (the quantum

\* Corresponding author.

well is asymmetric due to the electric field), are also observable [4].

A significant variation of the polarization  $P^{\text{cw}}$  of the PL line has been measured as a function of the excitation energy;  $P^{\text{cw}}$  is maximum when exciting in the vicinity of the  $E1^*H1^*$  transition and decreases steeply as soon as the excitation energy approaches the  $E1^*L1^*$  transition. Moreover  $P^{\text{cw}}$  exhibits a secondary maximum for an excitation energy corresponding to the  $E2H1$  transition. The dependence on the applied bias of  $P_{E1^*H1^*}$ , the polarization of the PL line when exciting at the  $E1^*H1^*$  transition energy, and consequently its dependence on  $N_s$ , is depicted in Fig. 1a. As  $N_s$  increases from  $10^{11}$  to  $10^{12} \text{ cm}^{-2}$ ,  $P_{E1^*H1^*}$  decreases from 65% to 10%; under the same conditions  $P_{E2H1}$ , the polarization when exciting the quantum well structure at the  $E2H1$  transition energy, remains constant at about 20%.

Time-resolved PL measurements after circularly polarized excitation give access to three different quantities: the initial polarization  $P(0)$  of the system at  $t = 0$ , the spin relaxation time  $\tau_s$  and the PL decay time  $\tau_R$ . For a given bias, the dependence of  $P(0)$  on the excitation energy is similar to the one observed for the polarization  $P^{\text{cw}}$  after cw excitation. In the same range of excitation energy, no significant variation of the recombination time and spin relaxation time is observed. The dependence of  $P(0)$  on the bias voltage is shown in Fig. 1a ( $\diamond$ ). In Fig. 1b,  $\tau_R$  and  $\tau_s$  are shown as a function of the applied voltage; while  $\tau_s$  remains fairly constant and of the order of 1 ns,  $\tau_R$  decreases from 300 to 100 ps as the bias goes from 0 to 8 V. This decrease of  $\tau_R$  occurs at the same voltage as the decrease of the cw PL efficiency and coincides with the appearance of a reverse current in the p-i-n diode. This variation is likely related to an evolution of the nonradiative channels responsible for the carriers recombination.

Photoluminescence from our n-modulation doped quantum well originates from band-to-band recombination of electrons of the Fermi sea and photoexcited holes. Due to the presence of a 2D electron gas, when the quantum well is excited at its  $E1^*H1^*$  transition, heavy holes are created at

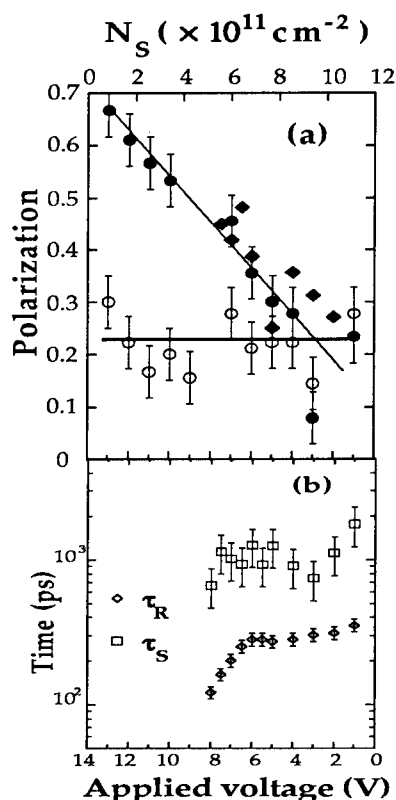


Fig. 1. (a) CW polarizations  $P_{E1^*H1^*}$  ( $\bullet$ ) and  $P_{E2H1}$  ( $\circ$ ) for excitation energies corresponding to the  $E1^*H1^*$  and  $E2H1$  transition energies of the 75 Å quantum well as a function of the applied voltage (lower scale) or the electron density (upper scale). The initial polarization measured in time-resolved experiments is also reported ( $\diamond$ ). (b) Recombination time  $\tau_R$  ( $\diamond$ ) and spin relaxation time  $\tau_s$  ( $\square$ ) as a function of the applied bias.

$k_{\parallel} = k_F$ , without superimposed excitation of light holes. The application of a bias, modulating the electron concentration, and consequently  $k_F$ , allows one to study the optical properties of heavy hole photocreated at different in-plane wavevectors.

In our time-resolved measurements the population of photocreated electrons (estimated to  $10^{10} \text{ cm}^{-2}$ ) is always at least one order of magnitude smaller than  $N_s$ . In our cw experiments, the concentration of photocarriers per unit time is of the order of  $10^{17} \text{ cm}^{-2} \text{ s}^{-1}$  and a continuous pumping of the Fermi sea cannot occur [5]. Under these conditions any saturation effect due to a polarization of the Fermi sea can be neglected.

Thus, all our measurements are related to the properties of the holes.

Let us call  $G(k_{\parallel})$  the polarization rate of the photocreated holes. By relaxation towards the band edge, part of the polarization is lost. The initial polarization  $P(0)$  can therefore be written as a product,  $P(0) = \alpha \cdot G$ . The cw polarization  $P_{\text{E1*H1*}}$  and  $P(0)$  are related by  $P_{\text{E1*H1*}} = P(0)/(1 + 2\tau_R/\tau_S)$ . The large value of  $\tau_S$  ( $\sim 1$  ns) with respect to  $\tau_R$  ( $\sim 300$  ps) explains why  $P_{\text{E1*H1*}}$  is not significantly different from  $P(0)$  (Fig. 1a).

The decrease of  $P(0)$  with increasing initial  $k_{\parallel}$  cannot be related to the decrease of  $G(k_{\parallel})$ . Considering the first heavy hole level, due to the mixing of the valence bands at  $k_{\parallel} \neq 0$ ,  $\sqrt{\langle J_z^2 \rangle}$  ( $J_z$  is the projection of the angular momentum along the growth axis) varies [4] from  $3/2$  to  $1.25$  for  $k_{\parallel}$  varying from  $0$  to  $0.025 \text{ \AA}^{-1}$  ( $k_F$  at  $N_S = 10^{12} \text{ cm}^{-2}$ ). Consequently  $G$ , which equals  $1$  at vanishing wavevector, decreases with increasing  $k_{\parallel}$ , but this effect remains small. More important is the term  $\alpha$  which takes into account the fact that a hole population created at  $k_{\parallel} \neq 0$  is always detected at  $k_{\parallel} = 0$ .

The polarization may be lost during the relaxation path towards the band edge, through emission of acoustic phonons or elastic scattering by

ionized impurities or interface roughness. At a given time, a hole in a defined spin state suffers scattering which can relax its energy and/or its momentum. The final state can be either in the same branch (spin-conserving scattering with a characteristics time  $\tau_{\text{sc}}$ ) or in the other one (spin-flip scattering with  $\tau_{\text{sf}}$ ). Calculations show [2,4] that for large values of  $k_{\parallel}$  the two times  $\tau_{\text{sc}}$  and  $\tau_{\text{sf}}$  have the same order of magnitude and a probability of spin-flip exists. As  $k_{\parallel}$  decreases  $\tau_{\text{sc}}$  remains fairly constant; on the contrary  $\tau_{\text{sf}}$  increases dramatically with decreasing  $k_{\parallel}$  and near the band edge the spin-flip process becomes impossible. According to these calculations, the coefficient  $\alpha$ , which results from a succession of such events, should decrease substantially as the wavevector at which the holes are photocreated increases, and is very likely responsible for the experimental results depicted in Fig. 1a. On the contrary, whatever the applied voltage is, when exciting the system at the E2H1 transition energy, holes are always mainly created at  $k_{\parallel} = 0$  and the polarization  $P_{\text{E2H1}}$  does not depend on the bias.

For holes at  $k_{\parallel} = 0$ , a very long spin relaxation time is observed ( $\approx 1$  ns). This is in striking contrast with the bulk values ( $\tau_S^{\text{bulk}} \approx 1$  ps). We have previously interpreted these trends [4] in terms of assisted spin-flip scattering of a thermal distribution of holes near the band edge ( $k_{\parallel} \approx 0$ ). The calculations do predict a large increase of  $\tau_{\text{sf}}$  with decreasing  $k_{\parallel}$ , but the thermal averaged spin-flip time largely overestimates the measured value. In fact, a D'Yakonov–Perel-like mechanism [5] has to be considered for holes due to the presence of both an inversion asymmetry term associated with the GaAs zinc-blend lattice,  $H_{\text{lin}}(\mathbf{k})$ , and a parity breaking band-bending potential,  $\phi(z)$ . For a small asymmetry the corresponding  $k_{\parallel}$ -dependent spin-flip probability is given by [6]

$$1/\tau_{\text{DP}}(k_{\parallel}) = \frac{1}{2}\Omega^2(k_{\parallel})\tau_{\text{sc}}^*(k_{\parallel}),$$

where  $\hbar\Omega(k_{\parallel})$  is the parity splitting of the HH1 hole dispersions and  $\tau_{\text{sc}}^*(k_{\parallel})$  is the spin-conserving momentum relaxation time. The resulting spin-flip probability for the hole gas is given by the thermal average of  $1/\tau_{\text{DP}}$ . For  $\phi(z) = eFz$  we have  $\langle 1/\tau_{\text{DP}} \rangle \approx F^2$ , and the spin-flip time varies

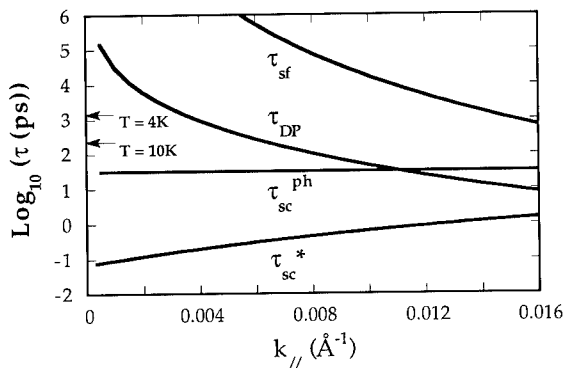


Fig. 2. Variation with the in-plane wavevector of  $\tau_{\text{sc}}^*$ ,  $\tau_{\text{sf}}$  and  $\tau_{\text{DP}}$  for a  $L = 75 \text{ \AA}$  GaAs/Ga<sub>0.7</sub>Al<sub>0.3</sub>As symmetric quantum well. Ionized impurities are located at  $z_{\text{imp}} = -L/2$  with an areal density of  $5 \times 10^{10} \text{ cm}^{-2}$ . The emission time of an acoustic phonon without spin flip,  $\tau_{\text{sc}}^{\text{ph}}$  is also reported. The arrows indicate  $\langle 1/\tau_{\text{DP}} \rangle^{-1}$ , the inverse of the thermal average at 4 and 10 K of  $1/\tau_{\text{DP}}$ .

rapidly with increasing bending, in contrast with  $\tau_S$  in Fig. 1b which is almost independent of  $N_S$ . Thus, the main contribution for  $\hbar\Omega$  should be given by  $H_{lin}$ . For the  $\tau_{sc}^*$  term both acoustical phonons emissions and ionized impurities scattering should be accounted for. We shown in Fig. 2 the variation with  $k_{||}$  of  $\tau_{sc}^*$ ,  $\tau_{DP}$  and  $\tau_{sf}$  for the symmetric  $L = 75 \text{ \AA}$  quantum well. The results have been obtained for ionized impurities scattering. Note that  $\tau_{DP}$  is smaller or much smaller than  $\tau_{sf}$ . For an areal density of  $N_{imp} \times 10^{10} \text{ cm}^{-2}$  located on a quantum well interface, at  $T = 4 \text{ K}$  we evaluate  $\langle 1/\tau_{DP} \rangle^{-1} \approx 260 \times N_{imp} \text{ ps}$ . For longitudinal acoustic (LA) phonon emission at  $4 \text{ K}$  in the framework of the deformation potential formalism [6,7] we evaluate  $\langle 1/\tau_{DP} \rangle^{-1} \approx 8 \text{ ps}$  for the same quantum well. The measured  $\tau_S \approx 1 \text{ ns}$  value should then correspond to an impurity concentration of about  $3 \times 10^{10} \text{ cm}^{-2}$ .

The previous discussion of the dependence of the polarization loss during the energy relaxation of the hole population is not essentially modified by the introduction of the D'Yakonov–Perel mechanism. As shown in Fig. 2 for large  $k_{||}$  the emission time of an acoustic phonon without spin-flip,  $\tau_{sc}^{ph}$ , is larger than  $\tau_{DP}$ . A large probability of polarization loss exists leading to a small value for the parameter  $\alpha$ . On the contrary, for  $k_{||} < 0.007 \text{ \AA}^{-1}$ ,  $\tau_{sc}^{ph}$  is much smaller than  $\tau_{DP}$  and the polarization should not be much affected by the relaxation process. A quantitative analysis of the influence of the energy relaxation on  $P(0)$  should include a modelization of the thermaliza-

tion of the hole population which is clearly beyond the scope of this paper.

In conclusion, according to our calculations the spin-flip time measured at the band edge should be strongly sample dependent and should increase with decreasing sample “quality”. This may explain why spin-flip time values ranging from  $5 \text{ ps}$  to  $1 \text{ ns}$  have been recently reported [4,8]. The first of these times should be related to a low efficient momentum-scattering mechanism (e.g. LA-phonon-assisted at low temperature), the second to an efficient one (e.g. ionized-impurity-assisted).

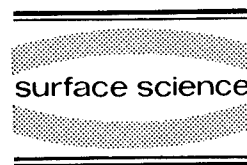
## 1. References

- [1] T. Uenoyama and L.J. Sham, Phys. Rev. Lett. 64 (1990) 3070.
- [2] R. Ferreira and G. Bastard, Phys. Rev. B 43 (1991) 9687.
- [3] C. Delalande, G. Bastard, J. Orgonasi, J.A. Brum, H.W. Liu and M. Voos, Phys. Rev. Lett. 59 (1987) 2690.
- [4] Ph. Roussignol, P. Rolland, R. Ferreira, C. Delalande, G. Bastard, A. Vinattieri, J. Martinez-Pastor, L. Carraresi, M. Colocci, J.F. Palmier and B. Etienne, Phys. Rev. B 46 (1992) 7292.
- [5] M.I. D'yakonov and V.I. Perel, in: Optical Orientation, Modern Problems in Condensed Matter Science, Vol. 8, Eds. F. Meier and B.P. Zakharchenya (North-Holland, Amsterdam, 1984).
- [6] R. Ferreira and G. Bastard, to be published.
- [7] G.L. Bir and G.E. Pikus, Fiz. Tverd. Tela (Leningrad) 2 (1960) 2287.
- [8] T.C. Damen, L. Vina, J.E. Cunningham, J. Shah and L.J. Sham, Phys. Rev. Lett. 67 (1991) 3432.



ELSEVIER

Surface Science 305 (1994) 267–270



## Plasmons localized at point charges in semiconductor quantum wells

S. Rudin <sup>\*,a</sup>, T.L. Reinecke <sup>b</sup>

<sup>a</sup> *U.S. Army Research Laboratory, Fort Monmouth, NJ 07703-5601, USA*

<sup>b</sup> *Naval Research Laboratory, Washington DC 20375-5347, USA*

(Received 13 April 1993; accepted for publication 4 May 1993)

### Abstract

The plasmon excitations of inhomogeneous carrier gases in semiconductor quantum wells in the presence of point charge impurities are investigated. The random phase approximation for the carrier gas yields an integral equation which expresses the condition that plasmons may be self-consistently localized in the vicinity of the impurity. The localized plasmon is a density wave trapped at the impurity site and exists in the electron (hole) gas only for negative (positive) impurity charge. Bound states of the intersubband plasmon are found for all densities of the carrier gas in a quantum well, a result which differs qualitatively from the bulk case. Numerical results for the binding energies are given for a range of relevant parameters.

### 1. Introduction

Both collective effects such as plasmons and also impurity bound states have been of considerable interest in recent studies of semiconductor quantum wells. The confinement provided by the heterostructure permits the investigation of the role of dimensionality on these properties. For example, recent experimental work suggests that plasmons may be bound by neutral donors in quantum wells [1]. The case of a plasmon bound at a point charge in a bulk electron gas was investigated earlier theoretically [2,3]. There it was found [3] that in a doped semiconductor bound plasmon states can exist only for densities

below a low threshold, which is not in the regime of physical interest. The physical picture of a bound plasmon in the bulk case is that the electron density is reduced in the vicinity of the negative point charge which lowers the plasmon energy there. The density nonuniformity causes plasmon scattering and may give rise to a bound plasmon state [2]. The latter is a density wave trapped at the impurity. Such states may have interesting effects on optical and transport properties.

In the case of a semiconductor quantum well (QW) with finite electron or hole density there are both intrasubband plasmons which are associated with a single carrier subband, and also intersubband plasmons which are associated with carrier transitions between two subbands [4,5]. The dispersion of the intrasubband plasmon begins

\* Corresponding author.



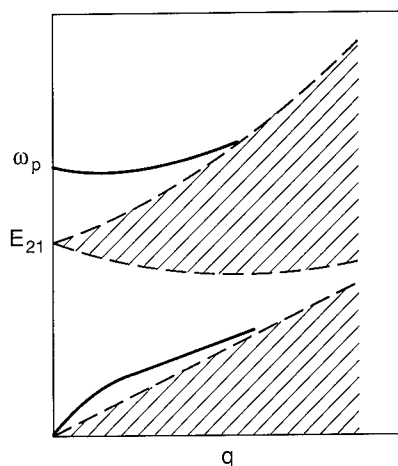


Fig. 1. Sketch of the energies of plasma excitations in a semiconductor quantum well vs wavevector. The lower solid curve represents an intrasubband plasmon, and the upper solid curve represents an intersubband plasmon.  $E_{21}$  is the energy separation between two subbands. The lightly hashed areas represent single particle excitations.

from zero energy and does not have an upper bound. On the other hand, for intersubband plasmons, as for the bulk plasmons, there is a lower bound to the energy dispersion curve. As will be seen from the discussion below this feature permits the existence of the bound state of the intersubband plasmon. The system which we study here is an electron or hole gas in the presence of a point charge. This model should represent physical systems containing ionized acceptors or donors. We note that such donors and acceptors are found to exhibit states of one, two or occasionally three electron charges. The extended intrasubband and intersubband plasma excitations in a quantum well are illustrated schematically in Fig. 1.

## 2. RPA for an inhomogeneous electron gas in a quantum well

The random phase approximation (RPA) is commonly used to derive the collective elementary excitations of the electron gas in a quantum well [4,5]. The extension to the inhomogeneous case is straightforward. The change of the total

carrier density in the presence of an external perturbation is

$$\delta\rho_{nm}^T(\mathbf{k}, \omega) = \delta\rho_{nm}(\mathbf{k}, \omega) + \delta\rho_{nm}^{\text{ext}}(\mathbf{k}, \omega), \quad (1)$$

where  $\mathbf{k}$  is a 2D wavevector and  $n, m$  are QW subband indices. We define the off-diagonal dielectric operator  $\epsilon$  in the momentum space in analogy to that in the homogeneous system so that

$$\delta\rho_{nm}^T(\mathbf{k}, \omega) = \sum_{ij, \mathbf{k}'} \epsilon_{nm, ij}^{-1}(\mathbf{k}, \mathbf{k}'; \omega) \delta\rho_{ij}^{\text{ext}}(\mathbf{k}', \omega). \quad (2)$$

Inverting Eq. (2) and defining the collective excitations by the condition  $\delta\rho^{\text{ext}} = 0$  while  $\delta\rho^T \neq 0$ , we obtain an equation for the collective excitations of the system:

$$\int d\mathbf{k}' \sum_{ij} \epsilon_{m, n, ij}(\mathbf{k}, \mathbf{k}'; \omega) \delta\rho_{ij}^T(\mathbf{k}', \omega) = 0. \quad (3)$$

The dielectric operator is evaluated in the RPA in terms of irreducible density propagator shown in Fig. 2. Defining

$$\chi = \Pi_{12}^R + \Pi_{21}^R, \quad (4)$$

$$g(\mathbf{k}) = \delta\rho_{12}^T(\mathbf{k}) + \delta\rho_{21}^T(\mathbf{k}), \quad (5)$$

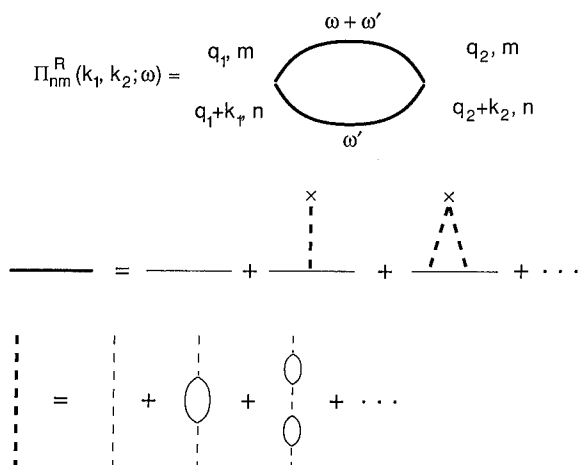


Fig. 2. The random phase approximation for the density propagator  $\Pi_{nm}$ . The thick solid line represents the one particle propagator of the system of independent carriers in the presence of the impurity. In the approximation employed here the impurity-carrier interaction is separately screened in the RPA.

we obtain an integral equation for the intersubband collective excitations

$$\sum_{k'} [\delta_{kk'} - \chi(k, k') V_{12,12}(k')] g(k') = 0. \quad (6)$$

In order to obtain an explicit integral equation from Eq. (6) we have to evaluate the polarization propagator  $\Pi_{nm}(k, k'; \omega)$  for a gas of independent electrons (or holes) interacting with an impurity via the Coulomb potential. We have developed an approximation for  $\Pi_{nm}$  using a spectral representation and evaluated it with what amounts to an infinite sequence of sum rules, as was suggested by Sham in the case of the bulk system [3]. In this way we have derived a good approximation for the kernel of the integral equation (6) together with a criterion for its validity.

### 3. Integral equation for localized intersubband plasmons

In the long wavelength approximation for the terms containing the unperturbed density  $n_0 \delta_{k,0}$  we obtain the following equation:

$$\begin{aligned} & [k^2 - (\mu E_{21}/\sigma)k - \mathcal{E}] g(k) \\ & + \frac{Z\alpha}{2n_0\sigma} \int \frac{d^2k'}{(2\pi)^2} 2E_{21} \\ & \times \delta n(k - k') g(k') = 0, \end{aligned} \quad (7)$$

where the energy parameter is defined as

$$\mathcal{E} = \frac{(\omega^2 - \omega_0^2)\hbar^2\epsilon_\infty}{4\pi e^2 n_0 \sigma(\omega)}, \quad (8)$$

and  $\omega_0$  is the frequency of the intersubband plasmon at  $k = 0$  in the absence of the impurity,  $\omega_{pl}(k = 0)$ ;  $\alpha$ ,  $\mu$  and  $\sigma(\omega)$  are the coefficients in long wavelength approximation (LWA) expansion for plasmon dispersion [4,5]. The intersubband plasmon dispersion has a lower bound given by  $\min\{\omega_{pl}(k)\}$ , and thus bound states may exist below it. Accordingly for bound states  $\mathcal{E} < 0$ .

Here  $\delta n(k)$  is the Fourier transformation of the change in the electron density due to the presence of an impurity of charge  $Ze$ . It is the

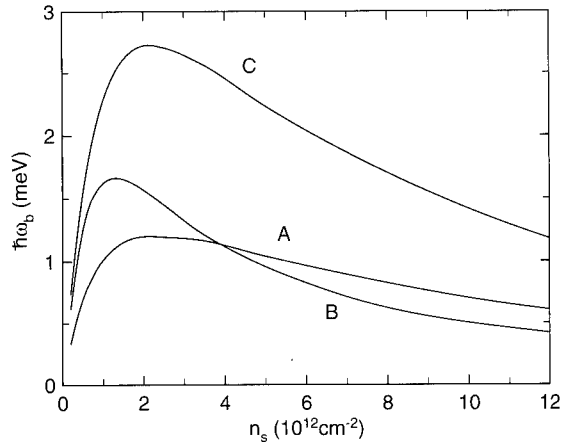


Fig. 3. The plasmon binding energy defined in Eq. (8) is shown here as a function of the effective two-dimensional density  $n_s = n_v L$ . The quantum well systems illustrated here are: (A) well width  $L = 100 \text{ \AA}$ ,  $m = 0.2 m_0$ ,  $\epsilon_\infty = 10.9$ ,  $|Z^*| = 2$ ; (B)  $L = 130 \text{ \AA}$ ,  $m = 0.2 m_0$ ,  $\epsilon_\infty = 10.9$ ,  $|Z^*| = 2$ ; (C)  $L = 100 \text{ \AA}$ ,  $m = 0.16 m_0$ ,  $\epsilon_\infty = 7.3$ ,  $|Z^*| = 2$ .

same charge density that appears in the Poisson equation for the response potential  $\phi_{res}$  when an external perturbation  $\phi_{ext}$  is applied. In linear screening approximation it can be evaluated in terms of QW form-factors.

The binding energy found from numerical solution of the integral equation for the  $l = 0$  angular momentum component is shown in Fig. 3 as a function of the two-dimensional density. The bound state equation has solutions only for  $Z < 0$ . By definition here the impurity charge is  $Ze$  for the electron gas and  $-Ze$  for the hole gas,  $Z^* = Z/\epsilon_\infty$ .

### 4. Discussion

In the corresponding bulk case [2,3] it was found that bound states exist only for densities below a certain threshold. This threshold density is so low for bulk semiconductors that the plasmon itself will not be observable. The situation in a quantum well is qualitatively different in that the solution of the bound state equation exists in principle at arbitrary densities. To understand this behavior qualitatively, let us neglect the linear term in  $k$  in the long wavelength approxima-

tion of the interaction matrix element. Let  $M$  be a plasmon “mass” defined by the inverse curvature of the plasmon dispersion at  $k = 0$ . Then the integral equation to leading order is similar to Schrodinger’s equation for a particle of mass  $M$  in an attractive 2D screened Coulomb potential with an effective charge

$$e^* = \frac{\alpha Z^* E_{21} m e}{2\pi M n \sigma},$$

and this potential has a bound state at arbitrary  $e^*$ .

The results given here suggest that bound plasmons may be observable for energies below the intersubband plasmon energy when the carrier mass is larger than  $0.1m_0$  and the well is not too narrow. The binding energy will be larger for larger values of the impurity charge  $Ze$  and for smaller dielectric constants. For example in a

GaAs QW the binding energy is small for the electron gas with its small mass, and the possibility of observing a bound plasmon state is better for holes as seen in Fig. 3. The bound state may be observable for an electron gas in a QW based on some II–VI materials due to the larger electron mass and smaller high frequency dielectric constant in them.

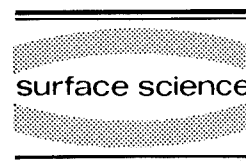
## 5. References

- [1] D. Gammon, B.V. Shanabrook and D. Musser, Phys. Rev. B 39 (1989) 1415.
- [2] E.A. Sziklas, Phys. Rev. 138 (1965) A1070.
- [3] L.J. Sham, in: Local Excitations in Solids (Plenum, New York, 1968) p. 665.
- [4] L. Wendler and R. Pechstedt, Phys. Status, Solidi (b) 138 (1986) 197.
- [5] J.K. Jain and S. Das Sarma, Phys. Rev. B 36 (1986) 5949.



ELSEVIER

Surface Science 305 (1994) 271–274



## Spin-resolved cyclotron resonance in a 2D electron gas

M.J. Yang <sup>\*</sup>, R.J. Wagner, P.J. Lin-Chung, B.V. Shanabrook, J.R. Waterman,  
W.J. Moore, J.L. Davis

*Naval Research Laboratory, Washington, DC 20375, USA*

(Received 19 April 1993; accepted for publication 22 June 1993)

### Abstract

We report the observation of spin-resolved cyclotron resonance of a 2DEG in an InAs quantum well. The data show that the  $g$ -factor of a 2DEG has a smaller energy dependence than that of bulk electrons. The reduction of the spin-splitting in a 2DEG can be accounted for by a calculation which includes the nonparabolicity of the band structure.

Although spin-resolved cyclotron resonance (CR) has been intensively searched for in the two-dimensional electron gas (2DEG) of high-mobility in GaAs/AlGaAs heterostructures, it has not been observed to date [1]. This has been attributed to suppressed spin-splitting due to electron–electron interactions. Recently, the observation of spin-resolved CR in a 2DEG in a strained InAs quantum well sandwiched by AlSb barriers has been reported [2]. Owing to the smaller band gap of InAs, the interaction between the conduction and the valence bands is stronger, and as a result, the  $g$ -factor has a stronger dependence on the electron energy, which is one of the fundamental criteria for observing spin-resolved CR.

The AlSb/InAs/AlSb single quantum well is grown by MBE on a GaAs(001) substrate with a thick AlSb buffer layer, where the InAs layer is under biaxial tension. It consists of a 1  $\mu\text{m}$  GaSb

and 1  $\mu\text{m}$  AlSb buffer layer, 10 periods of 25  $\text{\AA}$  GaSb/25  $\text{\AA}$  AlSb smoothing superlattice, a 200  $\text{\AA}$  AlSb lower barrier, a 149  $\text{\AA}$  InAs quantum well, a 500  $\text{\AA}$  top AlSb barrier, and a final capping layer of 30  $\text{\AA}$  GaSb. The carrier concentration is  $n_{2\text{D}} = 6.5 \times 10^{11} \text{ cm}^{-2}$  (see Fig. 1). The TO phonon energy of an InAs quantum well has been found to be shifted with respect to the bulk InAs TO phonon energy. Using elasticity theory, this shift has been used to deduce the tensile strain in the InAs quantum well. Moreover, the thickness of the InAs well is obtained by fitting the far infrared TO phonon absorption line intensity [3]. The magneto-optical experiments are performed at 4.2 K with a magnetic field of up to 13 T. At low  $B$ , the CR line shape is symmetric and the measured effective mass exhibits a constant value, as shown in Fig. 1. For  $B \geq 5$  T, the spectra show two discernible CR peaks originating from spin-conserving transitions between adjacent sets of spin-resolved Landau states. The separation between two CR peaks is larger at odd integer filling factor  $\nu$  than at even  $\nu$ , and the measured

<sup>\*</sup> Corresponding author.

cyclotron masses show variations correlated with the filling factor.

The experimental results are analyzed with the envelope-function approximation under a four-band  $k \cdot p$  model. We find that a calculation that only includes the nonparabolicity effect can qualitatively account for the data. However, in order to quantitatively explain the variation of the effective mass over a wide range of magnetic fields, we need to take into account the nonparabolicity, strain effects, and the effect of penetration of electron wave functions into the AlSb barriers [4]. Since our sample parameters have been experimentally determined, the only adjustable parameter in the calculation is an energy-dependent pre-factor  $\beta$  of the effective  $g$ -factor, i.e.,  $g_{2D}^*(E)$

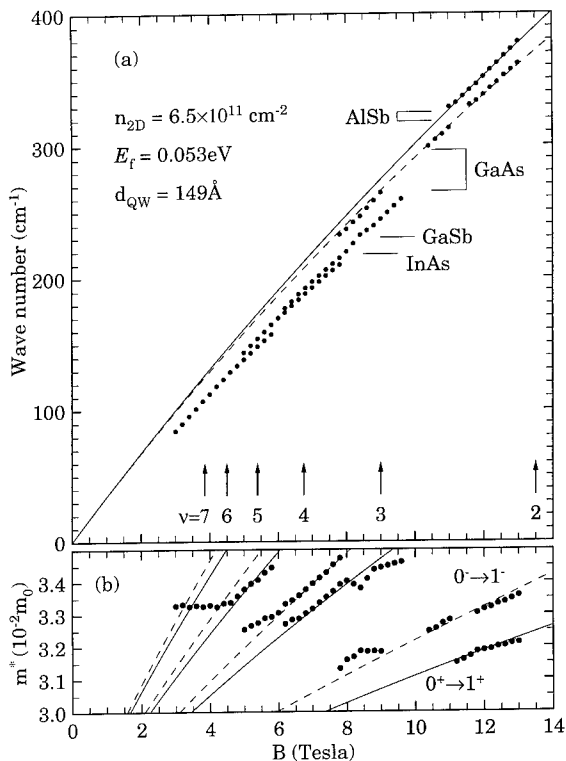


Fig. 1. (a) Dots: the measured resonance positions; solid (dashed) line: the calculated transition positions described in Ref. [4] for the lowest spin-up (-down) Landau level. The arrows mark the corresponding filling factor. Several lattice absorptions are also indicated. (b) Dots: the corresponding effective masses; solid (dashed) lines: the calculated effective masses described in Ref. [4] for spin-up (-down) transitions.

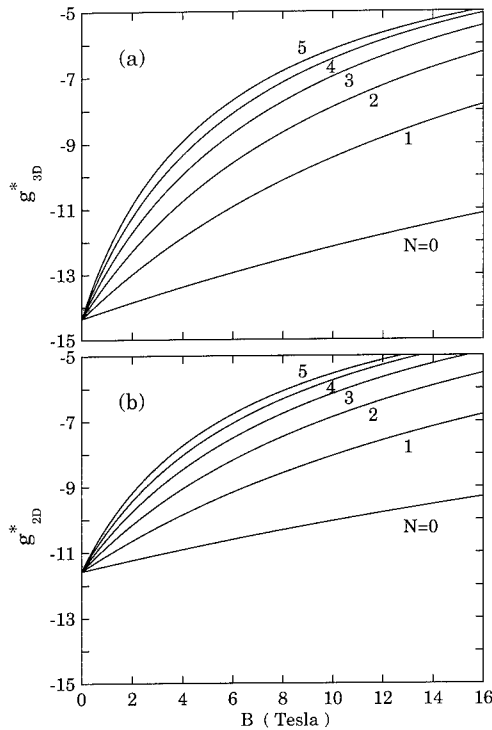


Fig. 2. The calculated  $g$ -factor for the first six Landau levels ( $N = 0, 1, \dots, 5$ ) as a function of magnetic field for (a) bulk electrons, and (b) 2D electrons.

$= g_{2D}^* + \beta E$ , where  $E$  is the electron energy above the bulk conduction minimum. The value of  $\beta$  is determined to be  $60 \text{ eV}^{-1}$  from the best fit to the experimental data. The obtained  $\beta$  is far smaller than the bulk band-edge value [5], and the reduction of  $\beta$  in a 2DEG will be shown in the following to be due to the fact that the electron energy is  $\sim 110 \text{ meV}$  above the bulk conduction band edge.

To calculate the energy-dependent  $g$ -factor, we follow the procedure outlined by Pidgeon and Brown [6], in which the nonparabolicity effect is automatically included. Fig. 2a shows the calculated  $g$ -factor for bulk InAs ( $g_{3D}^*$ ) as a function of magnetic field for different Landau levels [7]. Here we use the following parameters:  $P^2 = 10.85 \text{ eV}$ ;  $E_g = 0.42 \text{ eV}$ ;  $\Delta = 0.38 \text{ eV}$ ;  $\gamma_1 = 2.4513$ ;  $\gamma_2 = -0.2394$ ;  $\gamma_3 = 0.6806$ ;  $\kappa = -0.9294$ .

To calculate the  $g$ -factor for a 2DEG in a square well, we keep  $\gamma$ 's and  $\kappa$  unchanged. This

is because the InAs valence bands are not affected, to first order, by the presence of AlSb due to the staggered band alignment between AlSb and InAs. Although the strain effect can be considered by modifying the band parameters such as band gap and spin-orbit splitting, there is no simple way to include the penetration effect in Pidgeon and Brown's formalism. According to our previous study [4], the strain and penetration effects on the electronic band structure are opposite and of the same order of magnitude. For example, the electron effective mass is reduced with the inclusion of the strain effects, and increased due to the penetration effect. Although these two effects on the band structure do not cancel each other, a calculation which only includes the nonparabolicity effect can provide good insight into the  $g$ -factor when the electron energy is increased. To apply Pidgeon and Brown's formalism to the electron subband, we can simply add the subband energy ( $E_0 = 0.054$  eV for a well width of 149 Å) to the bulk band gap to define the effective band gap, and keep the remaining parameters unchanged. The results are plotted against magnetic field in Fig. 2b, as well as against the electron energy in Fig. 3. In both 3D and 2D cases, the effective  $g$ -value, roughly speaking, is not strongly dependent on the Landau level. It is clear that not only does the  $|g^*|$  decrease,  $\beta$ , the slope of the  $g$ -factor versus energy, is also smaller for a higher electron energy. It is easy to show that for  $N=0$ , the effective  $g$ -factor can be simplified to be:

$$g_{3D}^*(E) = -14.4 + 85.5E,$$

$$g_{2D}^*(E) = -11.6 + 65.4(E - E_0).$$

The calculation predicts a  $\beta$  of 65.4 for a 2DEG, and that is in excellent agreement with  $\beta = 60$  extracted from our data.

In conclusion, we have reported the observation of the spin-resolved cyclotron resonance of a 2DEG in an InAs quantum well. The splitting between the spin-up and spin-down transitions is found to be reduced substantially compared to the 3D electrons. A calculation that only includes the nonparabolicity effect provides good insight into the energy-dependent  $g$ -factor. It is found

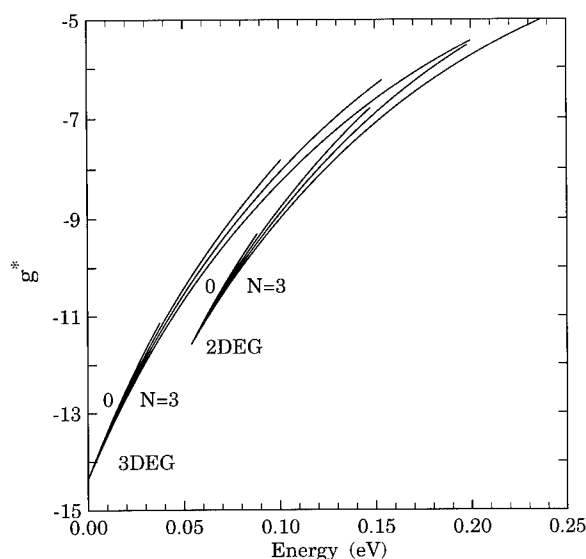


Fig. 3. The calculated  $g$ -factor as a function of electron energy for the first four Landau levels in 3D and 2D electron systems. Here energy is measured from the bulk conduction band edge.

that the reduction of spin-splitting in a 2DEG can be fully accounted for by the band structure effect.

One of the authors (M.J.Y.) is grateful to A.M. Chang, J.C. Ryan, and C.H. Yang for fruitful discussions. This work is supported by the Office of Naval Research.

## 1. References

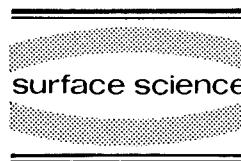
- [1] C.M. Engelhardt et al., *Surf. Sci.* 305 (1994) 23; J.G. Michels et al., *Surf. Sci.* 305 (1994) 33.
- [2] J. Scriba, A. Wixforth, J.P. Kotthaus, C. Bolognesi, C. Nguyen and H. Kroemer, *Semicond. Sci. Technol.* 8 (1993) S133; M.J. Yang, R.J. Wagner, B.V. Shanabrook, J.R. Waterman and W.J. Moore, *Phys. Rev. B* 47 (1993) 6807.
- [3] M.J. Yang, R.J. Wagner, B.V. Shanabrook, W.J. Moore, J.R. Waterman, M.E. Twigg and M. Fatemi, *Appl. Phys. Lett.* 61 (1992) 583.
- [4] M.J. Yang, P.J. Lin-Chung, B.V. Shanabrook, J.R. Waterman, R.J. Wagner and W.J. Moore, *Phys. Rev. B* 47 (1993) 1691.

- [5] From Fig. 8 of Ref. [7], the  $\beta$  is estimated to be 80 for bulk electrons, while in this paper, the  $\beta$  is calculated to be 85.5.
- [6] C.R. Pidgeon and R.N. Brown, Phys. Rev. 146 (1966) 575.
- [7] The parameters used in this work are different from those used by C.R. Pidgeon, D.L. Mitchell and R.N. Brown, Phys. Rev. 154 (1967) 737. This results in a different  $g$ -value, e.g., at band edge ( $-14.4$  versus  $-15$  in their case) and for the higher Landau level, e.g., the  $g$ -value never exceeds zero for  $E \leq 0.25$  eV in our calculation, while their results indicate the  $g$ -factor goes to zero at  $E \approx 0.24$  eV.



ELSEVIER

Surface Science 305 (1994) 275–279



## Cyclotron effective mass of holes in strained $\text{Si}_{1-x}\text{Ge}_x/\text{Si}$ quantum well structures

J.-P. Cheng <sup>\*,b</sup>, V.P. Kesan <sup>a</sup>, D.A. Grützmacher <sup>a</sup>, T.O. Sedgwick <sup>a</sup>

<sup>a</sup> IBM Research Division, T.J. Watson Research Center, Yorktown Heights, NY 10598, USA

<sup>b</sup> Francis Bitter National Magnet Laboratory, Massachusetts Institute of Technology, Cambridge, MA 02139, USA

(Received 20 April 1993; accepted for publication 15 June 1993)

### Abstract

A far-infrared magneto-optical study of cyclotron effective mass of quasi-two-dimensional holes in strained  $\text{Si}_{1-x}\text{Ge}_x/\text{Si}$  quantum wells has been carried out on a series of samples with different Ge compositions at low temperatures and high magnetic fields up to 23 T. The in-plane effective mass determined from cyclotron resonance energies decreases systematically from  $0.40m_0$  to  $0.29m_0$  as the Ge composition increases from  $x = 0.13$  to  $x = 0.37$ . The reduced in-plane mass and its variation with Ge composition are in good qualitative agreement with the strain effects on the valence band structure.

### 1. Introduction

In recent years,  $\text{Si}_{1-x}\text{Ge}_x/\text{Si}$  strained layer superlattices and heterostructures have attracted increasing attention due to their potential device applications and integration with the well-developed Si technology. When a  $\text{Si}_{1-x}\text{Ge}_x$  layer is pseudomorphically grown on a Si substrate, most of the band offset is in the valence band, and this has stimulated a great deal of interest to study the electronic properties of the valence band structure. The lattice mismatch between Si and Ge leads to an inherent compressive in-plane strain in the  $\text{Si}_{1-x}\text{Ge}_x$  alloy layer, which lifts the degeneracy of the heavy-hole ( $\frac{3}{2}, \frac{3}{2}$ ) and light-hole ( $\frac{3}{2}, \frac{1}{2}$ ) bands at the center of the Brillouin zone [1–4]. As a result, the band mixing is substantially

reduced near  $k = 0$ , and a quasi-two-dimensional hole gas (2DHG) occupying the ground (heavy-hole) subband of a strained  $\text{Si}_{1-x}\text{Ge}_x/\text{Si}$  quantum-confined structure is expected to have a lighter effective mass in the plane perpendicular to the growth direction [5–7]. The lighter in-plane hole mass has been observed for other strained layer systems, such as InGaAs/GaAs and InGaAs/AlGaAs quantum wells, in both Shubnikov–de Haas (SdH) oscillations and far-infrared (FIR) cyclotron resonance (CR) measurements [8–11]. For the strained  $\text{Si}_{1-x}\text{Ge}_x/\text{Si}$  system, magnetotransport measurements [12,13], studying the temperature dependence of the amplitude of SdH oscillations, have shown a strong disagreement among different structures, and the results thus are not conclusive.

In this paper we report a systematic FIR magneto-optical study carried out on a series of p-type modulation-doped  $\text{Si}_{1-x}\text{Ge}_x/\text{Si}$  multiple-quantum

\* Corresponding author.



tum-well (MQW) samples with widely varying Ge compositions ( $x = 0.13$ – $0.37$ ). The cyclotron resonance of 2DHGs has been observed at high magnetic fields (up to 23 T), and resonance energies are used to determine the in-plane effective mass. A lighter in-plane hole mass in the strained  $\text{Si}_{1-x}\text{Ge}_x$  layer is evidenced [14], and a systematic decrease in CR mass with increasing Ge composition has been clearly observed. These are qualitatively consistent with the expectation for the strain effects on the valence band structure, namely, a larger strain at higher Ge compositions will lead to a larger band splitting and smaller band mixing, and hence a lighter in-plane, band-edge effective mass.

## 2. Experimental

The three  $\text{Si}_{1-x}\text{Ge}_x/\text{Si}$  MQW structures used in this experiment were grown on n-Si(100) 30–100  $\Omega$  cm substrates by atmospheric pressure chemical vapor deposition (APCVD) [15]. Boron acceptors were modulation-doped in the Si barriers with the doping levels arranged in such a way that each  $\text{Si}_{1-x}\text{Ge}_x$  well would have the same sheet density. All samples have nominally the same barrier width of 300 Å and the same well width of 80 Å, which were confirmed by X-ray diffraction measurements. The X-ray diffraction spectra, together with dynamical diffraction simulations, showed that the  $\text{Si}_{1-x}\text{Ge}_x$  layers are fully strained for all samples. The important sample parameters are listed in Table 1, where the hole concentrations (per well) and the low-temperature mobilities are determined by dc magneto-transport measurements.

Table 1

Sample properties. Ge composition ( $x$ ) and well widths were determined by X-ray diffraction measurements; carrier concentrations (per well) and mobilities were determined by dc transport measurements at temperatures around 10 K

Sample	$x$	Well width (Å)	No. of wells	Density ( $10^{12}/\text{cm}^2$ )	Mobility ( $\text{cm}^2/\text{V}\cdot\text{s}$ )
1	0.13	80	4	0.8	2500
2	0.25	80	4	1.6	1700
3	0.37	80	1	2.3	1500

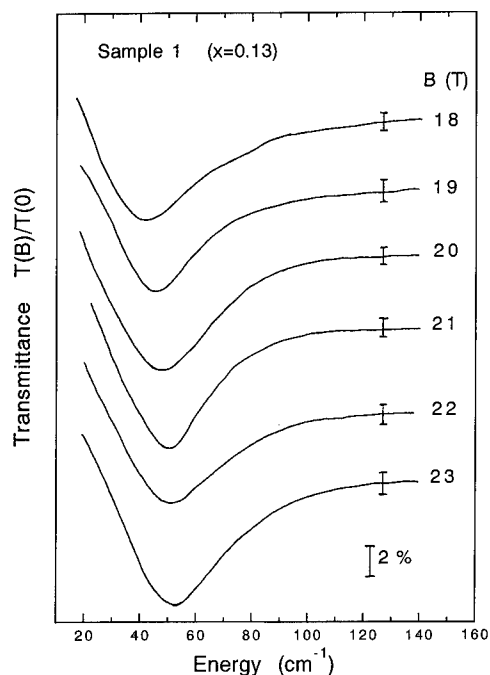


Fig. 1. Normalized transmission spectra for sample 1 ( $x = 0.13$ ) at several magnetic fields. Data were taken at 4.2 K. Error bars on the spectra indicate the typical noise level.

FIR magneto-transmission spectra were obtained with a repetitively scanned Fourier transform spectrometer in conjunction with a 23 T Bitter magnet at the Francis Bitter National Magnet Laboratory. A 4.2 K Si-composite bolometer detector was sealed in the same vacuum jacket as the sample, and a small amount of He exchange gas was used to accelerate the cooling process (however, too much exchange gas will diminish the detector response). Light pipes, reflecting mirrors and condensing-cone optics were used to guide the FIR light to the sample and detector. Sample substrates were wedged to avoid multiple-reflection interference, and all data were taken at liquid He temperatures.

## 3. Results and discussion

In Fig. 1 we show the magnetic field dependence of the FIR transmission spectra for sample 1 ( $x = 0.13$ ). All spectra in this figure were obtained at 4.2 K in the Faraday geometry (mag-

netic field is parallel to the direction of FIR light propagation and normal to the sample surface) and normalized by ratioing to a background spectrum taken at zero magnetic field. The linewidth of the CR spectra is generally broad with the half-width at half-maximum (HWHM) about  $20 \text{ cm}^{-1}$ . The line shape appears very asymmetric, i.e. the transmittance is divergent as energy approaches zero; this is due to the free-carrier absorption at  $B = 0$  in the background spectrum. With increasing magnetic field, the CR peak position (transmission minimum) moves continuously to higher energies. To verify the 2D property of the carriers, the normal to the sample surface was tilted about  $30^\circ$  away from the direction of magnetic field. The CR position was found to shift down to a lower energy (not shown in the figure) in comparison with the no-tilt case at the same magnetic field, which indicates that the holes are confined in the  $\text{Si}_{0.87}\text{Ge}_{0.13}$  quantum wells. From the slope of a plot of CR energy versus magnetic field (see Fig. 3 below), the cyclotron mass for this sample has been determined to be  $(0.40 \pm 0.02)m_0$ .

Fig. 2 shows typical transmission spectra for all three samples at the same magnetic field, 23 T. Data were taken at 4.2 K for samples 1 and 2 and at 3.0 K for sample 3. The spectra in the figure are normalized to a zero-field background, as discussed above. When the Ge composition increases, the resonance position clearly moves to higher energies, which implies a lighter effective mass for a larger Ge composition. Notice that the lineshape is more symmetric for sample 3 since its CR line appears at higher energy; hence it is less affected by the free-carrier absorption in the background spectrum.

The CR transition energy as a function of magnetic field normal to the sample surface ( $B \cos \theta$ , where  $\theta$  is the angle between the field direction and the normal to the sample surface) is plotted in Fig. 3 for all three samples. The solid symbols are for  $\theta = 0^\circ$  and the open symbols for  $\theta = 30^\circ$ . The error bars (omitted in the figure for a clear view) are typically  $\pm 5 \text{ cm}^{-1}$ , and are nearly the same for all data points. Within experimental error, all data points for each sample can be fitted reasonably well by a straight line passing

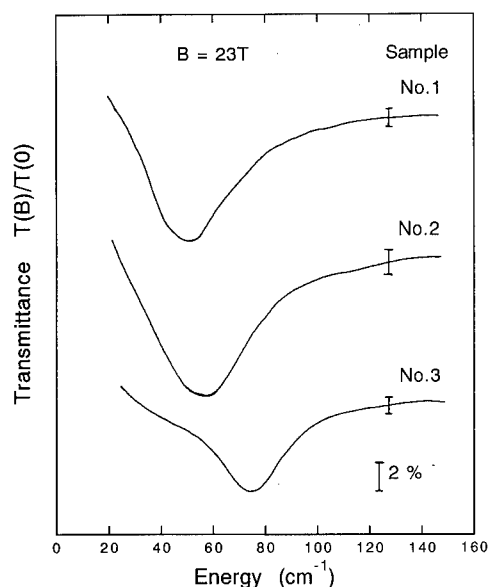


Fig. 2. Normalized transmission spectra for three samples at 23 T. Data were obtained at 4.2 K for samples 1 and 2, and 3.0 K for sample 3. Error bars on the spectra indicate the typical noise level.

through the origin, as shown in the figure. It is clear that the holes are confined in the strained  $\text{Si}_{1-x}\text{Ge}_x$  quantum wells for all samples, and a

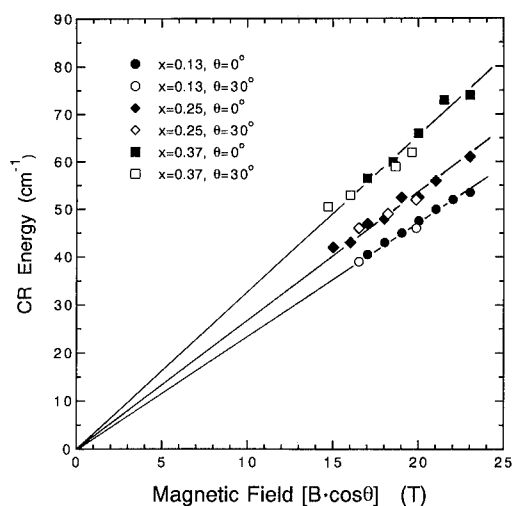


Fig. 3. A compilation of the CR transition energy as a function of magnetic field normal to the sample surface ( $B \cos \theta$ ) for three samples.  $\theta$  is the tilt angle between the direction of magnetic field and the normal to the sample surface. Solid symbols,  $\theta = 0^\circ$ ; open symbols,  $\theta = 30^\circ$ .

smaller Ge composition corresponds to a smaller slope of the straight line (thus a larger CR mass). The values of cyclotron effective mass for the three samples are listed below:

sample 1 ( $x = 0.13$ ) –  $(0.40 \pm 0.02)m_0$ ;

sample 2 ( $x = 0.25$ ) –  $(0.34 \pm 0.02)m_0$ ;

sample 3 ( $x = 0.37$ ) –  $(9.29 \pm 0.02)m_0$ .

The measured CR mass for sample 1 is in reasonable agreement with a previous transport measurement result [13], in which the hole mass in a  $\text{Si}_{0.85}\text{Ge}_{0.15}$  strained layer quantum well was determined to be  $(0.44 \pm 0.03)m_0$ . Since the 2D hole concentrations (per well) for all samples used in this study are comparable [16], we can infer that the in-plane effective mass of holes in  $\text{Si}_{1-x}\text{Ge}_x$  strained layers decreases with increasing Ge composition, which is qualitatively consistent with the expectation of the strain effects on the valence band structure.

If a linear-average method is used to estimate the effective mass for unstrained  $\text{Si}_{1-x}\text{Ge}_x$  alloy from bulk Si and Ge, the heavy hole mass at the band edge will be approximately  $0.5m_0$  for  $x = 0.13$  and  $0.45m_0$  for  $x = 0.37$ . Our measured effective masses are much smaller than these values and are consistent with the strain-induced, lighter in-plane mass. On the other hand, the measured values are systematically higher than the calculated values for the in-plane, band-edge mass for  $\text{Si}_{1-x}\text{Ge}_x/\text{Si}$  strained layers, which are typically about  $0.2m_0$  for the Ge composition range in our experiment [6,7]. It is most likely that the discrepancies between theory and experiment are due to the nonparabolicity effect in the valence bands. For the present samples, the carrier concentrations are high, and an estimate shows that the Fermi energies are substantially higher (10–20 meV) than the band-edge ( $k = 0$ ) (but still lower than the second subband), and the band mixing can be very strong; hence a large nonparabolicity and heavier effective mass are expected. Other factors, such as quantum confinement (shifting up the ground subband from bulk band-edge), wavefunction extension (sampling the heavier mass in the Si barriers), and warping of the energy surfaces for valence bands, may also enhance the

CR mass; the last one is especially important for high carrier concentrations [7].

#### 4. Summary

We have observed cyclotron resonance of quasi-2D holes confined in strained  $\text{Si}_{1-x}\text{Ge}_x/\text{Si}$  multiple quantum well structures at high magnetic fields. The measured CR mass is much smaller than the estimated heavy-hole mass for the unstrained  $\text{Si}_{1-x}\text{Ge}_x$  alloy, and it systematically decreases with increasing Ge composition. These observations are qualitatively consistent with a picture of strain-induced valence band splitting and reduction of band mixing. The discrepancy in the values of effective mass between theory and experiment may be due to the nonparabolicity effect at high hole concentrations.

#### 5. Acknowledgements

Most of this work was carried out at the Francis Bitter National Magnet Laboratory at MIT. We are very grateful to the staff, especially L. Rubin, for assistance. We would also like to thank S.S. Iyer and T.P. Smith III for their continued support and encouragement. One of us (JPC) thanks IBM for the support in the form of an IBM postdoctoral fellowship.

#### 6. References

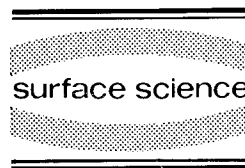
- [1] G.C. Osbourn, Phys. Rev. B 27 (1983) 5126.
- [2] G.C. Osbourn, J.E. Schirber, T.J. Drummond, L.R. Dawson, B.L. Doyle and I.J. Fritz, Appl. Phys. Lett. 49 (1986) 731.
- [3] R. People, Phys. Rev. B 32 (1985) 1405.
- [4] K.L. Wang, R.P. Karunasiri, J. Park, S.S. Rhee and C.H. Chern, Superlattices and Microstruct. 5 (1989) 201.
- [5] T. Manku and A. Nathan, Phys. Rev. B 43 (1991) 12634.
- [6] T. Manku and A. Nathan, J. Appl. Phys. 69 (1991) 8414.
- [7] S.K. Chun and K.L. Wang, IEEE Trans. Electron Devices ED-39 (1992) 2153.
- [8] J.E. Schirber, I.J. Fritz and L.R. Dawson, Appl. Phys. Lett. 46 (1985) 187.
- [9] S.Y. Lin, C.T. Liu, D.C. Tsui, E.D. Jones and L.R. Dawson, Appl. Phys. Lett. 55 (1989) 666.

- [10] S.Y. Lin, D.C. Tsui, J.F. Klem, E.D. Jones and L.R. Dawson, in: *MRS Proc. Symp. on Electrical, Optical and Developed Properties of Layered Structures*, Eds. J.R. Hayes, M.S. Hybertsen and E.R. Weber (Materials Research Society, Pittsburgh, 1990) p. 279.
- [11] M. Jaffe, J.E. Oh, J. Pamulapati, J. Singh and P. Bhat-tacharya, *Appl. Phys. Lett.* 54 (1989) 2345.
- [12] R. People, J.C. Bean, D.V. Lang, A.M. Sergent, H.L. Stormer, K.W. Wecht, R.T. Lynch and K. Baldwin, *Appl. Phys. Lett.* 45 (1984) 1231.
- [13] P.J. Wang, F.F. Fang, B.S. Meyerson, J. Nocera and B. Parker, *Appl. Phys. Lett.* 54 (1989) 2701.
- [14] J.-P. Cheng, V.P. Kesan, D.A. Grutzmacher, T.O. Sedgwick and J.A. Ott, *Appl. Phys. Lett.* 62 (1993) 1522.
- [15] P.D. Agnello, T.O. Sedgwick, D. Meyer and A.P. Ferro, in: *Proc. 1st Topical Symp. on Silicon Based Heterostruc-tures*, 37th American Vacuum Society Symposium, Eds. S.S. Iyer, D.C. Houghton and M.L. Green (Materials Research Society, Pittsburgh, 1990) p. 46.
- [16] When the carrier density differences are taken into ac-count for the nonparabolicity correction, our conclusions for the qualitative behavior of in-plane mass as a function of Ge composition should not change, since the samples showing heavier mass have lower carrier densities, and the mass would be even heavier when the density in-creases.



ELSEVIER

Surface Science 305 (1994) 280–284



# Far infrared emission from magnetically quantised 2DEGs in GaAs/(AlGa)As heterojunctions

N.N. Zinov'ev, R. Fletcher <sup>1</sup>, L.J. Challis <sup>\*</sup>, B. Sujak-Cyrul <sup>2</sup>, A.V. Akimov <sup>3</sup>,  
A.F. Jezierski

*Physics Department, Nottingham University, Nottingham, NG7 2RD, UK*

(Received 16 April 1993; accepted for publication 20 July 1993)

## Abstract

We present the first studies of far infrared cyclotron emission from magnetically quantised 2DEGs made using a broad band detector. Spectral resolution was obtained using the substrate as a Fabry–Pérot etalon together with a low pass filter. Information was obtained on the intensity in fields up to 3 T and currents up to 600  $\mu$ A. The experiments demonstrate that the system is well adapted for investigating the electron temperatures as a function of magnetic field. They also show that 20–30% of the emission occurs at frequencies significantly less than  $\omega_c$ .

## 1. Introduction

Two-dimensional electron gases (2DEGs) have been extensively studied by far infrared (FIR) transmission and reflection spectroscopy. Much less attention has been given to their emission spectrum particularly in magnetic fields where work has been restricted to three groups who used narrow band GaAs photodetectors. Their work confirmed that, in GaAs, the emission oc-

curs predominantly at the cyclotron frequency [1–3].

The present work describes a system developed for use as an electron thermometer. In magnetically quantised systems, the phonon relaxation rate by cyclotron phonon emission is predicted to decrease rapidly when  $q_c a > 1$ ;  $q_c = \omega_c/v_s$ , where  $\omega_c$  is the cyclotron frequency,  $v_s$  is the sound velocity and  $a$  is the “thickness” of the 2DEG [4]. Other processes are then likely to become important such as two-phonon emission [4] and edge-state relaxation [5]. To investigate the dependence of the relaxation rate on the cyclotron frequency we have developed a technique using a broad band detector which can be used to measure the intensity of the FIR emission and so the electron temperature over a range of magnetic fields. The paper also describes measurements of the total FIR intensity from 2DEGs

<sup>\*</sup> Corresponding author.

<sup>1</sup> Permanent address: Queen's University, Kingston, Ontario, Canada.

<sup>2</sup> Permanent address: Institute of Low Temperature and Structure Research, Wrocław, Poland.

<sup>3</sup> Permanent address: A.F. Ioffe Physical Technical Institute, St. Petersburg, Russian Federation.

in GaAs heterostructures as a function of current up to  $600 \mu\text{A}$  and magnetic field up to 3 T. The data are analysed to obtain values of the cyclotron mobility  $\mu_{\text{CR}}$  for the various samples.

## 2. Experimental arrangement

The sample is mounted on a copper post whose further end is in contact with liquid helium at 4 K. The sample and detector are located 1–2 mm from the two ends of an evacuated 18-cm copper light pipe of inner diameter 5 mm allowing the detector to be in an essentially field-free region while magnetic fields from a 0–7 T superconducting solenoid are applied normal to the sample.

Part of the FIR emission from the 2DEG travels towards the back surface of the substrate furthest from the 2DEG where it is reflected up towards the detector. The interference that occurs between the emission following these two light paths is well known but these may be the first experiments in which it has been used to obtain spectral information on the emission. The reflection was increased by polishing the back surface to be flat and parallel to the front and by polishing the copper mounting post to which it is glued. In the light path above the sample could be placed a low pass filter which has a sharp cut-off in transmission at  $\sim 15 \text{ cm}^{-1}$  falling as  $T_r \approx [1 + \exp(\nu - 15)/0.5]^{-1}$  ( $\nu$  in  $\text{cm}^{-1}$ ). The hot-electron detector was a thin InSb crystal of cross-section  $5 \times 5 \text{ mm}^2$  mounted on a  $5^\circ$  quartz wedge. The integral optical activity had a constant value of  $5.0 \text{ kV W}^{-1}$ . Its spectroscopic response is constant for  $\nu < 15 \text{ cm}^{-1}$ , but for  $\nu > 15 \text{ cm}^{-1}$  this fell as  $\exp[(\nu - 15)/15.4]$  with  $\nu$  in  $\text{cm}^{-1}$ . The filter, detector and amplifier system were supplied by QMC Instruments, Queen Mary and Westfield College, London University.

Most of the experiments were carried out on three single GaAs/(AlGa)As heterojunctions with the following sheet densities  $n$  (in  $10^{15} \text{ m}^{-2}$ ) and transport mobilities  $\mu_0$  (in  $\text{m}^2 \text{ V}^{-1} \text{ s}^{-1}$ ) NU276:  $n = 2.3$ ,  $\mu_0 = 22$ ; NU444:  $n = 3.4$ ,  $\mu_0 = 144$ ; NU711:  $n = 2.9$ ,  $\mu_0 = 80$ . The first two samples are standard 8-contact Hall bars with channel dimensions of  $2.5 \times 0.2 \text{ mm}^2$  and the third

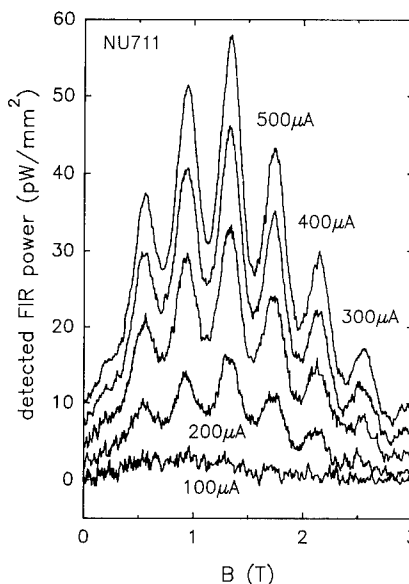


Fig. 1. The FIR power emitted from NU711 for various currents as a function of magnetic field.

has the shape of a cross in which each leg has dimensions  $4.0 \times 0.2 \text{ mm}^2$  and a contact at its extremity. The contact resistances were all less than  $50 \Omega$  so should contribute negligibly to the FIR emission. The 2DEGs were heated by current pulses of duration 10–120  $\mu\text{s}$  and the repetition rate was always kept below 1 kHz so that the rise in substrate temperature at the maximum power level was estimated to be less than 1 K. A resistor was connected in series with the sample to maintain approximately constant pulse current during the field sweeps though it also had the effect of restricting its maximum value to  $600 \mu\text{A}$ .

## 3. Results

Examples of measurements of the detected FIR power for different source-drain currents are shown as a function of magnetic field in Fig. 1 for NU711; similar results were obtained for NU276 and NU444. Measurements on NU711 were also made with the field applied at  $40^\circ$  to the 2DEG normal and the 2 sets of data are plotted against  $B \cos \theta$  in Fig. 2. Their similarity indicates that the FIR emission is due to the 2DEG.

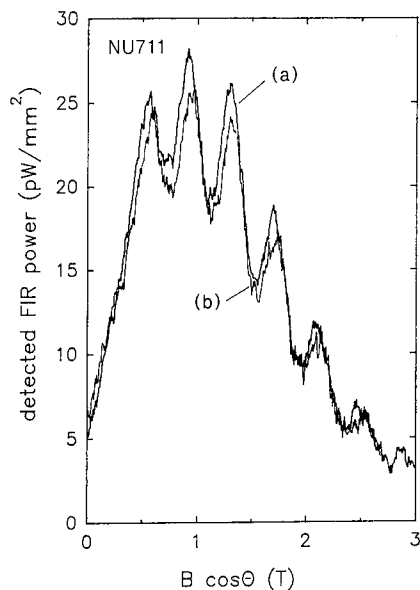


Fig. 2. The FIR power emitted from NU711 for a current of  $450 \mu\text{A}$  as a function of the normal component of magnetic field  $B \cos \theta$  for two directions of magnetic field ( $\theta = 0^\circ$  (a) and  $40^\circ$  (b)).

Oscillations observed in Fig. 2 have periods which, for the 3 samples, are in very good agreement with the period calculated assuming a nar-

row emission line at  $\omega_c$ . Because of the phase change of  $\pi$  on reflection at the back surface, the interference condition  $2d = m\lambda$  results in minima in the detected signal ( $d$  is the substrate thickness,  $\lambda = c/\nu_c\epsilon$  is the wavelength of the cyclotron radiation in the substrate of relative permittivity  $\epsilon$ ,  $c$  is the velocity of light and  $m$  is an integer). A further check was made by reducing the substrate thickness of all of the samples by  $\sim 25\%$ . The periods changed by the expected amounts. The amplitudes of the oscillations are determined by the emission linewidths which were deduced from the analysis given in Section 4.

The effect of inserting a low pass filter in the light path is demonstrated for sample NU711 in Fig. 3a which shows data with and without the filter. There appears to be no significant change for magnetic fields less than 1 T but the FIR signal drops rapidly over a narrow field region centred at about 1.07 T when the cyclotron frequency exceeds the cut-off frequency of the filter. Very similar results are found for samples NU276 and NU444 although the fall is noticeably broader for NU276 (Fig. 3b) in line with its greater cyclotron width evident in the oscillations. The intensity does not drop to zero when  $\nu_c > 15 \text{ cm}^{-1}$

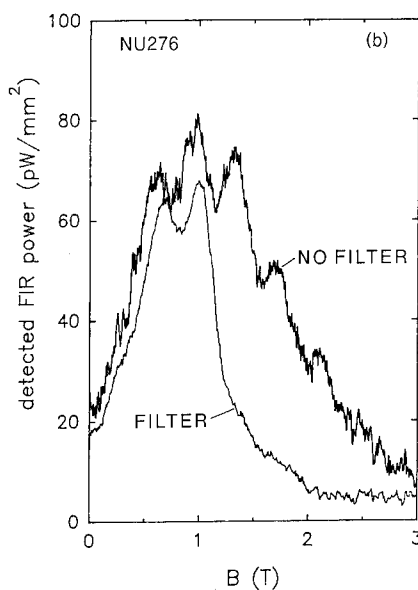
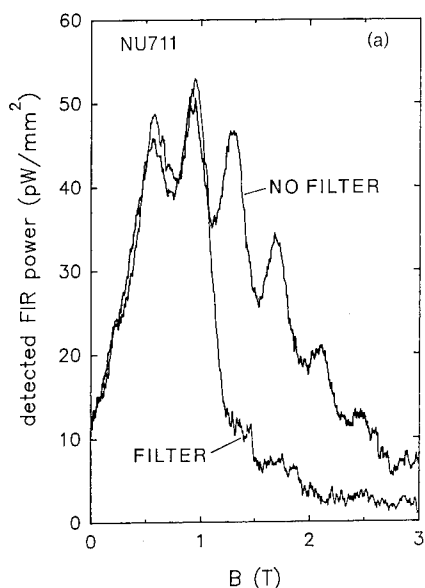


Fig. 3. The FIR power detected with and without a low pass filter for a current of  $500 \mu\text{A}$  (a) NU711 and  $460 \mu\text{A}$  (b) NU276.

but falls to a value between 0.2 and 0.3 of the intensity just below the cut-off. This implies that part of the emission occurs at  $\nu < \nu_c$  and since there is no similar fall at fields just below the cut-off when the filter is inserted at least for NU711 (this also appears to be the case for NU276 and NU444 though the data are less clear) this is not due to a broad tail on either side of  $\nu_c$ . We discuss this further in the next section.

#### 4. Discussion

The detector signal can be written

$$P_C^D = \int_0^\infty E(\omega) I(\omega) D(\omega) d\omega,$$

where  $E(\omega)$ ,  $I(\omega) d\omega$  and  $D(\omega)$  are respectively the emissivity of the 2DEG, the radiation emitted by a blackbody at temperature  $T_e$  of area equal to the 2DEG and the detector sensitivity. From electromagnetic theory,  $E(\omega)$  of a 2DEG of conductivity  $\sigma(\omega)$  at the surface of a transparent medium of relative permittivity  $\epsilon$  is given by

$$E(\omega) = \frac{4 \operatorname{Re} \sigma(\omega) / \epsilon_0 c}{|1 - i\sqrt{\epsilon} \cos \delta + \sigma(\omega) / \epsilon_0 c|^2},$$

where  $\delta = 2\pi d/\lambda$ , and from classical Drude theory

$$\sigma(\omega) = \frac{(ne^2\tau/m^*)(1 + i\omega\tau)}{(1 + i\omega\tau)^2 + \omega_c^2\tau^2},$$

where  $n$  is the sheet density and  $\tau$  is the electron relaxation time.

Curves calculated from these expressions at constant  $T_e$ , the standard expression for  $I(\omega) d\omega$  and the calibrated value of  $D(\omega)$  have similar structures to those found experimentally at constant current and have been used to determine values of  $\tau$  for the three samples. The corresponding values of  $\mu_{CR}$  in units of  $\text{m}^2 \text{V}^{-1} \text{s}^{-1}$  are NU276: 7, NU444: 10 and NU711: 15 which are all very much smaller than the values of  $\mu_0$  given earlier as expected from previous work on cyclotron resonance [6].

We next discuss the observation of FIR emission at frequencies less than  $\omega_c$ . In all three

samples this forms 20–30% of the total intensity at 1 T but decreases with field which might either imply that its intensity falls with magnetic field or that its frequency increases with field leading to a decrease in detector signal as the spectrum is moved through the filter cut-off.

At present neither the source nor the spectrum of this emission is known. We speculate, however, that it might possibly be a low frequency tail to the cyclotron line caused by part of the cyclotron energy being emitted as a phonon. The equivalent process in absorption was first discussed by Bass and Levinson [7] for a 3D system and has been seen experimentally for optical phonons [8]. Another possibility is that it might be associated with low-frequency magnetoplasmon modes of wavelength comparable to the width of the 2DEG (we are grateful to the referee for this suggestion). Emission arising through coupling to  $\omega_c$  would become weaker as  $\omega_c$  is increased in line with the decrease observed.

The theoretical relationship between FIR intensity and  $T_e$  at 1.2 T is shown in Fig. 4. A rough

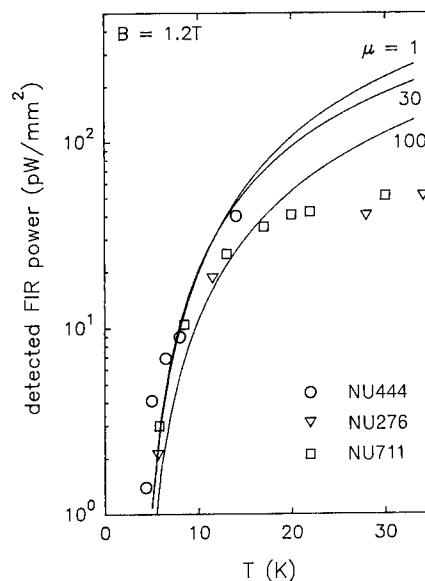


Fig. 4. The FIR intensity emitted for  $B = 1.2$  T as a function of  $T_e$ . The lines show theoretical values for a sample with  $n_s = 3 \times 10^{15} \text{ m}^{-2}$  and for different mobilities, and the points show experimental data for the corresponding input powers plotted using  $T_e$  values determined from Shubnikov–de Haas measurements [9].



comparison with the experimental FIR intensities can be made if, for a given input power density, we assume  $T_e$  values obtained from Shubnikov–de Haas measurements on low-mobility samples [9]; the agreement appears satisfactory up to about 15 K. The significance of this must be treated with caution at this stage since the  $T_e$  values were determined at the centre of the sample while the dissipation is believed to be greatest, at least for lower power inputs [10], at the diagonally opposite corners where the current enters and exits the 2DEG. It seems possible, however, that at these long wavelengths, the emissivity of the 2DEG in these corners is strongly reduced by the presence of the adjoining metal contacts.

In conclusion we note that the experiments suggest that the FIR emission technique has sufficient sensitivity to measure temperatures down to 5 K with the sample at 4 K, and should be capable of extension down to 2.5–3 K if the sample temperature were lowered to 1.5 K. Another advantage is that, for a given temperature, the intensity within a cyclotron line should be only rather weakly dependent on cyclotron mobility: the area under the line is almost independent of  $\mu_{CR}$  as can be seen from the curves in Fig. 4, because the increase in peak height is approximately balanced by the decrease in width.

## 5. Acknowledgements

We gratefully acknowledge help with the experiments by Dr. J.M. Chamberlain, Dr. T. Cheng,

Dr. M. Henini, Mr. B. Hill and Mr. J. Middleton, help with manuscript preparation by Mrs. L. Wightman, stimulating discussions with Professor R. Suris and theoretical colleagues from the Ioffe Physical Technical Institute and financial support from the Science and Engineering Research Council, the Royal Society and the European Commission.

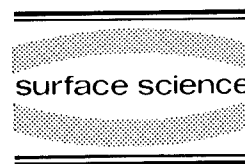
## 6. References

- [1] E. Gornik, R. Schwartz, D.C. Tsui, A.C. Gossard and W. Wiegmann, *Solid State Commun.* 38 (1981) 541.
- [2] K. von Klitzing, G. Ebert, N. Kleinmichel and H. Obloh, in: *Proc. 17th Int. Conf. on Phys. Semicond.*, San Francisco, 1984, Eds. J.D. Chadi and W.A. Harrison (Springer, New York, 1985) p. 271.
- [3] C. Chaubert, A. Raymond, W. Knap, J.Y. Mulot, M. Baj and J.P. Andres, *Semicond. Sci. Technol.* 16 (1991) 160.
- [4] V. Fal'ko and L.J. Challis, *J. Phys. Condensed Matter* 5 (1993) 3945.
- [5] A.Y. Shik, *Sov. Phys. Semicond.* 26 (1992) 481.
- [6] M.A. Hopkins, R.J. Nicholas, D.J. Barnes, M.A. Brummell, J.J. Harris and C.T. Foxon, *Phys. Rev. B* 39 (1989) 13302.
- [7] F.G. Bass and I.B. Levinson, *Sov. Phys. JETP* 22 (1966) 635.
- [8] B.D. McCombe, R.J. Wagner and G.A. Prinz, *Solid State Commun.* 8 (1970) 1687; E.J. Johnson and D.H. Dickey, *Phys. Rev. B* 1 (1970) 2676.
- [9] K. Hirakawa and H. Sakaki, *Appl. Phys. Lett.* 49 (1986) 889.
- [10] P.A. Russell, F.F. Ouali, N.P. Hewett and L.J. Challis, *Surf. Sci.* 229 (1990) 54; U. Klass, W. Dietsche, K. von Klitzing and K. Ploog, *Z. Phys. B* 82 (1991) 351.



ELSEVIER

Surface Science 305 (1994) 285–289



# Reflectivity, transport and magneto-optical studies of holes in the p-type HgZnTe/CdTe superlattice

J.B. Choi \*

*Department of Physics, Chungbuk National University, Cheongju, 360-763, South Korea*

J.R. Meyer, C.A. Hoffman

*Naval Research Laboratory, Washington, DC 20375, USA*

G. Karczewski, J.K. Furdyna

*Department of Physics, University of Notre Dame, Notre Dame, IN 47907, USA*

K.H. Yoo

*Department of Physics, Kyung Hee University, Seoul, South Korea*

J.P. Faurie

*Department of Physics, University of Illinois, Chicago, IL 60680, USA*

(Received 12 April 1993; accepted for publication 14 July 1993)

## Abstract

We report the first systematic experimental investigation of the anomalous properties of holes in a p-type HgZnTe/CdTe superlattice by performing reflectivity, transport and magneto-optical measurements. The transport and cyclotron resonance data are fully correlated with the polarization-dependent reflectivity, and show consistent behavior of two holes with different mobilities. The observed distinctive features of the holes are accurately explained by the extremely non-parabolic and anisotropic valence band structure.

Recent magnetotransport measurements on p-type Hg-based superlattices [1,2] have yielded extraordinarily high hole mobilities ( $> 10^5$  cm<sup>2</sup>/V · s), which is of great interest for potential

device applications. The existence of holes with such high mobilities corresponds to the extremely small in-plane hole effective masses and arises from the unique narrow-band-gap superlattice band structures, which are quite distinct from anything observed so far in wide-band-gap systems. Here we report the first systematic experi-

\* Corresponding author.

mental investigation of the anomalous properties of holes in a p-type HgZnTe/CdTe superlattice by performing reflectivity, transport and magneto-optical measurements. The transport and cyclotron resonance data are fully correlated with the polarization-dependent reflectivity and show consistent behavior of the holes.

Transport and cyclotron resonance experiments have been performed on a p-type 100 periods  $\text{Hg}_{1-x}\text{Zn}_x\text{Te}/\text{CdTe}$  superlattice grown by MBE on a GaAs(100) substrate. Nominal material parameters are  $x = 0.06$  for the composition, 70 Å for the HgZnTe well thickness, and 23 Å for the CdTe barrier thickness. Figs. 1 and 2 show the temperature-dependent electron and hole mobilities and cyclotron resonance data, which display consistent behavior. At low temperatures ( $T < 10$  K) two holes with different mobilities are obtained from the mixed conduction analysis, which account for the two-hole cyclotron resonances observed in the hole-active circular polarization of Faraday geometry (optical propagation parallel to  $B$ ). The hole cyclotron mass associated with the lower field resonance is found to be  $\sim 2.5 \times 10^{-3} m_0$ , which is extremely small and results in the ultrahigh hole mobility observed in transport. The second hole resonance corresponding to the lower mobility holes in transport is resolved only for high-resonance

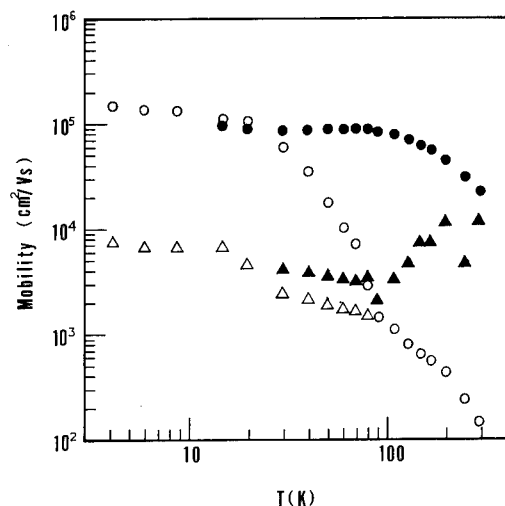


Fig. 1. Temperature dependence of electron and hole mobilities (holes, open marks; electrons, solid marks).

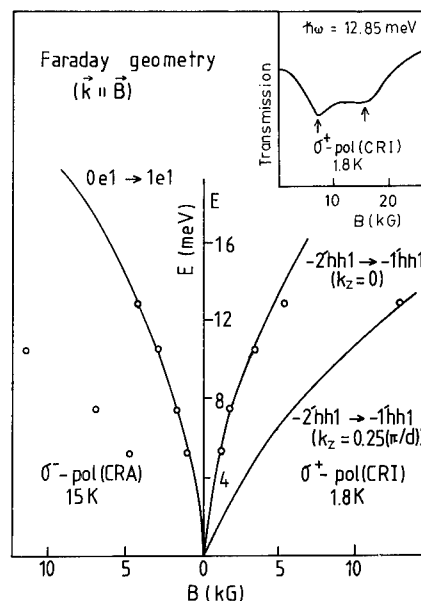


Fig. 2. FIR photon energies as a function of resonant magnetic fields in the Faraday geometry. The solid lines along data are the calculated inter-Landau level transitions.

magnetic fields because of its broader line width. The inset in Fig. 2 shows typical magnetotransmission for the wavelength 96.5  $\mu\text{m}$  at 1.8 K. With increasing temperature ( $T > 10$  K) thermally generated intrinsic electrons come to dominate the transport properties and they are also reflected in the cyclotron resonance data: two electron cyclotron resonances start to occur, while the intensities of the hole absorptions decrease. This thermal behavior of carriers indicates that the sample has an energy gap near zero ( $E_g < 10$  meV).

We have calculated the energy band structure in order to identify the hole magneto-optical transitions and explain the existence of two holes with different mobilities at low temperature and the abrupt decrease in their mobilities with increasing temperature. In calculating the band structure by a  $k \cdot p$  method, the best fit to the experimental data was obtained following slight adjustments of the Zn composition  $x$  and layer thicknesses. The value of the valence band offset  $\Lambda$  ( $\sim 500$  meV), defined as the difference between the HgZnTe and CdTe  $\Gamma_8$  valence band maxima, which cannot be uniquely determined by

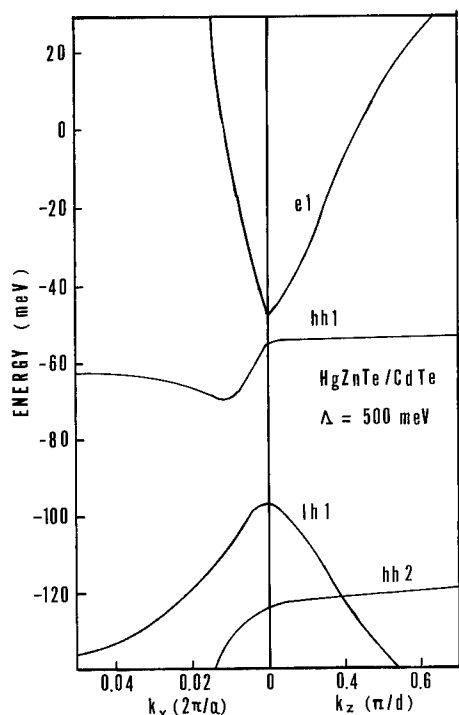


Fig. 3. Calculated superlattice energy dispersions in the growth and in-plane directions.

the cyclotron resonance data in the Faraday geometry alone [3,4] was independently determined by reflectivity data, as detailed later. Fig. 3 displays the resulting band structure of the superlattice for  $x = 0.04$ ,  $d_w = 73$  and  $d_B = 20$  Å. It shows that in contrast to the E1 band, the hh1 band is dispersionless in the growth-direction wavevector  $k_z$ , and this results in the mass broadening of holes for low temperatures [2]. The inter-Landau level transition,  $-2'hh1 \Rightarrow -1'hh1$ , can thus occur at two extremal positions of  $k_z$  over the zone. The lower field hole resonance is found to be very close to the transition occurring at  $k_z = 0$ , while the high field resonance can be fit by the transition occurring at  $k_z \approx 0.25 (\pi/d)$ . The hh1 band also shows a strong non-parabolicity of the dispersion with in-plane wavevector  $k_x$ , and the average effective mass over the thermal distribution increases with temperature. This causes the abrupt decrease in the hole mobility observed with increasing temperature. This thermal effect in hole effective mass also accounts for the tem-

perature dependence of the hole cyclotron resonance, which is observed for the wavelength 118.8  $\mu\text{m}$ . As the temperature increases from 1.8 to 50 K, the hole resonance becomes broader, and another very broad absorption associated with low-mobility holes starts to occur at the high-field side.

The existence of holes and their thermal properties should be confirmed by a direct measurement of hole intersubband transitions. This was done in our reflectivity experiment, which is also found to be crucial in determining  $\Delta$ . We have developed a reflectivity technique to enhance the polarization perpendicular to the superlattice plane. The broadband beam was incident at 45 degree to the back side of the sample, i.e., GaAs substrate. A conducting thin film was tightly attached to the front of the superlattice film in order to make the optical electric field of the photon to be predominantly perpendicular to the superlattice plane, which causes maximum optical coupling of the radiation to the vertical motion of electrons.

Fig. 4 displays the high-frequency reflectivity data of the superlattice. No appreciable structure was found between 900 and 3000  $\text{cm}^{-1}$ . In the polarization  $E \parallel z$  the data show a strong absorption at about 570  $\text{cm}^{-1}$  and a weak one at about 350  $\text{cm}^{-1}$ . The main absorption at 570  $\text{cm}^{-1}$

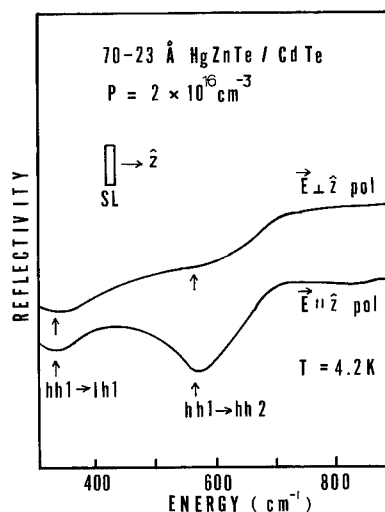


Fig. 4. Polarization dependence of reflectivity spectra at 4.2 K.

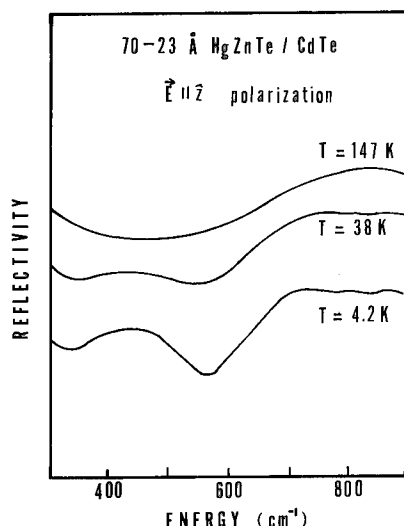


Fig. 5. Temperature dependence of reflectivity for polarization perpendicular to the superlattice plane.

shows a marked polarization dependence, and corresponds to the  $hh1 \Rightarrow hh2$  intersubband transition. On the other hand, the small absorption at  $350 \text{ cm}^{-1}$  has relatively little polarization dependence, and is associated with the  $hh1 \Rightarrow lh1$  transition (the polarization selection rule is less restrictive for interband transitions than intersubband transitions). Both absorptions also have temperature-induced broadenings, as shown in Fig. 5. We note that with increasing temperature, the  $hh1 \Rightarrow hh2$  absorption becomes weaker and its transition energy is found to shift to lower energy. This thermal behavior, similar to those in the transport and the hole cyclotron resonance data, can be explained by the strong non-parabolicity of the  $hh1$  in-plane energy dispersion  $E(k_x)$ . As temperature increases, thermally excited holes are distributed over the high-energy region of the  $hh1$  band, resulting in the small shift of  $hh1 \Rightarrow hh2$  transition to lower energy.

The observed transition energy of  $hh1 \Rightarrow hh2$  is found to fall in the range of values of about 70 meV. This result is crucial in determining the value of  $\Lambda$ . It is well known that strain moves the light-hole band  $lh1$  higher in energy with respect to the  $hh1$  band, while quantum confinement enhanced by a large  $\Lambda$  pushes  $lh1$  lower than  $hh1$

because of the large difference between light-hole and heavy-hole masses [5]. Therefore, for small  $\Lambda$  values the strain effect is dominant, and the hole Fermi level is in the  $lh1$  band. The intersubband transition is then  $lh1 \Rightarrow lh2$  whose transition energy is very large ( $\sim 200 \text{ meV}$ ) because of the small light-hole mass. Thus, the observed transition energy of about  $570 \text{ cm}^{-1}$  cannot be explained by any optical transitions between light-hole subbands. The assignment of the main absorption of  $570 \text{ cm}^{-1}$  to the  $hh1 \Rightarrow hh2$  intersubband transition implies that the Fermi level is in the  $hh1$  band, and this is possible only for a large value of the valence band offset. The theoretical value of  $\Lambda$  from a fit for the reflectivity data should be determined so as to be consistent with the transport and magneto-optical data. For  $x = 0.04$ ,  $d_w = 73 \text{ \AA}$  and  $d_B = 20 \text{ \AA}$ , the value of  $\Lambda = 500 \text{ meV}$  gives  $E(hh1 \Rightarrow hh2) = 70 \text{ meV}$ ,  $E(hh1 \Rightarrow lh1) = 45 \text{ meV}$  and a nearly zero band gap  $E_g = 7 \text{ meV}$ . The strain parameters are taken identical to those in HgTe [4], which may be justified for HgZnTe with low Zn content.

In summary, transport and magneto-optical measurements made on a p-type HgZnTe/CdTe superlattice show consistent behavior of two holes with different mobilities, which is explained by the extremely non-parabolic and anisotropic valence band structure. Properties of the holes were further investigated by reflectivity measurements, which led to identification of the two transitions,  $hh1 \Rightarrow hh2$  and  $hh1 \Rightarrow lh1$ . The main absorption of the  $hh1 \Rightarrow hh2$  at  $570 \text{ cm}^{-1}$  shows a strong polarization dependence and a temperature-induced broadening and shift in transition energy. Considering the compensating effect of the quantum confinement and strain on the position of hole subbands, this result also gives direct experimental evidence for a large value ( $\sim 500 \text{ meV}$ ) for the controversial valence band offset, but it should be noted that there are enough uncertainties in the Zn composition  $x$  and the layer thicknesses of the superlattice that slightly smaller values for the offset cannot be ruled out.

This work was partially supported by the Korea Science and Engineering Foundation through the Korea–United States International Coopera-

tive Research Program, the Korea Research Foundation, and the Agency for Defense Development in Korea.

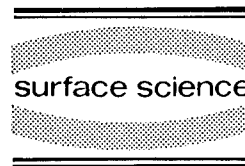
## 1. References

- [1] J.R. Meyer, C.A. Hoffman, F.J. Bartoli, J.W. Han, J.W. Cook, Jr., J.F. Schetzina, X. Chu, J.P. Faurie and J.N. Schulman, *Phys. Rev. B* 38 (1988) 2204.
- [2] C.A. Hoffman, J.R. Meyer, F.J. Bartoli, J.W. Han, J.W. Cook, J.F. Schetzina and J.N. Schulman, *Phys. Rev. B* 39 (1989) 5208.
- [3] N.F. Johnson, P.M. Hui and H. Ehrenreich, *Phys. Rev. Lett.* 61 (1988) 1933.
- [4] J.B. Choi, L. Ghenim, R. Mani, H.D. Drew, K.H. Yoo and J.T. Cheung, *Phys. Rev. B* 41 (1990) 10872.
- [5] J.R. Meyer, F.J. Bartoli, C.A. Hoffman and J.N. Schulman, *Phys. Rev. B* 38 (1988) 12457.



ELSEVIER

Surface Science 305 (1994) 290–294



# Crossing of cyclotron and spin resonances in a 2D electron gas

Vladimir I. Fal'ko

*Max-Planck-Institut für Festkörperforschung, Heisenbergstrasse 1, 70569 Stuttgart, Germany*

*Theory Department, Institute of Solid State Physics, Russian Academy of Sciences, Chernogolovka, 142432 Russian Federation*

(Received 2 June 1993; accepted for publication 19 June 1993)

## Abstract

We compare anticrossing of the cyclotron and spin resonances in spin-polarized and non-polarized phases of the degenerate two-dimensional Coulomb gas subjected to a strong tilted magnetic field. The spin-orbit coupling splits these resonances into three lines with the gaps between them exactly equal to  $\delta_{2n+1} = v_{so} p_F$  and  $\delta_{2n} = v_{so} p_F / \sqrt{2}$  at odd- and even-integer filling factors, respectively. The  $1/\sqrt{2}$  difference between  $\delta_{2n}$  and  $\delta_{2n+1}$  comes from the existence of an additional spin-density wave excitation in the polarized phase of interacting electrons at  $\nu = 2n$  and can be treated as a means to indicate the re-entrance of the system into it.

## 1. Introduction

In the present paper, we study the interplay of the electron-electron interaction in a 2D electron gas (in a single ideally pure heterostructure or quantum well) with spin-orbit coupling under specific conditions of artificial degeneracy of spin-split Landau levels [1]. This situation can be realized in the 2D electron gas by subjecting it to a strongly tilted magnetic field, so that the tilting makes up for the relative smallness of the electron  $g$ -factor [2,3] and provides  $\omega_c = eH_z/mc \approx \omega_s = \mu gH/\hbar$ . In this case the degenerate Landau levels with different spins are resonantly mixed and then split in the first order by spin-orbit interaction [4], and the analysis below deals with the influence of the Coulomb correlations on the fine structure of the cyclotron resonance (CR) near its crossing with the electron spin resonance (ESR).

The electron-electron interaction has two important consequences which make this crossing

different in the Coulomb and non-interacting gas. The first results from the fact that the crossings CR-ESR and CR-combined frequency resonance (CFR) are resolved by the exchange interaction [6], and mixing and splitting involve different hybridized collective modes, as compared to free electrons [4]. (But, according to Kohn's and Larmor's theorems [5–7], the crossing conditions remain the same as in the free gas model.)

Another feature of the interacting electron system consists of its transition to a collective spin-polarized state near the spin-split Landau level's crossing at even-integer filling factor, as predicted by Giuliani and Quinn [1] and, probably, observed by Koch et al. [3]. The exchange interaction of electrons stimulates the spin alignment, so that the electron gas at the CR-ESR crossing point has to be already polarized. The occupation of two excess Landau levels with the same spins produces a new spin-density wave mode which cannot manifest itself in ordinary spin resonance absorption but affects the fine

structure of CR at its crossing with ESR, so that we are able to propose the way for its indirect observation.

In studying this problem, we use the approach of inter-Landau-level excitons [8,6]. This approach is applicable to completely filled 2D Landau levels and, formally, requires that the planar cyclotron energy  $\hbar\omega_c$  be larger than the Coulomb energy  $e^2/\chi\lambda_H$ . It is based on the fact that the electrons from the filled Landau levels and the positive background of donors form a homogeneous neutral system [9] with chargeless excitations composed, as illustrated in Fig. 1, of an electron in one of the empty Landau levels (say,  $N=(n, \alpha)$ ) correlated with a hole (empty state) in one of the completely filled ones ( $N'=(n', \alpha')$ ,  $\alpha = \downarrow$  or  $\uparrow$ ). As long as such excitations are neutral, their total momenta  $Q$  are exact quantum numbers, in spite of the presence of a quantizing magnetic field. After accounting for the spin degree of freedom, we get the basic set  $\hat{\Psi}_{NN'}^+(Q)|0\rangle$  of low-lying excited states, where

$$\hat{\Psi}_{NN'}^+(Q) = \sum_p e^{ipQ_y} a_{N_p}^+ a_{N'-p-Q_x} \quad (1)$$

In Eq. (1) we use the gauge  $A=(-H_z y + H_y z, -H_x z, 0)$  and the dimensionless momenta  $Q$  and  $p$  measured in units  $1/\lambda_H$  of the inverse magnetic length  $\lambda_H + (\hbar c/eH_z)^{1/2}$ .

In terms of the excitons, Eq. (1), we can replace the exact many-body Hamiltonian of 2D electrons,  $\hat{H} = \hat{H}_0 + \hat{V}_{so} + \hat{U}$ , (where  $\hat{H}_0 = \sum \epsilon_N a_{N_p}^+ a_{N_p}$ ), by the set of finite-size matrices

$$H_{(\tilde{N}\tilde{N}')\chi(NN')} = \langle 0 | \hat{\Psi}_{\tilde{N}\tilde{N}'}^+(Q) \hat{H} \hat{\Psi}_{NN'}^+(Q) | 0 \rangle \\ - \delta_{\tilde{N}\tilde{N}'} \delta_{N'\tilde{N}'} \langle 0 | \hat{H} | 0 \rangle,$$

each acting in its own subspace of excitonic states with a fixed 2D momentum  $Q$  and total projec-

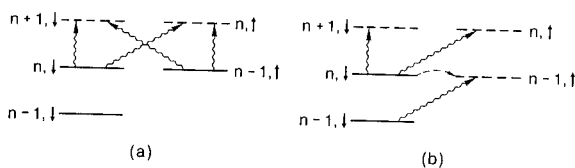


Fig. 1. Inter-Landau-level transitions involved into the exciton formation: (a)  $\nu = 2n + 1$ , (b)  $\nu = 2n$ .

tion of a spin to the axis  $\mathbf{h} = \mathbf{H}/H$ . The pairs of Landau level numbers  $(NN')$  and  $(\tilde{N}\tilde{N}')$  serve as indices and can be counted using the scheme of inter-Landau-level transitions from Fig. 1. Each matrix has a block-diagonal form with off-diagonal elements describing the conversion of one of the excitations,  $\hat{\Psi}_{NN'}^+(Q)|0\rangle$ , into another,  $\hat{\Psi}_{\tilde{N}\tilde{N}'}^+(Q)|0\rangle$ , in the course of Coulomb collisions or due to the spin-orbit coupling,

$$\hat{V}_{so} = \sum_{n,p} (a_{n\uparrow p}^+ a_{n+1\downarrow p} + \text{H.C.}) \sqrt{n+1} \alpha_{so},$$

$$\alpha_{so} = v_{so}(\mathbf{h}) \hbar / \lambda_H.$$

The spin-orbit coupling is treated below as a weak perturbation which mixes a finite number of collective modes (with  $\omega \approx \omega_c = \omega_s$ ) originally formed due to the electron-electron Coulomb interaction. The latter can be written, as usual, as

$$\hat{U} = \frac{1}{2} \int d\mathbf{x} d\mathbf{x}' \hat{\psi}^+(\mathbf{x}) \hat{\psi}^+(\mathbf{x}') \\ \times \frac{e^2}{\chi|\mathbf{x} - \mathbf{x}'|} \hat{\psi}(\mathbf{x}') \hat{\psi}(\mathbf{x}).$$

To designate intermediate stages of formal calculations, we use the definitions of Eq. (1), the algebra of operators  $a_{N_p}^+$  and  $a_{N'-p}$ , and the fact that all Landau levels (at  $T=0$ ) are either completely occupied or empty, and then find the form of the reduced matrix Hamiltonians  $H_{(\tilde{N}\tilde{N}')\chi(NN')}$  and diagonalize them.

## 2. CR fine structure at odd-integer filling factors

The case of the unit filling of the lowest Landau level,  $\nu = 1$ , provides us with the most clear example, because there is a single magnetoplasma mode,  $\omega_{pl} \approx \omega_c + Qe^2/2\hbar\chi$ , in the system which can be weakly coupled to a single spin exciton,  $\omega(Q \rightarrow 0) = \omega_s$  [8,6]. Therefore, the absorption peak near the crossing  $\omega_c = \omega_s$  is split by the spin-orbit coupling into two peaks of equal intensity,  $\omega_{\pm} = (\omega_c + \omega_s)/2 \pm \sqrt{(\omega_c - \omega_s)^2/4 + \delta_1^2}$ , which correspond to the usual anticrossing structure of the CR-ESR degeneracy point. The splitting gap between peaks is  $2\delta_1$ ,  $\delta_1 = |\alpha_{so}/\hbar| =$



$p_F v_{so}(\hbar)$ , where  $p_F$  is the zero field Fermi momentum in the gas [10].

With *higher odd-integer filling* there are four degenerate inter-Landau-level transitions near the crossing, as shown in Fig. 1a. Two of them correspond to transitions between neighboring Landau levels without change of spin, which, nevertheless, does not indicate the coexistence of two independent cyclotron resonances in the system. The electromagnetic field can only excite them in the combination  $\hat{\Psi}_{pl}^+$  which is in fact the real charge-density-wave eigenmode and has the linear dispersion  $\omega_{pl}(Q) = \omega_c + \pi \sigma_{xy} Q / \chi$  at small wave vectors coinciding with that of the classical magnetoplasma oscillations. Another mode,  $\hat{\Psi}_{sd}^+$ , is optically passive [6], but in the vicinity of CR–ESR crossing the spin–orbit coupling mixes it with  $\hat{\Psi}_{n\uparrow n\downarrow}^+$  and  $\hat{\Psi}_{pl}^+$  excitations, since at  $Q=0$  they all have the same energy. As to the combined frequency resonance mode  $\Psi_{n+1\downarrow n-1\uparrow}^+$ , its spectral position is shifted by the electron–electron exchange with respect to that of the single-particle transition,  $\omega = 2\omega_c - \omega_s + E_*$  (at  $\nu = 3$ ,  $E_* = -\sqrt{(\pi/2)} \frac{3}{16} e^2 / \chi \lambda_H$ ), so that the CR–ESR and CR–CFR crossings take place at different magnetic field tilting.

Now we have three collective modes ( $\hat{\Psi}_{n\uparrow n\downarrow}^+$ ,  $\hat{\Psi}_{pl}^+$ ,  $\hat{\Psi}_{sd}^+$ ) to be mixed, and after some algebra one can find the resulting collective excitations spectrum to be composed of the “unperturbed” cyclotron resonance mode,  $\omega_{CR} = \omega_c$ , with the relative efficiency  $I_{CR} \propto 1 - (2n+1)^{-2}$ , and mixed modes with the frequencies

$$\omega_{\pm} = \frac{\omega_c + \omega_s}{2} \pm \sqrt{\delta_{2n+1}^2 + \left(\frac{\omega_c - \omega_s}{2}\right)^2} \quad (2)$$

and relative efficiencies  $I_{\pm} = 0.5/(2n+1)^2$ . This gives us the unusual form of the fine structure of the CR near the crossing point shown in Fig. 2: two weak lines (satellites) which demonstrate the conventional anticrossing coexist with the unperturbed CR line. At any odd-integer filling factor the splitting gaps between satellites,

$$\delta_{2n+1} = \sqrt{2n+1} \left| \frac{\alpha_{so}}{\hbar} \right| = \frac{\sqrt{\nu} v_{so}(\hbar)}{\lambda_H} = p_F v_{so}(\hbar), \quad (3)$$

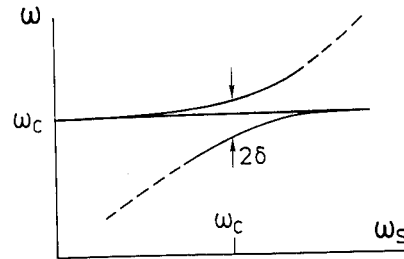


Fig. 2. The CR fine structure near the crossing.

are exactly equal to the zero magnetic field spin-splitting [10] at  $\nu = 1$ .

### 3. CR fine structure in the polarized phase at even-integer filling factors

The analysis of *even-integer filling factors* is more complex because of the complexity of the ground state of the system close to the artificial degeneracy point. It has been shown by Giuliani and Quinn [1] that, due to the inter-Landau-level exchange, the electron–electron interaction gives an earlier rise to the polarization transition in a 2D gas (i.e., at  $\omega_c > \omega_s$ ) than one could expect from the single-particle consideration. At  $\omega_c = \omega_s$ , where the CR–ESR crossing takes place, the gas in an ideally pure 2D system at  $T=0$  forms a polarized and homogeneous ground state. A weak spin–orbit coupling (at  $\nu = 2$  it should be  $|\alpha_{so}| \ll \frac{3}{16} E_c$ , where  $E_c = \sqrt{(\pi/2)} e^2 / \chi \lambda_H$  [11], which requires  $v_{so} \ll e^2 / \hbar \chi$ ) does not change this result and perturbs the above ground state and elementary quasiparticles in it only slightly. This is to say, that, in addition to a single cyclotron mode  $\hat{\Psi}_{2\downarrow 1\uparrow}^+$ , the polarized phase has two spin-flip excitation modes  $\hat{\Psi}_{0\uparrow 0\downarrow}^+$  and  $\hat{\Psi}_{1\uparrow 1\downarrow}^+$  related to the spin flip at different Landau levels, as shown in Fig. 1b. The block of the matrix Hamiltonian to describe these two is of the form

$$\begin{pmatrix} \frac{1}{2} E_c & -\frac{1}{2} E_c \\ -\frac{1}{2} E_c & \frac{1}{2} E_c \end{pmatrix},$$

and shows that real excitons are their symmetric and antisymmetric combinations,  $(\hat{\Psi}_{1\uparrow 1\downarrow}^+ \pm \hat{\Psi}_{0\uparrow 0\downarrow}^+) / \sqrt{2}$ . The symmetric mode frequency is

exactly equal (at  $Q = 0$ ) to the Zeeman splitting value, in agreement with Larmor's theorem. Only this mode can be excited by an external alternating magnetic field, whereas the antisymmetric spin wave with the energy  $\epsilon(Q \rightarrow 0) = \hbar\omega_s + E_c$  cannot be excited in an ordinary spin resonance.

This result allows us to state that there are only two completely degenerate modes at the point  $\omega_s = \omega_c$ : the magnetoplasmon and symmetric spin-density wave  $(\hat{\Psi}_{1\uparrow 1\downarrow}^+ + \hat{\Psi}_{0\uparrow 0\downarrow}^+)/\sqrt{2}$ , whereas the frequency of the excitation  $(\hat{\Psi}_{1\uparrow 1\downarrow}^+ - \hat{\Psi}_{0\uparrow 0\downarrow}^+)/\sqrt{2}$  is shifted by the value of  $E_c$  and takes no part in the resonant mixing. A more accurate analysis [11] shows that both of these two above-mentioned modes are decoupled from the continuum spectrum composed of pairs of "cyclotron" ( $\hat{\Psi}_{2\downarrow 1\downarrow}^+$ ) and spin +1 low-energy ( $\hat{\Psi}_{0\uparrow 1\downarrow}^+$ ) excitons, in agreement with Kohn's [5] and Larmor's theorems, and one can find their spin-orbit splitting gap as  $\delta_2 = p_F v_{so}(\hbar)/\sqrt{2}$ . This gap is  $1/\sqrt{2}$  factor reduced as compared to that at odd-integer filling factors. The origin of this difference can be traced at intermediate stages of calculations, after one notes that the direct spin-orbit coupling (initially, with the amplitude  $\sqrt{2}\alpha_{so}$ ) which exists only between  $\hat{\Psi}_{1\uparrow 1\downarrow}^+$  and  $\hat{\Psi}_{2\downarrow 1\downarrow}^+$  excitons has to be equally shared among symmetric and antisymmetric modes. Therefore, although the antisymmetric spin-density wave is optically passive, its existence sufficiently renormalizes the anticrossing of the CR and ESR, to allow its indirect observation.

In extending our analysis to the polarized state at higher even-integer filling factors, we should account for one additional inter-Landau-level mode  $\hat{\Psi}_{n\uparrow n-1\uparrow}^+$  in the basis (see Fig. 1b). This increases the number of actual excitons, but the appropriate choice of magnetoplasma and spin-density waves reduces the problem to that considered. That is, in the vicinity of a crossing the CR line acquires two weak satellites, similar to those at odd-integer filling, whereas the crossing of magnetoplasma modes  $\hat{\Psi}_{pl}^+$  and  $\hat{\Psi}_{sd}^+$  with antisymmetric spin +1 exciton can be ignored, because it occurs in the region of polarized phase instability. The CR acquires, therefore, a similar fine structure to that described by Fig. 1 with the only, though important, difference being that the

magnitude of the gaps  $\delta_{2n+2}$  between modes  $\omega_{CR}$  and  $\omega_{\pm}$ ,

$$\delta_{2n+2} = \sqrt{n+1} \left| \frac{\alpha_{so}}{\hbar} \right| = \sqrt{\frac{\nu}{2}} \frac{v_{so}(\hbar)}{\lambda_H} = \frac{p_F v_{so}(\hbar)}{\sqrt{2}}, \quad (4)$$

is reduced by the factor of  $1/\sqrt{2}$  in comparison with those at odd-integer filling.

#### 4. Summary

To summarize, the proposed theory of the cyclotron resonance fine structure near its crossing with the electron spin resonance in the 2D Coulomb gas subjected to a strong tilted magnetic field shows that the CR is, generally, composed of three lines, with the intensities evolving when the filling factor changes. One line is just at the unperturbed cyclotron resonance frequency; its relative intensity increases from zero (at  $\nu = 1, 2$ ) to almost 100% with occupation numbers higher than 3. The other two are split by the spin-orbit interaction and undergo a reverse evolution. After combining the results obtained for odd- and even-integer fillings, we obtain that the gaps which separate these split resonances are also filling-factor-dependent in such a way that they take the value of  $v_{so} p_F$  or  $v_{so} p_F/\sqrt{2}$  at  $\nu = 2n + 1$  and  $\nu = 2n$ , respectively, whereas the above parameter  $v_{so} p_F$  (the zero-field spin-splitting) is determined only by the sheet electron density and the heterostructure material but is independent of the magnetic field. This kind of Shubnikov-de Haas oscillations in the CR spectrum manifests re-entrance of the 2D system into a partially spin-polarized state and gives promise to find an indication of a new spin-density wave mode specific to this phase.

#### 5. Acknowledgements

The author thanks K. Efetov, K. von Klitzing and A. MacDonald for useful discussions and the Alexander von Humboldt Foundation for support.

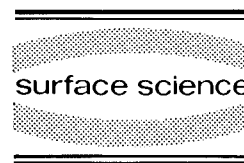
## 6. References

- [1] G.F. Giuliani and J.J. Quinn, Phys. Rev. B 31 (1985) 6228; Surf. Sci. 170 (1986) 316.
- [2] R.J. Nicholas et al., Phys. Rev. B 37 (1988) 1294.
- [3] S. Koch et al., Phys. Rev. B 47 (1993) 4048.
- [4] V.I. Fal'ko, Phys. Rev. B 46 (1992) 4320.
- [5] W. Kohn, Phys. Rev. 123 (1961) 1242.
- [6] C. Kallin and B.I. Halperin, Phys. Rev. B 30 (1984) 5655.
- [7] J.F. Janak, Phys. Rev. 178 (1969) 1416.
- [8] Yu.A. Bychkov, S.V. Iordanskii and G.M. Eliashberg, Pis'ma ZhETF 33 (1981) 152 (JETP Lett. 33 (1981) 143); Yu.A. Bychkov and E.I. Rashba, ZhETF 85 (1983) 1826 (Sov. Phys. JETP 58 (1983) 1062).
- [9] B. Janovici, Phys. Rev. Lett. 46 (1981) 386.
- [10] G. Lommer, F. Malcher and U. Rossler, Phys. Rev. Lett. 60 (1988) 728; B. Das, S. Datta and R. Reifenberger, Phys. Rev. B 41 (1990) 8278; B. Jusserand et al., Phys. Rev. Lett. 69 (1992) 848.
- [11] V.I. Fal'ko, unpublished.



ELSEVIER

Surface Science 305 (1994) 295–300



# Multicomponent envelope function problems: the ultimate concept

R. Winkler\*, U. Rössler

*Institut für Theoretische Physik, Universität Regensburg, D-93040 Regensburg, Germany*

(Received 15 April 1993; accepted for publication: 12 June 1993)

## Abstract

We present a new, powerful concept for solving the set of coupled equations of a multicomponent envelope function problem which is based on a quadrature method for the integral equations in momentum space. As an application of our method we discuss the dispersion of holes in AlAs/GaAs and Si/Si<sub>1-x</sub>Ge<sub>x</sub> quantum wells which have recently been probed experimentally by using resonant magneto-tunneling spectroscopy.

## 1. Introduction

Immense progress in heterostructure epitaxy has made possible the fabrication of a great variety of layered semiconductor structures. Due to the mastery of growth techniques such as molecular beam epitaxy (MBE) and metalorganic chemical vapor deposition (MOCVD) one can realize predesigned potential profiles and impurity distributions of the highest quality. In fact a point is reached where “do-it-yourself quantum mechanics” [1] is possible.

In theoretical studies on the electronic structure of layered semiconductors methods based on the envelope function approximation (EFA) are predominant [2]. The EFA can cope with periodic or aperiodic geometries of the structures as well as perturbations such as magnetic field, strain, or a built-in or external potential. Details of the underlying crystal potential are included in terms of bulk band structure parameters. Hence the EFA allows a comprehensive

description of electron and hole-like states that covers a wide range of aspects relevant for a comparison with experiments.

In position space the Schrödinger equation for the multicomponent envelope function is a set of coupled differential equations. Until now no general solution to the eigenvalue problem has been provided. Several methods have been suggested, each of them suited for certain problems but always requiring additional simplifications. A detailed discussion of existing approaches has recently been given elsewhere [3]. It is the aim of the present work to present a new, accurate method for the standardized solution of multicomponent envelope function problems which realises the full potential of the EFA thus giving us flexibility comparable with the methods of device fabrication. Simultaneously, it avoids unphysical “wing band” [18] and “spurious” solutions [19] which for some time have bothered researchers in this field [3].

\* Corresponding author. Fax: +49-941-943 4382; E-mail: roland.winkler@rphs1.physik.uni-regensburg.de.

## 2. Multiband Hamiltonians in momentum space

In position space the Hamiltonian for the envelope function is obtained from the  $\mathbf{k} \cdot \mathbf{p}$  matrix for the bulk band structure by replacing  $\mathbf{k} \rightarrow (\mathbf{k}_{\parallel}, (1/i)\partial_z)$  and adding to the diagonal the built-in or external potential  $V(z)$  [2]. In a generalized formulation the eigenvalue problem reads

$$\hat{H}(z) \Psi(z) = \mathcal{E} \Psi(z). \quad (1)$$

Here the  $N \times N$  matrix Hamiltonian  $\hat{H}$  acts on the spinor  $\Psi$ . We have

$$\hat{H} = \hat{H}^{(0)} + \hat{H}^{(1)} + \hat{H}^{(2)} \quad (2)$$

with matrix elements labeled according to the band edge Bloch functions

$$\begin{aligned} \hat{h}_{nn'}^{(0)} &= c_{nn'}^{(0)} + g_{nn'}^{(0)}(z), \\ \hat{h}_{nn'}^{(1)} &= c_{nn'}^{(1)}(1/i)\partial_z + \frac{1}{2} \left[ (1/i)\partial_z g_{nn'}^{(1)}(z) \right. \\ &\quad \left. + g_{nn'}^{(1)}(z)(1/i)\partial_z \right], \\ \hat{h}_{nn'}^{(2)} &= c_{nn'}^{(2)} [(1/i)\partial_z]^2 + (1/i)\partial_z g_{nn'}^{(2)}(z) \\ &\quad \times (1/i)\partial_z. \end{aligned} \quad (3)$$

Here  $c_{nn'}^{(\nu)}$  are complex constants and  $g_{nn'}^{(\nu)}(z)$  are complex functions of  $z$  due to the position-dependence of the band parameters. In general  $\hat{H}^{(0)}$  contains terms which result from the in-plane dispersion; in addition we have  $z$ -dependent band edge energies and a potential on its diagonal.  $\hat{H}^{(1)}$  represents off-diagonal terms proportional to momentum matrix elements multiplied by  $k_z = (1/i)\partial_z$  and  $\hat{H}^{(2)}$  results from remote band contributions of second order in  $k_z$ . Additional terms, such as those caused by homogeneous strain, can easily be included. Eq. (3) corresponds to the most commonly used Hermitian formulation of the operator  $\hat{H}$ .

In order to solve the eigenvalue problem we change over to momentum space. A Fourier transform leads to the coupled integral equations

$$\begin{aligned} \hat{H}(k) \Psi(k) &\equiv \int dk' \left[ C^{(0)} \delta(k - k') \right. \\ &\quad + G^{(0)}(k - k') + C^{(1)} k' \delta(k - k') \\ &\quad + \frac{1}{2}(k + k') G^{(1)}(k - k') \\ &\quad + C^{(2)} k'^2 \delta(k - k') \\ &\quad \left. + k k' G^{(2)}(k - k') \Psi(k') \right] \\ &= \mathcal{E} \Psi(k), \end{aligned} \quad (4)$$

where we have used  $k \equiv k_z$ . We apply a standard quadrature method [4] to solve the integral equations (4).

The appropriate boundary conditions at interfaces emerge from the Hermitian formulation of the operator  $\hat{H}$ . Hence, although we need not deal with these boundary conditions in momentum space, any solution  $\Psi(k)$  of Eq. (4) will satisfy them when transformed into position space. Therefore we can effortlessly investigate multiple quantum wells having an arbitrary number of interfaces.

We have checked the accuracy of our numerical method by comparing it with Andreani's exact analytical solution for the  $4 \times 4$  Luttinger Hamiltonian. Perfect agreement was obtained with Table 1 in Ref. [5].

## 3. Application to AlAs/GaAs and Si/Si<sub>1-x</sub>Ge<sub>x</sub> quantum wells

As an application of our method we discuss the dispersion of hole subbands in AlAs/GaAs and Si/Si<sub>1-x</sub>Ge<sub>x</sub> quantum wells. Recently this was probed experimentally by using resonant tunneling spectroscopy in high magnetic fields: When Hayden and coworkers [6–8] plotted the voltage position of peaks in the tunneling current  $I$  as a function of in-plane magnetic field  $B$ , they observed a striking similarity to calculated hole dispersion curves  $\mathcal{E}(k_{\parallel})$ . Using a perturbation approach it was argued that when holes are tunneling resonantly in a transverse magnetic field ( $B \parallel \hat{x}$ ) they acquire an in-plane momentum component

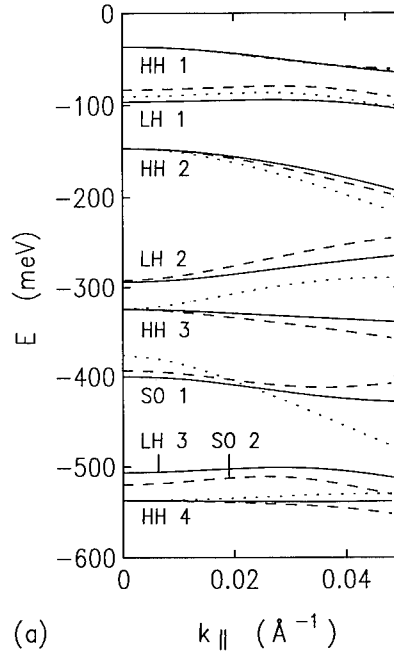
$$\hbar k_{\parallel} \equiv \hbar \Delta k_x = e B \Delta s, \quad (5)$$

where  $\Delta s$  is the average distance between the bound states in the well and those in the emitting accumulation layer. Here the gauge  $\mathbf{A} = (0, -Bz, 0)$  has been used.

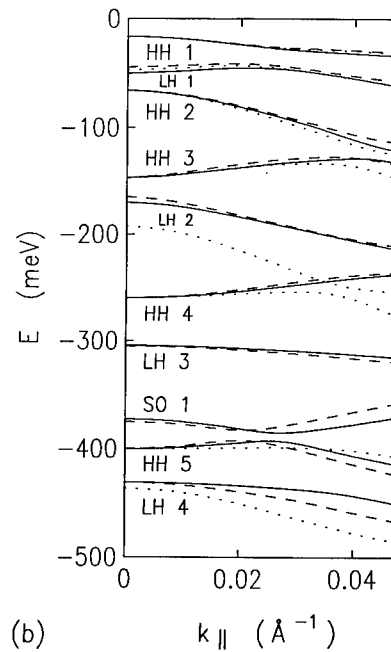
First we consider the 42 Å and the 68 Å AlAs/GaAs quantum wells used by Hayden et al. In Fig. 1 we compare the hole dispersion curves calculated by means of the  $4 \times 4$  Luttinger Hamiltonian ( $\Gamma_8^v$ ) with those from more complete multiband Hamiltonians taking into account the split-off valence band  $\Gamma_7^v$  and the lowest conduction band  $\Gamma_6^c$  [9]. Band parameters were taken from Ref. [10]. The explicit consideration of  $\Gamma_7^v$  and  $\Gamma_6^c$  clearly modifies the calculated subband dispersion  $\mathcal{E}(k_{\parallel})$  (spin-orbit splitting in bulk GaAs is 341 meV). In particular, it affects the HH–LH splitting which is relevant to the calculation of excitons. By means of our quadrature method it is also straightforward to compare the bound states in a quantum well with the resonant states in the double barrier structures actually used in Refs. [6–8]. But on the energy scale of Fig. 1 they cannot be distinguished. Anisotropy and electric-field-induced spin splitting are also of minor importance.

For a more quantitative comparison with the experiments of Hayden et al. we have to take into account that only some fraction  $V_e$  of the applied bias  $V$  drops between the emitter region and the quantum well; see Fig. 1 in Ref. [6]. Hence we self-consistently calculated the potential profile of the whole device as a function of applied bias  $V$  from which we could extract  $V_e$  and  $\Delta s$  (dashed lines in Fig. 2) [11].

Hayden et al. have pointed out that some charge  $N_w(V)$  will accumulate in the quantum well thus modifying the results in Fig. 2. They determined  $N_w(V)$  by probing the Landau level structure in a longitudinal magnetic field ( $\mathbf{B} \parallel \mathbf{I}$ ) and making use of  $N_w(V) = e/[\pi\hbar\Delta(1/B)]$  [12], where  $\Delta(1/B)$  is the reciprocal spacing of adjacent Landau levels at constant voltage  $V$ . When taking  $N_w(V)$  from Fig. 2b in Ref. [7] we obtain the solid lines in Fig. 2. However, we have to be careful when using these experimental values. The energy of Landau levels depends only weakly on whether these states are occupied or empty. Hence when neglecting anisotropy we



(a)



(b)

Fig. 1. Hole subband dispersion (a) of a 42 Å and (b) of a 68 Å AlAs/GaAs quantum well calculated by means of different multiband Hamiltonians:  $\Gamma_8^v$  (Luttinger Hamiltonian, dotted lines);  $\Gamma_8^v$  and  $\Gamma_7^v$  (dashed lines);  $\Gamma_8^v$ ,  $\Gamma_7^v$  and  $\Gamma_6^c$  (solid lines). The labeling of dispersion curves corresponds to the dominant spinor component at  $k_{\parallel} = 0$ .

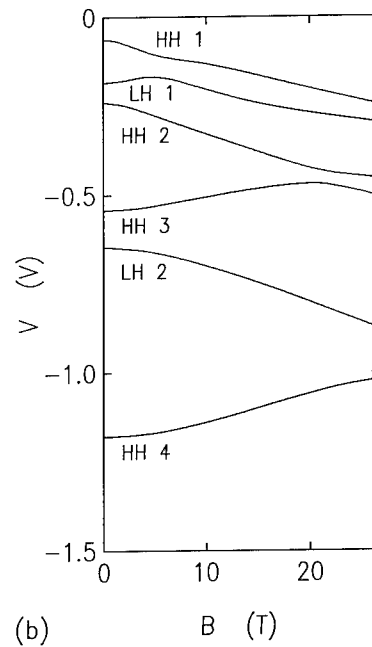
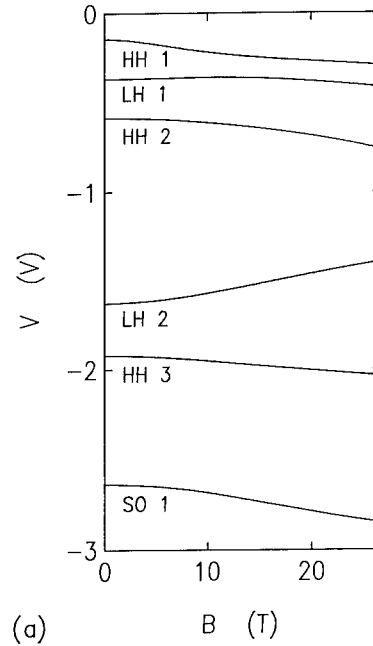
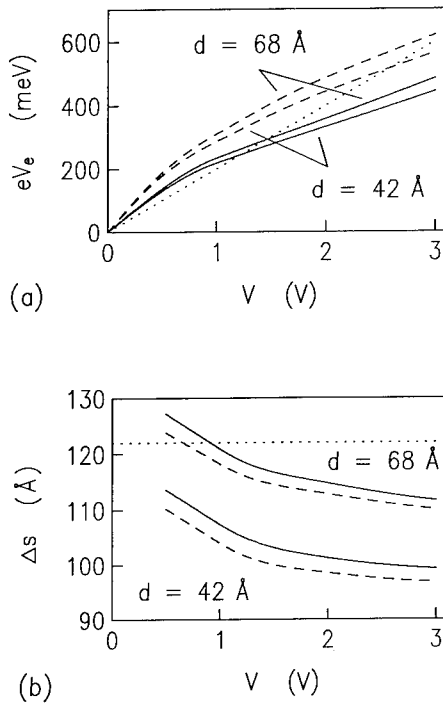


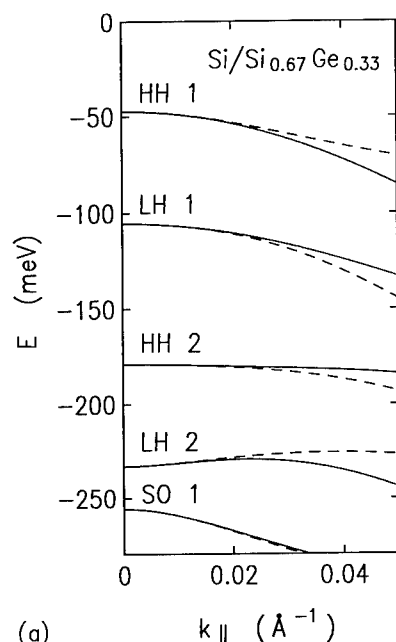
Fig. 3. Resonances in the  $I$ - $V$  characteristic as a function of transverse magnetic field, calculated for the two samples in Ref. [6] by using the solid lines in Figs. 1 and 2.

Fig. 2. (a) Potential difference  $eV_e$  between the emitter and the centre of the well and (b) average distance  $\Delta s$  between the bound states in the well and those in the emitting accumulation layer for the devices used in Ref. [6] (see Fig. 1 therein). Both quantities were calculated self-consistently as a function of applied bias  $V$  with (solid lines) and without (dashed lines) taking into account a charge build-up  $N_w(V)$  in the well. No experimental data on  $N_w(V)$  were available for the broader sample; hence in both cases we used Fig. 2b in Ref. [7]. Dotted lines refer to an estimate in Ref. [6].

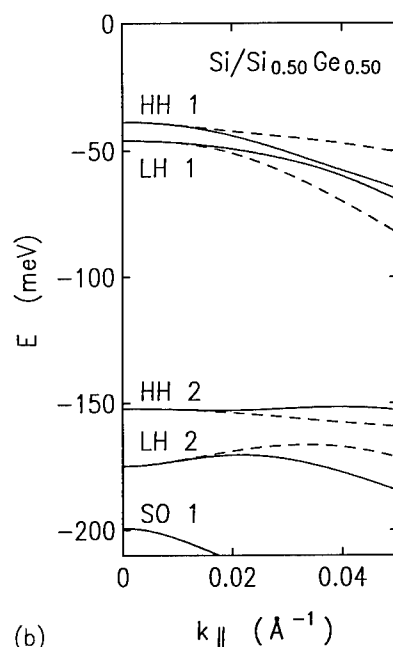
have  $k_{\parallel}^2(V) = 2\pi N_w(V) = 2e/[\hbar\Delta(1/B)]$ . From this we would expect that Fig. 2b in Ref. [7] should reflect the energy dispersion  $\mathcal{E}(k_{\parallel}^2)$  of the subbands in the well [12].

Fig. 2 was used to obtain a converted plot  $B$  versus  $V$  (Fig. 3) directly comparable with the experimental curves in Refs. [6–8].

The technique of Hayden et al. was used by Gennser et al. [13] to probe the anisotropic dispersion of holes in strained Si/Si<sub>1-x</sub>Ge<sub>x</sub> quantum wells. In Fig. 4 we show calculated results for the strained 40 Å Si/Si<sub>0.67</sub>Ge<sub>0.33</sub> and the 50 Å Si/Si<sub>0.5</sub>Ge<sub>0.5</sub> quantum wells used in Ref. [13]. Band parameters were taken from



(a)



(b)

Fig. 4. Hole subband dispersion (a) of the strained 40 Å Si/Si<sub>0.67</sub>Ge<sub>0.33</sub> and (b) of the 50 Å Si/Si<sub>0.5</sub>Ge<sub>0.5</sub> quantum wells of Ref. [13]. Both were calculated by means of a  $6 \times 6$  valence band Hamiltonian. Solid lines correspond to  $k_{\parallel}$  in the  $\langle 10 \rangle$  direction, dashed lines are for  $\langle 11 \rangle$ .

Ref. [14]. Our results differ to some extent from the measured values. In contrast to Ref. [13] (but in agreement with Ref. [8]) we find that the topmost subbands HH1 and LH1 show the strongest repulsion in the direction  $\langle 11 \rangle$  while they come closer in the  $\langle 10 \rangle$  direction. We encountered the same discrepancies when calculating the anisotropic subband dispersion for the strained AlAs/In<sub>0.1</sub>Ga<sub>0.9</sub>As quantum well investigated by Lin et al. [15].

A few comments are called for. In Ref. [16] Gennser et al. showed that almost the same resonances in the tunneling current can be observed both for a transverse ( $\mathbf{B} \perp \mathbf{I}$ ) and for a longitudinal ( $\mathbf{B} \parallel \mathbf{I}$ ) magnetic field. Obviously their findings appear to be incompatible with the interpretation of these experiments given by Hayden et al. Second, we want to remark that Smoliner et al. [17] showed both theoretically and experimentally that for tunneling 2D-electrons the resonances in the  $I$ - $V$  characteristic broaden considerably when a transverse magnetic field is applied. We might expect that this effect should be visible also in the case of resonant 2D-hole tunneling. For these reasons we suggest that the simple picture based on perturbation theory might be insufficient for an interpretation of the experimental data which were obtained in a magnetic field of up to 40 T.

#### 4. Summary and conclusions

We have presented a new concept for the solution of multicomponent envelope function problems which is based on a quadrature method for the integral equations in momentum space. The ansatz can be readily transferred to a wide range of Schrödinger-type eigenvalue problems. As an application we discussed the dispersion of holes in AlAs/GaAs and Si/Si<sub>1-x</sub>Ge<sub>x</sub> quantum wells which has recently been probed experimentally by means of resonant tunneling spectroscopy in high magnetic fields. Our calculations indicate that an interpretation of the experimental data by means of perturbation theory is inadequate.



## Acknowledgement

Work supported in part by the Deutsche Forschungsgemeinschaft.

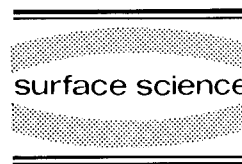
## References

- [1] L. Esaki, in: *Electronic Properties of Multilayers and Low-Dimensional Semiconductor Structures*, Eds. J.M. Chamberlain, L. Eaves and J.C. Portal (Plenum, New York, 1990) p. 1.
- [2] G. Bastard, *Wave Mechanics Applied to Semiconductor Heterostructures* (Les Editions de Physique, Les Ulis Cedex, 1988).
- [3] R. Winkler and U. Rössler, *Phys. Rev. B* 48 (1993) 8918.
- [4] C.T.H. Baker, *The Numerical Treatment of Integral Equations* (Clarendon, Oxford, 1977).
- [5] L.C. Andreani, A. Pasquarello and F. Bassani, *Phys. Rev. B* 36 (1987) 5887.
- [6] R.K. Hayden, D.K. Maude, L. Eaves, E.C. Valadares, M. Henini, F.W. Sheard, O.H. Hughes, J.C. Portal and L. Cury, *Phys. Rev. Lett.* 66 (1991) 1749.
- [7] R.K. Hayden, L. Eaves, M. Henini, D.K. Maude, J.C. Portal and G. Hill, *Appl. Phys. Lett.* 60 (1992) 1474.
- [8] R.K. Hayden, T. Takamasu, D.K. Maude, E.C. Valadares, L. Eaves, U. Ekenberg, N. Miura, M. Henini, J.C. Portal, G. Hill and M.A. Pate, *Semicond. Sci. Technol.* 7 (1992) B413.
- [9] H.-R. Trebin, U. Rössler and R. Ranvaud, *Phys. Rev. B* 20 (1979) 686.
- [10] Landolt-Börnstein, *New Series III, Vol. 17a: Semiconductors* (Springer, Berlin, 1982); H. Mayer and U. Rössler, *Phys. Rev. B* 44 (1991) 9048.
- [11] Integrals in  $k_{\parallel}$ -space have been evaluated by means of an analytic quadratic Brillouin zone integration scheme. R. Winkler, *J. Phys. Condens. Matter* 5 (1993) 2321.
- [12] D.C. Tsui, *Phys. Rev. B* 4 (1971) 4438; 8 (1973) 2657; 12 (1975) 5739.
- [13] U. Gennser, V.P. Kesan, D.A. Syphers, T.P. Smith III, S.S. Iyer and E.S. Yang, *Phys. Rev. Lett.* 67 (1991) 3828.
- [14] M.M. Rieger and P. Vogl, *Phys. Rev. B* 48 (1993) 14276.
- [15] S.Y. Lin, A. Zaslavsky, K. Hirakawa, D.C. Tsui and J.F. Klem, *Appl. Phys. Lett.* 60 (1992) 601.
- [16] U. Gennser, V.P. Kesan, D.A. Syphers, T.P. Smith III, S.S. Iyer and E.S. Yang, *Mater. Res. Soc. Symp. Proc.* 220 (1991) 397.
- [17] J. Smoliner, W. Demmerle, G. Berthold, E. Gornik, G. Weimann and W. Schlapp, *Phys. Rev. Lett.* 63 (1989) 2116.
- [18] S.R. White and L.J. Sham, *Phys. Rev. Lett.* 47 (1981) 879.
- [19] M.F.H. Schuurmans and G.W. 't Hooft, *Phys. Rev. B* 31 (1985) 8041.



ELSEVIER

Surface Science 305 (1994) 301–306



## 2DEG in strained Si/SiGe heterostructures

Frank F. Fang

*IBM T.J. Watson Research Center, Yorktown Heights, NY 10598, USA*

(Received 26 April 1993; accepted for publication 4 June 1993)

### Abstract

Low-temperature magnetotransport properties for the recent n-type modulation-doped Si/SiGe heterostructures are reported. The biaxially tensile-stressed (100)Si surface layers on stress-relieved SiGe substrates are shown to have all the well known MOSFET characteristics but with more than an order of magnitude higher mobility. The four-fold degeneracy of the ground subband can be completely resolved at a magnetic field as low as 2 T. FQHE at  $2/3$  and  $4/3$  are clearly discerned and the activation energy at the plateaus is about 1 K at 10 T. The ratios between scattering time and single-particle relaxation time are 4–10 for a great number of samples examined. Low-temperature mobility appears to be capped below  $2 \times 10^5 \text{ cm}^2 \text{ V}^{-1} \text{ s}^{-1}$  at present, as reported from several laboratories. Comparison of data and model calculations of Stern and Laux for the temperature-dependent mobility are made. Fixed charge and surface roughness appear to be the limiting parameters for the samples currently examined.

### 1. Introduction

Recently there has been considerable interest in studies of Si/SiGe heterostructures. The motivation was due mainly to the marked advances in material preparation both by MBE and by UHV-CVD, and breakthrough in strain relaxation of the alloy layers with minimal threading dislocations [1–3]. This opens up new possibilities of stressing the Si layers in a way that the band structures are favorably modified, together with the supposed smoothness of the interface, to give high electron mobility unforeseen in the much-studied MOSFET structures. This technique is viewed to provide significant leverage for Si-based technology in its already dominating position in semiconductor industry.

In a strained SiGe layer on a Si substrate, the valence-band offset in the low-Ge-fraction alloy layer has shown promising two-dimensional hole

gas (2DHG) accumulation and favorable heavy- and light-hole band splitting which allow detailed magnetotransport studies [4]. In this paper, we recount some recent advances of n-type modulation-doped Si/SiGe, which is still in an intensive stage of investigation among many laboratories in search for the mechanism that limits the currently observed low-temperature mobility to about  $2 \times 10^5 \text{ cm}^2 \text{ V}^{-1} \text{ s}^{-1}$  [5,6].

The lattice constant of silicon is  $5.43 \text{ \AA}$ , about 4% smaller than that of Ge ( $5.65 \text{ \AA}$ ). The alloy is then to have a lattice constant somewhere in-between depending on the relative composition. Until recently, stress-relieved alloy layers grown on silicon substrates always had an unacceptably high mismatch threading dislocation density. The discovery that gradual grading of the alloy composition provides relaxation of mismatch strain with drastically reduced threading dislocations in the growth direction [1–3] allows pseudomorphic

growth of good-quality thin Si layers on a larger and tunable crystalline lattice. An example (Fig. 1) by LeGoues et al. [1] shows cross-sectional images of samples grown by UHV-CVD, with single-step and graded alloy layer growth of a SiGe alloy on a Si substrate. The nearly defect-free graded alloy layer is clearly seen. The faults seen on the substrate side are believed to be generated by the Frank–Read mechanism [1], which provides partial stress relief for the film.

## 2. Strain-induced subbands

For a thin Si layer grown on this (100) substrate, the biaxial tensile strain reduces the cubic symmetry of the layer and, thus, lifts the degeneracy of the conduction-band edge. In this configuration, the energy of the two valleys with transverse effective mass parallel to the interface is lowered, while the other four are raised in accor-

dance with the respective deformation potentials. The situation is reminiscent of the electric-field-confined inversion layers [5] with electron subbands  $E_0$  (lower subband) and  $E_{0'}$ , except the splitting can be much greater. Assuming the lattice constant of the alloy can be linearly interpolated according to its composition, the  $E_0$  and  $E_{0'}$  subband splitting for the strained Si layer on the alloy substrate is shown in Fig. 2. Here,  $e_T = e_{xx} - e_{zz}$  is the total strain (where  $z$  is the growth direction), given by the lattice mismatch and Poisson's ratio. A theoretically derived uniaxial deformation potential by Van de Walle and Martin [6],  $\Xi_u = 9.3$  eV, is used for the strained conduction-band splitting.  $x$  is the Ge atomic fraction of the alloy. The initial splitting of 10–20 meV at  $x = 0$  is due to confinement of the inversion layer at the interface. For  $x = 0.3$ , as the most of the samples described here, the splitting is about 220 meV. Since the conduction-band edge of the unstrained SiGe alloy nearly coin-

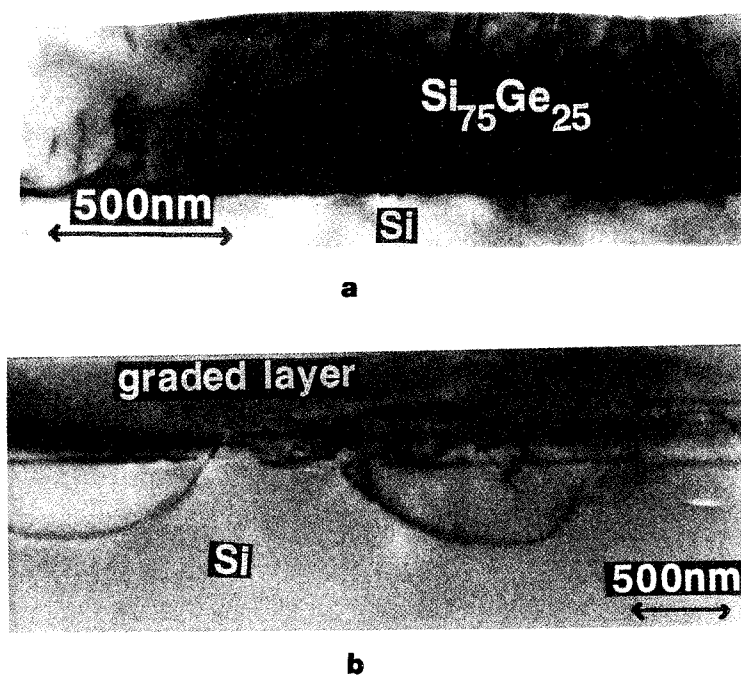


Fig. 1. Cross-sectional images of SiGe on Si heterostructures. Samples are grown by UHV-CVD. SiGe alloy is the top-most layer for each micrograph. (a) Uniform layer containing 25% Ge; dense lines of threading dislocation are clearly shown. (b) Graded layer where the Ge composition varies linearly from 0% to 25% throughout the film. No visible dislocation in the top layer is seen. (Courtesy of F.K. LeGoues.)

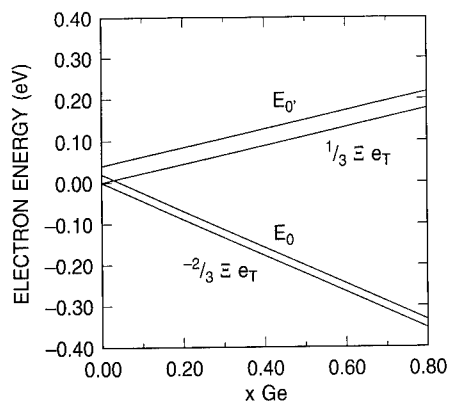


Fig. 2. Conduction-band splitting for a fully strained (100)Si on SiGe.  $x$  is the atomic fraction of Ge. The conduction-band deformation potential of 9.3 eV and a Poisson's ratio of 0.28 are used here. The initial splittings at  $x = 0$  are the confinement energies for the respective subband.

cides with that of the unstrained Si [5], the potential barrier for the  $E_0$  subband should be about 160 meV, depending upon the exact conduction-band alignment in the strain-free case. This strain-induced off-set allows for accumulating and confining electrons in the  $E_0$  subband with  $E_0'$  subband sufficiently high in energy to suppress inter-subband scattering, even at room temperature. To date, the room temperature mobilities of  $1800\text{--}2000\text{ cm}^2\text{ V}^{-1}\text{ s}^{-1}$  [7,8], higher than the of phonon-scattering-limited mobility of bulk Si, were reported.

### 3. Sample characterization

The Si layer is modulation-doped in a symmetrically clad SiGe cap layer with suitable spacer and dopants. The alloy layer adjacent to the Si substrate is linearly graded to 30% Ge mole fraction, and then a buffer layer up to  $1.5\text{ }\mu\text{m}$  with this Ge content is grown prior to the Si deposition. Details of the sample structures are described elsewhere [7–9]. The 2D carrier concentration as a function of spacer thickness is consistent with a charge-transfer model for a 160 meV barrier. A typical temperature-dependent Hall mobility of a sample with 15 nm spacer is shown in Fig. 3. The carrier concentration with-

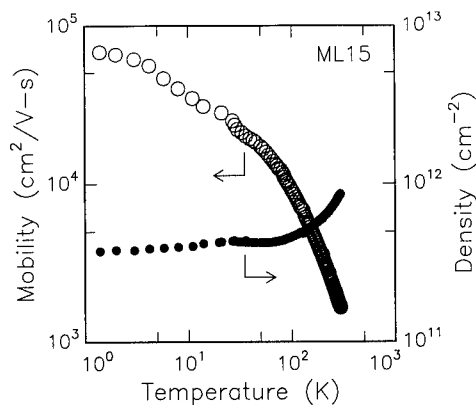


Fig. 3. A typical temperature dependence of channel Hall mobility and carrier concentration. The excess carriers above 100 K are due to residual dopants in the modulation-doping region.

out illumination for this sample is about  $4.3 \times 10^{11}\text{ cm}^{-2}$ . Room-temperature mobility is about  $2000\text{ cm}^2\text{ V}^{-1}\text{ s}^{-1}$ .

### 4. Magnetotransport

Magnetotransport shows all the well-known  $E_0$  subband characteristics of (100)Si inversion layers. However, because of its superior mobility, much more detailed structures show up at relatively lower magnetic fields compared with its MOSFET counterpart. Fig. 4 shows the longitu-

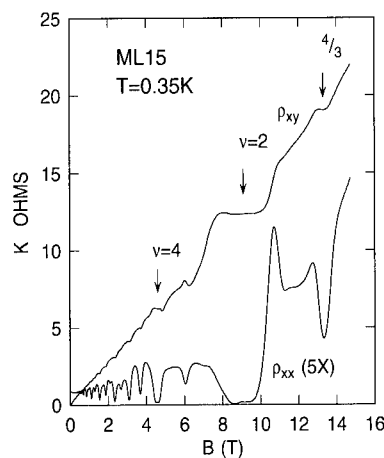


Fig. 4. Magnetoresistances at 0.35 K for the sample in Fig. 3.

dinal and Hall resistivities of the same sample as in Fig. 3 at 0.35 K. Lifting of the four-fold degeneracy for each Landau level, two for spin and two for valley, is well resolved at relatively low fields. Temperature dependence of the the SdH oscillation amplitude at low field gives an in-plane effective mass of  $0.2m_0$ , as expected for this subband. Tilted field experiments [10] indicate that the magnetic field filling factor  $\nu = 2, 6, 10$ , are due to spin splitting. For this sample, the coincident spin of adjacent Landau levels occurs at a magnetic field tilt angle of 69 degrees, which implies a many-body exchange-interaction-enhanced  $g$  factor of 3.6, surprisingly close to that found in MOSFET samples at the same carrier concentration [10], considering the qualitative differences in the sample configuration and in scattering rates. The valley splitting, characterized by the odd filling factors, can be resolved at about 2 T. The integer quantum Hall plateaus prominently appear at even filling factors. At the magnetic field  $B = 13.2$  T, corresponding to the hybrid fractional filling factor  $4/3$ , a clear  $\rho_{xy} = 3/4(hc/e^2)$  plateau and a corresponding  $\rho_{xx}$  dip are observed. There are also some structures between  $\nu = 2$  and  $4/3$  whose origin cannot be identified.

In Fig. 5 is shown the magnetoresistance for another sample with electron concentration  $3.6 \times 10^{11} \text{ cm}^{-2}$ , but lower mobility. The  $\nu = 2/3$

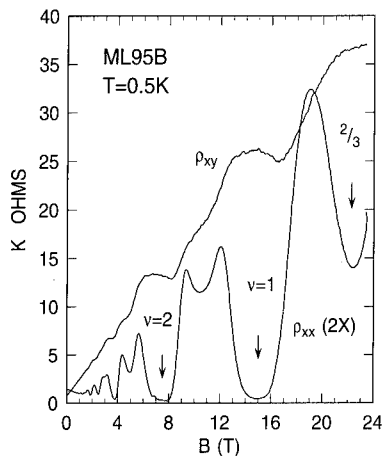


Fig. 5. Magnetoresistances of a sample with carrier concentration  $3.6 \times 10^{11} \text{ cm}^{-2}$ . (Work done at the National Magnetic Lab.)

FQHE at  $B = 23.5$  T is clearly discerned for the first time in this system. However, the expected  $\nu = 4/3$  state at 10.5 T cannot be unambiguously identified, probably due to low mobility and lower corresponding magnetic field compared with the sample in Fig. 4.

Activation energies  $\Delta$  for the  $\nu = 4/3, 2/3$  and the  $2/3$  states for the samples shown in Figs. 4 and 5, respectively, were measured by their temperature-dependent  $\rho_{xx}$  in the form of  $\exp(-\Delta/2T)$ . For the high-mobility sample, the activation energy for  $\nu = 4/3$  and  $2/3$  states are about 0.9 K at 13.5 T and 1.2 K at 27 T, respectively. For the low-mobility sample, the activation energy of the  $\nu = 2/3$  state is 1 K at 22.5 T. These low activation energies are to be compared with the values of 4–5 K reported for the high mobility  $((2-5) \times 10^6 \text{ cm}^2 \text{ V}^{-1} \text{ s}^{-1})$  and 8–9 K for the super-high mobility (over  $10^7$ ) GaAs/AlGaAs heterostructures [11]. As the activation energy is a measure of the mobility gap of these many-body coulomb-interaction ground states, it is not surprising that low mobility reflects greater level broadening, regardless of the nature of the intrinsic gap and the broadening mechanisms.

## 5. Scattering

It is well known that the electron mobility is governed by the scattering relaxation time. Only large-angle back-scattering events significantly degrade the mobility. On the other hand, the purity of a quantum coherent state is governed by the single-particle relaxation time which includes all the phase-breaking scattering events. Thus, it involves quantum-mechanical transition rates over all the angles. In the Si MOSFET, these two characteristic times are nearly equal [12], and this is taken as evidence of a short-range-scattering-dominated regime. In a high-quality modulation-doped sample such as the GaAs/AlGaAs structures, however, remote ion scattering is considered to be long range. The ratio between scattering relaxation time  $\tau_t$  and single-particle relaxation time  $\tau_s$  is considerably greater than unity [12,13]. Das Sarma and Stern have shown that in an ideal condition, this ratio depends strongly on

the spacer thickness [14]. For this reason, it may be used as a measure for the short-range scattering in the 2D-carrier channel region. Experimentally, the scattering relaxation time is obtained directly from mobility. The single-particle relaxation time is obtained by fitting the reciprocal magnetic damping at low fields of the SdH oscillation amplitude [12], which has the form  $P \exp(-\pi/\omega_c \tau_s)$  where  $\omega_c = eB/m$  is the cyclotron frequency.  $P$  is an appropriate pre-exponential factor, given in this case by  $\xi/\sinh \xi$ , where  $\xi = 2\pi^2 k_B T / \hbar \omega_c$  [15,12,16].

Data of this kind from various laboratories vary greatly, yielding ratios ranging from 11–26 from the Munich group [5]; 4 from the Bell group [17], and 4–11 from the IBM group [18]. Except for the high value of 26, these measured ratios are reasonably consistent with a recent model calculation of Stern and Laux [19], assuming  $10^{14} \text{ cm}^{-3}$  background acceptor density,  $10^{10} \text{ cm}^{-2}$  interface charges, and interface-roughness parameters rms height  $\Delta$  and lateral correlation length  $\Lambda$  equal to 1 and 20 nm, respectively. The low-temperature mobilities for all the samples reported above were about  $(1-2) \times 10^5 \text{ cm}^2 \text{ V}^{-1} \text{ s}^{-1}$ . The large difference in the ratio must be caused by great variations in the long-range scatterers. For instance, the non-uniform or gradual dopant concentration near the spacer edge, residual impurities inside the spacer region, etc.

## 6. Low-temperature mobility

A typical temperature-dependent mobility at low temperature is shown in Fig. 6. The negative temperature coefficient could in part be attributed to phonon scattering. The quantitative dependence must be sensitive to a combination of all other type of scattering with comparable rates. Recent model calculations reported by Stern and Laux [19] indeed show a variety of dependences by blending suitable parameters associated with different scattering mechanisms. Fig. 7 shows some experimental reciprocal mobility data fitted by such calculations [20]. The slopes of the experimental data suggest the mobility of the examined samples are limited by surface-roughness scatter-

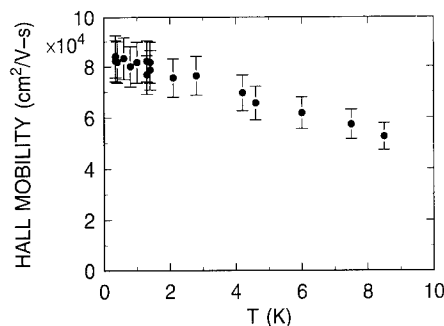


Fig. 6. A typical temperature-dependent Hall mobility at low temperature showing a pronounced negative temperature coefficient.

ing with rms height smaller than 0.8 nm and lateral correlation length about 1 nm. The data also suggest that interface charge is probably smaller than  $10^{10} \text{ cm}^{-2}$ , which is a typical number for a good MOSFET sample. A background acceptor-impurity density of  $10^{14} \text{ cm}^{-3}$  is assumed in the calculation.

In an unpublished report, Ming et al. [21] described some microscopic structures of the interfaces in SiGe/Si heterostructures revealed by a grazing-incidence X-ray scattering technique. They found that the rms height is around 0.5 nm, reasonably consistent with that implied for the

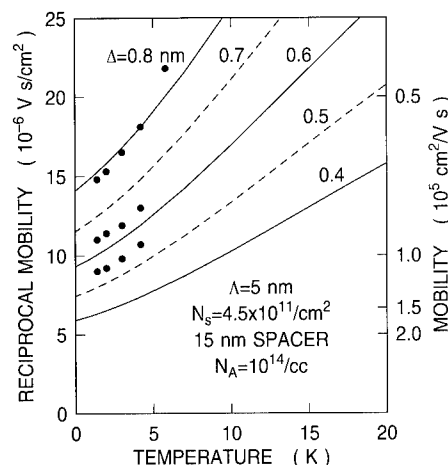


Fig. 7. Experimental reciprocal mobility data for samples with 15 nm spacer fitted with a model calculation of Stern and Laux. The background acceptor impurity and interface-charge densities are  $10^{14} \text{ cm}^{-3}$  and  $10^{10} \text{ cm}^{-2}$ , respectively. (See text.)

data in Fig. 7. However, they also reported a lateral correlation length of 70 nm which is much larger than the transport data implied. Since their samples are strained SiGe layers grown on (100)Si substrate by MBE, the comparison is certainly not relevant at this point. It would be very interesting and desirable if such microscopy could be performed on the samples for which the transport measurements have been carried out.

Within the scattering mechanisms considered in the model calculation, the data fitting seems to suggest that the currently observed mobilities of  $(1-2) \times 10^5 \text{ cm}^2 \text{ V}^{-1} \text{ s}^{-1}$  from various laboratories with different methods are likely limited by the background impurities in the Si inversion layer, the interface charge and the spacer distance. Surface roughness plays a prominent role, further degrading the mobility beyond the impurity and interface-charge-scattering limits. It would be interesting to have a gated structure to test the relative importance of the fixed-charge and surface-roughness scattering by varying the surface field and 2D electron density.

## 7. Conclusions

Strained Si on strain-relieved SiGe has shown significant improvement in the transport properties. The room-temperature mobility enhancement resulting from large subband splitting is of particular interest in the Si-based technology. With the mobility of up to  $2 \times 10^5 \text{ cm}^2 \text{ V}^{-1} \text{ s}^{-1}$ , valley splitting is observed at relatively low magnetic fields. FQHE plateaus are observed at  $\nu = 2/3$  and  $4/3$ . Temperature dependence of the electron mobility suggests that the fixed-charge scattering limits the present samples. It appears that in order to improve the mobility further, background impurities and the interface charge density need to be reduced. Surface roughness scattering should play an important role when more carriers are induced by field effect.

## 8. Acknowledgements

It is a pleasure to acknowledge stimulating discussions with F. Stern, S. Nelson and E. Men-

dez. Superb samples used in this work were generously supplied by B. Meyerson, S. Nelson and J. Chu. The able technical assistance of J. Nocera and M. Christie is gratefully acknowledged. F. LeGoues kindly permitted the use of the micrograph in Fig. 1. Careful reading of the manuscript by T. Theis is much appreciated.

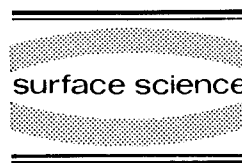
## 9. References

- [1] F.K. LeGoues, B.S. Meyerson and J.F. Morar, *Phys. Rev. Lett.* 66 (1991) 2903.
- [2] F. Schaffler, D. Tobben, H.-J. Herzog, G. Abstreiter and B. Hollander, *Semicond. Sci. Technol.* 7 (1992) 260.
- [3] E.A. Fitzgerald, Y.H. Xie, M.L. Green, D. Brasen, A.R. Kortan, J. Michel, Y.J. Mii and B.E. Weir, *Appl. Phys. Lett.* 59 (1991) 811.
- [4] F.F. Fang, P.J. Wang, B.S. Meyerson, J.J. Nocera and K.E. Ismail, *Surf. Sci.* 263 (1992) 175.
- [5] E.A. Fitzgerald, Y.-H. Xie, D. Monroe, P.J. Silverman, J.M. Kuo, A.R. Kortan, F.A. Thiel and B.A. Weir, *J. Vac. Sci. Technol. B* 10 (1992) 1807.
- [6] C.G. Van de Walle and R.M. Martin, *Phys. Rev. B* 34 (1986) 5621.
- [7] P.J. Wang, B.S. Meyerson, K. Ismail, F.F. Fang and J.J. Nocera, *Mater. Res. Soc. Symp. Proc.* 220 (1991) 403.
- [8] Y.J. Mii, Y.H. Xie, E.A. Fitzgerald, D. Monroe, F.A. Thiel and B.E. Weir, *Appl. Phys. Lett.* 59 (1991) 1611.
- [9] S.F. Nelson, K.E. Ismail, J.J. Nocera, F.F. Fang, E.E. Mendez, J.O. Chu and B.S. Meyerson, *Appl. Phys. Lett.* 61 (1992) 64.
- [10] F.F. Fang and P.J. Stiles, *Phys. Rev.* 174 (1968) 823.
- [11] R. Willett, H.L. Stormer, D.C. Tsui, A.C. Gossard, J.H. English and K.W. Baldwin, *Surf. Sci.* 196 (1988) 257.
- [12] F.F. Fang, A.B. Fowler and A. Hartstein, *Phys. Rev. B* 16 (1977) 4446.
- [13] M.A. Paalanen, D.C. Tsui and J.C.M. Hwang, *Phys. Rev. Lett.* 51 (1983) 2226.
- [14] S. Das Sarma and F. Stern, *Phys. Rev. B* 32 (1985) 8442.
- [15] T. Ando, Y. Matsumoto and Y. Uemura, *J. Phys. Soc. Jpn.* 39 (1975) 279.
- [16] P.T. Coleridge, *Phys. Rev. B* 44 (1991) 3793.
- [17] D. Monroe, Y.H. Xie, E.A. Fitzgerald and P.J. Silverman, *Phys. Rev. B* 46 (1992) 7935.
- [18] F.F. Fang, B.S. Meyerson, S.F. Nelson, J.O. Chu, J.J. Nocera, K.E. Ismail and E.E. Mendez, *Bull. Am. Phys. Soc.* 37 (1992) 550.
- [19] F. Stern and S.E. Laux, *Appl. Phys. Lett.* 61 (1992) 1110.
- [20] We are indebted to F. Stern and S.E. Laux for extending their calculation reported in Ref. [19] for appropriate fitting of the experimental data. Experimental data are in part provided by S.F. Nelson.
- [21] Z.H. Ming, A. Krol, Y.L. Soo, Y.H. Kao, J.S. Park and K.L. Wang, unpublished. We are grateful for a preprint prior to the publication.



ELSEVIER

Surface Science 305 (1994) 307–311



## Valence band Landau level mixing and anisotropy in $\text{Si}_{1-x}\text{Ge}_x$ investigated by resonant magnetotunneling

A. Zaslavsky \*, D.A. Grützmacher, S.Y. Lin, T.P. Smith III, T.O. Sedgwick

IBM Research Division, T.J. Watson Research Center, Yorktown Heights, NY 10598, USA

(Received 16 April 1993; accepted for publication 4 June 1993)

### Abstract

We report magnetotunneling measurements on strained p-Si/ $\text{Si}_{1-x}\text{Ge}_x$  double-barrier resonant tunneling structures in fields up to 30 T. In the  $I(V, B_{\parallel})$  characteristics of the first heavy-hole peak we observe satellite resonances corresponding to tunneling with  $\Delta n = 1$  and  $\Delta n = 2$  changes in Landau index  $n$ . The relative intensity of the satellite peaks excludes scattering as a possible mechanism and we attribute the  $\Delta n = 1, 2$  peaks to elastic tunneling made possible by Landau level mixing. The observed strong  $\Delta n = 2$  mixing could arise from the large  $E(k_{\perp})$  anisotropy in the  $\text{Si}_{1-x}\text{Ge}_x$  quantum well, which we probe by  $I(V, B_{\perp})$  measurements. From the shifts in the heavy-hole peak with in-plane  $B_{\perp}$  orientation we find that at large  $k_{\perp}$  the in-plane mass varies strongly between the  $\langle 110 \rangle$  (heavy) and  $\langle 100 \rangle$  (light) crystallographic directions.

Resonant magnetotunneling in double-barrier resonant tunneling structures (DBRTS) has become a powerful technique for probing two-dimensional (2D) subband states in quantum wells. If the tunneling carriers are described by a single, isotropic, parabolic band, like electrons in III–V heterostructures, the effects of a magnetic field parallel ( $B_{\parallel}$ ) and transverse ( $B_{\perp}$ ) to the tunneling direction are well understood. In a  $B_{\parallel}$  field, the states are constrained into evenly spaced Landau levels with in-plane harmonic oscillator wavefunctions  $\phi_n(r_{\perp})$ . The energy  $E$  and transverse momentum  $k_{\perp}$  conservation rules that govern tunneling from the emitter into the well at  $B = 0$  [1] are transformed into the conservation of  $E$  and

Landau index  $n$  [2,3]. As Landau levels successively align, the peak acquires a weak staircase-like structure [3], but in the absence of scattering or LO-phonon emission [4]  $B_{\parallel}$  cannot produce any structure in  $I(V, B_{\parallel})$  beyond the resonant peak. Conversely, in a  $B_{\perp}$  field, the energies and densities of states of the 2D subbands in the well are not strongly affected if the magnetic length is larger than the well width  $W$ . The main  $B_{\perp}$ -induced effect is the peak broadening and shifting to higher bias due to the  $\Delta k_{\perp} = eB_{\perp}\langle z \rangle/\hbar$  change in  $k_{\perp}$  as the carrier tunnels a distance  $\langle z \rangle$  from the emitter into the well [5,6]. If the in-plane dispersion  $E(k_{\perp})$  is isotropic, the peak shift  $\Delta V$  is obviously independent of  $B_{\perp}$  orientation in the plane; from  $E$  and  $k_{\perp}$  conservation  $\Delta V \sim B_{\perp}^2$  [5–7].

If the tunneling carriers cannot be described by a parabolic band, as in the case of p-type

\* Corresponding author.



III–V [8,9] and Si/Si<sub>1-x</sub>Ge<sub>x</sub> [10,11] DBRTS, magnetic field effects are more complex. Hole states in quantum wells belong to interacting heavy-hole (HH) and light-hole (LH) bands with nonparabolic and anisotropic dispersion; there are additional strain-induced complications in Si/Si<sub>1-x</sub>Ge<sub>x</sub> structures. We have measured  $I(V, B_{\parallel})$  to elucidate the valence band HH Landau level structure and  $I(V, B_{\perp})$  to probe the in-plane valence band anisotropy of strained Si<sub>1-x</sub>Ge<sub>x</sub> quantum wells. In  $I(V, B_{\parallel})$  characteristics we find strong Landau index-nonconserving satellite peaks in the first heavy-hole (HH<sub>0</sub>) resonance, which we interpret as the first observation of Landau level mixing [12–14] in transport. In the  $I(V, B_{\perp})$  data we find a strong dependence of peak bias on  $B_{\perp}$  orientation with respect to crystallographic axes: in the HH<sub>0</sub> subband the in-plane mass  $m_{\perp}^*$  is heavy along the  $\langle 110 \rangle$  and light along the  $\langle 100 \rangle$  axes.

Our p-Si/Si<sub>1-x</sub>Ge<sub>x</sub> DBRTS were grown by atmospheric pressure CVD, with 50 Å Si barriers cladding the Si<sub>0.75</sub>Ge<sub>0.25</sub> wells of thickness  $W = 35$  and 23 Å, and the double-barrier structure in turn surrounded by graded Si<sub>1-x</sub>Ge<sub>x</sub> emitter and collector regions (see Ref. [15] for details of the sample design and growth). The calculated DBRTS band diagram of the  $W = 35$  Å device under bias is shown in Fig. 1a; the zero-field  $I(V)$  characteristics of the two structures at  $T = 4.2$  K

are shown in Fig. 1b. Since the heavy–light hole strain splitting in Si<sub>0.75</sub>Ge<sub>0.25</sub>  $\Delta\epsilon \approx 40$  meV  $\gg kT$ , only the heavy-hole states are occupied in the emitter, and the  $I(V)$  curves exhibit resonant peaks corresponding to the tunneling of emitter heavy holes into the HH<sub>0</sub> and LH<sub>0</sub> subbands in the well. The peak-to-valley ratios are high for p-type DBRTS, reaching 4:1 for LH<sub>0</sub> peaks. The expected threshold and peak voltages for the resonances are also shown in Fig. 1b: we employed interpolated SiGe valence band parameters to calculate the energies of the HH<sub>0</sub> and LH<sub>0</sub> subbands; assumed the same parabolic  $E(k_{\perp})$  for the emitter and the HH<sub>0</sub> subband; took the LH<sub>0</sub> subband to be dispersionless [16]; and applied the standard  $E$  and  $k_{\perp}$  conservation rules [1]. Even in this naive model the agreement between the calculated and measured HH<sub>0</sub> peak positions is excellent. For the LH<sub>0</sub> peak the agreement is poor and a proper calculation of the LH<sub>0</sub> dispersion is clearly necessary.

The  $I(V, B_{\parallel})$  characteristics of the HH<sub>0</sub> peak in the  $W = 35$  Å DBRTS for increasing up to 30 T are shown in Fig. 2. While the main HH<sub>0</sub> peak position remains nearly unchanged at  $V_p = 140$  mV, already at  $B_{\parallel} = 7.5$  T a weak shoulder appears at higher bias. As  $B_{\parallel}$  increases, this shoulder develops into a strong satellite that shifts to higher  $V$  and dominates the main peak when  $B_{\parallel} = 30$  T, while for  $B_{\parallel} \geq 20$  T another, weaker

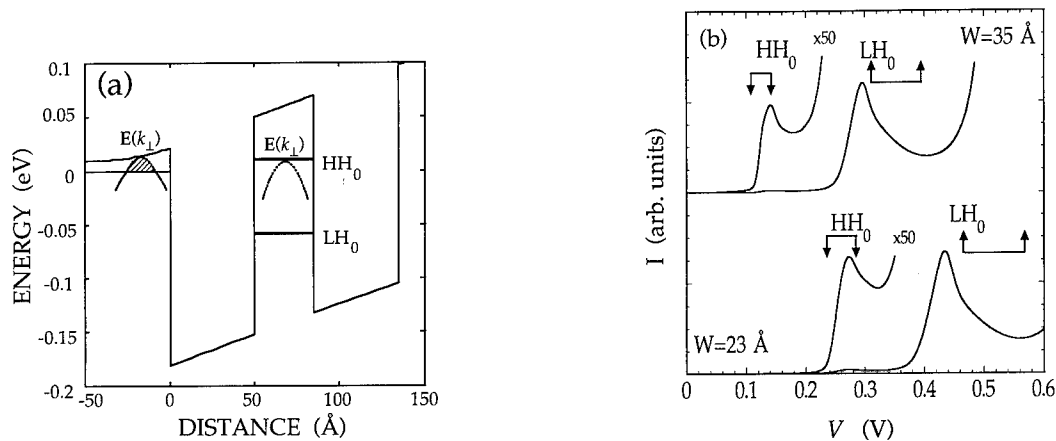


Fig. 1. (a) Calculated potential distribution of  $W = 35$  Å DBRTS under bias  $V = 140$  mV, with schematic  $E(k_{\perp})$  dispersion in the emitter and the HH<sub>0</sub> 2D subband (occupied emitter states are hatched). (b) Tunneling  $I(V, B = 0)$  characteristics at  $T = 4.2$  K of structures with  $W = 23$  and 35 Å. Arrows show the calculated threshold and peak voltages for the HH<sub>0</sub> and LH<sub>0</sub> peaks.

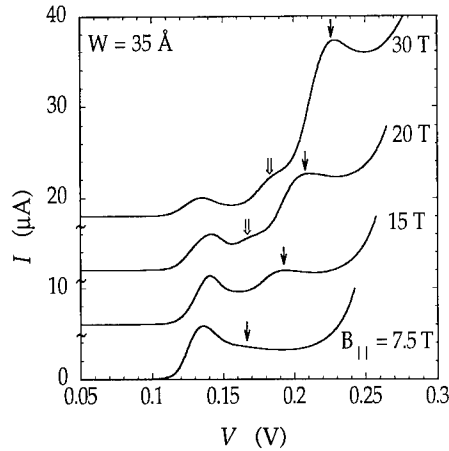


Fig. 2.  $I(V, B_{\parallel})$  characteristics at  $T = 4.2$  K of the  $W = 35$  Å structure at  $B_{\parallel} = 7.5, 15, 20$  and  $30$  T (curves displaced by  $6$   $\mu$ A for clarity). Solid ( $\Delta n = 2$ ) and open ( $\Delta n = 1$ ) arrows mark the Landau index nonconserving peaks.

satellite feature appears in between. The  $W = 23$  Å structure exhibits analogous behavior, with a stronger and a weaker satellite peaks shifting to higher bias with increasing  $B_{\parallel}$ .

The main and satellite peak positions of the  $HH_0$  lineshape are summarized in Fig. 3. Since the satellite peaks occur at higher bias than the main  $HH_0$  peak, they must arise from Landau index-nonconserving processes. From the  $B_{\parallel}$ -in-

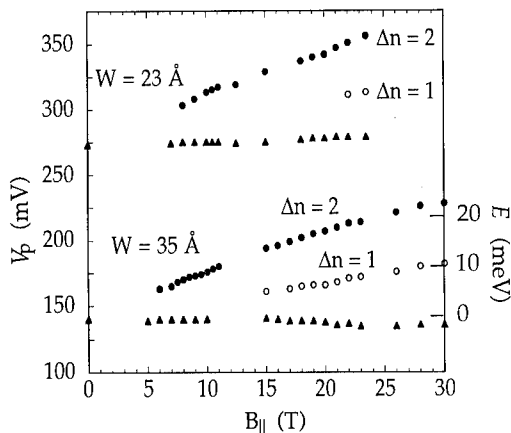


Fig. 3. Bias positions of the main (triangles) and satellite ( $\Delta n = 1$ , open circles;  $\Delta n = 2$ , filled circles) peaks versus  $B_{\parallel}$ . At right is the calculated energy scale of the Landau spectrum for the  $W = 35$  Å device; the zero of energy is arbitrarily set to the  $HH_0$  peak position at  $B_{\parallel} = 0$ .

duced shifts in satellite peak positions, we attribute the stronger satellite to  $\Delta n = 2$  tunneling and the weaker satellite to  $\Delta n = 1$  tunneling. A possible mechanism for these index-nonconserving peaks is scattering, which was invoked by Schubert et al. [17] to explain weak features observed in the conductance of the  $LH_0$  peak in similar p-Si/Si<sub>1-x</sub>Ge<sub>x</sub> DBRTS. Yet the strength of the  $\Delta n = 2$  satellite, which exceeds the main peak at high  $B_{\parallel}$ , together with the relative weakness of the  $\Delta n = 1$  satellite make a scattering mechanism unlikely. Although interface and impurity scattering can relax  $k_{\perp}$  conservation or, equivalently, Landau index conservation [17], it is unlikely to produce satellite peaks comparable in strength to the main, index-conserving peak. Moreover, the  $\Delta n = 1$  satellite is much weaker than  $\Delta n = 2$ , although the required change in  $k_{\perp}$  for  $\Delta n = 2$  tunneling is much larger if scattering is responsible. Consequently, instead of scattering-assisted tunneling, we interpret our data in terms of valence band Landau level mixing, which allows  $\Delta n \neq 0$  tunneling.

Essentially, our DBRTS in a  $B_{\parallel}$  field is described by an effective  $4 \times 4$  Hamiltonian  $H_{ij}$  in the  $|Jm_j\rangle$  basis [12–14]:  $J = 3/2$ ; the quantization axis is  $z \parallel B_{\parallel}$ ;  $i, j = 1, 2, 3, 4$  label the states  $m_j = 3/2, 1/2, -1/2, -3/2$  in that order; uniaxial strain contributes only to diagonal elements  $H_{ii}$  and splits the  $|3/2 \pm 3/2\rangle$  (HH) and  $|3/2 \pm 1/2\rangle$  (LH) bands by  $\Delta\epsilon$  [13]. In a magnetic field, all  $H_{ij}$  elements can be expressed in terms of harmonic oscillator raising and lowering operators  $a$  and  $a_{\pm}$ . If the anisotropy term  $(\gamma_3 - \gamma_2)a_{\pm}^2$  is ignored in the Hamiltonian, the four-component Landau level eigenfunctions  $\Psi_n$  can be written as a superposition of harmonic oscillator wavefunctions  $\phi_n(r_{\perp})$  [12,14]:

$$\Psi_n^{l,h} = [\zeta_{1,n}\phi_{n-2}; \zeta_{2,n}\phi_{n-1}; \zeta_{3,n}\phi_n; \zeta_{4,n}\phi_{n+1}], \quad (1)$$

where  $\zeta_{i,n}(z)$  are linear combinations of products  $c_i(z)|Jm_j\rangle$ , with  $c_i(z)$  determined by the boundary conditions on  $\Psi_n$ . The diagonal  $H_{ii}$  terms have the form  $(aa_{\pm} + 1/2)$  and would give rise to separate sets of heavy and light-hole Landau lev-

els with linear  $B_{\parallel}$  dependence, while the off-diagonal terms cause Landau level mixing. The relevant terms for  $\Delta n = 2$  level mixing are  $H_{13} \sim (\gamma_3 + \gamma_2)a^2 + (\gamma_3 - \gamma_2)a_+^2$ ; for  $\Delta n = 1$  mixing they are  $H_{12} \sim k_z a$  [14]. These terms mix oscillator functions  $\phi_m(r_{\perp})$  into the  $n$ th Landau level wavefunctions, where  $m = n, n \pm 1, n \pm 2$  (the closed form wavefunction (1) is no longer valid when the anisotropy term is included, but  $\phi_n(r_{\perp})$  remain the basis from which the Landau level  $\Psi_n$  are constructed). In a bulk crystal the common  $\phi_m$  of different Landau levels are multiplied by different orthogonal  $|J m_j\rangle$  functions, making  $n$  a constant of motion, but in a DBRTS the boundary conditions at the barrier interfaces [14] make  $\zeta_{i,n}(z)$  nonorthogonal at different  $z$ , allowing elastic tunneling from emitter to well between Landau levels with  $\Delta n = 1, 2$ .

The  $I(V, B_{\parallel})$  curves of Fig. 2 make it possible to obtain the separation between Landau levels by converting the voltage splitting between the main and satellite peaks into an energy scale, as done in Fig. 3 for the  $W = 35$  Å device. At low and moderate  $B_{\parallel}$  the  $\Delta n = 2$  peak shifts linearly with  $B_{\parallel}$ . If we take this energy separation as a measure of heavy-hole in-plane mass we obtain  $m_{\perp}^* = 0.29 \pm 0.04$ , heavier than predicted by interpolated valence band parameters, but in agreement with recent cyclotron resonance measurements on  $\text{Si}_{1-x}\text{Ge}_x$  quantum wells [18].

Without a true calculation of the mixed Landau level wavefunctions (1) in the quantum well our understanding of the relative strength of the  $\Delta n \neq 0$  satellite peaks remains qualitative. From the data in Fig. 2, we find that mixing with  $\Delta n = 1$  is about an order of magnitude weaker than  $\Delta n = 2$ . The weakness of  $\Delta n = 1$  satellite is consistent with the relevant  $H_{12} \sim k_z a$  term, since the resonant peaks occur when the 2D subbands are nearly aligned with the top of the band in the emitter (see Fig. 1a), so  $k_z$  is small [1]. The strong  $\Delta n = 2$  mixing we observe could imply a strong in-plane anisotropy described by the  $(\gamma_3 - \gamma_2)a_+^2$  term, especially since  $\Delta n = 2$  tunneling was not observed in III–V DBRTS [9]. We tested this hypothesis by performing  $I(V, B_{\perp})$  measurements versus in-plane  $B_{\perp}$  orientation, analogously to the earlier study by Gennser et al. [19]

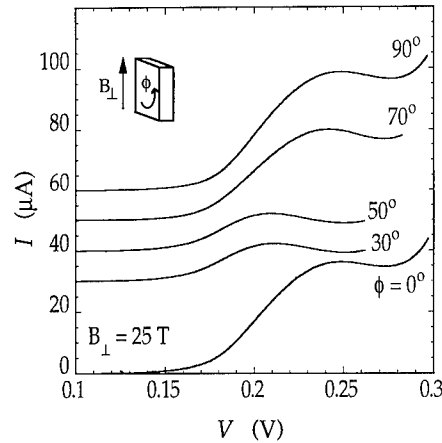


Fig. 4.  $I(V, B_{\perp} = 25$  T)  $\text{HH}_0$  peak of the  $W = 35$  Å DBRTS versus angle  $\phi$  between  $B_{\perp}$  and the  $\langle 100 \rangle$  axis (curves displaced for clarity). Inset contains the measurement geometry.

who reported  $B_{\perp}$  orientation dependence of peak positions in MBE-grown  $\text{Si}/\text{Si}_{1-x}\text{Ge}_x$  DBRTS.

Fig. 4 shows the strong variation in the  $\text{HH}_0$  peak as a function of the angle  $\phi$  between  $B_{\perp} = 25$  T and the  $\langle 100 \rangle$  axis in the  $W = 35$  Å DBRTS, together with the measurement geometry (inset). The  $B_{\perp}$ -induced peak shift  $\Delta V$  varies from  $\Delta V \approx 110$  mV when  $\phi = 0^\circ$  ( $B_{\perp} \parallel \langle 100 \rangle$  axis) to  $\Delta V \approx 75$  mV when  $\phi = 50^\circ$  ( $B_{\perp} \parallel \langle 110 \rangle$ ). The observed anisotropy, which is summarized for the  $W = 35$  Å structure in Fig. 5, follows the crystal symmetry, with the largest  $\Delta V$  occurring whenever  $B_{\perp}$  is aligned with a  $\langle 100 \rangle$  axis. By the simple geometrical construction in the inset of Fig. 5, showing schematically the states that can tunnel conserving  $E$  and  $k_{\perp}$ , assuming parabolic  $E(k_{\perp})$  dispersion with different curvature (different  $m_{\perp}^*$ ) along  $\langle 100 \rangle$  and  $\langle 110 \rangle$ , we immediately find that the effective heavy-hole mass  $m_{\perp}^*$  away from the  $k = 0$  band edge is markedly heavier along the  $\langle 110 \rangle$  than the  $\langle 100 \rangle$  axes. Due to band non-parabolicity further calculations are required to convert magnetotunneling data into real dispersion curves, but the  $E(k_{\perp})$  constant energy contour obtained by converting  $\Delta V(\phi)$  into an energy scale is consistent with the  $m_{\perp}^* \approx 0.29$  result obtained from  $I(V, B_{\perp})$  measurements that average over all  $k_{\perp}$ .

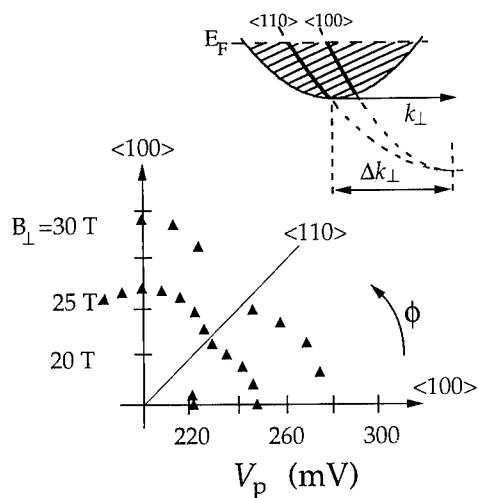


Fig. 5.  $HH_0$  peak position  $V_p$  versus  $\phi$  for  $B_{\perp} = 20, 25, 30$  T in  $W = 35$  Å DBRTS. Inset, schematic alignment of emitter and  $HH_0$  states with parabolic  $E(k_{\perp})$  of different curvatures for two crystallographic directions. States that can tunnel elastically are shown in boldtype.

In conclusion, we have experimentally observed satellite peaks in the heavy-hole  $I(V, B_{\parallel})$  characteristics of  $Si/Si_{1-x}Ge_x$  DBRTS due to index-nonconserving tunneling between Landau levels that cannot be attributed to scattering. We attribute these index-nonconserving peaks to strong Landau-level mixing and use the data to map out the energy spacing between Landau levels in strained  $Si_{1-x}Ge_x$  quantum wells. A possible explanation for the surprising strength of the  $\Delta n = 2$  level mixing is the large in-plane anisotropy of  $Si_{1-x}Ge_x$ , which we measured using  $I(V, B_{\perp})$  magnetotunneling as a function of  $B_{\perp}$  orientation in the plane. We find the  $HH_0$  subband to be highly anisotropic, with significantly smaller  $E(k_{\perp})$  curvature (heavier in-plane mass) in the  $\langle 110 \rangle$  direction.

We are pleased to acknowledge the assistance of the Francis Bitter National Magnet Laboratory

staff and D. Syphers. Work at IBM was partially supported by ONR (N0001492-C-0017).

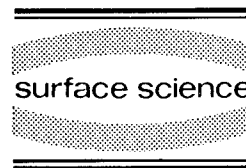
## 1. References

- [1] S. Luryi, Appl. Phys. Lett. 47 (1985) 490.
- [2] E.E. Mendez, L. Esaki and W.I. Wang, Phys. Rev. B 33 (1986) 2893.
- [3] V.J. Goldman, D.C. Tsui and J.E. Cunningham, Phys. Rev. B 35 (1987) 9387.
- [4] V.J. Goldman, D.C. Tsui and J.E. Cunningham, Phys. Rev. B 36 (1987) 7635.
- [5] L. Eaves, K.W.H. Stevens and F.W. Sheard, in: The Physics and Fabrication of Microstructures, Eds. M.J. Kelly and C. Weisbuch (Springer, New York, 1986) p. 343.
- [6] R.A. Davies, D.J. Newson, T.G. Powell, M.J. Kelly and H.W. Myron, Semicond. Sci. Technol. 2 (1987) 61.
- [7] A. Zaslavsky, Yuan P. Li, D.C. Tsui, M. Santos and M. Shayegan, Phys. Rev. B 42 (1990) 1374.
- [8] E.E. Mendez, W.I. Wang, B. Ricco and L. Esaki, Appl. Phys. Lett. 47 (1985) 415.
- [9] R.K. Hayden, L. Eaves, M. Henini, D.K. Maude, J.C. Portal and G. Hill, Appl. Phys. Lett. 60 (1992) 1474.
- [10] H.C. Liu, D. Landheer, M. Buchanan and D.C. Houghton, Appl. Phys. Lett. 52 (1988) 1809.
- [11] K.L. Wang, J. Park, S.S. Rhee, R.P. Karunasiri and C.H. Chern, Superlattices Microstruct. 5 (1989) 201.
- [12] J.M. Luttinger, Phys. Rev. 102 (1956) 1030.
- [13] G.E. Gurgenishvili, Fiz. Tverd. Tela 5 (1963) 2070 [Sov. Phys.-Solid State 5 (1964) 1510]; G.R. Khutsishvili, Fiz. Tverd. Tela 4 (1962) 2708 [Sov. Phys.-Solid State 4 (1963) 1986].
- [14] D.A. Broido and L.J. Sham, Phys. Rev. B 31 (1985) 888; L.J. Sham, in: High Magnetic Fields in Semiconductor Physics, Ed. G. Landwehr (Springer, New York, 1987) p. 288.
- [15] A. Zaslavsky, D.A. Grützmacher, Y.H. Lee, W. Ziegler and T.O. Sedgwick, Appl. Phys. Lett. 61 (1992) 2872 and references therein.
- [16] E.P. O'Reilly and G.P. Witchlow, Phys. Rev. B 34 (1986) 6030.
- [17] G. Schuberth, G. Abstreiter, E. Gornik, F. Schäffler and J.F. Luy, Phys. Rev. B 43 (1991) 2280.
- [18] J.-P. Cheng, V.P. Kesan, D.A. Grützmacher and T.O. Sedgwick, Appl. Phys. Lett. 62 (1993) 1522.
- [19] U. Gennser, V.P. Kesan, D.A. Syphers, T.P. Smith III, S.S. Iyer and E.S. Yang, Phys. Rev. Lett. 67 (1991) 3828.



ELSEVIER

Surface Science 305 (1994) 312–316



# Effect of electronic-state modulation on mobility in quantum wells

Takuma Tsuchiya <sup>\*,a</sup>, Tsuneya Ando <sup>b</sup>

<sup>a</sup> Fujitsu Laboratories Ltd., 10-1 Morinosato-Wakamiya, Atsugi 243-01, Japan

<sup>b</sup> Institute for Solid State Physics, University of Tokyo, 7-22-1 Roppongi, Minato-ku, Tokyo 106, Japan

(Received 3 May 1993; accepted for publication 14 June 1993)

## Abstract

The electron mobility limited by scattering from optical phonons is calculated for quantum wells with several thin barrier layers being inserted. The barrier insertion leads to a wavefunction modulation which enhances the mobility as long as it does not cause extra intersubband scattering. The dependence on the barrier height and the number of inserted layers is studied systematically.

## 1. Introduction

At room temperature, the mobility in polar semiconductors such as GaAs is limited by scattering from optical phonons. Reduction of the scattering strength is highly desirable for device applications and its possibility has been explored for many years. It is also one of the most challenging subjects in semiconductor physics. The purpose of this paper is to examine effects of wavefunction modulation on the mobility in GaAs/AlAs quantum wells.

There can be two ways in changing the electron–phonon interaction in polar semiconductors. One is modification of phonon modes in heterostructures. In fact, optical phonons are known to be strongly modified by the presence of

heterointerfaces [1]. However, recent reliable calculations based on lattice displacements obtained in lattice-dynamical calculations have given a disappointing result that the scattering strength is essentially independent of such phonon modification [2–5].

Another possible way to reduce scattering strength is a modulation of electron wavefunction. In fact, the scattering strength is characterized by the form factor for interaction with phonons determined by the electron wavefunction along the direction perpendicular to the layer. Because of the long-range Coulombic nature of the interaction, this form factor decreases rapidly with the decrease of the electron wavelength. The mobility can be enhanced, therefore, if the electron wavefunction has an appreciable amount of short-wavelength components.

In this paper, we calculate the electron mobility of GaAs/AlAs quantum wells with several thin barrier layers being inserted and explore a

\* Corresponding author.

possibility of mobility enhancement using wavefunction modulation. Its dependence on the barrier height and the number of inserted layers is calculated systematically. The model and the method are discussed briefly in Section 2, the result is presented in Section 3, and a short summary is given in Section 4.

## 2. Wavefunction modulated single quantum well

We consider GaAs/AlAs single quantum-well (SQW) structures with thin AlGaAs barrier layers being inserted in the GaAs well region. This will be denoted as wavefunction modulated SQW or WFMSQW( $N$ ) with  $N$  being the number of inserted AlGaAs layers. The thickness of each barrier layer inserted with equal spacing is chosen as 4 monolayers or 11.3 Å and the band discontinuity of the conduction-band bottom of GaAs and AlAs is assumed to be 800 meV.

A typical example of the band diagram and the wavefunction of the ground subband for an SQW and a WFMSQW(3) with three inserted barriers is given in Fig. 1. The total thickness is  $d = 124$  Å and the height of the barrier potential is chosen as 800 and 400 meV. The wavefunction in WFMSQW is modulated from that in SQW and the

modulation amplitude increases with the barrier height as is expected. These barriers modulate the electron wavefunction in such a way that it has an appreciable amount of short-wavelength components, which leads to a mobility enhancement as will be demonstrated below.

These thin barriers also cause a change of subband energies. In fact, the energy of a subband whose wavefunction does not have nodes at the position of barriers is raised by the barrier insertion. This causes a bunching of  $N + 1$  subbands in the presence of  $N$  equally spaced barriers. Thus, the thin barriers give rise to extra intersubband scattering in addition to the desired wavefunction modulation, which may lead to lowering of the electron mobility.

Because optical-phonon scattering is dominant at 300 K, we can neglect other scattering mechanisms such as impurities and acoustic phonons. The effective-mass approximation is employed for electronic states and the difference in the effective mass of well and barrier layers is neglected. Further, we consider the case of low electron sheet density ( $N_s = 2 \times 10^{11} \text{ cm}^{-2}$ ) for which the band bending is not important. We shall neglect the screening effect because of high phonon frequency ( $\geq 36$  meV), the low electron concentration, and high temperatures.

We employ a bulk-phonon model for optical phonons. In this model, the LO phonon of the bulk material of the well layer, i.e. GaAs in our structure, is assumed. It has been shown in previous papers [3–5] that the completeness of phonon modes leads to the conclusion that the scattering rate does not depend on details of individual phonon modes. In particular, the bulk phonon model gives quite accurate scattering rates for GaAs/AlAs systems at 300 K.

The electron mobility is calculated in the relaxation time approximation. All scattering processes, i.e. intersubband and intrasubband scattering with phonon emission and absorption, are taken into account. The relaxation time approximation is known to give only a crude estimate of the mobility for scattering from polar-optical-phonons [6], but is sufficient for the present purpose in which we are interested only in the relative difference between SQW and WFMSQWs.

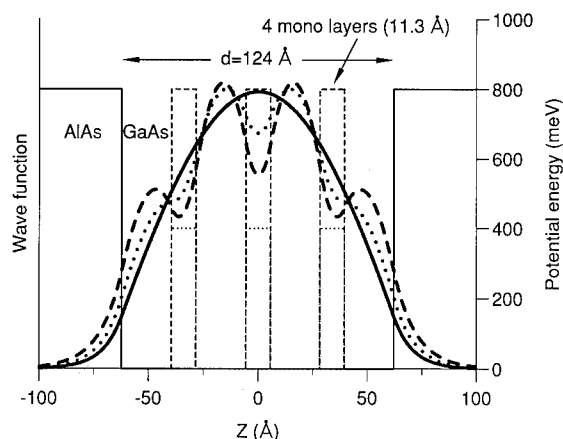


Fig. 1. Band diagram and wavefunctions of the lowest subband of SQW (solid line) and WFMSQW (dashed line for the barrier height 800 meV and dotted line for 400 meV) with layer thickness 124 Å. Three thin barriers are inserted in the WFMSQW.

Recently, Kawamura and Das Sarma [7] have shown that the relaxation time approximation overestimates the room temperature mobility only slightly.

### 3. Numerical results

The layer-thickness dependence of mobility at 300 K in SQW and WFMSQWs is shown in Fig. 2. For WFMSQWs the thickness of mini-well layers between barriers is varied in proportion to the total thickness  $d$  with the fixed barrier thickness. The mobility of SQW has a sharp peak at  $d = 136$  Å and becomes nearly independent of the thickness with small oscillations for  $d > 200$  Å. On the other hand, each WFMSQW has two large peaks. One is a sharp peak around  $d \leq 100$  Å and the other is a broad peak at  $d = 271, 407$ , and  $543$  Å, respectively, for  $N = 1, 2$ , and  $3$ .

For the layer thickness smaller than the first peaks, the mobility in WFMSQWs is larger than that in SQW. This enhancement is the result of the reduction in the electron–phonon interaction due to the wavefunction modulation. The amount of the enhancement is almost independent of the

number of thin barriers. This enhancement disappears quickly once the strong intersubband scattering starts to play a role and the mobility of WFMSQWs becomes smaller than that of SQW.

As the electron distribution is classical, the condition for the appearance of intersubband scattering due to LO phonon absorption into the subband  $l$  is given by

$$\hbar\omega_{\text{LO}} + \gamma k_{\text{B}}T \approx E_l - E_1, \quad (3.1)$$

where  $\hbar\omega_{\text{LO}}$  is the LO-phonon energy,  $E_l$  is the energy at the bottom of the  $l$ th subband,  $l = 1$  denotes the ground subband, and  $\gamma$  is a numerical coefficient of the order of unity. The thickness where the condition (3.1) is satisfied for the first excited subband with  $\gamma \approx 1.5$  is denoted by short vertical arrows in Fig. 2. It is clear that the peak thickness corresponds to the threshold for intersubband scattering. The peak well-thickness becomes smaller with the decrease of  $N$  because of decreasing  $E_2 - E_1$ .

The mobility at broad peaks of WFMSQWs is twice as high as that in SQW with the same layer thickness and is nearly the same as that of SQW at  $136$  Å. This is to be expected because mini-wells become nearly independent of each other for sufficiently thick WFMSQWs. In fact, for broad peaks, the total thickness can be obtained by multiplying the number of mini-wells to that of SQW at the mobility peak.

Fig. 3 shows calculated mobility for WFM-SQW(3) for varying barrier height. With decreasing barrier height, the first peak in the small thickness region approaches that for SQW and at the same time the second peak diminishes.

In Fig. 4 the results of the calculation for SQW and WFMSQW(3) at  $T = 120$  K are compared with the recent experiments of Zhu et al. [8]. The theoretical result is almost one order of magnitude larger than the experiments. This is partly because of the present relaxation time approximation which gives rather inaccurate mobility. However, the most significant cause of the discrepancy lies in the fact that the measured mobility is much lower than the known mobility in such systems [9]. The measured mobility in WFM-SQW(3) is  $\sim 1.5$  times as large as that in SQW for  $d = 124$  Å, where the calculation gives a lower

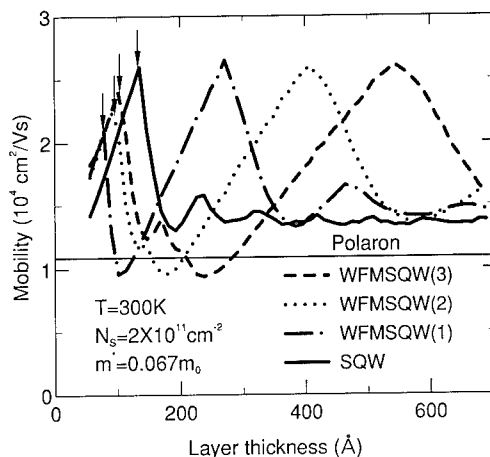


Fig. 2. Calculated mobility as a function of the layer thickness at 300 K in SQW (solid line) and WFMSQW( $N$ ) with varying  $N$ :  $N = 1$  (dash-dotted line),  $N = 2$  (dotted line), and  $N = 3$  (dashed line). The short vertical arrows indicate the thickness where condition (3.1) is satisfied for  $l = 2$  and  $\gamma \approx 1.5$ . The horizontal straight line denotes the polaron mobility in bulk GaAs.

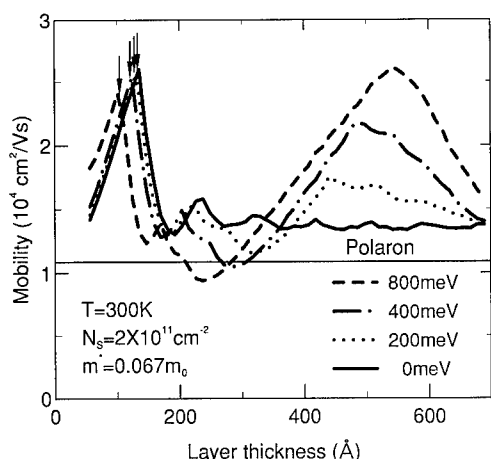


Fig. 3. Calculated mobility as a function of the layer thickness at 300 K in SQW (solid line) and WFMSQW(4) with varying barrier height: 800 meV (dashed line), 400 meV (dot-dashed line), and 200 meV (dotted line). The short vertical arrows indicate the thickness where condition (3.1) is satisfied for  $l=2$  and  $\gamma \approx 1.5$ . The horizontal straight line denotes the polaron mobility in bulk GaAs.

mobility in WFMSQW(3) than in SQW. The same is applicable to  $d = 210 \text{ \AA}$ .

Zhu et al. suggested that the observed en-

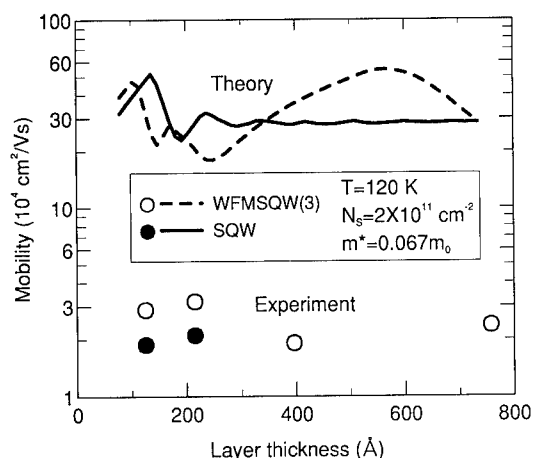


Fig. 4. Calculated and observed mobility at  $T = 120 \text{ K}$ . The solid and dashed lines show the calculated mobility in SQW and WFMSQW(3), respectively, and the filled and open circles show the measured mobility in SQW and WFMSQW(3), respectively.

hancement of the mobility in WFMSQW is due to modulation of optical phonons. This is quite unlikely, however. Although individual phonon modes can be strongly modified by the presence of hetero-interfaces, the completeness of the phonon modes leads to scattering strength independent of the modification as is discussed in Refs. [3–5]. Thus, origins of the discrepancy remain unknown.

#### 4. Summary and conclusion

Effects of electron-wavefunction modulation on the room temperature mobility is studied in GaAs/AlAs quantum wells. The modulation gives rise to two competing effects on the mobility: The first is the reduction in the strength of the electron–phonon interaction, leading to a mobility enhancement, and the second is the introduction of intersubband scattering, leading to a mobility reduction. An appreciable amount of the mobility enhancement can be achieved for appropriate values of parameters for which intersubband scattering is reduced as much as possible.

#### 5. Acknowledgments

One of the authors (T.T.) would like to thank T. Mimura, M. Abe, K. Hikosaka, and K. Joshin of Fujitsu Laboratories Ltd. for continuous encouragement. This work is supported in part by the Industry–University Joint Research Program “Mesoscopic Electronics.”

#### 6. References

- [1] See for example, J. Menéndez, *J. Lumin.* 44 (1989) 285.
- [2] H. Rücker, E. Molinari and P. Lugli, *Phys. Rev. B* 45 (1992) 6747.
- [3] T. Tsuchiya and T. Ando, *Semicond. Sci. Technol.* 7 (1992) B73.
- [4] T. Tsuchiya and T. Ando, *Phys. Rev. B* 47 (1993) 7240.
- [5] T. Tsuchiya and T. Ando, in: *Proceedings of the 21st*

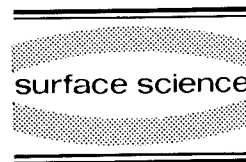


- International Conference on the Physics of Semiconductors, Eds. P. Jiang and H.-Z. Zheng (World Scientific, Singapore, 1993) p. 1004.
- [6] See for example, B.R. Nag, in: *Electron Transport in Compound Semiconductors*, (Springer, Berlin, 1980) p. 144.
- [7] T. Kawamura and S. Das Sarma, *Phys. Rev. B* 45 (1992) 3612.
- [8] X.T. Zhu, H. Goronkin, G.N. Maracas, R. Droopad and M.A. Strosio, *Appl. Phys. Lett.* 60 (1992) 2141.
- [9] L. Pfeiffer, K.W. West, H.L. Störmer and K.W. Baldwin, *Appl. Phys. Lett.* 55 (1989) 1888.



ELSEVIER

Surface Science 305 (1994) 317–321



## Wave function modification via controlled potential perturbation

K. Ensslin <sup>\*,a</sup>, H. Baum <sup>a</sup>, P.F. Hopkins <sup>b</sup>, A.C. Gossard <sup>b</sup>

<sup>a</sup> *Sektion Physik, LMU München, Geschwister-Scholl-Platz 1, 80539 München, Germany*

<sup>b</sup> *Materials Department, University of California, Santa Barbara, CA 93106, USA*

(Received 20 April 1993; accepted for publication 4 June 1993)

### Abstract

Parabolic quantum wells with a potential spike consisting of a small number (1,2,4) of AlAs-monolayers in the center of the well are investigated by means of low-temperature magnetotransport experiments. Intersubband scattering leads to a pronounced feature in the mobility versus carrier density characteristics when the second subband becomes populated. The strength of this feature decreases with increasing width of the AlAs spike which leads to conclusions on the overlap of the wave functions. In a magnetic field  $1/B$  periodic oscillations of the resistance arise that cannot directly be related to the carrier density of one specific subband.

### 1. Introduction

Synthetic potentials can be tailored in a very precise way using molecular beam epitaxy [1]. In particular, parabolic potentials have been realized in the conduction band of AlGaAs/GaAs heterostructures by varying the Al content appropriately. The single particle energy levels that arise after the parabolic potential well has been filled with electrons can be probed with magnetotransport experiments and a quantitative understanding of the details of the potential can be obtained [2]. Wave functions of electronic quantum levels can selectively be modified with a potential spike depending on the local position of the potential perturbation with respect to the maxima of the respective wave function [3]. Here parabolic quantum wells (PQW) are investigated that contain in the center of the well a potential spike consisting of 1, 2 or 4 monolayers of AlAs. The idea is to perturb strongly the wave function

of the lowest subband having a maximum in the center of the well. Simultaneously, the wave function of the second subband ideally has no amplitude in the center and will thus be very little influenced by the potential spike. This concept was used in Ref. [3] to probe directly the eigenstates of an undoped quantum well via optical spectroscopy. In our system, electrons that originate from the ionized donors outside the parabolic quantum well interact with each other leading to a self-consistent modification of the shape of the potential. A change in the charge density profile of the lowest quantum state will therefore directly influence the energy of the higher subband. Because of the mobile electrons in the well, the physical situation in our structures is more involved compared to undoped systems [3].

In this paper, we present experimental results that are based on magnetotransport techniques at liquid He-temperatures. This approach has been

proven useful to understand in detail the single-particle subband structure in unperturbed PQW [2]. The mobility  $\mu$  of the electrons is measured as a function of carrier density  $N_s$  that is controlled via a front-gate voltage. A distinct step-like feature arises in the  $\mu$  versus  $N_s$  curve once the second subband becomes populated. This characteristic becomes less pronounced for increasing width of the potential spike. We argue that this is caused by a decreasing overlap of the wave functions. In the limit of a strong potential spike the wave functions of the lowest two subbands tend to have their maxima in opposing halves of the well if the well is asymmetric. The low-field magnetoresistance reveals oscillations whose periodicities are analyzed by Fourier transformation. For higher carrier densities we find only one frequency in the power spectrum in spite of the fact that two subbands are occupied. Furthermore, this single frequency cannot directly be related to the charge density in the lowest subband.

## 2. Experimental results

The GaAs/Al<sub>x</sub>Ga<sub>1-x</sub>As parabolic quantum wells are grown by molecular beam epitaxy (MBE). The details of the growth sequence for the well without the spike are given in Ref. [2]. All wells investigated have the same curvature of the parabolic potential corresponding to an energy  $\hbar\omega_0 = 10$  meV. In the center of the well defined as the position of minimum Al content in the well without the spike, 1, 2 or 4 monolayers of AlAs are grown for the structures with potential perturbation. Two sets of samples were grown. One set consisting of a well without a spike and wells with a 2 monolayer spike at different positions within the well were grown. In this case the carrier densities ( $N_s \approx 5 \times 10^{11} \text{ cm}^{-2}$  at  $V_g = 0$ ) agree within 10% whether the samples contain potential spikes or not. The mobilities in the samples containing spikes are only reduced by about 10% with respect to the PQW without spike. On another date, after an MBE system opening, another set of samples was grown with 1, 2, and 4 monolayer potential spikes in the center of the well. A Hall bar pattern is mesa-

etched onto the samples and Ohmic contacts are alloyed onto the voltage pads. A front gate is evaporated onto the Hall bar to enable us to tune the total carrier density. In a PQW the width of the electron gas at the Fermi level as well as the position of the carrier distribution within the well are tuned with the gate voltage. The wave functions are thus shifted with respect to the center of the well once a gate voltage is applied. In the case of a potential spike in the center of the well in general the carrier distribution will not be symmetric with respect to the spike position. These considerations have to be kept in mind for the following discussion.

The low-frequency ( $\nu \approx 80$  Hz) transport experiments are performed in a superconducting magnet and the samples are cooled by He exchange gas at temperatures  $0.5 < T < 4.2$  K. The magnetic field is oriented perpendicular to the sample surface. Here we concentrate on the regime of small magnetic fields ( $B < 1.5$  T) where the influence of the magnetic field on the subband structure itself can be neglected. [2] The gate voltage dependence of the total carrier density can be obtained from the low-field Hall effect in good agreement with geometric considerations based on a capacitor model. From the resistance at zero field  $\rho_{xx}(B=0)$  an effective mobility of the electrons can be extracted. This mobility is plotted as a function of carrier density in Fig. 1 for four samples, one without a potential spike, and three different samples with 1, 2 and 4 monolayers of AlAs in the well. The curves are vertically offset for clarity. The sample without spike has a mobility that is roughly twice as high as for the other samples because it was grown at a different time. One pronounced feature occurs between  $N_s = (2-3) \times 10^{11} \text{ cm}^{-2}$  that is related to the onset of intersubband scattering due to the population of the second subband. The precise position of the feature on the  $N_s$ -axis depends on the details of the growth process and can probably not be compared for the different samples. For increasing strength of the potential spike the feature becomes weaker. One has to bear in mind that this occurs in the regime of negative gate voltages where the electron gas resides mostly in the lower half of the well towards the substrate-

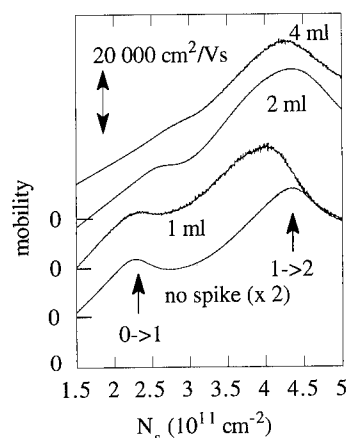


Fig. 1. Mobility as a function of carrier density for four parabolic quantum wells without AlAs spike and with 1, 2, and 4 monolayers of AlAs in the center of the well. The curves are vertically offset for clarity. The arrow in the upper left corner of the figure gives the scale for the mobility for the 3 samples with spike. The scale for the sample without spike is twice as large. The arrows are a guide to the eye and indicate where subbands become populated and intersubband scattering occurs. The temperature is  $T = 4.2$  K.

side of the sample, i.e. the wave function of the lowest subband has its maximum on one side of the potential spike. For symmetry reasons the wave function of the higher subband occupies mostly the opposing half of the well towards the surface-side of the sample. The stronger the potential spike the more these wave functions become separated and intersubband scattering will decrease. We argue that this is the reason why the feature in the  $\mu$  versus  $N_s$  curve that is related to intersubband scattering between the lowest two subbands vanishes for strong potential perturbations.

At high total carrier densities a third subband becomes slightly (less than  $0.5 \times 10^{11} \text{ cm}^{-2}$ ) populated (see arrow  $1 \rightarrow 2$  in Fig. 1) and intersubband scattering occurs among all three occupied subbands. Because of the large extent of the wave function of the third subband, the scattering rate increases and the mobility drops for increasing gate bias. Furthermore, the well is now closer to the symmetric situation where the wave functions of all occupied subbands extend on both sides of

the potential spike. Therefore, the presence of the potential spike should not significantly change the wave function overlap between the lowest three subbands. The intersubband scattering rate in this case is expected to be fairly independent of the strength of the spike in agreement with the experimental observation.

In the next paragraph we will focus on the effect of small magnetic fields on the transport properties of the PQW with 1 monolayer of AlAs in the center of the well. Fig. 2 presents a series of experimentally obtained traces for a series of gate voltages. The lowest lying curve for  $V_g = +200$  mV clearly displays only one set of  $1/B$  periodic oscillations. A Fourier power spectrum of this curve displays only one peak that gives a carrier density of roughly half the value as obtained from the Hall effect. The high-field magnetoresistance and Hall effect is dominated by a series of suppressed quantum Hall states which clearly indicates that more than one electronic subband is occupied [2]. For decreasing carrier density the curves in Fig. 2 indicate a second  $1/B$  periodicity which can be well resolved in the Fourier transform process. Fig. 3 summarizes the experimentally obtained values for the carrier

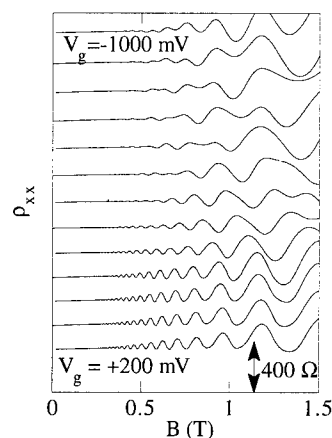


Fig. 2. Low-field magnetoresistance for the sample with 1 monolayer of AlAs in the center of the well. The curves are vertically offset for clarity. The gate voltage and therefore the total carrier density decreases from bottom to top. The temperature is  $T = 0.5$  K.

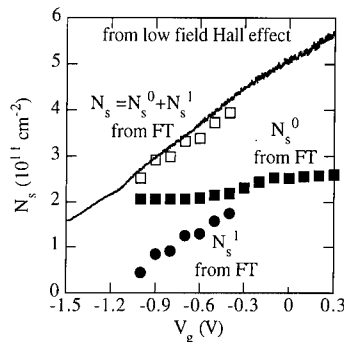


Fig. 3. Carrier densities as obtained from the low-field Hall effect (solid line) as well as from Fourier transform of the SdH oscillations (circles and squares) as a function of gate voltage.

densities as a function of gate bias. In the regime where two  $1/B$  periodic functions in the magnetoresistance can be identified via a Fourier transform, the sum of these two carrier densities is in good agreement with the value of total  $N_s$  as obtained from the low-field Hall effect. In this regime the usual analysis of the Shubnikov-de Haas (SdH) oscillations works fine and gives results in agreement with other experiments on electron gases with several occupied subbands, e.g. Ref. [4]. However, for  $-0.3 < V_g < +0.3$  V the interpretation of the data is not straightforward. This gate voltage regime covers the situation where the wave functions of the subbands are fairly symmetric with respect to the position of the spike. It appears counter-intuitive that only one period occurs in the low-field SdH-oscillations while simultaneously the high-field behavior as well as the value of the carrier density itself clearly suggest that more than one subband is occupied. In the following we discuss three scenarios that are unlikely to occur in our samples. (1) Very wide Landau levels in one subband, i.e. a very small scattering time of the carriers in this subband could explain why suddenly one oscillation period is missing. However, if that were the case, the resistance in general should go up and no deep minima in  $\rho_{xx}$  at high magnetic fields should be observable. Furthermore, the value of  $N_s$  as deduced from this single period should still be identifiable with the carrier density of a single subband. This is clearly not the case here. (2) A

populated third subband should also manifest itself in the SdH-oscillations and its low carrier density should lead to a clearly distinct peak in the power spectrum of the Fourier transform. This is not seen in the experimental data. (3) The lowest two subbands could have very similar carrier densities that may end up in a single period in the SdH oscillations. In that case the single frequency as deduced from the Fourier transform should give a carrier density that is half the value of what is obtained from the low-field Hall effect. This case is realized close to  $V_g = 0$ . However, for gate voltages  $V_g > 0$  the carrier density as deduced from the single period of the SdH oscillations should increase with increasing gate bias in contrast to the experimental observation (see solid squares in Fig. 3).

In the symmetric situation the self-consistent potential and the wave functions in our sample are very similar to the case of two coupled quantum wells [5] or wide square wells [6]. The suppression of odd-integer quantum Hall states in these systems has been observed and attributed to the competition between the interwell and intrawell Coulomb interactions. A phase transition for decreasing well coupling has been predicted [7]. To our best knowledge nobody has so far reported low-field effects that question the usual interpretation of SdH oscillations in a multi-subband or multi-well system. We suggest that in our samples intersubband Coulomb interactions can play a decisive role and modify the low-field SdH oscillations.

### 3. Conclusions

Parabolic quantum wells with a potential spike consisting of 1,2 or 4 monolayers of AlAs in the center of the well are investigated by means of magnetotransport experiments. The intersubband scattering rate decreases with increasing width of the potential spike in agreement with considerations for the wave function overlap. Once the subband wave functions are symmetric with respect to the position of the spike the experimental results imply that the usual interpretation of Shubnikov-de Haas oscillations in a multi-sub-

band system has to be questioned. We propose that this effect originates from Coulomb interaction between the electrons of different subbands.

#### 4. Acknowledgements

It is a pleasure to thank R. Jurk, M. Sundaram, A. Wixforth, and J.P. Kotthaus for very helpful discussions. We gratefully acknowledge financial support from the Deutsche Forschungsgemeinschaft and the U.S. Airforce (Grant AFOSR-91-0214).

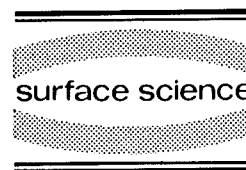
#### 5. References

- [1] M. Sundaram, S.A. Chalmers, P.F. Hopkins and A.C. Gossard, *Science* 254 (1991) 1326.
- [2] K. Ensslin, A. Wixforth, M. Sundaram, P.F. Hopkins, J.H. English and A.C. Gossard, *Phys. Rev. B* 47 (1993) 1366.
- [3] J.-Y. Marzin and J.-M. Gerard, *Phys. Rev. Lett.* 62 (1989) 2172.
- [4] H.L. Störmer, A.C. Gossard and W. Wiegmann, *Solid State Commun.* 41 (1982) 707.
- [5] G.S. Boebinger, H.W. Jiang, L.N. Pfeiffer and K.W. West, *Phys. Rev. Lett.* 64 (1990) 1793.
- [6] Y.W. Suen, J. Jo, M.B. Santos, L.W. Engel, S.W. Hwang and M. Shayegan, *Phys. Rev. B* 44 (1991) 5947.
- [7] L. Brey, *Phys. Rev. Lett.* 65 (1990) 903.



ELSEVIER

Surface Science 305 (1994) 322–326



## Non-uniform resonant coupling effect on 2D electron transport in $\delta$ -doped double quantum well structures

Y. Ohno <sup>\*,a,b</sup>, M. Tsuchiya <sup>c</sup>, T. Matsusue <sup>b</sup>, T. Noda <sup>b</sup>, H. Sakaki <sup>a,b,d</sup>

<sup>a</sup> Research Center for Advanced Science and Technology, University of Tokyo, 4-6-1 Komaba, Meguro-ku, Tokyo 153, Japan

<sup>b</sup> Institute of Industrial Science, University of Tokyo, 7-22-1 Roppongi, Minato-ku, Tokyo 106, Japan

<sup>c</sup> Department of Electronic Engineering, University of Tokyo, 7-3-1 Hongo, Bunkyo-ku, Tokyo 113, Japan

<sup>d</sup> Quantum Wave Project, JRDC, 4-3-24-302 Komaba, Meguro-ku, Tokyo 153, Japan

(Received 20 April 1993; accepted for publication 19 July 1993)

### Abstract

Effects of resonant coupling on 2D electron transport, especially the wavefunction-dependent scattering of electrons, have been studied in novel double quantum well (DQW) field effect structures in which a sheet of ionized donors is inserted in one of the wells. When the two relevant wavefunctions are modulated by a gate voltage  $V_g$  from localized ones to those extending over both wells, the channel resistance  $R$  shows a resonant increase, resulting in a peak-to-valley ratio of 2.5 in  $R-V_g$  characteristics at 1.5 K. Magnetic-field dependence of the channel resistivity has been investigated to elucidate features of resonant coupling at two different donor concentrations  $N_\delta$ . It has been found that the formation of coupled wavefunctions takes place uniformly only in the sample with low  $N_\delta$ , whereas the resonant coupling in the sample with high  $N_\delta$  ( $> 10^{15} \text{ m}^{-2}$ ) becomes substantially non-uniform or position dependent in the channel and leads to incomplete delocalization of wavefunctions.

The resonant coupling of electrons in double quantum wells (DQWs) has attracted much attention in the area of two-dimensional electron transport. For example, the coupling of two states is shown to affect both the integral and fractional quantum Hall effects [1]. It is also shown that the delocalization of wavefunctions in coupled DQWs results in the modulation of channel conductivity [2]. We have recently demonstrated that quite a large modulation in the channel conductivity can be realized by appropriate insertion of  $\delta$ -doping in one of the two wells [3]. In this paper, we study

transport properties of such impurity-inserted DQW structures to clarify the details of novel features in resonant coupling mainly from magnetoresistance measurements.

Samples we study here are selectively-doped DQW structures, consisting of two 150 Å GaAs QWs separated by a 22.5 Å undoped AlGaAs barrier. As shown in Fig. 1a, a sheet of Si donors is inserted at the center of the top QW (near the gate) to ensure that the mobilities of the two QWs are quite different and also to enhance the wavefunction dependence of scattering [2]. When the two levels in the DQW are out of resonance, the two wavefunctions are localized in each QW. In such a case, as will be discussed later, the

\* Corresponding author.

channel conductivity should be dominated by the bottom QW and be rather high, since electrons in the undoped bottom QW are isolated from the donors and in the high mobility state. When their energy difference  $\Delta E$  is reduced to bring the two levels in resonance by applying a proper gate voltage  $V_g$ , the interwell tunneling should be enhanced and also the interaction between  $\delta$ -doped impurities and electrons in the undoped QW. Therefore, the field-induced resonance should reduce the effective mobilities of electrons and give rise to a resistance maximum.

For this work we grew by molecular beam epitaxy two samples A and B with different sheet densities  $N_s$  of silicon:  $2 \times 10^{15} \text{ m}^{-2}$  for A and  $1 \times 10^{14} \text{ m}^{-2}$  for B, respectively. For each Hall-bar sample 200  $\mu\text{m}$  and 50  $\mu\text{m}$  wide an Al Schottky gate was deposited in vacuum. Ohmic contacts for source and drain were formed by alloying InSn to both QWs.

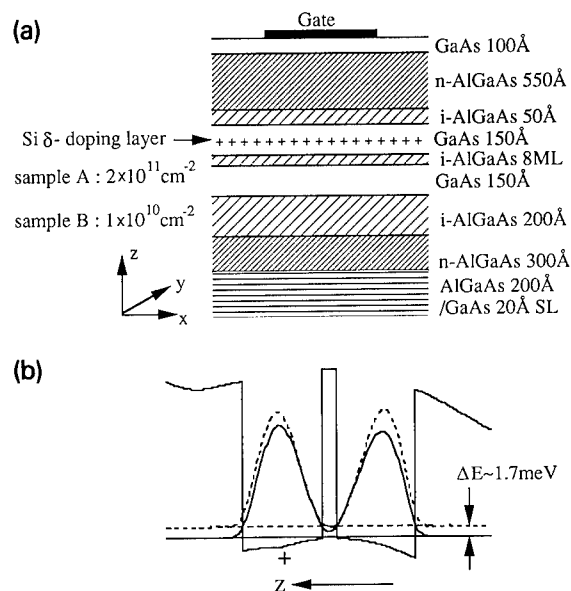


Fig. 1. (a) Schematic structure of  $\delta$ -doped double quantum wells formed on 10 periods of a 200 Å AlGaAs/20 Å GaAs superlattice and a 1000 Å GaAs buffer layer on semi-insulating GaAs substrates. The density of  $\delta$ -doped  $\text{Si}^+$  at the center of the top QW is  $2 \times 10^{15} \text{ m}^{-2}$  for sample A and  $1 \times 10^{14} \text{ m}^{-2}$  for sample B, respectively. (b) The potential profile and the squared wavefunction at resonance calculated by solving the Schrödinger and Poisson equations self-consistently for sample A.

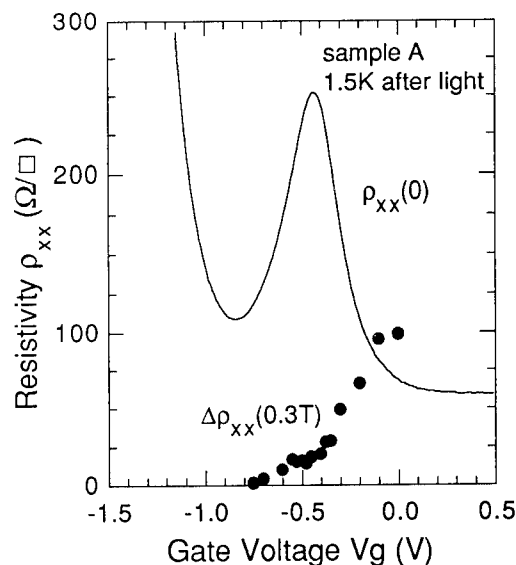


Fig. 2. The channel resistivity  $\rho_{xx}(0)$  of sample A at 1.5 K plotted as a function of gate voltage (solid line). The closed circles show the magnetoresistance  $\Delta\rho_{xx}$  at 0.3 T.

The channel resistivities  $\rho_{xx}$  were measured at 1.5 K by using an AC lock-in technique at 15 Hz with a 10 nA current source. A solid line in Fig. 2 shows the measured  $\rho_{xx}$  for sample A as a function of  $V_g$ . A prominent peak structure appears clearly at  $V_g \approx -0.5 \text{ V}$  with a peak-to-valley ( $P/V$ ) ratio of  $\sim 2.5$ , which was observed also for sample B in a similar manner (see Fig. 4). As described above, the peak of the resistance should correspond almost to the resonance condition where wavefunctions are coupled and delocalized. By solving the time-independent Schrödinger equation self-consistently, one can calculate the electronic states and electron mobilities. For example, it is found that symmetric and antisymmetric states are formed with  $\Delta E$  of 1.7 meV at resonance (see Fig. 1b). Here, the potential profile  $V(z)$  is assumed to be uniform in a plane parallel to the QWs by ignoring the in-plane fluctuation  $\delta V(x, y)$  of the potential.

Though the resonance of states is reflected in a resistivity peak, more detailed features can be extracted by studying the magnetoresistivity  $\Delta\rho_{xx}(B) = \rho_{xx}(B) - \rho_{xx}(0)$  with fields  $B$  perpendicular to the QWs. This is because the absence or the presence of magnetoresistivity depends



critically on the coupling condition of two states, as explained below. For a weak magnetic field, the conductivity tensor  $\sigma$  for electrons in multiple subbands can be expressed by

$$\begin{aligned}\sigma_{xx}(B) &= \sum \sigma_{xxi}(B) = \sum q\mu_i N_{Si} / [1 + (\mu_i B)^2], \\ \sigma_{xy}(B) &= \sum \sigma_{xyi}(B) = \sum q\mu_i^2 B N_{Si} / [1 + (\mu_i B)^2],\end{aligned}\quad (1)$$

where  $q$  is the electron charge,  $\mu_i$  and  $N_{Si}$  are the mobility and density of carriers for the  $i$ th subband, respectively. The resistivity  $\rho_{xx}(B)$  can be derived as  $\sigma_{xx}(B)/[\sigma_{xx}^2(B) + \sigma_{xy}^2(B)]$ . If electronic states in DQWs are not coupled and the current  $J$  is carried by two groups of electrons with different mobilities  $\mu_1$  and  $\mu_2$ , then  $\rho_{xx}(B)$  should depend on  $B$ . In particular, if  $\mu_1 B \gg 1$  and  $\mu_2 B \ll 1$ ,  $\rho_{xx}(B)$  can be expressed as [4]

$$\rho_{xx}(B) \approx 1/q \left[ N_{S2}\mu_2 + N_{S1}^2 / (N_{S2}\mu_2 B^2) \right]^{-1}, \quad (2)$$

from which one can readily see that  $\Delta\rho_{xx}(B)$  increases with  $B$ . In contrast, if  $J$  is borne by one type of electrons with a single mobility (including a single subband system),  $\Delta\rho_{xx}(B)$  should vanish as long as  $B$  is small enough to prevent the oscillation of  $\rho_{xx}(B)$  with  $B$ .

To examine these predicted behaviors, the weak-field  $\Delta\rho_{xx}(B)$  of both samples A and B were measured at various values of  $V_g$ . Fig. 3 shows curves of  $\Delta\rho_{xx}(B)$  of sample A as functions of magnetic field  $B$ , in which each zero-level of  $\Delta\rho_{xx}(B)$  corresponds to a set value of  $V_g$ . When  $V_g$  is sufficiently low ( $\leq -0.8$  V) and all the electrons are in the bottom (undoped) well,  $\Delta\rho_{xx}(B)$  is almost zero, which is in accordance with the prediction. When  $V_g$  is raised above  $-0.8$  V, where electrons occupy not only the bottom well but also the top (doped) well, one can readily see in Fig. 3 a parabolic increase of  $\Delta\rho_{xx}(B)$ , indicating that the current is carried by electrons with two different mobilities. Surprisingly, the parabolic increase of  $\Delta\rho_{xx}(B)$  persists even at the resonance point (see solid circles in Fig. 2), even though the ideal coupling should resolve the imbalance of  $\mu_1$  and  $\mu_2$  and make

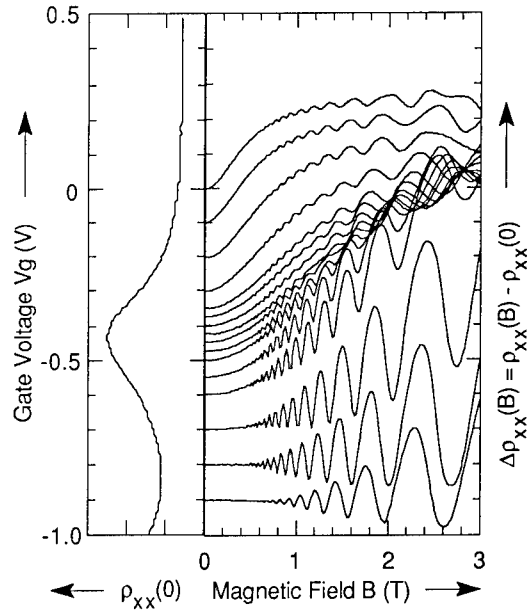


Fig. 3. The magnetoresistances  $\Delta\rho_{xx}(B)$  of sample A plotted as functions of  $B$  for different gate voltages. On the left-hand side,  $\rho_{xx}(0)$  is shown as a function of  $V_g$ . The origin of each  $\Delta\rho_{xx}(B)$  is offset along the vertical-axis so that the gate bias can be read for each  $\Delta\rho_{xx}(B)$  curve.

$\Delta\rho_{xx}(B)$  vanishingly small. To clarify and separate the contributions of the two quantum states, the field-dependence of  $\Delta\rho_{xx}(B)$  and Hall coefficients [5] as well as the period of Shubnikov–de Haas oscillation were analyzed to determine the mobilities and concentrations of electrons in each subband. It was found that the mobility  $\mu_1$  of the undoped QW channel is initially  $14 \text{ m}^2/\text{V} \cdot \text{s}$  at  $V_g = -0.8$  V (the valley of  $\rho_{xx}(0)$ ) but decreases to  $5 \text{ m}^2/\text{V} \cdot \text{s}$  at the estimated point of resonance or resistance peak. At this resonance point, the mobility  $\mu_2$  of the state originating from the doped well is found to be as low as  $\sim 1 \text{ m}^2/\text{V} \cdot \text{s}$  [6].

The magnetoresistance  $\Delta\rho_{xx}(B)$  of sample B is also studied and the result is shown by solid circles in Fig. 4. Note that  $\Delta\rho_{xx}(B = 0.3 \text{ T})$  is nearly zero at resonance in agreement with the prediction for an ideal resonant coupling model. For comparison, the channel resistivity  $\rho_{xx}(B = 0 \text{ T})$  is shown by the solid line in Fig. 4 and indicates that the field-induced resonance leads to the resistance peak also in the sample B. At the

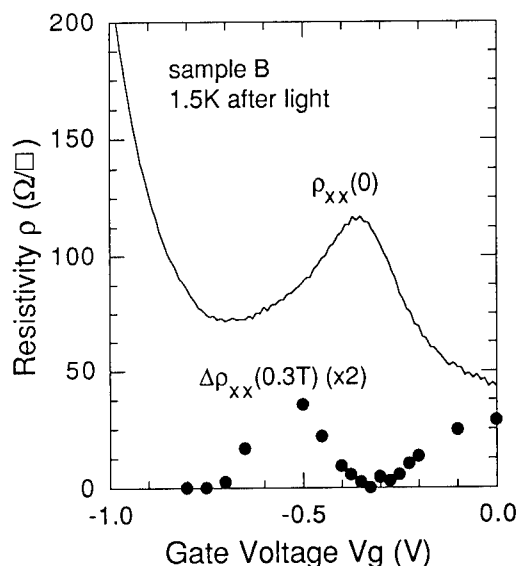


Fig. 4. The channel resistivity of sample B at 1.5 K plotted as a function of gate voltage (solid line). The closed circles show the magnetoresistance  $\Delta\rho_{xx}$  at 0.3 T, which becomes zero not only at  $V_g < -0.75$  V, where the top QW is depleted, but also in the region where  $V_g$  is slightly larger than that for the resistivity peak.

resonance point  $\mu$  and  $N_{S_{\text{total}}}$  are found to be  $6.5 \text{ m}^2/\text{V} \cdot \text{s}$  and  $8 \times 10^{15} \text{ m}^{-2}$  [7], respectively. We found that  $\mu_1 = 22 \text{ m}^2/\text{V} \cdot \text{s}$  and  $N_{S_1} = 4 \times 10^{15} \text{ m}^{-2}$  at the valley of  $\rho_{xx}(0)$  ( $V_g = -0.75$  V). Similarly, at  $V_g \approx 0$  V, we found  $\mu_2 = 6.7 \text{ m}^2/\text{V} \cdot \text{s}$  and  $N_{S_2} = 6.7 \times 10^{15} \text{ m}^{-2}$ , while  $\mu_1 = 22 \text{ m}^2/\text{V} \cdot \text{s}$  and  $N_{S_1} = 4.3 \times 10^{15} \text{ m}^{-2}$  indicating that mobilities are different under the uncoupled condition.

To explain the observed difference in  $\rho_{xx}(B)$  between these two samples, we should refine the model of resonant coupling. In sample B, the density of Si donors  $N_\delta = 1 \times 10^{14} \text{ m}^{-2}$  appears to be low enough to regard these dopants as a weak perturbation. Hence, the wavenumber  $k = (k_x, k_y)$  in the QW plane serves as a good quantum number and electron waves can propagate coherently in the channel. Indeed, the level broadening of both subbands estimated from their mobilities are smaller than the coupling energy  $\Delta E \approx 1.7 \text{ meV}$ . As a result, the resonant coupling of two levels takes place almost ideally and uniformly over the channel.

In contrast, the resonant coupling effect observed in sample A is certainly beyond the simple

model of the uniform resonance. For example, the fact that the measured  $\mu_2$  (less than  $1 \text{ m}^2/\text{V} \cdot \text{s}$ ) is far less than  $\mu_1$  ( $\sim 5 \text{ m}^2/\text{V} \cdot \text{s}$ ), even at resonance, indicates that the resonance enhances the tunneling only partly and does not lead to the complete delocalization of wavefunctions. These complications are due to the high density  $N_\delta = 2 \times 10^{15} \text{ m}^{-2}$  of donors that causes the substantial level broadening and potential fluctuation because of the overlapping of bound states. The resonant coupling under such a circumstance should be described by a refined model, in which the energy uncertainty  $\delta E_2$  and potential fluctuation  $\delta V$  in the doped well are taken into account. For instance,  $\delta E_2$  and potential fluctuation  $\delta V$  in the doped well are taken into account. For instance,  $\delta E_2$  given by the lower mobility  $\mu_2$  ( $\sim 1 \text{ m}^2/\text{V} \cdot \text{s}$ ) is comparable with (or greater than) the coupling energy  $\Delta E$ . Such a large  $\delta E_2$  suppresses the coherent propagation in both QWs and, therefore, prevents the formation of uniformly coupled states but, instead results in the position-dependent partial coupling. The features of such resonance should depend on both the energy broadening and the coupling energy, which will be discussed elsewhere.

In conclusion, we have investigated the resonant enhancement of ionized impurity scattering and the magnetoresistivity in impurity-inserted double quantum wells with low and high impurity concentrations  $N_\delta$ . We have shown that the gate-voltage-induced coupling of two quantum states takes place uniformly when  $N_\delta$  is low, but in the sample with high  $N_\delta$  the coupling is found to become quite local and the ground level in each QW maintains its identity.

The authors wish to acknowledge Dr. G. Fasol and Dr. H. Akiyama for useful discussions. This work is partly supported by a grant-in-aid from the Ministry of Education, Science and Culture, Japan.

## 1. References

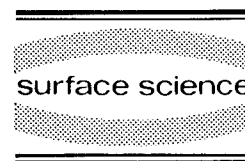
- [1] G.S. Boebinger, H.W. Jiang, L.N. Pfeiffer and K.W. West, Phys. Rev. Lett. 64 (1990) 1793; A.H. MacDonald, Phys. Rev. Lett. 65 (1990) 775.

- [2] A. Palevski, F. Beltram, F. Cappaso, L. Pfeiffer and K.W. West, Phys. Rev. Lett. 65 (1990) 1929.
- [3] Y. Ohno, M. Tsuchiya and H. Sakaki, Appl. Phys. Lett. 62 (1993) 1952.
- [4] M.J. Kane, N. Apsley, D.A. Anderson, L.L. Taylor and T. Kerr, J. Phys. C: Solid State Phys. 18 (1985) 5629.
- [5] W.A. Beck and J.R. Anderson, J. Appl. Phys. 62 (1987) 541.
- [6] Lower mobility  $\mu_2$  is uncertain since its conductivity is much less than that of higher mobility.
- [7] Two different periods of Shubnikov–de Haas oscillation could not be distinguished clearly from  $\rho_{xx}(B)$  at high magnetic fields. The accurate difference between  $N_{S_1}$  and  $N_{S_2}$ , which corresponds to  $\Delta E$ , is unknown from the experiment.



ELSEVIER

Surface Science 305 (1994) 327–332



## Disappearance of magnetophonon resonance at high magnetic fields in GaAs/GaAlAs heterojunctions

D.R. Leadley <sup>a,\*</sup>, R.J. Nicholas <sup>a</sup>, J. Singleton <sup>a,d</sup>, W. Xu <sup>b</sup>, F.M. Peeters <sup>b</sup>,  
J.T. Devreese <sup>b</sup>, L. van Bockstal <sup>c</sup>, F. Herlach <sup>c</sup>, J.A.A.J. Perenboom <sup>d</sup>,  
J.J. Harris <sup>e</sup>, C.T. Foxon <sup>f</sup>

<sup>a</sup> Department of Physics, Clarendon Laboratory, Parks Road, Oxford OX1 3PU, UK

<sup>b</sup> Departement Natuurkunde, Universiteit van Antwerpen, Universiteitsplein 1, B-2610 Antwerp, Belgium

<sup>c</sup> KU Leuven, Celestijnenlaan 200 D, B-3001 Leuven, Belgium

<sup>d</sup> University of Nijmegen, Toerooiveld 1, NL-6525 ED Nijmegen, The Netherlands

<sup>e</sup> Semiconductor IRC, Imperial College, London SW7 2BZ, UK

<sup>f</sup> Department of Physics, The University, Nottingham NG7 2RD, UK

(Received 20 April 1993; accepted for publication 1 June 1993)

### Abstract

Magnetophonon resonance is studied in the resistivity of high-mobility GaAs/GaAlAs heterojunctions. At high magnetic fields the oscillation amplitude decreases, leading to the complete disappearance of the fundamental resonance in some cases. This is in complete contrast to the behaviour seen in previous studies on many different materials which show an exponentially damped series of oscillations. The disappearance is explained by fully self-consistent calculations, including *all* the scattering processes to calculate the density of states and the resistivity. We find the Landau level width oscillates in field and the resonance amplitudes are determined by the relative importance of the elastic and inelastic scattering rates.

Magnetophonon resonance (MPR) may be observed in the resistivity  $\rho_{xx}$  of semiconductors as a series of oscillations due to the resonant absorption and emission of longitudinal optic (LO) phonons. The resonance occurs whenever the optic-phonon energy  $\hbar\omega_{LO}$  is equal to an integral multiple of the cyclotron energy:

$$\omega_{LO} = N\omega_c = NeB/m^*, \quad N = 1, 2, 3, \dots \quad (1)$$

In many previous studies [1,2] the MPR oscillations in  $\rho_{xx}$  have been described by an exponentially damped cosine series [3]

where the damping factor  $\gamma$  was originally found to be constant in magnetic field and to vary with temperature and sample mobility. This equation can also be derived as the first term of an harmonic expansion for the conductivity considering short-range scattering [4], and the empirical  $\gamma$  related to the theoretical Landau level (LL) width  $\Gamma$ . Although Eq. (2) has been applied to a wide variety of materials, quantitative agreement has

$$\frac{\Delta\rho_{xx}}{\rho_{xx}} \propto \cos(2\pi\omega_{LO}/\omega_c) \exp(-\gamma\omega_{LO}/\omega_c), \quad (2)$$

\* Corresponding author.

not always been possible since  $\gamma$  often varies with magnetic field [5,6].

In this paper we report MPR oscillations in the resistivity of high-mobility, low-electron-density GaAs/GaAlAs heterojunctions that are qualitatively different to any previous observations. Most strikingly the oscillations at the highest magnetic fields  $B$ , expected from Eq. (2) to be the strongest features in the resistivity  $\rho_{xx}$  completely disappear. The magnetoresistance has been measured in a large number of heterojunctions in pulsed fields up to 36 T at KU Leuven and steady fields to 30 T using the Nijmegen hybrid magnet. The samples were grown by MBE at Philips Research Laboratories to a standard HEMT design [7] with a range of undoped-GaAlAs spacer-layer thicknesses  $100 \text{ \AA} < L_z < 3200 \text{ \AA}$  and corresponding electron densities  $n_e$  from  $3.2$  to  $0.15 \times 10^{15} \text{ m}^{-2}$ .

The two extreme types of behaviour observed are illustrated in Fig. 1, which shows  $\rho_{xx}$  for samples with spacer layer widths of 400 and 3200 Å. To emphasise the oscillations a background resistance linear in  $B$  has been subtracted and the result expressed as a percentage of  $\rho_{xx}$  at  $B=0$ . The thinner spacer-layer sample G148 shows fairly conventional MPR, exhibiting the exponentially damped cosine series. However, the results are quite different for the wider spacer-layer sample G647, which also has a lower electron density. The oscillations at low magnetic field are well resolved and less damped than those for sample G148, but the amplitude peaks for the  $N=4$  resonance at 5.5 T, while the fundamental  $N=1$  resonance, expected to be the strongest, has become very weak with some indications of a more complicated lineshape. This behaviour can clearly not be explained by Eq. (2). Even for the  $L_z = 400 \text{ \AA}$  sample Eq. (2) does not give quantitative agreement with data, since the higher field peaks have not increased as much as expected [8].

The amplitude of the four highest field resonances are shown in Fig. 2 as a function of spacer-layer thickness. At low values of  $L_z$  the amplitude increases towards higher magnetic field (smaller  $N$ ), while for samples with a large  $L_z$  the reverse is true. Thus, there is a maximum

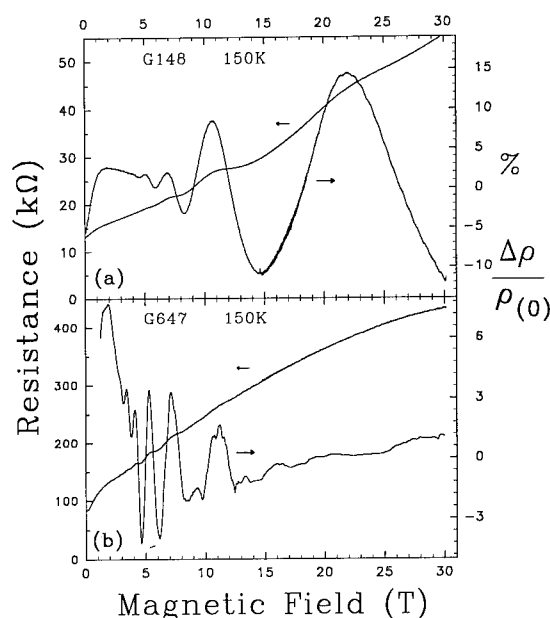


Fig. 1. (a) The magnetoresistance of sample G148, with a 400 Å spacer layer and  $n_e = 2.0 \times 10^{15} \text{ m}^{-2}$ , showing conventional MPR. The oscillations are enhanced by subtracting a background linear in  $B$  and expressing as a percentage of the zero-field resistivity (right scale). (b) The same for sample G647, with a 3200 Å spacer layer and  $n_e = 0.15 \times 10^{15} \text{ m}^{-2}$ , showing conventional MPR at low field but the disappearance of the fundamental resonance at high field.

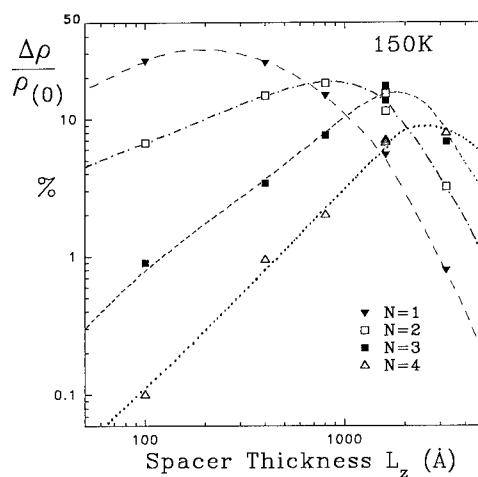


Fig. 2. Amplitude of the four highest field resonances as a function of undoped spacer layer thickness in the sample. The lines are to guide the eye.

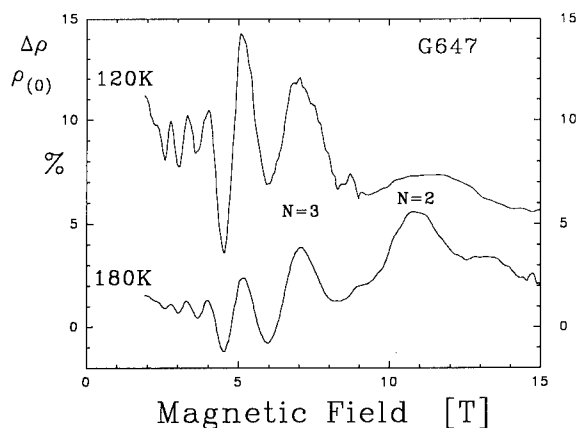


Fig. 3. MPR oscillations for sample G647 at 120 and 180 K. The  $N=2$  resonance disappears as the temperature is reduced.

amplitude which occurs at increasing  $L_z$  for higher harmonics. The temperature is also important, as seen in Fig. 3: for sample G647 the  $N=2$  resonance which is quite strong at 180 K has virtually disappeared at 120 K, while the  $N=3$  peak also weakens markedly relative to the  $N=4$  peak as the temperature is reduced.

All the samples studied follow the same general behaviour. (i) At low magnetic fields the oscillations increase in amplitude with increasing field as described by Eq. (2). (ii) At high magnetic fields the amplitudes decrease quite rapidly with increasing field and even disappear completely. (iii) The division between these two regions moves to lower magnetic field (a) at lower temperatures and (b) in samples with wider spacer layers (and, hence, smaller electron densities).

We explain the disappearance of the MPR at high magnetic fields by calculating  $\rho_{xx}$  with all the scattering processes included self consistently. It is essential to include the full self-consistency in calculating the density of states as well as the resistivity since each scattering mechanism is significantly affected by (and significantly affects) the temperature and magnetic-field dependence of the Landau level broadening.

Details of our calculations, based on a Green's Function approach to the quantum mechanical momentum balance equation, may be found in Ref. [9], where  $\rho_{xx}$  is calculated as a function of

temperature for fixed magnetic fields. The experimental values at a range of fields could be reproduced over the full temperature range (4–300 K) and showed that the high field resistivity is determined by the background impurity density to much higher temperatures than the zero-field mobility. Eq. (3) expresses the resistivity as the sum of elastic and inelastic scattering terms, each written as the product of a matrix element  $R_i$  and an energy integration over the joint density of initial and final states  $F_i$ . For the elastic scattering (subscript el) we include impurities (IMP) and deformation-potential-coupled acoustic phonons (A) and the inelastic scattering (in) is from LO phonons (O).

$$\rho_{xx} = (R_{\text{IMP}} + R_A)F_{\text{el}} + R_O F_{\text{in}}, \quad (3)$$

where

$$F_{\text{el}} = \sum_{M'M} (M' + M + 1) \int_{-\infty}^{\infty} dE \frac{\partial f(E)}{\partial E} \times \text{Im}[G_{M'}(E)] \text{Im}[G_M(E)],$$

and

$$F_{\text{in}} = \sum_{M'M} \int_{-\infty}^{\infty} dE (f(E) - f(E + \hbar\omega_{\text{LO}})) \times \text{Im}[G_{M'}(E + \hbar\omega_{\text{LO}})] \text{Im}[G_M(E)].$$

$\text{Im}[G_M(E)]$  is the imaginary part of the Green's function, which for the  $M$ th Landau level is  $G_M(E) = [E - E_M - \Sigma_M(E)]^{-1}$  with  $E_M = (M + 1/2)\hbar\omega_c$  and the self-energy

$$\begin{aligned} \Sigma_M(E) = \sum_{M'} [ & (W_{\text{IMP}} + W_A) G_{M'}(E) \\ & + W_O(N_0 + f(E - E_{M'})) \\ & \times G_{M'}(E + \hbar\omega_{\text{LO}}) \\ & + W_O(N_0 + 1 - f(E - E_{M'})) \\ & \times G_{M'}(E - \hbar\omega_{\text{LO}}) ]; \end{aligned} \quad (4)$$

$f(E)$  is the Fermi-Dirac electron-distribution function and  $N_0$  is the LO-phonon occupation number. The  $W_i$  are also matrix elements closely related to the  $R_i$ , the exact forms of which are given in Ref. [9]. Eqs. (3) and (4) must be solved self-consistently for  $G_M$ , and then the density of states and  $\rho_{xx}$  may be calculated.

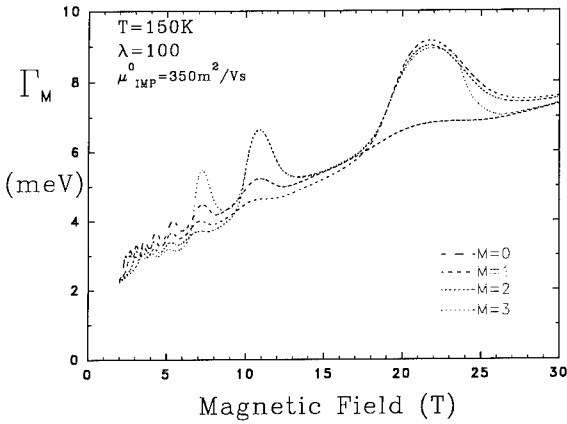


Fig. 4. The broadening of the first 4 Landau levels showing strong modulation in magnetic field. This modulation is much greater when electrons can both emit and absorb LO phonons as is the case for the  $M=1, 2$  and  $3$  levels around  $24$  T, but only for the  $M=2$  and  $3$  levels at  $12$  T.

The result of performing a full self-consistent calculation for the Landau level width is shown in Fig. 4 as a function of magnetic field. In marked contrast to calculations using a short-range scattering approximation which predict the same width for each LL and a monotonic  $\sqrt{B}$  increase, we see large increases at the MPR condition producing a level width that oscillates in field. These additions to the usual  $\sqrt{B}$  increase are different for each Landau level, because of the differences in energy averaging, and are greater when the electrons can emit as well as absorb LO phonons.

Thus, there are two sources of MPR oscillations in the resistivity: maxima in the overlap integral for inelastic scattering  $F_{in}$ , giving the expected increase in resistivity at resonance; and maxima in  $\Gamma$  from the oscillating LO-phonon contribution to the level broadening, which decrease both the elastic and inelastic scattering rates at resonance. The size of the resulting MPR oscillations in  $\rho_{xx}$  will depend on the relative sizes of the elastic and inelastic terms in Eqs. (3) and (4). In addition, the sharpness of the resonance will be different for the two cases, since they involve averages over different LLs with markedly different widths, as shown in Fig. 4. When the two effects produce similar amplitudes in opposite senses this results in a compensated

line shape rather than the complete disappearance of the MPR. This looks like the second derivative at a sharp peak, i.e. has a minimum at the resonance position with subsidiary maxima on either side. In the limits where one scattering process dominates, the MPR will be weak, as the oscillatory parts approximately cancel and the scattering rate remains constant.

To understand the factors that determine the observed MPR amplitudes it is necessary to investigate the matrix elements further. The  $W_i$  are proportional to the energy relaxation rate  $1/\tau_q$ , as the level broadening is sensitive to all scattering events. However, in evaluating the resistivity the momentum transferred in a scattering event has to be considered, so the  $R_i$  depend on the momentum relaxation rate  $1/\tau_l$ . For phonon scattering  $\tau_l \approx \tau_q$ , but for remote ionised impurity scattering  $\tau_l/\tau_q (= \lambda) \gg 1$ . Hence,  $W_{IMP}$  makes a relatively larger contribution to Eq. (4) than does  $R_{IMP}$  in Eq. (3). Therefore, if the inelastic terms increase relative to the elastic terms, the cross-over from domination by elastic to inelastic scattering will occur first in Eq. (3).

The inelastic terms depend on the LO-phonon population, so on increasing the temperature the MPR amplitude will first increase as  $R_O$  increases relative to  $R_{IMP}$ , and then decrease once  $W_O$  starts to dominate  $W_{IMP}$ . Thus, we have explained the observation of a maximum amplitude as a function of temperature [2]. This occurs at  $150$  K for the  $N=4$  resonance and at higher temperatures for the harmonics at higher magnetic fields since the elastic terms, being very sensitive to the number of states in a LL, increase faster than the elastic ones in field. At a fixed temperature, the amplitude will increase first with magnetic field as  $W_{IMP}$  overtakes  $W_O$  until  $R_{IMP}$  passes  $R_O$  leading to the suppression of the high field resonances seen in Figs. 1a and 3.

Fig. 5 shows calculations of  $\rho_{xx}$  for a sample with  $L_z = 400$  Å and  $n_e = 1 \times 10^{15} \text{ m}^{-2}$  at  $150$  K, using values of  $\lambda$  from  $1$  to  $1000$  but fixed total impurity density. This variation in  $\lambda$  corresponds to changing from isotropic impurity scattering appropriate to background impurities, to mostly small-angle scattering from remote ionised impurities. Several interesting aspects of the theory

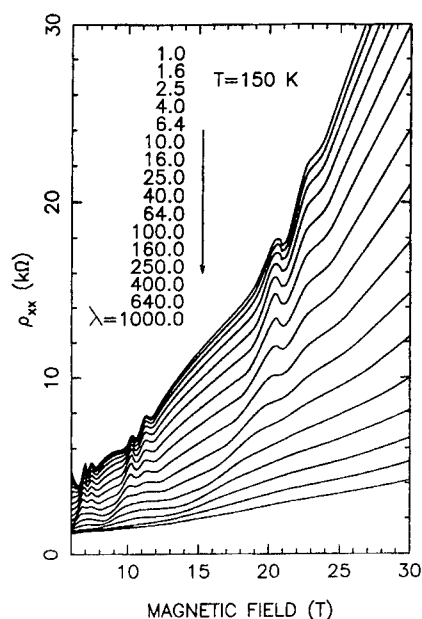


Fig. 5. The calculated magnetoresistance for a sample with  $n_e = 1 \times 10^{15} \text{ m}^{-2}$  at 150 K. The value of  $\lambda$  increases from 1 to 1000 as indicated. The parameters used correspond to sample G650, with a 400 Å spacer, for which  $\lambda$  is measured to be 150.

are apparent in this figure. When  $\lambda$  is small there is a large background magnetoresistance and a very pronounced differential lineshape. For large  $\lambda$  the resistance is much lower, since then most scattering events only involve a small change in momentum. Also the negative going part of the resonance is not observed as  $W_{\text{IMP}}$  is now much greater than  $R_{\text{IMP}}$ .

In these calculations both the oscillatory and background parts of  $\rho_{xx}$  are found directly, reproducing the experimental data. By contrast, earlier approaches only found the oscillatory part [4,10] or a constant background in the field region of interest [11,12]. If a self-consistent density of states is not used  $\rho_{xx}$  can only increase at the MPR condition Eq. (1), due to the maximum in the energy-overlap integral. This inevitably leads to larger oscillations at higher  $B$  where the number of states at the centre of the LLs is greater. Thus, the decrease in oscillation amplitude at high field, seen in Fig. 1b, could not be reproduced. Calculations that are not fully self-con-

sistent also lead to very substantial overestimates of the oscillations or use much larger values of  $\Gamma_0$  than predicted by the low-temperature mobility.

The general behaviour seen in the experiments has thus been explained: (i) At low magnetic fields and high temperatures OPS has a much greater effect on  $\rho_{xx}$  than does elastic scattering; so oscillations in the LO-phonon scattering rate  $F_{\text{in}}$  lead directly to MPR oscillations in  $\rho_{xx}$  as described phenomenologically by Eq. (2). (ii) At high magnetic fields the high DoS produced by narrow LLs means  $\rho_{xx}$  has a large contribution from elastic scattering. In this case the increase in  $\Gamma$  at a resonance in OPS reduces the elastic scattering, compensating for the increase in OPS and resulting in smaller MPR oscillations being observed in  $\rho_{xx}$ . By comparison in 3D or dirty samples there will always be a considerable number of states between the Landau levels and so only the resonances in  $F_{\text{in}}$  will be important and not the oscillating DoS. (iii) (a) At lower temperatures OPS is reduced relative to the elastic contribution and so case (ii) will be relevant at lower magnetic fields. (b) At a fixed temperature and magnetic field, where strong MPR is expected, the amplitude will be greatest in samples with the largest value of  $\lambda$  since then there will be the smallest oscillations in  $\Gamma$ .

In summary we find that in contrast to the large number of previous measurements of magnetophonon resonance in the resistivity where the amplitude of the resonances increases exponentially towards higher magnetic fields there is a strong reduction of amplitude at high magnetic fields. The amplitude decreases rapidly, leading to the complete disappearance of the  $N = 1$  resonance in certain situations, and a second differential form of lineshape for others. This can be explained by calculations that consider all the scattering mechanisms self-consistently in calculating both the density of states and the resistivity. The disappearance of the MPR is due to this self-consistency forcing the total scattering rate to remain constant.

D.R.L. acknowledges support from the Rutherford Appleton Laboratory. Part of this work was performed in the framework of contract



IT/SC/24 of the “Diensten voor Programmatie van het Wetenschapsbeleid” (Belgium).

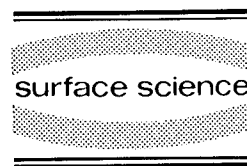
## 1. References

- [1] R.J. Nicholas, *Prog. Quantum Electron.* 10 (1985) 1.
- [2] R.J. Nicholas, in: *Landau Level Spectroscopy*, Eds. G. Landwehr and E.I. Rashba (Elsevier, Amsterdam, 1991) p. 777.
- [3] R.A. Stradling and R.A. Wood, *J. Phys. C* 1 (1968) 1711.
- [4] J.R. Barker, *J. Phys. C* 5 (1972) 1657.
- [5] G. Kido and N. Miura, *J. Phys. Soc. Jpn.* 52 (1982) 1734.
- [6] K. Senda, K. Shimomae, K. Kasai and C. Hamaguchi, *J. Phys. Soc. Jpn.* 47 (1979) 551.
- [7] C.T. Foxon, J.J. Harris, D. Hilton, J. Hewett and C. Roberts, *Semicond. Sci. Technol.* 4 (1989) 582.
- [8] D.R. Leadley, R.J. Nicholas, L. van Bockstal, F. Herlach, J.J. Harris and C.T. Foxon, *Solid State Sci.* 101 (Springer, Berlin, 1992) p. 623.
- [9] D.R. Leadley, R.J. Nicholas, W. Xu, F.M. Peeters, J.T. Devreese, J. Singelton, J. Perenboom, L. van Bockstal, F. Herlach, J.J. Harris and C.T. Foxon, *Phys. Rev. B* 48 (1993) 5457; *Physica B* 184 (1993) 197.
- [10] P. Warmenbol, F.M. Peeters and J.T. Devreese, *Phys. Rev. B* 37 (1988) 4694.
- [11] N. Mori, H. Murata, K. Taniguchi and C. Hamaguchi, *Phys. Rev. B* 38 (1988) 7622.
- [12] R. Lasnig and W. Zawadzki, *J. Phys. C* 16 (1983) 5435.



ELSEVIER

Surface Science 305 (1994) 333–336



## Current induced “spin” separation in p-doped asymmetric double quantum wells

G. Goldoni <sup>\*,a</sup>, A. Fasolino <sup>b</sup>

<sup>a</sup> *Scuola Internazionale Superiore di Studi Avanzati, via Beirut 2-4, 34014 Trieste, Italy*

<sup>b</sup> *Università degli Studi di Modena, Dipartimento di Fisica, Via Campi 213 / A, 41100 Modena, Italy*

(Received 19 April 1993; accepted for publication 5 May 1993)

### Abstract

In asymmetric double quantum wells, the “spin” splitting of the hole subbands at finite parallel momentum, due to the asymmetric potential, is related to a “spin” dependent delocalization of the wavefunction over the two wells. We show that the application of an electric field parallel to the interfaces in a p-doped asymmetric double quantum well can exploit such spin-dependent tunneling probability and separate carriers of opposite spins into the two wells, yielding a macroscopic magnetic moment of different magnitude and either the same or opposite direction in the two wells.

Asymmetric double quantum wells (ADQWs) are receiving much attention for the possibility of studying tunneling processes by optical means; due to the different size quantization of the two wells, selective excitation in one well is made possible and optical recombination after tunneling can be detected [1–3].

The hole subbands in GaAs/AlGaAs quantum wells (QWs) are complicated functions of the momentum parallel to the interfaces  $k_{\parallel}$ , due to the heavy (HH) and light (LH) hole mixing [4]. In asymmetric structures, in addition, the “spin” degeneracy is removed [5]. We have pointed out that in ADQW the “spin” splitting is crucially related to tunneling since the asymmetry comes into play only for states with penetration length

larger than the barrier and have shown that the “spin” splitting is related to a different delocalization of the two “spin” states over the two wells [6]. Due to time inversion symmetry, at  $\pm k_{\parallel}$  either  $\uparrow$  or  $\downarrow$  states tunnel preferentially to the adjacent well preventing polarized tunneling from being detected in any optical measurement which implies averaging over the reciprocal space. We suggest that the application of an in-plane electric field in p-doped ADQWs, by unbalancing the occupation of  $\pm k_{\parallel}$  states, may lead, through preferential tunneling, to the appearance of a macroscopic magnetic moment in the plane of the wells.

We consider GaAs/GaAlAs ADQWs grown along the  $x$  direction and we model the valence band by the Luttinger  $4 \times 4$  effective Hamiltonian, written in the basis  $J_z = (3/2, -1/2, 1/2, -3/2)$ , which we solve numerically to get energy levels and eigenfunctions [6]. At each in-plane wavevector  $k_{\parallel}$  the eigenstates can be labelled

\* Corresponding author.

with  $\uparrow$  or  $\downarrow$  since the Hamiltonian can be separated in two  $2 \times 2$  blocks [4,5]. With this labelling the eigenvalues of the two  $2 \times 2$  blocks display time reversal symmetry of  $E(k_{\parallel}, \uparrow) = E(-k_{\parallel}, \downarrow)$ , and, for centro-symmetric potentials, also  $E(k_{\parallel}, \uparrow) = E(k_{\parallel}, \downarrow)$ , i.e. “spin” degeneracy. Therefore we will use throughout “spin” as a way of labelling the Kramers related states, since neither the electron spin, nor the total angular momentum are good quantum numbers.

We show in Fig. 1a the first three  $\uparrow$  and  $\downarrow$  subbands of a 55/30/40 Å ADQW; the hole subbands of the parent single QWs (SQWs) are shown for comparison. The labels indicate the HH or LH character at  $k_{\parallel} = 0$  and the superscripts WW (wide well) or NW (narrow well) refer to the SQW from which the subbands arise. Appreciable splitting appears at  $k_{\parallel} \neq 0$ , particularly for the  $\text{HH}_1^{\text{NW}}$  and  $\text{LH}_1^{\text{WW}}$  subbands, as a consequence of the asymmetry. The splitting is due to different localization of the wavefunction of the two “spin” partners over the two wells as shown in Fig. 1b, where we plot, as a function of  $k_{\parallel}$ , the fraction of charge density of either “spin”

that delocalize in the adjacent well. Even if the NW and WW subbands in this ADQW are not in resonance, a finite amount of charge (up to  $\sim 25\%$ ) tunnels at finite  $k_{\parallel}$  into the adjacent well; the amount of delocalization is strongly “spin” dependent so that the spilling charge is basically of only one “spin” orientation. At negative  $k_{\parallel}$ ’s the opposite “spin” labelling applies so that on average no macroscopic polarization appears. Note also that this “spin” dependent delocalization is effective only over a limited range of  $k_{\parallel}$ , namely where spin–orbit coupling (linear in  $k_{\parallel}$ ) dominate over the quadratic kinetic energy.

We show next how the above “spin”- and  $k$ -dependence of the wavefunction can be exploited via an in-plane electric field to induce different populations of  $\uparrow$  and  $\downarrow$  “spins” in the two wells. In Fig. 2 we sketch a spin-split hole subband for a p-doped ADQW and the corresponding charge distribution in the device for each “spin” state at  $\pm k_{\parallel}$ . We have taken, as an example, a WW subband so that the wavefunctions are mainly localized in it, but for one of the two “spin”-split bands (the higher in energy) a

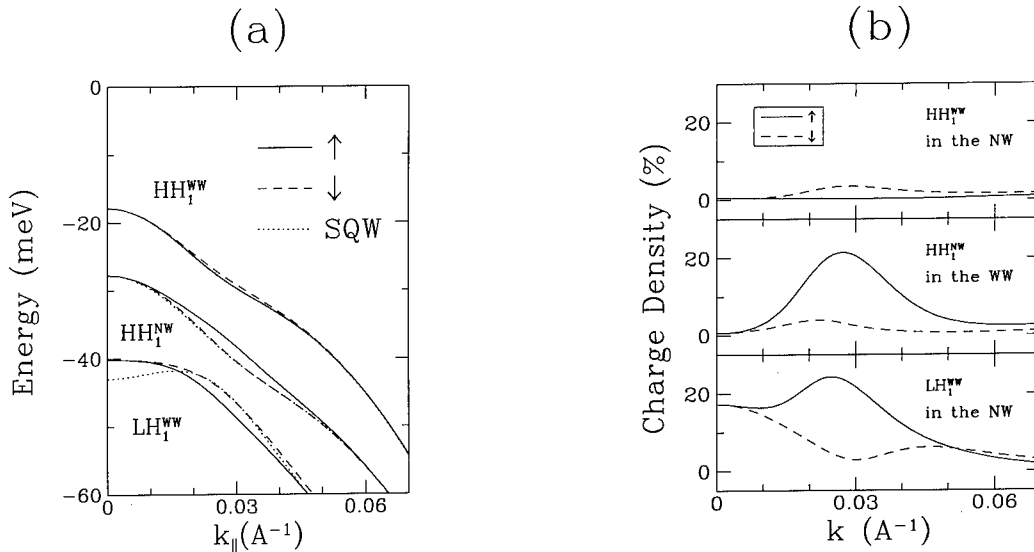


Fig. 1. (a) First three hole subbands of a GaAs/Al<sub>0.25</sub>Ga<sub>0.75</sub>As 55/30/40 Å ADQW, along the (10) in-plane direction. Solid lines:  $\uparrow$  states. Dashed lines:  $\downarrow$  states. Dotted lines: hole subbands of the 55 and 40 Å SQWs; The labels HH and LH refer to the character of the states at  $k_{\parallel} = 0$  and WW and NW to their localization. (b) Percentage of charge tunneling in the adjacent well for the three subbands in (a). Solid lines:  $\uparrow$  states. Dashed lines:  $\downarrow$  states. See text.

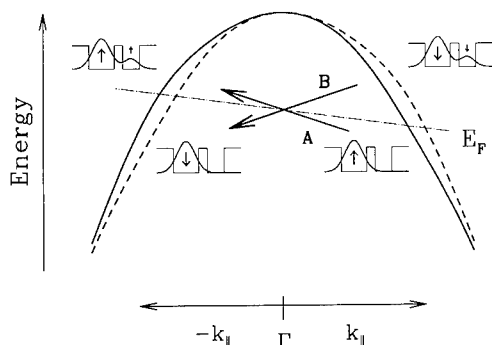


Fig. 2. Sketch of a "spin"-split subband in ADQW around  $k_{\parallel} = 0$ . Solid line:  $\uparrow$  states. Dashed line:  $\downarrow$  states. Dashed dotted line: Fermi energy with applied in-plane electric field. In the insets the charge density distributions of the "spin"-split subband is sketched. See text.

small fraction of "spin" is transferred to the NW (small arrows). Obviously, at zero electric field no net polarization appears since positive and negative  $k_{\parallel}$  are equally occupied and  $\uparrow$  and  $\downarrow$  transferred "spins" cancel out. If an in-plane external electric field  $E$  is applied, however, the Fermi surface displaces in the direction parallel to the field (dashed-dotted line in Fig. 2), and  $\uparrow$  and  $\downarrow$  transferred "spins" become unbalanced. The accumulation of "spin" of a given sign is only lim-

ited by the two spin-conserving scattering processes indicated by the arrows in Fig. 2, which tend to re-establish the equilibrium.

The labelling  $\uparrow \downarrow$  can be given a transparent physical meaning in terms of the expectation values of the components of the total angular momentum  $J$  calculated over  $\uparrow$  and  $\downarrow$  states. It can be shown that the only non-zero components of  $J$  are those in the plane of the interfaces: they constitute a two-component vector  $\langle J_{\parallel} \rangle$  which lies in the direction perpendicular to  $k_{\parallel}$  and with opposite direction for the two "spin" states. It is easy to show that  $\langle J_{\parallel} \rangle \rightarrow 0$  for HH while  $\langle J_{\parallel} \rangle \rightarrow \pm 1$  for LH as  $k_{\parallel} \rightarrow 0$ , since at small  $k_{\parallel}$  the two "spin" states are combinations of  $J_x = \pm 3/2$  and of  $J_x = \pm 1/2$  states, respectively. The modulus of  $\langle J_{\parallel} \rangle$  is shown in Fig. 3a as a function of  $k_{\parallel}$  for the three subbands of Fig. 1. Each pair of curves refers to the two "spin" states. For an asymmetric structure, the two curves are different and, consequently, a net magnetic moment arises; we show in Fig. 3b the sum of the two vectors  $\langle J_{\parallel} \rangle_{\uparrow}$  and  $\langle J_{\parallel} \rangle_{\downarrow}$  multiplied by the charge density  $\rho$  in either well. The results clearly show that preferential "spin" tunneling yields a net magnetic moment in each well. Note that the magnetic moment is different from zero in the same range of

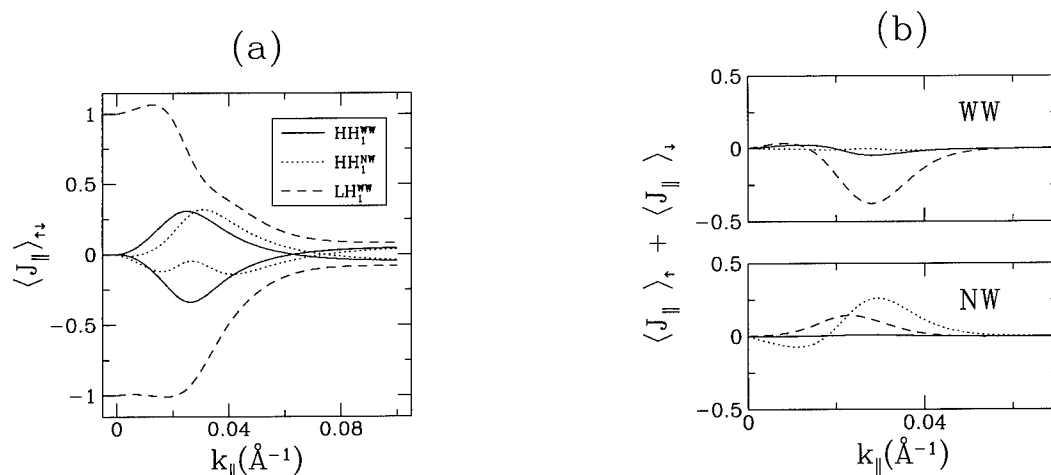


Fig. 3. (a) Total angular momentum in the plane of the interfaces and perpendicular to  $k_{\parallel}$  for the three subbands of Fig. 1a as a function of  $k_{\parallel}$ . Solid lines:  $\text{HH}_1^{\text{WW}}$  subband. Dashed lines:  $\text{HH}_1^{\text{NW}}$  subband. Dotted lines:  $\text{LH}_1^{\text{WW}}$  subband. For each subband, two curves are shown for  $\uparrow$ ,  $\downarrow$  states. The two curves are slightly different due to the asymmetry of the potential. Note also that  $\langle J_{\parallel} \rangle \rightarrow 0, \pm 1$  for pure HH and LH, respectively. (b) Total angular momentum summed over the two "spin" states and projected over the WW (left panel) and in the NW (right panel).

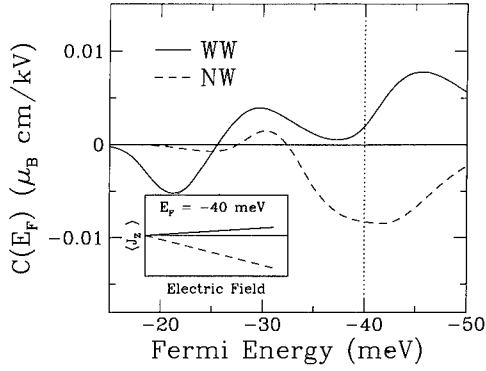


Fig 4. Calculated slope of  $\langle J_{\parallel} \rangle^W$  (solid line) and  $\langle J_{\parallel} \rangle^N$  (dashed line) as a function of the Fermi energy with  $\tau = 1$  ps and a temperature of 10 K. The  $\langle J_{\parallel} \rangle^{W(N)}$  appearing in the 55/30/40 Å ADQW with an applied electric field is sketched in the inset for an ADQW with the Fermi energy indicated by the vertical dotted line.

$k_{\parallel}$  where the wavefunctions delocalize, according to Fig. 1b. This magnetic moment, however, is reversed for negative values of  $k_{\parallel}$  so that it averages to zero, unless an electric in-plane field is used to unbalance the occupation of  $\pm k_{\parallel}$  states as we do next.

In order to estimate the average total angular momentum per electron  $\langle J_{\parallel} \rangle^{W(N)}$  in the WW (NW) we calculate

$$\langle J_{\parallel} \rangle^{W(N)} = \sum_{\sigma=\uparrow, \downarrow} \int \langle J_{\parallel} \rangle_{\sigma k_{\parallel}} \rho_{\sigma k_{\parallel}}^{W(N)} f_{k_{\parallel}} dk_{\parallel}, \quad (1)$$

where  $\rho_{\sigma k_{\parallel}}^{W(N)}$  is the charge density in the WW (NW) for a state at  $k_{\parallel}$  with “spin”  $\sigma$ ,  $\langle J_{\parallel} \rangle_{\sigma k_{\parallel}}$  is the expectation value of  $J_{\parallel}$  for that state and  $f_{k_{\parallel}}$  is the distribution function; a summation over all subbands is understood. We have introduced the above described scattering mechanisms within the relaxation-time approximation by assuming

$$f_{k_{\parallel}} = f_0 \left( k_{\parallel} - \frac{e\tau}{\hbar} E \right), \quad (2)$$

where  $f_0$  is the Fermi distribution function and  $\tau$  is the relaxation time for spin-conserving pro-

cesses [7]. This is appropriate for low fields and results in a linear dependence of  $\langle J_{\parallel} \rangle^{W(N)}$  on the modulus of the electric field  $E$  with a slope  $C(E_F)$  which only depends on the Fermi energy. Moreover, we have used the axial approximation for the in-plane dispersion of the hole subbands in calculating the above averages over  $k_{\parallel}$ . These approximations should not affect qualitatively the result, except for  $E_F$  near to the subband edges, since then  $(e\tau/\hbar)E \approx k_F$ .

In Fig. 4 we show the calculated slope  $C(E_F)$  as a function of the Fermi energy. The average momentum in either well has a finite value and either the same or opposite direction in the two wells. The ADQW under an applied electric field results in a system of spins with either ferromagnetic or antiferromagnetic coupling between the two layers. This could give rise to interesting new effects. In conclusion we have shown that an applied in-plane electric field in properly designed p-doped ADQW can give rise, through “spin” dependent tunneling, to a finite magnetization, with different orientation and magnitude in the two wells.

We thank J.C. Maan for useful discussions.

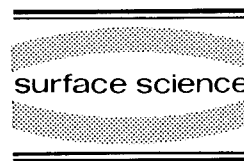
## 1. References

- [1] M. Nido, M.G.W. Alexander and W.W. Rühle, Appl. Phys. Lett. 56 (1990) 355.
- [2] P. Lefebvre, P. Bonnel, B. Gil and H. Mathieu, Phys. Rev. B 44 (1991) 5635.
- [3] Ph. Roussignol, A. Vinattieri, L. Carraresi, M. Colocci and A. Fasolino, Phys. Rev. B 44 (1991) 8873.
- [4] M. Altarelli, U. Ekenberg and A. Fasolino, Phys. Rev. B 32 (1985) 5138.
- [5] D.A. Broido and L.J. Sham, Phys. Rev. B 31 (1985) 888.
- [6] G. Goldoni and A. Fasolino, Phys. Rev. Lett. 69 (1992) 2567.
- [7] R. Ferreira and G. Bastard, Phys. Rev. B 43 (1991) 9687.



ELSEVIER

Surface Science 305 (1994) 337–342



## Quantum transport in $\text{InAs}_{1-x}\text{Sb}_x/\text{InSb}$ strained layer superlattices

Tan Le <sup>\*,a</sup>, A.G. Norman <sup>a</sup>, W.T. Yuen <sup>b</sup>, L. Hart <sup>a</sup>, I.T. Ferguson <sup>a</sup>, J.J. Harris <sup>a</sup>,  
C.C. Phillips <sup>b</sup>, R.A. Stradling <sup>a,b</sup>

<sup>a</sup> IRC in Semiconductor Materials, Imperial College, South Kensington, London SW7 2BZ, UK

<sup>b</sup> Physics Department, Imperial College, South Kensington, London SW7 2BZ, UK

(Received 26 April 1993; accepted for publication 25 May 1993)

### Abstract

The Shubnikov–de Haas (SdH) effect is observed in highly silicon doped  $\text{InAs}_{1-x}\text{Sb}_x/\text{InSb}$  strained layer superlattices with nominal  $x$  values of 0.8 and 0.9. Virtually 100% activation of the silicon as a donor is found provided that the growth temperature is kept below about 350°C. For the  $\text{InAs}_{0.2}\text{Sb}_{0.8}/\text{InSb}$  combination two-dimensional behaviour is observed. For  $\text{InAs}_{0.1}\text{Sb}_{0.9}/\text{InSb}$  up to three SdH periods are observed depending on the doping level and superlattice periodicity. These series do not follow the  $1/\cos\theta$  dependence typical of 2D. These SdH peaks can be interpreted quantitatively as “belly”, “neck” and “elliptic” orbits using a nearly-free electron model. Magnetic breakdown is believed to be present. Numerical calculations are presented for the band structure of the superlattices.

### 1. Introduction

$\text{InAs}_{1-x}\text{Sb}_x$  alloys represent the only III–V material system having a band gap capable of detecting in the atmospheric window centred at 10  $\mu\text{m}$  wavelength. The ten micron sensitivity arises from large band bowing effects. At low temperatures, the alloy band gap reaches a minimum value of about 0.14 eV for a composition ( $x$ ) = 0.65 (this gap corresponds to about 9  $\mu\text{m}$  wavelength). The band gap can be narrowed even further by growing strained layer superlattices (SLS) of  $\text{InAs}_{1-x}\text{Sb}_x/\text{InSb}$  (the lattice constants of InAs and InSb differ by 7%). Earlier work at Sandia Laboratories [1] has shown that good

quality SLS consisting of  $\text{InAs}_{0.13}\text{Sb}_{0.87}/\text{InSb}$  are possible and that a type II band alignment results with the conduction band edge in the alloy lying lower in energy than the band edge in InSb. Band edge photoluminescence at 12  $\mu\text{m}$  wavelength has been reported with this structure.

In this paper, we report the first Shubnikov–de Haas (SdH) measurements on highly silicon doped  $\text{InAs}_{1-x}\text{Sb}_x/\text{InSb}$  SLS with nominal  $x$  values of 0.8 and 0.9.

### 2. Sample structures

The samples were grown in a Vacuum Generators V80H MBE System. The superlattice consists of 100 quantum wells with a period of 200 (or 300) Å formed by 100 (150) Å InSb and 100

\* Corresponding author.

(150) Å InAs<sub>1-x</sub>Sb<sub>x</sub> layers, respectively, where  $x = 0.8$  and  $0.9$ . The compositions ( $x$ ) quoted are nominal. Double crystal X-ray diffraction measurements have confirmed that the superlattices are unrelaxed and some considerable deviation in the precise values of  $x$  were revealed in these measurements. The details of the samples investigated are given in Table 1.

The structures were all grown on semi-insulating GaAs substrates with typically 2  $\mu\text{m}$  thick InAs<sub>1-x</sub>Sb<sub>x</sub> buffer layers, where  $x = 0.90$  or  $0.95$ , respectively. For some samples InAs layers were also inserted between the GaAs substrate and the InAs<sub>1-x</sub>Sb<sub>x</sub> buffer. Apart from samples A and B, the samples were Si doped only in the wells.

Two growth temperatures were chosen, 440 and 340°C, in order to examine the amphoteric behaviour [2] of the silicon in these structures. The three structures grown at 440°C having InAs<sub>0.8</sub>Sb<sub>0.2</sub> in the wells (A to C) all have a carrier concentration deduced from the SdH effect, which is 60% of the silicon concentration. Sample D grown at a lower temperature of about 340°C shows approximately 100% activation. At this growth temperature, n-type silicon doping is possible up to concentrations of about  $10^{18} \text{ cm}^{-3}$  without significant autocompensation.

In a SLS structure, the hydrostatic component of the tension reduces the mean band gap while the biaxial component splits the degeneracy of the valence band maximum and introduces an

anisotropic valence band structure, with the highest band in the InAs<sub>1-x</sub>Sb<sub>x</sub> layers being light ( $J = 3/2$ ,  $m_j = 1/2$ ) along the growth direction. The unstrained valence band offset can be approximated [3] as  $(0.36 \pm 0.04) \cdot (x_b - x_w) \text{ eV}$ , where  $x_{b(w)}$  are the alloy compositions in the barriers (wells). For InAs<sub>0.2</sub>Sb<sub>0.8</sub>/InSb, the valence band offset is 72 meV. For a biaxial strained, direct gap semiconductor with [001] uniaxial strain, the energies of the conduction band ( $E_C$ ), out-of-plane light-hole ( $E_{LH}$ ) and heavy-hole ( $E_{HH}$ ) bands are given by:

$$E_C = E_G + a_c[2 - 2C_{12}/C_{11}]\epsilon,$$

$$E_H = [-a_v[2 - 2C_{12}/C_{11}] + b[1 + 2C_{12}/C_{11}]]\epsilon,$$

$$E_L = [-a_v[2 - 2C_{12}/C_{11}] - b[1 + 2C_{12}/C_{11}]]\epsilon.$$

$E_C$ ,  $E_H$  and  $E_L$  are the energies of the conduction, heavy-hole and light-hole band-edges;  $E_G$  is the unstrained bandgap of the alloy;  $a_c$  and  $a_v$  are the conduction and valence-band deformation potentials;  $b$  is the shear deformation potential;  $C_{mn}$  are the elastic constants; and  $\epsilon$  is the biaxial strain. In InAs<sub>0.2</sub>Sb<sub>0.8</sub>/InSb SLS,  $E_C$ ,  $E_H$  and  $E_L$  have values in relation to the unstrained valence band edge of InAs<sub>0.2</sub>Sb<sub>0.8</sub> of 350, 94 and 40 meV for the InSb barriers, and 118, -23 and 31 meV for InAs<sub>0.2</sub>Sb<sub>0.8</sub> wells, respectively. Conversely, for InAs<sub>0.1</sub>Sb<sub>0.9</sub>/InSb SLS these values are 292, 47 and 20 meV in the InSb barriers and 168, -11 and 16 meV in the InAs<sub>0.1</sub>Sb<sub>0.9</sub> wells.

Table 1  
Superlattice growth parameters and electrical data deduced from Hall and SdH measurements

Sample I.D.	Nominal Si density ( $10^{18} \text{ cm}^{-3}$ )		Sb composition ( $x$ ) in InAs <sub>1-x</sub> Sb <sub>x</sub> /InSb SLS	Well/barrier widths Å/Å	$T_s$ (°C)	$n^{\text{Hall}}$ ( $10^{18} \text{ cm}^{-2}$ )	$\mu^{\text{Hall}}$ ( $\text{cm}^2/\text{V} \cdot \text{s}$ )	$B_F$ (T)	$n^{\text{SdH}}$ ( $10^{18} \text{ cm}^{-2}$ )	Theory $E_F - E_C$ (meV)	Tilt behaviour
	Well	Barrier									
A	0.0	1.0	0.50	100/100	440	0.36	12000	12.8	0.62	111	2D fair
B	1.0	1.0	0.42	100/100	440	1.20	8000	24.8	1.20	164	2D good
C	1.0	0.0	0.62	100/100	440	0.62	11000	12.4	0.60	109	2D-like
D	1.0	0.0	0.60	100/100	330	1.28	4200	22.8	1.10	155	2D-like
E	0.2	0.0	0.95	100/100	340	0.13	45000	8.3	0.14	74	3D-like
F	0.5	0.0	0.92	100/100	340	0.41	26500	16.9	0.40	111	3D-like
G	0.5	0.0	0.98	150/150	340	0.39	27400	5.1	0.40	115	2 freq
								13.6			3 freq
								11.4			

The energy band structure of this novel strained layer superlattice system has been calculated by numerically solving the 1D Ben Daniel–Duke Hamiltonian [4]. By assuming the conduction band edge effective mass to be

$$m_{\text{alloy}}^*(0) = m_{\text{InSb}}^* \left( \frac{E'_g}{E_{\text{InSb}}^g} \right).$$

Here  $m_{\text{alloy}}^*(0)$  is the effective mass of the alloy at zero confinement energy, i.e.  $m_{\text{alloy}}^*$  is assumed to bow in the same way as the energy gap  $E_g$  in the In(As, Sb) system,  $E'_g$  equals the energy gap of the In(As, Sb) alloy. This assumption is in accord with interband magneto-optics [5]. The effective mass at an energy  $E$  above the conduction band edge is corrected for non-parabolicity before a new wavefunction and a new  $E$  are recalculated. The calculation proceeds self-consistently until the changes in  $E$  and  $m_{\text{alloy}}^*(E)$  are small in comparison with the uncertainty in the other parameters involved.

### 3. Results and discussion

#### 3.1. $\text{InAs}_{1-x}\text{Sb}_x/\text{InSb}$ SLS with $x \leq 0.8$

All four samples A, B, C and D with 80% nominal Sb wells exhibit a single SdH series. In

all these cases, the peaks moved upwards in field on tilting the magnetic field away from the axis of the superlattice. With sample A, however, the shift at a tilt angle of  $35^\circ$  was only about one third that expected from the  $1/\cos\theta$  relationship for an ideal two-dimensional electron gas. With the other samples, the  $1/\cos\theta$  dependence was exact to within experimental error. The deviation from the ideal relationship shows that there is significant penetration of the wavefunctions through the barrier regions for sample A.

Further evidence for superlattice tunnelling is provided by the observation of several peaks in the resistance when the magnetic field is applied parallel to the wells. Two weak peaks were also found with sample B in the parallel field orientation. However, the carrier concentration for this sample was higher than for the other three samples so the peaks observed in the parallel field orientation could also arise from diamagnetic depopulation. The energy band calculation for this sample shows that two electronic subbands should be occupied. Space charge effects resulting from the spatial transfer of the electrons and non-uniform distribution of the localised donors are fairly minor and not taken into account. We believe that the SdH peaks from higher subbands are not observed when the tilt angle is zero because the mobility is insufficient to satisfy the condition,

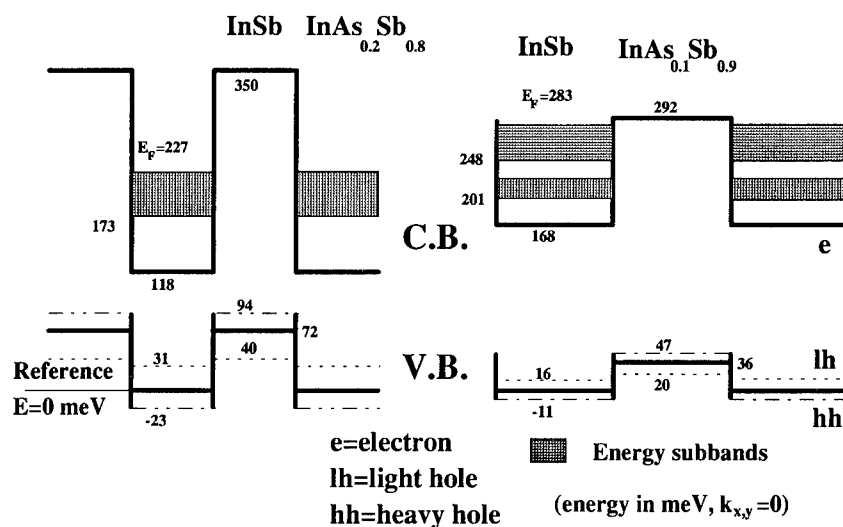


Fig. 1. Band structure and subband occupancies for samples C and G.



$\mu B \gg 1$ . It should also be noted that the electrons in a higher subband will have a considerably greater three-dimensional character.

The “Dingle temperature” term determining the amplitude of the SdH series may be written as  $\exp(-2\pi/\mu B)$  for a three-dimensional system but as  $\exp(-\pi/\mu B)$  for a 2DEG [6]. Consequently, the amplitude of the series from the higher subband is expected to be even more strongly damped in field. No structure is observed with the other two samples when  $\theta = 90^\circ$ . The results of the SdH and the Hall measurements are summarised in Table 1.

### 3.2. $\text{InAs}_{1-x}\text{Sb}_x/\text{InSb}$ SLS with $x \geq 0.9$

In contrast to the samples with  $x \approx 0.8$ , none of the superlattices with  $x \approx 0.9$  showed  $1/\cos\theta$  behaviour on tilting the field. This is not surprising since the Fermi energies on our band structure calculations are estimated to be only a few meV below the bottom of the barriers (Fig. 1).

Fig. 2 shows the magnetoresistance for sample F as a function of magnetic field for two orientations,  $\theta = 0^\circ$  and  $90^\circ$ . Two series are present. The fundamental field of the lower field series anomalously decreases with tilt angle with the fundamental field changing from 5.06 T at  $\theta = 0^\circ$  to 2.33 T at  $90^\circ$ . The higher frequency series is almost independent of tilt angle as is characteristic of 3D behaviour. With the other two samples studied at this composition ( $x \approx 0.9$ ), the highest

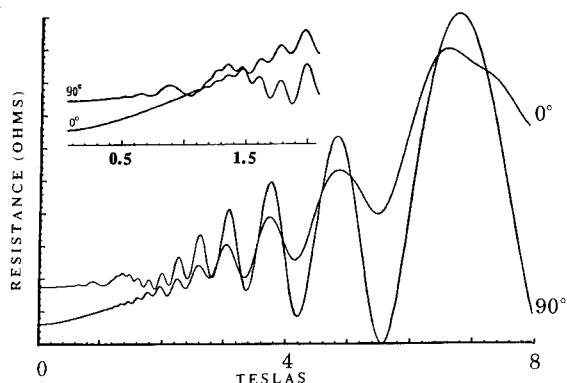
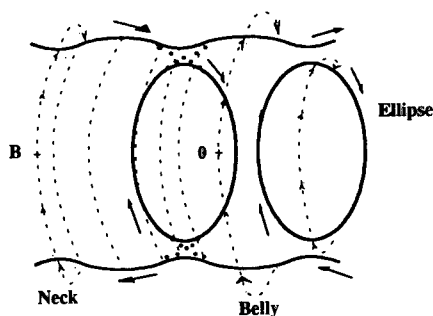


Fig. 2. Experimental recordings of resistance against field for sample F for  $\theta = 0^\circ$  to  $90^\circ$ .

### Fermi surface



Orbit  $\cdots \rightarrow$  B field perpendicular to superlattice planes  
 $\longrightarrow$  B field parallel to superlattice planes

Fig. 3. Nearly free electron model showing possible orbits (note neck orbit only present from  $\theta = 0^\circ$  to  $55^\circ$ ).

field series was also essentially independent of tilt angle.

Good agreement between carrier concentrations derived from the Hall and the SdH measurements is obtained if the 3D relationship  $(3\pi n)^{2/3} = (2e/\hbar)B_f$  is employed for the SdH case. These carrier concentrations are close to the intended doping concentrations.

The presence of two series for sample F, their dependence on tilt angle and the relative values of the fundamental fields can all be understood in terms of a nearly free electron model. The validity of such a model depends on there being strong tunnelling of the electron wavefunctions into the barriers as will happen when the Fermi energy is near the top of the wells. The Fermi vector,  $k_F = 2.27 \times 10^8 \text{ m}^{-1}$ , from the relation,  $k_F^3 = 3\pi^2 n_{3D}$  (for  $n_{3D} = 3.95 \times 10^{17} \text{ cm}^{-3}$ ), is greater than the minimum wavevector required to reach the first Brillouin zone boundary  $k_B = 1.57 \times 10^8 \text{ m}^{-1}$  (for  $a_0 = 200 \text{ \AA}$ ). Consequently, there is one intersection at the zone boundary resulting in two occupied minibands (Fig. 3 shows the Fermi surface on an extended zone scheme), and “belly”, “neck” and “elliptical” orbits are expected as indicated. The high field series is thought to originate from the belly orbit. This should become an open orbit in the  $\theta = 90^\circ$

configuration at low fields. However, the independence of tilt angle is thought to arise from the occurrence of magnetic breakdown at large tilt angles. There is a high probability for quantum tunnelling or “magnetic break-down” to occur when the magnetic field  $B$  is equal or greater than a critical field  $B_c$  applied along the superlattice planes, where

$$B_c = \frac{m^*}{\hbar e} \frac{(\Delta E)^2}{E_F},$$

see Ref. [7].  $\Delta E$  is the miniband gap at the zone boundary and  $E_F$  is the Fermi energy. Using the minigap which results from the band structure calculations,  $B_c$  is calculated to be 1.15 T (taking  $m^* = 0.015m_0$  for  $\text{InAs}_{0.1}\text{Sb}_{0.9}$  at zero confinement energy,  $\Delta E = 31$  meV and  $E_F = 111$  meV). The lower fundamental field is attributed to an elliptical orbit which becomes circular when  $\theta = 0^\circ$ . This picture explains rather well the anisotropy found experimentally except that neck orbits are not observed, probably because this series could

not be resolved in the Fourier analysis. The same model involving belly and elliptical orbits was used successfully to interpret the two series observed with “nini” doping superlattices in GaAs [8]. In this case also separate neck orbits were not observed.

In order to investigate further the validity of the nearly free electron model, structure G was grown with an identical concentration of dopant to sample F, but with the superlattice period increased from 200 to 300 Å. The change in superlattice period produces an additional series, as can be seen in Fig. 4, which shows the Fourier transform as a function of tilt angle.

The three fundamental fields behave in a quite distinct manner from each other with respect to tilt angle. Two series can be identified as belly orbit and elliptical orbit as these have similar characteristics to those found with sample F. The elliptical orbit could arise from the occupancy of the third Brillouin zone as would be expected as  $k_F$  remains as  $2.27 \times 10^8 \text{ m}^{-1}$ . The new wavevectors at the first two Brillouin zone boundaries

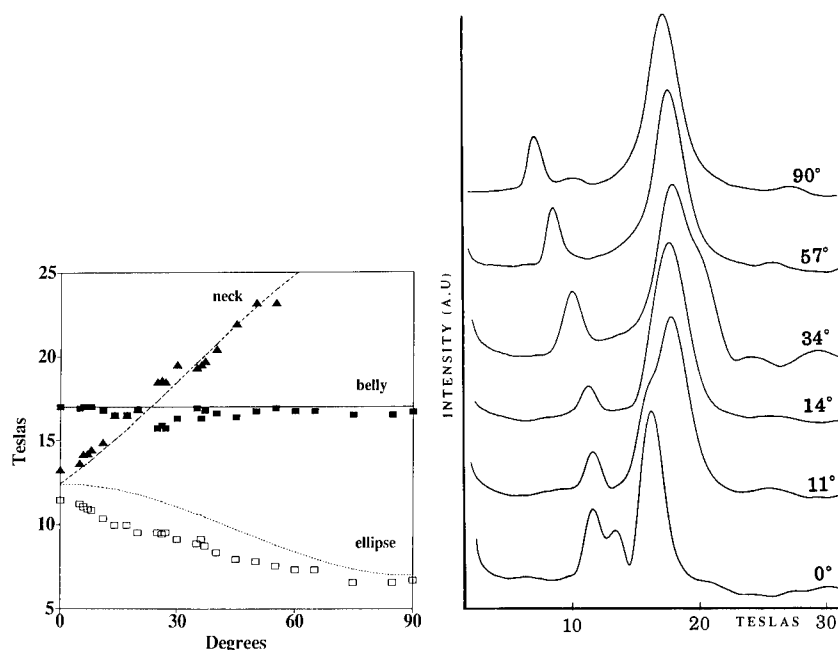


Fig. 4. Fourier transform of SdH data for a number of tilt angles for sample G (on the right). The left picture compares theory and experiment.

Table 2  
A comparison of theory and experiment for sample G

Theory			Experiment		
Angle ( $\theta$ )	$B^{\text{belly}}$	$B^{\text{neck}}$	$B^{\text{belly}}$	$B^{\text{neck}}$	$B^{\text{ellipse}}$
0	17.00	12.40	17.0	13.3	11.4
11	17.00	14.41	16.8	14.9	10.3
20	17.00	16.28	16.9	16.9	9.5
30	17.00	18.51	16.3	19.5	9.1
40	17.00	20.79	16.6	20.4	8.3
55	17.00	23.99	16.9	23.2	7.5
65	17.00	25.73	16.7		7.3
75	17.00	26.98	16.5		6.6
90	17.00	27.73	16.7		6.7

become  $k_B = 1.04 \times 10^8 \text{ m}^{-1}$  and  $2.08 \times 10^8 \text{ m}^{-1}$  on increasing the superlattice period. However, the extremal area predicted for the elliptical orbit with  $B$  parallel to the growth direction  $A$  is too small and any electron transfer back into the first two zones induced by a finite minigap only makes the fit worse.

We therefore believe that transfer between zones is significant, and that only two zones are occupied. The third period would then arise from the neck orbits associated with first zone electrons, i.e., the model is qualitatively identical to that employed for sample F with the exception that the neck orbits, which should be present also with sample F, are now resolved. The extremal cross-sectional areas, and hence the fundamental fields, were calculated as a function of tilt angle on a completely free electron model (i.e. neglecting the perturbations of the orbits away from the zone boundaries).

These fields are listed in Table 2 and shown in Fig. 4. It is seen that the observed behaviour is reproduced rather well theoretically without the use of any fitting parameter. The only variables used in the calculation are the superlattice period and the carrier density (i.e. the fundamental field of the belly orbit).

With the more lightly doped sample E, only a single series is observed. For the carrier concentration of  $1.35 \times 10^{17} \text{ cm}^{-3}$  deduced from this series,  $k_F = 1.58 \times 10^8 \text{ m}^{-1}$  which is virtually identical to  $k_B$ . No significant occupancy of the second zone is therefore anticipated. This sample

has the highest mobility of the samples investigated with  $45\,000 \text{ cm}^2/\text{V} \cdot \text{s}$  which is close to the bulk values for InSb at similar doping level.

#### 4. Summary

We have demonstrated that good quality  $\text{InAs}_{1-x}\text{Sb}_x/\text{InSb}$  SLS ( $x \geq 0.8$  with 1.3% mismatch) can be grown by MBE. n-Type silicon doping to greater than  $1 \times 10^{18} \text{ cm}^{-3}$  can be achieved in such structures which show a pronounced SdH effect.

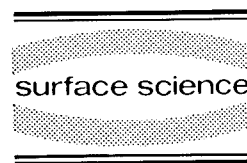
#### 5. References

- [1] S.R. Kurtz, G.C. Osbourn, R.M. Biefeld and S.R. Lee, Appl. Phys. Lett. 53 (1988) 216.
- [2] S.D. Parker, R.L. Williams, R. Droopad, R.A. Stradling, K.W. Barnham, S.N. Holmes, J. Lavery, C.C. Phillips, E. Skuras, R.H. Thomas, X. Zhang, A. Staton-Bevan and D.W. Pashley, Semicond. Sci. Technol. 4 (1989) 663.
- [3] S.R. Kurtz and R.M. Biefeld, Phys. Rev. B 44 (1991) 1143.
- [4] G. Bastard and J.A. Blum, IEEE, J. Quantum Electron. QE-22 (1986) 1625.
- [5] S.N. Smith, C.C. Phillips, R.H. Thomas, R.A. Stradling, B.N. Murdin and C.R. Pidgeon, Semicond. Sci. Technol. 7 (1992) 900.
- [6] T. Ando, J. Phys. Soc. Jpn. 37 (1974) 1233.
- [7] M. Cohen and L.M. Falicov, Phys. Rev. Lett. 7 (1961) 231.
- [8] R.L. Williams, E. Skuras, R.A. Stradling, R.B. Beall and J.J. Harris, Proc. Int. Conf. Phys. of Semicond., Warsaw (1988) 397.



ELSEVIER

Surface Science 305 (1994) 343–347



## Crossover from a two- to three-dimensional electronic structure in Si spike doped GaAs superlattices

A.B. Henriques\*, L.C.D. Gonçalves

*Instituto de Física, Universidade de São Paulo, Caixa Postal 20516, 01498 São Paulo, Brazil*

(Received 21 April 1993; accepted for publication 23 June 1993)

### Abstract

Periodically Si spike doped GaAs with the doping period in the range 100–830 Å was studied by magnetoresistance measurements in tilted fields and by photoconductivity. The angular dependence of the Shubnikov-de Haas oscillations, in conjunction with a self-consistent calculation of the miniband structure is used to construct the Fermi surface. When the doping period decreases, the superlattice potential weakens, and the magnetic breakdown of the superlattice Bragg reflection can be detected. Photoconductivity spectra are described by an absorption threshold at the Fermi energy, which is pushed upwards when the superlattice period decreases.

Spike doping is a technique which can be used to obtain carrier confinement in semiconductor microstructures. In spike doped GaAs, a sheet of shallow donor atoms is localized within a few monolayers of the crystal. The carriers, released from the shallow donors, are confined by a V-shaped space charge potential, a  $\delta$ -well. In periodically Si  $\delta$ -doped GaAs ( $\delta$ -superlattice), several equally spaced dopant sheets are introduced in the crystal. By varying the spacing between the dopant sheets, the strength of the interaction between adjacent  $\delta$ -wells can be tuned, and the system can be taken from a set of disconnected two-dimensional systems for the widely spaced wells to an essentially anisotropic three-dimensional system for the short period superlattice. The effect of an increasing coupling between adjacent wells when the superlattice period is made shorter has been detected by optical and magneto-transport studies of  $\delta$ -doped GaAs [1–4].

Periodically Si-doped GaAs grown by MBE was studied by Shubnikov-de Haas (SdH) measurements in tilted fields (0–9 Tesla) and by photoconductivity (PC) at 2 K. The samples were grown by MBE by S.M. Shibli of the Instituto de Física da Universidade de São Paulo. The spacing between the dopant sheets was varied from 830 down to 100 Å, while the doping level per period was kept constant at approximately  $2.0 \times 10^{12} \text{ cm}^{-2}$ .

First, the transverse SdH spectra (field applied parallel to the growth direction) will be discussed. Fig. 1 shows the inverse field Fourier transform for samples with a superlattice period in the range 830–100 Å. For the 830 Å sample, the  $\delta$ -wells are disconnected, and three peaks are detected, which correspond to the occupancy of three subbands. The occupancy of the ground-state ( $E_1$ ) subband, which contains most of the electronic charge, is detected only as a weak peak in the Fourier spectrum, because of its relatively lower mobility due to the strong localization, or short binding length, of

\* Corresponding author. Fax: +55 (11) 814-0503.

the E1 electrons [5]. When the  $\delta$ -well spacing is decreased, the binding length rises, and so does the relative strength of the peaks related to the ground-state miniband occupancy; simultaneously, the widths of the minibands increase, while the number of populated minibands is reduced. For the 100 Å sample, most of the electrons are in the ground-state miniband, which gives rise to a strong peak in the high frequency range of the Fourier spectrum.

The peaks  $B_i$  in the Fourier spectra are the extremal cross sections  $A_i$  of the Fermi surface in a plane perpendicular to the field direction, in units of  $\hbar/2\pi e$ . In order to interpret quantitatively the SdH data, it is necessary to know the shape of the Fermi surface, which we calculated self-consistently. The self-consistent procedure included the conduction band non-parabolicity and the exchange-correlation correction in the local density approximation. The input parameters were the superlattice period and the sheet carrier density per period. Details of the calculation procedure are given elsewhere [6].

The Fermi surface has the growth direction as its axis of symmetry, and can be represented by its rotationally symmetric cross section. The

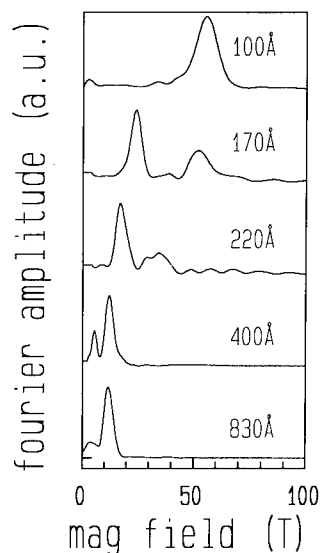


Fig. 1. Fourier spectra of the experimental recordings of the inverse field Shubnikov-de Haas oscillations. The nominal spacing between the  $\delta$ -wells for each curve is indicated.

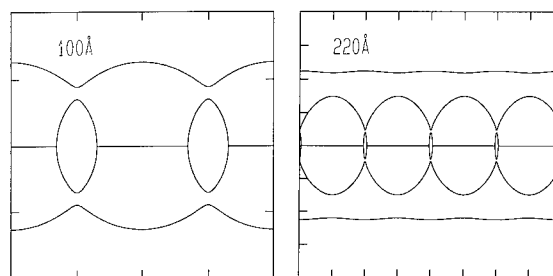


Fig. 2. Cross section of the Fermi surface of a  $\delta$ -superlattice in a plane containing the growth axis. The divisions on the axes are in units of  $\pi/a$  ( $a$  is the superlattice period, indicated for each structure).

Fermi surface for the 100 Å superlattice is shown in Fig. 2 in the extended zone scheme. The outer curve, recognized as a cylinder with periodically modulated cross section, is the Fermi surface for the E1 miniband, whereas the next miniband (E2) gives the lens-shaped surface centered around the minizone extremum.

If the superlattice period is increased, the Fermi surface for the second miniband gradually swells until it opens at the center of the Brillouin zone, thus changing gradually from lens-like to the periodically modulated cylinder shape, and the third miniband (E3) starts to be populated, which gives rise to a new Fermi lens-like surface at the minizone center, as for the 220 Å superlattice, also shown in Fig. 2. Conversely, if the superlattice period is reduced from 100 Å, electrons are transferred from the second to the first miniband, whose Fermi surface is more strongly modulated, and ultimately closes.

The electronic minibands described by an open Fermi surface will contribute to the transverse SdH oscillations with a “belly” and a “neck” frequency (which become degenerate in the uncoupled  $\delta$ -well limit) while the minibands described by a closed Fermi surface will be characterized by a single frequency. For an open (cylinder-like) Fermi surface, the extremal cross section in a plane perpendicular to the field direction will increase when the direction of the magnetic field is tilted, and will be finite only below a critical tilt angle,  $\theta_c$ , above which only open orbits in  $k$ -space are allowed. For a closed (lens-like) Fermi surface, the cross

section decreases when the field is tilted.

These opposite tendencies can be observed in Fig. 3, which shows the Fourier transform of the SdH spectra evolution as a function of the angle between the growth direction and the magnetic field ( $\theta$ ). For the 170 and 220 Å samples, a strong peak at low frequencies is displaced to the left when  $\theta$  increases, whereas a weak peak at high frequency moves to the right. The low frequency peak corresponds to a partially filled second miniband, and the high frequency one is due to a filled ground-state miniband. For the 400 Å structure, two peaks are detected at low frequencies; the lower frequency one, which is displaced to the left when the sample is tilted, is ascribed to a partially filled E3 miniband, and the one that moves to the right is ascribed to a full E2 miniband. In the 830 Å period structure, the peak positions scale as  $\cos \theta$ , as expected for a set of disconnected 2D systems. The 100 Å structure shows a single peak of constant frequency, which is indicative of a 3D electronic structure.

The angular dependence of the peak positions detected in the spectra of Fig. 3 is shown in Fig. 4. Also shown by solid lines are the theoretical cross sections of the Fermi surface. In the numerical calculations, the superlattice period was taken equal to the nominal value, and the total sheet carrier density,  $n_s$ , was adjusted to obtain the best agreement between the calculated extremal cross sections of the Fermi surface and the frequencies ( $B_i$ ) for  $\theta = 0$ . With the input parameters thus fixed, the extremal cross sections of the Fermi surfaces were calculated for all tilt angle

interval (0–90°).

The calculated Fermi surface extremal cross section dependence on  $\theta$  closely match the measured frequencies  $B_i$ , however, for some of the samples, described by an open Fermi surface, agreement is only obtained below the critical tilt angle  $\theta_c$ . This is the case for the E1 Fermi surface cross section of the 100 Å superlattice ( $\theta_c \sim 50^\circ$ ), the E2 of the 220 Å one ( $\theta_c \sim 60^\circ$ ), and the E3 of the 400 Å superlattice ( $\theta_c \sim 60^\circ$ ). Above these  $\theta_c$ , where no finite extremal cross sections for the corresponding Fermi surface miniband exist, the experimental curve persists.

The appearance of frequencies above the critical angle is interpreted in terms of a magnetic breakdown of Bragg reflection by the superlattice planes. The magnetic field strength required for an electron to cross a Bragg plane and transit between two minibands, separated by a gap of energy  $\Delta$ , is  $\hbar w_c E_F > \Delta^2$ , where  $w_c$  is the cyclotron frequency and  $E_F$  is the Fermi energy. The calculated magnetic fields required for the breakdown of Bragg reflection are shown in Table 1, and clearly support the hypothesis of magnetic breakdown.

The photoconductivity spectra at 2 K for the 170, 220 and 400 Å  $\delta$ -superlattices in the energy range near the GaAs band-edge were measured and are shown in Fig. 5. The spectra are described by a smooth absorption onset, which blue-shifts when the superlattice period decreases; this is a consequence of the increase of the Fermi energy [6]. The theoretical threshold for absorption from the  $n$ th hole miniband, indicated by arrows in Fig. 5, was estimated by

$$\hbar\nu_{\text{threshold}} = E_G + BGR - V_0 + E_F + H_{nF},$$

where  $E_G = 1.519$  eV,  $V_0$  is the potential barrier between the wells,  $E_F$  is the Fermi energy measured from the bottom of the well,  $H_{nF}$  is the hole energy at the Fermi wave vector, and  $BGR \sim -34$  meV, as estimated for a 3D electron gas [7].

In summary, we have studied the magnetoresistance oscillations in GaAs  $\delta$ -superlattices in tilted magnetic fields. These can be interpreted in terms of the shape of the Fermi surface, which

Table 1

Estimated magnetic field (Tesla) required for the breakdown of Bragg reflection of the electrons in the E1, E2 and E3 minibands

Superlattice period	E1	E2	E3
100 Å	1.7 <sup>a,b</sup>	–	–
170 Å	5.9	–	–
220 Å	8.5	< 1.0 <sup>a,b</sup>	–
400 Å	16.6	4.8	5.0 <sup>b</sup>

<sup>a</sup> Breakdown expected from  $\hbar w_c E_F > \Delta^2$ .

<sup>b</sup> Experimental points persist above  $\theta_c$ .

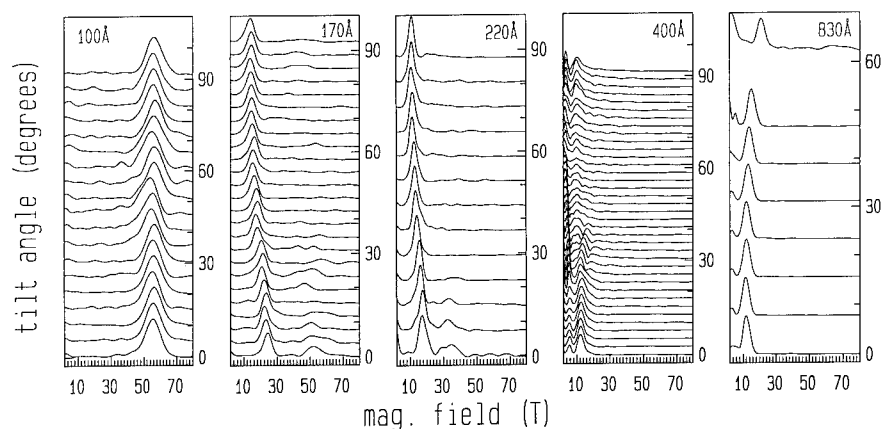


Fig. 3. Fourier transform on the inverse field Shubnikov–de Haas oscillations. The tilt angle to each curve is obtained by following the spectrum baseline to the right side. The spacing between the  $\delta$ -wells, corresponding to each set of curves, is indicated.

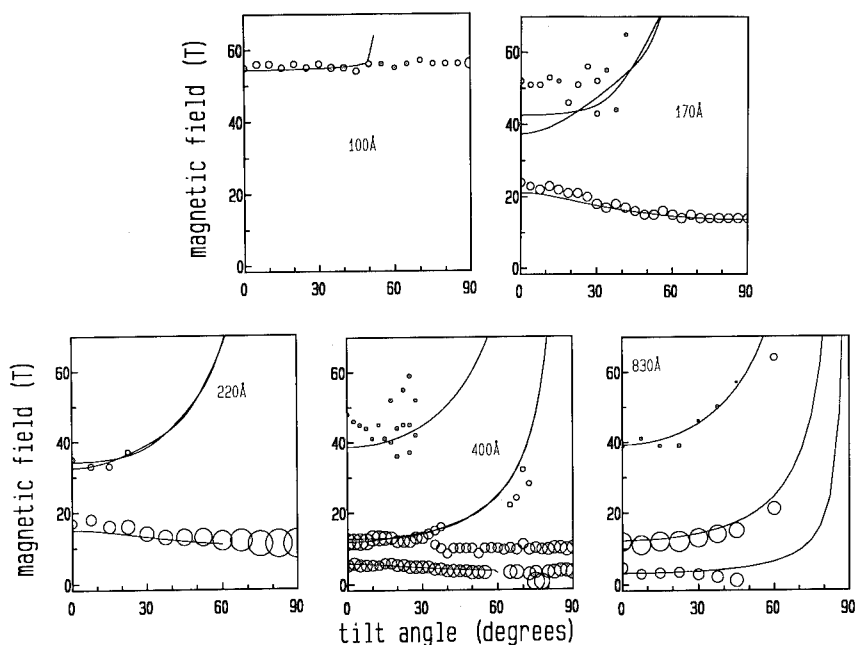


Fig. 4. Open circles show the frequencies  $B_i$ , obtained from the Fourier spectra of Fig. 3. The area of each circle is a measure of the relative intensity of the Fourier peak. Solid lines are the Fermi surface cross sections, obtained from the numerical calculations.

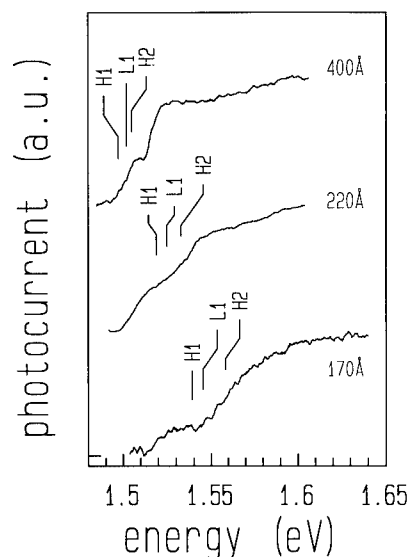


Fig. 5. Photoconductivity spectra of periodically spike doped GaAs. The spacing between the  $\delta$ -wells is indicated for each curve. Theoretical transition thresholds are indicated by arrows.

evolves progressively from the cylindrical shape in the uncoupled  $\delta$ -well limit, and approaches a sphere for the short period superlattices. It is shown that the magnetic breakdown of Bragg reflection plays an important role in these systems, and for a doping period below 100 Å the electronic structure is effectively three-dimensional. Photoconductivity spectra were also measured, and the spectra obtained are consistent with the interpretation of the transport data. The model used for the analysis of the experimental results

is simplified, since it does not take proper account of the effect of magnetic depopulation of the minibands [8], and also the effects of light on the self-consistent potential for electrons and holes and its consequences on the photoconductivity spectra [9].

This work is supported by the FAPESP Grant No. 91/3336–9 and the CNPq Grant No. 306335/88.

## References

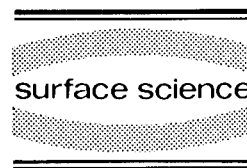
- [1] F. Koch, A. Zrenner and M. Zachau, in: *Two-Dimensional Systems: Physics and New Devices* (Springer, Berlin, 1986) p. 175.
- [2] R. Droopad, S.D. Parker, E. Skuras, R.A. Stradling, R.L. Williams, R.B. Beall and J.J. Harris, in: *High Magnetic Fields in Semiconductor Physics II* (Springer, Berlin, 1989) p. 199.
- [3] A.C. Maciel, M. Tatham, J.F. Ryan, J.M. Worlock, R.E. Nahory, J.P. Harbison and L.T. Florez, *Surf. Sci.* 228 (1990) 251.
- [4] Mao-Long Ke, J.S. Rimmer, B. Hamilton, J.H. Evans, M. Missous, K.E. Singer and P. Zalm, *Phys. Rev. B* 45 (1992) 14114.
- [5] S. Yamada and T. Makimoto, *Appl. Phys. Lett.* 57 (1990) 1022.
- [6] A.B. Henriques and L.C.D. Gonçalves, *Semicond. Sci. Technol.* 8 (1993) 585.
- [7] S. das Sarma, R. Jalabert and S.R.E. Yang, *Phys. Rev. B* 41 (1990) 8288.
- [8] A. Zrenner, H. Reisinger, F. Koch, K. Ploog and J.C. Maan, *Phys. Rev. B* 33 (1986) 5607.
- [9] B. Ulrich, C. Zhang and K. von Klitzing, *Appl. Phys. Lett.* 54 (1989) 1133.





ELSEVIER

Surface Science 305 (1994) 348–352



## Transverse magnetic focusing and the dispersion of GaAs 2D holes at (311)A heterojunctions

J.J. Heremans<sup>\*</sup>, M.B. Santos, M. Shayegan

*Department of Electrical Engineering, Princeton University, Princeton, NJ 08544, USA*

(Received 20 April 1993; accepted for publication 3 May 1993)

### Abstract

We report transverse magnetic focusing experiments on two-dimensional hole systems confined in square and triangular quantum wells grown on (311)A GaAs substrates. The focusing barriers are oriented along different crystallographic directions and allow us to derive the constant energy contours in  $k$ -space. The results indicate a nearly elliptical shape for these contours which we interpret in light of a lateral surface superlattice induced by corrugations at the heterojunction.

The use of transverse magnetic focusing (TMF) to determine the dimension and shape of Fermi surfaces was proposed by Tsoi, and subsequently was demonstrated in metals such as Bi, Sb, W, Cu and Ag [1]. Both the periodicity in magnetic field and the shape of the focusing singularities reflect the size and geometry of the momentum space orbit. TMF was also realized in two-dimensional electron systems at GaAs/AlGaAs heterojunctions, although here the circular Fermi surface cross-sections render the focusing spectra particularly simple [2–4]. Recently, TMF was achieved [5] in two-dimensional hole systems (2DHSs) at GaAs/AlGaAs heterojunctions, where the more intricate valence band structure of GaAs can display a subset of the variety of focusing spectra found in metals. Observation of TMF in 2DHSs was made possible by recent advances in the

growth of p-type heterostructures and quantum wells: molecular beam epitaxy (MBE) on the (311)A plane of the GaAs/AlGaAs system, and using Si as an acceptor dopant, has brought about a substantial improvement in the quality and mobility of the confined 2DHSs [5,6]. In this work we present a study of the directional dependence of TMF spectra taken on 2DHSs in triangular as well as square GaAs wells grown on (311)A substrates, and address the implications the experimental results bear on the in-plane energy versus wave vector dispersion relations of these systems.

TMF is achieved by drawing a current through one narrow opening (injector) and recording the voltage induced in a second opening (collector) separated from the injector by a focusing barrier of length  $L$ , as a function of a perpendicular magnetic field,  $B$  (lower part of Fig. 1). In a semi-classical model [7], under a magnetic field, the path in  $k$ -space coincides with the constant energy contours; in this case the contour defined

<sup>\*</sup> Corresponding author.

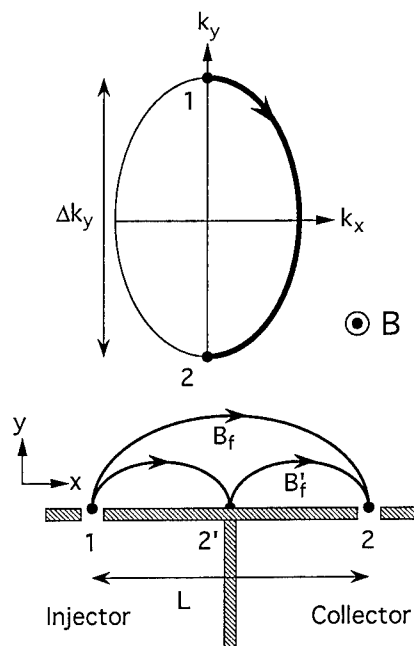


Fig. 1. Correspondence in the semi-classical model between hole paths in  $k$ -space (upper figure) and in real space (lower figure); the focusing barrier is indicated by the hatched area: the orbit 1–2 in  $k$ -space leads to the real space orbit 1–2 at field  $B_f$ , 1–2' at field  $B'_f = 2B_f$ . The first focusing peak occurs at  $B_f$ , the second at  $B'_f$ . In the semi-classical model we have  $B_f = (\hbar/eL)\Delta k_y$ .

by the Fermi energy  $E_F$  (Fig. 1). To this corresponds a path in real space of the same shape, but rotated by  $\pi/2$  and scaled by  $1/B$ . A chord of the real space orbit fits an integer number of times in  $L$  at those  $B$ -values where focusing peaks appear. The periodicity  $B_f$  of the signal can then be related to the  $k$ -space dimension  $\Delta k$ :  $B_f = (\hbar/eL)\Delta k$ . Hence, the experimental value of  $B_f$  should yield the value of  $\Delta k$  in the direction perpendicular to the focusing barrier. Orienting the barrier along different directions yields points on the constant energy contour at  $E_F$  (the Fermi surface, FS).

The sample growth on GaAs(311)A surfaces by MBE has been described elsewhere [6]. Briefly, 2DHSs were formed in both triangular and square wells. An anisotropy in the mobility  $\mu$  is a consistent feature of all our samples: along  $[2\bar{3}3]$  a higher  $\mu$  is found than along  $[01\bar{1}]$ . The ratio of these  $\mu$  is sample and density dependent, and

varies between 1.5 and 3. The triangular well was realized at a single  $\text{Al}_{0.35}\text{Ga}_{0.65}\text{As}/\text{GaAs}$  interface, separated from the Si dopant layer by a 210 Å spacer. For unprocessed samples of this type, typical sheet densities ( $p$ ) and  $[2\bar{3}3]$  mobilities ( $\mu_h$ ) were  $p = 2.7 \times 10^{15} \text{ m}^{-2}$  and  $\mu_h = 31 \text{ m}^2/\text{V} \cdot \text{s}$ , respectively. The square well samples consisted of a 150 Å wide GaAs layer, flanked on both sides by undoped  $\text{Al}_{0.30}\text{Ga}_{0.70}\text{As}$  spacers and Si dopant layers. Spacers in this case were either 450 Å (unprocessed  $p = 3.3 \times 10^{15} \text{ m}^{-2}$  and  $\mu_h = 120 \text{ m}^2/\text{V} \cdot \text{s}$ ) or 325 Å (unprocessed  $p = 4.5 \times 10^{15} \text{ m}^{-2}$  and  $\mu_h = 50 \text{ m}^2/\text{V} \cdot \text{s}$ ). Experimental data from all these systems exhibited qualitatively similar behavior; in this paper we concentrate on data for a square well sample with 450 Å spacers.

The focusing barriers, each of equal length ( $L = 3$  to  $6 \mu\text{m}$ ), were positioned adjacent to each other in a quarter circle, along 5 crystallographic directions ranging from  $[2\bar{3}3]$  to  $[01\bar{1}]$ . In this arrangement each constriction serves in turn as collector for one barrier and as injector for the neighboring barrier (Fig. 2). Lithographic constriction widths were  $0.8 \mu\text{m}$ . The TMF patterns were defined by wet etching, employing two different etchants: an  $\text{H}_2\text{SO}_4:\text{H}_2\text{O}_2:\text{H}_2\text{O}$  solution which yielded constrictions with beveled side walls for barriers parallel to  $[01\bar{1}]$ , and a more isotropically etching  $\text{H}_3\text{PO}_4:\text{H}_2\text{O}_2:\text{H}_2\text{O}$  solution. Using the latter, no beveling was noticed. Experimental results coincide for both cases. Also, the etch remained shallow and did not reach the 2DHSs. Thus intrusion of possible geometric etching effects in the observed focusing spectra is unlikely. Finally, a front gate was deposited over all active areas, permitting us to modify  $p$  and hence  $E_F$ . We determined  $p$  from the transverse magnetoresistance of a nearby Hall bar. The TMF measurements were performed at 0.45 K in a 4-terminal geometry, using a low frequency lock-in technique (more details can be found in Ref. [5]).

Fig. 3 shows typical TMF spectra, plotted as collector voltage normalized by injector current versus  $B$  (relevant parameters are included in the figure). Up to 5 periodic focusing peaks appear on an up-going slope for one polarity of  $B$ , while the reverse polarity yields a flat trace. As the

focusing barrier sweeps through the 5 orientations from  $[\bar{2}33]$  to  $[01\bar{1}]$ , the focusing spectra change in shape and periodicity  $B_f$ , the latter reaching the highest value for a barrier along  $[\bar{2}33]$ . This increase in  $B_f$  and variability in peak shapes was a consistent feature in all samples.

Fig. 4 shows a polar plot of the experimental  $B_f$  of Fig. 3 converted to  $\Delta k/2$  values for the different orientations. Also shown are such polar plots for two other  $p$  for the same sample ( $p$  was varied via the front gate). Each of these represents one quarter of the FS at different  $E_F$  in  $k$ -space. The inset compares one of our experimental contours with the Fermi circle that would be obtained for the same  $p$  assuming an isotropic dispersion. At a same  $p$ , the two contours should, of course, enclose the same area,  $S_k = 2\pi^2 p$ . The FS derived from the TMF data exhibits a marked elongation along the  $[01\bar{1}]$  direction, while along  $[\bar{2}33]$  the dimensions are correspondingly shortened, in accordance with the requirement of preservation of the area  $S_k$ . The experimental error in our data stems mostly from the precision

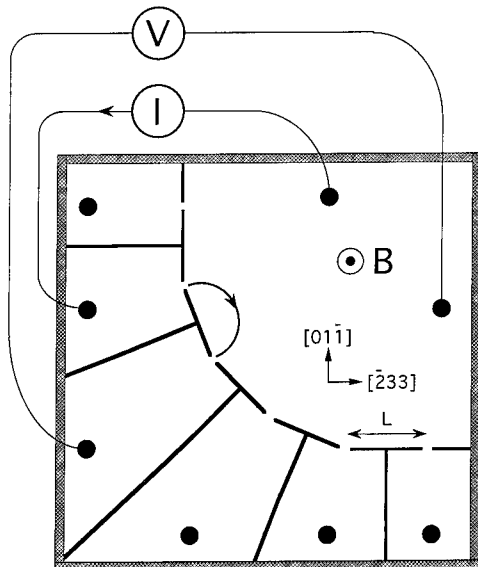


Fig. 2. Schematic representation of the sample geometry and 4-terminal measurement setup. The T-shaped focusing barriers are wet etched on the 2DHS, arranged in a quarter circle along different crystallographic orientations. Ohmic voltage and current contacts are represented by dots. The magnetic field is applied perpendicular to the sample plane.

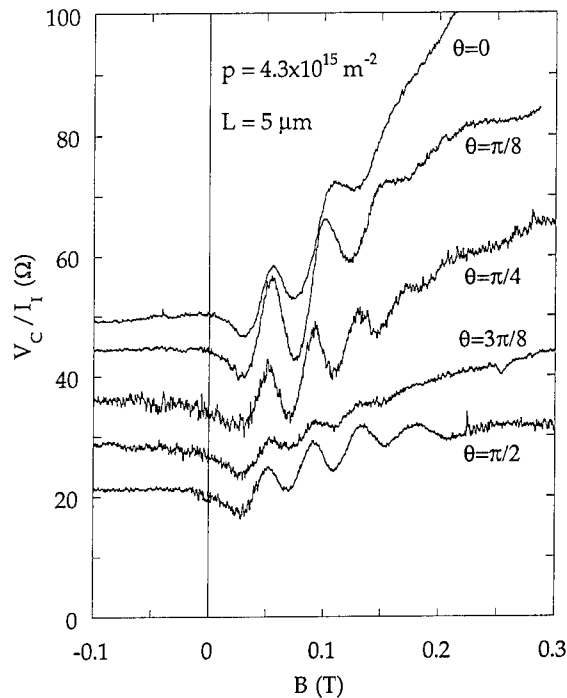


Fig. 3. TMF spectra for different orientations of the focusing barrier (collector voltage  $V_C$  normalized by injector current  $I_1$ ). The angle between the focusing barrier and the  $[\bar{2}33]$  direction is indicated by  $\theta$ . The spectra have been shifted up for clarity:  $\theta = 3\pi/8$  by 5  $\Omega$ ;  $\theta = \pi/4$  by 10  $\Omega$ ;  $\theta = \pi/8$  by 15  $\Omega$ ;  $\theta = 0$  by 20  $\Omega$ .

to which we can ascertain the focusing peak positions, rather than from lithographic deviations and we estimate it at about 7%. For the data of Figs. 3 and 4 this error can account for the discrepancy between  $S_k$  calculated from  $p$  and from the experimental FS. The distinct near-elliptical shape of the FS constitutes a common property of all samples investigated and, in the light of the semi-classical model, originates from the underlying dispersion of the 2DHS on GaAs(311)A surfaces, as we will discuss below.

The dispersion relations for the valence band of GaAs quantum wells at the (311)A surface have been previously studied theoretically [8], largely confirming resonant magnetotunneling spectroscopy experiments [9]. Higher subbands apparently display considerable nonparabolicity and anisotropy, while the lowest, heavy hole, subband remains quite free-hole-like up to high den-

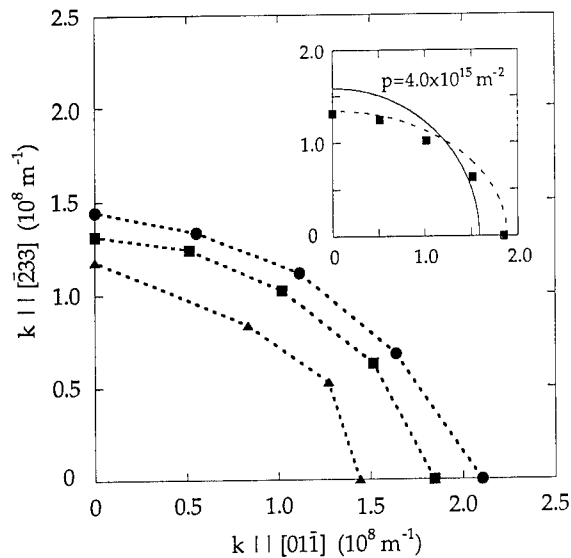


Fig. 4. Constant energy contours in  $k$ -space determined from TMF data at varying  $p$  (circles:  $p = 4.3 \times 10^{15} \text{ m}^{-2}$ ; squares:  $p = 4.0 \times 10^{15} \text{ m}^{-2}$ ; triangles:  $p = 3.1 \times 10^{15} \text{ m}^{-2}$ ). Inset: comparison between experimental points (squares), isotropic Fermi circle (solid curve) and Kronig–Penney calculation (dashed curve) for  $p = 4.0 \times 10^{15} \text{ m}^{-2}$ .

sities. Therefore in our samples, where only the lowest subband is occupied, the dispersion anisotropy (Fig. 4) and also the mobility anisotropy mentioned earlier are puzzling.

However, MBE on GaAs(311)A substrates has been reported [10] to induce interface corrugations along  $[233]$  and the transport anisotropy likely stems from this morphology. The corrugations, with a period of 32 Å, give rise to a one-dimensional lateral superlattice (LSL) along  $[011]$  for holes confined to a GaAs well [11]. Such a LSL modifies the dispersion along  $[011]$  while along  $[233]$  the dispersion should be unchanged from its free-hole form [12]. A straightforward Kronig–Penney calculation indicates that the LSL produces an elongation of the FS along the  $[011]$  direction compared to  $[233]$ . This is consistent with our TMF experiments. Let us note that for  $E_F$  values typically achieved in our 2DHSs,  $k_F$  amounts to about 1/10 of the Brillouin zone induced by this LSL. To account for the distortion observed in our data at these  $p$ , the LSL potential amplitude needed is about 200 to 300 meV, the value being sample dependent as ex-

pected for a growth related phenomenon. The FS obtained from the Kronig–Penney model (assuming for simplicity square barriers of width equal to half the period and height 300 meV) is plotted in the inset of Fig. 4. While a more realistic potential profile would be desirable, we feel that the qualitative features of the experimental data are well reproduced.

In conclusion, TMF employing a geometry of adjacent barriers in varying crystallographic directions enabled us to map out the constant energy contours in  $k$ -space for the heavy hole band of a 2DHS on the (311)A plane of GaAs. We interpret the data in a semi-classical model. Although the dispersion for the heavy hole band on (311)A surfaces is expected to be quite isotropic, nearly elliptical contours were deduced, with their long axis along the  $[011]$  orientation. We trace this shape back to the existence of a lateral superlattice, generated by growth induced corrugations along the  $[233]$  direction.

We thank K. Hirakawa for helpful discussions. This work was supported by the National Science Foundation, the Army Research Office and the IBM Corporation. The authors are affiliated with the Advanced Technology Center in Photonics and Opto-Electronic Materials established at Princeton University by the State of New Jersey.

## 1. References

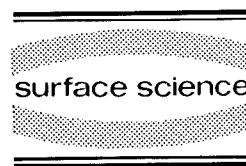
- [1] V.S. Tsoi, JETP Lett. 19 (1974) 70;  
V.S. Tsoi, JETP Lett. 22 (1975) 197;  
S.A. Korzh, Sov. Phys.-JETP 41 (1975) 70;  
V.S. Tsoi and I.I. Razgonov, Sov. Phys.-JETP 47 (1978) 597.
- [2] H. van Houten, C.W.J. Beenakker, J.G. Williamson, M.E.I. Broeckaart, P.H.M. van Loosdrecht, B.J. van Wees, J.E. Mooij, C.T. Foxon and J.J. Harris, Phys. Rev. B 39 (1989) 8556.
- [3] J. Spector, H.L. Stormer, K.W. Baldwin, L.N. Pfeiffer and K.W. West, Surf. Sci. 228 (1990) 283.
- [4] K. Nakamura, D.C. Tsui, F. Nihey, H. Toyoshima and T. Itoh, Appl. Phys. Lett. 56 (1990) 385.
- [5] J.J. Heremans, M.B. Santos and M. Shayegan, Appl. Phys. Lett. 61 (1992) 1652.
- [6] W.I. Wang, E.E. Mendez, Y. Iye, B. Lee, M.H. Kim and G.E. Stillman, J. Appl. Phys. 60 (1986) 1834;

- A.G. Davies, J.E.F. Frost, D.A. Ritchie, D.C. Peacock, R. Newbury, E.H. Linfield, M. Pepper and G.A.C. Jones, *J. Cryst. Growth* 111 (1991) 318;
- M.B. Santos, Y.W. Suen, M. Shayegan, Y.P. Li, L.W. Engel and D.C. Tsui, *Phys. Rev. Lett.* 68 (1992) 1188.
- [7] Our experiments involve samples with high sheet density and relatively wide injector and collector openings, so that the Fermi wavelength ( $\lambda_F$ ) is much smaller than the opening width ( $W$ ). Therefore, as in the case of TMF in metals, a semi-classical model is appropriate. In particular, we note that the quantum interference effects, manifested as reproducible fine structure superimposed on the focusing spectra, are essentially absent in our data (c.f. van Houten et al. [2] where  $\lambda_F \approx W$ , and also see G. Goldoni and A. Fasolino, *Phys. Rev. B* 44 (1991) 8369, for a theoretical discussion of subband structure effects on TMF in 2DHSs in the quantum mechanical regime).
- [8] E.C. Valadares, *Phys. Rev. B* 46 (1992) 3935.
- [9] R.K. Hayden, E.C. Valadares, M. Henini, L. Eaves, D.K. Maude and J.C. Portal, *Phys. Rev. B* 46 (1992) 15586.
- [10] R. Noetzel, N.N. Ledentsov, L. Daeweritz, K. Ploog and M. Hohenstein, *Phys. Rev. B* 45 (1992) 3507; R. Noetzel, N.N. Ledentsov and K. Ploog, *Phys. Rev. B* 47 (1993) 1299.
- [11] The presence of minigaps and the possibility of a LSL for 2D electrons at the vicinal Si/SiO<sub>2</sub> interfaces, such as (811), have been previously reported: T. Cole, A.A. Lakhani and P.J. Stiles, *Phys. Rev. Lett.* 38 (1977) 722; L.J. Sham, S.J. Allen, Jr., A. Kamgar and D.C. Tsui, *Phys. Rev. Lett.* 40 (1978) 472; see also, T. Ando, A.B. Fowler and F. Stern, *Rev. Mod. Phys.* 54 (1982) 437.
- [12] Irregularities in the periodicity or strength of the LSL's periodic potential may be responsible for the enhanced scattering and reduced mobility in the [01 $\bar{1}$ ] direction.



ELSEVIER

Surface Science 305 (1994) 353–357



## Intrinsic bistability in the electroluminescence spectrum and current–voltage characteristics of triple-barrier p–i–n resonant tunneling devices

P.A. Harrison <sup>\*,a</sup>, L. Eaves <sup>a</sup>, P.M. Martin <sup>a</sup>, M. Henini <sup>a</sup>, P.D. Buckle <sup>b</sup>,  
M.S. Skolnick <sup>b</sup>, D.M. Whittaker <sup>b</sup>, G. Hill <sup>c</sup>

<sup>a</sup> Department of Physics, University of Nottingham, Nottingham NG7 2RD, UK

<sup>b</sup> Department of Physics, University of Sheffield, Sheffield S3 7RH, UK

<sup>c</sup> Department of Electronic Engineering, University of Sheffield, Sheffield S1 3JD, UK

(Received 19 April 1993; accepted for publication 22 June 1993)

### Abstract

The electroluminescence spectrum and current–voltage characteristics of a forward biased triple-barrier p–i–n diode are investigated. The thin AlAs central barrier provides strong coupling between the two GaAs quantum wells. EL arises from the GaAs contact layers and both spatially direct and indirect recombination in the quantum wells. The latter line is much the stronger and shows a marked red shift with increasing bias. Two electron and two hole resonant peaks are observed in  $I(V)$  and in the intensity–bias plots of the EL emission lines. A pronounced intrinsic bistability is observed in both  $I(V)$  and the EL spectra. The effect of magnetic field on the EL spectra is investigated.

Resonant tunneling in double barrier heterostructures has attracted considerable attention since its first experimental realization [1]. Although most attention has focused on resonant tunneling (RT) of electrons in n-type devices, work has also been done on hole resonant tunneling in p-type devices [2]. Hole tunneling also plays an important role in the photoluminescence of n-type RT devices under optical excitation [3–6]. Recently, combined resonant tunneling of both electrons and holes in forward biased p–i–n

RT devices has been reported [7,8]. They incorporate two tunnel barriers in the undoped intrinsic (i) region and show strong electroluminescence (EL) emission due to electron–hole recombination in the quantum well (QW). EL is also observed from electrons (holes) which tunnel through both barriers and recombine as minority carriers in the opposite p-type (n-type) contact regions. An interesting feature of n-type RT devices is an intrinsic bistability effect in the current–voltage characteristics,  $I(V)$ , due to the buildup of space charge in the QW at resonance [9,10]. The bistability can also be observed in the variation with bias of both the PL intensity and photon energy of the emission from the QW [5,6].

\* Corresponding author.

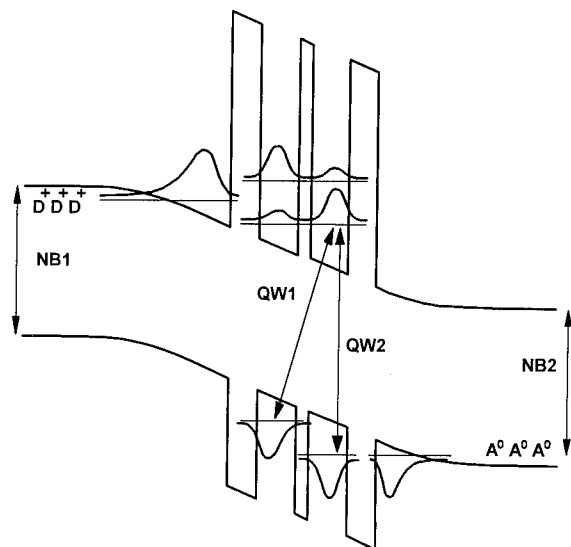


Fig. 1. Schematic band diagram of the device at 1.80 V forward bias, showing the electron and hole accumulation layers, the states of the quantum wells and the 4 electroluminescence transitions.

Here we report intrinsic bistability in both the EL emission spectra and  $I(V)$  characteristics of a triple-barrier p–i–n RT diode in which the two GaAs QWs, each of width 6.0 nm, are separated by a thin AlAs central barrier of thickness 0.85 nm. The two outer AlAs barriers are 5.1 nm thick. The EL from the QW corresponds to both spatially direct and indirect transitions. The intense spatially indirect emission undergoes a pronounced red shift with increasing forward bias and displays a marked intrinsic bistability in both its intensity and photon energy. A schematic band diagram of the device is shown in Fig. 1. Undoped GaAs spacers, of thicknesses 7.6 and 5.1 nm, separate the two outer barriers from the n- and p-doped contact layers, respectively. The dopings in these layers are graded from  $1 \times 10^{16}$  to  $2 \times 10^{18} \text{ cm}^{-3}$  for the n-type contact and from  $5 \times 10^{17}$  to  $2 \times 10^{18} \text{ cm}^{-3}$  for the p-type contact. The top n-type contact layer incorporates a  $1 \mu\text{m}$  thick  $\text{Al}_{0.33}\text{Ga}_{0.67}\text{As}$  window layer which allows efficient transmission of the EL from the QW [7]. The layers were fabricated into  $100 \mu\text{m}$  diameter mesas by optical lithography, with an annular Au–Ge contact to transmit the EL.

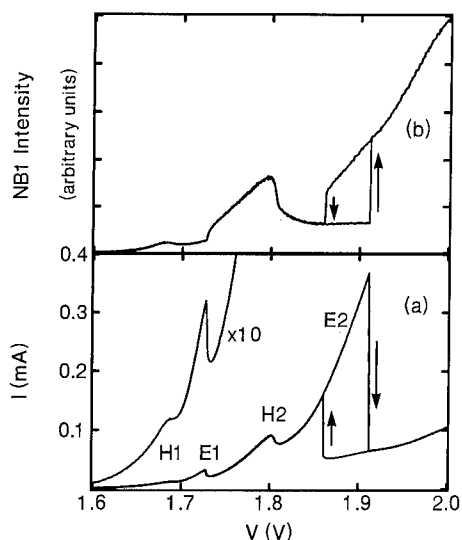


Fig. 2. (a) The current–voltage characteristics at 4 K; (b) Variation with bias of the intensity of the near-band edge luminescence line, NB1.

Fig. 2a shows the  $I(V)$  characteristics of the device at a temperature of 4 K. Four peaks are observed corresponding to electron (E) and hole (H) resonant tunneling into the QW states shown in Fig. 1. The tunneling occurs from two-dimensional (2D) electron and hole accumulation layers adjacent to the barriers. A strong intrinsic bistability is observed in the second electron resonance, E2. Over most of the range of forward bias, EL is observed from the quantum well. A typical EL spectrum is shown in Fig. 3. Four

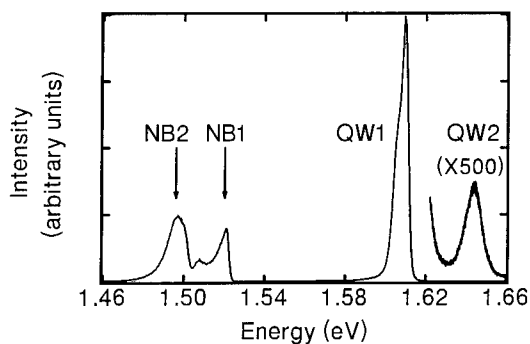


Fig. 3. Electroluminescence spectrum at a bias of 1.80 V showing the two near-band recombination lines and the two quantum well lines.

distinct EL lines are observed: two around 1.6 eV from the QWs and two around 1.5 eV due to near-band (NB) edge recombination. The higher energy emission line from the quantum well, QW2, is weak, having only  $\sim 10^{-3}$  of the intensity of QW1 at 1.8 V. Line NB1 at 1.521 eV is due to essentially free electron–hole recombination. The dependence of its intensity on bias is similar in form to the  $I(V)$  curves. Line NB2 at 1.487 eV is due to electron recombination at neutral acceptors. The bias dependence of the intensity of NB1 is shown in Fig. 2b. Note that it *increases* at voltages of 1.72 and 1.91 V, which correspond to the decreases in  $I(V)$  when the device is biased off the E1 and E2 resonances. Similarly, the intensity decreases at 1.86 V when the current increases at the low voltage side of the bistability loop. The intensity variation of NB1 indicates that it arises from holes that tunnel through both barriers to recombine as minority carriers in the n-type GaAs contact layers. It shows strong peaks on the hole resonances H1 and H2 in  $I(V)$  and decreases when the device is on an electron resonance since in this case the tunneling holes can recombine with the enhanced concentration of electrons in the conduction band QWs rather than pass through both barriers. This is confirmed in Fig. 4a which plots the intensity of one of the QW lines (QW1) as a function of bias. A peak in intensity is observed on the E1 line and also on H2. In addition, on the bistability loop of E2, the intensity of QW1 is higher when the electron resonant tunneling current is higher, corresponding to enhanced space charge buildup in the QW.

The bias-dependence of the intensity of the weak EL line QW2 is shown in Fig. 5a. This shows strong peaks at E1, H2 and E2 (the latter with bistability), similar to those in  $I(V)$ . No EL from the QW is observed on the H1 peak in  $I(V)$  since at this low bias the electron tunnel current is very low. The variations of the emission energy of the two EL lines from the QW, as a function of bias, are shown in Figs. 4b and 5b for QW1 and QW2, respectively. The emission energy of QW1 is voltage tunable and also shows a bistability around 1.9 V. The energy of the QW2 line has a much weaker dependence on  $V$ .

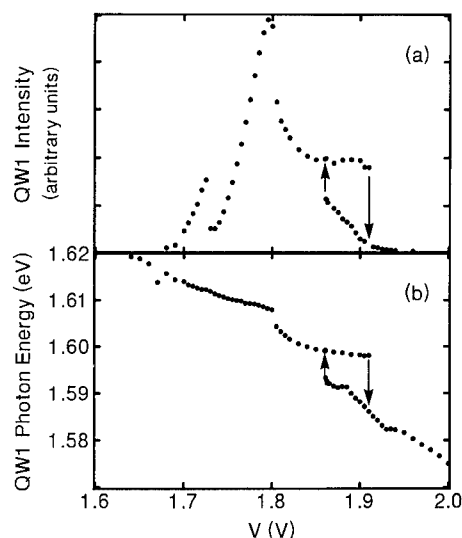


Fig. 4. Variation with bias of (a) the intensity of the spatially indirect recombination line, QW1; (b) the photon energy of QW1.

We can understand the  $I(V)$  characteristics and EL emission spectra by considering the effect of the applied bias on the confined electron and hole states in the quantum well [11–13]. The thin central barrier couples two quantum wells which in our device have the same thickness. Thus when

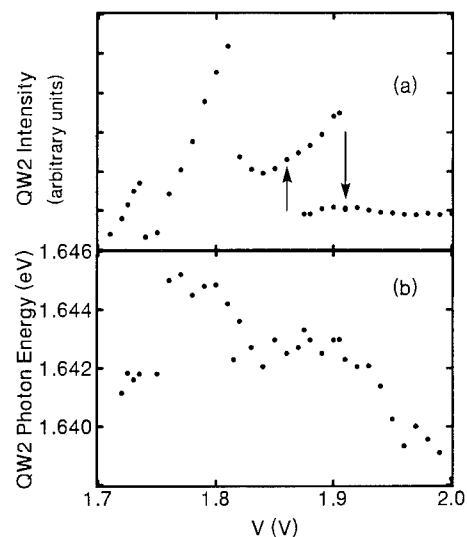


Fig. 5. Variation with bias of (a) intensity of the spatially direct recombination line QW2; (b) photon energy of QW2.



the device is biased at the flat-band voltage around 1.5 V, the electron (and hole) wavefunctions of the two lowest QW states will be of the familiar symmetric and antisymmetric form, extending over both quantum wells. At higher bias, the wavefunctions become increasingly localized in one or other of the two wells as shown in Fig. 1. This effect can be seen clearly in the  $I(V)$  characteristics: peak E1 is much weaker than E2 because of the much smaller tunneling probability from the emitter accumulation layer to the right-hand well. The localization effect is even more pronounced for holes than electrons because of their higher effective mass.

The voltage-induced confinement effect leads to the pronounced red shift of transition QW1 with increasing bias. In contrast, the shift of QW2 is much weaker, as it effectively corresponds to a spatially direct transition. Photoluminescence excitation (PLE) experiments confirm this model [14] and give a value for the symmetric–antisymmetric splitting of  $\Delta = 21$  meV at flat-band voltage, in quite good agreement with an effective mass model. The PLE also indicates that the QW1 and QW2 involve transitions to the lowest heavy hole states of the two wells.

Note that almost all of the observed EL arises from electrons in the lower E1 state of the conduction band QWs, even when the device is biased for resonant tunneling into E2. We attribute this to the rapid thermalization of electrons from E2 to E1 by the emission of optic phonons. From the PLE measurement we find that the E2–E1 splitting exceeds  $\hbar\omega_L = 36$  meV for  $V \geq 1.75$  V. Optic phonon emission occurs on a timescale  $\tau_{LO} \approx 0.3$  ps, much faster than the radiative recombination time ( $\tau_{rad} \approx 1$  ns) and the tunneling-out time, which we estimate to be 4 ns [15]. The much lower intensity of QW2 relative to QW1 indicates that the holes also relax their energy (H2  $\rightarrow$  H1) on a timescale much less than  $\tau_{rad}$ .

The existence of intrinsic bistability depends on a significant space-charge in the region of the QWs at resonance [9,10]. On the high current section of the bistability loop, the voltage drop across the emitter barrier remains approximately constant with increasing bias so that the energy alignment of the emitter and quantum well state

is maintained. The additional voltage is dropped across the collector barrier and is given by the space charge build-up in the QW. From magnetotunneling measurements we estimate that the electron sheet density in E1 at the peak of the E2 resonance in  $I(V)$  is  $\sim 3 \times 10^{11} \text{ cm}^{-2}$ . On the off-resonance, low current section of the loop, the energy of the QW state is below that of the emitter and the QW is uncharged. In a simple double-barrier p–i–n diode, charge buildup should be inhibited by recombination and the cancellation of electron and hole charge. It seems likely that the strong spatial separation of the electron and hole charge in this triple barrier device helps give rise to the observed bistability on E2, with the electron charge residing in E1.

Although both the QW1 and QW2 intensity plots show a bistability loop in the region of E2 similar to that in  $I(V)$ , the QW1 intensity steadily falls beyond the peak of the H2 resonance, and remains flat as the voltage is increased to the peak of E2. In contrast, QW2 shows a pronounced peak in intensity at the peak of E2. We attribute the different dependence of QW1 com-

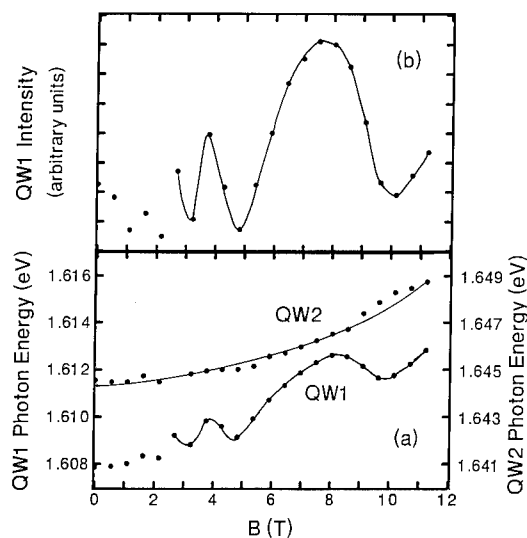


Fig. 6. (a) Variation of the energy of the QW1 and QW2 lines as a function of magnetic field; (b) variation of intensity of QW1 line as a function of  $B$ . The device is biased at  $V = 1.80$  V, on the peak of the H2 resonance.

pared to QW2 around E2 to either the decreasing overlap between E1 and H1 states with increasing bias or else the increasing transfer of holes to H1.

In the presence of a magnetic field,  $B$ , applied perpendicular to the plane of the QWs, the energy of the EL line QW2 shows a monotonic quadratic shift to higher energy, consistent with excitonic recombination. This is shown in Fig. 6a for a bias of 1.80 V, on the peak of the H2 resonance. The energy of the QW1 line also shifts to higher energy at a similar rate but with an oscillatory component, periodic in  $1/B$ . The intensity of QW1 also oscillates in a similar way – see Fig. 6b. Oscillatory structure of the same period is observed in the tunnel current  $I(B)$  and arises from the passage of Landau levels through the Fermi energy of the 2D electron gas in the accumulation layer on the n-type side [15]. These oscillations provide an accurate measure of the electron sheet density  $n_{\text{ea}}$  in this layer as a function of  $V$ . We attribute their appearance in the intensity and energy of the QW1 line to variations in the electric field in the quantum well region, caused by the change in  $n_{\text{ea}}$  when Landau levels are depopulated with increasing  $B$ . The spatially indirect QW1 line is especially sensitive to these variations.

In summary, we have observed intrinsic bistability in the EL emission and  $I(V)$  curves of a p–i–n triple barrier resonant tunneling diode. Spatially direct and indirect transitions are observed from the coupled wells. The latter emission is voltage tunable.

This work is supported by the Science and Engineering Research Council, UK and the European Community (ESPRIT Programme).

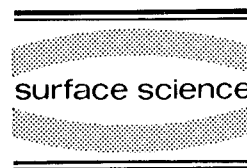
## 1. References

- [1] L.L. Chang, L. Esaki and R.L. Tsu, Appl. Phys. Lett. 24 (1974) 595.
- [2] R.K. Hayden, D.K. Maude, L. Eaves, E.C. Valadares, M. Henini, F.W. Sheard, O.H. Hughes, J.C. Portal and L. Cury, Phys. Rev. Lett. 66 (1991) 1749.
- [3] J.F. Young, B.M. Wood, G.C. Aers, R.L.S. Devine, H.C. Liu, D. Landheer, M. Buchanan, A.J. Springthorpe and P. Mandeville, Phys. Rev. Lett. 60 (1988) 2085.
- [4] N. Vojdani, D. Cote, D. Thomas, B. Sermage, P. Bois, E. Costard and J. Nagle, Appl. Phys. Lett. 56 (1990) 33.
- [5] M.S. Skolnick, D.G. Hayes, P.E. Simmonds, A.W. Higgs, G.W. Smith, H.J. Hutchinson, C.R. Whitehouse, L. Eaves, M. Henini, O.H. Hughes, M.L. Leadbeater and D.P. Halliday, Phys. Rev. B 41 (1990) 10754.
- [6] C.R.H. White, M.S. Skolnick, L. Eaves, M.L. Leadbeater, M. Henini, O.H. Hughes, G. Hill and M.A. Pate, Phys. Rev. B 45 (1992) 6721.
- [7] H.B. Evans, L. Eaves, C.R.H. White, M. Henini, P.D. Buckle, T.A. Fisher, D.J. Mowbray and M.S. Skolnick, Proc. NATO ARW on Frontiers of Optical Phenomena in Semiconductor Structures of Reduced Dimensions, July 1992, Yountville, USA; See also C.R.H. White, H.B. Evans, L. Eaves, P.M. Martin, M. Henini, G. Hill and M.A. Pate, Phys. Rev. B 45 (1992) 9513.
- [8] C. van Hoof, J. Genoe, R. Mertens, G. Borghs and E. Goovaerts, Appl. Phys. Lett. 60 (1992) 77.
- [9] V.J. Goldman, D.C. Tsui and J.E. Cunningham, Phys. Rev. Lett. 58 (1987) 1256.
- [10] E.S. Alves, L. Eaves, M. Henini, O.H. Hughes, M.L. Leadbeater, F.W. Sheard, G.A. Toombs, G. Hill and M.A. Pate, Electron. Lett. 24 (1988) 1190.
- [11] A. Alexandrou, J.A. Kash, E.E. Mendez, M. Zachau, J.M. Hong, T. Fukuzawa and Y. Hase, Phys. Rev. B 142 (1990) 9225.
- [12] T. Fukuzawa, E.E. Mendez and J.M. Hong, Phys. Rev. Lett. 64 (1990) 3066.
- [13] Y.J. Chen, E.S. Koteles, B.S. Elman and C.A. Armiento, Phys. Rev. B 36 (1987) 4562.
- [14] P.A. Harrison et al., to be published.
- [15] M.L. Leadbeater, E.S. Alves, F.W. Sheard, L. Eaves, M. Henini, O.H. Hughes and G.A. Toombs, J. Phys. Condensed Matter 1 (1988) 10605.



ELSEVIER

Surface Science 305 (1994) 358–362



# Excitonic correction to resonant tunneling

Gerrit E.W. Bauer

*Faculty of Applied Physics and DIMES, Delft University of Technology, 2628 CJ Delft, Netherlands*

(Received 16 April 1993; accepted for publication 13 June 1993)

## Abstract

Coulomb interlayer interactions are predicted to modify the tunneling process through a thin barrier when a large bias is applied. Magnetotunneling experiments between quasi-two-dimensional systems should provide evidence of bound excitonic states in terms of characteristic cusps in the tunneling resonance energy at integer filling factors.

The electron–electron interaction causes various effects on tunneling in small semiconductor structures, e.g. bistability in double-barrier resonant-tunneling devices [1], and the Coulomb blockade [2,3]. When the potential barrier is sufficiently thin, the Coulombic coupling between the half spaces can give rise to new effects like Coulomb drag between barrier-separated electron gases on transport *parallel* to the interfaces [4]. Here a theoretical discussion of the effects of the interlayer Coulomb interaction on the transport *normal* to the barrier, i.e., on the tunneling rate, is presented. Significant modifications are predicted for tunneling between quasi-two-dimensional (Q2D) systems [5–7], which are strongly modulated by an applied magnetic field. The theoretical findings should be verifiable by tunneling experiments in resonant tunneling diodes where the emitter is a quasi-two-dimensional electron or hole gas [7] or on independently contacted quantum wells separated by a few nanometers [5,6]. The recent discussion of Matveev and Larkin on correlation effects in impurity assisted tunneling [8] bears some relation to the present process.

The tunneling current through a single potential barrier can be obtained by treating the tunneling Hamiltonian,

$$H_T = \sum_{lr} \{T_{lr} d_r^\dagger c_l + \text{h.c.}\}, \quad (1)$$

as a perturbation, where  $T_{lr}$  denotes a tunneling matrix element and  $c_l$ ,  $d_r$  are annihilation operators of electron states  $l$  on the left and  $r$  on the right side of the junction, respectively. The current  $I_T$  through a barrier separating two metals can then, in general, be expressed in terms of the electron–hole Matsubara Green function  $G$  as [9]:

$$I_T(\Delta\mu) = -4e/\hbar \sum_{lr} \sum_{l'r'} T_{lr} T_{l'r'}^\dagger \times \text{Im } G(l, r, l', r'; -\Delta\mu/\hbar), \quad (2)$$

where  $\Delta\mu/e$  is the applied bias.

$$G(l, r, l', r'; i\omega) = - \int_0^\beta d\tau e^{i\omega\tau} \langle T_r d_r^\dagger(\tau) c_l(\tau) c_{l'}^\dagger(0) d_{r'}(0) \rangle, \quad (3)$$

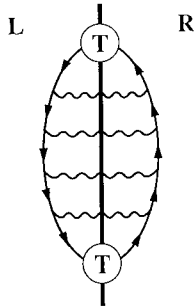


Fig. 1. Typical term in the diagrammatic series which is summed in the ladder approximation. The wavy line is the screened Coulomb interaction. The downward-directed arrows depict hole propagators on the left and the upward-directed arrows represent electron propagators on the right.

where  $T_\tau$  orders the imaginary time  $\tau$ , and  $\beta$  is the reciprocal temperature. When the Coulomb interaction is neglected, Eq. (2) reduces to the standard equation:

$$I_T(\Delta\mu) = (4\pi e/\hbar) \sum_{lr} |T_{lr}|^2 \delta(\Delta\mu + \xi_l - \chi_r) \times [f_L(\xi_l) - f_R(\chi_r)], \quad (4)$$

where  $\xi_l$ ,  $\chi_r$  and  $f_L$ ,  $f_R$  denote the single-particle energies and Fermi occupations of both sides, respectively. The novel aspect of the present problem is the dressing of the tunneling vertex by the interlayer Coulomb interaction, which is treated here in the ladder approximation and the statically screened interlayer Coulomb interaction [10]. A typical diagram of the terms to be summed is shown in Fig. 1.

To illustrate the general idea let us turn to a specific example, namely the tunneling between two Q2D systems [5–7]. Self-energies including image charge effects are treated in the quasi-particle approximation and are absorbed in the single-particle energies. The single-particle states are relabeled as  $l \rightarrow l, p$  and  $r \rightarrow r, k$  where  $l$  and  $r$  are now quantum well confinement states on respective sides and  $p, k$  denote in-plane wave vectors. Disregarding a small intersubband band mixing and the matrix character of many-subband screening, the Green function is diagonal in  $l$

(left) and  $r$  (right) and the Bethe–Salpeter equation reads:

$$\sum_{p''} \{ (i\hbar\omega + \xi_{lp} - \chi_{rk}) \delta_{p,p''} - V_{lr}^S(|p'' - p|) \} \times G_{lr}(p'', k'', p', k'; i\omega) = (f_L(lp) - f_R(rk)) \delta_{p,p'} \delta_{k,k'}, \quad (5)$$

with

$$V_{lr}^S(q) = \frac{2\pi e^2}{\kappa q \epsilon(q; 0)} F_{lr}(q), \quad (6)$$

where  $\kappa$  is the dielectric constant of the medium,  $\epsilon(q; 0)$  is the static dielectric function and  $F_{lr}(q)$  is a form factor.  $k' = p - p' + k$  and  $k'' = p - p'' + k$ , since the Coulomb interaction conserves transverse momentum.

It follows from Eq. (5) that the effect vanishes in a regime where linear response theory is applicable, since at equilibrium  $f_L - f_R = 0$  on average, and is maximized for the tunneling into a completely empty confinement state. This can be achieved by tunneling into an excited subband [5], which has the drawback of intersubband decay channels, however. Here a system is considered, in which the barrier distance is chosen such that the confinement state on the right is empty at zero bias (Fig. 2 shows the band profiles for an applied bias). Furthermore, the tunneling barrier on the right is assumed to be more transparent

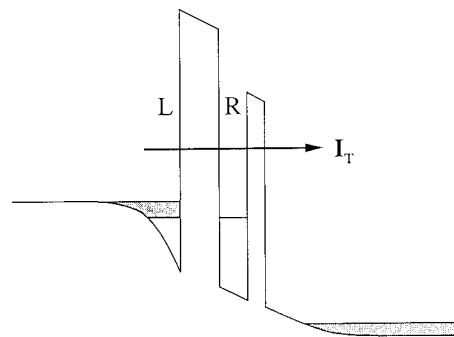


Fig. 2. Band diagram of a tunneling device under consideration in the present paper. Excitonic effects are strong when the left barrier is sufficiently thin but thick enough for the tunneling formalism to apply. The tunneling lifetime of the right barrier should be smaller than that of the left barrier to avoid charge accumulation.

than the barrier on the left such that charge accumulation does not occur. At zero temperature, Eq. (5) can be solved analytically when the interaction is short-ranged in the lateral direction ( $V_{lr}^S(q) \equiv \bar{V}$ ). Denoting by  $\mathbf{Q}$  the momentum transfer by the tunneling matrix element and considering only a single confinement state:

$$\sum_{p,p'} G(\mathbf{p}, \mathbf{p}', \mathbf{Q}; i\omega) = \frac{\sum_p G^{(0)}(\mathbf{p}, \mathbf{Q}; i\omega)}{1 + \bar{V} \sum_p G^{(0)}(\mathbf{p}, \mathbf{Q}; i\omega)}, \quad (7)$$

where

$$G^{(0)}(\mathbf{p}, \mathbf{Q}; i\omega) = \frac{f_L(\mathbf{p})}{i\hbar\omega - \xi_p + \chi_{p+\mathbf{Q}}}. \quad (8)$$

The tunneling current can now be obtained easily in different limiting cases. For the structures considered the single-particle dispersions are equal on the right and left side. When the wave vector is conserved, i.e.  $T_{p,p'} \equiv \delta_{p,p'} T_c$ , we have  $\mathbf{Q} = 0$  and

$$I_T^c(\Delta\mu) = (4e\pi/\hbar) |T_c|^2 N_L \delta(\Delta\mu + \rho_L \bar{V}). \quad (9)$$

The  $\delta$ -function tunneling resonance shifts to a lower bias by  $\rho_L \bar{V}$ , where  $\rho_L$  is the electron density (and  $N_L$  the number of electrons) in the left well. On the other hand, when the wave vector is not considered ( $T_{p,p'} \equiv T_{nc}$ ), the expression

$$I_T^{nc}(\Delta\mu) = (4e/\hbar) |T_{nc}|^2 \times \sum_{\mathbf{Q}} \sum_{p,p'} \text{Im} G(\mathbf{p}, \mathbf{p}', \mathbf{Q}; \Delta\mu) \quad (10)$$

is slightly more complicated and the result is displayed schematically in Fig. 3. The ohmic resistance at the threshold is reduced.

Physically, these results can be interpreted as an excitonic final-state effect. The electron which tunnels through the barrier forms a bound state with the hole left behind. The energy gain leads to a reduction of the tunneling resonance energy or resistance at threshold, respectively. The exciton binding energy scales with the electron density difference, reflecting the size of the phase space available to form a bound state, and the

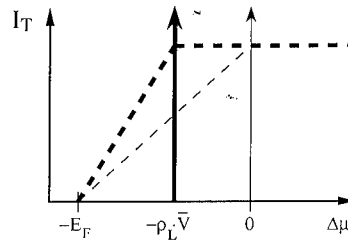


Fig. 3. Schematic tunneling rate  $I_T$  between two Q2D-systems as a function of an externally applied bias  $\Delta\mu$ . The results in the absence of excitonic effects (dashed lines) are modified by a wave-vector-independent interlayer interaction  $\bar{V}$  as shown for the two limiting cases of wave-vector conservation and non-conservation during tunneling.  $\Delta\rho_L$  is the electron density in the left well.  $\Delta\mu = 0$  corresponds to an applied voltage which aligns the subbands of both wells.

interlayer interaction strength. In contrast to conventional Wannier excitons the formation of the bound state does not cost kinetic energy, since the effective masses are equal. Therefore the binding energy can be large in spite of the screening. There is also no enhancement of the tunneling current.

A situation similar to that considered by Matveev and Larkin [8] can be obtained by letting the effective mass on the right side go to infinity and assuming a non- $k$ -conserving tunneling process. This process is not physically relevant for tunneling studies, but equivalent to the optical emission process caused by the electron capture of a neutral acceptor, where the *final* state is excitonic. While the process considered by Ref. [8] corresponds formally to X-ray core-hole absorption, the present one is *not* equivalent to X-ray emission, where the *initial* state is excitonic. The tunnel current in the present mean-field model then reads

$$I_T^\infty(\Delta\mu) = (4e/\hbar) |T_{nc}|^2 D_0 \times \text{Im} \frac{\ln(1 + E_F/\Delta\mu)}{1 + \bar{V} D_0 \ln(1 + E_F/\Delta\mu)}, \quad (11)$$

where  $D_0$  and  $E_F$  are the two-dimensional density of states and Fermi energy, respectively. The result in Fig. 4 is quite different from that in Fig. 3, displaying a split-off bound excitonic state. Higher order scattering processes merge the dis-

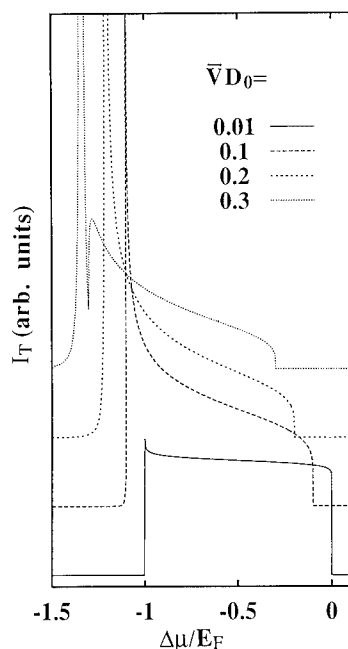


Fig. 4. Tunneling spectra of a 2D electron gas to a neutral, localized state on the right-hand side as a function of the interlayer interaction strength. The spectra are arbitrarily shifted with respect to each other. The bound state at the lower band edge has been convoluted by a Lorentzian.

crete state with the continuum for small binding energies, but the enhancement at the Fermi edge remains [8].

More involved calculations for the experimentally important case of full conservation of the wave vector [5–7] are necessary to investigate the effects of a more realistic interaction and applied magnetic fields. The numerical method of solving the Bethe–Salpeter equation is similar to that used for calculations of optical spectra of modulation-doped quantum wells [11], and details are given in Ref. [12]. Just like in the short-range interaction model, the tunneling current turns out to be dominated by the ground state tunneling resonance, which is plotted in Fig. 5 as a function of magnetic field normal to the interface. A strong modulation of the resonance is found. When the Landau levels are completely occupied, the exciton binding energy abruptly increases because of the reduced screening of the interlayer Coulomb interaction. This effect is

larger than the competing effect of the magnetic field dependence of the self-energies [13]. Downward cusps of the tunneling resonance at integer filling would therefore constitute a clear indication of the existence of interface bound states.

The bound state has a finite lifetime determined by the tunneling rates, by the lifetime of the hole ( $\sim 1$  ps [14]), and impurity and interface roughness scattering. Higher order scattering processes will also contribute to the broadening. Since the short-range potential is found here to be a good approximation, the calculation of the tunneling lineshape along the lines of Ref. [8] is possible, though the finite mass of the hole is a complicating factor [15]. The predicted effects are observable when the lifetime broadening is sufficiently smaller than the binding energies such that the interface bound states are well defined.

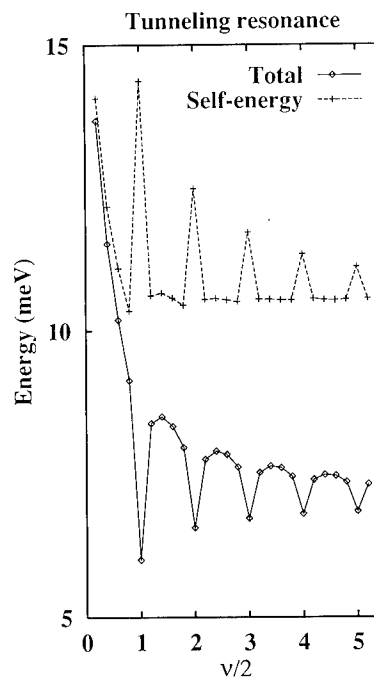


Fig. 5. Tunneling resonance energy as function of magnetic field normal to the interfaces. The filling factor is related to the density of  $\rho_L = 5 \times 10^{11} \text{ cm}^{-2}$  in the left well. The interwell distance is  $d = 200 \text{ \AA}$ . The zero of the applied bias has been chosen to correspond to the alignment of the non-interacting subbands. The dashed line shows the center of gravity of the tunneling spectrum when the exciton effect is neglected.

In conclusion, Coulomb local-field corrections to the tunneling rate have been investigated and significant effects on the 2D–2D (magneto) tunneling rate in the non-linear regime have been found for realistic device parameters.

This work is part of the research program of the “Stichting voor Fundamenteel Onderzoek der Materie (FOM)”, which is financially supported by the “Nederlandse Organisatie voor Wetenschappelijk Onderzoek (NWO)”.

### 1. Note added in proof

Very recently Boebinger et al. [Phys. Rev. B 47 (1993) 16608] carried out tunneling experiments on devices which are identical to those proposed here. These experiments support the important model assumption that a sharp tunneling resonance exists in high-mobility resonant tunneling diodes which do not accumulate charge. Furthermore, the increased broadening of the resonance at integer fillings demonstrates the importance of magnetic field dependent screening. Unfortunately, the resonance energy is dominated by the pinning of the emitter Fermi energy to that of the bulk, which means that the modulation of the latter has to be added to the resonance as calculated here. The excitonic correction is then only a relatively small contribution to the energy modulation and the experiments are inconclusive about its existence. Still excitonic effects should be very significant on the scale of many-body effects in the density of states of the left electron gas. An intriguing feature which cannot be explained by the present theory is the increased tunneling current at integer fillings. This could be

due to a modulation of the wave function perpendicular to the interfaces, or to higher order scattering effects, which are suppressed when the Fermi energy lies in a gap.

### 2. References

- [1] V.J. Goldman, D.C. Tsui and J.E. Cunningham, Phys. Rev. Lett. 58 (1987) 1256.
- [2] D.V. Averin and K.K. Likharev, in: Mesoscopic Phenomena in Solids, Eds. B.L. Altshuler, P.A. Lee and R.A. Webb (North-Holland, Amsterdam, 1991); C.W.J. Beenakker, Phys. Rev. B 44 (1991) 1646.
- [3] Yu.V. Nazarov, Zh. Eksp. Teor. Fiz. 95 (1989) 975 [Sov. Phys. JETP 68 (1989) 561]; M.H. Devoret et al., Phys. Rev. Lett. 64 (1990) 1824; S.M. Girvin et al., Phys. Rev. Lett. 64 (1990) 3183.
- [4] P.M. Solomon, P.J. Price, D.J. Frank and P.C. La Tulipe, Phys. Rev. Lett. 63 (1989) 2508; T.J. Gramila, J.P. Eisenstein, A.H. MacDonald, L.N. Pfeiffer and K.W. West, Phys. Rev. Lett. 66 (1991).
- [5] J. Smoliner, E. Gornik and G. Weimann, Phys. Rev. B 39 (1989) 12937.
- [6] J.P. Eisenstein, L.N. Pfeiffer and K.W. West, Appl. Phys. Lett. 58 (1991) 1497.
- [7] L. Eaves, R.K. Hayden, M.L. Leadbetter, D.K. Maude, E.C. Valadares, M. Henini, F.W. Sheard, O.H. Hughes, J.C. Portal and L. Cury, Surf. Sci. 263 (1992) 199.
- [8] K.A. Matveev and A.I. Larkin, Phys. Rev. B 46 (1992) 15337.
- [9] G.D. Mahan, Many-Particle Physics (Plenum, New York, 1981).
- [10] H. Haug and S. Schmitt-Rink, Prog. Quantum Electron. 9 (1984) 1.
- [11] G.E.W. Bauer, Phys. Rev. B 45 (1992) 9153.
- [12] G.E.W. Bauer, unpublished.
- [13] S. Katayama and T. Ando, Solid State Commun. 70 (1989) 97; T. Uenoyama and L.J. Sham, Phys. Rev. B 39 (1989) 11044.
- [14] S.K. Lyo, Phys. Rev. B 43 (1991) 7091.
- [15] T. Uenoyama and L.J. Sham, Phys. Rev. Lett. 65 (1990) 1048.

## Electron confinement in variable-area resonant tunnelling diodes using in-plane implanted gates

C.J. Goodings <sup>\*,a</sup>, H. Mizuta <sup>b</sup>, J.R.A. Cleaver <sup>\*,a</sup>, H. Ahmed <sup>a</sup>

<sup>a</sup> Cavendish Laboratory, Cambridge University, Cambridge CB3 0HE, UK

<sup>b</sup> Central Research Laboratory, Hitachi Ltd., Kokubunji 185, Tokyo, Japan

(Received 19 April 1993; accepted for publication 4 June 1993)

### Abstract

Novel variable-area resonant tunnelling diodes (RTDs) have been produced in which the confining potential originates from an implanted gate in the same plane as the quantum well. Results of experiments and numerical modelling have shown the confinement thus produced to be symmetric about the RTD barriers. Fine structure has been observed in large-area devices close to threshold which can be attributed to tunnelling through bound donor states in the active region of the device. Fine structure has also been seen in small-area devices which is consistent with the effects of lateral quantisation in the quantum well.

### 1. Introduction

The topic of small-area resonant tunnelling diodes (RTDs) has become of much interest recently, especially for the study of electron systems with reduced dimensionality. However, in the majority of such devices the degree of confinement is fixed during fabrication so that the most important parameter for quantisation effects, the size of the confinement potential, cannot be varied. Devices based on resonant tunnelling material in which the lateral confinement is controlled electrically are therefore of great interest for the study of electron systems with reduced dimensions.

Pioneering work has been reported in the past two years on RTD devices in which the lateral confinement is produced using a surface gate to deplete the underlying material [1–5]. However, such structures are inherently asymmetric – the confining potential originates at the surface gate which is above the plane of the resonant tunnelling barriers, leading to non-uniform lateral confinement of the quantum well. Such variations in the confinement have previously been shown to give a marked degradation of the peak-to-valley ratio (P/V) of the devices [6]. This paper describes work performed on in-plane gated variable-area RTDs (VARTDs) in which the confining potential originates in the same plane as the quantum well and so should be inherently more symmetric.

The device structure is depicted in cross-section in Fig. 1, and its fabrication has been de-

\* Corresponding author.



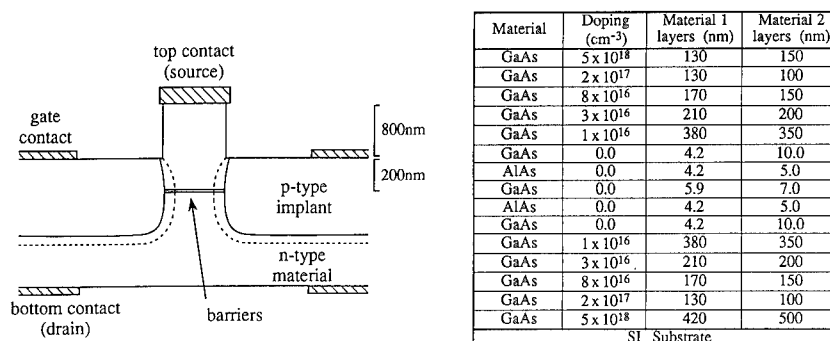


Fig. 1. Schematic cross-section of the in-plane gated RTD devices and layer structures of the materials used. The bottom contacts are displaced for clarity.

scribed elsewhere [7]. Current flows between the top and bottom contacts through the resonant tunnelling barriers, with lateral confinement being produced by an activated p-type gate region implanted into the n-type bulk material. By varying the reverse bias across the resulting p-n junction, the width of the depletion region, and hence the position of the confining potential and the area of the device, can be controlled. Results are reported here for devices fabricated on two materials, and the layer structures of these are also shown in Fig. 1. The conflict between the depth of the RTD barriers (required by the graded doping of the materials) and the maximum ion range in the material (for realistic implantation energies) is resolved by use of a pillar structure. A slight undercut to the top pad prevents implantation from occurring down the sides of the pillar, which can otherwise result in a large leakage between the top contact (source) and the gate.

## 2. Large-area devices

Measurements have been performed on various sizes of fixed-area devices fabricated by wet etching, and these show resonance voltages of +1.78 V (−1.84 V) and +0.64 (−0.76) for materials 1 and 2, respectively, as the bias magnitudes are increased (positive values refer to the top contact being positive with respect to the bottom contact). In both materials a large amount of hysteresis occurs in the resonance voltage for

increasing and decreasing sweeps of the bias due to the effects of charge build-up in the quantum well. The resonance voltages are significantly higher than those expected simply from the energy levels in the well due to the formation of a large depletion region in the low-doped layer on the collector side of the barriers [8] (where “collector” refers to the positively biased side of the device structure).

Typical characteristics for a 3 μm diameter device (lithographic dimension of the top pad) at 4.2 K fabricated on material 1 are shown in Fig. 2. As has been previously reported [7], this demonstrates control of the RTD device area at the resonant tunnelling barriers. The negative differential resistance (NDR) regions of the characteristics are vertical, but no hysteresis occurs similar to that seen in the large fixed-area devices. The peak current densities have been measured for both fixed-area and variable-area devices, and the values of the variable-area devices found to be similar to those for the fixed-area ones with charge build-up in the well. Current densities of  $540 \pm 20$  nA μm<sup>−2</sup> and  $2.0 \pm 0.1$  nA μm<sup>−2</sup> have been measured for VARTD devices on materials 1 and 2, respectively. The peak voltages have a weak dependence on gate bias which becomes more severe as the device size is reduced.

The principal advantage of this type of device over its surface-gated counterpart is the underlying symmetry of the implant about the RTD barrier layers. To verify this, the devices have

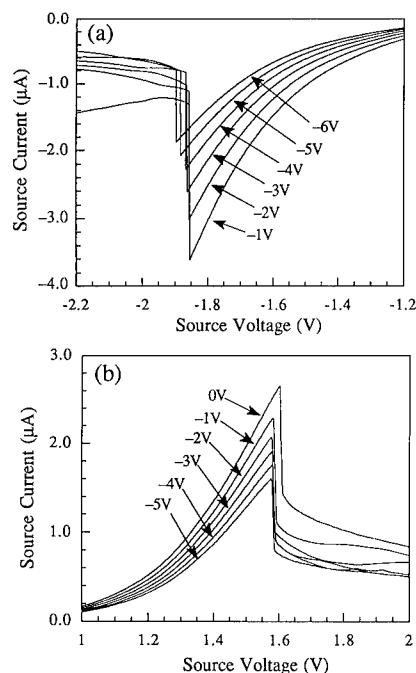


Fig. 2. Characteristics for a 3  $\mu\text{m}$  device on material 1 at 42 K for various gate biases.

been modelled using a 2D classical simulation [9] which takes account of the device structure, the graded doping within the material, the gaussian distribution of the implant and the lateral spread of the implant. The potential distribution for a 2  $\mu\text{m}$  device with a source–drain voltage of  $-1$  V and gate–drain voltage of  $-2$  V is shown in Fig. 3. Both the overall symmetry of the depletion around the barriers and the large voltage drop

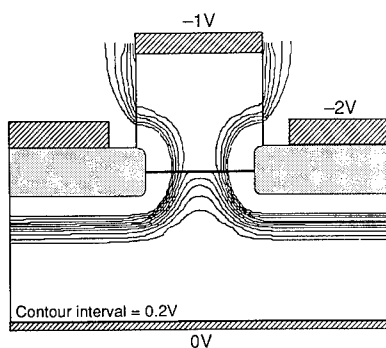


Fig. 3. Modelled potential distribution for a 2  $\mu\text{m}$  device showing the symmetry of the confining potential.

across the collector depletion region are apparent. The collector depletion, however, does appear to cause a non-uniform confinement potential immediately next to the barriers on the collector side, and this might be expected to degrade the P/V ratio of the device. Such a disadvantageous effect could be reduced by decreasing the collector depletion by use of a slightly higher doping concentration in the layers adjacent to the barriers.

The P/V ratios have been measured for a range of devices and are in broad agreement with the behaviour predicted by the above model. In particular, for a 2  $\mu\text{m}$  diameter device at 4.2 K, the P/V ratio is found to vary (with increasing gate bias) from 2.6 to 2.3 in reverse bias and from 2.5 to 2.2 in forward bias. Overall, the ratio is degraded from the large-area value of 5.9 for thin material, and this degradation increases slightly as the confinement is increased. However, the similarity between the results obtained with the channel both forward and reverse biased indicates the underlying symmetry of the confining implant.

The minimum electrical diameter of the devices fabricated on material 1 was 1  $\mu\text{m}$  – too large to show the effects of lateral quantisation. Nevertheless, fine structure has been seen for all these devices around the threshold voltage, even at a relatively high temperature of 4.2 K (Fig. 4). Typically, a weak series of plateaux occurs close to the device threshold with the structure being different in forward and reverse bias and becom-

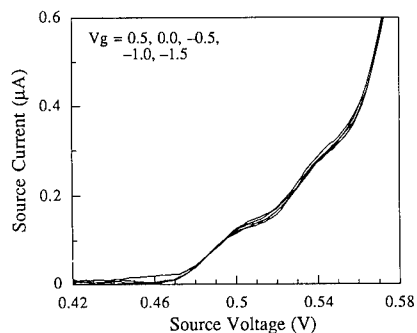


Fig. 4. Details of the  $I/V$  characteristics of a 4  $\mu\text{m}$  device on material 1 at 4.2 K showing typical fine structure found around threshold.

ing less distinct with increasing device size. Several possibilities exist for the origin of the fine structure. The first, lateral confinement, can be discounted due to the size of the devices and the invariance of the effect on gate bias. An alternative mechanism might be Coulomb blockade. However, this too should show a strong dependence on device area and hence on gate bias. Furthermore, for Coulomb blockade to be observed the electrostatic charging energy must be greater than the thermal broadening, and in these devices the capacitance is estimated to be a factor of at least 100 too large for this to be the case at 4.2 K.

The final possibility for the origin of the structure is tunnelling through donor or impurity states in the active region of the device, as observed by Dellow et al. [2,5] for a variable-area RTD confined by the depletion region from a surface gate. An ionised donor in the quantum well gives rise to a localised potential well and associated bound states through which electron tunnelling can occur for biases below the threshold voltage. The binding energy of such states depends on the position of the donors with a maximum occurring for donors in the centre of the well, and this maximum binding energy has been estimated to be about 14 meV for the present system. For large-area devices containing numerous such donors, the spread in energies due to their random distribution in the well leads to any structure becoming washed-out. However, for small devices with only a single or few donors, fine structure is expected around threshold as electrons tunnel through the bound states associated with the ionised donors.

The strongest structure is expected if only one donor is involved in the tunnelling process. In this case, only one electron at a time can contribute to the conduction, and so the plateau current,  $I$ , can be expressed as  $I = e/\tau_w$ , where  $\tau_w$  is the electron lifetime in the quantum well. Assuming that only single electron tunnelling is involved, this expression can be used to calculate the lifetime of carriers in the well. Table 1 shows the results obtained for three sizes of device, showing that the calculated lifetimes agree well with the approximate value of 500 ps derived for

Table 1

Measured values for the fine structure seen close to threshold for large-area devices on material 1 at 4.2 K and calculated carrier lifetimes in the quantum well (assuming single-electron tunnelling)

Top pad diameter ( $\mu\text{m}$ )	First plateau current (pA)	First plateau voltage (mV)	Calculated lifetime (ps)
2	500	820	320
3	250	560	640
4	150	500	1500

the large-area devices at resonance. One possible mechanism for the apparent dependence of the lifetimes on device size is the changing electric field across the collector barrier resulting from the action of the gate on the collector depletion region – for smaller devices the field is greater (indicated by the higher voltage for the first plateau) and the carrier lifetime in the well correspondingly shorter. Assuming a background doping of  $10^{14} \text{ cm}^{-3}$ , the number of donor states expected to be present in the quantum well is estimated to be between 1 and 5, consistent with the picture of single-electron or few-electron tunnelling. Since the position of a single donor state in the well is random and the symmetry of the forward and reverse bias characteristics depends upon the donor being positioned in the centre of the quantum well, there is a high probability of the characteristics showing asymmetry, as observed.

### 3. Small-area devices

A range of VARTDs with top pad diameters between 1.0 and 2.0  $\mu\text{m}$  has been fabricated to study possible lateral confinement effects, with material 2 being used to give a longer carrier lifetime in the quantum well. In particular, control of the electrical diameters down to zero has been demonstrated for devices with lithographic diameters of 1.2  $\mu\text{m}$  or less. The reverse-biased characteristics of a 1.2  $\mu\text{m}$  device are given in Fig. 5a. The device shows a reduction in the resonant current and an increase in the resonance voltage, along with a sharpening of the

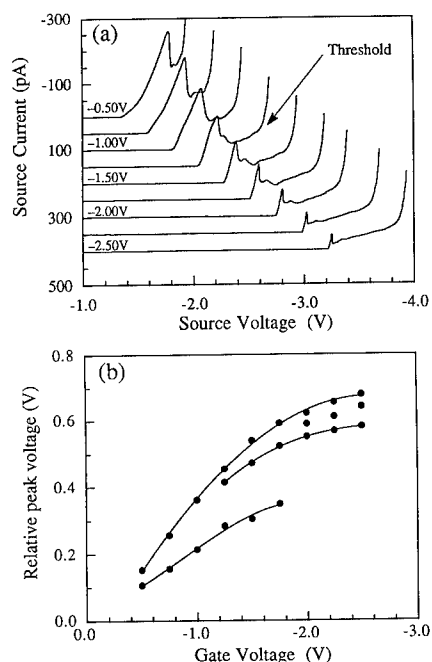


Fig. 5. Characteristics for a  $1.2 \mu\text{m}$  device on material 2 at 4.2 K showing (a) the measured  $I/V$  characteristics, and (b) the positions of the post-resonance fine structure relative to the turn-on voltage threshold of the p-n junction.

main resonance peak and extra structure in the valley current.

The voltage position of the observed fine structure can be calibrated relative to the p-n forward-bias thresholds (seen in the figure). Due to the unknown size of the depletion region on the collector side of the barriers, the absolute voltages of the peaks are not meaningful. However, the p-n threshold relates the source (emitter) voltage to the gate voltage, and so can be used as a reference point. Using this property, the energy of any levels responsible for the fine structure can be related to the energy of the emitter levels by considering the relative voltages between the p-n junction turn-on threshold and any observed structure. Values of relative peak voltage versus gate voltage are plotted for the observed peaks in Fig. 5b, which appears to show some splitting of the structure up to a gate voltage of about  $-2.0 \text{ V}$ , followed by a common shift in the relative peak positions.

The main interest in the fine structure is whether it might be due to lateral confinement effects [10,11]. To investigate this possibility, the lateral confinement potential has been modelled and has been found to be roughly parabolic in the plane of the barriers. As the gate bias is increased, the lateral confinement becomes progressively narrower until at about  $-2.0 \text{ V}$  a minimum size is reached, after which the lateral confinement well is simply shifted upwards in energy without alteration of shape. Such a result is consistent with the observations of a splitting of levels followed by a uniform shift. The modelling also successfully predicts an increased splitting and earlier levelling of the results obtained for the smaller devices. The sharpening of the resonance peaks with gate voltage may be due to a reduced charge build-up in the quantum well or, if lateral quantisation effects are occurring, to the splitting of a merged set of subbands into discrete states.

An approximate calculation can be performed to estimate the magnitude of the expected splitting of levels. Assuming a parabolic confining potential, and using the model to provide the size of the confinement, a level splitting in the quantum well of about  $5.5 \text{ meV}$  has been calculated for  $V_g = -1.5 \text{ V}$ . This can then be calibrated with the measured voltage by considering the position of the main resonance peak, resulting in a predicted peak separation of about  $150 \text{ mV}$ , which is consistent with that observed. Whilst this cannot be taken as conclusive proof of lateral quantisation in the well, the results clearly demonstrate the use of implanted-gate VARTDs to produce systems in which the lateral confinement effects become significant.

#### 4. Summary

In conclusion, a new method for the fabrication of variable-area RTDs has been demonstrated, in which the confining potential originates from an in-plane implanted gate. Both modelling and experimental results have been used to confirm the underlying symmetry of the device structure. Fine structure has been ob-

served in the  $I/V$  characteristics of relatively large area devices which has been attributed to the tunnelling of electrons through donor states in the active layers of the device. Finally, additional fine structure has been seen in the valley current of small-area devices which is consistent with the effects of level splitting in the quantum well due to lateral quantisation.

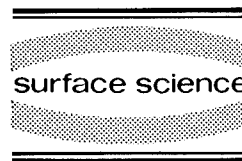
## 5. References

- [1] M.W. Dellow, P.H. Beton, M. Henini, P.C. Main and L. Eaves, *Electron. Lett.* 27 (1991) 134.
- [2] M.W. Dellow, P.H. Beton, C.J.G.M. Langerak, T.J. Foster, P.C. Main, L. Eaves, M. Henini, S.P. Beaumont and C.D.W. Wilkinson, *Phys. Rev. Lett.* 68 (1992) 1754.
- [3] P. Gu  ret, N. Blanc, R. Germann and H. Rothuizen, *Phys. Rev. Lett.* 68 (1992) 1896.
- [4] P. Gu  ret, N. Blanc, R. Germann and H. Rothuizen, *Semicond. Sci. Technol.* 7 (1992) B462.
- [5] M.W. Dellow, C.J.G.M. Langerak, P.H. Beton, T.J. Foster, P.C. Main, L. Eaves, M. Henini, S.P. Beaumont and C.D.W. Wilkinson, *Surf. Sci.* 263 (1992) 438.
- [6] P.H. Beton, M.W. Dellow, P.C. Main, T.J. Foster, L. Eaves, A.F. Jezierski, M. Henini, S.P. Beaumont and C.D.W. Wilkinson, *Appl. Phys. Lett.* 60 (1992) 2508.
- [7] C.J. Goodings, J.R.A. Cleaver and H. Ahmed, *Electron. Lett.* 28 (1992) 1535.
- [8] V.J. Goldman, D.C. Tsui and J.E. Cunningham, *Phys. Rev. B* 35 (1987) 9387.
- [9] H. Mizuta, K. Yamaguchi, M. Tanoue and S. Takahashi, *IEEE Trans. Electron Devices* ED-36 (1989) 2307.
- [10] Bo Su, V.J. Goldman, M. Santos and M. Shayegan, *Appl. Phys. Lett.* 58 (1991) 747.
- [11] S. Tarucha, Y. Hirayama, T. Saku and T. Kimura, *Phys. Rev. B* 41 (1990) 5459.



ELSEVIER

Surface Science 305 (1994) 369–374



## Electron transport via resonantly coupled energy levels in triple barrier structure investigated by magnetotunneling spectroscopy

H. Kurata <sup>\*,a,1</sup>, H. Sakaki <sup>a,b</sup>

<sup>a</sup> Quantum Wave Project, ERATO, Research Development Corporation of Japan, Keyaki-House 302, 4-3-24 Komaba, Meguro-ku, Tokyo 153, Japan

<sup>b</sup> Research Center for Advanced Science and Technology, University of Tokyo, 4-6-1 Komaba, Meguro-ku, Tokyo 153, Japan

(Received 23 May 1993; accepted for publication 13 July 1993)

### Abstract

Magnetotunneling spectroscopy in a series of GaAs/AlAs triple barrier diodes was performed to clarify the effect of scatterings and dimensionality of electronic states on the resonant tunneling transport. We found a variety of  $I$ - $V$  characteristics in such diodes and differences in the behavior of the observed peaks in a magnetic field. By analyzing  $I$ - $V$  characteristics in a magnetic field and magneto-oscillations of the tunnel current, we revealed that three different tunneling processes are responsible for the peaks.

Resonant tunneling in double barrier (DB) diodes in high magnetic fields has been studied extensively [1,2]. In particular, the DB structure with a large spacer layer (undoped or lightly doped GaAs layer) has attracted much attention, because its tunneling current is dominated by 2D–2D tunneling from the quantized energy level formed in the accumulation layer of the emitter to an energy level in the quantum well (QW) [3–5]. In this structure various features related to scattering-assisted processes have been revealed in a high magnetic field  $B_{\parallel}$  applied parallel to the current. However, the quantized states in the accumulation layer cannot be considered as an ideal 2D electron reservoir if we change the bar-

rier thickness for instance. We cannot neglect the electron transport process from the 3D highly doped layer to the accumulation layer when 2D–2D tunneling is faster. Moreover, a need for a self-consistent determination of energy levels in the accumulation layer makes the interpretation of the experimental results difficult. Hence it is not easy in such DB structures to examine 2D–2D tunneling processes systematically by changing the device structure. In triple barrier (TB) structures, we can arbitrarily control the strength of coupling of 2D states in two QWs by changing the thickness of the center barrier. In this case the change in barrier thickness does not substantially affect the position of quantized energy levels in the QWs. In addition, electron tunneling from the 3D emitter to 2D states in the QW can also be controlled in a TB structure. Hence the TB structure is suitable for examining systematically how the dimensionality of electronic states affects the

\* Corresponding author.

<sup>1</sup> Present Address: Fujitsu Laboratories, 10-1 Morinosato-Wakamiya, Atsugi-shi, Kanagawa 243-01, Japan.

resonant tunneling transport. In this work we performed magnetotunneling spectroscopy in magnetic fields  $B_{\parallel}$  at 4.2 K to reveal how the electron scattering affects various tunneling processes involved in the electron transport through the TB structure.

We prepared three GaAs/AlAs TB structures by molecular beam epitaxy (MBE) and fabricated mesa diodes with AuGeNi alloyed contacts by conventional photolithography techniques. The three TB structures have a 100 Å QW and a 50 Å QW separated by a center barrier of different thickness: 17 Å (6 monolayer (ML)) for sample A, 45 Å (16 ML) for B, and 31 Å (11 ML) for C, as shown in Fig. 1a. The outer barriers are all 31 Å (11 ML thick). The thickness of the collector-side

spacer layer (undoped GaAs) is 100 Å for A and B, and 300 Å for C. The spacer layer prevents the segregation of Si dopant during MBE growth, and also works to magnify the  $I$ - $V$  characteristics along the voltage axis. Since the emitter-side spacer (15 Å for all samples) is thin enough and the emitter ( $n^+$  GaAs) is heavily doped (nominally  $1 \times 10^{18} \text{ cm}^{-3}$ ), we can neglect the formation of an accumulation layer at the emitter. The  $I$ - $V$  characteristics of these samples at 4.2 K have shown a variety of peaks which are labeled P1, P2, and P3 as shown in Fig. 1. Note that only the positions of peaks in sample C shift to higher voltage as compared with those in other samples because of the thicker spacer. All the peaks in Fig. 1 are related to various tunneling paths be-

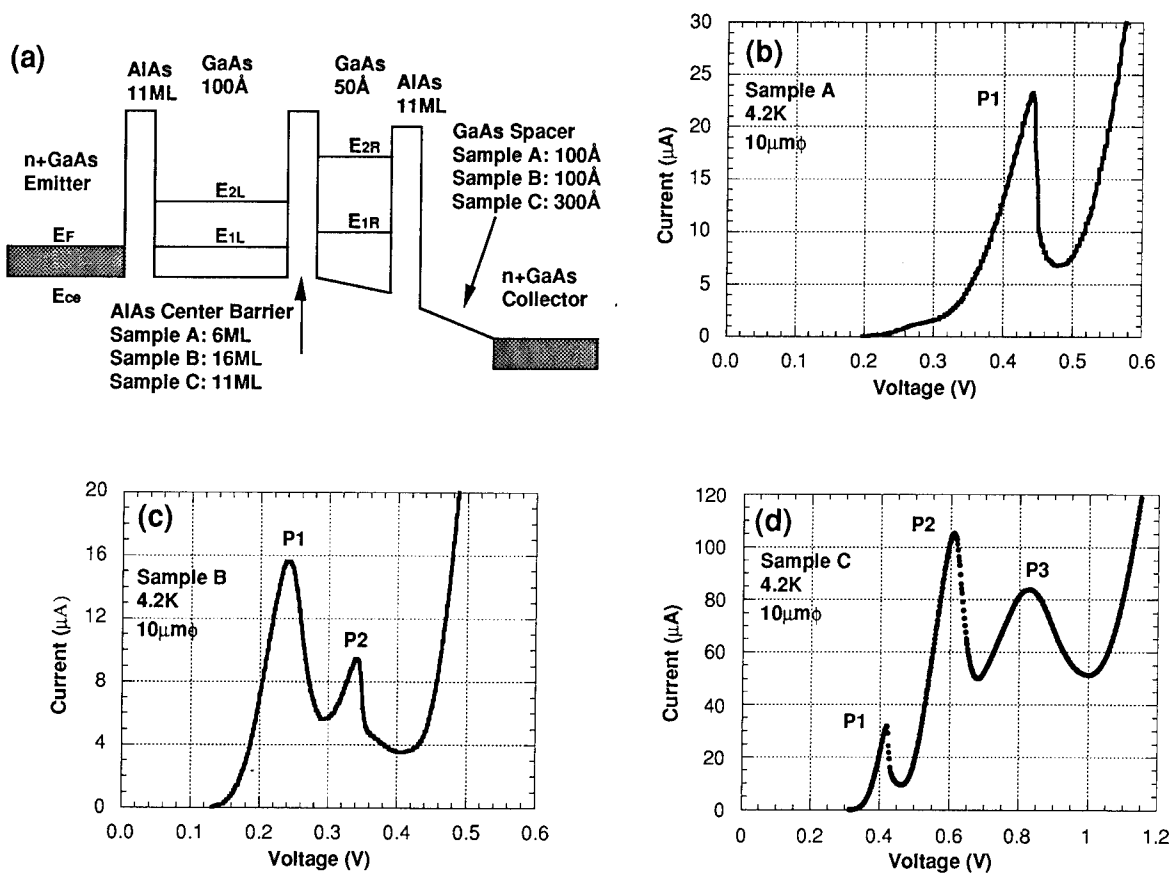


Fig. 1. (a) Schematic illustration of the triple barrier structure. The  $I$ - $V$  characteristics at 4.2 K are shown in (b) sample A, (c) sample B, and (d) sample C. The diameter of all diodes is  $10 \mu\text{m}$ . Note that the  $I$ - $V$  characteristics of sample C shift to higher voltage due to the thicker spacer.

tween the ground level of the emitter-side 100 Å QW (level  $E_{1L}$ ) and that of the collector side 50 Å QW (level  $E_{1R}$ ). These differences in  $I$ - $V$  characteristics result from the differences in dominant tunneling processes. They include (1) 3D–2D elastic tunneling from the emitter to  $E_{1L}$ , (2) 2D–2D elastic tunneling from  $E_{1L}$  to  $E_{1R}$ , and (3) 2D–2D scattering-assisted tunneling from  $E_{1L}$  to  $E_{1R}$ .

One can find three peaks (P1, P2, and P3) in the  $I$ - $V$  characteristics of sample C (Fig. 1d). As mentioned before, we attribute all the peaks to transport via ground levels  $E_{1L}$  and  $E_{1R}$  in each QW. The peaks P2 and P3 are not ascribed to the resonance between  $E_{1L}$  and  $E_{2R}$  (the second energy level in 50 Å QW), because we cannot explain the peak position considering the energy difference between  $E_{1R}$  and  $E_{2R}$  (400 meV). In addition, the similar current density of these peaks (40–140 A/cm<sup>2</sup>) shows that electron injection into  $E_{2L}$  (the second energy level in 100 Å QW) from the emitter is not involved. In this TB structure, tunnel current is mainly determined by the electron injection process from the emitter to 100 Å QW. Hence the current density is estimated by  $N_s/\tau_{IN}$ , where  $\tau_{IN}$  is the tunnel rate and  $N_s$  is the effective sheet concentration of electrons in the emitter. The tunnel rate  $\tau_{IN}$  is determined by the level broadening  $\Delta E$  associated with the finite lifetime of the energy levels in 100 Å QW. Thus the peak current density determined by the electron injection into  $E_{2L}$  must be one order of magnitude larger than that determined by the electron injection into  $E_{1L}$  according to the calculated energy width  $\Delta E$ .

The  $I$ - $V$  characteristics of sample C measured in fixed  $B_{||}$  showed two characteristic behaviors, as shown in Fig. 2. First, only the peak current density of P2 is reduced in high  $B_{||}$ ; the other two peaks (P1 and P3) are scarcely changed. Second, some additional structures appear in the  $I$ - $V$  characteristics and those of P3 do not change their position with increasing  $B_{||}$ . Such remarkable features indicate the difference in the origin of the three peaks. To confirm such features we also performed similar measurements in pulsed high magnetic field up to 35 T at 4.2 K. We show the change in the peak current of sample C in

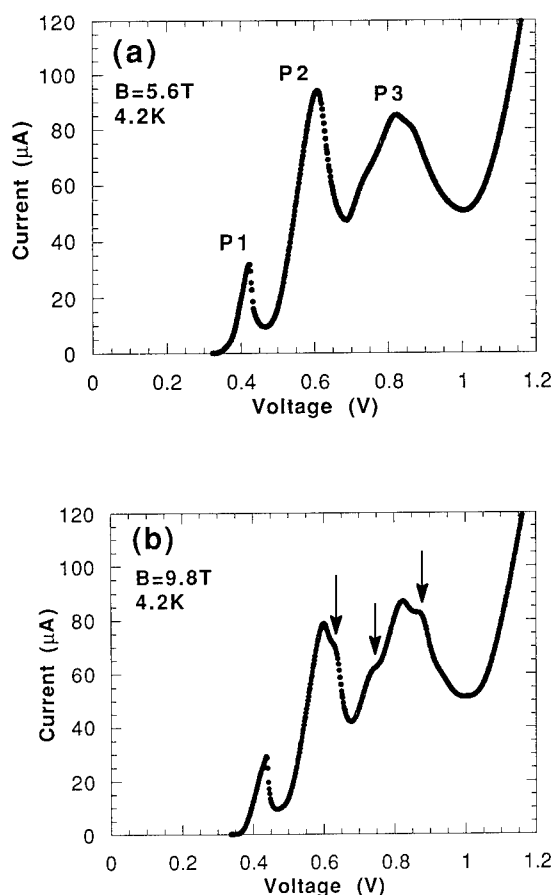


Fig. 2. The  $I$ - $V$  characteristics of sample C measured for the magnetic field of (a) 5.6 T and (b) 9.8 T at 4.2 K. One can find the reduction of P2 as compared with Fig. 1d. The additional structures are indicated by arrows in (b).

Fig. 3a. That of P1 in samples A and B is also plotted for comparison. One can find a drastic reduction of P2 in C. The positions of peaks and structures in sample C are shown in Fig. 3b. Most of the observed peaks do not change their position even in such high magnetic fields.

We have also examined the magneto-oscillation of tunnel currents for fixed bias voltage  $V_b$ . In sample C we can observe magneto-oscillations periodic in  $1/B$  near the onset of P1. However, we cannot observe clear magneto-oscillations for  $V_b$  above the valley region of P1. At  $V_b = 0.47 \text{ V}$ , the tunnel current is minimum in the valley region of P1 and the tunnel current remains almost constant with changing  $B_{||}$ . Since the current in-



creases again for higher  $V_b$ , the energy difference  $\delta E = E_{1L} - E_{1R}$  reaches the LO phonon energy  $\hbar\omega_{LO}$  at  $V_b = 0.47$  V. For higher  $V_b$   $\delta E$  becomes larger than  $\hbar\omega_{LO}$ , and the tunnel current should oscillate with the frequency  $B_f = m^*(\delta E - \hbar\omega_{LO})/e\hbar$ . However, while  $\delta E$  is not so different from  $\hbar\omega_{LO}$ , the scattering-assisted process with the change of Landau index is inhibited even for low magnetic field  $B_{||}$ . Hence, the probability of scattering-assisted tunneling from  $E_{1L}$  to  $E_{1R}$  decreases with increase in  $B_{||}$ . This can explain the decrease in the tunnel current for fixed  $V_b = 0.5$ – $0.6$  V. Therefore, we attribute the origin of P2 in C to scattering-assisted tunneling from  $E_{1L}$  to  $E_{1R}$ . Since the peak current density of P2 is

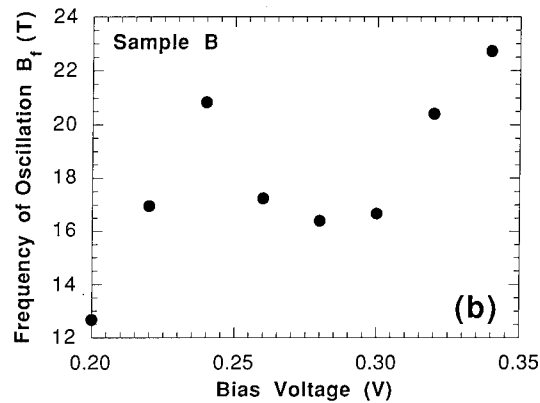
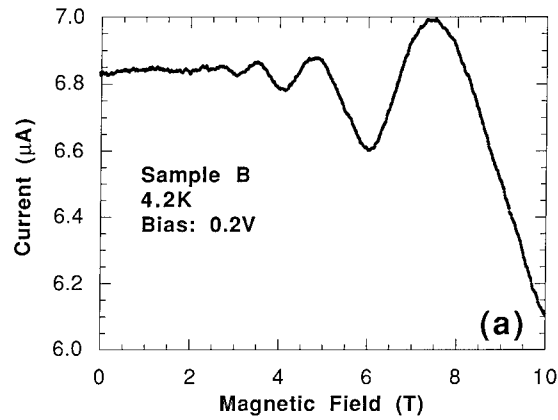


Fig. 4. (a) The oscillation of tunnel current observed in sample B for the bias voltage of 0.2 V. (b) The frequency of magneto-oscillation  $B_f$  for various bias voltages applied to sample B.

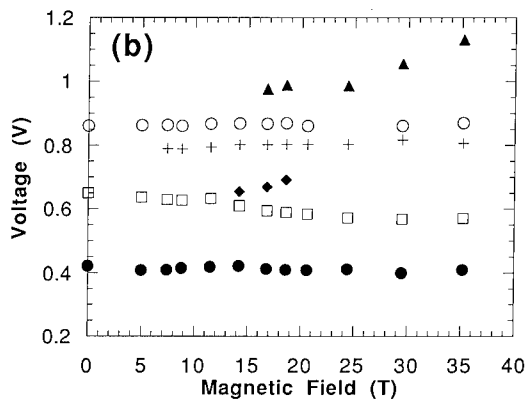
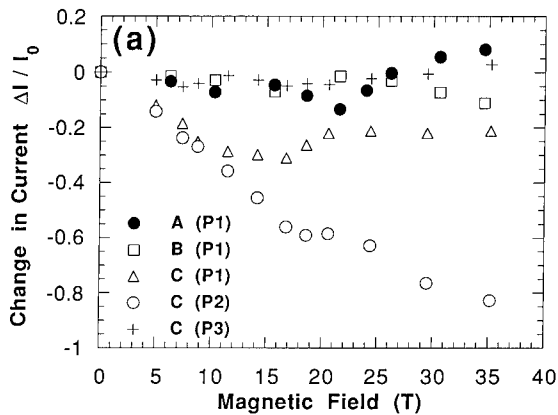


Fig. 3. (a) The change in the peak current normalized by zero field value is plotted for P1 in A, P1 in B, and all the peaks in C under magnetic field. (b) The positions of peaks in sample C under magnetic field.

larger than that of P1, the scattering-assisted process must be sufficiently efficient. This also suggests scattering by GaAs LO phonons. In addition, the number of injected electrons from the emitter to  $E_{1L}$  should increase with  $V_b$  to compensate for the decrease in the overlap of wavefunctions for  $E_{1L}$  and  $E_{1R}$  which leads to a slower scattering rate for higher  $V_b$ .

To compare with sample C, we measured magnetotunneling currents for fixed  $V_b$  in other samples. They showed magneto-oscillations periodic in  $1/B$ , as shown in Fig. 4a. The frequency of oscillation  $B_f = [\Delta(1/B)]^{-1}$  for various  $V_b$  applied to sample B is shown in Fig. 4b. The frequency  $B_f$  increases when  $V_b$  approaches the

peak voltage both in samples A and B. The maximum  $B_f = 23$  T for both A and B gives reasonable agreement with corresponding Fermi energy of the 3D emitter  $E_F$  estimated from the dopant concentration. These results show that the magneto-oscillations are due to the modulation of elastic 3D–2D tunneling processes in  $B_{||}$  [1]. Hence we can conclude that P1 in A and P2 in B appear when  $E_{1L}$  reaches the conduction band edge  $E_{ce}$  of the emitter. However, the peak P1 in B appears for lower  $V_b$  as compared with P1 in A. The position of P1 in C corresponds to P1 in B, if we assume uniform electric field over the TB structure and consider the shift of peaks to be caused by the thicker spacer. Hence, we attribute the origin of P1 in samples B and C to identical energy level alignment. The thicker center barrier of samples B and C results in a larger accumulation of electrons in  $E_{1L}$  and the accumulated electrons are expected to lower  $E_{1R}$  relative to  $E_{1L}$ . We can estimate the accumulated electron density from the frequency  $B_f$  of measured magneto-oscillations. Then we can deduce  $V_b$  for the onset of P1 which is determined by the resonance between  $E_{1L}$  and  $E_{1R}$ , if we consider the TB structure simply as a capacitance. Before the tunnel current starts to flow, the applied bias voltage  $V_b$  is associated with the electron in  $E_{1L}$  and the ionized donor at the collector. Hence,  $V_b$  is expressed by

$$V_b = \frac{eN_1}{\epsilon\epsilon_0}(b_1 + L_w + b_2 + L_s) + \frac{eN_1^2}{2N_D\epsilon\epsilon_0}, \quad (1)$$

where  $N_1$  is the sheet electron density in level  $E_{1L}$ , and  $N_D$  is the positive space charge due to the ionized donor in the depletion layer. In Eq. (1)  $b_1$ ,  $L_w$ ,  $b_2$ , and  $L_s$  represent the width of the center barrier, collector-side well, barrier, and spacer layer, respectively. The measured frequency  $B_f$  is 12.7 T at  $V_b = 0.2$  V for sample B and 10.5 T at  $V_b = 0.35$  V for sample C. Hence, we estimate the onset of P1 in B to be 0.19 V and that in C to be 0.28 V from Eq. (1). This reasonable agreement with experiment supports the interpretation that the shift of P1 to low  $V_b$  results from charge accumulation in  $E_{1L}$ . Hence, we can conclude that the current drop after P1 is due to

the inhibition of elastic 2D–2D tunneling from  $E_{1L}$  to  $E_{1R}$  in samples B and C. On the other hand, the single peak P1 in sample A cannot be explained by such a picture. Since P1 appears for higher  $V_b$ , the resonance between  $E_{1L}$  and  $E_{1R}$  is maintained until they reach the conduction band edge  $E_{ce}$  of the emitter. It can be ascribed to the strong coupling of  $E_{1L}$  and  $E_{1R}$  in sample A.

Finally we discuss the additional structures observed in sample C. The position of peaks in  $B_{||}$  is shown in Fig. 3b. One can find that the peak split from P3 (crosses in Fig. 3b) scarcely changes its position, whereas the additional peak which appears in the valley region of P3 (triangles in Fig. 3b) shifts with increasing  $B_{||}$ . The latter peak is ascribed to scattering-assisted processes which occur with the change of Landau index. If the structures in P3 are due to some scattering-assisted process, all should be associated with the process without the change of Landau index. We need further investigation to clarify the origin of P3 in sample C.

In summary, we have investigated a series of TB structures which are different in the coupling of 2D states. By magnetotunneling measurements we revealed that the different energy level alignment is the origin of observed numerous peaks. The drastic reduction of the peak current is ascribed to the inhibition of scattering-assisted 2D–2D tunneling processes in  $B_{||}$ . The origin of the first peak P1 depends on the strength of coupling of 2D energy levels and is attributed to 2D–2D elastic tunneling or 3D–2D elastic tunneling. Although we observed some structures whose positions are independent of magnetic field, their origins are not clear at present.

We acknowledge Professor N. Miura for extending to us the use of pulsed high magnetic fields and H. Noguchi for his collaboration.

## 1. References

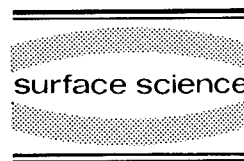
- [1] E.E. Mendez, L. Esaki and W.I. Wang, Phys. Rev. B 33 (1986) 2893.

- [2] V.J. Goldman, D.C. Tsui and J.E. Cunningham, *Phys. Rev. B* 35 (1987) 9387.
- [3] L. Eaves, G.A. Toombs, F.W. Sheard, C.A. Payling, M.L. Leadbeater, E.S. Alves, T.J. Foster, P.E. Simmonds, M. Henini, O.H. Hughes, J.C. Portal, G. Hill and M.A. Pate, *Appl. Phys. Lett.* 52 (1988) 212.
- [4] M.L. Leadbeater, E.S. Alves, L. Eaves, M. Henini, O.H. Hughes, A. Celeste, J.C. Portal, G. Hill and M.A. Pate, *Phys. Rev. B* 39 (1989) 3438.
- [5] D. Thomas, F. Chevoir, P. Bois, E. Barbier, Y. Guldner and J.P. Vieren, *Superlatt. Microstruct.* 5 (1989) 219.



ELSEVIER

Surface Science 305 (1994) 375–379



## Optical spectroscopy of inverted electron populations in double-barrier resonant-tunnelling structures

J.W. Cockburn <sup>a,\*</sup>, R.J. Teissier <sup>a</sup>, M.S. Skolnick <sup>a</sup>, P.D. Buckle <sup>a</sup>, D.M. Whittaker <sup>a</sup>,  
A.R.K. Willcox <sup>a</sup>, G.W. Smith <sup>b</sup>, G. Hill <sup>c</sup>, M.A. Pate <sup>c</sup>

<sup>a</sup> Department of Physics, University of Sheffield, Sheffield S3 7RH, UK

<sup>b</sup> Defence Research Agency, St. Andrew's Road, Malvern, Worcestershire WR14, 3PS, UK

<sup>c</sup> SERC Central Facility for III–V Materials, Department of Electronic and Electrical Engineering, University of Sheffield, Sheffield S1 3JD, UK

(Received 28 April 1993; accepted for publication 25 May 1993)

### Abstract

We present results of photoluminescence and electroluminescence spectroscopy carried out on GaAs/Al<sub>0.33</sub>Ga<sub>0.67</sub>As double-barrier resonant-tunnelling structures having quantum wells of either 200 or 250 Å width. At high bias, luminescence recombination is observed from electrons in highly excited ( $n > 2$ ) quantum-well (QW) states of the structures. Analysis of the luminescence intensities shows that when the structures are biased at the fourth electron resonance, a population inversion occurs between the  $n = 4$  and  $n = 3$  confined electron levels. In addition, when the 250 Å QW structure is biased at the fifth resonance, a population inversion occurs between the  $n = 5$  and  $n = 4$  confined levels. We show that such population inversions are explained by a rate-equation analysis of the excited-state populations.

When a double-barrier resonant-tunnelling structure (DBRTS) is biased such that electrons are injected into an excited quantum-well (QW) state, the relative populations of the QW electron levels are controlled by the inter-level scattering rates and the tunnelling-out rates from the QW. By measuring the relative intensities of luminescence recombination arising from electrons in the various QW levels, the relative populations of the levels can be determined. Electroluminescence

(EL) techniques have been employed recently to measure the population ratio of the  $n = 1$  (E1) and  $n = 2$  (E2) levels in DBRTS biased for tunnelling into E2, and it has been shown that this ratio is determined by the ratio of the intersubband scattering time  $\tau_i$  to the tunnelling out time from E1,  $\tau_1$  [1]. It has also been demonstrated that the population ratio can be altered by changing the collector (for electrons) barrier width in order to vary  $\tau_i$  [2].

In this paper we report results of photoluminescence (PL) and EL experiments which have been carried out in order to determine the rela-

\* Corresponding author.

tive populations of highly excited ( $n > 2$ ) electron states in DBRTS having QWs of either 200 or 250 Å width. The PL spectroscopy was carried out on the 200 Å QW sample (structure 1), which was grown by MBE on an  $n^+$  GaAs substrate and comprised the following layers: 0.50  $\mu\text{m}$   $n = 1.5 \times 10^{18} \text{ cm}^{-3}$  GaAs, 0.50  $\mu\text{m}$   $n = 2 \times 10^{17} \text{ cm}^{-3}$  GaAs, 100 Å undoped GaAs spacer, 85 Å undoped  $\text{Al}_{0.33}\text{Ga}_{0.67}\text{As}$  barrier, 200 Å undoped GaAs QW, 85 Å undoped  $\text{Al}_{0.33}\text{Ga}_{0.67}\text{As}$  barrier, 100 Å undoped GaAs spacer, 0.75  $\mu\text{m}$   $n = 2 \times 10^{17} \text{ cm}^{-3}$  GaAs, 0.25  $\mu\text{m}$   $n = 1 \times 10^{18} \text{ cm}^{-3}$  GaAs top contact.

EL experiments were performed on the sample having the 250 Å wide QW (structure 2), which consisted of a DBRTS grown within a p–n junction. When bias is applied to such a structure, both electrons and holes tunnel through the DBRTS, leading to EL recombination from the QW. Structure 2 was also grown by MBE on an  $n^+$  GaAs substrate, and comprised the following layers: 1.0  $\mu\text{m}$   $n = 1 \times 10^{18} \text{ cm}^{-3}$  GaAs, 500 Å  $n = 1 \times 10^{17} \text{ cm}^{-3}$  GaAs, 500 Å  $n = 1 \times 10^{16} \text{ cm}^{-3}$  GaAs, 85 Å undoped  $\text{Al}_{0.33}\text{Ga}_{0.67}\text{As}$  barrier, 250 Å undoped GaAs QW, 85 Å undoped  $\text{Al}_{0.33}\text{Ga}_{0.67}\text{As}$  barrier, 1000 Å  $p = 1 \times 10^{17} \text{ cm}^{-3}$  GaAs, 1.0  $\mu\text{m}$   $p = 1 \times 10^{18} \text{ cm}^{-3}$  top contact. Both structure 1 and structure 2 were processed into mesas with annular contacts to provide optical access.

For the experiments on structure 1, PL was excited with a 633 nm He–Ne laser. The  $I$ – $V$  characteristic obtained for structure 1 is shown in Fig. 1a (positive bias corresponds to top contact positive relative to substrate). At all biases, the most intense PL from the QW of structure 1 arises from recombination of E1 electrons with  $n = 1$  (HH1) heavy holes ( $E_{11h}$  recombination). This is because the majority of electrons injected into excited states of the structure scatter rapidly down to E1 before recombination occurs. Throughout most of the bias range of the E2 resonance, PL recombination from electrons injected into E2 ( $E_{21h}$  recombination) is obscured by overlap with the high-energy tail of the strong GaAs band-edge PL. However, at the peak of the resonance a weak  $E_{21h}$  feature becomes discernible at 1.554 eV. When the bias is increased

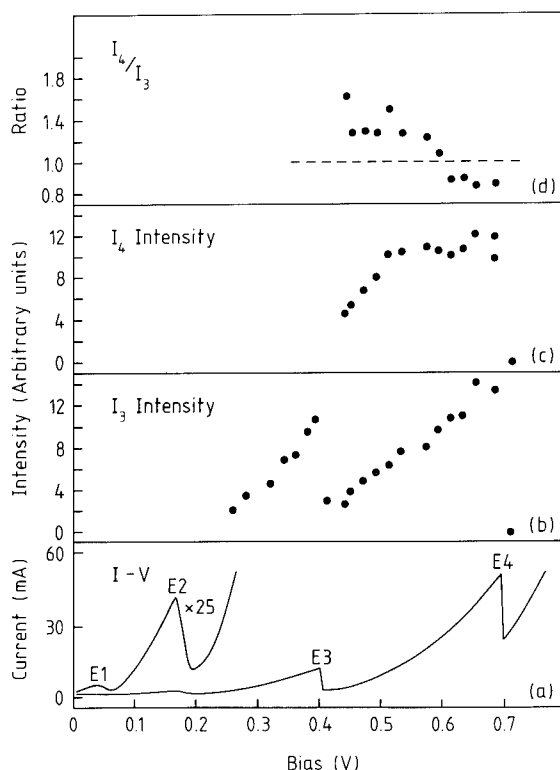


Fig. 1. (a) Current–voltage characteristic (5 K) for structure 1. (b)  $E_{31h}$  PL intensity ( $I_3$ ) versus bias. (c)  $E_{41h}$  PL intensity ( $I_4$ ) versus bias. (d)  $I_4/I_3$  PL intensity ratio versus bias.

to the onset of the E3 resonance, a PL peak emerges at an energy of 1.596 eV. This is due to  $E_{31h}$  recombination, which is calculated to occur at 1.593 eV. The integrated intensity ( $I_3$ ) of this peak, which is around four orders of magnitude smaller than that of the  $E_{11h}$  peak, is plotted versus bias in Fig. 1b. At the onset of the E4 resonance, a further PL peak is observed at an energy of 1.660 eV. This is due to  $E_{41h}$  recombination, calculated to occur at 1.650 eV. The  $E_{41h}$  intensity ( $I_4$ ) is plotted versus bias in Fig. 1c.

A representative PL spectrum in the 1.55 to 1.70 eV region, obtained at a bias of 0.5 V, is shown in Fig. 2. The spectrum clearly shows that  $I_4$  is greater than  $I_3$  at this bias. The  $I_4/I_3$  ratio is plotted versus bias in Fig. 1d. This shows that  $I_4$  is greater than  $I_3$  throughout much of the bias range of the E4 resonance. The electron population ratio of E4 and E3,  $n_4/n_3$ , may be deter-

mined from the PL intensity ratio using the relation

$$\frac{\alpha}{\beta} \frac{I_4}{I_3} = \frac{n_4}{n_3} \frac{f_4}{f_3}, \quad (1)$$

where  $\alpha$  ( $= 1.4 \pm 0.2$ ) accounts for the greater absorption of  $E_{41h}$  than  $E_{31h}$  PL in the GaAs top contact,  $\beta$  ( $= 1.6 \pm 0.1$ ) is the correction factor for the higher efficiency of the spectrometer/detector system at the  $E_{41h}$  energy and  $f_4/f_3$  is the ratio of the oscillator strengths for  $E_{41h}$  and  $E_{31h}$  transitions at the electric field of interest.  $f_4/f_3$  was calculated using values for the electric field obtained by comparing the bias dependence of the  $E_{11h}$  peak position with the calculated electric field dependence of the  $E_{11h}$  transition energy due to the quantum-confined Stark effect [3]. A Stark shift of 33 meV was observed at a bias of 0.5 V, corresponding to an electric field in the QW of  $5 \times 10^6$  V m $^{-1}$ . At this field  $f_4/f_3$  was calculated to be  $0.23 \pm 0.05$ , giving  $n_4/n_3 = 6 \pm 2$  at 0.5 V, indicating that an electron-population inversion is obtained between E3 and E4 when the structure is biased for tunnelling into E4.

As indicated in Fig. 3, when electrons tunnel into E4 they can subsequently either tunnel directly out of the QW, or tunnel sequentially through the QW after undergoing intersubband

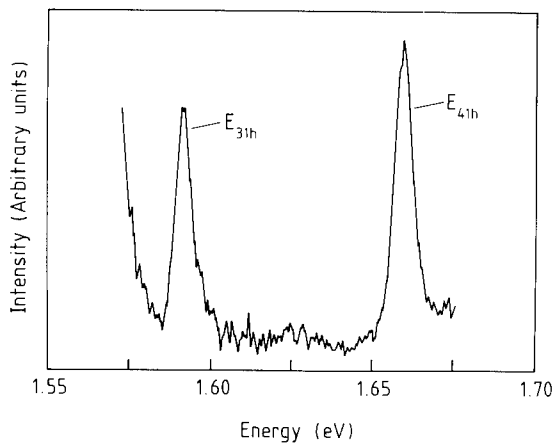


Fig. 2. PL spectrum obtained for structure 1 at a bias of 0.5 V and a temperature of 5 K showing  $E_{31h}$  and  $E_{41h}$  recombination.

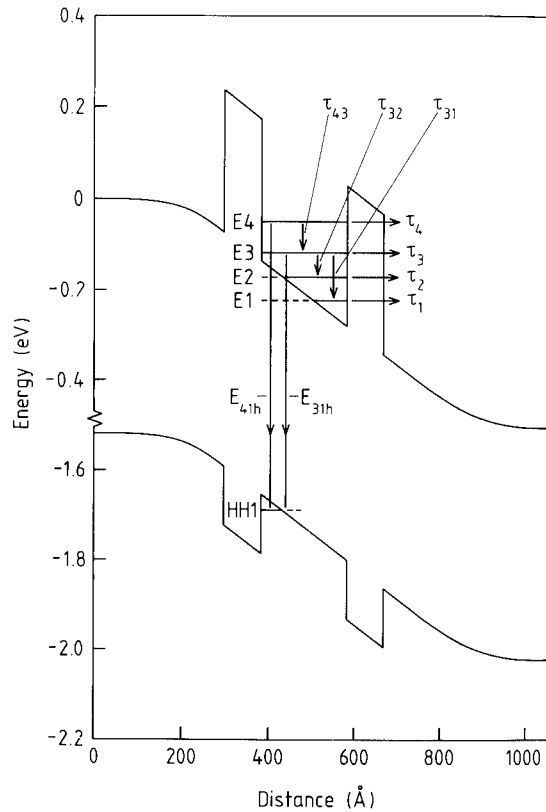


Fig. 3. Schematic band-edge diagram of structure 1 at a bias of 0.5 V.

scattering to lower QW levels. With the structure biased at the E4 resonance, the population of E3 obeys the following rate equation:

$$\frac{dn_3}{dt} = \frac{n_4}{\tau_{43}} - \frac{n_3}{\tau_3} - \frac{n_3}{\tau_{32}} - \frac{n_3}{\tau_{31}} - \frac{n_3}{\tau_{R3}}, \quad (2)$$

where  $\tau_{43}$ ,  $\tau_{32}$  and  $\tau_{31}$  are the intersubband scattering times from E4 to E3, E3 to E2 and E3 to E1, respectively;  $\tau_3$  is the tunnelling-out time from E3, and  $\tau_{R3}$  is the characteristic time for recombination with HH1 holes. The intersubband scattering time for subband spacings greater than the LO-phonon energy ( $\hbar\omega_{LO} = 36$  meV) is  $\sim 0.5$  ps [4,5], whereas  $\tau_3$  is calculated to be  $\sim 250$  ps at a bias of 0.5 V, and  $\tau_{R3}$  will very likely be greater than 10 ns [1]. Thus, the terms in Eq. (2) due to the tunnelling-out and recombination rates from E3 may be neglected in comparison with the

intersubband scattering terms to give, in the steady state,

$$\frac{n_4}{n_3} = \tau_{43} \left( \frac{1}{\tau_{32}} + \frac{1}{\tau_{31}} \right). \quad (3)$$

LO-phonon scattering of electrons between parallel, parabolic subbands separated by energy  $\Delta E$  requires the participation of a phonon of wavevector  $q \propto (\Delta E - \hbar\omega_{\text{LO}})^{1/2}$ . Since the strength of the Fröhlich interaction between electrons and LO phonons decreases with increasing  $q$  [5], the intersubband scattering time is expected to increase with  $\Delta E$  for  $\Delta E$  greater than  $\hbar\omega_{\text{LO}}$ . Thus,  $\tau_{43}$  ( $\Delta E = 67$  meV)  $>$   $\tau_{32}$  ( $\Delta E = 47$  meV) giving, from Eq. (3),  $n_4/n_3 > 1$ , consistent with our experimental observation of a population inversion between these subbands [6]. Ferreira and Bastard [5] have calculated the dependence of  $\tau_i$  on  $\Delta E$ . Using similar calculations for the intersubband scattering times in Eq. (3), we obtain  $n_4/n_3 \approx 2.3$ , in very reasonable agreement with our experimental measurements.

We now consider the EL experiments carried out on structure 2. The 5 K  $I$ - $V$  characteristics for this structure, for  $V > 1.5$  V, is shown in Fig. 4b. A forward bias of 1.5 V corresponds to zero bias in a conventional  $n$ - $i$ - $n$  DBRTS. At biases beyond 1.53 V, intense EL is observed due to  $E_{11h}$  recombination in the QW. In the bias range of the  $E_2$  resonance, the onset of an EL peak due to  $E_{21h}$  recombination is expected. However, in common with the PL experiments on structure 1, EL due to  $E_{21h}$  recombination is very weak, and does not become discernible from the high-energy tail of the GaAs band-edge EL until a bias of 1.68 V is reached. Calculation of the relative populations of  $E_2$  and  $E_1$  from the relative intensities of the  $E_{21h}$  and  $E_{11h}$  EL peaks, using Eq. (1), gives  $n_2/n_1 \approx 10^{-4}$ . This low value of  $n_2/n_1$  is surprising in view of the fact that rapid intersubband scattering from  $E_2$  to  $E_1$  by LO-phonon emission should not occur in this bias range, since the  $E_2$ - $E_1$  energy spacing remains below  $\hbar\omega_{\text{LO}}$  for biases up to about 1.9 V. Thus, intersubband scattering should be a relatively slow process ( $\tau_i \approx 100$  ps), proceeding via acoustic-phonon emission or scattering by impurities or interface de-

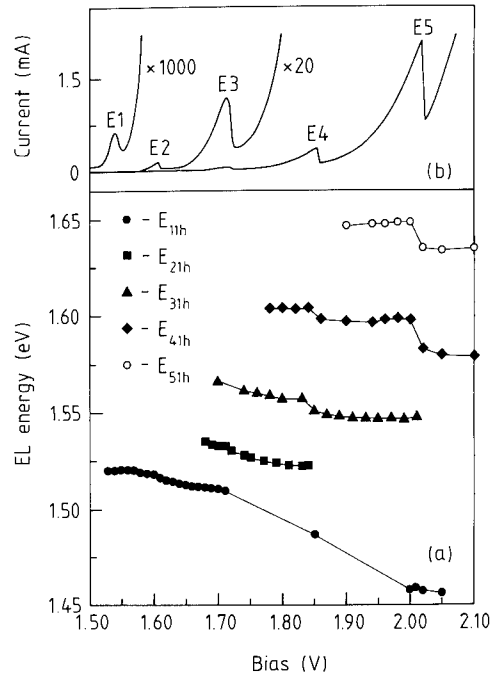


Fig. 4. (a) EL peak energies versus bias for structure 2. (b) 5 K  $I$ - $V$  characteristic for structure 2.

fects [5]. The low  $n_2/n_1$  ratio obtained here is comparable with values obtained from samples having  $E_2$ - $E_1$  spacings much greater than  $\hbar\omega_{\text{LO}}$  [1,2], strongly suggesting the occurrence of a rapid elastic scattering process between  $E_2$  and  $E_1$  in the present samples.

As the bias is increased so that electrons tunnel into higher excited states of the QW, further EL peaks emerge due to  $E_{31h}$ ,  $E_{41h}$ , and  $E_{51h}$  recombination. The observed energies of these peaks, together with those of the  $E_{11h}$  and  $E_{21h}$  peaks are plotted versus bias in Fig. 4a. The EL energies at the onset of  $E_{11h}$  (1.521 eV),  $E_{21h}$  (1.536 eV),  $E_{31h}$  (1.567 eV),  $E_{41h}$  (1.604 eV) and  $E_{51h}$  (1.647 eV) recombination are in very good agreement with the calculated transition energies (corrected for Stark shift of the HH1 and relevant electron levels under bias) of 1.520, 1.535, 1.568, 1.603 and 1.653 eV, respectively.

The Stark shift of the  $E_{11h}$  peak with bias was compared with the calculated electric field dependence of the  $E_{11h}$  energy in order to provide a calibration of QW electric field against device

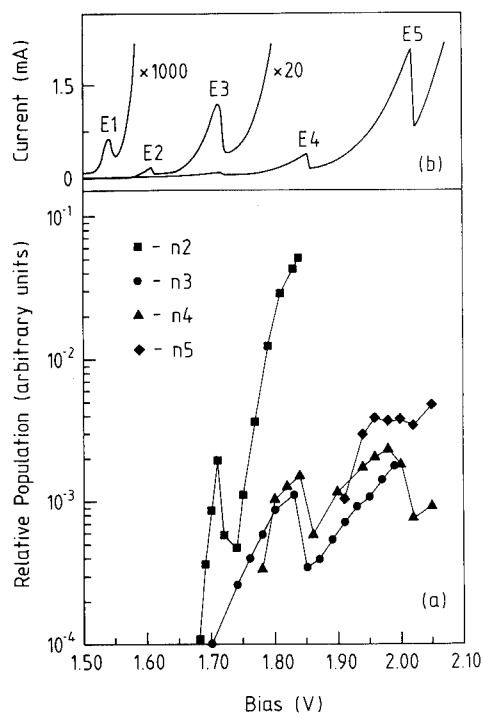


Fig. 5. (a) Relative populations of excited QW states of structure 2 versus bias; (b) as Fig. 4b.

bias. This enabled the oscillator strengths for the excited-state EL transitions to be calculated as a function of bias, allowing the bias dependence of the relative populations of the excited states to be calculated using Eq. (1). The results of this procedure are plotted in Fig. 5. This shows that as observed in structure 1, a population inversion occurs between E4 and E3 in the bias range of the E4 resonance. Furthermore, when structure 2 is biased for tunnelling into E5, a population inversion is obtained between E5 and E4 as well

as between E4 and E3. Since the E5–E4, E4–E3 and E3–E2 energy separations are all greater than  $\hbar\omega_{LO}$  [7], these population inversions can be explained by a rate-equation analysis similar to that carried out for structure 1 (Eqs. (2) and (3)).

In conclusion, we have used optical spectroscopy to study the relative populations of highly excited states of double-barrier resonant-tunnelling structures having a quantum well of either 200 or 250 Å width. We have shown that population inversions occur between highly excited states when the structures are biased at the E4 and E5 resonances, and that such population inversions are consistent with a rate analysis of the relative populations of the excited states.

## 1. References

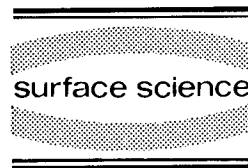
- [1] J.W. Cockburn, P.D. Buckle, M.S. Skolnick, D.M. Whittaker, W.I.E. Tagg, R.A. Hogg, R. Grey, G. Hill and M.A. Pate, *Phys. Rev. B* 45 (1992) 13757.
- [2] J.W. Cockburn, P.D. Buckle, M.S. Skolnick, D.M. Whittaker, W.I.E. Tagg, R. Grey, G. Hill and M.A. Pate, *Superlatt. Microstruct.* 12 (1992) 413.
- [3] D.A.B. Miller, D.S. Chemla, T.C. Damen, A.C. Gossard, W. Wiegmann, T.H. Wood and C.A. Burrus, *Phys. Rev. B* 32 (1985) 1043.
- [4] M.C. Tatham, J.F. Ryan and C.T. Foxon, *Phys. Rev. Lett.* 63 (1989) 1637.
- [5] R. Ferreira and G. Bastard, *Phys. Rev. B* 40 (1989) 1074.
- [6] For a similar three-level system, where instead the level separations are less than the LO phonon energy, S.J. Allen et al. (*Semicond. Sci. Technol.* 7 (1992) B1) have shown that a population inversion is not observed, since the acoustic-phonon scattering rate increases with increasing level separation (Ref. [5]).
- [7] Although the E3–E2 energy separation is only 32 meV under flat-band conditions, the Stark shift of the QW levels under bias leads to  $E3-E2 > \hbar\omega_{LO}$  for biases beyond 1.8 V.





ELSEVIER

Surface Science 305 (1994) 380–384



## Resonant inter-Landau-level tunneling of electrons and holes in superlattices

W. Müller <sup>\*,a</sup>, H.T. Grahn <sup>b</sup>, K. von Klitzing <sup>a</sup>, K. Ploog <sup>b</sup>

<sup>a</sup> Max-Planck-Institut für Festkörperforschung, Heisenbergstrasse 1, D-70569 Stuttgart 80, Germany

<sup>b</sup> Paul-Drude-Institut für Festkörperelektronik, Hausvogteiplatz 5-7, D-10117 Berlin, Germany

(Received 16 April 1993; accepted for publication 19 May 1993)

### Abstract

Inter-Landau-level tunneling of electrons and holes between two-dimensional (2D) systems is investigated in GaAs/AlAs superlattices. In one sample resonances due to electron tunneling up to  $\Delta n = 9$  ( $n$  is the Landau level index) are observed. The corresponding Landau fan can be constructed when conduction-band nonparabolicities are included. In a second sample resonances due to inter-Landau-level tunneling of holes are identified. The experimental results are discussed in view of the complex valence-band structure in the magnetic field.

A superlattice (SL) with almost vanishing miniband width can be viewed as a structure where tunneling takes place between 2D systems. A magnetic field applied perpendicular to the plane of the tunneling barrier leads to the quantization into Landau levels (LLs) and reduces the dimensionality of the states to 0D. The spectroscopy of inter-Landau-level tunneling resonances can be used as a tool to investigate the Landau level structure of electrons and holes as a function of the applied magnetic field.

Two samples are investigated in this study, sample 1 containing 40 periods of 9.0 nm GaAs and 4.0 nm AlAs, and sample 2 with 50 periods of 14.4 nm GaAs and 3.4 nm AlAs. In both samples the superlattice and two significantly larger wells are forming the intrinsic region of a p-i-n diode.

The p and n regions consists of highly doped  $\text{Al}_{0.5}\text{Ga}_{0.5}\text{As}$  layers. The samples were grown by molecular-beam epitaxy on a (100)-oriented n<sup>+</sup>-GaAs substrate and processed into mesas of 450 and 120  $\mu\text{m}$  diameter. Ohmic Cr/Au contacts were alloyed on the top and AuGe/Ni contacts on the substrate side. Under a reverse bias voltage  $V_A$  no carriers are injected via the contacts. The applied electric field is given by  $F_A = (V_{\text{BI}} - V_A)/W$ , where  $V_{\text{BI}}$  denotes the built-in voltage and  $W$  the width of the intrinsic region. Using an optical fiber the sample is illuminated in the bore of a magnet at an intensity of  $\sim 30 \text{ mW/cm}^2$  with a Ti-sapphire laser which is pumped by an Ar<sup>+</sup> laser. To achieve a rather homogeneous carrier distribution over the whole SL the wavelength of the Ti-sapphire laser is chosen to be 750 nm. The excited carrier concentration is estimated to be below  $10^9 \text{ cm}^{-2}$ . The photocurrent-voltage ( $I$ - $V$ ) characteristics are recorded with a Hewlett-Packard 4140B pA meter while the dif-

\* Corresponding author.

ferential conductivity–voltage ( $dI/dV - V$ ) traces are obtained using a standard ac modulation lock-in technique. All measurements are performed at a temperature of 1.5 K.

In sample 1 we observe LL tunneling of electrons. In Fig. 1 the absolute value of the photocurrent at 0 and 8 T applied perpendicular to the layers (parallel to the current) is plotted versus the applied voltage  $V_A$  for sample 1. The four maxima in the  $I-V$  trace at 0 T can be attributed to resonant coupling of adjacent wells in the SL. The maximum at  $-4.7$  V occurs when the first and second electronic subbands are aligned. The maxima at  $+0.75$  and  $-0.8$  V correspond to hole resonances between the lowest heavy hole (HH1) and light hole (LH1) subbands without and with LO-phonon (GaAs) emission. The resonance at  $-0.1$  V is due to LO-phonon-assisted tunneling between the lowest electronic as well as valence subbands. The  $I-V$  characteristics at 8 T show a large number of oscillations which can be better resolved by subtracting the 0 T trace from it (inset in Fig. 1). The period of the oscillations  $\Delta V_A$  corresponds to an energy difference  $\Delta E = ed\Delta V_A/W \approx 12.5$  meV which agrees well with the cyclotron energy  $\hbar\omega_c$  ( $\omega_c = eB/m^*$ ) using a slightly heavier electron effective mass  $m^*$  than in bulk GaAs.  $d$  denotes the period of the SL (13 nm). These resonances are therefore identified as

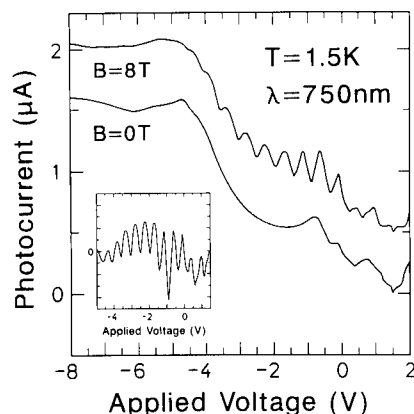


Fig. 1. Absolute value of the photocurrent at 0 and 8 T applied perpendicular to the layers vs applied voltage for sample 1. For clarity the trace at 8 T is shifted by  $0.5 \mu\text{A}$ . The inset shows the  $I-V$  characteristics at 8 T subtracted by the 0 T trace.

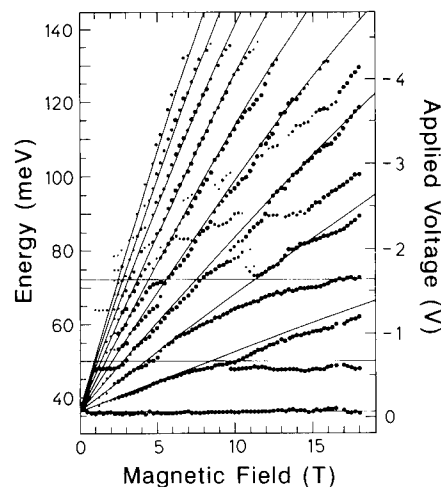


Fig. 2. Peak positions for LO-phonon-assisted LL tunneling (dots) for sample 1 and calculated Landau fan taking conduction-band nonparabolicities into account (solid lines). The energies of the GaAs LO phonon (36.2 meV), the AlAs LO phonon (50.1 meV), and twice the GaAs LO phonon (72.4 meV) are indicated by horizontal lines.

LL transitions of electrons between adjacent wells. The selection rule  $\Delta n = 0$  for resonant LL tunneling is broken by elastic scattering processes or inelastic scattering mechanisms such as optical phonon emission.

We will focus on the LO-phonon assisted resonances, which dominate in the  $I-V$  traces. In Fig. 2 the corresponding energy positions ( $E = edF_A$ ) of the resonance peaks above 30 meV are plotted versus the applied magnetic field. The size of the dots is proportional to the relative strength of the peaks in the  $I-V$  trace. A Landau fan originating from the GaAs LO-phonon assisted resonance at 36.2 meV is clearly resolved. Transitions with a change in the Landau index  $\Delta n$  from 0 up to 9 are visible. Due to the low carrier concentration, electrons are only injected from the  $n = 0$  LL into higher levels of the adjacent well. Because of the large barrier height and the weak coupling in this SL, the injected electrons relax to the ground level before tunneling into the next well can occur. Taking into account the conduction-band nonparabolicities [1] we calculate the  $0 \rightarrow n$  resonance energies. The corresponding Landau fan is plotted in Fig. 2. The experimental data are well described above twice the LO-phonon energy

( $2\hbar\omega_0$ ) of 72.4 meV. Below  $2\hbar\omega_0$  the transition energies are strongly renormalized, e.g. the  $\Delta n = 2$  resonance displays a LL anticrossing and splitting at  $2\hbar\omega_0$  for a magnetic field of 11.3 T. This magnetic field strength corresponds to  $\omega_c = \omega_0/2$ . In addition, at high magnetic fields a pinning at  $2\hbar\omega_0$  is apparent. These phenomena can be understood within the theory of 2D magnetopolarons [2]. A detailed discussion of the theoretical calculations and a quantitative comparison with the experimental data is presented in Ref. [3]. Resonant LL tunneling of electrons due to elastic scattering is also reported in Ref. [3]. Furthermore, resonances due to the emission of zone-folded acoustics phonons are identified.

Since both electrons and holes are excited, the question arises whether resonant LL tunneling of holes can also be observed in these structures. While there is some evidence for tunneling between hole LLs in sample 1 [3] it turns out that the magnetic field traces of sample 2 are dominated by hole resonances. In sample 2 the  $I$ - $V$  characteristics also exhibit a large number of oscillations in a perpendicular magnetic field, which however can be much better resolved in the  $dI/dV$ - $V$  characteristics, since their amplitude is much smaller than in sample 1. In Fig. 3 the  $dI/dV$ - $V$  traces at 0, 4 and 10 T are plotted

versus the applied voltage  $V_A$ . The zero intersects of the 0 T trace at +0.7 and -2.8 V correspond to resonant tunneling between the HH1 and LH1 subbands and to the resonance between the first and second electronic subbands, respectively. The dip at -0.6 V indicates the resonance due to LO-phonon-assisted tunneling. At 4 T the HH1-LH1 resonance is split into two distinct peaks. In addition, a series of oscillations evolves from the LO-phonon resonance. At 10 T the LO-phonon peak has become very pronounced and the oscillatory structure at higher electric fields dominates the spectrum. We want to emphasize two key features of the spectra. Firstly, we note that the spacing between peaks at electric fields beyond -2 V does not increase with increasing magnetic field as would be expected from LLs of electrons. Secondly, if one plots the position of the resonances as a function of the magnetic field, one observes a large number of anticrossings and splittings. This is accompanied by a strong modulation of the oscillator strength of the resonances resulting in regions of large and small amplitudes. We therefore identify the resonances as LL tunneling of holes. The anticrossing behaviour at higher electric fields, thus higher energies, reflects the interaction of LLs originating from the different hole subbands.

In order to get a better understanding of the underlying physics we calculate the valence-band LLs for a 14.4 nm GaAs/AlAs quantum well in the magnetic field. The HH-LH admixture is fully taken into account by a  $4 \times 4$  Luttinger Hamiltonian. For a detailed discussion of the theoretical calculation we refer to Ref. [4]. In the axial approximation the exact solution of the Hamiltonian for a magnetic field in the  $z$  direction (perpendicular to the layers) is then given by a linear combination

$$|\Psi\rangle = \alpha |n, \frac{3}{2}, -\frac{3}{2}\rangle + \beta |n-1, \frac{3}{2}, -\frac{1}{2}\rangle + \gamma |n-2, \frac{3}{2}, +\frac{1}{2}\rangle + \delta |n-3, \frac{3}{2}, +\frac{3}{2}\rangle, \quad (1)$$

with  $|m, J, J_z\rangle = 0$  for  $m < 0$ . The index  $n$  denotes the Landau orbital quantum number while  $J$  is the total angular momentum of the  $\Gamma_8$  valence-bands and  $J_z$  is its  $z$ -component. The wave-

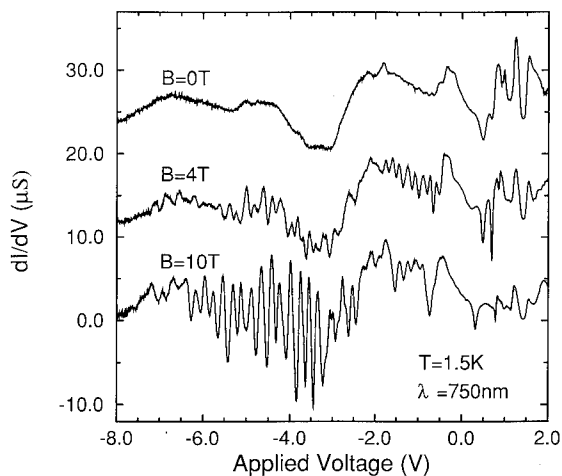


Fig. 3. Differential conductivity at 0, 4 and 10 T applied perpendicular to the layers vs applied voltage for sample 2. For clarity the traces at 0 and 4 T are shifted by 12 and 24  $\mu$ S, respectively.

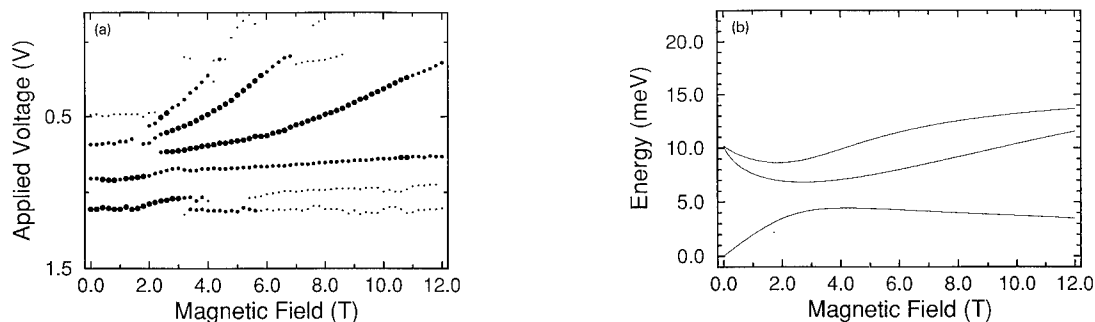


Fig. 4. (a) Positions of differential conductivity minima below the GaAs LO phonon emission line for sample 2. The size of the dots denotes the relative strength of the peaks. (b) Calculated transition energies from  $\text{HH1}(0^+)$  to  $\text{LH1}(1^+)$ ,  $\text{LH1}(2^-)$  and  $\text{HH1}(3^-)$ .

functions can be labeled according to their largest component in the limit  $B \rightarrow 0$ , i.e.  $\text{HH}i(n^\pm)$ , where  $i$  refers to the subband and a  $+$  or  $-$  sign to spin up or down. In a 14.4 nm quantum well the  $\text{HH1}(0^+)$  is the lowest level for all magnetic field strengths. We assume that due to the low carrier concentration holes are only injected from this level into higher levels of the adjacent well.

We now discuss which resonances can be observed in the experiment. Since their in-plane wavefunctions overlap according to Eq. (1) LL transitions from the  $\text{HH1}(0^+)$  into the  $\text{LH1}(1^+)$ ,  $\text{LH1}(2^-)$  and  $\text{HH1}(3^-)$  should be possible without a scattering process. In Fig. 4 the calculated resonances can be identified in the plot of the resonance positions below the GaAs LO-phonon emission line. The additional resonances observed in the experiment may be due to elastic scattering. On the other hand the Fröhlich interaction should mediate transitions between levels of different orbital quantum number under con-

servation of angular momentum. Therefore we expect tunneling resonances from the  $\text{HH1}(0^+)$  level into  $\text{HH}i(n^+)$  states with emission of an LO-phonon. In Fig. 5 we have plotted the calculated resonances and the experimentally observed resonances due to LO-phonon emission. It is apparent that not all calculated tunneling resonances are observed in the experiment. However, it is very likely that the probability for tunneling with LO-phonon emission into some levels is larger than into others and not even the same for all magnetic field strengths. The evaluation of such selection rules will require a detailed theoretical analysis and is beyond the scope of this paper. A tunneling resonance close to the AlAs LO-phonon energy at 50.1 meV can also be identified. Finally, it should be mentioned that the results of the calculations are very sensitive to the valence-band parameters used, especially in the case of wider quantum wells as studied in this experiment. Furthermore, a more complete calcu-

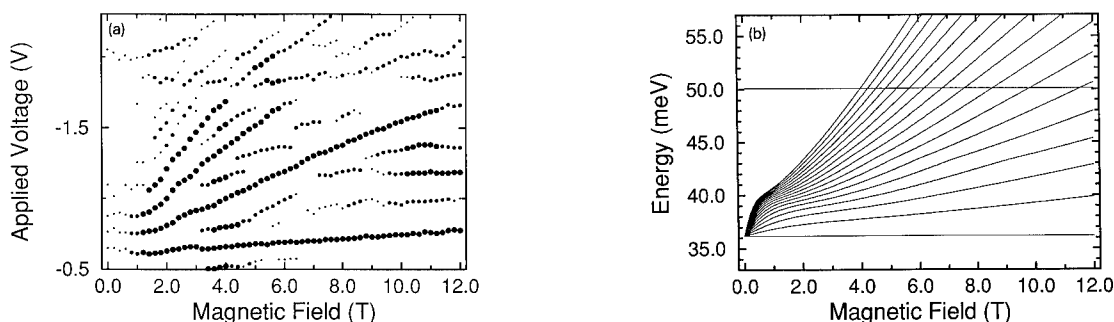


Fig. 5. (a) Positions of differential conductivity minima for LO-phonon-assisted LL tunneling for sample 2. The size of the dots denotes the relative strength of the peaks. (b) Calculated transition energies from  $\text{HH1}(0^+)$  to  $\text{HH1}(n^+)$  with  $n = 0, 1, \dots, 16$ .

lation should take into account the effect of the applied electric field, i.e. the shift of the levels due to the quantum-confined Stark effect.

In summary, we have presented a study of resonant LL tunneling between 2D systems. In sample 1 resonances of electrons up to  $\Delta n = 9$  are identified. The corresponding Landau fan can be simulated when conduction band nonparabolicities are included. In sample 2 LL tunneling resonances of holes are observed and compared to calculations taking into account the complex valence-band structure in the magnetic field. However, in order to obtain a better agreement more theoretical work is necessary. Finally, an open question originates from the fact that in one sample we observe LL tunneling of electrons while in the other sample the tunneling resonances are due to holes.

The authors would like to thank A. Fischer for sample growth and J. Weis and R.J. Haug for their expert help with the experiments. We especially thank A. Cros (Valencia, Spain) for giving us access to a computer program to calculate the hole subband structure in a magnetic field and for many helpful discussions. The work was partly supported by the Bundesminister für Forschung und Technologie.

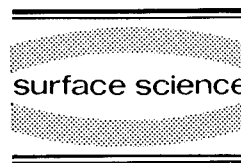
### 1. References

- [1] U. Ekenberg, Phys. Rev. B 40 (1989) 7714.
- [2] F.M. Peeters and J.T. Devreese, Phys. Rev. B 31 (1985) 3689.
- [3] W. Müller, H.T. Grahn, R.J. Haug and K. Ploog, Phys. Rev. B 46 (1992) 9800.
- [4] A. Cros, A. Cantarero, C. Trallero-Giner and M. Cardona, Phys. Rev. B 45 (1992) 6106.



ELSEVIER

Surface Science 305 (1994) 385–388



# Superlattice transport in intense terahertz electric fields

B.J. Keay <sup>\*,1</sup>, P.S.S. Guimaraes <sup>2</sup>, J.P. Kaminski, S.J. Allen, Jr.

*Center for Free-Electron Laser Studies <sup>3</sup>, Quantum Institute, Physics Department, UCSB, Santa Barbara, CA 93106-9530, USA*

P.F. Hopkins <sup>4</sup>, A.C. Gossard <sup>4</sup>

*Materials Department, University of California, Santa Barbara, CA 93106, USA*

L.T. Florez, J.P. Harbison

*Bellcore, Redbank, NJ 07701, USA*

(Received 21 April 1993; accepted for publication 10 July 1993)

## Abstract

The low DC field conductance and the nonlinear  $I$ – $V$  characteristics of GaAs/Al<sub>0.70</sub>Ga<sub>0.30</sub>As superlattices have been measured in the presence of intense electric fields produced by UCSB's free-electron lasers. The DC conductance exhibits oscillatory behavior as a function of terahertz field strength that resembles the zeroth-order Bessel function,  $J_0(edE^{AC}/\hbar\omega)$ , where  $e$ ,  $d$ , and  $E^{AC}$  are the electron charge, superlattice period and AC field strength, respectively. The  $I$ – $V$  characteristics, measured between 600 GHz and 3.1 THz, display new steps and plateaus. The dependence of the new structure of frequency suggests the presence of new conduction channels that are most naturally assigned to photon-mediated sequential tunneling.

## 1. Introduction

Since the pioneering work of Esaki and Tsu in 1970 [1] there has been much attention given to

the transport properties of superlattices in intense AC electric fields. The theoretical work is vast and contains several remarkable predictions, such as self-induced transparency, negative differential and absolute conductivity [2–7], and more recently the collapse of quasi-energy minibands [8]. Almost as remarkable as the theoretical predictions is the absence of experimental work to support them. However, if one examines the conditions necessary for the theories to be valid, this absence is not surprising. The simultaneous conditions of intense and high-frequency radiation requiring  $\omega\tau > 1$  and  $eE^{AC}d/\hbar\omega > 1$ , where  $d$  is the superlattice period and  $\tau$  is the

\* Corresponding author.

<sup>1</sup> Supported by the Army Research Office (DAAH-04-93-G-0082) and the NSF Science and Technology Center for Quantized Electronic Structures, Grant. No. DMR 91-20007.

<sup>2</sup> On leave from UFMG, Brazil; supported by CNPq, Brazil.

<sup>3</sup> Supported by the Office of Naval Research (N00014-92-J-1452).

<sup>4</sup> Supported by the Air Force Office of Scientific Research (AFOSR-91-0214).

mean scattering time, are not easily satisfied by conventional sources. However, for typical scattering times,  $\tau \approx 10^{12}$  s, the terahertz regime provides an obtainable compromise between the requirements of high frequency and high electric fields. These conditions, in the terahertz regime, can be satisfied by UCSB's free-electron lasers, which produce tunable radiation from 180 GHz to 4.8 THz at kilowatt power levels. Details of the UCSB lasers are given elsewhere [9].

In this article we report results of two transport measurements on semiconductor superlattices in the sequential tunneling regime subjected to intense terahertz radiation. The first measurement presented is of the low DC field conductance as a function of laser field strength, and the second measurement is of the current–voltage ( $I$ – $V$ ) characteristics of superlattices in the presence of intense terahertz radiation.

## 2. Experimental setup

Both the measurement of the low DC field conductance and the  $I$ – $V$  characteristics involved the same samples and experimental setup. The samples were 100 periods of MBE-grown superlattice with 33 nm wide quantum wells separated by 4 nm barriers. The superlattice was grown on an  $n^+$  GaAs substrate and capped by a 100 nm thick GaAs layer doped with Si to  $n = 2 \times 10^{18} \text{ cm}^{-3}$ , and the superlattice itself was uniformly doped with Si to  $n = 2 \times 10^{18} \text{ cm}^{-3}$ . Square mesas approximately 200  $\mu\text{m}$  wide and 3.7  $\mu\text{m}$  high were defined by standard lithographic techniques. Ni/AuGe/Ni/Au contacts were alloyed on both the substrate and the mesa for 45 s at 430°C. After bonding 25  $\mu\text{m}$  Au wires to both contacts, the samples were mounted in a temperature-controlled flow-type cryostat with Z-cut crystal quartz windows. The bonded Au wires acted as antennas to couple the radiation into the sample and the angle of incidence was adjusted to maximize the signal at different frequencies. The absolute coupling of radiation into the sample is not known. However, as will be discussed in the next section, qualitative comparisons of the data to simple conductance calculations suggest field strengths

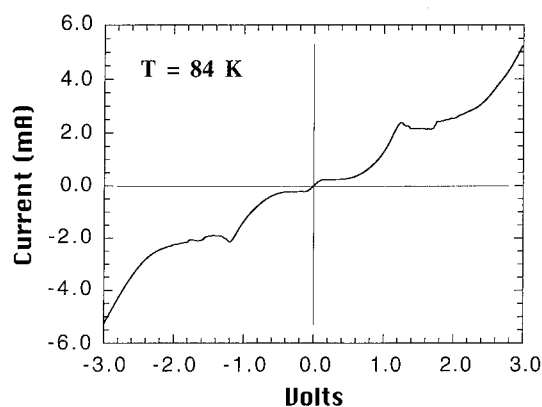


Fig. 1. Static  $I$ – $V$  characteristic at 84 K.

in the sample of several kV/cm, which are comparable to the free space electric fields.

Both the measurement of the low DC field conductance and the  $I$ – $V$  characteristic in the presence of the FEL can be discussed in terms of the static  $I$ – $V$ , which is shown in Fig. 1. The essential features of the static  $I$ – $V$  are explained by the alignment of the energy levels. At low bias the ground states are aligned and the electric field is uniform throughout the superlattice; this is characterized by an ohmic region in the  $I$ – $V$ . As the bias is increased the sample breaks into high and low electric field domains [10], with different state alignments in each domain. Eventually, the high field domain will encompass the entire sample and the electric field will be uniform again. This is characterized by a local maximum in the  $I$ – $V$  curve.

## 3. Low DC field conductance

The low DC field conductance shown in Fig. 2 was obtained by measuring the current through the sample at a fixed DC bias of 20 mV as the power into the sample was varied with attenuators. The oscillatory behavior of the conductance is very similar to that of the zeroth-order Bessel function,  $J_0(edE^{\text{AC}}/\hbar\omega)$ , whose appearance is common to theories on superlattices in intense AC electric fields. For superlattices in the sequential tunneling regime, transport in AC elec-

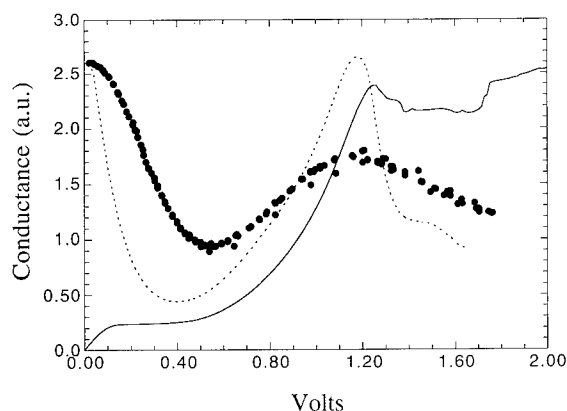


Fig. 2. The low-voltage conductance (solid points) and the model discussed in the text (dotted line) as a function of the incident terahertz electric field strength. The static  $I$ - $V$  (solid line) is shown for comparison.

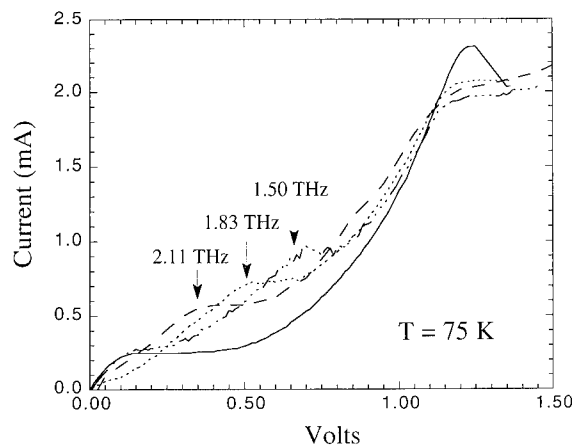


Fig. 3.  $I$ - $V$  characteristics at 75 K measured without (solid line) and with the sample in the presence of terahertz radiation at 2.11 THz (dashed lines), 1.83 THz (dotted line) and 1.50 THz (dash-dotted line).

tric fields can be thought of in terms of the formation of photon sidebands. In this picture the DC conductance at low field goes like  $J_0^2$ . Details of this theory can be found in Ref. [11].

As an alternate explanation, we present a simple empirical picture whose formulation starts with the static  $I$ - $V$ . In this scheme, an effective DC conductance is obtained by time averaging

the AC electric current over a single period of the laser field,

$$\sigma_{\text{DC}} = \frac{1}{T} \int_0^T dt \frac{I(E(t))}{E_0},$$

$$\text{where } E(t) = E_0 + E_1 \sin \omega t,$$

where  $E_0$  is the DC bias,  $E_1$  is the amplitude of the laser field, and the current as a function of

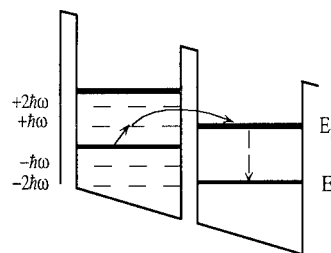
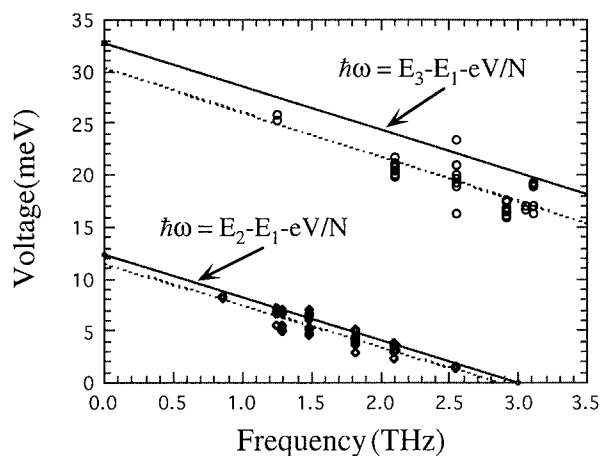


Fig. 4. The position in voltage of the AC-induced tunneling steps as a function of frequency. The solid lines are calculated, where  $N$  is the number of quantum wells, and the dotted lines are the best fits to the data.



electric field is obtained from the static  $I$ – $V$ . In Fig. 2 the second maxima in the conductance data and the calculation have been identified. This comparison suggests that a maximum electric field of 4.76 kV/cm has been coupled into the sample, which is close to the measured free space electric fields. In the model the  $I$ – $V$  characteristic and the concomitant domains must respond at terahertz frequencies.

#### 4. $I$ – $V$ characteristics in the presence of intense terahertz radiation

Fig. 3 shows the  $I$ – $V$  characteristics of the superlattice in the presence of the FEL at three different frequencies, where the solid line is the static  $I$ – $V$ . Most noteworthy is the appearance of new steps and plateaus in the presence of the FEL whose location in voltage varies as a function of frequency. In Fig. 4 we plot the location of the steps in voltage versus frequency, where the dotted lines are the best fits to the data and the solid lines are calculated using the envelope function approximation. It should be pointed out that the lower set of data in Fig. 4 corresponds to the region of the  $I$ – $V$  characteristic shown in Fig. 3 and the upper set of data corresponds to a higher voltage region of the  $I$ – $V$  not shown in Fig. 3.

The physical origin of the steps and plateaus can be understood in terms of sequential resonant tunneling into photon sidebands. In such a process, an electron absorbs a photon and is excited to a photon sideband  $\hbar\omega$  above the ground state, subsequently the electron tunnels into an excited state of the adjacent well and this is followed by the relaxation of energy back down to the ground state. The solid lines and the accompanying formulas in Fig. 4 are the mathematical statement of this process, and the energy level diagram with sidebands in Fig. 4 describes the process that corresponds to the lower set of data.

#### 5. Conclusion

We have observed photon-assisted sequential resonant tunneling in semiconductor superlattices

using terahertz radiation from the UCSB FELs. These new tunneling mechanisms can be explained in terms of well-to-well resonant tunneling from photon sidebands. We have also observed the oscillatory quenching of the DC conductivity as a function of AC field strength, although, the interpretation is still open to question. These set of measurements open the possibility of carrying out Büttiker and Landauer's gedanken experiment to measure the tunneling time [12,13]. Future measurements will focus on understanding the stimulated emission tunneling channels and how the quenching of the DC conductivity scales with laser frequency, superlattice parameters and temperature.

#### 6. Acknowledgements

These experiments would not have been possible without the expertise and commitment of the staff at the UCSB Center for Free-Electron Laser Studies, J.R. Allen, D. Enyeart, G. Ramian, D. White and B. Wallace.

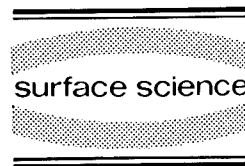
#### 7. References

- [1] L. Esaki and R. Tsu, IBM J. Res. Dev. 14 (1970) 61.
- [2] R. Tsu and L. Esaki, Appl. Phys. Lett. 19 (1971) 246.
- [3] Yu.A. Romanov, Opt. Spektrosk. 33 (1972) 917.
- [4] A.A. Ignatov and Yu.A. Romanov, Sov. Phys. Solid State 17 (1975) 2216.
- [5] A.A. Ignatov and Yu.A. Romanov, Phys. Status Solidi (b) 73 (1976) 327.
- [6] R.F. Kazarinov and R.A. Suris, Sov. Phys. Semicond. 6 (1972) 120.
- [7] For an extensive review, see: F.G. Bass and A.P. Teterov, Phys. Rep. 140 (1986) 37.
- [8] M. Holthaus, Phys. Rev. Lett. 69 (1992) 351.
- [9] G. Ramian, Nucl. Instrum. Methods A 318 (1992) 225.
- [10] K.K. Choi, B.F. Levine, R.J. Malik, J. Walker and C.G. Bethea, Phys. Rev. B 35 (1987) 4172.
- [11] P.K. Tien and J.P. Gordon, Phys. Rev. 129 (1963) 647.
- [12] M. Büttiker and R. Landauer, Phys. Rev. Lett. 49 (1982) 1739.
- [13] M. Büttiker, Electronic Properties of Multilayers and Low-Dimensional Semiconductor Structures, Eds. J.M. Chamberlain et al. (Plenum, New York, 1990) p. 297.



ELSEVIER

Surface Science 305 (1994) 389–392



## Terahertz response of resonant tunneling diodes

J.S. Scott <sup>\*,2,a</sup>, J.P. Kaminski <sup>a</sup>, S.J. Allen <sup>a</sup>, D.H. Chow <sup>b</sup>, M. Lui <sup>b</sup>, T.Y. Liu <sup>b</sup>

<sup>a</sup> University of California at Santa Barbara, Center for Free-Electron Laser Studies <sup>1</sup>, Santa Barbara, CA 93106, USA

<sup>b</sup> Hughes Research Laboratory, Malibu, CA 90265, USA

(Received 21 April 1993; accepted for publication 19 June 1993)

### Abstract

We have measured the broad-band terahertz response of state of the art InGaAs/AlAs and InAs/AlSb resonant tunneling diodes from 180 GHz to 3.6 THz using the free-electron lasers at UCSB. A tungsten whisker antenna in a conventional probe station is used to couple the far-infrared radiation into the device. Normalizing the resonant tunneling response with the off-resonant response allows us to circumvent the much slower RC time constant of the device and consequently enables a measurement of the relaxation time due to the quantum inductance.

### 1. Introduction

The potential applications of resonant tunneling diodes (RTDs) in high speed electronics has prompted extensive research into the fundamental limits of quantum transport in these systems. High speed operation of these devices has been demonstrated in picosecond switches [1] and high frequency negative resistance oscillators [2]. Limitations in the transport time are due to both the extrinsic RC time constant and the intrinsic “quantum well inductance”. Recently there has been substantial improvements in minimizing the RC time constant [3]. As improvements in reducing the extrinsic response times continue, the device response time will approach the limitation

imposed by the intrinsic response times due to the quasi-bound state escape time [4]. In this experiment it appears that we can avoid the extrinsic limitations of the RTD and measure intrinsic effects.

### 2. Resonant tunneling diodes

The resonant tunneling structures used in this present work are drawn from two different material systems. Both RTDs exhibit high peak-to-valley ratios and large current densities at room temperature, an important necessity in real device applications. The RTD based on the InGaAs/AlAs material system consists of 8 mL AlAs barriers, a 15 mL InGaAs quantum well and a 1000 Å depletion layer latticed matched to an InP substrate, and exhibits a room temperature peak current density of  $7.6 \times 10^4$  A/cm<sup>2</sup> and a peak-to-valley current ratio as high as 25:1. The DC room temperature current–voltage curve

\* Corresponding author.

<sup>1</sup> Office of Naval Research (N00014-92-J-1452).

<sup>2</sup> University of California MICRO program and the Hughes Aircraft Company (92-006).

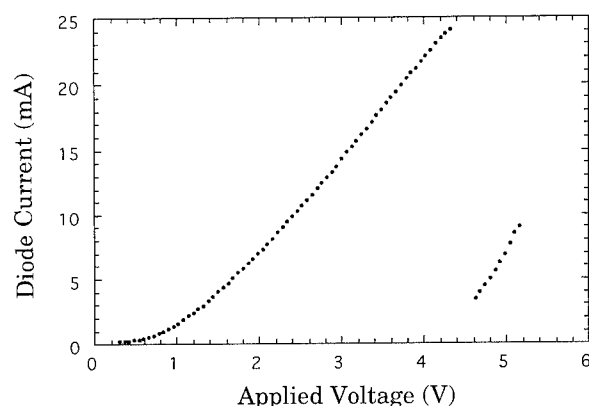


Fig. 1. DC  $IV$  curve for InGaAs/AlAs RTD.

is shown in Fig. 1. A second device based on the InAs/AlSb material system has 5 mL AlSb barriers, a 25 mL quantum well and a 500 Å depletion layer on a GaAs substrate and exhibits a room temperature peak current density of  $3.0 \times 10^5$  A/cm<sup>2</sup> and a peak-to-valley ratio of 3:1. This structure is similar to a device which has been observed to oscillate at 712 GHz [6]. All samples were grown by molecular beam epitaxy with heavily doped layers on either sides of the RTD structures. Electrical isolation of the diodes was accomplished by a simple wet mesa etch.

### 3. Experimental setup

Our terahertz radiation sources are the free-electron lasers at UCSB [5], which are capable of providing tunable high power far-infrared (FIR) radiation over the broad frequency range of 120 GHz to 5 THz.

Following the approach of Sollner and co-workers [6], we exploit the non-linearity in the current-voltage characteristic of a resonant tunneling diode to measure changes in the DC  $IV$  curve due to an applied terahertz field. An applied oscillating signal will shift the bias point of the RTD thereby producing a time averaged rectified response. For small, low frequency AC fields, the induced current in the device will be proportional to the second derivative of the DC  $IV$  curve.

The FIR is focused onto the 5  $\mu\text{m}$  square diodes in a conventional probe station with a tungsten probe tip acting as both the basic electrical contact for the diode as well as a broad band antenna coupling the radiation into the diode. A second probe tip, removed from the influence of the FIR, serves as the substrate contact. Using the diode as its own detector, at various terahertz frequencies both the DC current and the current induced by the terahertz radiation are measured as a function of the applied bias. We are particularly interested in comparing the response on and off resonance.

### 4. RTD rectified response

Shown in Fig. 2 is a plot of the induced current ( $\delta I$ ) in the diode, the diode response, as a function of the applied voltage. The frequency of the FIR is 3.6 THz. The diode response for voltages below the negative differential resistance onset voltage ( $V_{\text{NDR}} = 4.5$  V) corresponds to the resonant tunneling regime. Here the quasi-bound state in the quantum well remains above the emitter conduction band edge. The points above  $V_{\text{NDR}}$  represent the off-resonant condition, occurring when the well state has moved below the conduction band edge.

The frequency dependent, at a diode operating current of 2 mA, is shown in Fig. 3. The measured diode response is seen to be overwhelmed by antenna effects with the response

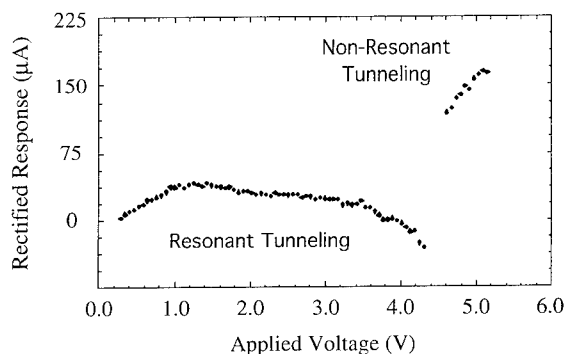


Fig. 2. RTD rectified response at 3.6 THz as a function of the DC bias point.

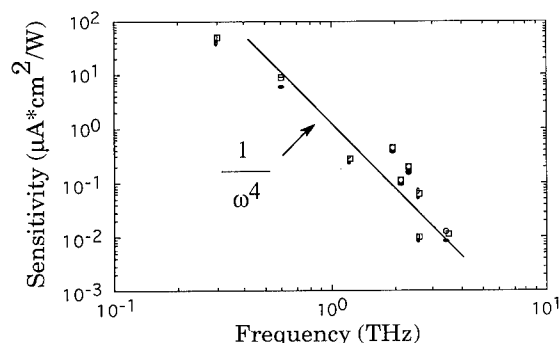


Fig. 3. InGaAs/AlAs frequency dependence.

exhibiting an inverse  $\omega^4$  behavior. With the device capacitance dominating, any intrinsic inductive effects due to the RTD are unobservable. To eliminate the device capacitance effects and essentially all extrinsic effects, the diode response in the resonant tunneling regime ( $\delta I_{\text{on-res}}$ ) is normalized by the off-resonant response ( $\delta I_{\text{off-res}}$ ). This serves to remove the antenna effects and it is the curve shapes which will carry the frequency dependence of the now *intrinsic* diode response.

The normalized frequency response,  $\delta I_{\text{on-res}}/\delta I_{\text{off-res}}$ , for the InGaAs/AlAs RTD and for the InAs/AlSb RTD is shown in Fig. 4. The InGaAs/AlAs RTD displays a roll off behavior at 650 GHz, and the InAs/AlSb RTD a roll off at 1.9 THz.

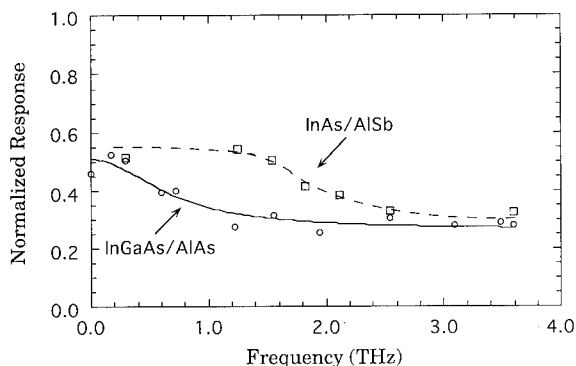


Fig. 4. The frequency response for the InGaAs/AlAs RTD and the InAs/AlSb RTD. The normalized rectified response for InGaAs/AlAs exhibits a roll off at 650 GHz and for InAs/AlSb a roll off at 1.9 THz.

This is not the RC roll off. By normalizing the rectified response we have eliminated the much slower RC time constant of the devices. The RC roll off actually occurs below 200 GHz, while the roll offs shown are well above this frequency.

To better understand this behavior we look to the lumped circuit model [4] which assumes a simple exponential relaxation of the tunneling current where the relaxation time  $\tau$  is modeled by a quantum inductance,  $L_{\text{qw}} = R\tau$ , where  $R$  is the tunneling resistance. We assume that the induced or rectified current relaxes in the same manner. The frequency dependence is then given by,

$$\delta I_{\text{induced}} \propto \frac{1}{1 + (\omega\tau)^2}.$$

For a simple relaxation of this type occurring in both the on and off resonant tunneling regimes, our normalized response would behave as,

$$\frac{\delta I_{\text{on}}}{\delta I_{\text{off}}} \propto \frac{1 + (\omega\tau_{\text{off}})^2}{1 + (\omega\tau_{\text{on}})^2}.$$

Using this form for the ratio of the relaxation of the induced current in the resonant and non-resonant state we can extract the two times  $\tau_{\text{on}}$  and  $\tau_{\text{off}}$ . The time  $\tau_{\text{on}}$  being the relaxation time associated with resonant tunneling and  $\tau_{\text{off}}$  the off-resonant tunneling time. The times can be obtained directly from the roll off point which is at  $\omega\tau_{\text{on}} = 1$  and from the ratio of the high frequency response to the low frequency response which gives the ratio of the relaxation times. For the InGaAs/AlAs RTD we obtain 170 and 240 fs, and for the InAs/AlSb, 85 and 45 fs for the relaxation times  $\tau_{\text{on}}$  and  $\tau_{\text{off}}$  respectively.

Although the linear response is expected to be dominated by the quantum well inductance at terahertz frequencies [7], published theories of the rectified response show either no relaxation [8] or internal resonances [9]. Wingreen [8] uses a transmission-coefficient approach to derive a coefficient of rectification. The form of the coefficient is such that at room temperature we would expect a flat, frequency independent, response. Frensley [9] on the other hand, working from a truly open quantum system premise uses a kinetic

theory based upon the Wigner–Weyl transformation of the density operator to model the AC small signal response of an GaAs/AlGaAs RTD. In this model the coefficient of rectification exhibits a region of resonant enhancement when the diode is biased in the NDR region. It must be noted that within this approach the susceptance is *positive* up to frequencies where optical transitions become important, well above our maximum frequency. This indicates that the rectified response is actually capacitive and not inductive as we have taken it to be here.

## 5. Conclusion

In conclusion, we have probed double barrier resonant tunneling diodes using terahertz radiation from the UCSB free-electron lasers. Normalizing the resonant tunneling rectified response with the off-resonant response enables a measurement of the intrinsic relaxation times associated with the *inductive* nature of the quantum well. From this simple relaxation model we extract intrinsic response times,  $\tau_{\text{on}}$  and  $\tau_{\text{off}}$ , associated with the tunneling current on and off resonance. For the InGaAs/AlAs RTD we obtain 170 and 240 fs, and for the InAs/AlSb, 85 and 45

fs for  $\tau_{\text{on}}$  and  $\tau_{\text{off}}$ , respectively. Finally, existing theories are not easily reconciled with these experiments.

## 6. Acknowledgments

The authors wish to thank the staff at the Center for Free-Electron Laser Studies, J.R. Allen, G. Ramian, D. White and in particular D. Enyeart for his expertise in the operation of the lasers.

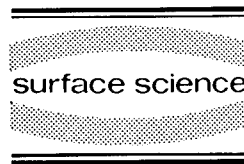
## 7. References

- [1] E. Ozbay, S.K. Diamond and D.M. Bloom, *Electron. Lett.* 26 (1990) 1046.
- [2] E.R. Brown, J.R. Soderstrom, C.D. Parker, L.J. Mahoney, K.M. Molvar and T.C. McGill, *Appl. Phys. Lett.* 58 (1991) 2291.
- [3] S. Allen, preprint/private communication.
- [4] E.R. Brown, C.D. Parker and T.C.L.G. Sollner, *Appl. Phys. Lett.* 54 (1989) 934.
- [5] G. Ramian, *Nucl. Instrum. Methods Phys. Res. A* 318 (1992) 225.
- [6] T.C.L.G. Sollner, W.D. Goodhue, P.E. Tannenwald, C.D. Parker and D.D. Peck, *Appl. Phys. Lett.* 43 (1983) 588.
- [7] Y. Fu and S.C. Dudley, *Phys. Rev. Lett.* 70 (1993) 65.
- [8] N.S. Wingreen, *Phys. Rev. Lett.* 56 (1990) 253.
- [9] W.R. Frensley, *Rev. Mod. Phys.* 62 (1990) 745.



ELSEVIER

Surface Science 305 (1994) 393–397



## Tunneling between highly correlated 2D electron systems

J.P. Eisenstein \*, L.N. Pfeiffer, K.W. West

*AT&T Bell Laboratories, Murray Hill, NJ 07974, USA*

(Received 21 April 1993; accepted for publication 17 June 1993)

### Abstract

Experiments on the tunneling between two parallel 2D electron gases at high magnetic fields are discussed. After reviewing the recent discovery of a broad high field tunneling gap tied to the Fermi level, several new results are presented. These include studies of the detailed shape of the gap near onset and evidence of the fractional quantum Hall effect in the tunneling characteristics. Finally, we present data suggesting that effects of Coulomb interactions on the tunneling may be separable into two distinct regimes.

Measurements revealing a new kind of Coulomb gap in the tunneling between two parallel 2D electron gases in GaAs double quantum wells at high magnetic fields have recently been reported [1]. In contrast to the sharply resonant tunneling characteristics seen at  $B = 0$ , which are consistent with a simple single-particle description of the tunneling process, at high fields a broad ( $\sim 2$  meV) region of quenched tunneling exists at the Fermi level (i.e. around zero bias). This suppression, or tunneling gap, exists over wide ranges of magnetic field and is not reflected in ordinary transport studies of the individual 2D layers (which display the integer and fractional Hall effects). This new gap cannot be explained within a non-interacting model of the 2D systems. Instead, we have argued [1] that it arises from the strongly correlated nature of 2D systems at high field, particularly in the lowest Landau level, and is not crucially dependent upon disorder. In

essence, the tunneling gap reflects the Coulomb energy required to rapidly inject an electron into this highly correlated system. The observed magnitude of the gap was found [1] to be quite consistent with this model. After briefly summarizing our earlier results, a number of new findings are reported here. Among these are studies of the detailed shape of the gap edge at high magnetic fields, fingerprints of the fractional quantum Hall effect (FQHE) on the tunneling and, finally, evidence that a boundary exists between two distinct tunneling regimes, both of which support a tunneling gap.

The double quantum well (DQW) samples used here consist of two 200 Å wide GaAs wells separated by a 175 Å wide  $\text{Al}_{0.3}\text{Ga}_{0.7}\text{As}$  barrier. Each well contains a 2D electron gas with a density around  $n_{1,2} \approx 1.6 \times 10^{11} \text{ cm}^{-2}$  and mobility of  $3 \times 10^6 \text{ cm}^2/\text{V} \cdot \text{s}$ . Separate ohmic contacts to the individual 2D layers are established using a selective depletion technique [2]. In addition to standard magneto-transport measurements on each layer, these contacts also allow for the application

\* Corresponding author.

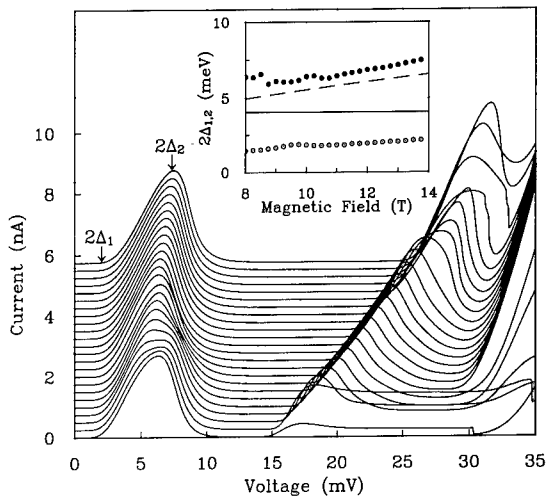


Fig. 1. Tunneling  $I$ - $V$  characteristics at  $T = 0.6$  K for magnetic fields from  $B = 8$  T to 13.75 T in steps of 0.25 T. The curves are vertically offset for clarity. Inset: Magnetic field dependence of the onset ( $2\Delta_1$ ) and peak ( $2\Delta_2$ ) voltages. The solid line is the Coulomb energy  $E_C = e^2/\epsilon\langle a \rangle$  while the dashed line is  $0.4e^2/\epsilon l_0$ .

of an inter-layer voltage  $V$  and the measurement of the resulting tunneling current  $I$ . Both  $I$  versus  $V$  and  $dI/dV$  versus  $V$  characteristics can be obtained. At  $B = 0$  sharply resonant tunneling characteristics are observed. Within a single-particle picture of the electron gases this follows from the twin constraints of energy and momentum conservation. In fact, the observed tunneling linewidth ( $\Gamma_0 \approx 0.3$  meV) provides a new and direct measure of the electronic lifetime in each layer [3].

High magnetic fields destroy the sharply resonant tunneling signatures seen at  $B = 0$ . In Fig. 1 low temperature  $I$ - $V$  characteristics are shown for magnetic fields between  $B = 8$  and almost 14 T. For this field range the Fermi level in each 2D layer lies in the lower spin branch of the lowest Landau level, with the filling factor ranging from  $\nu = 0.83$  to 0.48. (The figure contains data for  $V > 0$  only since the tunnel current was found to be closely antisymmetric in voltage for the present case of equal densities in the two layers.) As the figure shows, the tunnel current is extremely small over a range of voltages near  $V = 0$ . Above about  $V \approx 2$  mV the tunnel current rises into a

broad peak centered near  $V \approx 7$  mV, before falling to near zero again in wide high energy gap. A second peak, whose position is linearly dependent upon the magnetic field, is found at still higher voltage; this has been identified as due to tunneling into the empty first excited Landau level [1]. Both the gap around  $V = 0$  and the broad peak near 7 mV are due to *intra*-lowest Landau level tunneling events. These features are not strongly sensitive to the magnetic field, at least over the range covered in Fig. 1.

We have argued that a tunneling gap which tied the Fermi level is intrinsic to Landau quantized 2D systems. Put simply, the gap reflects the Coulomb energy required to rapidly inject (extract) a magnetically localized electron into (from) the highly correlated quantum liquid which the 2D electron system is in the extreme quantum limit. Since at short distances this liquid resembles a Wigner crystal, we may liken the tunneling process to the creation of a vacancy-interstitial pair. Ignoring excitonic effects, the energy required to create such a defect will be of order of the classical Coulomb energy  $E_C = e^2/\epsilon\langle a \rangle$  with the mean interparticle spacing  $\langle a \rangle = 2(\pi n)^{-1/2}$ . The inset to Fig. 1 contains the magnetic field dependence of the onset ( $2\Delta_1$ ) and peak ( $2\Delta_2$ ) voltages for the intra-Landau level tunnel current. (The onset is defined as that voltage where the current equals 1% of the peak value.) As the inset shows,  $E_C$  (the solid horizontal line) is about midway between  $2\Delta_1$  and  $2\Delta_2$ . The weak field dependence of these parameters is expected since the electrons are not point-like, but are only localized to within a magnetic length  $l_0 = (\hbar/eB)^{1/2}$  which is comparable to the inter-particle spacing at these filling factors.

The existence of a tunneling gap which is relatively insensitive to the filling factor seems, at first, at odds with the conventional picture of a 2DES in the extreme quantum limit where energy gaps exist only at certain fractional fillings. At  $\nu = 1/2$  for example, no FQHE state exists in a single layer system [4] and yet we find a substantial tunneling gap. The resolution of this apparent paradox lies in the time scale for tunneling. As long as the tunneling occurs faster than the liquid state can respond, through the emission of

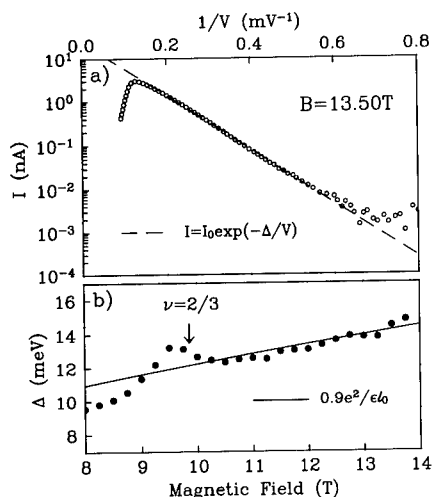


Fig. 2. Analysis of  $I$ - $V$  data in gap region. (a) Typical  $\log(I)$  vs.  $1/V$  plot. Data taken at  $B = 13.5 \text{ T}$  and  $T = 0.6 \text{ K}$ . Dashed line represents fit to Eq. (1). (b) Magnetic field dependence of extracted gap parameter  $\Delta$ . Solid line is  $0.9e^2/\epsilon l_0$ .

collective modes, the injected “interstitial” electron will clearly represent an excited state of the system. As time evolves the liquid will relax this defect and the ground state of the  $(N + 1)$ -particle system, with uniform density, will be established. Reasonable estimates of the relevant time scales support this scenario [1].

Several important issues have been ignored in this model, e.g. the role of disorder, *inter*-layer correlation effects, the fractional quantum Hall effect, etc. While considerably more experimental work is required to fully explore these issues, a more detailed analysis of the existing data is clearly desirable. We begin by analyzing the shape of the tunneling gap. Fig. 2a displays a typical high magnetic field  $I$ - $V$  characteristic near zero bias, with  $\log(I)$  plotted against  $1/V$ . The data are well represented, for over two decades in current, by the functional form

$$I = I_0 \exp(-\Delta/V). \quad (1)$$

This dependence contrasts markedly with the algebraic Coulomb gaps appropriate to strongly localized 2D conductors [5] or the logarithmic suppressions predicted [6] in the diffusive regime. It is also at odds with the conclusions of Ashoori

et al. [7] who first reported an apparent magnetic field-induced suppression of tunneling into a single 2D electron gas. While no  $I$ - $V$  characteristics were obtained, Ashoori et al. inferred, from measurements of temperature dependence of the zero bias tunneling conductance, a partial suppression of the tunneling density of states *linear* in energy about the Fermi level. Even after allowing for the necessary convolution of the spectral functions for each layer, our data are inconsistent with these earlier results [7].

Recently, He, Platzman and Halperin [8] have theoretically investigated tunneling between two disorder-free 2D electron systems in a high magnetic field. From numerical exact diagonalizations of finite systems they find, in addition to a strong suppression of the tunneling density of states around the Fermi level, a peak in the intra-Landau level tunnel current near  $V \approx 0.4e^2/\epsilon l_0$ . As the inset to Fig. 1 shows, this is in good agreement with the experiment. Using the recent Chern-Simons theory of Halperin, Lee and Read [9] for the half-filled Landau level, He et al. [8] also present analytical results suggesting that Eq. (1) should closely approximate the  $I$ - $V$  characteristic in the gap. While our data are consistent with Eq. (1), the value of  $\Delta$  we extract, around  $0.9e^2/\epsilon l_0$  as shown in Fig. 2b, is some seven times smaller than the value of  $2\pi e^2/\epsilon l_0$  predicted by He et al. Whether this quantitative disagreement is fundamental, or merely the result of various neglected issues (e.g. finite thickness corrections, *inter*-layer correlations, disorder, etc.), is not yet known. Nevertheless, the qualitative agreement between theory and experiment supports the notion that the observed tunneling gap is an intrinsic feature of 2D electron systems in the extreme quantum limit [10].

The weak magnetic field dependence of the measured tunneling spectra suggests that the fractional quantum Hall effect represents a relatively subtle effect in an already strongly correlated system. Nevertheless, the FQHE is apparent in the  $I$ - $V$  characteristics. In Fig. 2b, where the field dependence of the energy parameter  $\Delta$  defined in Eq. (1) is shown, a significant upward bump is found around the  $\nu = 2/3$  FQHE  $B = 9.9 \text{ T}$ . (A similar feature can be seen in the onset



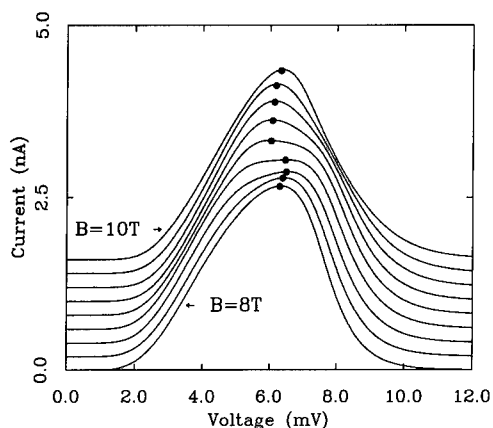


Fig. 3.  $I$ - $V$  characteristics between  $B = 8$  T and 10 T in steps of 0.25 T. Curves are vertically offset. Solid dots placed where current is a maximum. Note weak splitting of spectrum around 9 T. This is consistent with  $\nu = 2/3$  in one of the layers.

energy  $2\Delta_1$  displayed in Fig. 1.) While it is not yet clear to us how to interpret this bump, it seems reasonable that the incompressibility of an FQHE state would “harden” the tunneling gap. At a more subtle level, the FQHE at  $\nu = 2/3$  also appears to produce structure in the intra-Landau level tunneling peak. Fig. 3 shows a blow-up of the  $I$ - $V$  data from  $B = 8$  to 10 T with a barely resolved splitting of the peak observed around 9 T. The solid dots, placed at the maximum current, show that the lineshape appears to gradually shift spectral weight from the high energy component of the “doublet” to the low energy one as the field is increased and the  $2/3$ -state is traversed [11]. This splitting is reminiscent of features observed in recent luminescence studies of the FQHE [12]. Given these observations, it seems likely that tunneling will provide a fruitful new way to study the incompressible quantum liquids underlying the FQHE.

So far we have concentrated on high magnetic fields. Nevertheless, these samples reveal interaction effects on tunneling at fields as low as  $B = 0.5$  T. (At this field, and at very low temperature, a weak dip in the tunneling conductance at zero bias is first observable, as Fig. 4 demonstrates.) While intermediate magnetic fields have not yet been thoroughly studied, qualitative evidence suggesting that the effects of electron–electron

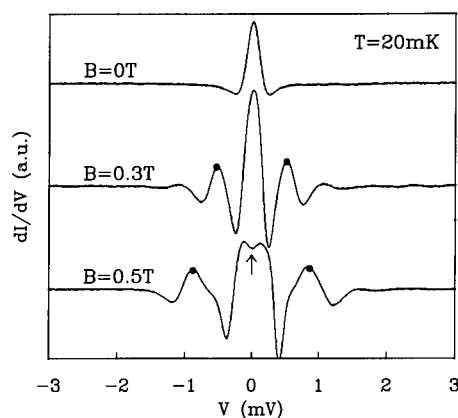


Fig. 4. Low field tunneling conductance curves at  $T = 20$  mK. Single peak at  $B = 0$  is split into a Landau fan by a weak field. By  $B = 0.5$  T a small suppression of the tunneling conductance appears at zero bias. The solid dots are placed at voltages corresponding to the cyclotron energy  $\pm \hbar\omega_c$ .

interactions on tunneling may be separable into two distinct regimes has been found. Fig. 5 contains a plot of the field dependence of the half-width of the tunnel resonance. This half-width is simply defined (see the inset to Fig. 5) as the voltage of the first zero crossing of  $dI/dV$ . The data shown were taken at high temperature,  $T = 6$  K, so as to suppress all quantum Hall states within the field range and thus eliminate technical difficulties with the associated extremely small sheet conductivities [1]. As Fig. 5 shows, the half-width gradually rises with field from  $B = 0$  to  $\sim 4$  T where it abruptly begins to increase much

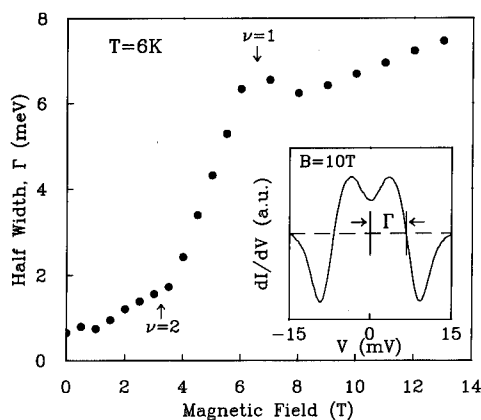


Fig. 5. Magnetic field dependence of half-width of tunnel resonance measured at  $T = 6$  K. Inset defines half-width.

more rapidly. By about  $B = 6$  T this steep rise ends and a gentle increase resumes. We have already argued [1] that in the high field case the very broad tunneling linewidths reflect the strong Coulomb interactions in the 2D system and that disorder plays a minor role. Below  $B \approx 5$  T this is not obviously the case and it is plausible that interactions and disorder are of comparable importance to the tunneling linewidth. In any case, Fig. 5 clearly suggests a distinction can be made between a low and high field tunneling regime. It seems reasonable to speculate that the boundary between these regimes depends upon the relative importance of disorder and electron–electron interactions. We note in passing that the transition between these two regimes occurs roughly over the filling factor interval  $2 > \nu > 1$ . The relevance of this correspondence will be tested in future experiments on samples with different densities.

In conclusion, we have reviewed our recent tunneling studies of high mobility double layer 2D electron systems. The central result is the observation of a deep and broad gap at the Fermi level in the tunneling density of states at high magnetic fields. A simple model has been suggested in which this gap is an intrinsic feature of the strongly correlated 2D electron systems in the extreme quantum limit and disorder plays at most a subsidiary role. The detailed shape of the gap has been compared with the predictions of a recent theory of tunneling in clean 2D systems at half-filling of the lowest Landau level and qualitative agreement is found. The fractional quantum Hall effect is observable in the tunneling

characteristics although an interpretation of the signature is lacking. Finally, we have presented data suggesting that the effects of interactions upon the tunneling can be separated into two regimes and we have speculated that disorder plays a role in defining this division.

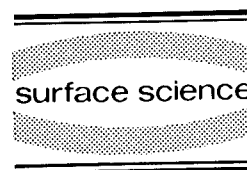
## 1. References

- [1] J.P. Eisenstein, L.N. Pfeiffer and K.W. West, *Phys. Rev. Lett.* 69 (1992) 3804.
- [2] J.P. Eisenstein, L.N. Pfeiffer and K.W. West, *Appl. Phys. Lett.* 57 (1990) 2324.
- [3] S.Q. Murphy, J.P. Eisenstein, L.N. Pfeiffer and K.W. West, *Bull. Am. Phys. Soc.* 38 (1993) 591.
- [4] Owing to the large barrier thickness, the present samples do not support the novel inter-layer FQHE states reported in Eisenstein et al., *Phys. Rev. Lett.* 68 (1992) 1383.
- [5] A.L. Efros and B.I. Shklovskii, in: *Electron–Electron Interactions in Disordered Systems*, Eds. A.L. Efros and M. Pollak (Elsevier, Amsterdam, 1985) p. 409.
- [6] B.L. Altshuler, A.G. Aronov and P.A. Lee, *Phys. Rev. Lett.* 44 (1980) 1288.
- [7] R.C. Ashoori, J.A. Lebens, N.P. Bigelow and P.H. Silsbee, *Phys. Rev. Lett.* 64 (1990) 681.
- [8] Song He, P.M. Platzman and B.I. Halperin, preprint.
- [9] B.I. Halperin, P.A. Lee and N. Read, *Phys. Rev. B* 47 (1993), in press.
- [10] A Coulomb gap in a clean classical 2D system with quenched kinetic energy has been predicted by A.L. Efros, *Phys. Rev. Lett.* 68 (1992) 2208.
- [11] The magnetic field location of a given filling fraction depends on the bias voltage  $V$ , via the interlayer capacitance. See Ref. [1].
- [12] See B.B. Goldberg et al., in: *Low Dimensional Electronic Systems*, Eds. G. Bauer, F. Kuchar and H. Heinrich (Springer, Berlin, 1992), and the references cited therein.



ELSEVIER

Surface Science 305 (1994) 398–399



# One-electron Green's function and electron tunneling in a two-dimensional electron system in a strong magnetic field

Song He <sup>\*,a</sup>, P.M. Platzman <sup>a</sup>, B.I. Halperin <sup>b</sup>

<sup>a</sup> AT&T Bell Laboratories, Murray Hill, NJ 07974, USA

<sup>b</sup> Department of Physics, Harvard University, Cambridge, MA 02138, USA

(Received 19 April 1993; accepted for publication 24 May 1993)

## Abstract

We investigate the properties of the one-electron Green's function in an interacting two-dimensional electron system in a strong magnetic field, which describes an electron tunneling into such a system. From finite-size diagonalization, we find that its spectral weight is suppressed near zero energy, reaches a maximum at an energy of about  $0.2e^2/\epsilon l_c$ , and decays exponentially at higher energies. We propose a theoretical model to account for the low-energy behavior. For the case of Coulomb interactions between the electrons, at even-denominator filling factors such as  $\nu = 1/2$ , we predict that the spectral weight varies as  $e^{-\omega_0/|\omega|}$ , for  $\omega \rightarrow 0$ .

In a recent experiment [1] examining the bulk tunneling of a bilayer system subjected to low temperatures and high magnetic fields, the experimental  $I$ - $V$  characteristics exhibited a strong suppression of the tunneling current at low biases and a broad, pronounced peak in the neighborhood of  $eV_{\max} \approx 0.4e^2/\epsilon l_c$ , where  $\epsilon$  is the dielectric constant, and  $l_c$  is the magnetic length.

Here we present a summary of our work [2] on the theory of this type of tunneling experiment using the tunneling Hamiltonian approximation which relates the tunneling current to the spectral weight  $A_{\pm}(\omega)$  of the one-electron Green's function  $G_{\pm}(\omega)$  in the individual layers.

We have presented simple arguments for the behaviors of  $A_{\pm}(\omega)$ . At low energies, we have

argued that the spectral weight is strongly suppressed due to the small overlap between the initial state when an extra electron is added to an  $N$ -electron system and the low-lying states in the resultant  $(N+1)$ -electron system. We have argued that the energies  $\bar{\omega}_{\pm}$  around which  $A_{\pm}(\omega)$  exhibit a maximum can be estimated to be the self-energies of one extra electron or hole added to the system in the lowest Landau level. According to our estimation, we find that the tunneling peak energy  $eV_{\max} \approx \bar{\omega}_{+} + \bar{\omega}_{-} \approx 0.4e^2/\epsilon l_c$ , the coefficient being roughly independent of  $\nu$  in the range of  $0.2 < \nu < 0.8$ . We have also performed finite-size diagonalization for systems of up to 10 electrons to study the behavior of  $A_{\pm}(\omega)$  at energies comparable to  $eV_{\max}$ . Fig. 1 is a typical numerical result we obtained, where we show the histograms of the spectral weight  $A_{\pm}(\omega)$  for a compressible system of 8 electrons and at an  $N_{\phi} = 17$  close to  $\nu = 1/2$ . Our numerical calcula-

\* Corresponding author.

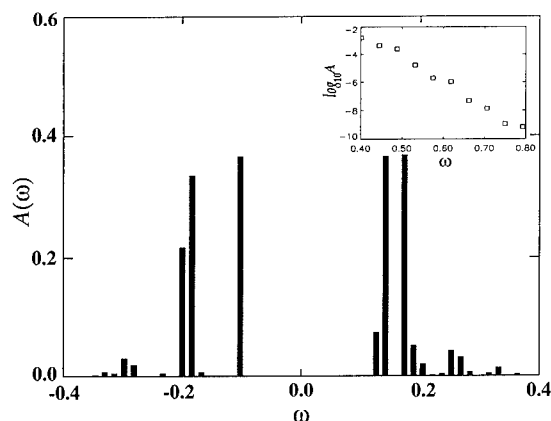


Fig. 1. The histograms of the spectral weight  $A(\omega)$  of the one-electron Green's function at a compressible state obtained for an 8-electron system with flux number  $N_\phi = 17$ ;  $\log_{10} A(\omega)$  is shown in the inset; all energies are measured from the chemical potential.

tions suggest that  $eV_{\max} \approx 0.4 \approx 0.6e^2/\epsilon l_c$  in the filling factor range  $1/3 < \nu < 2/3$ .

In order to understand the precise form of the suppression of the tunneling current at small biases, we have constructed a model for the low-energy behavior of  $A_{\pm}(\omega)$  by coupling the added electron to the density fluctuations in the rest of

the system. We find, for a disorder-free system at compressible filling factors such as  $\nu = 1/2$ , with Coulomb interaction, that the spectral weight  $A_{\pm}(\omega) \approx e^{\omega_0/|\omega|}$  as  $\omega \rightarrow 0$ , due to the existence of a diffusive mode [4] at low energies. The tunneling  $I$ - $V$  characteristics are determined to be  $I \approx e^{-V_0/V}$  with  $V_0 = 2\pi e^2/\epsilon l_c$  at  $\nu = 1/2$ . We have also discussed the effects of inter-layer coupling and impurity scattering on the tunneling. Comparison with the recent experiment [5] is made.

The authors are grateful for helpful conversations with J.P. Eisenstein, R. Ashoori, P.A. Lee, and R.H. Morf. Work at Harvard was supported in part by NSF grant DMR-91-15491.

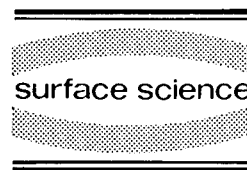
## 1. References

- [1] J.P. Eisenstein, L.N. Pfeiffer and K.W. West, Phys. Rev. Lett. 69 (1992) 3804.
- [2] Song He, P.M. Platzman and B.I. Halperin, Phys. Rev. Lett. 68 (1993) 3460.
- [3] K.D. Schotte and U. Schotte, Phys. Rev. 182 (1969) 479.
- [4] B.I. Halperin, P.A. Lee and N. Read, Phys. Rev. B 47 (1993) 7312.
- [5] J.P. Eisenstein, private communication.



ELSEVIER

Surface Science 305 (1994) 400–404



# Coupled electron–hole transport: generalized random-phase approximation and density functional theory

H.C. Tso

*Department of Physics, Queen's University, Kingston, Ontario, Canada K7L 3N6*

P. Vasilopoulos

*Department of Physics, Concordia University, 1555 de Maisonneuve Blvd. West, Montréal, Québec, Canada H3G 1M8*

F.M. Peeters

*Department of Physics, University of Antwerp (ULA), B-2610 Antwerp, Belgium*

(Received 15 April 1993; accepted for publication 1 June 1993)

## Abstract

Coulomb coupling between spatially separated two-dimensional electron and hole gases, when an electric field is applied to only one of them, is studied as function of temperature and electron (hole) gas density. The coupling is described in the random-phase approximation (RPA) and in a generalized RPA (GRPA) which takes into account exchange processes to all orders of the Hartree–Fock potential within the Hubbard approximation [Phys. Rev. 111 (1958) 442; Proc. R. Soc. London A 243 (1957) 336]. Due to the exclusion principle at low densities, electrons (holes) of the same spin are kept *so far apart* that only electrons (holes) of *different* spin screen each other. The GRPA coupling is stronger than the RPA one and leads to a larger transimpedance  $R_T$ . The temperature dependence of  $R_T$  agrees very well with that measured by Sivan et al. [1] for relatively high densities. The GRPA result for square wells is still below the experimental value, but it can be improved with a self-consistent calculation of the envelope function and of the mean separation between the gases.

## 1. Introduction

Coulomb coupling between two spatially separated electron gases, when a current is driven through only one of them, has been predicted [2] and observed [3,4] to influence the transport properties of the gases. Recently, transport measurements have been reported [1] in a system composed of a two-dimensional (2D) electron gas and a 2D hole gas. The gases are spatially separated by a barrier of width  $d = 200$  Å. The bar-

rier is high and thick enough to prevent tunneling and recombination but thin enough to allow for sizable Coulomb interaction between carriers in different gases. Current is allowed to flow in the electron gas and a drag voltage is developed and measured in the hole gas. The calculated [1] RPA results for the temperature and density dependence of the coupling were a factor of 5 to an order of magnitude smaller than the experimental results for temperatures ( $T$ ) between 9 and 50 K. A similar discrepancy between theory and

experiment [4] in an electron–electron system, for  $T \leq 7$  K, has been explained, *within* RPA, by a phonon-mediated Coulomb coupling important only at these very low temperatures [5] and most pronounced for *equal* electron densities. Thus, this mechanism cannot explain the high-temperature [1] results. Another mechanism would be electron–hole binding but this was estimated [1] to be very weak. Previously, we have shown [6] that the RPA treatment of the Coulomb scattering [1,5] overestimates the screening and renders the coupling stronger. The reported [6] GRPA transimpedance  $R_T$ , though in good agreement with the experiment, is still smaller than the experimental value especially for low densities. Here, we present briefly the GRPA results and show that the one-particle square well function of Ref. [6], should be replaced by a more realistic one that is determined self-consistently by density functional theory (DFT). This reduces the mean separation between the two gases and brings  $R_T$  closer to the experimental value.

## 2. Generalized random phase approximation

In this section we model the electron–hole system with two infinitely deep quantum wells, of width  $b$ , with their centers and their closest edges separated by a distance  $a$  and  $d$ , respectively. For the densities of interest, only the lowest level is occupied in either well. The many-body Hamiltonian pertinent to the experiment [1] is  $H(t) = H_h(t) + H_e(t) + H_{he}(t)$ .  $H_e$  is the Hamiltonian of the electrons in the drive well and contains electron–electron, electron–impurity, and electron–phonon interactions; the same holds for the Hamiltonian of the holes in the drag well  $H_h$  and  $H_{he}$  is the Coulomb interaction between holes and electrons in the two wells. With this Hamiltonian we obtain [6] the coupled momentum-balance equations:

$$-\frac{m_e^*}{e} \frac{\partial j_e}{\partial t} + en_e E = F^{eh} + F^e, \quad (1)$$

$$en_h \frac{V_D}{L} i + \frac{m_h^*}{e} \frac{\partial j_h}{\partial t} = F^{he} + F^h. \quad (2)$$

Here,  $V_D$  is the measured drag voltage and develops when the current is not allowed to flow; if the current flows,  $V_D$  vanishes. Further,  $L$  is the length of the specimen,  $n_e(n_h)$  the 2D electron (hole) density of the drive (drag) well,  $j_h(j_e)$  the 2D current density,  $m_h^*(m_e^*)$  the effective mass,  $E = Ei$  the electric field applied only in the drive well, and  $F^e(F^h)$  the frictional force due to scattering by phonons and impurities.

For weak electric fields, we write  $j_{e,h} = \pm n_{e,h} p e v_d^{e,h}$  with  $v_d^e(v_d^h)$  the drift velocity (+ for electrons, – for holes). Then the forces can be linearized over the drift velocities giving  $F^{he} = \Omega_{he} m_h^* (v_d^h - v_d^e)$ , where  $\Omega_{he}$  is the relaxation frequency per unit area due to the Coulomb coupling. In the steady state and for zero drag current, Eq. (2) gives the transimpedance  $R_T \equiv V_D/I_e = m_h \Omega_{he} / e^2 n_h n_e$ . The RPA result for  $\Omega_{he}$  is [6]

$$\Omega_{he} = -2\hbar \int_{-\infty}^{\infty} \frac{d\omega}{2\pi} \sum_{q_{\parallel}} \frac{|F(q_{\parallel}) v(q_{\parallel}; a)|^2}{|\epsilon_{+}(q_{\parallel}; \omega)|^2} \times q_{\parallel}^2 \frac{\partial n(\omega')}{\partial \omega'} \bigg|_{\omega' = -\omega} \text{Im}[\Pi_{+}^{h(0)}] \text{Im}[\Pi_{+}^{e(0)}], \quad (3)$$

with  $\Pi_{+}^{h,e(0)}(q_{\parallel}; \omega)$  the equilibrium hole (electron) polarizability,  $F(q_{\parallel})$  the form factor, and

$$\begin{aligned} \epsilon_{\pm}(q_{\parallel}; \omega) = & [1 - v(q_{\parallel}; 0) F(q_{\parallel}) \Pi_{\pm}^{h(0)}(q_{\parallel}; \omega)] \\ & \times [1 - v(q_{\parallel}; 0) F(q_{\parallel}) \Pi_{\pm}^{e(0)}(q_{\parallel}; \omega)] \\ & - |v(q_{\parallel}; a) F(q_{\parallel})|^2 \Pi_{\pm}^{h(0)}(q_{\parallel}; \omega) \\ & \times \Pi_{\pm}^{e(0)}(q_{\parallel}; \omega) \end{aligned} \quad (4)$$

the retarded (advanced) dielectric function in RPA; here  $v(q_{\parallel}; a) = (2\pi e^2 / q_{\parallel}) \exp(-q_{\parallel} a)$ . For temperatures  $T > 10$  K,  $\Omega_{he}$  behaves approximately linearly with  $T$  as shown by the dashed curve in Fig. 2. Figs. 1 and 2 show that there is a marked difference between the RPA calculations and the experimental results similar to that of Ref. [1]. This difference tends to be larger at

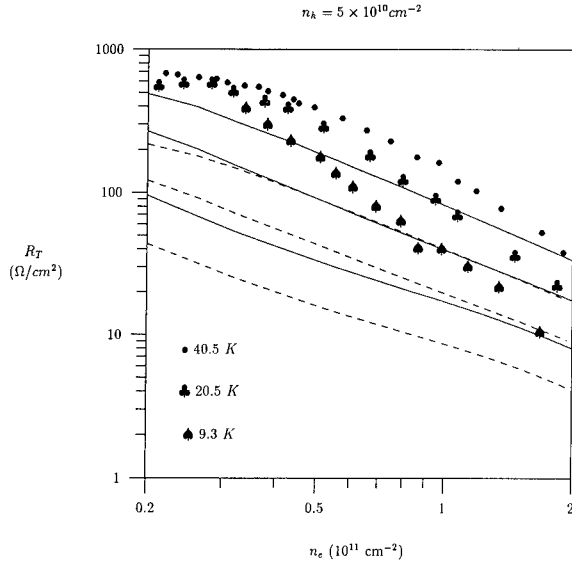


Fig. 1. Transimpedance  $R_T$  per square versus electron density  $n_e$  for three temperatures, with fixed hole density  $n_h = 5 \times 10^{10}/\text{cm}^2$ . The solid and dashed curves are the GRPA and RPA results, respectively.

lower densities as shown in Fig. 1. This is because the RPA is good [7] only for very high densities. An extra term shown, e.g., in Fig. 1b of Ref. [6],

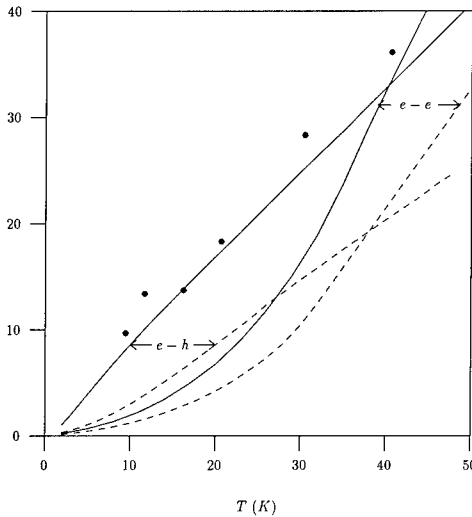


Fig. 2. Transimpedance  $R_T$  per square versus temperature  $T$  for fixed densities. Curves e-h:  $n_e = 2 \times 10^{11}/\text{cm}^2$ ,  $n_h = 5 \times 10^{10}/\text{cm}^2$ . Curves e-e: in both wells  $n_e = 1.5 \times 10^{11}/\text{cm}^2$ . All curves are marked as in Fig. 1.

should be included in the self-energy that takes into account the exchange process of holes and electrons. It can be ignored at high densities but not at low densities as shown by Abrikosov et al. [8]. Including this term and considering only scattering near the Fermi levels, we obtain an effective interaction  $\bar{v}_{\pm}(q_{\parallel}; \omega) = v(q; a)/\epsilon_{\pm}^G(q_{\parallel}; \omega)$ , where the GRPA dielectric function  $\epsilon_{\pm}^G(q_{\parallel}; \omega)$  is given by Eq. (4) with  $v(q_{\parallel}; 0)F(q_{\parallel})$  replaced by  $v_{\text{HF}}^h(q_{\parallel}; 0)$  and  $v_{\text{HF}}^e(q_{\parallel}; 0)$  on the first line, and  $|\dots|^2$  by  $v_{\text{HF}}^h(q_{\parallel}; a)v_{\text{HF}}^e(q_{\parallel}; a)e^{-2q_{\parallel}a}$  with

$$v_{\text{HF}}^{h,e}(q_{\parallel}; a) = \frac{2\pi e^2}{q_{\parallel}} \left[ F(q_{\parallel}) - \frac{1}{4} \frac{q_{\parallel}}{k_F^{h,e} + q_{\parallel}} \right. \\ \left. \times F(q_{\parallel} + k_F^{h,e}) e^{-k_F^{h,e}a} \right]. \quad (5)$$

The second term on the right-hand side of Eq. (5) is the exchange term and occurs only for carriers of *parallel* [7] spin. As a result, only carriers of *antiparallel* spin and a portion of them with *parallel* spin will participate, statistically speaking, in the screening for  $q_{\parallel} \gg k_F$ , i.e., for low densities, as carriers of the same spin are kept apart by the Pauli exclusion principle. For very low densities, carriers of the same spin can be so far apart that they have almost no effect on the screening at all. If the carriers in both wells are of the same type,  $-1/4$  in the exchange becomes [7]  $-1/2$  because there is no exchange between an electron and a hole. Thus  $\Omega_{\text{he}}$  takes the form of Eq. (3) with  $\epsilon_{\pm}(\dots)$  replaced by  $\epsilon_{\pm}^G(\dots)$ .

The calculated  $R_T$  is shown in Figs. 1 and 2 by the solid (GRPA) and dashed (RPA) curves. In Fig. 1  $R_T$  is shown as function of  $n_e$  for fixed  $n_h$ . The solid symbols are the experimental results of Ref. [1]. We have used  $m_h^* = 6.7m_e^*$  and the parameters of the experiment. Noticing the *logarithmic* scale, it is seen that the density dependence of  $R_T$ , in the GRPA, is better than the RPA result especially at high densities. In Fig. 2  $R_T$  is plotted versus temperature for an electron-hole (e-h) system. The agreement between the GRPA and the experimental result is very good; this is mainly due to the rather high gas densities involved. For contrast, we also show  $R_T$  for the same structure with electrons in both wells (e-e).

For all densities, the GRPA result is below the experimental one. This is because the square well function that we used is not very realistic; see below.

### 3. Density functional theory

To obtain the true envelope functions, we model the system with two triangular wells and barriers high enough to make the electron and hole wave functions vanish at the distant side of the barrier and thus avoid tunnelling. The electron energy density functional for the three-dimensional (3D) densities  $n_e$ ,  $n_h$  is given by [9]

$$E_e[n_e] = C_1 n_e^{2/3} + \frac{C_2}{n_e^2} \left( \frac{\partial n_e}{\partial z} \right)^2 - C_3 n_e^{1/3} + e^2 \int d\mathbf{r}_2 \frac{[n_e(\mathbf{r}_2) - 2n_h(\mathbf{r}_2)]}{2|\mathbf{r} - \mathbf{r}_2|} + v_{\text{ext}}, \quad (6)$$

where  $C_1 = 3(3\pi^2)^{2/3}/10$ ,  $C_2 = 1/8$ ,  $C_3 = 3(3\pi^2)^{1/3}/4\pi$ , and  $v_{\text{ext}}$  is the external (triangular) potential. The first two terms are the Thomas–Fermi and von Weizsäcker terms; the third and fourth terms are the exchange and Hartree interactions, respectively.  $E_h[n_h]$  is given by Eq. (6) with  $n_e$  interchanged with  $n_h$ . Minimizing  $\int d\mathbf{r} n_p(\mathbf{r}) E_p[n_p(\mathbf{r})]$ ,  $p \equiv e$  or  $h$ , and assuming the  $n_e$  depends weakly on  $n_h$  and vice versa, we obtain the coupled equations

$$-2C_2 \frac{\partial^2 n_p}{\partial z^2} + \frac{C_2}{n_p} \left( \frac{\partial n_p}{\partial z} \right)^2 + \left( \frac{5}{3} C_1 n_p^{2/3} + \phi_H^p + v_{\text{ext}} \right) n_p = \mu_p n_p, \quad (7)$$

where  $\phi_H^e(\mathbf{r}) = \int d\mathbf{r}_2 [n_e(\mathbf{r}_2) - n_h(\mathbf{r}_2)]/|\mathbf{r} - \mathbf{r}_2|$  and  $\mu_p$  is the chemical potential. The layer separation,  $a_C$ , obtained by capacitance measurement, is related to the density  $n_e$  by  $a_C = d + 2 \int d\mathbf{r} n_e(\mathbf{r}) z / \int d\mathbf{r} n_e(\mathbf{r})$  for  $n_e = n_h$ . Eq. (7) is solved numerically with barrier height 0.3 eV and the confining electric field adjusted to give  $a_C - d = 50$  Å. The normalized DFT electron density, which is symmetric to the hole one with respect to the barrier center for  $n_e = n_h$ , and its counter-

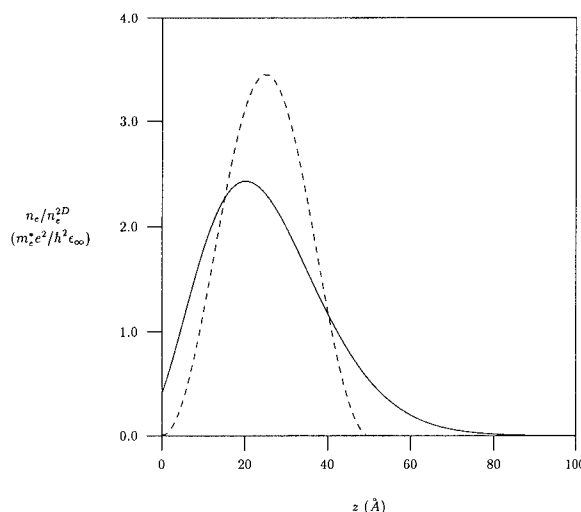


Fig. 3. Normalized 3D electron density  $n_e/n_e^{2D}$  versus position along the  $z$  axis; the barrier is between  $-200$  and  $0$  Å.

part for square wells are plotted in Fig. 3. It is seen that the layer separation for the more realistic triangular wells (solid curve) is 240 Å [6] and 250 Å for square wells (dashed curve) used in Ref. [6]. This renders the mean separation  $a$  smaller, cf. Eq. (5), and the coupling stronger. Full calculations for  $R_T$  are in progress.

### 4. Summary

We have shown that the reported [1] deviations of the density and temperature dependences of the Coulomb coupling between an electron gas and a hole gas, spatially separated from each other, from the RPA results are mostly due to an overestimation of the screening when treated within RPA. Most of the results, especially the temperature dependence, can be explained by employing a GRPA which takes into account exchange processes, absent from RPA, to all orders of the Hartree–Fock potential within the Hubbard approximation. The remaining discrepancy between experiment and the GRPA results can partially be accounted for by a self-consistent calculation of the envelope function and of the mean separation between the gases.



## 5. Acknowledgements

This work was partially supported by NSERC Grant No. OGPIN028 (H.C.T., P.V.) and NATO Grant No. NATO: 5-2-05/RG No. 890123 (P.V., F.M.P.).

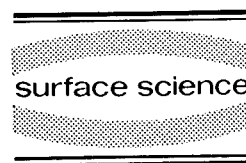
## 6. References

- [1] U. Sivan, P.M. Solomon and H. Shtrikman, Phys. Rev. Lett. 68 (1992) 1196.
- [2] M.B. Pogrebinskii, Sov. Phys. Semicond. 11 (1977) 372; P.J. Price, Physica B 117, (1983) 750;
- I.I. Boiko and Yu.M. Sirenko, Phys. Status Solidi 159 (1990) 805.
- [3] P.M. Solomon et al., Phys. Rev. Lett. 63 (1989) 2508.
- [4] T.J. Gramila et al., Phys. Rev. Lett. 66 (1991) 1216.
- [5] H.C. Tso, P. Vasilopoulos and F.M. Peeters, Phys. Rev. Lett. 68 (1992) 2516.
- [6] H.C. Tso, P. Vasilopoulos and F.M. Peeters, Phys. Rev. Lett. 70 (1993) 2146.
- [7] P. Nozières and D. Pines, Rev. 111 (1958) 442; J. Hubbard, Proc. R. Soc. London A 243 (1957) 336.
- [8] A.A. Abrikosov, L.P. Gorkov and I.E. Dzyaloshinski, Methods of Quantum Field Theory in Statistical Physics (Dover, New York, 1963) p. 336.
- [9] W. Kohn and P. Vashishta, Theory of the Inhomogeneous Electron Gas, Eds. S. Lundqvist and N.H. March (Plenum, New York, 1983) p. 79.



ELSEVIER

Surface Science 305 (1994) 405–407



## Observation of an abrupt double-to-single-layer transition in a double-quantum-well structure

Y. Katayama <sup>\*,1</sup>, D.C. Tsui, H.C. Manoharan, M. Shayegan

*Department of Electrical Engineering, Princeton University, Princeton, NJ 08544, USA*

(Received 19 April 1993; accepted for publication 14 June 1993)

### Abstract

We report the first observation of an abrupt double-to-single-layer transition in a GaAs/AlAs double-quantum-well (DQW) structure. The transition is observed as a sharp decrease in the 4-terminal resistance measured as a function of the bias applied to the front gate of the device. Data on the Shubnikov–de Haas oscillations taken at different gate voltages reveal that this abrupt change in resistance is associated with the transition from a double- to a single-layer two-dimensional electron system in the DQW.

Recently, transport measurements in DQW (double-quantum-well) systems have been of wide interest [1–4]. The small interlayer spacing comparable to the intralayer mean electron distance suggests the important roles of interlayer physics such as tunneling, interlayer Coulomb interaction, and exchange effects. Even at zero magnetic field, the transport coefficient shows structure arising from the inter-well tunneling as a function of the gate voltage [5]. The Coulomb interaction between two parallel two-dimensional electron gases (2DEGs) were experimentally studied and the scattering rate was obtained [6]. Theoretically, it has been pointed out that the exchange

effect can lead to an instability in a low-density symmetric DQW [7].

Here, we report the first observation of an abrupt double-to-single-layer transition in a GaAs/AlAs DQW structure, in which we believe the interlayer Coulomb interaction [6] and exchange effect [7] are playing the dominant role. The transition was observed as a sharp decrease in the 4-terminal resistance as a function of the top gate voltage,  $V_g$ , accompanied by the change in Shubnikov–de Haas (SdH) oscillation patterns from double-layer-like to single-layer-like.

Our device structure has a 70 Å AlAs barrier sandwiched between two 150 Å GaAs wells, with  $n \approx 1.4 \times 10^{11}/\text{cm}^2$  and  $\mu \approx 3.7 \times 10^5 \text{ cm}^2/\text{V} \cdot \text{s}$  in each well when density is balanced at  $V_g = +0.25 \text{ V}$ . We fabricated an H-shaped mesa which has 4 leads. The active region was completely covered by an Al Schottky gate. Resistance was measured in the 4-terminal configuration as a

\* Corresponding author.

<sup>1</sup> On educational leave from IBM Research, Tokyo Research Laboratory, 1623-14, Shimotsuruma, Yamato-shi, Kanagawa-ken, 242 Japan.

function of  $V_g$  using the standard Lock-in detection technique. A constant current excitation of 10 nA at 13 Hz was used throughout the measurement. The experiment was conducted using a  $\text{He}^3$  cryostat whose base temperature was 0.3 K.

Fig. 1 shows the resistance versus  $V_g$ . At  $T = 0.3$  K, the transition is seen as a sharp decrease in resistance by more than 50% at  $V_g \approx -0.46$  V. The characteristic energy scale of the transition is a few meV (see  $T = 15$  and 77 K traces in Fig. 1). Data on the SdH oscillations taken at different gate voltages above and below the transition are shown in Fig. 2. The appearance of single-frequency oscillations for  $V_g < -0.46$  V and oscillations showing beating for  $V_g > -0.46$  V is evidence that this abrupt change in resistance is indeed associated with the transition from a double- to a single-layer two-dimensional electron system in the DQW. The beating structure at  $V_g = -0.44$  V, where the densities of the two wells are expected to be far off balanced, may have a similar origin to the one observed in the 2 subband systems [8,9].

The sharp resistance drop at  $T = 0.3$  K is surprising. It cannot be explained by a simple parallel resistor model which treats two layers independently or other lumped circuit modeling of the DQW [10]. They only result in a monotonic change of resistance as a function of  $V_g$  like the  $T = 77$  K trace in Fig. 1. Therefore, some inter-

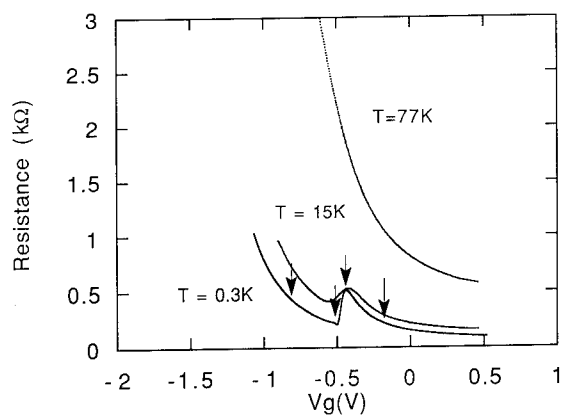


Fig. 1. 4-terminal resistances at  $B = 0$  for three different temperatures. Arrows indicate the positions of the gate voltages at which SdH oscillations are measured and shown in Fig. 2.

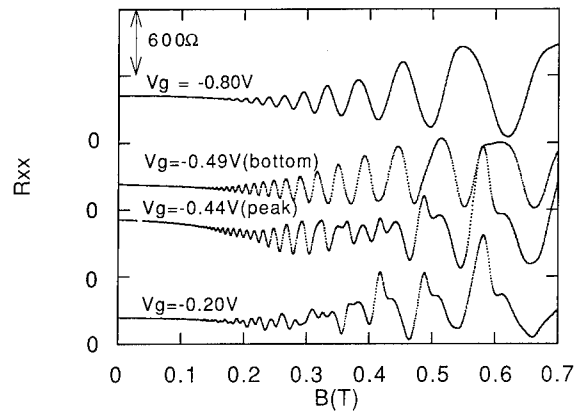


Fig. 2. SdH oscillations demonstrating an abrupt electronic transition from a double- to a single-layer system. Beatings indicative of a system of two 2DEGs with different densities are apparent.

layer physics must be playing a role. Tunneling, which was the reason for the resistance peak observed in Ref. [5], is not relevant, since the transition in our case, at  $V_g \approx -0.46$  V, is far away from the  $V_g = +0.25$  V, where the densities in the two wells are balanced. In the following, we give an explanation for our experimental findings based on interlayer Coulomb drag [6] and the exchange effect [7] in DQW systems.

The decrease in resistance is explained by the disappearance of the interlayer Coulomb drag [6] due to transfer of electrons out of the top well. The electrons in the top well are an order of magnitude closer in distance to the bottom electron layer than the remote donors (900 Å away), but an order of magnitude less in density just before the transition (at  $V_g = -0.44$  V, the density of the top layer  $n_1$  is estimated to be 14% of the density of the bottom layer  $n_2$ ). Therefore, the scattering rate of the bottom-layer electrons due to the electrons in the top layer is comparable to that due to the remote donors, if we assume a similar scattering mechanism for both the electrons in the top well and the remote donors above the well. The amount of the resistance drop in our data is consistent with this estimation.

The sudden depletion of the top well, which causes the sharp resistance drop, is considered to be a result of the exchange-driven instability pre-

dicted by Ruden and Wu [7]. In our case, where the wells are asymmetric, the total relevant energy of the system  $E_{\text{total}}$  can be written as

$$E_{\text{total}} = \frac{1}{2}D^{-1}[(n_1 - \Delta n)^2 + (n_2 + \Delta n)^2] - D^{-1}(n_2 - n_1)\Delta n + \frac{2\pi e^2}{\kappa_0}d\Delta n^2 - \frac{4e^2}{3\kappa_0}\left(\frac{2}{\pi}\right)^{1/2} \times [(n_1 - \Delta n)^{3/2} + (n_2 + \Delta n)^{3/2}],$$

where  $D$  is the two-dimensional density of states,  $\kappa_0$  is the dielectric constant of the medium between the two 2DEGs,  $d$  is the distance between the 2DEGs,  $\Delta n$  is the density of the transferred electrons, and  $n_1$ ,  $n_2$  are the densities of the individual wells. The second term is due to the subband-edge energy difference between the two wells. Fig. 3 gives the calculated  $E_{\text{total}}$  normalized

by  $D^{-1}n_2^2$  as a function of the transferred electron ratio  $\Delta n/n_1$  for three different ratios of  $n_1$  to  $n_2$ . We take  $n_2 = 1.4 \times 10^{11}/\text{cm}^2$ ,  $d = 220 \text{ \AA}$ , and  $\kappa_0 = 12$ . This calculation demonstrates that as  $n_1$  decreases, a larger fraction of electrons in the top well is transferred to the bottom well due to the exchange interaction, consistent with our experimental findings.

In conclusion, we report the first observation of an abrupt double-to-single-layer transition in a DQW structure, which is seen as a sharp decrease in the 4-terminal resistance as a function of the gate voltage.

Y.K. acknowledges the financial support from the IBM Japan overseas scholarship program and H.C.M. acknowledges the fellowship support from the Fannie and John Hertz Foundation. This work is supported in part by the NSF.

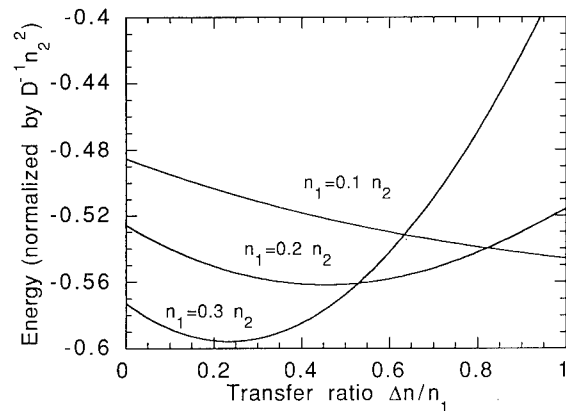


Fig. 3. The calculated total energy of the two 2DEGs as a function of the fractional density  $\Delta n/n_1$  of electrons transferred from the top well to the bottom well for three different ratios of  $n_1$  to  $n_2$ . We fix  $n_2 = 1.4 \times 10^{11}/\text{cm}^2$ .

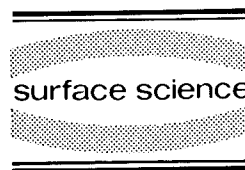
## 1. References

- [1] G.S. Boebinger, H.W. Jiang, L.N. Pfeiffer and K.W. West, Phys. Rev. Lett. 64 (1990) 1793.
- [2] A.H. MacDonald, P.M. Platzman and G.S. Boebinger, Phys. Rev. Lett. 65 (1990) 775.
- [3] J.P. Eisenstein, G.S. Boebinger, L.N. Pfeiffer, K.W. West and Song He, Phys. Rev. Lett. 68 (1992) 1383.
- [4] J.P. Eisenstein, L.N. Pfeiffer and K.W. West, Phys. Rev. Lett. 68 (1992) 3804.
- [5] A. Palevski, F. Beltram, F. Capasso, L. Pfeiffer and K.W. West, Phys. Rev. Lett. 65 (1990) 1929.
- [6] T.J. Gramila, J.P. Eisenstein, A.H. MacDonald, L.N. Pfeiffer and K.W. West, Phys. Rev. Lett. 66 (1991) 1216.
- [7] P.P. Ruden and Z. Wu, Appl. Phys. Lett. 59 (1991) 2165.
- [8] P.T. Coleridge, Semicond. Sci. Technol. 5 (1990) 961.
- [9] S.E. Schacham, E.J. Haugland and S.A. Alterovitz, Phys. Rev. B 45 (1992) 13417.
- [10] Y. Katayama and D.C. Tsui, Appl. Phys. Lett. 62 (1993) 2563.



ELSEVIER

Surface Science 305 (1994) 408–418



## Magnetotransport in antidot arrays

D. Weiss <sup>\*</sup>, K. Richter <sup>1</sup>, E. Vasiliadou, G. Lütjering

Max-Planck-Institut für Festkörperforschung, D-70569 Stuttgart, Germany

(Received 7 May 1993; accepted for publication 28 July 1993)

### Abstract

We study magnetotransport in lateral two-dimensional superlattices with periods on the order of 100 nm. Pronounced low-field transport anomalies reflect the interplay of two characteristic lengths of the system, the cyclotron radius  $R_c$  and the period  $a$ . Measurements at very low temperatures reveal quantum oscillations, periodic in the magnetic field  $B$ , which are superimposed upon the commensurability anomalies in the magnetoresistance  $\rho_{xx}$ . We show that the latter effect can be interpreted in terms of *quantized periodic orbits* which takes into account the chaotic nature of the classical phase space.

### 1. Introduction

Today's semiconductor technology provides a means to confine electrons in "boxes" with nanometer dimensions in all three spatial directions. Electron transport through these "artificial atoms" where the nuclear charge is replaced by the confining potential displays unique behavior and is used to probe the "atomic levels" of such a quantum dot structure [1]. In analogy, the coupling of quantum dots into a planar artificial lattice opens up the possibility to study the physical properties of artificial crystals. Just as individual quantum dots are characterized by energy levels analogous to atomic levels, artificial crystals possess a band structure, where the properties of the constituent "atoms" are controlled by the

superimposed periodic (confining) potential. Two examples of possible periodic potential shapes, both of them experimentally realized, are sketched in Fig. 1. For a weak periodic potential the electron energy (Fermi energy) is well above the potential modulation (Fig. 1a), whereas for a strong potential the Fermi energy intersects the repulsive potential peaks (Fig. 1b). Due to the characteristic shape of the latter type of potential, complementary to the one used to confine electrons in a quantum dot, we call it *antidot* potential [2–4]. Such artificial crystals allow one to search for qualitatively new phenomena not accessible in natural crystals. One prominent example in this context is the fractal energy spectrum of Bloch electrons in a magnetic field [5–7].

Recently, it has been observed that the magnetoresistance  $\rho_{xx}$  displays  $1/B$ -periodic low field oscillations when a high-mobility 2DEG is subjected to a *weak* periodic potential [8–11]. A weak (sinusoidal) periodic potential transforms the discrete Landau levels into Landau bands

<sup>\*</sup> Corresponding author.

<sup>1</sup> Present address: Division de Physique Théorique, Institut de Physique Nucléaire, 91406 Orsay Cedex, France.

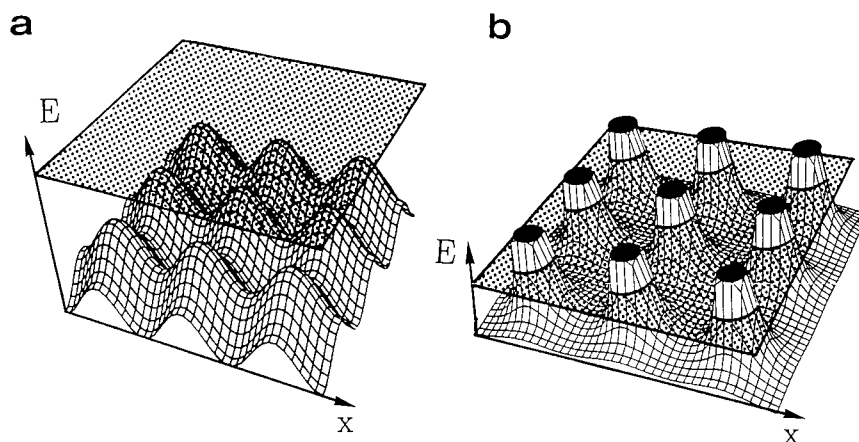


Fig. 1. (a) Weak and (b) strong modulation of the conduction band edge in the  $x$ - $y$  plane of the two-dimensional electron gas. The position of the Fermi energy is depicted by the dotted planes.

[12,13]. The resulting band structure can be calculated perturbatively for both one- and two-dimensional periodic potentials (see Ref. [7] and references therein). The oscillating bandwidth with

minima at  $2R_c = (\lambda - 1/4)a$  is the origin of the observed oscillatory behavior of  $\rho_{xx}$  (and  $\rho_{yy}$ ). Here,  $R_c$  is the classical cyclotron radius at the Fermi energy  $\epsilon_F$ , and  $\lambda$  is an integer oscillation

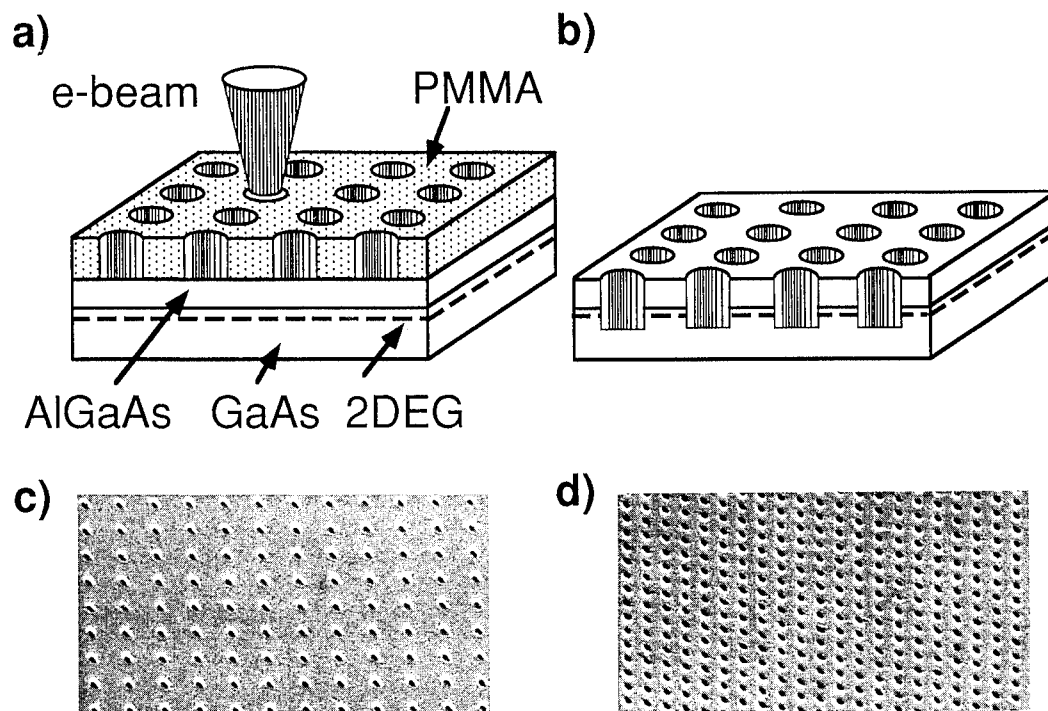


Fig. 2. Fabrication (schematically) of an antidot array by e-beam lithography (a) and subsequent etching of the holes through the 2DEG (b). An electron micrograph of a 300 nm square antidot lattice tilted by  $45^\circ$  is shown in (c), a 200 nm lattice in (d).

index. The picture of Landau band formation breaks down in an antidot lattice: the strong potential mixes Landau levels with different quantum numbers  $n$ , and a complicated band structure emerges.

Here we summarize our experimental results on magnetotransport in antidot arrays and sketch our current understanding of the phenomena observed. For a more complete collection of important related work, we refer to recent review articles [14–16]. Before going on to the experimental results, it is useful to specify some characteristic quantities of the system. Distinct transport anomalies stem from the commensurability between the cyclotron radius  $R_c$  and the period  $a$ . In a 2DEG the cyclotron radius,  $R_c = \hbar\sqrt{2\pi n_s}/eB$ , is directly connected to the carrier density  $n_s$  and the magnetic field  $B$ . In order to observe these effects it is necessary that the electron mean free path,  $l_e = v_F\tau$ , dependent on the Fermi velocity  $v_F$  and the Drude relaxation time  $\tau$ , is much longer than the period  $a$ . The Fermi wavelength  $\lambda_F = \sqrt{2\pi/n_s}$ , which is a measure of the extent of the wavefunction at zero field, however, is still smaller than the period  $a$  which is typically between 200 and 400 nm. Hence, electron transport can be treated in a semi-classical picture where the electrons bounce like balls ballistically through the antidot lattice (for related phenomena see also Ref. [15]). Classically, the motion of a particle in an antidot type of potential is known to be chaotic [17]. We show below that this classical electron dynamics leaves distinct marks in the experiments. In terms of an artificial band structure we face a situation where many bands are occupied; their number increases quadratically with the period  $\sim a^2 n_s/2$ . For antidot periods larger than the Fermi wavelength  $\lambda_F$  the electrons in such artificial crystals obey semi-classical rules.

## 2. Fabrication of antidot arrays

The starting point for the fabrication of lateral surface superlattices is a high-mobility two-dimensional electron gas (2DEG) formed at the interface of GaAs/AlGaAs heterojunctions. The

high mobility is an essential ingredient which assures that the electron mean free path,  $l_e$ , is much longer than the period  $a$  of the superimposed periodic potential. Typical mean free paths range from 5 to 10  $\mu\text{m}$  before patterning. The nanofabrication process is sketched in Fig. 2. The periodic array of antidots is written into the PMMA-resist layer by using a highly focused electron beam (Fig. 2a). Besides a square arrangement of antidots with periods from  $a = 200$  nm to  $a = 400$  nm, we have also fabricated triangular and rectangular arrays. After development, the holes in the PMMA are transferred into the heterojunction by reactive ion etching techniques [18]. After etching *through* the electron gas we expect an effective potential for the electrons similar to the one sketched in Fig. 1b; the conduction band is bent up at the antidot positions (due to charged surface states) and defines forbidden regions for the electrons. The effective antidot diameter  $d$  consists of the lithographic diameter plus a surrounding depletion region which can be reduced by brief illumination [19]. The antidot array is part of a conventional Hall bar geometry sketched in the top inset of Fig. 3b.

## 3. Magnetotransport experiments

In Fig. 3 we compare the magnetoresistance  $\rho_{xx}$  and the Hall resistance  $\rho_{xy}$  of patterned and unpatterned areas of the device. Pronounced low-field anomalies dominate the  $\rho_{xx}$  and  $\rho_{xy}$  trace of the antidot array in a regime where the transport coefficients are usually described by the Drude expressions  $\rho_{xx} = m^*/e^2 n_s \tau$ , and  $\rho_{xy} = B/en_s$  with the electron effective mass  $m^*$ . A double peak structure in  $\rho_{xx}$  for  $B$  values where  $R_c \approx 0.5a$  and  $R_c \approx 1.5a$  holds documents striking deviations from the simple Drude results. The  $\rho_{xx}$  peaks are accompanied by (nonquantized) steps in the Hall resistance displayed in Fig. 3b. At higher  $B$  values where the cyclotron diameter becomes smaller than the period  $a$ ,  $\rho_{xx}$  drops quickly, Shubnikov–de Haas (SdH) oscillations commence, and  $\rho_{xy}$  begins to display quantized Hall plateaus. In this high field regime the traces of patterned and unpatterned segments become

essentially identical indicating that the intrinsic high mobility is preserved between the antidots. At zero field, however, the mobility is limited by scattering off the antidots and the corresponding mean free path becomes comparable to the antidot spacing  $a$ . A remarkable anomaly in the  $\rho_{xy}$ -trace is the quenching of the Hall resistance close to  $B = 0$ ; the magnified quench is displayed in the inset of Fig. 3b. We address this effect in more detail below.

The number of peaks and steps resolved in the low  $B$  regime critically depends on the effective diameter  $d$  and the period  $a$  of the antidots. The zero-field resistance is directly controlled by the normalized cross section  $d/a$  and the carrier density  $n_s$ . In Fig. 4 we compare the magnetore-

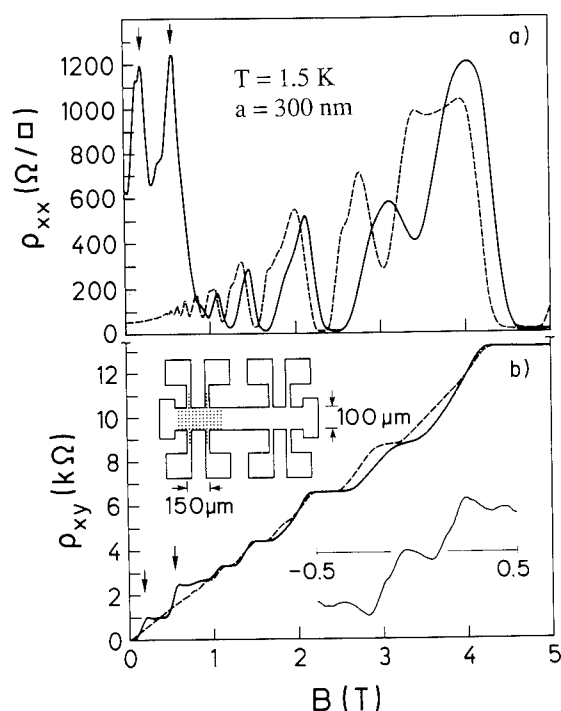


Fig. 3. (a) Magnetoresistance and (b) Hall resistance in patterned (solid line) and unpatterned (dashed line) sample segments at 1.5 K after brief illumination. In the patterned segment,  $n_s$  (determined from the periodicity of the Shubnikov-de Haas oscillations at higher  $B$ ) is slightly higher after illumination ( $n_s = 2.4 \times 10^{11} \text{ cm}^{-2}$ ). The arrows mark magnetic field positions where  $R_c/a \approx 0.5$  and 1.5. Top inset of (b): Sketch of the sample geometry. Bottom inset: Magnification of the quench in  $\rho_{xy}$  about  $B = 0$ . From Ref. [4].

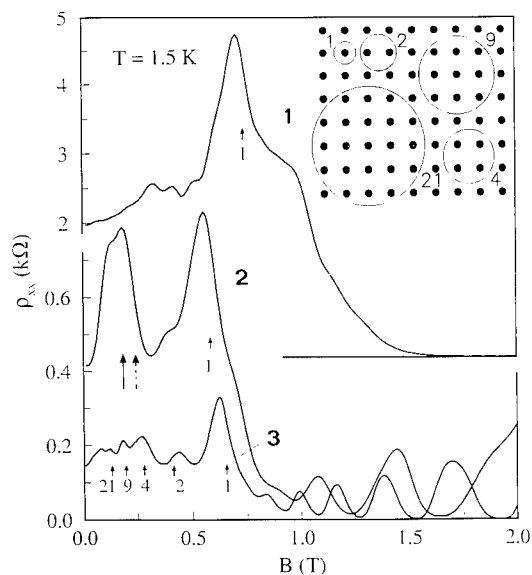


Fig. 4. Low- $B$  anomalies from three different samples. For smaller  $d/a$  more structure in  $\rho_{xx}$  evolves. All peaks in trace 3 can be ascribed to commensurate orbits around 1, 2, 4, 9 and 21 antidots, as is sketched in the inset. Corresponding  $R_c/a$  values, marked by arrows, are 0.5, 0.8, 1.14, 1.7 and 2.53, respectively. The dashed arrow for trace 2 marks the position of an unperturbed cyclotron orbit around four antidots ( $R_c/a = 1.14$ ). The shift of the corresponding resistance peak towards lower  $B$  indicates the deformation of the cyclotron orbit in a “soft” potential [17]. From Ref. [4].

distance curves of three samples with periods  $a = 200$  nm (top trace) and  $a = 300$  nm (bottom traces). In curves with smaller zero-field resistance a progressively greater number of peaks becomes resolved. Sample 3 exhibits the largest sequence of new  $\rho_{xx}$  peaks and  $\rho_{xy}$  plateaus. At each peak,  $R_c$  can be associated with a commensurate (circular) orbit encircling a specific number of antidots sketched in the inset of Fig. 4. Although the low-field maxima in trace 3 are well described by unperturbed circular cyclotron orbits, the simple orbit analysis fails to explain the prominent low  $B$  peak in curve 2: the  $R_c/a$  value of  $\sim 1.5$  deduced from the peak position at  $\sim 0.18$  T is not commensurate with the lattice. Model calculations show that this distinct peak stems from electrons on chaotic trajectories trapped on paths around four antidots [17]. Compared to the free electron case our the “orbit-around-four-antidots-peak” is shifted towards



lower  $B$  and provides a first experimental signature of chaotic electron dynamics.

The sequence of peaks observed in experiment reflects the geometry of the antidot lattice. In Fig. 5 we display  $\rho_{xx}$  data taken from a rectangular and hexagonal antidot lattice; a characteristic sequence of peaks reflects the particular “crystallographic” arrangement of the antidots. In a rectangular lattice the magnetoresistance strongly depends on the direction of current flow as can be seen from the data in Fig. 5a. The peak corresponding to an orbit around one antidot can only be probed if the current flows along the larger

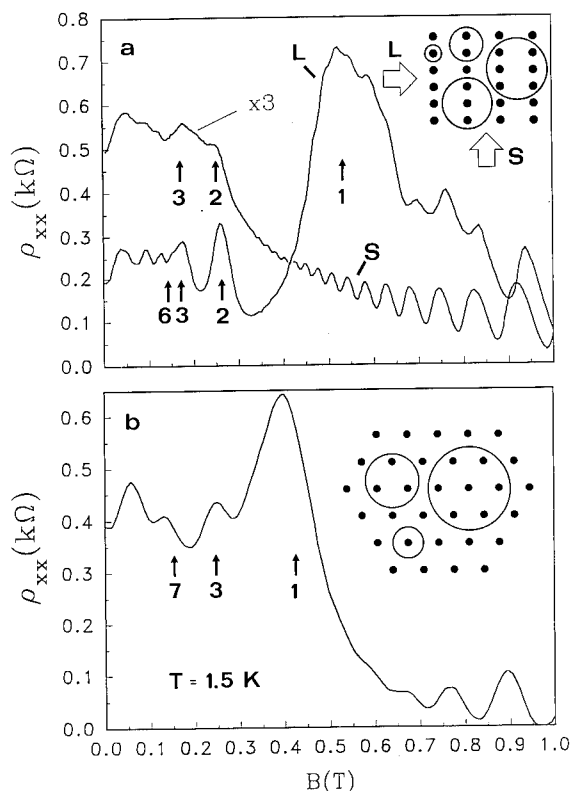


Fig. 5. (a) Magnetoresistance in a rectangular ( $a_x = 790$  nm,  $a_y = 410$  nm) and (b) hexagonal ( $a = 410$  nm) antidot array. In (a) “L” and “S” indicate the direction of current flow with respect to the long and the small period of the lattice as is sketched in the inset.  $B$ -positions corresponding to free cyclotron orbits around 1, 2, 3 and 6 antidots for  $R_c/a = 0.5, 1, 1.5$  and  $1.83$ , respectively, are marked. In the hexagonal lattice (b) arrows mark orbits around 1, 3 and 7 antidots at  $R_c/a$  values  $0.5, 0.87$  and  $1.37$ .

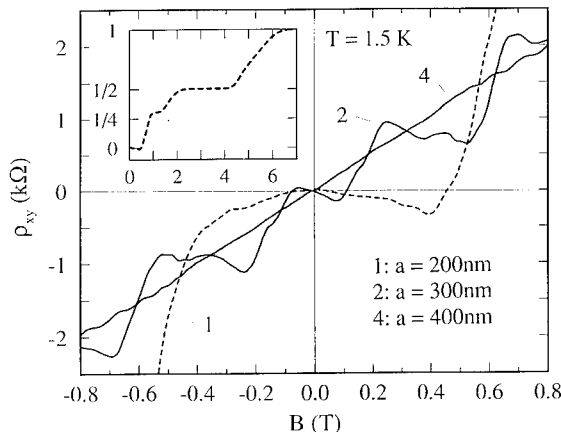


Fig. 6. Quenching of  $\rho_{xy}$  around  $B = 0$  for three samples with different periods  $a$ . For the sample with the smallest period  $a = 200$  nm we find the quench over a  $B$ -range of nearly 1 T. High field  $\rho_{xy}$ -data (in units of  $h/e^2$ ) of sample 1 up to 7 T are displayed in the inset. Sample 2 exhibits a negative slope of  $\rho_{xy}$  around  $B = 0$  indicating electron motion opposite to the Lorentz force.

lattice constant. The transport anomalies in such rectangular antidot lattices have been studied by Schuster et al. [20]. The magnetoresistance in a hexagonal lattice, displayed in Fig. 5b, shows peaks when the cyclotron orbit fits around 1, 3, and 7 antidots (see also Refs. [21,22]), hence reflecting the most stable commensurate orbits in this geometrical arrangement.

The quenching of the Hall resistance in antidot lattices came as a surprise. While such quenching has been observed in small, *mesoscopic* junctions where the electron motion between the sample boundaries can take place ballistically [23], the antidot array itself is macroscopic; its dimensions are large compared to  $l_e$ . In Fig. 6 we display the data of three antidot samples with different periods (but with comparable antidot diameter): the magnetic field range over which the Hall resistance is quenched decreases with increasing lattice constant. For  $a = 400$  nm the  $\rho_{xy}$  trace around  $B = 0$  becomes very close to the result expected from the Drude formulas. The quenching of the Hall resistance is just another example which underlines the importance of the classical chaotic electron dynamics discussed in the next section.

#### 4. Pinball model and chaotic electron dynamics

The fact that some of the peak positions in  $\rho_{xx}$  can be associated with circular commensurate orbits has stimulated an explanation based on a modified Drude picture, denoted as the pinball model [4]. Such a semi-classical description is supported by the experimental fact that the transport anomalies reported so far continue to be manifested up to high temperatures  $T \approx 50$  K. The basic assumption of the model is that electrons on commensurate orbits do not contribute to transport since they are trapped for a long time in the vicinity of an antidot. For such impaled orbits the repulsive potential at each antidot provides a local restoring force against drift induced by electric fields. The “removal” of an electron from transport requires a long lifetime of an electron on a pinned orbit, obtained when the mobility between the antidots is preserved. In this picture, the “reduction” of the carrier density for commensurate magnetic fields increases both  $\rho_{xx}$  and  $\rho_{xy}$ . The model involves three different pools of electrons: *pinned*, *scattered*, and *drifting* ones which are sketched in Fig. 7a. While the fraction  $f_p$  of pinned orbits reduces the carrier density for commensurate  $B$ , the fraction of scattered electrons,  $f_s$ , carries the current at low  $B$ . These electrons scatter as in a pinball game; their scattering time  $\tau'$  is of the order  $a/v_F$ . At higher  $B$ , both pinned and scattered trajectories die out and become replaced by drifting ones which, due to the suppression of backscattering sketched in Fig. 7b, are characterized by the intrinsic scattering time  $\tau \gg \tau'$  of the 2DEG. This is the origin of the pronounced negative magnetoresistance observed in experiment when  $R_c$  becomes smaller than  $a/2$ . The size of the different fractions depends on the magnetic field and has to be determined numerically. For these calculations we assumed a hard wall potential: hence the electrons between the antidots move on circles or arcs with cyclotron radius  $R_c$ . Each pool of carriers is characterized by a specific Drude resistivity. In a patterned sample each contingent contributes to the total resistivity which is obtained from the inverted sum of the individual conductivity tensors [4]. The result of a

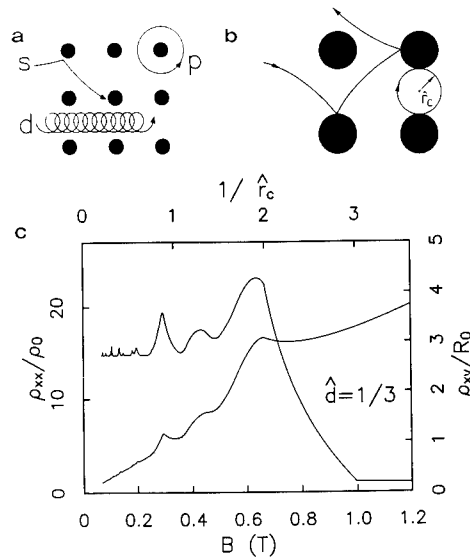


Fig. 7. (a) scattered (s), pinned (p) and drifting (d) trajectories. (b) Trajectories which connect neighboring antidots are suppressed once the cyclotron radius  $R_c$  becomes smaller than  $(a-d)/2$ . The suppression of backscattering is the origin of the negative magnetoresistance observed in experiment. (c) Calculated  $\rho_{xx}$  and  $\rho_{xy}$  traces for the parameters of sample 3. Features attributed to orbits around 1, 2 and 4 antidots (at  $R_c/a \approx 0.5, 0.8$  and  $1.14$ ) are most prominent. The top axis is given in units of the normalized cyclotron radius  $\hat{r}_c = R_c/a$ . From Ref. [4].

model calculation with parameters relevant for trace 3 of Fig. 3 ( $d/a = 1/3$ ) is shown in Fig. 7c. Remarkable similarities with the experiment are evident: the commensurability effects associated with orbits around 1, 2, and 4 antidots are quite prominent in both  $\rho_{xx}$  and  $\rho_{xy}$ .

Not explained by the model, however, is the magnetic field position of the low  $B$  peak of sample 2 in Fig. 3 and the quenching of the Hall effect. This is due to the omission of an essential ingredient in our model: the finite slope of the potential around each antidot which causes deviations from a circular cyclotron motion. The pinball model works as long as the length over which the antidot potential varies is small compared to  $a-d$ : then deviations from strictly circular trajectories occur only in the immediate locale of each antidot. For larger  $d/a$  (higher zero field resistance) the validity of the pinball model becomes more and more questionable. In general, the

electron dynamics in a “soft” antidot potential can not be described in terms of circular cyclotron motion characteristic for conventional electron gases in the limit  $\omega_c \tau \gg 1$  ( $\omega_c = eB/m^*$ : cyclotron frequency). One way to obtain information about the electron dynamics is to solve the classical equations of motion in a model antidot potential. Using such an approach Lorke et al. [24] calculated the conductivity tensor from the Einstein relation. Fleischmann, Geisel and Ketzmerick (FGK) applied a Kubo-type ansatz [17]. Using a model potential  $U(x,y) = U_0[\sin(\pi x/a)]^\beta$

sketched in Fig. 8a they start from the classical Hamiltonian

$$H = \epsilon_F = \frac{1}{2m^*} (\mathbf{p} - e\mathbf{A})^2 + U(x,y) \quad (1)$$

( $\mathbf{p}$  is the electron momentum and  $\mathbf{A}$  the vector potential) and integrate the Hamiltonian equations of motion. The numerical results are trajectories  $x(t)$ ,  $y(t)$ , and corresponding velocities  $v_x(t) = \dot{x}$ ,  $v_y(t) = \dot{y}$  [17]. The phase space is generally divided into regions with regular cyclotron-like motion and chaotic motion. This is illustrated

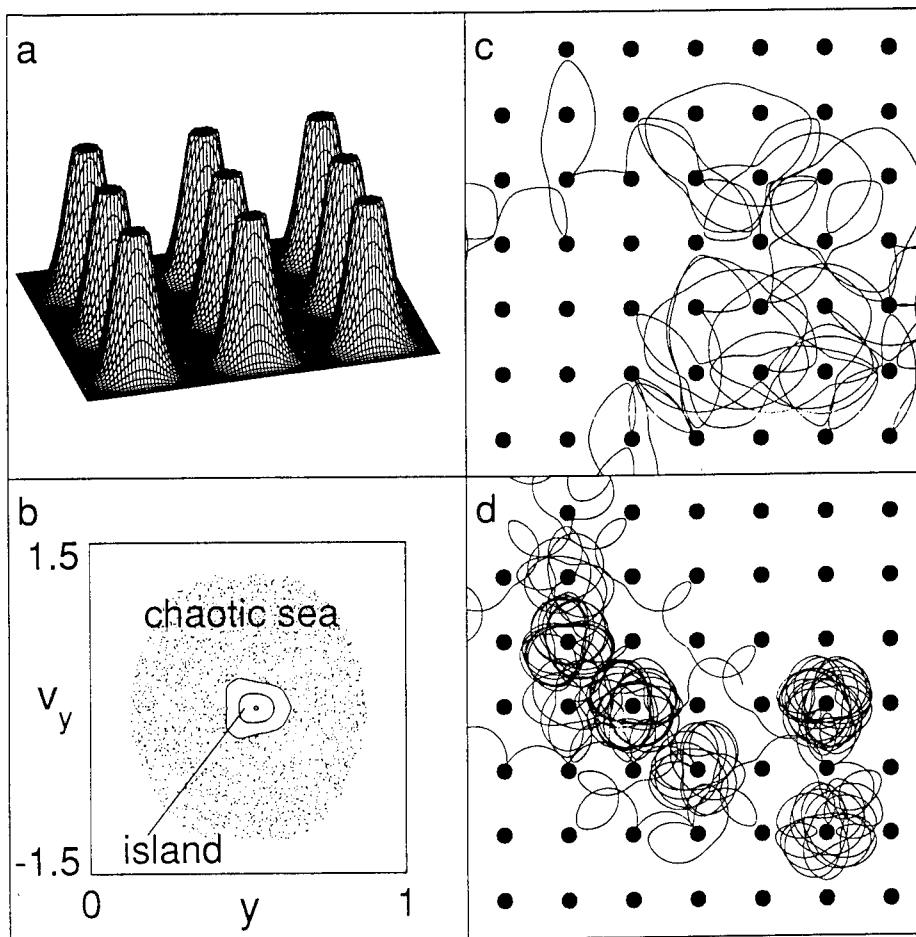


Fig. 8. (a) Antidot model potential. The steepness of the potential is controlled by the parameter  $\beta$ ; here:  $\beta = 4$ . (b) Phase space map showing regions of regular and chaotic motion. The point in the center represents an intersection with a cyclotron-type orbit of radius  $\sim 0.5a$  around one antidot at  $(x,y) = (0,0)$ . (c) Real space trajectories for an incommensurate ( $R_c = a$ ) and (d) commensurate ( $2R_c = a$ ) magnetic field value [28].

in the Poincaré surface of section  $(y, v_y)$  at  $x(\text{mod } a) = 0$  in Fig. 8b; an island of regular motion is clearly distinguishable from the sea of chaotic motion. The points surrounding the stable island stem from *one* chaotic electron trajectory scattered throughout the antidots lattice. Figs. 8c and 8d display chaotic real space trajectories close to the island of regular motion for an incommensurate and commensurate magnetic field value, respectively. The electrons within the stable island behave as the pinned electrons of our simple pinball model: they do not contribute to transport [17]. Surprisingly, however, Fleischmann et al. found that it is not primarily pinned orbits but chaotic trajectories whirling around the antidots (displayed in Fig. 8d) at commensurate  $B$ 's which are responsible for the emergence of the  $\rho_{xx}$  peaks. Their contribution to the conductivity  $\sigma$  can be expressed via the Kubo-type formula

$$\sigma_{ij} \propto \int_0^\infty e^{-t/\tau} \langle v_i(t) v_j(0) \rangle dt. \quad (2)$$

The indices  $i, j$  stand for  $x$  or  $y$  and the bracket denotes averaging over phase space. The integral is taken only over chaotic trajectories. Note that the unperturbed chaotic motion is “cut off” by the intrinsic scattering time  $\tau$ . Straightforward evaluation of equations based on Eq. (2) results in  $\rho_{xx}$  [17] and  $\rho_{xy}$  traces [25] which can be compared with experiment. The classical electron dynamics leaves distinct marks found in experiment. The shift of the “orbit-around-four-antidots-peak” (Fig. 3, trace 2) towards lower magnetic fields can be reproduced within the FKG model, and reflects “squeezed” orbits around four antidots, connected to an augmented cyclotron frequency. The FKG model also successfully describes the quenching of the Hall effect: the suppression of the Hall voltage is due to trajectories channeling over many periods in positive and negative direction along the main axes of the (square) antidot array. This guiding, and therefore the quenching, is less significant if the lattice is more open (larger periods, see Fig. 6). The calculated Hall resistance  $\rho_{xy}$  involving the chaotic trajectories via Eq. (2) shows a quenching of the Hall effect and even a negative Hall resis-

tivity (due to preferential scattering) as in experiment [25].

## 5. Magnetotransport experiments: quantization of periodic orbits

The magnetotransport experiments described in the previous sections were carried out at temperatures where quantum effects in the low magnetic field range in which the commensurability effects dominate were negligible. In this section, we explore transport in a temperature regime where the *quantization* of classical electron motion comes into play [26,27]. Measurements of  $\rho_{xx}$  at  $T \approx 0.4$  K display quantum oscillations superimposed upon the low  $B$  resistance anomalies. Corresponding data for sample 1 with  $d/a \approx 0.5$  are shown in Fig. 9a, where we compare  $\rho_{xx}$  from both patterned and unpatterned sample segments. In the unpatterned part,  $1/B$ -periodic Shubnikov-de Haas (SdH) oscillations reflect the Landau energy spectrum. The quantum oscillations in the antidot segment reveal quite different behavior. The oscillations are *periodic* in  $B$  with a period  $\Delta B \approx 0.105 T \approx h/ea^2$  corresponding to the addition of approximately one flux-quantum through the antidot unit cell. At 4.7 K, the quantum oscillations are smeared out while the characteristic  $\rho_{xx}$  peak at  $2R_c = a$ , attributed to trapped electrons whirling around one antidot (see Fig. 8d), persists. The oscillations periodic in  $B$  dominate only the low  $B$  regime ( $2R_c > a - d$ ); at high  $B$ , the sample behaves as if unpatterned, and  $\rho_{xx}$  displays minima which are  $1/B$ -periodic reflecting quantization of essentially *unperturbed* cyclotron orbits (Fig. 9a, left inset). In Fig. 9b we plot the oscillation index  $\eta$  for both the high and low field regime versus inverse magnetic field positions of the  $\rho_{xx}$  minima. At high  $B$ ,  $\eta$  is the filling factor  $\nu = n_s h/eB$  counting the number of occupied (spin-split) Landau levels. At low  $B$  the antidot potential strongly mixes different Landau levels and the filling factor loses its physical meaning.

Deviations from a linear  $1/B$  dependence in Fig. 9b can be assigned to the periodic orbits shown for an intermediate and low  $B$  value in the

insets of Fig. 9b. These orbits play a central role in explaining the positions of the  $\rho_{xx}$  extrema. This is evident from the calculated action  $\tilde{S}(B)$  (see below) of these orbits, displayed in Fig. 9b.  $B$ -periodic oscillations as shown in Fig. 9a, however, are *not an inherent* property of antidot

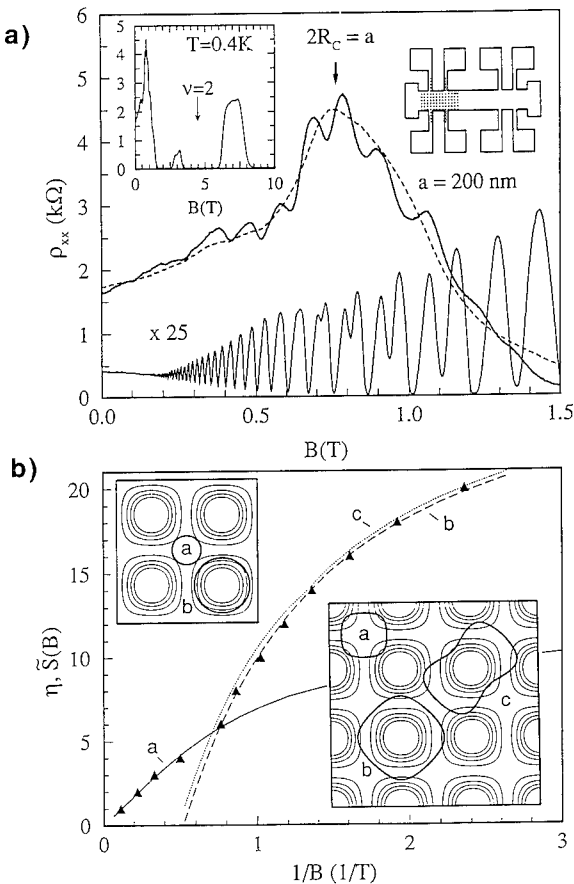


Fig. 9. (a)  $\rho_{xx}$  measured in the patterned (top traces) and unpatterned (bottom trace) segment of the same sample for  $T = 0.4$  K (solid lines) and  $4.7$  K (dashed line). The left inset displays the  $\rho_{xx}$  trace from the patterned segment up to  $10$  T; the filling factor  $\nu = 2$  is marked. At high  $B$ , the emergence of SdH oscillations reflects the quantization of essentially unperturbed orbits. Right inset: sketch of the sample layout. (b) The triangles mark all (up to  $10$  T)  $1/B$  positions of the  $\rho_{xx}$  minima. At high  $B$  the resistance minima lie equidistant on the  $1/B$  scale; at low  $B$  the spacing becomes periodic in  $B$ . Solid, dashed and dotted lines are calculated reduced actions  $\tilde{S}(B)$  of orbits (a) (b) and (c), respectively. These orbits are shown for  $1/B = 0.6 \text{ T}^{-1}$  (top) and  $1/B = 2.7 \text{ T}^{-1}$  (bottom inset). The potential steepness in the calculation was  $\beta = 2$ . From Ref. [26].

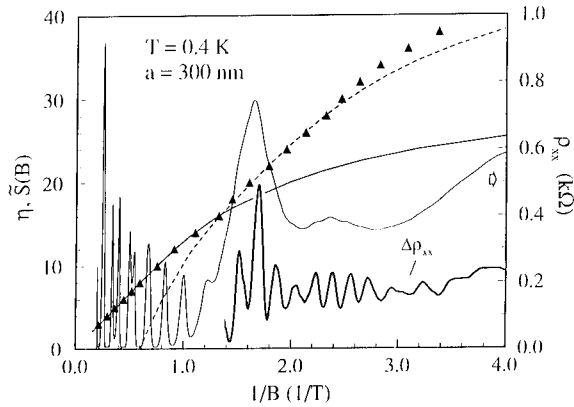


Fig. 10.  $\rho_{xx}$  and  $\Delta\rho_{xx}$  (arbitrary units) vs.  $1/B$ . The oscillation index  $\eta$  labels  $\rho_{xx}$  minima positions on the  $1/B$  scale (triangles). Dashed line: Calculated action  $\tilde{S}(B)$  for an orbit between four antidots. Solid line:  $\tilde{S}(B)$  for electron encompassing one antidot. From Ref. [26].

arrays. Data taken from a superlattice with smaller  $d/a \approx 0.4$  are shown in Fig. 10. In contrast to the data of Fig. 9a the  $\rho_{xx}$  minima are periodic in  $1/B$  over nearly the entire field range but display similar deviations for intermediate  $B$  where the low field anomalies begin to disappear (between  $0.6$  and  $1$  T). Again, the experimental data are best described by the action calculated for an orbit between four, and around one, antidot. The crossover from  $B$ -periodic to  $1/B$ -periodic oscillations, dependent on the normalized cross section  $d/a$ , together with the fact that the antidot array is much larger than the phase breaking length in a 2DEG [29], suggest that the  $B$ -periodic oscillations observed in experiment are *not* the usual Aharonov–Bohm oscillations observed, for example, in metal rings. This picture is in contrast to previous work [14,30]. In the following we assume that, as usual for quantum transport,  $\rho_{xx} \propto d^2(E, B)$  probes the electron density of states  $d(E, B)$  at the Fermi energy  $\epsilon_F$  [31].

To obtain information about  $d(E, B)$  one can go through quantum mechanical calculations [32] and obtain complicated spectra which are hard to interpret. Another approach is to use the method of semi-classical quantization of chaotic systems developed by Gutzwiller and others [33]. The problem to be solved is to quantize the electron motion in a classical phase space dominated by

chaotic trajectories like the ones displayed in Figs. 8c and 8d. It turns out that a smoothed density of states of such a chaotic system can be obtained from its *periodic orbits*. The orbits which turned out to be relevant in our system (see Refs. [26] and references therein) are displayed in the insets of Fig. 9b. Due to finite temperatures and impurity broadening effects we need to consider only the shortest periodic orbits. Note that these orbits are of negligible measure in a sea of non-periodic motion. The periodic orbits cause a modulation of  $d(E, B)$  with maxima given by the quantized action

$$S(B) = \oint (m^* v + eA) dr$$

$$= m^* \oint v dr - eB\mathcal{A}(B) = 2\pi\hbar N, \quad (3)$$

where  $N = (n + \gamma/2 + \alpha/4)$  contains the quantum number  $n$ , the winding number  $\gamma$  and the Maslov index  $\alpha$ .  $B\mathcal{A}(B)$  in Eq. (3) is the enclosed flux through a periodic orbit and  $v$  is the electron velocity given by Eq. (1). To compare with experiment we calculate the reduced action  $\tilde{S}(B)$

$$\tilde{S}(B) \equiv 2 \frac{S(B)}{\hbar} - \gamma(B) - \frac{\alpha}{2} - 1 = 2n;$$

$$n = 1, 2, \dots, \quad (4)$$

where  $2n$  now labels *minima* in  $d(E, B)$ . Note, that the  $y$ -axis of Figs. 9b and 10 represents  $\tilde{S}$ , where even  $\eta$  are described by Eq. (4). At high  $B$ ,  $2n$  is the filling factor  $\nu$ . The calculated traces of  $\tilde{S}(B)$  are shown in Figs. 9b and 10. The three periodic orbits, displayed in the insets of Fig. 9b, are sufficient to explain the minima positions of  $\rho_{xx}$ . These are (i) an orbit *between* four antidots, denoted as (a), (ii) an orbit *around* one antidot, (b), and (iii) orbit (c) emerging from a *bifurcation* of orbit (b).

The  $\tilde{S}(B)$  curves in Fig. 9b and 10 differ in the steepness of the model potential; we use  $\beta = 2$  and  $d/a = 0.5$  for the solid, dashed and dotted lines in Fig. 9b, and  $\beta = 4$  and  $d/a = 0.4$  for the traces in Fig. 10. Since  $d/a$  values are taken from the experiment [4]  $\beta$  is the only free parameter.

The magnetic field dependence of  $\tilde{S}(B)$  can be explained in a simplified approach evaluating the

$B$  dependence of the enclosed area  $\mathcal{A}$ . For unperturbed cyclotron motion  $S(B) = eB\mathcal{A}$  holds,  $\mathcal{A}(B) = \pi R_c^2$  scales with  $1/B^2$ , and  $1/B$ -periodic resistance oscillations result. At high  $B$ , orbit (a) is essentially unperturbed and in this realm oscillations periodic in  $1/B$  are prominent in Figs. 9b and 10. At lower  $B$  where  $2R_c$  is comparable to the period  $a$ , an essentially unperturbed cyclotron motion requires a sufficiently “open” antidot lattice (small  $d/a$ , large  $\beta$ ).  $1/B$ -periodic oscillations between  $1/B = 1.3 \text{ T}^{-1}$  and  $2.5 \text{ T}^{-1}$  in Fig. 10 document such behavior. Deviations from  $\mathcal{A}(B) \propto 1/B^2$  destroy the  $1/B$ -periodicity: smaller action is caused by impeding the expansion of a cyclotron orbit.  $B$ -periodic oscillations result when  $\mathcal{A}$  is independent of  $B$ . This condition is closely fulfilled by orbit (b) calculated for  $\beta = 2$ ,  $d/a = 0.5$  and shown in the bottom inset of Fig. 9b. This trajectory encloses an area  $\sim a^2$  causing the  $B$ -periodic oscillations with  $\Delta B \approx h/ea^2$  displayed in Fig. 9a.

## 6. Acknowledgements

The present work was done in close collaboration with P. Grambow, A. Menschig, R. Bergmann, H. Schweizer, M.L. Roukes, K. von Klitzing, K. Eberl, K. Ploog, and G. Weimann. We are grateful to R. Fleischmann, T. Geisel, R.R. Gerhardt, and D. Pfannkuche for many helpful discussions. The work was supported by the German Bundesministerium für Forschung und Technology under grant 01BM121/8.

## 7. References

- [1] See related work in the current proceedings.
- [2] M.L. Roukes and A. Scherer, *Bull. Am. Phys. Soc.* 34 (1989) 633.
- [3] K. Ensslin and P.M. Petroff, *Phys. Rev. B* 41 (1990) 12307.
- [4] D. Weiss, M.L. Roukes, A. Menschig, P. Grambow, K. von Klitzing and G. Weimann, *Phys. Rev. Lett.* 66 (1991) 2790.
- [5] M. Ya. Azbel, *Sov. Phys. JETP* 19 (1964) 634.
- [6] R.D. Hofstadter, *Phys. Rev. B* 14 (1976) 2239.
- [7] D. Pfannkuche and R.R. Gerhardt, *Phys. Rev. B* 46 (1992) 12606.

- [8] D. Weiss, K. von Klitzing, K. Ploog and G. Weimann, *Europhys. Lett.* 8 (1989) 179.
- [9] D. Weiss, K. von Klitzing, K. Ploog and G. Weimann, *Surf. Sci.* 229 (1990) 88.
- [10] R.R. Gerhardts, D. Weiss and U. Wulf, *Phys. Rev. B* 43 (1991) 5192.
- [11] D. Weiss, A. Menschig, K. von Klitzing and G. Weimann, *Surf. Sci.* 263 (1992) 314.
- [12] R.R. Gerhardts, D. Weiss and K. von Klitzing, *Phys. Rev. Lett.* 62 (1989) 1173.
- [13] R.W. Winkler, J.P. Kotthaus and K. Ploog, *Phys. Rev. Lett.* 62 (1989) 1177.
- [14] D.K. Ferry, *Prog. Quantum Electron.* 16 (1992) 251.
- [15] C.W.J. Beenakker and H. van Houten, in: *Solid State Physics*, Eds. H. Ehrenreich and D. Turnbull (Academic Press, Boston, MA, 1991) p. 1.
- [16] W. Hansen, J.P. Kotthaus and U. Merkt, in: *Semiconductors and Semimetals*, Eds. R.K. Willardson, A.C. Beer and E.P. Weber (Academic Press, San Diego, CA, 1992) p. 279.
- [17] R. Fleischmann, T. Geisel and R. Ketzmerick, *Phys. Rev. Lett.* 68 (1992) 1367.
- [18] D. Weiss, P. Grambow, K. von Klitzing, A. Menschig and G. Weimann, *Appl. Phys. Lett.* 58 (1991) 2960.
- [19] G. Müller, D. Weiss, K. von Klitzing, K. Ploog, H. Nickel, W. Schlapp and R. Lösch, *Phys. Rev. B* 46 (1992) 4346.
- [20] R. Schuster, K. Ensslin, J.P. Kotthaus, M. Holland and C. Stanley, *Phys. Rev. B* 47 (1993) 6843.
- [21] H. Fang and P.J. Stiles, *Phys. Rev. B* 41 (1990) 10171.
- [22] T. Yamashiro, J. Takahara, Y. Takagaki, K. Gamo, S. Namba, S. Takaoka and K. Murase, *Solid State Commun.* 79 (1991) 885.
- [23] M.L. Roukes, A. Scherer, S.J. Allen, Jr., H.G. Craighead, R.M. Ruthen, E.D. Beebe and J.P. Harbison, *Phys. Rev. Lett.* 59 (1987) 3011.
- [24] A. Lorke, J.P. Kotthaus and K. Ploog, *Phys. Rev. B* 44 (1991) 3447.
- [25] R. Ketzmerick, R. Fleischmann and T. Geisel, preprint.
- [26] D. Weiss, K. Richter, A. Menschig, R. Bergmann, H. Schweizer, K. von Klitzing and G. Weimann, *Phys. Rev. Lett.* 70 (1993) 4118.
- [27] The influence of an antidot array on  $n_s$  extracted from SdH oscillations at high and low  $B$  was studied by G.M. Sundaram, N.J. Bassom, R.J. Nicholas, G. J. Rees, P.J. Heard, P.D. Prewett, J.E.F. Frost, G.A.C. Jones, D.C. Peacock and D.A. Ritchie, *Phys. Rev. B* 47 (1993) 7348.
- [28] Figure provided by R. Fleischmann.
- [29] A. Yacoby, U. Sivan, C.P. Umbach and J.M. Hong, *Phys. Rev. Lett.* 66 (1991) 1938.
- [30] F. Nihey and K. Nakamura, *Physica B* 184 (1993) 398.
- [31] T. Ando, A.B. Fowler and F. Stern, *Rev. Mod. Phys.* 54 (1982) 438.
- [32] H. Silberbauer, *J. Phys.: Condensed Matter* 4 (1992) 7355.
- [33] *Chaos in Classical and Quantum Mechanics*, Ed. M.C. Gutzwiller (Springer, Berlin, 1990).

## Scattering of ballistic electrons by magnetic flux tubes

A.K. Geim<sup>1</sup>, S.J. Bending<sup>\*</sup>, I.V. Grigorieva

*School of Physics, University of Bath, Claverton Down, Bath BA2 7AY, UK*

(Received 20 April 1993; accepted for publication 25 May 1993)

### Abstract

We have observed a pronounced change in the conductance of a high-mobility two-dimensional electron gas (2DEG) caused by additional scattering of electrons at magnetic flux tubes (vortices) which are formed at the 2DEG by a superconducting 'gate' layer. The experimental results are in good agreement with theory if account is taken of the small-angle nature of electron–vortex scattering.

There has been much interest in the last few years in a hybrid system in which an extremely inhomogeneous magnetic field created by a type-II superconductor is projected down onto a two-dimensional gas below [1–7]. This system can be fabricated by gating a GaAlAs/GaAs heterostructure 2DEG with a type-II superconducting film. An applied magnetic field is segregated within and near the superconductor into a distribution of magnetic flux tubes (vortices) with characteristic diameter  $d \approx 2\lambda$  ( $\lambda \approx 0.1 \mu\text{m}$  and is the magnetic field penetration depth). Nonlocal weak localization [1–3], mesoscopic fluctuations caused by a single vortex [4], asymmetry of electron–vortex scattering and diffraction of 2D electrons at vortices [5–8] were investigated in this hybrid system. A point of fundamental interest here is the fact that the size of the magnetic tubes can be

much smaller than transport relaxation lengths, in which case the transport is essentially nonlocal. Moreover, under the conditions that vortices are spatially well separated (so that electrons are only influenced by vortices along a small part of their paths) and are randomly distributed, they can be considered as additional artificial scatterers introduced into a 2DEG. Fig. 1a illustrates this aspect for the case of ballistic transport.

In this paper we report a contribution to the longitudinal resistivity of a 2DEG which arises due to the extra scattering of ballistic electrons in a random distribution of vortices. Some evidence for such a contribution has already been reported in Ref. [5], but the present results, which were obtained in a very high-mobility 2DEG, are much clearer and allow quantitative analysis. In addition, we have a direct proof that the observed increase in the resistance is not caused by modification of the weak localization magnetoresistance [1–3].

We have employed two GaAlAs/GaAs heterostructures with electron concentrations,  $n = (0.365 \text{ and } 4.13) \times 10^{15} \text{ m}^{-2}$  and  $\mu = 76 \text{ and } 104$

<sup>\*</sup> Corresponding author.

<sup>1</sup> On sabbatical from Institute of Microelectronics Technology, Russian Academy of Sciences, Chernogolovka 142432, Russian Federation.



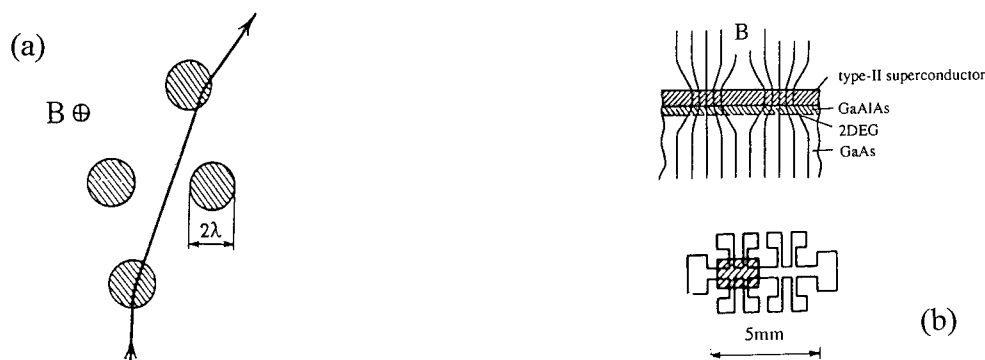


Fig. 1. (a) Schematic motion of ballistic electrons through the vortices. (b) The 2DEG-superconductor hybrid system and our experimental geometry.

$\text{m}^2/\text{V} \cdot \text{s}$ , respectively. The elastic mean free path of electrons,  $l$ , is  $11 \mu\text{m}$  for the material with high electron concentration and  $2.4 \mu\text{m}$  for the heterostructure with lower  $n$ . Each sample used in the experiment contained two identical structures with Hall bar geometry fabricated on the same chip (see Fig. 1b). A lead superconducting film ( $\approx 0.1 \mu\text{m}$  thick) was deposited on one of the Hall bars, while the other was used as a control to compare results for the cases of uniform magnetic field and the distribution of vortices. To avoid ambiguity arising from an inevitable difference between electron concentrations under the deposited metal gate and under the free surface, a 3 nm layer of aluminium oxide was initially deposited over the whole chip, providing the same surface conditions for both Hall bars.

Lead films of these thicknesses are known to be type-II superconductors and have a very small value of  $\lambda$  [9]. Our films had the transition temperature  $T_c = 7.2 \text{ K}$  (the same value as for the bulk material) and upper critical field of  $\sim 1200 \text{ G}$  at  $1.3 \text{ K}$ . These measured parameters allowed us to calculate all other superconducting parameters of the films [9,4]. In particular, we estimate  $\lambda \approx 60 \text{ nm}$  at  $1.3 \text{ K}$  and  $80 \text{ nm}$  at  $4.2 \text{ K}$ . We have also taken into account spatial broadening of vortices when they emerge from the superconductor. For the heterostructures used the distance between the 2DEG and the superconductor was  $70 \text{ nm}$  and our numerical calculations [4] based on the Clem model of a vortex yield  $d \approx 210 \text{ nm}$

for the vortex diameter at the 2DEG at  $1.3 \text{ K}$  and  $240 \text{ nm}$  at  $4.2 \text{ K}$ .

In our experiments it was important to avoid macroscopic inhomogeneities of the magnetic field inside the sample which could arise due to vortex pinning. Upon sweeping the applied magnetic field, pinning prevented vortices from spreading easily into the film and caused large macroscopic field gradients. This inhomogeneity completely obscures all other effects due to the distribution of vortices. To avoid these pinning effects, we performed measurements in the so-called 'field-cooling' regime, i.e. every change of the applied magnetic field  $B$  was followed by heating the sample to a temperature above  $T_c$  and then cooling it in the magnetic field down to  $1.3$  or  $4.2 \text{ K}$ . This procedure is known to provide a homogeneous distribution of vortices over the superconductor [9]. A typical distribution of vortices in the field-cooling regime in our superconducting films is shown in Fig. 2 where the micrograph was obtained with the decoration technique [9,10]. Note that vortices do not form a regular lattice in our strongly pinned superconductor (the measured critical current is about  $10^5$ – $10^6 \text{ A/cm}^2$ ) but vortex separations are still more or less equal throughout the film. For more experimental details we refer to our previous papers [4,11].

Fig. 3a shows the low-field magnetoresistivity  $\rho^U$  of the control (ungated) sample for the structure with the low electron concentration. The

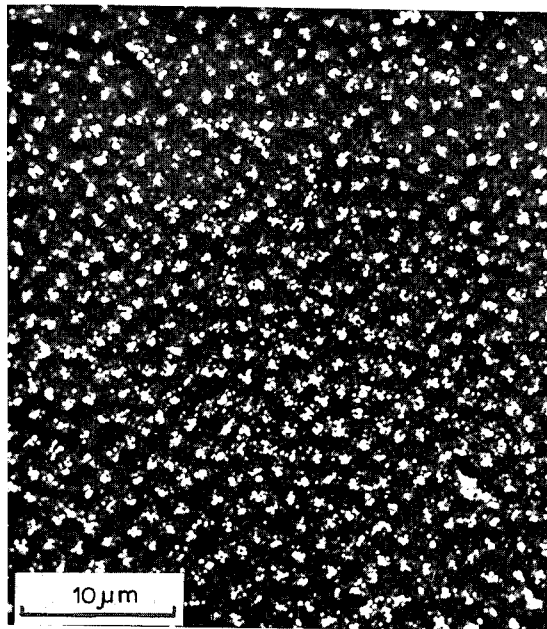


Fig. 2. Typical distribution of vortices in low magnetic fields imaged with the decoration technique ( $B = 10$  G). Bright spots against the dark background are vortices.

resistance has a very sharp peak due to weak localization in magnetic fields below 20 G and saturates to a fairly constant value in the higher fields. The low-field behaviour can be fitted to the Kawabata theory of weak localization [11] which yields the electron phase-breaking length  $L_\phi \approx 10$   $\mu\text{m}$  at 1.3 K and  $\approx 5$   $\mu\text{m}$  at 4.2 K. The weak localization peak strongly depends on temperature. Its value decreases by a factor of 4

upon increasing temperature from 1.3 to 4.2 K. The width of the peak becomes wider as temperature increases. The weak localization peak is also observed in the magnetoresistance  $\rho^G$  of the sample gated with the superconductor but it completely disappears in the differential magnetoresistance  $\rho^V = \rho^G - \rho^U$  (see Fig. 3b). What remains represents the effect of vortices on the 2DEG resistivity. We emphasize the following important features of the differential (electron–vortex) resistivity  $\rho^V$ : (1)  $\rho^V$  is positive and, at 4.2 K, exceeds the weak localization magnetoresistance; (2) it depends linearly on  $B$  at fields below 40 G; (3) it extends far beyond the region of the weak localization peak and completely disappears at fields above 400 G; and (4)  $\rho^V$  has a weak temperature dependence. We note that vortices are known to effect weak localization but this influence is negligibly small in magnetic fields above  $\phi_0/L_\phi^2$  [1–3,12]. The latter value corresponds to one vortex (one flux quantum  $\phi_0 = h/2e$ ) per the phase-coherent volume,  $L_\phi^2$ , and it is less than 1 G in our experiment. Furthermore, the micro-inhomogeneity of the magnetic field leads to an increase in the weak localization correction, and the net effect would be a negative differential magnetoresistance for the 2DEG, in contrast to what we observe. The weak localization behaviour has been investigated in detail in Refs. [1–3,13] and for a relatively high-mobility 2DEG it will also be the subject of a further publication. The size of the correction is below the limit of resolution in this experiment.

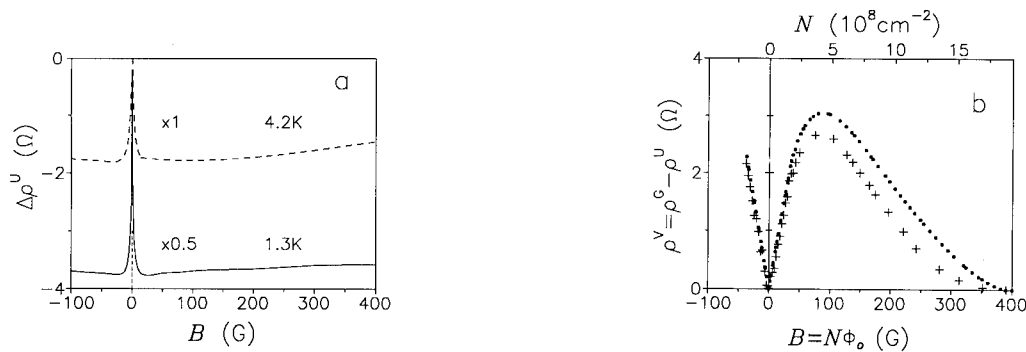


Fig. 3. (a) Magnetoresistance of the control sample with  $n = 0.365 \times 10^{15} \text{ m}^{-2}$  at 1.3 K (dots) and 4.2 K (crosses). (b) The residual electron–vortex resistivity  $\rho^V = \rho^G - \rho^U$  at 1.3 K (dots) and 4.2 K (crosses).

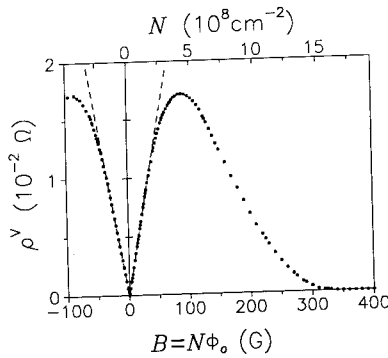


Fig. 4. The electron-vortex resistivity for the 2DEG with  $n = 4.13 \times 10^{15} \text{ m}^{-2}$ .

The electron-vortex resistance  $\rho^V$  in the sample with  $n = 4.13 \times 10^{15} \text{ m}^{-2}$  is shown in Fig. 4. It is readily seen that it has the same functional form as in the sample with lower  $n$  but the overall magnitude is smaller by a factor of about 100.

Let us first qualitatively explain the functional form of  $\rho^V$ . In low applied fields vortices are spatially well separated and their effects on the 2DEG are additive. Since the concentration of the scatterers (vortices) increases with the applied field  $B$  as  $N = B/\phi_0$ , the magnetoresistance  $\rho^V$  is linear at these fields. In large external fields the distance between individual vortices,  $L(\mu\text{m}) \approx 5[B(\text{G})]^{-1/2}$ , decreases to a value comparable with the vortex diameter and magnetic fields due to adjacent vortices strongly overlap. Consequently the inhomogeneity rapidly smears out, yielding a somewhat uniform magnetic field at the 2DEG although superconductivity in the gate is not destroyed. This smearing results in a vanishing difference between the gated and control samples and explains the high-field decay of  $\rho^V$  seen in Figs. 3 and 4.

To explain quantitatively the observed values of the linear magnetoresistance and the two orders of magnitude difference between the samples with different electron concentrations we shall view the vortices as independent scatterers introduced into the 2DEG [5–8] (see Fig. 1a). As pointed out earlier, the vortices are randomly distributed because of strong pinning in our samples (see Fig. 2). The resistivity due to the vortices with concentration  $N$  can be expressed by

the standard formula:  $\rho^V = m^*/ne^2\tau$ , where  $\tau$  is the transport mean-free time for this type of scattering. The transport time is equal to the interval between electron collisions with the vortices,  $\tau^* = 1/Ndv_F$  in case of large-angle scattering ( $\theta \approx 1$ ) and  $\tau \approx \tau^*\theta^{-2}$  for  $\theta \ll 1$  (where  $v_F$  is the Fermi velocity). Note that in both cases  $\rho^V \propto 1/\tau^* \propto N \propto B$ . The maximum angle  $\theta_m$ , by which an electron is deflected when passing through a vortex, can be estimated as  $\theta_m = \omega_c\tau_{tr} = \lambda_F/2d$ , where  $\omega_c$  is the cyclotron frequency in a characteristic field inside the vortices  $b = \phi_0/d^2$ ,  $\tau_{tr} = d/v_F$  is the transit time through the vortex and  $\lambda_F$  is the Fermi wavelength. This angle is equal to  $\sim 0.4$  and  $\sim 0.1$  for the samples with low and high electron concentrations, respectively. Using the expressions given above, we find:

$$\rho^V/\rho_i = (0.3/\pi^3)(\lambda_F/d)^2(ld/\phi_0)B \quad \text{for } \theta \ll 1, \quad (1a)$$

$$\rho^V/\rho_i = (ld/\phi_0)B \quad \text{for } \theta \approx 1, \quad (1b)$$

where  $\rho_i$  is the resistivity due to the impurity scattering. In Eq. (1a) we use the numerical coefficient obtained in the rigorous calculations of Ref. [8]. Note that in the limit of small-angle scattering the electron-vortex resistivity depends on the electron concentration as  $\rho^V \propto \rho_i \lambda_F^2 \propto \rho_i n^{-1} \propto n^{-2}$ . This dependence explains the observed difference of  $\rho^V$  for different  $n$ .

For the sample with high  $n$ , where  $\theta_m \approx 0.1$ , theory gives the magnetoresistance slope  $\rho^V/B \approx 5 \times 10^{-4} \text{ } \Omega/\text{G}$  in the limit  $\theta \ll 1$ . This result is in good agreement with the experimental value of  $3 \times 10^{-4} \text{ } \Omega/\text{G}$ . For the sample with lower  $n$  ( $\theta_m \approx 0.4$ ) the experimental slope is  $6 \times 10^{-2} \text{ } \Omega/\text{G}$ , which is substantially larger but still close to the small-angle limit value of  $2 \times 10^{-2} \text{ } \Omega/\text{G}$ . The corresponding value for the case of  $\theta \approx 1$  is  $6 \text{ } \Omega/\text{G}$ , indicating that the experimental situation is still very far from large-angle scattering. The same conclusion follows from the temperature dependence of the magnetoresistance slopes in Fig. 3b. For small-angle scattering  $\rho^V \propto 1/d$  (where  $d$  is the vortex diameter) while for  $\theta \approx 1$  we get the inverse dependence (see Eq. (1)). The experimental data show a decrease in the elec-

tron–vortex resistivity of 15% as temperature increases from 1.3 to 4.2 K. The decrease indicates the small-angle scattering limit and its value is in agreement with the expected broadening of the vortex diameter from 210 to 240 nm.

In conclusion, a randomly distributed magnetic field which is modulated on a scale less than the elastic electron mean-free path causes an extra contribution to the resistivity of a 2DEG. We show that the situation can be quantitatively described by the small-angle scattering of 2D electrons by the field inhomogeneities.

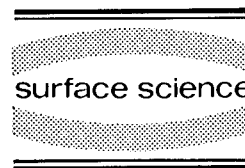
### 1. References

- [1] A.K. Geim, JETP Lett. 50 (1989) 389.
- [2] S.J. Bending, K. von Klitzing and K. Ploog, Phys. Rev. Lett. 65 (1990) 1060.
- [3] J. Rammer and A.L. Shelankov, Phys. Rev. B 36 (1987) 3135.
- [4] A.K. Geim, V.I. Falko, S.V. Dubonos and I.V. Grigorieva, Solid State Commun. 82 (1992) 831.
- [5] A.K. Geim, S.V. Dubonos and A.V. Khaetskii, JETP Lett. 51 (1990) 121.
- [6] A.K. Geim, S.J. Bending and I.V. Grigorieva, Phys. Rev. Lett. 69 (1992) 2252.
- [7] A.V. Khaetskii, J. Phys. C 3 (1991) 5115.
- [8] D.A. Kuptsov and M.Yu. Moiseev, J. Phys. I 1 (1991) 1165.
- [9] R.P. Huebener, Magnetic Flux Structures in Superconductors, Vol. 6 of Springer Series in Solid State Physics (Springer, Berlin, 1979).
- [10] I.V. Grigorieva and L.Ya. Vinnikov, J. Low-Temp. Phys. 74 (1989) 81.
- [11] A.K. Geim, I.V. Grigorieva and S.V. Dubonos, Phys. Rev. B 46 (1992) 324.
- [12] A. Kawabata, J. Phys. Soc. Jpn. 53 (1984) 3540.
- [13] S.J. Bending and A.K. Geim, Phys. Rev. B 46 (1992) 14912.



ELSEVIER

Surface Science 305 (1994) 424–427



## Resistivity and Hall resistance of a two-dimensional electron gas in the presence of magnetic flux tubes

L. Brey<sup>a</sup>, H.A. Fertig<sup>\*,b</sup>

<sup>a</sup> Departamento Física Materia Condensada C-XII, Facultad de Ciencias, Universidad Autónoma, E-28049 Madrid, Spain

<sup>b</sup> Department of Physics and Astronomy, University of Kentucky, Lexington, KY 40506-0055, USA

(Received 18 April 1993; accepted for publication 11 June 1993)

### Abstract

We compute the Hall and diagonal resistivities of a two-dimensional electron gas in the presence of randomly placed magnetic flux tubes. It is found that there is a suppression of the Hall conductance below its expected value for the corresponding uniform magnetic field case at low electron densities, in agreement with recent experiments. At densities somewhat lower than achieved thus far experimentally, we find resonances in the transport coefficients due to Landau level structures in the flux tubes. A classical calculation of the Hall resistance reproduces the broad features of the Hall conductance for integral or half-integral numbers of flux quanta in each flux tube.

In recent years, there has been increasing interest in the behavior of the two-dimensional electron gas (2DEG) in inhomogeneous magnetic fields. Such systems are of interest because they offer a new and unusual way of introducing an external potential in the electron gas, that does not necessarily involve adding random impurities to the system. The subject has also attracted some very recent attention because of a possible connection with the  $\nu = \frac{1}{2}$  Hall effect [1].

In practice, such inhomogeneous magnetic fields are made possible by depositing a thin superconducting film above the 2DEG, so that the field is broken up into vortex lines just above the electron gas [2,3]. If the ratio of the superconducting flux quantum  $hc/2e$  to the magnetic

field  $B$  is large compared to the area of a typical vortex line, then to a first approximation one may think of the magnetic field as being confined only to small regions of the electron gas. For large magnetic fields, the vortices form a hexagonal lattice, leading one to investigate the behavior of electrons in a periodic magnetic field [4,5]. For low enough magnetic fields, the positions of the vortices will be random, due to inhomogeneities in the superconducting film. We consider the latter situation in this work.

In this work, we will investigate the Hall effect in this system using a Boltzmann equation approach. Recent experiments [3] have investigated this quantity, and have found that at high electron densities, the Hall resistivity is essentially the same as in a uniform magnetic field, while at lower densities, it becomes suppressed below this value. Past theoretical work anticipated the former result [6], although the latter is largely unex-

\* Corresponding author.

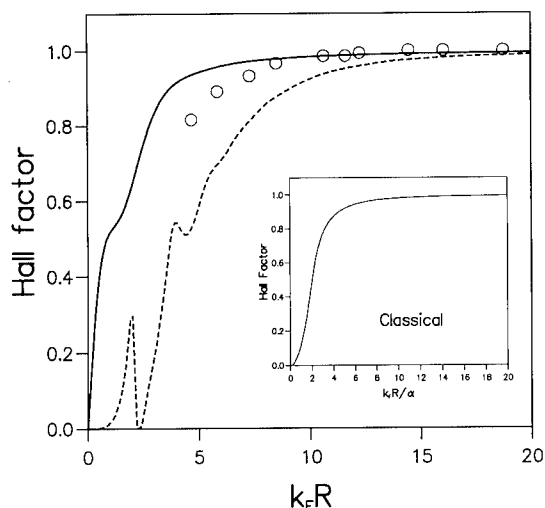


Fig. 1. Hall factor  $F_H$  as a function of  $k_F R$  for flux tubes containing  $\alpha = 0.5$  (solid line) and  $\alpha = 2.5$  (dashed line) flux quanta  $hc/e$ . Circles are data taken from Ref. [3]. Inset:  $F_H$  as calculated classically.

plained. Below, we will show explicitly that there is indeed a suppression of the Hall resistivity in a simple model of flux tubes randomly distributed through an electron gas, when  $k_F R < 1$ , where  $k_F$  is the Fermi wavelength and  $R$  the radius of a flux tube. This suppression is largely a result of the ineffectiveness of the flux tube as a scatterer if it is too narrow, and can be understood in a purely classical model. We also find that there can be resonances in the Hall resistivity due to the Landau level structure in the flux tubes, and that there are interesting oscillations in both the Hall resistance and the diagonal resistance as a function of the flux in each vortex, which is a consequence of the Aharonov–Bohm effect.

A typical result is illustrated in Fig. 1, where we plot the Hall factor, defined as  $F_H(k_F R) = \rho_{xy} n_s e c / B$ , where  $\rho_{xy}$  is the Hall resistivity,  $n_s$  the sheet density, and  $B$  is the spatially averaged magnetic field. The flux parameter  $\alpha$ , which is the number of flux quanta contained in a single flux tube, is taken to be 0.5, as is expected for the experiment of Ref. [3]. We note also that, throughout this paper, we assume for simplicity that the magnetic field is uniform inside the flux tube. One can see a “knee” in the Hall factor

near  $k_F R = 2$ , which may be traced back to a scattering resonance through the first Landau level in the region of the magnetic field. (Such resonances can be quite pronounced for larger values of  $\alpha$ , leading to non-monotonic behavior in  $F_H$ ; this is also illustrated in Fig. 1.) For comparison, the experimental points, as taken from Ref. [3], are plotted as well, with their assumption that  $R = 1000 \text{ \AA}$ . One can see good qualitative agreement here. We note that the choice of  $R$  is somewhat arbitrary, as the field profile inside the flux tube is not really uniform; we find that the agreement between experiment and theory can be made quantitative if we use an effective radius of  $R = 650 \text{ \AA}$ .

In Fig. 2, we illustrate (for  $\alpha = 1/2$  and  $\alpha = 5/2$ ) the quantity  $m^* / \hbar n_L \tau(k_F R)$ , where  $m^*$  is the effective mass,  $n_L$  is the number of vortices per unit area, and  $\tau(k_F R)$  is the elastic mean lifetime for scattering off the vortices. This quantity is proportional to the diagonal resistivity  $\rho_{xx}$ , and so is easily measured experimentally. It is interesting to see that there is a peak in the resistivity near  $k_F R = 2$ , which once again we interpret as a scattering resonance. Not surprisingly, similar plots for larger values of  $\alpha$  reveal a number of such resonances. It is also interesting

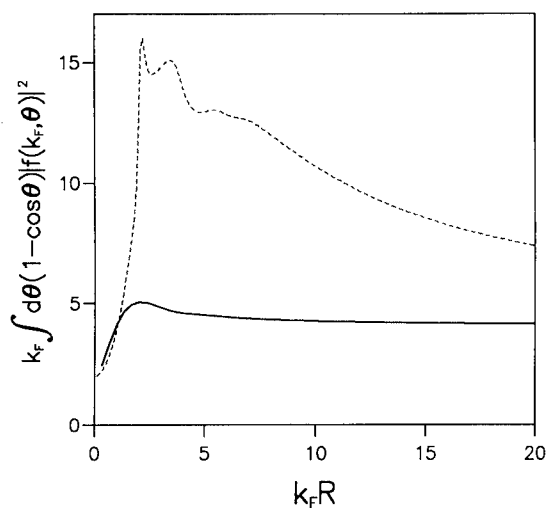


Fig. 2. Unitless measure of the inverse scattering time due to the flux quanta, as given in Eq. (7), for  $\alpha = 0.5$  (solid line) and  $\alpha = 2.5$  (dashed line).

to look at this quantity for fixed  $k_F R = 2$ , as a function of  $\alpha$ . One finds oscillations of period one, which are a manifestation of the Aharonov–Bohm effect. Similar oscillations are present in the Hall factor, although they are not as pronounced.

We now discuss the derivation of our results. In the symmetric gauge, and in polar coordinates  $(r, \theta)$ , the eigenstates  $\psi(qr)$  of an electron in the presence of a single flux tube of radius  $R$  can be written, for large distances  $r$ , as [7]

$$\lim_{r \rightarrow \infty} \psi(qr) = e^{iqx} + f(q, \theta) \frac{e^{iqr}}{\sqrt{r}}, \quad (1)$$

where  $f(q, \theta)$  is the total scattering amplitude, given by

$$f(q, \theta) = -\frac{1}{\sqrt{2\pi}q} e^{-i\pi/4} \left( e^{i\theta/2} \frac{\sin \pi\alpha}{\sin \theta/2} + \sum_{m=-\infty}^{\infty} e^{2i\delta_m} \frac{2i\Delta_2}{\Delta_1 + i\Delta_2} e^{im\theta} \right), \quad (2)$$

and

$$\delta_m = \frac{\pi}{2} (m + |m - \alpha|). \quad (3)$$

In these expressions  $q$  is related to the electron energy,  $\epsilon$ , by the relation  $\epsilon = \hbar^2 q^2 / 2m^*$ .

From the total scattering amplitude it is possible to calculate the  $T$ -matrix element between two plane waves of wavevector  $\mathbf{k}$  and  $\mathbf{k}'$ , both with the same magnitude  $k$ , and forming an angle  $\theta$  between them:

$$f(k, \theta) = -\frac{im^*}{2\hbar^2} \sqrt{\frac{2}{\pi k}} e^{-i\pi/4} \langle \mathbf{k}' | T | \mathbf{k} \rangle. \quad (4)$$

In terms of this matrix element, the transition probability from the state  $|\mathbf{k}\rangle$  to the state  $|\mathbf{k}'\rangle$  is given by the Golden rule

$$W_{\mathbf{k}, \mathbf{k}'} = \frac{2\pi}{\hbar} n_L |\langle \mathbf{k}' | T | \mathbf{k} \rangle|^2 \delta(\epsilon(\mathbf{k}') - \epsilon(\mathbf{k})). \quad (5)$$

Note that since the scattering is due to a magnetic field  $f(q, \theta) \neq f(q, -\theta)$ , and therefore

$W_{\mathbf{k}, \mathbf{k}'} \neq W_{\mathbf{k}', \mathbf{k}}$ . The Boltzmann equation, in the presence of an electric field  $\mathbf{E}$ , takes the form

$$-e\mathbf{E} \frac{1}{\hbar} \frac{\partial}{\partial \mathbf{k}} g(\mathbf{k}) = - \sum_{\mathbf{k}'} (W_{\mathbf{k}, \mathbf{k}'} g(\mathbf{k}) [1 - g(\mathbf{k}')] - W_{\mathbf{k}', \mathbf{k}} g(\mathbf{k}') [1 - g(\mathbf{k})]) - \frac{g(\mathbf{k}) - g_0(\mathbf{k})}{\tau_i}. \quad (6)$$

Here,  $\mathbf{E}$  is the applied electric field,  $g(\mathbf{k})$  is the number of electrons in the volume element  $d\mathbf{k}$  about the point  $\mathbf{k}$ , and  $g_0(\mathbf{k})$  is the equilibrium Fermi distribution. The last term of Eq. (7) describes collisions with the usual impurities, so that  $\tau_i$  is the relaxation time in absence of magnetic field.

It may be shown [6] that this equation is identical to the Boltzmann equation in a uniform magnetic field and a random impurity potential, with a total relaxation time  $\tau$  of the form

$$\frac{1}{\tau(kR)} = n_L \frac{\hbar k}{m^*} \int_0^{2\pi} d\theta (1 - \cos \theta) |f(k, \theta)|^2 + \frac{1}{\tau_i}, \quad (7)$$

and an effective magnetic field  $B_{\text{eff}} = BF_H(kR)$ , where the Hall factor  $F_H(kR)$ , is given by the expression

$$F_H(kR) = \frac{k}{2\pi\alpha} \int_0^{2\pi} |f(k, \theta)|^2 \sin \theta d\theta. \quad (8)$$

Note that both the Hall factor and the relaxation time only depend on the dimensionless quantity  $kR$ .

We illustrate in Fig. 1 the Hall factor in the case of vortices with magnetic flux  $\alpha = 0.5$  and 2.5. Note the two following limits in Fig. 1: (a)  $F_H \rightarrow 0$  when  $k_F R \rightarrow 0$ . This happens because in this limit there is no magnetic field. This behavior is precisely reproduced by our classical model below. (b)  $F_H \rightarrow 1$  when  $k_F R \rightarrow \infty$ , coinciding with the semiclassical result [6]. However, for  $2\alpha$  not precisely equal to an integer, we find  $F_H$  may either be suppressed or elevated from the semiclassical value. Such behavior, we shall see, does not arise in the classical model, and appears to be

a purely quantum effect. Physically, this is a result of the Aharonov–Bohm effect, for which there is a relative phase shift of electron paths traversing either side of the flux tube, even without passing through it. Thus, the vector potential *outside* the flux tube is capable of scattering electrons, an effect which never arises classically.

In Fig. 2, we illustrate the variation of the dimensionless quantity

$$k_F \int_0^{2\pi} d\theta (1 - \cos \theta) |f(k, \theta)|^2 \quad (9)$$

versus  $k_F R$  for different values of the magnetic flux  $\alpha$ . This quantity is related with the inverse of the scattering time due to the presence of vortices. From Eq. (7) the value of this function in  $k_F R = 0$  is  $2 \sin \pi \alpha^2$ . This function develops a maximum at the values of  $k_F R$  which correspond to the first Landau levels of the magnetic field in the disk. As  $\alpha$  increases more structure is observed because the Landau levels are more separated in energy. In high mobility samples (mean free path around  $10^4$ – $10^5$  Å), and at magnetic field around 150 G, the scattering time due to the vortices can be shorter than that due to the usual impurities.

Finally, we now show that much of the behavior illustrated in Fig. 1 may be understood from a purely classical approach. We begin by noting

$$|f(k, \theta)|^2 = d\sigma/d\theta, \quad (10)$$

where  $d\sigma/d\theta$  is the differential cross-section in two dimensions. Noting that the scattering angle  $\theta$  is a unique function of the impact parameter  $s$ , it is not difficult to show that  $d\sigma/d\theta = ds/d\theta$ , so that

$$F_H(k_F R) = \frac{k_F}{2\pi\alpha} \int_{-R}^R ds \sin \theta(s). \quad (11)$$

By integrating Newton's equation, one may explicitly compute  $\theta(s)$ . We find the resulting form of  $F_H$  to be a universal function of the parameter  $k_F R/\alpha$ , and plot it in the inset of Fig. 1. One can thus see the suppression of  $F_H$  near small  $k_F R$ , which in the classical case is simply the statement that the cross-section of an infinitely thin solenoid

is zero. For large  $k_F R$ , the semiclassical result [6] is recovered.

In conclusion, we have studied the Hall effect and the elastic scattering time for a two-dimensional electron gas scattered by random magnetic flux tubes using a Boltzmann equation approach. Our results give reasonable agreement with experiment for the suppression of the Hall effect at low electron densities. We find resonances in both the Hall and diagonal resistivities as a function of  $k_F R$  that correspond to Landau level energies in the flux tubes. At large  $k_F R$ , the Hall resistivity takes the value expected for a uniform magnetic field, provided the number of flux quanta contained in each tube is integral or half-integral. This result may be understood from a purely classical approach. For other values of the flux in a tube, one gets deviations from the classical result even at large  $k_F R$ , due to the Aharonov–Bohm effect.

We thank C. Tejedor and N. Garcia for helpful discussions. The authors acknowledge the support of the CICyT of Spain, Contract No. MAT 91 0210, and of the NSF, Grant No. DMR-92-02255.

## 1. References

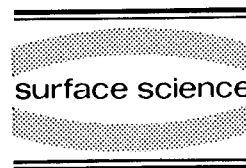
- [1] B.I. Halperin, P.A. Lee and N. Read, Phys. Rev. B 47 (1993) 7312.
- [2] S.J. Bending, K. von Klitzing and K. Ploog, Phys. Rev. Lett. 65 (1990) 1060.
- [3] A.K. Geim, S.J. Bending and I.V. Grigorieva, Phys. Rev. Lett. 69 (1992) 2252; A.K. Heyn et al., JETP Lett. 51 (1990) 121.
- [4] D. Yoshioka and Y. Iye, J. Phys. Soc. Jpn. 56 (1987) 448; P. Vasilopoulos and F.M. Peeters, Superlatt. Microstruct. 4 (1990) 393; F.M. Peeters and P. Vasilopoulos, Phys. Rev. B 47 (1993) 1466; D.P. Xue and Gang Xiao, Phys. Rev. B 45 (1992) 5986.
- [5] D.P. Arovas and F.D.M. Haldane, Bull. Am. Phys. Soc. 35 (1990) 583.
- [6] A.V. Khaetskii, J. Phys. C 3 (1991) 5115.
- [7] Y. Aharonov, C.K. Au, E.C. Lerner and J.Q. Lang, Phys. Rev. D 29 (1984) 2396.





ELSEVIER

Surface Science 305 (1994) 428–433



# Electronic states and collective excitations of a two-dimensional electron gas in spatially modulated magnetic fields

Xiaoguang Wu, Sergio E. Ulloa \*

*Department of Physics and Astronomy, Condensed Matter and Surface Sciences Program, Ohio University,  
Athens, OH 45701-2979, USA*

(Received 20 April 1993; accepted for publication 13 June 1993)

## Abstract

We have studied a two-dimensional (2D) electron gas in the presence of a perpendicular magnetic field spatially modulated along the plane, and in the regime of strong modulation. This magnetically modulated system is different in several respects from an electrostatically modulated one. It is found that the modulation period plays the role of controlling the effective modulation strength. For example, in a unidirectional modulation, the 2D electron gas undergoes a crossover of two- to one-dimensional behavior, as the modulation period increases. Both single-particle electronic states and collective excitations of the system are studied in detail. Anticipating the experimental realization of such systems, we focus our calculations on a realistic range of physical parameters.

## 1. Introduction

Recently, two-dimensional (2D) electronic systems with external modulations on the electron lateral motion have attracted considerable attention [1,2]. These tunable devices are typically realized with various electrostatic modulation methods [1]. In this paper, however, we study a 2D electron gas (2DEG) in the presence of a perpendicular magnetic field spatially modulated in the lateral directions. We show that this magnetically modulated system (MMS) is quite different from an electrostatically modulated system (EMS), despite obvious similarities. We show that the modulation period plays the role of controlling the effective modulation strength, which leads

to some interesting properties. We anticipate that a realistic MMS is intrinsically in the strong modulation regime [3], and generalize the conventional perturbative treatment [4] to include inter-Landau level couplings. Our work is complementary to the reported theoretical studies of MMS, which focus on the transport properties in the weak modulation limit [5].

In the following, we study MMS's with either a one-dimensional (1D) or a 2D lateral modulation. Both single-particle electronic states and collective excitation spectra are investigated. Conclusions appear in the last section.

## 2. 1D modulation

In this section, we study a 2DEG in a magnetic field modulated along one of the lateral direc-

\* Corresponding author.

tions. The modulated field is modelled as  $B_z(x) = B_0 + B_1 \sin(2\pi x/a)$ .  $B_0$  and  $B_1$  give the strength of the uniform and modulation fields, respectively. The modulation introduces two length scales: the spatial period of the modulation  $a$ , and the magnetic length  $l = \sqrt{\hbar c / eB_0}$ . The system can be characterized by two dimensionless quantities:  $p = a/l$  and  $s = B_1/B_0$ . We are interested in the regime  $s \approx 1$ . The single-particle energy levels and wavefunctions can be obtained by diagonalizing the Hamiltonian in the uniform-field Landau level basis, typically including 15 Landau levels.

The upper and middle panels of Fig. 1 show energy levels and electron density profiles of the MMS. In the absence of modulation, all Landau levels are degenerate and independent of the cyclotron center  $x_0 = l^2 ky/a$ . The degeneracy is partially lifted by the modulation and the energy becomes  $x_0$ -dependent. When  $s$  is fixed, such dependence becomes stronger as  $p$  increases. This is because the modulation terms in the Hamiltonian are directly proportional to either  $p$  or  $p^2$ . Thus, in a MMS,  $p$  directly controls the effective modulation strength, while in an EMS,  $p$  plays no corresponding role.

Fig. 1 shows that with a fixed  $s$ , the system displays a trend toward forming an array of 1D structures, as  $p$  increases. The 1D limit can be reached for  $p \gg 1$ . The physical reason behind this behavior can be easily understood. The spatial spreading of the electron wavefunction is governed by the magnetic length. When  $p$  is large enough, the local magnetic length determines the electron packing density. The higher the local field, the higher the local density. For an EMS, however, one finds that the density distribution becomes smoother as  $p$  increases,

since the potential felt becomes smoother, typically. We have also considered the effect of the self-consistent potential due to the nonuniform

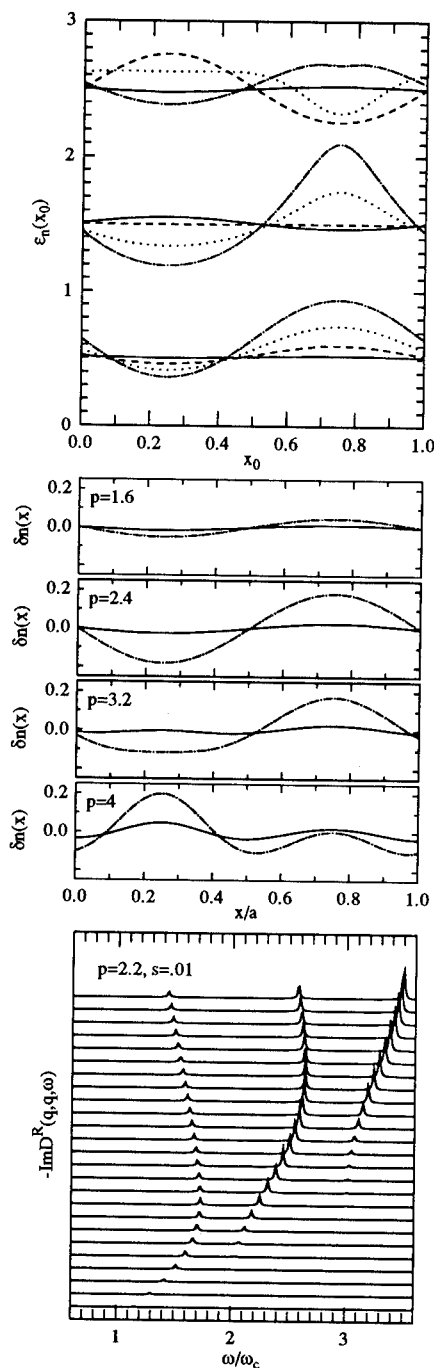


Fig. 1. 1D MMS. Upper panel: energy levels versus the cyclotron center in dimensionless units,  $x_0 = l^2 ky/a$ .  $s = 1$  is kept fixed for  $p = 1.6$  (solid), 2.4 (dashed), 3.2 (dotted), and 4 (dash-dotted). Middle panel: electron density profile along the  $x$ -axis with (solid) or without (dash-dotted) the self-consistent potential. Lower panel: collective excitation spectrum for a nearly unmodulated system ( $s = 0.01$ ) for increasing  $q$  values from 0.02 (bottom curve) to 0.5 (top) in steps of 0.02.

electron density distribution, whose main effect is to flatten out the electron distribution in competition with the magnetic field effect. However, following the physical reasoning above, we expect that when  $p \gg 1$ , the magnetic field effect eventually dominates, and the 2D to 1D-like transition behavior is still exhibited.

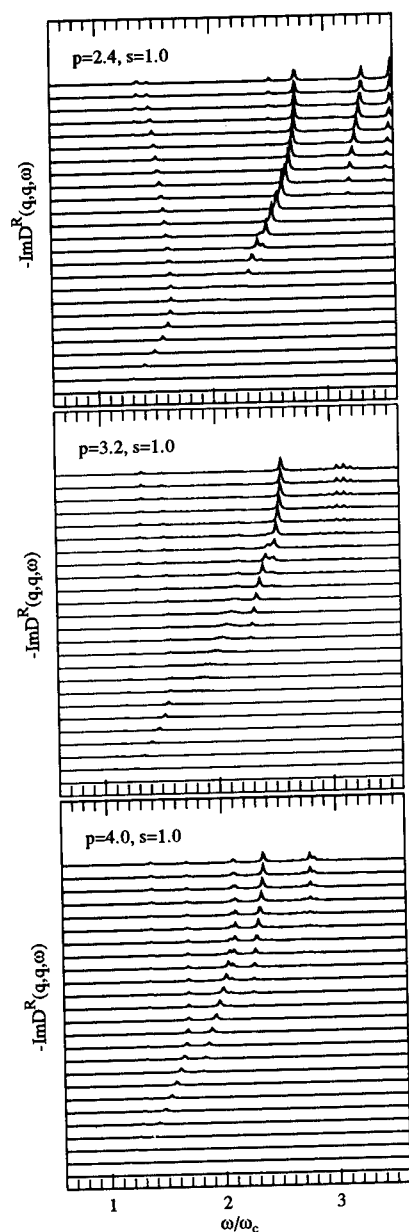


Fig. 2. Collective excitation spectra for various  $p$  in a 1D MMS.  $q$  varies as in Fig. 1.

Next, we study the collective excitations of this MMS. The density correlation function  $D^R(q_x, q'_x, \omega)$  ( $q_y = 0$ ) is evaluated within the random phase approximation (RPA) for simplicity [6]. The lower panel of Fig. 1 shows the excitation spectra for various  $q = q_x a / 2\pi$  at a vanishing  $s = 0.01$ . For each  $q$ , the origin of the curve is shifted upward equally. The peak structures in the curve are identified as the characteristic collective excitations at those frequencies, and the height of the peak gives a relative measure of the excitation coupling strength to an external probe. In Fig. 1, we recover the well-known magnetoplasmons of a 2DEG in a uniform magnetic field [7], as expected.

In Fig. 2, we study the excitation spectrum for a fixed  $s = 1$ , with  $p = 2.4, 3.2$  and  $4$ . For small  $p = 2.4$ , the system is more 2D-like, and so is its excitation spectrum. The effectively weak level modulation emerges only as the splitting of modes, most apparent at large  $q$ . This can be understood intuitively as resulting from mode-folding into the first Brillouin zone,  $|q| \leq 0.5$ , accompanied by a splitting at the zone edge ( $q = 0.5$ ), as introduced by the periodic modulation. A similar phenomenon and description appear in the study of an EMS [2]. However, in contrast to the EMS case, as  $p$  increases, the effective modulation strength increases, thus the splitting at  $q = 0.5$  becomes larger, and the folded modes gain strength. As  $p$  increases further, the folded modes intersect each other, resulting in a complicated redistribution of the oscillator strength among all the modes, even though the energy levels are not overlapping each other yet.

### 3. 2D modulation

In this section we study a MMS with the magnetic field modulated in both lateral  $x$ - and  $y$ -directions. The field is assumed to be  $B_z = B_0 + (B_1/2)[\sin(2\pi x/a) + \sin(2\pi y/a)]$ . We use Landau levels of a 2DEG without modulation as the basis set in calculating the eigenstates, and we limit the magnetic field to rational flux values, i.e.  $\phi/\phi_0 = n_p/n_q$ , where  $n_p$  and  $n_q$  are integers,  $\phi = B_0 a^2$ , and  $\phi_0 = hc/e$  [4]. Since the modula-

tion can no longer be treated as a perturbation for  $s \approx 1$ , we have generalized the earlier calculations to include inter-Landau level couplings, which lead to a Harper equation in matrix form [4] (details will be shown elsewhere). The system is well characterized with  $p$  and  $s$ .

For the rational field modulation, each Landau level splits into  $n_p$  sub-levels, and becomes

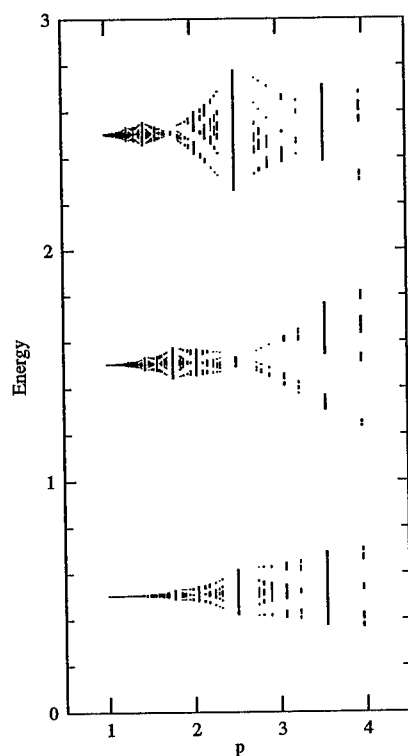


Fig. 3. 2D MMS. Upper panel: energy levels versus  $p$ .  $s=1$ , and  $n_p \leq 6$ . Lower panel: electron density profile for  $n_p = n_q = 1$ , with Fermi level at  $0.6 \hbar \omega_c$ .

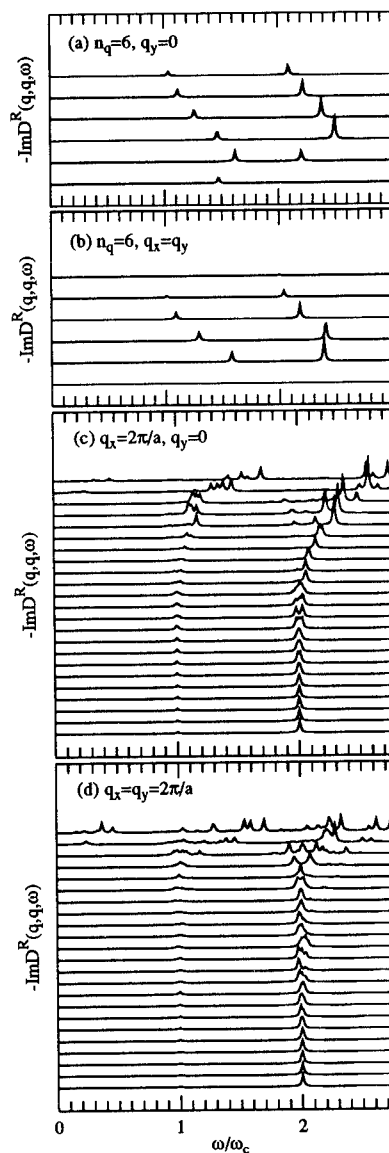


Fig. 4. Collective excitation spectra. (a) and (b):  $q$ -dependence; (c) and (d):  $p$ -dependence.  $n_p \leq 3$  and  $1 \leq p \leq 4$ .  $s=1$  in all panels.

cyclotron center dependent (Harper broadening [4]). In Fig. 3 (upper panel), the width of the lowest three Landau levels and their splittings, are shown for various  $p$  values. It is clear that the band width oscillates versus  $p$  in a non-monotonic fashion. The structure of the energy spectrum resembles the well-known Hofstadter butterfly [4], but with marked differences. For

example, the energy spectrum is no longer a periodic function of  $n_p/n_q$  [4] due to inter-Landau level couplings. For small  $p$  values ( $\approx 1$ ), the broadening is small, while for larger  $p$  the broadening becomes considerable. This again shows that the effective modulation strength is controlled by  $p$ . The lower panel of Fig. 3 shows the electron density profile for  $n_p = n_q = 1$ , with Fermi level at  $0.6 \hbar\omega_c$ .

Next, we study the collective excitation spectrum, as we wish to explore the possibility of observing the highly structured Hofstadter-type spectrum of Fig. 3. We will focus on the regime where the magnetic flux is just a few times  $\phi_0$ . The RPA is used for simplicity. The wavevector dependence of the excitation spectra is shown in Figs. 4(a) and (b) for  $n_p = 1$ ,  $n_q = 6$ ,  $s = 1$ .  $q$  is in two different directions: (a)  $q_y = 0$ , and (b)  $q_x = q_y$ . Different curves correspond to different  $q_x$ , starting with 0.05 (bottom curve), and then on from 0.1 to 0.5 (top) in steps of 0.1. The origin of each curve is shifted, so the dispersion can be seen. Since  $p$  is small, so is the effective modulation strength, the spectra resemble that of a 2DEG in a uniform magnetic field [7]. However, the spectra are anisotropic, because of the loss of rotational symmetry due to the modulation.

In Figs. 4(c) and (d), the excitation spectra are shown for various magnetic fields. The wavevector is fixed: in (c)  $q_x = 2\pi/a$ ,  $q_y = 0$ , and in (d)  $q_x = q_y = 2\pi/a$ ;  $s = 1$ . The fields ( $n_p$  and  $n_q$ ) are chosen such that  $n_p \leq 3$  and  $1 \leq p = (2\pi n_p/n_q)^{1/2} \leq 4$ . Twenty-three curves are plotted in order of increasing  $p$  from the bottom of each panel upwards, and the origin of each curve is shifted equally for clarity. The amplitudes of all curves have been rescaled in order to show the structures of all curves (for smaller  $p$ , the amplitude is smaller). We only observe single peaks around  $n\omega_c$  ( $n = 1, 2$ ) for small  $p$ . As  $p$  increases, the single peak develops into multiple-peak structures. However, the number of peaks does not directly correspond to the number of levels split from one Landau level by the modulation, both because of transition matrix element and depolarization shift effects. The intra-level contribution to the excitation spectra can also be seen at low frequencies ( $\omega/\omega_c \sim 0.4$ ), but only for larger  $p$

values. The spectra are anisotropic, as expected. Note that the zone-folding picture can no longer be used to describe the field dependence, since it predicts that the modes should deviate away from  $n\omega_c$  first, and then fall back, as  $p$  increases from a small value. This is not observed.

#### 4. Conclusions

We have studied a 2DEG in spatially modulated magnetic fields. It is found that the MMS becomes strongly modulated, when the modulation period becomes several times larger than the magnetic length. In the 1D modulation, the system shows a trend to a dimensional crossover. The collective excitation spectra also show strong modulation effects. In the 2D modulation, we find that multiple-peak structures develop either as the wavevector increases from the long wavelength limit, or as the magnetic field increases. Although the excitation spectra do not directly map the Hofstadter-type energy spectrum, because of complicated oscillator strength distributions, an interesting and certainly nontrivial spectrum is found nevertheless. It is desirable to implement experimentally the MMS studied here and observe the predicted spectra.

#### 5. Acknowledgements

This work was supported by the US Department of Energy, Grant No. DE-FG02-91ER45334.

#### 6. References

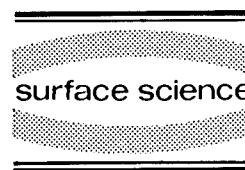
- [1] W. Hansen et al., Phys. Rev. Lett. 58 (1987) 2586; P.H. Beton et al., Phys. Rev. B 42 (1990) 9689; A. Lorke et al., Phys. Rev. Lett. 64 (1990) 2559; D. Weiss et al., Phys. Rev. Lett. 66 (1991) 2790; J. Alsmeier et al., Phys. Rev. B 41 (1990) 1699; H. Fang et al., Phys. Rev. B 41 (1990) 10171; K. Kern et al., Phys. Rev. Lett. 66 (1991) 1618; G. Berthold et al., Phys. Rev. B 45 (1992) 11350.
- [2] P. Vasilopoulos et al., Phys. Rev. Lett. 63 (1989) 2120; U. Wulf et al., Phys. Rev. B 42 (1990) 7637; G.R. Aizin et al., Sov. Phys.-JETP 60 (1984) 844; W. Que et al., Phys. Rev. B 43 (1991) 14079;

- R.R. Gerhardts, *Phys. Rev. B* 45 (1992) 3449;  
 T. Deruelle et al., *Phys. Rev. B* 45 (1992) 9082.
- [3] An MMS may be implemented by evaporating narrow strips of superconducting materials onto the surface close to the 2DEG, as the spatial modulation of the magnetic field results from the Meissner effect at low temperatures. See S.J. Bending et al., *Phys. Rev. B* 42 (1990) 9859; A.K. Geim et al., *JETP Lett.* 51 (1990) 121.
- [4] P.G. Harper, *Proc. Phys. Soc. London A* 68 (1955) 874; M.Ya. Azbel, *Sov. Phys.-JETP* 19 (1964) 634;
- D.R. Hofstadter, *Phys. Rev. B* 14 (1976) 2239;  
 D.J. Thouless et al., *Phys. Rev. Lett.* 49 (1982) 405.
- [5] B.A. Dubrovin et al., *Sov. Phys.-JETP* 52 (1980) 511; Deng Ping Xue et al., *Phys. Rev. B* 45 (1992) 5986; F.M. Peeters et al., *Phys. Rev. B* 47 (1993) 1466.
- [6] G.D. Mahan, *Many Particle Physics* (Plenum, New York, 1981).
- [7] K.W. Chiu and J.J. Quinn, *Phys. Rev. B* 9 (1974) 4724; Xiaoguang Wu et al., *B* 36 (1987) 9760.



ELSEVIER

Surface Science 305 (1994) 434–437



# Two-dimensional tunneling through magnetic barriers

A. Matulis <sup>a</sup>, F.M. Peeters <sup>\*,b</sup>, P. Vasilopoulos <sup>c</sup>

<sup>a</sup> Semiconductor Physics Institute, Vilnius, Lithuania

<sup>b</sup> Departement Natuurkunde, Universiteit Antwerpen (UIA), B-2610 Antwerpen, Belgium

<sup>c</sup> Department of Physics, Concordia University, Montréal, Québec, Canada H3G 1M8

(Received 23 April 1993; accepted for publication 22 June 1993)

## Abstract

We propose a new system consisting of magnetic tunneling barriers. A theoretical investigation is made of electrons moving in a plane tunneling and ballistically through these magnetic barriers. The differences between the usual tunneling problem and the tunneling through magnetic barriers are pointed out. A resonant tunneling structure consisting of such magnetic tunneling barriers is proposed and exhibits pronounced resonant structure.

## 1. Introduction

Recently, MBE growth has been used to stabilize thin films of the bulk metastable ferromagnetic intermetallic compound  $\tau$ -MnAl on AlGa/GaAs heterostructures. It was possible [1] to orient the easy magnetization direction of the films perpendicular to the substrate. Patterning of the ferromagnetic films will allow one to construct various magnetic structures. Another possibility is to put type-II superconducting gates [2] on top of a heterostructure and to destroy the superconductivity along a thin narrow line. In doing so the two-dimensional electron gas (2DEG) underneath it will interact with a nonhomogeneous magnetic field [2–5]. In this paper we study electron transmission through various magnetic tun-

neling structures and investigate the possibility of resonant tunneling.

## 2. Formulation of the problem

We consider a 2DEG in the  $(x, y)$  plane with a magnetic field  $B$  directed along the  $z$ -direction which is modulated along the  $x$ -direction. We assume that the vector potential is taken in the Landau gauge  $A = (0, A, 0)$  and thus the magnetic field is  $B_z \equiv B(x) \equiv dA(x)/dx$ . Let us introduce the following characteristic parameters: (i) the frequency  $\omega_c = eB_0/mc$  with  $B_0$  some typical magnetic field which later on will be taken equal to the height of the magnetic barrier, and (ii) the length  $l_B = \sqrt{\hbar c/eB_0}$ . From now on we will express all quantities in dimensionless units: (1) the magnetic field  $B(x) \rightarrow B_0 B(x)$ , (2) the vector potential  $A(x) \rightarrow B_0 l_B A(x)$ , (3) the coordinate  $r \rightarrow l_B r$ , (4) the velocity  $v \rightarrow l_B \omega_c v$ , and (5) the energy  $E \rightarrow \hbar \omega_c E$ .

\* Corresponding author.

In these dimensionless units, the stationary Schrödinger equation describing the electron tunneling process becomes

$$\left\{ \frac{\partial^2}{\partial x^2} + \left[ \frac{\partial}{\partial y} + iA(x) \right]^2 + 2E \right\} \Psi(x, y) = 0. \quad (1)$$

The electron motion in the presence of a magnetic field is inherently a 2D problem, but with our choice of Landau gauge the problem can be considerably simplified by choosing the electron wavefunction in the following form,  $\Psi(x, y) = \exp(iqy)\psi(x)$ , where  $q$  is the electron wavevector in the  $y$ -direction. The wavefunction  $\psi(x)$  satisfies the 1D Schrödinger equation

$$\left\{ \frac{d^2}{dx^2} - [A(x) + q]^2 + 2E \right\} \psi(x) = 0, \quad (2)$$

where the function

$$V(x) = \frac{1}{2} [A(x) + q]^2 \quad (3)$$

can be interpreted as a wavevector dependent electric potential. In the present case in which the magnetic field is nonuniform only along one direction there is a formal analogy between the magnetic field and the electric potential given by the following relation:  $B(x) = (dV(x)/dx)/\sqrt{2V(x)}$ .

### 3. Method of solution

The simplest way to consider the electron tunneling problem is by making use of the matrix

$$T(x, x_0) = \begin{pmatrix} u(x) & v(x) \\ u'(x) & v'(x) \end{pmatrix}, \quad (4)$$

where the functions  $u(x)$  and  $v(x)$  satisfy Eq. (2) and the boundary conditions  $u(x_0) = 1$ ,  $u'(x_0) = 0$ ,  $v(x_0) = 0$  and  $v'(x_0) = 1$ . Matching by means of the  $T$ -matrix the wavefunction  $\psi_-(x) = A \exp(ik_-x) + B \exp(-ik_-x)$  on the left side of the barrier structure with that on the right side  $\psi_+(x) = \exp(ik_+x)$ , we obtain

$$A = T_{11}^{-1} + \frac{k_+}{k_-} T_{22}^{-1} + i \left( \frac{1}{k_-} T_{21}^{-1} - k_+ T_{12}^{-1} \right), \quad (5)$$

and finally the electron transmission probability through the barrier is given by

$$t(E, q) = \frac{k_+}{k_- |A|^2}. \quad (6)$$

Here  $k_{\pm} = \sqrt{2(E - V(\pm\infty))}$  is the electron wavevector in the  $x$ -direction on the left and right barrier sides, respectively, and the symbol  $T^{-1}$  stands for the inverse matrix.

We also evaluated the electron current through the barrier in the ballistic regime. Following Ref. [6] the conductance is introduced as the electron flow averaged over half the Fermi surface

$$\sigma = \int_{-\pi/2}^{\pi/2} d\phi \cos \phi t(E_F, \sqrt{2E_F} \sin \phi). \quad (7)$$

Here  $\phi$  is the angle of incidence relative to the  $x$ -direction. The conductance is presented in units of  $e^2 m v_F l / h^2$ , where  $l$  is the length of the barrier structure in the  $y$ -direction.

### 4. Results and discussion

We evaluated the transition probabilities (6) and the conductance (7) by integrating numerically Eq. (2) and calculating the  $T$ -matrix (4). Fig. 1 shows the electron transmission through a simple magnetic barrier (see inset of Fig. 1) for

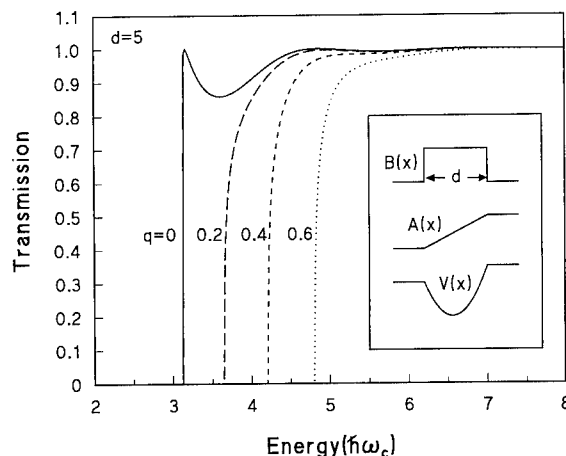


Fig. 1. Electron transmission through a magnetic barrier as a function of the electron energy for different values of the incident wavevector.



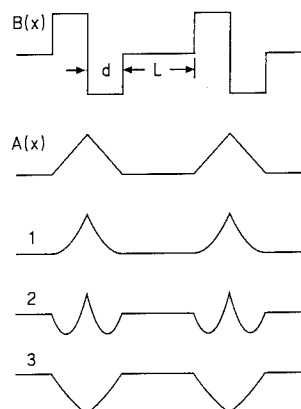


Fig. 2. A complex magnetic structure: barrier- and well-like regions correspond to opposite directions of the magnetic field. We show the magnetic field  $B(x)$ , the vector potential  $A(x)$ , and the potential  $V(x)$  for: (1)  $q \geq 0$ , (2)  $-d < q < 0$ , and (3)  $q < -d$ .

different values of the incident wavevector. The magnetic structure consists of a barrier  $B(x) = \theta(d^2/4 - x^2)$ , where  $\theta(x) = 1(x \geq 0)$ ,  $0(x < 0)$  is the step function. In the same inset we show the corresponding vector potential  $A(x) = x\theta(d^2/4 - x^2)$  and the potential  $V(x)$  for the case when  $|q| < d/2$ . We see that the electron transition through the magnetic barrier is analogous to the transition over an electric potential well. In Fig. 1 we observe that the transmission has some weak oscillations. Only in the case of  $q = 0$ , when the potential  $V(x)$  is symmetric and for specific values of the barrier width, has the transmission some resonant structure at low energies due to the presence of a virtual level in the quantum well. When  $|q| > d/2$  the potential  $V(x)$  has the shape of a step.

Next we consider the structure depicted in Fig. 2 which exhibits resonant tunneling. The magnetic structure consists of the barrier of Fig. 1 immediately followed by a well which is the identical reverse of the barrier. This basic structure is repeated after some distance  $L$ . The potential  $V(x)$  has different shapes depending on the value of  $q$ . For  $q \geq 0$  (curve 1) it consists of two simple potential barriers while for  $q < 0$  it is more complicated: depending on the absolute value of  $q$  it may consist of two quantum wells (curve 3) or of two double wells (curve 2). As a consequence,

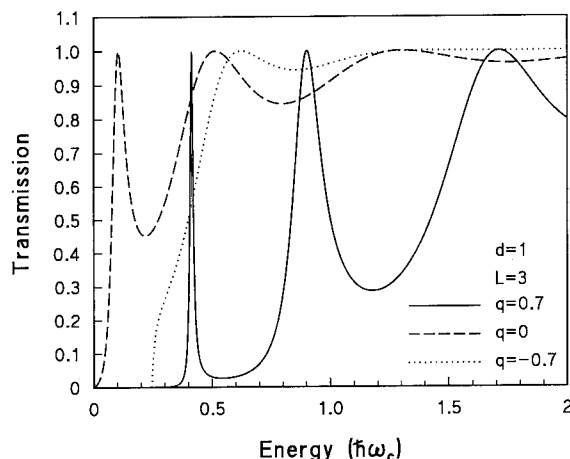


Fig. 3. Transmission coefficient for the structure of Fig. 2 for different values of the electron wavevector  $q$ .

dramatically different transmission coefficients are obtained in the three cases, as is shown in Fig. 3. For positive  $q$ -values there are well pronounced spikes of resonant tunneling, whereas for negative  $q$ -values there are only weak oscillations. This electron transmission anisotropy is clearly seen in Fig. 4 where we show the contour plot of the electron transmission in the velocity component plane ( $v_x = k_x$ ,  $v_y = q + A(-\infty)$ ). Notice that in contrast to the case without magnetic field, now the transmission probability manifests

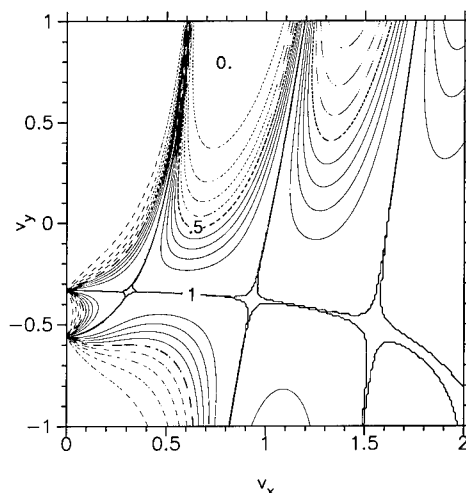


Fig. 4. Contour plot of the electron transmission probability in the  $(v_x, v_y)$  plane for the structure of Fig. 2.

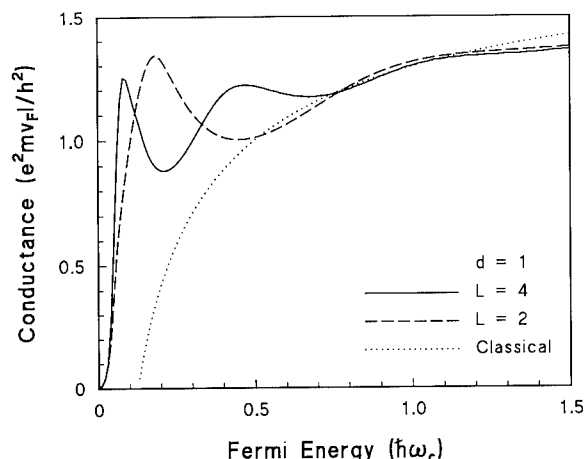


Fig. 5. The conductance through the structure of Fig. 2. The dotted line shows the conductance calculated classically.

the essential  $v_y$  (or  $q$ ) dependence and, consequently, such magnetic structures have well pronounced directional filter properties.

In Fig. 5 the current (scaled with the voltage, which then becomes the conductance) through the above structure is shown versus the Fermi energy. In spite of the averaging, the spikes at low energy are still pronounced and are closer in energy with increasing  $L$  as expected intuitively. For purposes of comparison we have also considered a classical treatment of ballistic transport through the above structure. In this case, tunneling is completely determined by the first barrier and does not depend on the separation  $L$ . In this case, the transmission coefficient is either 1 (if  $-\pi/2 < \varphi < \varphi_0$ ,  $\varphi_0 = \arcsin(1 - d/v_F)$ ) or 0 (if  $\varphi_0 < \varphi < \pi/2$ ). The corresponding averaged current is shown in Fig. 5 by the dotted curve.

In conclusion, we mention some essential differences between the usual tunneling and tunneling through magnetic barriers: (1) now the tunneling process is inherently two-dimensional, (2) the transmission probability essentially depends on the electron velocity ( $v_y$ ) along the magnetic barrier structure, and (3) the transmission probability can be affected by the bound energy levels in the magnetic barriers.

## 5. Acknowledgments

This work is supported by the Belgian National Science Foundation (NFWO), the Interuniversity Microelectronics Center (IMEC, Leuven) and by the Collaborative Research Grant: NATO-5-2-05/RG No. 890123. One of us (A.M.) acknowledges the support of the EEC through the programme: "Cooperation in Science and Technology with Central and Eastern European Countries".

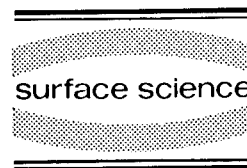
## 6. References

- [1] T. Sands, J.P. Harbison, M.L. Leadbeater, S.J. Allen, Jr., G.W. Hull, R. Ramesh and V.G. Keramides, *Appl. Phys. Lett.* 57 (1990) 2609.
- [2] A.K. Geim, *JETP Lett.* 50 (1989) 390; S.J. Bending, K. von Klitzing and K. Ploog, *Phys. Rev. Lett.* 65 (1990) 1060.
- [3] P. Vasilopoulos and F.M. Peeters, *Superlatt. Microstruct.* 4 (1990) 393; *Phys. Scri. T* 39 (1991) 177; F.M. Peeters and P. Vasilopoulos, *Phys. Rev. B* 47 (1993) 1466.
- [4] P.P. Vil'ns and M.V. Éntin, *Sov. Phys. Semicond.* 22 (1988) 1209 [*Fiz. Tekh. Poluprovodn.* 22 (1988) 1905].
- [5] D. Yoshioka and Y. Iye, *J. Phys. Soc. Jpn.* 56 (1987) 448.
- [6] M. Büttiker, *Phys. Rev. Lett.* 59 (1986) 1761.



ELSEVIER

Surface Science 305 (1994) 438–442



# Influence of a periodic potential on the integer quantum Hall effect

B. Huckestein \*, R.N. Bhatt

*Department of Electrical Engineering, Princeton University, Princeton, NJ 08544, USA*

(Received 21 April 1993; accepted for publication 12 May 1993)

## Abstract

We calculate the Hall conductivity for a disordered non-interacting two-dimensional electron gas in a strong magnetic field under the influence of a periodic potential. We investigate under which experimental conditions the unusual behavior of the Hall effect in the system could be observed.

## 1. Introduction

In recent years, advances in nanofabrication techniques have allowed the preparation of periodic submicron structures in semiconductor heterojunctions. These lateral surface superlattices [1,2] can take various forms: the periodic potential can be one- (1D) or two-dimensional (2D), and it can cause a weak or strong modulation. For strong modulation the two-dimensional electron gas (2DEG) forms either an array of quantum dots for attractive potential or it contains a regular array of scatterers known as “antidots”. Magnetoresistance and Hall effect measurements on these systems reveal interesting phenomena [3,4]. In the samples used, the period of the periodic potential was typical of the order of a few hundred nm. In this regime much of the physics can be explained by classical arguments [2,5].

The spectrum of a 2DEG in a strong perpendicular magnetic field and a weak periodic potential shows a very rich, self-similar structure known as the Hofstadter butterfly [6]. The emergence of subband gaps in this spectrum leads to a similarly intricate structure of the Hall conductivity as a function of magnetic field and filling factor [7,8]. Much of the present experimental effort is directed toward observing signatures of this spectrum. However, the effects of disorder will close the subband gaps associated with the Hofstadter butterfly and hence the corresponding features in the Hall conductivity will be smoothed out [9].

In this paper we investigate the influence of a disorder potential on the Hall conductivity of a 2DEG in a strong magnetic field. Since we are interested in the observability of the butterfly spectrum we will restrict ourselves to the situation where both the periodic potential and the disorder are weak compared to the magnetic field. Thus we do not treat cases like “antidot” arrays [4]. We have performed numerical calculations to estimate conditions that need to be met in order

\* Corresponding author.

to observe signatures of the Hofstadter butterfly in the Hall conductivity.

## 2. Calculational method

We first briefly review some basic features of a 2DEG in a strong magnetic field and weak periodic potential. For a square periodic potential with only one Fourier component and the same amplitude  $E_0$  and period  $a$  in both directions

$$V(\mathbf{r}) = 2E_0 \left[ \cos\left(\frac{2\pi}{a}x\right) + \cos\left(\frac{2\pi}{a}y\right) \right]. \quad (1)$$

Each Landau level splits into  $p$  subbands if the number of unit cells per flux quantum  $\alpha = \Phi_0/a^2B = 2\pi l_c^2/a^2$  is a rational number  $q/p$  [6,8]. Each subband carries the same number of states so that the filling factor  $\nu$  in the  $t$ th gap is given by  $\nu = t/p$ . The eigenvalues  $E$  of the Hamiltonian  $H = (\mathbf{p} - e\mathbf{A})^2/2m + V(\mathbf{r})$  are related to the eigenvalues  $\lambda$  of Harper's equation [6] by [11]

$$E = (n + 1/2)\hbar\omega_c + E_0 e^{-\pi\alpha/2} L_n(\pi\alpha)\lambda. \quad (2)$$

The Hall conductivity  $\sigma_{xy}$  in each gap is quantized in multiples of  $e^2/h$  as in the case of the gaps between Landau levels. Its value  $\sigma_{xy} = \sigma e^2/h$  is given by the Diophantine equation

$$\sigma = \nu - s\alpha = (t - sq)/p \quad (3)$$

with integer  $s$  and  $\sigma$  [7]. Each gap is then uniquely defined by its quantum numbers  $\sigma$  and  $s$ .

The calculations of the Hall conductivity that we present here are based on scaling studies of the localization length [10]. We calculate the localization length of long cylinders and apply a finite size scaling analysis to obtain the critical energy for which the localization length of the infinite system diverges using the same method used previously for single Landau levels without periodic potential [12–14]. We use the periodic potential given in Eq. (1). Our calculations of the localization length show that for weak disorder each subband that carries a non-zero Hall conductivity contains at least one energy with diverging localization length characteristic of critical states [10]. These critical states are separated by

mobility gaps. We assume that the Hall conductivity in these gaps can be calculated from Eq. (3) as in the case of no disorder. This is justified since the Hall conductivity can only change from its zero disorder value if a critical state crosses the Fermi energy. Thus, as long as we observe a mobility gap we know the value of the Hall conductivity.

As the disorder is increased these mobility gaps close. When a gap has closed, the Hall conductivity will no longer be given by Eq. (3). In this case it can be calculated by keeping track of the number of critical states that cross the Fermi energy and their contribution to the Hall conductivity. For this we use the following argument. Let us assume the subband below the particular mobility gap that just has closed contributes  $\sigma_1$  to the Hall conductivity and the subband above  $\sigma_2$ . When the gap has closed these subbands will behave like one subband with Hall conductivity  $\sigma_1 + \sigma_2$ . If  $\sigma_1$  and  $\sigma_2$  have opposite signs this means that critical states with positive and negative Hall conductivity have “annihilated”. The Hall conductivity of the combined bands is then due to the remaining states of the majority type. Our calculations of the localization length suggest that these remaining states stay at the same energy that they had for very weak disorder. We have assumed this to be the generic behavior in our calculations.

For example, in the case  $\alpha = 3/5$ , the Hall conductivity in the first 5 gaps takes on the values  $-1, 1, 0, 2, 1$  so that the Hall conductivity of the 5 subbands is  $-1, 2, -1, 2, -1$ . The first subband gaps to close with increasing disorder are the gaps between subbands 1 and 2 and between 4 and 5. If we keep the Fermi level fixed between subbands 4 and 5 and increase the disorder, the critical state with Hall conductivity  $-1$  in subband 5 moves through the Fermi level and “annihilates” with a state from subband 4 leaving a state with Hall conductivity 1 in subband 4. Thus we know that the Hall conductivity changes from 2 to 1.

For  $\alpha = 2/5$  and  $3/5$  the mobility gaps close when the strength  $\Gamma$  of the disorder is about twice the size of the mobility gap at low disorder [10]. Here  $\Gamma$  is the width of the disorder broad-

ened Landau band in the absence of a periodic potential [12,14]. We assume that this can be applied to other gaps we study. Since it is numerically rather involved to calculate the actual mobility gap at low disorder we replace it in our calculations with the spectral gap at zero disorder. This generically overestimates the effect of disorder. Thus, for the above example, the mobility gap is more than twice as large as the spectral gap. However, for the largest gaps in the Hofstadter butterfly, the difference is probably less severe.

### 3. Hofstadter butterfly and system parameters

For a system with fixed carrier density  $n_{2D}$  the parameter  $\alpha$  is proportional to the filling factor  $\nu = 2\pi l_c^2 n_{2D}$ ,  $\alpha = \nu/\nu_0$  with  $\nu_0 = n_{2D} a^2$ .  $\nu_0$  can be interpreted as the filling factor at which one flux quantum penetrates each unit cell of the lattice. It determines in which gap the Fermi energy is situated at a given filling factor. The Hall conductivity then depends on the filling factor via

$$\sigma = \nu(1 - s/\nu_0) \quad (4)$$

with integer  $\sigma$  and  $s$ . The widest gaps are the easiest to observe experimentally since these are least sensitive to disorder. The primary gaps are given by the trajectories  $\alpha = \nu + m$  and  $\alpha = 1 - \nu + m$  with integer  $m$ . In addition, a particular

Hall conductivity is easier to observe if the Fermi level stays in the same gap over a wide range of filling factors. This singles out the case  $\alpha = \nu$  corresponding to  $\nu_0 = 1$  as being particularly advantageous. However, this value is not easily achievable experimentally since it requires both very low carrier density and very short period.

For large values of  $\nu_0$  that are more readily achievable the Hall conductivity will only deviate from the value in the absence of a periodic potential for large filling factors and over small regions of filling factor. The reason for this is that in the widest gaps  $s$  takes on values of smallest absolute magnitude. The gaps between Landau levels at  $\nu = n$  are characterized by  $s = 0$  and  $\sigma = n$ . For  $|s|$  much smaller than  $\nu_0$ , Eq. (4) has solutions with  $\sigma = n$  for  $\nu = n\nu_0/(\nu_0 - s)$ . Thus, as long as  $n - 1/2 < \nu < n + 1/2$  the Hall conductivity will be the same whether these gaps are open or not. Only for sufficiently large  $n$  will this not be the case.

### 4. Numerical calculations

The Fermi level can be in a gap for rational values of  $\alpha = q/p$  and  $\nu = t/p$ . From this it follows that  $\nu_0$  has to be rational, too. We assumed the disorder to be proportional to the square root of the magnetic field,  $\Gamma = \Gamma_0/\sqrt{\nu}$ . In self-consistent Born approximation (SCBA) [15]  $\Gamma_0$  is

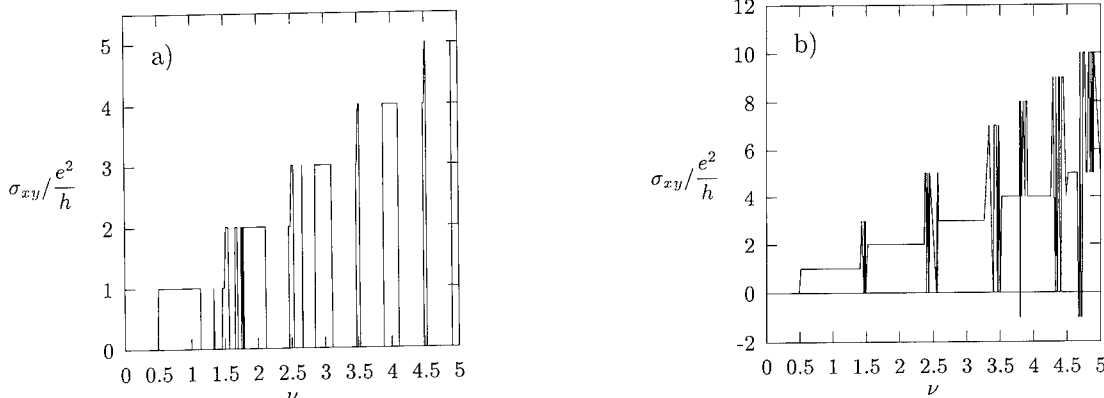


Fig. 1. (a) Dimensionless Hall conductivity for  $\nu_0 = 1$ ,  $\Gamma_0 = 0.124$  meV and  $E_0 = 0.1$  meV as a function of filling factor  $\nu$ . (b) The same for  $\nu_0 = 10/11$  and  $\Gamma_0 = 0.118$  meV.

given by  $\Gamma_0 = \sqrt{4e\hbar^3 n_{2D}/m^* \mu}$ , where  $m^*$  is the effective mass and  $\mu$  is the low field mobility.

We obtained the widths of the spectral gaps from Eq. (2) and the spectrum of Harper's equation that we calculated for rational  $\alpha$  and denominators  $p$  up to 50. We made sure that in all cases the width of the Landau bands broadened by disorder and periodic potential was less than the Landau level spacing so that our single band approximation remained valid. We chose  $\nu_0 = f/g$  with integer  $f$  and  $g$  and calculated the Hall conductivity in every possible gap with denominators up to 50 according to the procedure outlined above. In the figures we plot the Hall conductivity at these filling factors. The straight lines connecting these points are a guide to the eye.

In order to show how drastically a periodic potential can change the Hall conductivity we first present the most interesting case we have studied, namely  $\nu_0 = 1$  for sufficiently low disorder. The Hall conductivity shown in Fig. 1a is calculated for a periodic potential of  $E_0 = 0.1$  meV and a disorder strength  $\Gamma_0 = 0.124$  meV. Using SCBA with an effective mass of  $0.068m_0$  for GaAs this corresponds to a mobility  $\mu = 10^6$  cm<sup>2</sup>/V·s, a carrier density  $n_{2D} = 2 \times 10^{10}$  cm<sup>-2</sup>, and a period  $a = 70.7$  nm. The gaps with zero Hall conductivity remain open for most filling factors and the Hall conductivity vanishes for about 70% of a Landau band.

This effect is very sensitive to the exact value

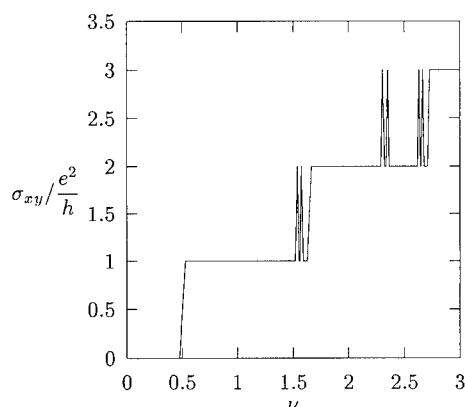


Fig. 2. Dimensionless Hall conductivity for  $\nu_0 = 10$ ,  $\Gamma_0 = 0.553$  meV and  $E_0 = 1$  meV as a function of filling factor  $\nu$ .

of  $\nu_0$  as can be seen from Fig. 1b where the same parameters as in Fig. 1a were used except for a lower density  $n_{2D} = 1.82 \times 10^{10}$  cm<sup>-2</sup> ( $\nu_0 = 10/11$ ). The very rich structure that develops persists only over very short intervals of filling factor.

Fig. 2 shows an example where even for high values of  $\nu_0$  a signature of the Hofstadter butterfly might be observable. A density  $n_{2D} = 10^{11}$  cm<sup>-2</sup> and a period  $a = 100$  nm leads to  $\nu_0 = 10$  that was used for the figure. Due to the higher density a stronger periodic potential  $E_0 = 1$  meV can be used without overlapping neighboring Landau levels. The disorder was  $\Gamma_0 = 0.553$  meV corresponding in SCBA to a mobility of  $2.5 \times 10^5$  cm<sup>2</sup>/V·s. The region where the filling factor drops to 1 near  $\nu = 1.6$  has a width of 0.04–0.08.

## 5. Conclusion

In the above discussion the effect of a finite temperature has been neglected. The largest gaps in the spectrum, e.g. for  $\alpha = 5/4$ , have a width of about  $0.6E_0$ . For  $E_0 = 0.1$  meV this corresponds to a temperature of 0.7 K. Thus at least the largest gaps should be observable at mK temperatures.

The clean systems necessary to observe the Hofstadter butterfly also show the fractional quantized Hall effect (FQHE). The effect of the FQHE is weakest for half-integer filling [16]. However, at these filling factors  $\nu$  the gaps in the Hofstadter butterfly close. The most favorable filling factors to observe the Hofstadter butterfly in the presence of the FQHE thus seems to be  $\nu = \text{odd multiples of } 1/4$ , where the FQHE is weak [16] but the primary gaps in the butterfly are strongest. Since the observation of non-trivial effects of the Hofstadter butterfly depends on the periodicity of the potential through  $\nu_0$ , these requirements on  $\nu$  and  $\nu_0$  are not in conflict.

The periodic potential used in these calculations contained only one Fourier component while realistic potentials might contain a whole Fourier spectrum. The effect of higher Fourier components on the present analysis remains to be considered.

In summary, we have presented calculations of the Hall effect in 2DEGs under the influence of a strong magnetic field, a disorder potential, and a periodic potential. We have estimated bounds on the strength of the disorder and the strength and period of the periodic potential.

## 6. Acknowledgements

One of us (B.H.) wants to thank A.H. MacDonald for stimulating discussions and NATO and DFG for support through scholarships. A portion of the calculations was done on the Princeton MasPar, supported in part by a DEC-DPRI grant and NSF CISE Instrumentation grant CDA-9121709.

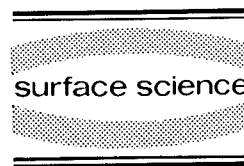
## 7. References

- [1] D. Weiss, *Festkörperprobleme, Advances in Solid State Physics*, Vol. 31, Ed. U. Rössler (Vieweg, Braunschweig, 1991).
- [2] C. Beenakker and H. van Houten, *Solid State Physics*, Vol. 44, Eds. H. Ehrenreich and D. Turnbull (Academic Press, San Diego, CA, 1991) p. 1.
- [3] R. Gerhardts, D. Weiss and U. Wulf, *Phys. Rev. B* 43 (1991) 5192.
- [4] D. Weiss, M.L. Roukes, A. Menschig, P. Grambow, K. von Klitzing and G. Weimann, *Phys. Rev. Lett.* 66 (1991) 2790.
- [5] R. Fleischmann, T. Geisel and R. Ketzmerick, *Phys. Rev. Lett.* 68 (1992) 1367.
- [6] D.R. Hofstadter, *Phys. Rev. B* 14 (1976) 2239.
- [7] D. Thouless, M. Kohmoto, M. Nightingale and M. den Nijs, *Phys. Rev. Lett.* 49 (1982) 405.
- [8] A.H. MacDonald, *Phys. Rev. B* 28 (1983) 6713.
- [9] H. Aoki, *Surf. Sci.* 263 (1992) 137.
- [10] B. Huckestein, to be published.
- [11] This is Eq. (6) of Ref. [8] that erroneously contains a factor 2.
- [12] B. Huckestein and B. Kramer, *Phys. Rev. Lett.* 64 (1990) 1437.
- [13] B. Huckestein, *Physica A* 167 (1990) 175.
- [14] B. Huckestein, *Europhys. Lett.* 20 (1992) 451.
- [15] T. Ando and Y. Uemura, *J. Phys. Soc. Jpn.* 36 (1974) 959.
- [16] S. Kivelson, D.-H. Lee and S.-C. Zhang, *Phys. Rev. B* 46 (1992) 2223; B. Halperin, P.A. Lee and N. Read, *Phys. Rev. B* 47 (1993) 7312.



ELSEVIER

Surface Science 305 (1994) 443–447



## Negative magnetoresistance and anomalous diffusion of two-dimensional electrons in a disordered array of antidots

G.M. Gusev <sup>\*,1,a</sup>, P. Basmaji <sup>a</sup>, Z.D. Kvon <sup>b</sup>, L.V. Litvin <sup>b</sup>, Yu.V. Nastaushev <sup>b</sup>,  
A.I. Toropov <sup>b</sup>

<sup>a</sup> Instituto de Física e Química de São Carlos, Universidade de São Paulo, São Paulo, Brazil

<sup>b</sup> Institute of Semiconductor Physics, Russian Academy of Sciences, Siberian Branch, Novosibirsk, Russian Federation

(Received 8 April 1993; accepted for publication 29 June 1993)

### Abstract

Negative linear magnetoresistance of two-dimensional (2D) electrons in a disordered array of antidots has been found. The existence in a magnetic field of trajectories which roll along the array of antidots was suggested. These trajectories have a mean free path larger than the average value for electrons with ordinary diffusion.

Magnetic field decreases electron mean free path, therefore the magnetoresistance of semiconductors and metals is positive. However, at low temperature and weak magnetic field negative magnetoresistance has been observed [1]. This phenomenon has been explained from a quantum standpoint. The crossed electron trajectories increase the backscattering probability due to the interference at the crossing point. Magnetic field suppresses this interference because of the Aharonov–Bohm effect, the backscattering probability decreases, and as a result negative magnetoresistance appears [1]. From a classical standpoint the negative magnetoresistance is a result of increase of electron elastic length or appear-

ance of the carriers with mean free path larger than the average value. In Ref. [2] Wagenhuber et al. have found theoretically that this probability exists in a 2D electron gas in a lateral two-dimensional lattice. At some value of lattice potential in a magnetic field the anomalous diffusion of electrons arises. This is characterized by a linear increase of the mean square displacement of carriers,  $\langle x^2 \rangle^{1/2} \approx t^{1+\alpha}$ , with  $\alpha = 1$ . It is responsible for violation of the exponential distribution of a portion of particles with mean free path, and thus, electrons with anomalously large elastic length appear. However, the influence of this effect on the electron transport, in particular magnetoresistance, was not considered.

One type of two-dimensional lateral superlattice with strong repulsive potential is an array of antidots [4], which is produced in a 2D electron gas by holes with submicron diameter fabricated by etching or irradiation by ions. This system has attracted attention also because it allows various

\* Corresponding author.

<sup>1</sup> Permanent address: Institute of Semiconductor Physics, Russian Academy of Sciences, Siberian Branch, Novosibirsk, Russian, Federation.



arrangements of antidots to be simulated, square [3,4], hexagonal [5], two-dimensional quasicrystals [6], and disordered [7,8].

In this work the magnetoresistance of 2D electrons in a periodic and disordered lattice of antidots has been studied, and a negative magnetoresistance which grows with degree of disorder has been found.

The test samples were Hall bridges based on GaAs/AlGaAs heterostructures with a 2D electron gas. The parameters of the initial heterostructures were electron density,  $n_s = 5 \times 10^{11} \text{ cm}^{-2}$ , and mobility,  $\mu = (2-5) \times 10^5 \text{ cm}^2/\text{V} \cdot \text{s}$ . A lattice of antidots, produced by electron-beam lithography and reactive ion etching, covered a part of the sample between the potential probes. The antidot diameter was  $0.15\text{--}0.2 \text{ }\mu\text{m}$ . The effective diameter,  $a$ , which consists of a lithographic diameter and a depletion length, was  $0.2\text{--}0.3 \text{ }\mu\text{m}$ . Samples in which the array of antidots is disordered with various degrees of disorder were made for the experiments (Fig. 1). The disordering of the lattice was accomplished in the following way. A random number generator determined the shift in the position of the antidots in the direction of the neighboring antidots. The deviations of antidots from their periodic arrangement in the lattice with period  $d = 0.7 \text{ }\mu\text{m}$  at the peak were  $\Delta = 0.0, 0.1, 0.25$ , and  $0.35 \text{ }\mu\text{m}$ . We also measured mesoscopic samples with size  $4 \times 4 \text{ }\mu\text{m}^2$ , average periodicity  $d = 0.6 \text{ }\mu\text{m}$ , and  $\Delta = 0.3 \text{ }\mu\text{m}$ . Thus, the short-range order of the system was violated, but its long-range order was preserved.

The magnetoresistance was measured by the four-terminal method at frequencies of 70–700 Hz in a magnetic field,  $B$ , up to 0.4 T, and at temperatures of 1.7–4.2 K. Electron scattering by the antidot lattice was dominant in our samples, from this the mean free path,  $l$ , at  $B = 0$  was found to be 0.4, 0.17, 0.21, and  $0.4 \text{ }\mu\text{m}$  for samples with different degrees of disorder. We see that the behavior of  $l$  is nonmonotonic with disorder. With an increase of  $\Delta$ , the length  $l$  initially decreases, and increases again. Similar nonmonotonic behavior has been observed recently in samples with a quasiperiodic (Penrose tiling) lattice of antidots [6], which is an intermediate type of

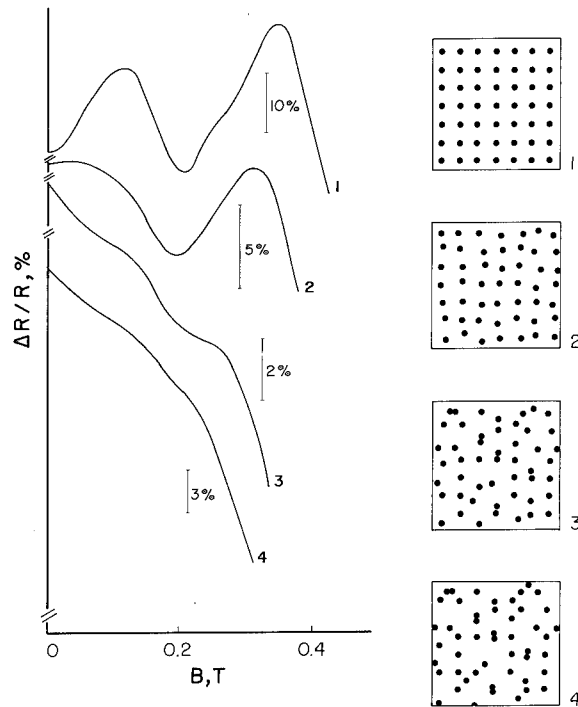


Fig. 1. Magnetoresistance dependence on  $B$  for a sample with different degrees of antidot disorder and for a periodic lattice:  $d = 0.7 \text{ }\mu\text{m}$ : (1)  $\Delta = 0.0$ ; (2)  $\Delta = 0.1$ ; (3)  $\Delta = 0.25$ ; (4)  $\Delta = 0.35 \text{ }\mu\text{m}$ ;  $T = 4.2 \text{ K}$ .

array between periodic and disordered. In this case the length  $l$  initially decreases with increase of the basic triangle size in the Penrose cell, and then increases again. This behavior has not been explained, and further theoretical analysis of the scattering in this system is required.

Fig. 1 shows the magnetoresistance for samples with various degrees of disorder as a function of magnetic field. We see commensurability oscillations for all samples when the cyclotron diameter,  $R_L$ , is comparable to the lattice period. The oscillation amplitude decreases with increase of  $\Delta$ , and the position of the last peak shifts to lower magnetic field [8]. The preservation of long-range order in our sample is responsible for oscillations in the disordered antidot lattice. Fig. 1 shows that for the periodic lattice, the second peak maximum is higher than the peak maximum which lies at lower magnetic field. However, for the array with disorder degree  $\Delta = 0.1 \text{ }\mu\text{m}$  their amplitudes are equal, i.e., negative magnetoresis-

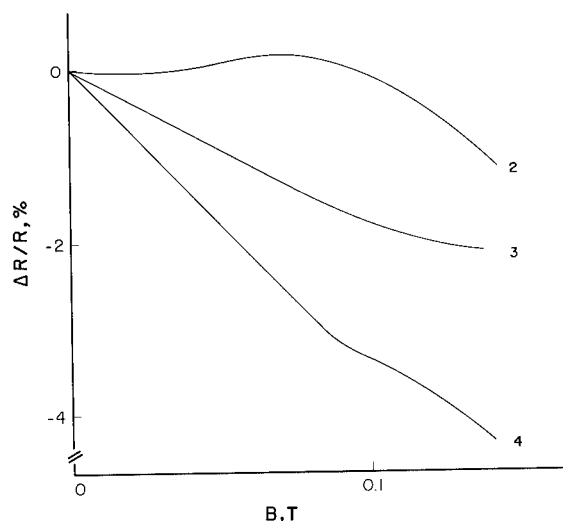


Fig. 2. Magnetoresistance dependence on  $B$  for low magnetic field. (2)  $\Delta = 0.1$ ; (3)  $\Delta = 0.25$ ; (4)  $\Delta = 0.35 \mu\text{m}$ ;  $T = 4.2 \text{ K}$ .

tance (nMR) appears, but it is not visible due to the oscillations. With increase of disorder degree nMR at low  $B$  is observed. Fig. 2 shows the low field part of the nMR for samples with a disordered array of antidots. We see that the magnetoresistance is linear for low magnetic field and

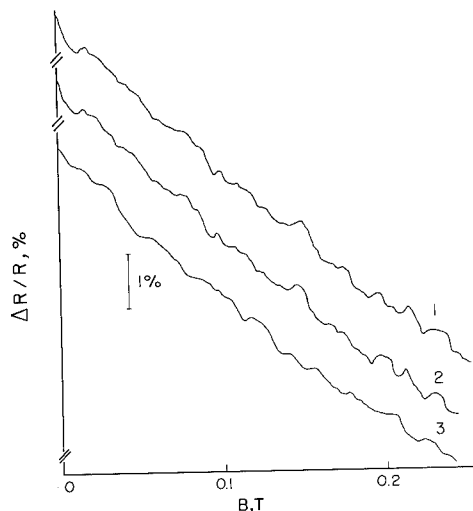


Fig. 3. Magnetoresistance of the mesoscopic samples with disordered lattice of antidots measured after different intervals of time: (1) 0 min, (2) 5 min, (3) 40 min;  $d = 0.6 \mu\text{m}$ ,  $\Delta = 0.3 \mu\text{m}$ ,  $T = 1.7 \text{ K}$ .

increases with increasing disorder. We did not find this magnetoresistance to be temperature dependent at temperatures 1.7–4.2 K, which proves that this nMR has a classical origin. Fig. 3 shows the magnetoresistance of a mesoscopic sample with period  $d = 0.6 \mu\text{m}$  measured after different intervals of time. We also see linear negative magnetoresistance which does not depend on the temperature. Against the background of this magnetoresistance, there are fluctuations. The pattern of these fluctuations as a function of  $B$  is changed in time. We believe, that the fluctuations of magnetoresistance are due to the interference of electron trajectories scattered by the antidot lattice. However, more experiments are necessary in this system. We also believe that linear negative magnetoresistance has the same nature as for macroscopic samples. We should note that we measured all samples before the patterning of antidots and observed no negative magnetoresistance in this region of magnetic field.

For Hall bridge samples  $\rho_{xx} = \sigma_{xx} / (\sigma_{xx}^2 + \sigma_{xy}^2)$ , where  $\rho_{xx}$  is the resistivity, and  $\sigma_{xx}$ ,  $\sigma_{xy}$  are the diagonal and Hall parts of the conductivity.  $\rho_{xx}$  is constant in magnetic field for one group of charge carriers. Thus, the appearance of negative magnetoresistance at low magnetic field is a result of an increase of the total conductivity; however, the coexisting Drude contribution decreases the total conductivity,

$$\sigma_{xx} = \sigma_0 / [1 + (\omega_c \tau)^2],$$

where  $\omega_c$  is the cyclotron frequency,  $\tau$  is the elastic scattering time, and  $\sigma_0$  is the Drude conductivity at zero magnetic field. In our case for weak magnetic field the Drude contribution to conductivity is small, and the observed negative magnetoresistance corresponds to a positive magnetoconductance,  $\Delta\sigma_{xx} > 0$ , although at stronger magnetic field  $\Delta\sigma_{xx} < 0$ . The Drude conductivity and  $\sigma_{xy}$  exactly compensate, and we observe only negative magnetoresistance.

In a one-dimensional lateral superlattice with strongly modulated potential, a positive magnetoresistance has been observed [9,10]. It was analyzed from the classical standpoint and explained

by the formation of open electron orbits, which drift in the crossed external magnetic field and in periodic superlattice electric field. For the periodic antidot lattice, as mentioned above, at low magnetic field commensurability oscillations have been found. With increase of  $B$ , when  $2R_L < d$ , negative magnetoresistance has been observed [3,4]. Increase of electrons scattered by antidots and localization around antidots are responsible for this magnetoresistance. In this case the magnetic field is strong, and  $\rho_{xx} \approx \rho_{xy}$ , where  $\rho_{xy}$  is the Hall resistivity. Thus, because of  $\rho_{xx} \approx \rho_{xy}$ , a decrease in resistivity signifies a decrease in the conductivity, i.e. localization, in contrast to the weak magnetic field case, where  $\rho_{xx} \approx 1/\sigma_{xx}$ .

There are two models which explain commensurability oscillations in an antidot lattice. The first model considers electron orbits which are not scattered by antidots [4]. A portion of these orbits,  $f_p$ , oscillates as a function of magnetic field, but the amplitude of these oscillations are too small to explain conductivity oscillations. In this case Fleischmann et al. [11] calculated the contribution of the chaotic trajectories which lie in the phase volume near the regular pinned orbits. The resultant conductivity is [11]

$$\sigma \approx (1 - f_p) \int dt e^{-t/\tau} \langle v_i(t) v_j(0) \rangle,$$

where  $\langle v_i(t) v_j(0) \rangle$  is the velocity correlation function. Fleischmann et al. have found, that the main contribution to the conductivity is determined by chaotic orbits, which are localized around antidot groups. The other model also considered the electron motion in the antidot lattice from the standpoint of dynamical chaos theory [12]. But in this model stable trajectories which roll along the lattice row have been found. These trajectories, in contrast to localized orbits considered in the first model, increase the total conductivity. However, as in the first model, the contribution of these trajectories to conductivity is not sufficient to explain the oscillation amplitudes. Therefore, nearby chaotic trajectories with the same dynamics should be included in the electron diffusion coefficient calculation. The runaway trajectories contribution to conductance

can be found from the theory for resistance of point contacts [12],

$$\sigma = \frac{2e^2}{h} k_F \frac{d-a}{\pi} \frac{L}{d} \frac{2S}{\pi^2},$$

where  $S$  is the fraction of phase space which is filled by runaway trajectories,  $L$  is the length of the sample, or  $L = l$ , and  $k_F$  is the electron wave vector. The diffusion coefficient for quasi-runaway trajectories was calculated through numerical simulation. Thus, one model analyzes “islands of pinned trajectories” and a nearby sea of chaotic orbits with the same dynamics [11], and the other one considers “islands of runaway trajectories” surrounded by a sea of electron orbits with anomalous diffusion [12]. Agreement of theory with experiment without adjustable parameters has been obtained in Ref. [11]; therefore, the contribution of chaotic orbits to conductivity is dominant. The existence of commensurability oscillations in the disordered antidot lattice (Fig. 1), as indicated above, gives evidence of the stability of pinned electron trajectories when short-range order is violated. The reason can be connected to the fact that the chaotic orbits are localized within several superlattice periods. In mesoscopic samples we observe no commensurability oscillations (Fig. 3). Therefore, more than 4 periods are necessary for these oscillations. In a disordered antidot array some long-range order is preserved, therefore these orbits are not destroyed in contrast to the regular trajectories which are determined by short-range order. It should be noted, that the runaway trajectories considered in model [12] have a diffusion coefficient divergence, since the relation  $\langle x(t) \rangle \geq t$  holds for these electrons. Similar trajectories with anomalous diffusion have been predicted in a superlattice with weak periodic potential [2]. These orbits appear in weak magnetic field. For the antidot array the same situation occurs if  $d/a \gg 1$ ; however, at finite magnetic field the portion of runaway trajectories should oscillate as a function of  $B$ . For the samples investigated in our work, the ratio  $d/a = 3.5$ , and trajectories with anomalous diffusion at low magnetic field are not prevented by shadowing antidots in the next rows. The situation is differ-

ent for a disordered antidot lattice. In this case runaway trajectories could appear not only for commensurability conditions, as in the periodic system, but at any magnetic field. Two reasons are responsible for the existence of anomalous diffusion trajectories, correlation of the electron cyclotron radius, and distance between antidots in any magnetic field because of disorder and accidental absence of shadowing of these orbits. Thus, the negative magnetoresistance observed in the disordered antidot lattice could be due to the existence of trajectories with anomalous diffusion in the magnetic field. Also the probability of appearance of these orbits increases with disorder increase, and growth of the magnetoresistance value is expected, as observed in experiments (Fig. 2). The runaway trajectory is analogous to the edge states in classically strong magnetic field [13]. The conductance of these trajectories can be written in the form

$$\sigma = e^2 N / h,$$

where

$$N \approx k_F R_L / 2;$$

thus  $\sigma \approx B^{-1}$ ; however, conductivity decreases with  $B$ . Recently, linear magnetoresistance in a quantum point contact has been observed, which was negative due to a difference in the value of the edge current inside and Hall current outside of the contact [14]. Our situation is similar, however, the difference between Hall and diagonal components of anomalous currents is not clear.

In summary, the samples with disordered antidot lattice, in contrast to the periodic array, have revealed linear negative magnetoresistance which is temperature independent. Against the magnetoresistance background commensurability oscillations, which are due to chaotic orbit localization, have been found. We believe that the trajectories which roll along rows of the lattice and pinned orbits remain stable when the short-range lattice order is violated. The small ratio  $d/a$  is responsible for this stability. Further antidot lat-

tice experimental work with larger  $d/a$  ratios and theoretical analysis of the transition from order to disorder are required.

This work is supported by CNPq and FAPESP (Brazil).

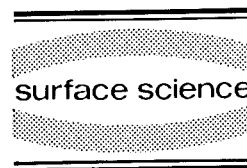
## 1. References

- [1] P. Lee and T.V. Ramakrishnan, *Rev. Mod. Phys.* 57 (1985) 287.
- [2] J. Wagenhuber, T. Geisel, P. Niebauer and G. Obermair, *Phys. Rev. B* 45 (1992) 4372.
- [3] K. Ensslin and P. Petroff, *Phys. Rev. B* 41 (1990) 12307; G.M. Gusev, V.T. Dolgoplov, Z.D. Kvon, A.A. Shashkin, V.M. Kudryashov, L.V. Litvin and Yu.V. Nastaushv, *JETP Lett.* 54 (1991) 364; A. Lorke, J.P. Kotthaus and K. Ploog, *Phys. Rev. B* 44 (1991) 3447.
- [4] D. Weiss, M.L. Roukes, A. Menschig, P. Grambow, K. von Klitzing and G. Weimann, *Phys. Rev. Lett.* 66 (1991) 2790.
- [5] T. Yamashiro, J. Takahara, Y. Takagaki, K. Gamo, S. Namba, S. Takaoka and K. Murase, *Solid State Commun.* 79 (1991) 885.
- [6] G.M. Gusev, P. Basmaji, D.I. Lubyshev, L.V. Litvin, Yu.V. Nastaushv and V.V. Preobragenskii, *Phys. Rev. B* 47 (1993) 9928.
- [7] G.M. Gusev, Z.D. Kvon, L.V. Litvin, Yu.V. Nastaushv, A.K. Kalagin and A.I. Toropov, *JETP Lett.* 56 (1992) 173.
- [8] G.M. Gusev, Z.D. Kvon, L.V. Litvin, Yu.V. Nastaushv, A.K. Kalagin and A.I. Toropov, *Abstracts of the Sixth International Conference on Superlattice and Microstructures*, Sian, People's Republic of China (1992) 198.
- [9] P.H. Beton, E.S. Alves, P.C. Main, L. Eaves, M.W. Dellow, M. Henini, O.H. Hughes, S.P. Beamont and C.D.W. Wilkinson, *Phys. Rev. B* 42 (1990) 9229.
- [10] C.W.J. Beenakker, *Phys. Rev. Lett.* 62 (1989) 2020.
- [11] R. Fleischmann, T. Geisel and R. Ketzmerick, *Phys. Rev. Lett.* 68 (1992) 1367.
- [12] E.M. Baskin, G.M. Gusev, Z.D. Kvon, A.G. Pogosov and M.V. Entin, *JETP Lett.* 55 (1992) 678.
- [13] M. Buttiker, *Phys. Rev. B* 38 (1988) 9375.
- [14] H. van Houten, C.W.J. Beenakker, P.H. Loosdrecht, T.J. Thornton, H. Ahmed, M. Pepper, C.T. Foxon and J.J. Harris, *Phys. Rev. B* 37 (1988) 8534.



ELSEVIER

Surface Science 305 (1994) 448–452



## Anti-collimation of ballistic electrons by a potential barrier

P.T. Coleridge <sup>\*</sup>, R.P. Taylor <sup>1</sup>, A.S. Sachrajda, J.A. Adams <sup>2</sup>

*Institute for Microstructural Science National Research Council, Ottawa, Ontario, K1A 0R6, Canada*

(Received 19 April 1993; accepted for publication 4 June 1993)

### Abstract

A pair of Quantum Point Contacts separated by a continuous barrier have been fabricated using the surface gate technique. Transport measurements for each component of this system and for various combinations have shown both additive and non-additive behaviour. The results are explained by a combination of reflection by the barrier of electrons collimated by the Quantum Point Contacts and transport by diffusion across the barrier.

When ballistic electrons in a 2D electron gas (2DEG) are controlled by surface gates two well-established phenomena are the collimation of electrons leaving a Quantum Point Contact (QPC) and the refraction of electrons under partially depleted gates [1]. We have investigated a structure involving two QPCs separated by a continuous gate to study the interaction between these two effects. The structures were fabricated on two sets of 2DEG material with densities (after illumination) of about  $3.6 \times 10^{11}/\text{cm}^2$ . The mobilities for the two samples were approximately  $0.45$  and  $0.39 \times 10^6 \text{ cm}^2/\text{V} \cdot \text{s}$ , significantly lower than values measured in bulk material before fabrication. Surface gates, of evaporated Ti/Pt, were defined using e-beam lithography in PMMA with the dimensions shown in Fig. 1. Four termi-

nal resistance measurements were made at 1.2 K, across the gated region of the Hall Bar, using low-frequency AC techniques with typical measuring currents of 200 nA. It was generally observed that the quantised steps were not as well defined as in similar devices without a central gate and for the central gate the steps (measured in a magnetic field) appeared at resistance values that were typically 20 to 50% too low. Measurements were made after the sample had been illuminated. This implies electron densities underneath the gates that are smaller than in the

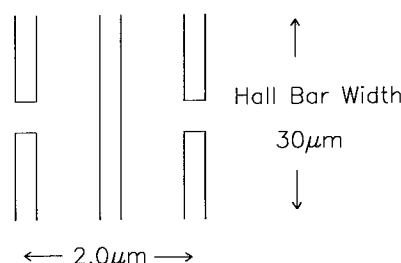


Fig. 1. Lithographic dimensions of the gates used to define the two QPCs and continuous centre gate.

<sup>\*</sup> Corresponding author.

<sup>1</sup> Present address: University of New South Wales, P.O. Box 1, Kensington, NSW 2033, Australia.

<sup>2</sup> Present address: Nottingham University, Nottingham NG7 2RD, UK.

bulk. It was found that applying modest positive voltages to nominally unactivated gates had the effect of improving the homogeneity (as indicated by the low-field Shubnikov–de Haas oscillations) and also tended to improve the quality of conductance steps for other (activated) gates.

Figure 2 shows the four-terminal resistance of the device with a small positive voltage on the central gate. Each QPC separately shows the characteristic negative magnetoresistance associated with magnetic depopulation of the Landau levels in the bulk 2DEG. With both QPCs formed the high-field magnetoresistance (above about 0.15 tesla) is just the sum of the effects of the separate QPCs (with the appropriate correction for double counting of the bulk contribution) but at the lower fields there is a dip and small central peak. The dip is attributed to the well-known effect [2,3] of collimated electrons propagating ballistically through both QPCs. The extra peak is a new effect although hints of such a peak can sometimes be seen in other published data [4]. The exact size and shape of this small peak was not highly reproducible and seemed to depend on the history of voltages applied to the various gates.

Figure 3 shows the effect of applying negative voltages to the central gate. Initially the dip attributed to collimation and the extra peak are

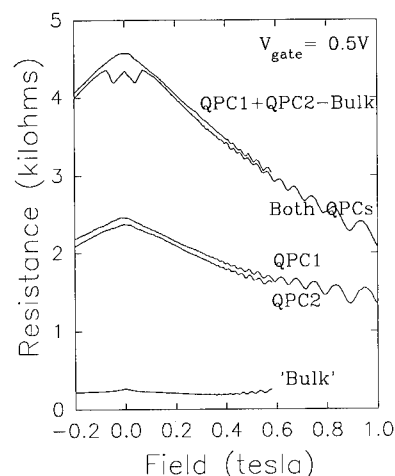


Fig. 2. Magnetoresistance curves in the first sample without a barrier between the two QPCs.

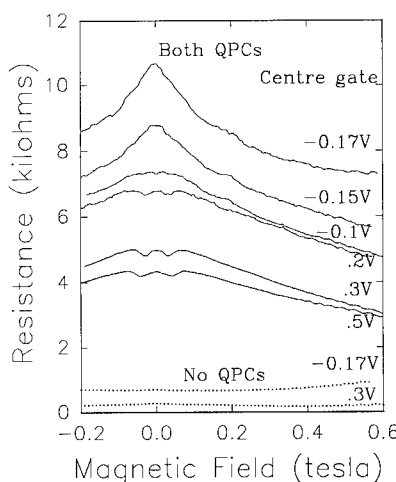


Fig. 3. Effect of activating the centre gate in the first sample with (solid curves) and without (dotted curves) the QPCs formed.

suppressed followed by a general rise in resistance of the device and then the evolution of a larger and wider central peak. The most negative voltage shown ( $-0.17$  V) corresponds to an electron density underneath the central gate about 20% of the bulk value. At low magnetic fields the resistance due to the centre gate is highly non-additive. For example the extra resistance of the gate by itself is about 50 ohms but with the QPCs formed it adds a resistance of about 4000 ohms. In the second sample (see Fig. 4) the dip due to collimation, which should appear with a positive voltage on the centre gate, and the associated small peak, are much less well-defined. With the central gate activated the general rise in resistance is also less pronounced but the broad peak appears very clearly. In both samples the broad peak appears with either or both QPCs activated and in the second sample there is little evidence of any interaction between the two QPCs. In this case the resistances of the QPCs (with the centre gate activated but held constant) are additive. This is illustrated explicitly in Fig. 4 where the dotted curves, which show the sum of the magnetoresistances of the first QPC with the centre gate and the second QPC with the centre gate, are in good agreement with the total resistance for both QPCs.

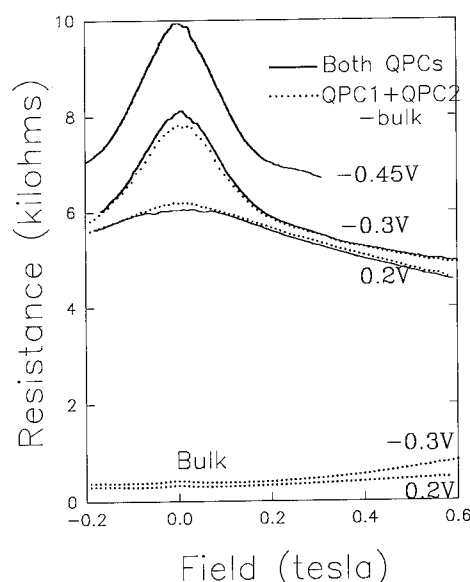


Fig. 4. Magnetoresistance curves for sample 2. Dotted curves show the sum of the resistances for each QPC separately.

The most important features of these results are: (1) the general increase in resistance which seems to vary from sample to sample; (2) the broad peak which always appears when the central barrier is well established and (3) the small 'blip' which seems to be associated in some way with ballistic propagation through the two QPCs, which is not always well defined, and which is suppressed by activation of the centre gate.

For a single QPC the negative magnetoresistance is, within the Landauer–Büttiker formalism [5], given by the number of occupied subbands in the QPC ( $N_{\text{QPC}}$ ) and in the bulk ( $N_{\text{bulk}}$ ) [3]. For moderate magnetic fields  $N_{\text{QPC}}$  is independent of field and  $N_{\text{bulk}}$  is the number of Landau levels so the four-terminal longitudinal resistance of a QPC,  $(h/2e^2)(1/N_{\text{QPC}} - 1/N_{\text{bulk}})$ , has a negative slope equal to the Hall slope. If the total resistance for two QPCs is just the sum of two terms of this form then this implies complete suppression of any ballistic transport between the QPCs as is, indeed, observed experimentally under some conditions (cf Fig. 2). For a continuous gate there is a slightly different behaviour. For fields above about 0.25 tesla, when the cyclotron diameter is less than the width of the gate, the 2DEG be-

neath the gate will behave like 'bulk' material of reduced density with the number of Landau levels,  $N_{\text{gate}}$ , smaller than  $N_{\text{bulk}}$ . The appropriate term  $(h/2e^2)(1/N_{\text{gate}} - 1/N_{\text{bulk}})$  will then give rise to a positive magnetoresistance. In practice this may be suppressed by parasitic conduction across the gate. At lower fields, when the cyclotron diameter is larger than the gate width, the resistance will increase with increasing barrier height with a complicated magnetic field dependence. Experience with broad isolated gates suggests that it starts approximately independent of field followed by the transition to the linear, high-field slope [6,7]. The behaviour seen in Fig. 3 is generally consistent with this picture. In the second sample (Fig. 4) the overall background rise in resistance appears only for the most negative voltages on the centre gate. With  $-0.3$  V on the centre gate the measured resistance for both QPCs is quite accurately given by the sum of the separate contributions from each QPC. In this case it seems that strong scattering within the gate region produces almost complete equilibration between the two reservoirs, shown schematically in Fig. 5 as  $\mu_1$  and  $\mu_2$ , between the QPCs and the centre barrier. By contrast in the first sample the background rise is nonadditive implying the persistences of some form of coherent transport across the centre gate which, in this sample at least, is not suppressed by a magnetic field.

The broad central peak, which appears when the barrier is formed, is the most robust feature in the data. In both samples the contributions from the separate QPCs are additive, i.e.

$$R(\text{QPC1} + \text{Barrier}) + R(\text{QPC2} + \text{Barrier}) \\ = R(\text{QPC1} + \text{QPC2} + \text{Barrier})$$

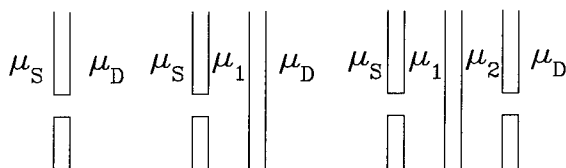


Fig. 5. Schematic representation of reservoirs with different gate configurations.

but the effect of the central barrier on one or both of the QPCs is highly nonadditive:

$$R(\text{QPC1} + \text{Barrier}) > R(\text{QPC1}) + R(\text{Barrier}).$$

The peak appears when the density of electrons under the centre gate is of order 50% or less of that in the bulk, i.e. when the barrier is large and provides a significant probability of reflection. It is attributed to ballistic reflection of electrons, by the barrier, back through the QPC producing a nonadditive increase in the resistance. Application of a magnetic field deflects the back-reflected electrons away from the QPC and suppresses the resistance increase. This is the converse of the situation for two QPCs alone where deflection of the collimated beam by a magnetic field reduces the transmission and increases the resistance. The width of the peak should be given by the magnetic field at which the cyclotron radius is equal to the spacing between the QPC and the centre gate. When allowance is made for depletion this is approximately 0.65  $\mu\text{m}$ , corresponding to a field of about 0.14 tesla, which is in good agreement with the experimentally observed width. The additivity of the contributions from two QPCs follows naturally from this explanation. With the barrier in place there is strong equilibration within each of two reservoirs  $\mu_1$  and  $\mu_2$  (see Fig. 5) and suppression of ballistic propagation through both QPCs. This suppression is made complete by magnetic fields strong enough that the electrons are confined to skipping orbits along the edges of the gates defining the QPCs.

The smaller, central, 'blip' is less well-understood. It is tentatively attributed to an interplay between diffusive and ballistic transport. Although most obvious under conditions of collimated ballistic transport through two QPCs a similar blip, with the same width but smaller amplitude, can also be seen in the 'bulk' term (Fig. 2). Extensive measurements [7] have established that it is a property of a bulk 2DEG and appears even in Hall bars with no gates provided there is some inhomogeneity in the system. Inhomogeneity is always likely to be present in gated samples that have been illuminated because of shadowing by the surface gates. In an inhomoge-

neous sample the current distribution in the low field regime, i.e.  $\mu B \ll 1$  (where  $\mu$  is the mobility), will be determined by the path of maximum conductivity. In the high-field regime ( $\mu B \gg 1$ ), by contrast, the current associated with the Hall term ( $\sigma_{xy}$ ) dominates and the current path will be determined by a local Hall resistance, i.e. by density variations. The blip is associated with the change in current distribution that accompanies the transition from low field to high field which occurs when  $\mu B \approx 1$ . Experiments in several samples and as a function of illumination, confirm that the width of the blip is, indeed, given by this expression. Furthermore, the width is found to be insensitive to temperature up to about 7 K, i.e. over the temperature range for which  $\mu$  does not change. This insensitivity to temperature also eliminates weak localisation as the origin of the blip.

If the blip is attributed to the low-field/high-field transition in the presence of inhomogeneities it is still necessary to explain why it is so amplified in the QPC/barrier/QPC structure. Within the Landauer–Büttiker formalism ballistic transport through a QPC is described in terms of a set of transmission and reflection coefficients connecting reservoirs in which equilibration occurs. The reservoirs are usually identified with the contacts and diffusive transport in the bulk 2DEG connecting the QPC to the contacts is ignored. More generally, and particularly in the low-field regime, the reservoirs might better be identified with regions of bulk 2DEG material, of order a few mean free paths from the QPC, within which the energy of the electrons is equilibrated by diffusive transport.

In zero magnetic field the extra resistance produced by a continuous gate can be described purely in terms of classical diffusive transport. For the samples considered here this resistance is typically 50 ohms and the resistivity of the bulk 2DEG is  $\sim 50$  ohms/ $\square$  so the spatial extent of the perturbation produced by the gate is of order the width of the Hall bar (30  $\mu\text{m}$ ). If the reservoirs determining ballistic transport through a QPC are the regions of 2DEG several mean free paths away, say 10 or 20  $\mu\text{m}$ , then the introduction, as close as 1  $\mu\text{m}$  to the QPC, of a large



perturbation in the current distribution of the bulk 2DEG would be expected to significantly change the effective chemical potential of the reservoirs and the way they couple to the QPC. The transition from low field to high field will similarly affect ballistic transport through the QPCs and this is reflected in an amplified version of the blip.

Generally the two samples behave somewhat differently at low magnetic fields. In the second sample not only was collimation between the two QPCs difficult to observe but also the continuous gate seemed more efficient at producing additive behaviour. This is attributed to inhomogeneities associated within the gates of the second sample resulting in predominantly random scattering rather than coherent refraction under the continuous gate. This is likely the result of differences in the fabrication process (the gate sensitivities were somewhat different in the two cases) and, in this context, it is interesting to note that though the second sample started with material having a higher mobility it actually ended up, after processing, with a lower mobility.

In summary, experiments on a system of two QPCs separated by a continuous gate have shown

simultaneously ballistic backscattering by the barrier and diffusive transport across the barrier. To explain some of the results it is assumed, in the low-field regime, that the reservoirs involved in ballistic transport through the QPCs are situated not in the contacts but in the bulk 2DEG, and that they are affected by inhomogeneities in the system.

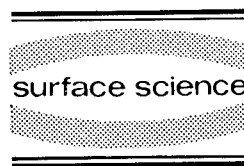
## 1. References

- [1] For a review see, e.g., C.W.J. Beenakker and H. van Houten, *Solid State Physics*, Vol. 44, Eds. H. Ehrenreich and D. Turnbull (Academic Press, New York, 1991).
- [2] D.A. Wharam, M. Pepper, H. Ahmed, J.E.F. Frost, D.G. Hasko, D.C. Peacock, D.A. Ritchie and G.A.C. Jones, *J. Phys. C* 21 (1988) L887.
- [3] C.W.J. Beenakker and H. van Houten, *Phys. Rev. B* 39 (1989) 10445.
- [4] See, e.g., P.C. Main, B.R. Davidson, P.H. Beton, L. Eaves, J.R. Owers-Bradley, A.J.M. Neves, S.P. Beaumont and C.D.W. Wilkinson, *J. Phys.: Condens. Matter* 2 (1990) 6541.
- [5] R. Landauer, *IBM J. Res. Dev.* 1 (1957) 223; 32 (1988) 306; M. Büttiker, *Phys. Rev. Lett.* 57 (1986) 1761.
- [6] R.J. Haug, J. Kukera, P. Streda and K. von Klitzing, *Phys. Rev. B* 39 (1989) 10892.
- [7] P.T. Coleridge, unpublished.



ELSEVIER

Surface Science 305 (1994) 453–459



## Charge oscillations in edge states and double-frequency Aharonov–Bohm effects around a tunable obstacle

P.J. Simpson <sup>\*</sup>, C.J.B. Ford, D.R. Mace, I. Zailer, M. Yosefin, M. Pepper <sup>1</sup>,  
J.T. Nicholls, D.A. Ritchie, J.E.F. Frost, M.P. Grimshaw, G.A.C. Jones

*Cavendish Laboratory, Madingley Road, Cambridge CB3 0HE, UK*

(Received 19 April 1993; accepted for publication 20 May 1993)

### Abstract

We have observed a new phenomenon of charge oscillations in small isolated edge states in the quantum Hall regime. We have developed a unique method of contacting an isolated metal dot independently of the other gates, using a patterned layer of insulator. Using this technique we have made two individually tunable ballistic channels in parallel. In a perpendicular magnetic field edge states form a ring around the dot, with a variable constriction on either side across which they can communicate. Electrons orbiting around the ring interfere with themselves, and a series of single particle (SP) states forms. By fine-tuning the individual constriction widths we can generate huge Aharonov–Bohm (AB) oscillations, and extremely well defined oscillations. In addition, in certain field ranges, we observe a very clear double AB frequency, at times completely losing a distinguishable fundamental frequency. We propose that the discreteness of the SP states gives rise to a charging effect, which modifies the tunnelling of the outermost edge state through the device, and also acts to evenly intersperse the energy levels of all the edge states encircling the dot.

The technique of using electron-beam lithography to pattern sub-micron metal Schottky gates on the surface of a GaAs–AlGaAs heterostructure, containing a high-mobility two-dimensional electron gas (2DEG), has become widely used since its conception in 1986 [1]. By applying a negative bias to the gates, the 2DEG beneath is depopulated, and so may be confined to a variety of patterns. Using a dot gate connected to the surrounding metallisation by a metal bridge over

an insulating layer, both Aharonov–Bohm rings [2], and two ballistic channels in parallel [3] have been fabricated. A later etching technique introduced an independent, but uncontrollable, dot [4].

In this new work, we have used a layer of insulator to separate a second metallisation layer contacting a dot gate from the surrounding pattern. We have reproduced the early design of three Schottky gates defining two ballistic channels in parallel, see inset Fig. 1, but with independent control over all three gates. The materials used had mobilities between 100 and 200  $\text{m}^2/\text{V}\cdot\text{s}$ , and carrier concentrations between 2 and  $4 \times 10^{15} \text{ m}^{-2}$ . The experiments were per-

<sup>\*</sup> Corresponding author. Fax: +44 (223) 337271.

<sup>1</sup> Also at: Toshiba Cambridge Research Centre, 260 Cambridge Science Park Cambridge, Cambridge CB4 4WE, UK.

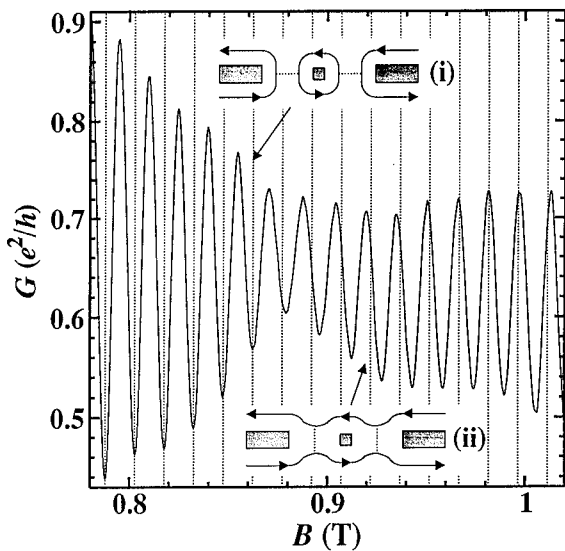


Fig. 1. A phase change in the Aharonov–Bohm oscillations that occurs when an edge state that is mostly transmitted (upper inset) becomes mostly reflected (lower inset).

formed on a dilution refrigerator at temperatures  $< 100$  mK, using standard phase-sensitive measurements at voltages sufficiently low to avoid electron heating. Either the two-terminal conductance or the four-terminal resistance was measured. In the first case a small magnetic field dependent correction for the series resistance was later subtracted; in the second case the Hall resistance measured close to the device was subsequently added. Both methods allow the true number of edge states propagating through the device to be determined.

In a perpendicular magnetic field greater than about 0.2 T, electrons in the 2DEG condense into Landau levels. Current is carried in a set of parallel edge states around the sides of the Hall bar, as the electrons become confined to the edges of the sample by the Lorentz force. If the Fermi energy  $E_F$  lies between Landau levels, there is no electron scattering across the sample, and no voltage drop along an edge. By placing a semi-transparent barrier across the Hall bar, edge states can be reflected to the opposite side, giving resistance plateaux-like the quantised Hall plateaux.

In our case, the encircling edge states form a ring around the dot, with a path length so small (a few microns) that it is less than the phase coherence length at the temperatures used in the experiment. The phase accumulated around the ring depends not only on the path length, but also on an additional contribution from the Aharonov–Bohm (AB) effect. Each time the flux enclosed by the ring changes by one flux quantum,  $h/e$ , there is a change in phase around the ring of  $2\pi$ . Hence there is a set of allowed SP states, each corresponding to a phase change of an integer multiple of  $2\pi$  around the ring. These states all lie within Landau levels, which rise in energy as they approach the edge of the depletion region formed by the dot. Hence states enclosing less area have higher energy, and thus shorter wavelengths. For a given applied field, the difference in radii between consecutive SP states is dependent on the amount of flux enclosed, the path length, and the wavelength.

A given edge state can be either mostly transmitted, or mostly reflected from the constrictions formed (see insets, Fig. 1, where the lines indicate the possible paths of the edge states). This influences the phase of the AB oscillations. If an edge state is mostly transmitted (Fig. 1i) with backscattering arising from tunnelling across the constrictions, then the degree of scattering across the device will increase when there is an SP state around the dot. Thus the device resistance increases. If an edge state is mostly reflected (Fig. 1ii) then an allowed SP state around the ring corresponds to an increase in transmission of that edge state through the constrictions, and causes a decrease in resistance. Therefore when an edge state responsible for AB becomes more reflected than transmitted, a phase change of  $\pi$  occurs in the oscillations. Fig. 1 shows a region in which such a phase change is observed. We have also seen phase changes of  $\pi$  in the space of a single oscillation. Perfect symmetry between the channels is not necessary for this to occur, since it is always the wider constriction which controls the backscattering. The period of the oscillation is approximately 15 mT, which corresponds to adding  $h/e$  of flux to a ring of radius  $0.3 \mu\text{m}$ , which implies a depletion width of  $0.15 \mu\text{m}$ .

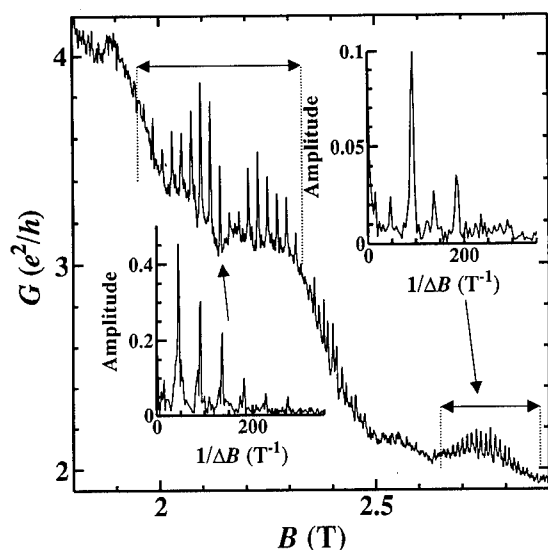


Fig. 2. An example of spiked Aharonov–Bohm oscillations. Around  $B = 2.2$  T, the ordinary single frequency oscillations are seen; the inset shows the Fourier transform of the data. The six peaks indicate that electrons make several orbits around the dot before phase coherence is lost. Spiked double frequency is seen above 2.6 T.

around a dot of lithographic radius  $0.15 \mu\text{m}$ . The lithographic constriction width between the dot and each arm is  $0.45 \mu\text{m}$ .

If an electron orbits around the ring more than once, then it will enclose additional flux in pro-

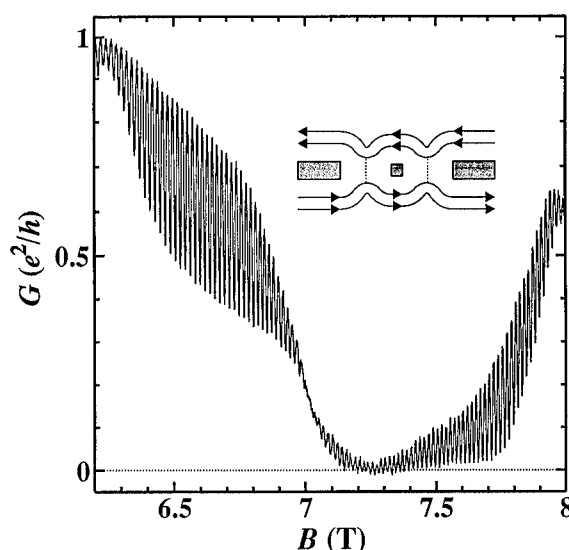


Fig. 3. Aharonov–Bohm oscillations close to pinch-off. Very fine tuning of the device was required to obtain these large oscillations; the peak to valley ratio can be in excess of 20:1.

portion to the number of orbits. For instance, an electron orbiting twice will give rise to an oscillation in resistance with a frequency twice that of the fundamental. We have observed very spiked AB oscillations (Fig. 2), corresponding to very well defined energy levels, as the electron orbits up to six times (or more) around the ring, as

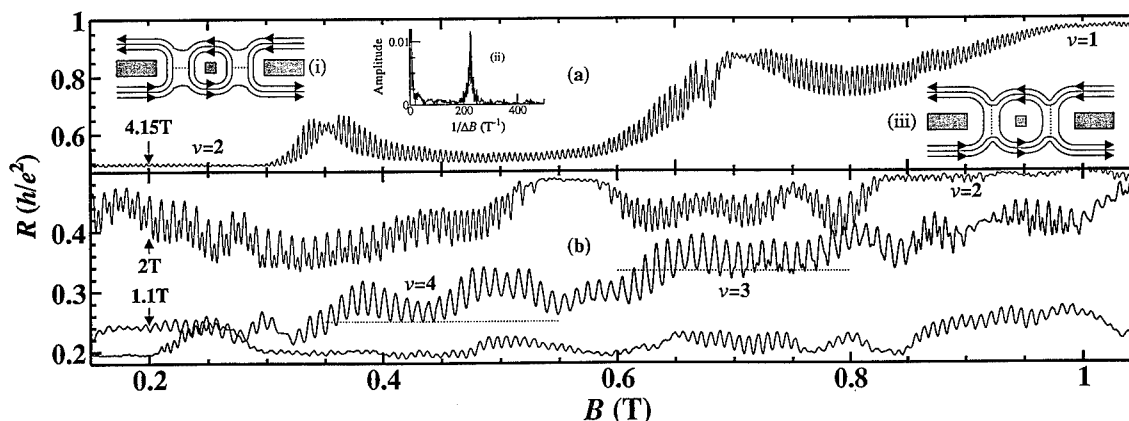


Fig. 4. A field sweep at constant gate voltage from 0.15 to 5 T. The sweep has been divided into four parts for clarity, and the section between 2.85 and 4.1 T omitted. The number of edge states,  $\nu$ , transmitted through the device is as labelled. Insets (i) and (iii) show the behaviour of the edge states schematically. Inset (ii) is a Fourier transform of the data of Fig. 4a. This device has a larger ring than that of Fig. 2.

shown in the Fourier transform (lower inset, Fig. 2). It is interesting to note that the spiked data is obtained when an edge state is mostly reflected. This is exactly contrary to what we might expect from the requirement for a well-defined ring. In principle a given edge state can oscillate between being fully transmitted and fully reflected according to the degree of interference around the ring. Consequently the largest AB oscillations occur as we reflect the final edge state. We have seen totally reflected edge states become up to a third transmitted (Fig. 3), and almost fully transmitted edge states become up to half reflected (Fig. 1). These large oscillations depend on the existence of a high degree of symmetry between the channels.

Below 0.2 T edge states are not defined, and oscillations are not observed (Fig. 4b, lowest curve). As the field increases and Landau levels form, we observe the usual  $h/e$  oscillations (lowest curve). In this particular example, these continue uninterrupted until at around 1.65 T a second oscillation briefly appears, interspersed between the first-harmonic peaks. The phase relation between the second oscillation and the fundamental changes as the field increases. As the third edge state is increasingly reflected, the

amplitude of the second oscillation grows and becomes comparable to that of the fundamental. Now the second oscillation remains precisely  $\pi$  out of phase from the fundamental. As the second edge state is reflected (Fig. 4a) the second oscillation can become indistinguishable from the fundamental, and so a pure double frequency is observed. The Fourier transform of such double frequency oscillations (Fig. 4a<sub>ii</sub>) shows no other discernible frequency. Comparison with the spiked AB oscillations of Fig. 2 shows that this is therefore not the effect of an electron orbiting twice around the ring.

We have seen this effect in all the devices that we have measured (over 10), in which the dots ranged in size from 0.1 to 0.3  $\mu\text{m}$ . The effect is quite tolerant of a large amount of asymmetry between the channels. It does not seem to depend on whether the propagating edge states are spin-split, but it does seem necessary for the number of edge states in the constrictions to be less than four. Conversely, when there are more than two edge states in the channels, for instance the upper curve in Fig. 4b, no corresponding higher frequencies are seen. When the temperature is increased, the two sets of oscillations smear out at the same rate. Squeezing one con-

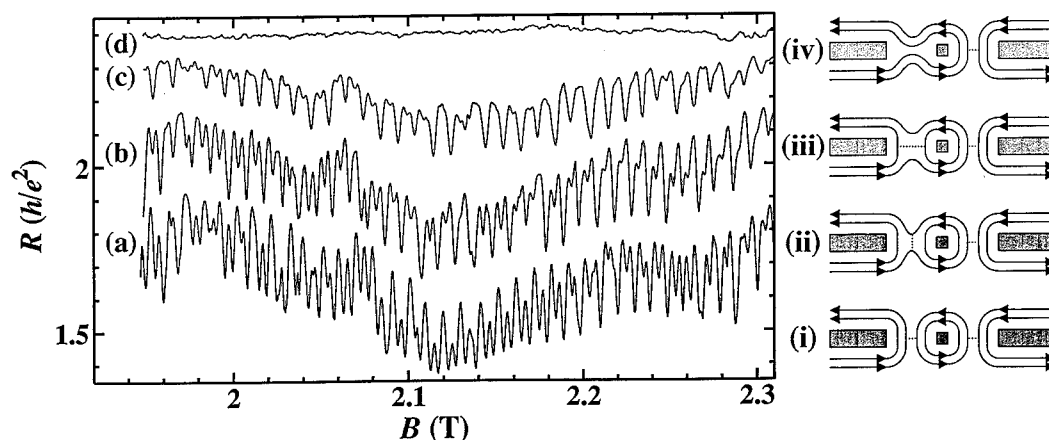


Fig. 5. Double frequency Aharonov–Bohm oscillations. Curve (a) shows the oscillations when the device is well-balanced, i.e. when the two constrictions are of similar width. For subsequent curves, the width of one constriction is reduced by increasing the bias on one arm. In curve (c), the amplitude of the second frequency is diminished. Nevertheless, both oscillations disappear completely at the same gate bias (d). Curves (b), (c) and (d) are vertically offset by 0.25, 0.4 and 0.44  $h/e^2$  respectively for clarity. (i)–(iv) show the behaviour of the edge states schematically.

striction does not eliminate the second oscillation before AB oscillations are destroyed altogether (Fig. 5).

We propose an explanation of these results based on the idea of edge state charging. In recent years Coulomb blockade (CB) has become a frequently observed phenomenon in semiconductor systems in which a 2DEG is confined to a cavity [5]. For a cavity containing a limited number of electrons, tunnelling into the cavity only occurs when there is no change in the charging energy  $q^2/C$  of the cavity (where  $q$  is the net charge of the cavity and  $C$  is the capacitance between the cavity and the rest of the system), i.e., tunnelling is blocked unless the net charge within the cavity can change from  $-e/2$  to  $e/2$ . CB oscillations in a cavity have been observed when the conductance is in excess of  $e^2/h$  [6]. In our case we have an isolated ring, and not a cavity. Isolation arises when the Fermi energy lies within the energy gap between Landau levels, as opposed to the confinement induced by a Schottky gate. It is then the discreteness of the SP states that allows charging. If the field is increased, the area of a state containing a given number of flux quanta  $h/e$  will decrease, and all the states will move inwards. A net negative charge will then build up within the edge state until it reaches  $-e/2$ . Then in an identical manner to conventional CB, an electron may leave the highest occupied orbit with no energy cost, and the net charge becomes  $e/2$ .

Normally we cannot detect the ladders of SP states formed in the inner edge states encircling the dot, as tunnelling is suppressed by the exponential decay of the wavefunctions away from the edge. Other work has shown that depopulation of inner edge states within a cavity can be detected by observing the modulation of CB oscillations in a magnetic field [7]. The double frequency might be explained if charging associated with the inner SP states influences the transmission coefficients of the outermost edge state. Charging of an inner edge state alters the local potential landscape, changing the amount of overlap, and therefore scattering, between states in the outermost edge state on opposite sides of the channels. Thus what appears as a double frequency arises from

two sets of  $h/e$  oscillations,  $\pi$  out of phase due to a Coulombic repulsion between the levels. It has been shown [8] that in a system exhibiting both CB and AB oscillations, the two effects are commensurate.

Examination of Fig. 4a shows that a double frequency persists even when there is only one fully-transmitted edge state through the constrictions, with the second almost fully reflected. It is difficult to picture how an extended state can be considered to charge, but a clue is provided by the spiked AB (Fig. 2). This shows that an extremely well-defined SP state (and therefore charging) is actually always formed by the transmission of an otherwise totally reflected edge state. The fact that the squeezing of one channel does not kill the second frequency (Fig. 5) can also be explained by considering the spiked AB. As one channel is narrowed, the outermost edge state becomes reflected from that constriction (Fig. 5ii). However, it can still tunnel across and therefore form a ladder of SP states. Pinching the constriction still further starts to reflect the inner edge state, at which point the outer most one ceases to form a ring (Fig. 5iii). Thus only the AB in the inner state is left, and it can only be felt through its effect on the outer edge state, which is itself no longer charging, and therefore less sensitive. Thus virtually no single oscillations from the innermost edge state are seen before it no longer forms a ring. Eventually, neither state is transmitted through the constriction, and AB oscillations cease (Fig. 5iv and d).

Notable is the indistinguishability of the conventional and charging AB, of which Fig. 4a is an extreme example. This may be due to the limitation of the amplitude of the oscillations by the tunnelling probabilities through each constriction rather than only due to the interference around the ring [9]. We do not know why no third oscillation is seen when there are clearly three edge states forming rings around the dot (upper curve, Fig. 4b).

We have applied a bias between source and drain to determine the energy level spacing. The bias populates edge states on one edge up to a chemical potential  $\mu_L$  which is higher than that on the far edge,  $\mu_R$ . At the constrictions, there

are therefore empty states in the loop into which tunnelling may occur. We use a small AC voltage on top of the DC voltage and measure the AC current, yielding  $dG/dV_{DC}$ . Due to the series resistance on each side of the device, both  $\mu_L$  and  $\mu_R$  are modulated by the AC, and hence we pick up simultaneously the density of states at both potentials. We see a peak in conductance when an SP state lines up with  $\mu_L$  or  $\mu_R$ . As the DC bias is incremented, each peak splits, giving us a calibration of the level spacing with field (Fig. 6). When peaks an  $h/e$  period apart cross, the DC bias is equivalent to the energy spacing between states. Thus, allowing for about 10% of the DC bias being dropped in the series resistance, the splitting is  $\sim 190 \mu\text{eV}$  at 1.7 T.

If we assume a parabolic potential well in the constrictions, of width  $0.1 \mu\text{m}$  at  $E_F \sim 2\hbar\omega_c \sim 14 \text{ meV}$  and at  $B = 1.7 \text{ T}$ , then the slope of the potential is  $\sim 560 \mu\text{eV/nm}$  at  $E_F$ . The difference in radius  $r$  of consecutive SP states is  $\delta r \sim h/(2\pi e r B) \sim 0.54 \text{ nm}$  at a radius of  $0.35 \mu\text{m}$ . Thus their energy separation is  $\sim dE/dr \delta r \sim 300 \mu\text{eV}$ . This approximation is in rough agreement with the measured value quoted above. At

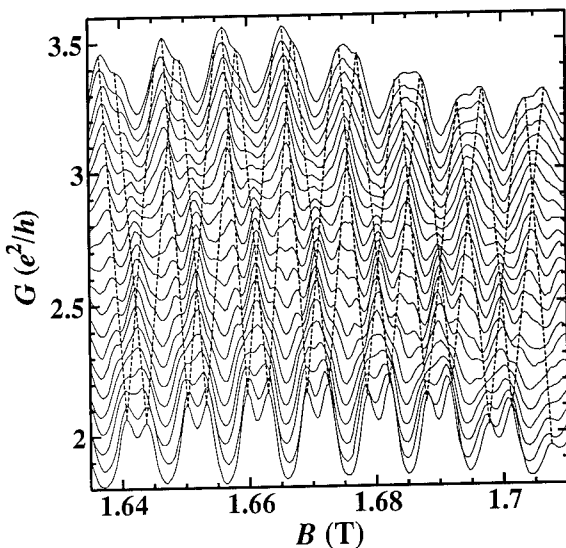


Fig. 6. The Aharonov–Bohm oscillations as a function of DC bias applied between source and drain. The lowest curve is for zero DC bias, the DC bias is incremented by  $10 \mu\text{V}$  between each curve, that for the top curve is  $210 \mu\text{V}$ . Each peak splits into two; the dashed lines are a guide to the eye.

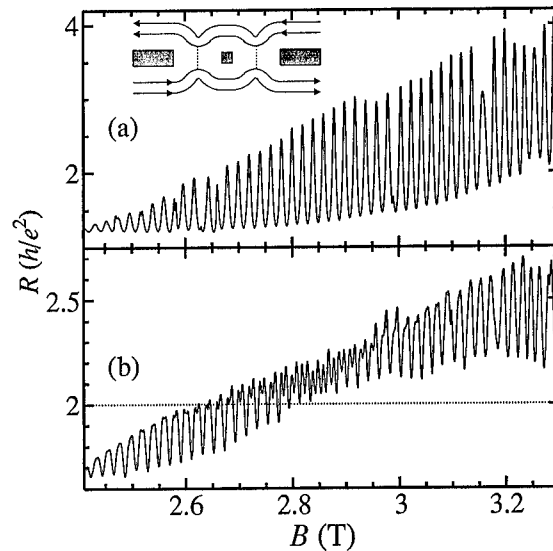


Fig. 7. (a) Large Aharonov–Bohm oscillations as the last edge state is reflected from the constrictions. (b) The same oscillations as a constant DC current is applied between source and drain. The current corresponds to a voltage bias of about  $60 \mu\text{V}$ .

$B = 3.3 \text{ T}$ , the shift is harder to determine, but it seems to be less by about a factor of two, as expected from the above formulae.

If we now apply a DC current or voltage bias to the device where only one edge state is transmitted, an interesting phenomenon occurs (Fig. 7): extra dips appear in the  $h/e$  oscillations. These correspond to a second set of oscillations which is  $\pi$  out of phase with the original set. These rapidly take over, and the original set fades away.

This phenomenon resembles the peak splitting which occurs under DC bias at lower fields (Fig. 6). In the latter case, however, the splitting is gradual. The two phenomena are therefore not necessarily related. At present we do not have an explanation for the effect. It occurs for both positive and negative biases although it is more marked for one bias direction. It occurs at currents of around  $1.5\text{--}2.5 \text{ nA}$ , which corresponds to a voltage of about  $60 \mu\text{V}$ . (The AC current superimposed is  $0.1 \text{ nA}$ .) Above and below these currents, the oscillations appear normal (with a sin-

gle-frequency) and the amplitude becomes small by the time the current reaches 5 nA.

In conclusion a new fabrication technique has given us unprecedented control over an isolated dot, allowing fine tuning of the constriction widths that control the tunnelling across the device. We have seen exceptionally well-defined, and extremely large, Aharonov–Bohm oscillations. When between one and four edge states propagate through the constrictions, a second oscillation is observed, precisely interspersed with the first. This we attribute to edge state charging, arising from the discreteness of the SP states. The effect of this is to modify the transmission of the outermost edge state through the constrictions as the potential landscape is changed, and hence the detection of the SP states in the inner edge states is possible. This model fits the observed effects of squeezing one channel, the charging of an apparently extended edge state, and the similarity between conventional Aharonov–Bohm oscillations and those arising from the electrostatic influence of charging. Applying a DC bias has allowed the measurement of the energy level spacing with field.

We would like to thank Dr. D. Khmelnitskii for helpful discussions. This work was partly

funded by SERC and the ESPRIT Basic Research Action project number 6536. D.A.R. acknowledges the support of Toshiba Cambridge Research Centre Ltd.

## 1. References

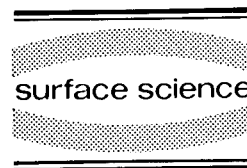
- [1] T.J. Thornton, M. Pepper, H. Ahmed, D. Andrews and G.J. Davies, *Phys. Rev. Lett.* 56 (1986) 1198.
- [2] C.J.B. Ford, T.J. Thornton, R. Newbury, M. Pepper, H. Ahmed, G.J. Davies and D. Andrews, *Superlatt. Microstruct.* 4 (1988) 541.
- [3] C.G. Smith, M. Pepper, R. Newbury, H. Ahmed, D.G. Hasko, D.C. Peacock, J.E.F. Frost, D.A. Ritchie, G.A.C. Jones and G. Hill, *J. Phys.: Condens. Matter* 1 (1989) 6763–6770.
- [4] J.A. Simmons, S.W. Hwang, D.C. Tsui and M. Shayegan, *Superlatt. Microstruct.* 11 (1992) 223.
- [5] U. Meirav, M.A. Kastner and S.J. Wind, *Phys. Rev. Lett.* 65 (1990) 771.
- [6] A.A.M. Staring, B.W. Alphenaar, H. van Houten, L.W. Molenkamp, O.J.A. Buyk, M.A.A. Mabe-soone and C.T. Foxon, *Phys. Rev. B* 46 (1992) 12869.
- [7] B.W. Alphenaar, A.A.M. Staring, H. van Houten, M.A.A. Mabe-soone, O.J.A. Buyk and C.T. Foxon *Phys. Rev. B* 46 (1992) 7236.
- [8] R.P. Taylor, A.S. Sachrajda, P. Zawadzki, P.T. Coleridge and J.A. Adams, *Phys. Rev. Lett.* 69 (1992) 1989.
- [9] L.P. Kouwenhoven, B.J. van Wees, C.J.P.M. Harmans and J.D. Williamson, *Surf. Sci.* 229 (1990) 290.





ELSEVIER

Surface Science 305 (1994) 460–464



## Control of ballistic electrons in (AlGa)As/GaAs heterostructures by means of superconducting niobium gate structures

T. Schäpers <sup>\*</sup>, F. Müller, A. Förster, B. Lengeler, H. Lüth

*Institut für Schicht- und Ionentechnik, Forschungszentrum Jülich (KFA), P.O. Box 1913, D-5170 Jülich, Germany*

(Received 20 April 1993; accepted for publication 12 June 1993)

### Abstract

Superconducting gate structures on a modulation doped (AlGa)As/GaAs heterostructure were used to control a ballistic electron beam within the high mobility 2DEG. A local and variable magnetic field was produced by superconducting current loops. The magnetic field induced by the loops was analysed by means of an external magnetic field as well as by an electron interference experiment. The maximum field obtained by two superconducting loops was 0.4 mT. In addition, a gate structure containing a superconducting ring between two opposite split gates was prepared in order to detect magnetic flux quantisation.

In recent years a large variety of experiments on ballistic electron transport in two-dimensional electron gases (2DEG) have been reported. Since a long transport mean free path is essential for investigations in the ballistic transport regime, most experiments are based on high-mobility 2DEG in modulation doped (AlGa)As/GaAs heterostructures grown by molecular beam epitaxy [1,2]. For collimated emission as well as for detection of ballistic electron beams most often split-gate point contacts are used [3–6]. Control of ballistic electrons is achieved by applying an external magnetic field [7] or/and by means of electrostatic refractive elements like lenses [8,9] or prisms [10]. Because of the large Fermi wavelength in a 2DEG (typically 50 nm) electron interference effects are also observable in the bal-

listic transport regime, as was demonstrated by a modified Young's double slit experiment [11]. In this letter we describe for the first time the control of ballistic electrons by means of superconducting gate structures on top of an (AlGa)As/GaAs heterostructure.

The niobium gate structures were fabricated on a modulation doped (AlGa)As/GaAs heterostructure grown by molecular beam epitaxy. The distance of the 2DEG from the surface was 150 nm. Standard van der Pauw measurements at 4.2 K showed a carrier density of  $2.6 \times 10^{15} \text{ m}^{-2}$  and a mobility of  $104 \text{ m}^2/\text{V} \cdot \text{s}$  resulting in a transport mean free path of  $9 \text{ } \mu\text{m}$ . For all samples a 40 nm thick niobium gate structure was defined by electron beam lithography.

A schematic layout of the sample with two current loops is given in Fig. 1. Between the point contacts two  $1 \text{ } \mu\text{m}$  wide current loops L1 and L2 separated by  $1 \text{ } \mu\text{m}$  are defined. The split-gates were separated  $3.6 \text{ } \mu\text{m}$  from each other. A colli-

<sup>\*</sup> Corresponding author.

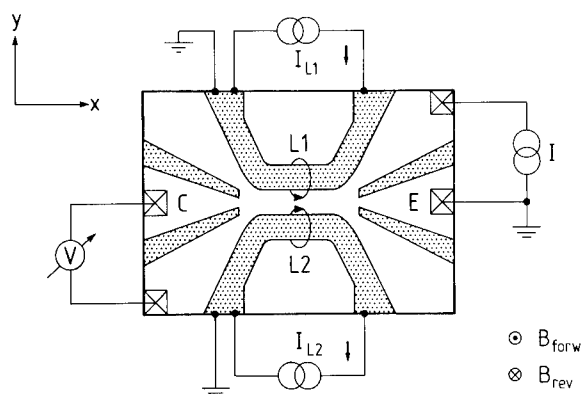


Fig. 1. Diagram of the gate structure and the measurement configuration.

mated beam of ballistic electrons is generated by driving a current through the emitter point contact *E*. The detection of the ballistic carriers through the collector point contact is accomplished by measuring the voltage drop  $V_C$  at the collector. The resistance of the emitter as well as the collector split-gate are adjusted to 6.0 k $\Omega$ . All measurements were performed in the dark.

The current loops are connected to a constant-current source with floating potential. An additional contact is used to define the ground potential of the superconducting loops, Fig. 1. This configuration ensures that electrostatic deflection of ballistic electrons caused by the loops can be excluded. The maximum supplied current of  $\pm 2$  mA is in all cases below the experimentally determined critical current of  $> 3$  mA. For the structure shown in Fig. 1, the magnetic field components in the area between the point contacts are orientated in the same directions; they are produced by two opposite currents  $I_{L1} = -I_{L2}$  through both loops. The magnitude of the field generated by the loops is determined by comparison with the collector signal dependence on an external magnetic field.

The collector voltage  $V_C$  as a function of an external magnetic field is shown in Fig. 2 for different currents  $I_{L1}$ ,  $-I_{L2} = \pm 1$  mA and 0 mA flowing through loop L1 and L2, respectively. The general shape of all three curves is determined by the deflection of the injected electrons by the external magnetic field; it represents the

angular distribution of the collimated electron beam [7]. The observed fine structure is reproducible on one and the same sample. It can be explained by interferences between electrons being scattered on impurities in the region between the point contacts [12]. A comparison of the curves in Fig. 2 clearly shows that a current flowing through the superconducting loops L1 and L2 shifts the initial distribution.

The observed shift in Fig. 2 is explained by a magnetic field produced by the current flowing in the superconducting loops. In Fig. 1 the orientation of the magnetic field is shown for a forward current in loop L1 and a reverse current in L2. In the area between both loops the magnetic field is orientated in a forward direction as shown in Fig. 1. This additional field causes a shift of the initial curve ( $I_{L1} = I_{L2} = 0$  mA) towards smaller external field values. Reversal of the current in the loops yields a shift in the opposite direction due to an additional reverse magnetic field.

According to Fig. 2, the total shift between the maximum current values  $I_{L1}$ ,  $-I_{L2} = 2$  mA and  $I_{L1}$ ,  $-I_{L2} = -2$  mA amounts to  $\pm 0.40$  mT. In order to estimate the expected shift, the magnetic field produced by a superconducting strip was calculated according to Rhoderik and Wilson [13]. In the calculation the width of the superconducting strip as well as the distance from the 2DEG was taken into account. Considering the spatial

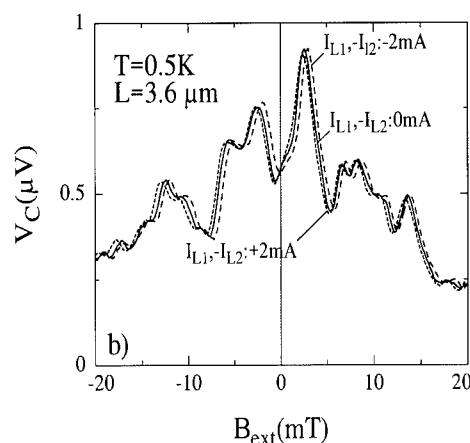


Fig. 2. Collector voltage as a function of an external magnetic field for different currents through the loops.

field dependence described in Ref. [13] and assuming a current of 2 mA in both strips leads to a magnetic field of 0.8 mT at the center between both strips. In this estimation the bending of the strips in the vicinity of the collector and emitter split gates is neglected; therefore the calculated value is higher by a factor of 2 as compared to the experimentally determined shift of 0.4 mT/2 mA.

In order to further elucidate the influence of the current loops on the ballistic electron transport an interference experiment, analogous to the experiment described in Ref. [11], on a structure with two gate fingers and only one current loop was performed. The width of the wider gate finger was 600 nm and that of the narrower one 400 nm. The separation between the point contacts was 5.6  $\mu\text{m}$ .

The propagation of an electron along each path  $\Gamma$  from the emitter E to the collector point contact C is described by a complex amplitude

$$\phi(\Gamma) = \text{const} \times \exp \left( \frac{i}{\hbar} \int_{\Gamma} \frac{m^*}{2} v^2 + e\varphi(\mathbf{r}) - e\mathbf{A}(\mathbf{r}) \cdot \mathbf{v} dt \right), \quad (1)$$

where  $\mathbf{v}$  is the electron velocity,  $\mathbf{r}$  the position of the electron,  $m^*$  the effective electron mass and  $e$  the electron charge.  $\varphi(\mathbf{r})$  and  $\mathbf{A}(\mathbf{r})$  are the electric and the vector potential, respectively. The total amplitude  $\Phi = \sum_{\text{all } \Gamma} \phi(\Gamma)$  for all possible paths  $\Gamma$  existing between E and C results in a transmission probability  $T_{\text{EC}} = |\Phi|^2$  for the electron transport from the emitter to the collector. Since the measured collector voltage  $V_C$  is determined by  $T_{\text{EC}}$ , a change of the latter is easily detected by measuring the voltage drop at the collector point contact. Biasing one of the gate fingers with a small, negative voltage results in a partial depletion of the 2DEG underneath the gate and, hence, in a phase change of the paths passing underneath this gate due to the electric potential  $\varphi$  and the reduction of the electron velocity  $\mathbf{v}$ . Beside the effect of a partial depletion of the 2DEG, the phase of an electron path is also modified by applying a magnetic field  $\mathbf{B} = \text{rot } \mathbf{A}$ .

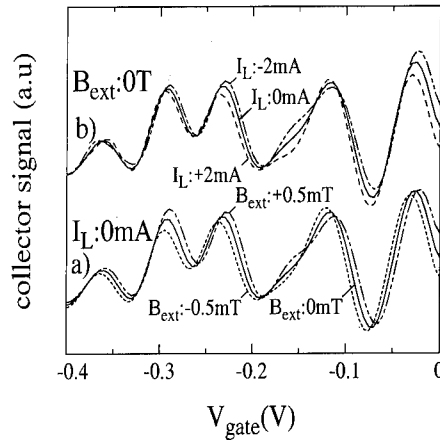


Fig. 3. Dependence of the collector signal on the gate voltage. The initial oscillation is shifted by an external magnetic field (a) and by a magnetic field generated by a current through the superconducting loop.

The measured collector signal  $V_C$  as a function of the voltage on a gate finger for different external magnetic fields is shown in Fig. 3a. The traces are obtained by using the 600 nm wide gate finger. The observed oscillations result from the interference of electron paths underneath and beside the gate finger. Applying an external transverse magnetic field in the forward direction causes a shift of the initial curve to lower gate voltages, whereas a reverse magnetic field shifts the initial oscillation in the opposite direction.

Fig. 3b illustrates the effect on the collector voltage caused by current  $I_L$  flow through the superconducting loop, while keeping the external magnetic field at zero. Referring to Fig. 3b, a reverse current of  $-2$  mA produces a shift of the initial curve towards lower gate voltages, while a forward current causes a shift in the opposite direction. These shifts of the initial oscillation can be explained by a magnetic field generated by the current through the loop as shown by a direct comparison with the results in Fig. 3a. A reverse current produces a magnetic field in the forward direction in the area between the point contacts, while a forward current generates a magnetic field in the opposite direction.

The positions of the maxima in Fig. 3b were determined in order to estimate the magnitude of the magnetic field generated by the loops. This

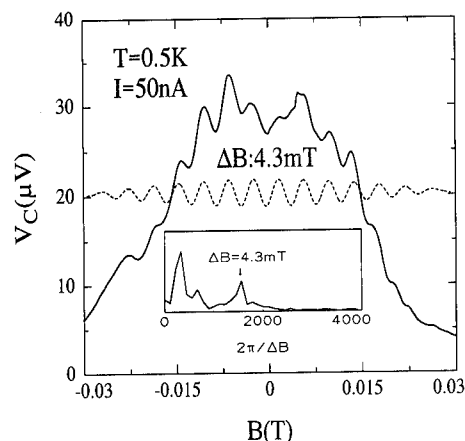


Fig. 4. Collector signal in dependence of an external magnetic field for the superconducting ring structure. The  $\Delta B = 4.3$  mT period can clearly be seen in the Fourier spectrum (inset). The dashed line shows the back transformation of the  $\Delta B = 4.3$  mT peak.

analysis shows that a current of  $I_L = 2$  mA is comparable to the effect induced by an external field of 0.35 mT. In contrast to the external magnetic field, the field distribution produced by the loop is inhomogeneous; therefore the field determined for the superconducting loops represents only an average value.

In order to detect the magnetic flux quantisation in a superconducting ring by using a ballistic electron beam, a ring-shaped niobium gate was placed between two opposite split gates. The area of the ring opening was  $0.46 \mu\text{m}^2$ , while the split gates were separated by  $3.6 \mu\text{m}$ .

The dependence of the collector signal on an external magnetic field at a temperature of 0.5 K is shown in Fig. 4. Superimposed on the overall shape of the collector signal, which is produced by a collimated ballistic electron beam, is a periodic structure. This periodic structure can be observed more clearly in the back transformation of the peak marked in the Fourier spectrum (Fig. 4, inset). The period of the oscillation is  $\Delta B = 4.3$  mT.

The origin of the oscillations can be explained by magnetic flux quanta, which enter the ring via a weak link in the superconducting film. Although no weak link in the form of a geometrical constriction was prepared intentionally in the ring,

this weak link can originate from grain boundaries or impurities in the superconducting film. The discontinuous increase of the magnetic field inside the superconducting ring leads to a modulated deflection of the ballistic electron beam flowing underneath the ring.

From the periodicity of the oscillation the effective opening area of the ring can be deduced. By using  $\Delta B = 4.3$  mT and the magnetic flux quantum  $\phi_0 = h/2e$  an area of  $0.48 \mu\text{m}^2$  was determined, which fits very well to the geometrical opening area of  $0.46 \mu\text{m}^2$ .

In conclusion, we have demonstrated the control of ballistic electrons by means of superconducting gate structures, which opens the possibility to control the current flow in a ballistic device by means of a local and variable magnetic field integrated in a circuit. The magnetic field generated by a superconducting current loop was analysed by an external magnetic field as well as an interference experiment. The maximum magnetic field produced by two loops was 0.4 mT. In addition, magnetic flux quantisation in a superconducting ring was detected by means of a ballistic electron beam flowing underneath the ring.

The authors would like to acknowledge G. Mülleijans, C. Krause and G. Hallmanns for technical support.

## 1. References

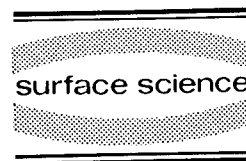
- [1] C.T. Foxon, J.J. Harris, D. Hilton, J. Hewitt and C. Roberts, *Semicond. Sci. Technol.* 4 (1989) 582.
- [2] L.N. Pfeiffer, K.W. West, H.L. Störmer and K. Baldwin, *Appl. Phys. Lett.* 55 (1989) 1880.
- [3] B.J. van Wees, H. van Houten, C.W.J. Beenakker, J.G. Williamson, L.P. Kouwenhoven, D. van der Marel and C.T. Foxon, *Phys. Rev. Lett.* 60 (1988) 848.
- [4] D.A. Wharam, T.J. Thornton, R. Newbury, M. Pepper, H. Ahmed, J.E.F. Frost, D.G. Hasko, D.C. Peacock, D.A. Ritchie and G.A.C. Jones, *J. Phys. C* 21 (1988) L209.
- [5] C.W.J. Beenakker and H. van Houten, *Phys. Rev. B* 39 (1989) 10445.
- [6] L.W. Molenkamp, A.A.M. Staring, C.W.J. Beenakker, R. Eppenga, C.E. Timmering, J.G. Williamson, C.J.P.M. Harmans and C.T. Foxon, *Phys. Rev. B* 41 (1990) 1274.
- [7] H. van Houten, C.W.J. Beenakker, J.G. Williamson, M.E.I. Broekaart, P.H.M. van Loosdrecht, B.J. van Wees,

- J.E. Mooij, C.T. Foxon and J.J. Harris, *Phys. Rev. B* 39 (1989) 8556.
- [8] J. Spector, H.L. Störmer, K.W. Baldwin, L.N. Pfeiffer and K.W. West, *Appl. Phys. Lett.* 56 (1990) 1290.
- [9] U. Sivan, M. Heiblum, C.P. Umbach and H. Shtrikman, *Phys. Rev. B* 41 (1990) 7937.
- [10] J. Spector, H.L. Störmer, K.W. Baldwin, L.N. Pfeiffer and K.W. West, *Appl. Phys. Lett.* 56 (1990) 2433.
- [11] A. Yacoby, U. Sivan, C.P. Umbach and J.M. Hong, *Phys. Rev. Lett.* 66 (1991) 1938.
- [12] D.R.S. Cumming, H. Ahmed and T.J. Thornton, *Appl. Phys. Lett.* 60 (1992) 2755.
- [13] E.H. Rhoderik and E.M. Wilson, *Nature* 194 (1962) 1167.



ELSEVIER

Surface Science 305 (1994) 465–469



# Metal/2DEG contact – a microscopic model

Y.B. Levinson

*Department of Physics, Weizmann Institute of Science, Rehovot 76100, Israel*

(Received 19 April 1993; accepted for publication 28 June 1993)

## Abstract

A model for a metal contact to a high mobility 2DEG is considered. The model takes into account strong elastic and inelastic electron scattering in the metal and the difference in Fermi surfaces of the metal and of the 2DEG. The thermalization probability for an electron which is incident on the contact is calculated.

## 1. Introduction

Recent experiments on the quantum Hall effect (QHE) draw attention to the properties of the current and voltage contacts to the two-dimensional electron gas (2DEG) [1–5]. A contact is called “ideal” when a carrier incident on the contact is adsorbed and thermalized in the contact. If there is a non-zero probability for the carrier to be reflected back to the 2DEG the contact is called “non-ideal”. In the case when some of the current contacts are not ideal the edge states are nonequally populated. If this population is probed by non-ideal voltage contacts, deviations in the QHE are possible [6]. Split-gate quantum point contacts can be driven from ideal to non-ideal by changing the gate voltage [2,3,5]. The question is much more complicated in the case of alloyed AuGe contacts. It is generally believed that in this case a low-resistance ohmic contact is achieved due to the presence of a heavily doped  $n^+$  layer between the metal and the GaAs, where the carrier transport occurs mainly through tunneling [7,8]. In the contact domain the electrons undergo strong scattering,

while in the 2DEG the scattering is negligible. The problem of penetration of a ballistic particle into a strongly scattering medium is known (for 3D geometry) from astrophysics and neutron physics (the Milne problem) [9]. The probability to be captured (thermalized) in a scattering half-space is  $w = (\tau_e/\tau_e + \tau_i)^{1/2}$ , where  $\tau_e$  and  $\tau_i$  are the elastic and inelastic scattering times, respectively. Hence, all 3D contacts must be non-ideal, since in metals and semiconductors at low temperatures  $\tau_i \gg \tau_e$  and  $w = (\tau_e/\tau_i)^{1/2} \ll 1$ .

The problem of electron thermalization in the metal/2DEG contact differs from the Milne problem at least in two points: (i) the electron gas is 2D, while the metal is 3D; (ii) there is additional reflection at the metal/semiconductor interface due to potential barriers and/or different Fermi surface in the metal and the semiconductor [10].

The paper is organized as follows. In Section 2 we discuss the model of the contact. The model neglects the 3D geometry of the metal and also the potential barrier at the metal/semiconductor interface but takes into account different Fermi spheres in the metal and the semiconductor. In

Section 3 we present the results for the 2D Milne problem (the solution will be given elsewhere). Using these results, we derive an integral equation for the backscattering angular distribution and calculate the thermalization probability in Section 4.

## 2. Model of the contact and formulation of the problem

We neglect the 3D geometry of the contact and consider a 2D model shown in Fig. 1. The 2DEG plane is divided in three regions. On the left there is a ballistic domain S (semiconductor) with no scattering, low electron density and small Fermi wavevector  $k_{FS}$ . On the right there is a domain M (metal) with strong elastic and inelastic scattering, high electron density and large Fermi wavevector  $k_{FM}$ . In between we assume a transition domain T (heavily doped semiconductor), the width of which,  $d$ , is large compared with the electron Fermi wavelength. Due to the smoothness of the transition region electrons traverse it adiabatically. An electron which is incident on T from S travels to M without reflection. The angle between the  $z$  axis and the electron momentum is changed to conserve its transversal component  $k_{\perp}$  (see Fig. 1). As to an electron which is incident on T from M the situation

depends on the angle of incidence  $\phi$ . If  $|\phi| < \bar{\phi} \equiv \sin^{-1}(k_{FS}/k_{FM})$  the electron travels to S without reflection. In the case  $|\phi| > \bar{\phi}$  the electron is totally and specularly reflected back to M.

The evolution of the electron distribution in M for zero temperature is given by the Boltzmann equation

$$v \cos \phi \frac{\partial f}{\partial z} = -\frac{f-n}{\tau_e} - \frac{f}{\tau_i}. \quad (1)$$

Here  $f(z, \phi)$  is the nonequilibrium part of the electron distribution at the Fermi surface,  $v$  is the Fermi velocity and

$$n(z) = \frac{1}{2\pi} \int_0^{2\pi} d\phi f(z, \phi) \quad (2)$$

is the nonequilibrium electron “density”. The first term in the RHS of Eq. (1) is responsible for elastic scattering, the second for inelastic scattering (thermalization).

The problem is as follows. An electron beam is coming from S with the angle of incidence  $\theta_0$ , the angular distribution being  $\delta(\theta - \theta_0)$  and the flux along  $z$  being  $J_0 = \cos \theta_0$ . We are interested in the thermalization probability  $w = (J_0 - J')/J_0$ , where  $J'$  is the total flux reflected back to S after the electrons undergo scattering in M.

Some models exist for a contact between 3D and 2D systems [11–13]. But these models do not take into account electron scattering and cannot

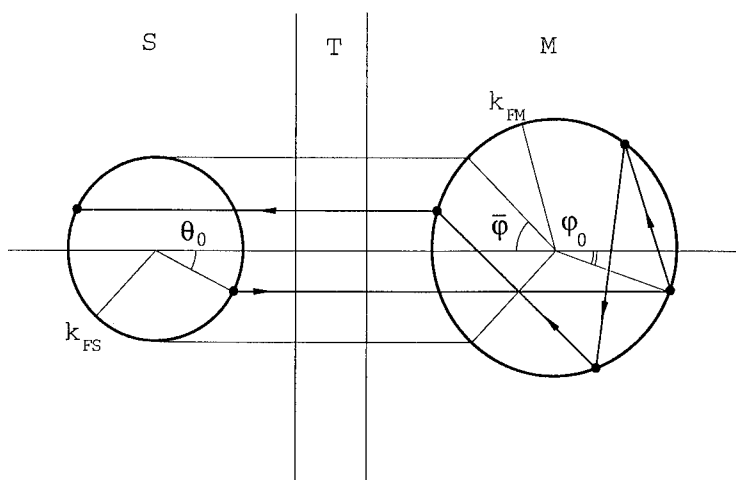


Fig. 1. Fermi circles in the 2DEG and the contact.

be used to calculate the electron thermalization probability.

### 3. 2D Milne problem

Assume the right half-plane ( $z > 0$ ) contains uniformly distributed scattering centers, while the left one ( $z < 0$ ) contains no such centers. A beam of particles with velocity  $v$  is coming from  $z = -\infty$  with angle of incidence  $\phi_0$ . The beam penetrates into the right half-space and is scattered according to Eq. (1). This equation is to be solved with the boundary condition at  $z = 0$ :  $f(0, \phi) = \delta(\phi - \phi_0)$ ,  $\cos \phi > 0$ . We are interested in the reflection matrix which is the angular distribution of particles scattered back to the left half-space:  $R(\phi_0 \rightarrow \phi) = f(0, \phi)$ ,  $\cos \phi < 0$ .

Using methods similar to those given in Ref. [9] one can find

$$R(\phi \rightarrow \pi - \psi) = \frac{\lambda}{2\pi} \frac{\cos \phi}{\cos \phi + \cos \psi} H_\lambda(\cos \phi) H_\lambda(\cos \psi), \quad (3)$$

where both angles  $\phi$  and  $\psi$  vary from  $-\pi/2$  to  $+\pi/2$ , the parameter  $\lambda = \tau_i/(\tau_e + \tau_i)$ , and the function  $H$  is given by

$$H_\lambda(\cos \phi) = \exp \left\{ \frac{1}{2\pi} \int_{-\infty}^{+\infty} \frac{dt \cos \phi}{1 + t^2 \cos^2 \phi} \times \left[ -\ln \left( 1 - \frac{\lambda}{\sqrt{t^2 + 1}} \right) \right] \right\}. \quad (4)$$

### 4. Thermalization probability

First let us calculate the thermalization probability for the 2D Milne problem, i.e. when  $k_{FS} = k_{FM}$  and  $\bar{\phi} = \pi/2$ . In this case

$$w = 1 - \frac{1}{\cos \phi_0} \int d\phi R(\phi_0 \rightarrow \pi - \phi) \cos \phi. \quad (5)$$

Introduce into Eq. (5) the matrix  $R$  from Eq. (4) and calculate the integral over  $\phi$ . This yields

$$w = \sqrt{1 - \lambda} H_\lambda(\cos \phi_0). \quad (6)$$

This result differs from  $w$  in 3D geometry only in the function  $H$  which is different in 2D.

To calculate the thermalization probability  $w$  with the account of the reflections in the transition domain  $T$  consider in  $M$  the domain  $0 < z < z_0$ , where  $z_0$  is arbitrary, subject to  $z_0 \ll v\tau_e, v\tau_i$ . Scattering can be neglected in this domain and hence the electron distribution depends only on  $\phi$ . It follows from the adiabatic properties of  $T$  that for  $0 < z < z_0$ :

$$f_+(\phi) = f_-(\pi - \phi), \quad |\phi| > \bar{\phi}, \quad (7)$$

$$f_+(\phi) = (\cos \theta_0 / \cos \phi_0) \delta(\phi - \phi_0), \quad |\phi| < \bar{\phi}. \quad (8)$$

Here  $f_+$  and  $f_-$  are distributions of particles moving to the right and to the left,  $\phi_0$  is the angle of refraction, which corresponds to the angle of incidence  $\theta_0$  (see Fig. 1). The cosine ratio in Eq. (8) comes from flux conservation. The distributions  $f_+$  and  $f_-$  are also connected through the reflection from the domain  $z > z_0$ :

$$f_-(\phi) = \int d\phi' f_+(\phi') R(\phi' \rightarrow \phi), \quad (9)$$

where the matrix  $R$  is given by Eq. (5). Introducing  $f_+$  from Eqs. (7) and (8) into Eq. (9), we obtain an integral equation for  $f_-$ :

$$f_-(\phi) - \int_{|\phi'| > \bar{\phi}} d\phi' f_-(\pi - \phi') R(\phi' \rightarrow \phi) = \frac{\cos \theta_0}{\cos \phi_0} R(\phi_0 \rightarrow \phi). \quad (10)$$

From the solution of this equation one can calculate the thermalization probability

$$w = 1 - \frac{1}{\cos \theta_0} \int_{|\pi - \phi| < \bar{\phi}} d\phi f_-(\phi) |\cos \phi|. \quad (11)$$

First let consider the situation when  $\bar{\phi} \ll 1$  and  $\delta \equiv 1 - \lambda \ll 1$ . In this case  $\phi_0$  is small and Eq. (10) can be reduced to

$$\begin{aligned} f_-(\phi) - \int_{|\phi'| < \bar{\phi}} d\phi' f_-(\pi - \phi') R(\phi' \rightarrow \phi) \\ = R(0 \rightarrow \phi) \cos \theta_0 - R(0 \rightarrow \phi) \\ \times \int_{|\phi'| < \bar{\phi}} d\phi' f_-(\pi - \phi'). \end{aligned} \quad (12)$$



In this equation the LHS gives electron redistribution in angles, while the RHS gives electron income to the domain  $0 < z < z_0$  (first term) and electron escape from this domain (second term). When  $\bar{\phi}$  is small, the RHS can be neglected in first approximation. In this approximation one can put  $\lambda = 1$  in the LHS. As a result, we have

$$f_{-}(\phi) = \int d\phi' f_{-}(\pi - \phi') R(\phi' \rightarrow \phi) |_{\lambda=1}. \quad (13)$$

Using some properties of functions  $H$  for  $\lambda = 1$  we can see that the solution is  $f_{-}(\phi) = A = \text{const.}$  The meaning of this solution is obvious. Since  $\lambda = 1$  electrons are totally (diffusively) reflected from the boundary  $z = z_0$ . Since  $\bar{\phi} = 0$  electrons are totally (specularly) reflected from the boundary  $z = 0$ . As a result of sequential reflections an isotropic angular distribution is established. Going to the second approximation we introduce the isotropic solution of Eq. (13) into Eq. (12), giving

$$A - A[1 - \delta^{1/2} H_{\lambda}(\cos \phi)]$$

$$= (\cos \theta_0 - 2\bar{\phi}A) \frac{\lambda}{2\pi} H_{\lambda}(1) \frac{H_{\lambda}(\cos \phi)}{1 + \cos \phi}. \quad (14)$$

In Eq. (14) we can put  $\lambda = 1$ , retaining the factor  $\delta^{1/2}$ . To find  $A$  we integrate Eq. (14) over  $\phi$ , using the relation

$$\begin{aligned} & \frac{1}{2\pi} H_1(1) \int d\phi \frac{H_1(\cos \phi)}{1 + \cos \phi} \\ &= H_1(1) - 1 \equiv c = 1.53 \dots \end{aligned} \quad (15)$$

As a result,

$$f_{-}(\phi) = A = \frac{c \cos \theta_0}{2\pi \delta^{1/2} + 2c\bar{\phi}}. \quad (16)$$

Substituting this distribution into Eq. (11), we obtain the thermalization probability

$$w = \frac{\delta^{1/2}}{\delta^{1/2} + c\bar{\phi}/\pi} \quad (17)$$

valid for  $\bar{\phi} \ll 1$  and  $\delta \ll 1$ .

It follows from Eq. (17) that the thermalization probability is enhanced, compared with the simple 2D Milne problem and if  $\bar{\phi} \ll \delta^{1/2}$  the contact is ideal, since in this case  $w \approx 1$ . Even in the

case that the contact is not ideal, its reflection coefficient is independent on the angle of incidence  $\phi_0$  and hence it populates all the electron states of the 2DEG to the same extent.

One can easily understand why the metal M is a trap when  $\bar{\phi} \ll \pi$ . The electron which comes from S has a momentum  $k$  directed nearly along  $+z$ . After scattering, the electron gains a transverse component  $k_{\perp}$ . Hence after most scattering events  $k_{\perp} > k_{\text{FS}}$ , and as a result the electron cannot go back to the semiconductor S and has to wait for a “lucky” scattering at the end of which the momentum is directed nearly along  $-z$ .

If  $\bar{\phi}$  is not small and/or  $\delta$  is not small, one can calculate  $w$  using the Schwinger variational method, see Ref. [9]. We apply this variational method to the integral equation (10) and integral in Eq. (5), using the simplest trial functions. As a result we obtain

$$\begin{aligned} 1 - w &= \frac{H_{\lambda}(\cos \phi_0) - 1}{\cos \phi_0} \\ &\times \frac{2 \sin \bar{\phi}}{\pi - \int_{|\phi| > \bar{\phi}} [H_{\lambda}(\cos \phi) - 1]}. \end{aligned} \quad (18)$$

To test this approach let us consider first the case  $\bar{\phi} = \pi/2$  and compare the variational approximation with the exact result from Eq. (6). The two results agree if

$$H_{\lambda}(\cos \phi) = \frac{1 + \frac{1}{2}\pi \cos \phi}{1 + \frac{1}{2}\pi \sqrt{1 - \lambda} \cos \phi}. \quad (19)$$

From the properties of functions  $H$  one can see that Eq. (19) is a good approximation to the exact  $H_{\lambda}$ . The second test of Eq. (18) is the case  $\bar{\phi} \ll \pi$ ,  $1 - \lambda \ll 1$ . One can see that in this case Eq. (18) leads to Eq. (17).

In conclusion, we present some numerical values relevant to the above discussed contact model. Typical Fermi wave-vectors are:  $k_{\text{FM}} \approx 10^8 \text{ cm}^{-1}$  and  $k_{\text{FS}} \approx 10^6 \text{ cm}^{-1}$ , giving the transmission angle  $\bar{\phi} \approx 10^{-2}$ . Rough estimates for scattering times in metals at low temperatures are:  $\tau_e \approx 10^{-4} \text{ s}$  and  $\tau_i \approx 10^{-10} \text{ s}$  giving  $\delta \approx 10^{-4}$ . The width of the transition region,  $d \approx 100 \text{ nm}$ , compared to  $\lambda_{\text{FS}} \approx 50 \text{ nm}$ .

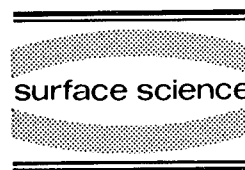
## 5. References

- [1] S. Komiyama, H. Hirai, S. Sasa and S. Hiyamizu, *Phys. Rev. B* 40 (1989) 12566.
- [2] B.J. van Wees, E.M.M. Willems, C.J.P.M. Harmans, C.W.J. Beenakker, H. van Houten, J.G. Williamson, C.T. Foxon and J.J. Harris, *Phys. Rev. Lett.* 62 (1989) 1181.
- [3] B.J. van Wees, E.M. Willems, L.P. Kouwenhoven, C.J.P.M. Harmans, J.G. Williamson, C.T. Foxon and J.J. Harris, *Phys. Rev. B* 39 (1989) 8066.
- [4] S. Komiyama, H. Hirai, S. Sasa and T. Fujii, *Solid State Commun.* 73 (1990) 91.
- [5] B.W. Alphenaar, P.L. McEuen, R.G. Wheeler and R.N. Sacks, *Phys. Rev. B* 64 (1990) 677.
- [6] M. Buttiker, *Phys. Rev. B* 38 (1988) 9375.
- [7] T.S. Kuan, P.E. Batson, T.N. Jackson, H. Rupprecht and E.L. Wilkie, *J. Appl. Phys.* 54 (1983) 6952.
- [8] N. Braslau, *J. Vac. Sci. Technol.* 19 (1981) 803.
- [9] P.M. Morse and H. Feshbach, *Methods of Theoretical Physics* (McGraw-Hill, New York, 1953).
- [10] V.F. Gantmakher and Y.B. Levinson, *Carrier Scattering in Metals and Semiconductors* (North-Holland, Amsterdam, 1987).
- [11] A.M. Kriman and P.P. Ruden, *Phys. Rev. B* 32 (1985) 8013.
- [12] R. Frohne and S. Datta, *J. Appl. Phys.* 64 (1988) 4086.
- [13] S.G. Petrosyan and A. Yu. Shik, *Sov. Phys. JETP* 69 (1989) 1261.



ELSEVIER

Surface Science 305 (1994) 470–475



# Superconductors coupled with a two-dimensional electron gas in GaAs/AlGaAs and InAs/AlGaSb heterostructures

J.R. Gao <sup>\*,a</sup>, J.P. Heida <sup>a</sup>, B.J. van Wees <sup>a</sup>, T.M. Klapwijk <sup>a</sup>, G. Borghs <sup>b</sup>, C.T. Foxon <sup>c</sup>

<sup>a</sup> Department of Applied Physics and Materials Science Centre, University of Groningen,  
Nijenborgh 4, 9747 AG Groningen, Netherlands

<sup>b</sup> IMEC, Kapeldreef 75, B-3030, Leuven, Belgium

<sup>c</sup> Philips Research Laboratories, Redhill, UK

(Received 10 May 1993; accepted for publication 12 June 1993)

## Abstract

We fabricated superconducting Sn/Pd contacts to a two-dimensional electron gas (2DEG) in GaAs/AlGaAs heterostructures by an alloying technique. A dip around zero bias and peaks at finite voltages have been observed in the differential resistance of a 2DEG between two superconductors. The resistance dip may be a result of Andreev reflection at 2DEG-superconductor interfaces and the peaks are probably due to the Josephson coupling between two very close superconducting islands in a superconducting contact region, which may be formed by alloying. Alternatively, we made superconducting Nb contacts to a 2DEG in an InAs/AlGaSb quantum well structure. The resistance of Nb-2DEG-Nb devices shows a clear indication of Andreev reflection.

## 1. Introduction

A weak link usually consists of a normal metal sandwiched between two superconductors (S). Using a semiconductor (Sm) instead of a normal metal, the supercurrent through such a system would depend on the carrier concentration, which can be varied, for instance, by means of a gate voltage. Most of the experiments so far have focused on systems with semiconductors in which there is considerable impurity scattering [1,2]. S-Sm-S systems using a high mobility two-dimensional electron gas (2DEG), such as that in

GaAs/AlGaAs heterostructures or InAs quantum well structures, are interesting from both fundamental and technological points of view. In these systems transport can be ballistic as well as phase coherent. The supercurrent in these systems is expected to be carried by bound states due to coherent Andreev reflection (AR) [3,4]. The absence of impurity scattering in the high mobility 2DEGs makes a direct comparison with theory possible. In addition, the supercurrent can be observed in the S-2DEG-S systems with a relatively large separation  $L_{sm}$ , e.g.  $L_{sm} = 0.5 \mu\text{m}$ , between the two superconductors [5]. This leaves space to define gates. It is therefore possible to realize both superconducting quantum point contacts, in which the supercurrent is predicted [6] to increase stepwise as the contact width becomes

\* Corresponding author.

wider, and other three terminal superconducting devices.

The transparency of a S–Sm interface determines the probability of AR, which plays a crucial role in the (super)current transport. At a S–Sm interface, a Schottky barrier is present except for the case for InAs. In addition, a 2DEG in a GaAs/AlGaAs heterostructure is formed typically 80 nm below the surface. To make highly transparent contacts to the GaAs/AlGaAs 2DEG an alloying process is needed. Superconducting contacts to a GaAs/AlGaAs accumulation layer were first made by Ivanov et al. [7] using a combination of Sn/In. The supercurrent was observed in a S–2DEG–S weak link. However, transport in the 2DEG was diffusive because of the low mobility. Contacts to a high mobility GaAs/AlGaAs 2DEG were later reported by Lenssen et al. [8] using Sn/Ti. Although they achieved highly transparent S–Sm interfaces, characteristics for the superconducting contacts could be observed only below 0.4 K.

We succeeded in making superconducting contacts to a high mobility GaAs/AlGaAs 2DEG using a new combination of Sn/Pd. Here we report our recent measurements on S–2DEG–S structures with a short electron gas between two superconductors. We observed new features in the differential resistance which we tentatively interpret as the formation of superconducting contacts to the 2DEG. We also report a result on Nb–2DEG–Nb devices using an InAs/GaAlSb quantum-well structure.

## 2. Results and discussion

### 2.1. GaAs/AlGaAs heterostructures

Fig. 1 shows a schematic top view of S–2DEG–S devices. Two close superconducting contacts with widths of 20  $\mu\text{m}$  are defined on a GaAs/AlGaAs sample using Sn/Pd. The separation between the two superconductors, as defined lithographically, is about 1.5  $\mu\text{m}$ . Each superconducting contact is attached by a pair of Au/Ti contacts (not shown) to allow for four terminal measurements. We used devices with two differ-

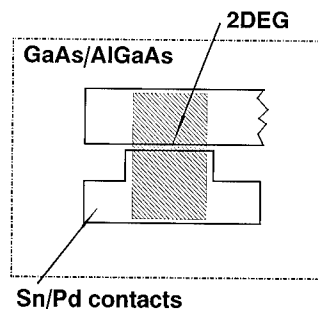


Fig. 1. A schematic top view of a S–2DEG–S device with a short channel 2DEG in GaAs/AlGaAs heterostructures contacted with two superconductors.

ent configurations: one has no mesa structure; the other has a mesa structure which defines a channel of width 16  $\mu\text{m}$ , as shown in the figure.

Our starting material is a usual MBE grown GaAs/AlGaAs heterostructure, which consists of a 4  $\mu\text{m}$  GaAs buffer layer, a 20 nm undoped AlGaAs spacer layer, a 40 nm Si-doped AlGaAs layer, and a 20 nm undoped GaAs cap-layer. The sheet electron density and mobility of our samples at 1.2 K are  $3.6 \times 10^{11} \text{ cm}^{-2}$  and  $4 \times 10^5 \text{ cm}^2/\text{V} \cdot \text{s}$ , the latter giving an electron mean free path  $l_e$  of 2.6  $\mu\text{m}$ .

The device fabrication is as follows. After mesa etching, contact patterns are defined by using standard photolithography. The native oxide of GaAs is removed in a solution of  $\text{HCl}:\text{H}_2\text{O} = 1:1$  for 2 min. Immediately afterwards the samples are loaded into the e-gun evaporation system and 15 nm Pd and 250 nm Sn are evaporated. To form ohmic and superconducting contacts, alloying takes place on a hot plate in forming gas or  $\text{N}_2$  for a short time at around 500°C. The Pd is used as a first layer to prevent the oxidation of GaAs and to reduce out-diffusion of Ga or As [9]. The Sn is used because it can form ohmic and superconductor contacts to GaAs [10] (the critical temperature of Sn  $T_c = 3.7 \text{ K}$  and its superconducting gap  $2\Delta(0) \approx 1.2 \text{ meV}$ ). Furthermore, compounds of  $\text{Pd}_x\text{Sn}_y$  which can be possibly formed during alloying are also superconductors. Some of them are known to have  $T_c$  between 0.4 and 3.3 K [11].

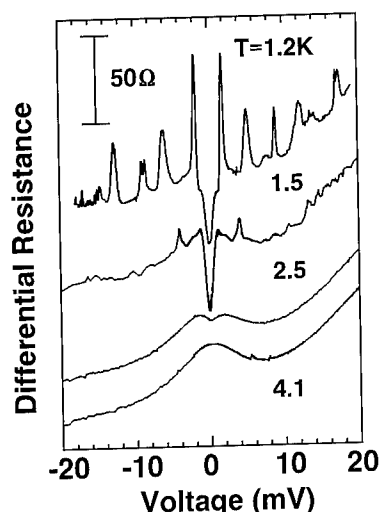


Fig. 2. The differential resistance of a GaAs/AlGaAs S-2DEG-S device as a function of voltage bias at four temperatures. For clarity there are offsets in the Y-direction. The normal state resistance taken at  $V = -15$  mV for four temperatures equals  $370 \Omega$ .

Fig. 2 shows the differential resistances of a S-2DEG-S device without mesa structure, measured at four temperatures. At 1.2 K a resistance dip around zero bias with a value of  $\sim 10\%$  the normal state resistance  $R_N$  is found. From 2 mV several reproducible peaks on the resistance were observed as the bias increases. These phenomena have been observed in three similar devices. We note that the peaks are not periodic and their detailed features are device-dependent. With increasing temperature the peaks damp quickly, but the dip decreases only slowly. Meanwhile, the bias position of the peaks shifts towards zero value. In one of the devices, we systematically studied the temperature dependence of the bias and current positions, which follows the BCS superconductor gap. However, the bias values are larger than  $2\Delta/e$  for Sn. Above 4 K all the features disappear. Instead, a broad hump arises around zero bias with the position of its minima at 5 mV; it vanishes at temperatures above 10 K. It should be noted that not all devices tested show the phenomena of dip and peaks, but they do give a similar hump in the resistance. Additionally, the resistance shows a slightly changed background.  $R_N$  taken at  $V = -15$  mV equals

$370 \Omega$ , and is independent of temperature. This value is dominated by two interface resistances since the resistance of the channel amounts to  $5 \Omega$ .

Applying a magnetic field yields similar behaviour as increasing temperature. The differential resistances versus bias measured at several magnetic fields are plotted in Fig. 3. All features are suppressed by a field of 0.35 T. The rise of the averaged resistance with the field is due to the magnetoresistance of the channel. The features in the zero field curve do not precisely reproduce those given in fig. 2; we attribute that to several thermal cycles.

To further examine the superconducting contacts we measured the temperature dependence of the resistance of the same sample applied with and without biases. The results are given in Fig. 4. As shown in the figure, zero bias resistance starts to decrease markedly as temperature is reduced below 4 K. In contrast, resistances obtained at biases of 3 and 6 mV are almost independent of temperature.

Because of its relatively long channel, no supercurrent is expected in this device in the temperature range we used. From Figs. 2–4 we conclude that the observed properties must be associated with the superconducting contacts. Which

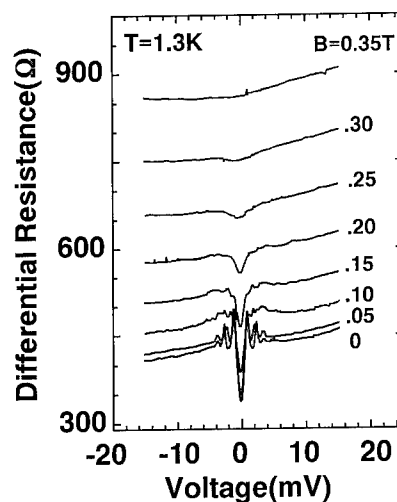


Fig. 3. The differential resistance as a function of bias for the same device as in Fig. 2, measured at several magnetic fields.

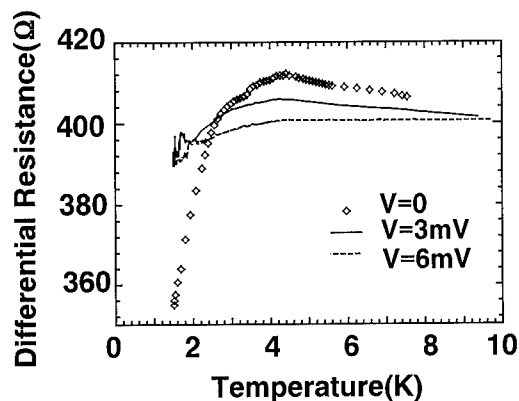


Fig. 4. The differential resistance as a function of temperature for the same device as in Fig. 2, biased at  $V = 0, 3$  and  $6$  mV, respectively.

material is responsible for the superconductor? Roughly speaking, the observed  $T_c$  is  $3.8 \pm 0.3$  K, suggested by the transition behaviour in Fig. 4, and it seems to be consistent with both Sn and  $\text{Pd}_x\text{Sn}_y$ . On the other hand, the critical field  $H_c \approx 0.35$  T inferred from Fig. 3 is much higher than that of Sn (0.03 T), suggesting that the superconductor is not pure Sn but  $\text{Pd}_x\text{Sn}_y$ .

At a S–Sm interface, for an incoming electron from the semiconductor with an energy (relative to the Fermi energy) below the superconductor gap, two types of scattering processes may take place: the electron can be either normally reflected or retro-reflected as a hole. The latter process is so-called Andreev reflection. Its probability is determined by the transmission coefficient  $T_N$ . According to the Blonder, Tinkham and Klapwijk (BTK) model [12], at an ideal S–Sm interface ( $T_N = 1$ ) the current will be doubled due to AR. Consequently, the resistance below the superconductor gap will be reduced to  $R_N/2$ . However, at a non-ideal interface, due to an interface barrier such as a Schottky barrier or the Fermi momentum mismatch,  $T_N$  is usually smaller than unity, thus AR can be largely suppressed.

In our case the resistance dip was observed at temperatures below  $T_c$  and at biases below 2 mV, which is approximately consistent with  $2\Delta/e$ . Following the BTK model we attribute the dip to AR. On the other hand, because of the occur-

rence of AR one might deduce  $T_N \approx 1$ . However, this does not agree with the value determined by the experimental  $R_N$  which gives a much smaller value,  $T_N \approx 0.04$ . The latter was determined by comparing  $R_N$  (370  $\Omega$ ) with the Sharvin resistance [13]  $R_s = 14$   $\Omega$  for the GaAs/AlGaAs 2DEG. We explain the observation of AR in our system with a large  $R_N$  value by assuming that AR takes place at a small part of the interface which is highly transparent. We speculate that the transparent part is due to the formation of several small superconducting islands of  $\text{Pd}_x\text{Sn}_y$ , induced by alloying. Here we discussed our result by naively applying the BTK model. It should be pointed out that, because of the assumption of a delta function potential, the BTK model might not apply to the alloyed contacts, in which the interface barrier may have a finite thickness, and may be inhomogeneous laterally.

The observed peaks may be understood by further assuming that there is Josephson coupling between two very close superconducting islands in a superconducting contact region. A peak may occur each time the applied current exceeds a critical current of the two coupled islands. As we mentioned before, the temperature dependence of the biases or currents corresponding to the peak position follows that of the BCS gap. In other words, it differs from the temperature dependence of the critical current for a Josephson junction such as a Sn–I–Sn [14]. This may be due to complicated configuration of the superconducting islands. Furthermore, in the magnetic fields a critical current of Josephson junctions decreases quickly and oscillates with the field. In Fig. 3 the peaks are suppressed by weak fields, but they do not give oscillating features with the field. For the latter it is not clear that this is due to a large magnetic field step used or that there are no oscillating features.

## 2.2. InAs / AlGaSb quantum well structures

In this part, we will present a measurement on a different system, Nb–2DEG–Nb using an InAs/AlGaSb quantum well structure. There are two advantages of using an InAs 2DEG. First, Schottky barriers are not present at Nb–InAs

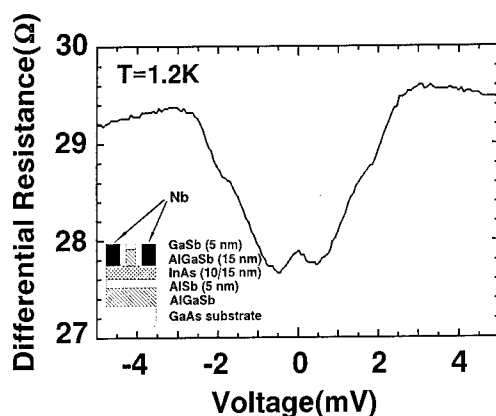


Fig. 5. The differential resistance vs bias voltage for an InAs Nb-2DEG-Nb device, measured at 1.2 K. Inset gives a schematic cross-section view of the device. The separation between two Nb electrodes is  $0.7 \mu\text{m}$ .

interfaces and thus highly transparent contacts may be expected. Second, the fabrication is simple because of no need for an alloying process. The device fabrication is summarized as follows; the top layers of GaSb and AlGaSb were first removed, and after a sputter cleaning of the InAs surface two superconducting Nb electrodes were deposited by sputtering.

Fig. 5 shows the differential resistance as a function of bias for a Nb-2DEG-Nb device, measured at 1.2 K. The device is illustrated schematically in the inset. The separation between the two Nb electrodes is  $0.7 \mu\text{m}$ , which is smaller than  $l_e$  ( $\sim 1 \mu\text{m}$ ). A drop of the resistance with a value of  $\sim 10\% R_N$  below 3 mV, corresponding to  $2\Delta$ , is due to AR. A feature observed around  $V=1.5$  mV, may be subharmonic energy gap structure [15] due to multiple AR. A small peak occurs around zero bias, which has not yet been understood. The observed  $R_N$  is around  $30 \Omega$ , close to the Sharvin resistance  $R_s = 10 \Omega$  for the InAs 2DEG. We therefore conclude that  $T_N$  is high although it may not equal unity. This explains the clear observation of AR in our Nb-2DEG-Nb devices using an InAs/AlGaSb structure. Similar systems using InAs quantum well structures have also been studied recently by other groups [5,16].

### 3. Conclusions

In summary, S-2DEG-S devices, two superconductors coupled with a short channel GaAs/AlGaAs 2DEG, have been fabricated successfully. Complicated features have been observed in the differential resistance of the devices at temperatures below 4 K, and their dependence on temperature and magnetic field suggests the formation of superconducting contacts to the 2DEG. The superconductor is expected to be  $\text{Pd}_x\text{Sn}_y$  formed during alloying. The observed resistance dip around zero bias may be a result of Andreev reflection. In addition, Nb-2DEG-Nb devices using an InAs/AlGaSb quantum well structure has also been studied and a drop of the resistance below the superconductor gap is a clear signature of Andreev reflection.

### 4. Acknowledgements

We would like to thank L.W. Molenkamp and B.W. Alphenaar for their discussions. This work has benefitted from conversations with K.-M.H. Lenssen and C.J.P.M. Harmans. This project is supported by the Dutch program on high  $T_c$  superconductivity and the NWO through the FOM.

### 5. References

- [1] For a review, see A.W. Kleinsasser and W.L. Gallagher, *Superconducting Devices*, Eds. S. Ruggiero and D. Rudman (Academic Press, Boston, 1990) p. 325.
- [2] Also see, T.M. Klapwijk, W.M. van Huffelen and D.R. Heslinga, *IEEE Trans. on Applied Superconductivity* 3 (1993) 2873.
- [3] A.F. Andreev, *Zh. Eksp. Teor. Fiz.* 46 (1964) 1825; [*Sov. Phys. JETP* 19 (1964) 1228].
- [4] I.O. Kulik, *Sov. Phys. JETP* 30 (1970) 1745; J. Bardeen and J.L. Johnson, *Phys. Rev. B* 5 72 (1972); R. Kummel, U. Günsenheimer and R. Nicolsky, *Phys. Rev. B* 42 (1990) 3992; B.J. van Wees, K.-M.H. Lenssen and C.J.P.M. Harmans, *Phys. Rev. B* 44 (1991) 470.
- [5] J. Nitta, T. Akazaki, H. Takayanagi and K. Arai, *Phys. Rev. B* 46 (1992) 14286.
- [6] C.W.J. Beenakker and H. van Houten, *Phys. Rev. Lett.* 66 (1991) 3056;

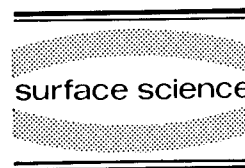
- A. Furusaki, H. Takayanagi and M. Tsukada, Phys. Rev. Lett. 67 (1991) 132.
- [7] Z. Ivanov, T. Claeson and T. Andersson, Jpn. J. Appl. Phys. 26, Sup. 26-3 (1987).
- [8] K.M.H. Lenssen, M. Matters, C.J.P.M. Harmans, J.E. Mooij, M.R. Leys, W. van der Vleuten and J.H. Wolter, IEEE Trans. on Applied Superconductivity 3 (1993) 1961.
- [9] T.C. Shen, G.B. Gao and H. Morkoc, J. Vac. Sci. Technol. B 10 (1992) 2113.
- [10] J.R. Gao, J.P. Heida, B.J. van Wees, S. Bakker, T.M. Klapwijk and B.W. Alphenaar, Appl. Phys. Lett. 63 (1993) 334.
- [11] Handbook of Chemistry and Physics, 63rd ed. (CRC Press, Boca Raton, FL).
- [12] G.E. Blonder, M. Tinkham and T.M. Klapwijk, Phys. Rev. B 25 (1982) 4515.
- [13] Y.V. Sharvin, Sov. Phys. JETP 21 (1965) 655.
- [14] T. van Duzer and C.W. Turner, Principles Superconductive Devices and Circuits (Elsevier, New York)
- [15] M. Octavio, M. Tinkham, G.E. Blonder and T.M. Klapwijk, Phys. Rev. B 27 (1983) 6739.
- [16] C. Nguyen, H. Kroemer and E.L. Hu, Phys. Rev. Lett., 69 (1992) 2847.





ELSEVIER

Surface Science 305 (1994) 476–479



# Influence of gate voltage on the transport properties of superconductor/2DEG systems

K.-M.H. Lenssen<sup>a,\*</sup>, L.A. Westerling<sup>a</sup>, C.J.P.M. Harmans<sup>a</sup>, J.E. Mooij<sup>a</sup>,  
M.R. Leys<sup>b</sup>, W. van der Vleuten<sup>b</sup>, J.H. Wolter<sup>b</sup>

<sup>a</sup> Department of Applied Physics, Delft University of Technology, P.O. Box 5046, NL-2600 GA Delft, Netherlands

<sup>b</sup> Department of Applied Physics, Eindhoven University of Technology, P.O. Box 513, NL-5600 MB Eindhoven, Netherlands

(Received 19 April 1993; accepted for publication 4 June 1993)

## Abstract

Highly transmissive, superconducting contacts of  $\mu\text{m}$ -scale have been made to the two-dimensional electron gas in GaAs/AlGaAs heterostructures, in combination with lateral gate structures. We present results of resistance measurements at  $T \approx 10$  mK on a sample with a quantum point contact between two superconducting Sn/Ti contacts. New effects due to phase-coherent Andreev reflection have been observed. The conductance is found to be quantized with enhanced steps  $> 2e^2/h$ , which is attributed to Andreev reflection. At zero gate voltage an enhancement of weak localization by Andreev reflection has been measured for the first time, while at a higher gate voltage indications of an excess conductance due to reflectionless tunneling have been found.

## 1. Introduction

The properties of electrical transport in low-dimensional systems are, in fact per definition, strongly determined by the boundaries. It is therefore obvious that new physical effects will be encountered, if some boundaries can be formed by superconductors. Since we recently succeeded in making superconducting, highly transmissive contacts to the two-dimensional electron gas (2DEG) in GaAs/AlGaAs heterostructures [1], it is now possible to enter this challenging new field in mesoscopic physics.

The interest in coupling superconductors (S) to semiconductors (N) is by now more than a decade old [2]. This combination opens the way to three-terminal devices in which superconducting effects can be modulated by, e.g., a gate volt-

age. But also from a more fundamental point of view superconductor/semiconductor systems are very interesting, especially if the semiconductor is phase-coherent or ballistic. In this case the electron transport can be conveniently described by a generalized Landauer–Büttiker formalism [3,4].

It has been predicted, that the critical current in a superconducting quantum point contact will be quantized [5,6]. But even in the absence of a supercurrent through the semiconductor, new effects caused by Andreev reflection are expected [7,8]. An electron (from N) with an excitation energy below the superconducting gap  $\Delta$  cannot enter the superconductor, because there are no states available. The incident electron can be retroreflected as a hole, while a Cooper-pair is created in the superconductor. Analogously, an incident hole can be reflected as an electron at the NS interface. The probability for this process

\* Corresponding author. Fax: +31 (15) 617868.

of Andreev reflection is strongly dependent on the transmission of the interface [9]. In particular at interfaces with semiconductors a Schottky barrier can introduce normal reflection and decrease the probability for Andreev reflection dramatically.

Recently, several effects at or near NS interfaces have been theoretically described. The unit of the conductance quantization will be doubled ( $4e^2/h$  instead of  $2e^2/h$ ) in a quantum point contact near an ideal NS interface due to Andreev reflection [4]. The measurement of an excess conductance that is described in Ref. [10] has been attributed to phase-coherent Andreev reflection in Refs. [4,11]. To observe this effect the transmission of the NS interface does not have to be very high. If the NS interface is however very transmissive, it is predicted that weak localization effects in the N region will be enhanced by Andreev reflection [4,12].

In the following, besides measurements which show an excess conductance, we will also discuss the first experimental evidence for quantization of the conductance with enhanced steps and for enhancement of weak localization by Andreev reflection.

## 2. Sample fabrication

GaAs/AlGaAs heterostructures are very suitable for studying these effects, because of their high mobility 2DEG and their excellent gating properties. The material we used for these experiments was grown by molecular beam epitaxy and consists of a GaAs substrate with a 4  $\mu\text{m}$  undoped GaAs layer, a 40 nm undoped  $\text{Al}_{0.33}\text{Ga}_{0.67}\text{As}$  spacer, a 38 nm n-doped  $\text{Al}_{0.33}\text{Ga}_{0.67}\text{As}$  layer and a 17 nm undoped GaAs caplayer. The electron mobility is  $110 \text{ m}^2/\text{V}\cdot\text{s}$  and the electron density is  $2.4 \times 10^{15} \text{ m}^{-2}$  (at  $T \approx 5 \text{ K}$ ).

The coupling between the 2DEG and a superconductor is the major problem, because the 2DEG is situated typically 100 nm below the surface of the heterostructure. The diffusion process which we developed for making highly transmis-

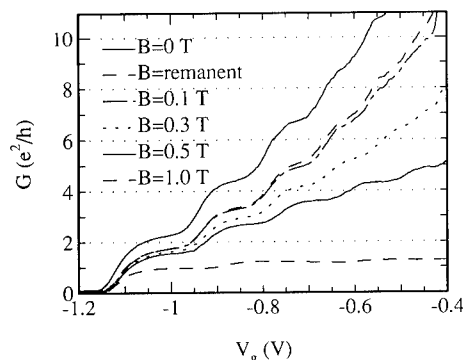


Fig. 1. The differential conductance as a function of the gate voltage defining the quantum point contact.

sive superconducting Sn/Ti contacts has been described elsewhere [1,13].

The sample consists of two 10  $\mu\text{m}$  wide superconducting Sn/Ti contacts at a distance of 800 nm from each other. In the space between the contacts a quantum point contact (width  $\approx 150 \text{ nm}$ , length  $\approx 90 \text{ nm}$ ) is situated. Both Sn/Ti contacts end in two bond pads. Four larger Sn/Ti contacts are added at the corners of the sample to enable test measurements. The sample is surrounded by a wide gate (a “moat gate”) for device isolation. All three patterns (contacts, wide gate and quantum point contact) were defined by electron beam lithography and aligned by automatic marker search on especially prepared gold markers (with an inaccuracy below 30 nm).

## 3. Results

The differential conductance of the SNS system as a function of the voltage on the gate defining the quantum point contact is presented in Fig. 1. Clearly, it can be seen that the conductance is quantized in units larger than  $2e^2/h$ . This is especially remarkable, since in normal quantum point contacts the plateaus are below the theoretical quantization values because of a series resistance. In this case even the uncorrected measured plateaus are above the values from the normal theory. We attribute this to Andreev reflection.

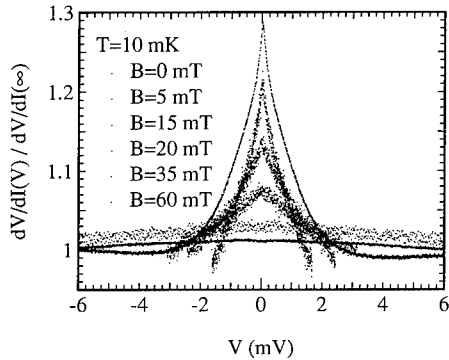


Fig. 2. The normalized differential resistance at  $V_g = 0$  mV as a function of the bias voltage for several magnetic fields.

The effect is very sensitive to magnetic fields. Already the remanent field of the superconducting magnet (of tens of mT) can destroy it. The  $B$ -values are the applied fields; the remanent field is not known. Note that for  $B = 0$  T the steps are approximately equidistant. This means that there is no series resistance of importance. At magnetic fields in the order of 0.1 T or larger the series resistance begins to increase significantly. This could be explained by a suppression of phase-coherent Andreev reflection. Around  $B = 1$  T the conductance seems to be quantized in units of  $e^2/h$ , because the spin degeneracy is lifted.

The  $dV/dI$ - $V$ -curves are strongly dependent on the gate voltage, as can be seen by comparing Figs. 2 and 3 at gate voltage  $V_g = 0$  mV with Fig. 4 at  $V_g = -890$  mV. In Fig. 2 the normalized  $dV/dI$ - $V$ -characteristics at zero gate voltage are presented, below 4 K (Fig. 3). Here a sharp resistance peak exists around zero voltage, which we believe is due to Andreev reflection enhanced weak localization. This peak disappears rapidly in magnetic fields below 0.04 T. This shows that the effect is suppressed, if time reversal symmetry is broken. When temperature increases, the peak becomes smaller and smaller and has disappeared completely.

When the enhancement of the weak localization is suppressed, the sign of the temperature dependence becomes slightly positive instead of negative. Besides by increased temperature, a DC voltage, and a magnetic field, this suppress-

sion can also be achieved by a voltage on the gate. The occurrence of enhanced weak localization requires that the NS interface is practically barrier-free [12]. By means of the gate voltage a potential barrier can be induced, and the transmission is lowered.

Fig. 4 shows some  $dV/dI$ - $V$ -characteristics at a gate voltage of  $V_g = -890$  mV for different magnetic fields. For low magnetic fields the curve shows now a resistance dip around zero bias, which is suppressed in higher fields or at higher temperatures ( $T \approx 1$  K). This excess conductance can be explained by reflectionless tunneling and can arise due to the reduced transmission [12]. Probably this is the same effect as described in Ref. [10], but now measured in a GaAs/AlGaAs heterostructure.

#### 4. Conclusions

We have observed new effects due to phase-coherent Andreev reflection. The conductance of the quantum point contact is quantized in units larger than  $2e^2/h$ . Enhancement of weak localization by Andreev reflection has been measured at zero gate voltage. This can be suppressed by increased temperature, a DC voltage and a small magnetic field, but also by a gate voltage. At a gate voltage of  $-890$  mV indications for an excess conductance due to reflectionless tunneling have been found. The occurrence of enhanced weak localization shows again that the supercon-

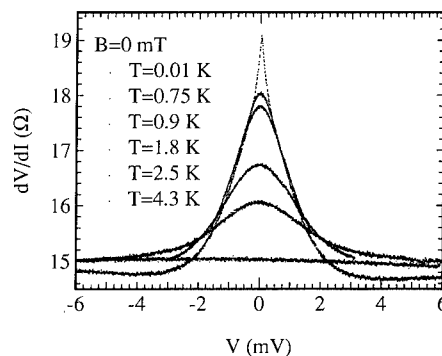


Fig. 3. The differential resistance at  $V_g = 0$  mV as a function of the bias voltage at several temperatures.

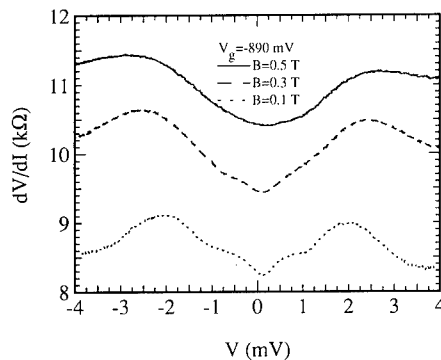


Fig. 4. The differential resistance at  $V_g = -890$  mV as a function of the bias voltage for several magnetic fields.

ducting contacts we have made are very transmissive and thus very suitable to study phase-coherent and ballistic effects in SNS structures.

#### Acknowledgements

We would like to thank the Delft Institute of Micro-Electronics and Submicron technology (DIMES) for the use of its facilities. This research was financially supported by the Dutch Foundation for Fundamental Research on Matter (Stichting FOM).

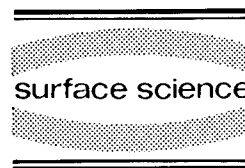
#### References

- [1] K.-M.H. Lenssen, M. Matters, C.J.P.M. Harmans, J.E. Mooij, M.R. Leys, W. van der Vleuten and J.H. Wolter, *IEEE Trans. Appl. Superconductivity* 3 (1993) 1961.
- [2] T.D. Clark, R.J. Prance and A.D.C. Grassie, *J. Appl. Phys.* 51 (1980) 2736.
- [3] B.J. van Wees, K.-M.H. Lenssen and C.J.P.M. Harmans, *Phys. Rev. B* 44 (1991) 470.
- [4] C.W.J. Beenakker, *Phys. Rev. B* 46 (1992) 12841.
- [5] A. Furusaki, H. Takayanagi and M. Tsukada, *Phys. Rev. Lett.* 67 (1991) 132.
- [6] C.W.J. Beenakker and H. van Houten, in: *Proc. Int. Symp. on Nanostructures and Mesoscopic Systems*, Santa Fe, NM, USA, May 1991.
- [7] A.F. Andreev, *Zh. Eksp. Teor. Fiz.* 46 (1964) 1823 [*Sov. Phys. JETP* 19 (1964) 1228].
- [8] A.F. Andreev, *Zh. Eksp. Teor. Fiz.* 49 (1965) 655 [*Sov. Phys. JETP* 22 (1966) 455].
- [9] G.E. Blonder, M. Tinkham and T.M. Klapwijk, *Phys. Rev. B* 25 (1982) 4515.
- [10] A. Kastalsky, A.W. Kleinsasser, L.H. Greene, R. Bhat, F.P. Milliken and J.P. Harbison, *Phys. Rev. Lett.* 67 (1991) 3026.
- [11] B.J. van Wees, P. de Vries, P. Magnée and T.M. Klapwijk, *Phys. Rev. Lett.* 69 (1992) 510.
- [12] I.K. Marmorkos, C.W.J. Beenakker and R.A. Jalabert, *Phys. Rev. B* 48 (1993) 2811.
- [13] K.-M.H. Lenssen, M. Matters, C.J.P.M. Harmans, J.E. Mooij, M.R. Leys, W. van der Vleuten and J.H. Wolter, *Appl. Phys. Lett.* 63 (1993) 2079.



ELSEVIER

Surface Science 305 (1994) 480–489



# Conductance fluctuations in a quantum dot in the tunneling regime: crossover from aperiodic to regular behavior

C.M. Marcus <sup>\*,1</sup>, R.M. Westervelt

*Department of Physics and Division of Applied Sciences, Harvard University, Cambridge MA 02138, USA*

P.F. Hopkins, A.C. Gossard

*Materials Department, University of California, Santa Barbara CA 93106, USA*

(Received 28 April 1993; accepted for publication 16 July 1993)

## Abstract

We discuss magnetoconductance fluctuations in a  $\sim 1 \mu\text{m}$  GaAS/ $\text{Al}_x\text{Ga}_{1-x}\text{As}$  quantum dot in the shape of a chaotic stadium billiard with point contact leads. Here we emphasize measurements carried out in the tunneling regime, where each lead carries less than one fully conducting channel. We discuss various crossover phenomena as the magnetoconductance fluctuations evolve from aperiodic structure at low fields ( $B \lesssim 0.5 \text{ T}$ ) into periodic, Aharonov–Bohm-like oscillations at higher fields.

## 1. Introduction

Over the last few years, the transport of electrons through small confined geometries has proven to be a remarkably rich experimental system, despite the apparent simplicity of the physical situation: an island of electrons – for instance, a gate-confined two-dimensional electron gas (2DEG) in a semiconductor heterostructure – is connected to reservoirs of bulk 2DEG via quantum point contacts which serve as quasi-1D chan-

nels [1–8]. At low temperatures these structures, so-called quantum dots or Coulomb islands, show significant fluctuations in their conductance as a function of applied magnetic field or Fermi energy (which can be controlled via gate voltages). Depending on the regime under investigation, a number of physical mechanisms – indeed, often wholly different physical pictures – have been invoked to explain these fluctuations. For instance, in open, multichannel disordered mesoscopic systems, quasi-random conductance fluctuations with universal rms amplitude  $\sim e^2/h = (25.8 \text{ k}\Omega)^{-1}$  are understood in terms of quantum interference of phase coherent electrons following diffusive trajectories [9]. On the other hand, in nearly isolated quantum dots ( $G_{\text{dot}} \ll e^2/h$ ),

\* Corresponding author.

<sup>1</sup> Present address: Department of Physics, Stanford University, Stanford CA 94305-4060, USA.

conductance fluctuations due to Coulomb blockade are associated with the discrete nature of the electronic charge; phase coherence is not generally considered central to this effect [4].

To date, most magnetotransport experiments in quantum dots in the tunneling regime ( $G_{\text{dot}} < e^2/h$ ) have been carried out at relatively large magnetic fields, where transport becomes simpler due to the formation of edge states. At fields above a few tesla, edge states become electrically isolated from one another, and each becomes subject to Coulomb blockade. At *small* magnetic fields, i.e., prior to the formation of well separated edge states, this picture breaks down: in the low-field tunneling regime, transport in quantum dots becomes a complicated problem involving an interplay of charging, quantum interference, and, for ballistic devices – structures in which the elastic mean free path  $\ell$  exceeds all device dimensions – a sensitivity to the confining geometry [10].

This paper describes magnetoconductance measurements in a  $\sim 1 \mu\text{m}$  ballistic GaAs/ $\text{Al}_x\text{Ga}_{1-x}\text{As}$  quantum dot in the shape of a stadium billiard (Fig. 1a) with magnetic field applied perpendicular to the plane of the dot, at a refrigerator temperature of 16 mK. The range of magnetic fields investigated covers  $B = 0$  to  $B \approx 2.2$  T. To characterize the observed conductance

fluctuations, we identify various crossover fields in going from low to high magnetic field. It is also significant that these measurements were carried out in the barely-tunneling regime,  $G_{\text{dot}} \lesssim e^2/h$ , which is itself an interesting crossover regime. As described below, the barely-tunneling regime is of particular interest in extending the applicability of semiclassical methods to problems in quantum chaos [11–13].

We are not suggesting that the low-field regime is uncharted territory in mesoscopic conductance studies. On the contrary, fluctuations at low fields have been widely investigated experimentally [14–16] and theoretically [9,17] in *disordered* metals and semiconductors, where the motion along at least one spatial direction is diffusive. However, little is known about the low-field regime in either ballistic devices or in tunneling quantum dots. Recent experiments [5], as well as numerics and semiclassical theory [18,19], indicate that magnetoconductance of open, ballistic dots with multichannel leads show aperiodic fluctuations at low magnetic fields, much like what is seen in disordered mesoscopic samples, though apparently not requiring disorder to produce the effect. For ballistic structures in general, the source of “randomness” that gives rise to aperiodic fluctuation is chaotic scattering from the walls of the device.

The underlying connection between chaos and aperiodic conductance fluctuations has been addressed recently within a semiclassical theoretical model [18], according to which electrons follow classical trajectories but carry phase information allowing for quantum interference. The semiclassical approach is only appropriate for multichannel leads and so is of questionable applicability for quantum dots in the tunneling regime. This requirement of multichannel leads can be understood by comparing the characteristic escape time  $\tau_{\text{esc}}$  from the scattering region with the characteristic quantum time scale  $\tau_{\text{H}} = \hbar/\Delta$ , where  $\Delta$  is the mean energy level spacing. Generally, a semiclassical approach is appropriate on time scales short compared to  $\tau_{\text{H}}$  [11]. In the semiclassical regime, the ratio of escape time to quantum time is given by  $\tau_{\text{esc}}/\tau_{\text{H}} = 2\pi(N_{\text{a}} + N_{\text{b}})^{-1}$ , where  $N_{\text{a}}$  and  $N_{\text{b}}$  are the number of channels in leads a

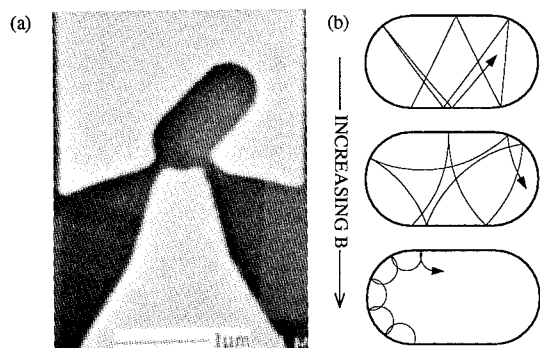


Fig. 1. (a) Electron micrograph of the stadium quantum dot, with  $1 \mu\text{m}$  bar for size scale. (b) Schematic picture of electron trajectories inside of the stadium, indicating the effect of increasing magnetic field. For the dot in (a) these trajectories correspond to  $B = 0, 0.17$ , and  $1.4$  T, from top to bottom.

and b. This expression shows that as the number of channels decreases, one necessarily leaves the semiclassical regime, *independent* of the size of the quantum dot. An equivalent statement in terms of energy is that there is a crossover from overlapping to isolated resonances as the leads become single channel, independent of dot area, and that a semiclassical approach is applicable only in the regime of overlapping resonances [11].

The standard theoretical approaches to *disordered* mesoscopic systems [9] are of uncertain applicability to transport in ballistic quantum dots for several reasons. First, these methods assume diffusive transport in at least one spatial direction. Second, many-body effects such as charging are generally not taken into account. Third, by assuming diffusive transport one effectively equates the time required for a trajectory to become well mixed (ergodic),  $\tau_{\text{erg}}$ , with the escape time, i.e. the time to diffuse through the system  $\tau_{\text{diff}} = \hbar/E_c$ , where  $E_c$  is the Thouless energy. In a ballistic quantum dot, these two times are not the same – either may be larger – with the ratio depending on the geometry of the dot and the size of the openings. Finally, one is unable to investigate non-generic features in transport by these methods: all trajectories and all regions of phase space are taken to be equivalent so that structure associated, for instance, with weakly unstable periodic orbits in a ballistic dot [5] – the analog of wave function scars in closed systems [20] – are not revealed. Incidentally, this last limitation also applies to random matrix approaches [21]: only generic transport features associated with a particular matrix ensemble, or physical symmetry, are explored.

What the above discussion intends to make clear is that the physics of conductance fluctuations in tunneling quantum dots occupies a poorly understood middle ground lying between Coulomb blockade systems, edge state systems, and disordered mesoscopic systems. The rest of the paper is organized as follows: Section 2 gives experimental details and parameters; Section 3 presents low-field behavior; Section 4 discusses the crossover from aperiodic to periodic conductance oscillations, comparing semiclassical, quantum, and charging pictures. Finally, in Section 5,

we point out a possible detection of multiple edge states and compare the observed conductance oscillations to an electrostatic model of edge states presented recently by Chklovskii, Shklovskii and Glazman (CSG) [22].

## 2. Experimental details

Magnetoconductance was measured in a ballistic quantum dot in the shape of a stadium billiard with two point contact leads, shown in Fig. 1a. Fabrication of the stadium dot, along with a similar circular dot on the same sample, has been described previously [5]. The pair of dots were fabricated on an  $\text{Al}_{0.3}\text{Ga}_{0.7}\text{As}$  heterostructure using Cr/Au (20 Å/80 Å) gates patterned via electron-beam lithography and standard liftoff techniques. The total distance from electron gas layer to the surface is 420 Å, with a Si  $\delta$ -doping layer ( $N_D = 6 \times 10^{12} \text{ cm}^{-2}$ ) set back 200 Å from the electron gas layer. After lithographic processing, a mobility  $\mu$  of  $265\,000 \text{ cm}^2/\text{V}\cdot\text{s}$  and a sheet density  $n$  of  $3.8 \times 10^{11} \text{ cm}^{-2}$  was measured at 16 mK with all gates shorted to the electron gas, and the sample cooled in the dark. We infer a slightly lower sheet density of  $\sim 3.6 \times 10^{11} \text{ cm}^{-2}$  within the dot based on an amplitude modulation of conductance oscillations at fields above 1 T. The modulation is periodic in  $1/B$ , and presumably corresponds to Landau levels in the dot passing through the Fermi surface, and so provides a measure of the density within the dot. The value  $n \approx 3.6 \times 10^{11} \text{ cm}^{-2}$  is also consistent with a characteristic resistance dip assumed to be due to curved trajectories aimed directly from one lead to the other (this feature is visible in Fig. 3 around  $B \approx 0.5 \text{ T}$ , and also in Fig. 1 of Ref. [5] for the circular dot). The elastic (transport) mean free path is  $\ell = 2.6 \mu\text{m}$ . The lithographic size of the dot, as measured from SEM micrographs, is  $0.58 \mu\text{m} \times 1.25 \mu\text{m}$ .

The conductance of the leads can be adjusted via the applied gate voltage, typical gate voltages are  $V_g \approx -0.6 \text{ V}$ . Unfortunately, the design of the present structure does not allow the conductances of the two point contacts to be individually tuned. Measurements were carried out in a dilu-

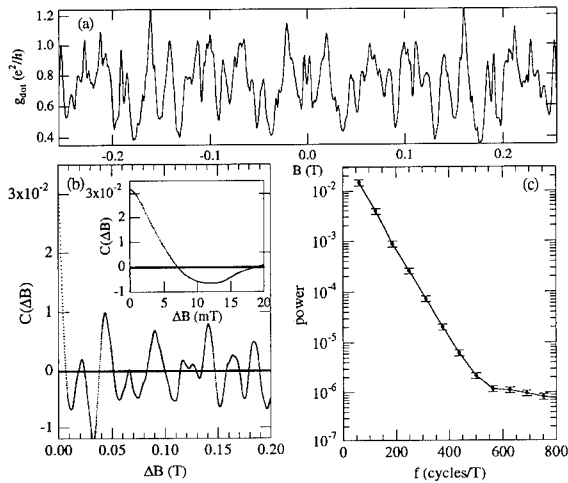


Fig. 2. (a) Conductance  $g_{\text{dot}}(B)$  of the stadium dot at 16 mK as a function of perpendicular magnetic field,  $B$ . (b) Autocorrelation function  $C(\Delta B)$  (defined in text) of conductance fluctuations, with  $C(0) = \text{var}[\delta g(B)]$ . Inset shows  $C(\Delta B)$  for small  $\Delta B$ . (c) Average power spectrum of fluctuations over the range shown in (a). Error bars are small due to averaging, which also reduces frequency resolution.

tion refrigerator using standard ac lock-in techniques with an 11 Hz current bias. The voltage drop across the sample was kept below  $2 \mu\text{V}$  in all runs to avoid excessive heating of the electrons. Voltages were measured in a four-probe configuration, but because nearly all of the voltage was dropped across the two-lead sample, the magnetoconductance approximately satisfies the two-probe symmetry,  $G(B) = G(-B)$ .

### 3. Aperiodic fluctuations at low field

Fig. 2a shows the magnetoconductance of the dot  $g_{\text{dot}}(B) = (h/e^2)G_{\text{dot}}(B)$  as a function of applied perpendicular magnetic field. The mean conductance is  $\bar{g}_{\text{dot}} \approx 0.75$ . At low fields, before the formation of edge states, the mean conductance of the dot  $\bar{g}_{\text{dot}}$  can be related to mean conductances of the individual point contacts a and b by the resistors-in-series form,  $\bar{g}_{\text{dot}} \approx \bar{g}_a \bar{g}_b / (\bar{g}_a + \bar{g}_b)$  [2]. Here, averages are over  $B$ , within a suitably small range where the average does not change very much. For equally opened

point contacts,  $\bar{g}_a = \bar{g}_b \equiv \bar{g}$ , this gives  $\bar{g}_{\text{dot}} = \bar{g}/2$ . For single-channel leads, each with transmission probability  $T$ , the mean conductance through the dot is simply given by  $\bar{g}_{\text{dot}} = T$ . Thus, assuming equal leads, we take the requirement to be in the tunneling regime as

$$\bar{g}_{\text{dot}} < 1 \quad \text{tunneling regime (equal leads)}. \quad (1)$$

For unequal leads, say with a ratio of conductances  $\kappa > 1$ , this tunneling condition becomes  $\bar{g}_{\text{dot}} < 2/(\kappa + 1)$ . As an example, if the conductances of the two leads differ by a factor of 1.5, the tunneling condition becomes  $\bar{g}_{\text{dot}} < 0.8$ . This condition simply assures that both leads have conductance less than unity. By this criterion it is reasonable to identify the data in Fig. 2a as in the weakly tunneling regime.

The conductance fluctuations in Fig. 2a are very similar in appearance to what is seen when the leads are opened and carry several channels each. To the eye, the fluctuations appear aperiodic, though maintaining the rough symmetry  $g_{\text{dot}}(B) = g_{\text{dot}}(-B)$ . The data do not show a large ballistic weak localization feature as seen in the more open structures. The dependence of ballistic weak localization, i.e. quantum-enhanced backscattering, on the degree of openness of the dot has not yet been studied in detail. The fluctuating part of the conductance  $\delta g(B)$  is separated from the background conductance of  $\sim \bar{g}_{\text{dot}}$  by subtracting a smooth (cubic polynomial) fit to  $g(B)$ . The autocorrelation of the resulting fluctuations,  $C(\Delta B) = [\delta g(B + \Delta B) \delta g(B)]$ , is shown in Fig. 2b. A close-up of the small  $\Delta B$  region, shown in the inset of Fig. 2b, indicates that the fluctuations have a correlation length of  $\sim 4 \text{ mT}$  which is of the order of, but smaller than the field associated with one flux quantum through the dot, which is  $(\Phi_0/\text{dot area}) \approx 9 \text{ mT}$ . Away from  $\Delta B \approx 0$ ,  $C(\Delta B)$  shows large fluctuations which may be related to non-generic small-area trajectories within the structure. In principle, these features in  $C(\Delta B)$  provide an effective “area spectroscopy” of the stadium. Fig. 2c shows the averaged power spectrum  $S(f)$  of the fluctuations, where  $f$  is the magnetic frequency in units of cycles/T. The spectrum shown is computed by averaging 62 FFT power spectra from half-over-



lapping 128-point segments covering the range in Fig. 2a, using Blackman–Harris third-order windowing. Assuming that the fluctuations do not change their statistics over the range investigated, the power spectrum  $S(f)$  will be equivalent to the Fourier transform of  $C(\Delta B)$ . Empirically, the power spectrum is exponential over four orders of magnitude in power,

$$S(f) \approx S_0 e^{-f/f_0}, \quad (2)$$

with a least-squares fit to  $\ln(S(f))$ , giving  $f_0 = 50$  cycles/T.  $S(f)$  reaches the noise floor at a magnetic frequency of  $\sim 500$  cycles/T, roughly 5 times the frequency associated with one flux quantum through the area of the dot:  $f_{\text{dot}} = \text{area}/\Phi_0 = 108$  cycles/T. This suggests that the exponential spectrum includes phase coherent trajectories with areas up to  $\sim 5$  times the area of the dot due to multiple bounces within the structure. The exponential form is similar to what one expects based on a semiclassical model of chaotic scattering [18], but not exactly: semiclassically, the theoretical result is slightly concave down on a log scale,  $S_{\text{sc}}(f) = S_0(1 + f/f_0) e^{-f/f_0}$ , where  $f_0 = A_{\text{esc}}/\Phi_0$  and  $A_{\text{esc}}$  characterizes the classical distribution of areas swept out by trajectories before escaping from the billiard,  $P(A) \approx e^{-A/A_{\text{esc}}}$ . Indeed, when the leads of the stadium dot carry several channels – here one expects the semiclassical model to apply – the experimental spectra are better fit by the semiclassical form than by the straight exponential [5]. In the weak tunneling regime, the spectrum reflects a relative enhancement of long dwell times compared to the semiclassical regime. Theoretically expected forms for  $S(f)$  in the tunneling regime – ignoring the effects of charging – have been calculated [23], and reveal a relative enhancement of the high-frequency part of the spectrum in the tunneling regime in agreement with our observations.

Because the stadium billiard is chaotic in the absence of disorder, one would not expect a moderate degree of disorder – inevitable in real devices – to qualitatively affect the above observations. Moderate disorder in the static potential felt by the electrons will only further randomize the already chaotic trajectories.

#### 4. Crossover from aperiodic to periodic oscillations at larger magnetic field

As the applied magnetic field is swept to above  $\sim 0.5$  T, the aperiodic structure seen at low fields is replaced by a nearly periodic oscillatory structure, as seen in Fig. 3. At intermediate fields,  $0.5 \text{ T} < B < 1 \text{ T}$ , the oscillations still have a large amplitude variation which becomes more regular above  $B \approx 1 \text{ T}$ .

A simple semiclassical picture which accounts for the transition at  $B \approx 0.5 \text{ T}$  is shown schematically in Fig. 1b: as the magnetic field increases, the classical cyclotron radius  $r_{\text{cycl}} = \Phi_0/\lambda_F B \approx 100 \text{ nm}/B[\text{T}]$  shrinks, becoming smaller than the minimum radius of curvature  $\rho_{\text{min}}$  of the dot. At this point, electrons no longer scatter chaotically within the dot but instead move in orderly skipping orbits around the edges [24], as shown schematically in the bottom panel of Fig. 1b. Once this condition is satisfied, the dot behaves essentially as a ring, and one should expect periodic Aharonov–Bohm oscillations [1,25]. The semiclassical critical field where this transition occurs is

$$B_{\text{sc}} = \Phi_0/\lambda_F \rho_{\text{min}}, \quad (3)$$

which for our dot gives  $B_{\text{sc}} = 0.46 \text{ T}$ , where we use  $\rho_{\text{min}} = 0.22 \mu\text{m}$ , assuming a depletion width of  $75 \text{ nm}$  (the value  $75 \text{ nm}$  is discussed below). This semiclassical prediction for the critical field, Eq. (3), appears consistent with the data in Fig. 3.

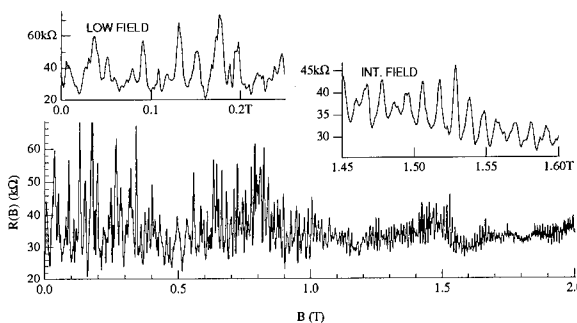


Fig. 3. The entire crossover from low to high field fluctuations is visible in this plot of resistance  $R(B)$  versus field  $B$  from  $B = 0$ – $2 \text{ T}$ . Insets show resistance at low field,  $B \leq 0.2 \text{ T}$ , exhibiting aperiodic fluctuations and at intermediate field,  $B \approx 1.5 \text{ T}$ , where the fluctuations are periodic.

There are a number of other characteristic magnetic fields which also might reasonably be considered as indicating the onset of “the edge state regime”. For instance, Glazman and Jonson [26] considered the model problem of edge states moving in a non-disordered, hard-wall potential characterized, as above, by a single radius of curvature. They introduced the notion of a global adiabatic regime which exists at a sufficiently high magnetic field that scattering between edge states *induced by the curvature of the wall* is suppressed. Treating the case of a soft step with radius of curvature  $\rho$ , they find the critical field at which the scattering between all occupied edge states is suppressed,

$$B_{gl} = B^* [0.23 \ln(2\pi\rho/\lambda_F)]^{1/2} (\lambda_F/\rho), \quad (4)$$

where  $B^* = \hbar k_F^2/2e$  is a characteristic field related to Landau level depopulation. Applying this result to our stadium dot, we set  $\rho = \rho_{\min} = 0.22 \mu\text{m}$  in Eq. (4) and find  $B_{gl} = 1.3 \text{ T}$ . The characteristic field  $B_{gl}$  has a different physical significance than  $B_{sc}$  found above:  $B_{sc}$  indicates the field above which electrons move around the edges in skipping orbits, all cutting roughly equal areas;  $B_{gl}$  indicates the field above which electrons are not scattered from one edge state to another.

In the field range 1.2–1.4 T, we observe an interesting beating phenomenon which may be related to entering a global adiabatic regime. We speculate that in this region, two marginally independent edge states participate in transport, each giving rise to Aharonov–Bohm oscillations with differing periods. Periods differ because the edge states reside at different distances from the edge of the dot and, therefore, cut different areas. The region of interest is shown in Fig. 4a, along with the power spectrum of  $\delta g(B)$  (Fig. 4b) which covers the same field range as in Fig. 4a. In Section 5 we apply the analysis of CSG [22] to determine the approximate locations and Aharonov–Bohm frequencies of the edge channels, and find them to be roughly consistent with Fig. 4b. Fig. 4c shows similar beating observed in the circular quantum dot, also in the tunneling regime. In the case of the circle, the beating is

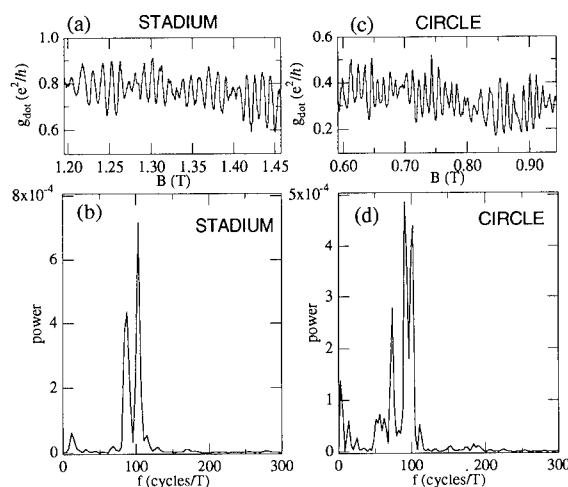


Fig. 4. (a) Beating between two frequencies in the stadium dot observed at  $B \approx 1.2$ –1.4 T, (b) the power spectrum (unaveraged FFT with Hann windowing) of the conductance fluctuations over the field range shown in (a). (c) Similar beating is also observed in a circular quantum dot [5] at lower fields than for the stadium. (d) The circle data show at least three distinct peaks in the power spectrum.

observed at a lower field,  $T \approx 0.6$ –0.9 T, and contains at least three distinct spectral components. We note that while the circle and stadium quantum dots investigated have roughly equal areas, the minimum radius of curvature for the circle is considerably larger,  $\rho_{\min}^{(\text{circle})} = 0.38$  and, correspondingly,  $B_{gl}^{(\text{circle})}$  is smaller. From Eq. (4), we estimate  $B_{gl}^{(\text{circle})} \approx 0.82$ , which is consistent with the range where beating is seen in the circle.

So far we have ignored the role of charging, despite the fact the tunneling regime is where Coulomb blockade effects are most important. We believe we can ignore charging in the data presented above for two reasons. First, we are sweeping magnetic field rather than gate voltage, so the total number of electrons within the dot is not changing. Second, we are still at relatively low fields, so the insulating barriers that prevent electrostatic equilibration *between* Landau levels are not very effective. On the other hand, if we wish to be more quantitative, for instance to find where in the dot edge states reside, we need to consider the electrostatics of the dot. This analysis will also allow us to estimate one more magnetic field scale which appears at yet higher fields than

considered above: the field at which the insulating regions between edge states become sufficiently large that *tunneling* between edge states (as opposed to scattering) is suppressed. At this characteristic scale, which we term  $B_{\text{Coul}}$ , individual bound edge states become electrically isolated and so are subject to Coulomb blockade.

### 5. Electrostatics of edge states in the stadium dot

In this section we apply the analysis of CSG [22] to the stadium dot and extract two quantities relevant to the data presented above. First, by considering the locations and corresponding areas of the set of edge states as a function of field, we estimate the expected frequencies of Aharonov–Bohm-like conductance oscillations associated with individual edge states. We then compare these estimates with the stadium power spectrum, Fig. 4b. Second, because CSG also derive an expression for the widths of the insulating regions between edge states, we can identify a field scale above which the insulating regions become wider than the magnetic length  $l_B =$

$(\hbar/eB)^{1/2}$ . We identify this field as  $B_{\text{Coul}}$ , the crossover field where tunneling between edge states becomes strongly suppressed.

CSG extend the one-electron model of edge channels by noting that near the edge of the 2DEG, the electron density profile  $n(x)$  is primarily determined by electrostatics of the confined electrons. Within this picture, the magnetic field acts as a perturbation of the zero-field charge distribution, with edge state locations determined accordingly. Furthermore, they treat the electrostatics problem self-consistently, so that regions with partially filled Landau levels act as metallic regions and screen potential gradients, while regions with integer filling factor act as insulating regions. These arguments are essentially those used by McEuen et al. [4] in their analysis of the addition spectrum of a small quantum dot in high fields. CSG define a length scale  $l = V_g \epsilon / 4\pi n_0 e$  characterizing the self-consistent density profile, and show that in zero field the density  $n(x)$  varies according to

$$n(x) = n_{\text{dot}} \left( \frac{x-l}{x+l} \right)^{1/2}, \quad (5)$$

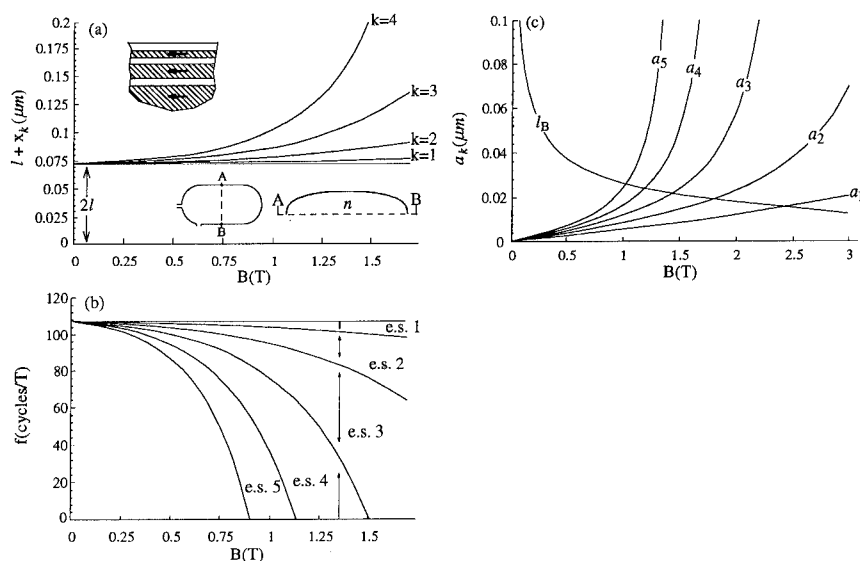


Fig. 5. (a) Distances  $l + x_k(B)$  between the gate and edge state borders. Upper inset shows edge state bands separated by insulating gaps; lower inset shows the zero-field density along the cut A–B, indicating the relative size of the depletion region and the density curvature, based on Eq. (5). (b) Aharonov–Bohm frequencies associated with edge state borders. (c) Widths of insulating regions  $a_k$  as a function of field for  $k = 1$ –5. Also shown is the magnetic length.  $B_{\text{Coul}}$  is defined by the condition  $a_1(B) = l_B$ .

saturating to the value  $n_{\text{dot}}$  at large distances from the edge. Using our experimental values  $V_g = -0.61$  V and  $n = n_{\text{dot}} = 3.6 \times 10^{11} \text{ cm}^{-2}$ , we find  $l = 37$  nm for our stadium dot. The depletion width, defined as the distance between the edge of the confining gate and the point where the electron density falls to zero is  $2l = 75$  nm.

In a magnetic field, electron states become quantized into Landau levels, each of which can hold a density of electrons  $n_L = 2B/\Phi_0 = 4.8 \times 10^{10} \text{ cm}^{-2} B[\text{T}]$  including spin degeneracy. At the edge of the 2DEG, a given Landau level becomes empty when the density at that position can be fully accommodated by lower Landau levels. Simple filling of Landau levels according to Eq. (5) gives the following expression for the locations  $x_k$  where the  $k$ th Landau level becomes depopulated,

$$x_k(B) = l \left( \frac{n_{\text{dot}}^2 + k^2 n_L^2}{n_{\text{dot}}^2 - k^2 n_L^2} \right). \quad (6)$$

The  $k + 1$ th edge state, according to this picture, thus consists of a band of finite width located between  $l + x_k(B)$  and  $l + x_{k+1}(B)$  from the gate edge. The field dependent area  $A_k(B)$  associated with the edge state boundary located a distance  $l + x_k(B)$  from the gate edge can be readily computed given the geometry of the dot. Then, by defining the phase  $\phi_k$  of an Aharonov–Bohm oscillation associated with the  $k$ th boundary as

$$\phi_k = 2\pi \frac{A_k(B)B}{\Phi_0}, \quad (7)$$

one may identify a field-dependent frequency  $f_k(B)$  associated with each edge state border given by  $f_k(B) = (2\pi)^{-1} d\phi_k/dB$ . We note that because the areas themselves depend on  $B$ , there will be a negative contribution to  $f_k(B)$ , reflecting the fact that as the field is increased the edge state borders move inward, a point which has been emphasized previously [1]. The calculated frequencies  $f_k(B)$  for  $k = 0-6$  are shown in Fig. 5b for the stadium dot. We propose that Aharonov–Bohm oscillations associated with the  $(k + 1)$ th edge state will contribute to the power spectrum of conductance fluctuations in a frequency band between  $f_k(B)$  and  $f_{k+1}(B)$ . Notice

that at  $B \approx 1.25$  T, where the number of occupied (spin-degenerate) Landau levels is  $\nu = n_{\text{dot}}/n_L \approx 6$ , only three edge states will contribute to the frequency spectrum in ranges that are fully separated from zero; above 1.5 T the third edge state as well intersects the zero-frequency axis. We observe that the two peaks in Fig. 4b are consistent with the theoretical frequencies associated with edge states (e.s.) 1 and 2. We cannot account for the structure of Fig. 4b in any great detail, however. For example, why the broad frequency band associated with edge state 3 is not seen is not understood, unless we speculate that edge state 3 is too far from the edges to couple to the leads. Indeed, for the circle, Fig. 4d, we see three strong peaks which may be associated with three edge states. This difference is reasonable given that the circle data is at a lower field than the stadium data, and so all edge states reside closer to the edge of the sample.

A competition between electrostatic energy and the energy scale  $\hbar\omega_c$  set by Landau level quantization causes insulating regions of thickness  $a_k(B)$  to form between edge state bands. In this insulating region, an integer number of Landau levels are occupied, making the electron gas incompressible. The width  $a_k(B)$  can be found by balancing the energy associated with moving an electron to a lower Landau level – an energy gain of  $\hbar\omega_c$  – against the energy cost of distorting the zero-field charge distribution. The resulting widths obtained by CSG, using boundary conditions appropriate for outer edge states (see comments following Eq. (19') in Ref. [22]), are

$$a_k^2(B) = \frac{4\hbar\omega_c\epsilon}{\pi^2 e^2 n'(x_k)}, \quad (8)$$

where  $n'(x_k)$  is the derivative  $dn(x)/dx$  evaluated at  $x_k(B)$  and  $\epsilon$  is the dielectric constant of the material. As the magnetic field increases, the insulating gaps become wider, with the inner gaps widening most quickly. The first five gap widths for the stadium dot as a function of magnetic field are shown in Fig. 5c. Also shown on the same scale is the magnetic length  $l_B$ . Ignoring the effects of disorder, a rough criterion for the value of magnetic field above which edge states become

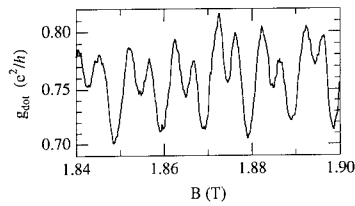


Fig. 6. Alternating peaks in conductance observed at higher field, a possible signature of Coulomb blockade of individual edge states.

electrically isolated from one another is the condition  $a_1(B) = l_B$ . We take this to define  $B_{\text{Coul}}$ , the field above which Coulomb blockade of bound edge states can operate. In our dot,  $B_{\text{Coul}} \approx 2.5$  T. We emphasize the approximate nature of this definition.

Finally, we note that at magnetic fields of  $\sim 1.9$  T we observe an interesting alternation in conductance oscillation peak heights, shown in Fig. 6. This behavior is not seen at lower fields or above this field up to  $\sim 2.2$  T. A similar effect has recently been reported by Sachrajda et al. [27] at somewhat higher fields,  $B \approx 3.4$  T. These authors attribute their alternating peak heights to charging effects, which they argue lead to a strict alternation of conduction via a pair of spin-split Landau levels. At present we do not know of a good picture to explain the alternation observed in Fig. 6 at these low fields. We speculate however, that such an effect may be attributable to charging effects, indicating that the spin-degenerate edge channels are behaving as effectively isolated islands.

In conclusion, we have investigated magneto-conductance fluctuations in a ballistic quantum dot at millikelvin temperatures in the low-to-intermediate magnetic field regime. The dot is connected to the bulk 2DEG via tunneling point contact leads. At low fields,  $B \lesssim 0.5$  T, we observe conductance fluctuations with an exponential power spectrum, similar to what is seen in quantum dots with multichannel point contact leads. At intermediate fields,  $B \approx 0.5$ – $2$  T, there is a crossover to periodic, and multiply periodic, conductance oscillations. To distinguish various regimes encountered along the way, we investigated three characteristic crossover fields:  $B_{\text{sc}}$ ,

above which the semiclassical electron trajectories within the structure change from chaotic to regular;  $B_{\text{gl}}$ , above which is the so-called global adiabatic regime, where scattering between edge states due to wall curvature is suppressed; and finally  $B_{\text{Coul}}$  above which tunneling between edge states is suppressed, making bound edge states susceptible to Coulomb blockade. For the stadium-shaped dot studied, these fields were found to be  $B_{\text{sc}} \approx 0.46$  T,  $B_{\text{gl}} \approx 1.3$  T, and  $B_{\text{Coul}} \approx 2.5$  T. We also used an electrostatic model of edge states [22] to calculate conductance oscillation frequencies for several edge states. These results were consistent with the experimentally observed multiply periodic conductance oscillations observed around  $B \approx 1.3$  T in the stadium dot. Finally, we speculated that an alternation in conductance peak height observed at  $B \approx 1.9$  T may indicate the onset of Coulomb blockade of individual confined edge states.

## 6. Acknowledgements

The authors thank B. Altshuler, A.T. Johnson, L. Kouwenhoven and P. McEuen for informative discussions. Research supported at Harvard by the ONR under N00014-89-J-1592 and N00014-89-J-1023 and the NSF under DMR-91-19386, and at UCSB by the AFOSR under 91-0214.

## 7. References

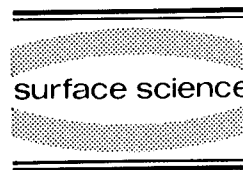
- [1] B.J. van Wees et al., Phys. Rev. Lett. 62 (1989) 2523.
- [2] L.P. Kouwenhoven et al., Phys. Rev. B 40 (1989) 8083.
- [3] P.L. McEuen et al., Phys. Rev. Lett. 66 (1991) 1926.
- [4] P.L. McEuen et al., Phys. Rev. B 45 (1992) 11419.
- [5] C.M. Marcus, A.J. Rimberg, R.M. Westervelt, P.F. Hopkins and A.C. Gossard, Phys. Rev. Lett. 69 (1992) 506.
- [6] B.W. Alphenaar et al., Phys. Rev. B 46 (1992) 7236.
- [7] R.P. Taylor, A.S. Sachrajda, P.T. Zawadzki, P.T. Coleridge and J.A. Adams, Phys. Rev. Lett. 69 (1992) 1989.
- [8] A.T. Johnson, L.P. Kouwenhoven, W. de Jong, N.C. van der Vaart and C.J.P.M. Harmans, Phys. Rev. Lett. 69 (1992) 1592.
- [9] B.L. Altshuler, JETP Lett. 41 (1985) 648.
- [10] R.A. Jalabert, A.D. Stone and Y. Alhassid, Phys. Rev. Lett. 68 (1992) 3468.

- [11] N. Argaman, Y. Imry and U. Smilansky, *Phys. Rev. B* 47 (1993) 4440.
- [12] B.L. Altshuler and B.I. Shklovskii, *Sov. Phys. JETP* 64 (1986) 127.
- [13] C.H. Lewenkopf and H.A. Weidenmüller, *Ann. Phys.* 212 (1991) 53.
- [14] W.J. Skocpol et al., *Phys. Rev. Lett.* 56 (1986) 2865.
- [15] A. Benoit, C.P. Umbach, R.B. Laibowitz and R.A. Webb, *Phys. Rev. Lett.* 58 (1987) 2343.
- [16] G. Timp, in: *Mesoscopic Phenomena in Solids*, Eds. B.L. Altshuler, P.A. Lee and R.A. Webb (Elsevier, New York, 1991).
- [17] B. Kramer, Ed., *Quantum Coherence in Mesoscopic Systems*, NATO ASI Series B, Vol. 254 (Plenum, New York, 1991).
- [18] R.A. Jalabert, H.U. Baranger and A.D. Stone, *Phys. Rev. Lett.* 65 (1990) 2442.
- [19] K. Nakamura and H. Ishio, *J. Phys. Soc. Jpn.* 61 (1992) 3939.
- [20] E.J. Heller, *Phys. Rev. Lett.* 53 (1984) 1515.
- [21] A.D. Stone, P.A. Mello, K.A. Muttalib and J. Pichard, in: *Mesoscopic Phenomena in Solids*, Eds. B.L. Altshuler, P.A. Lee and R.A. Webb (Elsevier, Amsterdam, 1991).
- [22] D.B. Chklovskii, B.I. Shklovskii and L.I. Glazman, *Phys. Rev. B* 46 (1992) 4026.
- [23] B.D. Simons and B.L. Altshuler, *Phys. Rev. Lett.* 70 (1993) 4063; V.N. Prigodin, K.B. Efetov and S. Iida, *Phys. Rev. Lett.* 71 (1993) 1230; B. Altshuler, personal communication.
- [24] M. Robnik and M.V. Berry, *J. Phys. A* 18 (1985) 1361.
- [25] U. Sivan, Y. Imry and C. Hartzstein, *Phys. Rev. B* 39 (1989) 1242.
- [26] L.I. Glazman and M. Jonson, *J. Phys. Condensed Matter* 1 (1989) 5547.
- [27] A.S. Sachrajda et al., to be published.



ELSEVIER

Surface Science 305 (1994) 490–494



## Universal fluctuation effects in chaotic quantum dots

A. Douglas Stone \*, Henrik Bruus

*Applied Physics, Yale University, P.O. Box 2157, New Haven, CT 06520, USA*

(Received 19 April 1993; accepted for publication 19 May 1993)

### Abstract

We show that quantum dots with classically chaotic dynamics exhibit universal quantum fluctuation effects in a number of physical properties. Specifically, the distribution of Coulomb blockade resonance amplitudes and the correlation function of the quantum dot energy levels with shape distortion have universal forms which are shown to agree well with numerical results from a billiard model of quantum dots. These universal statistical properties are experimentally accessible through transport and capacitance measurements of single dots; a clear experimental signature may be obtained by their sensitivity to a weak magnetic field. Integrable models for quantum dots are found to have non-universal statistical properties.

The analogy between semiconductor quantum dots and “artificial atoms” has been widely noted and has been the basis for various model calculations which include the effects of size quantization and Coulomb interactions. However, unlike natural atoms, the potential which confines the electrons within each quantum dot will vary from dot to dot due both to variations in the fabrication process leading to confinement and to the weak potential fluctuations arising from randomly located remote donors. Although these potential variations are small enough that treating these systems as short-range disordered (i.e. elastic mean free path smaller than sample size) is not realistic, they are likely to be large enough to generate chaotic classical motion for trapped electrons. It is now understood that there are strong similarities between the behavior of disordered quantum systems and simple quantum sys-

tems which are classically chaotic, and that therefore quantum-chaotic systems should exhibit many of the mesoscopic fluctuation effects characteristic of disordered system [1–5]. Quantum dots are of particular interest because they are *isolated* quantum systems with relatively large level-spacing  $\Delta\epsilon$  ( $\sim 0.05$  meV or  $\sim 500$  mK) and therefore can be studied in the regime  $kT < \Delta\epsilon$  where one expects the maximal effect due to quantum-chaotic fluctuations.

In fact there are many experimental measurements on single quantum dots which indicate the presence of such fluctuations. Three examples are: (1) The amplitude of the Coulomb-blockade (CB) oscillations fluctuates non-monotonically by as much as an order of magnitude between adjacent peaks [6–8]. (2) The amplitude pattern is completely rearranged in an apparently random (but reproducible) fashion by magnetic fields of order 20 mT [8,3]. (3) Recent capacitance measurements of the spectrum of single dots show non-monotonic variations as a function of mag-

\* Corresponding author.

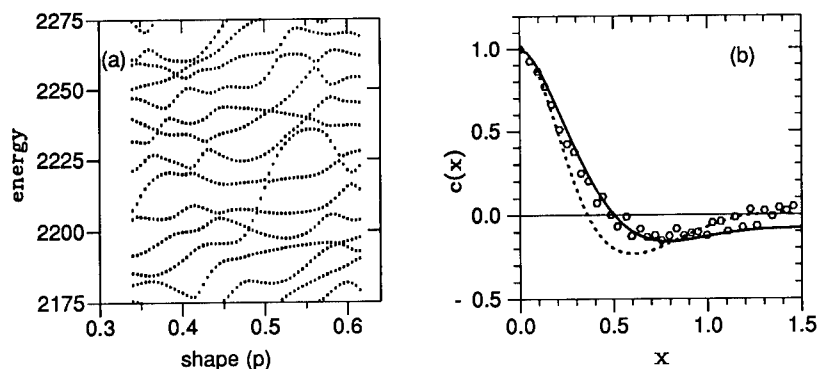


Fig. 1. Features of the 2d quantum dot with a hard-wall boundary given by  $w(z) = \cos(p)z + \sin(p)/\sqrt{2}z^2$ ,  $|z|=1$ . In (a) are shown the (even parity) energy levels 268 to 279 vs. shape parameter  $p$ . In (b) is shown the correlation function,  $c(x)$ , defined in Eq. (1). The full (broken) curve corresponds to the orthogonal (unitary) case. The open circles are our numerical results.

netic field not related to Landau level formation [9].

In earlier work, Jalabert et al. [2] used random-matrix theory to predict the distribution of CB amplitudes and tested their prediction by calculating transmission resonances through irregularly-shaped quantum dots. The model stud-

ied there had three disadvantages: First, the classical mechanics generated by the dot potential was essentially unknown, although undoubtedly chaotic. Second, no characterization of the spectrum in isolation was possible. And third, for technical reasons the time-reversal symmetry breaking transition predicted by the analytic the-

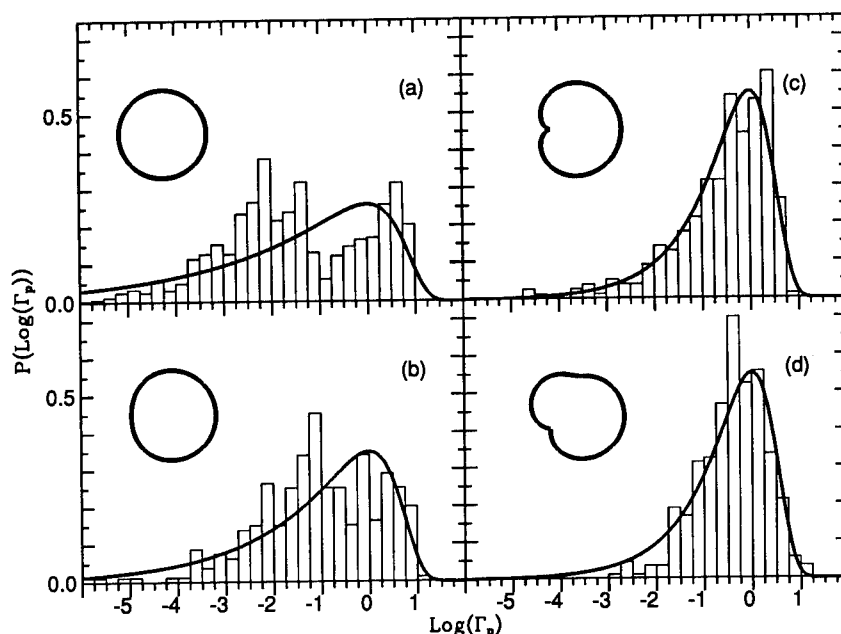


Fig. 2. The distribution of the partial decay width,  $\Gamma_p$ , for four different shapes of the quantum dot. Shown are histograms representing our numerical results,  $\chi^2$  distributions (full curves) serving as a guide for the eye ( $\nu = 0.33, 0.50, 1.00$ , and  $1.00$ , respectively), and as inserts the particular shapes of the dot. In (a), (b), and (c) we used the simple quadratic map with  $p = 0.0, 0.2$ , and  $0.5$ , respectively. In (d) we used the cubic map with  $\phi = \pi/3$ ,  $b = c = 0.2$ , and  $a = 0.913$ . In (a) the model is integrable, in (b) it is nearly integrable, and in both (c) and (d) it is fully chaotic.



ory was difficult to test quantitatively. Here we study a quantum billiard model [12–14] which corrects all of these deficiencies (although we need to introduce one further assumption to connect our results to scattering theory [3]).

The model we study consists of all two-dimensional infinite potential wells with boundaries given by the cubic conformal mapping  $w(z) = az + bz^2 + ce^{i\phi}z^3$  (where  $a, b, c$  are chosen to fix the area to the value  $\pi$ ). Often it suffices to set  $c = 0$  in which case  $a = \cos(p)$ ,  $b = \sin(p)/\sqrt{2}$  and  $p$  is the single parameter which varies the shape. The mapping is conformal for  $0 \leq p \leq 0.615$ . At  $p = 0$  we have a circular well with integrable classical motion (angular momentum is conserved) and Bessel function eigenstates. For  $p \approx 0.34$  the curvature at  $z = -1$  vanishes and the well begins to develop a concave region which leads to fully chaotic classical dynamics [12]. The shape of the well for four different parameter choices is shown in Fig. 2 (insets). The basic simplification of the model is that the Schrödinger equation for the energy levels of irregular billiards with non-zero  $p$ -values may be solved by a very efficient numerical procedure which exploits the change of variables defined by the inverse conformal transformation [13].

In Fig. 1 we plot typical high energy levels as function of shape. Note the rapid pseudo-random oscillations for very small shape distortions. We can characterize this fluctuating spectrum by the correlation function of the derivatives of the energy levels with respect to  $p$ . Recent work [5,10] indicates that when properly rescaled this type of correlation function has a universal form in chaotic quantum systems. Defining  $C(0) = \langle ([\partial\epsilon/\partial p](1/\Delta\epsilon))^2 \rangle$  and  $x = \sqrt{C(0)}p$  the rescaled correlation function takes the form

$$c(x) = \left\langle \frac{\partial\epsilon_i(\bar{x}+x)}{\partial\bar{x}} \frac{\partial\epsilon_i(\bar{x})}{\partial\bar{x}} \frac{1}{\Delta\epsilon^2} \right\rangle. \quad (1)$$

We find good agreement with the behavior obtained from disordered quantum dots for the first few correlation lengths and then a substantial deviation as seen in other work [5,10]. It follows from the rescaling that the correlation “length” in shape is just  $p_c \approx 1/\sqrt{C(0)}$ .  $p_c$  decreases with increasing energy as expected due to the shorten-

ing of the electron wavelength. The strong dependence of the energy levels on shape has implications for the properties of quantum dot arrays. Since there is likely to be significant shape variation between dots one does not expect the formation of superlattice bands due to the random mismatch of energy levels on adjacent dots. In fact no such band-formation effects were observed in recent experiments [11] at zero or low magnetic field; it is only at fields  $B > 2$  T that the mini-gaps appeared due to the formation of narrow Landau bands. Thus our results suggest that quantum dots are not in general well-described as identical “artificial atoms”.

Not only will the spectrum of quantum dots fluctuate with shape (or magnetic field) but the probability density of the eigenstates of a given dot will fluctuate from level to level. We attribute the CB amplitude fluctuations to spatial fluctuations in the probability density of the quasi-bound states [2]. In the regime  $\bar{\Gamma} < kT < \Delta\epsilon < e^2/C$ , (where  $\bar{\Gamma}$  is the mean level width and  $e^2/C$  is the charging energy) a single level controls each Coulomb blockade peak [15,16] and large amplitude fluctuations are observed. Due to thermal broadening the width of all CB peaks are  $\sim kT$ , whereas the amplitude [16] is given by

$$g_{\max} = \frac{e^2/h}{4\pi kT} \frac{\Gamma_{\lambda}^{\ell}\Gamma_{\lambda}^r}{(\Gamma_{\lambda}^{\ell} + \Gamma_{\lambda}^r)} = \frac{e^2}{4\pi h} \frac{\bar{\Gamma}}{kT} \alpha_{\lambda}, \quad (2)$$

where  $\Gamma_{\lambda} = \Gamma_{\lambda}^{\ell} + \Gamma_{\lambda}^r$  is the total decay width for level  $\lambda$  and  $\Gamma_{\lambda}^{\ell}, \Gamma_{\lambda}^r$  are the partial decay widths into the right and left leads. The factor  $\alpha_{\lambda}$  in Eq. (2) is a dimensionless measure of the *area* under the  $T = 0$  resonance, hence the observed amplitude fluctuations reflect the fluctuations in these areas.

It is possible using the  $R$ -matrix theory developed for compound nuclear scattering [17] to express the level widths of Eq. (2) in terms of states  $X_{\lambda}(x, y)$  of the dot in isolation (with appropriate boundary conditions); details are given elsewhere [4,3]. We assume that the resonance wavefunctions  $X_{\lambda}$  are described by the orthogonal random-matrix ensemble when time-reversal symmetry is present ( $B = 0$ ) and by the unitary random-matrix ensemble when TR is broken (suf-

ficiently high magnetic field). We note that this assumption should be reasonable even in the presence of strong interactions as long as one applies it to the self-consistent single-particle states, as is done, e.g., when analyzing shell model calculations of the nucleus. If  $X_\lambda$  are described by random-matrix theory then the distribution of partial widths  $\Gamma_p$  should have a  $\chi^2_\nu$  distribution with  $\nu = 1, 2$  degrees of freedom [2]. This distribution should be universal in the chaotic regime, i.e. two different shapes both of which generate chaotic classical dynamics should have the same distribution of level widths (even though the individual levels are quite different (see Fig. 1)). However, if the system approaches integrability then non-universal distributions differing from  $\chi^2$  should arise. Precisely this behavior is confirmed by numerical calculations of the partial width distribution for the conformal billiard model as seen in Fig. 2, where only the fully chaotic models (c) and (d) fit a  $\chi^2_{\nu=1}$  distribution reasonably well.

Having confirmed that random matrix theory works well in the chaotic regime, one can derive [2,4] from this ansatz the probability density  $\mathcal{P}_\nu(\alpha)$ , where  $\nu = 2$  for the orthogonal case and  $\nu = 4$  for the unitary case. One finds

$$\mathcal{P}_2(\alpha) = \sqrt{\frac{2}{\pi\alpha}} e^{-2\alpha} \quad (3)$$

$$\mathcal{P}_4(\alpha) = 2 e^{-4\alpha} \int_0^\infty dz e^{-z} \sqrt{\frac{z+4\alpha}{z}}. \quad (4)$$

$\mathcal{P}_2$  and  $\mathcal{P}_4$  are plotted in Fig. 3 where they are compared to numerical data obtained by evaluating  $\alpha$  for the wavefunctions of the conformal model for the case  $\nu = 2, 4$ . The time-reversal symmetry-breaking needed to study  $\nu = 4$  is achieved by adding an Aharonov–Bohm flux to the center of the quantum dot [14]. Note the substantial suppression of small peak amplitudes caused by breaking TR symmetry. This reduces substantially the variance of  $\alpha$ , and from Eqs. (3) and (4) one finds  $\Delta\alpha_4^2/\Delta\alpha_2^2 = 32/45 \approx 0.71$ .

If this suppression of CB amplitude fluctuations due to TR symmetry breaking is to be observable the magnetic field necessary to induce the TR transition be small compared to that needed for Landau level formation. Landau level formation strongly suppresses the fluctuations [8]; the classical analogue of this effect is the suppression of chaos by the formation of stable skipping orbits. Adapting arguments by Berry and Robnik [14,3], we find that the flux,  $\Phi_c$ , needed to break TR symmetry for a dot of area  $A$  is  $\Phi_c \approx (\hbar v_F/\Delta\epsilon\sqrt{A})^{-1/2}\hbar/e$ . In the experimental systems of interest this corresponds to a field of order a few times 10 mT, much smaller than that needed for edge-state formation. Thus the statistical effect of time-reversal symmetry breaking predicted by our theory should be observable experimentally by making histograms of the amplitudes as a function of magnetic field. It is hoped that careful experimental tests of this type will be performed in the near future.

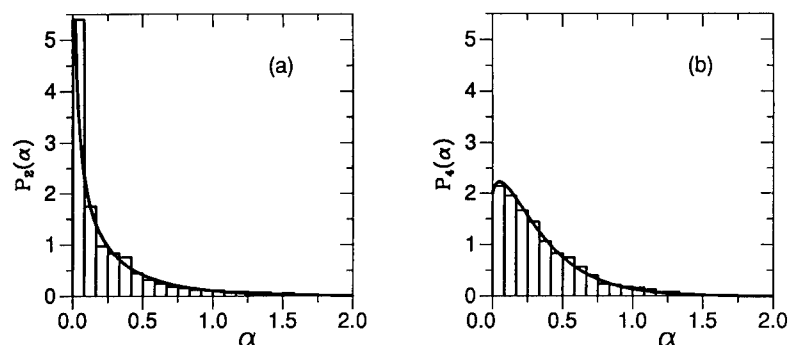


Fig. 3. Predicted distribution of peak amplitudes  $\alpha$  in the presence of time-reversal symmetry (a) and absence (b), compared to the numerically generated amplitudes obtained from the cubic model in the fully chaotic case (same shape as in Fig. 2d).

A.D.S. gratefully acknowledges the contributions of his earlier collaborators R.A. Jalabert and Y. Alhassid. H.B. is supported by Grant No. 11-9454 from the Danish Natural Science Research Council. We want to thank B. Simons for helpful conversations and for sharing the numerical curves in Fig. 1b. This work was partially supported by ARO grant DAAH04-93-G-0009.

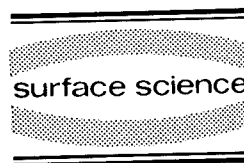
## 1. References

- [1] R.A. Jalabert, H.U. Baranger and A.D. Stone, *Phys. Rev. Lett.* 65 (1990) 2442.
- [2] R.A. Jalabert, A.D. Stone and Y. Alhassid, *Phys. Rev. Lett.* 68 (1992) 3468.
- [3] A.D. Stone and H. Bruus, *Physica B* 189 (1993) 43.
- [4] A.D. Stone, R.A. Jalabert and Y. Alhassid, in: Springer Series in Solid-State Sciences, Vol. 109, Eds. H. Fukuyama and T. Ando (Springer, Berlin, 1992) p. 39.
- [5] A. Szafer and B. Altshuler, *Phys. Rev. Lett.* 70 (1993) 587.
- [6] U. Meirav, M.A. Kastner and S.J. Wind, *Phys. Rev. Lett.* 65 (1990) 771.
- [7] L.P. Kouwenhoven et al., *Z. Phys. B* 85 (1991) 367.
- [8] E. Foxman, P. McEuen, M. Kastner, U. Meirav and S. Wind, unpublished.
- [9] R. Ashoori et al., *Physica B* 189 (1993) 117.
- [10] B. Simons and B.L. Altshuler, *Phys. Rev. Lett.* 70 (1993) 4063.
- [11] L.P. Kouwenhoven et al., *Phys. Rev. Lett.* 65 (1990) 361.
- [12] M. Robnik, *J. Phys. A* 16 (1983) 3971.
- [13] M. Robnik, *J. Phys. A* 17 (1983) 1049.
- [14] M.V. Berry and M. Robnik, *J. Phys. A* 19 (1984) 649.
- [15] Y. Meir, N. Wingreen and P.A. Lee, *Phys. Rev. Lett.* 66 (1991) 3048.
- [16] C.W.J. Beenakker, *Phys. Rev. B* 44 (1991) 1646.
- [17] A.M. Lane and R.G. Thomas, *Rev. Mod. Phys.* 30 (1958) 257.



ELSEVIER

Surface Science 305 (1994) 495–500



## Weak localization and conductance fluctuations in a chaotic quantum dot

M.J. Berry <sup>\*,a</sup>, J.A. Katine <sup>a</sup>, C.M. Marcus <sup>b</sup>, R.M. Westervelt <sup>a,c</sup>, A.C. Gossard <sup>c</sup>

<sup>a</sup> Department of Physics and Division of Applied Sciences, Harvard University, Cambridge, MA 02138, USA

<sup>b</sup> Department of Physics, Stanford University, Stanford, CA 94305, USA

<sup>c</sup> Materials Department, University of California, Santa Barbara, CA 93106, USA

(Received 22 April 1993; accepted for publication 4 June 1993)

### Abstract

We report detailed measurements of reproducible, aperiodic fluctuations in the magnetoconductance of a submicron, stadium-shaped quantum dot with quantum point contacts. We study the prominent dip at  $B = 0$  that is associated with a ballistic analog of the weak localization effect, and find its properties to be in agreement with semiclassical arguments.

Theorists have long been fascinated by the quantum mechanical limit of classically chaotic systems – a field known as quantum chaos [1]. Chaotic scattering and its connection to random matrix theory has been studied in nuclear and atomic physics [2]. Recently, mesoscopic conductance fluctuations have been recognized as manifestations of quantum chaos [3–6]. Advances in precision, submicron electron beam lithography have made it possible to fabricate devices in which electrons travel ballistically at low temperatures and maintain their phase coherence over distances larger than the device size [7]. These devices have exhibited many novel transport features associated with classical trajectories [8–11]. Marcus et al. [8] studied transport in a chaotically-shaped billiard and have found signatures of

chaotic scattering and quantum interference in conductance fluctuations. These signatures are predicted in recent semiclassical theories [4,5]. In this approach, the conductance through the billiard is calculated with the Landauer formula,  $G = e^2/h \text{Tr}[t * t]$ , where the complex transmission matrix,  $t_{mn}$ , is evaluated by summing the semiclassical Green function for all trajectories in the billiard that connect incoming mode  $m$  to outgoing mode  $n$ .

In this paper, we present experimental data with reproducible, aperiodic fluctuations and a prominent zero field dip in the low temperature ( $T = 0.15$  K to  $T = 4.2$  K) magnetoconductance of a stadium-shaped quantum dot. A conductance dip at  $B = 0$  arises from the coherent backscattering of time reversed pairs of trajectories each starting and ending in the same transverse mode of one of the two contacts, analogous to the weak localization effect [12]. Weak localization in bal-

\* Corresponding author.

listic microstructures, reported by Marcus et al. [8], is distinct from two-dimensional weak localization, because trajectories bounce from the stadium walls, rather than diffuse in a disordered potential. The theory of weak localization in ballistic microstructures is an interesting topic of current research, having important differences from the traditional theory of weak localization in the bulk; see Baranger et al. [5]. The characteristic magnetic field necessary to destroy the zero field dip is determined by the typical area that paths enclose before they dephase or leave the billiard: constructive interference is lost when a fraction of a flux quantum threads this area. The magnetoconductance dip evolves smoothly in temperature. Superimposed upon the  $B = 0$  conductance dip are fluctuations that arise from quantum interference between all paths other than those returning to their starting mode. These fluctuations, which also appear away from  $B = 0$ , rearrange dramatically as the coupling into the stadium is varied; their root mean squared amplitude grows with increasing average conductance and is smaller than universal conductance fluctuations [13].

The experiment was carried out using a GaAs/Al<sub>0.3</sub>Ga<sub>0.7</sub>As heterostructure containing a near surface 2D electron gas (depth = 420 Å). The gas has a sheet density  $n_s = 4.4 \times 10^{11} \text{ cm}^{-2}$  and mobility  $\mu = 350\,000 \text{ cm}^2/\text{V} \cdot \text{s}$ , giving a mean free path,  $l = 3.8 \text{ } \mu\text{m}$ . It is important to use a near surface gas because we want the lithographic shape of our dot to be most nearly reflected in the shape of the equipotential contours at the electron gas. Gates are patterned with electron beam lithography and Cr/Au metallization. The gas under the gates was depleted by a negative voltage bias, forming a stadium-shaped region of electron gas that electrons are forced to travel through. We vary the magnetic field perpendicular to the plane of the gas and measure the magnetoresistance with standard ac lock-in techniques, using  $I_{\text{bias}} = 1 \text{ nA}$  and  $f = 11 \text{ Hz}$ . The sample was cooled first in a  $^3\text{He}$  cryostat, then in a dilution refrigerator for the lowest temperatures.

An electron micrograph of the stadium is shown in Fig. 1. The lithographic size is  $1.3$

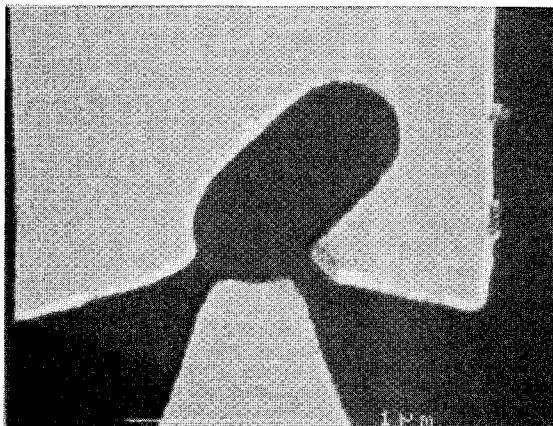


Fig. 1. Electron micrograph of the stadium at 35 000 X (length bar =  $1 \text{ } \mu\text{m}$ ). Bright regions are metallic gates, dark regions are the GaAs surface. Quantum point contacts are at a  $90^\circ$  angle to each other to avoid direct transmission.

$\mu\text{m} \times 0.6 \text{ } \mu\text{m}$ . After subtracting a depletion width of 65 nm [14], the area is  $0.55 \text{ } \mu\text{m}^2$ . The dimensions are much larger than the Fermi wavelength ( $\lambda_F = (2\pi/n_s)^{1/2} = 38 \text{ nm}$ ), so that the semiclassical picture is appropriate inside the stadium. The point contacts have lithographic width  $\sim 190 \text{ nm}$  and contain up to six transverse modes when the gas is depleted under the gate.

There are two important characteristic fields. The first,  $B_\phi$ , occurs when a flux quantum threads the area of the device,  $B_\phi = \Phi_0/(\text{area}) \approx 8 \text{ mT}$ . The second,  $B_{\text{cyc}}$ , is the field at which the cyclotron radius equals the radius of curvature of the stadium,  $B_{\text{cyc}} = \Phi_0/(\lambda_F \text{ radius}) \approx 0.4 \text{ T}$ . This separation in characteristic fields allows us to effectively ignore the bending of trajectories at small fields,  $B \ll B_{\text{cyc}}$ , and only consider magnetic field dependence through the Aharonov–Bohm phase. The phase coherence time was measured with a split gate technique [15] on an adjacent sample from the same wafer at  $T = 1.5 \text{ K}$ , giving a value of  $\tau_\phi \approx 33 \text{ ps}$ . Trajectories with lengths up to the ballistic phase breaking length,  $l_\phi \equiv v_F \tau_\phi \approx 10 \text{ } \mu\text{m}$ , contribute to quantum interference, indicating that paths undergo many bounces before losing coherence.

Plotted in Fig. 2 are four consecutive magnetoresistance sweeps on the stadium at  $T = 1.5 \text{ K}$ .

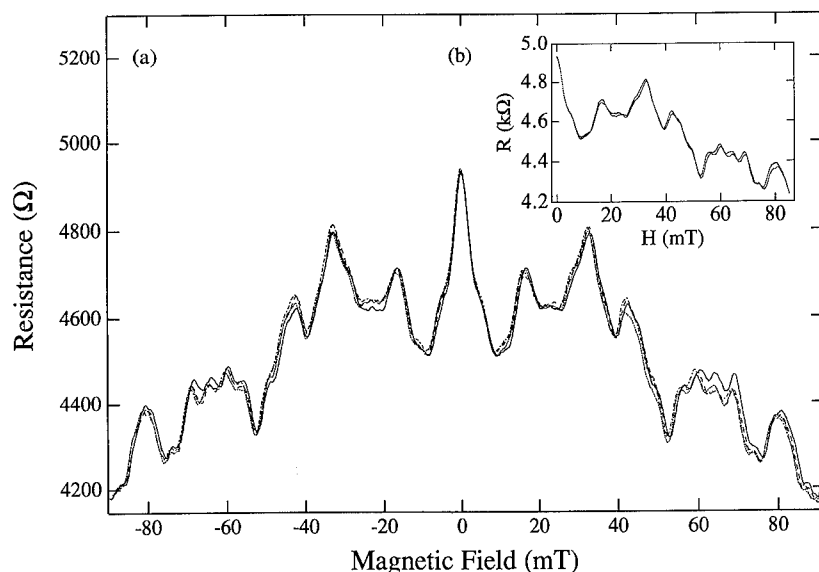


Fig. 2. (a) Four consecutive magnetoresistance sweeps on the stadium at  $T = 1.5$  K. (b) Magnetoresistance at both  $+B$  and  $-B$  plotted vs.  $|B|$ , showing approximate two-probe symmetry.

They show a prominent zero field resistance peak and symmetric, aperiodic fluctuations around that peak. The zero field peak is associated with a ballistic analog of the weak localization effect, while the conductance fluctuations are due to statistical variations in quantum interference between paths which do not return to their originating contact mode. The conductance fluctuations reproduce over four consecutive sweeps and remain stable until the temperature is cycled – even cycling the gate voltage does not effect them. We swept the gate voltage at  $B = 0$  and found that the conductance had several plateaus due to quantization in the point contacts. Because the gate voltage sweep simultaneously changes the width of both point contacts, we did not necessarily expect the sweep to have plateaus. If we assume that the resistance of the two point contacts adds in series [16], we can infer that the data shown here was taken on a conductance plateau corresponding to approximately five transverse modes ( $G \approx 10 e^2/h$ ) in each lead. In the inset, one of the four magnetoresistance sweeps is folded over with negative  $B$  plotted versus  $|B|$ . The plot shows that the magnetore-

sistance is even in  $B$ , as expected for two-probe symmetry. The small deviations arise in the wide regions of the electron gas because four indium contacts are used to measure resistance.

The temperature dependence of the conductance fluctuations is shown in Fig. 3. The curves have been converted to conductance, so that the zero field feature now appears as a dip. The stadium was biased on another plateau in the point contact characteristic corresponding to approximately three modes in each lead. The temperature was varied from  $T = 1.50$  K to  $T = 4.25$  K in eleven logarithmically spaced steps. The conductance fluctuations evolve smoothly in temperature, with the zero field dip dropping monotonically as temperature is lowered.

Semiclassical analysis by Baranger et al. [5] predicts that the zero field dip is a Lorentzian, so we fit to this functional form. A typical curve fit is shown in Fig. 3b. Some error is introduced by conductance fluctuations superimposed upon the  $B = 0$  dip as discussed above. Plotted in Fig. 4 are the height  $\Delta\sigma_0$  and width  $B_c$  (half width half maximum) of the dip, which were taken from the curve fit parameters at each temperature. The

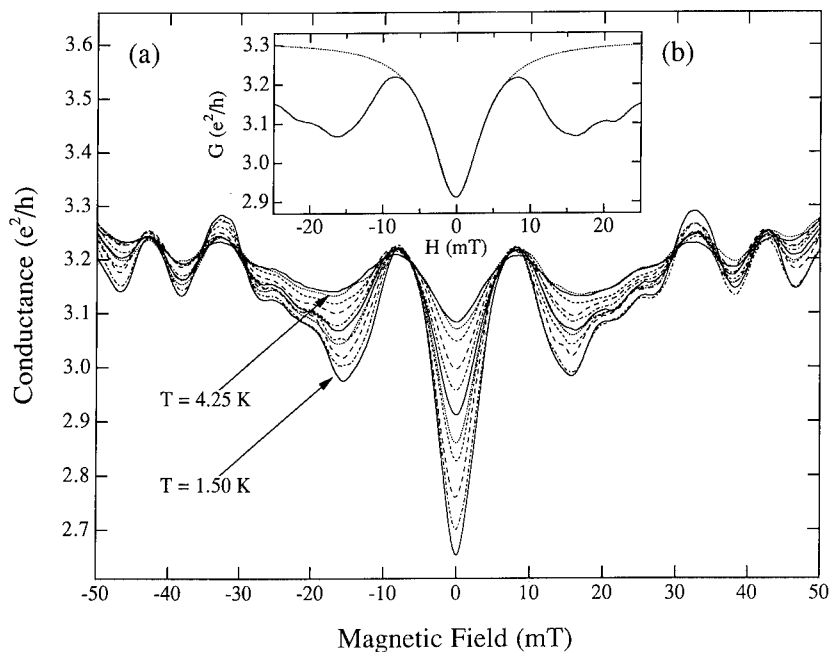


Fig. 3. (a) Magnetoconductance for 11 different temperatures logarithmically spaced in the interval  $T = 1.50$  K to  $T = 4.25$  K. (b) Lorentzian curve fit (dashed) to the zero field conductivity dip at  $T = 2.55$  K (solid).

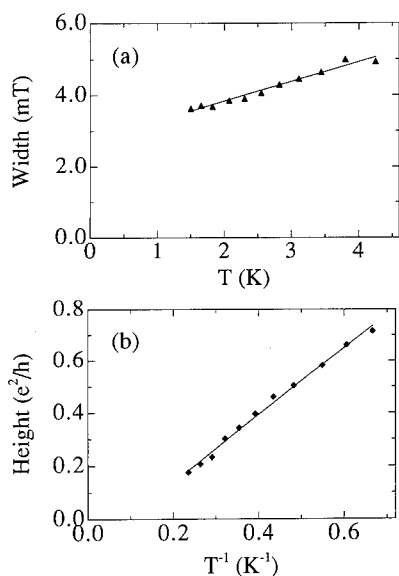


Fig. 4. (a) Width ( $B_c$ ) vs.  $T$ . (b) Height ( $\Delta\sigma_0$ ) vs.  $T^{-1}$ . Taken from  $g(B) = g(0) - \Delta\sigma_0 / [1 + (B/B_c)^2]$ . Error bars ( $\delta B_c \approx 1\%$ ,  $\delta\sigma_0 \approx 0.5\%$ ) not visible on this scale.

height grows by a factor of four between  $T = 4.25$  K and  $T = 1.50$  K, varying as  $\Delta\sigma_0 \propto 1/T$ . The width  $B_c = 3.6$  to  $5.0$  mT is less sensitive to temperature, as shown.

Semiclassical arguments predict that the zero field dip should get taller and narrow slightly at low temperature. The characteristic area enclosed by pairs of time reversed paths returning to their originating mode is not the device area – it instead depends on the distribution of closed trajectory areas which remain coherent inside the stadium. The stadium shape is convenient, because classical trajectories inside it are highly chaotic; their initial direction being randomized after only a few bounces off of the walls [17]. The distribution of trajectory areas is approximately given by a simple exponential:  $N(A) \approx \exp(-2\pi\alpha|A|)$ , with only one parameter,  $\alpha$  [4,18]. The characteristic area  $(2\pi\alpha)^{-1}$  is finite, because trajectories only remain on the stadium for a finite time before exiting or losing their

phase. Temperature alters quantum interference in two ways. First, finite temperature truncates the distribution of trajectory lengths at the phase breaking length ( $l_\phi$ ), shifting the characteristic area to a smaller value [19]. Second, thermal broadening of the Fermi surface damps conductance fluctuations. Weak localization is less sensitive to thermal smearing, because each time reversed pair of paths contributes to the zero field conductance dip [7].

The height  $\Delta\sigma_0$  of the zero field feature is expected to be proportional to the fraction of time reversed pairs returning to the origin which remain phase coherent. This fraction increases as temperature is lowered. The width  $B_c$  depends directly on the characteristic area  $(2\pi\alpha)^{-1}$ . But unlike the bulk theory,  $B_c$  cannot increase indefinitely because it is rare to find backscattering paths whose area is much smaller than the stadium area. This effect puts an upper limit on  $B_c$  and prevents it from changing rapidly in temperature. These semiclassical arguments are consistent with the measured data if we assume a power law dependence for the phase breaking rate [20]. In contrast, the traditional weak localization theory predicts a weaker and much narrower peak with its width of  $\sim 0.04$  mT [12].

Finally, we examine the statistics of conductance fluctuations. The rms fluctuation,  $\langle(\delta G)^2\rangle^{1/2}$ , at  $T = 1.5$  K (squares) and  $T = 0.15$  K (circles) is plotted versus the average conductance,  $\langle G \rangle$  in Fig. 5a. A third order polynomial background was first subtracted from the magnetoconductance data to remove the slow trend evident in Fig. 2 [8]. While  $G_{\text{rms}}$  at high temperature was rather insensitive to the analysis technique,  $G_{\text{rms}}$  at low temperature varied by  $\sim 20\%$  depending on the background subtraction scheme. The rms fluctuation increases monotonically with average conductance, reaching a maximum value of  $0.35 e^2/h$  with roughly six transverse modes in the leads. The data for both temperatures have not yet reached UCF amplitude [13] at the largest  $G_{\text{ave}}$ . The high temperature data extrapolate to  $G_{\text{rms}} = 0$  at zero conductance. However, at low temperature the intercept is  $0.1 e^2/h$ , implying that the rms fluctuation must drop steeply in the tunneling regime ( $G_{\text{ave}} < 1$ ).

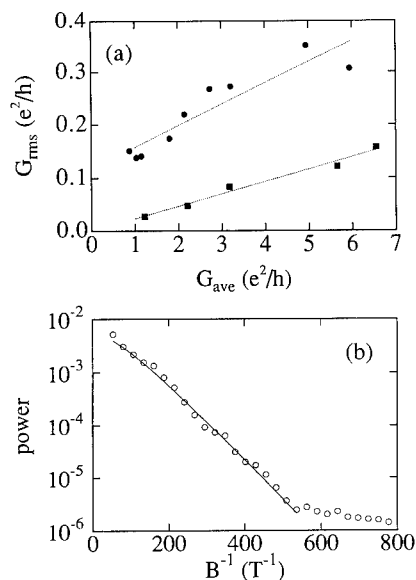


Fig. 5. (a) Root mean square conductance fluctuation ( $G_{\text{rms}}$ ) vs. average conductance ( $G_{\text{ave}}$ ) at  $T = 1.5$  K (square) and  $T = 0.15$  K (circle) with linear fits (dashed) drawn as a guide to the eye. (b) Fit to the averaged power spectrum of the conductance fluctuations vs.  $1/B$ .

The power spectrum of the conductance fluctuations versus  $1/B$  is shown in Fig. 5b at  $T = 0.15$  K. To obtain the statistical behavior of the fluctuations, we average 15 overlapping power spectra in the field range  $|B| = 0.05$  to  $0.30$  T [8]. Assuming that the distribution of trajectory areas is the same over our field range, the power spectrum equals the Fourier transform of the magnetic field autocorrelation function [4,8]

$$S(f) = S_0(1 + 2\pi f\alpha\Phi_0) \exp(-2\pi f\alpha\Phi_0),$$

where  $f$  is expressed in cycles/T. The data fit this form reasonably well over three orders of magnitude in power, giving a value of  $(2\pi\alpha)^{-1} = 0.21 \mu\text{m}^2$ , which is  $\sim 0.4$  times the device area. Periodic orbits inside the stadium typically have areas roughly half the device area or less [8]. If we assume that the characteristic area for time reversed paths returning to the same contact mode is the same as for all paths, we can compare the characteristic field implied by this value of  $\alpha$  [5],  $B_c = \alpha\Phi_0/2 = 1.5$  mT, to the experimental width of the  $B = 0$  conductance dip. The



measured width at  $T = 0.15$  K is 2.2 mT, indicating approximate agreement.

The authors thank J.H. Baskey, S.H. Yang, and D.J. Mar for assistance in carrying out the measurements, P.F. Hopkins for help in sample fabrication, and H.U. Baranger for useful discussions. The work at Harvard was supported in part by the ONR under N00014-89-J-1592 and the NSF under DMR-91-19386, and at UCSB by the AFOSR under 91-0214; one of us (M.J.B.) acknowledges support from the NSF and one of us (R.M.W.) acknowledges support from the Center for Quantized Electronic Structures and the Institute for Theoretical Physics at UCSB.

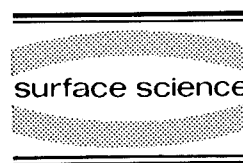
## 1. References

- [1] M.C. Gutzwiller, *Chaos in Classical and Quantum Mechanics* (Springer, New York, 1990), and references therein.
- [2] T.A. Brody, J. Flores, J.B. French, P.A. Mello, A. Pandey and S.S. Wong, *Rev. Mod. Phys.* 53 (1981) 385; *Irregular Atomic Systems and Quantum Chaos*, Ed. J.C. Gay (Gordon and Breach, London, 1992).
- [3] M. Robnik and M.V. Berry, *J. Phys. A* 18 (1985) 1361; M.C. Gutzwiller, *J. Math. Phys.* 12 (1971) 343; E. Doron, U. Smilansky and A. Frenkel, *Physica D* 50 (1991) 367; E.J. Heller, *Phys. Rev. Lett.* 53 (1984) 1515.
- [4] R.A. Jalabert, H.U. Baranger and A.D. Stone, *Phys. Rev. Lett.* 65 (1990) 2442.
- [5] H.U. Baranger, R.A. Jalabert and A.D. Stone, in: *Transport Phenomena in Mesoscopic Systems*, Eds. H. Fukuyama and T. Ando (Springer, New York, 1992). The authors find that off-diagonal terms make a significant contribution to the magneto-resistance, resulting in a net effect that is smaller than that predicted by coherent backscattering alone.
- [6] R.V. Jensen, *Chaos* 1 (1991) 101.
- [7] C.W.J. Beenakker and H. van Houten, in: *Solid State Physics*, Vol. 44, Eds. H. Ehrenreich and D. Turnbull (Academic Press, San Diego, CA, 1991), and references therein.
- [8] C.M. Marcus, A.J. Rimberg, R.M. Westervelt, P.F. Hopkins and A.C. Gossard, *Phys. Rev. Lett.* 69 (1992) 506.
- [9] M.L. Roukes, A. Scherer, S.J. Allen, H.G. Craighead, R.M. Ruthen, E.D. Beebe and J.P. Harbison, *Phys. Rev. Lett.* 59 (1988) 3011; C.J.B. Ford, S. Washburn, M. Büttiker, C.M. Knoedler and J.M. Hong, *Phys. Rev. Lett.* 62 (1989) 2724; G. Timp, A.M. Chang, P. Makiewich, R. Behringer, J.E. Cunningham, T.Y. Chang and R.E. Howard, *Phys. Rev. Lett.* 59 (1987) 732.
- [10] D. Weiss, M.L. Roukes, A. Menschig, P. Grambow, K. von Klitzing and G. Weiman, *Phys. Rev. Lett.* 66 (1991) 2790; A. Lorke, J.P. Kotthaus and K. Ploog, *Phys. Rev. B* 44 (1991) 3447.
- [11] H.J. Stöckmann and J. Stein, *Phys. Rev. Lett.* 64 (1990) 2215; E. Doron, U. Smilansky and A. Frenkel, *Phys. Rev. Lett.* 65 (1990) 3072.
- [12] S. Chakravarty and A. Schmid, *Phys. Rep.* 140 (1986) 193; G. Bergmann, *Phys. Rep.* 107 (1984) 1.
- [13] B.L. Altshuler, *JETP Lett.* 41 (1985) 648; P.A. Lee and A.D. Stone, *Phys. Rev. Lett.* 55 (1985) 1622.
- [14] Determined from the difference between the lithographic width (190 nm) and the electron gas width ( $W = 3\lambda_F/2 \approx 60$  nm) with 3 transverse modes in the point contacts.
- [15] M.J. Berry, J.A. Katine, R.M. Westervelt and A.C. Gossard, to be published; data were analyzed in the limits channel width  $W < l$  and  $h/2\pi eB > Wl$  [7].
- [16] L.P. Kouwenhoven, B.J. van Wees, W. Kool, C.J.P.M. Harmans, A.A.M. Staring and C.T. Foxon, *Phys. Rev. B* 40 (1989) 8083; we also must assume that both point contacts are on the same plateau.
- [17] Bennetin and Strelcyn, *Phys. Rev. A* 17 (1978) 773; this result is for a closed stadium.
- [18] The exponential form for  $N(A)$  breaks down at small areas even in the absence of disorder.
- [19] C.M. Marcus, R.M. Westervelt, P.F. Hopkins and A.C. Gossard, *Phys. Rev. B* 48 (1993) 2460.
- [20] K.K. Choi, D.C. Tsui and K. Alavi, *Phys. Rev. B* 36 (1987) 7751; the phase breaking rate has a crossover at  $T_0 = h/2\pi k\tau = 0.6$  K:  $\tau_\phi^{-1} \propto T^2 \ln T$  for  $T > T_0$  and  $\tau_\phi^{-1} \propto T$  for  $T < T_0$ .



ELSEVIER

Surface Science 305 (1994) 501–506



## Magnetotransport in a chaotic scattering cavity with tunable electron density

M.W. Keller <sup>\*,a</sup>, O. Millo <sup>1,a</sup>, A. Mittal <sup>a</sup>, D.E. Prober <sup>a</sup>, R.N. Sacks <sup>b</sup>

<sup>a</sup> Department of Applied Physics, Yale University, New Haven, CT 06520-2157, USA

<sup>b</sup> United Technologies Research Center, East Hartford, CT 06108, USA

(Received 19 April 1993; accepted for publication 18 June 1993)

### Abstract

We have measured the resistance versus magnetic field and Fermi energy for two stadium-shaped cavities in which chaotic scattering is expected. We fit the power spectra of the magnetoresistance fluctuations to semiclassical chaotic scattering theory and find a characteristic field which scales with cavity dimensions as predicted by classical simulations. Measurements of conductance versus Fermi energy indicate a significant contribution from short, non-chaotic paths. We have also studied the energy-averaged conductance as a function of magnetic field. We observe a ballistic weak localization effect similar to that predicted by recent calculations.

### 1. Introduction

The 2D electron gas of a clean GaAs/AlGaAs heterostructure can be confined to a cavity small enough that large angle elastic scattering is dominated by the walls rather than random impurities. At temperatures of about 0.1 K, inelastic scattering is weak enough that electrons can traverse a 1  $\mu\text{m}$  cavity several times while maintaining phase coherence. The electron wavelength is still much smaller than the cavity, however, so that electron transport may be described semiclassically. Such a cavity is thus useful in testing the predictions of

the semiclassical theory of chaotic scattering [1,2]. This theory predicts random fluctuations in the resistance of a chaotic cavity such as a stadium when a perpendicular magnetic field is applied or when the electron density is changed. There is also a recent prediction for a weak localization effect which reflects the chaotic nature of the cavity [3]. The observation of a difference between magnetoresistance fluctuations in nominally chaotic and non-chaotic cavities has been reported previously [4]. In this paper we report the observation of the scaling of magnetoresistance fluctuations with cavity size. We also find evidence for an important contribution from short, non-chaotic paths. Finally, we study the weak localization in the cavity as a function of Fermi energy and find an energy-averaged effect in agreement with recent numerical studies [3].

\* Corresponding author.

<sup>1</sup> Permanent address: Racah Institute of Physics, Hebrew University of Jerusalem, Jerusalem, Israel, 91904.

## 2. Fabrication and measurement

Our samples are fabricated from GaAs/Al GaAs heterostructures having bulk mobility of  $60 \text{ m}^2/\text{V} \cdot \text{s}$  and density of  $2.6 \times 10^{15} \text{ m}^{-2}$ . After fabrication the mobility of a small cavity is difficult to assess, but the density is found to be similar to the bulk. Confinement of the electron gas is achieved by patterning a Ti/Au metal mask with electron-beam lithography and exposing it to low energy ( $\sim 200 \text{ eV}$ ) Xe ions [5], which makes the unprotected areas insulating. The metal mask is a self-aligned Schottky barrier gate which allows the density to be varied over a small range without significantly changing the shape of the cavity.

The data we present here are from a sample with two cavities whose shape and dimensions are given in the insets of Fig. 2. The offset lead geometry was chosen to eliminate direct paths which do not interact with the edges of the cavity. The change in electron density with gate voltage is calibrated from the change in one or more minima of the Shubnikov–de Haas oscillations. We estimate an electron density of  $(2.1 + 2.3V_g) \times 10^{15} \text{ m}^{-2}$ , where  $V_g$  is the gate voltage in volts, over the range  $|V_g| \leq 0.1 \text{ V}$ . The sample is mounted in a dilution refrigerator and all data presented here are measured with the mixing chamber at  $50 \text{ mK}$ . The actual electron temperature is estimated to be  $100 \text{ mK}$  or slightly higher [6]. The voltage drop across the cavity is always less than  $10 \mu\text{V}$ .

## 3. Magnetoresistance fluctuations

Fig. 1 shows the magnetoresistance of the two stadia measured with  $V_g = -0.02 \text{ V}$ . Both stadia show random, reproducible fluctuations but on different magnetic field scales. The data are not symmetric about  $B = 0$  because we make a true four probe measurement. We have interchanged current and voltage leads and find that the Onsager relation for four probe measurements [7] is satisfied.

The theory of quantum chaotic scattering pre-

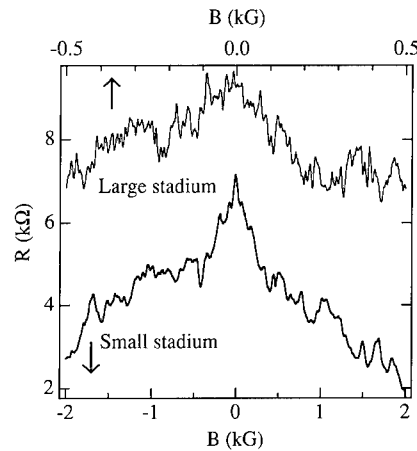


Fig. 1. Magnetoresistance of the small and large stadia with  $V_g = -0.02 \text{ V}$ ,  $T \approx 100 \text{ mK}$ .

dicts the following form for the power spectrum  $S(f)$  of the fluctuations [1]:

$$S(f) = S(0)(1 + 2\pi\phi_0\alpha f) e^{-2\pi\phi_0\alpha f}, \quad (2)$$

where  $f$  is inverse magnetic field,  $\phi_0 = h/e$  is the flux quantum, and  $\alpha$  is a parameter that characterizes the chaotic dynamics of classical particles scattering in a cavity of the same shape. Specifically,  $\alpha$  determines the probability  $P$  that a classical particle will enclose an area  $A$  before escaping the cavity according to

$$P(|A|) \propto e^{-2\pi\alpha|A|}. \quad (3)$$

The power spectra of the data in Fig. 1 are shown in Fig. 2 [8]. The smooth lines are fits to (2) for  $0.006 \leq f \leq 0.022 \text{ G}^{-1}$  (small stadium) and for  $0.024 \leq f \leq 0.184 \text{ G}^{-1}$  (large stadium). The lower bound corresponds to an area of about  $(2\pi\alpha)^{-1}$ , which is approximately the smallest area for which (3) is expected to hold [1]. The upper bound is the largest  $f$  for which (2) remains a good fit to the data (found iteratively). It is always larger than  $(\phi_0\alpha)^{-1}$ . The fits give  $\phi_0\alpha = 61.3 \text{ G}$  (small stadium) and  $8.5 \text{ G}$  (large stadium). The frequency interval used in the fit affects the value of  $\phi_0\alpha$  by as much as  $\pm 20\%$ . Fig. 3 shows the range of  $\phi_0\alpha$  values which give reasonable fits over some frequency interval, for measurements at several values of  $V_g$ . The bar at  $V_g = 0$  represents several measurements separated by thermal cy-

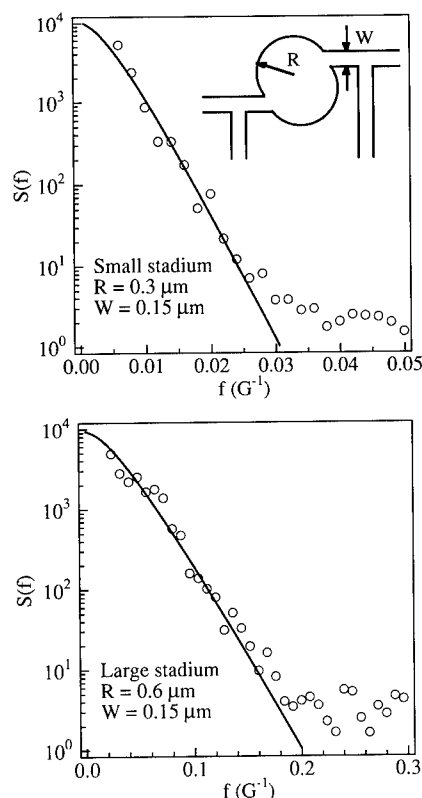


Fig. 2. Power spectra of the data in Fig. 1 (circles) and fits to Eq. (2) (lines). Insets: Stadium shape with leads and dimensions for each stadium.

cles to  $T \geq 77$  K. There is no apparent trend in  $\phi_0\alpha$  with  $V_g$ , which indicates the size and shape of the cavity are independent of  $V_g$  over the

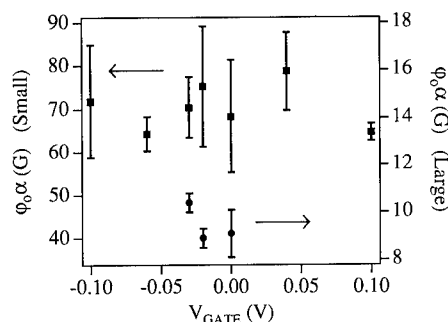


Fig. 3. Characteristic field  $\phi_0\alpha$  of the small (squares) and large (circles) stadia for several gate voltages. The bars give the range of values which give good fits and the points are the mean values.

Table 1  
Characteristic field  $\phi_0\alpha$  for both stadia

Stadium	$\phi_0\alpha$ (G)	
	Simulation	Experiment
Small	23	70
Large	3.5	9.3

Simulation values are from Ref. [9]. Experimental values are average values for several thermal cycles and gate voltages.

range shown. The mean  $\phi_0\alpha$  for each stadium over all  $V_g$  is shown in Table 1.

The expected value of  $\phi_0\alpha$  for a stadium can be found by numerical simulation of classical particles scattering in the cavity [1]. Our stadium shape with offset leads has not been simulated, but simulations for symmetric stadia with directly opposite leads may be used as a first estimate. For symmetric stadia, simulations [9] give the values of  $\phi_0\alpha$  shown in Table 1. The experimental value of  $\phi_0\alpha$  for each stadium is about three times larger than the simulation value, indicating the typical enclosed areas in our stadia are about three times smaller than expected. Jensen [2] has argued that a tendency for trajectories to circulate in one direction before being backscattered exists in the symmetric stadium with  $R \gg W$ . This effect increases the typical area enclosed by a factor of about four. Our experimental results indicate a much weaker circulation effect, which is likely due to the cavity edges not being perfectly smooth. A more realistic simulation of our shape would be helpful. It is important to note that the ratio of the two experimental values agrees fairly well with the prediction from the simulations, indicating that the fluctuations scale with cavity size as expected. Also note that the ratio is not simply the inverse ratio of the total cavity areas. Jensen [2] has derived an analytical expression for  $\phi_0\alpha$  in terms of  $R$  and  $W$  for symmetric stadia. His result predicts values of 18 G for the small stadium and 3.8 G for the large stadium.

#### 4. Conductance versus wavevector

Fig. 4 shows the conductance of the small stadium as a function of Fermi wavevector at

$B = 0$ . Again we observe random but reproducible fluctuations. These fluctuations are also expected to have a power spectrum predicted by semiclassical theory [1]. This aspect of the data is still under investigation and will be discussed elsewhere.

Here we focus on the contribution of short, non-chaotic paths to the conductance. Two such paths are suggested in the inset of Fig. 4. Path 1 goes directly between the two leads and path 2 bounces once off each side of the cavity. In the semiclassical picture, the transmission of these two paths has a phase factor  $\exp[ik_F(L_1 - L_2)]$ , where  $L_1$  and  $L_2$  are the path lengths. This phase will oscillate as  $k_F$  is changed, and if such a pair of paths contributes strongly to the conductance, the Fourier power of  $G(k_F)$  will show a peak at the frequency of the oscillation,  $1/\Delta k_F = (L_1 - L_2)/2\pi$ . The (unaveraged) Fourier power of  $G(k_F)$  for the small stadium at several values of  $B$  is shown in Fig. 5. At  $B = 0$  there are two peaks present, indicating two pairs of paths make an important contribution. At  $B = 20, 35$ , and  $50$  G (not shown), the same two peaks are found with nearly the same amplitudes. At  $B = 70$  G, the higher frequency peak begins to disappear and a new peak appears at low frequency. The lower frequency peaks persist until  $B = 350$  G, the largest field used. The magnetic field causes the paths to curve, and a path will cease to contribute strongly to the conductance when it no

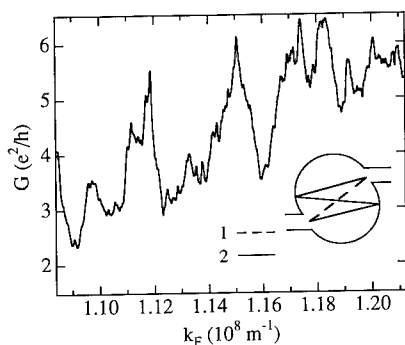


Fig. 4.  $G(k_F)$  for the small stadium at  $B = 0$ . The wavevector range shown corresponds to  $-0.1 \leq V_g \leq 0.1$  V. The number of modes in the leads,  $k_F W/\pi$ , changes from 5.2 to 5.8 over this range. Inset: A possible pair of short paths inside the cavity (see text).

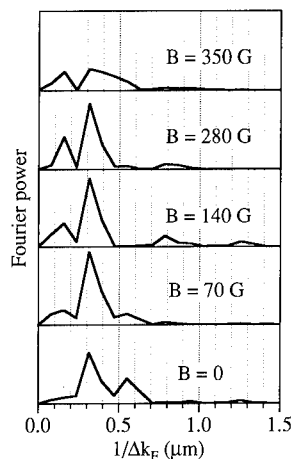


Fig. 5. Fourier power of  $G(k_F)$  for the small stadium, after subtraction of a linear background from  $G(k_F)$ .

longer enters the opposite lead. A higher frequency peak presumably involves a longer path, and thus will be affected by a smaller field, consistent with our observations.

At this point we cannot identify the exact paths which are responsible for the observed peaks in the Fourier spectra. It would be helpful to have similar data for a range of cavity sizes. Unfortunately, the ability to vary the density in the large stadium was lost before such data could be obtained. Nonetheless, our results show that some pairs of relatively short paths are important and that the longer paths which reflect the chaotic classical dynamics of the cavity do not completely determine the conductance [10]. This was mentioned in reports of numerical studies [1], but has not been measured previously.

## 5. Weak localization

The data for the small stadium in Fig. 1 show a pronounced peak at  $B = 0$ . This feature has a width comparable to  $\phi_0 \alpha$ , and was identified previously [4] as a weak localization (WL) effect due to breaking of time reversal symmetry by the magnetic field. We do not find a strong peak at  $B = 0$  for all values of  $V_g$ , nor after every thermal cycle to  $T \geq 77$  K for  $V_g = 0$ . WL always produces negative magnetoresistance, but when fluctua-

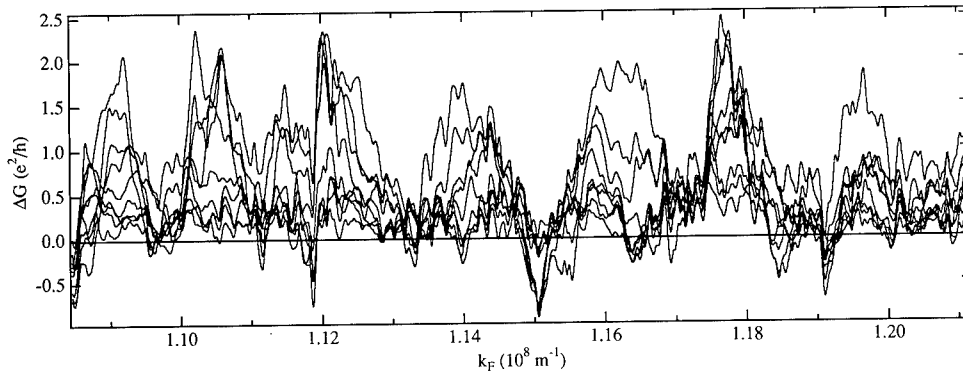


Fig. 6.  $\Delta G(k_F, B) \equiv G(k_F, B) - G(k_F, 0)$  for the small stadium at  $B = 20, 35, 50, 70, 100, 140, 210, 280$ , and  $350$  G. The traces are generally in order of increasing  $B$  from bottom to top.

tions are also present, the net magnetoresistance can be of either sign. The WL can only be distinguished from the fluctuations by performing an ensemble average. In our sample the gate allows us to average over Fermi energy.

The WL can be expressed as the change in conductance  $\Delta G(k_F, B) \equiv G(k_F, B) - G(k_F, 0)$ . This is shown in Fig. 6 for several values of  $B$ . This plot explicitly shows the variation in the WL effect as we access different members of the ensemble of the cavity by changing  $k_F$ . For some members the effect is large and for others it is small, and both positive and negative effects are seen. The energy-averaged WL effect is simply the mean of  $\Delta G$  over the entire range of Fig. 6, and it is shown in Fig. 7. We find  $\langle \Delta G \rangle$  increases sharply for small  $B$  and then rises more slowly for

$B$  larger than about  $1.5\phi_0\alpha$ . In Ref. [3], the energy-averaged change in conductance was calculated from numerically-generated  $G(k_F)$  traces in the same fashion as described here. Very similar behavior was found for  $\langle \Delta G \rangle$  versus  $B$  in stadium-like structures with no direct paths between the leads.

Ref. [3] also explored the effect of cavity shape on the weak localization effect. It was found that the effect is qualitatively different in chaotic and non-chaotic cavities, and that the symmetry of the cavity affects the size of the effect by a substantial amount. Ongoing studies are aimed at testing these predictions.

## 6. Conclusion

We have observed fluctuations in the resistance of chaotic cavities as a function of magnetic field which scale with the cavity size as expected from simulations of classical particles. There appears to be a weaker circulation effect in our cavities than is seen in simulations of shapes with symmetric leads and perfectly smooth edges. We find peaks in the power spectrum of  $G(k_F)$  which indicate an important contribution from pairs of short, non-chaotic paths. We have measured weak localization as a function of energy and we observe an energy-averaged weak localization effect similar to the effect seen in recent calculations [3].

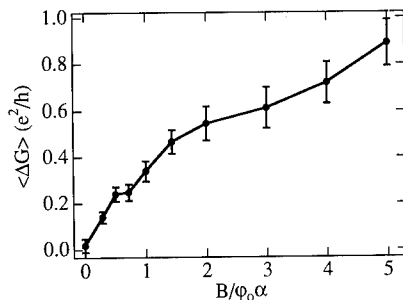


Fig. 7. Mean  $\Delta G$  for the wavevector range shown in Fig. 6. The field scale has been normalized using  $\phi_0\alpha = 70$  G. The point at  $B = 0$  is the difference between two  $G(k_F)$  traces at  $B = 0$  taken before and after all the other traces (three days apart).

## 7. Acknowledgements

We thank R.G. Wheeler, A.D. Stone, and H.U. Baranger for helpful discussions. Research supported by NSF DMR 9112752 and equipment purchased under NSF DMR 9112451.

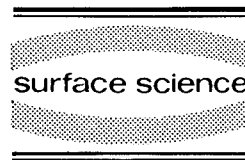
## 8. References

- [1] R.A. Jalabert, H.U. Baranger and A.D. Stone, *Phys. Rev. Lett.* 65 (1990) 2442;
- [2] E. Doron, U. Smilansky and A. Frenkel, *Physica D* 50 (1991) 367.
- [3] R.V. Jensen, *Chaos* 1 (1991) 101.
- [4] H.U. Baranger, R.A. Jalabert and A.D. Stone, in: *Transport Phenomena in Mesoscopic Systems*, Eds. H. Fukuyama and T. Ando (Springer, New York, 1992); H.U. Baranger, R.A. Jalabert and A.D. Stone, *Phys. Rev. Lett.*, to be published.
- [5] C.M. Marcus et al., *Phys. Rev. Lett.* 69 (1992) 506.
- [6] A. Scherer and M.L. Roukes, *Appl. Phys. Lett.* 55 (1989) 377.
- [7] A. Mittal et al., *Proceedings of LT20*, to appear in *Physica B* (1994).
- [8] M. Buttiker, *Phys. Rev. Lett.* 57 (1986) 1761.
- [9] The power spectra are logarithmic averages of the Fourier transforms of 15 half-overlapping segments, each containing about 500 G for the small stadium and 130 G for the large stadium.
- [10] W.A. Lin and J.B. Delos, private communication.



ELSEVIER

Surface Science 305 (1994) 507–510



# Conductance fluctuations of 2D electrons in a strong magnetic field

D.E. Khmelnitskii \*, M. Yosefin

*Cavendish Laboratory, Cambridge University, Madingley Road, Cambridge CB3 0HE, UK*

(Received 19 April 1993; accepted for publication 12 June 1993)

## Abstract

We study the universal conductance fluctuations (UCF) in two-dimensional mesoscopic systems in the presence of a strong magnetic field when the Hall conductance  $\sigma_{xy}$  is not negligible compared to  $\sigma_{xx}$ . We find that the Hall component of the diffusion current modifies the boundary conditions for the diffuson and gives rise to a qualitatively new behavior of the UCF. In particular, when  $\sigma_{xy}$  is larger than  $\sigma_{xx}$ , the magnetic field correlation length  $B_c$  is proportional to  $\sigma_{xx}$  instead of the usual inverse proportionality leading to oscillations in  $B_c$  in phase with the Shubnikov–de Haas oscillations of  $\sigma_{xx}$ .

## 1. Introduction

The properties of a two-dimensional electron gas in a strong magnetic field are dominated by the integer quantum Hall effect, which corresponds in its extreme form to a strong localization. Nevertheless, if the size of a sample is smaller than the localization length, the dissipative conductivity  $\sigma_{xx}$  can be larger than the quantum unit  $e^2/h$ . Large values of  $\sigma_{xx}$  coexist in this regime with large values of the Hall conductivity  $\sigma_{xy}$ . Mesoscopic conductance fluctuations in this regime can be studied by the standard perturbative techniques. Here we will focus our attention on the new features of the fluctuations which appear as a result of a nonvanishing  $\sigma_{xy}$ .

## 2. Correlation function

The conductance fluctuations can be described by means of the correlation function

$$F_B(\Delta B) = \langle \delta G(B + \Delta B) \delta G(B) \rangle, \quad (1)$$

which can be calculated by conventional diagrammatic techniques [1–4]. The physical meaning of these diagrams corresponds to representation of the electron propagator in a form of a Feynman path integral. At strong magnetic fields where the cooperon contribution is suppressed, it is sufficient to consider only diffusive paths shown in Fig. 1. The sum over all such paths is the diffuson  $P_\omega(\mathbf{r}, \mathbf{r}')$ . Formal evaluation of this sum gives

$$P_\omega(q, y, y') = \sum_{n=0}^{\infty} \frac{\phi_n^L(y) \phi_n^{R*}(y')}{-i\omega + \Lambda_n(q)}. \quad (2)$$

\* Corresponding author.



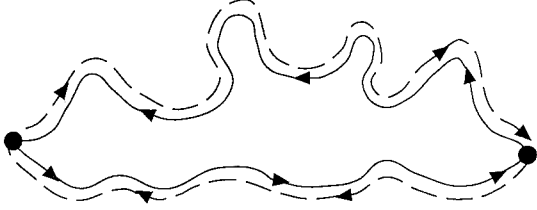


Fig. 1. Trajectories contributing to the diffusion. Solid line corresponds to magnetic field  $B$ , and the dashed line corresponds to  $B + \Delta B$ .

Here  $\phi_n^L$  and  $A_n$  are the eigenfunctions and eigenvalues of the diffusion equation

$$\mathcal{D} \left[ q^2 - \frac{d^2}{dy^2} \right] \phi_n^L(y) = A_n \phi_n^L(y). \quad (3)$$

We will consider long narrow samples of length  $L$  and width  $w \ll L$ . Solutions of this equation should then satisfy the condition of vanishing of the transverse diffusion current on the boundary  $y = 0, w$ . At strong magnetic fields this current is proportional not only to the transverse gradient (conventional diffusion with diffusion coefficient  $\mathcal{D}$ ), but also to the longitudinal gradient (Hall diffusion with Hall diffusion coefficient  $\mathcal{D}_H$ ). The total diffusion current is therefore given by

$$J = -\mathcal{D} \nabla \psi(\mathbf{r}) - \mathcal{D}_H \hat{z} \times \nabla \psi(\mathbf{r}). \quad (4)$$

The transverse component of the diffusion current (4) vanishes at the boundary provided the eigenfunctions  $\phi_n^L(y)$  satisfy the condition

$$\left( \frac{d}{dy} + i\gamma q \right) \phi_n^L(y) = 0 \quad (5)$$

at the boundaries  $y = 0, w$ . Here  $\gamma$  is the ratio of the Hall and the longitudinal diffusion coefficients. From the Einstein relations it follows that it is also equal to the ratio between Hall and longitudinal conductivities  $\gamma = \mathcal{D}_H / \mathcal{D} = \sigma_{xy} / \sigma_{xx}$ .

An easy way to solve Eq. (3) with boundary conditions (5) is by noticing that the functions  $\chi_n(y) = (d/dy + i\gamma q) \phi_n^L(y)$  satisfy the same equation with simpler boundary conditions  $\chi_n =$

0. Therefore  $(d/dy + i\gamma q) \phi_n^L(y) = \sin(n\pi y/w)$ . Inverting this relation, we find

$$\phi_n^L(y) = \begin{cases} A_0 \exp(-i\gamma q y) & \text{if } n = 0, \\ A_n \left[ \frac{n\pi}{w} \cos \frac{n\pi}{w} y - i\gamma q \sin \frac{n\pi}{w} y \right] & \text{if } n \neq 0, \end{cases} \quad (6)$$

where  $A_n$  is a normalization constant. The corresponding eigenvalues are

$$A_n = \begin{cases} \mathcal{D}(1 + \gamma^2)q^2 & \text{if } n = 0, \\ \mathcal{D} \left( q^2 + \frac{\pi^2 n^2}{w^2} \right) & \text{if } n \neq 0. \end{cases} \quad (7)$$

In the  $n = 0$  eigenmode the transverse current vanishes identically. From (7) it follows that the diffusion constant for this mode is enhanced in the presence of a magnetic field by a factor  $1 + \gamma^2$ . This effective diffusion constant corresponding to the  $n = 0$  mode is coupled by the Einstein relation,

$$\frac{1}{\rho_{xx}} = e^2 \nu \mathcal{D}(1 + \gamma^2), \quad (8)$$

not to the longitudinal conductivity  $\sigma_{xx}$ , but rather to inverse resistivity  $1/\rho_{xx} = (\sigma_{xx}^2 + \sigma_{xy}^2)/\sigma_{xx}$ .

Since the boundary conditions (5) are not self-adjoint, we need to consider also the right eigenfunctions  $\phi_n^R(y)$  which satisfy the same equation, but with the adjoint boundary conditions  $(d/dy - i\gamma q) \phi_n^R(y) = 0$ . Comparison of this condition with the boundary condition (5) satisfied by  $\phi_n^L$  gives  $\phi_n^R(y) = \phi_n^{L*}(y)$ . From the biorthogonality relation  $\langle \phi_n^R | \phi_n^L \rangle = \delta_{nn'}$ , it then follows that the eigenfunctions  $\phi_n^L$  satisfy

$$\int_0^w \phi_n^L(y) \phi_n^L(y) dy = \delta_{nn'}. \quad (9)$$

The amplitude of the conductance fluctuations at strong magnetic fields can now be easily determined by using the standard expression of the correlation function (1) in terms of the eigenfunctions and eigenvalues of the diffusion [1–5]. At low temperatures only the lowest eigenvalue gives

a significant contribution and the diffuson can be approximated as

$$P_w^{(0)}(q, y, y') = \frac{A_0^2 e^{-i\gamma q(y+y')}}{-i\omega + \mathcal{D}(1+\gamma^2)q^2}. \quad (10)$$

Using (10), we find that at low temperatures the amplitude of the conductance fluctuations depends explicitly on  $\gamma$ :

$$F_B(\Delta B = 0) \approx \left(\frac{e^2}{h}\right)^2 \frac{1}{\sqrt{1+\gamma^2}} \frac{L_T^3}{L^3}. \quad (11)$$

Here,  $L_T$  is the thermal length,  $L_T = \sqrt{\hbar \mathcal{D}/T}$ .

The low temperature result (11) holds provided  $L_T > w\sqrt{1+\gamma^2}$ . At higher temperatures the contribution of other eigenvalues cannot be neglected, and for  $L_T < w$  they dominate the behavior of the fluctuations. Since only the  $n = 0$  eigenvalue depends on  $\gamma$ , for  $L_T < w$  we obtain the standard 2d expression for the fluctuation amplitude.

### 3. Correlation field $B_c$

The dependence of the correlation function (1) on the field difference  $\Delta B$  can be determined by an introduction of  $\Delta B$  into both the diffusion equation (3) and the boundary conditions (5). This can be achieved by making the substitution  $\nabla \rightarrow \nabla - i(e/\hbar c)\mathbf{A}$ . It is convenient to choose the gauge  $A_x = -\Delta B y$ ,  $A_y = \gamma \Delta B y$  which corresponds to the substitution  $q \rightarrow q - (e\Delta B/\hbar c)y$ ,  $d/dy \rightarrow d/dy + i\gamma(e\Delta B/\hbar c)y$ . In this gauge the magnetic field difference  $\Delta B$  cancels out of the boundary conditions. We thus find that at finite  $\Delta B$  the eigenfunctions and the eigenvalues of the diffuson can be determined from the equation

$$\mathcal{D} \left[ \left( q - \frac{e\Delta B}{\hbar c} y \right)^2 - \frac{d^2}{dy^2} + 2i\gamma \frac{e\Delta B}{\hbar c} y \frac{d}{dy} + \gamma^2 \left( \frac{e\Delta B}{\hbar c} \right)^2 y^2 \right] \phi_n^L(y) = A_n \phi_n^L(y), \quad (12)$$

subject to the boundary condition (5). Corrections to the eigenvalues to leading order in  $\Delta B$  can be determined by using the explicit form of the

unperturbed eigenfunctions (6). In particular, we find

$$\Delta A_0 = \mathcal{D}(1+\gamma^2) \frac{w^2}{12} \left( \frac{e\Delta B}{\hbar c} \right)^2. \quad (13)$$

Substitution of this correction into the low-temperature form of the diffuson yields the correlation field  $B_c$

$$B_c \approx \frac{(hc/e)T}{\hbar \mathcal{D}(1+\gamma^2)} \approx e c \nu T \rho_{xx}, \quad (14)$$

where we have used the Einstein relation (8).

From Eq. (14), it follows that in the low temperature limit  $L_T > w\sqrt{1+\gamma^2}$ , the correlation field  $B_c$  is proportional to the longitudinal resistivity  $\rho_{xx}$ . In the limit  $\sigma_{xy} = 0$  this result agrees with the standard theory of universal conductance fluctuations which predicts that  $B_c$  should be inversely proportional to the longitudinal conductivity  $\sigma_{xx}$ . However, in the high field regime where  $\sigma_{xy} > \sigma_{xx}$ ,  $\rho_{xx}$  is proportional to  $\sigma_{xx}$ . The standard theory therefore predicts oscillations in  $B_c$  180° out of phase with Shubnikov–de Haas oscillations in  $\rho_{xx}$ , whereas we find oscillations *in phase* with SdH oscillations.

Experimental observation of the conductance fluctuations in the high field regime has been reported recently by a number of groups [6–9]. Oscillations in  $B_c$  in phase with SdH oscillations were observed in at least one of these experiments [9].

### 4. Acknowledgements

We are grateful to D. Cobden and A. Morgan for communicating to us their data prior to publication.

### 5. References

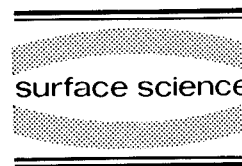
- [1] P.A. Lee and A.D. Stone, Phys. Rev. Lett. 35 (1985) 1622.
- [2] B.L. Altshuler, JETP Lett. 41 (1985) 648.
- [3] B.L. Altshuler and D.E. Khmelnitskii, JETP Lett. 42 (1986) 359.
- [4] P.A. Lee, A.D. Stone and H. Fukuyama, Phys. Rev. B 35 (1987) 1039.

- [5] S. Xiong and A.D. Stone, Phys. Rev. Lett. 68 (1992) 3757.
- [6] G. Timp, A.M. Chang, J.E. Cunningham, T.Y. Chang, P. Mankiewich, R. Behringer and R.E. Howard, Phys. Rev. Lett. 58 (1987) 2814.
- [7] A.K. Geim, P.C. Main, P.H. Beton, P. Streda, L. Eaves, C.D.W. Wilkinson and S.P. Beaumont, Phys. Rev. Lett. 67 (1991) 3014.
- [8] A.K. Geim, P.C. Main, P.H. Beton and L. Eaves, Phys. Rev. Lett. 69 (1991) 1248.
- [9] A. Morgan et al., to be published.



ELSEVIER

Surface Science 305 (1994) 511–515



## Tunneling into classically chaotic orbits in quantum wells

T.M. Fromhold, M.L. Leadbeater, L. Eaves \*, T.J. Foster, P.C. Main, F.W. Sheard

*Department of Physics, University of Nottingham, Nottingham NG7 2RD, UK*

(Received 20 April 1993; accepted for publication 11 May 1993)

### Abstract

Resonant tunneling diodes with wide quantum wells are investigated in the presence of a large magnetic field oriented at various angles to the plane of the well. The current–voltage characteristics exhibit a large number of resonant peaks, even when the electron motion in the quantum well is classically chaotic. We show that the spacing of the peaks in the chaotic region is determined by the period of unstable periodic orbits in the potential well and provides direct evidence of an effect analogous to period doubling.

The quantum mechanical description of classically chaotic systems is one of the most interesting and challenging problems in contemporary physics [1,2]. An impressive body of theoretical work already exists, but to date the range of experiments studying quantum chaos has been limited. Most experimental work has focused on the spectroscopy of the highly excited states of atoms in high magnetic fields [3] and on the ionisation of atoms in strong microwave fields [4]. In condensed matter physics, recent experiments have explored the effect of chaos on quantum transport [5–7].

In this paper we describe a new and flexible experiment for studying electrons in a quantum mechanically confined system under conditions when their motion is classically chaotic. Fig. 1a shows two infinite potential barriers, with a uniform electric field  $E$  along the normal to the barrier interfaces ( $-E\parallel x$ ). Electrons moving clas-

sically between the barriers undergo specular reflection from the left-hand (emitter) and right-hand (collector) barrier. If a magnetic field  $B$  is applied at an angle  $\theta = 0^\circ$  or  $\theta = 90^\circ$  to  $x$  the electron orbits are periodic. At intermediate tilt

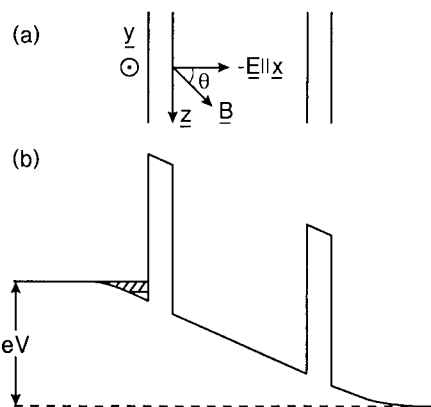


Fig. 1. (a) Plan view of the classical double barrier system in the tilted field geometry. (b) Schematic conduction band profile of a resonant tunneling diode. The hatched region represents the 2D accumulation layer.

\* Corresponding author.

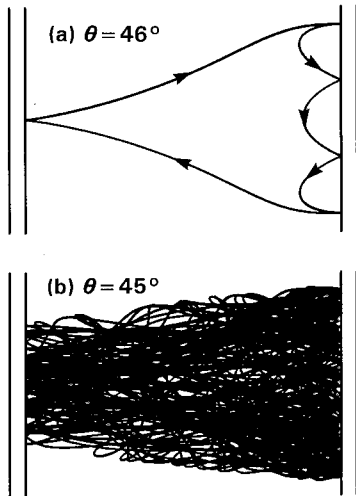


Fig. 2. Projection on the  $x$ - $y$  plane of classical orbits for a 60 nm potential well with  $E = 3.5 \times 10^6 \text{ V m}^{-1}$ ,  $B = 11.4 \text{ T}$  and (a)  $\theta = 46^\circ$ , (b)  $\theta = 45^\circ$ . The effective mass in GaAs is used.

angles the electron motion comprises a constant acceleration along  $B$  and a cycloidal drift in the orthogonal plane. Specular reflection at the barrier interfaces repeatedly resets the boundary conditions for the cycloidal motion and, when the cyclotron radius is sufficiently small, produces orbital segments which rapidly become uncorrelated and are collectively chaotic. For general initial velocity at the emitter barrier, the motion is aperiodic. However, periodic orbits do occur for certain starting velocities as shown in Fig. 2a. Note that if  $\theta$  is reduced by only one degree, the motion becomes aperiodic (Fig. 2b). This extreme sensitivity to the initial conditions is the defining characteristic of classical chaos.

At high quantum numbers ( $n \geq 20$ ) the energy-level spectrum of the potential well is very complicated [8] corresponding to the classically chaotic domain. By reducing the barriers to a finite height as in a double-barrier tunnel structure, the level pattern is qualitatively unchanged but we may now probe this spectrum using resonant tunneling spectroscopy.

Our structure consists of a GaAs quantum well of width  $w = 120 \text{ nm}$  enclosed by two  $\text{Al}_{0.4}\text{Ga}_{0.6}\text{As}$  tunnel barriers of thickness  $b = 5.6 \text{ nm}$  (Fig. 1b).

Full details of the layer composition are given elsewhere [9]. Electrons tunnel into the quantum well from the occupied states of a two-dimensional accumulation layer. The resonant peaks in the current-voltage characteristic  $I(V)$  are superimposed on a monotonically increasing back-

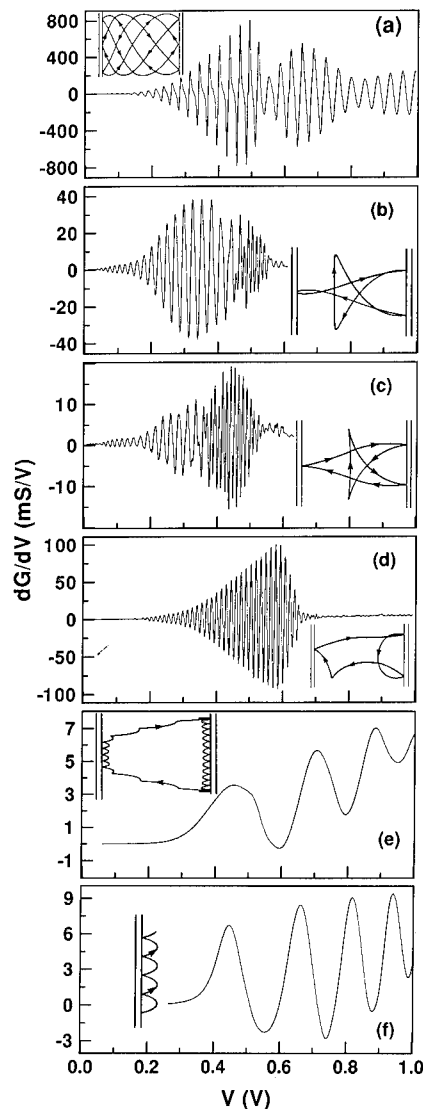


Fig. 3.  $dG/dV$  plots for a resonant tunneling diode containing a 120 nm wide quantum well with  $B = 11.4 \text{ T}$  and (a)  $\theta = 0^\circ$ , (b)  $\theta = 15^\circ$ , (c)  $\theta = 20^\circ$ , (d)  $\theta = 40^\circ$ , (e)  $\theta = 80^\circ$ , (f)  $\theta = 90^\circ$ . The resonances are related to the classical periodic orbits (inset) projected onto the  $x$ - $y$  plane.

ground which we suppress by taking second derivative plots,  $d^2I/dV^2$ . Fig. 3 shows measurements of  $dG/dV = d^2I/dV^2$  for a range of tilt angles with  $B = 11.4$  T.

At  $\theta = 0^\circ$ , a series of resonant tunneling peaks is observed with a voltage spacing  $\Delta V \approx 30$  mV [10]. The beating, at around 550 and 850 mV, is due to an “over the barrier” quantum interference effect at the collector barrier [10]. Oscillatory structure in  $I(V)$  persists up to tilt angles of just over  $50^\circ$ , but it decreases in amplitude and changes its periodicity with increasing  $\theta$ . For  $0^\circ \leq \theta < 10^\circ$  the voltage separation  $\Delta V$  decreases gradually as  $\cos^2\theta$  [11]. At larger tilt angles the oscillatory structure changes dramatically. In particular, at  $\theta = 15^\circ$ , the spacing,  $\Delta V$ , of the oscillations decreases by a factor of  $\sim 2$  to a value of  $\sim 12$  mV at voltages above  $\sim 460$  mV, with the more widely spaced oscillations persisting at lower bias. The boundary between these two regions is very distinct and moves steadily to lower bias with increasing angle. At  $\theta \geq 24^\circ$ , the shorter period oscillations dominate the  $I(V)$  curves in the range of voltage up to 800 mV. For  $15^\circ < \theta < 50^\circ$ , their period is almost constant. For angles between  $50^\circ$  and  $60^\circ$ , no regular oscillatory structure is observed. For  $\theta > 60^\circ$  a new series of much more widely-spaced oscillations is observed in  $dG/dV$ . The voltage separation of these resonances decreases as  $B$  approaches  $90^\circ$ , c.f Figs. 3e and 3f.

In a classical picture, electrons in the potential well execute regular helical orbits for  $\theta = 0^\circ$  (Fig. 3a) and skipping orbits for  $\theta = 90^\circ$  (Fig. 3f). Quantisation of these orbits in the quasiclassical regime gives an energy-level splitting  $\Delta\epsilon = h/\tau$ , where  $\tau$  is the periodic time for return to the emitter barrier. This is related to the voltage separation between adjacent peaks in the  $dG/dV$  plots by  $\Delta V = f\Delta\epsilon/e$ , where the factor  $f \approx 2$  depends on the potential distribution in the structure. The larger  $\Delta V$  values at  $\theta = 90^\circ$  compared with  $\theta = 0^\circ$  are attributable to the shorter return times of the skipping orbits [12].

Although the energy spectrum of a classically chaotic system is complex, regular clusterings of levels occur which are related to the unstable periodic orbits of the system. This produces oscillatory structure in the smoothed density of states

and the energy period  $\Delta\epsilon_P$  is related to the unstable orbit period  $T_P$  by  $\Delta\epsilon_P = h/T_P$  [1,2]. Our experiments probe the density of states of the quantum well so the voltage spacings  $\Delta V$  are directly related to the unstable periodic orbits by  $\Delta V = fh/eT_P$ . We have therefore used numerical simulations to search for periodic orbits in a potential well which has impenetrable barriers but is otherwise identical to that in the device. The starting velocities at the emitter barrier are chosen to be consistent with the momenta of the occupied states in the accumulation layer. The orbital paths are then obtained by numerical solution of Newton's equations, including specular reflection at the barrier interfaces. For  $\theta < 10^\circ$ , the allowed periodic orbits are all modified corkscrew trajectories which collide only once with each barrier per period, as shown in Fig. 4a. When  $\theta = 20^\circ$ , modified corkscrew orbits exist for  $V < 400$  mV. When  $V = 200$  mV a second type of

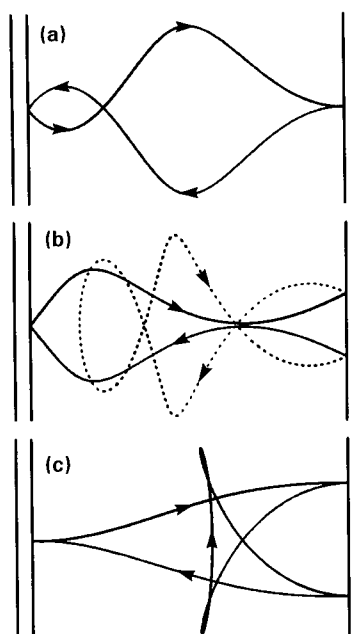


Fig. 4. Periodic classical orbits calculated for a 120 nm wide well ( $B = 11.4$  T and  $\theta = 20^\circ$ ) projected onto the  $x-y$  plane. With increasing electric field the corkscrew orbits (a) evolve into star-shaped orbits (c) via a period-doubling transition (b).

periodic orbit is observed (Fig. 4b). Electrons in these orbits make two successive collisions with the collector barrier before returning to their starting point on the emitter barrier. The path between the two successive collisions on the collector barrier (dotted curve in Fig. 4b) almost intersects with the emitter barrier. The period  $T_D$  for these orbits is almost twice that for the modified corkscrew orbits. However, for  $V = 200$  mV,  $T_D \approx 1.2$  ps is much greater than the LO phonon emission time  $\tau_{LO} \approx 0.2$  ps [13] of hot electrons in GaAs. At this voltage the energy-level clusters corresponding to the classical period-doubled orbit are therefore not resolved in the  $dG/dV$  plot. As  $V$  is increased, the orbital segment between successive collisions with the collector barrier is pulled away from the emitter barrier so that the total path length and orbital period both fall. The closely-spaced energy level clusters associated with the period-doubled orbit dominate the resonant structure in  $dG/dV$  for  $V > 375$  mV, when  $T_D$  becomes comparable with  $\tau_{LO}$ . The orbital path then passes close to the centre of the quantum well between successive collisions with the collector barrier as shown in Fig. 4c. Electrons in these star-shaped orbits therefore travel almost twice the distance in the  $x$ -direction as electrons in the modified corkscrew orbits. The period for the star-shaped orbits (0.62 ps for  $V = 400$  mV,  $\theta = 20^\circ$ ) is almost twice that for the corkscrew orbits (0.35 ps for  $V = 400$  mV,  $\theta = 0^\circ$  and  $20^\circ$ ). The separation of energy level clusters corresponding to the star-shaped orbits is therefore approximately half that for the corkscrew orbits. This is the origin of the reduction of  $\Delta V$  by a factor  $\sim 2$ , which is observed with increasing voltage for tilt angles in the range  $10^\circ \leq \theta \leq 24^\circ$ . From the above orbital periods we calculate values of  $\Delta V = 30$  and 13 mV for resonances associated with the corkscrew and star-shaped orbits, respectively. These values are in good agreement with the measured peak spacings of 30 and 12 mV. Within the allowed range of initial velocities the corkscrew and star-shaped orbits coexist over a limited range of  $\theta$  and bias and the two periods observed in  $dG/dV$  at around 350 mV for  $\theta = 20^\circ$  provide evidence for this. Similar star-shaped orbits occur for tilt angles in the range  $10^\circ < \theta < 50^\circ$

and account for all the high-frequency resonant structure ( $\Delta V \approx 15$  mV) in  $dG/dV$ . Although the shape of the orbits changes with  $\theta$  and  $V$ , the topology does not (compare Figs. 3b–d) and the period remains  $\sim 0.6$  ps, which accounts for the slow variation of  $\Delta V$ .

For  $50^\circ < \theta < 60^\circ$ , the classical star-shaped orbits are replaced by more complicated periodic orbits. However, the period of these orbits greatly exceeds  $\tau_{LO}$  so that no regular structure is resolved in  $dG/dV$ . For  $\theta > 60^\circ$ ,  $B_z$  is sufficiently high that the electrons in classical periodic orbits make several skips along the emitter barrier before traversing the well, as shown in Fig. 3e. The total orbital period  $T = 3$  ps is much greater than  $\tau_{LO}$  so that the associated energy level clusters are not resolved. However, the time interval  $\tau_s$  of each skip along the emitter barrier (0.08 ps for  $\theta = 80^\circ$  and  $V = 590$  mV) is almost 40 times smaller than  $T$ . We can give a quantitative explanation for the gradual reduction of  $\Delta V$  with increasing  $\theta > 60^\circ$  by using the skipping times  $\tau_s$  rather than the total orbital period to determine the spacing of the clusters in the energy eigenvalue spectrum of the quantum well.

It should be noted that the range of allowed starting velocities does not give perfectly periodic orbits over the entire range of  $\theta$  and applied voltage. However, orbits which are almost periodic over several LO phonon emission times ( $> 10$  ps) do occur over the measured range of tilt angles and bias voltages. Most of the resonant structure in  $I(V)$  is presumably due to these almost-periodic orbits.

In summary, we have shown that the classical motion of electrons in a potential well is chaotic in the presence of a tilted magnetic field. Our studies highlight the potential of the resonant-tunneling diode for studying chaos in a system which shows clear quantum behaviour. The resonant structure observed in  $dG/dV$  is analogous to the Garton–Tomkins resonances [14] in the absorption spectrum of highly-excited hydrogenic atoms in high magnetic fields. However, in our structures the device parameters can be tailored so that, in a classical picture, the electrons are injected into periodic orbits with specified topologies and return times.

We are grateful to Dr. M. Henini for growing the layers used in this study. This work is supported by SERC.

## 1. References

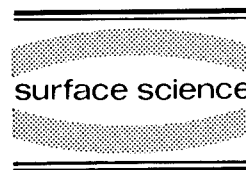
- [1] M.V. Berry, Proc. R. Soc. London A 413 (1987) 183.
- [2] R.V. Jensen, Nature 355 (1992) 311.
- [3] H. Hasegawa, M. Robnik and G. Wunner, Prog. Theor. Phys. Suppl. 98 (1989) 198.
- [4] K.A.H. van Leeuwen, G.V. Oppen, S. Renwick, J.B. Bowlin, P.M. Koch, R.V. Jensen, O. Rath, D. Richards and J.G. Leopold, Phys. Rev. Lett. 55 (1985) 2231.
- [5] R. Fleischmann, T. Geisel and R. Ketzmerick, Phys. Rev. Lett. 68 (1992) 1367.
- [6] D. Weiss, M.L. Roukes, A. Menschig, P. Grambow, K. von Klitzing and G. Weimann, Phys. Rev. Lett. 66 (1991) 2790.
- [7] C.M. Marcus, A.J. Rimberg, R.M. Westervelt, P.F. Hopkins and A.C. Gossard, Phys. Rev. Lett. 69 (1992) 506.
- [8] G. Marx, K. Lier and R. Kümmel, in: High Magnetic Fields in Semiconductor Physics III, Springer Series in Solid-State Sciences, Vol. 101, Ed. G. Landwehr (Springer, Berlin, 1992) p. 180.
- [9] M.L. Leadbeater, E.S. Alves, L. Eaves, M. Henini, O.H. Hughes, A. Celeste, J.C. Portal, G. Hill and M.A. Pate, J. Phys.: Condensed Matter 1 (1989) 4865.
- [10] E.S. Alves, M.L. Leadbeater, L. Eaves, M. Henini and O.H. Hughes, Solid State Electron. 32 (1989) 1627.
- [11] C. Kutter, V. Chitta, J.C. Maan, V.I. Fal'ko, M.L. Leadbeater, M. Henini and L. Eaves, Phys. Rev. B 45 (1992) 8749.
- [12] T.M. Fromhold, F.W. Sheard and G.A. Toombs, Proc. 20th Int. Conf. on Physics of Semiconductors, Eds. E.M. Anastassakis and J.D. Joannopoulos (World Scientific, Singapore, 1990) p. 1250.
- [13] A.F.J. Levi, R.J. Späh and J.H. English, Phys. Rev. B 36 (1987) 9402.
- [14] W.R.S. Garton and F.S. Tomkins, Astrophys. J. 158 (1969) 839.





ELSEVIER

Surface Science 305 (1994) 516–519



## Low-temperature equilibrium vertical transport through a two-dimensional electron gas

P.C. van Son <sup>\*,a,1</sup>, F.P. Milliken <sup>a</sup>, E.E. Mendez <sup>a</sup>, W.I. Wang <sup>b</sup>

<sup>a</sup> IBM Research Division, Thomas J. Watson Research Center, P.O. Box 218, Yorktown Heights, NY 10598, USA

<sup>b</sup> Department of Electrical Engineering, Columbia University, New York, NY 10027, USA

(Received 19 April 1993; accepted for publication 4 June 1993)

### Abstract

We have studied tunneling transport through a high-mobility two-dimensional electron gas in a GaSb/AlSb/InAs/AlSb/GaSb heterostructure. In high perpendicular magnetic fields and at temperatures below 1 K the tunneling conductance shows deviations from regular Shubnikov–de Haas oscillations. An overall decrease in conductance with decreasing temperature is attributed to the formation of a Coulomb gap in the tunneling density of states. Reproducible conductance fluctuations are due to resonant tunneling possibly through interface-related states.

Resonant tunnel diodes fabricated from InAs/AlSb/GaSb-type heterostructures show special properties because transport involves the valence band of GaSb and the conduction band of InAs [1–5]. At room temperature they show high peak-to-valley ratios and large current densities [2,3], which is important for device applications. At low temperatures, the diodes are ideally suited for studying the properties of a high-mobility two-dimensional electron gas (2DEG). The valence band edge of GaSb lies at a higher energy than the conduction band edge of InAs. In the heterostructure shown in Fig. 1 charge is transferred

from the GaSb electrodes to the InAs quantum well (the AlSb layers act as tunnel barriers). If a magnetic field is applied perpendicular to the plane of the quantum well, the electrons condense into Landau levels. The corresponding

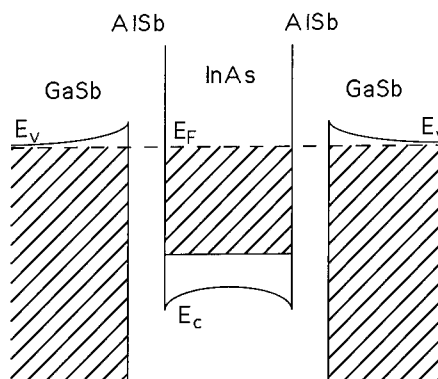


Fig. 1. Schematic band diagram.

\* Corresponding author.

<sup>1</sup> On leave from Department of Applied Physics, University of Groningen, The Netherlands. Present address: Department of Applied Physics, Delft University of Technology, Lorentzweg 1, NL-2628 CJ Delft, The Netherlands.

change in the density of states is reflected in the tunneling current through the structure. It can be studied both at zero bias as a function of magnetic field as well as at fixed magnetic field as a function of applied DC voltage. The results at temperatures of 1 K and higher are well understood [4,5]. In this paper we describe new features that show up in the zero-bias conductance in high magnetic fields at temperatures below 1 K. These include an overall decrease in conductance with decreasing temperature and the appearance of reproducible conductance fluctuations.

The samples are GaSb/AlSb/InAs/AlSb/GaSb double-barrier structures grown by MBE on p-GaSb substrates. The InAs quantum well is 15 nm wide and the barriers are 4 nm (samples I and II) or 2.5 nm (sample III), yielding electron densities in the well of  $1.2 \times 10^{12} \text{ cm}^{-2}$  and  $1.4 \times 10^{12} \text{ cm}^{-2}$  respectively. Macroscopic individual diodes (typically  $125 \times 125 \mu\text{m}^2$ ) are defined by wet mesa-etching. Two dilution-refrigerator systems were used for the measurements (10 mK/9 T and 45 mK/14 T). The conductance or the (differential) resistance was measured using a small AC modulation; the electronic set-up has been carefully optimized to prevent outside interference from reaching the sample.

The main features of our results are shown in Fig. 2. The 1100 mK curve shows the expected Shubnikov–de Haas oscillations with a resistance maximum each time an integral number of Landau levels is occupied (the intermediate maxima are due to spin splitting). At lower temperatures three new features are apparent. First, there is an overall increase of the resistance in a high perpendicular magnetic field with decreasing temperature all the way down to 11 mK. The effect is stronger in the Shubnikov–de Haas resistance minima, thereby reducing the modulation depth of the oscillations. Although the increase is observed in all samples, the overall strength of the effect can be quite different even in nominally identical samples. Note that there is no effect at zero magnetic field, nor if the field is directed in the plane of the quantum well. Second, reproducible resistance fluctuations show up in this macroscopically large sample and become more

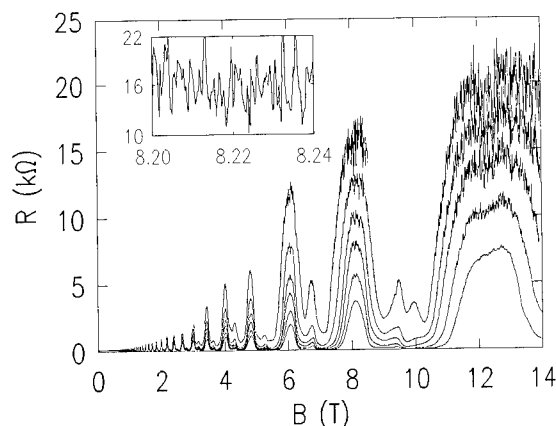


Fig. 2. Zero-bias resistance (sample I) as a function of magnetic field for several temperatures (from top to bottom: 11 mK (up to 8.6 T), 44 mK, 101 mK, 193 mK, 400 mK and 1100 mK). The inset shows the resistance fluctuations at 11 mK on an expanded magnetic field scale (note that the resolution of the magnetic field sweeps in the main figure is not high enough to capture the full amplitude of the fluctuations).

pronounced as the temperature decreases. The inset is a high-resolution magnetic field trace that shows the full extent of the fluctuations (in contrast to the main figure). Third, an additional resistance maximum develops with decreasing temperature around 10 T that can not be accounted for by a straightforward analysis.

Before we discuss these three observations in more detail we point out that in none of the tunneling measurements shown here the parallel momentum of the charge carrier is conserved (the excess momentum is absorbed e.g. by an impurity or by interface roughness). As has been shown before in samples from the same wafer [5], the reduced (differential) conductance at temperatures lower than 40 K and at applied voltages not exceeding 60 mV is due to the fact that conducting channels that do conserve parallel momentum are not available under those conditions. The nonconservation of parallel momentum cannot somehow be responsible for the resistance increase in Fig. 2 because it would similarly affect the resistance at  $B = 0$ , which it does not. The fact that parallel momentum is not conserved makes the zero-bias conductance a fairly straight-

forward probe of the total density of states of the 2DEG around the Fermi level.

The increase in zero-bias resistance with decreasing temperature is mirrored in the sharp minimum in the differential conductance versus applied voltage at low temperatures (Fig. 3(a)) showing that only the density of states around the Fermi level is affected. The fact that the resistance increase does not yet seem to saturate at 11 mK means that the density-of-states minimum at the Fermi level must be very sharp, possibly singular. A similar observation has been reported by Ashoori et al. [6] regarding tunneling from a GaAs quantum well to a doped GaAs substrate. They tentatively attributed the effect to the formation of a Coulomb gap in the tunneling density of states [7]. In comparison, our samples show a sharper and deeper density-of-states minimum. We speculate that the large sample-to-sample variations that we observe are due to relatively small variations in the actual minimum value of the density of states at the Fermi level.

The conductance fluctuations are due to resonant tunneling through well-defined charge-carrier states that shift through the Fermi level as a function of magnetic field. As the fluctuations appear on both Shubnikov–de Haas maxima and

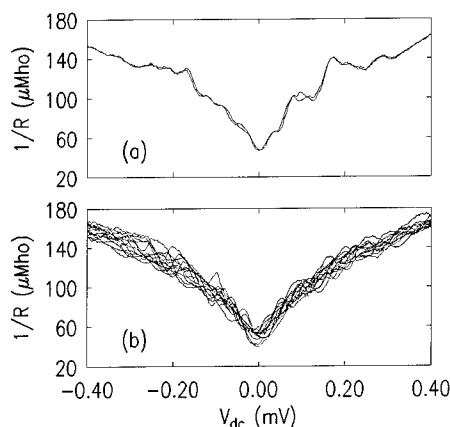


Fig. 3. Inverse differential resistance (sample I) versus DC voltage at  $B = 12$  T and  $T = 45$  mK. (a) Fixed magnetic field; the two sweeps demonstrate the reproducibility of the fluctuations. (b) Magnetic field drifting down at a rate of 5 mT between successive voltage sweeps (showing the amplitude of the fluctuations).

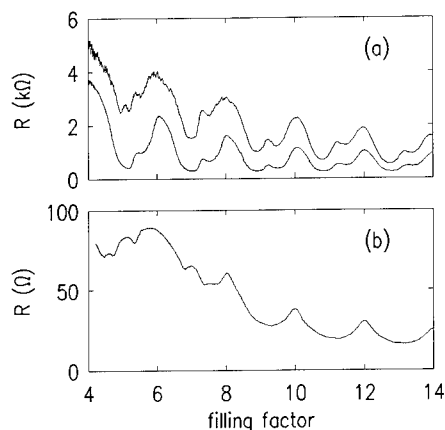


Fig. 4. Zero-bias resistance as a function of magnetic field. (a) Sample II,  $T = 45$  mK (upper curve) and  $T = 400$  mK (lower curve). (b) Sample III,  $T = 45$  mK.

minima, the states are not likely linked to the localized states of the quantum Hall effect. The resonant-tunneling mechanism is independent of the formation of a Coulomb gap in the 2DEG as is shown in Fig. 3(b). When a voltage is applied, the average differential conductance increases drastically but the amplitude of the fluctuations remains the same. The fluctuation peaks are still thermally broadened at 45 mK indicating that the actual resonances are very sharp. This means that the tunneling rates from the electrodes to the resonant state must be low but very symmetric. Possibly the resonances are due to electron states strongly localized at the InAs/AlSb interfaces.

Finally, we discuss the additional resistance peak in the third Landau level (i.e. between filling factors 4 and 6) at low temperatures. Figure 4 shows the resistance versus filling factor of two other samples one of which has thinner AlSb barriers. That sample (Fig. 4(b)) does not show spin splitting in the Shubnikov–de Haas oscillations but at 45 K it features a three-fold splitting in both the third and the fourth Landau level. The effect may be due to the resolution at these low temperatures of the Landau levels of the holes in the GaSb electrodes. The hole quantization cannot be directly responsible for the splitting because it would only give broad Shubnikov–de Haas oscillations due to the low hole density

and mobility. However, the electron and hole densities are not constant as a function of magnetic field [4]. The charge transfer between InAs and GaSb is constantly adjusted to the actual values of the densities of states at the Fermi level. This interaction may be the key to the understanding of the anomalous three-fold splitting of the Shubnikov–de Haas oscillations.

In conclusion, we have studied vertical transport through a 2DEG in the InAs quantum well of a type II heterostructure. At temperatures below 1 K the zero-bias conductance shows interesting deviations from the usual Shubnikov–de Haas oscillations in high perpendicular magnetic fields. These include an overall decrease in the conductance that is attributed to the formation of a Coulomb gap in the tunneling density of states and the appearance of conductance fluctuations possibly due to resonant tunneling through interface-related states.

One of us (P.C.v.S.) would like to thank the IBM Research Division for its hospitality during

his visit and acknowledges the Royal Dutch Academy of Arts and Sciences (KNAW) for financial support. This work has been partially supported by the Army Research Office.

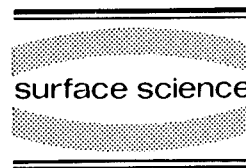
## 1. References

- [1] L. Esaki, L.L. Chang and E.E. Mendez, *Jpn. J. Appl. Phys.* 20 (1981) L529.
- [2] J.R. Söderström, D.H. Chow and T.C. McGill, *Appl. Phys. Lett.* 55 (1989) 1094.
- [3] L.F. Luo, R. Beresford, K.F. Longenbach and W.I. Wang, *Appl. Phys. Lett.* 57 (1990) 1554.
- [4] E.E. Mendez, H. Ohno and L. Esaki, *Phys. Rev. B* 43 (1991) 5196.
- [5] E.E. Mendez, J. Nocera and W.I. Wang, *Phys. Rev. B* 45 (1992) 3910.
- [6] R.C. Ashoori, J.A. Lebens, N.P. Bigelow and R.H. Silsbee, *Phys. Rev. Lett.* 64 (1990) 681.
- [7] Recently this interpretation has been considered theoretically [A.L. Efros, *Phys. Rev. Lett.* 68 (1992) 2208]. A related effect is found in experiments on tunneling between two 2DEGs [J.P. Eisenstein, L.N. Pfeiffer and K.W. West, *Phys. Rev. Lett.* 69 (1992) 3804; A.L. Efros and F.G. Pikus, to be published].



ELSEVIER

Surface Science 305 (1994) 520–526



# Coulomb blockade in the presence of adiabatically transmitted edge channels

B.W. Alphenaar <sup>\*,1</sup>, A.A.M. Staring, H. van Houten

*Philips Research Laboratories, 5600 JA Eindhoven, The Netherlands*

C.T. Foxon <sup>2</sup>

*Philips Research Laboratories, Redhill RH1 5HA, UK*

(Received 30 April 1993; accepted for publication 3 June 1993)

## Abstract

We present measurements of the conductance of a quantum dot in the presence of 2, 1, and 0 adiabatically transmitted edge channels. In all three cases periodic conductance oscillations are observed as a function of gate voltage. By using the oscillations observed in the absence of edge channels as an electron counter we demonstrate that the oscillations observed in the presence of edge channels are due to the influence of Coulomb charging. Using the temperature dependence of the conductance oscillations we have then estimated the activated Coulomb charging energy.

## 1. Introduction

There has been a great deal of experimental and theoretical work devoted to the study of quantum dots fabricated by selectively depleting the two-dimensional electron gas (2DEG) of an AlGaAs/GaAs heterostructure. An example of such a dot device is shown schematically in Fig. 1a. Three gates labelled A, C, and D are used to create two quantum point contacts (QPCs) which

connect the dot to large 2DEG leads. The density in the dot is varied independently of the QPC conductances by the voltage on gate B. When the dot is formed the gaps between gates B and C are pinched off.

In a high magnetic field, electron transport in the leads occurs through edge channels (which form where each Landau level crosses the Fermi energy near the edge of the sample). Selective reflection of edge channels is possible at a QPC, whose conductance is approximately given by [1]

$$G_{\text{pc}} \approx \frac{e^2}{h} (N_{\text{trans}} + t), \quad (1)$$

with  $N_{\text{trans}}$  the number of edge channels that are fully transmitted over the barrier in the constriction. The  $(N_{\text{trans}} + 1)$ th edge channel (correspond-

\* Corresponding author.

<sup>1</sup> Current address: Hitachi Cambridge Laboratory, Cavendish Laboratory, Cambridge CB3 0HE, UK.

<sup>2</sup> Current address: Department of Physics, University of Nottingham, Nottingham NG7 2RD, UK.

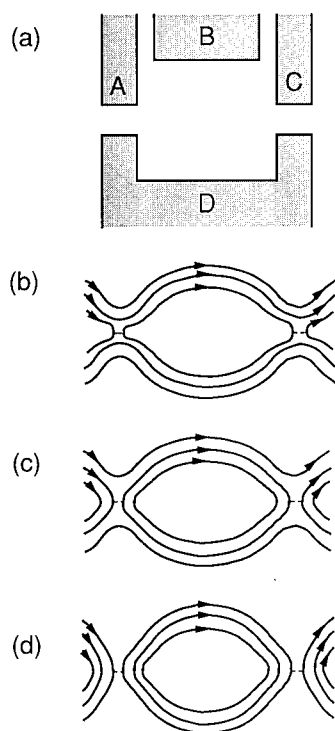


Fig. 1. (a) Schematic drawing of the quantum dot devices. The dimensions of the rectangle formed by the gates is  $750 \times 800 \text{ nm}^2$  for device I and  $700 \times 900 \text{ nm}^2$  for device II. (b)–(d) Current paths through the dot in the presence of 2, 1, or 0 adiabatically transmitted edge channels as adjusted by  $V_A$  and  $V_C$ .

ing to the lowest energy Landau level confined to the dot) tunnels with a transmission probability  $t \leq 1$ . Edge channels corresponding to higher energy Landau levels are nearly completely reflected.

The electron states localized in the dot form a discrete energy spectrum, each state being associated with a particular confined Landau level. This results in two relevant energy scales: an inter-Landau level spacing  $\Delta E$ , and a smaller intra-Landau level spacing  $\delta E$  [2]. For a non-interacting electron gas, a peak in the conductance due to resonant tunnelling is observed if a confined state of the  $(N_{\text{trans}} + 1)$ th Landau level lines up with the Fermi level in the leads,  $E_F$ . Periodic conductance oscillations are then expected both as a function of electron density (varied by means of the voltage  $V_B$  on electrode B), and as a function of magnetic field. Evidence for such

oscillations (sometimes referred to in the literature as Aharonov–Bohm oscillations [3]) have been demonstrated experimentally as a function of magnetic field [4] and gate voltage [5], in the regime where one or more edge channels are transmitted adiabatically (i.e.,  $N_{\text{trans}} = 2, 1$  as shown in Figs. 1b and 1c).

It has become clear, though, that this non-interacting electron approximation is not valid if the conductance of the point contacts  $G_{\text{pc}} < e^2/h$ , i.e., if there are no adiabatically transmitted edge channels present ( $N_{\text{trans}} = 0$  as in Fig. 1d). In this regime, tunnelling through a quantum dot is governed by single-electron charging effects [6]. These effects are known to be important if the capacitance of the dot  $C$  is small so that the maximum charging energy  $e^2/2C \gg kT$ . Single-electron charging has been demonstrated experimentally by observations of Coulomb blockade oscillations, i.e., periodic oscillations in the conductance as a function of voltage on a gate capacitively coupled to the dot. The Coulomb charging energy is typically much larger than either of the quantum confinement energies  $\Delta E$  or  $\delta E$ ; modifications in the amplitude and position of the Coulomb blockade oscillations due to the confined energy spectrum have only been observed at milliKelvin temperatures [7,2,8].

It has been widely assumed that Coulomb charging can be ignored if the conductance of the point contacts  $G_{\text{pc}} > e^2/h$ , as is the case if one or more edge channels are adiabatically transmitted. Coulomb charging effects do disappear in the analogous zero-field case where the barriers in the QPCs are low enough that a non-tunnel current flows [9]. However, if isolated current paths exist with conductance less than  $e^2/h$ , Coulomb charging can still be important, even if the total device conductance is greater than  $e^2/h$ . Such a situation occurs in a high magnetic field where the current carrying edge channels are separated by a tunnel barrier consisting of an incompressible electron gas. This allows for single-electron charging of the confined edge channels even in the presence of adiabatically transmitted edge channels.

In a recent paper [10], we demonstrated the importance of Coulomb charging in the presence

of adiabatically transmitted edge channels. In this paper, we present more extensive data from measurements of two additional quantum dot devices that confirm this conclusion. We give a direct comparison of the conductance versus gate voltage for different barrier transparencies, so that 2, 1, or 0 adiabatically transmitted edge channels are present in addition to the confined levels. We observe periodic conductance oscillations as a function of gate voltage for all three barrier transparencies and use the oscillations observed in the full Coulomb blockade regime (no adiabatically transmitted edge channels) as a novel electron counter to calibrate the period of the oscillations observed in the presence of adiabatically transmitted edge channels. In this way we demonstrate that even in the presence of the transmitted channels the conductance oscillations cannot be satisfactorily described in terms of resonant tunnelling without invoking Coulomb charging.

## 2. Experiment

The geometry of our two quantum dot devices (I and II) is shown schematically in Fig. 1a [11]. As described in the introduction, four gates (labelled A–D) define a rectangle on the surface of an AlGaAs/GaAs heterostructure with a 2DEG of mobility  $\mu \approx 10^6 \text{ cm}^2/\text{V} \cdot \text{s}$  and density  $n_s \approx 3 \times 10^{11} \text{ cm}^{-2}$ . The lithographic dimensions of device I are  $750 \times 800 \text{ nm}^2$  and those of device II are  $700 \times 900 \text{ nm}^2$ . When the gates are negatively biased, a quantum dot is formed in the underlying 2DEG, and is connected through QPCs to two-dimensional leads. Two-terminal conductance measurements are made across the dot using an AC lock-in technique with an excitation voltage below  $10 \text{ } \mu\text{V}$ . In our experiments, the voltage on gate D is left fixed, and the voltages on gates A and C are adjusted to control the transmission through the tunnel barriers in the QPCs. The conductance is then measured as a function of the voltage on gate B which determines the electron density in the dot.

Fig. 2 shows the results of conductance measurements of device I as a function of  $V_B$  for a

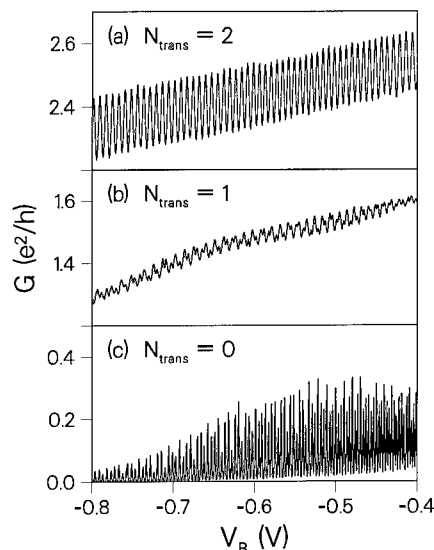


Fig. 2. Conductance of device I as a function of the voltage on gate B for  $B = 3.5 \text{ T}$  and  $T = 50 \text{ mK}$ . In the top, middle, and bottom trace (a)–(c) the QPCs are adjusted to conductances of  $2.5$ ,  $1.5$ , and  $0.5 \text{ } e^2/h$ , respectively. The three cases correspond to the three current paths shown in Figs. 1b–d.

magnetic field of  $B = 3.50 \text{ T}$  and a temperature of  $50 \text{ mK}$ . The QPCs are adjusted so that there are  $N_{\text{trans}} = 2$ ,  $1$ , and  $0$  edge channels adiabatically transmitted through the dot for traces (a), (b), and (c), respectively. This corresponds to the following QPC conductances: (a)  $2e^2/h < G_{\text{pc}} < 3e^2/h$ , (b)  $e^2/h < G_{\text{pc}} < 2e^2/h$ , and (c)  $G_{\text{pc}} < e^2/h$ . Each trace shows a series of nearly periodic oscillations in the conductance as a function of  $V_B$ , however, the period of the oscillations varies from trace to trace. There are 53 oscillations in (a), 80 in (b), and 102 in (c), indicating that the period in (a) is about twice that in (c) while the period in (b) is about 1.2 times that in (c).

Fig. 3 compares the conductance oscillations from measurements made at four different magnetic fields ( $2.75$ ,  $3.50$ ,  $4.20$ , and  $4.60 \text{ T}$ ). In each case the QPCs are adjusted so that  $2e^2/h < G_{\text{pc}} < 3e^2/h$ , in other words  $N_{\text{trans}} = 2$ . Between  $2.75$  and  $4.60 \text{ T}$  periodic conductance oscillations are observed whose period increases with magnetic field – the amplitude of the oscillations drops off rapidly outside of this field range. In the  $N_{\text{trans}} = 1$  case (not shown) oscillations are observed for

magnetic fields less than 7 T and the period of the oscillations again increases with increasing magnetic field. For the  $N_{\text{trans}} = 0$  case, however, oscillations are observed irrespective of the magnetic field and the period of the oscillations is field independent.

### 3. Model

The Coulomb charging energy for the closed dot  $e^2/2C \approx e^2/8\epsilon d \approx 2.5 \times 10^{-4}$  eV, is more than an order of magnitude greater than the estimated confined-energy spacing  $\delta E \approx 4\hbar^2/m^*d \approx 2.0 \times 10^{-5}$  eV. Thus, the very regular oscillations observed in the absence of adiabatically transmitted edge channels (the bottom trace in Fig. 2) can safely be attributed to the Coulomb blockade effect. The gate voltage separation between peaks is then  $\sim e/C_{\text{gate}}$ , where  $C_{\text{gate}}$ , the capacitance between gate B and the dot, is assumed to be independent of  $G_{\text{pc}}$ . This is reasonable since  $G_{\text{pc}}$  is much more sensitive to changes in voltages  $V_A$  and  $V_C$  than are the size of the dot and the dot–gate separation (which together determine  $C_{\text{gate}}$ ).

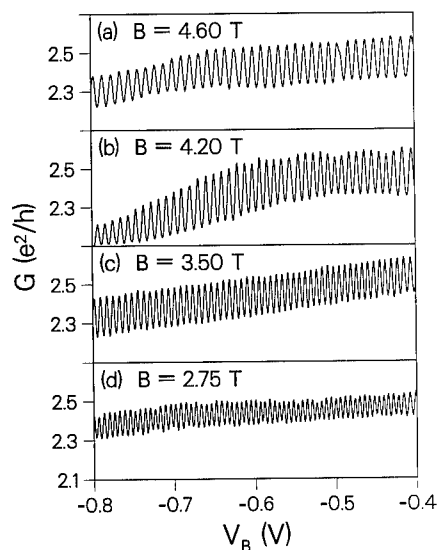


Fig. 3. Conductance of device I as a function of the voltage on gate B for  $G_{\text{pc}} = 2.5 e^2/h$  ( $N_{\text{trans}} = 2$ ) and  $T = 50$  mK at four different magnetic fields.

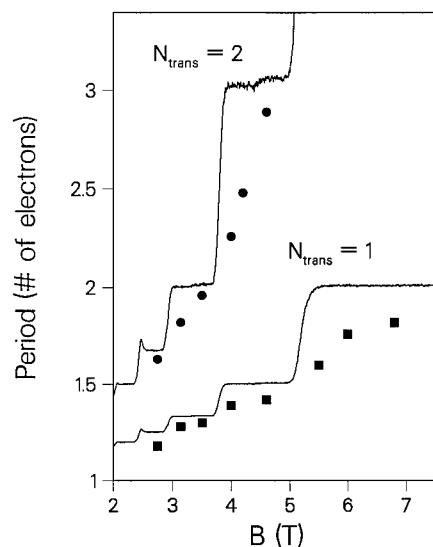


Fig. 4. Period of the conductance oscillations (in units of electrons per peak) versus magnetic field for  $G_{\text{pc}} = 2.5 e^2/h$  (circles) and  $G_{\text{pc}} = 1.5 e^2/h$  (squares). The solid lines are theoretical fits for  $N_{\text{trans}} = 2, 1$  adiabatically transmitted edge channels (see text).

This implies that the number of electrons removed from the dot as a function of  $V_B$  is independent of the number of edge channels adiabatically transmitted through the dot. Since each Coulomb blockade peak corresponds to the removal of one electron from the dot, we can use the Coulomb blockade oscillations as a tool to determine the number of electrons corresponding to each peak in the upper traces in Fig. 2. This is given by the number of peaks for  $N_{\text{trans}} = 1$  or 2 divided by the number of Coulomb blockade peaks counted for  $N_{\text{trans}} = 0$ . The results of this procedure performed on a set of measurements of the type shown in Figs. 2 and 3 are plotted versus magnetic field in Fig. 4. The number of electrons per peak is considerably larger for  $N_{\text{trans}} = 2$  than for  $N_{\text{trans}} = 1$ . In both cases, an increase in magnetic field results in an increase in the number of electrons per peak.

We now discuss the origin of the periodic conductance oscillations for  $G_{\text{pc}} > e^2/h$  (traces (a) and (b) in Fig. 2). As described in Ref. [10], the oscillations observed in the presence of adiabatically transmitted edge channels vanish at rel-



atively low temperatures – for  $N_{\text{trans}} = 1$  and 2 the oscillations disappear at 200 and 500 mK, respectively. These temperatures are comparable to the estimated confined energy spacing,  $\delta E \approx 235$  mK. In addition, it is difficult to estimate the charging energy, since it is influenced by the presence of the adiabatically transmitted edge channels. We thus first consider the simpler non-interacting case in which Coulomb charging is ignored.

As discussed in the introduction, in the absence of Coulomb charging a peak in the conductance is observed due to resonant tunnelling when an electron state of the outermost confined Landau level lines up with the Fermi energy in the leads. The frequency at which this occurs corresponds to the rate at which electrons are removed from the outermost confined Landau level. The total number of spin-split Landau levels in the dot  $N_{\text{dot}}$  are made up of the  $N_{\text{conf}}$  Landau levels of guiding center energy  $E_g$  below the barrier height  $E_b$  and the  $N_{\text{trans}}$  additional Landau levels that are occupied in the dot but fully transmitted over the barriers in the QPCs ( $E_g > E_b$ ). For the  $N_{\text{trans}} = 0$  case, it has been demonstrated that the electron states associated with the confined Landau levels are ordered in a cyclical fashion and, thus, each of the  $N_{\text{conf}}$  Landau levels is depleted at approximately the same rate as a function of  $V_B$  [2]. We assume that the  $N_{\text{trans}}$  Landau levels are depleted at a similar rate, so that we must remove  $N_{\text{dot}}$  electrons in order to remove one from the outermost confined Landau level. Since  $N_{\text{dot}} \propto 1/B$ , this argument predicts that the number of electrons per peak should decrease rather than increase with magnetic field, in contradiction with the observed results (Fig. 4). This discrepancy could in principle be eliminated if resonant tunnelling through electron states of the confined Landau levels with index higher than  $N_{\text{trans}} + 1$  also contribute to the conductance of the dot. The tunnelling rate, however, decreases exponentially with decreasing  $E_g$  [12], thus, there should be an order of magnitude modulation of conductance peak heights due to resonant tunnelling through states belonging to consecutive Landau levels confined in the dot [13]. This is not observed in our experiment, however [14].

We can model the results of Fig. 4 though, if we take Coulomb charging into account for  $G_{\text{pc}} > e^2/h$ . We extend recent arguments for the  $N_{\text{trans}} = 0$  case [15] to our problem by considering a separate Coulomb charging energy for the  $N_{\text{conf}}$  Landau levels existing in the presence of the adiabatically transmitted edge channels. This is reasonable, since a magnetically induced tunnel barrier consisting of an incompressible electron gas exists between each of the edge channels. Tunnelling electrons thus face a non-zero Coulomb charging energy associated with a change in the electron population of the confined Landau levels. This leads to Coulomb blockade oscillations as a function of gate voltage with a period corresponding to the removal of an electron from *any one of the*  $N_{\text{conf}}$  Landau levels. The removal of electrons from one of the  $N_{\text{trans}}$  Landau levels does not give rise to a conductance peak because charge in these levels is not localized and can therefore be changed continuously. This implies that

$$\frac{\text{electrons}}{\text{peak}} = \frac{N_{\text{conf}} + N_{\text{trans}}}{N_{\text{conf}}} = \frac{N_{\text{dot}}}{N_{\text{conf}}}. \quad (2)$$

Fig. 4 shows solutions of Eq. (2) for  $N_{\text{trans}} = 1$  and  $N_{\text{trans}} = 2$ . We determine  $N_{\text{dot}}$  by measuring the conductance of the dot with the two QPCs completely open ( $V_A = V_C = 0$ ); using Eq. (1), this is proportional to the number of edge channels between gates B and D. The agreement between our model and the experimental results is reasonably good. In both cases, the number of electrons per peak is seen to increase as  $N_{\text{dot}}$  decreases from 5 to 3. Clearly, this model, which includes Coulomb charging, is able to account for the experimental observations, while the non-interacting model discussed above does not. This demonstrates the importance of Coulomb charging even in the presence of adiabatically transmitted edge channels.

#### 4. Discussion

In our phenomenological model, the presence of the  $N_{\text{trans}}$  adiabatically transmitted Landau levels enters only in the form of a nearby electron

reservoir, coupled capacitively to both the gates and the confined Landau levels. This enhances the effective capacitance and decreases the charging energy  $e^2/2C$ . The assumed increase in  $C$  with the number of adiabatically transmitted edge channels can account for the reduction of the activation energy with increasing barrier transparency as described in Ref. [10]. A more quantitative description is contained in two recent theoretical papers which calculate the charging energy of the confined Landau levels in the presence of adiabatically transmitted edge channels [16,17]. Both use an extension of the self-consistent model introduced by McEuen et al. [15] in which the distribution of electrons among the Landau levels is arranged to minimize the total energy of the dot assuming a Thomas–Fermi electron–electron interaction. The number of electrons occupying each confined Landau level is constrained to be an integer, whereas it is an unconstrained positive real number for an extended edge channel. This model predicts an appreciable Coulomb charging energy in the presence of adiabatically transmitted edge channels that oscillates as a function of electron density. According to Marmorkos and Beenakker [16], for  $B = 2$  T,  $N_{\text{dot}} = 2$  and  $N_{\text{trans}} = 1$ , the charging energy reaches a maximum of  $E_{\text{act}} \approx 0.1$  meV  $\approx 1.2$  K.

Experimentally, we can determine an activation energy from the temperature dependence of the conductance oscillations. Fig. 5 shows the temperature dependence of a conductance maximum and minimum for device II at  $B = 3.5$  T,  $N_{\text{trans}} = 2$ , and  $N_{\text{dot}} = 4$ . The conductance minimum shows an activated behavior with  $E_{\text{act}} = 4.7$   $\mu$ eV, while the maximum is virtually temperature independent [18]. This is in qualitative agreement with the theory. However, the theoretically determined activation energy is much larger than that determined experimentally. This discrepancy could be due to the fact that the model does not accurately match the device geometry used in the experiment [17]. While the model is appropriate for a device in which the density is controlled by a back gate as used by McEuen et al. [7,15], the device in our experiment has a side gate which varies both the density and the lateral confinement.

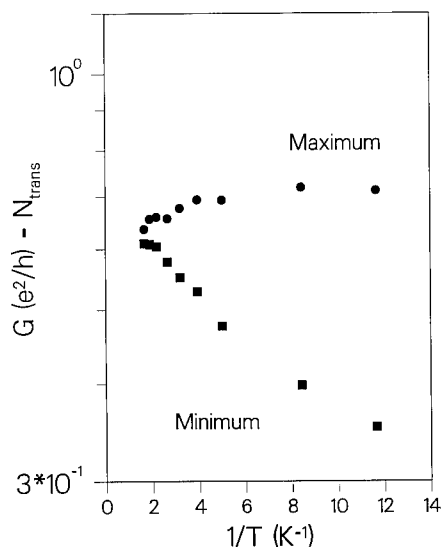


Fig. 5. Temperature dependence of a maximum and a minimum in the conductance of device II as a function of inverse temperature for  $B = 3.5$  T and  $N_{\text{trans}} = 2$ .

In addition, Kinaret and Wingreen [17] introduce an effective capacitance model in which the charge distribution is directly related to the capacitances among the Landau levels and the gate. The increase in the period of the conductance oscillations for increasing  $N_{\text{trans}}$  is then attributed to the decrease in effective capacitance between the confined Landau levels and the gate. As the upper Landau level is depleted, it shrinks, and its geometrical capacitance is thus reduced. This predicts that the charge per peak as shown in Fig. 4 grows smoothly with magnetic field, rather than in steps, as is predicted by our phenomenological model. On this point the experimental results are not entirely conclusive. In Fig. 4, the period increases smoothly with magnetic field for the  $N_{\text{trans}} = 2$  case, however, steps are apparent for the  $N_{\text{trans}} = 1$  case.

In conclusion, we have studied the conductance of a quantum dot in the presence of 2, 1, or 0 adiabatically transmitted edge channels. We observe periodic conductance oscillations as a function of gate voltage in all three cases, and demonstrate that the number of electrons added to the dot per peak is determined by the ratio of the total number of Landau levels in the dot to

the number confined to the dot. Our results demonstrate that the formation of Landau levels in a high magnetic field causes single-electron charging effects to be of importance for barrier conductances greater than  $e^2/h$ . Using the temperature dependence of the conductance oscillations we have then estimated the activated Coulomb charging energy. The discrepancy between the experimentally determined activation energy and that predicted theoretically suggests that a more complete theoretical treatment of the problem is still needed.

## 5. Acknowledgements

The authors would like to thank C.W.J. Beenakker, P.L. McEuen and L.W. Molenkamp for useful discussions and M.A.A. Mabe-soone and O.J.A. Buyk for expert technical assistance. In addition, B.W.A. is grateful for the support of Hitachi Cambridge Laboratory during the preparation of this manuscript.

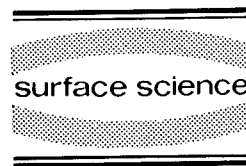
## 6. References

- [1] B.J. van Wees, L.P. Kouwenhoven, H. van Houten, C.W.J. Beenakker, J.E. Mooij, C.T. Foxon and J.J. Harris, *Phys. Rev. B* 38 (1988) 3625.
- [2] A.A.M. Staring, B.W. Alphenaar, H. van Houten, L.W. Molenkamp, O.J.A. Buyk, M.A.A. Mabe-soone and C.T. Foxon, *Phys. Rev. B* 46 (1992) 12869.
- [3] J.K. Jain, *Phys. Rev. Lett.* 60 (1988) 2074; U. Sivan and Y. Imry, *Phys. Rev. Lett.* 61 (1988) 1001.
- [4] B.J. van Wees, L.P. Kouwenhoven, C.J.P.M. Harmens, J.G. Williamson, C.E.T. Timmering, M.E.I. Broekaart, C.T. Foxon and J.J. Harris, *Phys. Rev. Lett.* 62 (1989) 2523.
- [5] R.J. Brown, C.G. Smith, M. Pepper, M.J. Kelly, R. Newbury, H. Ahmed, D.G. Hasko, J.E.F. Frost, D.C. Peacock, D.A. Ritchie and G.A.C. Jones, *J. Phys. C* 1 (1989) 6291.
- [6] For a recent review of Coulomb blockade in semiconductor nanostructures, see: H. van Houten, C.W.J. Beenakker and A.A.M. Staring, in: *Single Charge Tunneling*, NATO Advanced Study Institute, Series B: Physics, Eds. H. Grabert and M.M. Devoret (Plenum, New York, 1992).
- [7] P.L. McEuen, E.B. Foxman, U. Meirav, M.A. Kastner, Y. Meir, N.S. Wingreen and S.J. Wind, *Phys. Rev. Lett.* 66 (1991) 1926.
- [8] A.T. Johnson, L.P. Kouwenhoven, W. de Jong, N.C. van der Vaart, C.J.P.M. Harmens and C.T. Foxon, *Phys. Rev. Lett.* 69 (1992) 1592; E.B. Foxman, P.L. McEuen, U. Meirav, N.S. Wingreen, Y. Meir, P.A. Belk, N.R. Belk, M.A. Kastner and S.J. Wind, *Phys. Rev. B* 47 (1993) 10020.
- [9] L.P. Kouwenhoven, N.C. van der Vaart, A.T. Johnson, W. Kool, C.J.P.M. Harmens, J.G. Williamson, A.A.M. Staring and C.T. Foxon, *Z. Phys. B* 85 (1991) 367.
- [10] B.W. Alphenaar, A.A.M. Staring, H. van Houten, M.A.A. Mabe-soone, O.J.A. Buyk and C.T. Foxon, *Phys. Rev. B* 46 (1992) 7236.
- [11] For a more exact description of the device geometries see Ref. [2] for device I, and A.A.M. Staring et al. *Physica B* 175 (1991) 226, for device II.
- [12] H.A. Fertig and B.I. Halperin, *Phys. Rev. B* 36 (1987) 7969.
- [13] Y. Meir, N.S. Wingreen and P.A. Lee, *Phys. Rev. Lett.* 66 (1991) 771; C.W.J. Beenakker, *Phys. Rev. B* 44 (1991) 1646.
- [14] The more modest amplitude modulation of the conductance peaks that we observe in the middle and bottom traces of Fig. 2 can be explained in terms of tunnelling through the confined states associated with only the  $(N_{\text{trans}} + 1)$ th Landau level. The fact that a more dramatic amplitude modulation is not observed suggests that we are in the near classical regime where  $\Delta E \geq kT \geq \delta E$ . See Ref. [2].
- [15] P.L. McEuen, E.B. Foxman, J.M. Kinaret, U. Mierav, M.A. Kastner, N.S. Wingreen and S.J. Wind, *Phys. Rev. B* 45 (1992) 11419.
- [16] I.K. Marmorkos and C.W.J. Beenakker, *Phys. Rev. B* 46 (1992) 15562.
- [17] J.M. Kinaret and N.S. Wingreen, preprint.
- [18] By definition, the activation energy equals  $kT$  at the temperature where the conductance minimum decreases to  $1/e$  of its high temperature value. Thus, in Fig. 5, where the minimum decreases by less than an order of magnitude between 500 and 50 mK, the activation energy corresponds to a temperature of 55 mK even though the oscillations survive to a temperature of 500 mK.



ELSEVIER

Surface Science 305 (1994) 527–535



## Electron–electron interactions and the magnetoconductance of submicron quantum dots

A. Sachrajda \*, R.P. Taylor, C. Dharma-wardana, J.A. Adams, P. Zawadzki, P.T. Coleridge

*Institute For Microstructural Sciences, NRC, Ottawa, Canada K1A 0R6*

(Received 19 April 1993; accepted for publication 14 July 1993)

---

### Abstract

The magnetoconductance of quantum dots at high magnetic fields has been studied experimentally and theoretically as a function of the quantum dot barrier height. It is found that even when the dot is not Coulomb blockaded, electron–electron interactions are required to explain the magnetoconductance oscillations.

---

### 1. Introduction

Conductance oscillations due to discrete electron effects have been observed in quantum dots both as a function of electron number [1] and magnetic field [2]. The former are the well known Coulomb blockade oscillations (CBO), whereas the magnetoconductance oscillations (MCO) arise when discrete states and fully transmitted edge states participate in the conductance. The MCO effect is sometimes referred to as the high field Aharonov–Bohm (AB) effect. In this paper we reinterpret the MCO effect in terms of an interacting-electron picture. We find a new regime where both effects coexist and use this coexistence to infer from our measurements and theory both the spin quantum number and the Landau

level index of the discrete state closest to the Fermi level. In Section 2 we identify experimentally the barrier conductance conditions necessary for the observation of each effect. In Section 3 results are presented for the barrier regime in which the two effects co-exist both as a functions field and electron density. A theoretical model is presented in Section 4 in which we show that the MCO are dominated by electron–electron interactions within the dot and the screening effect of fully transmitted edge states.

The experiments were performed on a variety of dots defined using the lateral gate depletion technique. The TiPt gates were deposited upon high-mobility 2DEGs in GaAs/AlGaAs heterostructures using conventional e-beam techniques. The samples were then placed on a metallic gate which acted as a backgate for changing the sample carrier density and the number of electrons in the dot. More details on the sample geometry are published elsewhere [3].

---

\* Corresponding author.

## 2. Quantum dot barrier conditions for the observation of the coulomb blockade and magnetoconductance oscillations

The experiment of Van Wees et al. [2] was performed on a  $1.5\ \mu\text{m}$  diameter dot and was interpreted as resonant tunnelling through the single-electron levels in the dot. At resonance the conductance through the dot was enhanced. In addition to one trapped edge state in the dot, a number,  $N_{\text{FS}}$ , of edge states were fully transmitted through the dot and also through the quantum point contact (QPC) barriers at the entrance and exit of the dot. Adiabatic transport (i.e., no communication between edge states) was believed to be crucial to the observation of the effect. The period of the MCO was found not to be simply related to the area of the dot via  $\Delta B = h/eA$ . This discrepancy was accommodated by considering that the area  $A$  changed as the magnetic field,  $B$ , was swept. In this paper we will present an alternative explanation using the interacting-electron picture. In our early experiments [4] we did not observe any periodic MCO for dots with diameters greater than  $1.0\ \mu\text{m}$ . For dots between  $1.0$  and  $0.5\ \mu\text{m}$  large aperiodic magnetoconductance structures (MCS) which persisted to relatively high temperatures ( $> 2\ \text{K}$ ) could be observed. Most significantly the conductance through the dot at the minima dropped below that given by the fully transmitted edge states. Fig. 1a shows an example of such behaviour for a  $1\ \mu\text{m}$  diameter dot (NB, in Fig. 1 the edge state configuration of Fig. 9a is achieved at  $5.8\ \text{T}$ ). The MCS were not present in magnetic field ( $B$ ) sweeps when only the individual QPC barriers were defined. The MCS [3] provide evidence of the coupling between the fully transmitted edge states and the trapped edge states. The random nature of the MCS implies that the coupling is related to the impurity potential. A similar signature of non-adiabaticity in a different geometry has previously been studied experimentally by Ford et al. [5] and theoretically by Kirzenow et al. [6]. When dots (diameter  $\leq 0.5\ \mu\text{m}$ ) were studied [3] periodic MCO oscillations were observed superimposed on these larger MCS at temperatures below  $500\ \text{mK}$  (see Fig. 1b). It was

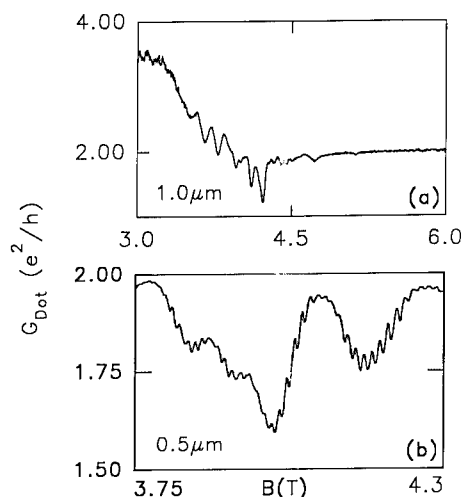


Fig. 1. The magnetoconductance of quantum dots with diameters (a)  $1\ \mu\text{m}$  (b)  $0.5\ \mu\text{m}$  (see text for details).

found in addition [3] that both the MCS and the MCO existed even when the QPC barriers were set to allow only fully transmitted edge states (i.e., there was no tunnelling across the QPC barrier). Fig. 9a illustrates the edge state configuration for the observation of the MCO. The fully transmitted edge states at the top and bottom of the dot, are filled to different chemical potentials (they originate from different contact reservoirs). Tunnelling through the discrete states of the dot, however, achieves a partial equilibration of this chemical potential difference. At resonance the conductance through the dot is lowered. We therefore distinguish this resonant reflection (RR) mechanism from the resonant transmission (RT) mechanism of Van Wees et al. [2]. The RR process will occur whenever the inner discrete energy levels of the dot are depopulated. Fig. 2 shows the equivalent oscillations observed when either the backgate (i.e., mainly the dot density) or one of the top gates (i.e., mainly the dot area) is swept. The consequences of electron–electron interactions and spin conservation during the RR process will be dealt with in Section 4.

CBO were first observed in semiconductor nanostructures by Scott–Thomas et al. [1]. The orthodox theory [7] assumes that the dot is well isolated (i.e., the barrier resistance  $> h/e^2$ ). Ex-

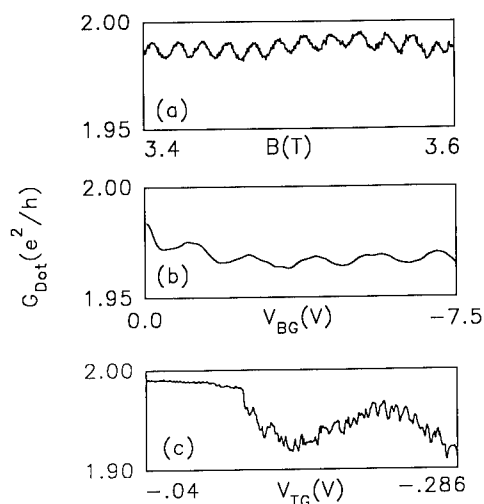


Fig. 2. The resonant reflection mechanism observed by sweeping (a)  $B$ , (b) the backgate voltage  $V_{BG}$  and (c) the top-gate voltage  $V_{TG}$ .

perimentally, however, we have found that the condition for observation of the CBO is that less than one mode (but only slightly less) has to be fully transmitted in each barrier. Fig. 3 shows the maximum barrier conductance for which we could observe CBO as a function of magnetic field. The sharp transition from  $\sim e^2/h$  to  $2e^2/h$  occurs when spin resolution is achieved. The CBO persisted to 2 K and had a gate voltage period independent of field from 0 to 13 T.

Consider the situation of Fig. 9a for which the RR oscillations were observed both as a function

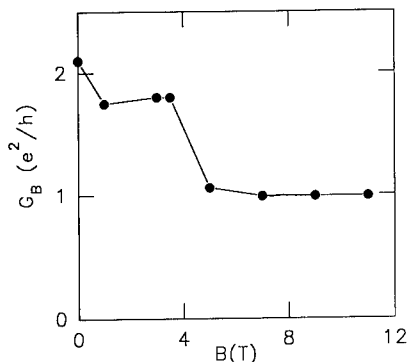


Fig. 3. The  $B$  dependence of the maximum barrier conductance at which Coulomb blockade oscillations were observed.

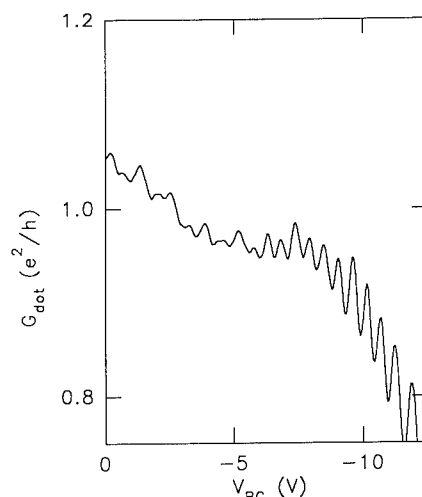


Fig. 4. A backgate voltage sweep in the Coulomb blockade regime.

of field and backgate. There were two edge states transmitted through the barriers: spin up and spin down (NB, however our measurements showed that in the barriers themselves the edge states were not fully spin resolved). When the QPC barrier conductance was set  $\ll 2e^2/h$  we only observed CBO as a function of backgate voltage. The two sets of oscillations had different temperature dependencies and periods. In the next section we present results on an intermediate barrier conductance regime in which both sets of oscillations coexist.

### 3. Coexistence of the RR and CB effects

In Fig. 4 we show the backgate voltage dependence of the conductance of the dot at  $B = 3.5$  T which for this dot corresponds to the edge state configuration illustrated in Fig. 9. As the voltage is swept the number of electrons in the dot changes resulting in CBO with uniform amplitude that can be seen at the more negative gate voltages. The backgate also affects the barrier height in the QPCs at the entrance and exit to the dot and at the low negative voltage end (Fig. 4) RR effects may be expected to be observed. For this particular sweep we observe that at this high

conductance end of the sweep every second CBO peak is suppressed. A suppression of the peak is exactly what would be expected if the two effects (i.e., RR and CB) coexisted. Every time the trapped level is depopulated there is a decrease in conductance due to the resonant backscattering (RR) process which occurs. Electrons are removed from the dot at the CBO peaks. Therefore, an observation of the suppression of the peaks can be used to identify when an inner trapped level is being removed from the dot. The CBO themselves count every electron leaving the dot. It can therefore be deduced from Fig. 4 that as the dot is depopulated every second electron comes from the “inner” trapped level. For an isolated dot calculations show that this is what is expected. On warming the sample to above 700 mK the doublet structure disappears, leaving only a single-period equal-amplitude CBO. Again this is consistent with our explanation since the RR oscillations (RRO) only persist to 500 mK. However, Fig. 4 is not typical. We have repeated the measurements by cooling the samples down twice and by making measurements after different amounts of illumination. In most sweeps [3] we observed a more complicated behaviour than the simple one shown in Fig. 4. In each case, however, a single-period and equal-amplitude oscillation was observed on warming the sample up to 700 mK.

Fig. 5 shows a series of Fourier transforms of typical gate voltage sweeps for different barrier conditions. In Fig. 5d the barrier height was high enough that only the CBO were observed. In Fig. 5a the barrier was low allowing full transmission of the edge states across the barrier (Fig. 9a) so that only the RRO were observed. They could be distinguished by their temperature dependencies as mentioned above. For intermediate barrier conditions two additional peaks could usually be observed with temperature dependencies very similar to the RR effect. These occurred at half and a quarter the frequency of the CB oscillations. Since the CBO involve every electron these frequencies correspond to the removal of every second and fourth electron. It is also important to note that in the region where the two effects coexist the RRO have changed their period to

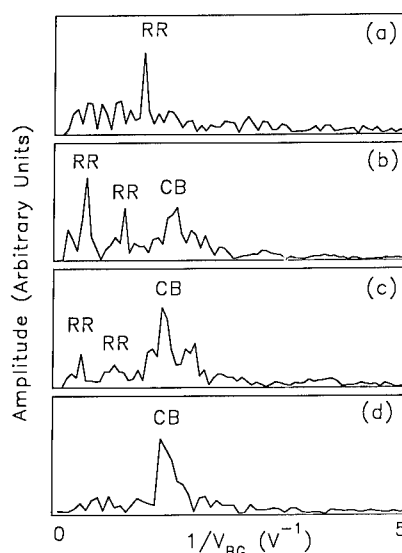


Fig. 5. Fourier transforms of backgate voltage sweeps under different barrier conditions.

become commensurate with the CBO. Commensurability is required because both effects involve the removal of electrons from the dot but the CBO count every single electron removed from the dot. The major difference between the sweeps on different cooldowns and after different illuminations was the relative strength of the two RR peaks in the Fourier transforms in the intermediate regime. In fact, Fig. 4 was a special case where the peak corresponding to every fourth electron was very small. The RR process is a “magneto-fingerprint” of the exact impurity potential of the dot and, therefore, might be expected to vary with different cooldown and illumination. In order to explain the origin of the fourth electron peak in the Fourier spectrum it is only necessary to consider the fact that it is highly likely (in the absence of magnetic impurities) that spin would be conserved in RR tunnelling. One would therefore expect to observe separate tunnelling processes for the two spin directions. It is easily shown that on including the Zeeman term the single-electron levels of the trapped inner edge state would be alternatively spin up and down. As a result each spin direction should give a RR minimum corresponding to the depletion of every fourth electron.

An alternative explanation of the above peak amplitude behaviour above might result from the different tunnelling probabilities of electrons related to the spatial position of the wavefunctions of the trapped states in relation to the tunnelling barrier. Indeed such an effect has been observed by Alphenaar et al. [8] who observed a periodic variation in the amplitude of the conductance peaks with a period determined by the number of trapped edge states. This was observed, however, for a well isolated dot. Our effect, on the other hand, occurs only in the intermediate regime. CBO were studied from 0 to 13 T and no other periodic behaviour in the peak conductance was observed other than in this regime. Also experiments performed as a function of magnetic field, i.e., at constant electron density, give further proof that a coexistence of RR and CB effects is the origin of the period doubling.

We now consider the significance of the above effects involving every second and fourth electron for experiments in which the field is swept. Firstly, we note that the period and amplitude of oscillations when the edge states are fully transmitted were remarkably constant (NB, over a field range of 0.6 T no detectable change in period was observed). Within the original resonant tunnelling explanation of the effect one could immediately infer from this that either these oscillations are due to a single-spin species or that by coincidence the Zeeman splitting is equal to half the bare level spacing. The latter case is easily shown not to be the case by tilting the sample in a magnetic field (Fig. 6). As the sample is tilted the Zeeman term is proportional to  $B$  while the Coulomb term varies as the normal component of the field,  $B \cos \theta$ . In fact the period varies as  $B \cos \theta$ . Thus, at first sight it would appear as if the RRO were due to RR tunnelling through a single-spin species (the same arguments could of course be made for our gate voltage sweeps). Fig. 7a is a field sweep in the RR regime where the barrier height is set to allow the outer edge state to be fully transmitted. A single-period oscillation is seen. For reasons which will become clear below we label the oscillations "a" through "d". Fig. 7b shows a field sweep after a very small increase in the barrier height. Two effects are

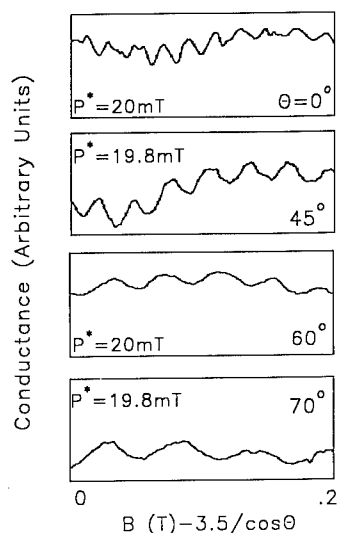


Fig. 6. Resonant reflection oscillations at different tilt angles,  $\theta$ .  $p^* = \Delta B \cdot \cos \theta$ .

visible. Firstly, a small change in period occurs, similar to the change observed in backgate voltage sweeps. Further increases in barrier height (i.e., top-gate voltage,  $V_{TG}$ ) had a much smaller effect on the period. Secondly, an apparent suppression of every second peak can be seen (i.e., at point "c"). When the barrier height is raised further (Fig. 7c), triangular MCO begin to ap-

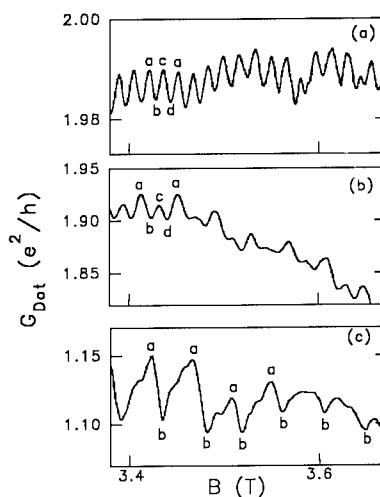


Fig. 7. Resonant reflection oscillations for different barrier conditions (see text for details).



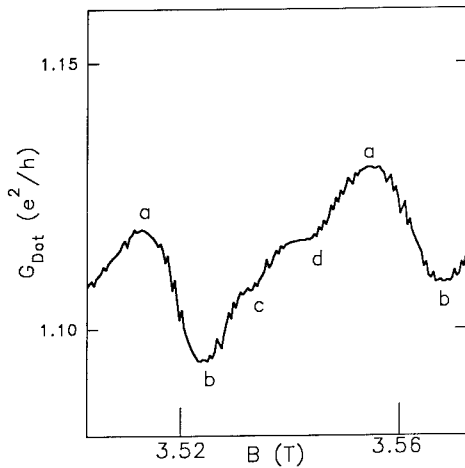


Fig. 8. Expanded view of one of the oscillations from Fig. 7c.

pear. In Fig. 8 one such triangular structure is enlarged. From the spacing of the minima we are able to identify the two troughs, “b” and “d” which were present in Figs. 7a and 7b. One of the two troughs is much shallower (i.e., “d”). However, point “c” is also a trough now. Finally, at the high field end of 7c only the isolated troughs associated with point “b” are visible. Note that our explanation of RR as a mechanism for the MCO leads trivially to conductance troughs, whereas conductance peaks would be expected for resonant transmission. We note also that points “a” through “d” are equally spaced in field.

#### 4. The effects of electron–electron interactions and spin on the RR process

In order to understand the above data, it is necessary to include the effect of electron–electron interactions [9]. Fig. 9 shows edge state schematics as a function of barrier height to be compared with the data in Figs. 7 and 8. Consider Fig. 9a, using the notation of Fig. 9 the RR process for the down spins can be described as  $\chi_d \rightarrow \phi_d \rightarrow \chi'_d$ , where electrons from the upper edge tunnel through the confined levels ( $\phi_d$  and  $\phi_u$  for down-spin and up-spin levels, respectively) to the lower edge and, thus, partially equilibrate

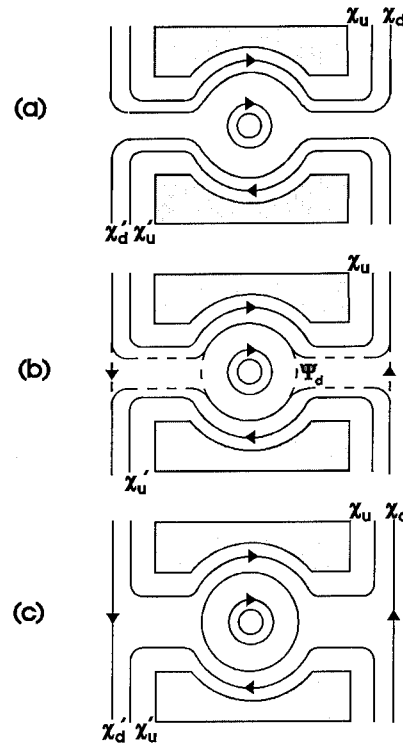


Fig. 9. Edge state schematics.  $X_u$  and  $X_d$  represent spin-up and spin-down edge states, respectively.  $\Psi_d$  represents a mixed state. (See text for details.)

the chemical potential difference between the two edges causing a conductance drop. Spin is conserved in the process so that an equivalent pro-

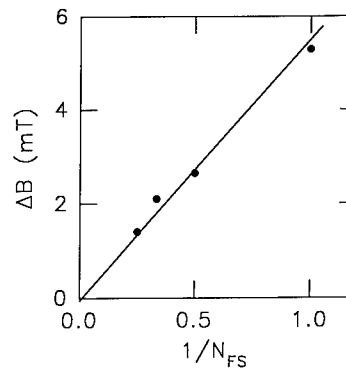


Fig. 10. The period of the RT oscillations observed by Van Wees et al. [2] (solid circles). The solid line shows the trend predicted by the model.

cess exits for the up spins  $\chi_u \rightarrow \phi_u \rightarrow \chi'_u$ . We define the associated reflection probabilities of the respective edge states by  $R_d$  and  $R_u$ . At their respective resonances their values are almost identical since they are essentially tunnelling probabilities connecting the edge and confined states, differing only in their spin.

A simple calculation of the single-particle (SP) spectrum shows that consecutive resonances involve the reflection of electrons of opposite spin. If electron–electron interactions are taken into account this SP picture is invalidated and the magnetoconductance becomes a probe of the “addition” energy, i.e., the change in ground-state energy (or at finite temperatures free energy) of the system on incrementing the number of electrons in the QDs confined states. Resonances occur when this addition spectrum equals  $E_F$  (or more generally the chemical potential,  $\mu$ , at finite temperatures). Although the exact form of the potential is not known detailed simulations [10] show that even for external potentials quite different from the parabolic form the single-energy levels  $\epsilon_l^0$  are quite similar to those of the parabolic confinement discussed by Fock [11]. Two quantum numbers  $n, l$  and the spin quantum number  $s$  characterize the levels. The Landau levels occur in the limit  $\omega_0/\omega_c \approx 0$ , where  $\omega_0$  and  $\omega_c$  are the parabolic and cyclotron frequencies, respectively. It is necessary to consider the change in ground-state energy as the system goes from an  $N$  electron system to an  $N+1$  electron system. If the number of fully transmitted edge states is kept constant then only the total energy of the trapped states is relevant. The ground-state energy of the  $N$  electron system can be written down using density functional theory (DFT). According to DFT the electrons in a magnetic field see not only their usual Coulomb interactions (i.e., Hartree term) but also an exchange correlation potential  $V_{xc}$  and vector potential  $A_{xc}$ . One may for simplicity assume that the SP energies are calculated using B and ignore the effect of  $A_{xc}$ . Some recent calculations [12] have in fact found it adequate to ignore both  $A_{xc}$  and  $V_{xc}$  (i.e., the Hartree approximation). The effect of the  $V_{xc}$  is to introduce an exchange–correlation energy  $e_{xc}^i$  for each energy level.

Thus, we can write

$$E(N) = \sum_i \epsilon_i^0 n_i + \sum_{ij} u_{ij} n_i n_j + \sum e_{xc}^i n_i, \quad (1)$$

where  $n_i, n_j = 1$  for occupied states and zero otherwise, and  $u_{ij}$  is the Coulomb interaction between electrons in levels  $i$  and  $j$ . The occupied states are for  $i$  and  $j$ , to  $N$ . On adding an extra electron we need to include one more Kohn–Sham state in the summations. Hence, the addition spectrum is given by

$$\begin{aligned} \Delta E(N+1, N) &= E(N+1) - E(N) \\ &= \epsilon_{(N+1)}^0 + \sum_{i < N+1} u_{i(N+1)} + e_{xc}^{(N+1)}, \end{aligned} \quad (2)$$

and tunnelling can occur if  $\Delta E(N+1, N) = E_F$ .

The elements in Eq. (2) can be given explicitly in terms of the Kohn–Sham wavefunctions of the trapped states,  $\phi_i(z)$ . In particular,

$$\begin{aligned} u_{i(N+1)} &= \langle \phi_i(z) \phi_{(N+1)}(z') | \\ &\quad (e^*)^2 / |z - z'| \\ &\quad | \langle \phi_i(z) \phi_{(N+1)}(z') \rangle / K_{qd}. \end{aligned} \quad (3)$$

The effective charge  $e^*$  already contains the effect of the background dielectric constant of the semiconductor. The electrons in the fully transmitted edge states are “metallic” and contribute an additional screening contribution to the screening function of the quantum dot,  $K_{qd}$ . We can define an average electron separation  $\langle r_{i(N+1)} \rangle$  by the equation

$$u_{i(N+1)} = (e^*)^2 / (\langle r_{i(N+1)} \rangle K_{qd}), \quad (4)$$

and define

$$\begin{aligned} U_{(N+1)} &= \sum_{i < N+1} u_{i(N+1)} \\ &= ((e^*)^2 / K_{qd}) \sum_{i < (N+1)} (r_{i(N+1)})^{-1}. \end{aligned} \quad (5)$$

Therefore,

$$\Delta E(N, N+1) = \epsilon_{(N+1)}^0 + U_{(N+1)} + e_{xc}^{(N+1)}. \quad (6)$$

If we assume that  $U$  is the dominant energy scale of the problem and is independent of  $N$  for

a reasonable range of  $N$  then we can explain the single period of Fig. 7a even though every second oscillation is due to tunnelling of electrons of different spin. It is interesting to note that  $U$  is a microscopic description of the charging energy of the usual Coulomb blockade theory which is written in terms of an effective capacity of the quantum dot. The consequences of the screening function will be dealt with later.

Let us now consider how the  $X_s \rightarrow \phi_s \rightarrow X_s$ , with  $s = u$  or  $d$ , process is affected if we increase the barrier height (Fig. 7b and 7d), i.e. The conductance of the barrier  $G_B < 2$ . Under our experimental conditions, neither of the spin-resolved edge state is then fully transmitted across the barrier (i.e., we are not in the fully adiabatic regime in the barriers). However, the edge state with  $s = d$  is preferentially reflected at the barriers. For simplicity we assume that the edge state with  $s = u$  is still fully transmitted and described by  $X_u$  (see Fig. 9b). But the  $X_d$  state becomes quasi-confined and is represented as a mixed state  $\Psi_d$

$$\Psi_d = aX_d(n_L) + b\phi_d(n_L, \beta) + \dots, \quad (7)$$

where  $X_d$  and  $\phi_d(\beta)$  are the wavefunctions of the extended and confined part of the mixed state.  $\phi_d(n_L, \beta)$  is the confined spin-down state closest to the Fermi energy and is associated with the same Landau level index,  $n_L$  (in this case  $n_L = 1$ ), as its partner but has a discrete angular momentum index  $\beta$ . The ellipsis in Eq. (7) indicates that other confined states also contribute to the mixed state but for simplicity we make the obvious assumption that  $\phi_d(n_L, \beta)$  is dominant. The values  $a^2$  and  $b^2$  represent the probabilities that a  $s = d$  electron entering the dot appears in the extended or confined component of the mixed state, and their values are determined by the boundary conditions at the first QPC barrier which match  $\Psi_d$  to the incoming edge state. It is important to note, however, that matching the boundary conditions for maximum transmission at the first QPC does not guarantee that they are matched at the second QPC. For selected boundary conditions the net effect of the mixing in of  $\phi_d(n_L, \beta)$  is to decrease transmission across the dot. That is in

addition to the RR via the  $X_s \rightarrow \phi_s \rightarrow X_s$  path we now have an additional reflection denoted by  $R_{\text{int},d}$ . This reflection process, which occurs at  $B$  fields corresponding to maxima in  $b^2$  does NOT directly involve the inner confined levels  $\phi_d(n'_L, l)$  where  $n'_L$  is the Landau level index of the inner level (i.e., 2 in this experiment).

Point “b” in Fig. 6 represents the  $R_u$  resonance and is therefore unaffected by the mixed state. Point “d” represents the  $R_d$  process and becomes gradually weaker as more of the spin-down edge state is reflected at the barriers. This can be seen in the triangular structure in Fig. 8 where the “d” resonance is clearly much weaker than the “b” resonance. Finally, when the  $G_B \ll 2$  this “d” resonance disappears since the edge state is totally reflected at the barrier (see Fig. 9c for the edge state configuration). This creates a “period doubling” for MCO. We associate the dip at point “c” in Figs. 7b, 7c and 8 with the  $R_{\text{int},d}$  mechanism described above and illustrated in Fig. 9b. This mechanism is also not present when the edge state is fully reflected at the barriers.

We now return to the role of the fully transmitted edge states in the experiment. In Eq. (3) it is explicitly indicated that the Coulomb energy  $U$  is screened by  $K_{\text{qd}}$ . If the dot contains only trapped states the polarizability  $K_{\text{qd}}$  is negligible and  $K_{\text{qd}} = K_{\text{qd}}^0$ . Here tunnelling will involve all the usual Coulomb blockade effects. When fully transmitted edge states are present the polarizability increases dramatically. They act as metallic strips and are polarizable because virtual excitations to empty states lying just above  $E_F$  become possible since there is no gap at  $E_F$  in the regions penetrated by the edge state. If we assume to first order that the polarizability of all of the fully transmitted edge states is the same, then

$$K_{\text{qd}} = K_{\text{qd}}^0 + N_{\text{FS}}\pi_{\text{FS}}, \quad (8)$$

with

$$K_{\text{qd}}^0 < N_{\text{FS}}\pi_{\text{FS}}.$$

It should be also noted that  $\omega_0$  is affected since the confining potential is also screened and is now represented by  $\omega_0/N_{\text{FS}}\pi_{\text{FS}}$ , where  $\pi_{\text{FS}}$  is

the static polarizability of an edge state. Thus, one effect of  $N_{\text{FS}}$  is to decrease the SP energy separation.

From this simple picture we can predict that the period of the oscillations should (if we make all the above assumptions) be proportional to the inverse number of fully transmitted edge states. Our dots did not show MCO for a sufficient number of  $N_{\text{FS}}$  to confirm this prediction, but in Fig. 9 we plot the period from the original MCO experiment by Van Wees et al. against the inverse of the number of fully transmitted edge states. As can be seen the agreement is excellent, suggesting strongly that even for the  $1.5 \mu\text{m}$  dot charging effects dominated the MCO period.

In conclusion we have reported results in a regime where the MCO and CB effects coexist. We have shown that they can be understood only if electron–electron interactions are taken into account. The screening effect of the fully transmitted edge states largely determines the period of the MCO. We have used our results to reinterpret the original MCO experiment previously interpreted as an Aharonov–Bohm effect.

## 5. Acknowledgements

We wish to acknowledge the contribution of J.A. Adams, P. Marshall, M. Davies and P. Chow-Chong in the fabrication of the samples.

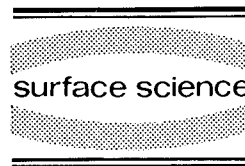
## 6. References

- [1] J.H.F. Scott-Thomas et al., Phys. Rev. Lett. 62 (1989) 583.
- [2] B.J. Van Wees et al., Phys. Rev. Lett. 62 (1989) 2523; R.J. Brown et al., J. Phys. C 1 (1988) 6291.
- [3] R.P. Taylor et al., Phys. Rev. Lett. 69 (1992) 1989.
- [4] R.P. Taylor et al., Surf. Sci. 263 (1992) 247.
- [5] C.J.B. Ford et al., Phys. Rev. B 43 (1991) 7339.
- [6] G. Kirczenow and E. Castano, Phys. Rev. B 43 (1991) 7343.
- [7] D.V. Averin and K.K. Likharev, in: Quantum Effects in Small Disordered Systems, Eds. B.L. Altschuler, P.A. Lee and R.A. Webb (Elsevier, Amsterdam, 1991).
- [8] B.W. Alphenaar et al., Phys. Rev. B 46 (1992) 14178.
- [9] M.W.C. Dharma-wardana, R.P. Taylor and A.S. Sachrajda, Solid State Commun. 84 (1992) 631.
- [10] A. Kumar, S.E. Laux and F. Stern, Phys. Rev. B 42 (1990) 5166.
- [11] Z. Fock, Z. Phys. 47 (1928) 466.
- [12] P.L. McEuen et al., Phys. Rev. B 45 (1992) 11419.



ELSEVIER

Surface Science 305 (1994) 536–540



## Coulomb blockade of Andreev reflection in the NSN single-electron transistor

Travis M. Eiles <sup>\*,a,b,1</sup>, Michel H. Devoret <sup>c</sup>, John M. Martinis <sup>a</sup>

<sup>a</sup> National Institute of Standards and Technology, Boulder, Colorado, USA,

<sup>b</sup> Department of Physics, University of Colorado, Boulder, Colorado, USA,

<sup>c</sup> Service de Physique de l'Etat Condensé, CEA-Saclay, Gif-sur-Yvette, France

(Received 3 May 1993; accepted for publication 26 May 1993)

### Abstract

We have measured at low temperatures the current through a submicrometer superconducting island connected to normal-metal leads by ultrasmall tunnel junctions. At low bias voltages, the current changes from being  $e$ -periodic in the applied gate charge to  $2e$ -periodic. We interpret this  $2e$ -periodic current as a manifestation of a sequence of Andreev reflection events which transports two electrons at a time across the island. This behavior is clear evidence that there is a difference in total energy between ground states of an even or odd number of electrons.

The behavior of systems with a small number of quantum particles, like atomic nuclei, depends on whether the total number of particles is even or odd. The pairing of electrons in a superconductor may lead to an observation of this effect in an isolated sample with a macroscopic ( $\sim 10^9$ ) number of such particles. At very low temperatures, a simple view is that all the electrons should condense into the BCS ground state if their number is even. However, an odd number of electrons will require one electron to remain in an excited quasiparticle state of energy  $\Delta$ . Is it possible to observe these even-odd parity effects in a mesoscopic superconductor?

The superconductor can be conveniently investigated by connecting it to metal leads by two

ultrasmall tunnel junctions which only weakly perturb the system. The junctions allow us to probe the energy of the island versus the electron number. To do this, two conditions must be met. First, junction resistances  $R_T$  must exceed the resistance quantum  $R_K = h/e^2$  to ensure that the charge state of the island is well defined. Furthermore, the Coulomb energy of the island  $E_C = e^2/2C$ , where  $C$  is its capacitance, must exceed  $k_B T$  so that single-electron tunneling occurs. We present current-voltage characteristics for a sample with normal leads (NSN) [1]. In this case the mechanism of tunneling is understood more readily than in the all-superconducting case (SSS) where Josephson tunneling and its interaction with the electromagnetic environment play a major role [2].

In order to externally vary the charge state of the island, a gate voltage is capacitively coupled to the island. This gate continuously polarizes the island with a gate charge  $Q = C_g V_g$ . For a nor-

\* Corresponding author.

<sup>1</sup> Present address: Semiconductor Physics Department, Sandia National Laboratories, Albuquerque, NM, USA.

mal-metal island at zero temperature, the zero-bias conductance vanishes unless the gate charge removes the Coulomb energy barrier, which occurs at charges  $Q/e = n + 1/2$ , where  $n$  is an integer. The associated current will be  $e$ -periodic with the gate charge as depicted in Fig. 1b. However, if the island is superconducting, the gap energy significantly alters the situation. In Fig. 1c we show  $E_n$  vs  $Q$  for various values of the electron number. Now single-electron tunneling can possibly occur for values of  $Q/e$  different from  $n + 1/2$ . However, for conduction to occur the same quasiparticle state has to be filled and emptied as the charge moves through the junctions. One expects a very low conductance ( $< (100 \text{ G}\Omega)^{-1}$ ) from this channel [3]. Since Cooper pair tunneling is excluded, we must consider a higher-order process allowing the simultaneous tunneling of two electrons. We envision a process where two electrons enter the island through one junction and form a Cooper pair, followed by the disappearance of another Cooper pair as two electrons exit the island. This process is identical to Andreev reflection at each S-I-N junction.

The schematic of the device is shown in the lower inset of Fig. 2, as well as the actual physical layout in the upper left. The sample was fabricated by electron-beam lithography and double-angle evaporation. The Al island was 350 nm thick and was spatially separated from its extra-

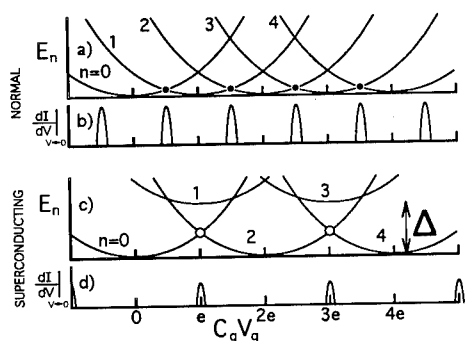


Fig. 1. System energy vs gate voltage for several values of the excess number of electrons in the (a) normal or (c) superconducting island. The gate continuously polarizes the island accounting for the parabolic relationship between energy and gate charge  $C_g V_g$ . In the superconducting case (c), states with an odd number of electrons are elevated by  $\Delta$ . Zero-bias conductance is shown in (b) and (d) for the two cases.

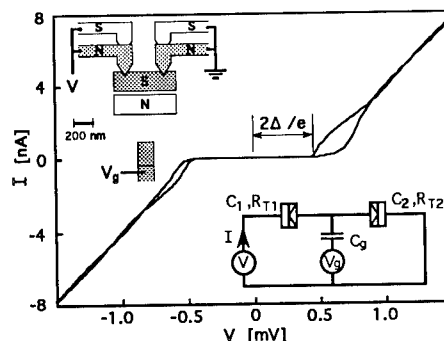


Fig. 2. Large-scale  $I$ - $V$  characteristic with gate charge adjusted for maximum and minimum gap. The sharp current rise at  $2\Delta/e$  is indicative of two NS junctions in series. The lower inset is the device schematic; the upper inset is the actual layout.

neous twin left over from the double angle evaporation. The normal leads consisted of a 5 nm Al buffer layer overlaid by a 55 nm layer of gold. The buffer layer was used to promote adhesion; its superconductivity should be suppressed completely by its proximity to the much thicker gold layer. The large-scale current-voltage characteristics are presented in Fig. 2 with the gate voltage adjusted to give maximum and minimum gaps on the positive-voltage side. The current sharply rises at a voltage compatible with the usual measured gap of Al. The device parameters could be found from the large-scale characteristics; we obtained  $R_{T1} \approx R_{T2} \approx 65 \text{ k}\Omega$ ,  $E_c/e = 126 \text{ }\mu\text{V}$  and  $\Delta/e = 235 \text{ }\mu\text{V}$ .

Figure 3 is a plot of the device voltage versus gate voltage for a series of constant current biases. The current biases range from 3 pA for the contour at the lowest voltage, to 2.05 nA for the contour near 800  $\mu\text{V}$ . In accordance with the  $I$ - $V$  curves in Fig. 2, currents on the scale of a few pA begin to appear only as the voltage approaches  $2\Delta/e$ , where two quasiparticle excitations can be created. Above this voltage, the  $V$ - $V_g$  curves form a characteristic sawtooth pattern. Threshold lines following the slopes of the curves are drawn, which indicate the voltages that must be exceeded for single-electron tunneling to be allowed. As will be discussed below, there is a cotunneling process which yields current below these thresholds; this accounts for the rounding

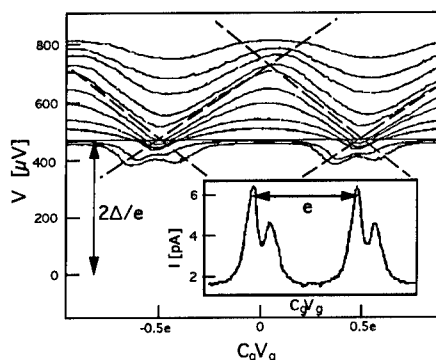


Fig. 3. Bias voltage vs gate voltage for several values of the current. The bias currents in pA are: 3, 6, 33, 67, 175, 343, 762, 1070, 1460, 1750 and 2050. Well above  $2\Delta/e$ , the contours form the sawtooth pattern characteristic of the normal single-electron transistor. Near  $Q/e = n + 1/2$ , current is observed below  $2\Delta/e$ . The inset is a plot of current vs gate charge for  $V = 430 \mu\text{V}$ . The double peak structure is found at voltages just under  $2\Delta/e$ .

of the  $V-V_g$  curves within the threshold lines. An unusual feature in the data is seen where the threshold lines cross at  $2\Delta/e$  and the Coulomb gap is eliminated by the gate voltage. Currents on the scale of several pA occur here for voltages slightly less than  $2\Delta/e$ . This suggests the excitation of quasiparticles within the gap or possibly thermal activation. Another interesting aspect to this current is the double-peak structure in the dependence on gate charge as shown in the inset. There is a relative minimum in the current where the Coulomb gap for two-quasiparticle excitations is completely removed. We observe that the current peaks appear to follow the threshold lines below the gap voltage  $2\Delta/e$ .

At bias voltages exceeding twice the superconducting gap we observed modulation of the current with gate charge very similar to that in the normal-metal transistor, but with the voltage origin being offset by  $2\Delta/e$ . For voltages less than the Coulomb gap and in the range  $2\Delta/e < V < 2(\Delta + E_c)/e$ , the current from two sequential single-electron tunneling events should be exponentially small. However, we observe a smooth increase of the current with voltage, similar to the current produced by inelastic cotunneling in the

normal-state single-electron transistor [4,5]. In this second-order process, electrons simultaneously tunnel through both junctions and the current is thus inversely proportional to the product of the junction resistances. The charge state of the island is unchanged after this process, although electron-like and hole-like quasiparticles must still be created. The inelastic nature of the process thus requires voltages greater than  $2\Delta/e$  in order to excite the quasiparticles in the island. The theory for inelastic cotunneling is used to calculate at maximum gap and  $T = 0$  the current  $I = (R_K/\pi R_1 R_2) (C/e)^2 (\delta V^2 \Delta/e + 2\delta V^3/3\pi)$ , where  $\delta V = V - 2\Delta/e$ . The data shown in Fig. 4 are taken for maximum Coulomb gap, and are in good agreement with the theoretical curves calculated from our measured parameters.

In Fig. 5 we show experimental  $I$  vs  $V_g$  data taken at 35 mK for two bias voltages: (a)  $V = 478 \mu\text{V} \approx 2\Delta/e$  and (b)  $V = 63 \mu\text{V} \approx \Delta/4e$ . At the larger voltage, where quasiparticle tunneling is allowed, the data are  $e$ -periodic as expected. The low-voltage data have twice the period of the higher voltage data, and the current peaks are positioned at minima of the high-voltage data. This behavior is exactly predicted by the simple Coulomb blockade model incorporating an energy asymmetry between even and odd states which was depicted above in Fig. 1.

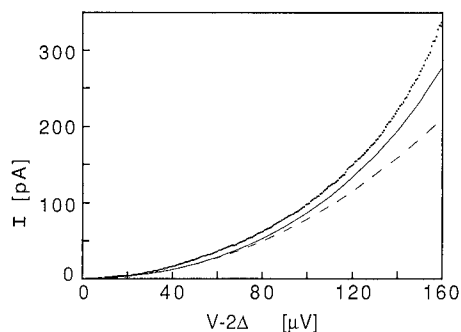


Fig. 4. Current-voltage characteristic for voltages beyond  $2\Delta/e$ , adjusted for maximum gap. Points are experimental data. The solid curve is the result of the calculation of the cotunneling rate, including both quadratic and cubic terms. The dashed line shows the contribution of the quadratic term only.

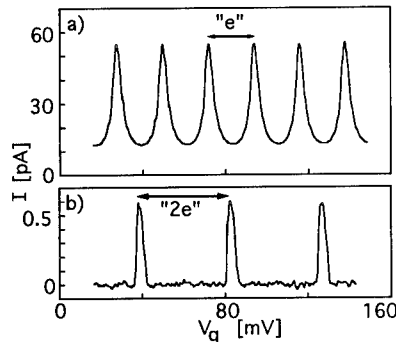


Fig. 5. Current vs gate voltage curves for bias voltages (a)  $V = 478 \text{ mV} \approx 2\Delta/e$  and (b)  $V = 63 \text{ mV} \approx \Delta/4e$ . Periodicities of the gate charge are indicated by the arrows.

Figure 6 shows  $I$ - $V$  characteristics for three values of the charge bias. The  $2e$ -periodicity is evident in the different characteristics between the  $Q = 0$  and  $Q = e$  data. The curve for  $Q = 1.06e$  shows a small Coulomb gap opening up at the origin. This behavior is markedly different from what is seen in the SSS device where the charge transfer is coherent and has a supercurrent-like current-voltage characteristic. The gap at the origin points to an incoherent process where voltage thresholds for each junction must be exceeded in order that sequential tunneling occurs.

To summarize the  $2e$ -periodic data, we note that the current mechanism must lead to (1) sequential transport in two-electron increments across the junctions, (2) linear conductance near

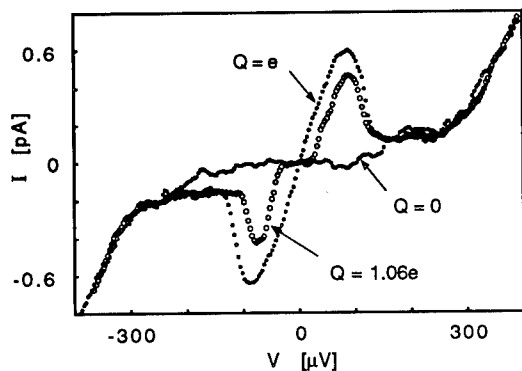


Fig. 6. Current-voltage characteristics at small voltages for three values of the charge bias.

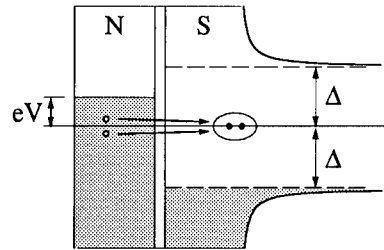


Fig. 7. Schematic depiction of the two-electron tunneling process involving a normal metal (N) and a superconductor (S) separated by a tunnel barrier. The holes created in the left electrode have energies  $\epsilon_1$  and  $\epsilon_2$ , where  $\epsilon_1 + \epsilon_2 = 2 \text{ eV}$ . These two electrons form a Cooper pair in the superconductor and thus no quasiparticle excitations are created.

the origin, and (3) a limiting voltage beyond which the current decreases quickly. Figure 7 is a depiction of the two-electron process responsible for the low-voltage current. At bias voltages less than  $\Delta/e$ , the single-electron tunnel events are impossible since a quasiparticle of energy  $\Delta$  must be created. However, a two-electron process, which creates two holes in the normal metal and one Cooper pair in the superconductor, is possible. For a single junction, the conductance for the process is

$$G_{\text{NS}} = R_K^{-1} \sum_m T_m^2,$$

where  $T_m$  is the transmission coefficient for the  $m$ th transverse mode [6]. This is similar to the Landauer conductance formula, except that here  $T_m$  is squared because two electrons tunnel simultaneously across a junction. The transmission coefficient is related to the normal state conductance by

$$\sum_m T_m = R_K G_{\text{NN}}/2.$$

If  $T_m$  is constant for each channel, then the conductance from two-electron tunnel events becomes  $G_{\text{NS}} = R_K/4M_{\text{eff}}(R_T)^2$  where  $M_{\text{eff}}$  is the effective number of conduction channels. This single-junction calculation can be extended to the double-junction NSN system to include the lowering of the intermediate state energies due to the Coulomb interaction [6,7]. The zero-bias conductance of  $100 \text{ M}\Omega$  we measure is consistent with a



value of  $M_{\text{eff}}$  of about 100 which is reasonable considering the granularity of the Al films.

Figure 6 shows that when the charge bias is adjusted for  $Q/e = 2n + 1$ , the current decreases rapidly above about 100  $\mu\text{V}$ . This decrease can be explained by noting that there are two possible conduction channels: (1) the  $(0 \rightarrow 2 \rightarrow 0)$  process described above, and (2) the  $(0 \rightarrow 1 \rightarrow 0)$  process where the same quasiparticle state is filled and then emptied. Because the  $(1 \rightarrow 0)$  transition rate is very low, state 1 is occupied for a long time and thus blocks the  $(0 \rightarrow 2 \rightarrow 0)$  channel from contributing a current. The voltage at which the Andreev reflection disappears can be found by computing when state 1 becomes occupied [7]. This occurs when the free-energy difference between the 0 and 1 states goes to zero, which gives a voltage  $2(\Delta - E_c - k_B T \ln N_{\text{eff}})/e = 160 \mu\text{V}$ , where  $N_{\text{eff}}$  is the effective number of available quasiparticles [2]. This prediction is in reasonable agreement with our data, and will fit our data if we choose a value of  $\Delta$  that is only 10% less than what is given above.

Although the conductance remained fairly constant with temperature, the peak current decreased linearly with increasing temperature and disappeared at  $T_0 = 130 \text{ mK}$ , as shown in Fig. 8. At zero bias voltage and gate charges  $Q/e = 2n + 1$ , the energy difference between even and odd

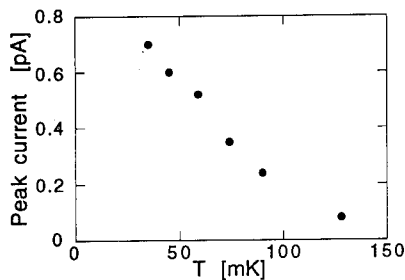


Fig. 8. Plot of the maximum current of the  $2e$ -periodic peak versus temperature. The peak disappears at  $T_0 = 130 \text{ mK}$ .

levels is  $\Delta - E_c$ . Thus the odd level becomes significantly populated when the temperature reaches  $k_B T_0 = (\Delta - E_c)/\ln N_{\text{eff}} = 140 \text{ mK}$  [1]. Our measured threshold temperature is in good agreement with this simple thermodynamic prediction.

In conclusion, we have clearly observed the energy difference between even and odd states in a small superconductor. This observation was made possible by a tunneling mechanism similar to Andreev reflection occurring through NIS tunnel junctions. It is the combined effect of the Coulomb blockade and the superconducting gap that gives this system its interesting and unusual properties. Because single-electron tunneling events are blocked by the Coulomb energy, second-order tunneling processes can be clearly observed.

We acknowledge helpful discussions with D. Esteve and L. Glazman. This work was supported in part by the Office of Naval Research under Contract No. N00014-92-F-0003.

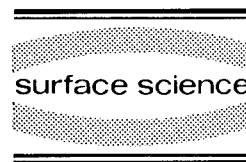
## 1. References

- [1] T.M. Eiles, J.M. Martinis and M.H. Devoret, Phys. Rev. Lett. 70 (1993) 1862.
- [2] M.T. Tuominen, J.M. Hergenrother, T.S. Tighe and M. Tinkham, Phys. Rev. Lett. 69 (1992) 1997.
- [3] D.V. Averin and Yu.V. Nazarov, Phys. Rev. Lett. 69 (1992) 1993.
- [4] T.M. Eiles, G. Zimmerli, H.D. Jensen and J.M. Martinis, Phys. Rev. Lett. 69 (1992) 148.
- [5] D.V. Averin and A.A. Odintsov, Phys. Lett. A 140 (1989) 251; D.V. Averin and Yu.V. Nazarov, Phys. Rev. Lett. 65 (1990) 151.
- [6] T.M. Eiles, J.M. Martinis and M.H. Devoret, Physica B 189 (1993) 210.
- [7] F.W.J. Hekking, L.I. Glazman, K.A. Matveev and R.I. Shekhter, Phys. Rev. Lett. 70 (1993) 4138.



ELSEVIER

Surface Science 305 (1994) 541–546



## Correlation effects on transport through few-electrons systems

J.J. Palacios <sup>\*,a</sup>, L. Martin-Moreno <sup>b</sup>, C. Tejedor <sup>a</sup>

<sup>a</sup> Departamento de Física de la Materia Condensada, Universidad Autónoma de Madrid, Cantoblanco, 28049, Madrid, Spain

<sup>b</sup> Instituto de Ciencia de Materiales (CSIC), Universidad Autónoma de Madrid, Cantoblanco, 28049, Madrid, Spain

(Received 26 April 1993; accepted for publication 4 June 1993)

### Abstract

We study lateral tunneling through a quantum box including electron–electron interactions in the presence of a magnetic field which breaks single particle degeneracies. The conductance at zero temperature as a function of the Fermi energy in the leads consists of a set of peaks related to changing by one the electron occupancy in the box. We find that the position and heights of the peaks are controlled by many-body effects. We compute the conductance up to 8 electrons for several cases where correlation effects dominate. In the range of intermediate fields spin selection rules quench some peaks. At low and high fields the behavior of the conductance as a function of the number of electrons is very different due to big changes in the many-body ground state wavefunctions.

The increasing ability for producing extremely small cavities where only a few electrons ( $N \leq 10$ ) coexist, allows the study of many-body effects on the lateral tunneling through such structures [1]. The concept of capacitance is too simple to describe effects, like exchange and correlation, which should be extremely important in those small systems. In many cases, the experiments are performed in the presence of a high magnetic field  $B$ . The aim of this paper is to show that correlation effects are crucial, even in the case in which the system is not in the fractional quantum Hall regime. A Keldysh framework [2] is used to obtain the conductance of a square quantum box, in the linear response regime, including electron–electron interaction. The leads are as-

sumed to behave like a Fermi liquid, i.e., electrons there can be described in terms of quasiparticles. Hartree, exchange and correlation interactions among all the electrons confined in the box are included in order to calculate conductances. We include a cut-off in the two-dimensional Coulomb interaction to take into account the finite width of actual systems.

We analyze lateral magnetotunneling including many body effects in the dot by using a Keldysh formalism [2–4]. We take two equal barriers separating the box from each lead. So, the current is given by [2]

$$J = \frac{-2e}{h} \int d\omega [f_L(\omega) - f_R(\omega)] \text{Im}[\text{tr}\{\Gamma G^r\}],$$

where  $f_L$  and  $f_R$  are the Fermi distributions of the left and right leads respectively and  $G^r$  is the non-equilibrium retarded Green's function including all the many-body effects as well as the

\* Corresponding author.

coupling to the leads given by  $\Gamma$ . In a single particle basis,

$$G_{i,j}^r(t) = -i\theta(t)(\langle d_i(t)d_j^\dagger \rangle + \langle d_j^\dagger d_i(t) \rangle),$$

and

$$\Gamma_{i,j}(\omega) = 2\pi \sum_l \rho_l(\omega) \langle i|V|l \rangle \langle l|V|j \rangle.$$

$d_i$  and  $d_j^\dagger$  are the annihilation and creation operators of box states  $|i\rangle$  and  $|j\rangle$  respectively, the angular brackets in  $G_{i,j}^r$  mean thermal average,  $V$  is the potential that couples the box to the leads, these having eigenstates  $|l\rangle$  and density of states  $\rho_l$ . It is important to realize that the coupling  $\Gamma$  can be obtained as output of a single-particle calculation of tunneling. We concentrate in the linear regime at zero temperature so that thermal averages become expectation values in the ground state,  $G^r$  being the equilibrium retarded Green's function at zero temperature. The total Hamiltonian is represented in the basis of antisymmetrized configurations  $\alpha^{(N)} = \{n_i\}$ , where  $n_i$  are the occupations of single particle states  $|i\rangle$  verifying  $n_i = 0$  or 1 and  $\sum_i n_i = N$ . The many-body eigenstates with energies  $E_\beta^{(N)}$  of a box with  $N$  electrons are written as  $\Phi_\beta^{(N)} = \sum_\alpha c_{\alpha,\beta} \alpha^{(N)}$ . In this basis, the equilibrium Green's function  $g^r$  for an isolated box takes, in the Lehmann representation, the form

$$g_{i,j}^{r(N)}(\omega) = \lim_{\eta \rightarrow 0} \sum_\beta \left[ \frac{\Delta_{i,j}^{(N)\beta+}}{\omega + E_0^{(N)} - E_\beta^{(N+1)} + i\eta} + \frac{\Delta_{i,j}^{(N)\beta-}}{\omega - E_0^{(N)} + E_\beta^{(N-1)} + i\eta} \right],$$

where the numerators are spectral weights  $\Delta_{i,j}^{(N)\beta+} = \langle \Phi_0^{(N)} | d_i | \Phi_\beta^{(N+1)} \rangle \langle \Phi_\beta^{(N+1)} | d_j^\dagger | \Phi_0^{(N)} \rangle$  and  $\Delta_{i,j}^{(N)\beta-} = \langle \Phi_0^{(N)} | d_i^\dagger | \Phi_\beta^{(N-1)} \rangle \langle \Phi_\beta^{(N-1)} | d_j | \Phi_0^{(N)} \rangle$ . The calculation of the conductance  $G = eJ/\Delta\mu$ , requires the coupling to the leads by using a self-energy  $\Sigma^r = (g^r)^{-1} - (G^r)^{-1}$ . The interaction and the coupling to the leads must be solved simultaneously. Such an analysis has been done only for the Anderson Hamiltonian [4–6]. A Kondo-like peak appears in the density of states at the Fermi energy and at zero temperature due to correlations to the leads. This would give rise

to perfect transparency. The existence of the Kondo effect requires degeneracy, usually of spin, of the single-particle levels. If the degeneracy is broken by the Zeeman term due to magnetic field, the Kondo peak shifts away from the Fermi energy and, again, correlations to the leads are not important for the properties at such energy [5]. Therefore, in our problem with magnetic field, we neglect correlations in the coupling to the leads and consider the self-energy  $\Sigma^r$  only as the non-interacting, single-particle self-energy  $\Sigma^{sp}$ . A very good approximation for the single-particle self-energy is to consider that the coupling to the leads only broadens the levels  $i, j$  but does not shift or mix them, i.e.  $\Sigma_{i,j}^{sp} \approx -i\Gamma_{i,j}\delta_{i,j}$ . Then, the conductance in the presence of the magnetic field becomes

$$G = \frac{e^2}{h} \sum_{N,i} \left[ \frac{\Delta_{i,i}^{(N)+}\Gamma_{i,i}^2(E_F)}{(E_F - \delta V - E_0^{(N+1)} + E_0^{(N)})^2 + \Gamma_{i,i}^2} \times \frac{\Delta_{i,i}^{(N)-}\Gamma_{i,i}^2(E_F)}{(E_F - \delta V + E_0^{(N-1)} - E_0^{(N)})^2 + \Gamma_{i,i}^2} \right],$$

where, for zero temperature and well-resolved resonances, the only significant contribution comes from  $\beta \equiv 0$ .  $E_F$  is the Fermi level of the leads and  $\delta V$  gives the bottom of the box potential with respect to those of the leads. The conductance reduces to a set of peaks, each one related to the variation of the discrete number  $N$ . This is achieved when the Fermi level at the leads verifies  $E_F \approx \delta V \pm E_0^{(N \pm 1)} \mp E_0^{(N)}$ . The position of each peak of the conductance is a many-body feature, a result also obtained [3,7] in the very different regime  $k_B T \gg \Gamma$ . Correlation effects reflect on the height of each peak [3], which is given by  $\sum_i \Delta_{i,i}^{(N)}$ . The width of each peak is given by the single particle coupling  $\Gamma_{i,i}$ .

We apply the above discussed scheme to a square box defined by two barriers built up in a wire (along the  $y$  direction) of width  $W$  by means of transverse (i.e. in the  $x$  direction) gate potentials. These gate potentials create two effective barriers of width  $l_b$  and height  $V_b$  separated from each other by the distance  $W$ . In such a square geometry, only solutions for isolated boxes with

$N=2$  and  $B=0$  have been calculated [8]. We work with a strong perpendicular magnetic field described in a Landau gauge ( $A=Bxu_y$ ). Each single particle state will be labelled as  $i \equiv (n, k, \sigma)$ , where  $\sigma$  is the spin index and  $n$  and  $k$  are the discrete quantum numbers related to spatial shape of the wavefunction. These single particle states are straightforwardly obtained from the diagonalization of the Hamiltonian represented in a basis of sines and cosines in the  $x$  and  $y$  directions. From these wavefunctions, the broadenings  $\Gamma_{i,i}$ , required for the calculation of

the conductance, are obtained using their expressions given before.

We present here results of the calculation for a square box of side  $W=100$  nm. We use its single particle eigenfunctions to describe electron–electron interactions within the box. The calculation of each matrix element of the total Hamiltonian reduces to compute four-dimensional integrals involving single particle wavefunctions. By diagonalizing the Hamiltonian one obtains the energies of  $N$  electrons in the box as well as the eigenstates in the form of linear

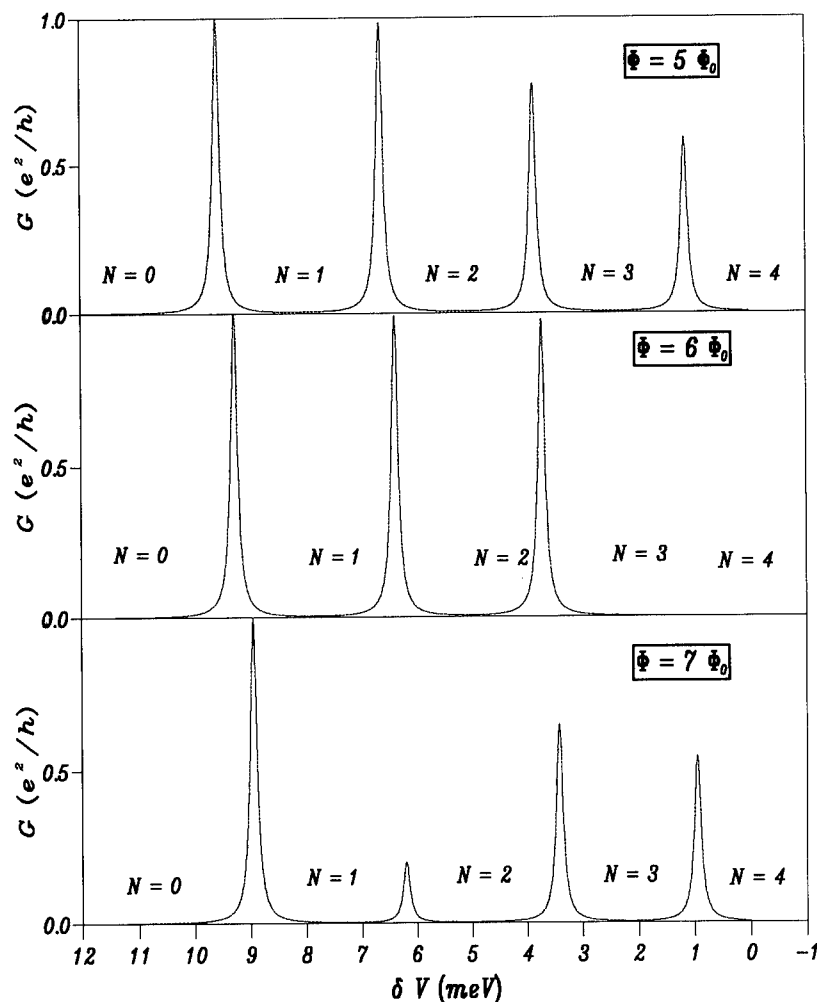


Fig. 1. Many-body conductance  $G$  of a box with  $W=100$  nm and  $E_F=11.5$  meV as a function of the dot bottom potential between  $B=2$  and  $3$  T.

combinations of configurations. The box is defined by two barriers of width  $l_b = 25$  nm. In order to have weak coupling between the box and the leads we take a barrier height  $V_b = 12$  meV. Following the experimental procedure, we fix the Fermi energy of the leads at  $E_F = 11.5$  meV and move the box bottom potential  $\delta V$ .

There are three regimes of  $B$  depending on the characteristics of the many-body ground states. Firstly, we present results in the intermediate regime of magnetic fields. The main result is that the ground state of the box with  $N$  electrons changes its multiplet symmetry when varying the magnetic field. This has an important

implication: for some ranges of  $B$  the difference between the total spin of  $N$  and  $N \pm 1$  electrons is larger than  $1/2$ . Then, the spectral weights are zero and the conductance of the box, when passing from  $N$  to  $N + 1$  electrons, disappears. Later on, following with the variation of the field, the multiplet character of the ground state changes once again and the difference  $1/2$  is restored and the peak of the conductance appears once again. This is observed in Fig. 1 in the conductance of our square box with magnetic fields corresponding to have 5, 6 and 7 flux quanta through the box (this implies to cover a range between 2 and 3 T). Since we fix the energy difference between the

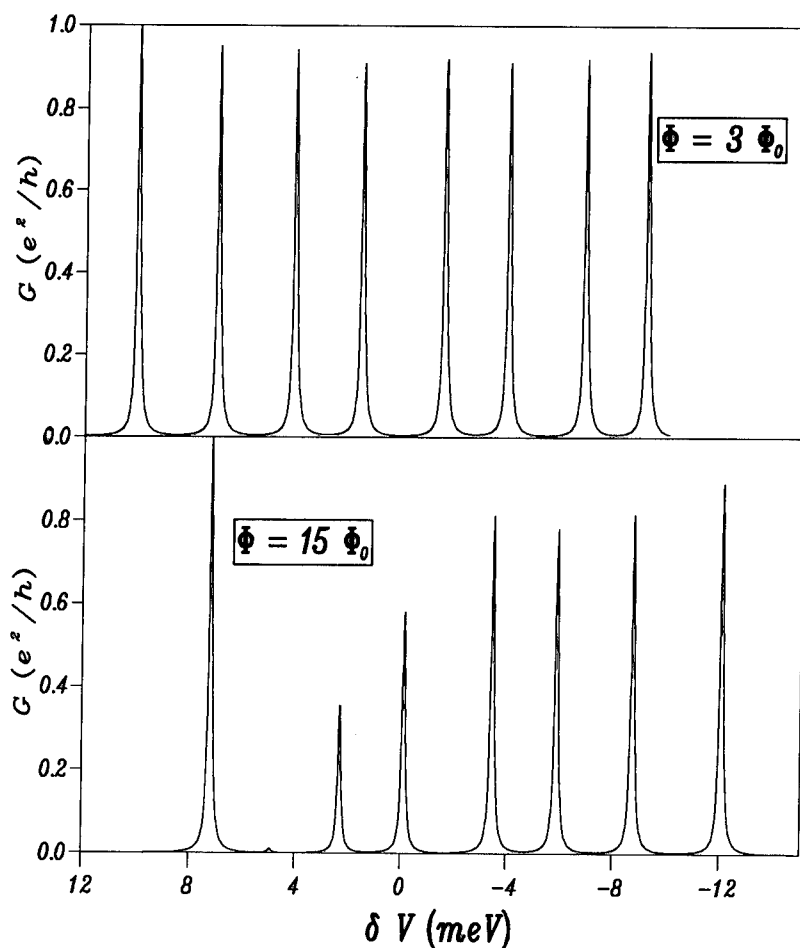


Fig. 2. Many-body conductance  $G$  of a box with  $W = 100$  nm and  $E_F = 11.5$  meV as a function of the dot bottom potential for  $B = 1.25$  and  $6.25$  T.

top of the barrier and the Fermi energy of the leads, the broadening of all the peaks is practically the same. The numbers within the figure stand for the number of electrons within the box. For the lower field, the conductance decreases when  $N$  increases, due to the decrease of the spectral weights. When the magnetic field increases, the peak corresponding to 4 electrons disappears because the ground state of 3 electrons has a total spin  $S = 3/2$  while the ground state of 4 electrons has a total spin  $S = 0$  so that the spectral weight is zero. This gives a zero in the conductance intensity although a small lowering of the bottom of the dot potential would allow the introduction of the electron in the dot without implying current (i.e. conductance) in the whole system. For an even higher field, the ground state of the dot with 3 electrons recovers  $S = 1/2$  and the peak conductance corresponding to 4 electrons appears once again. The spectral weights  $\Delta_{i,i}^{(N)}$  give both the spin selection rules discussed above and strong reductions in some peaks intensity. For instance, at the higher field, the peak corresponding to 2 electrons becomes rather small because the ground state corresponds to single particle wavefunctions in the outer region of the box due to Coulomb repulsion while the 1 electron ground state is situated in the inner region so that the spectral function reduces significantly. This is similar to the orbital angular momentum rule obtained in circular dots [3,9]. The peaks have been shifted with respect to the single particle result by the charging effect that, in this case, is rather constant with the number of particles.

Let us now discuss the high and low field regimes in which there are no questions related to total spin selection rules. Fig. 2 gives the conductance of the box containing up to 8 electrons for magnetic fields in two different regimes. For 3 flux quanta through the box ( $B = 1.25$  T) the many-body wavefunctions are rather complicated including all the possible spin configurations, while for 15 flux quanta ( $B = 6.25$  T) the  $N$ -electrons ground state is spin polarized. Due to the big differences in the wavefunctions, the peaks behave in a very different way. For the lower field (i.e. for non-polarized wavefunctions) the peaks

are rather high, presenting a minimum for the transition between 5 and 6 electrons and tending to  $e^2/h$  for increasing  $N$ . For the higher field (i.e. for spin polarized wavefunctions) the spectral weights present a stronger variation but the peaks also tend to have a conductance  $e^2/h$ . It must be stressed that we are presenting conductances coming from ground state properties at fixed magnetic field, something different to previous works [3] where, in order to study the fractional regime, the system is not maintained in its ground state. Some other minor results can also be extracted from Fig. 2: (1) the charging energy is not totally constant and (2) for the high field, once again, the peak for 2 electrons is very small because it relates  $N$ -electron wavefunctions with very different spatial distribution.

In summary, we have computed the conductance of a box in the presence of a magnetic field at zero temperature including all the electron-electron interaction without any restriction in the spin configuration. The conductance consists of a set of peaks with their position and intensity determined by many-body effects while their width is essentially given by the coupling between single particle states in the box and in the leads. In the intermediate range of fields, the ground state of  $N$  electrons changes its multiplet character with the variation of the magnetic field implying selection rules that quench some conductance peaks. The ground state wavefunctions have big differences between the low and the high field regimes. Therefore, the spectral weights imply different behaviors of the conductance peaks as a function of the number of electrons in both field regimes.

This work has been supported in part by the Comision Interministerial de Ciencia y Tecnologia of Spain under contracts MAT 91 0201 and MAT 91 0905-C02-01 and by the Commission of the European Communities under contract SSC-CT90-0020.

## 1. References

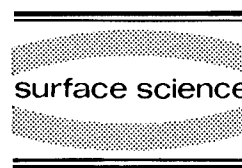
- [1] M.A. Kastner, Phys. Today, January (1993), p. 24, and references therein.

- [2] Y. Meir and N.S. Wingreen, Phys. Rev. Lett. 68 (1992) 2512.
- [3] J.M. Kinaret et al., Phys. Rev. B 45 (1992) 9489; 46 (1992) 4681.
- [4] S. Hershfield, J.H. Davies and J.W. Wilkins, Phys. Rev. B 46 (1992) 7046.
- [5] T.K. Ng and P.A. Lee, Phys. Rev. Lett. 61 (1988) 1768; L.I. Glazman and M.E. Raikh, JETP Lett. 47 (1988) 452.
- [6] Y. Meir, N.S. Wingreen and P.A. Lee, Phys. Rev. Lett. 66 (1991) 3048.
- [7] C.W.J. Beenakker, Phys. Rev. B 44 (1991) 1646; C.W.J. Beenakker, H. van Houten and A.A.M. Staring, Phys. Rev. B 44 (1991) 1657.
- [8] G.W. Bryant, Phys. Rev. Lett. 59 (1987) 1140; W. Hausler, B. Kramer and J. Masek, Z. Phys. B 85 (1991) 435; T. Brandes, W. Hausler, K. Jauregui, B. Kramer and D. Weinmann, preprint.
- [9] P.A. Maksym and T. Chakraborty, Phys. Rev. Lett. 65 (1990) 108; Phys. Rev. B 45 (1992) 1947; U. Merkt, J. Huser and M. Wagner, Phys. Rev. B 43 (1991) 7320.



ELSEVIER

Surface Science 305 (1994) 547–552



# Charging effects in small-area modulation-doped double-barrier heterostructures

S. Tarucha \*, T. Honda, T. Saku, Y. Tokura

*NTT Basic Research Laboratories, Musashino-shi, Tokyo 180, Japan*

(Received 23 April 1993; accepted for publication 15 June 1993)

## Abstract

Charging effects on resonant tunneling are studied in modulation-doped double-barrier heterostructures. We observe a blockade of the tunneling current around zero-bias in small-area devices, while in large-area devices we observe a tunneling current with a zero-threshold bias due to the modulation doping. The blockade voltage width varies in proportion to the inverse square of the conducting diameter, and agrees well with the calculated charging energy for a single electron. At the high voltage end of this blockade region we observe step-like current-voltage features and fine structure in the form of small peaks and shoulders. This fine structure is related to the interplay between charging and size quantization effects.

## 1. Introduction

Quantum mechanical effects in a semiconductor quantum dot lead to the formation of zero-dimensional (0D) states with discrete energies. Tunneling through the 0D states is impeded by a single-electron charging effect or Coulomb blockade when an electron is substantially delayed in the dot during transport. The charging effect has been demonstrated in lateral transport through a quantum dot formed in a two-dimensional electron gas (2DEG) when size quantization is negligible [1–3]. A signature for combined 0D states and charging has recently been observed in a similar but smaller quantum dot [4]. The size quantization effect in resonant tunneling has been

well defined in vertical transport through a small-area double-barrier heterostructure (DBH), which shows a series of peaks in the current versus voltage ( $I$ – $V$ ) characteristics due to resonance associated with the 0D states in the well [5–7]. The charging effect is not important in this DBH because the tunneling electron is not delayed in the well [5]. The charging effect has been studied in small-area asymmetric DBHs [8,9]. For these asymmetric tunnel barrier structures, the  $I$ – $V$  characteristic shows a stepwise increase of the tunneling current with increasing bias voltage, known as a Coulomb staircase [10]. In these structures, however, Coulomb blockade, which is a good measure of charging energy, is masked by a large threshold bias needed to align the 0D state with the Fermi energy in the contact. This paper reports on the charging effects observed in a small-area *modulation-doped* DBH for which size quantization and charging effects coexist. The

\* Corresponding author.



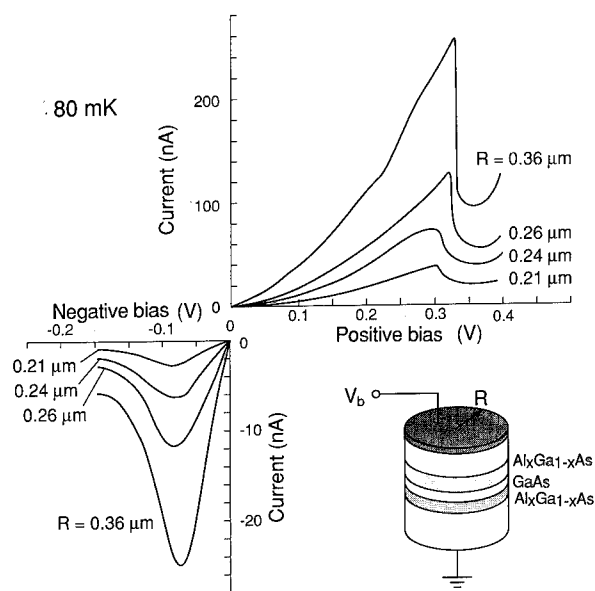


Fig. 1.  $I$ - $V$  characteristics of small-area devices.

DBH has an asymmetry in barrier thickness leading to a large difference in the transmission coefficients of the emitter and collector barriers. The modulation doping generates surplus electrons in the well. Therefore, the DBH when it is sufficiently large, shows a zero-threshold bias for resonance. This enables us to observe Coulomb blockade in the small-area device when the tunneling current is suppressed around zero-bias, and to determine the single-electron charging energy. At the high voltage end of the Coulomb blockade we observe a Coulomb staircase modulated by fine structure, which is related to the interplay between the charging and size quantization effects.

## 2. Samples

A schematic diagram of our DBH devices is shown in Fig. 1. The DBH consists of a 10.2 nm thick  $\text{Al}_{0.3}\text{Ga}_{0.7}\text{As}$  barrier, a 6.0 nm thick GaAs well, and a 8.8 nm thick  $\text{Al}_{0.3}\text{Ga}_{0.7}\text{As}$  barrier. Each  $\text{Al}_{0.3}\text{Ga}_{0.7}\text{As}$  barrier is selectively doped to  $1 \times 10^{11} \text{ cm}^{-2}$  in the center, and is adjacent to a 2 nm thick GaAs spacer and a n-GaAs contact doped to  $1 \times 10^{18} \text{ cm}^{-3}$ . Five sheets of Si with an

areal density of  $1 \times 10^{11} \text{ cm}^{-2}$  are embedded in the upper contact close to the surface for the purpose of fabricating a non-alloyed contact. In the WKB approximation the transmission coefficient through the second barrier (thicker collector barrier),  $T_c$ , is smaller than that through the first barrier (thinner emitter barrier),  $T_e$ , by a factor of  $\sim 8$  around zero bias. Due to the differing thickness of the barriers the average steady-state number of electrons in the well,  $\langle n \rangle$ , increases in the positive bias region and decreases in the negative bias region when the bottom contact is grounded. A large area device fabricated from the DBH exhibits a tunneling current with a zero-threshold bias, a large current peak at 0.3 V and a small current peak at  $-0.08$  V. A large area device fabricated from a similar DBH without selectively doped barriers exhibits a tunneling current with a threshold of 0.1 V and a peak at 0.37 V in positive bias and a threshold of  $-0.071$  V and a peak at  $-0.16$  V in negative bias. We analyze the differences in negative bias where the band bending effect is small, and estimate for the modulation-doped DBH that the confined level is  $4 \pm 1$  meV below the Fermi energy in the contacts at 0 V and the electron density in the well is  $(1.1 \pm 0.3) \times 10^{11} \text{ cm}^{-2}$ . The DBH is processed into small-area devices with a geometrical radius  $R$  between 0.21 and  $1.0 \mu\text{m}$  using electron-beam lithography and wet chemical etching.

## 3. Charging effects

Fig. 1 shows the  $I$ - $V$  characteristics of devices with  $R$  ranging from 0.36 to  $0.21 \mu\text{m}$ . The principle resonance is visible in all cases. The sidewall depletion width,  $W$ , is determined to be  $0.13 \mu\text{m}$  from measurements of peak current versus  $R$  [6]. The smallest device has a conducting diameter of  $2(R - W) = 0.16 \mu\text{m}$ , from which we estimate that 15 to 27 electrons accumulated in the well at zero bias. We have previously reported that a series of current peaks due to resonant tunneling through the 0D states confined in the well dominates the  $I$ - $V$  characteristic of a small-area undoped DBH [7]. When the DBH is laterally de-

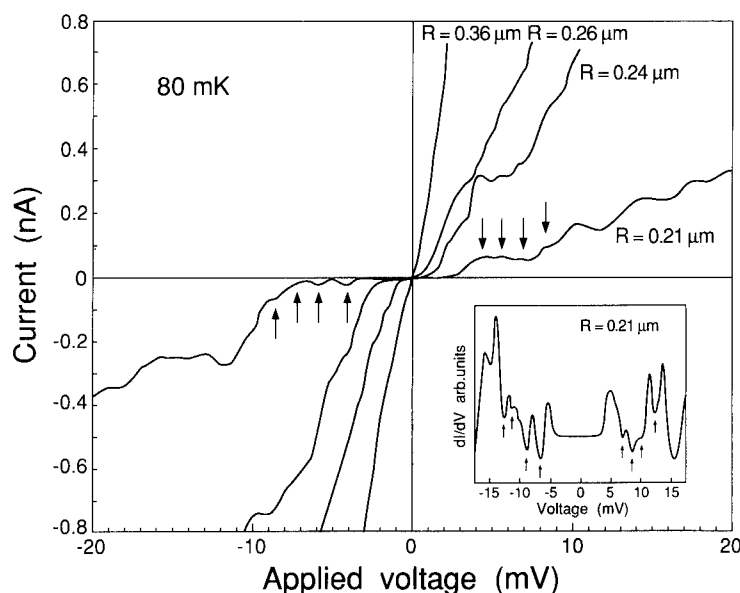


Fig. 2. Details of the  $I$ - $V$  characteristics (Fig. 1) in the low bias region.

pleted or  $R - W \ll R$  [7], the lateral confinement of the harmonic potential forms 0D subbands with a good degeneracy. The existence of a conducting region in the DBH readily lifts the degeneracy, and reduces the subband energies. This probably obscures the underlying effect of size quantization in the  $I$ - $V$  curves in Fig. 1. The effect of size quantization is also not important in the contact because the heavy doping leads to a small sidewall depletion and strong inelastic scattering.

Fig. 2 shows Fig. 1 in the low bias region on an expanded scale. The tunneling current is rapidly suppressed around 0 V for the devices with  $R \leq 0.26 \mu\text{m}$ . This current suppression appears more pronounced for the smaller devices. The voltage width,  $\Delta V$ , over which the tunneling current is used as a direct measure of the charging energy  $e\Delta V/2 = e^2/C$ , where  $C$  is the total capacitance. Here, we assume that most of the applied voltage drops uniformly across the DBH around 0 V since the tunneling current in large devices with  $R \geq 0.36 \mu\text{m}$  increases monotonically with voltage. The charging energy thus obtained,  $E_c$ , is plotted as a function of  $R$  in Fig. 3. The electrochemical potential of the dot is nearly equal to that of the reservoirs, emitter and collector con-

tacts, in the vicinity of 0 V. This is not the case for an undoped DBH because a large threshold bias for resonance gives rise to a large band bending. Consequently, the total capacitance of the tunnel junctions is well defined by  $C = \pi(R - W)^2 \epsilon_r \cdot (1/d_e + 1/d_c)$ , where  $d_e$  and  $d_c$  are respectively the emitter and collector barrier thicknesses, and  $\epsilon_r$  is the dielectric constant of  $\text{Al}_{0.3}\text{Ga}_{0.7}\text{As}$ . The solid line in Fig. 3 shows the calculated charging energy  $E_c = e^2/C$  and reproduces well the values derived from  $\Delta V$ . The effect of electron-electron interactions in the dot is

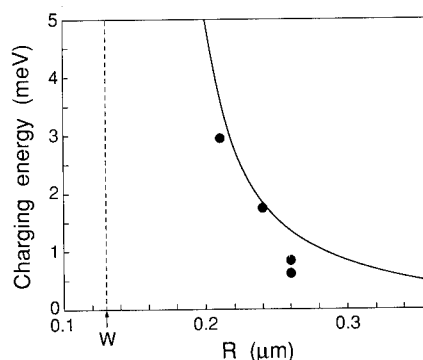


Fig. 3. Charging energy as a function of geometrical DBH radius. The dotted line indicates the sidewall depletion width.

$$I_0 = \frac{e}{\hbar} \frac{T_e E_F T_c E_0}{T_e E_F + T_c E_0}, \quad (1)$$

#### 4. Coexistence of size quantization and charging effects

Figure 1 is a plot of level energy (meV) versus dot radius ( $\mu\text{m}$ ) for a parabolic quantum dot. The y-axis represents Level energy (meV) from 0 to 25, and the x-axis represents Dot radius ( $\mu\text{m}$ ) from 0.14 to 0.30. Multiple curves are shown, labeled 1, 2, 3, and 4, representing different energy levels. The energy decreases as the dot radius increases. An inset diagram shows a parabolic quantum dot with radius  $R$  and width  $W$ .

through the 0D state from the three-dimensional contact can give rise to a sharp current peak when the Fermi energy in the contact and the 0D state align [7]. The average energy separation  $\Delta E$  of the 0D states at  $R = 0.21 \mu\text{m}$  is 0.5 to 1 meV in the vicinity of  $E_F$ . The value of  $2\Delta E/e$  is comparable to the average separation between the small current peaks indicated by the arrows in Fig. 2, whose positions are well defined in the derivative  $dI/dV$ . Therefore, we expect that the Coulomb staircase is modulated by the existence of the 0D states. This view is consistent with the change of the fine structure at higher temperatures as well as in the presence of a magnetic field. Fig. 5 shows the  $I$ - $V$  curves for the device with  $R = 0.21 \mu\text{m}$  in positive bias at different temperatures. The staircase structure remains up to 4.2 K although Coulomb blockade becomes less critical as the temperature increases. The fine structure becomes ambiguous at 4.2 K when the thermal broadening  $kT$  of the 0D state is comparable to the subband separation. Application of a weak magnetic field parallel to the direction of tunneling gives rise to a complicated change in the fine current structure. We observe a splitting of the small peaks or shoulders to high

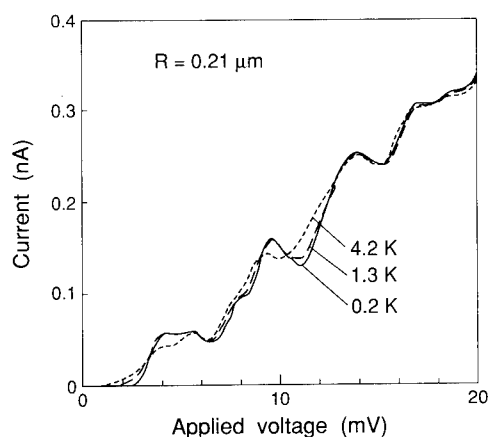


Fig. 5.  $I$ - $V$  curves in the low positive bias for the device with  $R = 0.21 \mu\text{m}$  at different temperatures.

and low energies as the magnetic field is increased up to 1 T. This behavior can be related to the lifting of the degenerate 0D states in the presence of weak magnetic field. A discussion of the magnetic field dependence will appear in a later publication.

The appearance of fine structure from the size quantization effect superimposed on the Coulomb staircase has already been predicted theoretically [1]. The negative differential resistance can be a characteristic of resonant tunneling through well-defined 0D states [7,12]. Addition of one more electron to the quantum dot is blocked by the charging energy as long as the surplus electrons reside in the dot, which is the case when  $T_e/T_c \gg 1$ . Otherwise, the escape of an electron from the dot induces resonant tunneling through the 0D states before compensating for the charging energy. This probably occurs in our device because the ratio  $T_e/T_c \approx 8$  is not large enough. We also speculate that the dot may not be localized from the reservoirs strongly enough to define  $\langle n \rangle$  as an integer although this issue has not yet been investigated. However, the present arguments are not yet fixed. It is still necessary to develop a more elaborate theory to account for the interplay between the charging and size quantization effect since the size quantization effect is stronger than expected. In the negative bias direction, fine structure in the tunneling current similar to that in the positive bias is observed, as

shown by the arrows in Fig. 2, although the staircase is not seen. This is unexpected in our model since the subtraction of one more electron from the dot is blocked by the charging energy in negative bias. The tunneling current in the small devices with  $R \leq 0.26 \mu\text{m}$  increases more steeply with voltage in the negative bias than in positive bias. This implies that  $\langle n \rangle$  is not so well defined in negative bias as in positive bias. Therefore, following the preceding discussion, we would anticipate a more predominant effect of size quantization on the  $I$ - $V$  characteristic in negative bias than in positive bias.

## 5. Conclusions

We observe Coulomb blockade of resonant tunneling in small-area modulation-doped DBHs and determine the charging energy as a function of conducting diameter. Coulomb blockade is followed by step-like current-voltage characteristics with extra structure, which is related to the interplay between the charging and size quantization effects.

## 6. Acknowledgments

We thank Yoshiro Hirayama, David G. Austing, Yoshiji Horikoshi, and Tatsuya Kimura for useful discussions.

## 7. References

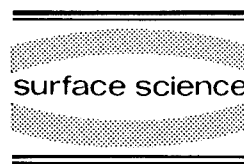
- [1] J.H.F. Scott-Thomas, S.B. Field, M.A. Kastner, H.I. Smith and D.A. Antoniadis, Phys. Rev. Lett. 62 (1989) 583.
- [2] U. Meirav, M.A. Kastner, M. Heiblum and S.J. Wind, Phys. Rev. B 40 (1989) 5871.
- [3] H. van Houten and C.W.J. Beenakker, Phys. Rev. Lett. 63 (1989) 1893.
- [4] A.T. Johnson, L.P. Kouwenhoven, W. de Jong, N.C. van der Vaart, C.J.P. Harmans and C.T. Foxon, Phys. Rev. Lett. 69 (1992) 1592.
- [5] M.A. Reed, J.N. Randall, R.J. Aggarwal, R.J. Matyi, T.M. Moore and A.E. Wetsel, Phys. Rev. Lett. 60 (1988) 535.
- [6] S. Tarucha, Y. Hirayama, T. Saku and T. Kimura, Phys. Rev. B 41 (1990) 5459.

- [7] S. Tarucha, Y. Tokura and Y. Hirayama, *Phys. Rev. B* 44 (1991) 13815.
- [8] Bo Su, V.J. Goldman and J.E. Cunningham, *Science* 255 (1992) 313.
- [9] M. Tewordt, L. Martin-Moreno, J.T. Nicholls, M. Pepper, M.J. Kelly, V.J. Law, D.A. Ritchie, J.E.F. Frost and G.A.C. Jones, *Phys. Rev. B* 45 (1992) 14407.
- [10] A.N. Korotkov, D.V. Averin and K.K. Likharev, *Physica B* 165&166 (1990) 927.
- [11] D.V. Averin, A.N. Korotov and K.K. Likharev, *Phys. Rev. B* 44 (1991) 6199.
- [12] A. Groshev, T. Ivarov and V. Valtchinov, *Phys. Rev. Lett.* 66 (1991) 1082.



ELSEVIER

Surface Science 305 (1994) 553–557



## A non-invasive voltage probe to measure Coulomb charging

C.G. Smith <sup>\*</sup>, M. Field, M. Pepper <sup>1</sup>, D.A Ritchie, J.E.F. Frost, G.A.C. Jones,  
D.G. Hasko

*Cavendish Laboratory, University of Cambridge, Cambridge CB3 0HE, UK*

(Received 19 April 1993; accepted for publication 15 July 1993)

### Abstract

We have fabricated a quantum box device in close proximity to a one-dimensional (1D) ballistic channel, but in a separate circuit. This is achieved using electron beam lithography to define sub-micron gates on a modulation doped GaAs/GaAlAs heterostructure containing a high mobility electron gas. When the 1D channel is biased in the tunneling regime it is extremely sensitive to neighbouring electric fields, and therefore the potential variation in the quantum box. The resistance variation with voltage in this channel is calibrated by applying a known voltage to the quantum box and in this way the Coulomb charging energy is measured in a non-invasive manner. The Coulomb charging caused by removal of electrons from the dot is detectable while immeasurably small currents flow through the dot. The measured charging energy is 500  $\mu\text{eV}$  which compares well with that calculated from a measurement of the total capacitance between all the surrounding conducting regions and the quantum box.

### 1. Introduction

Theoretical suggestions for non-invasive measurements of voltage and chemical potential in sub-micron devices have been discussed in the literature for some time [1]. To measure voltage a capacitance technique is required, while to measure chemical potential one would require a weakly coupled voltage probe. In this paper we will discuss the realization of a technique to measure the single electron charging energy in a semiconductor quantum box in a non-invasive manner [2]. The charging voltage on a metal

island has been investigated using the known properties of a similar metal CB device fabricated nearby [3]. Recently there has been a great deal of work in the field of single electron charging or Coulomb blockade (CB). Such effects were first observed in granular metal films [4] and later in sub-micron metal–oxide–metal junctions [5]. In the light of the initial transport measurements through a lateral quantum dot defined using Schottky gates above a high mobility GaAs/GaAlAs heterostructure [6], it was suggested [7] that such a structure should show CB oscillations in the conductance with changing gate voltage. These CB oscillations were subsequently observed in such structures [8].

In order to make a non-invasive measurement of the electrostatic potential on the quantum dot in the CB regime we needed to make use of

<sup>\*</sup> Corresponding author.

<sup>1</sup> Also at: Toshiba Cambridge Research Centre, 260 Cambridge Science Park, Milton Road, Cambridge CB4 4WE, UK.

capacitance coupling so that no charge flows from the dot. Typically a 2DEG area of  $0.5 \mu\text{m}$  square has a capacitance of  $10^{-16}$  F while the capacitance coupling to the dot of a 2DEG  $0.1 \mu\text{m}$  away is of the order  $10^{-17}$  F. Thus the addition of one electron onto the dot would put  $1/10$  of an electron onto the neighbouring 2DEG area. A voltmeter connected to this region would be unable to measure this voltage as a charge of greater than  $1/10$  of an electron would be required to make such a measurement. What was required was a method of miniaturising our voltmeter and putting this next to the quantum box. The solution was to use a ballistic point contact next to the quantum box, but in a separate circuit. When such a channel is biased in a tunneling regime it is very sensitive to surrounding voltages, so the voltage change on the dot due to the addition of single electrons then causes the resistance of this channel to alter.

## 2. Measurement of charging energy

Fig. 1 is an electron micrograph of the gate pattern defined by electron beam lithography on our device. The bar down the middle separates two circuits, one with a quantum box defined by the three gates on the right-hand side of the bar, and the other with a ballistic point contact defined between the gate on the left and the bar. The gates were fabricated on top of a two-dimensional electron gas (2DEG) with a mobility of  $120 \text{ m}^2 \text{ V}^{-1} \text{ s}^{-1}$  and a carrier concentration of  $3.61 \times 10^{15} \text{ m}^{-2}$ . The 2DEG resides  $70 \text{ nm}$  below the surface. Voltage probes on either side of the box and the ballistic point contact made it possible to measure their conductance simultaneously.

By putting a negative voltage of  $-0.8 \text{ V}$  on the bar down the middle (G1 in Fig. 2) the two circuits can be electrically isolated so that even when a DC bias voltage of more than  $100 \text{ mV}$  is applied a current of less than  $1 \text{ pA}$  flows between them. By adjusting the gates G3, G4 and G5 on the right of the bar, CB oscillations in the conductance measured from top to bottom are observed. The conductances are measured using a  $10 \mu\text{V}$  AC applied voltage and a current ampli-

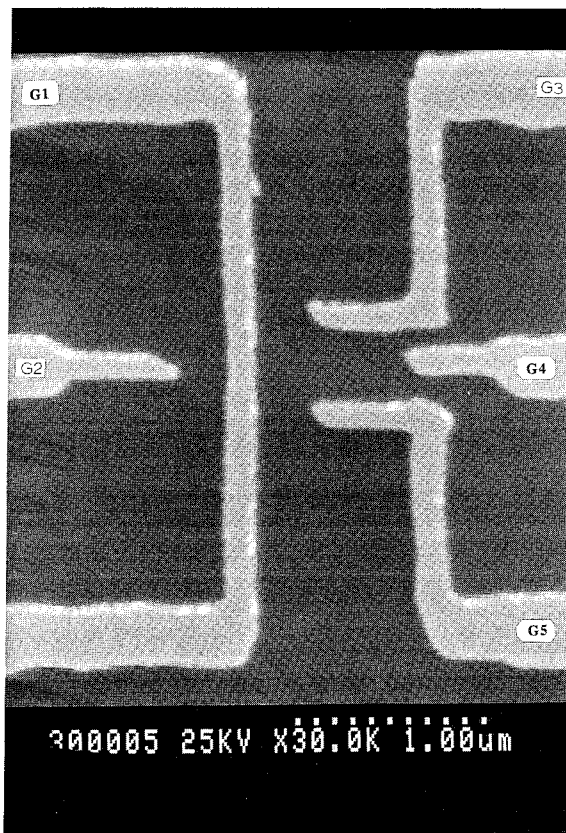


Fig. 1. An electron micrograph of sample showing the gates G1, G2, G3, G4 and G5.

fier. All the measurements were performed in a dilution refrigerator with a base temperature  $T < 20 \text{ mK}$ . The gates G5 and G3 form two barriers and the gate G4 is used as a plunger to change the area of the confined 2DEG dot. From Aharonov–Bohm-like oscillations [9] when the conductance is greater than  $2e^2/h$  we deduce that the area of the dot is approximately  $0.65 \times 0.24 \mu\text{m}^2$ . With the conductance less than  $2e^2/h$ , sweeping the plunger G4 results in periodic oscillations of period  $12.3 \text{ mV}$ . These oscillations are independent of magnetic field indicating that they are due to single electron charging. In parallel with this measurement the resistance of the channel between the gates G1 and G2 is measured with the resistance set greater than  $h/2e^2$  (typically  $100 \text{ k}\Omega$ ). We chose a resistance greater than the quantized value, because then the transmis-

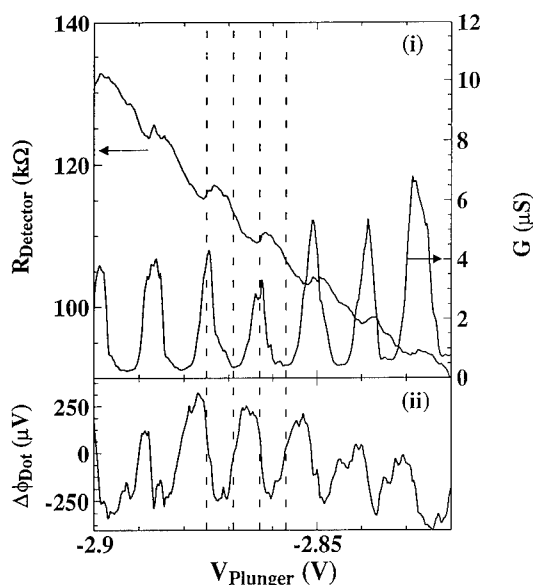


Fig. 2. (i) The CB oscillations in the dot against plunger voltage, with the detector resistance also shown. (ii) The calibrated dot potential variation.

sion probability must be less than one. In other words the electrons are tunneling through a barrier. As we are measuring the resistance of the detector with a constant current of 1 nA and the detector resistance is around 100 k $\Omega$  we have a bias voltage of around 100  $\mu V$  on the detector, a value comparable with the tunneling barrier height. This level of current was required to ensure a sensible signal-to-noise ratio.

As the screening in the plane of the 2DEG is not perfect the potential seen by the dot is sensitive to all the surrounding gates including G2. The capacitance between all these gates and the regions of 2DEG can be deduced from the period of the CB oscillation with an applied DC voltage to each gate or area of 2DEG. The total capacitance of the dot is then the sum of all these values and comes to  $C_{\Sigma} = 2.9 \times 10^{-16}$  F. This implies that the charging energy of the dot  $\Delta E = e^2/C_{\Sigma} = 550$   $\mu eV$ .

In Fig. 2 the conductance of the dot and the resistance of the detector are shown. The conductance in the quantum box oscillates from 0.2 to 6  $\mu S$  while the resistance of the detector rises from 90 to 120 k $\Omega$ . On this background there are dips

which correspond with the peaks in the conductance in the neighbouring circuit. The rising background is due to direct coupling between the gate G4 (plunger) and the detector. Although it is useful to measure relative potentials, it is far more useful to measure the absolute change in potential. To obtain this information the detector had to be calibrated. To achieve this the voltage on the plunger was removed so that a voltage could be applied directly to the 2DEG region between the tunnel barriers of the CB dot. The variation in resistance with voltage applied to the 2DEG is then recorded and was found to be nearly linear and not exponential. This occurs because the bias voltage across the barrier is large compared to the barrier in the detector; however, the exact form of the relation is unimportant. Although in this calibration procedure the leads connected to the dot also float up to the applied voltage, this modification to the resistance of the detector is small because of the greater distance of these regions. The rising background due to the plunger G4 is corrected for by raising the temperature of the device until there is no CB structure in the detector. When this high temperature background is subtracted from the low temperature curve and the calibration with the applied 2DEG potential is used we get a non-invasive measurement of the potential on the dot. As the bias voltage across the detector is of the order of 100  $\mu V$  the temperature dependence of the detector is weak for temperatures less than 1 K. It is worth noting that the structure in the detector is washed out by a temperature of 500 mK while the CB in the dot itself is lost at around 1.2 K. The signal in the detector is being lost when the thermal smearing is comparable to the change in the barrier height due to the CB potential in the box. This implies a value of 40  $\mu eV$  for the detector modulation.

Returning to Fig. 2, the bottom curve shows the amplitude of the potential oscillations in the quantum dot. The first thing to notice is that the amplitude of the oscillations in potential are of the order 500  $\mu eV$  in good agreement from that calculated from our estimate of  $e^2/C_{\Sigma}$ . This is around 12 times larger than the modulation it causes in the detector. This value fits nicely with



the ratio of the total capacitance,  $C_\Sigma$ , to the capacitance from the dot to the detector, which comes to 14. The second obvious feature of this graph is that peaks in the conductance through the box correspond to the points of inflection in the potential. This is to be expected, because we are measuring the time averaged potential on the dot as a current of 0.6 nA flows at the peaks in the conductance. This corresponds to 600 million electrons per second passing through the dot making it oscillate from  $+e^2/C_\Sigma$  to  $-e^2/C_\Sigma$  every nano-second. As the time constant in the detector circuit is 300 ms no potential is measured. Changing the gate voltage off a peak in conductance, means that the probability of finding an electron in the dot or outside the dot is no longer identical. If we are on the left of the peak the voltage on the plunger is more negative so the electron spends less time on the dot and the detector becomes more positive. The potential of the dot reflects the difference between the charge on the dot that would minimise the charging energy and the percentage time an electron is on the dot. In the case of extremely narrow conductance peaks, this can lead to a sawtooth wave form for the dot potential [10].

As a check of the charging energy one can measure the temperature dependence of the conductance troughs in the quantum box when showing CB. From a plot of the log of these conductance minima against  $1/T$ , the two activation energies  $W_1$  and  $W_2$  can be deduced. Where  $W_1$  is the difference between the Fermi energy in the leads and the next available state in the dot, and

$W_2$  is the energy difference between the highest states in the dot to the first available state in the leads. The total conductance is given by

$$G = G_1 \exp(-W_1/kT) + G_2 \exp(-W_2/kT),$$

where  $G_{1,2}$  are the conductances through the dot due to the two levels. The Arrhenius plot of  $\ln(G)$  versus  $1/T$  gives a straight line with an intercept of  $11.4 \mu\text{S}$  and a slope with an activation energy of  $50 \mu\text{eV}$ . We would expect a value of  $e^2/2C_\Sigma = 250 \mu\text{eV}$  for the activation energy and a value of twice the conductance in the peaks for the intercept of  $12 \mu\text{S}$ . This discrepancy between  $e^2/C_\Sigma$  and the activation energy has been noted before [8], and may be due to co-tunneling. The charging energy being reduced by an electron being ejected from the far end at the same time as an electron enters. The reduction in the energy will then be given by the ratio of the tunneling time through one barrier to the RC time constant for the dot.

### 3. The detector signal when the conductance in the box is small

By continually sweeping the plunger voltage to more negative values the capacitance effect on the barriers reduces the conductance through the dot, until it can no longer be measured. At the same time the oscillations in the detector become sharper and can be followed for a further 110 periods, until the voltage is  $-4.05 \text{ V}$ . After this point the signal vanishes. This is shown in Fig. 3. The detector has to be reset slightly to take into

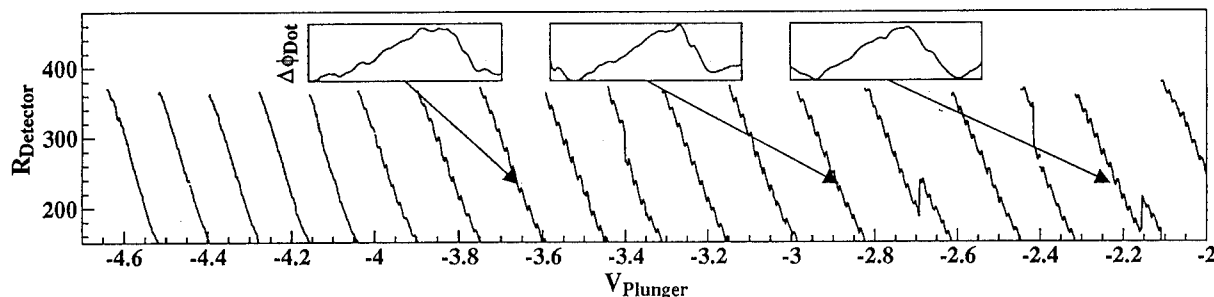


Fig. 3. The detector resistance when the dot conductance is immeasurably small. The detector resistance is reset to  $150 \text{ k}\Omega$  whenever it is driven above  $360 \text{ k}\Omega$  by the capacitance effect of the plunger on the detector. The insert shows the development of the sawtooth shape.

account the effect of the plunger on the detector. At more negative voltages the oscillations disappear and the effect of the plunger on the detector becomes greater suggesting the dot is no longer screening it. To see if this is the last electron in the dot we must estimate the likely number of electrons to start with. To do this we can use the Aharonov–Bohm-like oscillations seen when the conductance is greater than  $2e^2/h$ . These occur when a magnetic field is applied such that Landau levels are formed in the 2DEG, which results in edge states circulating round the dot. The conductance then oscillates periodically in  $B$  with a period of  $h/eA$ , where  $A$  is the area of the box. The measured period is 20 mT, which corresponds to an area of  $2.1 \times 10^{-13} \text{ m}^2$  [9]. At a constant magnetic field similar oscillations are seen as the plunger voltage  $V_{\text{pl}}$  is changed altering the area by  $dA$ . As we have a value for  $dV_{\text{pl}}/dA$  ( $3.3 \times 10^{13} \text{ V m}^{-2}$  measured from the Aharonov–Bohm-like oscillations) and  $dV_{\text{pl}}/dN$  (12.2 mV measured from the Coulomb blockade oscillations) we therefore can calculate  $dN/dA$ , the carrier concentration in the dot. This calculation results in a value of  $2.57 \times 10^{15} \text{ m}^{-2}$ , which is 20% lower than the sheet carrier concentration in the 2DEG away from the gates. When this is combined with the calculated area of the dot one obtains 532 for the number of electrons in the dot.

From these estimates we can deduce that the loss of signal in the detector is not due to the removal of the last electron, but must be due to an increase in the barriers to the dot by such an extent that no electrons can flow within the time constant of the measurement of the detector. It is worth noting that as the barriers become higher the potential measured on the detector becomes more sawtooth in nature reflecting the narrower, but immeasurably small amplitude conductance peaks.

#### 4. Conclusion

By defining a quantum box in one circuit and a ballistic constriction in another nearby circuit, we

have been able to use the constriction biased in the tunneling regime as a non-invasive voltage probe of single electron charging on the dot. The constriction can be calibrated to an accuracy of  $50 \mu\text{V}$ , giving a value of  $500 \mu\text{V}$  for the charging energy on the dot. The detector can still be used to show the sawtooth shape of the potential, even though the current through the dot is immeasurably small. The activation energy of the dot is a factor of five smaller than the measured, and calculated value of the charging energy in the dot. This may be a result of co-tunneling of electrons through the dot.

#### 5. Acknowledgements

This work was supported by the Science and Engineering Research Council and Esprit Project No. BRA6536.

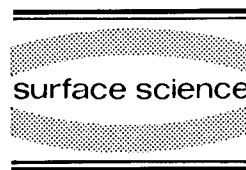
#### 6. References

- [1] R. Landauer, *Z. Phys. B (Condensed Matter)* 68 (1987) 217.
- [2] M. Field, C.G. Smith, M. Pepper, D.A. Ritchie, J.E.F. Frost, G.A.C. Jones and D.G. Hasko, *Phys. Rev. Lett.* 70 (1993) 1311.
- [3] P. Lafarge, H. Pothier, E.R. Williams, D. Esteve, C. Urbina and M.H. Devoret, *Z. Phys. B (Condensed Matter)* 85 (1991) 327.
- [4] I. Giaever and H.R. Zeller, *Phys. Rev. Lett.* 20 (1968) 1504.
- [5] D.V. Averin and K.K. Likharev, in: *Mesoscopic Phenomena in Solids*, Eds. B.L. Al'tshuler, P.A. Lee and R.A. Webb (Elsevier, Amsterdam, 1991).
- [6] C.G. Smith, M. Pepper, H. Ahmed, J.E.F. Frost, D.G. Hasko, D.C. Peacock, D.A. Ritchie and G.A.C. Jones, *J. Phys. C* 21 (1988) L893.
- [7] L.I. Glazman and R.I. Shekhter, *J. Phys. (Condensed Matter)* 1 (1989) 5811.
- [8] U. Meirav, M.A. Kastner, M. Heiblum and S.J. Wind, *Phys. Rev. B* 40 (1989) 5871.
- [9] R. Brown, C.G. Smith, M. Pepper, H. Ahmed, J.E.F. Frost, D.G. Hasko, D.C. Peacock, D.A. Ritchie and G.A.C. Jones, *J. Phys. (Condensed Matter)* 1 (1989) 6291.
- [10] L.P. Kouwenhoven, N.C. van der Vaart, A.T. Johnson, W. Kool, C.J.P.M. Harmans, J.G. Williamson, A.A.M. Staring and C.T. Foxon, *Z. Phys. B (Condensed Matter)* 85 (1991) 367.



ELSEVIER

Surface Science 305 (1994) 558–565



## Energy levels of an artificial atom probed with single-electron capacitance spectroscopy

R.C. Ashoori <sup>\*,1</sup>, H.L. Stormer, J.S. Weiner, L.N. Pfeiffer, K.W. Baldwin, K.W. West

*AT&T Bell Laboratories, Murray Hill, NJ 07974, USA*

(Received 31 May 1993; accepted for publication 30 June 1993)

### Abstract

We have recently developed a spectroscopic technique which allows direct measurement of quantum energy levels. The method is based on observation of the capacitance signal resulting from single electrons tunneling into discrete quantum levels. The electrons tunnel between a metallic layer and confined states of a microscopic capacitor fabricated in GaAs. Charge transfer occurs only for bias voltages at which a quantum level resonates with the Fermi energy of the metallic layer. This creates a sequence of distinct capacitance peaks whose bias positions directly reflect the electronic spectrum of the confined structure. Using this “single-electron capacitance spectroscopy”, we map the magnetic field dependence of the ground state energies of a single quantum dot containing from 0 to 50 electrons. Along with a spectroscopic measurement of the dot’s ground states, we probe tunneling rates of electrons to individual quantum states. The experimental spectra reproduce many features of a noninteracting electron model with an added fixed charging energy. However, in detailed observations deviations are apparent: exchange induces a two-electron singlet–triplet transition, self-consistency of the confinement potential causes the dot to assume a quasi two-dimensional character, and features develop which are suggestive of the fractional quantum Hall effect.

Several years ago, it became evident that semiconductor technology had, at least in one sense, begun to touch the ultimate limits of miniaturization. Several experiments, such as the resonant tunneling system of Reed et al. [1] made it clear that it might be feasible to produce a “quantum dot or artificial atom” containing as few as one electron. Over the last few years, many other methods have been developed to study these sys-

tems. Among these are gated resonant tunneling devices [2], far infrared spectroscopy [3,4], conventional capacitance studies of arrays [5,6], and photoluminescence spectroscopies [7]. Recently, two techniques have been developed which allow spectroscopic study of the ground state (GS) energies in *individual* quantum dots with a resolution limited only by the temperature of the electronic system [8,9].

A key question to be answered by spectroscopic studies on quantum dots is the role of the electron–electron interaction in modifying the dot’s electronic level structure. Bryant [10] has addressed this question for quantum dots con-

\* Corresponding author.

<sup>1</sup> Present address: Department of Physics, Massachusetts Institute of Technology, Cambridge, MA 02139, USA.

taining just two electrons. He finds a continuous evolution of the level structure, from single-particle-like states in the limit of a very small dot, to a level structure dominated by the electron–electron interaction in larger dots. Since the confinement potential in semiconductor quantum dots can be controlled at will, a large range of this continuum which is not accessible in atomic physics can be examined.

In the presence of magnetic field ( $B$ ), the electron–electron interaction is expected to affect the electronic level structure of a quantum dot in interesting ways. For instance, Maksym and Chakraborty [11] find in their calculations that electrons in their GS in a quantum dot undergo discrete increases of angular momentum of several  $\hbar$  as  $B$  is increased, reminiscent of transitions between different fractional quantum Hall states. In order to investigate experimentally such novel phenomena, we have undertaken a high resolution study of the GS energy levels and tunneling rate spectra of a single quantum dot in magnetic field.

In a previous paper [8], we have introduced single-electron capacitance spectroscopy (SECS). The method allows the direct measurement of the energies of quantum levels of an individual small structure (dot) as a function of magnetic field ( $B$ ). When the Fermi energy of an electrode becomes resonant with a quantum level of a nearby dot, single electrons can tunnel back and forth between the electrode and the dot through a tunnel barrier (see Fig. 1a). The resulting charge induced by this motion on the opposite electrode of a “tunnel capacitor” is detected by an on-chip, highly sensitive transistor. Using this technique, we were able to detect spatially distinct localized states in a small tunnel capacitor. We now use SECS to measure the GS energies of a single quantum dot containing  $N$  electrons in which charge nucleates in only one central location.

To measure the capacitance signal from single electrons moving back and forth across the tunnel barrier, we have incorporated our device into a “bridge on a chip”, with a standard capacitor and detector located very close to the tunnel capacitor. As a detector, we use a cryogenic high electron mobility transistor (HEMT) with input shunt

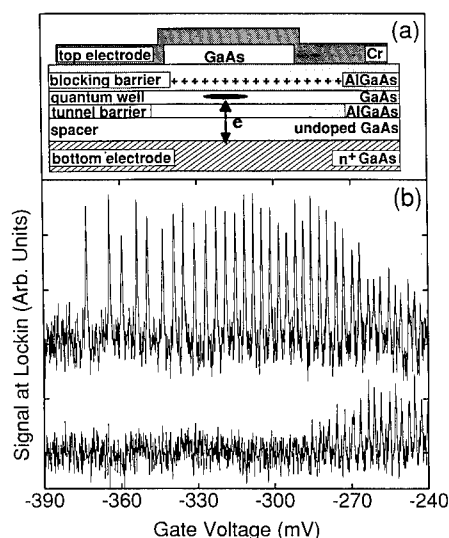


Fig. 1. (a) Schematic of sample. (b) Capacitance data vs. gate bias for the quantum dot sample in zero magnetic field. The top and bottom traces show the signal resulting from electron tunneling in-phase and electron tunneling in  $90^\circ$  lagging phase with the 210 kHz excitation voltage, respectively.

capacitance of  $\approx 0.3$  pF. It is positioned within 2 mm of the bridge. We mount the HEMT with its two-dimensional electron gas parallel to the magnetic field, and we find its characteristics practically unaffected by an applied field in this geometry.

The basic configuration of our GaAs samples has been described previously [8], although the semiconductor structure has been slightly modified for the present experiments. A schematic of the sample is shown in Fig. 1a. The layer sequence is as follows: 3000 Å  $n^+$ -doped ( $4 \times 10^{17} \text{ cm}^{-3}$ ) GaAs bottom electrode; 600 Å undoped GaAs spacer layer; 125 Å undoped  $\text{Al}_{0.3}\text{Ga}_{0.7}\text{As}$ /GaAs superlattice tunnel barrier; 175 Å quantum well (vertically confines the quantum dot); 500 Å  $\text{Al}_{0.3}\text{Ga}_{0.7}\text{As}$  blocking barrier; and a 300 Å GaAs cap layer. The blocking barrier contains a Si delta doped layer 200 Å from the well edge. The wide 600 Å spacer layer and the superlattice tunnel barrier [12] were implemented to prevent Si atoms from migrating into the well [8]. Lateral confinement is provided by first patterning a 3500 Å diameter circular metallic disk on top of the sample surface and using this as an

etch mask to etch down to the AlGaAs blocking barrier surface. The 3500 Å diameter top electrode is contacted for measurement by overlaying it with a 1.5 μm diameter metal disk. All measurements are taken at 0.35 K.

Fig. 1b displays capacitance versus gate bias data for the quantum dot sample. The top trace is the signal observed in-phase with the excitation voltage. A first peak appears at −373 mV and arises as the lowest electronic state of the dot becomes resonant with the Fermi energy of the  $n^+$  electrode. With increasing positive gate bias, subsequent electrons tunnel onto the quantum dot. Unlike our previous results in a larger dot, the peaks are spaced rather uniformly, with their separation decreasing slightly with increasing electron number. The constancy of the peak heights attests to the quantization of charge that is being moved onto the dot.

Beyond the 25th peak, the peak heights in the top trace of Fig. 1b drop due to a decrease in the tunneling rate. This interpretation is confirmed by measuring the signal at the dot in 90° lagging phase, shown in the bottom trace of Fig. 1b, where peaks occur only for  $N \geq 25$ . This behavior is unambiguous evidence that the tunneling rate of electrons is becoming smaller than the 210 kHz excitation frequency. A slow tunneling rate causes an electron to “wait” a length of time before it tunnels in response to the excitation voltage, and its motion thus lags the excitation. The present experiment thus allows both a tunneling rate spectroscopy based on the height and phase of capacitance peaks as well as an energy level spectroscopy based on the positions of the peaks.

We have developed an understanding of why the tunneling rates decrease in these samples with increasing electron number based upon stud-

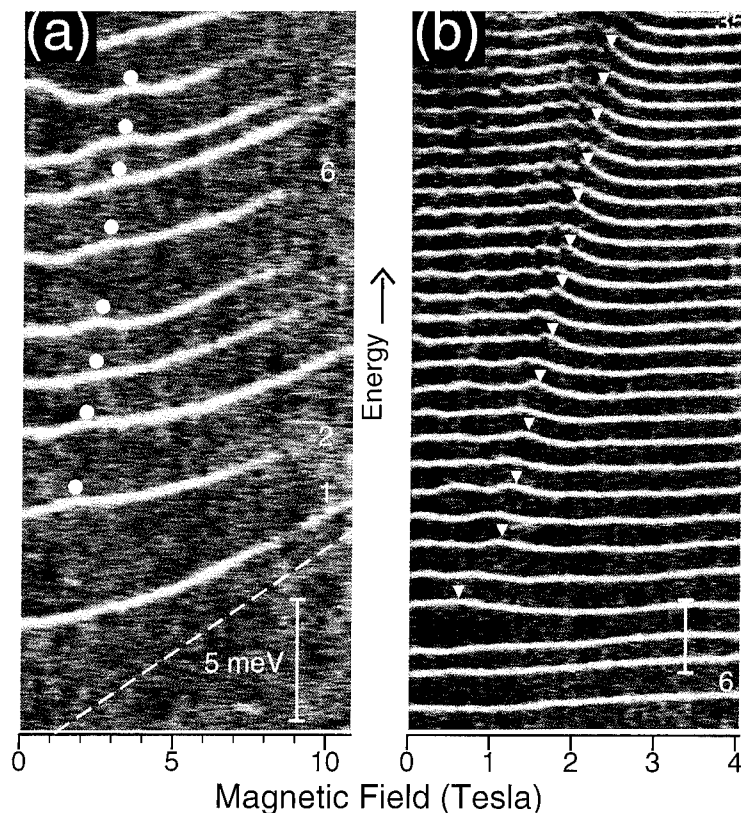


Fig. 2. Grey scale plots of the sample capacitance as a function of both magnetic field and gate bias. The vertical bars in both (a) and (b) represent an energy of 5 meV. The dashed line follows the zero point energy in magnetic field for a free electron,  $\hbar\omega_c/2$ .

ies of different wafers with different undoped spacer layers just below the tunnel barrier. Briefly, the geometry of our samples suggests that the tunneling problem can be separated into transverse (in the plane of the quantum well) and longitudinal (in the direction of tunneling) parts [13]. The large 600 Å spacer layer acts as a long and low ( $< 20$  meV high) tunnel barrier. As the dot fills up with electrons, their bound state energy in the quantum well is lowered with respect to this barrier, reducing the tunneling rate.

The regime of a few electrons in a dot has been probed by relatively few experiments [14]. We now use SECS in  $B$ -field to study this domain with unprecedented resolution. Fig. 2 is a grey scale image of the dot capacitance as a function of gate bias and  $B$ -field applied perpendicular to the plane of the dot. The white and black regions correspond to the highest and lowest capacitance, respectively. The gate bias scale is converted to an energy scale [8] by division by a lever-arm of  $2.0 \pm 0.1$  for this structure. This lever-arm was determined from capacitance measurements on large area mesas made on the same wafer.

Fig. 2 represents the  $B$ -field evolution of the first 35  $N$ -electron GS energies of the quantum dot. The field dependence of the lowest energy state in Fig. 2a is smooth and is well described by the first electron in a cylindrically symmetric parabolic potential [15]  $\frac{1}{2}m^*\omega_0^2r^2$  with  $\hbar\omega_0 = 5.4$  meV. The high field asymptote of this curve follows the dashed line in Fig. 2a with slope  $\hbar\omega_c/2$ . From the classical turning points of the lowest bound state we deduce a dot diameter of 408 Å.

In contrast to the first electron, the evolution of the ground state energy of two electrons shows a pronounced “bump” and a change of slope at about 1.5 T (see dot on 2nd electron). We interpret this feature as a singlet–triplet crossing. Considering noninteracting states, the first two electrons in the dot fall into a two-fold (spin) degenerate ground state for  $B = 0$ . At higher field, the energy difference between the ground orbital state and the first excited state shrinks, and the Zeeman effect causes a level crossing at 25 T for  $\hbar\omega_0 = 5.4$  meV.

Electron–electron interactions significantly re-

duce the  $B$ -field for this singlet–triplet crossing. Wagner, Merkt, and Chaplik [16] have calculated its position for parabolic quantum dots. For  $\hbar\omega_0 = 5.4$  meV, the crossing is expected at 3.6 T, about a factor of 2 higher than seen in Fig. 2a. The discrepancy may arise from the assumption of a strictly parabolic potential in the calculation. Such a singlet–triplet crossing has not been observed in atomic physics experiments due to the exceedingly high  $B$ -field required ( $4 \times 10^5$  T for He). The weak binding of electrons in our quantum dot along with the small electronic mass shifts it to attainable fields.

The singlet–triplet crossing should exist *even in the absence* of a Zeeman splitting, arising solely from the electron–electron interaction [16]. The angular momentum quantum number  $m$  of the two electrons in the ground state increases with  $B$ , being equal to zero only at low field [11,16]. The energy difference between single-particle states of progressively larger angular momenta decreases with increasing  $B$ ; in higher fields, it becomes advantageous for the system to place electrons in states of successively higher angular momenta (larger orbit radii) in order to decrease the Coulomb repulsion between electrons. To maintain exchange antisymmetry of the two-electron wavefunction, the system undergoes singlet–triplet (triplet–singlet) crossings as  $m$  switches from even (odd) to odd (even) numbers.

The Zeeman energy moves the first singlet–triplet crossing to yet lower fields. Moreover, at higher fields the Zeeman effect may force for the system to remain in a spin triplet, allowing only transitions between odd  $m$  states. For our GaAs dot, the nature of transitions beyond the initial singlet–triplet crossing depends sensitively on the value of  $\hbar\omega_0$  for the dot as well as on the precise shape of the bare confining potential. These transitions cause smaller changes of slope in the two-electron GS energy, and we do not attempt to label them here.

The data of Fig. 2a, display several unexpected features. The bump seen in the GS energy of the two-electron system seems to progress through the few-electron system (white dots). Its position shifts monotonically to higher fields with increasing  $N$ , producing a clear “ripple” through the

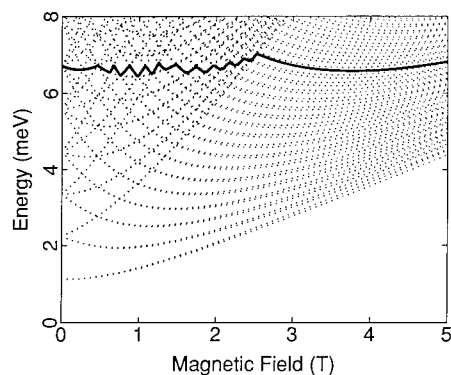


Fig. 3. Theoretical Darwin–Fock states for a parabolic quantum dot with  $\hbar\omega_0 = 1.12$  meV (dotted curves). The bold solid curve displays the magnetic field evolution of the 35th electron.

data set. It seems likely that these features are also spin related. Finally, selected traces of Fig. 2a show a distinct intensity loss with increasing  $B$  resulting from an unexplained decreased tunneling rate. At a lower excitation frequency (65 kHz rather than 210 kHz), all capacitance peaks continue smoothly to our maximum field of 10.8 T, except at  $N=2$ , for which the tunneling rate drops precipitously at 8 T.

Fig. 2b shows the ground state energies of the dot for  $N=6$ –35 on an expanded field scale. In order to interpret the general features of this data set, we turn first to Fig. 3. This graph reproduces the highly intertwined single-particle states of a cylindrically symmetric parabolic potential with  $\hbar\omega_0 = 1.12$  meV in a  $B$ -field.  $N$  electrons in this system fill the  $N$  lowest energy states. The GS energy of the  $N$ th electron should thus oscillate as levels cross as indicated in bold for the 35th electron GS. The oscillations cease at about 2 T.

In magnetic field, Landau level structure develops in the dot. Because the density is higher near the dot center than at the edges, and in magnetic field, levels of larger Landau index  $\nu$  may be filled there rather than at the dot edge. As the field is increased, the degeneracy of the lower  $\nu$  levels increases, and electrons move from the higher  $\nu$  states at the dot center to the lower  $\nu$  states which become available at the dot edge.

Taking the Landau level index  $\nu$  for the dot to be given by the Landau level occupancy at the dot center, the position of the last crossing in Fig. 3 can thus be identified with  $\nu = 2$ . At this field, all electrons have moved into the lowest Landau level, and at the dot center, there are two electrons (one spin up and one spin down) per flux-quantum passing through the dot.

In order to incorporate the electron–electron interaction to lowest order into this picture, we follow the constant interaction (CI) model [9,17,18]. It consists of single-particle states each separated by a magnetic field independent charging energy. In Fig. 2b, the development of the  $\nu = 2$  positions are clearly visible (white triangles). Beyond  $N = 10$ , the  $\nu = 2$  positions for each successive electron agree well with the CI model using a constant  $\hbar\omega_0 = 1.12$  meV. Curiously, the tunneling rates are attenuated around  $\nu = 2$  at large  $N$ . At  $\nu = 2$ , the electrons in the dot center are in a quantum Hall state, and we speculate that tunneling suppression arises from the incompressibility of this state.

Fig. 4 zooms in on the  $\nu = 2$  region for  $N = 21$ –33. These data are taken at 125 kHz to achieve well developed capacitance peaks. The oscillations expected from the CI model are clearly visible. Although the qualitative agreement between experiment and the simple model of Fig. 3 is satisfying, there exist some remarkable differences: oscillations in the GS energy appear only very close to  $\nu = 2$ , and GS energies drop abruptly as the field is increased beyond  $\nu = 2$ . While we presently have no explanation for the existence of oscillations only close to the  $\nu = 2$  region and their relative phases, we believe that the energy drop beyond  $\nu = 2$  is related to the nonparabolicity of the self-consistent potential.

Hartree calculations [19] show that the bottom of the dot's confinement potential is “flattened” considerably by the presence of electrons, and in the interior can be considered as a small two-dimensional (2D) system. In a 2D system there exist well known sudden drops in the chemical potential as Landau levels depopulate in  $B$ -field. As  $N$  is increased the dot approaches a 2D system, giving rise to the enhanced chemical potential drop at  $\nu = 2$  seen in our data.

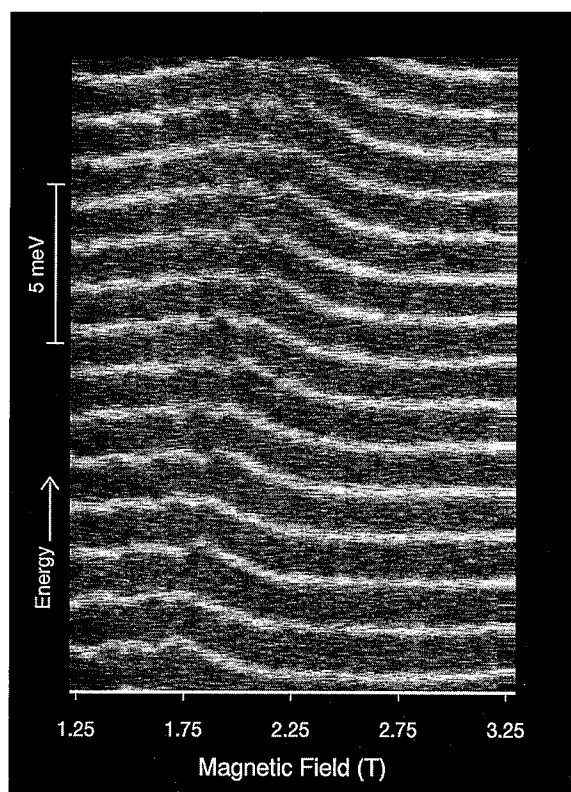


Fig. 4. Grey-scale capacitance data for  $N = 21$ –33. The data set zooms in on the  $\nu = 2$  region.

The identification of the  $\nu = 2$  position allows us to determine the size of the dot, calculate its charging energy and compare it with the observed gate bias spacing between successive electrons [17]. Since for large  $N$  the potential around the dot center is approximately constant, we can define a capacitance of the dot to external electrodes. With capacitances  $C_{\text{top}}$  and  $C_{\text{bott}}$  of the dot to the top and bottom plates, respectively, the electrostatic lever-arm is  $(C_{\text{bott}} + C_{\text{top}})/C_{\text{bott}}$ . Ignoring the comparably small quantum level spacings, successive electron additions occur when the electrostatic potential in the dot changes by an amount,  $e/(C_{\text{top}} + C_{\text{bott}})$ . Accounting for the lever-arm, electron additions are spaced by  $e/C_{\text{top}}$  in gate bias.

In a dot with a flat-bottom potential, the area of the dot  $A$  is related to the Landau level filling fraction  $\nu$  by  $A = N(h/eB\nu)$ . For the 30th elec-

tron,  $\nu = 2$  occurs at about 2.2 T, which translates into a dot diameter of 1900 Å. Assuming parabolic confinement with  $\hbar\omega_0 = 1.1$  meV rather than flat-bottom confinement decreases the dot area by only 2%. A simple parallel plate capacitor model neglecting fringing fields yields  $e/C_{\text{top}} = 4.2$  mV, only  $\sim 25\%$  larger than the measured gate bias spacing of 3.3 mV between capacitance peaks. The dot sizes determined this way compare very well with sizes calculated using our own classical relaxation method [20] computer simulations. An alternate way of determining the dot size is by looking at Fig. 4 and noting that each oscillation seen here corresponds to adding an additional flux quantum to the dot [21]. The size of the dot determined from the oscillation period is, to within experimental error, the same as that determined above.

As we move to yet higher  $N$ , approaching the 2D limit, additional features become apparent in our spectra. Fig. 5, taken at 125 kHz, displays the chemical potentials of the dot containing 33–50 electrons. Similar to Fig. 4, we observe the steep drop in chemical potential at  $B$ -fields just beyond  $\nu = 2$  (at about 2.3 T for  $N = 33$ ). The same behavior is now apparent at  $\nu = 4$  (at about 1.2 T for  $N = 33$ ). We attribute the accentuation of these features to the increasingly 2D character of the system at high filling. A more precise understanding of the chemical potential steps will require a self-consistent calculation of the dot's edges [22].

Pursuing further the transition between a quantum dot and a finite-sized 2D electron system, we now examine the region  $\nu < 2$  at  $B$  above 4 T. We observe a sequence of “bumps” shifting only slightly to higher  $B$  with higher  $N$ . These features are inexplicable in terms of any CI model which all predict that successive traces oscillate  $180^\circ$  out of phase [9,18]. We note also, that unlike the predictions of a single particle model which predicts features with a periodicity of one flux quantum through the dot, the bumps seen in the  $\nu < 2$  regime have a periodicity of about three flux quanta. We hypothesize that the bumps seen in Fig. 5 are of many-particle origin reminiscent of the fractional quantum Hall effect (FQHE). In the FQHE the chemical potential of the system



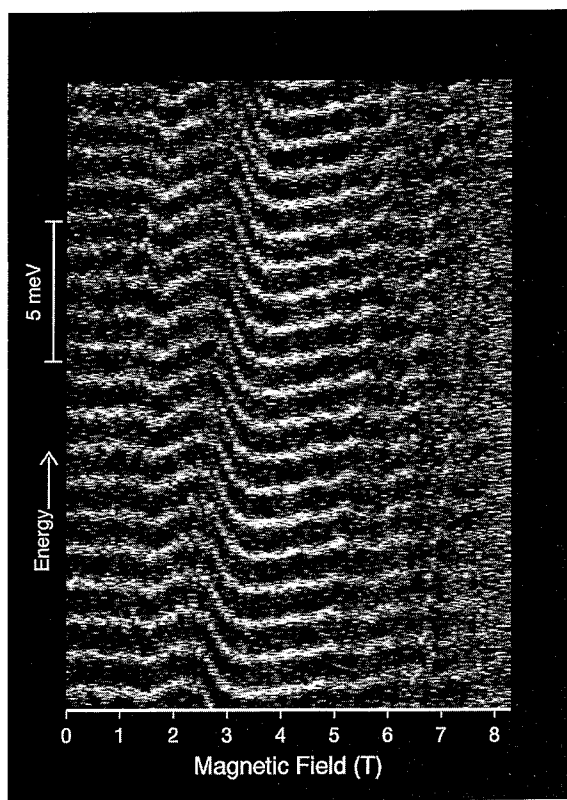


Fig. 5. Sample capacitance as a function of gate bias and magnetic field for  $N=33$  (lowest full trace) up to 50. The vertical bar represents an energy of 5 meV.

undergoes maxima between FQHE steps and minima at the steps [23]. The features seen in Fig. 5 are 0.2–0.5 meV in height, not unlike the characteristic energy range of the FQHE at such  $B$ -fields. Moreover, the decrease in tunneling rates (intensity) between the bumps, may reflect the energy gaps in the FQHE. These features grow monotonically in prominence as more electrons are added to the dot, suggesting a two-dimensional origin. The size and distribution of the electron density within the dot vary with  $B$ -field, and it is thus difficult to assign a precise value of  $\nu$  at dot center for fields beyond  $\nu=2$ . Finally, given the nonuniformity of the electron density, we expect the electron gas to form incompressible and compressible regions, with the FQHE chemical potential minima occurring with the central

portion of the dot at a  $\nu$  value appropriate for the FQHE [24].

We note that at high magnetic fields, for all electron numbers, tunneling rates tend to be suppressed. This effect appears analogous to an observed tunneling suppression in the two-dimensional electron gas [25]. In that case, the suppression arises as a zero-bias anomaly which develops due to a magnetic field induced Coulomb gap. We speculate that a similar phenomenon is occurring here, although a detailed study of the temperature and excitation dependence of the tunneling suppression will be required to confirm this hypothesis.

In summary, SECS has permitted a detailed survey of the  $N$ -electron ground states of a quantum dot in magnetic field. There are several salient features of the data set. We observe the singlet–triplet transition in the two electron dot. An unusual “ripple” is seen to run through the data for fewer than 10 electrons in the dot, and it appears that the ripple is caused by correlations between spin-flips in the dot containing different numbers of electrons. Anomalous behavior is seen in both the ground state energies and the tunneling rates to the dot around integer Landau level filling fractions. Finally, features appear at high magnetic field and large electron number which are suggestive of the development of the FQHE.

We thank S.J. Pearton for help preparing the quantum dots and L.I. Glazman, P. Hawrylak, P.A. Lee, A.H. MacDonald, B.I. Shklovskii, and N. Wingreen for helpful discussions.

## 1. References

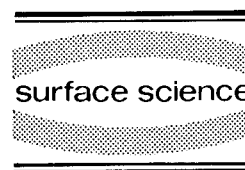
- [1] M.A. Reed, J.N. Randall, R.J. Aggarwal, R.J. Matyi, T.M. Moore and A.E. Wetsel, *Phys. Rev. Lett.* 60 (1988) 535.
- [2] M.W. Dellow et al., *Phys. Rev. Lett.* 68 (1992) 1754.
- [3] Ch. Sikorski and U. Merkt, *Phys. Rev. Lett.* 62 (1989) 2164.
- [4] B. Meurer, D. Heitmann and K. Ploog, *Phys. Rev. Lett.* 68 (1992) 1371.
- [5] W. Hansen, T.P. Smith, III, K.Y. Lee, J.A. Brum, C.M. Knoedler, J.M. Hong and D.P. Kern, *Phys. Rev. Lett.* 62 (1989) 2168;

- see comment by, R.H. Silsbee and R.C. Ashoori, Phys. Rev. Lett. 64 (1990) 1991.
- [6] R.C. Ashoori, R.H. Silsbee, L.N. Pfeiffer and K.W. West, in: *Nanostructures and Mesoscopic Systems*, Eds. M. Reed and W. Kirk (Academic Press, New York, 1992) pp. 323–334.
- [7] K. Brunner, U. Bockelmann, G. Abstreiter, M. Walther, G. Böhm, G. Tränkle and G. Weimann, Phys. Rev. Lett. 69 (1992) 3216.
- [8] R.C. Ashoori, H.L. Stormer, J.S. Weiner, L.N. Pfeiffer, K.W. Baldwin and K.W. West, Phys. Rev. Lett. 68 (1992) 3088.
- [9] P.L. McEuen, E.B. Foxman, U. Meirav, M.A. Kastner, Yigal Meir, N.S. Wingreen and S.J. Wind, Phys. Rev. Lett. 66 (1991) 1926.
- [10] G.W. Bryant, Phys. Rev. Lett. 59 (1987) 1140.
- [11] P.A. Maksym and T. Chakraborty, Phys. Rev. Lett. 65 (1990) 108.
- [12] U. Meirav, M. Heiblum and Frank Stern, Appl. Phys. Lett. 52 (1988) 1268.
- [13] J.A. Lebens, R.H. Silsbee and S.L. Wright, Appl. Phys. Lett. 51 (1987) 840.
- [14] B. Meurer, D. Heitmann and K. Ploog, Phys. Rev. Lett. 68 (1992) 1371;  
Bo Su, V.J. Goldman and J.E. Cunningham, Science 255 (1992) 313.
- [15] C.G. Darwin, Proc. Cambridge Philos. Soc. 27 (1930) 86.
- [16] M. Wagner, U. Merkt and A.V. Chaplik, Phys. Rev. B 45 (1992) 1951.
- [17] R.H. Silsbee and R.C. Ashoori, Phys. Rev. Lett. 64 (1990) 1991.
- [18] P.L. McEuen, E.B. Foxman, J. Kinaret, U. Meirav, M.A. Kastner, N.S. Wingreen and S.J. Wind, Phys. Rev. B 45 (1992) 11419.
- [19] A. Kumar, S.E. Laux and F. Stern, Phys. Rev. B 42 (1990) 5166.
- [20] K.J. Binns and P.J. Lawrenson, *Analysis and Computation of Electric and Magnetic Field Problems* (Pergamon, Oxford, 1973).
- [21] U. Sivan and Y. Imry, Phys. Rev. Lett. 61 (1988) 1001.
- [22] D.B. Chklovskii, B.I. Shklovskii and L.I. Glazman, Phys. Rev. B 46 (1992) 4026.
- [23] T. Chakraborty and P. Pietiläinen, *The Fractional Quantum Hall Effect* (Springer, Berlin, 1988).
- [24] J.M. Kinaret, Y. Meir, N.S. Wingreen, P.A. Lee and Xiao-Gang Wen, Phys. Rev. B 45 (1992) 9489;  
A.H. MacDonald and M.D. Johnson, Phys. Rev. Lett. 70 (1993) 3107.
- [25] R.C. Ashoori, J.A. Lebens, N.P. Bigelow and R.H. Silsbee, Phys. Rev. Lett. 64 (1990) 681; Phys. Rev. B 48 (1993) 4616.



ELSEVIER

Surface Science 305 (1994) 566–570



# Evidence for spin singlet–triplet transitions of two electrons in a quantum dot observed via single-electron tunneling

Bo Su <sup>\*,a</sup>, V.J. Goldman <sup>a</sup>, J.E. Cunningham <sup>b</sup>

<sup>a</sup> Department of Physics, State University of New York, Stony Brook, NY 11794-3800, USA

<sup>b</sup> AT&T Bell Laboratories, Holmdel, NJ 07733, USA

(Received 20 April 1993; accepted for publication 6 July 1993)

## Abstract

We report magnetotunneling in a double-barrier resonant tunneling nanometer device in the single-electron charging regime, in particular for the case of two electrons in the well. Sharp rising steps appear in current–voltage characteristics, the  $N$ th step appearing at a voltage  $V_N$  when the Coulomb blockade for tunneling of  $N$ th electron into the well is overcome. The first current step width is  $\Delta V_1 = V_2 - V_1$  (the second step width is  $\Delta V_2 = V_3 - V_2$ ), corresponding to the difference of energies required for having two (three) electrons and having one (two) electron(s) in the well. As a function of magnetic field, we observe  $\Delta V_1$  to exhibit upward cusps, while  $\Delta V_2$  exhibits downward cusps at the same magnetic field. Such behavior is expected to manifest the spin singlet–triplet transitions of the two-electron state confined in a quantum dot.

## 1. Introduction

Quantum dots fabricated from double-barrier resonant tunneling structures (DBRTS) have their uniqueness in studying electron transport both in the size quantization regime and in the single-electron charging regime. By utilizing asymmetric DBRTS, single-electron charging effects may be largely separated from those due to size quantization. Recently, we have reported the observation of single-electron charging in nanometer DBRTS devices [1–3]. The heterostructure material is asymmetric with one barrier much less transparent than the other. When the emitter barrier is less transparent than the collector barrier, the

current reflects resonant tunneling of just one electron at a time through size-quantized well states; the current peaks and/or steps (depending on device parameters) appear in current–voltage characteristics ( $I$ – $V$  curves). When the emitter barrier is more transparent than the collector barrier, electrons accumulate in the well; the total number of electrons in the dot increases with bias in increments of one, *starting from zero*, up to 35 in one device [2,3], all electrons are “extra”.

Incremental electron occupation of the well leads to sharp steps of the tunneling current, the  $N$ th step appears at a voltage  $V_N$  when the Coulomb blockade for tunneling of the  $N$ th electron into the well is overcome. We find that the energy for adding the first electron is much different from that needed to add the second elec-

\* Corresponding author.

tron, and the energy for the second electron is different from that for the third. This is, in part, because the intrawell electron–electron interaction energy per electron depends on the total number of electrons in the dot and, in part, because of the different spatial extent of electron distributions for different size-quantized well states. In this presentation, we report an experimental study of single-electron charging as a function of magnetic field, in particular when there are two electrons in the well. Electron–electron interaction and the Pauli exclusion principle lead to spin singlet–triplet transitions of the ground state of two electrons as a function of magnetic field [1,3].

## 2. Samples and experimental

Our DBRTS material was grown by molecular beam epitaxy. The active layer consists of a 9 nm GaAs well sandwiched between a 10 nm  $\text{Al}_{0.34}\text{Ga}_{0.66}\text{As}$  barrier and a 11.5 nm  $\text{Al}_{0.36}\text{Ga}_{0.64}\text{As}$  barrier (substrate side). The GaAs emitter and collector electrodes are Si-doped to  $2 \times 10^{17} \text{ cm}^{-3}$ ; nominally undoped spacers of 10 and 8 nm are inserted before and after, respectively, the double-barrier region in order to limit Si concentration in the well. The wafer has a 100 nm non-alloyed Al ohmic contact grown in situ, so that no heat treatment of the devices was needed. The double-barrier region is  $\sim 300 \text{ nm}$  below the surface of the wafer.

Devices of nominal diameter  $D = 0.5\text{--}3 \mu\text{m}$  were defined by electron beam lithography and wet chemical etching. As discussed elsewhere [4], the “electrical size” of devices is smaller than  $D$  by about 350 nm because of etching undercut and surface depletion, as illustrated in Fig. 1. Areas unexposed to the electron beam define devices so that possible electron bombardment damage of the GaAs material is minimized. More details of the fabrication process can be found in Ref. [3]. Measurements were done in a top-loading dilution refrigerator with the sample immersed in the mixture. The  $I$ – $V$  curves of the devices were measured using a very-low-noise voltage source biasing circuit.

## 3. Theory

Wagner, Merkt and Chaplik [5] have calculated the energy levels of two electrons in a 2D parabolic confining potential as a function of magnetic field  $B$  in GaAs. They found that the electron–electron interaction and the Pauli exclusion principle lead to spin singlet and triplet transitions of the ground state of two electrons in quantum dots as a function of magnetic field. The angular momentum  $m\hbar$  of the ground state of two electrons, where  $m$  is an integer, increases, as magnetic field is increased, as to reduce electron–electron interaction energy. A higher angular momentum means higher rotational energy; on the other hand, the average distance between

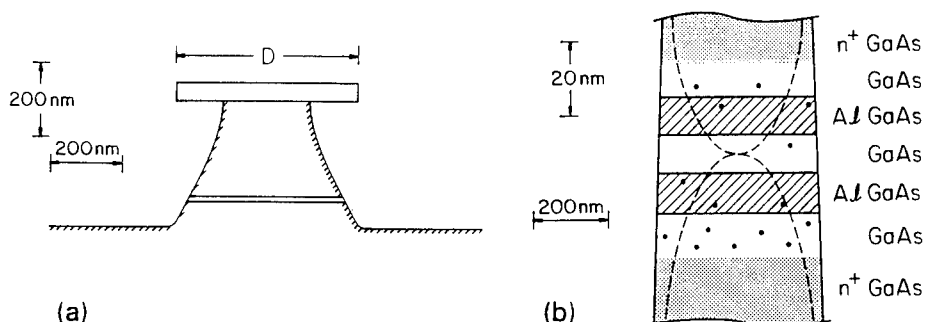


Fig. 1. (a) Cross section of a nanometer DBRTS device; the metal ohmic contact has diameter  $D$ , and the two barriers are represented as two horizontal lines. (b) The double-barrier region expanded vertically by a factor of ten. Dotted regions are doped intentionally; large dots represent unintentional donors, and the dashed lines give an equipotential resulting from the GaAs surface depletion.

the two electrons is increased and Coulomb energy is smaller. As a result of the competition of the two energies, the ground states in the sequence of  $m = 0, -1, -2, -3, \dots$  appear as  $B$  is increased. Since, according to the Pauli exclusion principle, the total spin of two electrons is  $\frac{1}{2}[1 - (-1)^m]$ , this leads to an alternating sequence of singlet and triplet ground states. The  $B$ -fields at which singlet–triplet transitions occur depend on the dot size (curvature of the confining potential).

At low  $B$ , the spin singlet  $m = 0$  state has lower energy. As  $B$  increases, this energy rises, while the energy of the  $m = -1$  spin triplet state drops. At certain  $B$ , these two states cross, forming an upward cusp. At yet higher  $B$ , such singlet–triplet crossings form a series of upward cusps. If the ground state energy of the two electrons in a quantum dot could be measured experimentally as a function of  $B$ , a series of upward cusps should appear on an otherwise smooth curve and the upward cusps indicate the transitions between the spin singlet and triplet states.

#### 4. Results and discussion

The  $I$ – $V$  curve of the nanometer device in the positive bias reflects the one-electron-at-a-time tunneling through an increasing number of size-quantized well states [3]. We model the depletion potential in the plane of the dot as a 2D parabolic well so that the single-electron energy spectrum is given by  $E_M = \hbar\omega_0(M + 1)$ . We obtain  $\hbar\omega_0 = 4$  meV from the magnetotunneling data [3]. Both magnetotunneling data [3] and a Hartree numerical calculation [6] suggest that a parabolic potential models the confining potential well.

We will focus our attention on the negative bias of the device when the collector barrier is less transparent than the emitter barrier. Fig. 2 shows magnetotunneling  $I$ – $V$  curves taken with magnetic field applied parallel to the tunneling direction (perpendicular to the barriers). Up to six or seven steps can be seen in the data of Fig. 2. After overcoming the Coulomb blockade, the lowest well state is occupied most of the time. In contrast to the positive bias, even though the only tunneling electron can tunnel through several of

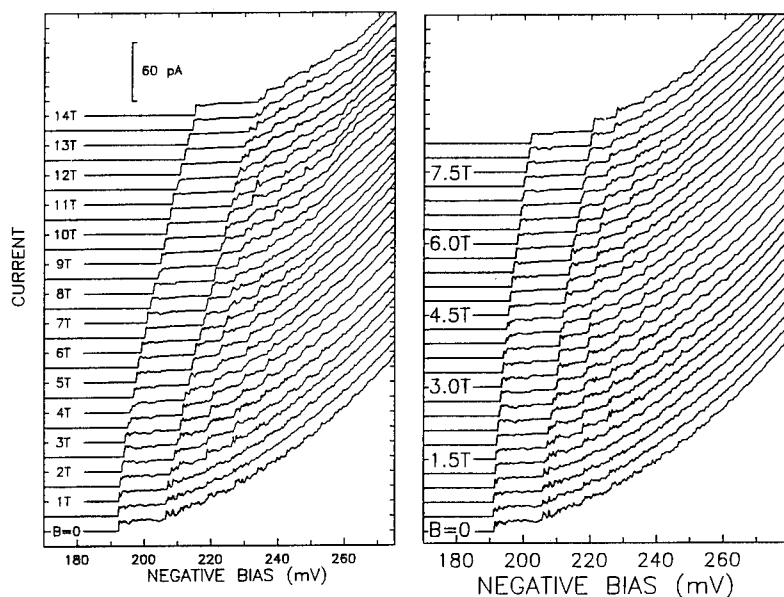


Fig. 2. Magnetotunneling data versus negative bias at 20 mK. The curves shown were taken every 0.5 T in the left field and every 0.3 T in the right field, and are offset vertically by 15 pA. Each current step corresponds to an increase by one in the number of electrons in the well ( $N_w = 0$  at low bias).

the lowest well states, after the first current step the current stays nearly constant until it is energetically possible to have two electrons in the well at the same time, when the second step occurs. Similarly, each subsequent current step occurs when it is energetically possible to have one more electron in the well. Thus, the  $I$ - $V$  curves of Fig. 2 reflect single-electron charging of the well by an incrementally-increasing number of electrons dynamically stored in the well. We define  $\Delta V_N$  as the voltage extent of the  $N$ th current step in the negative bias, corresponding to the number of electrons in the well equal to  $N_W$ . As discussed before, each step in the “staircase” corresponds to increase of  $N_W$  by one, starting from zero. If the total energy of the  $N_W$  many-electron state is denoted as  $E_N$ , then the change in energy required to add  $N_W$ th electron is  $(\Delta E)_N = E_N - E_{N-1}$ ; this corresponds to the voltage  $V_N$ , when the  $N$ th step occurs. Therefore,  $\Delta V_N = (V_{N+1} - V_N)$  corresponds to  $(\Delta E)_{N+1} - (\Delta E)_N = E_{N+1} - 2E_N + E_{N-1}$ . A step width  $\Delta V_N$  thus corresponds to the change in total energy required for adding the  $(N_W + 1)$ th electron into the well. The first width,  $\Delta V_1$ , gives the energy difference between having just one and having two electrons in the well; the second width,  $\Delta V_2$ , gives the energy difference between having two and three electrons in the well; thus we have  $\Delta V_1 = \alpha(E_2 - 2E_1)$  and  $\Delta V_2 = \alpha(E_3 - 2E_2 + E_1)$ , where  $\alpha$  is the energy-to-bias conversion coefficient ( $\alpha = 3.7$  mV/meV for this device as determined from thermal activation, see Ref. [3]) and  $E_N$  is the lowest total energy required to have  $N_W$  electrons in the well, including the many-body kinetic energies and many-electron Coulomb energies, both charging and intrawell. In Fig. 3, we plot  $\Delta V_1$  and  $\Delta V_2$  as a function of  $B$ .

There are two possible spin states when there are two electrons in the well: spin singlet and spin triplet. At zero  $B$ , the singlet state has lower energy than the triplet state; at some  $B$ , the  $S_z = -1$  triplet state crosses the  $S_z = 0$  singlet state [1]. Experimentally, we observe evidence for the splitting of the second current step into two substeps in the  $I$ - $V$  curve in the negative bias (with more or less clarity for different devices, Refs. [1–3]); following our work, this phe-

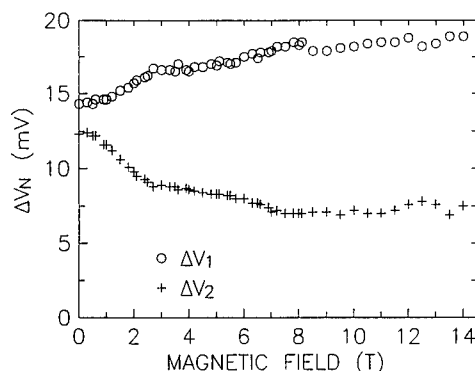


Fig. 3. The voltage extent of the first two current steps in the negative bias,  $\Delta V_1$  and  $\Delta V_2$ , as a function of  $B$ . Three upward and downward cusps in  $\Delta V_1$  and  $\Delta V_2$ , respectively, occur at roughly the same  $B$ , marking the transitions of spin singlet-triplet states of two electrons. The bias-to-energy conversion is 0.27 meV/mV [3].

nomenon was modeled theoretically by Chen and Ting [7]. The first crossing of the triplet and singlet states occurs at  $B = 2.7 \pm 0.3$  T. This crossing is reflected as cusps in  $\Delta V_1$  and  $\Delta V_2$  at the same  $B$  in Fig. 3: an upward cusp in  $\Delta V_1$  and a downward cusp in  $\Delta V_2$ . In addition, at higher  $B$ , there are two more cusps in  $\Delta V_1$  and  $\Delta V_2$ , upward and downward, respectively, at about the same  $B$ : one at  $8.0 \pm 0.5$  T and another at  $12 \pm 1$  T.

Both  $\Delta V_1$  and  $\Delta V_2$  contain  $E_2$ , with plus in  $\Delta V_1$  and minus in  $\Delta V_2$ . Therefore, the upward cusps in  $E_2$  are reflected as upward cusps in  $\Delta V_1$  and downward cusps in  $\Delta V_2$  so long as  $E_3$  and  $E_1$  are smooth functions of  $B$ . The ground state is unique. For one electron in the well,  $E_1$  is a smooth function of  $B$ . For three electrons, one would expect many transitions between different total angular momentum states on a much smaller energy scale [8], less than what can be resolved in our experiments. This is evidenced by the fact that in the  $\Delta V_2$  data in Fig. 3 no other clear cusps are seen except the three also present in the  $\Delta V_1$  data. Thus, we treat  $E_3$  as a smooth function of  $B$ . From the numerical calculations of Ref. [5], the values of  $B$  at which spin singlet-triplet transitions occur for  $\hbar\omega_0 = 4$  meV and Lande factor  $g^* = -0.44$  are  $2.8 \pm 0.2$  T,  $8.5 \pm 0.5$  T and  $9.9 \pm 0.5$  T. They are in a reasonable agreement with the experimental values.

As expected,  $\Delta V_1$  is greater than  $\Delta V_2$  because the Coulomb repulsion per electron is greatest for two electrons in the well. Screening by the electrodes reduces the Coulomb energy. For electron concentration in the electrodes  $n_E = 2 \times 10^{17} \text{ cm}^{-3}$ , the screening length is  $\sim n_E^{-1/3} = 15 \text{ nm}$ . This length is in addition to the barrier thickness of about 10 nm, the screening charges would be about  $\lambda = 25 \text{ nm}$  away from the electrons in the well. The in-plane separation of electrons in the well is on the order of  $a/2 = (2\hbar/m^*\omega_0)^{1/2}$ , on average; for  $\hbar\omega_0 = 4 \text{ meV}$  and  $N_W = 2$ ,  $a/2 = 24 \text{ nm}$ . Thus the separation of electrons in the well and the distance to the screening charges are comparable. An estimation of the expectation value of the two-electron repulsion energy, cut off for electron separations greater than  $\lambda$ , shows that the screening reduces the bare repulsion by a factor of  $2 \pm 0.5$  (for  $N_W = 2$ ) for the parameters of this device. Even though the two-electron repulsion is screened by the electrodes, it still plays an important role in determining the energy of the two-electron ground state; for, if the two-

electron repulsion was totally screened, no spin singlet–triplet transitions would occur and the spin singlet state would remain as the ground state as  $B$  is swept.

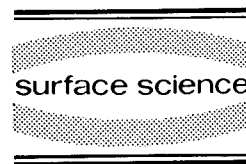
## 5. References

- [1] V.J. Goldman, B. Su and J.E. Cunningham, in: *Nanostructures and Mesoscopic Systems*, Eds. W.P. Kirk and M.A. Reed (Academic Press, New York, 1991) p. 173.
- [2] B. Su, V.J. Goldman and J.E. Cunningham, *Science* 255 (1992) 313.
- [3] B. Su, V.J. Goldman and J.E. Cunningham, *Phys. Rev. B* 46 (1992) 7644.
- [4] B. Su, V.J. Goldman, M. Santos and M. Shayegan, *Appl. Phys. Lett.* 58 (1991) 747.
- [5] M. Wagner, U. Merkt and A.V. Chaplik, *Phys. Rev. B* 45 (1992) 1950.
- [6] F. Stern, S.E. Laux and A. Kumar, private communication and in this conference.
- [7] L.Y. Chen and C.S. Ting, *Phys. Rev. B* 44 (1991) 5916.
- [8] See, e.g., P.A. Maksym and T. Chakraborty, *Phys. Rev. Lett.* 65 (1990) 108; P. Hawrylak and D. Pfannkuche, *Phys. Rev. Lett.* 70 (1993) 485.



ELSEVIER

Surface Science 305 (1994) 571–575



# Coulomb oscillation amplitude enhancement and envelope modulation in a magnetic field and activated tunneling

M. Stopa \*, Y. Aoyagi, T. Sugano

*RIKEN, The Institute of Physical and Chemical Research, Frontier Research System, 2-1 Hirosawa, Wako-Shi, Saitama 351-01, Japan*

(Received 21 April 1993; accepted for publication 27 July 1993)

## Abstract

We have calculated the self-consistent electronic structure, in a magnetic field  $B$ , for a lateral quantum dot patterned electrostatically on a GaAs/AlGaAs heterostructure for  $N$ , the number of electrons in the dot, of order 100. We have derived an expression for the dot–contact–gates system free energy which is expressed in terms of the self-consistent electrostatic potential  $\Phi$  and electron energy levels  $\epsilon_p$ , both of which are functions of  $N$ ,  $B$  and gate voltage  $V_g$ . The self-consistent calculation results are also employed to compute the elements of the device capacitance matrix. The magneto-spectrum shows a significant variation with  $N$ , in contrast to the constant interaction model, which relates to recently observed periodic envelope modulation of Coulomb oscillation amplitudes in a magnetic field.

## 1. Introduction

The Coulomb blockade in semiconductor systems arises from the electrostatic interaction of many electrons quantum mechanically confined to a submicron region, typically a quantum dot. The analysis of its properties is therefore naturally amenable to the application of self-consistent electronic structure techniques, which solve the quantum mechanical problem and the electrostatic problem together. Heretofor, however, two principal impediments to progress in that application have been: (1) the restriction of self-consistent electronic structure calculations in these systems to small electron number ( $N < 20$ ),

and (2) the absence of a suitable method of calculating the total free energy of an interacting dot–contact–gate system from the results of the structure calculation, once the non-interacting levels and capacitance parameters of the semi-classical theory have been abandoned.

In this paper we present further results from, and somewhat more detail of our solution to these two problems. Experimental results which have been unexplained by the semi-classical theory are addressed, with particular emphasis on the Coulomb oscillation amplitude structure and the influence of a magnetic field thereon.

## 2. Calculation

We solve the Poisson and Schrödinger equations self-consistently in 3D [1] for a typical lat-

\* Corresponding author.



eral semiconductor quantum dot patterned electrostatically on a GaAs/AlGaAs 2DEG heterostructure. The results in this paper are for a dot similar in gate arrangement but about 30% smaller in the 2DEG plane (by length) than that fabricated by Kouwenhoven et al. [2]. We include a wide region of the source and drain contacts wherein the electron density is determined by a two-dimensional Thomas–Fermi approximation supplemented by the calculated  $z$ -subband (growth direction) wavefunction. As in the work of Kumar et al. [1] we discretize the Poisson equation on a non-uniform mesh (typically  $65 \times 65 \times 18$ ) and employ a pre-conditioned bi-conjugate gradient solver to determine the electrostatic potential for a given input charge density and boundary conditions. Our approach to the solution of the effective mass Schrödinger equation for the dot electrons differs from that of Ref. [1]. Rather than discretization on a mesh we proceed as follows [3].

At each iteration, at each point  $(\rho(x_i, y_j), \phi(x_i, y_j))$  in the 2D ( $65 \times 65$ ) plane, we solve the  $z$ -part of Schrödinger equation,

$$\begin{aligned} & \left[ -\partial_z^2 + e\Phi_{\rho,\phi}(z) + V_B(z) \right] \xi_n^{\rho,\phi}(z) \\ & = \epsilon_n(\rho, \phi) \xi_n^{\rho,\phi}(z), \end{aligned} \quad (1)$$

where  $\Phi_{\rho,\phi}(z)$  is the electrostatic potential from the preceding iteration solution to the Poisson equation.  $V_B(z)$  is the band offset potential which, for numerical purposes, we take as a *square well* of width 200 Å. The solution of Eq. (1), in addition to providing the charge  $z$ -distribution in the contacts, reduces the three-dimensional equation in the dot to a multi-component 2D equation. If we ignore subband coupling terms, we obtain

$$\begin{aligned} & \left[ -\frac{1}{\rho} \partial_\rho \rho \partial_\rho - \frac{1}{\rho^2} \partial_\phi^2 - i\mu_B B_0 \partial_\phi + \frac{1}{4} \mu_B^2 B_0^2 \rho^2 \right. \\ & \left. + \epsilon_n(\rho, \phi) \right] f_n(\rho, \phi) = E_n f_n(\rho, \phi) \end{aligned} \quad (2)$$

(with  $\hbar = 2m^* = 1$ ). Here,  $\mu_B$  is the effective Bohr magneton and  $B_0$  the magnetic field. To solve this equation we first Fourier decompose  $\epsilon_n(\rho, \phi)$  and solve for the azimuthally symmetric

part (for each azimuthal  $m$ ) by expanding in Bessel functions. This procedure converges well as the number of zeroes in the highest retained Bessel function increases, provided that the magnetic field is not too strong ( $B_0 < 0.5$  T). For stronger fields we find that an expansion in so-called “Darwin–Fock” states is more efficient. Indeed, even at zero magnetic field this latter basis can be used and, for a sufficient number of eigenfunctions, compares well with the Bessel function expansion. The non-azimuthally symmetric part of  $\epsilon_n(\rho, \phi)$  is then diagonalized in a basis:

$$\psi(\rho, \phi, z) = \sum_{N,n,m} \alpha_{N,n,m} f_{N,n,m}(\rho) \xi_n^{\rho,\phi}(z) e^{im\phi}, \quad (3)$$

where  $f_{N,n,m}(\rho)$  is the  $N$ th solution for the  $n$ th  $z$ -subband and  $m$ th angular momentum of the azimuthally symmetric part of the Hamiltonian. Inputs to the calculation are: dot electron number  $N$ , surface gate voltages  $V_i$ , donor concentration  $n_d$  and device dimensions. Results of the calculation are energy levels  $\epsilon_p$ , wave functions  $\psi_p(\mathbf{r})$ , electrostatic potential  $\Phi(\mathbf{r})$ , electron density (for both the dot and the contacts)  $\rho_{el}(\mathbf{r})$  and induced gate charges  $Q_i$  (from the surface electric fields). Typically we vary  $N$  and one of the gate voltages,  $V_C$ , on grids of values to obtain the results throughout a region of the  $N$ – $V_C$  plane.

To calculate the total interacting free energy we begin from the classical expression

$$\begin{aligned} & F(\{n_p\}, Q_i, V_i) \\ & = \sum_p n_p \epsilon_p^0 + \frac{1}{2} \sum_i Q_i V_i - \sum_{i \neq \text{dot}} \int dt V_i(t) I_i(t), \end{aligned} \quad (4)$$

where the first sum is over non-interacting dot energies  $\epsilon_p^0$ , with occupancies  $\{n_p\}$ , the second sum is over all gates, contacts and the dot (including ion donor impurity charge), and the final sum is over contacts and gates only. From the definition of the *self-consistent* energies  $\epsilon_p = \langle \psi_p | -\nabla^2 + V_B(z) + e\Phi(\mathbf{r}) | \psi_p \rangle$  and the quantum expression for the electrostatic energy,  $Q_{\text{dot}} V_{\text{dot}} \rightarrow$

$\sum_p \langle \psi_p | e\Phi(\mathbf{r}) | \psi_p \rangle$ , we can write, for the quantum case:

$$\sum_p n_p \varepsilon_p^0 + \frac{1}{2} Q_{\text{dot}} V_{\text{dot}} \rightarrow \sum_p n_p \varepsilon_p - \frac{1}{2} \int d\mathbf{r} \rho_{\text{el}}(\mathbf{r}) \Phi(\mathbf{r}) + \int d\mathbf{r} \rho_{\text{ion}}(\mathbf{r}) \Phi(\mathbf{r}), \quad (5)$$

which is the standard correction for the double counting in a mean field approximation. For the energy from the power supplies we make an adiabatic approximation that the voltage on the gates and contacts remains nearly constant throughout the electron tunneling process. This is in contrast to a current limited approximation. We may then write the total free energy as

$$F(\{n_p\}, N, V_i) = \sum_p n_p \varepsilon_p - \frac{1}{2} \int d\mathbf{r} \rho_{\text{el}}(\mathbf{r}) \Phi(\mathbf{r}) + \frac{1}{2} \int d\mathbf{r} \rho_{\text{ion}}(\mathbf{r}) \Phi(\mathbf{r}) - \frac{1}{2} \sum_{\text{contacts}} \int d\mathbf{r} \rho_{\text{cont}}(\mathbf{r}) \Phi(\mathbf{r}) - \frac{1}{2} \sum_i Q_i V_i, \quad (6)$$

where the energy levels, density, potential and induced charges are implicitly functions of the electron number on the dot, the magnetic field and the applied gate voltages. (Spin-splitting is also included in the magnetic field case). Note that the occupation number dependence of these terms is ignored. Calculation of the self-consistent structure at various temperatures in the 0–2 K range, an effective test of the sensitivity to variation of the occupancies, shows only small change of the electronic structure.

### 3. Results

Fig. 1 shows the dot self-capacitance (total capacitance to ground) and gate to dot capacitance as a function of the changing electron number and changing gate voltage. (In the experiments the gate voltage is varied and the electron

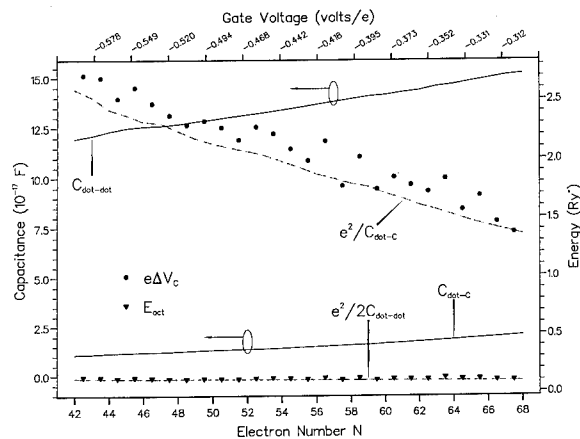


Fig. 1. Capacitances (solid lines, scale at left), classical resonance spacing and activation energy and resonance spacings (circles) and activation energies (triangles) from conductance calculation, all as a function of gate voltage and electron number.

number changes correspondingly.) Capacitances can be easily computed by changing  $N$  by some small fraction and “measuring” the change in both the dot potential minimum and the induced charges on the gates and contacts. A slightly more sophisticated averaging process, employing a notion of “local capacitance” is discussed in Ref. [4]. Note that as  $N$  increases the dot grows and hence the capacitances increase. Calculations of the conductance and its temperature dependence, also discussed in Ref. [4], give the resonance spacing and the conductance minima activation energies. In Fig. 1, these are compared with the values expected from the semi-classical model,  $e^2/C_{\text{dot-gate}}$  and  $e^2/2C_{\text{dot-dot}}$ , respectively.

In the semi-classical, or “constant interaction” (CI) model [5,6], the single-particle states are assumed to be independent of the electrostatics, that is, neither a function of  $N$  nor the gate voltages. While we have found [7] that this approximation is somewhat justifiable for the zero field case, the application of a small magnetic field causes the spectrum, particularly at the Fermi surface, to become strongly dependent on  $N$ . This is shown in Fig. 2, where the levels, measured relative to the potential minimum of the dot, are plotted for  $B = 1$  T as a function of

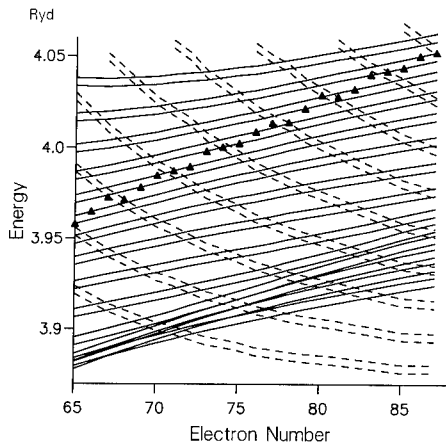


Fig. 2. Self-consistent single particle energies at fixed magnetic field,  $B = 1$  T, as a function of electron number. Gate voltage (not shown) also varies such that the electron number is that  $N$  which minimizes the free energy of the dot for that voltage. Dashed lines are in the lowest Landau level ( $n = 1$ ), solid lines are  $n = 2$ . Constant spin-splitting is clearly visible. Triangles mark the  $N$ th level (the quasi-Fermi surface).

changing  $N$ . ( $V_c$  also changes in the figure with changing  $N$ .) The pairs of rising solid lines are (spin-split) second Landau level ( $n = 2$ ) states. The decreasing dashed lines show the lowest Landau level ( $n = 1$ ) states. Triangles mark the  $N$ th or quasi-Fermi level. The structure is easily explained. As  $N$  increases, the triangular potential confining the electrons to the GaAs/AlGaAs interface becomes steeper and the binding to the interface,  $\epsilon_n(\rho, \phi)$ , increases. However, in a magnetic field the  $n = 1$  states at the Fermi energy orbit at the dot perimeter. As  $N$  increases the dot “wall” moves outward. The various states, which are characterized by orbits, each enclosing some fixed magnetic flux, remain stationary in space. Thus the states at the edge decrease in energy, in proportion to their angular momentum, as they “slide” down the wall. This results in a pattern of level crossings between outer,  $n = 1$  states and inner,  $n = 2$  states.

Note that in the device model, as in the experimental device, the dot is pinched by laterally disposed surface gates in order to vary the number of electrons in the dot. Therefore the dot is not, in general, circularly symmetric. Rather, it is commonly fairly oblong. Nonetheless, our calcu-

lations, which have so far extended to about  $N = 100$ , show no evidence of chaotic level variation for any magnetic field. Recent calculations by Jalabert et al. [8] of the non-interacting spectrum for a quantum dot have shown that, as a function of small distortions in the dot shape from perfect circularity, the energy levels evolve in a seemingly chaotic fashion. Though this may well suggest that, for a sufficiently large dot, chaotic dynamics become applicable, it is our opinion that the sensitivity of the spectrum to small distortions, which these authors have found in a small dot, are a mathematical artifact of the infinitely hard wall confining potential which they employ.

Recent experiments by Staring et al. [9] have shown a periodic amplitude modulation (envelope) of the Coulomb oscillations in the quantum Hall regime. The number of oscillations per major (envelope) period was found to approximately equal the filling factor  $\nu$ . Staring et al. present a CI model explanation for this phenomenon. However, inspection of Fig. 2 leads to a slightly different interpretation. Note that, due to the level crossings, the Fermi energy passes periodically through the decreasing  $n = 1$  levels. If, as assumed in Ref. [9], the coupling of those states to the source and drain far exceeds that of the inner Landau level, then thermally activated tunneling will produce an amplitude modulation which peaks when the quasi-Fermi energy is nearest to (or equal to) an  $n = 1$  energy level. Note that in this,  $\nu = 4$ , case the number of oscillations per envelope period would not be exactly four (Fig. 2 would give a value of 3.5). However, careful examination of the published experimental data does not convincingly show that the number of oscillations must be an integer.

#### 4. References

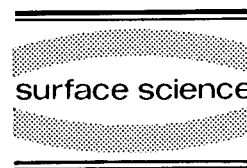
- [1] A. Kumar, S. Laux and F. Stern, Phys. Rev. B 42 (1990) 5166.
- [2] L.P. Kouwenhoven, N.C. van der Vaart, A.T. Johnson, C.J.P.M. Harmans, J.G. Williamson, A.A.M. Staring and C.T. Foxon, Proceedings of the German Physical Society meeting, Münster 1991; Festkörperprobleme/Advances in Solid State Physics, Vol. 31.

- [3] Dimensional decoupling of Schrödinger's equation has been used in other contexts. For application to the quasi-one-dimensional problem see, for example, G. Bastard, J.A. Brum and R. Ferreira, *Solid State Phys.* 44 (1991) 229.
- [4] M. Stopa and Y. Tokura, in: *Science and Technology of Mesoscopic Structures*, Eds. S. Namba, C. Hamaguchi and T. Ando (Springer, Tokyo, 1992).
- [5] C.W.J. Beenakker, *Phys. Rev. B* 44 (1991) 1646; D.V. Averin, A.N. Korotkov and K.K. Bikharev, *Phys. Rev. B* 44 (1991) 6199.
- [6] P.L. McEuen, E.B. Foxman, J. Kinaret, U. Meirav, M.A. Kastner, N.S. Wingreen and S.J. Wind, *Phys. Rev. B* 45 (1992) 11419.
- [7] M. Stopa, *Phys. Rev.*, submitted.
- [8] R.A. Jalabert, A.D. Stone and Y. Alhassid, *Phys. Rev. Lett.* 68 (1992) 3468.
- [9] A.A.M. Staring, B.W. Alphenaar, H. van Houten, L.W. Molenkamp, O.J.A. Buyk, M.A.A. Mabesoone and C.T. Foxon, *Phys. Rev. B* 46 (1992) 12869.



ELSEVIER

Surface Science 305 (1994) 576–579



# Magneto-optics of quantum wires grown on V-grooved substrates

A.S. Plaut <sup>\*,a,b</sup>, K. Kash <sup>a,1</sup>, E. Kapon <sup>a</sup>, D.M. Hwang <sup>a</sup>, E. Colas <sup>a</sup>

<sup>a</sup> Bellcore, Red Bank, NJ 07701-7040, USA

<sup>b</sup> Exeter University, Exeter EX4 4QL, UK

(Received 29 April 1993; accepted for publication 18 June 1993)

## Abstract

AlGaAs/GaAs undoped quantum wires (QWRs) grown by organometallic chemical vapour deposition on V-grooved substrates have been studied by photoluminescence (PL) and photoluminescence excitation (PLE) in zero and finite magnetic fields. From the study of the diamagnetic shift of the peaks as a function of wire width and orientation with respect to the magnetic field, we have deduced one-dimensional effective masses for the lowest subband transitions.

Fabrication of semiconductor structures exhibiting two-dimensional (2D) confinement has taken many forms over the past few years [1–3]. In-situ growth of crescent-shaped quantum wires (QWRs) on V-grooved substrates has the advantage, over post-growth processing, of producing wires with interfaces of comparable quality to that currently available in quantum well (QW) structures. Lasers incorporating such crescent-shaped QWRs show peaks in the optical gain spectra at energies corresponding to transitions between the quasi-1D subbands [4–6], and operate at room temperature with sub-mA threshold currents [7].

Here, we report the results of magneto-optical measurements, for all three orthogonal magnetic field directions, on crescent-shaped QWRs of

various widths, with subband separations of up to 45 meV in the conduction band. We are therefore able to study systematically the dependence of the diamagnetic shift of the 1D exciton on subband index, field direction and wire size. Analysis of the quadratic shifts has enabled us to determine exciton reduced masses for the ground state of these 1D systems.

These crescent-shaped quantum wires are grown by organometallic chemical vapour deposition (OMCVD) on a GaAs(100) substrate patterned with [011]-oriented V-grooves [8]. A transmission electron microscopy (TEM) cross-sectional image of a part of a vertically-stacked array of GaAs/AlGaAs QWRs from sample A is shown in Fig. 1. Sample A was grown at 670°C on a 3.5  $\mu\text{m}$  pitch grating. It consists of a 0.7  $\mu\text{m}$  Al<sub>0.45</sub>Ga<sub>0.55</sub>As cladding layer, followed by ten periods of (nominally) 2 nm GaAs QWs separated by 50 nm thick Al<sub>0.45</sub>Ga<sub>0.55</sub>As barriers. The complete recovery of the radius of curvature at the bottom of the groove during barrier layer

\* Corresponding author.

<sup>1</sup> Present address: Department of Physics, Case Western Reserve University, Cleveland, OH 44106, USA.

growth results in a vertical array of nearly identical GaAs wires. In the case of sample A, each crescent is 5.5 nm thick at its centre and  $\sim 35$  nm in full geometrical width. Sample B was grown at 750°C and consisted of an 8.5 nm thick and  $\sim 65$  nm wide GaAs crescent sandwiched between  $\text{Al}_{0.7}\text{Ga}_{0.3}\text{As}$  barriers [10]. In sample C, grown at 670°C, the GaAs crescents were 8.3 nm thick and  $\sim 40$  nm in geometrical width. Note that the effective wire widths are much smaller than the geometric ones due to the tapering of the quantum well layers [4].

The energy-band structure of the QWRs was evaluated using the model described in Ref. [4]. For sample A, the calculated energy separation between the ground and first excited QWR subbands for electrons, heavy holes and light holes are 44.6, 11.1 and 30.4 meV, respectively. The corresponding values for sample B are 21.7, 3.9 and 16.7 meV. The effective width  $W_{\text{eff}}$  of the wires defined by where  $E_{\text{confinement}}^{\text{electron}}(y) = E_1$ , where  $E_1$  is the lowest electron subband energy [9], is

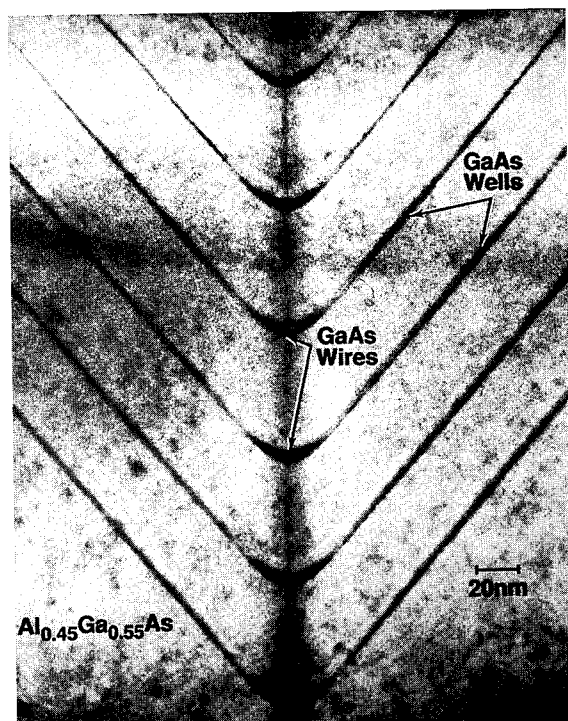


Fig. 1. TEM cross-sectional image of a vertically-stacked array of GaAs/AlGaAs crescent-shaped QWRs.

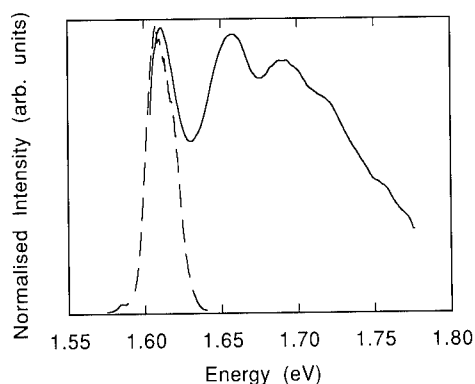


Fig. 2. PLE (solid curve) and PL (dashed curve) spectra at 27.5 K at  $B = 0$  T for sample A.

much smaller than the geometric width. For electrons in the ground state  $W_{\text{eff}} = 9.5$  nm for sample A and  $W_{\text{eff}} = 16$  nm for sample B.

The non-equilibrium carriers were created using a Ti:sapphire laser, and the low temperature (4 K or  $24 \pm 4$  K) photoluminescence (PL) and photoluminescence excitation (PLE) spectra were recorded in the Faraday configuration with the laser beam always parallel to the sample growth direction ( $z$ -direction). For the PLE measurements the spectrometer was set to the low energy side of the PL peak. Measurements were taken in magnetic field ( $B$ ) up to 7 T using an optical cryostat.

In Fig. 2 we show both the PL and PLE spectra for sample A at zero magnetic field, taken using light polarised parallel to the axis of the wire. The PLE peak energy for the second excited transition in sample A as a function of magnetic field has been plotted in Fig. 3 for all three magnetic field directions:  $B_x$ ,  $B_y$  and  $B_z$ . The three curves are slightly displaced relative to each other due to inhomogeneity across the sample, and the necessity of repositioning the sample in order to achieve the three experimental arrangements. When the field is applied along the wire ( $B_x$ ) the PLE peak energy appears essentially independent of magnetic field up to 7 T, but if the magnetic field is applied either perpendicularly or laterally, then a clear diamagnetic shift is observed. For sample A the magnitudes of the shifts are very similar for magnetic fields in

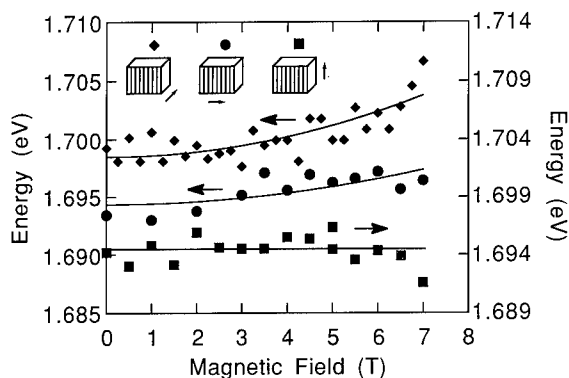


Fig. 3. PLE peak positions for the second excited state of sample A as a function of magnetic field applied perpendicularly ( $B_z$ ) (diamonds), laterally ( $B_y$ ) (circles) and along the wires ( $B_x$ ) (squares). The lines are theoretical fits to the data for  $B_z$  and  $B_y$  and a guide to the eye for  $B_x$ . The arrows in the inset indicate the magnetic field axis.

the  $y$ - and  $z$ -directions. In this case, the wire width in the  $y$ -direction ( $W_{\text{eff}}$ ) is 9.5 nm and the quantum well reaches its maximum thickness of 5.5 nm in the  $z$ -direction at the centre of the QWR. Thus one would expect the diamagnetic shifts to be significantly greater for these two directions of magnetic field than that for  $B_x$  (assuming no anisotropy with bulk crystallographic direction [11]) and, at the same time, fairly similar to each other; in agreement with what we find experimentally.

The diamagnetic coefficients of the PL energy, with the magnetic field applied perpendicularly ( $B_z$ ), were determined as  $18 \pm 5.2 \mu\text{eV}/\text{T}^2$ ,  $24 \pm 3.0 \mu\text{eV}/\text{T}^2$ , and  $26 \pm 2.9 \mu\text{eV}/\text{T}^2$  for sample A, B and C, respectively. This trend is consistent with greater diamagnetic shifts for wider wires. PL peak energy can be ambiguous, however, due to the presence of competing processes, such as localised states which can provide alternative radiative recombination paths. We do indeed find that the slope of the PL transition is significantly greater than that of the corresponding PLE for the same transition. Our PLE data, therefore, give a much more reliable measure of the diamagnetic shift of the one-dimensional exciton than PL [11].

By fitting the experimentally determined dia-

magnetic shifts from the PLE data of sample A using first-order perturbation theory [11,12], we can derive reduced exciton masses ( $\mu$ ) for the lowest 1D subband in each sample. From the fitted value of  $\mu$ , we have calculated an averaged Bohr radius of 7.8 nm for sample A. We have also determined the anisotropic diamagnetic shifts for several higher subbands. These shifts increase with increasing energy of the subband in accordance with the associated increase in wavefunction extent and corresponding decrease in binding energy. However, the application of the bulk exciton model in order to relate the confinement-induced contraction of the exciton radius to an anisotropic effective mass is not appropriate for excitons associated with higher subbands of the quantum wire. We will include an appropriate model for the calculation of binding energies in a future publication.

Using the less accurate measurements of the diamagnetic shifts of the PL gives consistently smaller values (67–70%) for the reduced exciton masses and correspondingly larger values for the Bohr radii.

Since upper bounds on the diamagnetic coefficients were employed, the derived reduced masses are lower bounds –  $\mu = 0.085m_0$  for the lowest subband in sample A ( $m_0$  is the free electron mass). This lower bound is significantly larger than the bulk value of  $0.058m_0$  and also greater than the values obtained by similar measurements in quantum wells [13–16].

Similar work on etched quantum wires [17] which claimed a 15% enhancement in the excitonic mass was analysed using an isotropic reduced mass which was based on experimental data taken in only one magnetic field orientation ( $B_z$ ), an approach found here and elsewhere [11] to be inadequate.

In summary, we have derived the most accurate values, to date, for the anisotropic reduced masses in QWRs, from the diamagnetic shifts of the ground state of QWRs of various widths. The diamagnetic shift was found to depend on the orientation of the wires with respect to the magnetic field, with the shift being least when the wires were oriented parallel to the field. The shift was also found to increase, as expected, with the

width of the wire and with increasing energy of the subband transition.

We wish to thank N. Pulsford, G.P. Srivastava, M. Boero, M. Lawless and C.D.H. Williams for helpful discussions. One of us (A.S.P.) is grateful for financial support from SERC, UK.

## 1. References

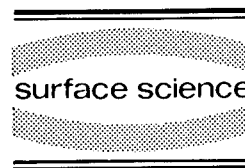
- [1] K. Kash, *J. Lumin.* 46 (1990) 69.
- [2] R. Nötzel, N.N. Ledentsov, L. Däweritz, M. Hohenstein and K. Ploog, *Phys. Rev. Lett.* 67 (1991) 3812.
- [3] K. Brunner, U. Bockelmann, G. Abstreiter, M. Walther, G. Böhm, G. Tränkle and G. Weimann, *Phys. Rev. Lett.* 69 (1992) 3216.
- [4] E. Kapon, D.M. Hwang and R. Bhat, *Phys. Rev. Lett.* 63 (1989) 430.
- [5] E. Kapon, S. Simhony, R. Bhat and D.M. Hwang, *Appl. Phys. Lett.* 55 (1989) 2715.
- [6] E. Kapon, D.M. Hwang, M. Walther, R. Bhat and N.G. Stoffel, *Surf. Sci.* 267 (1992) 593.
- [7] S. Simhony, E. Kapon, E. Colas, D.M. Hwang, N.G. Stoffel and P. Worland, *Appl. Phys. Lett.* 59 (1991) 2225.
- [8] R. Bhat, E. Kapon, D.M. Hwang, M.A. Koza and C.P. Yun, *J. Cryst. Growth* 93 (1988) 850.
- [9] E. Kapon, M. Walther, J. Christen, M. Grundmann, E. Colas and D. Bimberg, in: *Low-Dimensional Electronic Systems*, Vol. 111 of Springer Series in Solid State Sciences, Eds. G. Bauer, F. Kuchar and H. Heinrich (Springer, Berlin, 1992) p. 300.
- [10] E. Kapon, K. Kash, E.M. Clausen, Jr., D.M. Hwang and E. Colas, *Appl. Phys. Lett.* 60 (1992) 477.
- [11] Y. Nagamune, Y. Arakawa, S. Tsukamoto, N. Nishioka, S. Sasaki and N. Miura, *Phys. Rev. Lett.* 69 (1992) 2963.
- [12] S. Taguchi, T. Goto, M. Takeda and G. Kido, *J. Phys. Soc. Jpn.* 57 (1988) 3256.
- [13] N. Miura, Y. Isawa, S. Tarucha and H. Okamoto, *Proc. 17th Int. Conf. Physics of Semiconductors* (Springer, New York, 1984) p. 359.
- [14] W. Ossau, B. Jäkel, E. Bangert, G. Landwehr and G. Weimann, *Surf. Sci.* 174 (1986) 188.
- [15] G. Duggan, *Phys. Rev. B* 37 (1988) 2759.
- [16] A.S. Plaut, J. Singleton, R.J. Nicholas, R.T. Harley, S.R. Andrews and C.T.B. Foxon, *Phys. Rev. B* 38 (1988) 1323.
- [17] M. Kohl, D. Heitmann, P. Grambow and K. Ploog, *Phys. Rev. Lett.* 63 (1989) 2124.





ELSEVIER

Surface Science 305 (1994) 580–584



## Fermi-edge singularities in InGaAs and GaAs quantum wires

M. Fritze <sup>a</sup>, A.V. Nurmikko <sup>\*,a</sup>, P. Hawrylak <sup>b</sup>

<sup>a</sup> Division of Engineering and Department of Physics, Brown University, Providence, RI 02912, USA

<sup>b</sup> National Research Council, Ottawa, Ontario K1A 0R6, Canada

(Received 30 May 1993; accepted for publication 11 August 1993)

### Abstract

Strong Fermi-edge singularities (FES) were observed in the magnetoluminescence spectra of InGaAs quantum wires of electronic widths of  $L_{\text{ww}} \approx 500$  Å. These quasi-1-dimensional (1D) many-electron/one-hole correlation effects cause a large shift in spectral weight from the band-edge to the conduction Fermi energy, when compared with unpatterned (2D) structures. While the FES effects in the InGaAs quantum wires are associated with spatially direct transitions, we have also observed related effects in GaAs, where a Schottky gate bias is needed to induce the effect due to the dominantly spatially indirect nature of the transitions.

Among the several interband spectroscopic studies of doped quantum well wires (QWWs) there has been only limited experimental work on many electron–hole correlations, exemplified by the Fermi-edge singularity (FES) [1–3] which has been studied in a number of quasi-2D and 3D electron systems experimentally and theoretically. Here we address the issue of Fermi-edge singularities in n-type doped QWWs in a regime of electron concentration which is sufficiently high ( $E_F \approx 20$  meV), so that the emission from electrons at the top of the Fermi sea can be clearly distinguished from those at the bottom of the conduction band potential well.

The QWWs were fabricated from n-type asymmetrically doped InGaAs and GaAs single quantum well (SQW) samples of well thicknesses  $L_w = 150$  Å, containing relatively high electron con-

centrations ( $n_s \approx 1 \times 10^{12} \text{ cm}^{-2}$ ), which were patterned by laser holographic lithography and selective (but weak) shallow chemical etching. The advantage of a higher initial concentration is also a more robust electronic and optical system with respect to QWW processing. Typical geometrical wire widths of 1000–2000 Å were produced, with typical electron densities of  $n_{1D} \approx 10^6 \text{ cm}^{-1}$  and the carriers residing in approximately  $L_{\text{QWW}} \approx 500$  Å wide effective lateral potential of  $V_{\text{QWW}} \approx 10$ –20 meV modulation depth.

Fig. 1a shows a reference photoluminescence (PL) spectrum obtained from the unpatterned portion of an InGaAs SQW sample at  $T = 1.8$  K. The emission is dominated by electrons at the bottom of the  $N = 1$  conduction subband, recombining with holes in the  $N = 1$  valence subband. The electron density is obtained directly from the width of the PL spectrum ( $n_s = 9 \times 10^{11} \text{ cm}^{-2}$ ), in very good agreement with transport (Hall) measurements. Fig. 1b shows PL spectra for the

\* Corresponding author.

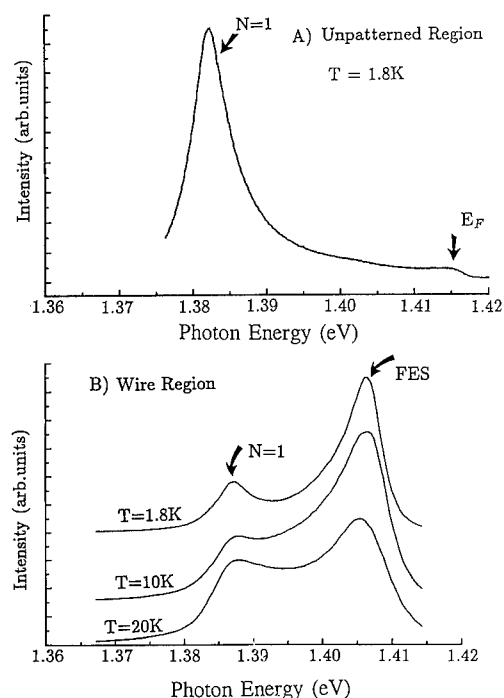


Fig. 1. (a) PL spectrum of unpatterned InGaAs single quantum well at  $T = 1.8$  K. Note the  $N = 1$  transition as well as the cutoff at  $E_F$ . (b) Spectrum from an InGaAs quantum well wire sample as a function of temperature. Note the strong shift of spectral weight to  $E_F$  compared with the unpatterned case.

very same sample, but now obtained in the QWW region. The lineshape of the spectrum now shows a strong enhancement at higher energies (at  $E_F$ ) compared to the unpatterned case. There is no indication of the QWW subband structure in the emission spectrum, presumably due to broadening by scattering. The intensity of the  $N = 1$  emission remained nearly comparable to the unpatterned case, suggesting that the sample fabrication did not have major adverse effects. From the temperature dependence of the 'FES' peak we infer a characteristic energy of 30 K. This general behaviour is characteristic of Fermi-edge singularities observed by PL in quasi-2D and 3D systems due to valence hole localization, although now with a larger binding energy [4–6]. We attribute this enhancement to the quantization of the electron motion by the wire potential. Also, we argue below that the emissions in Fig. 1b

correspond to spatially direct transitions in the QWW as indicated in Fig. 3.

The enhancement at  $E_F$  is not contradicted by the lack of observing the QWW subband structure in the emission spectrum. This follows as the experiment samples over many wires (and inhomogeneities within each wire). Because all the wires have a common chemical potential  $\mu$ , the averaging over the distribution of wires with fluctuating width masks out the subband structure in the noninteracting portion of the emission spectrum, but leaves the spectral structure close to the common chemical potential (FES) unchanged.

Fig. 2a shows the PL spectrum of the QWW portion for our sample in a perpendicular magnetic field,  $B_z = 3$  T at  $T = 1.8$  K. Beyond a low-field regime, we observed generally clear

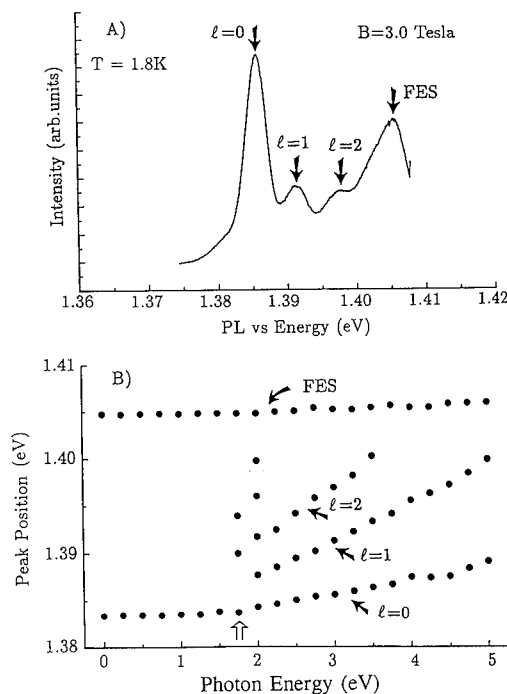


Fig. 2. (a) Typical PL spectrum of the InGaAs QWW sample in a perpendicular magnetic field at  $T = 1.8$  K. Except for the FES region, the electron Fermi sea is Landau quantized. (b) Fan plot of the transition energies versus field  $B$ . Note the diamagnetic shift of the FES peak. The open arrow marks the transition from QWW confined regime to Landau behavior for the lowest Landau level.

Landau quantization across the Fermi sea (indicated here by the level indices  $l = 0, 1, 2$ ), except for the electrons at the Fermi edge where the FES feature remained unaffected but for a diamagnetic-type shift. This behavior supports the notion of the FES peak being of excitonic character. The field dependence of some of the relevant emission energies are summarized in the fan plot of Fig. 2b. For low magnetic fields, Landau quantization is inhibited by the lateral width of the QWW potential, but becomes allowed when the cyclotron diameter becomes smaller than the electronic wire confinement width. A clear transition from confined to Landau level behavior occurs for the lowest  $N = 1$  Landau level at  $B = 1.75$  T for this QWW sample (marked by an open arrow). Note the change in 'slope' for  $l = 0$  at  $B = 1.75$  T according to  $E_n = E_0 + (n + 1/2)[(h\omega_c)^2 + (h\omega_0)^2]$ , where  $h\omega_0$  is the (approximately) parabolic wire confinement potential. For unpatterned portion of the samples, Landau-level quantization was readily observed at low magnetic fields  $B < 1$  T. Our data yield a typical electronic confinement width of  $L_{\text{QWW}} = 550$  Å. Using a simple sinusoidal potential model, we obtain 1D subband spacings of  $\Delta E \approx 1.3$  meV for the electrostatic potential depth of  $V_{\text{QWW}} \approx 20$  meV in this sample.

Important differences were found when comparing the PL spectra of the InGaAs QWWs with those obtained in comparably prepared GaAs structures. A new spectral feature, redshifted from the band-edge by about 10 meV, was very clearly introduced by the presence of the QWW. This emission, not encountered in any of the InGaAs QWW samples, is due to the *spatially indirect* electron–hole recombination (Fig. 3), analogous to luminescence in nipi-structures. The peak shifts continuously towards the  $N = 1$  direct transition with increasing laser excitation power, hence reflecting the screening out of the relatively shallow 1D modulation potential. The difference between the emission energy measured at very low laser powers ( $\sim 1$  μW) and the  $N = 1$  direct band-edge transition yields the 1D modulation depth in a typical sample of  $V_{\text{QWW}} \approx 10$  meV, i.e. a shallower 1D modulation depth than the InGaAs QWWs above, where  $V_{\text{QWW}} \approx 20$

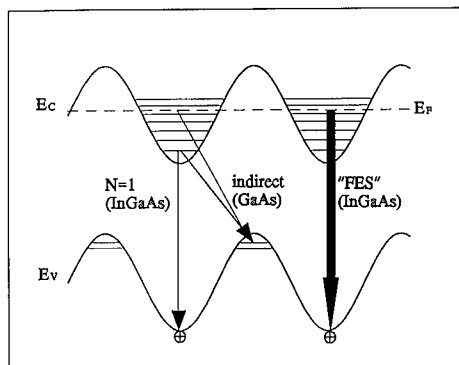


Fig. 3. Real-space schematic energy diagram depicting the QWW potential profile and the key interband transitions discussed in the text. The transition labelled 'FES' indicates the process which gives rise to the edge singularity effect in the InGaAs wires.

meV. The spatially indirect nature of the recombination also reduces the electron–hole correlation at the Fermi energy and consequently no FES feature was observed at higher energies. In order to tune the 1D potential modulation depth and the electron–hole overlap, Schottky gates were evaporated on this sample. For a narrow range of gate voltages of  $V_g \approx (-5 \pm 0.5)$  V, a distinct PL peak appeared, corresponding to electron recombination at the Fermi level and displaying a temperature dependence similar to the FES feature observed in the InGaAs QWW's. In spite of the enhancement at the high energy edge, however, the overall emission intensity near  $E_F$  remained much lower than in the case of InGaAs QWWs.

In interpreting the presence of the strong FES-like features in our InGaAs QWW structures, and the need for a Schottky-gate to produce such (weaker) effects in the GaAs case, we consider in Fig. 3 schematically the conduction and valence band potential for the quantum wires together with some of the key optical transitions, both spatially direct and indirect. In the electrostatically defined QWW structures, both one- and many-electron effects can lead to PL enhancements near  $E_F$ . For a spatially *indirect* transition, the electron–hole overlap increases with increasing 1D subband index. From simple calculations

for a sinusoidal potential, this one-electron matrix element can in fact increase by several orders of magnitude. Beyond the one-electron picture, the increased overlap effect is also most likely responsible for the enhancements in the electron–hole interaction observed at  $E_F$  in the GaAs QWWs. Furthermore, the presence of the spatially indirect transition at the band edges, and the weak emissions at  $E_F$  are consistent with the presence of free holes which thermalize rapidly to the valence band minimum, following photoexcitation. Ongoing experiments show that the luminescence decay time of this feature is long (tens of ns), shortening with increasing intensity of excitation, supporting our interpretation.

On the other hand, the much larger optical intensities at  $E_F$  and the distinct presence of an edge singularity in the (ungated) InGaAs QWWs can only be reconciled with a *spatially direct* transition, shown schematically in Fig. 3. First, there is no evidence for the spectrally redshifted band-edge transitions. Also given the larger wire modulation depth ( $V_{\text{QWW}} \approx 20$  meV), calculations now show a much reduced optical cross section for these transitions. We argue that spatially direct transitions are dominant in the InGaAs QWWs due to partial hole localization by alloy potential fluctuations which inhibit and/or retard the thermalization process of the holes to the (indirect) valence band maximum. In this fashion, a sizable hole population remains available in steady state for the spatially direct transitions (which possess large optical cross-sections). For a normally disordered alloy, we calculate that the mean localization energy for our In composition ( $x = 0.15$ ) is approximately 15 meV for a heavy hole, i.e. a value comparable with both  $V_{\text{QWW}}$  and  $E_F$ . Hence, the strong FES features observed in our structures are made possible by a combination of (at least partial) hole localization and closely spaced conduction subbands which enhance the electron–hole Coulomb scattering near  $E_F$ . In part then, our results agree with the recent calculations (for spatially direct case) that strong singularities in QWWs can only be observed with hole localization, although in our case we have departed from the strict 1D limit that the theory has addressed.

The problem of Fermi-edge singularities in doped quantum well systems of 2D and 3D dimensionality has been extensively studied [7]. Strong correlations between the electrons at  $k_F$  and the photoholes at  $k = 0$  are the basis for such many-body exciton complexes which are frustrated by the requirement of momentum conservation. Evidence for singularities was originally observed in InGaAs quantum wells in which the holes were localized by some form of alloy disorder [4]. They were subsequently observed in GaAs QWs with free holes in two circumstances: (i) in case of small values of the Fermi energy ( $E_F \sim$  a few meV) [8], and (ii) in cases where a higher, empty conduction subband was in near proximity to  $E_F$  (within a few meV) to provide a virtual scattering channel, permitting electrons with  $k \approx k_F$  to couple to holes at  $k = 0$  [6].

Theoretically, many-electron/one-hole correlations are expected to be stronger in the 1D case due to the lack of hole recoil such a confined system (only excitations of  $k = 0$  and  $k = 2k_F$  are allowed). Roughly, the recoil energy is given by  $E_r \sim (m_e^*/m_h^*)E_F$  and should remain small in comparison with the binding energy of the FES. On the other hand, the importance of hole localization in forming a FES in QWW systems is the subject of some discussion [9,10]. Generally, the calculations only consider the 1D quantum limit (1 occupied subband), in contrast to our experimental circumstances. Hence, in addition to the hole localization and electron confinement, the subband interference effect could be expected to be of importance here. In that sense, our observations in the QWW structures may be compared to the FES's observed recently in wide parabolic wells (quasi-3D systems) [11], since we are dealing with a number of occupied closely spaced subband levels ( $\Delta E \approx 1$ –2 meV). These closely spaced subbands allow intersubband scattering to couple electrons at  $k_F$  to holes at  $k = 0$ , thus enhancing the formation of the FES.

## 1. Acknowledgement

This work was supported by the National Science Foundation Grants DMR-9112329 and DMR-9121747.

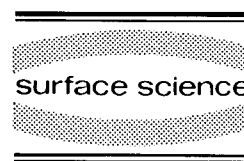
## 2. References

- [1] J.M. Calleja, A.R. Goni, B.S. Dennis, J.S. Weiner, A. Pinczuk, S. Schmitt-Rink, L.N. Pfeiffer, K. West, J.F. Muller and A.E. Ruckenstein, *Solid State Commun.* 79 (1991) 911.
- [2] J.M. Calleja, J.S. Weiner, A.R. Goni and A. Pinczuk, in: *Optics of Semiconductor Nanostructures*, Eds. E. Gobel, F. Henneberger and S. Schmitt-Rink (Akademie-Verlag, Berlin, 1993)
- [3] F. Hirler, R. Kuchler, R. Strenz, G. Abstreiter, G. Bohm, J. Smoliner, G. Trankle and G. Weiman, *Surf. Sci.* 263 (1992) 563.
- [4] M.S. Skolnick, J.M. Rorison, K.J. Nash, D.J. Mowbray, P.R. Tapster, S.J. Bass and A.D. Pitt, *Phys. Rev. Lett.* 58 (1987) 2130.
- [5] G. Livescu, D.A.B. Miller, D.S. Chemla, M. Ramaswamy, T.Y. Chang, N. Sauer, A.C. Gossard and J.H. English, *IEEE J. Quantum Electron.* QE-24 (1988) 1677.
- [6] W. Chen, M. Fritze, W. Walecki, A.V. Nurmikko, D. Ackley, J.M. Hong and L.L. Chang, *Phys. Rev. B* 45 (1992) 8464;
- W. Chen, M. Fritze, A.V. Nurmikko, J.M. Hong and L.L. Chang, *Phys. Rev. B* 43 (1991) 10388;
- W. Chen, M. Fritze, A.V. Nurmikko, D. Ackley, C. Colvard and H. Lee, *Phys. Rev. Lett.* 64 (1990) 2434.
- [7] See, e.g. J.F. Mueller, A. Ruckenstein and S. Schmitt-Rink, *Mod. Phys. Lett.* 5 (1991) 135;
- J.F. Mueller, *Phys. Rev. B* 42 (1990) 11189;
- P. Hawrylak, *Phys. Rev. B* 44 (1991) 6262, 11236, 3821.
- [8] A.J. Turberfield, R.A. Ford, I.N. Harris, J.F. Ryan, C.T. Foxon and J.J. Harris, *Phys. Rev. B* 47 (1993) 4794.
- [9] P. Hawrylak, *Solid State Commun.* 81 (1992) 525.
- [10] T. Ogawa, A. Furusaki and N. Nagaosa, *Phys. Rev. Lett.* 68 (1992) 3638;
- F.J. Rodriguez and C. Tejedor, *Phys. Rev. B* 47 (1993) 1506.
- [11] M. Fritze, W. Chen, A.V. Nurmikko, J. Jo, M. Santos and M. Shayegan, *Phys. Rev. B* 45 (1992) 408; *Phys. Rev. B*, in press.



ELSEVIER

Surface Science 305 (1994) 585–590



# Photoluminescence intensity and multiple phonon Raman scattering in quantum dots: evidence of the bottleneck effect

P.D. Wang <sup>\*</sup>, C.M. Sotomayor Torres, H. McLelland, S. Thoms, M. Holland, C.R. Stanley

*Nanoelectronics Research Centre, Department of Electronics and Electrical Engineering, University of Glasgow, Glasgow G12, 8QQ, UK*

(Received 30 May 1993; accepted for publication 28 June 1993)

## Abstract

We report a systematic study of photoluminescence efficiency in dry etched quantum well dots. Luminescence degradation is observed on decreasing the quantum dot lateral size. Furthermore, luminescence quenching is more pronounced in quantum dots with a thicker quantum well than those with a thinner one. This effect is attributed to the reduced carrier relaxation in 0D system. Resonant Raman scattering and “hot” exciton luminescence have also been observed in dry etched GaAs/AlGaAs quantum dots in which quantum confinement effects are found with decreasing dot sizes. Up to 4th-order multiphonon processes have been observed through photoluminescence and photoluminescence excitation in quantum dots. These results are direct evidence of the bottleneck effect. Lateral patterning of quantum wells strongly localises excitons in three-dimensional quantum confinement regime (0D system). The observation of resonant Raman scattering and hot exciton luminescence up to high temperature demonstrates the high stability of localised excitons.

## 1. Introduction

Recent years have seen increased research activities in the optical properties of one- and zero-dimensional (1D and 0D) semiconductor wires and dots. The optical band-to-band oscillator strength and non-linear properties increase with the decreasing dimensionality due to the increased concentration of density of states at the band edge [1]. However, most useful optical devices such as lasers, rely on a fast carrier relaxation process for efficient radiative recombina-

tion. Several theoretical papers have suggested slower relaxation processes in quantum dots: the so-called bottleneck effect [2,3]. It is mainly due to the discrete energy levels in the quantum dots which drastically reduce the electron (exciton)–phonon interaction. In a quantum dot, first-order electron–LO phonon Fröhlich coupling is forbidden, and carrier relaxation has to rely on the inefficient electron–acoustic phonon coupling. The resulting strongly reduced relaxation of hot carriers is expected to limit the luminescence efficiency in quantum dots in  $< 200$  nm lateral sizes. Experimental evidence has partly supported the theoretical predictions [4,5]: it has been shown that for large dot diameter ( $L$ ), specially  $L > 200$

<sup>\*</sup> Corresponding author.

nm in GaAs/GaAlAs, the emission yield is better modelled invoking predominantly surface recombination velocity effects, whereas for  $L < 200$  nm the data fit better the limits set by the bottleneck effect [4]. Fabrication techniques can induce defects which are also responsible for luminescence degradation. In this paper, we report a systematic study of photoluminescence efficiency of etched quantum dots containing quantum wells of different thickness. We find that the luminescence intensity dependence on dot diameter is stronger for dots with thicker quantum wells than for dots with thinner quantum wells. Multiphonon processes are invoked to interpret resonant Raman scattering (RRS) from dots. Both results lend support to the bottleneck effect and indicate the importance of multiphonon processes in the relaxation of hot carriers in nanostructures.

## 2. Photoluminescence efficiency in dry etched quantum well dots

The quantum dots were fabricated using electron beam lithography and dry etch techniques. Single quantum wells with different thicknesses ( $L_z$ ) were fabricated. To reduce the lateral exciton localisation due to interface roughness, three monolayers of AlAs were grown on both quantum well interfaces. All wafers were fabricated and then etched in the same batch to minimise any external uncertainties involved in the fabrication processes. The details of fabrication process have been reported elsewhere [4]. Fig. 1 shows the normalised luminescence intensity as a function of dot sizes for different quantum well thickness. It is clearly seen that the luminescence intensity decreases with decreasing dot lateral sizes. Moreover, the PL intensity of dots containing thinner quantum wells ( $L_z$ ) is less quenched than those with larger  $L_z$ . This can be understood qualitatively from electron–LA phonon scattering processes in a 0D quantum dot. The strong quenching of the phonon scattering in 0D systems occurs when the phonon wave vector  $q$  exceeds  $\sim 2\pi/L_v$ . Here  $L_v$  indicates the smallest of the three quantum dot dimensions.  $L_z$  is

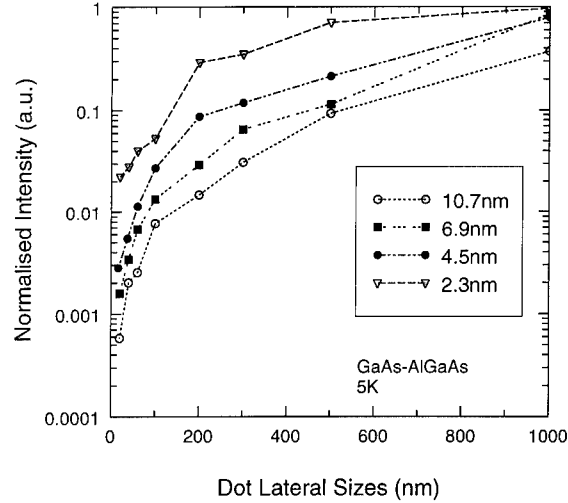


Fig. 1. Photoluminescence intensity from quantum dots with different quantum well thickness as a function of dot lateral size. Open circles, full squares, full circles and inverted open triangles denote  $L_z = 10.7$ , 6.9, 4.5 and 2.3 nm. The intensity is normalised to that of the control areas for each dot array.

usually the smallest dimension. This indicates that the coupling to a LA phonon with a given energy can be enhanced by decreasing  $L_z$ . For an infinite quantum well potential, it can be shown that the lateral threshold size corresponding to the onset of reduced relaxation is proportional to the  $L_z^{0.5}$ . For even smaller  $L_z$  of real quantum wells with finite potential barrier, the effective confinement becomes weaker due to the leakage of the wave function into the barrier leading to higher threshold again.

Quantitatively, we calculate the luminescence efficiency of a quantum dot with a square flat shape by studying the transition rates of LA phonon scattering of two quantum dot levels. The transition rates between two levels can be taken as

$$\omega_{if} = \frac{D^2}{2\rho\hbar c_s^2} \left[ n_B + \begin{Bmatrix} 0 \\ 1 \end{Bmatrix} \right] \frac{q_{if} M_z(q_{if})}{L_x L_y} \times (2 + \delta_{ll'} + \delta_{mm'}), \quad (1)$$

where

$$q_{if} = \frac{E_{if}}{\hbar c_s} = \frac{\pi^2 \hbar}{2m^* c_s} \left( \frac{l'^2 - l^2}{L_x^2} + \frac{m'^2 - m^2}{L_y^2} \right). \quad (2)$$

Here we denote  $(l, m, n)$  as the standard quantum numbers of energy levels in this quantum dot system.  $l$ ,  $m$  and  $n$  correspond to the quantization in the  $x$ ,  $y$ , and  $z$  directions, respectively.  $D = 8.6$  eV is the deformation potential,  $\rho = 5300$  kg/m<sup>3</sup> is the volume density and  $c_s = 3700$  m/s is the phonon sound velocity in GaAs.  $M_z(q_{if})$  is the  $z$ -component of the matrix element.

Again, it can be seen that the above theoretical consideration is based on the comparison between the phonon wave vector  $q = \Delta E / \hbar c_s$  and the extent of the Fourier transform of the wave functions, namely,  $\pi/L_x$ ,  $\pi/L_y$ ,  $\pi/L_z$ . Quasimomentum conservation of phonon scattering is required in order that the matrix element is non-zero. For lateral confinement greater than the characteristic “phonon length”  $L_1 = \hbar/2m^*c_s$  ( $L_1 = 1.4$   $\mu\text{m}$  for GaAs), energy conservation requires  $q > \pi/L_x$ ,  $\pi/L_y$ . This means that only phonons with a large  $q_z$  can interact with the carriers. However, with further confinement, i.e.,  $\Delta E > \hbar c_s \pi/L_z = 0.6$  meV,  $M_z(q)$  will also vanish since  $M_z(q) \propto q^{-6}$ , or  $\omega_{if} \propto L_x^8$ , a rather steep dependence when  $L_x$  is reduced for additional lateral confinement. This sets in the quenching of the luminescence. In GaAs, one expects the quenching to occur at  $(L_1 L_z)^{1/2} = 120$  nm in the lateral dimension for a 10 nm quantum well. In practice, the threshold sizes were taken to be those at which the luminescence efficiency dropped by two orders of magnitude with respect to that of a control mesa. Fig. 2 shows a comparison of experimental data with the theoretical calculations. The dashed line represents a theoretical calculation assuming a constant radiative and non-radiative lifetime  $\tau$  for different quantum well thickness. For larger  $L_z$  value, it shows  $L_z^{0.5}$  dependence as predicated by theory. For  $L_z < 2$  nm, the threshold starts to increase again reflecting the weaker effective confinement due to the wave function leakage in the growth direction. However, the experimental results exhibit a stronger  $L_z$  dependence, i.e.,  $\propto L_z^{1.2}$ . In the theoretical model discussed above, we assume a constant lifetime for different quantum well width  $L_z$ . This assumption is incorrect. It is well known that the exciton localisation is drastically different for quantum well thickness ranging from 2 to

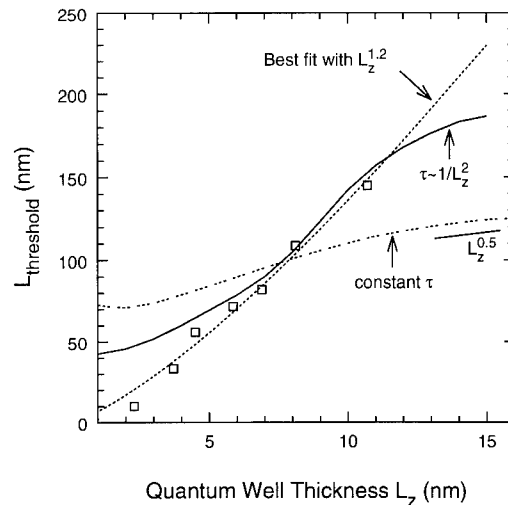


Fig. 2. The luminescence threshold as a function of well thickness  $L_z$ . The dotted line is a least squares fit to the experimental data. The dashed line is the theoretical calculation assuming a constant carrier lifetime. The solid line is the same calculation, assuming a carrier lifetime  $\tau \propto 1/L_z^2$ , as explained in the text.

10 nm [6]. The exciton localisation will in turn affect its diffusion. This arises from the exciton diffusion coefficient  $D \approx L_z^2$  [6]. The most important non-radiative process in dry etched dots is due to exciton migration to the surface [4]. The interface exciton localisation changes the exciton diffusion in such a way that it influences the quantum dot carrier lifetime. It is based on these arguments that the assumption of the exciton radiative lifetime  $\tau \propto 1/L_z^2$  becomes reasonable. The solid line in Fig. 2 is based on the same model, but assuming  $\tau \propto 1/L_z^2$ . It gives a reasonable fit to the experimental data. This systematic experimental study of luminescence yield indicates the stronger quenching of luminescence in quantum dots with a thicker quantum well compared to those with a thinner one, in agreement with the theoretical predictions based on the bottleneck effect.

### 3. Multiple phonon relaxation in quantum dots: resonant Raman scattering and hot exciton luminescence (HEL)

The bottleneck effect occurs because the energy quantisation forbids the first-order Fröhlich



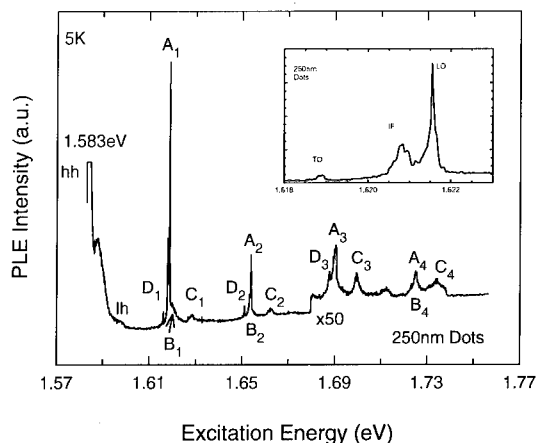


Fig. 3. The PLE spectra of a 250 nm dot array. The details of labelling are discussed in the text. The inset is a blow-up of the first-order Raman line  $A_1$  of 250 nm dots. It can be seen clearly that some fine structure is superimposed on the interface (IF) mode. This demonstrates the mixing of optical phonons.

interactions which offer a faster scattering rate ( $10^{12} \text{ s}^{-1}$  for LO phonon scattering as compared to  $10^9 \text{ s}^{-1}$  for LA scattering). Inoshita and Sakaki [7] consider the multiphonon processes in the quantum dots. They emphasised the role of two-phonon processes based on the second-order perturbation method. For an energy separation of  $\Delta E > 0.5 \text{ meV}$ , 2LA contribution is significant with a relaxation time of the order of 10 ns. For  $|\Delta E - \hbar\omega_{\text{LO}}| < 3 \text{ meV}$ , the relaxation time can be smaller than 1 ns incorporating  $\text{LO} \pm \text{LA}$  processes. In other words, the multiphonon process ( $n\text{LO} \pm \text{LA}$ ) helps to create a window of rapid (sub-nanosecond) relaxation around the longitudinal optical phonon energy.

Fig. 3 shows the PLE spectra of a 250 nm quantum dot array. The quantum dots are fabricated through the same electron beam lithography, but through a deep dry etch process. The side wall damage significantly reduces the effective sizes of the dots. Wang et al. [8] have performed Raman scattering to analyse the surface dead layer thickness induced by the dry etch processes. It was shown that the top surface damage depth induced by RIE saturated at approximately  $\sim 35 \pm 5 \text{ nm}$ . The side wall damage, how-

ever, arises from a different mechanism and can be three to four times as high as the surface one [8]. On the basis of these considerations, the “active” dot size in our 250 nm dots is expected to be around  $2R_a = 30 \pm 10 \text{ nm}$ . Indeed, the fact that our 200 nm dot array of the same process did not show any detectable photoluminescence signal reveals the existence of a dead layer in these samples. Heitmann et al. [9] also reported a similar dry etch damage depth in their quantum wires fabricated under similar conditions.

We modelled the 0D exciton states in a cylindrical quantum disk structure. Without Coulomb interaction, the wave function of the electron-hole pair can be written as

$$\psi_{nml} \propto \cos(k_e z_e) \cos(k_h z_h) J_l(r_e \rho_e) \times J_l(r_h \rho_h) e^{il\theta_e} e^{il\theta_h}, \quad (3)$$

where  $J$  is the Bessel function describing the lateral wave function of carriers,  $k$  is the  $z$  direction quantised wave vector,  $r$  is the lateral wave vector, and  $l$  is an integer due to rotational invariance of the wave function. Subscripts  $e$  and  $h$  refer to electrons and holes. Based on the complete separation of vertical and lateral wave functions, the system eigenenergy is given by:

$$E_0 = E_n + E_{ml} = E_n + \frac{\hbar^2 r_{ml}^2}{2\mu} + \frac{\hbar^2 K_{\text{ex}}^2}{2M}. \quad (4)$$

Here  $\mu$  is the reduced mass and  $M$  the centre mass of electron-hole pairs. The system can be described more accurately by taking into account Coulomb interactions. The 0D exciton eigenenergy then is  $E_{\text{ex}} = E_0 - E_B$ , where  $E_B$  is the binding energy of 0D excitons. Assuming a 40 nm diameter dot, the first three lateral subband energies of  $n = 1$  ground state are calculated to be  $E_{m0} = 9.25, 48.75$  and  $119.8 \text{ meV}$ . The calculated ground state energy using the above model is in a good agreement with experiments which shows a 9.04 meV blue shift as compared with the starting material. The light hole transition observed in Fig. 3 for 250 nm dots is very weak. This could be due to the unfavourable selection rules for the light holes in 1D and 0D system, or it could be due to the side wall non-radiative recombination.

The striking sharp features in the PLE spectra in Fig. 3 are the four series of oscillatory structures labelled  $A_n$ ,  $B_n$ ,  $C_n$  and  $D_n$ . When the detector is scanned across the whole heavy hole (hh) exciton resonance region, all of the oscillatory peaks shift simultaneously such that their corresponding energy spacing is maintained at 36.5 meV. Series  $A_n$  and  $B_n$  extrapolate directly to the detection energy, while  $C_n$  extrapolates 9.8 meV higher, roughly at the light hole (lh) peak position of the spectrum of 250 nm dot arrays. This is discussed below. Series  $D_n$  has a 36.5 meV period with  $D_1$  33.4 meV above the detector energy. The inset of Fig. 3 shows the  $A_1$  peak which comprises a sharp LO phonon mode and the interface phonon mode.

From the above discussion, it is clear that the  $A_n$  series corresponds to the LO phonons. The  $D_n$  series is related to TO phonons. These two series arise from either RRS or HEL processes. There has been long debate over whether these lines belong to HEL or RRS. RRS is a coherent process within the exciton dephasing time involving virtual intermediate states, whereas HEL is an incoherent process involving the indirect creation of excitons with large  $K$  vector and subsequent relaxation through LO-phonon emission. In other words, the main difference between the RRS and HEL is that in the latter case, the relaxation is scattered through real exciton states in accordance with the energy and momentum (wave vector) conservation laws, whereas in the former case the excitons take part only as virtual intermediate states. The separate electron and hole relaxation processes are ruled out here since they will give an oscillation period corresponding to  $T = \hbar\omega_{\text{LO}}(1 + m_e/m_h)$ , i.e., 42–44 meV in GaAs system. Series  $B_n$  and  $C_n$  are assigned to hot exciton luminescence or the multiphonon cascade of excitons with the thermalised steady state distributions. The other evidence for this quasi-equilibrium energy distribution can be seen more clearly by examining the  $B_1$  emission:  $B_1$  has a high energy tail. This line shape represents the Maxwellian type of acoustic phonon assisted thermalisation since the first-order LO phonon coupling is forbidden. The peak position of the  $B_n$  series can be written as  $E = E_{\text{ex}} + \hbar\omega_{\text{LO}} +$

$\hbar^2q^2/2M$  due to this additional acoustic phonon thermalisation. Here,  $qa_B \approx 1$  since  $a_B$ , the exciton Bohr radius, is a measure of the range of the potential well which binds the exciton. The calculated peak position is about 0.65 meV above the strong phonon series, in quite good agreement with experiment.

As shown from energy calculations of Eq. (4), the separation of energy levels matches  $n\text{LO} \pm \text{LA}$  phonon scattering windows, e.g., multiphonon processes in 250 nm dots involve virtual state transitions ( $E_{30} - E_{20} \approx 2\text{LO} + \text{LA}$ ). They may be therefore more accurately described by RRS involving high-order scattering. We only calculate  $l = 0$  related states, there is a series of additional  $l$  related states to increase the multiphonon relaxation probabilities. Multiple phonon processes contribute to quantum dot luminescence when quantized levels in 0D dots are appropriately spaced to match the rapid carrier relaxation windows.

#### 4. Exciton confinement in quantum dots

Usually HEL has been observed in wide-gap II–VI semiconductors [10] among other systems. Recently, similar HEL or multiple phonon RRS has been observed in III–V low-dimensional semiconductor structures such as coupled quantum wells [11], multiple quantum wells [12] and corrugated superlattice [13]. In a 0D quantum dot system strong localisation of excitons is present due to the 3D confinement barrier. Such localisation of excitons is equivalent to the bottleneck effect which arises from the 3D quantum confinement. The strong localisation and high binding of excitons can also be demonstrated by their temperature dependence. The sharp multiphonon lines in 250 nm dots persist up to 30–35 K. In a 3D system, the sharp lines disappear after 8 K as demonstrated by Cohen and Sturge [14] in their  $\text{CdS}_x\text{Se}_{1-x}$  system. The acoustic-phonon-assisted hopping process diminishes after excitons can be thermalised above the mobility edge (delocalised state). In a 2D system, the multiphonon lines or RRS disappear above 15–20 K, demonstrating weaker binding of excitons. Apart from the tem-

perature dependence, the damping characteristics of the sharp phonon line observed in PLE provides an estimate of the localisation potential. For the 250 nm dots with effective radius of  $15 \pm 5$  nm, the localisation energy can be estimated to be  $> 100$  meV. Exciton localisation also manifests itself experimentally in the Stokes shift between the absorption- and emission-related transition. The Stokes shift ranges from 1.3 meV, through 3.01 meV to 4.43 meV in 500, 300 and 250 nm dots as compared to 0.5 meV in a control sample, demonstrating the increasing exciton localisation with reduction in dimensionality.

## 5. Conclusion

In conclusion, the poor luminescence of quantum dots is attributed to inefficient energy relaxation. The experimental studies on luminescence reported here add support to this interpretation. Multiphonon relaxation can help carriers to relax efficiently. Recently, Bockelmann and Egeler [15] consider the Coulomb scattering (Auger effect) in high density electron-hole plasma as an efficient carrier relaxation mechanism. A high plasma density of  $10^{12} \text{ cm}^{-2}$  is quite usual in laser operation. They show that the electron scattering rate can be comparable to the LO scattering ( $10^{12} \text{ s}^{-1}$ ). Therefore, whether the acoustic phonon related bottleneck effect limits the performance of quantum-dot-based optoelectronic devices remains to be seen. The multiphonon processes also point to the strong localisation of excitons due to the three-dimensional quantum confinement in the 0D system. The decrease in emission yield from quantum dots with decreasing quantum well thickness is the clear demonstration of the slower acoustic phonon scattering rate in 0D, in good agreement with theoretical predictions [16].

## 6. Acknowledgements

This work is supported by the Science and Engineering Research Council (Grant No. GR/H 44714). We are grateful to S.P. Beaumont for useful discussions and critical reading of the manuscript.

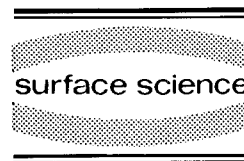
## 7. References

- [1] S. Schmitt-Rink, D.A.B. Miller and D.S. Chemla, *Phys. Rev. B* 35 (1987) 8113.
- [2] U. Bockelmann and G. Bastard, *Phys. Rev. B* 42 (1990) 8947.
- [3] H. Benisty, C.M. Sotomayor Torres and C. Weisbuch, *Phys. Rev. B* 44 (1991) 10945.
- [4] P.D. Wang, C.M. Sotomayor Torres, H. Benisty, C. Weisbuch and S.P. Beaumont, *Appl. Phys. Lett.* 61 (1992) 946; more details, see P.D. Wang et al., *SPIE*, 1676 (1992) 172.
- [5] E.M. Clausen, Jr., H.G. Graighead, J.P. Harbison, A. Scherer, L.M. Schiavone, B. Van der Gaag and L.T. Florez, *J. Vac. Sci. Technol. B* 7 (1989) 2011.
- [6] D. Oberhauser, K.H. Pantke, J.M. Hvam, G. Weimann and C. Klingshirn, *Phys. Rev. B* 47 (1993) 6827.
- [7] T. Inoshita and H. Sakaki, *Phys. Rev. B* 46 (1992) 7260.
- [8] P.D. Wang, M.A. Foad, C.M. Sotomayor Torres, S. Thoms, M. Watt, R. Cheung, C.D.W. Wilkinson and S.P. Beaumont, *J. Appl. Phys.* 71 (1992) 3754.
- [9] D. Heitmann, H. Lage, M. Kohl, R. Cingolani, P. Grambow and K. Ploog, *Int. Phys. Conf. Ser. No. 123* (1992) 109.
- [10] S. Permogorov, *Phys. Status Solidi (b)* 68 (1975) 9.
- [11] F. Clerot, B. Deveaud, A. Chomette, A. Regreny and B. Sermage, *Phys. Rev. B* 41 (1990) 5756.
- [12] N.N. Ledentsov, R. Nötzel, P.S. Kop'ev and K. Ploog, *Appl. Phys. A* 55 (1992) 533.
- [13] R. Nötzel, N.N. Ledentsov, L. Däweritz, K. Ploog and M. Hohenstein, *Phys. Rev. B* 45 (1992) 3507; also R. Nötzel, N.N. Ledentsov and K. Ploog, *Phys. Rev. B* 47 (1993) 1299.
- [14] E. Cohen and M.D. Sturge, *Phys. Rev. B* 25 (1982) 3828.
- [15] U. Bockelmann and T. Egeler, *Phys. Rev. B* 46 (1992) 15574.
- [16] U. Bockelmann, in: *Phonons in Nanostructures*, Eds. J.P. Leburton, J. Pascual and C.M. Sotomayor Torres (Kluwer, Dordrecht, 1993), p. 415.



ELSEVIER

Surface Science 305 (1994) 591–596



## Information on the confinement potential in GaAs/AlGaAs wires from magnetoluminescence experiments

F. Hirler <sup>\*</sup>, R. Strenz, R. K  chler, G. Abstreiter, G. B  hm, G. Weimann

*Walter Schottky Institut, TU-M  nchen, D-85748 Garching, Germany*

(Received 30 April 1993; accepted for publication 4 June 1993)

### Abstract

Shallow etched wires, dots and antidots have been prepared from remote-doped GaAs/AlGaAs quantum wells. The luminescence of electrons and holes separated into adjacent lateral regions was studied with a magnetic field applied in the growth direction. The spatially indirect luminescence was found to shift in energy and become direct at high magnetic fields. Details of the shape of the confinement potential were obtained by simulating the energy shift numerically.

In recent years a great effort has been undertaken to explore the basic properties of semiconductor nanostructures. In periodically modulated structures the application of magnetic fields is widely used, which results either in new phenomena such as edge magnetoplasmons [1] and resonances in magnetoresistance due to classically closed orbits [2], or yields insight into the properties of the lateral confinement. The interaction of the magnetic field with the confining electric field leads to a hybridization and a shift of the one-dimensional subband energies, which can be detected by, for example, magnetic depopulation [3], magnetoluminescence [4,5], magnetotunneling [6] and magnetophonon resonances [7]. These experiments give information on the strength of the lateral confinement potential, but a parabolic model is often assumed for its shape.

In this paper we study the magnetic field behaviour of plasma-like and excitonic spatially indirect photoluminescence (PL), as well as the spatially indirect luminescence of shallow etched wires, dots and antidots. We simulate the indirect PL spectra numerically and find that the energy shift with magnetic field is strongly dependent on the shape of the confining potential.

Remote-doped GaAs/AlGaAs single quantum well samples grown by molecular beam epitaxy were used for the preparation of shallow etched nanostructures. A typical layer sequence consisted of an 80   GaAs quantum well grown on a GaAs/Al<sub>0.4</sub>Ga<sub>0.6</sub>As superlattice, followed by a 200   undoped Al<sub>0.4</sub>Ga<sub>0.6</sub>As spacer layer, a 500   thick Si-doped Al<sub>0.4</sub>Ga<sub>0.6</sub>As layer ( $N_D = 2 \times 10^{18} \text{ cm}^{-3}$ ) and a 100   GaAs cap layer. The corresponding electron density and mobility of the 2DEG at 4.2 K under illumination were  $6.5 \times 10^{11} \text{ cm}^{-2}$  and  $265\,000 \text{ cm}^2/\text{V} \cdot \text{s}$ , respectively. In order to create a photoresist pattern with a typi-

<sup>\*</sup> Corresponding author.

cal period of  $a = 500$  nm, holographic lithography was applied. The wire, dot or antidot structure was transferred into the sample with a wet chemical  $\text{NaOH}/\text{H}_2\text{O}_2/\text{H}_2\text{O}$  etchant. The etch process was stopped inside the  $\text{AlGaAs}$  spacer layer, so that surface defects were separated by more than  $100 \text{ \AA}$  from the active  $\text{GaAs}$  quantum well. The induced potential modulation in the structured samples separated the carriers laterally. The electrons occupy the area of the conduction band minima below the unetched regions, while the laser-induced holes accumulate in the valence band maxima below the etched regions. The width of the conducting electron channel was monitored during etching via the resistance of the electron gas at room temperature. The lateral quantization of the nanostructured samples was verified by magnetic depopulation [6] under laser illumination at  $1.5 \text{ K}$ . We observed that the Fermi energy was not reduced within the wires, and find an electronic subband spacing due to lateral quantization to be about  $2 \text{ meV}$  near the Fermi energy. The optical measurements were performed with a Dilor triple-grating spectrometer with a multichannel detector system and an optical fibre  $110 \text{ }\mu\text{m}$  in diameter at  $T = 1.5 \text{ K}$ . The PL was excited typically at a wavelength of  $700 \text{ nm}$ . The magnetic field was aligned along the growth direction.

For shallow etched quantum wires, dots and antidots, three types of luminescence features could be observed, as sketched in the inset of Fig. 1. Their basic properties are discussed in Ref. [8]. The indirect luminescence was observed in quantum wires and dots, as well as antidots. This is due to spatially indirect transitions of the separated carriers with a low transition probability as a consequence of the low overlap of the wavefunctions. The other types of recombinations are both direct in real space and involve hot, laser-generated carriers with a lower occupation density, but a much larger overlap compared to the states involved in indirect transitions. Below the etched areas with low carrier densities, excitonic transitions take place which lead to a sharp luminescence peak. From the regions with high electron density below the unetched areas, a plasma-like luminescence is emitted whose width is given

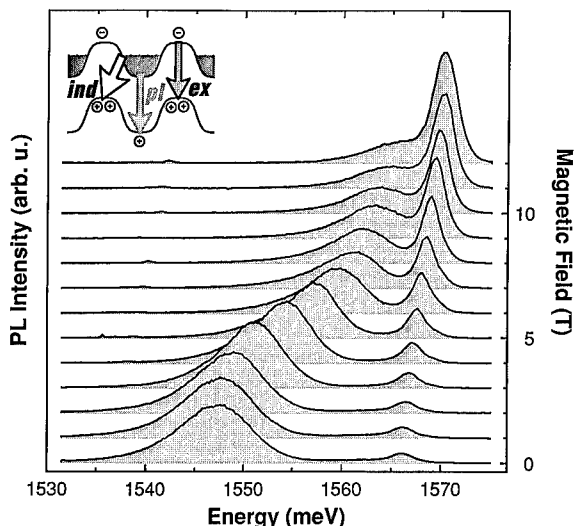


Fig. 1. PL spectra of a wire sample of period  $a = 500 \text{ nm}$  at various magnetic fields.

by the Fermi energy and whose onset is redshifted with respect to the exciton because of bandgap renormalization. Under standard conditions (excitation densities below  $100 \text{ mW}/\text{cm}^{-2}$ , without magnetic field) the excitonic luminescence is observed in quantum wires and dots while the plasma luminescence can be seen only in antidots.

Fig. 1 shows the PL spectra of a quantum wire sample of  $500 \text{ nm}$  period for magnetic fields of  $1\text{--}12 \text{ T}$ . The broad low-energy luminescence due to spatially indirect recombinations is located at energies below the fundamental gap of the well at zero magnetic field. The peak position stays almost constant up to  $1.5 \text{ T}$ , then increases rapidly and shifts finally with a smaller slope above  $6 \text{ T}$ . The excitonic luminescence reveals a rather moderate shift and gains in intensity with respect to the indirect one.

Fig. 2 shows the peak positions as a function of magnetic field of the spectra in Fig. 1 and, in addition, the indirect peaks of two further sets of spectra recorded at different laser excitation densities. The indirect transition energies shift with increasing excitation upwards because additional carriers flatten the potential modulation due to electrostatic screening. The dependence on magnetic field is determined by the localization of the

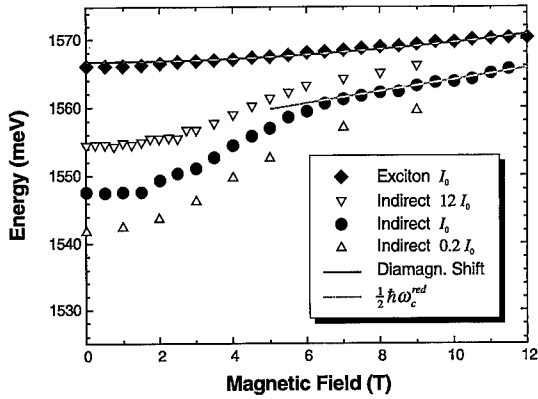


Fig. 2. Peak positions of excitonic as well as indirect luminescence for various excitation densities with  $I_0 \approx 16 \text{ mW cm}^{-2}$ .

wavefunctions by the applied field. Up to 1.5 T all three data sets reveal almost constant transition energies due to the fact that the overlap and the position of the PL maximum is determined entirely by the lateral confinement. The relevant length scales are the width of the cyclotron wavefunction at  $E_F$  with a value of about 300 nm at 1 T as typical magnetic length which is larger than the spatial separation of electrons and holes, which depends on the potential shape. With a further increase in  $B$ , the magnetic localization starts to dominate, such that only holes closer to the walls and therefore higher in energy have reasonable overlap with the electrons at the Fermi energy. The luminescence peak shifts upwards. At fields above 6 T the parabolic magnetic potential dominates. The shift exhibits a slope close to  $\frac{1}{2}\hbar\omega_c^{\text{red}}$  ( $\omega_c^{\text{red}} = eB(1/m^*e + 1/m^*h)$ ), as the transitions are almost direct at such high fields. The different steepnesses for the three excitation densities shift the vertex of the magnetic parabola which causes the observed shift in the transition energies. The excitonic peak energies vary only negligibly with excitation density. The excitonic luminescence shifts upwards by 4.2 meV at 12 T as observed also for the unstructured, homogeneously etched reference sample. The solid line gives the diamagnetic, quadratic shift using the equation in Ref. [9] (cgs units):

$$\Delta E_{1s} = D_2 \frac{\epsilon^2 \hbar^4}{4\mu^* c^2 e^2} H^2,$$

with the reduced exciton mass  $\mu^*$  and a parameter  $D_2$  related to the exciton dimensionality. With the experimentally determined proportionality constants for a 75 Å GaAs/Ga<sub>0.65</sub>Al<sub>0.35</sub>As well of Ref. [9], we get good agreement with our experimental values. A very similar behaviour of indirect and excitonic recombinations is found for dots and antidots. Antidots always reveal, in contrast to wires and dots, a plasma luminescence which splits above 2 T into a Landau ladder with up to five branches. The transitions are allowed transitions with the same Landau level quantum number for electrons and holes ( $n_L^e = n_L^h$ ) at a sample temperature of  $T = 1.5 \text{ K}$ . In the as-grown samples, such Landau level number-conserving transitions are observed only at higher temperatures ( $T \geq 40 \text{ K}$ ). At  $T = 1.5 \text{ K}$  as-grown samples exhibit only transitions with  $n_L^h = 0$  because hole states with higher  $n_L^h$  are not thermally occupied. The plasma luminescence in antidots, consequently, is due to hot holes.

For a more quantitative understanding of the behaviour, we simulate the spectra numerically. A purely two-dimensional system with a periodic lateral wire confinement  $V(x)$ , free motion in  $y$ -direction and the magnetic field perpendicular to the two-dimensional system is assumed. In Landau gauge with the vector potential  $A = B(0, x, 0)$  and the Ansatz  $\Psi(x, y) = e^{ik_y y} \varphi(x)$ , the Schrödinger equation becomes:

$$\left( -\frac{\hbar^2}{2m^*} \frac{\partial^2}{\partial x^2} + \frac{m^* \omega_c^2}{2} (x - x_0)^2 + V(x) \right) \varphi(x) = E \varphi(x), \quad (1)$$

with the effective mass  $m^*$ , the cyclotron frequency  $\omega_c = eB/m^*$ , and the centre coordinate of the magnetic parabola  $x_0 = \hbar k_y / eB$ . We choose the potential  $V(x)$  of the form:

$$V(x) = \frac{V_0}{2} - \frac{V_0}{2} \sin \left[ N \arctan \left( \sigma \frac{x}{a} \right) \right], \quad \text{for } -\frac{a}{4} \leq x \leq \frac{a}{4}, \quad (2)$$

with  $V_0$  being the total modulation amplitude,  $\sigma$  a parameter describing the steepness of the walls and  $N = \pi/2 \arctan^{-1}(\sigma/4)$  a normalization factor. The limit  $\sigma \rightarrow 0$  results in a sinusoidal poten-

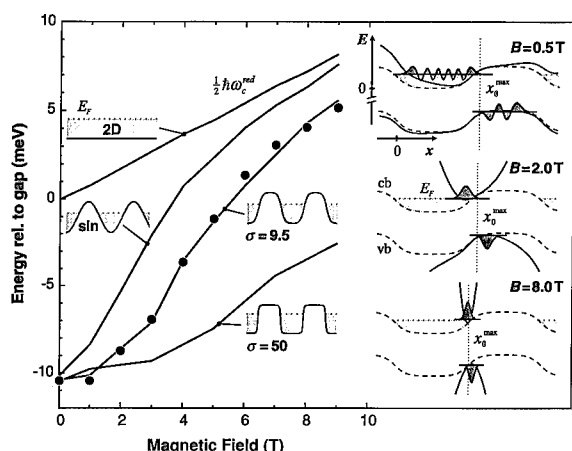


Fig. 3. Experimental (filled circles) and simulated (lines) indirect peak positions relative to the fundamental gap as a function of magnetic field. The insets are calculated for the parameters of the best fit and show the wavefunctions giving maximum transition probability.

tial,  $\sigma \rightarrow \infty$  in a rectangular one. For other values of  $x$ ,  $V(x)$  is determined by successively mirroring at values  $a/4 + l \cdot a/2$  ( $l$  integer). To obtain the PL spectra, Eq. (1) is discretized for electrons and holes and the matrix eigenvalues problem is solved on a grid of typically 200 points. For the determination of the occupation probability a Fermi–Dirac distribution is assumed for electrons and a Boltzmann distribution for holes. Thus hot carriers are neglected and no significant structure due to direct transitions is found. The parameters for the effective masses  $m^{*e} = 0.075m_0$  and  $m^{*h} = 0.23m_0$  are determined experimentally from as-grown samples [10]. To calculate the spectra for nonzero magnetic fields, the spectra of a large number of the centre coordinates  $x_0$  within half a period (symmetry) are added. Due to conservation of  $k_y$  in optical transitions, the same values of  $x_0$  have to be used for electrons and holes.

The insets in Fig. 3 show the electron and hole wavefunction giving maximum transition rate, together with the corresponding total potential for three values of  $B$ . The position of the corresponding vertex of the magnetic parabola  $x_0^{\max}$  is indicated by a dotted vertical line. The dashed lines denote the pure electrostatic potential, the solid lines the sum of electrostatic plus magnetic

one with a different curvature for electrons and holes due to the different effective masses. For all values of  $B$ , electron states near the Fermi energy exhibit the largest overlap with the spatially separated holes because they penetrate deeper into the barrier. At  $B = 0.5$  T, the total potential differs only slightly from the electrostatic confinement. As the occupation density of the holes decreases exponentially with increasing hole energy, holes low in energy but with still sufficient overlap yield highest transition rates. The increasing magnetic field starts to squeeze the wavefunction spatially, thus reducing the overlap such that hole states closer to the walls and higher in energy are favoured although their occupation density is smaller. The PL peak shifts to higher energies and the PL intensity decreases. It is clear that the extent of the shift depends especially on the steepness of the walls. In the case of a rectangular confinement for example an increase of hole energy will have a rather small effect on the overlap with respect to smoother potential shapes. At 8 T, the total potential is almost completely determined by the magnetic term and the bandgap is almost direct, such that the behaviour is similar to 2D Landau levels with a slope close to  $\frac{1}{2}\hbar\omega_c^{\text{red}}$ . The steepness of the wall results in a shift of the vertices of the magnetic parabolas which shifts the PL maxima to lower energies (see Fig. 2).

Fig. 3 shows the indirect peak positions of Fig. 1 relative to the fundamental gap of the 80 Å well as well as the simulated peak positions without lateral confinement, for a sinusoidal potential ( $\sigma \rightarrow 0$ ), a potential of the shape of Eq. (2) with a steepness of  $\sigma = 9.5$  and an almost rectangular confinement with  $\sigma = 50$ . The confinement potentials are also depicted. For the 2D case as test potential, the simulated luminescence maximum at  $B = 0$  T is equal to the gap and shifts like the difference of ground electron and hole Landau levels, as expected. For the other three potential shapes the total modulation amplitude  $V_0$  is chosen to give the experimental peak position at  $B = 0$  T resulting in  $V_0 = 33.7$  meV for the sinusoidal ( $\sigma \rightarrow 0$ ) as well as the  $\sigma = 9.5$  case and  $V_0 = 31$  meV for  $\sigma = 50$ . The modulation amplitude is smaller for the almost rectangular case,

because the lowest-energy holes already have a large overlap, and electrons below the Fermi energy with an occupation probability of 1 have almost the same overlap compared to states at  $E_F$  with occupation probability of 0.5. The transition of the luminescence from an indirect type at low fields to a direct one at high fields is much slower for a more rectangular shape, because the spatial separation of electrons and lowest energy holes is already rather small at low fields. The best fit of our model to the experimental data in Fig. 3 results in a confinement potential with  $\sigma = 9.5 \pm 2$  and  $V_0 = (33.7 \pm 2)$  meV.  $\sigma$  and  $V_0$  are here the only fitting parameters; all other parameters such as the Fermi energy  $E_F = 21.3$  meV and the carrier temperature  $T^e = T^h = 5$  K, are extracted from experimental data (see also Ref. [10]). The adjacent lateral confinement potential exhibits much steeper walls compared to a purely sinusoidal potential, but also a much flatter bottom part compared to a parabolic confinement. From self-consistent calculations of quantum wires, such as those of Laux et al. [11], it is known that when starting with a parabolic confinement without carriers, an increase in electron density leads to a flattening of the bottom of the parabola and to steeper walls. The potential shape determined here is in good qualitative agreement with such calculations.

The analysis shows, that for the determined potential shape, 15 electron subbands are occupied with a subband spacing increasing from 0.8 meV for the lowest electron states to 1.7 meV close to the Fermi energy. These values are consistent with magnetotransport experiments where we obtain a subband spacing at the Fermi energy of about 2 meV under similar conditions. The hole subband spacing is smaller due to the higher effective mass and is increasing from 0.4 to 0.9 meV at a hole energy of 21 meV. Due to the large number of occupied subbands, we expect only a small variation in the confinement potential with magnetic field due to electron redistribution and neglect it in our model. Furthermore, the slope of the walls, which determines the indirect peak position predominantly, remains constant if the number of electrons is not modified. A fit to the experimental data for different exci-

tation conditions presented in Fig. 2 confirms the variation of the modulation amplitude. We obtain 28.7 and 38.2 meV for the highest and the lowest excitation densities, respectively. A systematic variation of  $\sigma$  is not observed indicating only small changes in the electron carrier density.

We also investigated samples with a smaller Fermi energy,  $E_F = 15.6$  meV, where we find for all recorded laser excitations also a varying modulation amplitude, but an almost independent steepness parameter,  $\sigma = 3.7 \pm 1$ . The potential is therefore more sinusoidal than that of the sample with  $E_F = 21.3$  meV. To investigate the influence of the width of etched or unetched regions on the positions of the maxima, simulations are performed for potentials with other periods  $a$ , but very similar wall shapes. The deviation of the calculated energy positions is small and of the same magnitude as the deviation of the wall shapes. Our method is therefore sensitive to the wall properties, but rather insensitive to the width of the confining potential. Detailed information on the width has to be extracted from other experiments such as magnetic depopulation or confined plasmons [12].

In conclusion, magnetoluminescence provides insight into the basic properties of the three types of luminescence features observed in wires, dots and antidots. The shift of the indirect luminescence is a consequence of magnetic localization and allows us to extract details of the lateral confinement. The excitonic luminescence reveals a rather moderate shift that is well described as a diamagnetic excitonic shift. The plasma luminescence in antidots splits into a Landau ladder and is due to a non-thermalized hole distribution.

We acknowledge financial support provided by the Deutsche Forschungsgemeinschaft via SFB 348, and by Siemens AG.

## 1. References

- [1] K. Kern, D. Heitmann, P. Grambow, Y.H. Zhang and K. Ploog, Phys. Rev. Lett. 66 (1991) 1618.
- [2] D. Weiss, M.L. Roukes, A. Menshig, P. Grambow, K. von Klitzing and G. Weimann, Phys. Rev. Lett. 66 (1991) 2790.

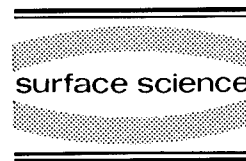


- [3] K.-F. Berggren, T.J. Thornton, D.J. Newson and M. Pepper, *Phys. Rev. Lett.* 57 (1986) 1769.
- [4] A.S. Plaut, H. Lage, P. Grambow, D. Heitmann, K. von Klitzing and K. Ploog, *Phys. Rev. Lett.* 67 (1991) 1642.
- [5] Y. Nagamune, Y. Arakawa, S. Tsukamoto, M. Nishioka, S. Sasaki and N. Miura, *Phys. Rev. Lett.* 69 (1992) 2963.
- [6] F. Hirler, J. Smoliner, E. Gornik, G. Weimann and W. Schlapp, *Appl. Phys. Lett.* 57 (1990) 261.
- [7] G. Berthold, J. Smoliner, C. Wirner, E. Gornik, G. Böhm, G. Weimann, M. Hauser, C. Hamaguchi, N. Mori and H. Momose, *Semicond. Sci. Technol.* 8 (1993) 735.
- [8] F. Hirler, R. Strenz, R. Küchler, G. Abstreiter, G. Böhm, J. Smoliner, G. Tränkle and G. Weimann, *Semicond. Sci. Technol.* 8 (1993) 617.
- [9] D.C. Rogers, J. Singleton, R.J. Nicholas, C.T. Foxon and K. Woodbridge, *Phys. Rev. B* 34 (1986) 4002.
- [10] R. Küchler, G. Abstreiter, G. Böhm and G. Weimann, *Semicond. Sci. Technol.* 8 (1993) 88, and references therein.
- [11] S.E. Laux, D.J. Frank and F. Stern, *Surf. Sci.* 196 (1988) 101.
- [12] T. Egeler, G. Abstreiter, G. Weimann, T. Demel, D. Heitmann, P. Grambow and W. Schlapp, *Phys. Rev. Lett.* 65 (1990) 1804.



ELSEVIER

Surface Science 305 (1994) 597–600



# Magneto-optics of interacting electrons in quantum dots

Pawel Hawrylak \*

*Institute for Microstructural Sciences, National Research Council of Canada, Ottawa, Canada K1A 0R6*

(Received 19 April 1993; accepted for publication 18 June 1993)

## Abstract

We study the electronic states of an exciton coupled to interacting electrons in a quantum dot in a strong magnetic field. The exciton is composed of a localized valence hole and a photoexcited electron. The exciton is strongly coupled to the electron system because the hole binds a photo-excited electron and one of the electrons from the quantum dot. Detailed calculations for an exciton coupled to one- and two-electron dots are presented.

## 1. Introduction

Quantum dots are artificial atoms created in semiconductor heterostructures by laterally confining a few two-dimensional electrons [1–3]. The role of electron–electron interactions in parabolic quantum dots has been recently studied by several authors [4–6]. As a result of the competition of kinetic, Zeeman, and electron–electron interaction energies, both the spin and the angular momentum of the ground state of the electron system change with increasing magnetic field through a series of “magic numbers”. We have shown recently [6] that the sequence of different ground states leads to discontinuous shifts of the acceptor-related recombination spectrum. The size and the sign of the discontinuity are direct measures of electron–electron and final state interactions. This is possible because of the charge neutrality of the photoexcited acceptor. Here we study in detail the effect of the attractive valence

hole potential on the spectrum of the photoexcited system.

## 2. The model

We consider a two-dimensional quantum dot containing  $N$  electrons. In the interband absorption process an electron–valence hole pair is created. We consider a model where an electron is added to the dot while a valence hole is localized in the centre of the dot. The final-state Hamiltonian of the dot plus an electron–hole pair describes a system of  $N + 1$  electrons with mass  $m$  confined by a parabolic potential with a characteristic energy  $\omega_0$  in a magnetic field  $B$  normal to the plane of the dot interacting with the attractive valence hole potential:

$$H = \sum_{i=1}^{N+1} \left\{ \frac{1}{2m} \left( \mathbf{p}_i + \frac{e}{c} \mathbf{A}_i \right)^2 + \frac{1}{2} m \omega_0^2 \mathbf{r}_i^2 + g \mu B S_z^i - \frac{e^2}{\epsilon_0 |\mathbf{r}_i|} \right\}$$

\* Corresponding author.

$$+ \sum_{i < j; i, j=1}^{N+1} \frac{e^2}{\epsilon_0 |\mathbf{r}_i - \mathbf{r}_j|}. \quad (1)$$

The vector potential is given in the symmetric gauge  $\mathbf{A} = (\mathbf{B} \times \mathbf{r})/2$ ,  $\epsilon_0$  is the background dielectric constant, and  $g$  is the effective  $g$ -factor. We take  $\hbar = 1$ .

In order to diagonalize the single-particle Hamiltonian of the dot, we introduce a pair of harmonic oscillator lowering (raising) operators  $(a, b)$  for each particle, e.g.:

$$z = (a + b^\dagger) \sqrt{l_0^2/2\Omega} \quad \text{and} \quad \partial_z = (b - a^\dagger) \sqrt{2\Omega/l_0^2},$$

where  $z = (x - iy)/2$ ,  $l_0 = 1/(m\omega_c)^{1/2}$  is the magnetic length,  $\omega_c$  is the cyclotron energy and  $\Omega = (1 + (2\omega_0/\omega_c)^2)^{1/2}$ . The single-particle Hamiltonian for an electron in the dot reduces to the Hamiltonian of a two-dimensional harmonic oscillator with eigenenergies  $E_{N,M} = \Omega_+(N + 1/2) + \Omega_-(M + 1/2)$ , eigenstates  $|M, N\rangle$  given by  $|M, N\rangle = (b^\dagger)^M (a^\dagger)^N |0\rangle / (N!M!)^{1/2}$  and two frequencies  $\Omega_{+(-)} = \{\sqrt{\omega_c^2 + 4\omega_0^2} + (-)\omega_c\}/2$ . The many electron states can be classified by a total spin  $S$ , its projection  $S_z$ , and the  $z$ -component of the total angular momentum  $R = \sum(M_i - N_i)$ . In the initial state (no valence hole) the relative motion and the center of mass motion (CM) can be separated. Only the relative motion is affected by the electron–electron interactions. The construction of the many electron states from the product of spin and harmonic oscillator states for  $N$  electrons is accomplished by a generalized Jacobi transformation into harmonic oscillator states describing  $N - 1$  degrees of freedom of the relative motion of electrons. These states transform according to the  $(N - 1)$ -dimensional representation of the group of permutations  $S_N$ . This procedure was described in Ref. [6]. In the final state we carry out an identical procedure for the  $(N + 1)$ -electron system in the presence of the valence hole potential. The valence hole potential couples CM and relative motion of all  $N + 1$  electrons in the quantum dot. The energy spectrum of final and initial Hamiltonian is diagonalized numerically for each value of the total angular momentum  $R$  using correlated states as a basis. The confining potential is  $\omega_0 = 4$  meV,

Zeeman energy  $\Delta E = g\mu B = 0.03$  meV/T, and other parameters, such as the effective mass and the dielectric constant, are appropriate for GaAs.

### 3. Results

We first consider the simplest case of the interband spectroscopy of an empty quantum dot. For illustrative purposes we consider the strong magnetic field limit ( $\Omega_+ \gg \Omega_-$ ). Initially, there is vacuum: no electrons and no excitons (Fig. 1a). After absorption, an electron–hole pair is created. The energy spectrum of an interacting electron–hole pair (exciton) as a function of angular momentum  $R$  is shown in Fig. 1b. The energy scale  $E_0 = Ry\sqrt{2\pi}a_0/l_0$  is the binding energy of an exciton in the high magnetic field limit. Fig. 1c shows the energy spectrum of the photoexcited carrier in the absence of electron–hole interactions. In this limit the energy spectrum is given simply by  $E_M = \Omega_-M + (\Omega_+ + \Omega_-)/2$ . The electron–hole interaction lowers the energy of different free-electron states (in all the figures the energies have been shifted for clarity).

We now turn to the spectroscopy of a quantum dot with one electron. The energy spectrum of initial states is shown in Fig. 2a for magnetic field  $B = 10$  T. The ground state is the zero angular momentum, spin-down  $|-\rangle$  state for all mag-

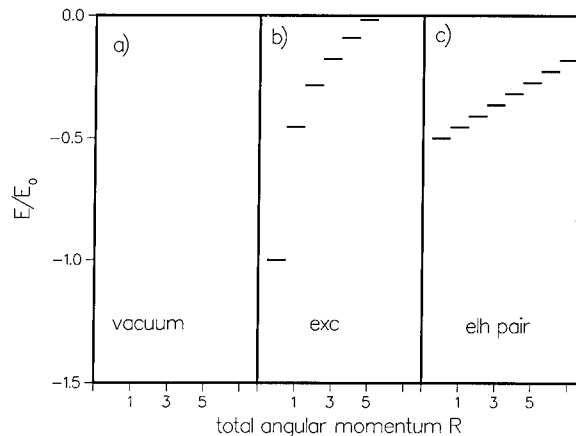


Fig. 1. (a) Energy spectrum of an empty quantum dot in the strong magnetic field limit; (b) single-exciton spectrum; (c) single electron–hole pair spectrum, no valence hole potential.

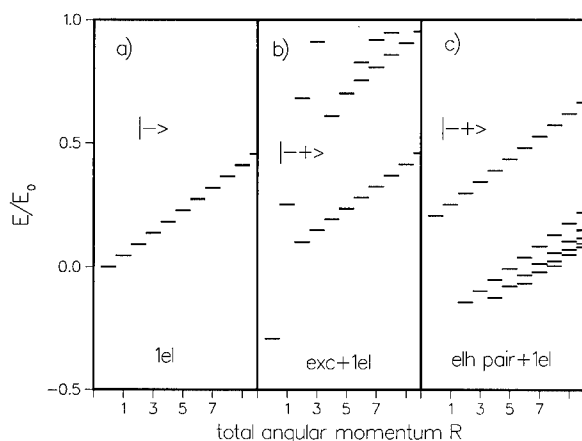


Fig. 2. (a) One-electron spectrum of a quantum dot in the strong magnetic field limit; (b) spin-singlet exciton spectrum; (c) spin-singlet exciton spectrum, no valence hole potential.

netic fields. In the absorption process only the transition to the zero angular momentum state is allowed, forcing the spin of the photoexcited carrier to be reversed  $|+\rangle$ . The final two-electron state is spin-singlet. The energy of the final state is determined by the competition of the attractive interaction with the valence hole and a repulsive interaction between two electrons. In the singlet state both electrons lower their energy by occupying the zero angular momentum state and the distinction between the photoexcited and initial-state electrons is completely lost. The one electron + exciton (the two-electron + hole) complex energy spectrum as a function of the total angular momentum  $R$  is shown in Fig. 2b. The ground state  $R=0$  is bound, and there is a Coulomb barrier at  $R=1$  to be overcome before the exciton can ionize ( $R>1$  spectrum). This is to be contrasted with Fig. 1c, where the attractive hole potential was off, i.e. we consider the injection of the electron-valence hole pair. The final state spectrum is now the spectrum of the spin-singlet two-electron dot.

We now turn to the interband spectroscopy of a two-electron quantum dot, an artificial helium atom. The spin triplet  $S=1$  ground state of the two-electron dot is determined by repulsive electron-electron interactions. We show the energy spectrum in the strong magnetic field limit of the triplet state in Fig. 3a. For  $B=10$  T the ground

state is at  $R=3$ . To what extent can interband spectroscopy provide information about the ground state of the dot? In Fig. 3b we show the spectrum of an exciton coupled to the two-electron dot. This is now a three electron + valence hole problem, with a single photoexcited electron having a reversed spin. The total spin of the excited state is  $S=1/2$ . The ground state has an angular momentum  $R=2$ , which is lower than the angular momentum of the initial ground state. This implies a very strong rearrangement of electrons in the presence of an exciton. We can again think of this state as consisting of two electrons, one photoexcited and one from the two-electron dot attracted by the hole and repelling the third electron. Clearly, there is little overlap of the initial and final states. In Fig. 3c we show the excitation spectrum of the three electron complex without the valence hole potential (electron-valence hole pair complex). The angular momentum  $R=7$  of the ground state is very different, and hence the ground state and the excitation spectrum depend strongly on the final state interactions.

We now calculate the difference in energies of the lowest-energy photoexcited state and the initial state (ground state of the two-electron dot) as a function of the magnetic field. In calculations we use the subspace of two quasi-Landau levels ( $N=0, 1$ ) as the minimum subspace yielding

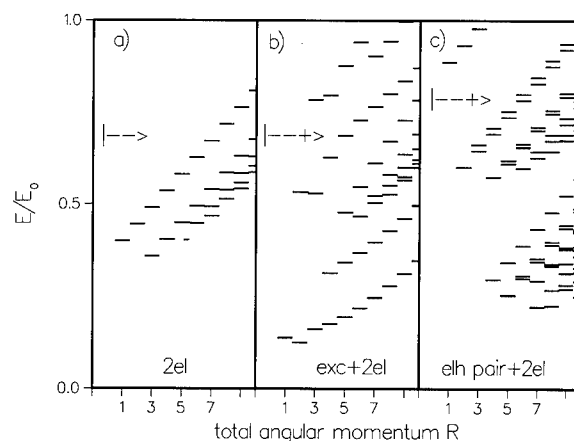


Fig. 3. (a) Spin triplet two-electron spectrum in the strong magnetic field limit; (b) spin-1/2 two-electron + exciton spectrum; (c) same as (b), but no valence hole potential.

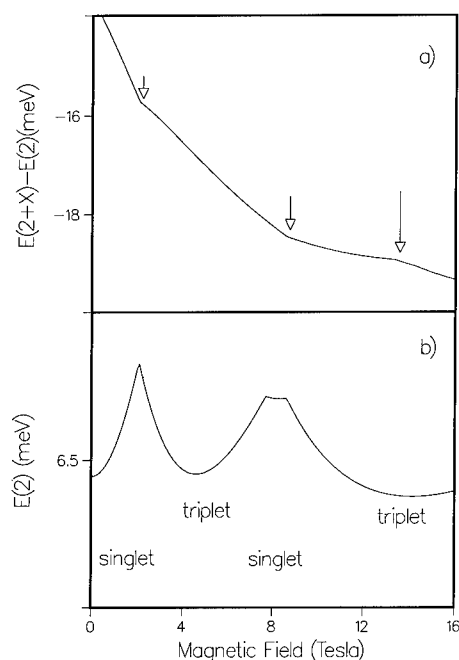


Fig. 4. (a) Transition energy as a function of magnetic field corresponding to Fig. 3b; (b) ground state energy of a two-electron dot. Different singlet and triplet states are visible.

qualitatively correct spin-induced transitions in the two- and three-electron cases. In Fig. 4a we show the absorption threshold given by the difference between the lowest-energy state of the exciton + quantum dot system and the ground state energy of the quantum dot:  $\omega = E(2+X) - E(2)$ . The arrows identify structures in the transition

energy  $\omega$ . These structures are related to the spin and angular momentum changes of the two-electron dot, shown in Fig. 3b, and to changes in the photoexcited system (last arrow). Hence, because of the strong correlations induced in the final state, the energy structure in the absorption energy reflects changes in the spin and angular momentum of the initial state. In the absence of the valence hole potential the transition energy  $\omega$  is equal to the chemical potential of the two-electron atom.

In summary, excitons coupled to electrons in quantum dots are a sensitive and nontrivial probe of the ground and excited states of the strongly interacting electron system.

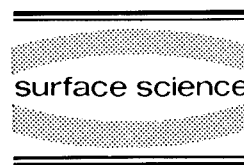
#### 4. References

- [1] For a recent review and references, see T. Chakraborty, *Comments Condensed Matter Phys.* 16 (1992) 35.
- [2] Ch. Sikorski and U. Merkt, *Phys. Rev. Lett.* 62 (1989) 2164; B. Meurer, D. Heitman and K. Ploog, *Phys. Rev. Lett.* 68 (1992) 1371.
- [3] P.L. McEuen, E.B. Foxman, Jari Kinaret, U. Meirav, M.A. Kastner, N.S. Wingreen and S.J. Wind, *Phys. Rev. B* 45 (1992) 11419.
- [4] P.A. Maksym and T. Chakraborty, *Phys. Rev. Lett.* 65 (1990) 108; *Phys. Rev. B* 45 (1992) 1947.
- [5] D. Pfannkuche and R.R. Gerhardts, *Phys. Rev. B* 44 (1991) 13132.
- [6] P. Hawrylak and D. Pfannkuche, *Phys. Rev. Lett.* 70 (1993) 485.



ELSEVIER

Surface Science 305 (1994) 601–605



# Magnetoplasmons and FIR response of an antidot array

G.Y. Wu <sup>\*,1</sup>, Y. Zhao

*Department of Electrical Engineering, Princeton University, Princeton, NJ 08544, USA*

(Received 20 April 1993; accepted for publication 30 July 1993)

## Abstract

We present a theory of the magnetoplasmons of two-dimensional antidot arrays. A variational Wigner–Seitz model is proposed within the hydrodynamic picture to calculate the magnetoplasma modes. Hydrodynamic solutions of the modes are quantized into plasmons. Moreover, by considering the first-order absorption process, in which one photon is converted into one plasmon, we analytically derive the far-infrared (FIR) response of the structures. We directly compare our model to the experiments and obtain quantitative agreement. However, in addition to the observed  $\nu^+$  and  $\nu^-$  modes, we predict the existence of a mode degenerate with  $\nu^+$  at zero magnetic field, but with an oscillator strength decreasing rapidly with magnetic field. Our work provides an explanation for the recently observed FIR anomaly as well as a model for future studies of electron grid/antidot structures.

The physics of the two-dimensional electron gas (2DEG) is currently a subject of great interest. With the recent advancement of nanostructure technology, the study of uniform 2DEGs has extended to that of lateral superlattices (LSLs). Among these interesting systems, the dynamic response of the uniform 2DEG, the LSLs of quantum wires, and the LSLs of quantum dots can largely be understood within the Kohn theorem, which states that, for a homogeneous electron gas or inhomogeneous system confined by parabolic potentials, the long-wavelength response is due to the center-of-mass motion of electrons [1]. However, the LSLs of grids/

antidots, lacking such properties, show many peculiarities in the magneto-optical [2,3] and magnetotransport measurements [4]. In recent far-infrared (FIR) studies of the grid structure, Kern et al. [2] and Zhao et al. [3] observed, in the presence of magnetic field  $B$ , new resonances  $\nu^+$  and  $\nu^-$  other than the electron cyclotron resonance (CR). They show an anomalous level-crossing-like feature in the  $\omega$ – $B$  dispersion, which was attributed to the breakdown of Kohn's theorem [3]. The high-frequency  $\nu^+$  branch starts at small  $B$  with a negative slope, and then increases in frequency with  $B$ , eventually approaching the CR. A second low-frequency  $\nu^-$  branch begins with zero frequency at  $B = 0$ , rises with  $B$ , and shows a slightly negative slope at high  $B$ . Moreover, the oscillator strength transfers from the  $\nu^+$  to the  $\nu^-$  with increasing  $B$ , suggesting a mixing of the two modes. The plasma origin of the  $\nu^+$  mode was demonstrated by Zhao et al. from a density-

\* Corresponding author: On leave from the Department of Electrical Engineering, Tsing-Hua University, Hsin Chu, Taiwan 300.

<sup>1</sup> Present address: Department of Physics, University of California at San Diego, La Jolla, CA 92093-0319.

dependence study [3]. On the other hand, the foregoing anomaly has not been experimentally observed or theoretically predicted in similar investigations of the 2D structures where the Kohn theorem holds [5–8]. Therefore, the grid/antidot structures constitute interesting systems to theorists from the viewpoint of understanding the consequence of breakdown of the Kohn theorem. In this work, we develop a model for the magnetoplasma modes and the FIR response of the grid/antidot structure, and directly compare our model to the experiments. Our work provides not only an explanation for the observed FIR anomaly, but also a model for the future study of electron grid/antidot structures.

We picture the system as a thin layer of 2DEG sitting at the heterostructure interface (with the coordinate  $x=0$ ) and penetrated by a square lattice of holes. The structure is bounded by two metal gates located at  $x=x_1$  and  $x_2$ .  $B$  is taken to be along the  $x$ -axis. Consistent with the experiments, we shall assume the length scales  $l \sim d \gg r_s$ , where  $l$  is the plasma characteristic length,  $d$  is the lattice constant of the antidot array, and  $r_s$  is the interelectron spacing. Further, an estimate using the experimental parameters yields  $l \gg a^*$ , where  $a^*$  is the effective Bohr radius, which permits us to neglect compressibility effects.

The physics of long- $l$  plasma modes belongs to the hydrodynamic limit, in which one needs to deal only with coarse-grain averages. In the present theory, we focus on the three hydrodynamic quantities  $n(y, z, t)$ ,  $V(y, z, x, t)$ , and  $\mathbf{v}(y, z, t)$ , where  $n$  is the electron density fluctuation,  $V$  is the electric potential fluctuation, and  $\mathbf{v}$  is the velocity field. They are governed by the laws of conservation, i.e. particle conservation and momentum conservation, plus Coulomb's law. We look for the normal modes with harmonic time dependence  $e^{-i\omega t}$ . They satisfy the plasma equation [5–7]:

$$(n_s e/m)(\partial^2/\partial y^2 + \partial^2/\partial z^2)V_0 + (\omega_c^2 - \omega^2)n = 0, \quad (1)$$

where  $V_0$  is the potential fluctuation at the  $x=0$  plane,  $n_s$  is the average electron density,  $\omega_c$  is the CR frequency. This equation needs to be solved simultaneously with the Poisson equation.

We propose a variational Wigner–Seitz (WS) model that reduces the complicated problem to essentially that of a (circular) WS cell, and treats the intracell and intercell Coulomb interactions. The plan is to study the so-called screened limit first, and to use it as the guideline for setting up a model later for the general situation where the Coulomb interactions are important.

In the screened limit, e.g.  $x_1 \rightarrow 0$ , Coulomb interactions in the 2DEG are reduced by the nearby metal gate. In this limit, the electric field lines are perpendicular to the metal gate, and one can picture it as a pair of parallel plates, i.e. a capacitor, with the upper end grounded. This capacitor approximation results in a local linear relationship between  $V_0$  and  $n$ , with  $V_0 = -ex_1 n/e_1$ , where  $e_1$  is the dielectric constant of the upper layer of the heterostructure. With this relation, the Poisson equation is solved, and the number of unknowns is reduced. Substituting this relation into the plasma equation, one obtains an equation in the electron density  $n$ .

To solve it for the periodic array of antidots, we write with the Bloch theorem  $n(y, z) = e^{i(q_y y + q_z z)} n_c(y, z)$ , where  $\mathbf{q} = (q_y, q_z)$  is a wavevector in the  $yz$ -plane, and  $n_c$  is cell-periodic. For the present problem, it suffices to focus on the  $\mathbf{q} = 0$  solutions, since these are the modes excitable with the FIR, which has a very long wavelength compared to the lattice constant of the array. The Bloch theorem transforms the many-cell problem to a one-cell one, and reduces the number of boundaries, i.e. hole edges, where we need to force the solution to satisfy some sort of boundary condition, to just one.

However, the reduced problem requires the additional specification of boundary condition at the cell boundary. We derive it by introducing the idea of WS method [9]. First, we approximate the WS unit cell as a circular disk, thus enhancing the actual square symmetry. With this, the solution can be written as  $n(y, z) = n(r) e^{ijs}$ , where  $(r, s)$  are the polar coordinates, and  $j$  is an azimuthal index. The boundary condition can be taken as:

$$n(r)|_{r=r_0} = 0 \quad (dn/dr)|_{r=r_0} = 0 \quad \text{for } j = \text{odd (even)}, \quad (2)$$

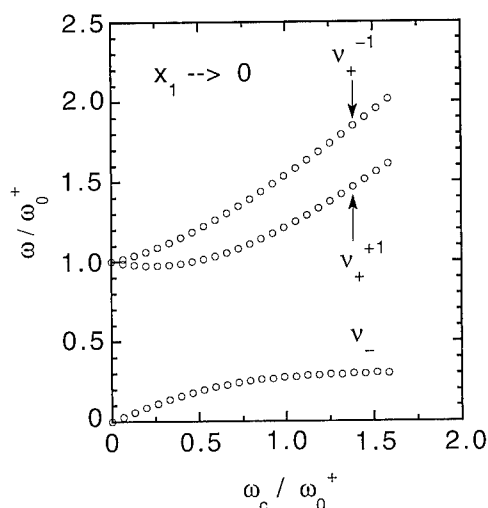


Fig. 1. The  $B$  dispersion of low-lying plasma modes in the screened approximation.  $\omega_0^+$  is the zero-field  $\nu_+^{+1}$  (or  $\nu_+^{-1}$ ) mode frequency. The relevant parameters are  $r_i = 700 \text{ \AA}$ , and  $r_0 = 1000 \text{ \AA}$ .

where  $r = r_0$  is the boundary of the circular cell, which we take to have the same area as the actual one. The reasoning behind (2) is as follows. Take  $|j| = 1$ , for example. At time  $t = 0$  ( $\pi/2\omega$ ), with the density fluctuation in each unit cell equal to  $n(r) \cos(s)$  ( $n(r) \sin(s)$ ), the sign of charge changes as we cross the cell boundary horizontally (vertically). Hence,  $n(r)$  at the boundary must be zero. The angular dependence of  $n$  is such that the electron gas within each unit cell forms a dipole, implying that the  $|j| = 1$  modes are excitable by long-wavelength electric fields. Moreover, we require that  $v_r|_{r=r_i} = 0$  at the hole edge, as a result of the elastic reflection of an electron from the edge. With equal angles of incidence and reflection for the edge reflection, this condition follows from taking the coarse-grain average of the electron velocity,  $(1/N_e)\sum v_i$ . It means that the macroscopic current does not penetrate into the holes.

The solution to the above problem can be written analytically as Bessel functions. We plot the solutions of low-lying modes in Fig. 1. They consist of three branches. Two of them  $\nu_+^{+1}$  (with  $j = 1$ ) and  $\nu_+^{-1}$  (with  $j = -1$ ), have higher frequencies than the CR; whereas, the third branch,  $\nu_-$  (with  $j = 1$ ), is lower in frequency than the

CR. This figure contains several features observed in the experiment. Notice in particular that, near  $B = 0$ , the  $\nu_+^{+1}$  branch shows a negative  $B$  dispersion. However, there are differences between this result and the experiment. The calculated frequency of the  $\nu_-$  branch saturates at high  $B$ , while the experiments observed a slightly negative dispersion in this limit, a characteristic of the edge magnetoplasmons (EMP) [5–7]. Further, besides the  $\nu_+^{+1}$  branch, the theory predicts the existence of another eigenmode,  $\nu_+^{-1}$ , which is degenerate with the  $\nu_+^{+1}$  mode at  $B = 0$ . The existence of the  $\nu_+^{-1}$  mode is simply a consequence of symmetry, which can be reasoned as follows. At  $B = 0$ , the two  $\nu_+$  modes are degenerate but with opposite rotations. In the presence of  $B$ , the symmetry becomes broken, lifting the degeneracy.

So far, we have established a useful model that, even with several critical approximations, is able to provide a clear qualitative picture for the physics of the structures. In the actual experiments, however, the metal gates were distant from the 2DEG, and did not effectively screen down the Coulomb interactions. In such general cases, the model predicts plasma modes that are too soft. For a true and quantitative understanding of the grid structures, it is essential to incorporate the effects of intracell and intercell Coulomb interactions. In view of the success of the screened model, we shall generalize it with the constraint that, in the limit  $x_1 \rightarrow 0$ , the generalized model reduces to the screened one. The generalization is achieved via a variational approach.

In the following, we give a brief account of the variational approach. First, we construct reasonable trial functions for  $n(y, z)$  and  $V_0(y, z)$ . They are defined on the circular WS cell and taken to have the separable form  $f(r) e^{ijs}$ . By an argument parallel to the one leading to (2), we impose the conditions (we focus on the  $|j| = 1$  case)

$$V_0(r)|_{r=r_0} = 0, \quad v_r|_{r=r_i} = 0, \quad (3)$$

$$n(r)|_{r=r_0} = 0, \quad (4)$$

which reflect the physics involved in the grid structure, i.e. the dipole formation and the edge



reflection within each cell. We then cast the plasma equation plus these boundary conditions into an integral equation via the use of a Green's function. We treat the e–e interactions in the following approximate way. We create a square lattice formed with the circular WS cells, and embed the trial functions into the lattice. For  $|\mathbf{r} - \mathbf{R}_i| > r_0$ , the functions are set to zero, where  $\mathbf{R}_i$  are the centers of the cells. We consider the e–e interactions in this artificial lattice and solve the Poisson equation in its reciprocal space. We note that, as long as the artificial lattice cell is close in size to the real lattice cell, the estimate of Coulomb effects based on using the artificial lattice should be reasonable.

We now turn to the discussion of FIR response. We assume that the FIR radiation is incident normal to the 2DEG, which is consistent with the experimental situation, and hence we neglect retardation effects due to the finite light velocity. We consider only the dominant one-photon process, in which a photon is absorbed and the excited state containing a plasmon is created. In view of this, the plasma eigenmodes obtained with our model have to be quantized to properly represent the quanta of excitations (plasmons). This is carried out in the language of second

quantization. First, we write the energy fluctuation in our model:

$$H = (n_s m / 2) \int v^2 d^2 r + (1/2) \int (-e) n V_0 d^2 r. \quad (5)$$

The eigenmodes obtained from solving the integral equation are inserted in (5) and quantized by requiring  $H = \hbar \omega$ , meaning that the energy fluctuation contained in the excited state is due to the presence of one plasmon. With the amplitudes of the fluctuations so fixed, the velocity field operator, for example, is written as

$$\hat{\mathbf{u}}(\mathbf{r}, t) = -i/\sqrt{2} \sum_k (\mathbf{v}_k(\mathbf{r}) b_k(t) - \text{h.c.}), \quad (6)$$

where  $b_k$  is the lowering operator for the  $k$ th mode,  $\mathbf{v}_k(\mathbf{r})$  is the quantized velocity field, and h.c. denotes the Hermitian conjugate. The interaction Hamiltonian between a plasmon and the light can be expressed as:

$$H' = \int n_s (-e) \hat{\mathbf{u}} \cdot \mathbf{A}_{\text{ext}} d^2 r,$$

where  $\mathbf{A}_{\text{ext}}$  is the vector potential of the light. The optical matrix element  $\langle l_k | H' | 0 \rangle$  is evaluated between the ground state  $|0\rangle$  and the ex-

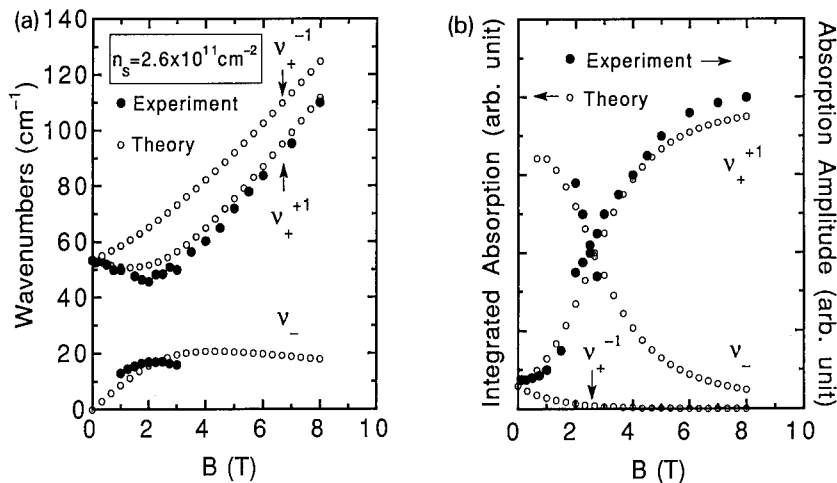


Fig. 2. (a) The left panel shows the  $B$  dispersion of low-lying modes for the GaAs/GaAlAs heterostructure of Zhao et al. [3]. (b) The right panel shows the absorption versus  $B$ . The parameters used by the theory are directly taken from Ref. [3]. For the parameters not listed here, we take  $e_1 = e_2 = 13$ , and  $m = 0.067m_e$  from the CR data of the experiment.

cited state  $|l_k\rangle$  containing one plasmon of the  $k$ th mode. In the FIR limit, the absorption integrated over a resonance frequency  $\omega_k$  is written in terms of the matrix element:

$$\int a(\omega') d\omega' \approx |\langle l_k | \hat{\mathbf{u}} \cdot \mathbf{e} | 0 \rangle|^2 / \omega_k, \quad (7)$$

where  $\mathbf{e}$  is the polarization vector of the electric field. An evaluation of  $\langle l_k | \hat{\mathbf{u}} \cdot \mathbf{e} | 0 \rangle$  results in the selection rule  $j = \pm 1$  for the unpolarized FIR excitation.

We compare our theory to the experiment of Zhao et al. [3] in Fig. 2. Quantitative agreement is achieved. Similar agreement was found when comparing the theory with the experiment of Kern et al. [2] in the case of InGaAs/InAlAs. Notice the appearance of slightly negative dispersion at high  $B$  in the calculation of the  $\nu_-$  branch, which was absent in the screened model. As shown in Fig. 2b, the absorption intensity transfers from the  $\nu_-$  branch to the  $\nu_+^{+1}$  branch as  $B$  increases. Notice that the strength of the  $\nu_+^{-1}$  mode decreases rapidly with  $B$ . If we assume that the resonance width of the absorption is mode-independent and does not change with  $B$ , the results here can be directly compared with the experimental transmission spectra, which are shown in the plots for comparison. The values of  $B$  at which the  $\nu_-$  and  $\nu_+^{+1}$  branches have equal strengths agree with the experiment. We have also computed for other  $|j| = 1$  modes with higher frequencies and found that their strengths are smaller by orders of magnitude, indicating that the oscillator strength has been exhausted by the low-lying modes [10].

In summary, we have developed a theory of the magnetoplasmons of electron grid/antidot structures. The calculated mode frequencies and FIR absorption agree with the experiments. We interpret the interesting features of such systems as the result of an interplay of  $B$  and the unique geometry of the grid structure. It removes the existence of any  $j = -1$  EMP mode, and suppresses the oscillator strength of the  $\nu_+^{-1}$  mode, as it has the opposite sense of rotation to the cyclotron motion. On the other hand, the  $\nu_+^{+1}$  mode and the  $\nu_-$  mode, having the same sense, can share the oscillator strength. Finally, we note

that it should be interesting to carry out a polarized FIR experiment, in which the absorption peak of the  $\nu_+^{+1}$  mode would be suppressed by the selection rule, to verify the existence of the  $\nu_+^{-1}$  mode predicted by our theory.

During our work, Lorke et al. [11] reported numerical simulations of LSLs within the independent-particle picture, which contained some qualitative features for the grid structures.

We are grateful to Professor D.C. Tsui for many valuable discussions and for his constant support during this work. One of us (G.Y. Wu) thanks Princeton University for the hospitality received during his visit, and the NSC of ROC for sponsoring the visit. This work was supported by the AFOSR under grant No. AFOSR-91-0353.

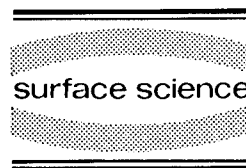
## 1. References

- [1] W. Kohn, Phys. Rev. 123 (1961) 1242;  
L. Brey, N.F. Johnson and B.I. Halperin, Phys. Rev. B 40 (1989) 10647.
- [2] K. Kern, D. Heitmann, P. Grambow, Y.H. Zhang and K. Ploog, Phys. Rev. Lett. 66 (1991) 1618.
- [3] Y. Zhao, D.C. Tsui, M. Santos and M. Shayegan, R.A. Ghanbari, D.A. Antoniadis and H.I. Smith, Appl. Phys. Lett. 60 (1992) 1510.
- [4] R. Fleischmann, T. Giesel and R. Ketzmerick, Phys. Rev. Lett. 68 (1992) 1367, and references therein.
- [5] D.B. Mast, A.J. Dahm and A.L. Fetter, Phys. Rev. Lett. 54 (1985) 1706;  
A.L. Fetter, Phys. Rev. B 33 (1986) 5221.
- [6] D.C. Glatli, E.Y. Andrei, G. Deville, J. Poitrenaud and F.I.B. Williams, Phys. Rev. Lett. 54 (1985) 1710.
- [7] J.-W. Wu, P. Hawrylak and J.J. Quinn, Phys. Rev. Lett. 55 (1985) 879.
- [8] C.C. Grimes and G. Adams, Phys. Rev. Lett. 36 (1976) 145;  
S.J. Allen, D.C. Tsui and R.A. Logan, Phys. Rev. Lett. 38 (1977) 980;  
A. Lorke, J.P. Kotthaus and K. Ploog, Phys. Rev. Lett. 64 (1990) 2559;  
T. Demel, D. Heitmann, P. Grambow and K. Ploog, Phys. Rev. Lett. 66 (1991) 2657, and references therein.
- [9] The original WS method was developed to study the  $S$  states of metal band structures. See E. Wigner and F. Seitz, Phys. Rev. 43 (1933) 804.
- [10] The optical absorptions in the screened model display the same patterns of variations with  $B$  as discussed in this paragraph.
- [11] A. Lorke, I. Jejina and J.P. Kotthaus, Phys. Rev. B 46 (1992) 12845.



ELSEVIER

Surface Science 305 (1994) 606–609



# FIR spectroscopy of the intra-Landau level excitations of strongly correlated quantum dots

X.C. Xie \*

*Department of Physics, Oklahoma State University, Stillwater, OK 74078, USA*

S. Das Sarma

*Department of Physics, University of Maryland, MD 20740, USA*

Song He

*Department of Physics, AT&T Bell Laboratory, Murray Hill, NJ 07974, USA*

(Received 20 April 1993; accepted for publication 15 June 1993)

## Abstract

By directly diagonalizing the many-body interacting Hamiltonian for two model confinement potentials, we calculate the dipole-allowed optical transition spectra for a few electrons confined in a small quantum dot subjected to a strong external magnetic field. We find substantial many-body corrections to the optical transition energies for quartic and flat-bottomed-parabolic confinement in contrast to the well-studied *purely* parabolic confinement, where optical transitions are known to be unaffected by interaction effects by virtue of the generalized Kohn's theorem.

There has been considerable recent interest in the electronic properties of quantum dots where the electron motion is quantized in all three directions. While much attention has focused [1,2] on the tunneling of electrons in and out of quantum dots and the associated Coulomb blockade effects, the electronic properties of a single isolated quantum dot where electronic motion is quantum mechanically confined in all three dimensions is also quite interesting, particularly in

the presence of a strong external magnetic field which can be used to tune the properties of the system. Based on our experience with the physics of strongly correlated two-dimensional fractional quantum Hall liquids, one expects interesting electron–electron interaction effects in quantum dots under strong external magnetic fields. In this paper we present numerical results for the optical transition energy and magnetization of small quantum dots containing a few ( $\sim 6$ ) electrons as a function of the external magnetic field on the system. The two main features of our calculations are using the realistic Coulomb interaction between the electrons and treating the confinement

\* Corresponding author.

potential in a number of semi-realistic simple models.

Our theoretical technique is the exact diagonalization of few-electron quantum dot systems within the lowest Landau level approximation. This technique has been extremely successful [3] in studying the fractional quantum Hall effect. Using our exact diagonalization technique we obtain the lowest dipole-allowed optical transition energy as a function of the magnetic field. Our exact numerical results for the optical transition energies exhibit considerable correlations arising from electron interaction effects which should be experimentally observable in small quantum dots with non-parabolic confinement potential.

Earlier theoretical work on the elementary excitation spectra in quantum dots mostly used parabolic confinement not only because of its calculational simplicity but also because it is a reasonable model for electrostatically defined confinement. Optical (or, more generally, magneto-optical) properties of parabolically confined quantum dots are, however, trivial due to the validity of the generalized Kohn's theorem which asserts [4,5] that the optical transition energy of the interacting parabolic system is exactly the same as that of the bare, non-interacting system. This exact cancellation of many-body correlation effect on the optical spectra [6] of parabolically confined quantum dots arises from the separability of the interacting Hamiltonian into center-of-mass and relative coordinates, which is possible only for a quadratic confining potential. This theorem, however, provides no clue about the correlation correction to the optical spectra of non-parabolically confined quantum dots. We mention that the absence of correlation effects in the magneto-optical spectra of parabolically confined quantum dots is now accepted to be experimentally established [5,6]. There have been earlier theoretical investigations [7,8] of the effects of non-parabolic confinement potential on the optical properties of dots. In Ref. [6], the authors studied the magneto-optical response of two-electrons in non-parabolic quantum dots. In Ref. [7] the non-parabolic effect is included by considering two coupled parabolic quantum dots and magneto-optical properties are studied as well. In

both of these cases [7,8] the deviation from non-parabolicity is only a small perturbation to the system, and the magneto-optical spectra have only small corrections compared with the parabolic case. In contrast, our calculated magneto-optical spectra exhibit very strong many-body correlation effects.

In this paper we calculate the interacting magneto-optical spectra of quantum dots for two different model non-parabolic confinement potentials,

$$V(\mathbf{r}) = V_0(r - r_0)^{2n}\theta(r - r_0), \quad (1)$$

with  $n = 2$  and  $r_0 = 0$  (model I) defining a quartic confinement as our first model, and  $n = 1$  and non-zero  $r_0$  (model II) defining a flat-bottomed-parabolic confinement as our second model. We note that our quantum dot is a disc-shaped two-dimensional structure (i.e.  $\mathbf{r}$  in Eq. (1) is a two-dimensional position vector in the  $x$ - $y$  plane with the magnetic field along the  $z$  direction), which is a reasonable model for many lithographically defined structures where the confinement along one direction ( $z$ ) is much stronger than that in the other two directions, and the system is effectively a finite disc-shaped two-dimensional system (i. e. a dot which is shaped like a disc). At no loss of generality, all our numerical results are for such quantum disc structures. We consider the magnetic field to be strong enough to spin-polarize the system, concentrating entirely on the lowest spin-split Landau level. All our calculations neglect spin effects, and Landau level mixing effects as well. Our exact diagonalization calculations employ 6-electron systems in the quantum dot assuming all the electrons in the lowest spin-split Landau level. For high magnetic fields this is certainly a reasonable approximation. We expect our results to be qualitatively valid in the presence of Landau level mixing effects, but the quantitative validity [4] of the magneto-optical transition energies may not be better than 10% due to the neglect of higher Landau levels. We also assume a spin polarized system which is certainly a valid approximation at higher ( $> 3$ – $4$  T) magnetic fields. Relaxing this approximation would introduce additional structure and compli-

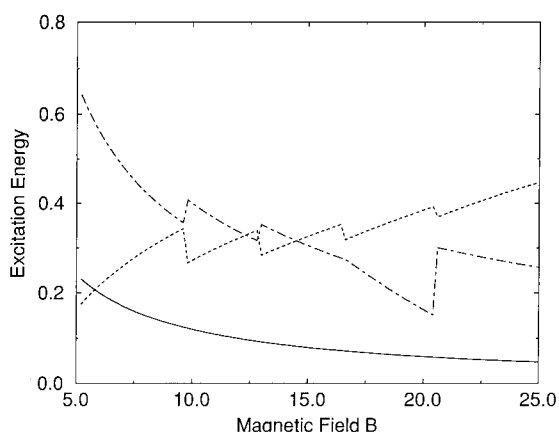


Fig. 1. The calculated dipole-allowed magneto-optical transition energies as a function of the magnetic field for a 6-electron quantum dot system for the quartic confinement (model I) with  $V_0 = 0.05e^2/l$  and  $r_0 = 0$ , where  $l$  is the magnetic length at  $B = 5$  T. The dash-dotted, dotted, and solid lines correspond, respectively, to interacting  $E_+$ ,  $E_-$ , and the non-interacting dipole transition energies.

cations into our calculated numerical results as singlet–triplet transitions start playing a role. Again, our basic result, prediction of correlation-induced non-monotonic structure in the magneto-optical spectra of small non-parabolic quantum dots, is unaffected by this approximation.

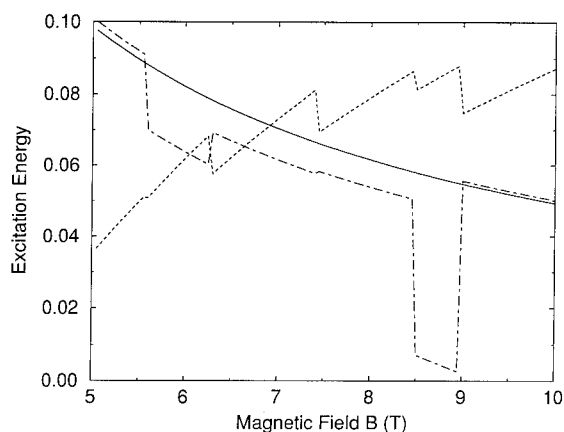


Fig. 2. The same as in Fig. 1 for a quantum dot with the flat-bottomed parabolic confinement (model II) with  $V_0 = 0.05e^2/l$  and  $r_0 = l$ , where  $l$  is the magnetic length at  $B = 5$  T.

In Figs. 1 and 2 we show for the two model confinements our calculated magneto-optical spectra for dipole-allowed optical transitions in the quantum dots. The calculations are carried out at temperature  $T = 0$ . Energy is measured in units of  $e^2/\epsilon l$ , where  $l$  is the magnetic length at magnetic field  $B = 5$  T, and  $\epsilon$  is the dielectric constant of the material. This energy unit is roughly  $60/\epsilon$  meV, which is 4.5 meV for GaAs material. The length parameter  $r_0$  is measured in units of magnetic length at  $B = 5$  T, which is approximately 11.5 nm. The other parameter  $V_0$  is also measured in units of  $e^2/\epsilon l$  at  $B = 5$  T. There are two possible dipole-allowed optical transitions given by  $L_z \rightarrow L_z \pm 1$  which correspond to the two possible circular polarization modes of the absorbed photon. We refer to these transition energies as  $E_{\pm}$  modes, respectively. For the non-interacting case, the ground state is always the lowest possible  $L_z$  state and, therefore, only the  $E_+$  mode is allowed. We emphasize that for a parabolic quantum dot system, the interacting and non-interacting magneto-optical spectra are identical (by virtue of the generalized Kohn's theorem). For the non-parabolic quantum dots on the other hand, as can be seen from Figs. 1 and 2, correlation effects are substantial in the magneto-optical spectra. In particular, the magneto-optical transition energies show the same kind of non-monotonic sharp structures (and jumps at particular *magic* magnetic field values) as the corresponding thermodynamic properties do. Any observation of non-monotonic behavior in the magneto-optical spectra of small quantum dots as a function of the external magnetic field, as shown in Figs. 1 and 2, will be rather strong direct evidence in support of correlation effects in quantum dot systems. The important point to note is that, while the *non-interacting* magneto-optical spectra of the non-parabolic dots studied here are qualitatively the same as that of the parabolic systems, the interacting spectra are *qualitatively* and strikingly different, as is obvious from the results shown in Figs. 1 and 2. The correlation effects produce striking non-monotonic features (manifested as spikes and jumps in Figs. 1 and 2 at various magic magnetic field values) associated with the sudden changes in the

ground states of the system (switching among various  $L_z$  values) as a function of the magnetic field arising from the competition between confinement and electron–electron interaction.

In summary, we have used the direct diagonalization technique in the lowest spin-split Landau level to calculate the elementary excitation spectra and the magneto-optical properties of small quantum dots (containing six electrons) with non-parabolic confinement potentials. Non-parabolic confinement, by allowing mixing between center of mass and relative coordinates, gives rise to substantial correlation effects on the dipole-allowed magneto-optical transition energies. This is in contrast to parabolically [4–6] confined quantum dot structures, where correlation effects cancel out in the magneto-optical spectra. For two different model confinement potentials, the quartic confinement and the flat-bottomed parabolic confinement, our calculated magneto-optical transition energies show correlation-induced non-monotonic behavior as a function of the external magnetic field. In particular, the calculated magneto-optical energies show correlation-driven sharp structures and jumps at various specific magnetic field values.

This work is supported in part by the National Science Foundation Materials Theory (DMR) program.

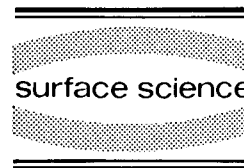
## 1. References

- [1] M.A. Kastner, Rev. Mod. Phys. 64 (1992) 849; C.W.J. Beenakker, H. van Houten and A.A.M. Staring, in: Single Charge Tunneling, Eds. H. Grabert and M.H. Devoret (Plenum, New York, 1991), and references therein.
- [2] R.C. Ashoori, H.L. Stormer, J.S. Weiner, L.N. Pfeiffer, K. Baldwin and K.W. West, Phys. Rev. Lett. 68 (1992) 3088, and preprint (1992).
- [3] R.E. Prange and S.S.M. Girvin, Eds., The Quantum Hall Effect (Springer, New York, 1990); T. Chakraborty and P. Pietilainen, The Fractional Quantum Hall Effect (Springer, Heidelberg, 1988).
- [4] P.A. Maksym and T. Chakraborty, Phys. Rev. Lett. 65 (1990) 108.
- [5] Q.P. Li, K. Karrai, S.K. Yip, S. Das Sarma and H.D. Drew, Phys. Rev. B 43 (1991) 11768; P. Bakshi, D.A. Broido and K. Kempa, Phys. Rev. B 42 (1990) 7416.
- [6] C. Sikorski and U. Merkt, Phys. Rev. Lett. 62 (1989) 2164; U. Merkt, Adv. Solid State Phys. 30 (1990) 77.
- [7] D. Pfannkuche and R.R. Gerhardts, Phys. Rev. B 44 (1991) 13132.
- [8] T. Chakraborty, V. Halonen and P. Pietilainen, Phys. Rev. B 43 (1991) 14289.



ELSEVIER

Surface Science 305 (1994) 610–614



## Quantum dots in tilted magnetic fields

B. Meurer <sup>\*,1</sup>, D. Heitmann <sup>2</sup>, K. Ploog <sup>3</sup>

*Max-Planck-Institut für Festkörperforschung, Heisenbergstrasse 1, D-70506 Stuttgart, Germany*

(Received 20 April 1993; accepted for publication 4 June 1993)

### Abstract

Arrays of field-effect confined quantum dots with diameters down to 100 nm have been prepared from  $\text{Al}_x\text{Ga}_{1-x}\text{As}/\text{GaAs}$  heterostructures. In far-infrared spectroscopy, transitions are induced between the 2–3 meV separated quantum levels of the lateral confinement. In tilted magnetic fields  $B$ , we observe a resonant coupling to states arising from the confinement in the growth direction. The level spacing in this  $z$ -direction is found to be only a few meV in our samples and thus comparable to the level spacing of the lateral confinement. The excitation spectrum that we observe is determined by the *total* magnetic field  $B$ . Thus the quantum dots are essentially *three-dimensional* objects. We observe a similar transition to a three-dimensional behavior in two-dimensional electron gases with small subband spacings.

Low-dimensional quantum confined electronic systems in semiconductors have recently attracted much interest. An ultimate limit is a quantum dot, an artificial atom, where few electrons are confined in all three dimensions [1–7]. Most systems so far have been realized by lateral structuring of a two-dimensional (2D) electronic system with various methods. In these systems, the lateral confinement of the electrons in the  $x$ - $y$  plane is usually assumed to be much smaller than

the one in the growth direction  $z$ . Therefore, the quantum dots are treated in a limit that we refer to as a “quantum-dot disk” in the following.

We report here on field-effect confined quantum dot arrays in GaAs, where both the lateral confinement energy and the confinement energy in the  $z$ -direction are typically several meV. This leads to interesting coupling effects between states confined in the  $z$ -direction and the quantum dot states confined in the lateral directions. In far-infrared (FIR) spectroscopy, transitions between the quantum levels of the lateral confinement are excited. In tilted magnetic fields  $B$ , we observe a resonant coupling with states in the growth direction. The experimental dispersion can be well described with the model of a three-dimensional harmonic atom, as calculated by Li et al. [8]. For magnetic fields above the coupling regime the resonance frequencies are determined by the total magnetic field, indicating that the

\* Corresponding author.

<sup>1</sup> Present address: Laboratoire de Physique de la Matière Condensée, Ecole Normale Supérieure, 24 rue Lhomond, F-75231 Paris Cedex 05, France.

<sup>2</sup> Institut für Angewandte Physik, Universität Hamburg, Jungiusstrasse 11, D-20355 Hamburg, Germany.

<sup>3</sup> Paul-Drude-Institut für Festkörperelektronik, Hausvogteiplatz 5–7, D-10117 Berlin, Germany.

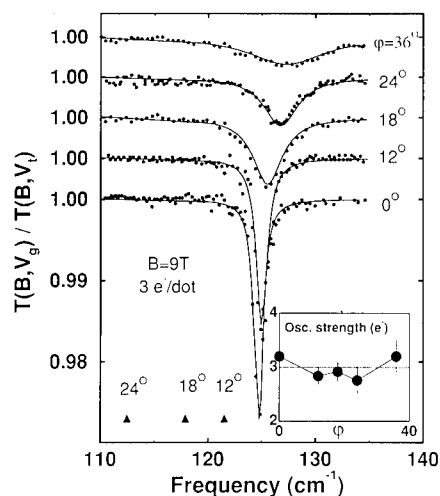


Fig. 1. Experimental FIR transmission spectra (symbols) and fits (solid lines) for quantum-dot sample no. 1 with  $a = 200$  nm at  $B = 9$  T and tilt angles  $\varphi$  up to  $36^\circ$ . The adjusted gate voltage  $V_g$  defines quantum dots with three electrons. The inset shows the integrated absorption strength in units of the electron number as a function of  $\varphi$ . The integrated absorption strength remains constant within the experimental error. The triangles mark the expected resonance frequency of a quantum-dot disk. (The expected resonance frequency of the quantum-dot disk for  $\varphi = 36^\circ$  is about  $\omega_r = 100$   $\text{cm}^{-1}$  and thus out of scope.) The spectral resolution is set to  $0.25$   $\text{cm}^{-1}$  and the temperature is  $T = 2.2$  K.

excitation of the quantum dots is three-dimensional.

The quantum-dot structures have been prepared starting from  $\text{Al}_{0.32}\text{Ga}_{0.68}\text{As}/\text{GaAs}$  heterostructures grown by molecular beam epitaxy. An additional Si  $\delta$ -doped layer was deposited at a distance of 330 nm below the interface. The  $\delta$ -layer is semitransparent for the FIR radiation and acts as a back gate to charge the dots. On top of the heterostructure, we prepared by holographic lithography a periodic photoresist dot array with periods  $a$  ranging from 500 nm down to 200 nm. A semitransparent NiCr front gate was then evaporated onto the photoresist structure. Contacts were alloyed outside the gate area to the  $\delta$ -doped back contact, so that via a negative gate voltage we could confine the electrons under the photoresist dots and vary the number of electrons [1,2,4,7]. The band bending at the position of the back gate results in systems with small energy separations in the  $z$ -direction. FIR transmission spectroscopy was carried out with a Fourier transform spectrometer at  $T = 2.2$  K. We recorded the normalized transmission of unpolarized radiation,  $T(V_g)/T(V_l)$ , for different mag-

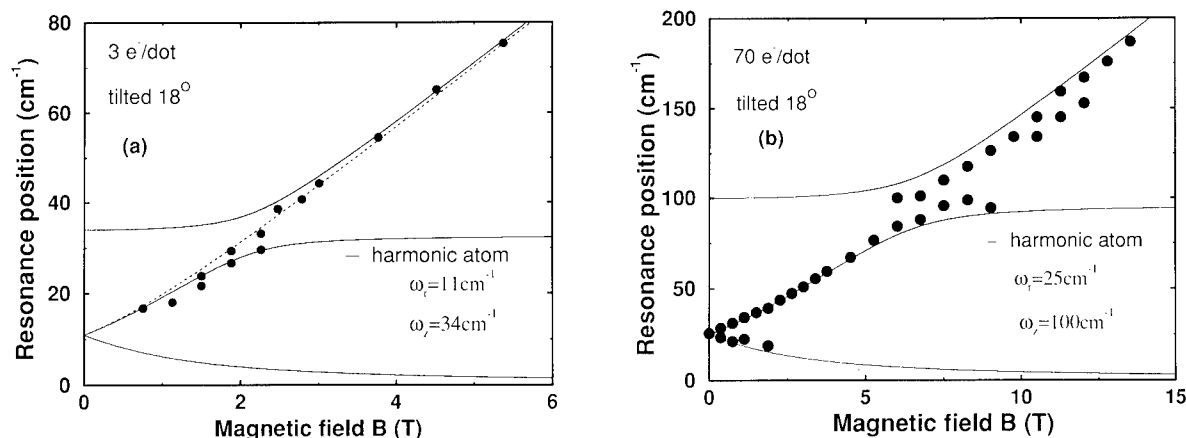


Fig. 2. (a) Magnetic field dispersion of the resonance frequencies (symbols) for sample no. 1 at fixed tilting angle  $\varphi = 18^\circ$ . The solid lines are calculated in the model of a harmonic atom with the confinement frequencies  $\omega_x = 11$   $\text{cm}^{-1}$  in the  $x$ - $y$  plane and  $\omega_z = 34$   $\text{cm}^{-1}$  in the  $z$ -direction. The dashed lines are the theoretical and experimental results at  $\varphi = 0^\circ$ . (Note that for the  $\omega^-$  mode, the dashed and solid curves are identical within the linewidth.) (b) In comparison, the results of sample no. 2 with  $a = 500$  nm and 70 electrons in the quantum dots are shown. For this sample we find  $\omega_x = 25$   $\text{cm}^{-1}$  and the best fits we obtained with an  $\omega_z = 100$   $\text{cm}^{-1}$ .



netic fields  $B$  and tilt angles  $\varphi$ .  $V_t$  is the threshold voltage of the dot system.

Fig. 1 shows FIR transmission spectra for a sample with a period of  $a = 200$  nm, labeled no. 1 in the following, at fixed magnetic field  $B = 9$  T and different tilt angles  $\varphi$ . The adjusted gate voltage  $V_g$  defines isolated dots with three electrons. The number of electrons is stabilized by a high Coulomb energy of about 15 meV in these small structures [7]. For  $B = 9$  T there is resonant absorption at  $\omega_r \approx 125$  cm<sup>-1</sup> with an amplitude of about 3% (for  $\varphi = 0^\circ$ ). For increasing tilt angle  $\varphi$ , the resonance shifts slightly to higher frequencies and broadens while the integrated absorption strength does not vary with  $\varphi$ . The nearly constant resonance frequency is a surprising observation. For a strong  $z$ -confinement, the quantum-dot disk limit, we would expect a decrease of the resonance frequency because of the smaller in-plane magnetic field. The expected cosine-law is indicated by triangles in Fig. 1 and does not at all describe the experiment.

The experimental magnetic field dispersions at  $\varphi = 0^\circ$  are shown as dashed lines in Fig. 2a. Such a dispersion has been observed previously [1,3,4,7]. It consists at  $B = 0$  of one resonance,  $\omega_r$ , which splits for  $B > 0$  into two resonances: one increases with increasing  $B$  and approaches the cyclotron frequency  $\omega_c = eB/m^*$  and the other decreases with  $B$ . This  $B$ -dispersion directly reflects transitions in the one-particle excitation spectrum of a two-dimensional parabolic confinement in a magnetic field [9]. With regard to the selection rules [1,10], the excitation frequencies are:

$$\omega_r^\pm(B) = \pm \omega_c/2 + \sqrt{(\omega_c/2)^2 + \omega_r^2}. \quad (1)$$

This result describes well the dispersion at  $\varphi = 0^\circ$ . The splitting at small magnetic fields in the few electron system is caused by deviations of the external lateral confinement potential from the parabolic shape [11].

If we follow the FIR resonances at a fixed value of  $\varphi = 18^\circ$  in their dependence on the magnetic field  $B$ , we find the dispersion marked by symbols (●) in Fig. 2a. In comparison, Fig. 2b shows the result of sample no. 2 with a period

$a = 500$  nm and 70 electrons in the quantum dots adjusted. Both samples show a splitting of the dispersion, which is caused by a resonant interaction with states confined in the  $z$ -direction. It increases with increasing  $\varphi$  and resembles the resonant subband-Landau-level coupling (RSLC) previously observed in tilted-field cyclotron resonance (CR) experiments on 2D systems [12], and similarly as an anti-crossing behavior in 1D systems [13].

To explain the experimentally observed behavior, we have chosen the model of a three-dimensional quantum-dot atom, as it has been proposed by Li et al. [8]. They calculated the resonance frequencies in the form of a cubic equation in  $\omega^2$ . For a circular symmetry in the  $x$ - $y$  plane this equation reads:

$$\omega^6 - \omega^4(\omega_c^2 + 2\omega_r^2 + \omega_z^2) + \omega^2\{\omega_c^2[\omega_r^2 \sin^2(\varphi) + \omega_z^2 \cos^2(\varphi)] + \omega_r^2(\omega_r^2 + \omega_z^2)\} - \omega_r^4\omega_z^2 = 0, \quad (2)$$

where  $\omega_r$  is the resonance frequency of the lateral confinement,  $\omega_z$  is the resonance frequency of the confinement in the  $z$ -direction and  $\varphi$  is the tilt angle. We have solved this equation numerically, and we have chosen  $\omega_z$  to obtain a good fit of the data. The solid lines in Figs. 2a and 2b mark the results of the fits. For sample no. 1 with  $\omega_r = 11$  cm<sup>-1</sup> we find an  $\omega_z = 34$  cm<sup>-1</sup> and for sample no. 2 with  $\omega_r = 25$  cm<sup>-1</sup> an  $\omega_z = 100$  cm<sup>-1</sup>. Qualitatively, the model of the parabolic atom describes well the observed frequency dispersions of the quantum dots in tilted magnetic fields. In particular it describes that at large fields, the resonance frequencies are determined by the total rather than the perpendicular magnetic field. The model does not describe the magnitude in  $\Delta\omega$  of the splitting and an additional structure (Fig. 2b at about  $\omega = 150$  cm<sup>-1</sup>), which is probably caused by a resonant interaction with a next higher state in the  $z$ -direction. The assumption of a harmonic potential in the  $z$ -direction is obviously too simple to describe these details, whereas in general, the applied model explains well all important features of the experimental  $B$ -dispersions. Thus we can con-

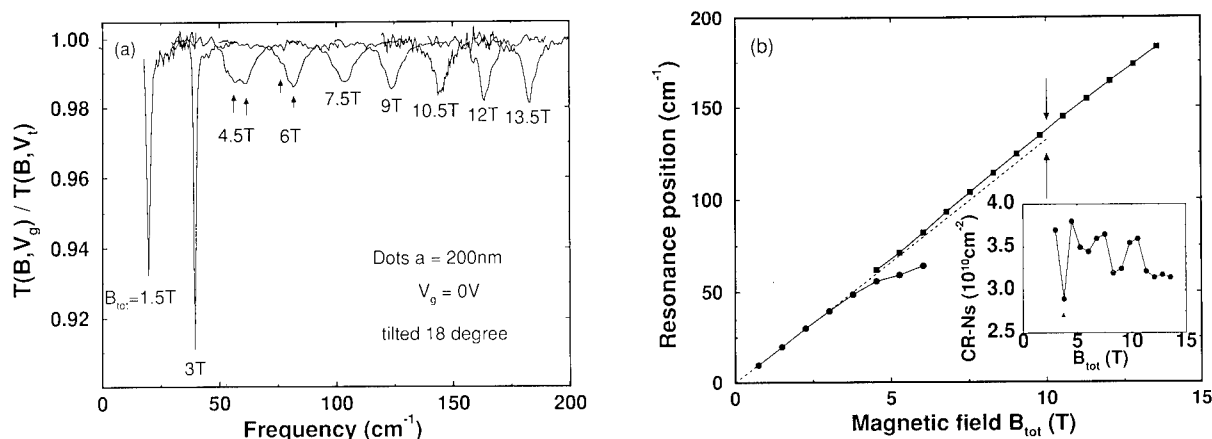


Fig. 3. (a) Experimental cyclotron resonance spectra of sample no. 1 at  $\varphi = 18^\circ$  and  $V_g = 0$ . The arrows ( $\uparrow$ ) mark the resonant coupling regime with the 2D-intersubband resonance at  $\omega_z \approx 65 \text{ cm}^{-1}$ . (b) Magnetic field dispersion of the resonances in (a). Above the coupling, the cyclotron frequency depends on the total magnetic field and not on the component in the 2D-plane (dashed line).

clude that the excitation of our quantum dots is indeed *three-dimensional*.

An additional experimental observation in Fig. 1 is the broadening of the resonances, that we believe to be intrinsic. CR in 2D systems has a smaller linewidth at  $\varphi = 90^\circ$  [14] and in tilted fields two excitations, a 3D-CR and a 2D inter-subband resonance (ISR) are possible [15]. If, as in our experiments, three-dimensional motion of electrons is possible, the resonance frequency depends on the center coordinate of the motion which leads to a broadening of the experimental spectra.

In the following, we will show that also in 2D-systems with small intersubband spacings, a transition to a three-dimensional excitation becomes observable. The small subband spacings were realized in the same heterostructures with back gate layer that were used for defining the quantum dot systems. By applying a certain gate voltage during cool down, sample no. 1 (from above) had a 2D-density of only  $N_s = 3.5 \times 10^{10} \text{ cm}^{-2}$  at  $T = 2.2 \text{ K}$ , as determined from the integrated absorption strength of the CR. At  $V_g = 0$  the system is practically 2D. Fig. 3 shows (a) the cyclotron resonance spectra at  $\varphi = 18^\circ$  and (b) the corresponding  $B$ -dispersion for sample no. 1 at  $V_g = 0$ , where no quantum dots are formed. Below the coupling regime with the excited sub-

band, we observe a CR with a linewidth  $b$  of about only  $1 \text{ cm}^{-1}$ . It drops in frequency with the expected  $\cos(\varphi)$  law. At about  $65 \text{ cm}^{-1}$ , we observe the resonant subband-Landau-level coupling. Above the coupling, the resonance frequency is independent of  $\varphi$  showing that the excitation is three-dimensional. Similar transitions were reported for 2D-systems in wide parabolic quantum wells [16], where the intersubband spacings are also very small, and in luminescence experiments on Be-doped 1D-systems [17].

In summary, we have presented FIR transmission experiments on quantum dots in tilted magnetic fields. The quantum-dot systems show a resonant interaction with states confined in the growth direction from which we can determine the level spacing in the  $z$ -direction. The level spacing turns out to be comparable with the one in the lateral direction. Thus we can excite a three-dimensional motion in the quantum dots. This is manifested in the observation that at large magnetic fields the dispersion of the resonance frequencies depends on the total rather than on the perpendicular component of the magnetic field. We observe a similar behaviour in 2D-electron gases with small subband spacings.

We wish to acknowledge most useful discussions with Daniela Pfannkuche, R.R. Gerhardt

and V. Fal'ko and with U. Merkt from Hamburg University. We thank R. Nötzel, A. Fischer and M. Hauser for the MBE growth of our samples, H. Lage and C. Lange for expert help with the preparation of the dots and Y. Guldner from the Ecole Normale Supérieure for a critical reading of the manuscript. This work was supported by the Bundesministerium für Forschung und Technologie. One of us (B.M.) would like to acknowledge financial support from the European Union.

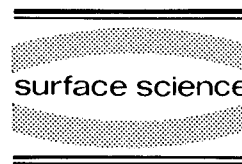
## 1. References

- [1] Ch. Sikorski and U. Merkt, *Phys. Rev. Lett.* 62 (1989) 2164.
- [2] W. Hansen, T.P. Smith, III, K.Y. Lee, J.A. Brum, C.M. Knoedler, J.M. Hong and D.P. Kern, *Phys. Rev. Lett.* 62 (1989) 2168.
- [3] T. Demel, D. Heitmann, P. Grambow and K. Ploog, *Phys. Rev. Lett.* 64 (1990) 788.
- [4] A. Lorke, J.P. Kotthaus and K. Ploog, *Phys. Rev. Lett.* 64 (1990) 2559.
- [5] P.L. McEuen, E.B. Foxman, U. Meirav, M.A. Kastner, Y. Meir and N.S. Wingreen, *Phys. Rev. Lett.* 66 (1991) 1926.
- [6] R.C. Ashoori, H.L. Stormer, J.S. Weiner, L.N. Pfeiffer, S.J. Pearton, K.W. Baldwin and K.W. West, *Phys. Rev. Lett.* 68 (1992) 3088.
- [7] B. Meurer, D. Heitmann and K. Ploog, *Phys. Rev. Lett.* 68 (1992) 1371.
- [8] Q.P. Li, K. Karrai, S.K. Yip, S. Das Sarma and H.D. Drew, *Phys. Rev. B* 43 (1991) 5151.
- [9] V. Fock, *Z. Phys.* 47 (1928) 446.
- [10] U. Merkt, Ch. Sikorski and J. Alsmeier, in: *Spectroscopy of Semiconductor Microstructures*, Eds. G. Fasol, A. Fasolino and P. Lugli (Plenum, New York, 1989) p. 89.
- [11] D. Pfannkuche and R.R. Gerhardt, *Phys. Rev. B* 44 (1991) 5887.
- [12] Z. Schlesinger, J.C.M. Hwang and S.J. Allen, *Phys. Rev. B* 50 (1983) 2098.
- [13] K. Kern, D. Heitmann, R.R. Gerhardt, P. Grambow, Y.H. Zhang and K. Ploog, *Phys. Rev. B* 44 (1991) 1139.
- [14] U. Merkt, *Phys. Rev. B* 32 (1985) 6699.
- [15] S. Oelting, U. Merkt and J.P. Kotthaus, *Surf. Sci.* 170 (1986) 402.
- [16] C. Kutter, V. Chitta, J.C. Maan, V.I. Fal'ko, M.L. Leadbeater, M. Henini and L. Eaves, *Phys. Rev. B* 45 (1992) 8749.
- [17] I.V. Kukushkin, V.I. Fal'ko, K. von Klitzing, K. Ploog and D. Heitmann, *JETP Lett.* 53 (1991) 335.



ELSEVIER

Surface Science 305 (1994) 615–619



## The influence of reduced dimensionality on the spin-splitting in GaAlAs/GaAs quantum wires

J. Wróbel <sup>\*,a,b,f</sup>, F. Kuchar <sup>c</sup>, K. Ismail <sup>d</sup>, K.Y. Lee <sup>d</sup>, H. Nickel <sup>e</sup>, W. Schlapp <sup>e</sup>, G. Grabecki <sup>f</sup>, T. Dietl <sup>f</sup>

<sup>a</sup> Institut für Festkörperphysik, Universität, A-1090 Wien, Austria

<sup>b</sup> L. Boltzmann Institut für Festkörperphysik, Kopernikusgasse 15, A-1060 Wien, Austria

<sup>c</sup> Institut für Physik, Montanuniversität, A-8700 Leoben, Austria

<sup>d</sup> IBM Thomas J. Watson Research Center, Yorktown Heights, NY 10598, USA

<sup>e</sup> Forschungsinstitut der Deutschen Bundespost, D-6100 Darmstadt, Germany

<sup>f</sup> Institute of Physics Polish Academy of Sciences, PL 02-668 Warszawa, Poland

(Received 21 April 1993; accepted for publication 1 July 1993)

### Abstract

We study the role of reduced dimensionality on the quantum magnetotransport in quasi-ballistic GaAlAs/GaAs quantum wires. We observe strong “antiresonances” in  $G(B)$ , related to the backscattering of edge currents induced by disorder. We find that the spin-related conductance plateaux are strongly suppressed due to the many-body effects. In the device with low carrier density we have been able to induce the spin-splitting and observe the  $e^2/h$  plateau in high magnetic fields. From the temperature dependence of this plateau we show that the  $g$ -factor in wires is indeed much smaller than in the 2D case. We find also that the scattering rate at the “antiresonance” depends linearly on the temperature.

The reduced dimensionality of the electron gas has a strong effect on the quantum magnetotransport in quasi-ballistic 1D structures. For example the increased role of the edge states can cause two types of phenomena not observed in 2D systems. First, at magnetic fields for which the Fermi level is close to a new 1D-subband threshold, a pronounced conductance dip (“antiresonance” [1]) should be observed, since the states carrying current in the opposite directions are close to the center of the wire and the impurity

induced backscattering then is strong [2]. The second effect is connected with the total many-body energy of the 1D electron gas. In wires, the positive kinetic energy of edge-skipping electrons cannot be neglected as compared to the negative Coulombic exchange term. As a result, in 1D systems the *non*-spin-split quantum state can be energetically favorable [3], as opposed to the 2D case [4]. Therefore, the exchange enhancement of the  $g$ -factor, under certain conditions, is absent and such an effect should be observable in the transport properties. To our knowledge, however, most of the conductance versus magnetic field data were reported for short ( $\leq 1 \mu\text{m}$ ) point

\* Corresponding author.

contacts, whereas the described theories apply only to long (or strictly speaking – infinitely long) quantum wires.

In this work, we verify both of the above theoretical predictions by comparing the magnetotransport properties of a wide 2D sample with data obtained for narrow and relatively long quasi-1D structures. We studied non-gated GaAlAs/GaAs heterojunction wires of length  $L = 20 \mu\text{m}$  and geometric width  $W = 0.6$  and  $0.8 \mu\text{m}$  (samples 1 and 2, respectively), in magnetic fields  $B$  up to 13 T. We measured the two-terminal conductance  $G$  in the temperature range 0.04–5 K, using a He-3 cryostat for the higher temperatures and a dilution refrigerator for the lowest temperatures.  $G$  as a function of magnetic field  $B$  was recorded using standard lock-in techniques with ac currents of 1–10 nA at 17–313 Hz.

Our two-terminal devices were formed by e-beam lithography and prepared by a deep etching technique from a GaAlAs/GaAs heterostructure (2D electron density  $n_s = 4.1 \times 10^{11} \text{ cm}^{-2}$  and mobility  $\mu^{2D} \approx 1 \times 10^6 \text{ cm}^2/\text{V} \cdot \text{s}$ ,  $T = 4 \text{ K}$ ). The black lines in the insert of Fig. 1 are etched grooves defining the wire. The large metallic contacts (shaded areas) are close to the wire, the distance being of the order of the device width. The series resistance is negligibly small since the quantization of  $G$  at  $2e^2/h$  is exact.

Nevertheless, the mobility in wires was reduced as compared to the 2D case; the estimated values were within the range  $\sim (0.25\text{--}0.5) \times 10^6 \text{ cm}^2/\text{V} \cdot \text{s}$ , which correspond to a mean free path  $l$  of several microns. To compare our Q1D data with the pure 2D behavior, we measured also the *two-terminal* conductance of a wide ( $W = 2 \text{ mm}$ ,  $L/W = 4$ ) heterostructure sample with  $n_s$  and  $\mu^{2D}$  comparable to sample 2.

The real width of the electron gas in our wires was smaller than the lithographic one. This is due to a sidewall depletion region, which reduces the physical width of the device [5]. In order to reduce the depletion regions and make sample 1 conducting, it was illuminated with a red light emitting diode (LED).

To determine the sample parameters, we analyzed the magnetoconductance oscillations regarding depopulation of the hybrid magnetoelec-

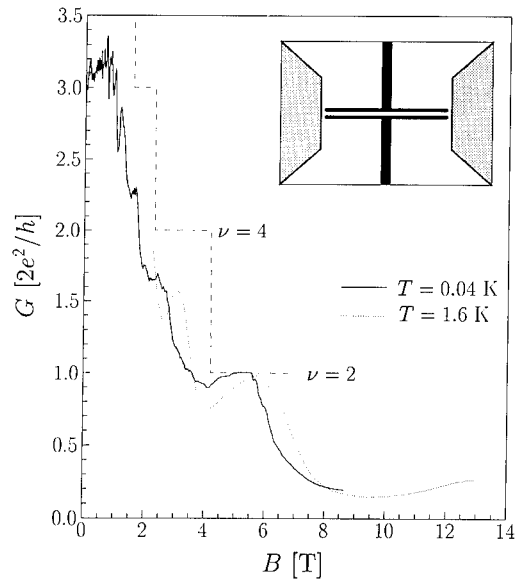


Fig. 1.  $G(B)$  for sample 1 at  $T = 0.04 \text{ K}$ ; estimated parameters:  $W = 0.30 \pm 0.03 \mu\text{m}$ ,  $n_L \approx 7 \times 10^6 \text{ cm}^{-1}$ ,  $\hbar\omega_0 \approx 0.65 \text{ meV}$ ,  $\mu^{2D} \approx 0.42 \times 10^6 \text{ cm}^2/\text{V} \cdot \text{s}$ . The dashed line was calculated for an idealized ballistic sample (at  $T = 0 \text{ K}$ ) assuming parabolic confinement and the parameters given above. The dotted line shows high field data, recorded at  $T = 1.6 \text{ K}$ , for slightly higher ( $n_L \approx 10 \times 10^6 \text{ cm}^{-1}$ ) carrier density. Insert: sample design (details see text).

tric levels as a function of magnetic field. We plotted the level indices against  $1/B$  ( $B$  corresponding to minima of  $G$ ) and fitted these data to the formula derived in Ref. [6] for a parabolic confinement. As fit parameters, we obtained the 1D subband separation  $\hbar\omega_0$  and linear density  $n_L$ . From the high magnetic field limit we obtained the 2D density  $n_s$ . The width of the wire was then estimated as  $W = n_L/n_s$ , enabling us to infer other parameters, e.g., the mobility at  $B = 0$ . The values of the parameters obtained from this analysis are given in the figure captions.

Fig. 1 shows the magnetoconductance of sample 1, measured after illumination with the red LED). For comparison, we calculated the magnetoconductance of an ideal ballistic wire, assuming the parabolic confinement potential. Results are shown by the dashed line. Since an external field lowers the number of occupied subbands, according to the Landauer–Büttiker formula [7] it gives a steplike decrease of  $G$  for an ideal sample.

In the real sample with disorder, the conductance at low magnetic fields is strongly reduced as compared to the ballistic case due to the impurity-induced backscattering within the wire [5]. At higher fields, however, the scattering is suppressed, and around  $B = 5$  T there is an exact plateau corresponding to  $G = 1$ . Interestingly, near the transitions from one magnetoelectric subband to another, minima in the conductance (the “antiresonances”) are observed. Around those minima, the aperiodic conductance fluctuations are visible at our lowest temperatures. They are presumably due to the quantum interference effects connected with the back and forth scattering of electrons.

Such a magnetic field behavior of a disordered wire was recently theoretically predicted by Kinaret and Lee [2]. They considered the *two-terminal* conductance (at  $T = 0$ ) as a transmission problem for edge currents. At low magnetic fields, edge states are wide and electrons can easily scatter. As a result, the conductance is reduced. For high magnetic fields the backscattering is strong when the Fermi energy reaches the bottom of one of the quantized levels. This is because the states of the higher subband become located near the center of the wire and electrons can more easily scatter across the sample to the opposite edge (and opposite direction of motion). This produces the “antiresonance” in  $G$  at the magnetic field value for which, in an ideal sample, the perfect step would be seen. The measured conductance is still reduced just after decoupling of the upper channel, presumably due to the backscattering via localized edge-type currents encircling the center of the wire. For still higher fields the flat plateau should reappear, as it is indeed observed in the experiment for  $B > 5$  T.

Let us consider now the spin-splitting problem. Clearly, in Fig. 1 there is no evidence for the antiresonance/plateau structure corresponding to  $G = 1.5$  ( $\nu = 3$ ) and even more important to  $G = 0.5$  ( $\nu = 1$ ). We attribute it to the suppression of spin-splitting in 1D devices, as predicted in Ref. [3]. For our sample at  $B > 6$  T the conductance continues to decrease, whereas if the spin-splitting were large (as in 2D), one should observe a wide and well developed plateau with

value  $e^2/h$ . To compare our data with theory, we calculate the total many-body energy  $E_{\text{tot}}$  of a GaAlAs/GaAs heterojunction wire using Eqs. (12) and (13) from Ref. [3], where it is assumed that only the lowest (degenerate or not) level is occupied and that the confinement is parabolic. For a given electron density  $n_L$  the concept of a critical magnetic field  $B_{\text{cr}}$  can be introduced. For  $B < B_{\text{cr}}$  the spin-splitting is suppressed. With increasing field the kinetic energy of carriers is reduced, the exchange and Zeeman energies start to dominate and the transition to a spin-split phase occurs at  $B = B_{\text{cr}}$ . For smaller level separation ( $\hbar\omega_0$ ) or smaller  $n_L$  such a phase transition occurs at a smaller  $B_{\text{cr}}$ .

For sample 1 we have  $B_{\text{cr}} \approx 15$ –20 T corresponding to  $\hbar\omega_0 = 0.65$  meV and  $n_L = (7$ – $10) \times 10^6 \text{ cm}^{-1}$ . This explains why the spin-splitting is not observed at lower fields. Note, however, a weak increase of  $G$  visible above 10 T (at  $T = 1.6$  K). Does it mean that the spin-splitting reappears when  $B$  approaches  $B_{\text{cr}}$ ? To check this we need a sample with smaller critical field.

Fig. 2 shows data for sample 2 ( $W_{\text{geo}} = 0.8 \text{ }\mu\text{m}$ ), which was *not illuminated* before the measurement. The linear carrier density and the level separation  $\hbar\omega_0$  are smaller than in sample 1; however, the physical widths are almost the same.

Let us first consider the data recorded at the lowest temperature ( $T = 0.35$  K). The general behavior of  $G(B)$  is the same as for sample 1. As a function of magnetic field, we observed the strong antiresonances at the magnetoelectric subband onsets, but not for  $G = 1.5$ . For  $B > 3.7$  T the conductance decreases below 0.5; however, at higher fields the wide plateau corresponding to  $\nu = 1$  develops. For sample 2, theory gives  $B_{\text{cr}} \approx 9$  T, which is still above but close to fields where the  $\nu = 1$  plateau reappears in the experiment.

Is the assumption about the quenching of spin-splitting really necessary to explain our data? One might argue that the  $g$ -factor in wires shows, in fact, the same oscillating behavior as in a 2D electron gas, and therefore both spin states can be simultaneously decoupled from the current/voltage probes [8]. Even though it might be true for smaller fields and large filling factors, the assumption of reduced spin-splitting is still neces-

sary to explain the high field region where only one channel is occupied and the theory of Kinaret and Lee applies. We think that the small-spin splitting in the 1D case can be directly inferred from the temperature dependence of the high-field magnetoconductance data.

For this purpose we analyzed the temperature dependence of the reflection coefficient  $\mathcal{R} = 0.5 - G$  in the center of the  $\nu = 1$  plateau (at  $B = 7.3$  T). For  $T \lesssim 1$  K this dependence is rather weak; however, at higher  $T$  the conductance decreases strongly, and  $\mathcal{R}$  shows approximately an activated behavior. Since we are at the center of a plateau, the Fermi level is already located between the spin-split levels. The electrons which are thermally activated to the upper empty subband are scattered back. This might explain the activated behavior of the reflection coefficient. A similar analysis can be applied to the 2D sample. The insert in Fig. 2 shows the two-terminal conductance of the wide 2D device for several temperatures. Note the much weaker dependence of

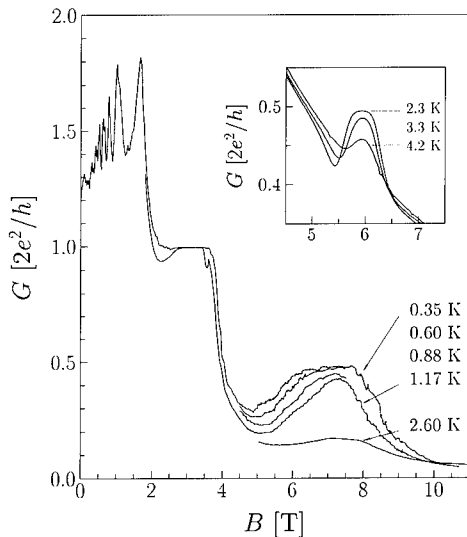


Fig. 2.  $G(B)$  for sample 2 at  $T = 0.35, 0.60, 0.88, 1.17$  and  $2.6$  K; estimated parameters:  $W \approx 0.33 \pm 0.03 \mu\text{m}$ ,  $n_L = (5.0 \pm 0.2) \times 10^6 \text{ cm}^{-1}$ ,  $\hbar\omega_0 = 0.46 \pm 0.2 \text{ meV}$ ,  $\mu^{2D} \approx 0.24 \times 10^6 \text{ cm}^2/\text{V}\cdot\text{s}$ . The insert shows data for the 2D sample with  $n_s = 1.4 \times 10^{11} \text{ cm}^{-2}$ . Note the expanded scales of both  $B$  and  $G$  axes, as compared to the main figure. Near  $5$  T, the temperature dependence of the 2D data is opposite to that of the 1D data.

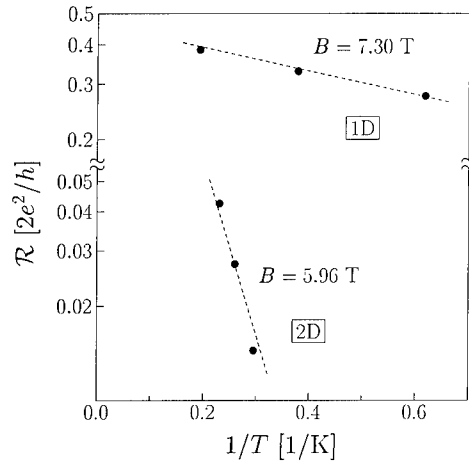


Fig. 3.  $\mathcal{R} = 0.5 - G$  vs  $1/T$  for 1D and 2D samples presented in Fig. 2;  $\mathcal{R}$  is plotted on a logarithmic scale. Conductance was taken for  $B$  corresponding to the center of the  $\nu = 1$  plateaux (dashed lines are guides to the eye).

$G$  at the center of plateau. This is demonstrated in the next figure.

Fig. 3 shows  $\ln \mathcal{R}$  versus  $1/T$  measured at  $T = 1.6, 2.6$  and  $5$  K for sample 2 (in Fig. 2 data at  $2.6$  K are shown). Also, the corresponding data for the 2D sample are presented. In our interpretation, the slopes of dashed lines ( $E_R$ ) should be proportional to the energy separation between the spin-split levels. The large quantitative difference in its values ( $E_R \approx 1$  and  $17$  K, respectively) shows clearly the much smaller spin-splitting in the 1D sample, as compared to the 2D device. In terms of  $g$ -factor,  $2 E_R$  corresponds to  $|g^*| \approx 8.2$  (2D at  $B = 5.95$  T) and to  $|g^*| \approx 0.4$  (1D at  $B = 7.3$  T).

Another large difference, in this case also qualitative, is visible at magnetic fields below the quantized plateaux. In wires the “antiresonances” are apparently deeper at higher temperatures (see also Fig. 1), whereas in the 2D case the trend is opposite. Let us study the temperature dependence of the conductance minima in more detail, since it might give more insight to the mechanisms responsible for backscattering in quantum wires.

At magnetic fields just below  $6$  T (Fig. 2), the Fermi level must be located close to the bottom of the upper occupied subband. Interestingly,  $G$

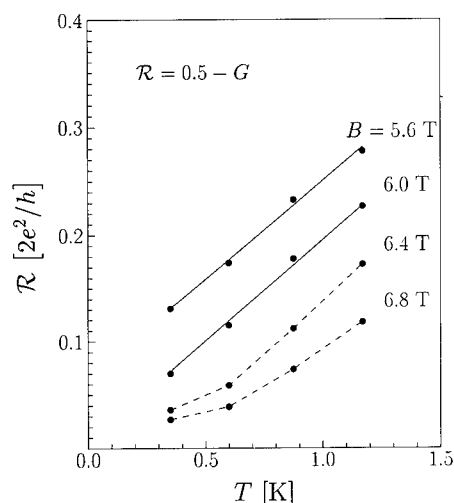


Fig. 4.  $\mathcal{R} = 0.5 - G$  vs temperature for  $T \leq 1.17$  K. Lines are guides to the eye. Data were taken at the “antiresonance” (solid lines) and for magnetic fields closer to the quantized plateau (dashed lines).

shows here a much stronger temperature dependence for  $T \leq 1$  K, as compared to the center of the plateau. Fig. 4 shows  $\mathcal{R}$  versus temperature for  $T \leq 1.17$  K. At magnetic fields corresponding to the “antiresonance”  $\mathcal{R}$  depends linearly on the temperature. Note also, that the straight solid line for  $B = 5.6$  T extrapolates to a non-zero value for  $T \rightarrow 0$ . It indicates that the “antiresonances” exist also at  $T = 0$  when the scattering is purely elastic. At higher magnetic fields, the conductance approaches the quantized plateau and both the scattering and the temperature dependencies are weaker at lowest  $T$  (dashed lines).

The same temperature dependence was observed for higher, light induced, electron densities in the device. Furthermore,  $\mathcal{R}$  was proportional to  $T$  also for other conductance minima, indicating that such a behavior is typical for the “antiresonances”. As it is known, in 3D metals the inverse of the momentum relaxation time is proportional to  $T$  for acoustic phonon scattering. We think that also in our case the linear temperature dependence of the scattering rate is due to

the nonelastic interaction with acoustic phonons. In other words, the phonon emission makes the “antiresonance” deeper with increasing  $T$ . Such a mechanism, involving the impurity-assisted inter- and intraband emission of acoustic phonons was recently discussed in Ref. [9].

To separate the role of disorder from the spin-related properties, we measured also  $G(B)$  of a shorter ( $L = 1.5 \mu\text{m}$ ,  $W_{\text{geo}} = 0.4 \mu\text{m}$ ) gated wire. The preliminary results obtained for  $T = 1.6$ – $4.2$  K show that also here the spin-related conductance plateaux are strongly suppressed; however, the temperature dependence of  $G$  is weaker as compared to the long ( $L = 20 \mu\text{m}$ ) samples. Furthermore, the conductance “antiresonances” are not observed, as should be expected in this nearly disorder free sample.

In conclusion, the high field two-terminal conductance of a quantum wire is not just a result of  $\sigma_{xx}$  and  $\sigma_{xy}$  conductivity tensor component mixing. The strong backscattering and large temperature dependence show the influence of reduced dimensionality on the spin properties of 1D systems.

This work was supported by the “Bundesministerium für Wissenschaft und Forschung”, Austria, grant no. 30.405/3 and 45.283/2.

## 1. References

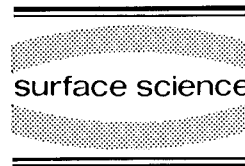
- [1] B. Kramer, J. Mašek, V. Špička and B. Velický, Surf. Sci. 229 (1990) 316.
- [2] J.M. Kinaret and P.A. Lee, Phys. Rev. B 43 (1991) 3847.
- [3] J.M. Kinaret and P.A. Lee, Phys. Rev. B 42 (1990) 11768.
- [4] T. Ando and Y. Uemura, J. Phys. Soc. Jpn. 37 (1974) 1044.
- [5] J. Wróbel, F. Kuchar, K. Ismail, K.Y. Lee, H. Nickel and W. Schlapp, Surf. Sci. 263 (1992) 261.
- [6] J.F. Weisz and K.-F. Berggren, Phys. Rev. B 40 (1989) 1325.
- [7] M. Büttiker, Phys. Rev. Lett. 57 (1986) 1761.
- [8] S. Komiyama, H. Nii, M. Ohsawa, S. Fukatsu, Y. Shiraki, R. Itoh and H. Toyoshima, Solid State Commun. 80 (1991) 157.
- [9] T. Martin and S. Feng, Phys. Rev. B 44 (1991) 9084.





ELSEVIER

Surface Science 305 (1994) 620–623



# Determination of the quantum wire potential and hot electron spectroscopy using point contacts

G. Fasol<sup>a</sup>, Y. Nagamune<sup>b</sup>, J. Motohisa<sup>a</sup>, H. Sakaki<sup>a,b</sup>

<sup>a</sup> ERATO Quantum Wave Project, 4-6-1 Komaba, Meguro-ku, Tokyo 153, Japan

<sup>b</sup> Research Center for Advanced Science and Technology, 4-6-1 Komaba, Meguro-ku, Tokyo 153, Japan

(Received 19 April 1993; accepted for publication 23 June 1993)

## Abstract

The internal potential seen by electrons within the quantum wire region of split-gate point contacts is determined using the thermal spread of the electron distribution function as an “internal reference”. The determination of the internal potential is used to analyze the energy distribution of hot electrons propagating between two quantum point contacts spaced distances up to 17  $\mu\text{m}$  apart. Even for a spacing of 17  $\mu\text{m}$  there is evidence that the electrons have not reached thermal equilibrium after propagating for this length.

Hot electron transport, and hot electron cooling, are both of great importance and have been investigated intensively using optical and transport methods. Transport techniques have been used for hot electron spectroscopy in transistor structures both for structures where electrons propagate perpendicular to epitaxial growth planes as well as for structures where transport is parallel to the growth planes (see Ref. [1]). In the latter case split-gate quantum point contacts or gates are used to analyze the electron energy distribution. One of the major obstacles in this type of transport spectroscopy is to determine the “internal potential” seen by electrons inside the detector structure, i.e. to calibrate the spectrometer. In Ref. [2] this has been done by calibrating against the LO phonon frequency, which is well known, while in Ref. [3] magnetic focussing was used.

In the present work we analyze hot electron transport over long distances using spectrometer

structures consisting of two separated split-gate quantum point contacts [4]. In order to perform spectrometry, the external voltage applied to the gate electrodes has to be related to the “internal” potential seen by electrons inside the microstructure. The thermal spread of the electron distribution is used here as an internal reference to determine the “internal” potential.

In the present work, we use the thermal spread of the electron Fermi-distribution as the internal standard of energy. This method is schematically illustrated in Fig. 1. We use the assumptions of the Landauer–Büttiker transport theory [5], which can be extended to finite electron energy distributions and finite temperatures (see, e.g. Ref. [6]). We assume that electrons are emitted from the right hand and left hand side electrodes according to their thermal distributions, and we neglect dissipation within the point contact “wires”. The total current is determined by the difference between the current moving left and the current moving right. Note that the famous Landauer–Büttiker formula comes in two ver-

\* Corresponding author. Fax: +81 (3) 3466-8308.

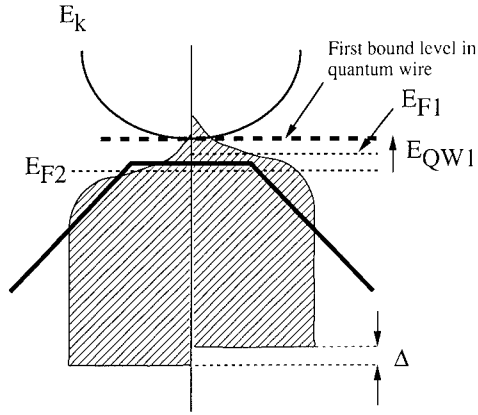


Fig. 1. Schematic energy diagram of a quantum point contact, as used here for injection and detection of carriers.

sions: a “two-point-version” and a “four-point-version”. Since our contacts are far away from the obstruction the two-point-version is applicable. Thus we obtain for the current  $I$  through a quantum point contact, as shown in Fig. 1:

$$I = \int_{E_{QW1}}^{\infty} dE e \left[ v_E \frac{dn}{dE} \right] T(E) \quad (1)$$

$$\times \left[ \frac{1}{\exp(\beta(E - e\Delta) + 1)} - \frac{1}{\exp(\beta E + 1)} \right].$$

We assume that the transmission factor  $T(E)$  is independent of  $E$  in the region we study, and set  $T(E) \approx \Gamma$ . We estimate  $\Gamma \approx 0.8$  from the magnitude of the conductivity at the plateau of the quantum point contact characteristics. The integration over energy in Eq. 2 can be performed easily. We assume that only the lowest conduction level within the constriction contributes to transport and we obtain for the conductivity  $G$

$$G = \Gamma \frac{2e^2}{h} \left[ \frac{1}{\exp(\beta E_{QW1}) + 1} \right]. \quad (2)$$

Thus the separation of the first bound level in the quantum point contact can be determined with reference to the Fermi level in the surrounding 2D “contact” area as long as only one subband is contributing to the transport.

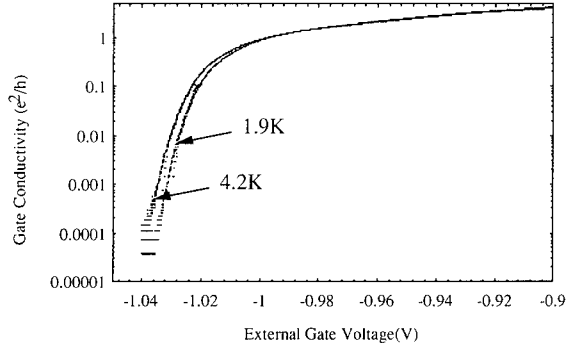


Fig. 2. Conductance of a quantum point contact in the low transmission region. The characteristic shows strong temperature dependence, which we use here to deduce information about the position of the first bound level with respect to the Fermi level in the base region of our structure.

The spectrometer structures were fabricated using electron beam epitaxy onto MBE grown GaAs/Al<sub>x</sub>Ga<sub>1-x</sub>As modulation doped heterostructures. Hot electron spectrometers were made, consisting of two-point contacts formed by split-gates separated by distances between 2 and 18  $\mu\text{m}$ . The gap between the electrodes, where the point contacts are formed, is 0.25  $\mu\text{m}$ .

Fig. 2 shows measurements of the conductivity of the drain-side split-gate point contact as a function of externally applied gate voltage. It can be seen that the conductivity decreases approximately exponentially as the applied voltage is increased into the total cut-off region. The figure shows a measurement for temperatures of 4.2 and 1.9 K. The temperature dependence indi-

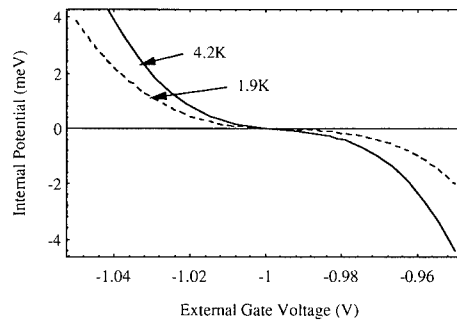


Fig. 3. Position of the first bound level in a quantum point contact with respect to the Fermi level in the base region as a function of the voltage applied externally to the gate.

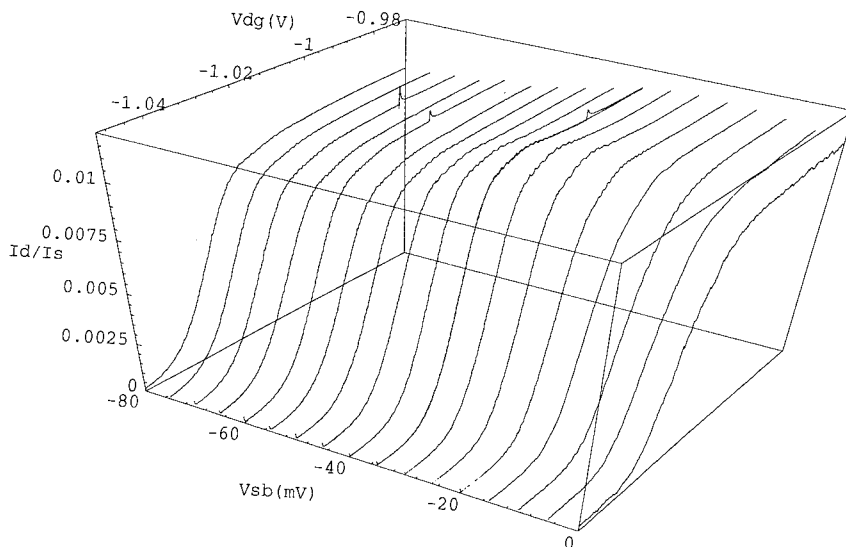


Fig. 4. Current transfer ratio  $I_d/I_s$  as a function of externally applied drain gate voltage  $V_{dg}$  for different source–base bias voltages  $V_{sb}$ . The temperature is 4.2 K, source–drain separation is 17.84  $\mu\text{m}$ , carrier density is  $0.34 \times 10^{12} \text{ cm}^{-2}$ , and mobility of the 2D gas is  $7.0 \times 10^5 \text{ cm}^2/\text{V s}$ .

cates the dependence of the transmission characteristic on the electron distribution. Using Eq. 2 we derive the internal potential in the point contact (corresponding to the energy of the first bound level). The resulting potential is shown as a function of the externally applied voltage for a typical point contact in Fig. 3. We do not have a full explanation for the discrepancy between the potential values determined for the two different temperatures. This discrepancy points to the main limitations of the present analysis: assuming constant transmission  $T(E)$ , and neglecting contributions from higher subbands. Further factors may be the temperature dependence of screening, and also the influence of temperature dependent scattering.

We injected electrons with varying excess energies into the 2DEG formed between the two point contacts, varying the external voltage applied to the second point contact. The excess energy is applied by biasing an ohmic contact formed to the source region with respect to the base region. The base region is connected to ground. The current transfer ratio is measured by determining the ratio of the current

injected into the source region with respect to the current through the drain region. Fig. 4 shows the transfer ratio  $I_{\text{drain}}/I_{\text{source}}$  as a function of external drain gate voltage for different injection bias voltages. The measurement is at a temperature of 4.2 K, the carrier density is  $n = 0.34 \times 10^{12} \text{ cm}^{-2}$ , and the mobility is  $\mu = 7.0 \times 10^5 \text{ cm}^2/\text{V s}$ . The spacing of the source gate and the drain gate is 17.8  $\mu\text{m}$ . Fig. 5 shows the first derivatives of the current transfer curves from Fig. 4. Injection energies in the range of 0 to 80 mV were studied here.

The derivatives of the transfer ratio in Fig. 5 are expected to be closely related to the energy spectrum of the electrons as they arrive at the drain gate after propagating for 17.8  $\mu\text{m}$ . The figure clearly shows a shift of the energy distribution to higher energies as the injection energy is increased, while a broad tail at higher energies develops. For low injection voltages the width of the main peak is approximately  $3kT$  as expected, while it broadens considerably for higher injection energies. Fig. 4 shows clearly a reduction of the peak transmission probability as the injection energy exceeds an energy of around 40 meV,

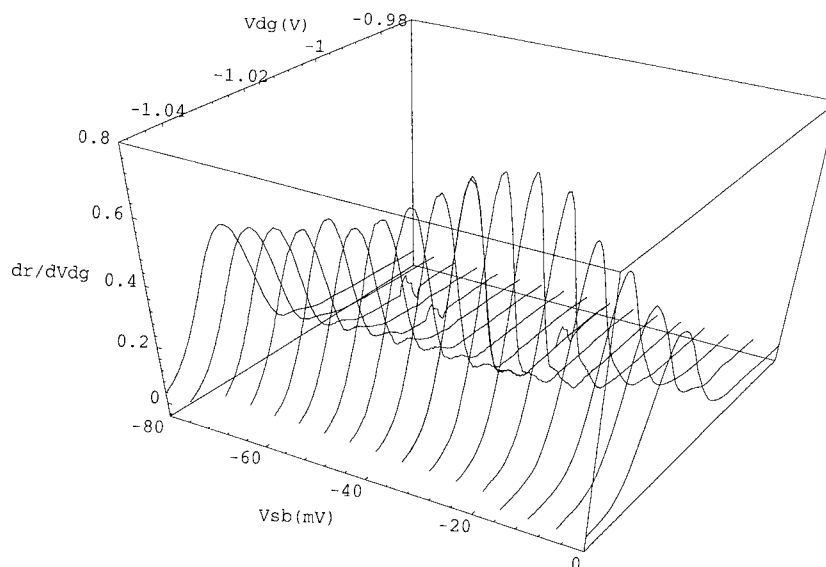


Fig. 5. First derivative of the current transfer ratio  $dr/dV_{dg}$  as a function of externally applied drain gate voltage  $V_{dg}$  for different injection bias voltages  $V_{sb}$ . (Derived from the data in Fig. 4.)

and Fig. 5 shows a similar effect for the first derivative of the transmission spectrum, also indicating the effect of LO phonon scattering when the injection energy exceeds the LO phonon energy of 36.4 meV.

In summary, we have observed the energy distribution of hot electron beams after they have propagated through distances up to 17  $\mu\text{m}$ . Even after this long distance, the electron distribution has not fully thermalized. A new method is proposed to determine the position of the first bound level within a quantum point contact constriction, and thus the “internal potential”, seen by electrons within the structure. Thus the thermal energy distribution of electrons is used as an internal energy scale.

The authors would like to express their gratitude to Professor Yasuhiko Arakawa for many helpful discussions. Support by the NTT Endowed Chair at RCAST and the “Sakaki Quantum Wave Project” of ERATO is gratefully acknowledged.

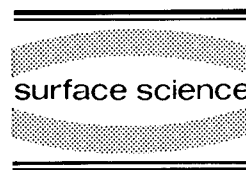
## References

- [1] M. Heiblum, M.I. Nathan, D.C. Thomas and C. Knoedler, *Phys. Rev. Lett.* 55 (1985) 2200; S. Muto, K. Imamura, N. Yokoyama, S. Hiyamizu and H. Nishi, *Electron. Lett.* 21 (1985) 555; J.R. Hayes and A.F.J. Levi, *IEEE J. Quantum Electron.* 22 (1986) 1744; A.P. Long, P.H. Beton and M.J. Kelly, *Semicond. Sci. Technol.* 1 (1986) 63; P. Matthews, M.J. Kelly, D.G. Hasko, J.E.F. Frost, D.A. Ritchie, G.A.C. Jones, M. Pepper and H. Ahmed, *Semicond. Sci. Technol.* 7 (1992) B536.
- [2] U. Sivan, M. Heiblum and C.P. Umbach, *Phys. Rev. Lett.* 63 (1989) 992.
- [3] J.G. Williamson, H. van Houten, C.W.J. Beenakker, M.E.I. Broekaart, L.I.A. Spendeler, B.J. van Wees and C.T. Foxon, *Phys. Rev. B* 41 (1990) 1207.
- [4] B.J. van Wees et al., *Phys. Rev. Lett.* 60 (1988) 848; D.A. Wharam et al., *J. Phys. C* 21 (1988) L209.
- [5] M. Büttiker, Y. Imry, R. Landauer and S. Pinhas, *Phys. Rev. B* 31 (1985) 6207.
- [6] P.F. Bagwell and T.P. Orlando, *Phys. Rev. B* 40 (1989) 1456.
- [7] I.B. Levinson, *Sov. Phys. JETP* 68 (1989) 1257.
- [8] L.P. Kouwenhoven, B.J. van Wees, C.J.P.M. Harmans, J.G. Williamson, H. van Houten, C.W.J. Beenakker, C.T. Foxon and J.J. Harris, *Phys. Rev. B* 39 (1989) 8040.



ELSEVIER

Surface Science 305 (1994) 624–628



## Resonant tunnelling between edge states in mesoscopic wires

A.K. Geim<sup>a</sup>, P.C. Main<sup>\*,a</sup>, C.V. Brown<sup>a</sup>, R. Taboryski<sup>b</sup>, H. Carmona<sup>a</sup>, T.J. Foster<sup>a</sup>,  
P.E. Lindelof<sup>b</sup>, L. Eaves<sup>a</sup>

<sup>a</sup> Department of Physics, University of Nottingham, Nottingham, NG7 2RD, UK

<sup>b</sup> Niels Bohr Institute, The Oersted Laboratory, DK-2100 Copenhagen, Denmark

(Received 20 April 1993; accepted for publication 19 May 1993)

### Abstract

We report measurements of the magnetoresistance of long ( $> 50 \mu\text{m}$ ), narrow ( $< 1 \mu\text{m}$ ) quantum wires fabricated from a high mobility two-dimensional electron gas. We observe that, at low filling factors, the Shubnikov–de Haas oscillations split into a series of sharp peaks which we attribute to resonant tunnelling between edge states through localized states in the bulk. The results are in excellent agreement with the theoretical model of Jain and Kivelson.

In the quantum Hall régime of a high mobility two-dimensional electron gas (2DEG) the edge state model of electron transport [1,2] has provided considerable insight. Even between Hall plateaux, where the longitudinal resistance is non-zero, it has been possible to understand the measured resistance in terms of macroscopic transmission probabilities between edge channels [3,4]. In mesoscopic samples fabricated from narrow wires ( $\sim 1 \mu\text{m}$ ) various authors [5–7] have reported temperature dependent resistance fluctuations within the Shubnikov–de Haas oscillations (SdHO). These fluctuations have been ascribed either to universal conductance fluctuations (UCF) [6,8] or to resonant tunnelling between edge states through a localized state in the bulk 2DEG [5,9]. In this paper we present results from a narrow sample in which we observe similar but much stronger fluctuations than have been

reported earlier. We are able to rule out UCF as the source of these fluctuations and we provide quantitative evidence that their origin lies in resonant tunnelling between edge states through *several* localized states in the bulk.

The inset to Fig. 1 shows the topology of the wires used in the experiment. They were fabricated by electron beam lithography from GaAs/(AlGa)As heterostructures with a low temperature mobility of  $20 \text{ m}^2 \text{ V}^{-1} \text{ s}^{-1}$  and electron density  $4.3 \times 10^{11} \text{ cm}^{-2}$  in the 2DEG after fabrication. The conducting width of all sections of the wire is  $\sim 1 \mu\text{m}$ . Probe pair B and H are  $10 \mu\text{m}$  from pair C and G, which in turn are  $20 \mu\text{m}$  from probes D and F. The measurement leads have a relatively very long length of  $50 \mu\text{m}$ . For a four-wire resistance measurement we use the normal convention that  $R_{ijkl} = V_{kl}/I_{ij}$ , where  $V_{kl}$  is the voltage difference between contacts k and l due to a current passing between i and j. A typical local magnetoresistance trace is shown in Fig. 1a for the configuration  $R_{EADB}$  at a temper-

\* Corresponding author.

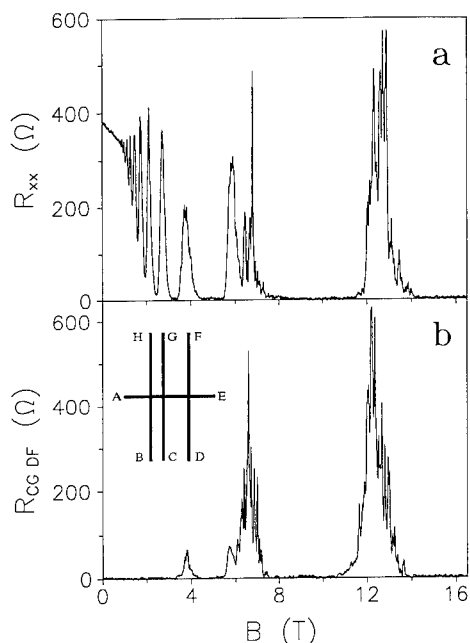


Fig. 1. Magnetoresistance traces at 0.3 K for local (a) and non-local (b) configurations. Inset: Schematic representation of the wire geometry.

ature of 0.29 K with the magnetic field,  $B$ , applied perpendicular to the 2DEG. For notation purposes we label each resistance zero in terms of the filling factor  $\nu = h/(e^2 R_H)$ , where  $R_H$  is the Hall resistance. In Fig. 1,  $\nu = 2$  at  $B = 9$  T. Pronounced, reproducible resistance fluctuations are visible for filling factors  $\nu < 4$ . For comparison, a non-local resistance curve corresponding to  $R_{CGDF}$ , where the voltage contacts are remote from the classical current path, and taken at the same temperature is also shown in Fig. 1b. Again, large fluctuations are visible in the SdHO.

In Fig. 2a we plot the magnetoresistance at  $T = 300$  mK in the local configuration of Fig. 1a between  $\nu = 2$  and  $\nu = 4$ . The resistance minimum shown by the dashed line is  $\nu = 3$  so that the SdHO on either side of the line correspond to the chemical potential being in Landau levels of different spin polarization, as shown schematically by the arrows. The fluctuations are far stronger in the right hand SdHO; an observation which is true in all configurations. In Fig. 2b we show the SdHO between  $\nu = 1$  and  $\nu = 2$  for the

same conditions as in Fig. 2a. It is immediately clear that the quasi-period of the fluctuations is not the same in different SdHO. In Fig. 2a the two SdHO have approximately the same number of peaks even though the strength is very different. Furthermore, the number of peaks in the SdHO shown in Fig. 2b is also approximately the same. This contrasts sharply with the observation of a  $B$ -independent quasi-period reported by Simmons et al. [5] for their much weaker structure. In Fig. 2c we plot the equivalent SdHO as in Fig. 2a but for a non-local configuration  $R_{CDBH}$  in which the voltage probes are  $10 \mu\text{m}$  from the classical current path. There is a similar distinction between the spin-split levels.

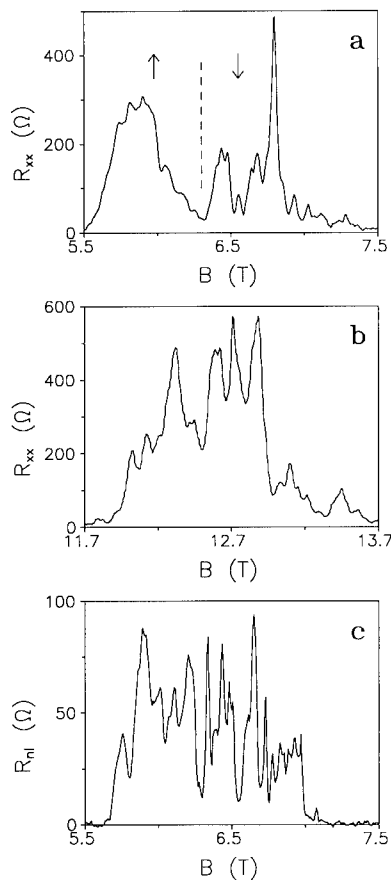


Fig. 2. Magnetoresistance at 0.3 K for local configuration for (a)  $5.5 < B < 7.5$  T, (b)  $11.7 < B < 13.7$  T and (c) for the non-local configuration,  $R_{CDBH}$  for  $5.5 < B < 7.5$  T.

Conductance fluctuations have been observed in the quantum Hall régime by several authors [5–7]. The origin of the fluctuations has been ascribed to UCF [6,8], resonant tunnelling between edge states through a single localized state in the bulk of the wire [5,9] and Coulomb blockade [7]. None of these explanations is able to explain our observations. The fluctuations we observe in the non-local geometry are  $\sim 100\%$  of the total resistance and yet the separation between the current and voltage probes can be as much as  $30 \mu\text{m}$ , a large distance compared with phase coherence length at this temperature ( $\sim 5 \mu\text{m}$ ). It follows that the fluctuations are not UCF. Also, Simmons et al. [5] ascribe the quasi-periodicity of their fluctuations to the Aharonov–Bohm effect in a single localized state in the bulk of the wire. In that case the fluctuations are more visible near the resistance minima and are very sharp and difficult to observe in the centre of the peaks [5,9], in contrast to our observations.

Our results can be explained in terms of a model related to that first proposed by Jain and Kivelson [9]. The resistance fluctuations are caused by resonant tunnelling between edge states but through a number of parallel channels rather than through a single localized state. Essentially, we associate each resistance peak with a particular resonant channel. For a particular channel to be resonant requires sufficient overlap between the wavefunctions of the edge and bulk states and a whole number of flux quanta threading the localized orbit. In our sample, changing  $B$  reduces the wavefunction overlap sufficiently that, before another flux quantum can thread the orbit, the resonance amplitude has fallen drastically. This explains the observation that within any Landau level the number of fluctuations is approximately the same. If the origin of the fluctuations were explained in terms of tunnelling through a single state the quasi-period would be due to a flux quantum threading the area of the localised state and would be approximately independent of  $\nu$ .

The model of Jain and Kivelson makes specific predictions for the temperature and magnetic field dependence of an individual resonant tunnelling peak. Fig. 3 shows the temperature de-

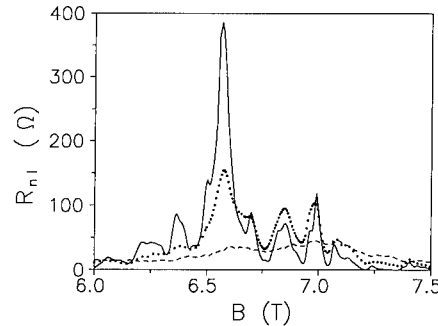


Fig. 3. Magnetoresistance in the non-local configuration  $R_{\text{ACDF}}$  at  $T = 0.28 \text{ K}$  (solid line),  $0.8 \text{ K}$  (dotted line) and  $3 \text{ K}$  (dashed line).

pendence of a SdHO measured in the non-local geometry  $R_{\text{ACDF}}$ . For  $6.2 < B < 6.7 \text{ T}$  there is a monotonic temperature dependence, with the peaks being stronger and sharper at lower temperatures. For  $6.7 < B < 7.2 \text{ T}$ , the temperature dependence is much more complicated and is discussed in more detail below. We consider the strong central feature in Fig. 3 which exhibits a strong and monotonic dependence on temperature. According to Ref. [9] the resistance peak due to a resonant channel is described by

$$R(\mu, T) \approx (k_{\text{B}}T)^{-1} \exp[|\mu - E_0|/k_{\text{B}}T], \quad (1)$$

where  $R(\mu, T)$  is the resistance peak due to a resonant state with energy  $E_0$  and  $\mu$  is the chemical potential. The equation is valid provided that  $k_{\text{B}}T$  is larger than the natural linewidth of the resonance. In Fig. 4a we plot  $d(\ln R)/d(\hbar\omega_c)$  versus  $1/T$  for the principal peak in Fig. 3, shown by the open circles. We also plot the maximum value of  $d(\ln R)/d(\hbar\omega_c)$  at a given  $T$  for the rest of the fluctuations, as shown by the filled circles. This plot assumes that  $\mu \approx (N - \frac{1}{2})\hbar\omega_c \pm g^*\mu_{\text{B}}B$ , where  $N$  is the number of filled (spin degenerate) Landau levels,  $g^*$  is the effective Landé  $g$ -factor and  $\mu_{\text{B}}$  is the Bohr magneton. The value of  $g^*$  is not well known, is oscillatory and for this Landau level the Zeeman term is negative. The slope,  $d\mu/d(\hbar\omega_c)$ , of the best line drawn through the points is 0.9, which gives a value of  $g^* = 17$  which is consistent with values determined from activation plots [10]. In Fig. 4b we plot  $\ln R$  versus  $\ln T$  for the amplitude of the strongest peak (open circles) in Fig. 3

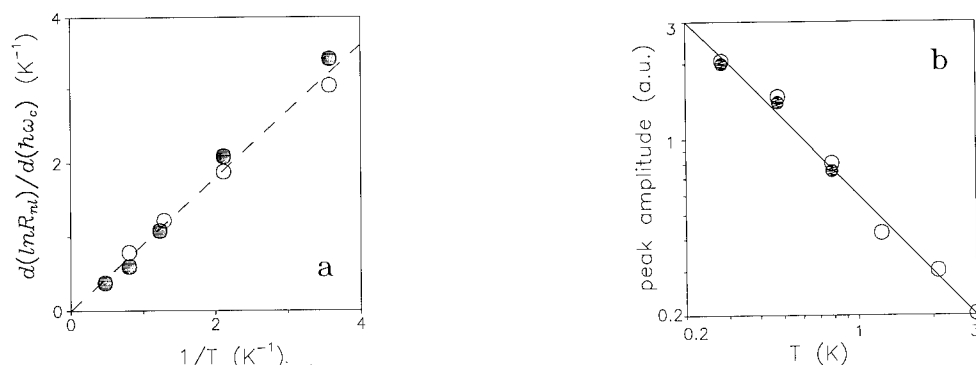


Fig. 4. (a)  $d(\ln R)/d(\hbar\omega_c)$  versus  $1/T$  for principal peak of Fig. 3 (open circles). See text for explanation of filled circles. (b)  $\ln R$  versus  $\ln T$  for two peaks of Fig. 3.

and the peak immediately to its left (filled circles). Referring to Eq. (1) we see  $R \propto T^{-1}$  at the peak maximum which is represented by the line in Fig. 4b. The agreement with the experimental data is excellent.

Two features of the experimental data are not explained directly by the model. The first is the asymmetry of the strength of the fluctuations (see Figs. 2a and 2c). Referring to Fig. 5, which is a schematic representation of the Landau levels in our device, the fluctuations are weak when the chemical potential,  $\mu$ , is in a Landau level where the nearest totally filled level is only separated by the Zeeman energy. This situation is represented by line  $\mu_x$  in Fig. 5. When  $\mu$  is in position  $\mu_y$ , where the nearest filled level is an energy  $\hbar\omega_c$  away, the fluctuations are strong. We can understand these observations by considering a Landauer–Büttiker [1] picture for the edge states. At

$\mu_x$ , because the Zeeman energy splitting is relatively small, it is easy for electrons in the partially-filled level to equilibrate with electrons in the filled level. This tends to smooth out fluctuations, which are always due to resonances in the uppermost level, since the current is shared between the two uppermost levels. With the chemical potential at  $\mu_y$  the nearest filled level is an energy  $\hbar\omega_c$  away and equilibration is much harder because the wavefunction overlap between the adjacent edge states is much smaller. The second unexplained experimental observation is the non-monotonic temperature dependence of some of the features as displayed in Fig. 3. In terms of Fig. 5, we obtain the expected  $T$  dependence at  $\mu_y$  and the non-monotonic behaviour when the chemical potential is at  $\mu_z$ . This observation remains something of a puzzle. Most probably, the non-monotonic behaviour is related to other effects which are known to occur in devices of this sort [3] for example, temperature-dependent equilibration between edge states and/or contact transmission coefficients.

To summarize, we have observed profound aperiodic structure in the SdHO of long, narrow quantum wires in the quantum Hall régime. We are able to rule out UCF as a possible explanation of the effect and instead, we are able to compare our data successfully with a model based on resonant tunnelling through localized states in the bulk of the wire. Comparison between different SdHO indicates that it is likely that the fluctuations are due to a number of resonant chan-

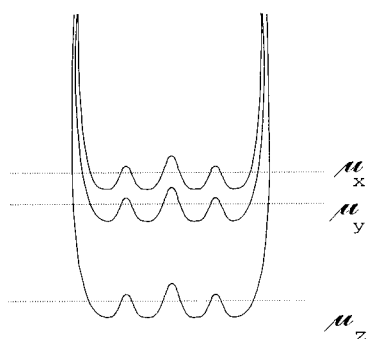


Fig. 5. Schematic diagram of Landau levels. The dashed lines represent  $\mu$  at three different magnetic fields.



nels. We note that if two particular four-wire resistance measurements share a particular contact, then there is also a correlation between the fluctuations observed for a given SdHO. The different spin-split Landau levels show different strengths of fluctuation which can be explained in terms of inter-edge scattering. We note, finally, that in our mesoscopic samples, in which the width is much larger than the magnetic length, the resistance within the SdHO is determined by single electron tunnelling paths across the width of the sample.

### 1. Acknowledgements

This work is funded by the SERC (UK). H.C. is supported by CNPq (Brasil) and A.K.G. and C.V.B. by SERC.

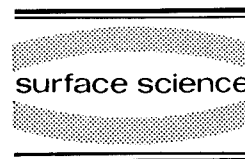
### 2. References

- [1] M. Büttiker, Phys. Rev. B 38 (1988) 9375.
- [2] For a recent review see R.J. Haug, Semicond. Sci. Tech. 8 (1993) 131.
- [3] S. Komiyama, H. Hirai, M. Oshawa, Y. Matsuda, S. Sasa and T. Fujii, Phys. Rev. B 45 (1992) 11085.
- [4] P.L. McKuen, A. Szafer, C.A. Richter, B.W. Alphenaar, J.K. Jain, A.D. Stone, R.G. Wheeler and R.N. Sacks, Phys. Rev. Lett. 64 (1990) 2062.
- [5] J.A. Simmons, S.W. Hwang, D.C. Tsui, H.P. Wei, L.W. Engel and M. Shayegan, Phys. Rev. B 44 (1991) 12933.
- [6] G. Timp, P.M. Mankiewich, P. de Vegvar, R. Behringer, J.E. Cunningham, R.E. Howard and H.U. Baranger, Phys. Rev. B 39 (1989) 6227.
- [7] J.K. Jain and S. Kivelson, Phys. Rev. Lett. 60 (1988) 1542.
- [8] S. Xiong and A.D. Stone, Phys. Rev. Lett. 68 (1992) 3757.
- [9] A.B. Fowler, G.L. Timp, J.J. Wainer and R.A. Webb, Phys. Rev. Lett. 57 (1986) 138.
- [10] R.J. Nicholas, R.J. Haug, K. von Klitzing and G. Weimann, Phys. Rev. B 37 (1988) 1294.



ELSEVIER

Surface Science 305 (1994) 629–632



## Gate tuned transition to the insulating phase of one-dimensional electrons in high magnetic fields

S.W. Hwang <sup>\*</sup>, D.C. Tsui, M. Shayegan

*Department of Electrical Engineering, Princeton University, Princeton, NJ 08544, USA*

(Received 19 April 1993; accepted for publication 21 July 1993)

### Abstract

We report experimental results on charge transport in a low disorder and low density one-dimensional electron system. We find a gate tuned transition to an insulating phase at high magnetic fields and conductance oscillations as a function of density in this  $B$ -induced insulating phase. A careful study of the temperature dependence and the current–voltage characteristics of these conductance oscillations is made and the results fit the recent theoretical model of one-dimensional Wigner solid.

Recently, Scott-Thomas et al. [1] found, in a narrow Si inversion layer, periodic conductance oscillations as a function of the density. They interpreted the oscillations as manifestation of a one-dimensional charge-density-wave (1D CDW) [2] pinned by impurities in the channel. The pinning energy is maximized whenever the density is commensurate with an integer number of electrons between two pinning centers, resulting in periodic oscillations of the conductance as the electron density is changed. Subsequently, the formation of a one-dimensional Wigner solid (1D WS) in a low disorder and low density one-dimensional electron system (1D ES) was theoretically studied by Averin and Likharev [3], and by Glazman, Ruzin, and Shklovskii (GRS) [4]. Both theoretical papers emphasize that in the low density limit, when  $n_{1D} < (1/a_B)$  (where  $n_{1D}$  is the

1D electron density and  $a_B$  is the Bohr radius,  $\sim 100 \text{ \AA}$  in GaAs), the electrons are expected to form a 1D WS pinned by weak potential fluctuations in the channel. In a more recent paper, Averin and Nazarov (AN) [5] calculated the temperature ( $T$ ) dependence of the maxima and minima of such conductance oscillations, based on the charge density wave tunneling theory of Larkin and Lee [6].

In principle, the  $n_{1D}a_B < 1$  regime can be reached by simply decreasing the channel width ( $W$ ). In a usual split-gate channel fabricated on high density GaAs/ $\text{Al}_x\text{Ga}_{1-x}\text{As}$  2D ES, the  $n_{1D}a_B < 1$  condition is expected to be obtained by biasing the gate strongly such that the channel is near pinch-off. In reality, however, such channels have strong disorder and it has not been possible to maintain an ideal, open channel near pinch-off. One way of overcoming this problem is to fabricate a split-gate channel on a low density, low disorder 2D ES. In this case, the  $n_{1D}a_B < 1$  limit can be reached even when  $W$  is not extremely

<sup>\*</sup> Corresponding author.

small and the channel is still far away from pinch-off.

In this paper, we report experimental results on charge transport in the low disorder and low-density ( $n_{1D}a_B < 1$ ) regime where the formation of 1D WS is anticipated. The sample is a  $1\ \mu$  wide split-gate channel fabricated on a wafer of GaAs/Al<sub>x</sub>Ga<sub>1-x</sub>As heterostructure with an extremely low two-dimensional density,  $n_{2D} = 6.5 \times 10^{10}\ \text{cm}^{-2}$  and high mobility,  $\mu = 10^6\ \text{cm}^2/\text{V}\cdot\text{s}$ . In this sample,  $W$  and  $n_{1D}$  can be varied in a wide range by biasing the split-gate bias,  $V_g$ .

The details of charge transport characteristics at  $B = 0$  and at low  $B$  is reported elsewhere [7] and can be summarized as follows: (1) At  $B = 0$ , quantized conductance steps, at integer multiples of  $2e^2/h$ , are observed in our channel. The fabricated channel length is  $1.2\ \mu\text{m}$  at  $V_g = 0$  and an even longer channel is expected for more negative  $V_g$ . To our knowledge, the conductance quantization in such a long channel fabricated on such a low 2D electron density wafer has not been observed before [8]. Analysis of these quantized steps shows that we can change  $n_{1D}$  in a wide range, reproducibly reaching the  $n_{1D}a_B < 1$  regime (corresponding to the bias range,  $-2.2 < V_g < -1.45\ \text{V}$ ), and more importantly, that unprecedentedly smooth and weak potential fluctuations are obtained in the channel. (2) In the

presence of  $B$ , we observe the integer (IQHE) and fractional quantum Hall effect (FQHE) states (well defined  $1/3$  state) in the channel. Analysis of the IQHE states shows that the channel has a  $V_g$  dependence on the electron density predicted by the calculation of split-gate channel with no disorder [9].

For  $B$  higher than that for the  $1/3$  FQHE state, the channel becomes an insulator. Fig. 1a shows the diagonal resistance across the channel,  $R_n$ , at  $V_g = -1.855\ \text{V}$  in the  $\nu < 1$  regime, at  $T = 35, 112, 300\ \text{mK}$ . Qualitatively, the  $T$  dependence of  $R_n$  changes drastically in the range,  $3.5 < B < 4.2\ \text{T}$ , showing an almost constant  $R_n$  at low  $B$  and a rapid increase of  $R_n$  with decreasing  $T$  at high  $B$ . Fig. 1b shows in better detail the  $T$  dependence at fixed  $B$  in this range from  $B = 3.0$  to  $4.6\ \text{T}$ . It is clear that there are two distinct regimes showing two different  $T$  dependences. For  $B < 3.8\ \text{T}$ , the 1D channel is metallic in that  $R_n$  is approximately independent of  $T$ ; for  $B > 3.8\ \text{T}$ ,  $R_n$  increases as  $T$  decreases and the channel behaves as an insulator. This is especially apparent for the  $B > 4.0\ \text{T}$  data, where the increase is rapid and  $R_n$  is approaching to  $\infty$  as  $T \rightarrow 0$ . This transition of the 1D channel into an insulating state can therefore be characterized by a  $B$  field,  $B_{M-I}$ , which is  $\sim 3.8\ \text{T}$  at  $V_g = -1.855\ \text{V}$ .

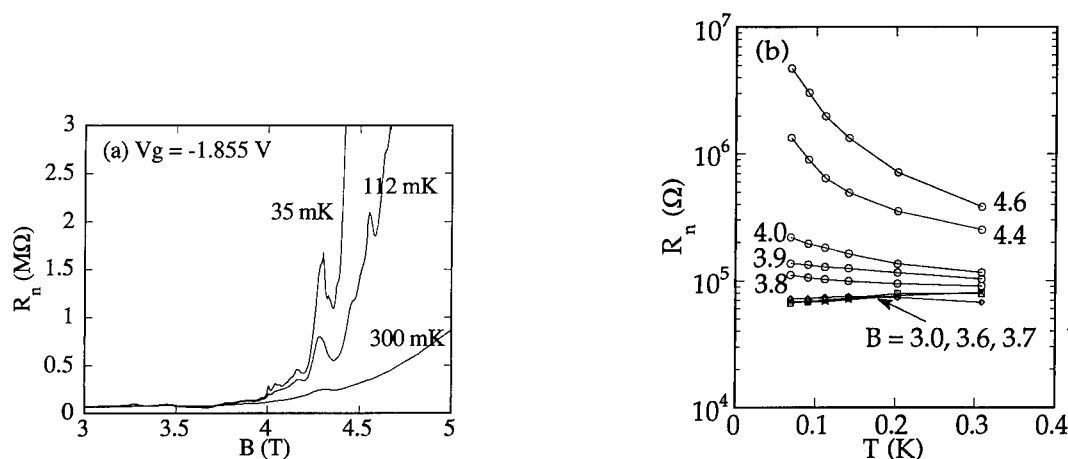


Fig. 1. (a) The diagonal resistance,  $R_n$ , at  $V_g = -1.855\ \text{V}$  in the  $\nu < 1$  regime, at  $T = 35, 112, 300\ \text{mK}$ . Notice a dramatic change in the  $T$  dependence of  $R_n$  in the range,  $3.5 < B < 4.2\ \text{T}$ . (b) More quantitative  $T$  dependence of  $R_n$  at fixed  $B$  in the range,  $3.0 < B < 4.6\ \text{T}$ .

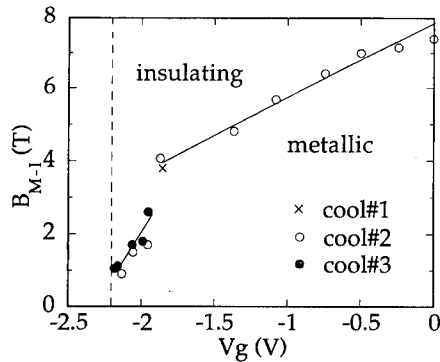


Fig. 2.  $(B, V_g)$  phase diagram showing the  $B_{M-1}$  deduced from the data of 3 different cool-downs. Two straight lines are eye-guide lines.

We have investigated the  $T$  dependences of  $R_n$  as a function of  $B$  and  $V_g$ , and the  $B_{M-1}$  deduced from the data taken from 3 cool-downs are summarized in Fig. 2. The vertical dashed line in the figure indicates the  $V_g$  below which the channel is already insulating at  $B = 0$  (the conductance of the channel,  $G < e^2/h$ ,  $V_g < -2.2$  V), and the IQHE is not observed. The upper left part of the graph is the  $B$  field induced insulating phase where  $R_n$  increases with decreasing  $T$ . The lower right part is the metallic phase where the QHE states are observed. The IQHE states are observed in the entire bias range on the right-hand side of the dashed line mentioned above and the FQHE states are observed at  $V_g > -1.9$  V.  $B_{M-1}$  clearly varies with  $V_g$ , being smaller at larger  $-V_g$ . In terms of the Landau level filling factor, the transition occurs in the range  $0.28 < \nu < 0.33$ , when  $2.8 \times 10^{10} \text{ cm}^{-2} < n_{2D} < 6.5 \times 10^{10} \text{ cm}^{-2}$  ( $V_g > -1.9$  V), and at larger filling factors ( $0.57 < \nu < 0.77$ ), when  $n_{2D} < 2.8 \times 10^{10} \text{ cm}^{-2}$  ( $V_g < -1.9$  V).

In our low disorder and low density ( $n_{1D}a_B < 1$ ) one-dimensional channel, a pinned 1D WS is clearly a possible ground state for the observed  $B$ -induced insulating phase and the most striking characteristic of charge transport in such an insulator is the oscillations predicted in the conductance as a function of electron density. We also systematically studied conductance traces as a function of density (which is tuned by a backgate bias,  $V_{BG}$ ) in the entire  $(V_g, B)$  plane of the

phase diagram, Fig. 2. We find that the conductance oscillations are observed in the insulating phase  $n_{1D}a_B < 1$  regime ( $V_g < -1.45$  V). Fig. 3 is a demonstration of the fact that conductance oscillations are observed only in the  $B$ -induced insulating phase, showing a set of  $G$  versus  $V_{BG}$  data, taken at  $V_g = -2.061$  V, for several  $B$ 's for  $B < 2.7$  T. As seen in Fig. 2,  $B_{M-1} \approx 1.7$  T at this  $V_g$ . In the metallic regime ( $B = 0$  and 1 T), there are no conductance oscillations. In particular, at  $B = 1$  T,  $G$  shows a wide plateau of  $e^2/h$ , suggesting the  $\nu = 1$  IQHE state in the narrow channel. When the channel is in the insulating phase ( $B = 2.0, 2.5$ , and  $2.7$  T data), conductance oscillations appear. These oscillations become sharper and more developed as  $B$  increases. Fig. 3f shows the Fourier transform of the data taken at  $B = 2.7$  T, clearly showing a peak corresponding to a dominant oscillation periodicity of  $0.83$  V.

A careful study of the  $T$  dependences and the current-voltage ( $I$ - $V$ ) characteristics of these oscillations was made and the results were analyzed in terms of the 1D WS model of GRS and AN. The most important prediction of the AN model

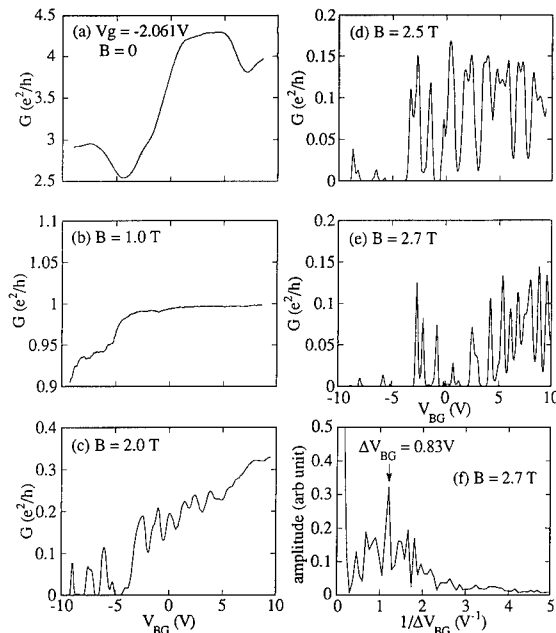


Fig. 3. A set of  $G$  vs.  $V_{BG}$  data taken at  $V_g = -2.061$  V, for several  $B$ 's for  $B < 2.7$  T.

is that both the conductance maxima ( $G_{\max}$ ) and the conductance minima ( $G_{\min}$ ) follow power law dependences on  $T$ , and as a result, both  $G_{\max}$  and  $G_{\min}$  increase with increasing  $T$ . Our data show wide  $V_{\text{BG}}$  ranges where both  $G_{\max}$  and  $G_{\min}$  increase with  $T$ . We fit the data with the predicted power law and obtain parameters in reasonable agreement with estimation. We also observe a sharp threshold in the  $I$ - $V$  taken from the oscillation data. When  $V$  is smaller than the threshold voltage, the differential conductance also fits the power law predicted by GRS, again with reasonable parameters [7].

In conclusion, we have studied our low density low disorder 1D ES at high  $B$ . We identify a transition into a  $B$ -field-induced insulating phase. More importantly, we observe conductance oscillations, predicted to occur in 1D WS, in this  $B$ -induced insulating phase in the  $n_{\text{1D}}a_{\text{B}} < 1$  low density limit. The analysis of the observed conductance oscillations shows that many of the quantitative and qualitative features of our data are consistent with the 1D WS model. In particular, the  $T$  dependences and the  $I$ - $V$  characteris-

tics can be quantitatively explained by the 1D WS model with reasonable parameters.

This work is supported in part by the NSF and the ONR.

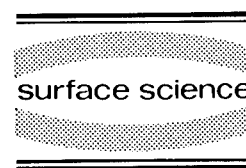
## 1. References

- [1] J.H.F. Scott-Thomas, S.B. Field, M.A. Kastner, H.I. Smith and D.A. Antoniadis, Phys. Rev. Lett. 62 (1989) 583.
- [2] For a review, see, G. Gruner, Rev. Mod. Phys. 60 (1988) 1129.
- [3] D.V. Averin and K.K. Likharev, Proceedings of 1991 International Symposium on Nanostructures and Mesoscopic Systems (Santa Fe, NM, May 1991).
- [4] L.I. Glazman, I.M. Ruzin and B.I. Shklovskii, Phys. Rev. B 45 (1992) 8454.
- [5] D.V. Averin and Yu.V. Nazarov, Phys. Rev. B 47 (1993) 9944.
- [6] A.I. Larkin and P.A. Lee, Phys. Rev. B 17 (1978) 1596.
- [7] S.W. Hwang, D.C. Tsui and M. Shayegan, to be published.
- [8] The conductance quantization in the 2–4  $\mu\text{m}$  channel fabricated on a  $2.0 \times 10^{11} \text{ cm}^{-2}$  density sample was reported by K. Ismail, S. Washburn and K.Y. Lee, Appl. Phys. Lett. 59 (1991) 1998.
- [9] L.I. Glazman and I.A. Larkin, Semicond. Sci. Technol. 6 (1991) 32.



ELSEVIER

Surface Science 305 (1994) 633–636



# Observation of 1D electron states at the boundary between an MOS and a Schottky contact on Si(100) by electron tunneling

U. Kunze \*, T. Drebingen, B. Klehn, J. Lindolf

*Institut für Technische Physik, Universität Erlangen-Nürnberg, D-8520 Erlangen, Germany*

(Received 12 April 1993; accepted for publication 15 June 1993)

## Abstract

Electron quantum wires on Si surfaces have been prepared at the boundary between a Schottky contact and an MOS structure with electron inversion layer at the Si–SiO<sub>2</sub> interface. In tunneling from the metal into the inversion layer and vice versa the spectroscopic signal  $d^2I/dV^2$  exhibits short-period oscillations which can be attributed to the 1D electron states at the edge of the 2D electron gas.

## 1. Introduction

The investigation of quantum effects in one-dimensional (1D) electronic systems depends sensitively on sophisticated microfabrication techniques. Narrow electron inversion channels on Si which showed lateral quantization have been prepared by means of X-ray [1], holographic [2], or electron-beam lithography [3], where the lateral confinement potential was formed electrostatically using the split-gate configuration. Typical 1D subband separations were about several meV, as determined from 1D conductance oscillations [1,3] or from far-infrared spectroscopy [2]. While optical intersubband resonances contain dominant collective contributions [2,4], tunneling spectroscopy is capable of giving directly the one-par-

ticle level energies. This technique has been successfully applied to split-gate-induced quantum wires in GaAs using vertical Schottky-barrier tunneling [5], lateral double-barrier tunneling [6,7], and lateral single-barrier tunneling [8]. Much larger 1D level separations than the typical 2–5 meV in nanolithographically defined structures have been achieved by regrowth of a 2D–1D–2D tunneling structure on the vertical cleavage plane of a conventional layered double-barrier device [9]. However, tunneling in Si quantum wires has not been reported so far. In this work we have performed a tunneling spectroscopy of a single Si quantum wire, where a novel self-aligned fabrication scheme based on standard photolithography is used to achieve a strong lateral confinement. The resulting 1D electron system is located at the edge of a 2D electron inversion layer. Features in the derivative  $d^2I/dV^2$  of the current( $I$ )–voltage( $V$ ) characteristics taken from appropriate metal–SiO<sub>2</sub>–Si (MOS) tunnel junctions indicate a 1D level separation of the order of 10 meV.

\* Corresponding author.

## 2. Sample preparation

Fig. 1 shows an idealized cross section of the investigated structures. The preparation started from  $0.3 \Omega \cdot \text{cm}$  p-type Si(001) wafers. Phosphorous diffusion through an oxide mask forms  $n^+$  source and drain contact wells of a conventional MOS field-effect transistor (FET). A simultaneous boron diffusion of the back side of the wafer provides the substrate contact. Subsequently, 200 nm field oxide and 5–10 nm gate oxide were grown by thermal oxidation in dry  $\text{O}_2$ . Close to the drain  $n^+$  well, a gate oxide edge was prepared along the [110] direction by etching in buffered hydrofluoric acid. A 50 nm Mg and a 200 nm Al capping layer were evaporated and the metal contact pads patterned by standard resist technology and wet-chemical etching. Finally, an Al layer was deposited on the substrate contact. For the sake of comparison, additional 2D MOS tunneling structures with gate-oxide thickness  $d_{\text{ox}} \approx 2.5 \text{ nm}$  were prepared on substrates of the same kind [10].

## 3. Basic considerations

Our motivation to search for a 1D charge accumulation at the  $\text{SiO}_2$  edge is based on two observations. (i) In planar MOS structures the electron density is roughly inversely proportional to the oxide thickness. In particular at  $d_{\text{ox}} \leq 50 \text{ nm}$  the oxide trapped charge has a negligible

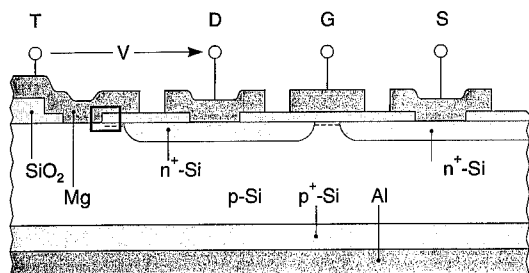


Fig. 1. Schematic cross-sectional view of the lateral tunneling structure (not to scale). T denotes the tunnel electrode and D, G and S the drain, gate and source contact of an additional MOSFET. The rectangle marks the tunneling region. The forward bias polarity is indicated.

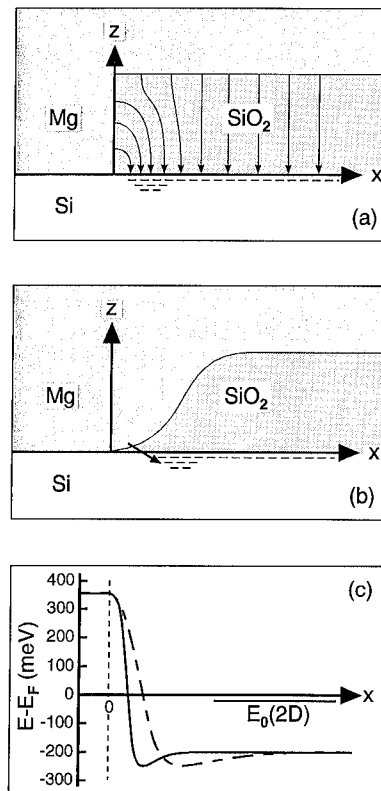


Fig. 2. (a) Expanded view of the abrupt oxide-step tunneling junction marked in Fig. 1. The mobile electron charge and the corresponding electric field pattern are schematically drawn. (b) Oxide thickness grading in a more realistic oxide step. The arrow indicates the tunneling path through the oxide. (c) Possible lateral variation of the conduction-band energy at the Si surface arising from an abrupt (solid) and graded (dashed) oxide step.

influence on the built-in potential [11]. (ii) The increase of  $N_s$  as  $d_{\text{ox}}$  decreases is limited at extremely thin  $\text{SiO}_2$  layer, at  $d_{\text{ox}} \approx 1.5 \text{ nm}$   $N_s$  drops abruptly to zero [12]. Now the Fermi level is pinned at interface gap states that probably are induced by the strong penetration of the metal wave function into the semiconductor. The barrier height of Mg Schottky contacts on air-exposed Si surfaces amounts to about 0.35 eV [13].

These observations result in a model of the oxide edge as depicted in Fig. 2. Due to the small separation between the metal and the Si– $\text{SiO}_2$  interface at the edge, the surface band bending should be enhanced and a lateral potential well is

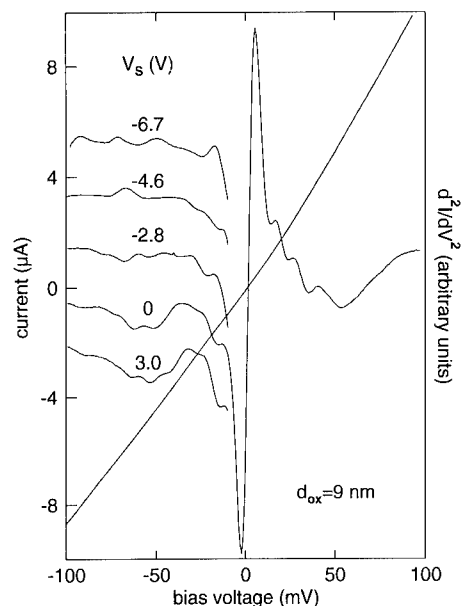


Fig. 3. Current( $I$ )–voltage( $V$ ) and second derivative  $d^2I/dV^2$  characteristic of a quantum wire junction with gate-oxide thickness  $d_{ox} = 9$  nm with different substrate bias  $V_s$ . Except for the  $V_s = 0$  curve only the reverse bias range is shown. The vertical displacement is for clarity.

formed. If we assume that the  $\text{SiO}_2$  thickness of a more realistic oxide edge is graded, the 1D confinement potential is widened (Figs. 2b and 2c). The depletion zone in the area with  $d_{ox} \leq 1.5$  nm leads to a finite separation between the metal and electron layer. The leakage current at the edge of the Schottky contact is carried by MOS tunneling. Electrical contact to the quantum wire is provided by the 2D electron channel. These extended subband states are resonant with the 1D subbands at energies  $E > E_0$ , where  $E_0$  is the energy of the lowest 2D subband.

#### 4. Results and discussion

The Figs. 3, 4 and 5 show  $I$ – $V$  and  $d^2I/dV^2$  characteristics of tunnel junctions measured at 4.2 K. In the characteristics of the 1D junctions (Figs. 3 and 4) short-periodic oscillations which are not observed in 2D junctions (Fig. 5) are imposed on the  $d^2I/dV^2$  background curves. We attribute these structures to 1D electron states of

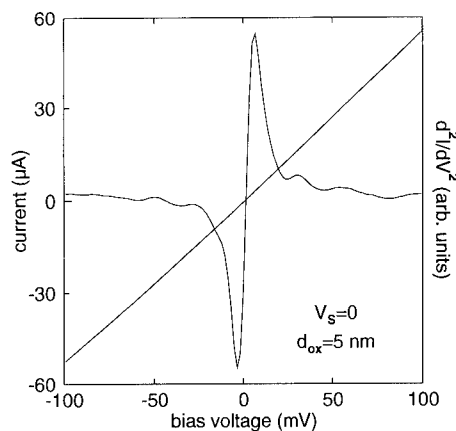


Fig. 4. Current( $I$ )–voltage( $V$ ) and second derivative  $d^2I/dV^2$  characteristic of a junction with gate-oxide thickness  $d_{ox} = 5$  nm.

the edge quantum well. At forward bias which corresponds to energies below the Fermi level, more oscillation periods occur in the characteristic shown in Fig. 3 than in that of Fig. 4. This indicates that the potential well is smaller in energy in the  $d_{ox} = 5$  nm sample compared with the 9 nm sample.

The energy position of the lowest 2D subband level in the adjacent electron channel can be estimated from the corresponding structure in the 2D junction characteristic, which yields  $E_F - E_0 = 44 \pm 1$  meV. Since  $d_{ox}$  of the gate oxide is larger by a factor of about 4 (2) the electron density should be lower by the same factor, i.e.  $E_F - E_0$  should be about 11 (22) meV in the 1D junction with  $d_{ox} = 9$  (5) nm. For the determination of the 1D level energies we tentatively use the bias positions of the dips in  $d^2I/dV^2$ . Strictly speaking this is wrong since in MOS tunneling

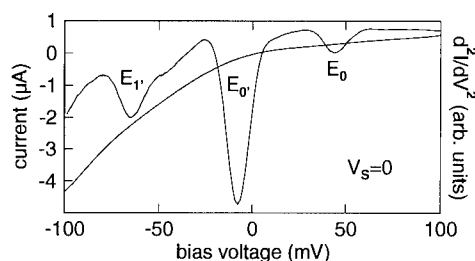


Fig. 5. Tunneling characteristics of an areal MOS junction. The 2D subband-edge induced structures are indicated.



the differential conductance  $dI/dV$  should reflect the density of states (DOS). Thus the oscillations in  $d^2I/dV^2$  are phase shifted with respect to the oscillatory 1D DOS. The series resistance  $R_s$  which causes a shift of the bias position due to the voltage drop can be estimated from the channel resistance of the additional MOSFET. While in the 9 nm sample this error is negligible as long as the reverse substrate voltages are smaller than  $V_s \approx 3$  V, in the 5 nm sample about half of the applied bias drops across  $R_s$ . Therefore, we restrict ourselves to the evaluation of the 9 nm sample data. The bias position of the dips at forward bias in Fig. 3 amounts to 14.4, 24.4 and 35.3 mV with an error of  $\pm 0.5$  mV and to  $53 \pm 1$  mV. The latter dip probably reflects a remainder of the 2D  $E_0$  level in the edge channel similar to that observed in magnetotunneling experiments on electron inversion layers [14]. The other three dips represent the energies of bound 1D subbands. The series of dips at reverse bias can tentatively be attributed to virtually bound 1D levels arising from quantum interference in the lateral potential well. Similar effects have been observed and numerically modeled in layered double-barrier structures [15]. However, the distinctness of these structures can hardly be understood from a smooth potential variation in the quantum well. It should also be noted that an alternative explanation in terms of tunneling via impurity states in the Si seems unlikely due to the regularity of the oscillation and its reproducibility in different junctions. Further experiments on samples with low doping level may provide an improved understanding.

Upon applying a substrate bias the dips are shifted in their bias position. A change of  $V_s$  from +3 to -3 V shifts the structures at forward bias by  $-2 \pm 0.5$  meV, i.e. the energy of the corresponding 1D levels rises relative to the Fermi level. This shift reflects the depopulation of the electron channel as the depletion charge density increases. At higher reverse  $V_s$  the series resistance sharply increases leading to a dominant  $R_s$  induced positive bias shift. The change of the reverse bias pattern demonstrates the effect of the depletion field on the level structure.

The width  $w$  of the edge quantum wire can be

estimated from the period of the oscillation. Assuming a parabolic well, the width is  $w^2 = 8E_F/m^*\omega^2$ , where  $E_F \approx 50$  meV is the Fermi energy of the 1D system,  $m^*/m = 0.2$  and  $\hbar\omega = 12 \pm 2$  meV is the oscillation period. The result of  $w = 33 \pm 6$  nm is about three times the oxide thickness, which supports the model of a smoothly graded oxide step. However, this model is inconsistent with the interpretation of the reverse bias oscillation as quantum interference effect.

## 5. Outlook

Quantum wires at the edge of a 2D electron channel, easily fabricated by a self-aligned process, offer a prospective field of tunneling studies on 1D electron systems in Si. Possible interesting parameters are the surface and the wire orientation and high magnetic fields.

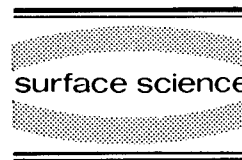
## 6. References

- [1] A.C. Warren, D.A. Antoniadis and H.I. Smith, *Phys. Rev. Lett.* 56 (1986) 1858.
- [2] J. Alsmeier, E. Batke and J.P. Kotthaus, *Phys. Rev. B* 40 (1989) 12574.
- [3] J.R. Gao, C. de Graaf, J. Caro, S. Radelaar, M. Offenberg, V. Lauer, J. Singleton, T.J.B.M. Janssen and J.A.A.J. Perenboom, *Phys. Rev. B* 41 (1990) 12315.
- [4] K. Kern, T. Demel, D. Heitmann, P. Grambow, K. Ploog and M. Razeghi, *Surf. Sci.* 229 (1990) 256.
- [5] F. Hirler, J. Smoliner, E. Gornik and G. Weimann, *Appl. Phys. Lett.* 57 (1990) 261.
- [6] S.Y. Chou, D.R. Allee, R.F.W. Pease and J.S. Harris, *Appl. Phys. Lett.* 55 (1989) 176.
- [7] K. Ismail, D.A. Antoniadis and H.I. Smith, *Appl. Phys. Lett.* 55 (1989) 589.
- [8] C.C. Eugster and J.A. del Alamo, *Phys. Rev. Lett.* 67 (1991) 3586.
- [9] A. Zaslavsky, D.C. Tsui, M. Santos and M. Shayegan, *Appl. Phys. Lett.* 58 (1991) 1440.
- [10] U. Kunze, *J. Phys. C* 17 (1984) 5677.
- [11] S. Kar, *Solid State Electron.* 18 (1975) 169.
- [12] P. Bauernschmitt, J. Lindolf and U. Kunze, *Microelectron. Eng.* 22 (1993) 105.
- [13] C.R. Crowell, H.B. Shore and E.E. LaBate, *J. Appl. Phys.* 36 (1965) 3843.
- [14] U. Kunze and G. Lautz, *Surf. Sci.* 142 (1984) 314.
- [15] R.C. Potter and A.A. Lakhani, *Appl. Phys. Lett.* 52 (1988) 1349.



ELSEVIER

Surface Science 305 (1994) 637–642



## Magnetophonon resonances in quantum wires

G. Berthold, J. Smoliner <sup>\*</sup>, E. Gornik, G. Böhm, G. Weimann

*Walter Schottky Institut, Technische Universität München, Am Coulombwall, D-8046 Garching, Germany*

T. Suski, P. Wisniewski

*UNIPRESS, Polish Academy of Sciences, Sokolowska 29, 01-142 Warsaw, Poland*

C. Hamaguchi, N. Mori, H. Momose

*Department of Electronic Engineering, Osaka University, Suita City, Osaka 565, Japan*

(Received 7 May 1993; accepted for publication 15 June 1993)

---

### Abstract

We have investigated the magnetotransport properties of quantum wires which were fabricated on high-mobility GaAs/GaAlAs modulation-doped heterostructures by laser holography. For high temperatures ( $\sim 150$  K), magnetoresistance structures are revealed, which are due to the occurrence of magnetophonon resonances in the wire. This effect is used to determine the polaron mass which is found to be about 10% larger than to the polaron mass in bulk GaAs. In addition, hydrostatic pressure is used to modify the electron density in these quantum wires. We observe an increase of the 1D subband energy spacing with a decreasing electron density and an enhancement of the magnetophonon resonance amplitudes.

---

The problem of a low-dimensional electron system coupled to the longitudinal optical phonons (LO) has generated considerable interest in recent years. In bulk material, structures in the second derivative of the sample resistance ( $d^2R/dB^2$ ), which are caused by magnetophonon resonances, were used to determine the effective mass and the LO phonon energy [1,2].

In two-dimensional systems, magnetophonon resonances were first reported by Tsui et al. [3]. The observed structures in  $d^2R/dB^2$  were used

to determine the polaron mass in a two-dimensional electron gas. Later, magnetophonon resonances were also investigated by cyclotron resonance measurements [4,5], where it was possible to determine the energy relaxation rates. Brummel and coworkers [6] have carried out very systematic measurements, where they studied the magnetophonon resonances in two-dimensional electron gas (2DEG) as a function of temperature, electron concentration and magnetic field orientation. The results of these measurements showed: (i) an increase of the magnetoresistance oscillations amplitude with decreasing carrier concentration, (ii) an anomalous increase of the

---

<sup>\*</sup> Corresponding author.

cyclotron mass with temperature, and (iii) a possible involvement of interface phonons in the studied interaction with the 2DEG. Theoretical considerations on magnetophonon resonances for two-dimensional electron systems were carried out by Hamaguchi et al. [7] and Mori et al. [8]. For example, these authors have interpreted the increase of the magnetophonon resonance amplitude with decreasing sheet electron density [6] by Landau level broadening due to increased remote impurity scattering. Most recently, magnetophonons were also observed in vertical transport experiments carried out on GaAs/AlGaAs superlattices [9].

For nanostructured systems, such as quantum wires, interesting magnetophonon effects were already predicted theoretically [10–13]. Vasileopoulos et al. [10] have shown that for 1D systems, the magnetophonon resonances should be shifted to lower fields. Most recently, detailed theoretical studies of the 1D transport in the magnetophonon regime were carried out by Mori et al. [11]. They pointed out that the magnetoconductivity  $\sigma_{xx}$  consists of two contributions. One is related to the current carried by the electron hopping motion between the localized cyclotron orbits through the electron–phonon interaction, and the other is caused by the current carried by electron motion affected by the confinement potential. The former exhibits maxima at the resonances and the latter results in minima at resonance for the magnetoconductivity  $\sigma_{xx}$ . Although there are experimental hints that phonons play an important role in nanostructures [14], there are only a few data on magnetophonon effects in quantum-wire structures.

In our previous paper [15] we have determined the 1D quantization energies and have correlated it with the procedure of wire preparation. The use of longer etching times resulted in a stronger potential modulation and larger 1D energy level spacing.

The aim of this paper is to analyze the magnetotransport properties of quantum wires at high temperatures ( $T \approx 150$  K) and under hydrostatic pressures. One of the purposes of the performed studies is to determine the polaron mass of the electrons in 1D systems. The obtained results

show that in the case of a 1D system the polaron mass is higher than the bulk GaAs value. In addition, the magnetophonon resonances allow us to estimate the energy spacing of the 1D structure. Applying hydrostatic pressure makes it possible to decrease the electron density in the studied wires, which is used to examine the 1D quantization energy as a function of electron density.

The investigated samples consist of an unintentionally p-doped GaAs layer grown on a semi-insulating substrate ( $N_A < 10^{14} \text{ cm}^{-3}$ ), followed by an undoped spacer ( $d = 100 \text{ \AA}$ ), and doped  $\text{Al}_x\text{Ga}_{1-x}\text{As}$  ( $d = 250 \text{ \AA}$ ),  $N_D = 4 \times 10^{18} \text{ cm}^{-3}$ ,  $x = 0.3$ ). The additional GaAs cap layer is highly n-doped ( $d = 150 \text{ \AA}$ ,  $N_D = 5.7 \times 10^{18} \text{ cm}^{-3}$ ).

Bar-shaped mesas were etched into the samples and ohmic contacts were aligned using a AuGe alloy. Using laser holography, multiple wire structures were prepared with a period of  $a = 410 \text{ nm}$ , a geometrical width of  $w = 200 \text{ nm}$  and a length of  $l = 100 \text{ }\mu\text{m}$ . The photoresist patterns are transferred into the GaAs by wet chemical etching ( $\text{H}_2\text{O} : \text{H}_2\text{O}_2 : \text{NaOH} = 500 : 300 : 1$ ). Note, that magnetophonon resonances are observed best in samples which are etched so deep that the quantum wires are almost depleted at  $T = 4.2 \text{ K}$ . Therefore, the optimum etch time for the quantum wires was 60 s. A schematic view of the multi-wire structure used in these studies is shown in Fig. 1. The mobility of the unstructured samples was  $\mu = 3.8 \times 10^5 \text{ cm}^2/\text{V} \cdot \text{s}$  and the electron density was  $n_s = 6.3 \times 10^{11} \text{ cm}^{-2}$  at  $T = 4.2 \text{ K}$ . To characterize the properties of these wires, magnetoresistance measurements were performed in a configuration where the magnetic field is applied perpendicular to the multiple wire structure. For high-pressure measurements the UNIPRESS clamp cell with light petroleum as a pressure transmitting medium has been employed. A calibrated highly Te-doped InSb pressure gauge was used to monitor the pressure at temperatures between  $T = 300 \text{ K}$  and  $4.2 \text{ K}$ .

To describe the obtained experimental results we first concentrate on the temperature dependence of the magnetoresistance in a quantum wire. The experimental data at ambient pressures are shown in Fig. 2. At low temperatures (Fig. 2,

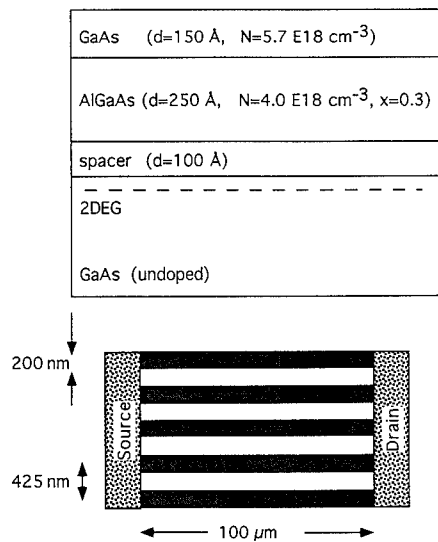


Fig. 1. Schematic view of the quantum-wire structures.

$T = 4.2$  K) Shubnikov–de Haas oscillations are observed above  $B = 1$  T. We have used this effect to determine the electron density corresponding to the different pressures applied to the samples. The negative magnetoresistance up to  $B = 3$  T, usually observed at low temperatures, is due to

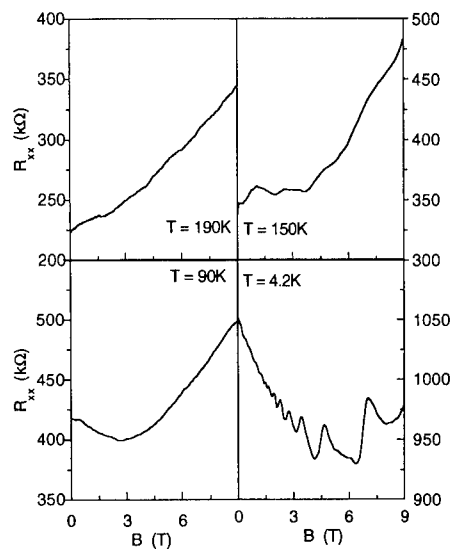


Fig. 2. Magnetoresistance for a multiple quantum-wire structure as a function of temperature. The maxima of magnetoresistance are clearly seen at  $T = 150$  K at magnetic fields  $B = 7, 4.5$  and  $2.8$  T.

the fact that the scattering processes in the quantum wire are more dominant than the boundary scattering [16]. For temperatures around  $T = 100$  K the Shubnikov–de Haas oscillations are washed out (Fig. 2), whereas at even higher temperatures ( $T \approx 130$ – $180$  K), additional structures are observed in the magnetoresistance  $R_{xx}$ , which are associated with magnetophonon resonances. The maxima observed in Fig. 2 for  $T = 150$  K at magnetic fields of  $B = 7, 4.5$  and  $2.8$  T represent these effects. For even higher temperatures the considered oscillations disappear (Fig. 2,  $T = 190$  K).

With applying hydrostatic pressure, the carrier density decreases due to lowering of the position of the Si-related level with respect to the bottom of the conduction band minima in both GaAs and AlGaAs [17]. Thus, electrons from the conducting channel are transferred to the Si donors located in the AlGaAs barrier. For the highest applied pressure, i.e.,  $p = 9$  kbar at  $T = 300$  K (which corresponds to  $p = 6$  kbar at  $T = 4.2$  K) carrier concentration, determined from the Shubnikov–de Haas effect, decreases from the value  $n_s = 6.3 \times 10^{11} \text{ cm}^{-2}$  to  $n_s = 4.2 \times 10^{11} \text{ cm}^{-2}$ . We estimate that the carrier concentrations determined at  $T = 4.2$  K characterize the sample at  $T = 150$  K within the accuracy of 20%. One may expect that the potential modulation as well as the screening phenomena will be influenced by the pressure-induced decrease in the carrier density. Concerning the variation in the magnetophonon resonances induced by a decrease in the carrier concentration (i.e., increasing applied pressure), we observed a shift of the corresponding maxima of the magnetoresistance to lower magnetic fields. In addition, the amplitude of the oscillations increases with decreasing  $n_s$ , which can be seen in Fig. 3, where the derivative of the measured magnetoresistance  $dR_{xx}/dB$  is plotted for two carrier densities ( $n_s = 6.3 \times 10^{11}$  and  $5.7 \times 10^{11} \text{ cm}^{-2}$ ).

To analyze the experimental data quantitatively, we assume a parabolic confinement  $V(y)$  for the quantum wires with  $V(y) = \frac{1}{2}m^*\Omega_0^2y^2$ , where  $y$  is the direction perpendicular to the wire,  $m^*$  is the electron effective mass (or polaron mass) and  $\Omega_0$  describes the strength of the

electrostatic potential. The corresponding subband spacing at  $B = 0$  T is given as  $\hbar\Omega_0$ . If the magnetic field is included using a Landau gauge, the subband spacing is equal to  $\hbar\Omega$  with  $\Omega^2 = \Omega_0^2 + \omega_c^2$  and  $\omega_c$  is the cyclotron frequency. According to Ref. [11], magnetoresistance maxima are expected each time, an integer ( $n$ ) multiple of the 1D subband spacing is equal to the LO-phonon energy:

$$n\hbar\sqrt{\omega_c^2 + \Omega_0^2} = \hbar\omega_{\text{LO}}. \quad (1)$$

Rewriting Eq. (1) in terms of  $B^2$ , we obtain:

$$B^2 = \left( \frac{m^*\omega_{\text{LO}}}{e} \right)^2 \frac{1}{n^2} - \left( \frac{m^*\Omega_0}{e} \right)^2. \quad (2)$$

If we consider the 2D case, which means  $\Omega_0 = 0$ , we obtain the usual magnetophonon peak positions, which are equidistant in  $1/B$ . Further, the polaron effective mass,  $m^*$ , can be determined from the slope of the curve if the phonon energy is known, or vice versa. In the case of a nanostructured sample, which means  $\Omega_0 > 0$ , the curve intersects the  $B^2$ -axis no longer at  $B = 0$ , which offers the possibility to determine the 1D subband energies from the magnetophonon peak positions. Note, that in contrast to magnetic depopulation measurements, this method offers the possibility to measure the subband spacing for samples, which are in the extreme quantum limit at low temperatures.

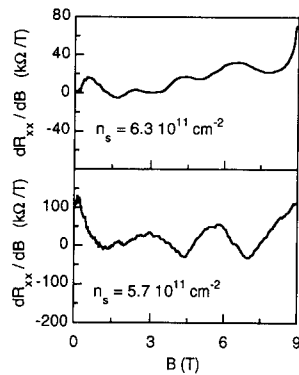


Fig. 3. The derivative  $dR_{xx}/dB$  for a quantum-wire structure at four different pressures (characterized by different carrier densities).

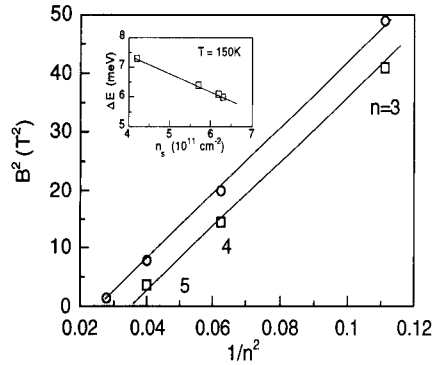


Fig. 4. The magnetophonon peak positions in  $B^2$  are plotted as a function of  $1/n^2$  for two different electron densities. The circles (upper line) correspond to  $n_s = 6.3 \times 10^{11} \text{ cm}^{-2}$  and the squares (lower line) to  $n_s = 5.7 \times 10^{11} \text{ cm}^{-2}$ . The inset shows the 1D subband energy spacing as a function of  $n_s$ .

Fig. 4 shows the results of the above considerations, where we have plotted the magnetophonon peak positions in  $B^2$  versus  $1/n^2$ . The peak positions for the two electron densities follow the predicted linear behavior in good agreement with the theoretical predictions. The slope of the linear dependence of  $B^2$  versus  $1/n^2$  in Fig. 4 can be used to determine the polaron mass  $m^*$  of the electrons in the quantum wire. If we assume the bulk GaAs LO phonon energy, the polaron mass of about  $m^* = 0.08$  ( $\pm 0.005$ ) is obtained. Values of the polaron mass  $m^*$  determined by magnetophonon effect in bulk GaAs [1] and 2D systems (see, e.g., Ref. [6]) do not exceed  $m_{\text{eff}}$  by more than 10%. Thus, we can conclude that in the studied 1D system the polaron mass  $m^*$  (at ambient pressures) is larger than  $m_{\text{eff}}$  in bulk GaAs by about  $20 \pm 5\%$ . Note, that within our experimental accuracy we do not observe changes of this 1D polaron mass  $m^*$  with increasing pressure, whereas in a two-dimensional electron system the effective mass increases about 7% between  $p = 0$  and  $p = 9$  kbar (see, e.g., Ref. [18]).

Using the polaron mass  $m^*$  we now determine the subband spacing from the intersection with the  $B^2$  axis due to formula (2) for a one-dimensional electron system (at ambient pressure). We obtain values of 6 meV. After applying hydrostatic pressure the electron density decreases and

the subband spacing increases as shown in the inset of Fig. 4. For the highest pressure (9 kbar) the electron density in the sample is  $n_s = 4.2 \times 10^{11} \text{ cm}^{-2}$  and the subband spacing is increased to 7.3 meV. Thus, the decrease in the carrier density produces an increase in the subband spacing as it is predicted by Laux et al. [19].

After having deduced the polaron mass of the electrons and the subband spacing in a quantum wire using the magnetic field position of the magnetophonon resonances, we now consider the amplitudes of these resonances (see Fig. 3). The observation of the increase in the magnetophonon oscillation amplitude with decreasing carrier concentration can be possibly explained in the way which was applied by Hamaguchi et al. [7] to the case of two-dimensional GaAs/AlGaAs structures. They propose to associate this amplitude value with the Landau level broadening due to remote impurity scattering. Changes in the number of ionized scattering centers in the AlGaAs barrier can be associated with the formation of pairs of positively and negatively charged Si-donor centers [20], which can lead to the decrease of the Landau level broadening.

To our knowledge of the literature, the strength of the observed resonances in our experiment strongly suggests, that magnetophonon scattering processes in quantum wires are enhanced, compared to 2D or 3D systems. This conclusion is consistent with the findings of Ref. [9], where very strong magnetophonon resonances were observed in vertical transport data on GaAs/AlGaAs superlattices. In their configuration the magnetic field is applied perpendicular to the layers of the sample, but parallel to the current, which formally, is also a kind of 1D transport.

In summary, the magnetotransport in quantum wires was investigated in the temperature regime between  $T = 2$  and  $T = 175$  K and under hydrostatic pressure up to 9 kbar. Magnetophonon resonances in the  $R_{xx}$  versus  $B$  curves are observed in the temperature range between  $T = 106$  and  $T = 175$  K. Application of hydrostatic pressure makes it possible to decrease the density of carriers in the quantum wires used in these measurements. According to the expectations it results in increasing a spacing between 1D energy

levels. In addition, pressure-induced changes in the distribution of charges in the quantum-wire structures enables us to observe an increase in the amplitude of magnetophonon oscillation as the carrier density is lowered. The determination of the polaron mass, performed under the assumption that electrons are interacting with LO phonons of bulk GaAs, gives a value of about 0.08 of the GaAs effective electron mass, which is 20% larger than the bulk value.

This work was sponsored by Deutsche Forschungsgemeinschaft, project No. SFB 348. The authors are grateful to W. Demmerle and R. Maschek for their assistance. T.S. and P.W. acknowledge the support by Grant No. 201609101 of the KBN, Poland. One of the authors (C.H.) acknowledges the support by the Grant-in-Aid for Scientific Research (A) and by the Grant-in-Aid for Scientific Research on Priority Area "Electron Wave Interference Effects in Mesoscopic Structures", from the Ministry of Education, Science and Culture, Japan. The support by the Grant-in-Aid for encouragement of young scientists to N.M. from the Ministry of Education, Science and Culture, Japan, is also acknowledged.

## 1. References

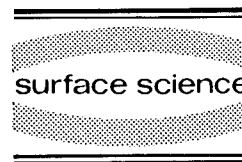
- [1] R.A. Stradling and R.A. Wood, *Solid State Commun.* 6 (1968) 701.
- [2] P.G. Harper, J.W. Hodby, R.A. Stradling, *Rep. Prog. Phys.* 37 (1973) 1.
- [3] D.C. Tsui, T. Englert, A.Y. Chao and A.C. Gossard, *Phys. Rev. Lett.* 44 (1980) 341.
- [4] P. Warmenbol, F.M. Peeters, X. Wu and J.T. Devreese, *Phys. Rev. B* 40 (1989) 6258.
- [5] P. Warmenbol, F.M. Peeters and J.T. Devreese, *Phys. Rev. B* 37 (1988) 4694.
- [6] M.A. Brummel, D.R. Leadley, J.R. Nicholas, J.J. Harris and C.T. Foxon, *Surf. Sci.* 196 (1988) 451.
- [7] C. Hamaguchi, N. Mori, H. Murata and K. Taniguchi, *High Magnetic Fields in Semiconductor Physics II*, Vol. 87 (Springer, Berlin, 1989).
- [8] N. Mori, H. Murata, K. Taniguchi and C. Hamaguchi, *Phys. Rev. B* 38 (1988) 7622.
- [9] N. Noguchi, H. Sakaki, T. Takamasu and N. Miura, *Phys. Rev. B* 45 (1992) 12148.

- [10] P. Vasilopoulous, P. Warmenbol, F.M. Peeters and J.T. Devreese, *Phys. Rev. B* 40 (1989) 1810.
- [11] N. Mori, H. Momose and C. Hamaguchi, *Phys. Rev. B* 45 (1992) 4536.
- [12] M.H. Degani and O. Hipolito, *Superlatt. Microstruct.* 5 (1989) 137.
- [13] E.S. Hellman and J.S. Harris, *Phys. Rev. B* 33 (1986) 8284;  
S. Briggs, B.A. Mason and J.P. Leburton, *Phys. Rev. B* 40 (1989) 12001;  
V.B. Campos, M.H. Degani and O. Hipolito, *Solid State Commun.* 79 (1991) 473.
- [14] K. Ismail, *Proc. Int. Symp. on Science and Technol. of Mesoscopic Structures*, Nara, 6–8 November 1991, to be published.
- [15] G. Berthold, J. Smoliner, M. Hauser, C. Wirner, E. Gornik, G. Böhm, G. Weimann, C. Hamaguchi, N. Mori and H. Momose, to be published.
- [16] T.J. Thornton, M.L. Roukes, A. Scherer and B.P. van de Gaag, *Phys. Rev. Lett.* 63 (1989) 2128.
- [17] T. Suski, E. Litwin-Staszewska, P. Wisniewski, L. Dmowski, W.H. Zhuang, G.B. Liang, D.Z. Sun and Y.P. Zhen, *J. Appl. Phys.* 63 (1988) 2307;  
R. Piotrkowski, J.L. Robert, E. Litwin-Staszewska and J.P. Andre, *Phys. Rev. B* 37 (1988) 1031.
- [18] L.G. Shantarama, A.R. Adams, C.N. Ahmad and R.J. Nicholas, *J. Phys. C* 17 (1984) 4429;  
G. Gregoris, J. Beerens, S. Ben Amor, L. Dmowski, J.C. Portal, F. Alexandre, D.L. Sivco and A.Y. Cho, *Phys. Rev. B* 37 (1988) 1262.
- [19] S.E. Laux, D.J. Frank and F. Stern, *Surf. Sci.* 196 (1988) 101.
- [20] T. Suski, P. Wisniewski, L.H. Dmowski, I. Gorczyca, J. Smoliner, E. Gornik, G. Weimann and G. Böhm, to be published.



ELSEVIER

Surface Science 305 (1994) 643–647



# Anharmonic periodic modulation in lateral surface superlattices

R. Cuscó <sup>\*,1</sup>, M.C. Holland, J.H. Davies, I.A. Larkin, E. Skuras, A.R. Long,  
S.P. Beaumont

*Nanoelectronics Research Centre, Department of Electronics and Electrical Engineering, Glasgow University, Glasgow G12 8QQ, UK*

(Received 19 April 1993; accepted for publication 13 June 1993)

## Abstract

We have measured the longitudinal magnetoresistance of a lateral surface superlattice with a period of 270 nm where the electrons are only 28 nm deep. The commensurability oscillations have a strong second harmonic content. This reflects a non-sinusoidal potential in the two-dimensional electron gas, a consequence of the shallow structure. The shape of the potential cannot be explained by a pinned GaAs surface and indicates that the surface charge is frozen or that the electrons feel an elastic strain field from the metal gates.

## 1. Introduction

Recent advances in molecular beam epitaxy and nanofabrication techniques have generated interest in a periodically modulated two-dimensional electron gas (2DEG). It is now possible to fabricate a lateral surface superlattice (LSSL) using surface gates on very high mobility GaAs/AlGaAs heterostructures in which the electron retains its phase coherence over many periods of the superlattice. The clearest manifestation of the modulation of the 2DEG is the appearance of a series of oscillations in the low-field magnetoresistance arising from the commensurability between the cyclotron orbit and the period of the potential [1,2]. The origin of these oscillations is now well understood [3,4] and most experimental

data [1,5,6] are adequately described by a semi-classical model [3] with a sinusoidal modulation potential.

In conventional high-mobility layers, where the 2DEG is formed deep below the surface (typically 100 nm), the high-order Fourier components of the surface potential are strongly attenuated causing a sinusoidal potential in the 2DEG [7]. It is predicted [6] that the semiclassical model will break down when  $(\hbar^2/2m)(2\pi/a)^2 > 16 eV$ , where  $V$  is the amplitude and  $a$  is the period of the periodic potential in the 2DEG. In this regime the electrons can tunnel through the barriers of the periodic potential and new effects are expected. The period of the gate must be reduced to approximately 50 nm for devices to operate in this regime, and the 2DEG must be brought closer to the surface without degrading its characteristics.

Here we report the fabrication of a superlattice device with a period of 270 nm on a shallow 2DEG at an interface only 28 nm below the

\* Corresponding author.

<sup>1</sup> Present address: Institute of Earth Sciences (Jaume Almera), Martí i Franquès s/n, 08028 Barcelona, Spain.



surface. We show that the improved coupling between the surface and the 2DEG strongly modifies the shape of the periodic potential in which electron transport takes place and makes it far from sinusoidal.

## 2. Samples and experimental procedure

The devices were fabricated on GaAs/(Al, Ga)As layers comprising a GaAs buffer, two 10 nm thick AlAs barriers separated by 2 nm of AlGaAs  $\delta$ -doped to  $4 \times 10^{16} \text{ m}^{-2}$ , and a 5.4 nm GaAs cap layer. Hall bars with three pairs of voltage probes were fabricated on this layer by electron beam lithography and wet etching. The channel was  $14 \mu\text{m}$  wide with  $30 \mu\text{m}$  between voltage probes. An interdigitated array of Schottky barrier gates between two of the pairs of voltage probes was formed by electron beam lithography followed by evaporation and lift-off of 15 nm Ti/15 nm Au. The width of each metal finger was 130 nm and the spacing between adjacent fingers was 140 nm. The interdigitation allows adjacent fingers to be differentially biased, although all fingers were held at zero potential in the experiments reported here; the effect of bias will be discussed in a future publication. The

array of gates fills the space between the voltage contacts to minimise the effect of ungated areas of 2DEG on the overall magnetoresistance.

The four-terminal magnetoresistance of the devices was measured using standard lock-in techniques in an Oxford Instruments Kelvinox dilution refrigerator. The ungated region of the device gave an electron density of  $3.3 \times 10^{15} \text{ m}^{-2}$  and a mobility of  $66 \text{ m}^2 \text{ V}^{-1} \text{ s}^{-1}$  at 4.2 K in the dark, with the mobility rising to  $81 \text{ m}^2 \text{ V}^{-1} \text{ s}^{-1}$  after brief illumination. In the gated region, with the gates held at 0 V, the electron density was  $3.2 \times 10^{15} \text{ m}^{-2}$  and the resistivity was twice the value of the ungated region.

We believe that the high mobility of these layers is largely due to electrons around the  $\delta$ -doped layer. Although these electrons have a low mobility and make a negligible direct contribution to transport, they screen the random potential due to the ionized donors and greatly enhance the mobility of the 2DEG from an expected value of only about  $6 \text{ m}^2 \text{ V}^{-1} \text{ s}^{-1}$  if the full random potential were operative. We have verified this by measuring the mobility and concentration of the 2DEG in another sample as a function of the voltage on a large uniform gate. A built-in potential associated with the Schottky gates could partly deplete the charge around the

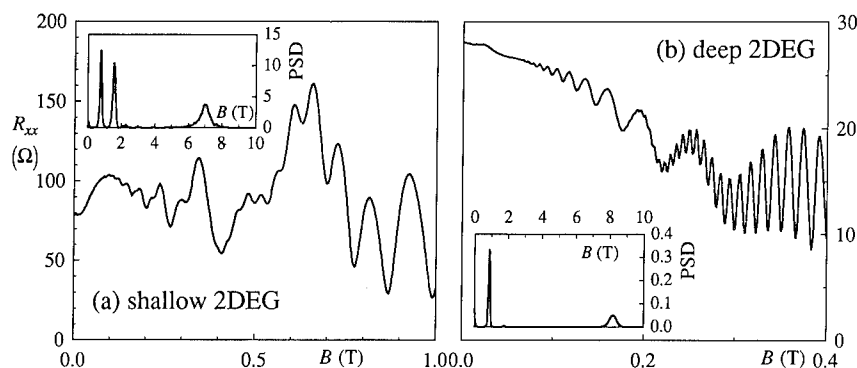


Fig. 1. Longitudinal magnetoresistance of (a) the shallow 2DEG at 1.2 K and (b) the deep 2DEG at 70 mK. The commensurability oscillations at low  $B$  are sinusoidal in the deep 2DEG (b) but show a strong second harmonic in the shallow structure (a). This is confirmed by the power spectral density (PSD, insets) obtained from Fourier transforms of the magnetoresistance treated as a function of  $1/B$ . The peak at 7–8 T is from the Shubnikov–de Haas effect while those at low frequency arise from commensurability oscillations. The second harmonic is strong in the shallow 2DEG (a) but absent from the deep 2DEG (b).

donors, increase the random potential and decrease the mobility of the gated region. However, this would require a very large built-in potential and we suspect that damage introduced during processing is responsible for the reduction in mobility.

### 3. Experimental results and analysis

Fig. 1a shows the longitudinal magnetoresistance of the gated region at  $T = 1.2$  K for zero gate voltage, with the current flow perpendicular to the equipotentials of the superlattice. These results were taken after the sample had been illuminated, but the same effects were visible with the sample in the dark. We observe Shubnikov–de Haas oscillations at high fields, and another series of oscillations periodic in  $1/B$  are clearly visible at low fields ( $B < 0.8$  T). These commensurability oscillations arise from enhanced diffusion in the direction of the equipotentials due to a resonance in the  $E \times B$  drift. This occurs [3] when the cyclotron radius  $R_c$  obeys  $2R_c = (n + \frac{1}{4})a$ , where  $n = 1, 2, \dots$ , and has been well studied in conventional deep 2DEGs [1,2,5,6]. Previous experiments have shown sinusoidal oscillations but in our devices the commensurability oscillations have a strong second harmonic content which is clearly visible in the raw data and is even more striking in the power spectrum of the magnetoresistance shown in the inset to Fig. 1a.

For comparison, we fabricated identical structures on a conventional modulation-doped layer where the 2DEG lies 90 nm below the surface. Their magnetoresistance at 70 mK after illumination is shown in Fig. 1b, and the commensurability oscillations are clearly sinusoidal. The power spectrum (inset) confirms that no significant higher harmonics are present.

We used a semiclassical model [3] to relate the amplitude of each harmonic of the commensurability oscillations to the amplitude of the corresponding harmonic of the electrostatic potential in the 2DEG. The harmonics were extracted by digitally filtering the experimental data and the

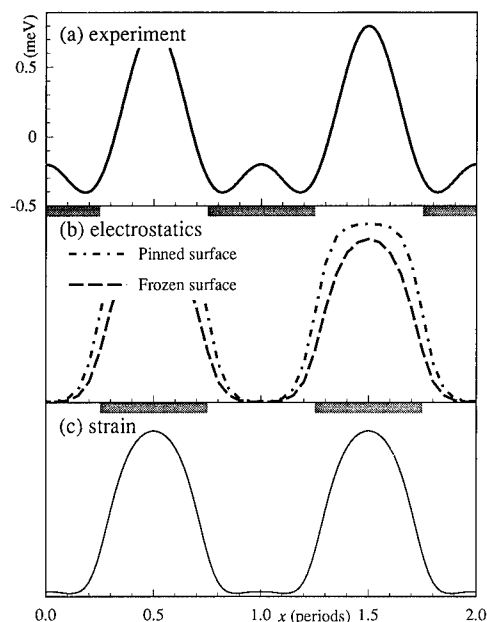


Fig. 2. Potential energy in 2DEG. (a) Experimental result reconstructed from commensurability oscillations for the shallow device. (b) Electrostatic calculations: chain curve, pinned surface; broken curve, frozen surface charge. (c) Potential due to strain caused by differential contraction between the GaAs and metal gate. The lateral positions of the gates are shown as grey rectangles in (b) and (c). The scales of the theoretical curves are arbitrary.

estimates of the potential were obtained from the theoretical expression

$$\frac{\delta\rho}{\rho} = \sum_{n=1}^{\infty} \left( \frac{eV_n}{E_F} \right)^2 \left( \frac{nl^2}{aR_c} \right) \cos^2 \left( \frac{2\pi nR_c}{a} - \frac{\pi}{4} \right), \quad (1)$$

where  $\rho$  is the resistivity,  $V_n$  is the peak amplitude of the  $n$ th harmonic of the periodic potential at the 2DEG,  $E_F$  is the Fermi energy and  $l$  is the mean free path. The phase of the commensurability oscillations as a function of  $B$  agrees with Eq. (1), but they give a density of  $3.8 \times 10^{15} \text{ m}^{-2}$  compared with  $3.3 \times 10^{15} \text{ m}^{-2}$  from the Shubnikov–de Haas peak. We have not yet resolved this discrepancy.

The strength of the modulation was found to be  $V_1 \approx 0.5$  meV for the fundamental (first harmonic) and  $V_2 \approx 0.3$  meV for the second harmonic. The potential energy at the 2DEG was

reconstructed from this and is shown in Fig. 2a. It resembles a truncated sine-wave as expected from the second harmonic in the commensurability oscillations. Note that Eq. (1) does not contain the *phases* of the harmonics of the potential energy. Although the phase between the first and second harmonics is fixed by symmetry, we cannot determine either the sign of the potential or whether the double minima lie under the gates or the gaps.

#### 4. Theoretical analysis

We have modeled the potential in the 2DEG, considering two possible sources. The first is an electrostatic field. No bias was applied to the gates so a built-in voltage under the Schottky gates, mentioned above, must be responsible. The potential in the 2DEG was calculated analytically and depends strongly on the boundary condition [8] applied to the exposed surface between the gates, as shown in Fig. 2b.

The usual assumption is that the Fermi energy on the surface is pinned at a fixed energy below the conduction band. This leads to a potential in the 2DEG that contains no significant content of even harmonics (chain curve), and is not in agreement with experiment. Pinning requires charge to be able to move between the 2DEG and the surface, which seems unlikely at low temperature, and a more realistic assumption may be that the charge on the surface is frozen (broken curve). This leads to a potential that contains a second harmonic although not as large as that seen experimentally. A typical built-in voltage on the gates is around 0.1 V which leads to 6 mV peak-to-peak in the 2DEG for both boundary conditions. Screening by the electrons around the donors reduces this by a factor of about 5, with a smaller effect on the shape. Thus electrostatics [9] predicts the right magnitude of potential in the 2DEG (although the sign is unknown), but too little of the higher harmonics.

A second possible source of this potential is mechanical strain. This has been used to confine electrons in potential wells by depositing deliberately a mis-matched stressor [10]. In our case the

strain arises because the gates are deposited at a relatively high temperature. The coefficient of expansion of the metal gates is greater than that of GaAs, so the gate acts as a stressor in tension when the sample is cooled. This produces a strain field within the semiconductor which couples to the electrons through the deformation potential. The potential energy was calculated analytically [9], assuming uniform longitudinal strain under the gates, and is shown in Fig. 2c. It has shallow double minima under the gaps, less pronounced than that seen experimentally, although they increase rapidly if the separation between the gates and 2DEG is reduced. The form of the potential energy agrees with numerical calculations [10], although the sign is reversed because our stressor is in tension. It is difficult to calculate the magnitude of the potential because the conditions under which the gate is deposited are not accurately known, but a potential of around 1 meV in the 2DEG seems reasonable. Thus strain offers the best single source of the periodic potential observed.

#### 5. Conclusions

We have shown that the construction of a surface superlattice on a shallow 2DEG leads to greater coupling between the gate potential and electrons in the channel. In turn, the periodic potential becomes non-sinusoidal and harmonics of the commensurability oscillations appear in the longitudinal magnetoresistance. The shape of the inferred potential is explained best by a strain field due to differential contraction between the metal gates and the semiconductor, although an electrostatic model in which the surface charge between the gate fingers is frozen also gives a fair description of the shape.

#### 6. Acknowledgements

This work was supported by UK SERC grant GR/80890 and partially by ESPRIT Basic Research Action 3133. R. Cuscó has benefited from a postgraduate scholarship from the Spanish Ministry of Education and Science.

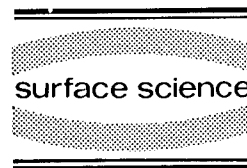
## 7. References

- [1] R.R. Gerhardts, D. Weiss and K. von Klitzing, *Phys. Rev. Lett.* 62 (1989) 1173.
- [2] R.W. Winkler and J.P. Kotthaus, *Phys. Rev. Lett.* 62 (1989) 1177.
- [3] C.W. Beenaker, *Phys. Rev. Lett.* 62 (1989) 2020.
- [4] C. Zhang and R.R. Gerhardts, *Phys. Rev. B* 41 (1990) 12850.
- [5] P.H. Beton, E.S. Alves, P.C. Main, L. Eaves, M.W. Dellow, M. Henini, O.H. Hughes, S.P. Beaumont and C.D.W. Wilkinson, *Phys. Rev. B* 42 (1990) 9229.
- [6] P.H. Beton, M.W. Dellow, P.C. Main, E.S. Alves, L. Eaves, S.P. Beaumont and C.D.W. Wilkinson, *Phys. Rev. B* 43 (1991) 9980.
- [7] J.P. Kotthaus and D. Heitmann, *Surf. Sci.* 113 (1982) 481.
- [8] S.E. Laux, D.J. Frank and F. Stern, *Surf. Sci.* 196 (1988) 101.
- [9] J.H. Davies and I.A. Larkin, *Phys. Rev. B*, to be published.
- [10] K. Kash, R. Bhat, D.D. Mahoney, P.S.D. Lin, A. Scherer, J.M. Worlock, B.P. Van der Gaag, M. Koza and P. Grabbe, *Appl. Phys. Lett.* 55 (1989) 681.



ELSEVIER

Surface Science 305 (1994) 648–653



## Fabrication and characterisation of multi-level lateral nano-devices

R.P. Taylor <sup>\*,1</sup>, Y. Feng, A.S. Sachrajda, J.A. Adams <sup>2</sup>, M. Davies, P.T. Coleridge, P. Zawadski

*I.M.S., National Research Council, Ottawa, Ontario, K1A 0R6, Canada*

(Received 19 April 1993; accepted for publication 11 May 1993)

### Abstract

The design of surface gate patterns, used to define nanostructures in AlGaAs/GaAs heterostructures, is greatly enhanced by the possibility of establishing electrical contact to, and independently biasing, a 100 nm wide isolated gate. We describe the fabrication of a multi-level metallisation architecture which can be used to contact a nanoscale central gate and monitor the transition from a quantum dot to ring geometry. We employ geometry induced quantum interference effects as a novel low temperature characterisation tool and report experiments in which the central electrode acts as an artificial impurity.

### 1. Introduction

Since its first demonstration in 1986 [1], the technique of employing surface gate designs to define submicron-sized geometries in the two-dimensional electron gas (2DEG) of AlGaAs/GaAs heterostructures has yielded a wide variety of low temperature experiments. The ability to incorporate an independent nanoscale gate into these patterns adds considerable flexibility to the scope of these highly topical devices. In this paper we describe the fabrication of a five gate device, shown in Fig. 1, which is designed to study the transition from a quantum dot to a ring. Previ-

ously these two distinct geometries, although the focus of a great deal of theoretical and experimental investigation [2–5], could only be studied by the fabrication of two separate nanostructures. The transition, achieved by tuning the bias applied to gate 5, requires the construction of a novel multi-layer metallisation architecture to contact to isolated gates with widths as small as 100 nm. Such a transition has implications for a variety of physical phenomena ranging from geometry induced quantum interference to Coulomb blockade [3] effects. By switching off gates 2 and 4 and tuning gate 5, the same device can be used to induce an artificial impurity of known size and position into a submicron wire. This fabrication technique can therefore also be used to assess the extent by which impurities affect nanostructure functionality, for example as a scattering site for quantum interference paths. We present low temperature magnetoresistance results both at low

\* Corresponding author.

<sup>1</sup> Present address: School of Physics, University of New South Wales, P.O. Box 1, Kensington, NSW, 2033, Australia.

<sup>2</sup> Present address: Department of Physics, University of Nottingham, Nottingham, NG7 2RD, UK.

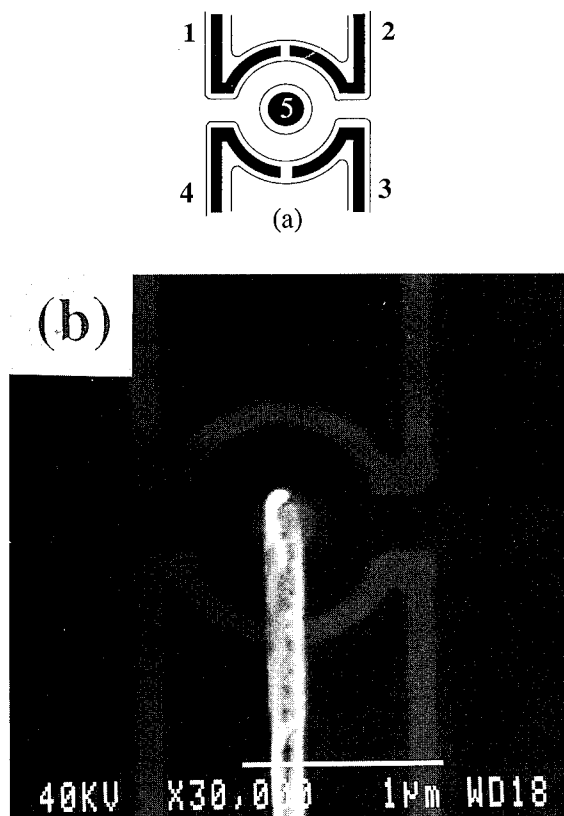


Fig. 1. (a). A schematic showing the surface gates (black) and associated depletion pattern (narrow lines) and (b) an SEM image of the completed device.

fields, where Aharonov–Bohm oscillations [6] are used as a characterisation tool, and at higher fields where we investigate a breakdown of the quantum Hall effect [7] due to tunnelling through the states bound to the artificial impurity. This is the first demonstration of the ability to separately address gates in the centre of a quantum dot or wire.

## 2. Device fabrication

The method of connecting devices using metal interconnects separated by an interlayer dielectric is a critical part of VLSI technology. To exploit this approach for nanostructure construction, a 10 nm alignment precision is required. For the device of Fig. 1 we successfully adopt this two

level metallisation architecture as the method of contacting the central electrode, gate 5. A layer of  $\text{Si}_3\text{N}_4$  is deposited over the device and then a 100 nm diameter hole is etched in the nitride to expose the central electrode, allowing contact to a fineline interconnect. The fabrication sequence of the device involves seven lithography steps for which both electron beam (EB) and optical (UV) exposure techniques are employed.

The initial two UV stages define a  $30\text{ }\mu\text{m}$  wide Hall bar. To reduce sidewall damage [8], a “shallow” etch technique depletes the 2DEG at a typical etch depth of 70 nm, compared to the 2DEG depth of 82 nm. The anisotropic etch  $\text{H}_3\text{PO}_4$  produces a mesa edge with a sloping profile, allowing fine surface gates (deposited later) to cross continuously. A 200 nm thick NiAuGe metallisation is then aligned to the mesa pattern and annealed to establish Ohmic contacts to the 2DEG. This metallisation stage also provides three sets of markers which are used at the first EB fabrication stage for course, medium and fine alignment (at 200, 100 and  $50\text{ }\mu\text{m}$  square field sizes, respectively). Details of these UV lithography stages are reported elsewhere [9]. We now consider the construction of the five gate nanostructure within this Hall bar geometry.

### 2.1. The surface gates

The EB lithography is performed using a modified JEOL JSM-840A scanning electron microscope (SEM). Poly(methyl methacrylate) (PMMA) is used as a spin-coated resist: A 110 nm thick bilayer (approximate molecular weights of 100 000 and 400 000 dissolved in o-xylene to give concentrations of 2% and 4% by weight in solution) is used to produce the Ti/Pt (10/40 nm) surface gates by lift-off [9]. Ti is chosen because of the reproducible Schottky barrier (0.7 eV) at the semiconductor interface, which is essential to minimise any leakage currents, and also because its adhesion properties are superior to those of Au and Al [9]. The Pt capping layer prevents oxidation of the Ti. In addition to the five gates seen in Fig. 1, three sets of markers are also deposited during this metallisation and these are used for precision alignment (at 50, 25 and 12.5

$\mu\text{m}$  square field sizes) in the subsequent EB fabrication stages. Gates 1 to 4 extend to cross the mesa edge of the Hall bar and then fan out to facilitate overlay by gate bonding pads. These Ti/Au (25/300 nm) gate bonding pads, defined by subsequent UV lithography and metal lift-off, terminate 5  $\mu\text{m}$  from the mesa edge and link gates 1 to 4 with 200  $\mu\text{m}$  square regions where wire bonding occurs. The thick top layer of Au is used to facilitate this bonding. This metallisation is therefore also deposited on top of the annealed Ohmic pads. The remaining four fabrication stages are used to establish an electrical link between gate 5 and its respective bonding pad.

## 2.2. The inter-layer insulator

Remote plasma enhanced chemical vapour deposition (R-PECVD) is used to establish a 100 nm thick conformal layer of  $\text{Si}_3\text{N}_4$  over the 50 nm high gates (confirmed by a subsequent cleave and SEM examination of a control sample) [10]. We note that initial attempts by conventional parallel-plate PECVD, in which the sample was immersed in the plasma, resulted in severe degradation of electron mobility in the device due to ion damage [9]. A 1  $\mu\text{m}$  thick layer of photoresist is now deposited and exposed by UV lithography, defining the etch mask for a subsequent  $\text{CHF}_3$  plasma etch. This step opens windows in the  $\text{Si}_3\text{N}_4$  layer above the gate bonding pads, the Ohmic contacts and also above selected alignment markers [9]. The unetched regions, in particular the 2DEG in the Hall bar, are protected from reactive ion etching (RIE) damage [11] by the  $\text{Si}_3\text{N}_4$  layer. For the Ohmic patterns, only the regions required for wire bonding are exposed, so minimising damage in the 2DEG regions below the Ohmic metallisation. To expose the central electrode, a 100 nm diameter circle is written by EB in a 240 nm thick bilayer of PMMA resist using a 12.5  $\mu\text{m}$  field size. The alignment of this pattern is achieved using three sets of alignment markers – one set, positioned below windows in the  $\text{Si}_3\text{N}_4$  at the sides of the Hall bar mesa, allows alignment at the 50  $\mu\text{m}$  field size. Two further sets (sufficiently visible through the 100 nm  $\text{Si}_3\text{N}_4$  layer) are positioned on the Hall bar

close to the gates, and allow further alignment [12] at 25 and 12.5  $\mu\text{m}$  field sizes. Using this resist pattern as an etch mask, an optimised  $\text{CHF}_3$  plasma establishes the hole above the electrode with a tapered profile required for the final metallisation process [9]. The central electrode both shields the 2DEG from ion damage during etching and also serves as an etch stop (over-etching would result in an unwanted potential perturbation in the 2DEG). Finally, the PMMA mask is stripped using an oxygen plasma and the surface solvent cleaned, readying the device for the final metallisation.

## 2.3. The metal interconnect

In Fig. 1b the first layer of gates, although darker, are still clearly seen through the 100 nm layer of  $\text{Si}_3\text{N}_4$ . The metal interconnect pattern, which traverses the  $\text{Si}_3\text{N}_4$  surface to link the central electrode to its bonding pad, is written in a 290 nm thick bilayer of PMMA in two stages. Approaching the dot (not shown), the interconnect has a width of 300 nm and is written at the 50  $\mu\text{m}$  field size, whilst a narrower 100 nm wide metal line (identical width to the gates defining the dot), drawn at the 12.5  $\mu\text{m}$  field size, traverses the dot region. The most critical stage is establishing a metallic link through the 100 nm hole in the  $\text{Si}_3\text{N}_4$ . Firstly, the hole must be etched completely down to the electrode. This is indicated during EB exposure of the resist when secondary electron contrast, seen as the electron beam reaches the surface gate, is only observed if the gate is not covered with nitride. To deposit the metal in the hole, a tapered profile is required in addition to a two stage metallisation procedure – an initial Ti/Pt/Au (10/20/40 nm) layer followed by Ti/Au (25/50 nm). In each case, the sample surface is tilted at 22° to the plane facing the electron beam evaporant sources (operating pressure of  $<10^{-7}$  Torr) and is rotated through 180° within this plane between the two metallisations. Fig. 1b reveals an alignment precision of approximately 10 nm and for a working device this precision is required at two stages (the hole to the central electrode, and then the interconnect to the hole). Success of the align-

ment scheme is due to a combination of the small exposure field ( $12.5 \mu\text{m}$ ), the high resolution of the 16 bit digital-to-analog converters in the pattern generator and the stability of the sample stage. Examination in an SEM, using a range of device tilt angles, is used to physically assess the hole “filling” procedure prior to electrical characterisation.

### 3. Electrical characterisation

Application of a negative voltage to the gates on the surface of the semiconductor, 1 to 4, defines a corresponding depletion profile in the 2DEG at the AlGaAs/GaAs interface. Electrons (with a mobility of  $10^6 \text{ cm}^2/\text{V}\cdot\text{s}$  and density of  $3.3 \times 10^{11} \text{ cm}^{-2}$  at 4.2 K) therefore pass through an enclosed region, or “dot”, via an entrance and an exit port. Alternatively, activation of just two diagonal gates, say 1 and 3, defines a narrow channel or “wire” for the electrons. Biasing gate 5 can therefore be used either to induce a transition from a dot into a ring, or to introduce a potential inhomogeneity, or “artificial impurity”, into a narrow wire. In Figs. 2 to 4, we focus on the wire geometry and use standard low current AC measurements to monitor the evolution of the magnetoresistance at 20 mK. In Fig. 2 we see a clear manifestation of the Aharonov–Bohm (AB) effect at  $-0.42 \text{ V}$ , a voltage which is typical for depletion under our gates. These magnetoresistance oscillations, of period  $\Delta B$ , result from the quantum interference between electron paths which enclose an area  $A$  around the artificial impurity. Calculations of  $A$ , using the equation  $A = h/e\Delta B$ , reveal an average trajectory diameter of 620 nm. This is consistent with values for the average width of the wire (850 nm) and the diameter of the impurity (400 nm), both calculated from the respective lithographic radii allowing for a depletion distance (obtained from calibration measurements of the entrance and exit ports [12]). The insets of Fig. 2 use this unique signature of the AB oscillations to calibrate the characteristic depletion action for the five gates. The average trajectory diameter, calculated from  $\Delta B$ , can be reduced or increased by, for example,

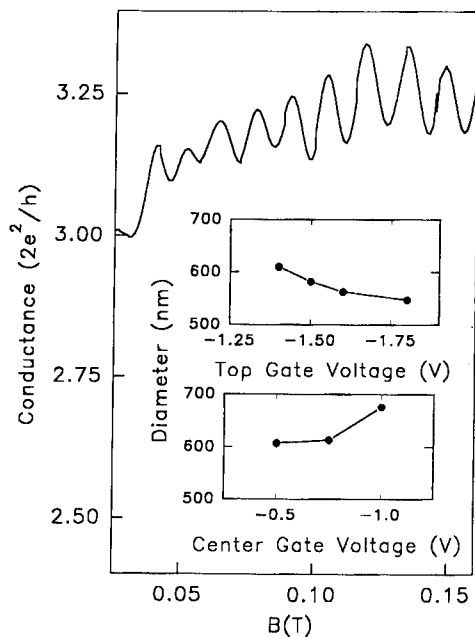


Fig. 2. Aharonov–Bohm oscillations, induced by the artificial impurity. The insets show their gate voltage dependences (see text for details).

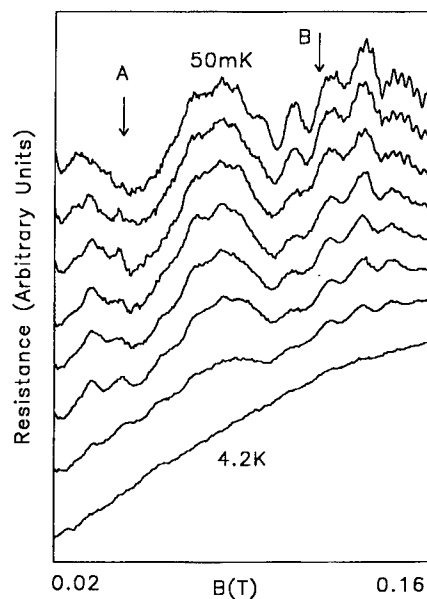


Fig. 3. Low field magnetoresistance taken at 50 mK (top), 200 mK, 400 mK, 620 mK, 840 mK, 1.2 K, 2 K and 4 K. For each trace, a background slope has been subtracted.



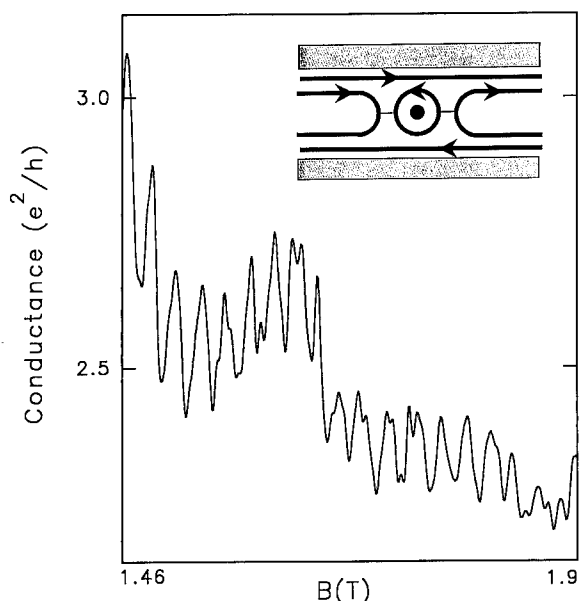


Fig. 4. Magnetoconductance oscillations at high magnetic fields. The inset is a schematic representation of the edge states and the tunnelling route via the artificial impurity. Two extra edge states, apparent for these fields, are also reflected at the impurity but are omitted for clarity.

tuning gates 3 (upper inset) and 5 (lower inset), respectively. Controlled variations in average diameter from 550 to 700 nm can be achieved. The AB effect relies on phase coherence of the partial waves associated with the electron trajectories, and we therefore include Fig. 3 to demonstrate the oscillations' sensitivity to electron temperature (see magnetic field range marked B. Note, details of the low field magnetoresistance regime, marked A, will be discussed elsewhere).

Finally, Fig. 4 reveals a set of high field magnetoconductance oscillations, which can be explained by an interplay of edge states with the artificial impurity, as represented schematically in the inset. At voltages sufficient to achieve depletion under the centre gate, a reduced electron density (relative to the bulk 2DEG) in the regions between the impurity and the wire sidewalls creates two parallel potential barriers which can be set to reflect some or all of the edge states. In this field regime, electrons from reflected edge states undergo resonant tunnelling [7] through the states bound to the artificial impurity. If we

assume the resonance condition, and hence the resulting periodic oscillations, are determined by a single particle spectrum of the bound states, the diameter for the impurity (450 nm) calculated from  $\Delta B$  is physically reasonable. However, as with the quantum dot geometry [14], it is likely that electron interactions will ultimately be required to explain the dynamics of the tunnelling process. At even higher fields, in the "adiabatic" regime, the total conductance on a plateau is given simply by the larger of the parallel conductances and no oscillations are seen. In contrast to previous studies of these phenomena [15], the above investigations benefit enormously from the ability to independently vary the two barriers while keeping the centre gate at a fixed voltage. This is possible for our structure since all five gates can be independently biased.

#### 4. Conclusions

We have demonstrated an architecture used to independently bias a nanoscale isolated gate. This approach to nanostructure design provides the flexibility to investigate continuous transitions between distinct geometries which previously could only be measured using two separately constructed nanostructures. The technique, which links a central electrode to a gate bonding pad for the device of Fig. 1, may equally be employed to interconnect to another nanostructure device. Whether used for intra- or inter-device interconnects, the approach offers significant advantages. The devices, which are sensitive to fringing electric fields, are shielded from the interconnect by the insulating electrical properties of the  $\text{Si}_3\text{N}_4$ . The encapsulation by a protecting layer also makes the structure robust, by reducing both physical and electrostatic charging damage during handling. Furthermore, the interconnects can travel over rather than around devices. Future modifications to the process are aimed at both improving its viability as a nanoscale metal interconnect technique, and also at providing previously unattainable geometries for the study of controllable quantum interference effects.

## 5. Acknowledgements

D. Landheer, P.A. Marshall and R. Barber for assistance in device fabrication.

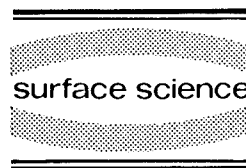
## 6. References

- [1] T.J. Thornton, M. Pepper, H. Ahmed, D. Andrews and G.J. Davies, *Phys. Rev. Lett.* 56 (1986) 1198.
- [2] S. Washburn and R.A. Webb, *Adv. Phys.* 35 (1986) 375.
- [3] R.P. Taylor, A.S. Sachrajda, P. Zawadzki, P.T. Coleridge and J.A. Adams, *Phys. Rev. Lett.* 69 (1992) 1989.
- [4] H. van Houten, C.W.J. Beenakker and A.M. Staring, in: *Single Electron Tunneling*, NATO ASI Series B, Eds. H. Grabert and M.H. Devrolet (Plenum, New York).
- [5] R.A. Jalabert, H.U. Baranger and A.D. Stone, *Phys. Rev. Lett.* 65 (1990) 2443.
- [6] Y. Aharonov and D. Bohm, *Phys. Rev. Lett.* 115 (1959) 485.
- [7] J.K. Jain, *Phys. Rev. Lett.* 60 (1988) 2074.
- [8] H. van Houten, B.J. Van Wees, H.G.J. Heijman and J.P. Andre, *Appl. Phys. Lett.* 49 (1986) 1781.
- [9] R.P. Taylor, J.A. Adams, M. Davies, P.A. Marshall and R. Barber, *J. Vac. Sci. Technol. B* 11 (1993) 628.
- [10] D. Landheer, N.G. Skinner, T.E. Jackman, D.A. Thomson, J.G. Simmons, D.V. Stevanovic and D. Khatamain, *J. Vac. Sci. Technol. A* 9 (1991) 2594.
- [11] S.I. Pearton, F. Ren, J.R. Lothian, T.R. Fullowan, R.F. Kopf, U.K. Chakrabarti, S.P. Hui, A.B. Emerson, R.L. Kosterlak and S.S. Pei, *J. Vac. Sci. Technol. B* 9, 5 (1991) 2487.
- [12] Softwear produced by JCN lithography systems, Bozeman, MT 59717, USA.
- [13] R.P. Taylor, A.S. Sachrajda, J.A. Adams, C.R. Leavens, P. Zawadzki and P.T. Coleridge, *Superlatt. Microstruct.* 11 (1992) 219.
- [14] M.W.C. Dharma-wardana, R.P. Taylor and A.S. Sachrajda, *Solid State Commun.* 84 (1992) 631.
- [15] S.W. Hwang, J.A. Simmons, D.C. Tsui and M. Shayegan, *Phys. Rev. B* 44 (1991) 13497.



ELSEVIER

Surface Science 305 (1994) 654–658



# Magnetotransport study of GaAs/AlGaAs quantum wires

R.G. Mani \*, K. von Klitzing, E. Vasiliadou, P. Grambow, K. Ploog

*Max Planck Institut für Festkörperforschung, Heisenbergstrasse 1, D-70569 Stuttgart, Germany*

(Received 19 April 1993; accepted for publication 1 June 1993)

## Abstract

We report low temperature ( $T < 2$  K) measurements of the two-terminal resistance in arrays of GaAs/AlGaAs wires and highlight localization-related effects.

## 1. Introduction

Experimental studies of localization which proceed from the metallic limit rely upon the use of the temperature,  $T$ , as a parameter for changing the effective sample size in order to confirm (length) scaling theories [1]. In such experiments, features observed in the electrical response reflect the  $T$ -variation of characteristic lengths involved in interference, i.e., the inelastic diffusion length, and interaction effects, i.e., the thermal diffusion length, and thereby reveal effective dimensionality which is partly determined by comparing characteristic lengths with the physical sample size. The utility of this method has been confirmed in 2D systems through weak localization studies at low magnetic fields,  $B$ , and scaling studies of transport in the quantum Hall regime [1,2]. Here, we apply this approach to quantum wires in order to: (a) trace out the ( $B = 0$ ) flow to the (1D) exponentially localized regime, if the latter is experimentally accessible by varying  $T$

[3], and (b) search for novel characteristics resulting from confinement, and phase coherence in the confined direction, in the low filling factor,  $\nu$ , high- $B$  limit [4].

## 2. Experiment

Transport studies were carried out on arrays of GaAs/AlGaAs wires manufactured by optical (holographic) lithography of MBE-grown GaAs/AlGaAs heterostructures characterized by  $n = 3 \times 10^{11} \text{ cm}^{-2}$  and  $\mu(4.2 \text{ K}) = 0.5 \times 10^6 \text{ cm}^2/\text{V} \cdot \text{s}$ . Typically, a photoresist wire grating served as a template for a shallow mesa etch of the (Si) n-doped AlGaAs layer in the heterostructure. Depletion below the etched regions partitioned the 2DEG into an array of electronic wires of periodicity  $\lambda = 730 \text{ nm}$  (see Fig. 2, left inset) and reduced the carrier density,  $n$ , well below the initial value. For the samples examined here, the mesa width  $W_M = 400 \text{ nm} > \lambda/2$  and the electrical wire width ranged between  $130 < W < 200 \text{ nm}$ .  $300 \mu\text{m}$  wide Au-Ge/Ni contacts provided electrical access to the quasi-1D system. Thus,

\* Corresponding author.

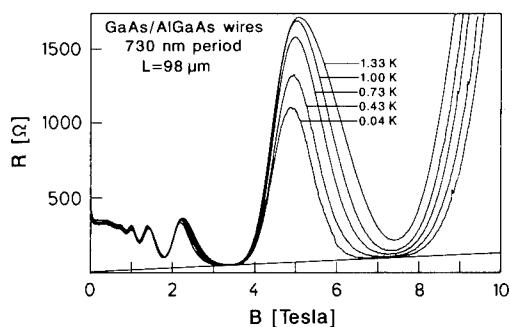


Fig. 1. The two-terminal resistance,  $R$ , vs the magnetic field,  $B$ .

these two-terminal resistance measurements included in-situ averaging of approximately 412 wires in parallel.

### 3. Overview

The transport characteristics of wires may be surveyed in a field sweep of the two-terminal resistance,  $R$ , which is shown in Fig. 1 for  $L = 98 \mu\text{m}$  long wires. At low  $B$ ,  $B < 0.2 \text{ T}$ , one observes negative magnetoresistance which increases in magnitude with decreasing  $T$ . Further increase in  $B$  indicates Landau quantization through the onset of Shubnikov-de Haas (SdH) oscillations. At low filling factors  $\nu < 4$  ( $B > 1.8 \text{ T}$ ), the SdH linewidth and amplitude exhibit strong  $T$ -dependence. In addition, the resistance minima saturate to a  $T$ -independent value at the lowest  $T$ , in the vicinity of  $\nu = 1$  ( $6 < B < 8.5 \text{ T}$ ) and  $\nu = 2$  ( $3 < B < 4 \text{ T}$ ), and the  $T$ -evolution of the lineshape around  $\nu = 1$  is reminiscent of the resistance minima in the IQHE regime.

Fig. 1 indicates that the two-terminal resistance,  $R$ , which includes both  $R_{xx}$  and  $R_{xy}$ , exhibits mostly  $R_{xx}$ -like characteristics at high  $B$ . This feature originates from the relatively large length  $L$  ( $98 \mu\text{m}$ ) to width ( $0.2 \mu\text{m}$ ) ratio ( $\sim 4.9 \times 10^2$ ) of the wires which enhances  $R_{xx}$  relative to  $R_{xy}$ . Yet, one might assume a quantized value for  $R$  in the vicinity of the  $\nu = 2$  minima, in order to estimate the number of electrically active wires,  $N_w = 260$ , in the sample. Then, the resistance per wire, for the low disorder configuration of Fig. 1,

may also be determined:  $N_w R(B = 0) \approx 85 \text{ k}\Omega/\text{wire}$ . Upon correlating the measured resistance at  $B = 0$  with  $n \approx 3 \times 10^8 \text{ m}^{-1}$  and  $N_w$ , the electronic mean free path in the wires,  $l \approx 1.4 \mu\text{m}$ , was found to be reduced relative to the unprocessed material,  $l \approx 4.8 \mu\text{m}$ . The confinement energy satisfies  $0.5 < \hbar\omega_0 < 1 \text{ meV}$ .

### 4. Low field transport

The magnitude of the low field ( $B < 0.2 \text{ T}$ ) feature pointed out in Fig. 1, was found to be strongly sensitive to the effective disorder in the wires, and relatively large effects could be observed when a low  $n$  (high-effective disorder) configuration was realized by utilizing the persistent photoconductivity effect. Here, we compare the high-effective disorder configuration in a set of  $77 \mu\text{m}$  and  $98 \mu\text{m}$  long wires fabricated on a single chip, which included a small change in  $n$  between the two sets of wires in order to investigate the influence of a differential change in disorder, i.e.,  $n(77 \mu\text{m}) < n(98 \mu\text{m})$  with  $\Delta n < 10\%$  (see SdH data, inset Fig. 2).

Examine Fig. 2. The  $B = 300 \text{ mT}$ , high- $T$  ( $T = 1.2 \text{ K}$ ) resistance for the two samples scale approximately with  $L$ ,  $R(98 \mu\text{m})/R(77 \mu\text{m}) = 1.13$ , and the resistance per wire, i.e.,  $N_w R(98 \mu\text{m}) = 265 \text{ k}\Omega$  and  $N_w R(77 \mu\text{m}) = 233 \text{ k}\Omega$ , exceeds  $h/e^2$ . The localization length in these wires,  $\alpha^{-1}$ , is estimated to be  $\alpha^{-1}(77 \mu\text{m}) = 8.5 \mu\text{m}$  and  $\alpha^{-1}(98 \mu\text{m}) = 9.5 \mu\text{m}$ . Note that a reduction in  $T$  produces rather large increases of  $R(B = 0)$  and  $R(B = 300 \text{ mT})$ , such that, although at  $T = 1.2 \text{ K}$  the longer wires show greater resistance in accord with expectations, the shorter low-mobility wires become substantially more resistive at the lowest  $T$ !

These low- $B$  data indicate that the magnetoresistance may be separated into two terms: a  $T$ -dependent,  $B$ -independent term which measures the  $B = 300 \text{ mT}$  value of the resistance,  $R'_1(T)$ , and a  $B$ - and  $T$ -dependent term,  $R'_2(T, B)$ . As the data exhibit a Lorentzian lineshape, they have been fit to  $R(T, B) = R'_1(T) + R'_2(T, B) = R'_1(T) + R_2(T)/[1 + (B/\Delta B(T))^2]$ . Best fits, shown in Fig.

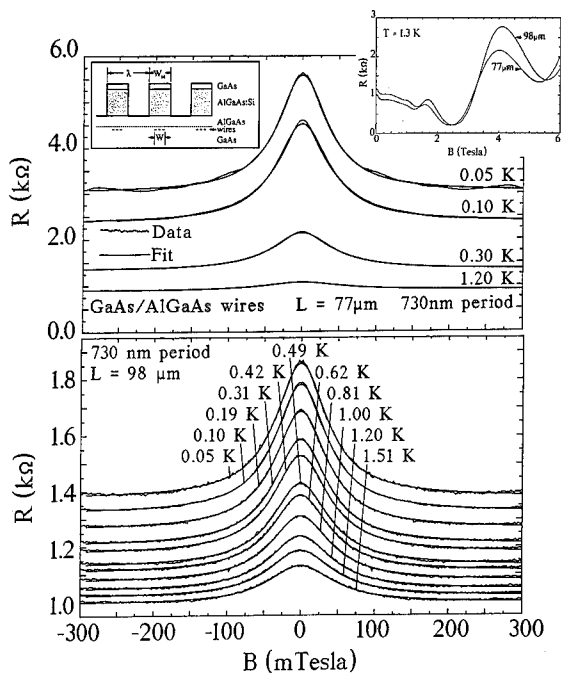


Fig. 2. (Inset left): Schematic of GaAs/AlGaAs wires. (Inset right): The Shubnikov-de Haas effect at  $T = 1.3$  K. Low- $B$  magnetoresistance in  $77 \mu\text{m}$  (top) and  $98 \mu\text{m}$  (bottom) wires. Data and fit (see text) are shown.

2, indicate that the empirical function describes the data within experimental uncertainties. A plausible alternative for  $R'_2(T, B)$ , the 1D weak localization prediction, provided consistently poorer fits to the same data.

The  $T$ -exponent characterizing  $R_2(T)$  may be extracted from Fig. 3, which shows that at relatively high  $T$ ,  $R_2(T) \approx T^\alpha$  with  $\alpha = -1.0 \pm 0.1$ . However, at the lowest  $T$ ,  $R_2(T)$  saturates to a nearly constant value. The exponent characterizing the  $B$ -independent term may be determined after subtraction of the classical resistance  $R_0$ , i.e.,  $R_1(T) = R'_1(T) - R_0$ ; which is estimated to be  $R_0(77 \mu\text{m}) = 499 \Omega$  and  $R_0(98 \mu\text{m}) = 726 \Omega$ . Fig. 3 (top) shows that  $R_1(T) \approx T^\beta$  with  $\beta = -0.5 \pm 0.1$ . A comparison of  $R_1(T)$  and  $R_2(T)$  indicates that  $R_1(T)$  continues to increase with decreasing  $T$  even after  $R_2(T)$  shows saturation.

The mechanisms responsible for  $R_1(T)$  and  $R'_2(T, B)$  may be identified by comparing with 1D predictions for the dirty metal limit [1]. Thus,  $R_1(T) \approx T^{-0.5}$  and the characteristic  $B$ -independ-

ence suggest that electron interactions are responsible for the variation of the background with  $T$ . The power law,  $R_2(T) \approx T^{-1}$ , and the suppression of the magnetoresistance with increased  $B$  suggest that  $R'_2(T, B)$  reflects quantum interference. However, the magnitude and the lineshape indicate that it differs quantitatively from the behavior observed in the weak disorder limit. The saturation of  $R_1(T)$  and  $R_2(T)$  for the  $98 \mu\text{m}$  wires demonstrate that the effective sample size may not be increased further by reducing  $T$ . Thus, the  $98 \mu\text{m}$  wires show zero-dimensional behavior as far as both interference and interaction effects are concerned, at the lowest  $T$ . The shorter ( $77 \mu\text{m}$ ), more disordered wires show mixed dimensionality at the lowest  $T$ . Here, the saturation of  $R_2(T)$  indicates 0D characteristics for interference effects while the continued increase of  $R_1(T)$  with decreasing  $T$  suggests 1D behavior for interaction effects. Thus, these ex-

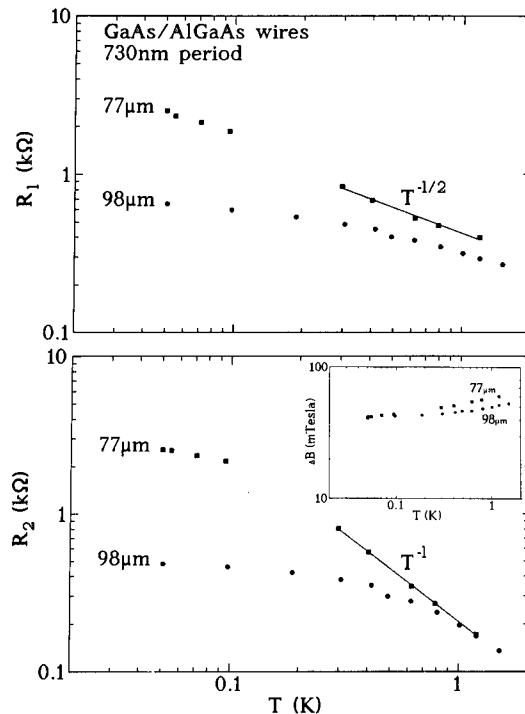


Fig. 3. Top: The interaction contribution,  $R_1(T) \approx T^{-1/2}$ , is shown vs  $T$ . Bottom: The interference contribution,  $R_2(T) \approx T^{-1}$  is shown for the same samples. Inset: The half-width,  $\Delta B$ , of the Lorentzian is shown vs  $T$ .

periments demonstrate that temperature can become a less effective tool for varying the effective sample size when characteristic lengths approach  $\alpha^{-1}$  and induce dimensional crossovers as far as interference and interaction effects are concerned. Then, further flow towards the exponentially localized regime, driven by temperature at  $B = 0$ , might call for a change in the mechanisms and a shift in the length scales which determine effective sample size at finite  $T$  [1].

### 5. High field transport

A striking feature in the data of Fig. 1 for  $\nu < 4$  is the strong  $T$ -induced, asymmetric narrowing in the linewidth of the SdH oscillations. The feature may be better examined for the  $N = 0 \downarrow$  oscillation, i.e.,  $3.5 < B < 7$  T, by removing a linear Hall effect from the two-terminal resistance and normalizing the amplitude. The result, plotted in Fig. 4 (inset), shows that linewidth narrowing occurs predominantly on the high- $B$  side with reduced  $T$ , while the low- $B$  side remains virtually unaffected by changing  $T$ . Similar behavior may also be seen in the  $N = 1$  SdH oscillation which spans the range  $1.8 < B < 3.5$  T in Fig. 1. The  $T$ -dependence of the half-width at half-maximum,  $\Delta B$ , on the high- $B$  side of the  $N = 0 \downarrow$  peak has

been plotted in Fig. 4 for three samples of dissimilar lengths; a fit to the data suggests that  $\Delta B \approx T^\kappa$  with  $\kappa = 0.4 (\pm 30\%)$ .

Scaling studies in the quantum Hall regime have examined symmetric narrowing of SdH oscillations [2], and they have attributed the effect to the progressive  $T$ -induced localization of states in the tails of the 2D Landau levels. The similarity of linewidth narrowing on the high- $B$  side of the SdH oscillations suggests that localization occurs on the low energy side of Landau levels in wires and 2D systems. However, the  $T$ -independent linewidth on the low- $B$  side in wires is unlike the standard 2D result, and it suggests the absence of localization on the high energy side of the 1D subbands.

We model these characteristics assuming parabolic confinement in wires, i.e.,  $V(x) = m^* \omega^2 x^2 / 2$  with  $\omega^2 = \omega_0^2 + \omega_c^2$ . Note that  $\omega_0$  defines the potential at  $B = 0$  and  $\omega_c = eB/m^*$ . For this potential,  $E_{n,k}(B) = (n + 1/2)\hbar\omega + \hbar^2 k^2 / 2m^*(B)$  with  $m^*(B) = m^*(1 + \omega_c^2/\omega_0^2)$ , while the electronic density of states (DOS),  $g(E) = (2\pi)^{-1} (2m^*(B)/\hbar^2)^{1/2} \Sigma(E - (n + 1/2)\hbar\omega)^{-1/2}$ , exhibits a  $E^{-1/2}$  singularity at the band edge (see inset (A), Fig. 5). Level broadening might be expected to smear out the  $E^{-1/2}$  singularity, produce a low energy tail in the DOS below the Landau subbands, and result in the localization of low energy states which lie near the band bottom.

The magnetoresistance in wires has been simulated using the model DOS of Fig. 5 (inset, (B)), which includes a mobility edge,  $E_m$ , at the subband bottoms. The field variation of the Fermi level,  $\zeta$ , is shown in Fig. 5 (top) for typical parameters. The diagonal conductivity  $\sigma_{xx}$ , which reflects delocalized initial and final states in the vicinity of  $\zeta$  through  $\sigma_{xx} \approx \int (-df/dE)g^2(E)dE$ , is plotted in Fig. 5 (bottom) for three values of  $E_m$ . Note that an increase in the fraction of localized states per Landau subband results in an asymmetric narrowing of the oscillations on the high field side, as observed in the data. The simulations may be connected to experiment by noting that  $T$  serves to vary the effective sample length by changing the inelastic diffusion length, as in the low- $B$  experiment. The resulting pro-

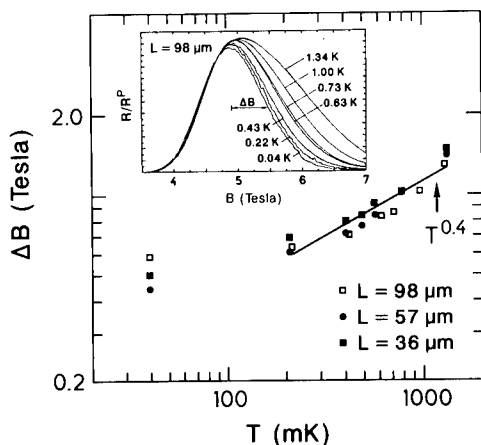


Fig. 4.  $\Delta B$  on the high field side of the SdH oscillation is shown vs  $T$  for three samples. Inset: The normalized resistance vs  $B$  for the  $N = 0$  (down) SdH oscillation.

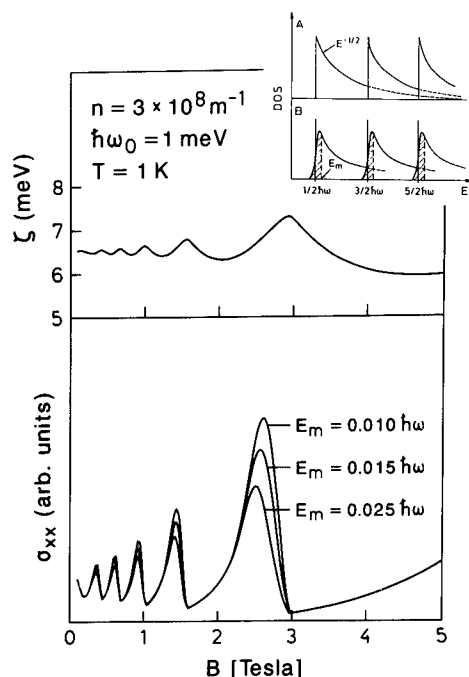


Fig. 5. Inset: (A) Ideal density of states for wires with parabolic confinement. (B) Model DOS for wires including localization.  $E_m$  marks the mobility edge. (Top) the  $B$ -variation of the Fermi level,  $\zeta$ . (Bottom) The diagonal conductivity,  $\sigma_{xx}$ , vs  $B$  for three values of  $E_m$ . Note the narrowing of the SdH oscillations on the high- $B$  side with increased  $E_m$ .

gressive localization of longer states near the subband bottoms with reduced  $T$  shifts the mobility edge to higher energies as in the simulations, and the asymmetric SdH narrowing follows power law variation with  $T$ , as observed in scaling studies of transport in the (2D) IQHE regime and in our results (Fig. 4) [2,4]. Thus, confinement plus phase coherence in the confined direction is responsible for these novel high- $B$  characteristics in wires.

## 6. Conclusion

The localization-dependent properties of GaAs/AlGaAs wires have been examined through a transport study over the low- ( $B < 300$  mT) and high-magnetic field regimes ( $B < 10$  T). We have shown that low field magnetoresistance in these wires is described by  $R(T, B) = R_0 + R_1(T) + R_2(T)/(1 + (B/\Delta B)^2)$ , where the  $T$ -dependent terms exhibit interaction- and interference-like power laws,  $R_1(T) \approx T^{-1/2}$  and  $R_2(T) \approx T^{-1}$ , at relatively high  $T$ , followed by saturation at the lowest  $T$ , which we have reasoned signifies a dimensional crossover as far as interaction and interference effects are concerned. The high field studies reveal strong temperature-induced asymmetric narrowing of Shubnikov-de Haas oscillations, which has been attributed to asymmetric localization on the low energy side of the 1D-Landau bands. Finally, the data (Fig. 1) also indicate that the two-terminal resistance exhibits a finite slope versus  $B$  in the vicinity of  $\nu = 1$  and  $\nu = 2$  at the lowest  $T$ ; this feature appears to suggest that Hall quantization need not occur in disordered quasi-1D systems [3].

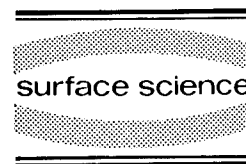
## 7. References

- [1] P.A. Lee and T.V. Ramakrishnan, Rev. Mod. Phys. 57 (1985) 287; D.J. Thouless, Phys. Rev. Lett. 39 (1977) 1167.
- [2] H.P. Wei et al., Phys. Rev. Lett. 61 (1988) 1294; A.M.M. Pruisken, Phys. Rev. Lett. 61 (1988) 1297; S. Koch et al., Phys. Rev. Lett. 67 (1991) 883.
- [3] R.G. Mani, K. von Klitzing and K. Ploog, Phys. Rev. B 48 (1993) 4571; and unpublished.
- [4] R.G. Mani and K. von Klitzing, Phys. Rev. B 46 (1992) 9877; T. Ando, Phys. Rev. B 42 (1990) 5626; R.G. Mani and K. von Klitzing, Z. Phys. B 92 (1993) 335.



ELSEVIER

Surface Science 305 (1994) 659–663



## Transport properties of dual quantum dots

K. Ogawa <sup>\*,a</sup>, R.J. Blaikie <sup>a</sup>, J.D. White <sup>a</sup>, J. Allam <sup>a</sup>, H. Ahmed <sup>b</sup>

<sup>a</sup> Hitachi Cambridge Laboratory, Hitachi Europe Limited, Madingley Road, Cambridge CB3 0HE, UK

<sup>b</sup> Microelectronics Research Centre, Cavendish Laboratory, University of Cambridge, Madingley Road, Cambridge CB3 0HE, UK

(Received 20 April 1993; accepted for publication 30 June 1993)

### Abstract

Transport properties of GaAs dual quantum dots are investigated by means of dual-channel current measurements. The total conductance of the dual quantum dots has a shoulder and a plateau near integer multiples of quantised conductance as if the dual quantum dots behave as a single quantum point contact. This novel behaviour in the total conductance is discussed on the basis of a multi-channel conductor model. Chemical-potential variation in the two-dimensional electron gas is proposed in three-terminal-like transport through the quantum dots.

### 1. Introduction

Electron waves in coupled quantum structures give rise to new aspects of transport phenomena in semiconductor low-dimensional systems [1,2]. Coupling between quantum structures will be highly pronounced in a system consisting of quantum dots because translational motion is eliminated in quantum dots. The coupling is viewed in analogy with chemical bonding in a molecule [3]. In this paper we have investigated transport properties of dual quantum dots, the simplest case of coupled quantum dots, by means of dual-channel current measurements and have discussed the results on the basis of a multi-channel conductor model. We have found that strong coupling between quantum dots leads to conductance quantisation over the dual quantum dots such as observed in a single quantum point con-

tact in spite of the fact that the dual channels of current have been measured independently [3,4].

### 2. GaAs dual quantum dots and dual-channel current measurements

The dual quantum dots investigated in this paper have been formed by lateral confinement of a two-dimensional electron gas (2DEG) at a GaAs/Ga<sub>0.7</sub>Al<sub>0.3</sub>As heterojunction. The lateral size of the dual quantum dots and coupling between quantum dots have been controlled by gate voltages applied through the four split gates as illustrated in Fig. 1. These split gates have been fabricated through evaporation of metals on top of the heterojunction wafers after electron-beam lithography. The quantum dots (QD1 and QD2) have a quadrilateral shape, typically 400 nm × 500 nm in diagonal dimension. The quantum dots are separated from each other by a potential barrier formed by two central gates with voltage  $V_T$ . The

\* Corresponding author.



potential barrier has been kept low enough to realise strong coupling between quantum dots as described in the next section. Gate voltages applied to confinement gates for QD1 and QD2 are  $V_1$  and  $V_2$ , respectively. Weak electric coupling between quantum dot and 2DEG reservoir enables transport measurements on the dual quantum dots.

Dual-channel current measurements have been performed at 4.2 K with the configuration shown in Fig. 1. This configuration is similar to that employed for the dual electron waveguides [1,2]. Alternating voltage bias  $V_{AC}$  ( $100 \mu V_{rms}$ ) has been applied to the source terminal in the side of the quantum dot on the left (QD1) and dual channels of current  $I_1$  and  $I_2$  through the drain terminals have been measured with lock-in amplifiers. Dual channels of conductances have been obtained from the relations,  $G_1 = I_1/V_{AC}$  and  $G_2 = I_2/V_{AC}$  as a function of gate voltage  $V_1$  applied to the confinement gate for QD1. In each measurement,  $V_1$  was scanned between 0.0 and  $-0.8$  V with both  $V_2$  and  $V_T$  fixed.

### 3. Experimental results and discussion

#### 3.1. Conductance characteristics

Conductance characteristics of the dual quantum dots are presented in Figs. 2 and 3. The dual-channel conductances  $G_1$  and  $G_2$  and the total conductance  $G_1 + G_2$  are plotted in units of quantised conductance  $2e^2/h$  as a function of

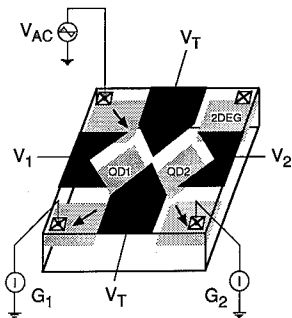


Fig. 1. Dual quantum dots and configuration of dual-channel current measurements.

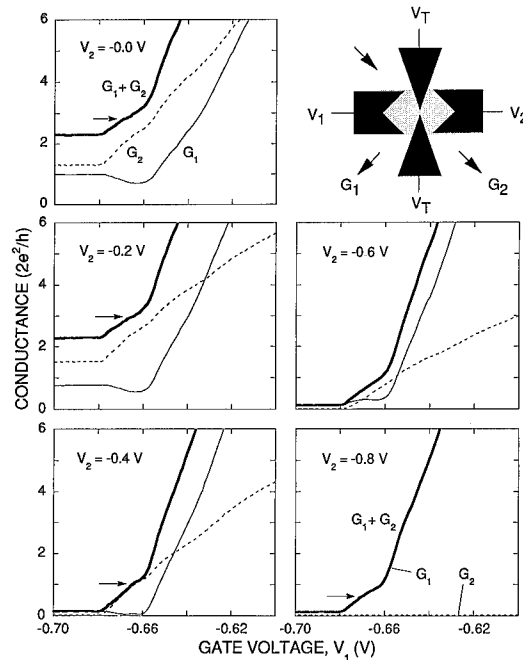


Fig. 2. Dual channels of conductance,  $G_1$  (solid line) and  $G_2$  (dashed) and the total conductance  $G_1 + G_2$  (bold) plotted against gate voltage,  $V_1$  applied to confinement gate for QD1. Voltage,  $V_2$ , for confinement gate for QD2 is changed between 0.0 and  $-0.8$  V (from left top to left bottom and right middle to right bottom) in  $-0.2$  V steps. The conductances are scaled in units of quantised conductance,  $2e^2/h$ , including spin degeneracy. The gate voltage,  $V_T$ , for the central barrier is  $-0.6$  V. The measurement configuration is illustrated at the right-top corner.

gate voltage  $V_1$  at 4.2 K with  $V_T = -0.6$  and  $-0.55$  V, respectively. As gate voltage  $V_1$  decreases, dual-channel conductances tend to decrease since the potential barrier between source 2DEG reservoir and QD1 increases and current transmission is reduced. Quantum dot 2 is less conductive when gate voltage  $V_2$  for QD2 is varied to more negative values. The QD2 is almost non-conducting with gate voltage  $V_2$  as strong as  $-0.8$  V.

The total conductance  $G_1 + G_2$  plotted against  $V_1$  yields a shoulder-like structure about an integer multiple of the quantised conductance irrespective of complicated behaviour of  $G_1$  and  $G_2$ . The shoulder occurs approximately at 3 for  $V_2 = 0.0$  or  $-0.2$  V in Fig. 2, or otherwise at 1 V in Figs. 2 and 3. A plateau, on which conductance is

slightly higher than 2, is also observed in the region where  $V_1$  is more negative than  $-0.68$  V, with  $V_T = 0.0$  or  $-0.2$  V. The dual-channel conductances vary in a complementary manner to each other according to the change in  $V_2$  between  $0.0$  and  $-0.2$  V or between  $-0.4$  and  $-0.8$  V. The dual quantum dots seem to be quantised as a single quantum point contact even though conductances through dual quantum dots are measured independently. The conductance at which the shoulder occurs seems to vary with change in  $V_2$ . The arrow in each graph in Figs. 2 and 3 indicates the shoulder. The shoulder appears, for example in Fig. 4, below the quantised conductance for  $V_2 = -0.4$  or  $-0.8$  V, while it is located almost at the quantised conductance for  $V_2 = -0.6$  V. A possible origin of this variation is discussed later in terms of chemical potential variation in the 2DEG.

Transport of the dual quantum dots is dominated by QD2 in a certain range of gate voltages

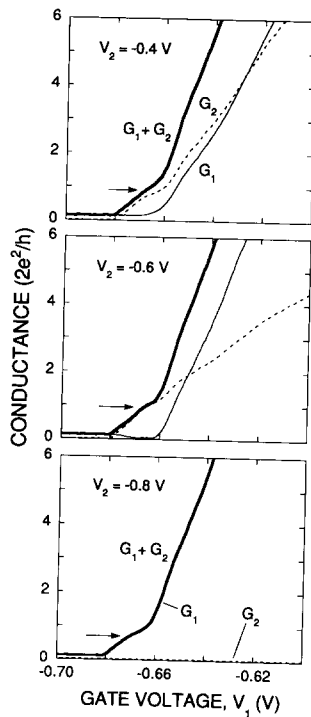


Fig. 3. Dual channels of conductance and their total conductance. Similar plots to those shown in Fig. 2 except  $V_2$  is between  $-0.4$  and  $-0.8$  V, and  $V_T = -0.55$  V.

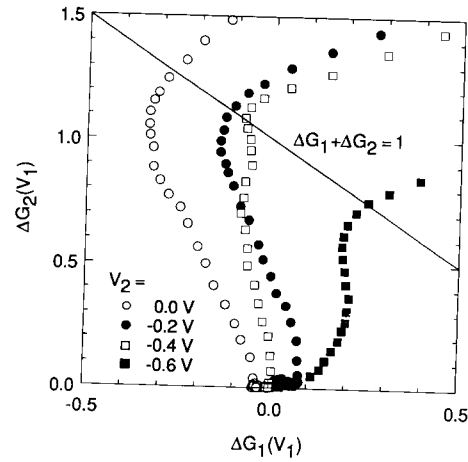


Fig. 4.  $\Delta G_2$  plotted as a function of  $\Delta G_1$ .  $\Delta G_1$  and  $\Delta G_2$  have been obtained as differences from the conductances measured in the experimental limit of confinement ( $V_1 = -0.8$  V). Four sets of the plots correspond to the dual-channel conductances with  $V_2 = -0.0$  to  $-0.6$  V by  $-0.2$  V step. The line indicates  $\Delta G_1 + \Delta G_2 = 1$ .

$V_1$  and  $V_2$ . The conductance  $G_2$  through QD2 is higher than  $G_1$  in a range, which becomes narrower with decreasing  $V_2$ . The transport is even like single-channel conduction through QD2, namely  $G_1 \approx 0$ , between  $V_1 = -0.660$  and  $-0.675$  for  $V_2 = -0.4$  V in Fig. 2 and for  $V_2 = -0.6$  V in Fig. 3. These features of the transport suggest that strong coupling between the quantum dots directly connects QD2 as well as QD1 with the source 2DEG terminal. On account of the strong coupling, the dual quantum dots should be treated as a multiple-mode conductor similar to a single quantum point contact [4,5]. A multi-channel conductor has been employed to explain the quantisation plateaux in a quantum point contact [4,6].

### 3.2. Multi-channel conductor model

The multi-channel conductor model is applied to the dual quantum dots, which are regarded as an obstacle in the model and the dual-channel conductances  $G_1$  and  $G_2$ ; the total conductance  $G_1 + G_2$  is expressed as [4,6]

$$G_1 = T_{01}\alpha_1 - T_{12}(\alpha_2 - \alpha_1), \quad (1)$$

$$G_2 = T_{02}\alpha_2 + T_{12}(\alpha_2 - \alpha_1), \quad (2)$$

and

$$G_1 + G_2 = T_{01}\alpha_1 + T_{02}\alpha_2. \quad (3)$$

Here, transport associated with only one electron subband is considered, and  $G_1$  and  $G_2$  are scaled in units of  $2e^2/h$ . The transmission coefficient  $T_{ij}$  represents transmission between terminals  $i$  and  $j$ , where the terminals 0, 1 and 2 correspond to the source terminal, the left drain terminal and the right drain terminal, respectively. The factors  $\alpha_1$  and  $\alpha_2$  are defined as  $\alpha_1 = V_{QD1}/V_{AC}$  and  $\alpha_2 = V_{QD2}/V_{AC}$  according to the definition of  $G_1$  and  $G_2$  in the dual-channel current measurements. Eq. (3) shows  $G_1 + G_2 = 1$  under the condition that resistance in 2DEG reservoir is negligible, namely  $\alpha_1 = \alpha_2 = 1$  and electron reflection back to the source is negligible,  $T_{01} + T_{02} = 1$ . This result of the model supports the idea that the total conductance of dual quantum dots will undergo conductance quantisation such as observed in a quantum point contact and electron waveguides [2,4]. The above condition, however, is not always satisfied and  $G_1 + G_2$  may deviate from 1. The conductance characteristics in Figs. 2 and 3 show that the condition is not satisfied and  $\alpha_1$ ,  $\alpha_2$  and  $T_{01} + T_{02}$  depend on gate voltage  $V_1$  and  $V_2$ . Gate-voltage dependences of  $\alpha_i$  and  $T_{ij}$  cause transport between the three source and drain terminals rather than two parallel transport channels from the source terminal to the drain terminals, as discussed below.

### 3.3. Three-terminal transport

To compare the conductance characteristics with Eqs. (1), (2) and (3), relative conductance  $\Delta G_2$  is plotted as a function of relative conductance  $\Delta G_1$  with  $V_T = -0.6$  V in Fig. 4. Each relative conductance has been obtained as a difference from the conductance measured in the experimental limit of confinement at  $V_1 = -0.8$  V:  $\Delta G_1 = G_1(V_1) - G_1(-0.8)$  and  $\Delta G_2 = G_2(V_1) - G_2(-0.8)$ . The four traces in Fig. 4 correspond to  $\Delta G_2 - \Delta G_1$  curves with  $V_2 = 0.0, -0.2, -0.4$  and  $-0.6$  V, respectively. These traces show a common feature that a large bend of a curve occurs at a point close to  $\Delta G_1 + \Delta G_2 = 1$ . In the  $\Delta G_2 - \Delta G_1$  space below  $\Delta G_1 + \Delta G_2 = 1$ , electron

transport can be described by Eqs. (1), (2) and (3). If  $V_2$  is  $-0.2$  V or weaker,  $\Delta G_1$  is negative and the curve has a negative slope. If  $V_2$  takes further more negative value,  $\Delta G_1$  as well as the slope tends to be positive. Transport between the two drain terminals, that is,  $T_{12} (\alpha_2 - \alpha_1)$ , is dominant compared with transport between the source terminal to each drain terminal,  $T_{01} \alpha_1$  and  $T_{02} \alpha_2$ , if  $V_2$  is weak and QD2 is weakly confined. Transport through the dual quantum dots is then described as electron transport between three terminals rather than parallel transport between the source and the drain terminals. This implies that  $\alpha_2 > \alpha_1$ : voltage or chemical potential difference is built in between the two drains in spite that each drain is connected to virtual grounds of lock-in amplifier. It is difficult to realise such an observable difference in chemical potential between the drain terminals if we regard 2DEG as a ideal metallic conductor. Even a small number of scattering centres, however, has a very strong effect on electron localisation in 2D [7]. A possible origin is, therefore, chemical potential variation due to weak localisation which is induced by interface roughness and impurities in 2DEG.

## 4. Conclusion

Transport properties of GaAs dual quantum dots have been investigated by means of dual-channel current measurements. The total conductance of the dual quantum dots yields a shoulder and a plateau. These structures are regarded as the sign of conductance quantisation such as observed in single point contacts on the basis of a multi-channel conductor model. Chemical-potential variation in the two-dimensional electron gas is suggested to cause the three-terminal transport through the quantum dots rather than dual-channel parallel transport.

## 5. References

- [1] C.C. Eugster and J.A. del Alamo, Phys. Rev. Lett. 67 (1991) 3586.

- [2] C.C. Eugster, J.A. del Alamo, M.J. Rooks and M.R. Melloch, *Appl. Phys. Lett.* 60 (1992) 642.
- [3] J.C. Phillips, *Bonds and Bands in Semiconductors* (Academic Press, New York, 1973) p. 9.
- [4] B.J. van Wees, H. van Houten, C.W.J. Beenakker, J.G. Williamson, L.P. Kouwenhoven, D. van der Marel and C.T. Foxon, *Phys. Rev. Lett.* 60 (1988) 848.
- [5] D.A. Wharam, T.J. Thornton, R. Newbury, M. Pepper, H. Ahmed, J.E.F. Frost, D.G. Hasko, D.C. Peacock, D.A. Ritchie and G.A.C. Jones, *J. Phys. C: Solid State Phys.* 21 (1988) L209.
- [6] M. Büttiker, Y. Imry, R. Landauer and S. Pinhas, *Phys. Rev. B* 31 (1985) 6207.
- [7] E. Abraham, P.W. Anderson, D.C. Licciardello and T.V. Ramakrishnan, *Phys. Rev. Lett.* 42 (1979) 673.

# Lateral transport through a single quantum dot with a magnetic field parallel to the current

J. Weis <sup>\*</sup>, R.J. Haug, K. von Klitzing, K. Ploog <sup>1</sup>

*Max-Planck-Institut für Festkörperforschung, Heisenbergstrasse 1, 70569 Stuttgart, Germany*

(Received 19 April 1993; accepted for publication 4 May 1993)

## Abstract

Transport through a quantum dot defined in a two-dimensional electron gas is investigated for a magnetic field parallel to the current direction. By measuring the differential conductance as a function of the gate-voltage for finite bias-voltage between the two electron reservoirs, excited states of the quantum dot are observable. Different excited states show a different magnetic field dependence. The observed shift of conductance resonances is affected by the diamagnetic shift of the two-dimensional electron gas in the leads.

## 1. Introduction

Quantum dots or zero-dimensional systems consist of a small number of electrons confined by a three-dimensional potential. By coupling a quantum dot with two electron reservoirs by weak tunnel junctions, electron transport through the quantum dot can be investigated. Due to the small total capacitance of the quantum dot, the electrostatic energy required to add an additional electron to the dot can exceed the thermal energy  $k_B T$  at low temperature. In this situation transport is inhibited. It is known as the Coulomb blockade of tunneling [1]. This effect has been observed in metallic systems, but also in semiconductor nanostructures, where the discreteness of the energy spectrum due to confinement effects

has to be taken into account [2]. By changing the voltage at a gate electrode capacitively coupled to the quantum dot, the electrostatic potential of the quantum dot is changed and the states of the quasi-isolated dot are shifted in energy relatively to the states of the electron reservoirs.

The conductance through the quantum dot as a function of the gate-voltage at low temperature and vanishing bias-voltage between the electron reservoirs exhibits well separated peaks. At the conductance peak the number of electrons in the dot oscillates between two neighbouring integers (i.e. between  $N$  and  $N + 1$ ). It is called the single-electron-tunneling regime. At more negative gate-voltage next to the conductance peak the number of electrons is fixed to  $N$ , while sweeping to more positive gate-voltage it is fixed to  $(N + 1)$  until the next conductance peak appears alternating between  $(N + 1)$  and  $(N + 2)$  electrons in the dot.

The energy necessary to add an electron to the quantum dot is changed when a magnetic field is

<sup>\*</sup> Corresponding author.

<sup>1</sup> Present address: Paul-Drude Institut für Festkörperelektronik, Hausvogteiplatz 5-7, 10117 Berlin, Germany.

applied. McEuen et al. [3] obtained the magnetic field dispersion of this energy by performing very detailed measurements of the changes in gate-voltage position and amplitude of conductance resonances. In their case the magnetic field was applied perpendicular to the two-dimensional electron gas (2DEG). Here we present investigations with a different magnetic field orientation: in our case the magnetic field is parallel to the 2DEG and parallel to the current. It is shown that one has to take into account the magnetic field dependence of the chemical potential of the electron reservoirs when extracting information about the magnetic field dispersion of the states of the quantum dot.

## 2. The experiment

The sample used in these experiments is based on a GaAs/Al<sub>0.33</sub>Ga<sub>0.67</sub>As heterostructure with a 2DEG, grown on an undoped GaAs substrate. The 2DEG has a sheet electron density of  $3.4 \times 10^{15} \text{ m}^{-2}$  with a mobility of  $60 \text{ m}^2/\text{V} \cdot \text{s}$  at a temperature of 4.2 K. A Hall bar was etched and ohmic contacts (AuGeNi) were alloyed to contact the 2DEG. To define the quantum dot, metallic split-gates, as shown schematically in the inset of Fig. 1, were deposited on the top of the Hall bar. The diameter of the area between the tips of the gates is about 350 nm. In addition to these top-gates, a metallic electrode (back-gate) on the reverse side of the substrate was used to change the electrostatic potential of the quantum dot. The distance between the 2DEG and the top-gates was 86 nm, the distance between the 2DEG and the back-gate was 0.5 mm.

The sample was mounted in the mixing chamber of a  $^3\text{He}/^4\text{He}$  dilution refrigerator with base temperature of 22 mK. To define the quantum dot, negative voltages ( $-0.7 \text{ V}$ ) were applied to the top-gates relative to an ohmic contact of the Hall bar. Electrostatic depletion below the top-gates divides the 2DEG into two areas, which act as leads, and the region of the quantum dot, which was then weakly coupled to the two leads by tunneling barriers. The tunneling barriers could be tuned by changing slightly the voltage

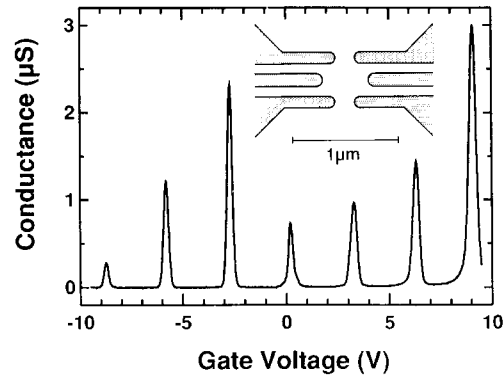


Fig. 1. Conductance versus back-gate voltage. Inset: Center of split-gate structure used to define the quantum dot.

applied to the different top-gate fingers. The two-terminal conductance through the quantum dot was measured by using an ac lock-in technique at a frequency of 13 Hz and an effective ac source-drain voltage of  $5 \mu\text{V}$ . In addition to the ac source-drain voltage, a dc voltage  $V_{\text{DS}}$  in the range of mV could be applied. For the measurements the top-gates were kept at fixed voltages.

## 3. The results

In Fig. 1 the measured conductance as a function of the back-gate voltage  $V_{\text{B}}$  is shown. Well separated conductance peaks are observable. Within the experimental resolution all the separations in gate-voltage between adjacent peaks are the same. In the Coulomb blockade model used for quasi-isolated quantum dots this separation is given by  $e/C_{\text{B}}$  for degenerate states, where  $C_{\text{B}}$  is the capacitance between the quantum dot and the back-gate [2]. We obtain  $C_{\text{B}} = (5.4 \pm 0.2) \times 10^{-20} \text{ F}$ . In changing the voltage  $V_{\text{G}}^i$  of each top-gate  $i$  by  $\Delta V_{\text{G}}^i$ , the conductance peaks shift slightly in the back-gate voltage  $V_{\text{B}}$  given by  $\Delta V_{\text{B}} = C_{\text{G}}^i/C_{\text{B}} \cdot \Delta V_{\text{G}}^i$  ( $C_{\text{G}}^i$  is the capacitance to top-gate  $i$ ). In a similar way the capacitances to the two leads can be obtained. Adding all capacitances results in a total capacitance of  $C_{\Sigma} = (1.2 \pm 0.1) \times 10^{-16} \text{ F}$ . The relation between electrostatic potential changes in the dot and changes in the back-gate voltage  $\Delta V_{\text{B}}$  is given by the ratio  $C_{\text{B}}/C_{\Sigma} = (4.5 \pm 0.2) \times 10^{-4}$ .

In Fig. 2 the measurements of the conductance versus back-gate voltage  $V_B$  are shown for different magnetic fields  $B$ , varying from  $-15$  to  $15$  T in  $0.5$  T steps. The conductance peaks are shifted to positive gate voltage  $V_B$  and the amplitudes of the peaks are modulated by the magnetic field. The dependence is symmetric for both directions of  $B$ . These measurements are expected to contain information about the magnetic field dependence of the energy that is necessary to add the  $(N+1)$ th electron to the dot (between ground-state of  $(N+1)$  and groundstate of  $N$  electrons). A change in peak amplitude has been correlated with a change in character of the lowest accessible state for the  $(N+1)$ th electron [3].

To obtain additional information about our system we performed measurements of the differential conductance  $dI/dV_{DS}$  versus back-gate voltage  $V_B$  for a finite dc bias voltage  $V_{DS} = -0.7$  mV. In Fig. 3 the differential conductance  $dI/dV_{DS}$  is plotted in linear greyscale versus  $V_B$  for the different values of  $B$  (white corresponds to  $dI/dV_{DS} \leq 0 \mu S$ , black corresponds to  $dI/dV_{DS} \geq 1 \mu S$ ). The gate-voltage regions, where single-electron tunneling (SET) occurs, are broadened since the difference between the electrochemical potentials of the two electron reservoirs has been increased.

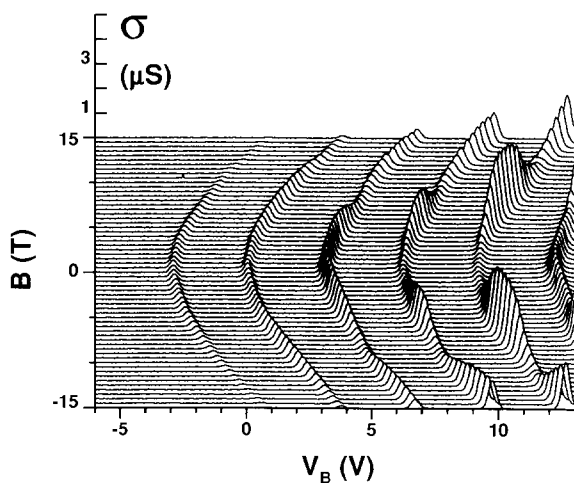


Fig. 2. Conductance  $\sigma$  versus back-gate voltage  $V_B$  for different magnetic fields  $B$  ( $-15$  to  $15$  T in  $0.5$  T steps) in a three-dimensional plot.

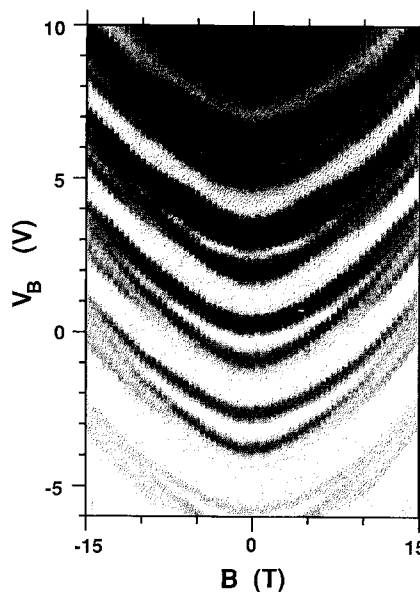


Fig. 3. Differential conductance  $dI/dV_{DS}$  given in a greyscale (white  $\leq 0 \mu S$ , black  $\geq 1 \mu S$ ) as a function of back-gate voltage  $V_B$  for different magnetic fields  $B$  ( $-15$  to  $15$  T in  $0.5$  T steps). The bias voltage  $V_{DS}$  was  $-0.7$  mV.

With  $N$  electrons enclosed in the quantum dot and sweeping  $V_B$  to positive values, transport through the dot starts when the energy necessary to add the  $(N+1)$ th electron becomes equal to the electrochemical potential of the emitter reservoir and stops when the energy falls below the electrochemical potential of the collector reservoir. Additional differential conductance peaks in the SET regime appear indicating new tunneling channels [4–6] since excited states of the  $N$  and  $N+1$  electron system are energetically accessible for transport. As visible in Fig. 3, the separation between these additional peaks changes with the magnetic field.

One possibility for a magnetic-field-induced change is Zeeman splitting due to different spin states. At  $15$  T the Zeeman splitting  $g\mu_B B$  is  $0.38$  meV for the  $g$ -factor of bulk GaAs ( $|g| = 0.44$ ). To analyse the results shown in Fig. 3 in more detail, the gate-voltage position of the two peaks visible in Fig. 3 around  $-3$  V are replotted in Fig. 4a versus  $B$ . Clearly the different shifts in  $V_B$  of the two peaks induced by  $B$  are visible. The data points in Fig. 4b show the magnetic field

dependence of the difference between these shifts, which appear to be linear with magnetic field. This fact suggests that the two peaks are connected with states which differ in their spin quantum number. A linear fit of the  $B$  dependence (given by the straight line in Fig. 4b) yields the slope  $dV_B/dB = (40 \pm 5) \text{ mV/T}$ . Relating this to the Zeeman splitting provides a  $g$ -factor of  $|g| = 0.31 \pm 0.04$ . This value is slightly smaller than  $g$ -factor values measured for the 2DEG in similar heterostructures by electron-spin resonance experiments [7].  $g$ -factors measured for 1D constrictions have been found to be larger [8]. The correct value for a quantum dot at the Al-GaAs/GaAs interface is not known.

Whereas the change in difference in gate-voltage position of the two peaks seems to be linear in  $B$ , the overall shift in gate-voltage position of one peak is nonlinear. The data points given in Fig. 4a can be fitted by a second-order polynomial in  $B$  ( $\delta V_B = \alpha B^2 + \beta B$ , with  $\alpha = (13 \pm 1) \text{ mV/T}^2$ , and  $\beta = (60 \pm 10) \text{ mV/T}$ , respectively,  $\beta = (100 \pm 10) \text{ mV/T}$ ). Both peak shifts are described by the same  $B^2$  dependence.

In interpreting these shifts one has to be careful. On the one hand the magnetic field influences the states in the quantum dot, on the other

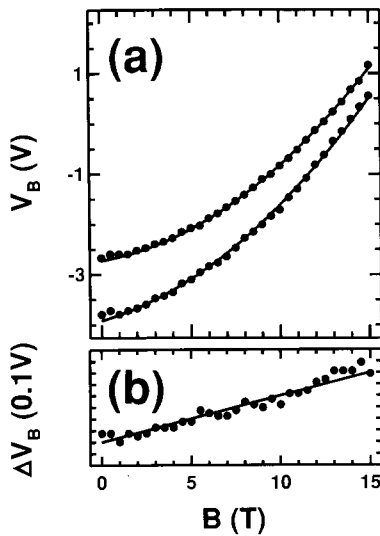


Fig. 4. (a) Gate-voltage position  $V_B$  of the two peaks observed in Fig. 3 around  $-3 \text{ V}$  plotted versus  $B$ . (b) Difference in gate-voltage of the two peaks (a) versus  $B$ .

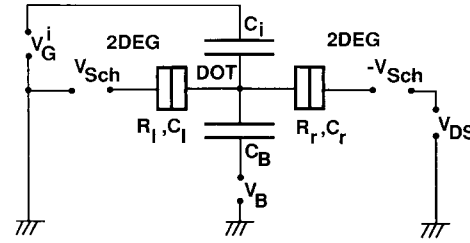


Fig. 5. Schematic capacitance circuit of the sample taking into account the Schottky voltages  $V_{\text{Sch}}$ .

hand the magnetic field also affects the 2DEG leads. The electronic states in the 2DEG are energetically shifted by the magnetic field, whereas the metallic electron reservoirs are hardly affected. Their electrochemical potential is fixed by the electrical circuit outside the magnet. To come to an equilibrium state between 2DEG and metallic electron reservoirs, electrons move from the 2DEG to the metal building up an intrinsic voltage at the interface (Schottky voltage) until the electrochemical potentials are equalised. The electrostatic potentials of the 2DEG leads are changed by  $\Delta V_{\text{Sch}} = \Delta \mu_{\text{ch}}^{\text{2DEG}}(B)/e$ , where  $\Delta \mu_{\text{ch}}^{\text{2DEG}}$  is the change of the chemical potential of the 2DEG. The quasi-isolated quantum dot is coupled to the 2DEG leads by capacitances. Therefore the electrostatic potential of the quantum dot is shifted due to the capacitance circuit given in Fig. 5, in addition to the energy change  $\Delta E_{N+1}^{\text{Dot}}(B)$  induced directly by the magnetic field to the energy necessary to add the  $(N+1)$ th electron. Consequently, shifts  $\delta V_B$  of resonance condition in the back-gate voltage  $V_B$  are given by

$$e \cdot C_B / C_{\Sigma} \cdot \delta V_B = \Delta E_{N+1}^{\text{Dot}}(B) - (C_r + C_l) / C_{\Sigma} \cdot \Delta \mu_{\text{ch}}^{\text{2DEG}}(B), \quad (1)$$

where  $C_r$  and  $C_l$  are the capacitances between the quantum dot and the 2D reservoirs.

In an in-plane-gate single-electron transistor [9], where also the gates consist of 2DEG only  $\Delta E_{N+1}^{\text{Dot}}(B) - \Delta \mu_{\text{ch}}^{\text{2DEG}}(B)$  should be observable. But in our structure, since the quantum dot is also capacitively coupled to metallic gates negligibly affected by the magnetic field, only the fraction  $(C_r + C_l) / C_{\Sigma} = 0.59 \pm 0.05$  of the diamagnetic shift of the 2DEG appears in formula (1).



Assuming that the change of the electron density in the 2DEG is negligible,  $\Delta\mu_{\text{ch}}^{2\text{DEG}}(B)$  is given by the diamagnetic shift  $\Delta E^{2\text{DEG}}(B)$  of the subband [10]. Assuming in addition that the quantum dot and the 2DEG have the same diamagnetic shift, we obtain  $\Delta E^{2\text{DEG}}(B)/B^2 = (14 \pm 2) \mu\text{eV}/\text{T}^2$  from the  $B^2$  dependence shown in Fig. 4 for the diamagnetic shift for this heterostructure.

#### 4. Conclusions

The resonance conditions for transport through the quantum dot are affected by the change of the chemical potential in the leads (2DEG) induced by the magnetic field. Direct information about the quantum dot is obtained by interpreting the difference of the shifts of differential conductance peak, which are observed at finite bias-voltage within one single-electron-tunneling regime.

#### 5. Acknowledgements

We gratefully acknowledge stimulating discussions with D. Pfannkuche and H. Pothier. We thank M. Riek, A. Gollhardt and F. Schartner for

their expert help with the sample preparation. Part of the work has been supported by the Bundesministerium für Forschung und Technologie.

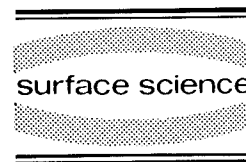
#### 6. References

- [1] Special Issue on Single Charge Tunneling, Z. Phys. B (Condensed Matter) 85, No. 3 (1991); H. Koch and H. Lübbig, Eds., in: Single-Electron Tunneling and Mesoscopic Devices, Springer Series in Electronics and Photonics, Vol. 31 (Springer, Berlin, 1992).
- [2] C.W.J. Beenakker, Phys. Rev. B 44 (1991) 1646.
- [3] P.L. McEuen, E.B. Foxman, U. Meirav, M.A. Kastner, Y. Meir, N.S. Wingreen and S.J. Wind, Phys. Rev. Lett. 66 (1991) 1926.
- [4] J. Weis, R.J. Haug, K. von Klitzing and K. Ploog, Phys. Rev. B 46 (1992) 12837.
- [5] A.T. Johnson, L.P. Kouwenhoven, W. de Jong, N.C. van der Vaart, C.J.P.M. Harmans and C.T. Foxon, Phys. Rev. Lett. 69 (1992) 1592.
- [6] E.B. Foxman, P.L. McEuen, U. Meirav, N.S. Wingreen, Y. Meir, P.A. Belk, N.R. Belk, M.A. Kastner and S.J. Wind, Phys. Rev. B 47 (1993) 10020.
- [7] M. Döbers, K. von Klitzing and G. Weimann, Phys. Rev. B 38 (1988) 5453.
- [8] N.K. Patel, J.T. Nicholls, L. Martin-Moreno, M. Pepper, J.E.F. Frost, D.A. Ritchie and G.A.C. Jones, Phys. Rev. B 44 (1991) 10973.
- [9] H. Pothier, J. Weis, R.J. Haug and K. von Klitzing, Appl. Phys. Lett. 62 (1993) 3174.
- [10] F. Stern, Phys. Rev. Lett. 21 (1968) 1687.



ELSEVIER

Surface Science 305 (1994) 669–673



# Aharonov–Bohm conductance oscillation of an antidot

Y. Takagaki, D.K. Ferry \*

*Center for Solid State Electronics Research, Arizona State University, Tempe, AZ 85287-6206, USA*

(Received 8 April 1993; accepted for publication 10 June 1993)

## Abstract

Magnetoconductance of a strip of two-dimensional electron gas is calculated in the presence of an antidot potential. We use both abrupt and smooth models for the antidot potential. An oscillation due to the Aharonov–Bohm effect is observed as a circulating edge state around the antidot is established. As short-range disorder is introduced, the amplitude of the oscillation is enhanced (suppressed) for magnetic fields below (above) the threshold of the circulating edge state. The position of the resonances in a magnetic field is found to be nearly independent of the moderate disorder.

## 1. Introduction

Recent experiments [1–3] have shown that the magnetoresistance of antidot arrays exhibits a periodic oscillation at low temperatures. The fine structure is superimposed on a slowly varying background oscillation due to commensurate classical orbits [2,4]. The amplitude of the rapid oscillation is suppressed in both weak and strong magnetic fields, and hence is a maximum at fields where the cyclotron orbit encircles a single antidot [3]. Since the period is in reasonable agreement with a change of magnetic flux  $h/e$  penetrating through the antidot, the oscillation has been interpreted in terms of an Aharonov–Bohm (AB)-type interference effect [5,6]. Surprisingly, the array may consist of thousands of antidots. Therefore, the observations indicate that the oscillation does not suffer from ensemble averaging,

in contrast to the conventional  $h/e$  oscillation observed in lithographically defined ring structures [7]. In dirty metals, the electron phase after traveling the AB loop is sample dependent due to phase shifts while being scattered from impurities. The purpose of this paper is to investigate the effects of random potentials on the AB interference in the antidot structures. We focus our attention on the role of an individual antidot. Quantum mechanical transmission through a strip of two-dimensional electron gas (2DEG) is numerically calculated in the presence of an antidot potential and short-range disorder. If the AB oscillation possesses sample specific phase due to the impurities, contributions from phase incoherent segments will average out in an array of antidots.

## 2. Numerical model

Our model geometry is illustrated in Fig. 1a, in which a single antidot potential  $V(x, y)$  is placed

\* Corresponding author.

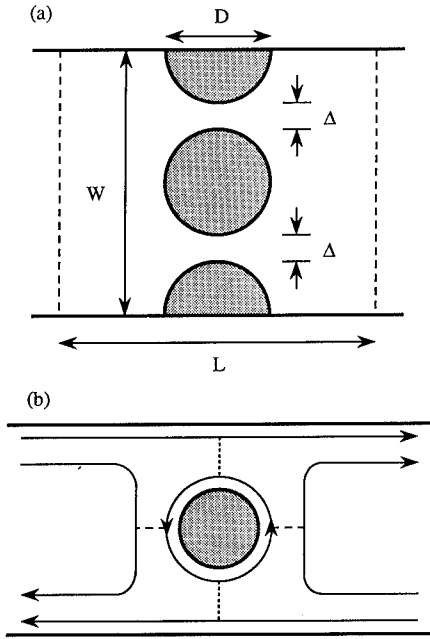


Fig. 1. (a) Schematic view of the model. The shaded regions represent the antidot potential. Short-range disorder is introduced in the area with length  $L = 57a$  (between the dashed lines). (b) Configuration of edge states at the Fermi energy.

at the center of a strip with width  $W$ . We consider a steep potential [ $V(x, y) = U$  in the antidot and 0 otherwise] and a smooth potential:

$$V(x, y) = \frac{U_0}{4} \left[ 1 + \cos\left(\frac{2\pi x}{W/2}\right) \right] \left[ 1 + \cos\left(\frac{2\pi y}{W/2}\right) \right],$$

$$|x| < W/4. \quad (1)$$

The neighboring antidots in the transverse direction are represented by the hard wall boundary and those in the longitudinal direction are neglected for the sake of simplicity. This roughly corresponds to a situation, in which the phase coherence length is comparable with the antidot period.

The conductance of the system is calculated by means of the lattice Green's function technique. The system is simulated by a square lattice with lattice constant  $a$ . We assume the Fermi wavelength to be  $\lambda_F = 9a$ . In the sample region with length  $L \approx 6.3\lambda_F$ , short-range disorder is introduced by modifying the site energy randomly in

an interval  $[-\Gamma/2, \Gamma/2]$ . In the following simulation, the magnetic field is graded to zero in the leads attached to the sample region since, in the absence of magnetic field, the transmission coefficient is simply given by a projection of the Green's function onto the transverse wave function [8].

### 3. Results and discussion

In the first part of this paper, we assume an abrupt potential with the diameter of the antidot being  $D = 21a$  ( $\approx 2.3\lambda_F$ ). The experiment by Nihei et al. [3] has shown that the oscillation appears as the distance between the antidots narrows. This can be explained in terms of multi-mode effects [6]. The two-terminal conductance of the ordered case ( $\Gamma = 0$ ) is plotted in Fig. 2 as a function of  $\hbar\omega_c/E_F$ , with  $\omega_c = eB/m$  being the cyclotron frequency. The curves represent the conductance for  $\Delta/\lambda_F \approx 1.1, 0.89$ , and  $0.67$ , i.e., the Fermi energy is placed above, near, and below the second subband threshold in the constrictions. The magnetic field penetrates the 2DEG region as well as the antidot region, and so no

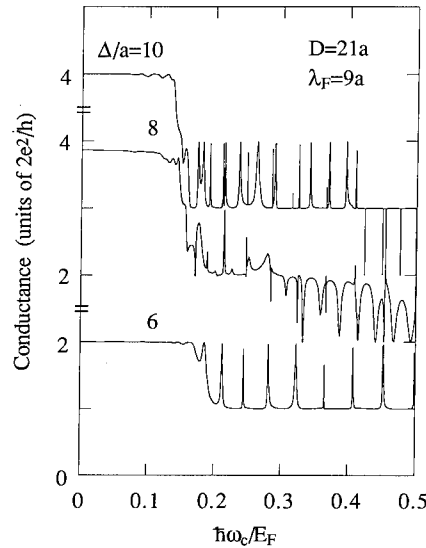


Fig. 2. The conductance of the wire as a function of magnetic field. The separation between the antidots  $\Delta$  is  $10a$  ( $\sim 1.1\lambda_F$ ),  $8a$  ( $\sim 0.89\lambda_F$ ) and  $6a$  ( $\sim 0.67\lambda_F$ ) from the top to the bottom.

AB structures are observed near zero field in the samples with a small ratio of “ring diameter to wire width”. Note that the two parallel constrictions have no correlation at  $B = 0$ , so that the conductance is nearly quantized in units of  $4e^2/h$  as  $\Delta$  is varied. The degeneracy breaks down for  $\hbar\omega_c/E_F > 0.2$ , where an edge state circulating around the antidot potential is well defined, and hence the conductance quantization appears in units of  $2e^2/h$ . In this regime, the conductance exhibits an oscillation due to AB interference, which consists of Lorentzian-shaped resonances with amplitude  $\sim 2e^2/h$ . One finds that the resonances can appear as either peaks or dips. The resonant reflection, which has been predicted by Jain and Kivelson [9], is due to tunneling between the antidots in the transverse direction (dotted line in Fig. 1b). On the other hand, the resonant transmission is due to tunneling between the classically reflected edge state in the wire and that around the antidot (dashed line in Fig. 1b) [6]. Therefore, the latter occurs only when the number of occupied Landau levels in the wire region away from the antidot is larger than that in the constriction. The resonance width is related to the strength of coupling between the edge states (traveling in the opposite directions for the resonant reflection and in the same direction for the resonant transmission) by the Breit–Wigner formula. The transport becomes adiabatic as the magnetic field is increased, resulting in a narrow resonance due to suppression of the inter-edge transition. At finite temperatures, the oscillation eventually disappears if the resonance width becomes much narrower than  $k_B T$  in strong fields. The oscillation is periodic when only the lowest mode is transmissive in the constrictions. On the other hand, if multiple edge states are occupied at the constrictions, contributions from different modes overlap, leading to aperiodic resonances. For the low field sinusoidal oscillation at  $\hbar\omega_c/E_F \approx 0.15$ , oscillations associated with different edge states add incoherently, and so one finds a destructive averaging effect.

Let us now consider impurity effects in a nearly clean system. In Fig. 3, the conductance is plotted for various values of  $\Gamma$  for a particular realization of disorder. We find that the oscillation is robust

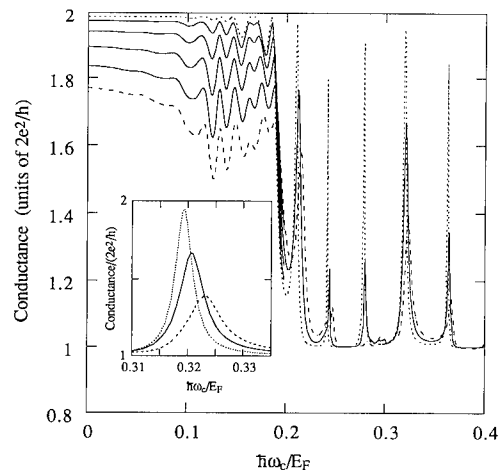


Fig. 3. The conductance of the wire as a function of magnetic field in the presence of short-range disorder. The strength of the disorder  $\Gamma/E_F$  is 0.0 (dotted line), 0.2, 0.4, 0.6, 0.8 and 1.0 (dashed line) for  $\hbar\omega_c/E_F < 0.2$  and 0.0 (dotted line), 0.6 (solid line), and 1.0 (dashed line) for  $\hbar\omega_c/E_F > 0.2$ . The peak at  $\hbar\omega_c/E_F \approx 0.32$  is expanded in the inset. The parameters for the abrupt antidot potential are  $D = 21a$ ,  $\Delta = 5a$ , and  $\lambda_F = 9a$ .

against the disorder. Note that, the mean free path at  $B = 0$  is  $\sim 16\lambda_F$  for  $\Gamma/E_F = 1.0$ . As the disorder is increased, the low field oscillation is enhanced, whereas the high field resonances are suppressed and broadened (Fig. 3, inset). The position of the resonances only slightly shifts to higher magnetic fields and is almost independent of the disorder even for  $\Gamma/E_F = 1.0$ , where the peak at  $\hbar\omega_c/E_F \approx 0.29$  is almost destroyed. This is in contrast to the AB oscillation in a quantum dot, for which the period becomes slow as disorder is introduced due to shrinkage of effective ring area [10]. The independence of the period from the presence of disorder can be explained in that the effective loop trajectory in the antidot passes through the center between the antidots. The edge state is pushed away from the boundary by disorder. The area shrinks to the bulk in the quantum dots while the trajectory is less affected in the antidots. Normally, an electron picks up additional phase when scattered from impurities. The AB oscillation is usually averaged to zero in an array of rings of metals [7]. This phase alteration may not be efficient if the sample dimensions are not much larger than the Fermi wave-

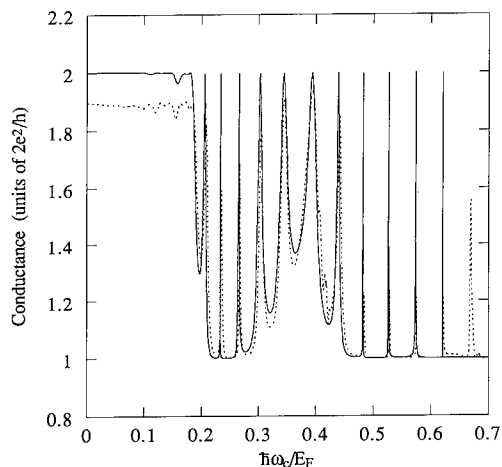


Fig. 4. The conductance as a function of magnetic field for the smooth potential. The solid and dotted lines correspond to  $\Gamma/E_F = 0.0$  and  $0.6$ , respectively.

length. Our result suggests that ensemble averaging, in the quantum Hall regime, is effectively invalid in geometries patterned with high mobility semiconductors.

We find that, in general, the period increases with increasing magnetic field, though the low field behavior considerably depends on the Fermi energy. The period of the peaks at  $\hbar\omega_c/E_F \approx 0.14, 0.2$  and  $0.4$  in Fig. 3 corresponds to an effective loop diameter of  $\sim 47a$ ,  $\sim 32a$  and  $\sim 27a$ , respectively. The reason that the effective diameter can be significantly larger than the period of the array ( $26a$ ) is due to neglect of antidots in the longitudinal direction. The shrinkage is also ascribed to an increased spatial separation between left- and right-moving edge states in high magnetic fields, which has been observed in experiments [3].

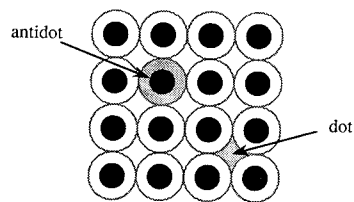


Fig. 5. Closed edge state loops (shaded areas) in antidot array. The filled circles and dotted lines represent antidot potential and edge states, respectively.

The transmission for the smooth potential is shown in Fig. 4. The parameter of the potential is chosen such that the distance of adjacent dots at the Fermi energy is  $\sim 0.71\lambda_F$ . One finds essentially the same result. The edge states come closer in space for the smooth potential, and so one finds broad resonances when compared to the case of the abrupt potential. The effective loop diameter in a range of magnetic field  $0.3 < \hbar\omega_c/E_F < 0.6$  is  $\sim 27a$ , which is comparable with the period of the antidots. The oscillation effectively disappears in high magnetic fields as the circulating edge state, which encloses the magnetic flux, is isolated from the current carrying edge state. The peaks become so narrow for  $\hbar\omega_c/E_F > 0.6$  that the resonance at  $\hbar\omega_c/E_F \approx 0.68$  does not appear in Fig. 4 in the absence of disorder. The peak appears clear for  $\Gamma/E_F = 0.6$  (dotted line) due to the disorder induced broadening.

#### 4. Conclusion

In conclusion, the magnetic field dependence of the transmission through a single antidot potential is found to show resonant reflection and transmission due to AB effect. The position of the resonances in magnetic field is insensitive to disorder. This suggests that the oscillation can survive ensemble averaging in moderate disorder. The clearest oscillation is expected to occur if only the lowest mode is transmitted between the antidots. In this situation, the oscillation in the antidot array may arise not only due to the circulating edge state around the antidots but also due to that in the quantum dot region (Fig. 5). However, the numerical result of Sivan et al. [10] indicates that the latter contribution is averaged out in the presence of randomness, and hence only the former one will appear in the resistance of macroscopic arrays.

#### 5. Acknowledgement

This work was supported in part by the Office of Naval Research.

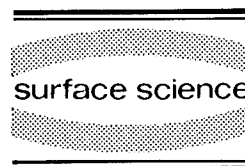
## 6. References

- [1] C.G. Smith, M. Pepper, R. Newbury, H. Ahmed, D.G. Hasko, D.C. Peacock, J.E.F. Frost, D.A. Ritchie, G.A.C. Jones and G. Hill, *J. Phys.: Condensed Matter* 2 (1990) 3405.
- [2] D. Weiss, M.L. Roukes, A. Menschig, P. Grambow, K. von Klitzing and G. Weimann, *Phys. Rev. Lett.* 66 (1991) 2790.
- [3] F. Nihei, S. Ishizaka and K. Nakamura, unpublished.
- [4] T. Yamashiro, J. Takahara, Y. Takagaki, K. Gamo, S. Namba, S. Takaoka and K. Murase, *Solid State Commun.* 79 (1991) 885.
- [5] D.K. Ferry, *Prog. Quantum Electron.* 16 (1992) 251.
- [6] Y. Takagaki and D.K. Ferry, unpublished.
- [7] C.P. Umbach, C. Van Haesendonck, R.B. Laibowitz, S. Washburn and R.A. Webb, *Phys. Rev. Lett.* 56 (1986) 386.
- [8] H.U. Baranger and A.D. Stone, *Phys. Rev. B* 40 (1989) 8169.
- [9] J.K. Jain and S.A. Kivelson, *Phys. Rev. Lett.* 60 (1988) 1542.
- [10] U. Sivan, Y. Imry and C. Hartzstein, *Phys. Rev. B* 39 (1989) 1242.



ELSEVIER

Surface Science 305 (1994) 674–677



# The AC Hall effect for electrons on liquid helium in ultra-high magnetic fields

P.J.M. Peters <sup>a</sup>, P. Scheuzger <sup>b</sup>, M.J. Lea <sup>c</sup>, W.P.N.M. Jacobs <sup>a</sup>,  
R.W. van der Heijden <sup>a,\*</sup>

<sup>a</sup> Department of Physics, Eindhoven University of Technology, P.O. Box 513, 5600 MB Eindhoven, Netherlands

<sup>b</sup> Hochfeld Magnetlabor, Max-Planck-Institut für Festkörperforschung, BP 166X, 38042 Grenoble Cedex, France

<sup>c</sup> Department of Physics, Royal Holloway, University of London, Egham, Surrey TW20 0EX, UK

(Received 12 April 1993; accepted for publication 11 May 1993)

## Abstract

Current–voltage phase shift measurements are reported between electrodes situated near the rim of an array located below a charged liquid helium surface. Data are taken in magnetic fields up to 20 T at a temperature near 2 K. Under these conditions, the ultra-quantum limit is reached, where the Landau level width is larger than the electron thermal energy. Interpreting the data in terms of the AC Hall effect, or edge magnetoplasmon, suggests that the Hall resistivity deviates from its classical value for fields greater than 10 T.

## 1. Introduction

Surface state electrons on liquid helium (SSE) form a classical two-dimensional electron gas in the sense that the electrons are non-degenerate, i.e. the Fermi energy is much smaller than the thermal energy  $kT$  at practical densities and temperatures. One of the most intriguing phenomena in degenerate systems (inversion layers and heterojunctions), namely the quantum Hall effects (QHE) [1] will therefore not occur in the SSE-system. In a strong magnetic field, the electrons in a non-degenerate system are, however, also subjected to the quantization of energy in the Lan-

dau levels. This quantization determines the transport properties in high magnetic fields [2–6].

Two strong-field regimes may be distinguished for the SSE. The first is the quantum limit, where the Landau level separation,  $\hbar\omega_c$ , is much larger than  $kT$ , but the Landau level width,  $2\Gamma$ , is much smaller than  $kT$ . The second regime is the ultra-quantum limit, where not only  $\hbar\omega_c \gg kT$ , but also  $\Gamma \gg kT$ . The level width  $2\Gamma$ , which might be written as  $\hbar/\tau(B)$  with  $\tau(B)$  the scattering time in a field, is determined by the scattering processes and is expected to decrease rapidly with decreasing temperature at a rate faster than  $T$ . The ultra-quantum limit will therefore not be reached by cooling down to practically realisable temperatures  $T \geq 10$  mK. Instead,  $\Gamma$  should be increased by increasing the temperature up to the highest possible temperature which is limited to

\* Corresponding author. Fax: +31 (40) 453587.

the  $\lambda$ -point of helium (2.17 K) to avoid boiling problems. Around the temperature of 2 K, scattering is completely determined by gas atom scattering and ripplon scattering is negligible. In this regime, far above the Wigner crystal phase transition [7], the electron correlations are not important and the level width and transport properties should be described by the early theory of Ando and Uemura [8] based on the self consistent Born approximation (SCBA). It was found experimentally that this theory reasonably well explains magnetoconductivity data in the gas atom scattering regime [2,3] even up to fields as high as 22 T [5]. The SCBA theory yields a semi-elliptic shape for the Landau levels with half width  $\Gamma = (2\hbar^2\omega_c/\pi\tau(0))^{1/2}$ , where  $\omega_c$  is the cyclotron frequency and  $\tau(0)$  the zero field scattering time. At 2 K and 20 T, using the zero field mobility of  $1.7 \text{ m}^2/\text{V} \cdot \text{s}$  [9], this gives  $2\Gamma/kT \sim 3.9$  while  $\hbar\omega_c/kT \sim 13$ . These values characterize the experimentally closest approach to the ultra-quantum limit,  $kT \ll \Gamma \ll \hbar\omega_c$ , where all electrons reside in the low-energy tail of the lowest Landau level. The SCBA-theory predicts a normal, linear Hall effect even in the quantum limit:  $\rho_{xy} = B/ne = h/\nu e^2$  ( $\rho_{xy}$  is the off-diagonal component of the resistivity tensor or Hall resistivity,  $B$  is the magnetic field,  $n$  the electron density,  $e$  the elementary charge,  $h$  the Planck constant and  $\nu = nh/eB$  the Landau level filling factor). The linear Hall effect was verified experimentally in the gas atom scattering regime up to well into the quantum limit [10,11]. It was noted previously [11] that the SCBA-theory predicts strong deviations from the linear Hall effect in the ultra-quantum limit with  $\rho_{xy} \propto B^{1/2}$ . The aim of the present work is to investigate the Hall effect in the ultra-quantum limit at temperatures of around 2 K in magnetic fields up to 20 T.

The measurement of the transport parameters, especially the Hall resistivity, for the SSE-system presents a considerable experimental problem because of the impossibility of attaching DC contacts to the sample. Therefore, one must resort to AC-capacitive coupling techniques. In strong magnetic fields such an AC-excitation leads to a localised edge mode [10,12]. Thanks to the inhomogeneous density distribution at the edge of the

SSE, the edge mode exists in the form of a moderately damped propagating wave called an edge magnetoplasmon for suitable frequencies and densities. Being first observed in the collisionless limit,  $\omega\tau \gg 1$  ( $\omega$  angular frequency,  $\tau$  scattering time) [13], it was recently shown that it exists down to very low, audio, frequencies [14]. It can be regarded as a dynamical Hall effect and is therefore also called the AC Hall effect. The dispersion relation, which under suitable circumstances can be measured, depends directly on  $\rho_{xy}$  as it should for a Hall effect. Here, we extend previous data around 2 K, that were essentially in the classical Hall effect regime [14], up to ultra-quantizing fields in an attempt to investigate  $\rho_{xy}$  in this limit.

## 2. Experimental

An array of electrodes with 14 mm diameter, shown in the inset to Fig. 2, was placed typically 0.5 mm below the helium surface. One of the outer electrodes, say 1, was excited with an AC-voltage  $V_0 \cos \omega t$ . The currents in- and out-of-phase with respect to the driving voltage, induced on one of the other outer electrodes (usually diametrically opposite to the driving one, e.g. 5) was measured using a current amplifier and dual-phase phase sensitive detector. Confining potentials were put on an upper plate and a surrounding circular guard ring. The homogeneity of the resistive magnet was sufficient to ignore helium level variations with magnetic field [5]. For each measuring frequency, the currents measured with the surface uncharged were subtracted from the data to account for stray resistances and capacitances. The measured phase shift was corrected for phase shifts of the current amplifier.

## 3. Results and discussion

Because at low frequencies and zero magnetic field the experimental system behaves as an RC-circuit, the convention is adopted to write the measured current as  $I = YV_0$ , where  $Y$  is defined



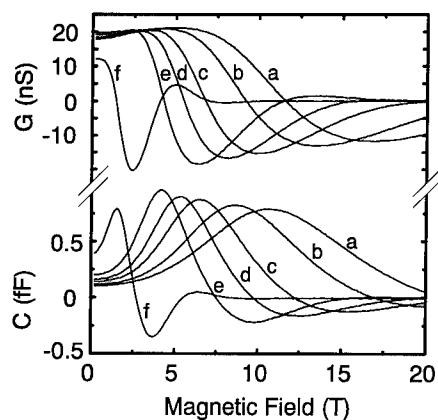


Fig. 1.  $G$  and  $C$  versus magnetic field.  $T = 2$  K,  $\omega/2\pi = 5$  kHz. From a to f,  $n$  is  $10.5, 8.2, 5.8, 4.7, 3.5$  and  $1.2 \times 10^{11} \text{ m}^{-2}$ .

as  $Y = G + j\omega C$ . A set of raw data is given in Fig. 1, for a fixed frequency at several densities.

The most convenient parameter to analyse is the phase shift  $\phi$ , defined as  $\phi = \arctan(G/\omega C)$ . This phase shift is proportional to the edge mode wavevector, and so to  $\rho_{xy}$ , in the edge mode regime, provided that the damping length is shorter than the sample circumference [14]. The  $\phi(B)$  curves obtained from the data of Fig. 1 are shown in Fig. 2. From Figs. 1 and 2, it follows that the phase increases with field, while the amplitude decreases, depending on the combina-

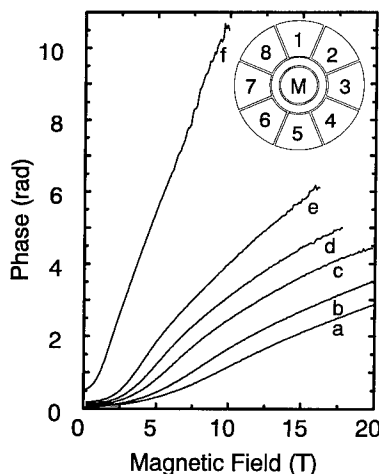


Fig. 2. Phase versus field for the data in Fig. 1. The inset shows the electrode geometry.

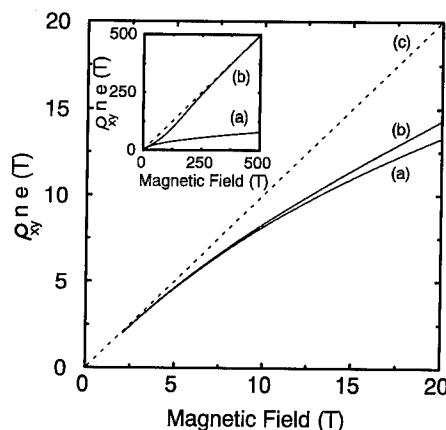


Fig. 3.  $\rho_{xy} (\times ne)$  versus field. (a) semi-elliptic and (b) Gaussian DOS, (c) linear. Inset: extended field range.

tion of frequency  $\omega$  and density  $n$  chosen, as these control the damping length [12,14]. When  $n$  and  $\omega$  are chosen so that the amplitude has become unmeasurably small in fields below 10 T, the  $\phi(B)$  curves are linear beyond some transient low-field region. The total measured phase shift is then about 10 rad. This is the behaviour reported before for fields less than 4 T [14] and now verified in an extensive series of measurements up to 10 T. A typical example of this is curve (f) in Figs. 1 and 2. The linear behaviour is in agreement with the expected linear Hall effect.

The situation changes significantly upon choosing lower frequencies and/or higher densities, so that there is an appreciable signal magnitude above 10 T. Firstly, as seen from Fig. 1, hardly one oscillation cycle (corresponding to a phase change of  $2\pi$ ) can be observed before the signal has decayed. Secondly, as seen from Fig. 2, there is hardly any region where  $\phi(B)$  is linear.

As to the physical interpretation of these observations, it is tempting to consider a nonlinear Hall effect as a cause. Fig. 3 shows a plot of  $\rho_{xy}$  calculated from the SCBA-theory [8,11] for the parameters of the experiment. The Hall effect is sublinear, tending to  $B^{1/2}$ ; the deviation is about 30% at 20 T.

There are several complications that hamper a firm interpretation of the data. A rigorous theory only exists for the limiting case where the width of the edge mode is comparable to the width of

the density-inhomogeneity at the edge [15]. Even then, the theory assumes  $\sigma_{xx} \ll \sigma_{xy}$  (diagonal and off-diagonal components of the conductivity tensor respectively), so that  $\sigma_{xy} = 1/\rho_{xy}$ . The results are expressed in  $\sigma_{xy}$  rather than  $1/\rho_{xy}$  but from a simplified analysis, the relevant parameter is expected to be  $1/\rho_{xy}$ . The SCBA-theory in the ultra-quantum limit predicts the opposite inequality, with  $\sigma_{xx}$  and  $\sigma_{xy}$  comparable at 2 K and 20 T. This means that the Hall angle ( $\arctan(\sigma_{xy}/\sigma_{xx})$ ) is no longer close to  $90^\circ$ , which in fact could also be related to the observed stronger damping in large fields.

The general situation has been studied in the transmission line approximation with a semi-empirical edge capacitance to yield the edge magnetoplasmon [14]. This simple model gives an extra contribution to  $k$  which depends on  $\rho_{xx}$  [12], at least in the limit where the spatial width of the edge mode is large compared to the width of the electron inhomogeneity at the edges. The two contributions should be distinguishable by their different  $n/\omega$  dependencies (square root and linear respectively). A preliminary result of such a detailed analysis yields a  $\rho_{xy}(B)$  curve that is surprisingly close to the theory shown in Fig. 3, but a fortuitous agreement cannot be ruled out.

As previously suggested [5], the shape of the tails of the Landau level could be important in the limit  $\Gamma \gg kT$ . In Fig. 3 therefore is also plotted the result for  $\rho_{xy}$  when a Gaussian density of states (DOS) is inserted phenomenologically in the SCBA-formulas [8,11]. The difference is not large in the presently used field region, but huge in the real ultra-quantum limit. Using a Gaussian DOS gives a classical, linear Hall effect again (see inset in Fig. 3)! This result is of interest in view of recent discussions on the universality of the Hall effect in degenerate systems. There, apart from the QHE-plateau regions, the Hall effect is always classical, even in the localised Wigner lattice regime where  $\rho_{xx}$  diverges [16].

We thank Dr. A.T.A.M. de Waele and Professor P. Wyder for their interest in this work.

Financial support from FOM-NWO, The Netherlands and SERC, UK (for M.J.L.) is gratefully acknowledged.

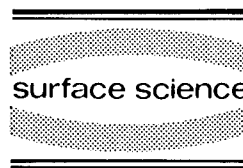
#### 4. References

- [1] R.E. Prange and S.M. Girvin, Eds., *The Quantum Hall Effects* (Springer, New York, 1987).
- [2] P.W. Adams and M.A. Paalanen, *Phys. Rev. B* 37 (1988) 3805.
- [3] R.W. van der Heijden, M.C.M. van de Sanden, J.H.G. Surewaard, A.T.A.M. de Waele, H.M. Gijsman and F.M. Peeters, *Europhys. Lett.* 6 (1988) 75.
- [4] A.O. Stone, P. Fozooni, M.J. Lea and M. Abdul-Gader, *J. Phys.: Condensed Matter* 1 (1989) 2743.
- [5] J. Neuenschwander, P. Scheuzger, W. Joss and P. Wyder, *Physica B* 165/166 (1990) 845; P. Scheuzger, J. Neuenschwander and P. Wyder, *Helv. Phys. Acta* 64 (1991) 170.
- [6] V.N. Grigor'ev, O.P. Kirichek, Yu.Z. Kovdria and Yu.P. Monarkha, *Sov. J. Low Temp. Phys.* 16 (1990) 219.
- [7] C.C. Grimes and G. Adams, *Phys. Rev. Lett.* 42 (1979) 795.
- [8] T. Ando and Y. Uemura, *J. Phys. Soc. Jpn.* 36 (1974) 959; T. Ando, Y. Matsumoto and Y. Uemura, *J. Phys. Soc. Jpn.* 39 (1975) 279.
- [9] M. Saitoh, *J. Phys. Soc. Jpn.* 42 (1977) 201.
- [10] M.J. Lea, A.O. Stone and P. Fozooni, *Europhys. Lett.* 7 (1988) 641.
- [11] R.W. van der Heijden, H.M. Gijsman and F.M. Peeters, *J. Phys. C* 21 (1988) L1165.
- [12] M.J. Lea, A.O. Stone, P. Fozooni and J. Frost, *J. Low Temp. Phys.* 85 (1991) 67.
- [13] D.B. Mast, A.J. Dahm and A.L. Fetter, *Phys. Rev. Lett.* 54 (1985) 1706; D.C. Glattli, E.Y. Andrei, G. Deville, G. Poitrenaud and F.I.B. Williams, *Phys. Rev. Lett.* 54 (1985) 1710.
- [14] M.J. Lea, A.O. Stone, P. Fozooni, P.J.M. Peters, A.M.L. Janssen and R.W. van der Heijden, *Surf. Sci.* 263 (1992) 677; P.J.M. Peters, M.J. Lea, A.M.L. Janssen, A.O. Stone, W.P.N.M. Jacobs, P. Fozooni and R.W. van der Heijden, *Phys. Rev. Lett.* 67 (1991) 2199.
- [15] V.A. Volkov and S.A. Mikhailov, in: *Modern Problems in Condensed Matter Sciences*, Vol. 27.2, Eds. V.M. Agranovich and A.A. Maradudin (North-Holland, Amsterdam, 1991) ch. 15, p. 855.
- [16] V.J. Goldman, J.K. Wang, Bo Su and M. Shayegan, *Phys. Rev. Lett.* 70 (1993) 647.



ELSEVIER

Surface Science 305 (1994) 678–693



## Author index

Abstreiter, G., see Hirler	305 (1994) 591
Adams, J.A., see Coleridge	305 (1994) 448
Adams, J.A., see Sachrajda	305 (1994) 527
Adams, J.A., see Taylor	305 (1994) 648
Ahmed, H., see Goodings	305 (1994) 363
Ahmed, H., see Ogawa	305 (1994) 659
Akimov, A.V., see Zinov'ev	305 (1994) 280
Allam, J., see Ogawa	305 (1994) 659
Allen, Jr., S.J., see Keay	305 (1994) 385
Allen, S.J., see Scott	305 (1994) 389
Alphenaar, B.W., A.A.M. Staring, H. van Houten and C.T. Foxon, Coulomb blockade in the presence of adiabatically transmitted edge channels	305 (1994) 520
Ando, T., see Tsuchiya	305 (1994) 312
Aoyagi, Y., see Stopa	305 (1994) 571
Ashoori, R.C., H.L. Stormer, J.S. Weiner, L.N. Pfeiffer, K.W. Baldwin and K.W. West, Energy levels of an artificial atom probed with single-electron capaci- tance spectroscopy	305 (1994) 558
Athas, G.J., see Klepper	305 (1994) 181
Baldwin, K.W., see Ashoori	305 (1994) 558
Bar-Ad, S., I. Bar-Joseph, Y. Levinson and H. Shtrikman, Time-resolved four wave mixing studies of a two-dimensional electron gas in a magnetic field	305 (1994) 234
Bar-Joseph, I., see Bar-Ad	305 (1994) 234
Barnes, D.J., see Dalton	305 (1994) 156
Basmaji, P., see Gusev	305 (1994) 443
Bastard, G., see Roussignol	305 (1994) 263
Bauer, G.E.W., Excitonic correction to resonant tunneling	305 (1994) 358
Baum, H., see Ensslin	305 (1994) 317
Beaumont, S.P., see Cuscó	305 (1994) 643
Bending, S.J., see Geim	305 (1994) 419
Benedict, K.A., see Eyles	305 (1994) 87
Berry, M.J., J.A. Katine, C.M. Marcus, R.M. Westervelt and A.C. Gossard, Weak localization and conductance fluctuations in a chaotic quantum dot	305 (1994) 495
Berthold, G., J. Smoliner, E. Gornik, G. Böhm, G. Weimann, T. Suski, P. Wisniewski, C. Hamaguchi, N. Mori and H. Momose, Magnetophonon reso- nances in quantum wires	305 (1994) 637
Besson, M., see Engelhardt	305 (1994) 23
Bhatt, R.N., see Huckestein	305 (1994) 438
Blaikie, R.J., see Ogawa	305 (1994) 659
Blom, F.A.P., see Van Haren	305 (1994) 172

- Boebinger, G.S., S.Q. Murphy, J.P. Eisenstein, L.N. Pfeiffer, K.W. West and S. He, New collective quantum Hall states in double quantum wells 305 (1994) 8
- Böhm, G., see Engelhardt 305 (1994) 23
- Böhm, G., see Hirler 305 (1994) 591
- Böhm, G., see Berthold 305 (1994) 637
- Borghs, G., see Gao 305 (1994) 470
- Brey, L. and H.A. Fertig, Resistivity and Hall resistance of a two-dimensional electron gas in the presence of magnetic flux tubes 305 (1994) 424
- Brooks, J.S., see Klepper 305 (1994) 181
- Brown, C.V., see Geim 305 (1994) 624
- Brown, S.A., A.G. Davies, A.C. Lindsay, R.B. Dunford, R.G. Clark, P.E. Simmonds, H.H. Voss, J.J. Harris and C.T. Foxon, Time-resolved magneto-photo-luminescence measurements of the integer QHE, fractional QHE and extreme quantum limit 305 (1994) 42
- Bruus, H., see Stone 305 (1994) 490
- Buckle, P.D., see Harrison 305 (1994) 353
- Buckle, P.D., see Cockburn 305 (1994) 375
- Burnett, J.H., H.M. Cheong, R.M. Westervelt, W. Paul, P.F. Hopkins, M. Sundaram and A.C. Gossard, Resonant inelastic light scattering in remotely doped wide parabolic GaAs/Al<sub>x</sub>Ga<sub>1-x</sub>As quantum wells in a magnetic field 305 (1994) 208
- Campbell, J.W., see Pudalov 305 (1994) 107
- Campbell, J.W., see D'Iorio 305 (1994) 115
- Carmona, H., see Geim 305 (1994) 624
- Carraresi, L., see Roussignol 305 (1994) 263
- Caulfield, J., see Doporto 305 (1994) 187
- Challis, L.J., see Eyles 305 (1994) 87
- Challis, L.J., see Zinov'ev 305 (1994) 280
- Chen, X., see Klepper 305 (1994) 181
- Chen, X.M. and J.J. Quinn, Numerical studies of the photoluminescence spectrum of quantum Hall systems 305 (1994) 71
- Cheng, J.-P., see Li 305 (1994) 215
- Cheng, J.-P., V.P. Kesan, D.A. Grützmacher and T.O. Sedgwick, Cyclotron effective mass of holes in strained Si<sub>1-x</sub>Ge<sub>x</sub>/Si quantum well structures 305 (1994) 275
- Cheong, H.M., see Burnett 305 (1994) 208
- Chklovskii, D.B. and P.A. Lee, Transport properties between quantum Hall plateaus 305 (1994) 133
- Choi, J.B., J.R. Meyer, C.A. Hoffman, G. Karczewski, J.K. Furdyna, K.H. Yoo and J.P. Faurie, Reflectivity, transport and magneto-optical studies of holes in the p-type HgZnTe/CdTe superlattice 305 (1994) 285
- Chow, D.H., see Scott 305 (1994) 389
- Clark, R.G., see Brown 305 (1994) 42
- Cleaver, J.R.A., see Goodings 305 (1994) 363
- Cockburn, J.W., R.J. Teissier, M.S. Skolnick, P.D. Buckle, D.M. Whittaker, A.R.K. Willcox, G.W. Smith, G. Hill and M.A. Pate, Optical spectroscopy of inverted electron populations in double-barrier resonant-tunnelling structures 305 (1994) 375
- Colas, E., see Plaut 305 (1994) 576
- Coleridge, P.T., R.P. Taylor, A.S. Sachrajda and J.A. Adams, Anti-collimation of ballistic electrons by a potential barrier 305 (1994) 448
- Coleridge, P.T., see Sachrajda 305 (1994) 527
- Coleridge, P.T., see Taylor 305 (1994) 648
- Colocci, M., see Roussignol 305 (1994) 263

Cox, R.T., see Kheng	305 (1994) 225
Cunningham, J.E., see Su	305 (1994) 566
Cuscó, R., M.C. Holland, J.H. Davies, I.A. Larkin, E. Skuras, A.R. Long and S.P. Beaumont, Anharmonic periodic modulation in lateral surface superlattices	305 (1994) 643
Dahl, M., see Heiman	305 (1994) 50
Dalton, K.S.H., M. van der Burgt, M. Lakrimi, R.J. Warburton, M.S. Daly, W. Lubczyński, R.W. Martin, D.M. Symons, D.J. Barnes, N. Miura, R.J. Nicholas, N.J. Mason and P.J. Walker, "Intrinsic" quantum Hall effect in InAs/Ga <sub>1-x</sub> In <sub>x</sub> Sb crossed gap heterostructures in high magnetic fields	305 (1994) 156
Daly, M.S., see Dalton	305 (1994) 156
Das Sarma, S., see Fertig	305 (1994) 67
Das Sarma, S., see Xie	305 (1994) 606
Davies, A.G., see Brown	305 (1994) 42
Davies, H.D.M., see Harris	305 (1994) 61
Davies, J.H., see Cuscó	305 (1994) 643
Davies, M., see Taylor	305 (1994) 648
Davis, J.L., see Yang	305 (1994) 271
Day, P., see Doporto	305 (1994) 187
De Lange, W., see Van Haren	305 (1994) 172
Delalande, C., see Roussignol	305 (1994) 263
Dempsey, J., see Gelfand	305 (1994) 166
Dennis, B.S., see Heiman	305 (1994) 50
Devoret, M.H., see Eiles	305 (1994) 536
Devreese, J.T., see Shi	305 (1994) 220
Devreese, J.T., see Leadley	305 (1994) 327
Dharma-wardana, C., see Sachrajda	305 (1994) 527
Dietl, T., see Wróbel	305 (1994) 615
D'Iorio, M., see Pudalov	305 (1994) 107
D'Iorio, M., V.M. Pudalov, S.V. Kravchenko and J.W. Campbell, Collective insulating state at zero magnetic field in a dilute 2D electron system	305 (1994) 115
Dolgoplov, V.T., G.V. Kravchenko, S.V. Kravchenko and A.A. Shashkin, Wigner solid in two-dimensional electron system in silicon in the extreme quantum limit?	305 (1994) 96
Doporto, M., J. Caulfield, S. Hill, J. Singleton, F.L. Pratt, M. Kurmoo, P.J.T. Hendriks, J.A.A.J. Perenboom, W. Hayes and P. Day, The influence of magnetic order in quasi-2D organic conductors	305 (1994) 187
Drebing, T., see Kunze	305 (1994) 633
Du, R.R., D.C. Tsui, H.L. Stormer, L.N. Pfeiffer and K.W. West, Experimental evidence for composite particles in the fractional quantum Hall effect	305 (1994) 18
Dunford, R.B., see Brown	305 (1994) 42
Dutta, M., see Wraback	305 (1994) 238
Eaves, L., see Harrison	305 (1994) 353
Eaves, L., see Fromhold	305 (1994) 511
Eaves, L., see Geim	305 (1994) 624
Eberl, K., see Kukushkin	305 (1994) 55
Eiles, T.M., M.H. Devoret and J.M. Martinis, Coulomb blockade of Andreev reflection in the NSN single-electron transistor	305 (1994) 536
Eisenstein, J.P., see Boebinger	305 (1994) 8
Eisenstein, J.P., L.N. Pfeiffer and K.W. West, Tunneling between highly correlated 2D electron systems	305 (1994) 393
Ekenberg, U., see Kash	305 (1994) 251

- Engel, L.W., D. Shahar, Ç. Kurdak and D.C. Tsui, Observation of finite-frequency scaling in the integer quantum Hall effect 305 (1994) 124
- Engelhardt, C.M., E. Gornik, M. Besson, G. Böhm and G. Weimann, Occurrence of a bulk-like electron phase in the cyclotron resonance of GaAs inversion channels in the extreme quantum limit 305 (1994) 23
- Ensslin, K., H. Baum, P.F. Hopkins and A.C. Gossard, Wave function modification via controlled potential perturbation 305 (1994) 317
- Esslinger, A., R.W. Winkler, C. Rocke, A. Wixforth, J.P. Kotthaus, H. Nickel, W. Schlapp and R. Lösch, Ultrasonic approach to the integer and fractional quantum Hall effect 305 (1994) 83
- Etienne, B., see Jusserand 305 (1994) 247
- Etienne, B., see Roussignol 305 (1994) 263
- Eyles, R.H., C.J. Mellor, A.J. Kent, K.A. Benedict, L.J. Challis, S. Kravchenko, N.N. Zinov'ev and M. Henini, Phonon measurements of the energy gap in the fractional quantum Hall state 305 (1994) 87
- Fal'ko, V.I., Crossing of cyclotron and spin resonances in a 2D electron gas 305 (1994) 290
- Fang, F.F., 2DEG in strained Si/SiGe heterostructures 305 (1994) 301
- Fasol, G., Y. Nagamune, J. Motohisa and H. Sakaki, Determination of the quantum wire potential and hot electron spectroscopy using point contacts 305 (1994) 620
- Fasolino, A., see Goldoni 305 (1994) 333
- Faurie, J.P., see Choi 305 (1994) 285
- Feng, Y., see Taylor 305 (1994) 648
- Ferguson, I.T., see Le 305 (1994) 337
- Ferreira, R., see Roussignol 305 (1994) 263
- Ferry, D.K., see Takagaki 305 (1994) 669
- Fertig, H.A., D.Z. Liu and S. Das Sarma, Photoluminescence and the Wigner crystal: can you see it? 305 (1994) 67
- Fertig, H.A., see Brey 305 (1994) 424
- Field, M., see Smith 305 (1994) 553
- Fletcher, R., see Zeitler 305 (1994) 91
- Fletcher, R., see Zinov'ev 305 (1994) 280
- Florez, L.T., see Keay 305 (1994) 385
- Ford, C.J.B., see Simpson 305 (1994) 453
- Ford, R.A., see Harris 305 (1994) 61
- Förster, A., see Schäpers 305 (1994) 460
- Foster, T.J., see Fromhold 305 (1994) 511
- Foster, T.J., see Geim 305 (1994) 624
- Foxon, C.T., see Michels 305 (1994) 33
- Foxon, C.T., see Brown 305 (1994) 42
- Foxon, C.T., see Harris 305 (1994) 61
- Foxon, C.T., see Zeitler 305 (1994) 91
- Foxon, C.T., see Leadley 305 (1994) 327
- Foxon, C.T., see Gao 305 (1994) 470
- Foxon, C.T., see Alphenaar 305 (1994) 520
- Fritze, M., A.V. Nurmikko and P. Hawrylak, Fermi-edge singularities in InGaAs and GaAs quantum wires 305 (1994) 580
- Fromhold, T.M., M.L. Leadbeater, L. Eaves, T.J. Foster, P.C. Main and F.W. Sheard, Tunneling into classically chaotic orbits in quantum wells 305 (1994) 511
- Frost, J.E.F., see Simpson 305 (1994) 453
- Frost, J.E.F., see Smith 305 (1994) 553
- Fukase, T., see Kawaji 305 (1994) 161
- Furdyna, J.K., see Choi 305 (1994) 285

- Gao, J.R., J.P. Heida, B.J. van Wees, T.M. Klapwijk, G. Borghs and C.T. Foxon, Superconductors coupled with a two-dimensional electron gas in GaAs/Al-GaAs and InAs/AlGaSb heterostructures 305 (1994) 470
- Gee, P., see Michels 305 (1994) 33
- Geim, A.K., S.J. Bending and I.V. Grigorieva, Scattering of ballistic electrons by magnetic flux tubes 305 (1994) 419
- Geim, A.K., P.C. Main, C.V. Brown, R. Taboryski, H. Carmona, T.J. Foster, P.E. Lindelof and L. Eaves, Resonant tunnelling between edge states in mesoscopic wires 305 (1994) 624
- Gelfand, B.Y., J. Dempsey and B.I. Halperin, Effects of electron–electron interactions on the ground state of quantum Hall edge states 305 (1994) 166
- Glozman, I., see Jiang 305 (1994) 120
- Goldman, V.J., see Su 305 (1994) 566
- Goldoni, G. and A. Fasolino, Current induced “spin” separation in p-doped asymmetric double quantum wells 305 (1994) 333
- Gonçalves, L.C.D., see Henriques 305 (1994) 343
- Goodings, C.J., H. Mizuta, J.R.A. Cleaver and H. Ahmed, Electron confinement in variable-area resonant tunnelling diodes using in-plane implanted gates 305 (1994) 363
- Gornik, E., see Engelhardt 305 (1994) 23
- Gornik, E., see Berthold 305 (1994) 637
- Gossard, A.C., see Burnett 305 (1994) 208
- Gossard, A.C., see Harris 305 (1994) 230
- Gossard, A.C., see Ensslin 305 (1994) 317
- Gossard, A.C., see Keay 305 (1994) 385
- Gossard, A.C., see Marcus 305 (1994) 480
- Gossard, A.C., see Berry 305 (1994) 495
- Goto, T., see Kawaji 305 (1994) 161
- Grabecki, G., see Wróbel 305 (1994) 615
- Grahn, H.T., see Müller 305 (1994) 380
- Grambow, P., see Mani 305 (1994) 654
- Grigorieva, I.V., see Geim 305 (1994) 419
- Grimshaw, M.P., see Simpson 305 (1994) 453
- Grützmacher, D.A., see Cheng 305 (1994) 275
- Grützmacher, D.A., see Zaslavsky 305 (1994) 307
- Guimaraes, P.S.S., see Keay 305 (1994) 385
- Gusev, G.M., P. Basmaji, Z.D. Kvon, L.V. Litvin, Yu.V. Nastaushev and A.I. Toropov, Negative magnetoresistance and anomalous diffusion of two-dimensional electrons in a disordered array of antidots 305 (1994) 443
- Gwinn, E.G., see Yuh 305 (1994) 202
- Halperin, B.I., Theories for  $\nu = 1/2$  in single- and double-layer systems 305 (1994) 1
- Halperin, B.I., see Gelfand 305 (1994) 166
- Halperin, B.I., see He 305 (1994) 398
- Hamaguchi, C., see Berthold 305 (1994) 637
- Hannahs, S.T., see Jiang 305 (1994) 120
- Harbison, J.P., see Keay 305 (1994) 385
- Harmans, C.J.P.M., see Lenssen 305 (1994) 476
- Harris, C.I., B. Monemar, P.O. Holtz, H. Kalt, M. Sundaram, J.L. Merz and A.C. Gossard, Exciton-capture mechanism at impurities in GaAs/Al<sub>x</sub>Ga<sub>(1-x)</sub>As quantum wells 305 (1994) 230
- Harris, I.N., H.D.M. Davies, R.A. Ford, J.F. Ryan, A.J. Turberfield, C.T. Foxon and J.J. Harris, Quasi-particle recombination and spatial ordering of 2D electrons in the extreme quantum limit 305 (1994) 61

Harris, J.J., see Michels	305 (1994)	33
Harris, J.J., see Brown	305 (1994)	42
Harris, J.J., see Harris	305 (1994)	61
Harris, J.J., see Zeitler	305 (1994)	91
Harris, J.J., see Leadley	305 (1994)	327
Harris, J.J., see Le	305 (1994)	337
Harrison, P.A., L. Eaves, P.M. Martin, M. Henini, P.D. Buckle, M.S. Skolnick, D.M. Whittaker and G. Hill, Intrinsic bistability in the electroluminescence spectrum and current-voltage characteristics of triple-barrier p-i-n resonant tunneling devices	305 (1994)	353
Hart, L., see Le	305 (1994)	337
Hasko, D.G., see Smith	305 (1994)	553
Haug, R.J., see Kukushkin	305 (1994)	55
Haug, R.J., see Weis	305 (1994)	664
Hawrylak, P., see Fritze	305 (1994)	580
Hawrylak, P., Magneto-optics of interacting electrons in quantum dots	305 (1994)	597
Hayes, W., see Doporto	305 (1994)	187
He, S., see Boebinger	305 (1994)	8
He, S., see Price	305 (1994)	126
He, S., P.M. Platzman and B.I. Halperin, One-electron Green's function and electron tunneling in a two-dimensional electron system in a strong magnetic field	305 (1994)	398
He, S., see Xie	305 (1994)	606
Heida, J.P., see Gao	305 (1994)	470
Heiman, D., A. Pinczuk, M. Dahl, B.S. Dennis, L.N. Pfeiffer and K.W. West, Time-resolved photoluminescence in the fractional quantum Hall regime	305 (1994)	50
Heitmann, D., see Meurer	305 (1994)	610
Hendriks, P.J.T., see Doporto	305 (1994)	187
Henini, M., see Eyles	305 (1994)	87
Henini, M., see Harrison	305 (1994)	353
Henriques, A.B. and L.C.D. Gonçalves, Crossover from a two- to three-dimensional electronic structure in Si spike doped GaAs superlattices	305 (1994)	343
Heremans, J.J., M.B. Santos and M. Shayegan, Transverse magnetic focusing and the dispersion of GaAs 2D holes at (311)A heterojunctions	305 (1994)	348
Herlach, F., see Leadley	305 (1994)	327
Hill, G., see Harrison	305 (1994)	353
Hill, G., see Cockburn	305 (1994)	375
Hill, S., see Michels	305 (1994)	33
Hill, S., see Doporto	305 (1994)	187
Hirakawa, K., see Kawaji	305 (1994)	161
Hirler, F., R. Strenz, R. Küchler, G. Abstreiter, G. Böhm and G. Weimann, Information on the confinement potential in GaAs/AlGaAs wires from magnetoluminescence experiments	305 (1994)	591
Hoffman, C.A., see Choi	305 (1994)	285
Holland, M., see Wang	305 (1994)	585
Holland, M.C., see Cuscó	305 (1994)	643
Holtz, P.O., see Harris	305 (1994)	230
Honda, T., see Tarucha	305 (1994)	547
Hopkins, P.F., see Burnett	305 (1994)	208
Hopkins, P.F., see Ensslin	305 (1994)	317
Hopkins, P.F., see Keay	305 (1994)	385
Hopkins, P.F., see Marcus	305 (1994)	480



- Huckestein, B. and R.N. Bhatt, Influence of a periodic potential on the integer quantum Hall effect 305 (1994) 438
- Hwang, D.M., see Plaut 305 (1994) 576
- Hwang, S.W., D.C. Tsui and M. Shayegan, Gate tuned transition to the insulating phase of one-dimensional electrons in high magnetic fields 305 (1994) 629
- Ismail, K., see Wróbel 305 (1994) 615
- Jacobs, W.P.N.M., see Peters 305 (1994) 674
- Jezierski, A.F., see Zinov'ev 305 (1994) 280
- Jiang, H.W., I. Glozman, C.E. Johnson and S.T. Hannahs, Magnetic-field-induced transition from an Anderson insulator to a quantum Hall conductor 305 (1994) 120
- Johnson, C.E., see Jiang 305 (1994) 120
- Jones, G.A.C., see Simpson 305 (1994) 453
- Jones, G.A.C., see Smith 305 (1994) 553
- Jusserand, B., D. Richards, H. Peric and B. Etienne, Raman scattering on modulation-doped quantum wells: intrinsic spin splitting of the GaAs conduction band 305 (1994) 247
- Kalt, H., see Harris 305 (1994) 230
- Kaminski, J.P., see Keay 305 (1994) 385
- Kaminski, J.P., see Scott 305 (1994) 389
- Kane, B.E., L.N. Pfeiffer and K.W. West, Junctions between coplanar 2D gases: a probe of boundary effects in the quantized Hall regime 305 (1994) 176
- Kapon, E., see Plaut 305 (1994) 576
- Karczewski, G., see Choi 305 (1994) 285
- Kash, J.A., M. Zachau, M.A. Tischler and U. Ekenberg, Optical measurements of warped valence bands in quantum wells 305 (1994) 251
- Kash, K., see Plaut 305 (1994) 576
- Katayama, Y., D.C. Tsui, H.C. Manoharan and M. Shayegan, Observation of an abrupt double-to-single-layer transition in a double-quantum-well structure 305 (1994) 405
- Katine, J.A., see Berry 305 (1994) 495
- Kawaji, S., K. Hirakawa, M. Nagata, T. Okamoto, T. Fukase and T. Goto, Magnetic field dependence of the device-width-dependent breakdown current in the quantum Hall effect 305 (1994) 161
- Keay, B.J., P.S.S. Guimaraes, J.P. Kaminski, S.J. Allen, Jr., P.F. Hopkins, A.C. Gossard, L.T. Florez and J.P. Harbison, Superlattice transport in intense terahertz electric fields 305 (1994) 385
- Keller, M.W., O. Millo, A. Mittal, D.E. Prober and R.N. Sacks, Magnetotransport in a chaotic scattering cavity with tunable electron density 305 (1994) 501
- Kent, A.J., see Eyles 305 (1994) 87
- Kesan, V.P., see Cheng 305 (1994) 275
- Kheng, K., R.T. Cox, Y. Merle d'Aubigné, M. Mamor, N. Magnea, H. Mariette, K. Saminadayar and S. Tatarenko, Negatively charged excitons  $X^-$  in the electron gas in  $\text{CdTe}/\text{Cd}_{1-x}\text{Zn}_x\text{Te}$  quantum wells 305 (1994) 225
- Khmelnitskii, D.E. and M. Yosefin, Conductance fluctuations of 2D electrons in a strong magnetic field 305 (1994) 507
- Kinoshita, N., see Klepper 305 (1994) 181
- Klapwijk, T.M., see Gao 305 (1994) 470
- Klehn, B., see Kunze 305 (1994) 633
- Klepper, S.J., J.S. Brooks, G.J. Athas, X. Chen, M. Tokumoto, N. Kinoshita and Y. Tanaka, Magnetic ordering and Fermi surface effects in the low-dimensional organic conductor  $\alpha\text{-(BEDT-TTF)}_2\text{RbHg(SCN)}_4$  305 (1994) 181

Kotthaus, J.P., see Esslinger	305 (1994) 83
Kozlov, V.G., see Walecki	305 (1994) 243
Kravchenko, G.V., see Dolgoplov	305 (1994) 96
Kravchenko, S., see Eyles	305 (1994) 87
Kravchenko, S.V., see Dolgoplov	305 (1994) 96
Kravchenko, S.V., see D'Iorio	305 (1994) 115
Kuchar, F., see Wróbel	305 (1994) 615
Küchler, R., see Hirler	305 (1994) 591
Kukushkin, I.V., R.J. Haug, K. von Klitzing, K. Eberl and K. Ploog, Time-resolved magnetoluminescence and Raman scattering measured in the regime of the fractional quantum Hall effect and of the Wigner solid	305 (1994) 55
Kunze, U., T. Drebingner, B. Klehn and J. Lindolf, Observation of 1D electron states at the boundary between an MOS and a Schottky contact on Si(100) by electron tunneling	305 (1994) 633
Kurata, H. and H. Sakaki, Electron transport via resonantly coupled energy levels in triple barrier structure investigated by magnetotunneling spectroscopy	305 (1994) 369
Kurdak, Ç., see Engel	305 (1994) 124
Kurmoo, M., see Doporto	305 (1994) 187
Kvon, Z.D., see Gusev	305 (1994) 443
Lakrimi, M., see Dalton	305 (1994) 156
Larkin, I.A., see Cuscó	305 (1994) 643
Le, T., A.G. Norman, W.T. Yuen, L. Hart, I.T. Ferguson, J.J. Harris, C.C. Phillips and R.A. Stradling, Quantum transport in $\text{InAs}_{1-x}\text{Sb}_x/\text{InSb}$ strained layer superlattices	305 (1994) 337
Lea, M.J., see Peters	305 (1994) 674
Leadbeater, M.L., see Fromhold	305 (1994) 511
Leadley, D.R., R.J. Nicholas, J. Singleton, W. Xu, F.M. Peeters, J.T. Devreese, L. van Bockstal, F. Herlach, J.A.A.J. Perenboom, J.J. Harris and C.T. Foxon, Disappearance of magnetophonon resonance at high magnetic fields in $\text{GaAs}/\text{GaAlAs}$ heterojunctions	305 (1994) 327
Lee, K.Y., see Wróbel	305 (1994) 615
Lee, P.A., see Chklovskii	305 (1994) 133
Lengeler, B., see Schäpers	305 (1994) 460
Lenssen, K.-M.H., L.A. Westerling, C.J.P.M. Harmans, J.E. Mooij, M.R. Leys, W. van der Vleuten and J.H. Wolter, Influence of gate voltage on the transport properties of superconductor/2DEG systems	305 (1994) 476
Levinson, Y., see Bar-Ad	305 (1994) 234
Levinson, Y.B., Metal/2DEG contact - a microscopic model	305 (1994) 465
Leys, M.R., see Lenssen	305 (1994) 476
Li, W.J., J.L. Wang, B.D. McCombe, J.-P. Cheng and W. Schaff, Spectroscopy of quasi-2D $\text{D}^-$ ions in the presence of excess electrons	305 (1994) 215
Li, Y., see Song	305 (1994) 139
Lin, S.Y., see Zaslavsky	305 (1994) 307
Lin-Chung, P.J., see Yang	305 (1994) 271
Lindelof, P.E., see Geim	305 (1994) 624
Lindolf, J., see Kunze	305 (1994) 633
Lindsay, A.C., see Brown	305 (1994) 42
Litvin, L.V., see Gusev	305 (1994) 443
Liu, D.Z., see Fertig	305 (1994) 67
Liu, T.Y., see Scott	305 (1994) 389
Long, A.R., see Cuscó	305 (1994) 643

- Lösch, R., see Esslinger 305 (1994) 83
- Lu, Y., see Wraback 305 (1994) 238
- Lubczyński, W., see Dalton 305 (1994) 156
- Lui, M., see Scott 305 (1994) 389
- Lüth, H., see Schäpers 305 (1994) 460
- Lütjering, G., see Weiss 305 (1994) 408
- Maan, J.C., see Zeitler 305 (1994) 91
- MacDonald, A.H., see Zheng 305 (1994) 101
- Mace, D.R., see Simpson 305 (1994) 453
- Magnea, N., see Kheng 305 (1994) 225
- Maijale, M.Z. and L.J. Sham, Exciton spin dynamics and polarized luminescence in quantum wells 305 (1994) 256
- Main, P.C., see Fromhold 305 (1994) 511
- Main, P.C., see Geim 305 (1994) 624
- Mamor, M., see Kheng 305 (1994) 225
- Mani, R.G., K. von Klitzing, E. Vasiliadou, P. Grambow and K. Ploog, Magneto-transport study of GaAs/AlGaAs quantum wires 305 (1994) 654
- Manoharan, H.C., see Suen 305 (1994) 13
- Manoharan, H.C., see Katayama 305 (1994) 405
- Marcus, C.M., R.M. Westervelt, P.F. Hopkins and A.C. Gossard, Conductance fluctuations in a quantum dot in the tunneling regime: crossover from aperiodic to regular behavior 305 (1994) 480
- Marcus, C.M., see Berry 305 (1994) 495
- Mariette, H., see Kheng 305 (1994) 225
- Martin, P.M., see Harrison 305 (1994) 353
- Martin, R.W., see Dalton 305 (1994) 156
- Martin-Moreno, L., see Palacios 305 (1994) 541
- Martinez-Pastor, J., see Roussignol 305 (1994) 263
- Martinis, J.M., see Eiles 305 (1994) 536
- Mason, N.J., see Dalton 305 (1994) 156
- Matsusue, T., see Ohno 305 (1994) 322
- Matulis, A., F.M. Peeters and P. Vasilopoulos, Two-dimensional tunneling through magnetic barriers 305 (1994) 434
- McCombe, B.D., see Li 305 (1994) 215
- McLelland, H., see Wang 305 (1994) 585
- Mellor, C.J., see Eyles 305 (1994) 87
- Mendez, E.E., see Van Son 305 (1994) 516
- Merle d'Aubigné, Y., see Kheng 305 (1994) 225
- Merz, J.L., see Harris 305 (1994) 230
- Meurer, B., D. Heitmann and K. Ploog, Quantum dots in tilted magnetic fields 305 (1994) 610
- Meyer, J.R., see Choi 305 (1994) 285
- Michels, J.G., S. Hill, R.J. Warburton, G.M. Summers, P. Gee, J. Singleton, R.J. Nicholas, C.T. Foxon and J.J. Harris, Cyclotron resonance to 100 mK of a GaAs heterojunction in the ultra-quantum limit 305 (1994) 33
- Milliken, F.P., see Van Son 305 (1994) 516
- Millo, O., see Keller 305 (1994) 501
- Mittal, A., see Keller 305 (1994) 501
- Miura, N., see Dalton 305 (1994) 156
- Mizuta, H., see Goodings 305 (1994) 363
- Momose, H., see Berthold 305 (1994) 637
- Monemar, B., see Harris 305 (1994) 230

Mooij, J.E., see Lenssen	305 (1994) 476
Moore, W.J., see Yang	305 (1994) 271
Mori, N., see Berthold	305 (1994) 637
Motohisa, J., see Fasol	305 (1994) 620
Müller, F., see Schäpers	305 (1994) 460
Müller, W., H.T. Grahn, K. von Klitzing and K. Ploog, Resonant inter-Landau-level tunneling of electrons and holes in superlattices	305 (1994) 380
Murphy, S.Q., see Boebinger	305 (1994) 8
Nagamune, Y., see Fasol	305 (1994) 620
Nagata, M., see Kawaji	305 (1994) 161
Nastaushev, Yu.V., see Gusev	305 (1994) 443
Newman, P.G., see Wraback	305 (1994) 238
Nicholas, R.J., see Michels	305 (1994) 33
Nicholas, R.J., see Dalton	305 (1994) 156
Nicholas, R.J., see Leadley	305 (1994) 327
Nicholls, J.T., see Simpson	305 (1994) 453
Nickel, H., see Esslinger	305 (1994) 83
Nickel, H., see Wróbel	305 (1994) 615
Noda, T., see Ohno	305 (1994) 322
Norman, A.G., see Le	305 (1994) 337
Nurmikko, A.V., see Walecki	305 (1994) 243
Nurmikko, A.V., see Fritze	305 (1994) 580
Ogawa, K., R.J. Blaikie, J.D. White, J. Allam and H. Ahmed, Transport properties of dual quantum dots	305 (1994) 659
Ohno, Y., M. Tsuchiya, T. Matsusue, T. Noda and H. Sakaki, Non-uniform resonant coupling effect on 2D electron transport in $\delta$ -doped double quantum well structures	305 (1994) 322
Okamoto, T., see Kawaji	305 (1994) 161
Palacios, J.J., L. Martin-Moreno and C. Tejedor, Correlation effects on transport through few-electrons systems	305 (1994) 541
Palmier, J.F., see Roussignol	305 (1994) 263
Pamulapati, J., see Wraback	305 (1994) 238
Pate, M.A., see Cockburn	305 (1994) 375
Paul, W., see Burnett	305 (1994) 208
Peeters, F.M., see Shi	305 (1994) 220
Peeters, F.M., see Leadley	305 (1994) 327
Peeters, F.M., see Tso	305 (1994) 400
Peeters, F.M., see Matulis	305 (1994) 434
Pepper, M., see Simpson	305 (1994) 453
Pepper, M., see Smith	305 (1994) 553
Perenboom, J.A.A.J., see Doporto	305 (1994) 187
Perenboom, J.A.A.J., see Leadley	305 (1994) 327
Peric, H., see Jusserand	305 (1994) 247
Peters, P.J.M., P. Scheuzger, M.J. Lea, W.P.N.M. Jacobs and R.W. van der Heijden, The AC Hall effect for electrons on liquid helium in ultra-high magnetic fields	305 (1994) 674
Pfeiffer, L.N., see Boebinger	305 (1994) 8
Pfeiffer, L.N., see Du	305 (1994) 18
Pfeiffer, L.N., see Heiman	305 (1994) 50

- Pfeiffer, L.N., see Kane 305 (1994) 176  
Pfeiffer, L.N., see Eisenstein 305 (1994) 393  
Pfeiffer, L.N., see Ashoori 305 (1994) 558  
Phillips, C.C., see Le 305 (1994) 337  
Pinczuk, A., see Heiman 305 (1994) 50  
Platzman, P.M., see Price 305 (1994) 126  
Platzman, P.M., see He 305 (1994) 398  
Plaut, A.S., K. Kash, E. Kapon, D.M. Hwang and E. Colas, Magneto-optics of quantum wires grown on V-grooved substrates 305 (1994) 576  
Ploog, K., see Kukushkin 305 (1994) 55  
Ploog, K., see Müller 305 (1994) 380  
Ploog, K., see Meurer 305 (1994) 610  
Ploog, K., see Mani 305 (1994) 654  
Ploog, K., see Weis 305 (1994) 664  
Polyakov, D.G. and B.I. Shklovskii, Conductivity peaks in the quantum Hall regime: broadening with temperature, current, and frequency 305 (1994) 151  
Pratt, F.L., see Doport 305 (1994) 187  
Price, R., P.M. Platzman, S. He and X. Zhu, Quantum Hall liquid–Wigner solid phase boundary 305 (1994) 126  
Prober, D.E., see Keller 305 (1994) 501  
Pudalov, V.M., M. D'Iorio and J.W. Campbell, Termination of the quantized Hall effect by the electron solid 305 (1994) 107  
Pudalov, V.M., see D'Iorio 305 (1994) 115  
Quinn, J.J., see Chen 305 (1994) 71  
Reinecke, T.L., see Rudin 305 (1994) 267  
Richards, D., see Jusserand 305 (1994) 247  
Richter, C.A., R.G. Wheeler and R.N. Sacks, Transitions between edge and bulk channels in the quantum Hall regime 305 (1994) 145  
Richter, K., see Weiss 305 (1994) 408  
Ritchie, D.A., see Simpson 305 (1994) 453  
Ritchie, D.A., see Smith 305 (1994) 553  
Rocke, C., see Esslinger 305 (1994) 83  
Rössler, U., see Winkler 305 (1994) 295  
Roussignol, Ph., R. Ferreira, C. Delalande, G. Bastard, A. Vinattieri, J. Martinez-Pastor, L. Carraresi, M. Colocci, J.F. Palmier and B. Etienne, Hole spin relaxation in a n-doped quantum well structure 305 (1994) 263  
Rudin, S. and T.L. Reinecke, Plasmons localized at point charges in semiconductor quantum wells 305 (1994) 267  
Ryan, J.F., see Harris 305 (1994) 61  
Sachrajda, A., R.P. Taylor, C. Dharma-wardana, J.A. Adams, P. Zawadzki and P.T. Coleridge, Electron–electron interactions and the magntoconductance of submicron quantum dots 305 (1994) 527  
Sachrajda, A.S., see Coleridge 305 (1994) 448  
Sachrajda, A.S., see Taylor 305 (1994) 648  
Sacks, R.N., see Richter 305 (1994) 145  
Sacks, R.N., see Keller 305 (1994) 501  
Sakaki, H., see Ohno 305 (1994) 322  
Sakaki, H., see Kurata 305 (1994) 369  
Sakaki, H., see Fasol 305 (1994) 620

- Saku, T., see Tarucha 305 (1994) 547
- Saminadayar, K., see Kheng 305 (1994) 225
- Santos, M.B., see Suen 305 (1994) 13
- Santos, M.B., see Heremans 305 (1994) 348
- Schaff, W., see Li 305 (1994) 215
- Schäpers, T., F. Müller, A. Förster, B. Lengeler and H. Lüth, Control of ballistic electrons in (AlGa)As/GaAs heterostructures by means of superconducting niobium gate structures 305 (1994) 460
- Scheuzger, P., see Peters 305 (1994) 674
- Schlapp, W., see Esslinger 305 (1994) 83
- Schlapp, W., see Wróbel 305 (1994) 615
- Scott, J.S., J.P. Kaminski, S.J. Allen, D.H. Chow, M. Lui and T.Y. Liu, Terahertz response of resonant tunneling diodes 305 (1994) 389
- Sedgwick, T.O., see Cheng 305 (1994) 275
- Sedgwick, T.O., see Zaslavsky 305 (1994) 307
- Shahar, D., see Engel 305 (1994) 124
- Sham, L.J., see Maialle 305 (1994) 256
- Shanabrook, B.V., see Yang 305 (1994) 271
- Shashkin, A.A., see Dolgoplov 305 (1994) 96
- Shayegan, M., see Suen 305 (1994) 13
- Shayegan, M., see Heremans 305 (1994) 348
- Shayegan, M., see Katayama 305 (1994) 405
- Shayegan, M., see Hwang 305 (1994) 629
- Sheard, F.W., see Fromhold 305 (1994) 511
- Shen, H., see Wraback 305 (1994) 238
- Shi, J.M., F.M. Peeters and J.T. Devreese, Transition energies of  $D^-$  centers in a superlattice 305 (1994) 220
- Shklovskii, B.I., see Polyakov 305 (1994) 151
- Shtrikman, H., see Bar-Ad 305 (1994) 234
- Simmonds, P.E., see Brown 305 (1994) 42
- Simpson, P.J., C.J.B. Ford, D.R. Mace, I. Zailer, M. Yosefin, M. Pepper, J.T. Nicholls, D.A. Ritchie, J.E.F. Frost, M.P. Grimshaw and G.A.C. Jones, Charge oscillations in edge states and double-frequency Aharonov–Bohm effects around a tunable obstacle 305 (1994) 453
- Singleton, J., see Michels 305 (1994) 33
- Singleton, J., see Doporto 305 (1994) 187
- Singleton, J., see Leadley 305 (1994) 327
- Skolnick, M.S., see Harrison 305 (1994) 353
- Skolnick, M.S., see Cockburn 305 (1994) 375
- Skuras, E., see Cuscó 305 (1994) 643
- Smith, C.G., M. Field, M. Pepper, D.A. Ritchie, J.E.F. Frost, G.A.C. Jones and D.G. Hasko, A non-evasive voltage probe to measure Coulomb charging 305 (1994) 553
- Smith, G.W., see Cockburn 305 (1994) 375
- Smith III, T.P., see Zaslavsky 305 (1994) 307
- Smoliner, J., see Berthold 305 (1994) 637
- Some, D., see Walecki 305 (1994) 243
- Song, A., H. Zheng, F. Yang and Y. Li, Direct determination of the density of states in two-dimensional systems by magnetocapacitances of biased double barrier structures 305 (1994) 139
- Sotomayor Torres, C.M., see Wang 305 (1994) 585
- Stanley, C.R., see Wang 305 (1994) 585
- Staring, A.A.M., see Alphenaar 305 (1994) 520

- Stone, A.D. and H. Bruus, Universal fluctuation effects in chaotic quantum dots 305 (1994) 490
- Stopa, M., Y. Aoyagi and T. Sugano, Coulomb oscillation amplitude enhancement and envelope modulation in a magnetic field and activated tunneling 305 (1994) 571
- Stormer, H.L., see Du 305 (1994) 18
- Stormer, H.L., see Ashoori 305 (1994) 558
- Stradling, R.A., see Le 305 (1994) 337
- Strenz, R., see Hirler 305 (1994) 591
- Su, B., V.J. Goldman and J.E. Cunningham, Evidence for spin singlet–triplet transitions of two electrons in a quantum dot observed via single-electron tunneling 305 (1994) 566
- Suen, Y.W., H.C. Manoharan, X. Ying, M.B. Santos and M. Shayegan, One-component to two-component transitions of fractional quantum Hall states in a wide quantum well 305 (1994) 13
- Sugano, T., see Stopa 305 (1994) 571
- Sujak-Cyruł, B., see Zinov'ev 305 (1994) 280
- Summers, G.M., see Michels 305 (1994) 33
- Sundaram, M., see Burnett 305 (1994) 208
- Sundaram, M., see Harris 305 (1994) 230
- Suski, T., see Berthold 305 (1994) 637
- Symons, D.M., see Dalton 305 (1994) 156
- Taboryski, R., see Geim 305 (1994) 624
- Takagaki, Y. and D.K. Ferry, Aharonov–Bohm conductance oscillation of an antidot 305 (1994) 669
- Tanaka, Y., see Klepper 305 (1994) 181
- Tarucha, S., T. Honda, T. Saku and Y. Tokura, Charging effects in small-area modulation-doped double-barrier heterostructures 305 (1994) 547
- Tatarenko, S., see Kheng 305 (1994) 225
- Taylor, R.P., see Coleridge 305 (1994) 448
- Taylor, R.P., see Sachrajda 305 (1994) 527
- Taylor, R.P., Y. Feng, A.S. Sachrajda, J.A. Adams, M. Davies, P.T. Coleridge and P. Zawadzki, Fabrication and characterisation of multi-level lateral nano-devices 305 (1994) 648
- Taysing-Lara, M., see Wraback 305 (1994) 238
- Teissier, R.J., see Cockburn 305 (1994) 375
- Tejedor, C., see Palacios 305 (1994) 541
- Thoms, S., see Wang 305 (1994) 585
- Tischler, M.A., see Kash 305 (1994) 251
- Tokumoto, M., see Klepper 305 (1994) 181
- Tokura, Y., see Tarucha 305 (1994) 547
- Toropov, A.I., see Gusev 305 (1994) 443
- Tso, H.C., P. Vasilopoulos and F.M. Peeters, Coupled electron–hole transport: generalized random-phase approximation and density functional theory 305 (1994) 400
- Tsuchiya, M., see Ohno 305 (1994) 322
- Tsuchiya, T. and T. Ando, Effect of electronic-state modulation on mobility in quantum wells 305 (1994) 312
- Tsui, D.C., see Du 305 (1994) 18
- Tsui, D.C., see Engel 305 (1994) 124
- Tsui, D.C., see Katayama 305 (1994) 405
- Tsui, D.C., see Hwang 305 (1994) 629
- Turberfield, A.J., see Harris 305 (1994) 61
- Ulloa, S.E., see Wu 305 (1994) 428

Van Bockstal, L., see Leadley	305 (1994) 327
Van der Burgt, M., see Dalton	305 (1994) 156
Van der Heijden, R.W., see Peters	305 (1994) 674
Van der Vleuten, W., see Lenssen	305 (1994) 476
Van Haren, R.J.F., F.A.P. Blom, W. de Lange and J.H. Wolter, Total suppression of the inter-edge-channel scattering in a GaAs/AlGaAs heterostructure	305 (1994) 172
Van Houten, H., see Alphenaar	305 (1994) 520
Van Son, P.C., F.P. Milliken, E.E. Mendez and W.I. Wang, Low-temperature equilibrium vertical transport through a two-dimensional electron gas	305 (1994) 516
Van Wees, B.J., see Gao	305 (1994) 470
Vasiliadou, E., see Weiss	305 (1994) 408
Vasiliadou, E., see Mani	305 (1994) 654
Vasilopoulos, P., see Tso	305 (1994) 400
Vasilopoulos, P., see Matulis	305 (1994) 434
Vinattieri, A., see Roussignol	305 (1994) 263
Von Klitzing, K., see Kukushkin	305 (1994) 55
Von Klitzing, K., see Müller	305 (1994) 380
Von Klitzing, K., see Mani	305 (1994) 654
Von Klitzing, K., see Weis	305 (1994) 664
Voss, H.H., see Brown	305 (1994) 42
Wagner, R.J., see Yang	305 (1994) 271
Walecki, W.J., D. Some, V.G. Kozlov and A.V. Nurmikko, Terahertz electromagnetic transients as probes of a two-dimensional electron gas	305 (1994) 243
Walker, P.J., see Dalton	305 (1994) 156
Wang, J.L., see Li	305 (1994) 215
Wang, P.D., C.M. Sotomayor Torres, H. McLelland, S. Thoms, M. Holland and C.R. Stanley, Photoluminescence intensity and multiple phonon Raman scattering in quantum dots: evidence of the bottleneck effect	305 (1994) 585
Wang, W.I., see Van Son	305 (1994) 516
Warburton, R.J., see Michels	305 (1994) 33
Warburton, R.J., see Dalton	305 (1994) 156
Waterman, J.R., see Yang	305 (1994) 271
Weimann, G., see Engelhardt	305 (1994) 23
Weimann, G., see Hirler	305 (1994) 591
Weimann, G., see Berthold	305 (1994) 637
Weiner, J.S., see Ashoori	305 (1994) 558
Weis, J., R.J. Haug, K. von Klitzing and K. Ploog, Lateral transport through a single quantum dot with a magnetic field parallel to the current	305 (1994) 664
Weiss, D., K. Richter, E. Vasiliadou and G. Lütjering, Magnetotransport in antidot arrays	305 (1994) 408
West, K.W., see Boebinger	305 (1994) 8
West, K.W., see Du	305 (1994) 18
West, K.W., see Heiman	305 (1994) 50
West, K.W., see Kane	305 (1994) 176
West, K.W., see Eisenstein	305 (1994) 393
West, K.W., see Ashoori	305 (1994) 558
Westerling, L.A., see Lenssen	305 (1994) 476
Westervelt, R.M., see Burnett	305 (1994) 208
Westervelt, R.M., see Marcus	305 (1994) 480
Westervelt, R.M., see Berry	305 (1994) 495
Wheeler, R.G., see Richter	305 (1994) 145



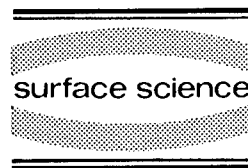
- White, J.D., see Ogawa 305 (1994) 659
- Whittaker, D.M., see Harrison 305 (1994) 353
- Whittaker, D.M., see Cockburn 305 (1994) 375
- Willcox, A.R.K., see Cockburn 305 (1994) 375
- Willett, R.L., Surface acoustic wave studies of electron correlations in the 2DES 305 (1994) 76
- Winkler, R. and U. Rössler, Multicomponent envelope function problems: the ultimate concept 305 (1994) 295
- Winkler, R.W., see Esslinger 305 (1994) 83
- Wisniewski, P., see Berthold 305 (1994) 637
- Wixforth, A., see Esslinger 305 (1994) 83
- Wixforth, A., Electronic excitations in parabolically confined electron systems 305 (1994) 194
- Wolter, J.H., see Van Haren 305 (1994) 172
- Wolter, J.H., see Lenssen 305 (1994) 476
- Wraback, M., H. Shen, J. Pamulapati, M. Dutta, P.G. Newman, M. Taysing-Lara and Y. Lu, Femtosecond studies of excitonic optical non-linearities in GaAs/Al<sub>x</sub>Ga<sub>1-x</sub>As multiple quantum wells under in-plane uniaxial strain 305 (1994) 238
- Wróbel, J., F. Kuchar, K. Ismail, K.Y. Lee, H. Nickel, W. Schlapp, G. Grabecki and T. Dietl, The influence of reduced dimensionality on the spin-splitting in GaAlAs/GaAs quantum wires 305 (1994) 615
- Wu, G.Y. and Y. Zhao, Magnetoplasmons and FIR response of an antidot array 305 (1994) 601
- Wu, X. and S.E. Ulloa, Electronic states and collective excitations of a two-dimensional electron gas in spatially modulated magnetic fields 305 (1994) 428
- Wyder, P., see Zeitler 305 (1994) 91
- Xie, X.C., S. Das Sarma and S. He, FIR spectroscopy of the intra-Landau level excitations of strongly correlated quantum dots 305 (1994) 606
- Xu, W., see Leadley 305 (1994) 327
- Yang, F., see Song 305 (1994) 139
- Yang, M.J., R.J. Wagner, P.J. Lin-Chung, B.V. Shanabrook, J.R. Waterman, W.J. Moore and J.L. Davis, Spin-resolved cyclotron resonance in a 2D electron gas 305 (1994) 271
- Ying, X., see Suen 305 (1994) 13
- Yoo, K.H., see Choi 305 (1994) 285
- Yosefin, M., see Simpson 305 (1994) 453
- Yosefin, M., see Khmelnitskii 305 (1994) 507
- Yuen, W.T., see Le 305 (1994) 337
- Yuh, E.L. and E.G. Gwinn, Transition from 2D to 3D collective response: surface sensitivity 305 (1994) 202
- Zachau, M., see Kash 305 (1994) 251
- Zailer, I., see Simpson 305 (1994) 453
- Zaslavsky, A., D.A. Grützmacher, S.Y. Lin, T.P. Smith III and T.O. Sedgwick, Valence band Landau level mixing and anisotropy in Si<sub>1-x</sub>Ge<sub>x</sub> investigated by resonant magnetotunneling 305 (1994) 307
- Zawadski, P., see Taylor 305 (1994) 648
- Zawadzki, P., see Sachrajda 305 (1994) 527
- Zeitler, U., R. Fletcher, J.C. Maan, C.T. Foxon, J.J. Harris and P. Wyder, Thermoelectric properties of GaAs/Ga<sub>1-x</sub>Al<sub>x</sub>As heterojunctions in the fractional quantum Hall regime 305 (1994) 91
- Zhao, Y., see Wu 305 (1994) 601
- Zheng, H., see Song 305 (1994) 139
- Zheng, L. and A.H. MacDonald, High temperature perturbation study of two-dimensional interacting electrons in a partly-filled Landau level 305 (1994) 101

- Zhu, X., see Price 305 (1994) 126  
Zinov'ev, N.N., see Eyles 305 (1994) 87  
Zinov'ev, N.N., R. Fletcher, L.J. Challis, B. Sujak-Cyrul, A.V. Akimov and A.F. Jezierski, Far infrared emission from magnetically quantised 2DEGs in GaAs/(AlGa)As heretojunctions 305 (1994) 280



ELSEVIER

Surface Science 305 (1994) 694–709



## Subject index

### *Band structure*

- J.A. Kash, M. Zachau, M.A. Tischler and U. Ekenberg, Optical measurements of warped valence bands in quantum wells 305 (1994) 251
- J.B. Choi, J.R. Meyer, C.A. Hoffman, G. Karczewski, J.K. Furdyna, K.H. Yoo and J.P. Faurie, Reflectivity, transport and magneto-optical studies of holes in the p-type HgZnTe/CdTe superlattice 305 (1994) 285
- R. Winkler and U. Rössler, Multicomponent envelope function problems: the ultimate concept 305 (1994) 295

### *Cadmium telluride*

- K. Kheng, R.T. Cox, Y. Merle d'Aubigné, M. Mamor, N. Magnea, H. Mariette, K. Saminadayar and S. Tatarenko, Negatively charged excitons  $X^-$  in the electron gas in CdTe/Cd<sub>1-x</sub>Zn<sub>x</sub>Te quantum wells 305 (1994) 225
- J.B. Choi, J.R. Meyer, C.A. Hoffman, G. Karczewski, J.K. Furdyna, K.H. Yoo and J.P. Faurie, Reflectivity, transport and magneto-optical studies of holes in the p-type HgZnTe/CdTe superlattice 305 (1994) 285

### *Chalcogens*

- J.B. Choi, J.R. Meyer, C.A. Hoffman, G. Karczewski, J.K. Furdyna, K.H. Yoo and J.P. Faurie, Reflectivity, transport and magneto-optical studies of holes in the p-type HgZnTe/CdTe superlattice 305 (1994) 285

### *Conductivity*

- R.L. Willett, Surface acoustic wave studies of electron correlations in the 2DES 305 (1994) 76
- V.T. Dolgoplov, G.V. Kravchenko, S.V. Kravchenko and A.A. Shashkin, Wigner solid in two-dimensional electron system in silicon in the extreme quantum limit? 305 (1994) 96
- M. D'Iorio, V.M. Pudalov, S.V. Kravchenko and J.W. Campbell, Collective insulating state at zero magnetic field in a dilute 2D electron system 305 (1994) 115
- S.J. Klepper, J.S. Brooks, G.J. Athas, X. Chen, M. Tokumoto, N. Kinoshita and Y. Tanaka, Magnetic ordering and Fermi surface effects in the low-dimensional organic conductor  $\alpha$ -(BEDT-TTF)<sub>2</sub>RbHg(SCN)<sub>4</sub> 305 (1994) 181
- M. Doporto, J. Caulfield, S. Hill, J. Singleton, F.L. Pratt, M. Kurmoo, P.J.T. Hendriks, J.A.A.J. Perenboom, W. Hayes and P. Day, The influence of magnetic order in quasi-2D organic conductors 305 (1994) 187
- J.B. Choi, J.R. Meyer, C.A. Hoffman, G. Karczewski, J.K. Furdyna, K.H. Yoo and J.P. Faurie, Reflectivity, transport and magneto-optical studies of holes in the p-type HgZnTe/CdTe superlattice 305 (1994) 285

- T. Tsuchiya and T. Ando, Effect of electronic-state modulation on mobility in quantum wells 305 (1994) 312
- K. Ensslin, H. Baum, P.F. Hopkins and A.C. Gossard, Wave function modification via controlled potential perturbation 305 (1994) 317
- Y. Ohno, M. Tsuchiya, T. Matsusue, T. Noda and H. Sakaki, Non-uniform resonant coupling effect on 2D electron transport in  $\delta$ -doped double quantum well structures 305 (1994) 322
- T. Le, A.G. Norman, W.T. Yuen, L. Hart, I.T. Ferguson, J.J. Harris, C.C. Phillips and R.A. Stradling, Quantum transport in  $\text{InAs}_{1-x}\text{Sb}_x/\text{InSb}$  strained layer superlattices 305 (1994) 337
- A.B. Henriques and L.C.D. Gonçalves, Crossover from a two- to three-dimensional electronic structure in Si spike doped GaAs superlattices 305 (1994) 343
- C.J. Goodings, H. Mizuta, J.R.A. Cleaver and H. Ahmed, Electron confinement in variable-area resonant tunnelling diodes using in-plane implanted gates 305 (1994) 363
- W. Müller, H.T. Grahn, K. von Klitzing and K. Ploog, Resonant inter-Landau-level tunneling of electrons and holes in superlattices 305 (1994) 380
- B.J. Keay, P.S.S. Guimaraes, J.P. Kaminski, S.J. Allen, Jr., P.F. Hopkins, A.C. Gossard, L.T. Florez and J.P. Harbison, Superlattice transport in intense terahertz electric fields 305 (1994) 385
- J.S. Scott, J.P. Kaminski, S.J. Allen, D.H. Chow, M. Lui and T.Y. Liu, Terahertz response of resonant tunneling diodes 305 (1994) 389
- J.P. Eisenstein, L.N. Pfeiffer and K.W. West, Tunneling between highly correlated 2D electron systems 305 (1994) 393
- H.C. Tso, P. Vasilopoulos and F.M. Peeters, Coupled electron-hole transport: generalized random-phase approximation and density functional theory 305 (1994) 400
- Y. Katayama, D.C. Tsui, H.C. Manoharan and M. Shayegan, Observation of an abrupt double-to-single-layer transition in a double-quantum-well structure 305 (1994) 405
- D. Weiss, K. Richter, E. Vasiliadou and G. Lütjering, Magnetotransport in antidot arrays 305 (1994) 408
- A.K. Geim, S.J. Bending and I.V. Grigorieva, Scattering of ballistic electrons by magnetic flux tubes 305 (1994) 419
- L. Brey and H.A. Fertig, Resistivity and Hall resistance of a two-dimensional electron gas in the presence of magnetic flux tubes 305 (1994) 424
- G.M. Gusev, P. Basmaji, Z.D. Kvon, L.V. Litvin, Yu.V. Nastaushev and A.I. Toropov, Negative magnetoresistance and anomalous diffusion of two-dimensional electrons in a disordered array of antidots 305 (1994) 443
- P.T. Coleridge, R.P. Taylor, A.S. Sachrajda and J.A. Adams, Anti-collimation of ballistic electrons by a potential barrier 305 (1994) 448
- J.R. Gao, J.P. Heida, B.J. van Wees, T.M. Klapwijk, G. Borghs and C.T. Foxon, Superconductors coupled with a two-dimensional electron gas in GaAs/Al-GaAs and InAs/AlGaSb heterostructures 305 (1994) 470
- K.-M.H. Lenssen, L.A. Westerling, C.J.P.M. Harmans, J.E. Mooij, M.R. Leys, W. van der Vleuten and J.H. Wolter, Influence of gate voltage on the transport properties of superconductor/2DEG systems 305 (1994) 476
- C.M. Marcus, R.M. Westervelt, P.F. Hopkins and A.C. Gossard, Conductance fluctuations in a quantum dot in the tunneling regime: crossover from aperiodic to regular behavior 305 (1994) 480
- A.D. Stone and H. Bruus, Universal fluctuation effects in chaotic quantum dots 305 (1994) 490
- M.J. Berry, J.A. Katine, C.M. Marcus, R.M. Westervelt and A.C. Gossard, Weak localization and conductance fluctuations in a chaotic quantum dot 305 (1994) 495
- M.W. Keller, O. Millo, A. Mittal, D.E. Prober and R.N. Sacks, Magnetotransport in a chaotic scattering cavity with tunable electron density 305 (1994) 501

- D.E. Khmelnitskii and M. Yosefin, Conductance fluctuations of 2D electrons in a strong magnetic field 305 (1994) 507
- P.C. van Son, F.P. Milliken, E.E. Mendez and W.I. Wang, Low-temperature equilibrium vertical transport through a two-dimensional electron gas 305 (1994) 516
- B.W. Alphenaar, A.A.M. Staring, H. van Houten and C.T. Foxon, Coulomb blockade in the presence of adiabatically transmitted edge channels 305 (1994) 520
- A. Sachrajda, R.P. Taylor, C. Dharma-wardana, J.A. Adams, P. Zawadzki and P.T. Coleridge, Electron–electron interactions and the magnetoconductance of sub-micron quantum dots 305 (1994) 527
- T.M. Eiles, M.H. Devoret and J.M. Martinis, Coulomb blockade of Andreev reflection in the NSN single-electron transistor 305 (1994) 536
- J.J. Palacios, L. Martin-Moreno and C. Tejedor, Correlation effects on transport through few-electrons systems 305 (1994) 541
- S. Tarucha, T. Honda, T. Saku and Y. Tokura, Charging effects in small-area modulation-doped double-barrier heterostructures 305 (1994) 547
- C.G. Smith, M. Field, M. Pepper, D.A. Ritchie, J.E.F. Frost, G.A.C. Jones and D.G. Hasko, A non-invasive voltage probe to measure Coulomb charging 305 (1994) 553
- B. Meurer, D. Heitmann and K. Ploog, Quantum dots in tilted magnetic fields 305 (1994) 610
- J. Wróbel, F. Kuchar, K. Ismail, K.Y. Lee, H. Nickel, W. Schlapp, G. Grabecki and T. Dietl, The influence of reduced dimensionality on the spin-splitting in GaAlAs/GaAs quantum wires 305 (1994) 615
- G. Fasol, Y. Nagamune, J. Motohisa and H. Sakaki, Determination of the quantum wire potential and hot electron spectroscopy using point contacts 305 (1994) 620
- A.K. Geim, P.C. Main, C.V. Brown, R. Taboryski, H. Carmona, T.J. Foster, P.E. Lindelof and L. Eaves, Resonant tunnelling between edge states in mesoscopic wires 305 (1994) 624
- S.W. Hwang, D.C. Tsui and M. Shayegan, Gate tuned transition to the insulating phase of one-dimensional electrons in high magnetic fields 305 (1994) 629
- G. Berthold, J. Smoliner, E. Gornik, G. Böhm, G. Weimann, T. Suski, P. Wisniewski, C. Hamaguchi, N. Mori and H. Momose, Magnetophonon resonances in quantum wires 305 (1994) 637
- R. Cuscó, M.C. Holland, J.H. Davies, I.A. Larkin, E. Skuras, A.R. Long and S.P. Beaumont, Anharmonic periodic modulation in lateral surface superlattices 305 (1994) 643
- R.P. Taylor, Y. Feng, A.S. Sachrajda, J.A. Adams, M. Davies, P.T. Coleridge and P. Zawadzki, Fabrication and characterisation of multi-level lateral nano-devices 305 (1994) 648
- R.G. Mani, K. von Klitzing, E. Vasiliadou, P. Grambow and K. Ploog, Magneto-transport study of GaAs/AlGaAs quantum wires 305 (1994) 654
- K. Ogawa, R.J. Blaikie, J.D. White, J. Allam and H. Ahmed, Transport properties of dual quantum dots 305 (1994) 659
- J. Weis, R.J. Haug, K. von Klitzing and K. Ploog, Lateral transport through a single quantum dot with a magnetic field parallel to the current 305 (1994) 664
- Y. Takagaki and D.K. Ferry, Aharonov–Bohm conductance oscillation of an antidot 305 (1994) 669
- Cyclotron resonance studies*
- C.M. Engelhardt, E. Gornik, M. Besson, G. Böhm and G. Weimann, Occurrence of a bulk-like electron phase in the cyclotron resonance of GaAs inversion channels in the extreme quantum limit 305 (1994) 23
- J.G. Michels, S. Hill, R.J. Warburton, G.M. Summers, P. Gee, J. Singleton, R.J. Nicholas, C.T. Foxon and J.J. Harris, Cyclotron resonance to 100 mK of a GaAs heterojunction in the ultra-quantum limit 305 (1994) 33

- A. Wixforth, Electronic excitations in parabolically confined electron systems 305 (1994) 194  
 M.J. Yang, R.J. Wagner, P.J. Lin-Chung, B.V. Shanabrook, J.R. Waterman, W.J. Moore and J.L. Davis, Spin-resolved cyclotron resonance in a 2D electron gas 305 (1994) 271  
 J.-P. Cheng, V.P. Kesan, D.A. Grützmacher and T.O. Sedgwick, Cyclotron effective mass of holes in strained  $\text{Si}_{1-x}\text{Ge}_x/\text{Si}$  quantum well structures 305 (1994) 275  
 V.I. Fal'ko, Crossing of cyclotron and spin resonances in a 2D electron gas 305 (1994) 290

### *Deuterium*

- W.J. Li, J.L. Wang, B.D. McCombe, J.-P. Cheng and W. Schaff, Spectroscopy of quasi-2D  $\text{D}^-$  ions in the presence of excess electrons 305 (1994) 215  
 J.M. Shi, F.M. Peeters and J.T. Devreese, Transition energies of  $\text{D}^-$  centers in a superlattice 305 (1994) 220

### *Electron scattering*

- Y.B. Levinson, Metal/2DEG contact – a microscopic model 305 (1994) 465

### *Gallium antimonide*

- J.R. Gao, J.P. Heida, B.J. van Wees, T.M. Klapwijk, G. Borghs and C.T. Foxon, Superconductors coupled with a two-dimensional electron gas in GaAs/AlGaAs and InAs/AlGaSb heterostructures 305 (1994) 470  
 P.C. van Son, F.P. Milliken, E.E. Mendez and W.I. Wang, Low-temperature equilibrium vertical transport through a two-dimensional electron gas 305 (1994) 516

### *Gallium arsenide*

- G.S. Boebinger, S.Q. Murphy, J.P. Eisenstein, L.N. Pfeiffer, K.W. West and S. He, New collective quantum Hall states in double quantum wells 305 (1994) 8  
 Y.W. Suen, H.C. Manoharan, X. Ying, M.B. Santos and M. Shayegan, One-component to two-component transitions of fractional quantum Hall states in a wide quantum well 305 (1994) 13  
 R.R. Du, D.C. Tsui, H.L. Stormer, L.N. Pfeiffer and K.W. West, Experimental evidence for composite particles in the fractional quantum Hall effect 305 (1994) 18  
 C.M. Engelhardt, E. Gornik, M. Besson, G. Böhm and G. Weimann, Occurrence of a bulk-like electron phase in the cyclotron resonance of GaAs inversion channels in the extreme quantum limit 305 (1994) 23  
 J.G. Michels, S. Hill, R.J. Warburton, G.M. Summers, P. Gee, J. Singleton, R.J. Nicholas, C.T. Foxon and J.J. Harris, Cyclotron resonance to 100 mK of a GaAs heterojunction in the ultra-quantum limit 305 (1994) 33  
 S.A. Brown, A.G. Davies, A.C. Lindsay, R.B. Dunford, R.G. Clark, P.E. Simmonds, H.H. Voss, J.J. Harris and C.T. Foxon, Time-resolved magneto-photoluminescence measurements of the integer QHE, fractional QHE and extreme quantum limit 305 (1994) 42  
 D. Heiman, A. Pinczuk, M. Dahl, B.S. Dennis, L.N. Pfeiffer and K.W. West, Time-resolved photoluminescence in the fractional quantum Hall regime 305 (1994) 50  
 I.V. Kukushkin, R.J. Haug, K. von Klitzing, K. Eberl and K. Ploog, Time-resolved magnetoluminescence and Raman scattering measured in the regime of the fractional quantum Hall effect and of the Wigner solid 305 (1994) 55  
 I.N. Harris, H.D.M. Davies, R.A. Ford, J.F. Ryan, A.J. Turberfield, C.T. Foxon and J.J. Harris, Quasi-particle recombination and spatial ordering of 2D electrons in the extreme quantum limit 305 (1994) 61  
 U. Zeitler, R. Fletcher, J.C. Maan, C.T. Foxon, J.J. Harris and P. Wyder, Thermoelectric properties of GaAs/ $\text{Ga}_{1-x}\text{Al}_x\text{As}$  heterojunctions in the fractional quantum Hall regime 305 (1994) 91

- H.W. Jiang, I. Glozman, C.E. Johnson and S.T. Hannahs, Magnetic-field-induced transition from an Anderson insulator to a quantum Hall conductor 305 (1994) 120
- A. Song, H. Zheng, F. Yang and Y. Li, Direct determination of the density of states in two-dimensional systems by magnetocapacitances of biased double barrier structures 305 (1994) 139
- K.S.H. Dalton, M. van der Burgt, M. Lakrimi, R.J. Warburton, M.S. Daly, W. Lubczyński, R.W. Martin, D.M. Symons, D.J. Barnes, N. Miura, R.J. Nicholas, N.J. Mason and P.J. Walker, "Intrinsic" quantum Hall effect in InAs/Ga<sub>1-x</sub>In<sub>x</sub>Sb crossed gap heterostructures in high magnetic fields 305 (1994) 156
- S. Kawaji, K. Hirakawa, M. Nagata, T. Okamoto, T. Fukase and T. Goto, Magnetic field dependence of the device-width-dependent breakdown current in the quantum Hall effect 305 (1994) 161
- R.J.F. van Haren, F.A.P. Blom, W. de Lange and J.H. Wolter, Total suppression of the inter-edge-channel scattering in a GaAs/AlGaAs heterostructure 305 (1994) 172
- B.E. Kane, L.N. Pfeiffer and K.W. West, Junctions between coplanar 2D gases: a probe of boundary effects in the quantized Hall regime 305 (1994) 176
- A. Wixforth, Electronic excitations in parabolically confined electron systems 305 (1994) 194
- E.L. Yuh and E.G. Gwinn, Transition from 2D to 3D collective response: surface sensitivity 305 (1994) 202
- J.H. Burnett, H.M. Cheong, R.M. Westervelt, W. Paul, P.F. Hopkins, M. Sundaram and A.C. Gossard, Resonant inelastic light scattering in remotely doped wide parabolic GaAs/Al<sub>x</sub>Ga<sub>1-x</sub>As quantum wells in a magnetic field 305 (1994) 208
- W.J. Li, J.L. Wang, B.D. McCombe, J.-P. Cheng and W. Schaff, Spectroscopy of quasi-2D D<sup>-</sup> ions in the presence of excess electrons 305 (1994) 215
- J.M. Shi, F.M. Peeters and J.T. Devreese, Transition energies of D<sup>-</sup> centers in a superlattice 305 (1994) 220
- C.I. Harris, B. Monemar, P.O. Holtz, H. Kalt, M. Sundaram, J.L. Merz and A.C. Gossard, Exciton-capture mechanism at impurities in GaAs/Al<sub>x</sub>Ga<sub>(1-x)</sub>As quantum wells 305 (1994) 230
- S. Bar-Ad, I. Bar-Joseph, Y. Levinson and H. Shtrikman, Time-resolved four wave mixing studies of a two-dimensional electron gas in a magnetic field 305 (1994) 234
- M. Wraback, H. Shen, J. Pamulapati, M. Dutta, P.G. Newman, M. Taysing-Lara and Y. Lu, Femtosecond studies of excitonic optical non-linearities in GaAs/Al<sub>x</sub>Ga<sub>1-x</sub>As multiple quantum wells under in-plane uniaxial strain 305 (1994) 238
- W.J. Walecki, D. Some, V.G. Kozlov and A.V. Nurmikko, Terahertz electromagnetic transients as probes of a two-dimensional electron gas 305 (1994) 243
- B. Jusserand, D. Richards, H. Peric and B. Etienne, Raman scattering on modulation-doped quantum wells: intrinsic spin splitting of the GaAs conduction band 305 (1994) 247
- J.A. Kash, M. Zachau, M.A. Tischler and U. Ekenberg, Optical measurements of warped valence bands in quantum wells 305 (1994) 251
- Ph. Roussignol, R. Ferreira, C. Delalande, G. Bastard, A. Vinattieri, J. Martinez-Pastor, L. Carraresi, M. Colocci, J.F. Palmier and B. Etienne, Hole spin relaxation in a n-doped quantum well structure 305 (1994) 263
- N.N. Zinov'ev, R. Fletcher, L.J. Challis, B. Sujak-Cyrul, A.V. Akimov and A.F. Jezierski, Far infrared emission from magnetically quantised 2DEGs in GaAs/(AlGa)As heterojunctions 305 (1994) 280
- K. Ensslin, H. Baum, P.F. Hopkins and A.C. Gossard, Wave function modification via controlled potential perturbation 305 (1994) 317
- Y. Ohno, M. Tsuchiya, T. Matsusue, T. Noda and H. Sakaki, Non-uniform resonant coupling effect on 2D electron transport in  $\delta$ -doped double quantum well structures 305 (1994) 322

- D.R. Leadley, R.J. Nicholas, J. Singleton, W. Xu, F.M. Peeters, J.T. Devreese, L. van Bockstal, F. Herlach, J.A.A.J. Perenboom, J.J. Harris and C.T. Foxon, Disappearance of magnetophonon resonance at high magnetic fields in GaAs/GaAlAs heterojunctions 305 (1994) 327
- G. Goldoni and A. Fasolino, Current induced “spin” separation in p-doped asymmetric double quantum wells 305 (1994) 333
- A.B. Henriques and L.C.D. Gonçalves, Crossover from a two- to three-dimensional electronic structure in Si spike doped GaAs superlattices 305 (1994) 343
- J.J. Heremans, M.B. Santos and M. Shayegan, Transverse magnetic focusing and the dispersion of GaAs 2D holes at (311)A heterojunctions 305 (1994) 348
- P.A. Harrison, L. Eaves, P.M. Martin, M. Henini, P.D. Buckle, M.S. Skolnick, D.M. Whittaker and G. Hill, Intrinsic bistability in the electroluminescence spectrum and current–voltage characteristics of triple-barrier p–i–n resonant tunneling devices 305 (1994) 353
- H. Kurata and H. Sakaki, Electron transport via resonantly coupled energy levels in triple barrier structure investigated by magnetotunneling spectroscopy 305 (1994) 369
- J.W. Cockburn, R.J. Teissier, M.S. Skolnick, P.D. Buckle, D.M. Whittaker, A.R.K. Willcox, G.W. Smith, G. Hill and M.A. Pate, Optical spectroscopy of inverted electron populations in double-barrier resonant-tunnelling structures 305 (1994) 375
- W. Müller, H.T. Grahn, K. von Klitzing and K. Ploog, Resonant inter-Landau-level tunneling of electrons and holes in superlattices 305 (1994) 380
- B.J. Keay, P.S.S. Guimaraes, J.P. Kaminski, S.J. Allen, Jr., P.F. Hopkins, A.C. Gossard, L.T. Florez and J.P. Harbison, Superlattice transport in intense terahertz electric fields 305 (1994) 385
- J.S. Scott, J.P. Kaminski, S.J. Allen, D.H. Chow, M. Lui and T.Y. Liu, Terahertz response of resonant tunneling diodes 305 (1994) 389
- J.P. Eisenstein, L.N. Pfeiffer and K.W. West, Tunneling between highly correlated 2D electron systems 305 (1994) 393
- Y. Katayama, D.C. Tsui, H.C. Manoharan and M. Shayegan, Observation of an abrupt double-to-single-layer transition in a double-quantum-well structure 305 (1994) 405
- D. Weiss, K. Richter, E. Vasiliadou and G. Lütjering, Magnetotransport in antidot arrays 305 (1994) 408
- G.M. Gusev, P. Basmaji, Z.D. Kvon, L.V. Litvin, Yu.V. Nastaushev and A.I. Toropov, Negative magnetoresistance and anomalous diffusion of two-dimensional electrons in a disordered array of antidots 305 (1994) 443
- T. Schäpers, F. Müller, A. Förster, B. Lengeler and H. Lüth, Control of ballistic electrons in (AlGa)As/GaAs heterostructures by means of superconducting niobium gate structures 305 (1994) 460
- J.R. Gao, J.P. Heida, B.J. van Wees, T.M. Klapwijk, G. Borghs and C.T. Foxon, Superconductors coupled with a two-dimensional electron gas in GaAs/AlGaAs and InAs/AlGaSb heterostructures 305 (1994) 470
- K.-M.H. Lenssen, L.A. Westerling, C.J.P.M. Harmans, J.E. Mooij, M.R. Leys, W. van der Vleuten and J.H. Wolter, Influence of gate voltage on the transport properties of superconductor/2DEG systems 305 (1994) 476
- C.M. Marcus, R.M. Westervelt, P.F. Hopkins and A.C. Gossard, Conductance fluctuations in a quantum dot in the tunneling regime: crossover from aperiodic to regular behavior 305 (1994) 480
- M.J. Berry, J.A. Katine, C.M. Marcus, R.M. Westervelt and A.C. Gossard, Weak localization and conductance fluctuations in a chaotic quantum dot 305 (1994) 495
- M.W. Keller, O. Millo, A. Mittal, D.E. Prober and R.N. Sacks, Magnetotransport in a chaotic scattering cavity with tunable electron density 305 (1994) 501



- B.W. Alphenaar, A.A.M. Staring, H. van Houten and C.T. Foxon, Coulomb blockade in the presence of adiabatically transmitted edge channels 305 (1994) 520
- A. Sachrajda, R.P. Taylor, C. Dharma-wardana, J.A. Adams, P. Zawadzki and P.T. Coleridge, Electron–electron interactions and the magnetoconductance of sub-micron quantum dots 305 (1994) 527
- C.G. Smith, M. Field, M. Pepper, D.A. Ritchie, J.E.F. Frost, G.A.C. Jones and D.G. Hasko, A non-evasive voltage probe to measure Coulomb charging 305 (1994) 553
- B. Su, V.J. Goldman and J.E. Cunningham, Evidence for spin singlet–triplet transitions of two electrons in a quantum dot observed via single-electron tunneling 305 (1994) 566
- M. Stopa, Y. Aoyagi and T. Sugano, Coulomb oscillation amplitude enhancement and envelope modulation in a magnetic field and activated tunneling 305 (1994) 571
- A.S. Plaut, K. Kash, E. Kapon, D.M. Hwang and E. Colas, Magneto-optics of quantum wires grown on V-grooved substrates 305 (1994) 576
- M. Fritze, A.V. Nurmikko and P. Hawrylak, Fermi-edge singularities in InGaAs and GaAs quantum wires 305 (1994) 580
- P.D. Wang, C.M. Sotomayor Torres, H. McLelland, S. Thoms, M. Holland and C.R. Stanley, Photoluminescence intensity and multiple phonon Raman scattering in quantum dots: evidence of the bottleneck effect 305 (1994) 585
- F. Hirler, R. Strenz, R. Küchler, G. Abstreiter, G. Böhm and G. Weimann, Information on the confinement potential in GaAs/AlGaAs wires from magnetoluminescence experiments 305 (1994) 591
- G.Y. Wu and Y. Zhao, Magnetoplasmons and FIR response of an antidot array 305 (1994) 601
- B. Meurer, D. Heitmann and K. Ploog, Quantum dots in tilted magnetic fields 305 (1994) 610
- J. Wróbel, F. Kuchar, K. Ismail, K.Y. Lee, H. Nickel, W. Schlapp, G. Grabecki and T. Dietl, The influence of reduced dimensionality on the spin-splitting in GaAlAs/GaAs quantum wires 305 (1994) 615
- A.K. Geim, P.C. Main, C.V. Brown, R. Taboryski, H. Carmona, T.J. Foster, P.E. Lindelof and L. Eaves, Resonant tunnelling between edge states in mesoscopic wires 305 (1994) 624
- S.W. Hwang, D.C. Tsui and M. Shayegan, Gate tuned transition to the insulating phase of one-dimensional electrons in high magnetic fields 305 (1994) 629
- R.P. Taylor, Y. Feng, A.S. Sachrajda, J.A. Adams, M. Davies, P.T. Coleridge and P. Zawadzki, Fabrication and characterisation of multi-level lateral nano-devices 305 (1994) 648
- R.G. Mani, K. von Klitzing, E. Vasiliadou, P. Grambow and K. Ploog, Magneto-transport study of GaAs/AlGaAs quantum wires 305 (1994) 654
- K. Ogawa, R.J. Blaikie, J.D. White, J. Allam and H. Ahmed, Transport properties of dual quantum dots 305 (1994) 659
- J. Weis, R.J. Haug, K. von Klitzing and K. Ploog, Lateral transport through a single quantum dot with a magnetic field parallel to the current 305 (1994) 664

### Germanium

- J.-P. Cheng, V.P. Kesan, D.A. Grützmacher and T.O. Sedgwick, Cyclotron effective mass of holes in strained  $\text{Si}_{1-x}\text{Ge}_x/\text{Si}$  quantum well structures 305 (1994) 275
- F.F. Fang, 2DEG in strained Si/SiGe heterostructures 305 (1994) 301
- A. Zaslavsky, D.A. Grützmacher, S.Y. Lin, T.P. Smith III and T.O. Sedgwick, Valence band Landau level mixing and anisotropy in  $\text{Si}_{1-x}\text{Ge}_x$  investigated by resonant magnetotunneling 305 (1994) 307

*Hall effect*

- B.I. Halperin, Theories for  $\nu = 1/2$  in single- and double-layer systems 305 (1994) 1
- G.S. Boebinger, S.Q. Murphy, J.P. Eisenstein, L.N. Pfeiffer, K.W. West and S. He, New collective quantum Hall states in double quantum wells 305 (1994) 8
- Y.W. Suen, H.C. Manoharan, X. Ying, M.B. Santos and M. Shayegan, One-component to two-component transitions of fractional quantum Hall states in a wide quantum well 305 (1994) 13
- R.R. Du, D.C. Tsui, H.L. Stormer, L.N. Pfeiffer and K.W. West, Experimental evidence for composite particles in the fractional quantum Hall effect 305 (1994) 18
- S.A. Brown, A.G. Davies, A.C. Lindsay, R.B. Dunford, R.G. Clark, P.E. Simmonds, H.H. Voss, J.J. Harris and C.T. Foxon, Time-resolved magneto-photoluminescence measurements of the integer QHE, fractional QHE and extreme quantum limit 305 (1994) 42
- D. Heiman, A. Pinczuk, M. Dahl, B.S. Dennis, L.N. Pfeiffer and K.W. West, Time-resolved photoluminescence in the fractional quantum Hall regime 305 (1994) 50
- X.M. Chen and J.J. Quinn, Numerical studies of the photoluminescence spectrum of quantum Hall systems 305 (1994) 71
- A. Esslinger, R.W. Winkler, C. Rocke, A. Wixforth, J.P. Kotthaus, H. Nickel, W. Schlapp and R. Lösch, Ultrasonic approach to the integer and fractional quantum Hall effect 305 (1994) 83
- R.H. Eyles, C.J. Mellor, A.J. Kent, K.A. Benedict, L.J. Challis, S. Kravchenko, N.N. Zinov'ev and M. Henini, Phonon measurements of the energy gap in the fractional quantum Hall state 305 (1994) 87
- U. Zeitler, R. Fletcher, J.C. Maan, C.T. Foxon, J.J. Harris and P. Wyder, Thermoelectric properties of GaAs/Ga<sub>1-x</sub>Al<sub>x</sub>As heterojunctions in the fractional quantum Hall regime 305 (1994) 91
- L. Zheng and A.H. MacDonald, High temperature perturbation study of two-dimensional interacting electrons in a partly-filled Landau level 305 (1994) 101
- V.M. Pudalov, M. D'Iorio and J.W. Campbell, Termination of the quantized Hall effect by the electron solid 305 (1994) 107
- H.W. Jiang, I. Glozman, C.E. Johnson and S.T. Hannahs, Magnetic-field-induced transition from an Anderson insulator to a quantum Hall conductor 305 (1994) 120
- L.W. Engel, D. Shahar, Ç. Kurdak and D.C. Tsui, Observation of finite-frequency scaling in the integer quantum Hall effect 305 (1994) 124
- R. Price, P.M. Platzman, S. He and X. Zhu, Quantum Hall liquid–Wigner solid phase boundary 305 (1994) 126
- D.B. Chklovskii and P.A. Lee, Transport properties between quantum Hall plateaus 305 (1994) 133
- C.A. Richter, R.G. Wheeler and R.N. Sacks, Transitions between edge and bulk channels in the quantum Hall regime 305 (1994) 145
- D.G. Polyakov and B.I. Shklovskii, Conductivity peaks in the quantum Hall regime: broadening with temperature, current, and frequency 305 (1994) 151
- K.S.H. Dalton, M. van der Burgt, M. Lakrimi, R.J. Warburton, M.S. Daly, W. Lubczyński, R.W. Martin, D.M. Symons, D.J. Barnes, N. Miura, R.J. Nicholas, N.J. Mason and P.J. Walker, “Intrinsic” quantum Hall effect in InAs/Ga<sub>1-x</sub>In<sub>x</sub>Sb crossed gap heterostructures in high magnetic fields 305 (1994) 156
- S. Kawaji, K. Hirakawa, M. Nagata, T. Okamoto, T. Fukase and T. Goto, Magnetic field dependence of the device-width-dependent breakdown current in the quantum Hall effect 305 (1994) 161
- B.Y. Gelfand, J. Dempsey and B.I. Halperin, Effects of electron–electron interactions on the ground state of quantum Hall edge states 305 (1994) 166
- R.J.F. van Haren, F.A.P. Blom, W. de Lange and J.H. Wolter, Total suppression of the inter-edge-channel scattering in a GaAs/AlGaAs heterostructure 305 (1994) 172

- B.E. Kane, L.N. Pfeiffer and K.W. West, Junctions between coplanar 2D gases: a probe of boundary effects in the quantized Hall regime 305 (1994) 176
- F.F. Fang, 2DEG in strained Si/SiGe heterostructures 305 (1994) 301
- L. Brey and H.A. Fertig, Resistivity and Hall resistance of a two-dimensional electron gas in the presence of magnetic flux tubes 305 (1994) 424
- B. Huckestein and R.N. Bhatt, Influence of a periodic potential on the integer quantum Hall effect 305 (1994) 438
- P.J. Simpson, C.J.B. Ford, D.R. Mace, I. Zailer, M. Yosefin, M. Pepper, J.T. Nicholls, D.A. Ritchie, J.E.F. Frost, M.P. Grimshaw and G.A.C. Jones, Charge oscillations in edge states and double-frequency Aharonov–Bohm effects around a tunable obstacle 305 (1994) 453
- D.E. Khmelnitskii and M. Yosefin, Conductance fluctuations of 2D electrons in a strong magnetic field 305 (1994) 507
- P.J.M. Peters, P. Scheuzger, M.J. Lea, W.P.N.M. Jacobs and R.W. van der Heijden, The AC Hall effect for electrons on liquid helium in ultra-high magnetic fields 305 (1994) 674

### *Heterostructures*

- S. Tarucha, T. Honda, T. Saku and Y. Tokura, Charging effects in small-area modulation-doped double-barrier heterostructures 305 (1994) 547

### *Indium antimonide*

- T. Le, A.G. Norman, W.T. Yuen, L. Hart, I.T. Ferguson, J.J. Harris, C.C. Phillips and R.A. Stradling, Quantum transport in  $\text{InAs}_{1-x}\text{Sb}_x/\text{InSb}$  strained layer superlattices 305 (1994) 337

### *Indium arsenide*

- K.S.H. Dalton, M. van der Burgt, M. Lakrimi, R.J. Warburton, M.S. Daly, W. Lubczyński, R.W. Martin, D.M. Symons, D.J. Barnes, N. Miura, R.J. Nicholas, N.J. Mason and P.J. Walker, “Intrinsic” quantum Hall effect in  $\text{InAs}/\text{Ga}_{1-x}\text{In}_x\text{Sb}$  crossed gap heterostructures in high magnetic fields 305 (1994) 156
- M.J. Yang, R.J. Wagner, P.J. Lin-Chung, B.V. Shanabrook, J.R. Waterman, W.J. Moore and J.L. Davis, Spin-resolved cyclotron resonance in a 2D electron gas 305 (1994) 271
- J.S. Scott, J.P. Kaminski, S.J. Allen, D.H. Chow, M. Lui and T.Y. Liu, Terahertz response of resonant tunneling diodes 305 (1994) 389
- J.R. Gao, J.P. Heida, B.J. van Wees, T.M. Klapwijk, G. Borghs and C.T. Foxon, Superconductors coupled with a two-dimensional electron gas in  $\text{GaAs}/\text{Al-GaAs}$  and  $\text{InAs}/\text{AlGaSb}$  heterostructures 305 (1994) 470
- P.C. van Son, F.P. Milliken, E.E. Mendez and W.I. Wang, Low-temperature equilibrium vertical transport through a two-dimensional electron gas 305 (1994) 516

### *Infrared spectroscopy*

- W.J. Li, J.L. Wang, B.D. McCombe, J.-P. Cheng and W. Schaff, Spectroscopy of quasi-2D  $\text{D}^-$  ions in the presence of excess electrons 305 (1994) 215
- J.-P. Cheng, V.P. Kesan, D.A. Grützmacher and T.O. Sedgwick, Cyclotron effective mass of holes in strained  $\text{Si}_{1-x}\text{Ge}_x/\text{Si}$  quantum well structures 305 (1994) 275
- X.C. Xie, S. Das Sarma and S. He, FIR spectroscopy of the intra-Landau level excitations of strongly correlated quantum dots 305 (1994) 606
- B. Meurer, D. Heitmann and K. Ploog, Quantum dots in tilted magnetic fields 305 (1994) 610

*Light scattering*

- J.H. Burnett, H.M. Cheong, R.M. Westervelt, W. Paul, P.F. Hopkins, M. Sundaram and A.C. Gossard, Resonant inelastic light scattering in remotely doped wide parabolic GaAs/ $\text{Al}_x\text{Ga}_{1-x}$ As quantum wells in a magnetic field 305 (1994) 208

*Luminescence*

- S.A. Brown, A.G. Davies, A.C. Lindsay, R.B. Dunford, R.G. Clark, P.E. Simmonds, H.H. Voss, J.J. Harris and C.T. Foxon, Time-resolved magneto-photoluminescence measurements of the integer QHE, fractional QHE and extreme quantum limit 305 (1994) 42
- D. Heiman, A. Pinczuk, M. Dahl, B.S. Dennis, L.N. Pfeiffer and K.W. West, Time-resolved photoluminescence in the fractional quantum Hall regime 305 (1994) 50
- I.V. Kukushkin, R.J. Haug, K. von Klitzing, K. Eberl and K. Ploog, Time-resolved magnetoluminescence and Raman scattering measured in the regime of the fractional quantum Hall effect and of the Wigner solid 305 (1994) 55
- I.N. Harris, H.D.M. Davies, R.A. Ford, J.F. Ryan, A.J. Turberfield, C.T. Foxon and J.J. Harris, Quasi-particle recombination and spatial ordering of 2D electrons in the extreme quantum limit 305 (1994) 61
- H.A. Fertig, D.Z. Liu and S. Das Sarma, Photoluminescence and the Wigner crystal: can you see it? 305 (1994) 67
- X.M. Chen and J.J. Quinn, Numerical studies of the photoluminescence spectrum of quantum Hall systems 305 (1994) 71
- A. Wixforth, Electronic excitations in parabolically confined electron systems 305 (1994) 194
- C.I. Harris, B. Monemar, P.O. Holtz, H. Kalt, M. Sundaram, J.L. Merz and A.C. Gossard, Exciton-capture mechanism at impurities in GaAs/ $\text{Al}_x\text{Ga}_{(1-x)}$ As quantum wells 305 (1994) 230
- M.Z. Maialle and L.J. Sham, Exciton spin dynamics and polarized luminescence in quantum wells 305 (1994) 256
- Ph. Roussignol, R. Ferreira, C. Delalande, G. Bastard, A. Vinattieri, J. Martinez-Pastor, L. Carraresi, M. Colocci, J.F. Palmier and B. Etienne, Hole spin relaxation in a n-doped quantum well structure 305 (1994) 263
- N.N. Zinov'ev, R. Fletcher, L.J. Challis, B. Sujak-Cyrul, A.V. Akimov and A.F. Jezierski, Far infrared emission from magnetically quantised 2DEGs in GaAs/(AlGa)As heterojunctions 305 (1994) 280
- P.A. Harrison, L. Eaves, P.M. Martin, M. Henini, P.D. Buckle, M.S. Skolnick, D.M. Whittaker and G. Hill, Intrinsic bistability in the electroluminescence spectrum and current-voltage characteristics of triple-barrier p-i-n resonant tunneling devices 305 (1994) 353
- J.W. Cockburn, R.J. Teissier, M.S. Skolnick, P.D. Buckle, D.M. Whittaker, A.R.K. Willcox, G.W. Smith, G. Hill and M.A. Pate, Optical spectroscopy of inverted electron populations in double-barrier resonant-tunnelling structures 305 (1994) 375
- A.S. Plaut, K. Kash, E. Kapon, D.M. Hwang and E. Colas, Magneto-optics of quantum wires grown on V-grooved substrates 305 (1994) 576
- M. Fritze, A.V. Nurmikko and P. Hawrylak, Fermi-edge singularities in InGaAs and GaAs quantum wires 305 (1994) 580
- P.D. Wang, C.M. Sotomayor Torres, H. McLelland, S. Thoms, M. Holland and C.R. Stanley, Photoluminescence intensity and multiple phonon Raman scattering in quantum dots: evidence of the bottleneck effect 305 (1994) 585
- F. Hirler, R. Strenz, R. Küchler, G. Abstreiter, G. Böhm and G. Weimann, Information on the confinement potential in GaAs/AlGaAs wires from magnetoluminescence experiments 305 (1994) 591

*Magnetic measurements*

- I.V. Kukushkin, R.J. Haug, K. von Klitzing, K. Eberl and K. Ploog, Time-resolved magnetoluminescence and Raman scattering measured in the regime of the fractional quantum Hall effect and of the Wigner solid 305 (1994) 55
- H.A. Fertig, D.Z. Liu and S. Das Sarma, Photoluminescence and the Wigner crystal: can you see it? 305 (1994) 67
- R.L. Willett, Surface acoustic wave studies of electron correlations in the 2DES 305 (1994) 76
- V.T. Dolgoplov, G.V. Kravchenko, S.V. Kravchenko and A.A. Shashkin, Wigner solid in two-dimensional electron system in silicon in the extreme quantum limit? 305 (1994) 96
- A. Song, H. Zheng, F. Yang and Y. Li, Direct determination of the density of states in two-dimensional systems by magnetocapacitances of biased double barrier structures 305 (1994) 139
- S.J. Klepper, J.S. Brooks, G.J. Athas, X. Chen, M. Tokumoto, N. Kinoshita and Y. Tanaka, Magnetic ordering and Fermi surface effects in the low-dimensional organic conductor  $\alpha$ -(BEDT-TTF)<sub>2</sub>RbHg(SCN)<sub>4</sub> 305 (1994) 181
- M. Doporto, J. Caulfield, S. Hill, J. Singleton, F.L. Pratt, M. Kurmoo, P.J.T. Hendriks, J.A.A.J. Perenboom, W. Hayes and P. Day, The influence of magnetic order in quasi-2D organic conductors 305 (1994) 187
- J.H. Burnett, H.M. Cheong, R.M. Westervelt, W. Paul, P.F. Hopkins, M. Sundaram and A.C. Gossard, Resonant inelastic light scattering in remotely doped wide parabolic GaAs/Al<sub>x</sub>Ga<sub>1-x</sub>As quantum wells in a magnetic field 305 (1994) 208
- J.M. Shi, F.M. Peeters and J.T. Devreese, Transition energies of D<sup>-</sup> centers in a superlattice 305 (1994) 220
- K. Kheng, R.T. Cox, Y. Merle d'Aubigné, M. Mamor, N. Magnea, H. Mariette, K. Saminadayar and S. Tatarenko, Negatively charged excitons X<sup>-</sup> in the electron gas in CdTe/Cd<sub>1-x</sub>Zn<sub>x</sub>Te quantum wells 305 (1994) 225
- S. Bar-Ad, I. Bar-Joseph, Y. Levinson and H. Shtrikman, Time-resolved four wave mixing studies of a two-dimensional electron gas in a magnetic field 305 (1994) 234
- W.J. Walecki, D. Some, V.G. Kozlov and A.V. Nurmikko, Terahertz electromagnetic transients as probes of a two-dimensional electron gas 305 (1994) 243
- N.N. Zinov'ev, R. Fletcher, L.J. Challis, B. Sujak-Cyrul, A.V. Akimov and A.F. Jezierski, Far infrared emission from magnetically quantised 2DEGs in GaAs/(AlGa)As heterojunctions 305 (1994) 280
- J.B. Choi, J.R. Meyer, C.A. Hoffman, G. Karczewski, J.K. Furdyna, K.H. Yoo and J.P. Faurie, Reflectivity, transport and magneto-optical studies of holes in the p-type HgZnTe/CdTe superlattice 305 (1994) 285
- R. Winkler and U. Rössler, Multicomponent envelope function problems: the ultimate concept 305 (1994) 295
- A. Zaslavsky, D.A. Grützmacher, S.Y. Lin, T.P. Smith III and T.O. Sedgwick, Valence band Landau level mixing and anisotropy in Si<sub>1-x</sub>Ge<sub>x</sub> investigated by resonant magnetotunneling 305 (1994) 307
- K. Ensslin, H. Baum, P.F. Hopkins and A.C. Gossard, Wave function modification via controlled potential perturbation 305 (1994) 317
- Y. Ohno, M. Tsuchiya, T. Matsusue, T. Noda and H. Sakaki, Non-uniform resonant coupling effect on 2D electron transport in  $\delta$ -doped double quantum well structures 305 (1994) 322
- D.R. Leadley, R.J. Nicholas, J. Singleton, W. Xu, F.M. Peeters, J.T. Devreese, L. van Bockstal, F. Herlach, J.A.A.J. Perenboom, J.J. Harris and C.T. Foxon, Disappearance of magnetophonon resonance at high magnetic fields in GaAs/GaAlAs heterojunctions 305 (1994) 327

- T. Le, A.G. Norman, W.T. Yuen, L. Hart, I.T. Ferguson, J.J. Harris, C.C. Phillips and R.A. Stradling, Quantum transport in  $\text{InAs}_{1-x}\text{Sb}_x/\text{InSb}$  strained layer superlattices 305 (1994) 337
- A.B. Henriques and L.C.D. Gonçalves, Crossover from a two- to three-dimensional electronic structure in Si spike doped GaAs superlattices 305 (1994) 343
- J.J. Heremans, M.B. Santos and M. Shayegan, Transverse magnetic focusing and the dispersion of GaAs 2D holes at (311)A heterojunctions 305 (1994) 348
- P.A. Harrison, L. Eaves, P.M. Martin, M. Henini, P.D. Buckle, M.S. Skolnick, D.M. Whittaker and G. Hill, Intrinsic bistability in the electroluminescence spectrum and current-voltage characteristics of triple-barrier p-i-n resonant tunneling devices 305 (1994) 353
- G.E.W. Bauer, Excitonic correction to resonant tunneling 305 (1994) 358
- J.P. Eisenstein, L.N. Pfeiffer and K.W. West, Tunneling between highly correlated 2D electron systems 305 (1994) 393
- S. He, P.M. Platzman and B.I. Halperin, One-electron Green's function and electron tunneling in a two-dimensional electron system in a strong magnetic field 305 (1994) 398
- Y. Katayama, D.C. Tsui, H.C. Manoharan and M. Shayegan, Observation of an abrupt double-to-single-layer transition in a double-quantum-well structure 305 (1994) 405
- D. Weiss, K. Richter, E. Vasiliadou and G. Lütjering, Magnetotransport in antidot arrays 305 (1994) 408
- A.K. Geim, S.J. Bending and I.V. Grigorieva, Scattering of ballistic electrons by magnetic flux tubes 305 (1994) 419
- X. Wu and S.E. Ulloa, Electronic states and collective excitations of a two-dimensional electron gas in spatially modulated magnetic fields 305 (1994) 428
- G.M. Gusev, P. Basmaji, Z.D. Kvon, L.V. Litvin, Yu.V. Nastaushev and A.I. Toropov, Negative magnetoresistance and anomalous diffusion of two-dimensional electrons in a disordered array of antidots 305 (1994) 443
- P.T. Coleridge, R.P. Taylor, A.S. Sachrajda and J.A. Adams, Anti-collimation of ballistic electrons by a potential barrier 305 (1994) 448
- T. Schäpers, F. Müller, A. Förster, B. Lengeler and H. Lüth, Control of ballistic electrons in (AlGa)As/GaAs heterostructures by means of superconducting niobium gate structures 305 (1994) 460
- K.-M.H. Lenssen, L.A. Westerling, C.J.P.M. Harmans, J.E. Mooij, M.R. Leys, W. van der Vleuten and J.H. Wolter, Influence of gate voltage on the transport properties of superconductor/2DEG systems 305 (1994) 476
- C.M. Marcus, R.M. Westervelt, P.F. Hopkins and A.C. Gossard, Conductance fluctuations in a quantum dot in the tunneling regime: crossover from aperiodic to regular behavior 305 (1994) 480
- M.J. Berry, J.A. Katine, C.M. Marcus, R.M. Westervelt and A.C. Gossard, Weak localization and conductance fluctuations in a chaotic quantum dot 305 (1994) 495
- M.W. Keller, O. Millo, A. Mittal, D.E. Prober and R.N. Sacks, Magnetotransport in a chaotic scattering cavity with tunable electron density 305 (1994) 501
- T.M. Fromhold, M.L. Leadbeater, L. Eaves, T.J. Foster, P.C. Main and F.W. Sheard, Tunneling into classically chaotic orbits in quantum wells 305 (1994) 511
- P.C. van Son, F.P. Milliken, E.E. Mendez and W.I. Wang, Low-temperature equilibrium vertical transport through a two-dimensional electron gas 305 (1994) 516
- A. Sachrajda, R.P. Taylor, C. Dharma-wardana, J.A. Adams, P. Zawadzki and P.T. Coleridge, Electron-electron interactions and the magnetotransport of sub-micron quantum dots 305 (1994) 527
- J.J. Palacios, L. Martin-Moreno and C. Tejedor, Correlation effects on transport through few-electrons systems 305 (1994) 541

- R.C. Ashoori, H.L. Stormer, J.S. Weiner, L.N. Pfeiffer, K.W. Baldwin and K.W. West, Energy levels of an artificial atom probed with single-electron capacitance spectroscopy 305 (1994) 558
- B. Su, V.J. Goldman and J.E. Cunningham, Evidence for spin singlet–triplet transitions of two electrons in a quantum dot observed via single-electron tunneling 305 (1994) 566
- M. Stopa, Y. Aoyagi and T. Sugano, Coulomb oscillation amplitude enhancement and envelope modulation in a magnetic field and activated tunneling 305 (1994) 571
- A.S. Plaut, K. Kash, E. Kapon, D.M. Hwang and E. Colas, Magneto-optics of quantum wires grown on V-grooved substrates 305 (1994) 576
- M. Fritze, A.V. Nurmikko and P. Hawrylak, Fermi-edge singularities in InGaAs and GaAs quantum wires 305 (1994) 580
- F. Hirler, R. Strenz, R. Kuchler, G. Abstreiter, G. Böhm and G. Weimann, Information on the confinement potential in GaAs/AlGaAs wires from magnetoluminescence experiments 305 (1994) 591
- P. Hawrylak, Magneto-optics of interacting electrons in quantum dots 305 (1994) 597
- G.Y. Wu and Y. Zhao, Magnetoplasmons and FIR response of an antidot array 305 (1994) 601
- X.C. Xie, S. Das Sarma and S. He, FIR spectroscopy of the intra-Landau level excitations of strongly correlated quantum dots 305 (1994) 606
- B. Meurer, D. Heitmann and K. Ploog, Quantum dots in tilted magnetic fields 305 (1994) 610
- J. Wróbel, F. Kuchar, K. Ismail, K.Y. Lee, H. Nickel, W. Schlapp, G. Grabecki and T. Dietl, The influence of reduced dimensionality on the spin-splitting in GaAlAs/GaAs quantum wires 305 (1994) 615
- A.K. Geim, P.C. Main, C.V. Brown, R. Taboryski, H. Carmona, T.J. Foster, P.E. Lindelof and L. Eaves, Resonant tunnelling between edge states in mesoscopic wires 305 (1994) 624
- S.W. Hwang, D.C. Tsui and M. Shayegan, Gate tuned transition to the insulating phase of one-dimensional electrons in high magnetic fields 305 (1994) 629
- G. Berthold, J. Smoliner, E. Gornik, G. Böhm, G. Weimann, T. Suski, P. Wisniewski, C. Hamaguchi, N. Mori and H. Momose, Magnetophonon resonances in quantum wires 305 (1994) 637
- R.P. Taylor, Y. Feng, A.S. Sachrajda, J.A. Adams, M. Davies, P.T. Coleridge and P. Zawadzki, Fabrication and characterisation of multi-level lateral nano-devices 305 (1994) 648
- R.G. Mani, K. von Klitzing, E. Vasiliadou, P. Grambow and K. Ploog, Magneto-transport study of GaAs/AlGaAs quantum wires 305 (1994) 654
- J. Weis, R.J. Haug, K. von Klitzing and K. Ploog, Lateral transport through a single quantum dot with a magnetic field parallel to the current 305 (1994) 664
- Y. Takagaki and D.K. Ferry, Aharonov–Bohm conductance oscillation of an antidot 305 (1994) 669

### *Magnetic structures*

- A. Matulis, F.M. Peeters and P. Vasilopoulos, Two-dimensional tunneling through magnetic barriers 305 (1994) 434

### *Niobium*

- T. Schäpers, F. Müller, A. Förster, B. Lengeler and H. Lüth, Control of ballistic electrons in (AlGa)As/GaAs heterostructures by means of superconducting niobium gate structures 305 (1994) 460

*Noble gases*

- P.J.M. Peters, P. Scheuzger, M.J. Lea, W.P.N.M. Jacobs and R.W. van der Heijden, The AC Hall effect for electrons on liquid helium in ultra-high magnetic fields 305 (1994) 674

*Organic substances*

- S.J. Klepper, J.S. Brooks, G.J. Athas, X. Chen, M. Tokumoto, N. Kinoshita and Y. Tanaka, Magnetic ordering and Fermi surface effects in the low-dimensional organic conductor  $\alpha$ -(BEDT-TTF)<sub>2</sub>RbHg(SCN)<sub>4</sub> 305 (1994) 181
- M. Dopporto, J. Caulfield, S. Hill, J. Singleton, F.L. Pratt, M. Kurmoo, P.J.T. Hendriks, J.A.A.J. Perenboom, W. Hayes and P. Day, The influence of magnetic order in quasi-2D organic conductors 305 (1994) 187

*Photoconductivity*

- A.B. Henriques and L.C.D. Gonçalves, Crossover from a two- to three-dimensional electronic structure in Si spike doped GaAs superlattices 305 (1994) 343

*Raman scattering*

- I.V. Kukushkin, R.J. Haug, K. von Klitzing, K. Eberl and K. Ploog, Time-resolved magnetoluminescence and Raman scattering measured in the regime of the fractional quantum Hall effect and of the Wigner solid 305 (1994) 55
- B. Jusserand, D. Richards, H. Peric and B. Etienne, Raman scattering on modulation-doped quantum wells: intrinsic spin splitting of the GaAs conduction band 305 (1994) 247
- P.D. Wang, C.M. Sotomayor Torres, H. McLelland, S. Thoms, M. Holland and C.R. Stanley, Photoluminescence intensity and multiple phonon Raman scattering in quantum dots: evidence of the bottleneck effect 305 (1994) 585

*Reflection spectroscopy*

- J.B. Choi, J.R. Meyer, C.A. Hoffman, G. Karczewski, J.K. Furdyna, K.H. Yoo and J.P. Faurie, Reflectivity, transport and magneto-optical studies of holes in the p-type HgZnTe/CdTe superlattice 305 (1994) 285

*Silicon*

- V.T. Dolgoplov, G.V. Kravchenko, S.V. Kravchenko and A.A. Shashkin, Wigner solid in two-dimensional electron system in silicon in the extreme quantum limit? 305 (1994) 96
- V.M. Pudalov, M. D'Iorio and J.W. Campbell, Termination of the quantized Hall effect by the electron solid 305 (1994) 107
- M. D'Iorio, V.M. Pudalov, S.V. Kravchenko and J.W. Campbell, Collective insulating state at zero magnetic field in a dilute 2D electron system 305 (1994) 115
- J.-P. Cheng, V.P. Kesan, D.A. Grützmacher and T.O. Sedgwick, Cyclotron effective mass of holes in strained Si<sub>1-x</sub>Ge<sub>x</sub>/Si quantum well structures 305 (1994) 275
- F.F. Fang, 2DEG in strained Si/SiGe heterostructures 305 (1994) 301
- A. Zaslavsky, D.A. Grützmacher, S.Y. Lin, T.P. Smith III and T.O. Sedgwick, Valence band Landau level mixing and anisotropy in Si<sub>1-x</sub>Ge<sub>x</sub> investigated by resonant magnetotunneling 305 (1994) 307
- A.B. Henriques and L.C.D. Gonçalves, Crossover from a two- to three-dimensional electronic structure in Si spike doped GaAs superlattices 305 (1994) 343
- U. Kunze, T. Drebing, B. Klehn and J. Lindolf, Observation of 1D electron states at the boundary between an MOS and a Schottky contact on Si(100) by electron tunneling 305 (1994) 633



*Silicon oxide*

- U. Kunze, T. Drebing, B. Klehn and J. Lindolf, Observation of 1D electron states at the boundary between an MOS and a Schottky contact on Si(100) by electron tunneling 305 (1994) 633

*Superconductivity*

- T. Schäpers, F. Müller, A. Förster, B. Lengeler and H. Lüth, Control of ballistic electrons in (AlGa)As/GaAs heterostructures by means of superconducting niobium gate structures 305 (1994) 460
- K.-M.H. Lenssen, L.A. Westerling, C.J.P.M. Harmans, J.E. Mooij, M.R. Leys, W. van der Vleuten and J.H. Wolter, Influence of gate voltage on the transport properties of superconductor/2DEG systems 305 (1994) 476

*Superlattices*

- T. Le, A.G. Norman, W.T. Yuen, L. Hart, I.T. Ferguson, J.J. Harris, C.C. Phillips and R.A. Stradling, Quantum transport in  $\text{InAs}_{1-x}\text{Sb}_x/\text{InSb}$  strained layer superlattices 305 (1994) 337
- R. Cuscó, M.C. Holland, J.H. Davies, I.A. Larkin, E. Skuras, A.R. Long and S.P. Beaumont, Anharmonic periodic modulation in lateral surface superlattices 305 (1994) 643

*Surface phonons and adsorbate vibrations*

- W. Müller, H.T. Grahn, K. von Klitzing and K. Ploog, Resonant inter-Landau-level tunneling of electrons and holes in superlattices 305 (1994) 380

*Surface plasmons*

- A. Wixforth, Electronic excitations in parabolically confined electron systems 305 (1994) 194
- E.L. Yuh and E.G. Gwinn, Transition from 2D to 3D collective response: surface sensitivity 305 (1994) 202
- S. Rudin and T.L. Reinecke, Plasmons localized at point charges in semiconductor quantum wells 305 (1994) 267
- G.Y. Wu and Y. Zhao, Magnetoplasmons and FIR response of an antidot array 305 (1994) 601

*Tunneling*

- A. Zaslavsky, D.A. Grützmacher, S.Y. Lin, T.P. Smith III and T.O. Sedgwick, Valence band Landau level mixing and anisotropy in  $\text{Si}_{1-x}\text{Ge}_x$  investigated by resonant magnetotunneling 305 (1994) 307
- G. Goldoni and A. Fasolino, Current induced “spin” separation in p-doped asymmetric double quantum wells 305 (1994) 333
- G.E.W. Bauer, Excitonic correction to resonant tunneling 305 (1994) 358
- C.J. Goodings, H. Mizuta, J.R.A. Cleaver and H. Ahmed, Electron confinement in variable-area resonant tunnelling diodes using in-plane implanted gates 305 (1994) 363
- H. Kurata and H. Sakaki, Electron transport via resonantly coupled energy levels in triple barrier structure investigated by magnetotunneling spectroscopy 305 (1994) 369
- J.W. Cockburn, R.J. Teissier, M.S. Skolnick, P.D. Buckle, D.M. Whittaker, A.R.K. Willcox, G.W. Smith, G. Hill and M.A. Pate, Optical spectroscopy of inverted electron populations in double-barrier resonant-tunnelling structures 305 (1994) 375
- W. Müller, H.T. Grahn, K. von Klitzing and K. Ploog, Resonant inter-Landau-level tunneling of electrons and holes in superlattices 305 (1994) 380
- J.S. Scott, J.P. Kaminski, S.J. Allen, D.H. Chow, M. Lui and T.Y. Liu, Terahertz response of resonant tunneling diodes 305 (1994) 389

- J.P. Eisenstein, L.N. Pfeiffer and K.W. West, Tunneling between highly correlated 2D electron systems 305 (1994) 393
- S. He, P.M. Platzman and B.I. Halperin, One-electron Green's function and electron tunneling in a two-dimensional electron system in a strong magnetic field 305 (1994) 398
- A. Matulis, F.M. Peeters and P. Vasilopoulos, Two-dimensional tunneling through magnetic barriers 305 (1994) 434
- T.M. Fromhold, M.L. Leadbeater, L. Eaves, T.J. Foster, P.C. Main and F.W. Sheard, Tunneling into classically chaotic orbits in quantum wells 305 (1994) 511
- P.C. van Son, F.P. Milliken, E.E. Mendez and W.I. Wang, Low-temperature equilibrium vertical transport through a two-dimensional electron gas 305 (1994) 516
- T.M. Eiles, M.H. Devoret and J.M. Martinis, Coulomb blockade of Andreev reflection in the NSN single-electron transistor 305 (1994) 536
- J.J. Palacios, L. Martin-Moreno and C. Tejedor, Correlation effects on transport through few-electrons systems 305 (1994) 541
- R.C. Ashoori, H.L. Stormer, J.S. Weiner, L.N. Pfeiffer, K.W. Baldwin and K.W. West, Energy levels of an artificial atom probed with single-electron capacitance spectroscopy 305 (1994) 558
- B. Su, V.J. Goldman and J.E. Cunningham, Evidence for spin singlet–triplet transitions of two electrons in a quantum dot observed via single-electron tunneling 305 (1994) 566
- M. Stopa, Y. Aoyagi and T. Sugano, Coulomb oscillation amplitude enhancement and envelope modulation in a magnetic field and activated tunneling 305 (1994) 571
- A.K. Geim, P.C. Main, C.V. Brown, R. Taboryski, H. Carmona, T.J. Foster, P.E. Lindelof and L. Eaves, Resonant tunnelling between edge states in mesoscopic wires 305 (1994) 624
- U. Kunze, T. Drebingner, B. Klehn and J. Lindolf, Observation of 1D electron states at the boundary between an MOS and a Schottky contact on Si(100) by electron tunneling 305 (1994) 633